

RĒZEKNES TEHNOLOĢIJU AKADĒMIJA  
Inženieru fakultāte

REZEKNE ACADEMY OF TECHNOLOGIES  
Faculty of Engineering

# **VIDE. TEHNOLOĢIJA. RESURSI**

XIV starptautiskās zinātniski praktiskās konferences rakstu krājums  
2023.gada 15.-16.jūnijs

**3.SĒJUMS**

# **ENVIRONMENT. TECHNOLOGY. RESOURCES**

Proceedings of the 14<sup>th</sup> International Scientific and Practical Conference  
June 15<sup>th</sup> – 16<sup>th</sup>, 2023

**Volume III**

Rēzekne  
2023

**VIDE. TEHNOLOĢIJA. RESURSI.** 14. starptautiskās zinātniski praktiskās konferences rakstu krājums. 2023. gada 15.-16. jūnijs. 3.sējums. Rēzekne: Rēzeknes Tehnoloģiju akadēmija, 2023. 374 lpp.

**ENVIRONMENT. TECHNOLOGY. RESOURCES.** Proceedings of the 14<sup>th</sup> International Scientific and Practical Conference on June 15-16, 2023. *Volume III*, Rezekne: Rezekne Academy of Technologies, 2023. pp. 374.

Rekomendējusi publicēšanai Rēzeknes Tehnoloģiju akadēmijas Inženieru fakultātes Dome 2023. gada 09. maijā.  
*Recommended for publication by the Council of Faculty of Engineering of Rezekne Academy of Technologies on May, 09<sup>th</sup>, 2023.*



ERDF co-funded project “Funding of international projects in research and innovation at Rezekne Academy of Technologies” No. 1.1.1.5/18/I/012

14.starptautiskās zinātniski praktiskās konferences “Vide. Tehnoloģija. Resursi” rakstu krājumu trijos sējumos ir pārstāvēti jaunākie pēdējo divu gadu pētījumi vides inženierzinātnē, vides un dabas aizsardzībā, ilgtspējīgā lauksaimniecībā, enerģētikā, materiālzinātnē, mehānikā, metālapstrādē, lāzeru tehnoloģijās, matemātiskajā modelēšanā, elektrotehnikā, vides ekonomikā un vadībā, informācijas tehnoloģijās un sociotehnisko sistēmu modelēšanā, vides izglītībā un ilgtspējīgas attīstības procesos.

Krājumos pārstāvēto pētījumu joma ir daudzpusīga un starpdisciplināra, balstīta uz starptautisko zinātnieku kolektīvu sasniegumu rezultātiem. Konferences rakstu krājumos iekļauti 143 zinātniskie raksti.

Konferences dalībnieki pārstāv 17 valstis.

*Proceedings of the 14<sup>th</sup> International Scientific and Practical Conference “Environment. Technology. Resources” include studies of the last two years in fields of engineering, environmental and nature protection, sustainable agriculture, energy, material science, mechanics, metalworking, laser technologies, mathematical modelling, electrical engineering, environmental economics and management, information technologies and sociotechnical systems modelling, environmental education and sustainable development. The research area presented in the proceedings is comprehensive and cross disciplinary-based, on advances of international researchers. The proceedings comprise 143 scientific papers. Conference participants represent 17 countries.*

<https://conferences.rta.lv/index.php/ETR/ETR2023>

Link to conference proceedings: <http://journals.rta.lv/index.php/ETR>



This journal is licenced under  
[Creative Commons Attribution 4.0 International \(CC BY 4.0\) License](https://creativecommons.org/licenses/by/4.0/)  
The author of the paper takes responsibility for the content of the paper.

Print ISSN 1691-5402  
Online ISSN 2256-070X

Published by Rezekne Academy of Technologies, 2023

### ***Scientific Committee Chairman***

Dr.sc.ing. Edmunds Teirumnieks, Rezekne Academy of Technologies, Latvia

### ***Scientific Committee Co-Chairmen***

Dr. Walter Leal, Hamburg University of Applied Sciences, Germany, Manchester Metropolitan University, United Kingdom

Dr.sc.ing. Andris Martinovs, Rezekne Academy of Technologies, Latvia

Dr.sc.ing. Artis Teilāns, Rezekne Academy of Technologies, Latvia

### ***Scientific Committee***

Dr.agr. Aleksandrs Adamovičs, Latvia University of Life Sciences and Technologies, Latvia

PhD Nikolaj Angelov, Technical University of Gabrovo, Bulgaria

PhD Andres Annuk, Estonian University of Life Sciences, Estonia

Dr. Dragen Antic, University of Nis, Serbia

Dr. agr. Lidia Antypova, Mykolayiv National Agrarian University, Ukraine

PhD Iluta Arbidāne, Rezekne Academy of Technologies, Latvia

Dr.sc.ing. Anita Avišāne, Riga Technical University, Latvia

DSc. Hristo Ivanov Beloev, Angel Kanchev University of Ruse, Bulgaria

PhD Sholpan Bekmukhanbetova, Kazakh Automobile and Road Institute, Kazakhstan

PhD Plamen Bogdanov, "Vasil Levski" National Military University, Bulgaria

Dr. Rene Brunsch, Apromace data systems GmbH, Germany

PhD Basar Caglar, Izmir Institute of Technology, Turkey

Dr. hab. Ing. Tadeusz Chrzan, Poltegor Institute, Poland

PhD Lubomir Dimitrov, Tehnical University of Sofia, Bulgaria

PhD Nikolaj Dolchinkov, "Vasil Levski" National Military University, Bulgaria

Dr. agr. Daina Feldmane, Latvia University of Life Sciences and Technologies, Latvia

Dr.sc.ing. Aleksandrs Gorbunovs, Riga Technical University, Latvia

Dr.sc.ing. Pēteris Grabusts, Rezekne Academy of Technologies, Latvia

Dr. agr. Elvyra Gruzdevienė, Flax museum, the branch of Eriskiai Cultural Center of the Panevezys District, Lithuania

Mg. Mart Hovi, Estonian University of Life Sciences, Estonia

Dr.sc.ing. Aivars Kaķītis, Latvia University of Life Sciences and Technologies, Latvia

Dr.paed. Ilmārs Kangro, Rezekne Academy of Technology, Latvia

Dr. paed. Janis Kapenieks, Riga Technical University, Latvia

PhD Atis Kapenieks, Riga Technical University, Latvia

PhD Tsanko Karadzhev, Technical University of Gabrovo, Bulgaria

PhD Veiko Karu, Tallinn University of Technology, Estonia

Dipl.-Kfm. Lars Kempt, Chemnitz University of Technology, Germany

PhD. Anna Khilya, Vinnytsia Mykhailo Kotsiubynskyi State Pedagogical University, Ukraine

Dr.sc.ing. Sergejs Kodors, Rezekne Academy of Technologies, Latvia

Dr.sc.ing. Ēriks Kronbergs, Latvia University of Life Sciences and Technologies, Latvia

Dr.sc.ing. Lyubomir Lazov, Rezekne Academy of Technologies, Latvia

Dr. Slobodan Lubura, University of East Sarajevo, Bosnia and Herzegovina

PhD Arturs Medveckis, University of Liepaja, Latvia

Dr.sc.ing. Linda Mežule, Riga Technical University, Latvia

PhD Ziedonis Miklašēvičs, Rezekne Academy of Technologies, Latvia

PhD Nikolai Minkovski, University of Forestry, Bulgaria

PhD Cristian-Emil Moldoveanu, Military Technical Academy "Ferdinand I", Romania

Dr.sc.ing. Ivan Mitev, Technical University Gabrovo, Bulgaria

PhD Nikolay Nedyalkov, Bulgarian Academy of Sciences, Bulgaria

Dr. Vlastimir Nikolic, University of Nis, Serbia  
PhD Eng. Ilie Nuca, Technical University of Moldova, Republic of Moldova  
Dr.chem. Sergejs Osipovs, Daugavpils University, Latvia  
Dr. Nenad Pavlovič, University of Nis, Serbia  
Dr.sc.ing. Desislava Petrova, Technical University of Gabrovo, Bulgaria  
Dr.agr. Liena Poiša, Rezekne Academy of Technologies, Latvia  
PhD Dimcho Pulov, Technical University of Gabrovo, Bulgaria  
Dr. agr. Gundega Putniece, Latvia University of Life Sciences and Technologies, Latvia  
Dr.sc.ing. Svetlana Polukoshko, Ventspils University College, Engineering Research Institute "VSRC", Latvia  
PhD Gabriel Raducanu, Air Force Academy Henri Coanda, Romania  
Dr. Anton Rassolkin, Tallinn University of Technology, Estonia  
Dr.phys. Gita Rēvalde, Riga Technical University, Latvia  
Dr.sc.ing. Andrejs Romanovs, IEEE Latvia Section, Riga Technical University, Latvia  
Dr.sc.ing. Andris Skromulis, Rezekne Academy of Technologies, Latvia  
PhD Gunars Strods, Rezekne Academy of Technologies, Latvia  
PhD Jolanta Šadauskiene, Kaunas University of Technology, Lithuania  
Dr.-Ing. Bambang Soemardiono, Institut Teknologi Sepuluh Nopember, Indonesia  
PhD Arita Takahashi, Riga Technical University, Latvia  
Dr.-Ing. Josef Timmerberg, Jade University of Applied Sciences, Germany  
Dr.habil.sc.ing Janis Viba, Riga Technical University, Latvia  
PhD Constantin-Iulian Vizitiu, Militar Technical Academy "Ferdinand I", Romania  
PhD Tsanka Zlateva-Petkova, Technical University of Gabrovo, Bulgaria  
PhD Erika Zubule, Rezekne Academy of Technologies, Latvia  
PhD Anda Zvaigzne, Rezekne Academy of Technologies, Latvia

### ***Organising Committee Chairman***

Dr.habil.geol. Gotfrīds Noviks, Rezekne Academy of Technologies, Latvia

### ***Organizing Commitee***

Dr.sc.ing. Egils Ginters, Riga Tehnical University, Latvia  
Dr.sc.ing. Pēteris Grabusts, Rezekne Academy of Technologies, Latvia  
DSc. Dimitar Grekov, Agricultural University, Bulgaria  
Dr.sc.ing. Aleksandrs Gorbunovs, Riga Technical University, Latvia  
Dr.sc.ing. Ēriks Kronbergs, Latvia University of Life Sciences and Technologies, Latvia  
Dr.sc.ing. Sergejs Kodors, Rezekne Academy of Technologies, Latvia  
Dr.sc.ing. Lyubomir Lazov, Rezekne Academy of Technologies, Latvia  
PhD Līga Mazure, Rezekne Academy of Technologies, Latvia  
PhD Magdalena Mitkova, Prof. Assen Zlatarov University Burgas, Bulgaria  
PhD Valyo Nikolov, Technical University of Sofia, Plovdiv Branch, Bulgaria  
Dr.sc.ing. Imants Nulle, Latvia University of Life Sciences and Technologies, Latvia  
Vilnis Rantins, Member of the Council of the Association of Mechanical Engineering and Metalworking Industries of Latvia, Latvia  
Dr.agr. Liena Poiša, Rezekne Academy of Technologies, Latvia  
Dr.geol. Valdis Segliņš, University of Latvia, Latvia  
Dr.sc.ing. Andris Skromulis, Rezekne Academy of Technologies, Latvia  
Dr.biol. Artūrs Škute, Daugavpils University, Latvia  
Dr.sc.ing. Artis Teilāns, Rezekne Academy of Technologies, Latvia  
PhD Ērika Teirumnieka, Rezekne Academy of Technologies, Latvia  
Dr.biol. Rasma Tretjakova, Rezekne Academy of Technologies, Latvia

## *Reviewers*

Dr.agr. Aleksandrs Adamovičs, Latvia University of Life Sciences and Technologies, Latvia  
PhD Nikolaj Angelov, Technical University of Gabrovo, Bulgaria  
PhD Andres Annuk, Estonian University of Life Sciences, Estonia  
Dr. agr. Lidiia Antypova, Mykolayiv National Agrarian University, Ukraine  
PhD Iluta Arbidane, Rezekne Academy of Technologies, Latvia  
Dr.oec. Dzintra Atstāja, BA School of Business and Finance, Latvia  
Dr.sc.ing. Anita Avišāne, Riga Technical University, Latvia  
PhD Sholpan Bekmukhanbetova, Kazakh Automobile and Road Institute, Kazakhstan  
PhD Ansis Ataols Bērziņš, Riga Tehnical University, Latvia  
PhD Aija Brakovska, Daugavpils University, Latvia  
Dr. Rene Brunsch, Apromace data systems GmbH, Germany  
PhD Basar Caglar, Izmir Institute of Technology, Turkey  
PhD Sarma Cakula, Vidzeme University of Applied Sciences, Latvia  
Dr. hab. Ing. Tadeusz Chrzan, Poltegor Institute, Poland  
Dr.sc.ing. Edgars Čubars, Rezekne Academy of Technologies, Latvia  
PhD Dimitar Diakov, Technical University of Sofia, Bulgaria  
PhD Dimitar Dichev, Technical University of Gabrovo, Bulgaria  
Prof. PhD Nikolay Dolchinkov, “Vasil Levski” National Military University, Bulgaria  
PhD Sandra Ezmale, Rezekne Academy of Technologies, Latvia  
Dr. agr. Daina Feldmane, Latvia University of Life Sciences and Technologies, Latvia  
Dr.sc.ing. Egils Ginters, Riga Tehnical University, Latvia  
Dr.sc.ing. Aleksandrs Gorbunovs, Riga Technical University, Latvia  
Dr.sc.ing. Pēteris Grabusts, Rezekne Academy of Technologies, Latvia  
Dr. agr. Elvyra Gruzdevienė, Flax museum, the branch of Eriskiai Cultural Center of the Panevezys District, Lithuania  
Mg. Mart Hovi, Estonian University of Life Sciences, Estonia  
Dr. agr. Sofija Jankauskiene, Lithuanian Research Centre for Agriculture and Forestry, Lithuania  
PhD Angelika Juško-Štekele, Rezekne Academy of Technologies, Latvia  
Dr.sc.ing. Aivars Kaķītis, Latvia University of Life Sciences and Technologies, Latvia  
Dr.paed. Ilmārs Kangro, Rezekne Academy of Technology, Latvia  
Dr. paed. Janis Kapenieks, Riga Technical University, Latvia  
PhD Atis Kapenieks, Riga Technical University, Latvia  
PhD Tsanko Karadzhev, Technical University of Gabrovo, Bulgaria  
PhD. Anna Khilya, Vinnytsia Mykhailo Kotsiubynskyi State Pedagogical University, Ukraine  
Dr.sc.ing. Sergejs Kodors, Rezekne Academy of Technologies, Latvia  
Dr.sc.ing. Ēriks Kronbergs, Latvia University of Life Sciences and Technologies, Latvia  
PhD Karīne Laganovska, Rezekne Academy of Technologies, Latvia  
Dr. Walter Leal, Hamburg University of Applied Sciences, Germany, Manchester Metropolitan University, United Kingdom  
Dr.oec. Jelena Lonska, Rezekne Academy of Technologies, Latvia  
Dr.sc.math. Maksims Marinaki, University of Latvia, Latvia  
Dr.sc.ing. Andris Martinovs, Rezekne Academy of Technologies, Latvia  
PhD Žanna Martinsone, Riga Stradiņš University, Latvia  
PhD Arturs Medveckis, University of Liepaja, Latvia  
Prof., Dr.habil.sc.ing. Jurijs Merkurjevs, Riga Technical University, Latvia  
PhD Ziedonis Miklašēvičs, Rezekne Academy of Technologies, Latvia  
PhD Nikolai Minkovski, University of Forestry, Bulgaria

Dr.sc.ing. Ivan Mitev, Technical University Gabrovo, Bulgaria  
Dr.habil.geol. Gotfrīds Noviks, Rezekne Academy of Technologies, Latvia  
PhD Eng. Ilie Nuca, Technical University of Moldova, Republic of Moldova  
Dr.chem. Sergejs Osipovs, Daugavpils University, Latvia  
PhD Jana Paidere, Daugavpils University, Latvia  
Dr.sc.ing. Jeļena Pečerska, Riga Technical University, Latvia  
Dr.sc.ing. Desislava Petrova, Technical University of Gabrovo, Bulgaria  
Dr.agr. Liena Poiša, Rezekne Academy of Technologies, Latvia  
Dr. agr. Valentīna Pole, IK Tava zeme, Latvia  
PhD Dimcho Pulov, Technical University of Gabrovo, Bulgaria  
Dr. agr. Gundega Putniece, Latvia University of Life Sciences and Technologies, Latvia  
Dr. Anton Rassolkin, Tallinn University of Technology, Estonia  
Dr.phys. Gita Rēvalde, Riga Technical University, Latvia  
PhD Jolanta Šadauskiene, Kaunas University of Technology, Lithuania  
Dr.sc.ing. Andris Skromulis, Rezekne Academy of Technologies, Latvia  
Dr.-Ing. Bambang Soemardiono, Institut Teknologi Sepuluh Nopember, Indonesia  
PhD Aina Strode, Rezekne Academy of Technologies, Latvia  
PhD Gunars Strods, Rezekne Academy of Technologies, Latvia  
PhD Arita Takahashi, Riga Technical University, Latvia  
Dr.sc.ing. Artis Teilāns, Rezekne Academy of Technologies, Latvia  
Dr.sc.ing. Edmunds Teirumnieks, Rezekne Academy of Technologies, Latvia  
Dr.-Ing. Josef Timmerberg, Jade University of Applied Sciences, Germany  
Dr.biol. Rasma Tretjakova, Rezekne Academy of Technologies, Latvia  
Dr.sc.ing. Imants Zarembo, Rezekne Academy of Technologies, Latvia  
PhD Tsanka Zlateva-Petkova, Technical University of Gabrovo, Bulgaria  
PhD Erika Zubule, Rezekne Academy of Technologies, Latvia  
PhD Anda Zvaigzne, Rezekne Academy of Technologies, Latvia

### ***Secretariat Chairman***

PhD Ērika Teirumnieka, Rezekne Academy of Technologies, Latvia

### ***Secretariat Members***

Dr.agr. Liena Poiša, Rezekne Academy of Technologies, Latvia  
Mg.sc.comp. Gundega Teilāne, Rezekne Academy of Technologies, Latvia



**ENGINEERING SCIENCES  
AND PRODUCTION  
TECHNOLOGIES,  
AND LASER  
TECHNOLOGIES**

# SATURS CONTENTS

## *Engineering Sciences and Production Technologies*

<b>Krasimir Ambarev, Stiliyana Taneva</b> STUDY OF THE INFLUENCE OF ROAD RESISTANCE ON THE FUEL CONSUMPTION OF A PASSENGER CAR WITH AN AUTOMATIC TRANSMISSION	15
<b>Krasimir Ambarev, Valyo Nikolov</b> EXPERIMENTAL STUDY OF TOXIC COMPONENTS IN THE EXHAUST GASES DURING THE OPERATION OF A CAR ENGINE WITH GASOLINE AND LPG	20
<b>Valentin Anguelov</b> THERMAL CHARACTERISTICS OF MATERIALS IN MODELLING OF WELDING PROCESSES	24
<b>Valeri Bakardzhiev, Sabi Sabev, Konstantin Chukalov, Plamen Kasabov</b> RESEARCH INTO THE ACCURACY OF HOLES IN 3D PRINTING USING TAGUCHI METHOD	36
<b>Valeri Bakardzhiev, Sabi Sabev, Plamen Kasabov, Konstantin Chukalov</b> RESEARCH INTO 3D PRINTING LAYER ADHESION IN ABS MATERIALS	41
<b>Vitaly Beresnevich, Marina Cerpinska, Martins Irbe, Janis Viba</b> CONVEYOR-TYPE SMALL HYDROPOWER PLANT FOR SHALLOW RIVER WATERS	46
<b>Oleksandr Byzkrovnyi, Kyrylo Smelyakov, Anastasiya Chupryna, Loreta Savulioniene, Paulius Sakalys</b> COMPARISON OF POTENTIAL ROAD ACCIDENT DETECTION ALGORITHMS FOR MODERN MACHINE VISION SYSTEM	50
<b>Ervin Blumbergs, Viktors Mironovs, Genadijs Sahmenko</b> COMPARATIVE STUDIES OF THE STRENGTH CHARACTERISTICS OF CONCRETE BLOCKS WITH TITANIUM AND IRON RODS (BARS)	56
<b>Genadi Cvetanov, Tsanko Karadzhov</b> OPTICAL GEOMETRIC DESIGN OF SMALL MODULAR CYLINDRICAL GEARS WITH ASYMMETRIC PROFILE	61
<b>Vladlen Devin, Serhii Yermakov, Oleg Gorbovy, Vitaliy Pidlisnyj, Oleksandr Semenov</b> RESEARCH ON WORKING BODIES OF HAMMER CRUSHERS EMPLOYING THE FINITE ELEMENT METHOD	65

<b>Vanya Dyakova, Hristina Spasova, Yoanna Kostova, Yana Mourdjeva, Georgi Stefanov</b>	69
EFFECT OF CU AS MINORITY ALLOYING ELEMENT ON GLASS FORMING ABILITY AND CRYSTALLIZATION BEHAVIOR OF RAPIDLY SOLIDIFIED AL-SI-NI RIBBONS	
<b>Vanya Dyakova, Yoanna Kostova, Hristina Spasova</b>	74
INFLUENCE OF NI AS MINORITY ALLOYING ELEMENT ON THE CORROSION BEHAVIOR OF AMORPHOUS AL-CU-MG ALLOYS IN CHLORIDE SOLUTION	
<b>Boyan Dochev, Desislava Dimova, Ivan Panov</b>	79
INVESTIGATING THE POSSIBILITY OF ALLOYING AN ALLOY ALSI25CU5CR WITH CO, CR AND MO USING METAL POWDER	
<b>Boyan Dochev, Desislava Dimova, Mihail Zagorski, Plamen Kasabov, Georgiya Kamburova</b>	83
INVESTIGATION OF THE STRUCTURE OF ALSI25CU4CR AND ALSI25CU5CR ALLOYS	
<b>Nikolay Todorov Dolchinkov</b>	90
RESULTS AND ANALYSIS OF ACHIEVED JOINT RESEARCH AND ACTIVITIES BETWEEN REZEKNE ACADEMY OF TECHNOLOGY AND VASIL LEVSKI NATIONAL MILITARY UNIVERSITY	
<b>Veselina Dukova, Roussi Minev, Emil Yankov</b>	94
STUDY OF TECHNOLOGICAL CHAINS FOR RAPID PROTOTYPING OF ORTHODONTIC DENTAL PRODUCTS	
<b>Deyan Gradinarov, Marina Manilova, Manahil Tongov</b>	99
EXPERIMENTAL REMOTE DETERMINATION OF THE STATIC CHARACTERISTIC OF THE ARC IN TIG WELDING	
<b>Georgi Iliev, Hristo Hristov</b>	106
MODELLING AND SIMULATION OF ELECTROPNEUMATIC POSITIONING SYSTEM INCLUDING THE LENGTH OF PNEUMATIC LINES	
<b>Georgi Iliev, Hristo Hristov</b>	112
MODELLING AND SIMULATION OF DYNAMIC PROCESSES OF PNEUMATIC LINES	
<b>Julieta Kaleicheva, Krassimir Kirov, Valentin Mishev, Rumyana Lazarova, Zdravka Karaguiozova</b>	119
EFFECT OF BORON ON THE WEAR BEHAVIOR OF HIGH CHROMIUM WHITE CAST IRONS	
<b>Karunamoorthy Rengasamy Kannathan, Andrejs Krasnikovs, Arturs Macanovskis</b>	124
INGREDIENTS DEGRADATION IN STEEL FIBER REINFORCED CONCRETE AFTER THERMAL LOADING	
<b>Pavlinka Katsarova, Kliment Georgiev, Adelina Vasileva, Marin Dimitrov</b>	129
DESIGN AND PRODUCTION OF A DEVICE FOR BASING AND FIXING CONIC DETAILS IN SINE BAR MEASUREMENTS	

<b>Evgeni Lyubomirov Kehayov, Georgi Borisov Ivanov, Georgi Georgiev Komitov</b> 3D MODEL OF THE MECHANICAL PART OF A WEED RECOGNITION SYSTEM IN AN AGRICULTURAL ROBOT IN 3D EXPERIENCE ENVIRONMENT	135
<b>Christo Kondoff, Rossen Mikhov, Leoneed Kirilov, Radostina Zaekova, Plamen Tashev</b> WORKING REGIMES FOR FRICTION STIR PROCESSING OF ALUMINIUM ALLOY A6061	139
<b>Angel Lengerov, Sabi Sabev, Stoyan Paliiski</b> EXPERIMENTAL STUDY OF SURFACE ROUGHNESS IN VIBRO-IMPACT CUTTING OF OPTICAL SLUGS	145
<b>Angel Lengerov, Kalin Krumov, Georgi Levicharov</b> STUDY OF THE KINEMATIC AND DYNAMIC OF INTERACTION OF A VIBRATING SYSTEM FOR CUTTING OPTICAL SLUGS	149
<b>Dimilyan Leonov, Angel Lengerov, Kalin Krumov, Hristo Metev</b> INCREASING THE QUALITY OF FORMING OF SPINNING DETAILS OF ALUMINUM ALLOYS BY CONTROLLING THE RESIDUAL STRESSES IN THEIR SURFACE LAYER	154
<b>Dimilyan Leonov, Hristo Metev, Kalin Krumov, Angel Lengerov</b> SOLVING FUNCTIONAL-TECHNOLOGICAL PROBLEMS USING A NON- PARAMETRIC APPROACH FOR CONTROL OF MICROGEOMETRY OF THE SURFACES OF DETAILS	159
<b>Georgi Levicharov, Angel Lengerov, Stoyan Paliiski</b> STUDY ABOUT THE INFLUENCE OF THE PROCESS PARAMETERS OF VIBRO IMPACT CUTTING OF OPTICAL SLUGS ON THE PRODUCTIVITY OF THE PROCESS	164
<b>Marin Jordanov Marinov</b> A GEOMETRICAL SYNTHESIS OF COMEZ TEXTILE MECHANISMS OF FINALLY REMOVED POSSIBILITIES	168
<b>Vaidotas Matutis, Loreta Savulioniene, Paulius Sakalys, Laura Gzegozevske</b> RESEARCH OF THE PRINCIPAL MODEL OF THE ELECTRIC ENERGY GENERATOR OF THE ELECTRIC CAR (STAGE COMBINATION OF MECHANICAL AND ELECTROMECHANICAL PARTS)	172
<b>Ruta Meiste, Sandra Jakštienė, Aušra Lankauskienė</b> IMPROVEMENT OF OPERATIONAL PROCESSES BY ENSURING WORK SAFETY IN PRODUCTION	176
<b>Ivan Mitev, Simeon Tsenkulovski</b> LOCAL PROCESSING OF NON-METAL MATERIALS WITH CONCENTRATED ENERGY FLOW	183

<b>Neli Nikolova</b> HUMAN CAPITAL IN THE CHANGING WORK ENVIRONMENT OF INDUSTRY 4.0	187
<b>Oleksandra Orda, Yevgen Nagornyy, Natalia Potaman</b> APPROACH TO THE FORMING OF RATIONAL TECHNOLOGY FOR THE EXPORT CARGOES DELIVERY IN SUPPLY CHAIN ON THE PRINCIPLES OF CO- MODALITY	194
<b>Angel Poparov, Agop Izmirliqn</b> CHARACTERISTICS OF MOVEMENTS WHEN CYLINDRICAL TURNING, DRILLING, COREDRILLING AND REAMING	200
<b>Angel Poparov, Agop Izmirliqn</b> CHARACTERISTICS OF MOTIONS IN FACING	204
<b>Dimcho Pulov, Tsanko Karadzhov</b> DEVELOPMENT OF A METHOD FOR CONTACTLESS TEMPERATURE MEASUREMENT IN 3 SPECTRAL RANGES	208
<b>Sabi Sabev, Plamen Kasabov, Konstantin Chukalov, Valeri Bakardzhiev</b> INFLUENCE OF ADDING POLYPROPYLENE(PP) INTO POLYETHYLENE(PE) ON MECHANICAL PROPERTIES OF GEOCELLS	214
<b>Sabi Sabev, Plamen Kasabov, Konstantin Chukalov, Valeri Bakardzhiev</b> DETERMINATION OF THE DYNAMIC MODULUS OF LINEAR DEFORMATIONS OF REINFORCED HIGHLY FILLED POLYMER CONCRETE COMPOSITES DURING CURING	219
<b>Silviya Salapateva, Iliya Chetrokov, Bano Stefanov</b> ALGORITHM FOR OPTIMIZATION OF IDLE TOOL MOVES WHEN MILLING COMPLEX SURFACES ON A TRIAXIAL CNC MILLING MACHINE	226
<b>Silviya Salapateva, Bano Stafanov</b> MATHEMATICAL MODELING OF THE SEQUENCE OF MACHINING SECTIONS OF COMPLEX SURFACES WHEN MILLING ON A TRIAXIAL CNC MACHINE TOOL	233
<b>Silviya Salapateva, Bano Stefanov</b> EXPERIMENTAL STUDIES OF AN ALGORITHM FOR MINIMIZING THE IDLE TOOL MOVES WHEN MILLING COMPLEX SURFACES ON TRIAXIAL CNC MACHINE TOOLS	240
<b>Kyrylo Smelyakov, Anastasiya Chupryna, Denys Sandrkin, Loreta Savulioniene, Paulius Sakalys</b> ADAPTIVE IMAGE ENHANCEMENT MODEL FOR THE ROBOT VISION SYSTEM	246
<b>Stiliyana Taneva, Krasimir Ambarev, Stanimir Penchev, Hristo Atanssov</b> FREQUENCY ANALYSIS OF AN ARM OF MACPHERSON SUSPENSION ON A PASSENGER CAR	252

<b>Manahil Tongov, Valentin Anguelov</b> PRACTICE ORIENTED HEAT SOURCE MODEL CALIBRATION	257
<b>Manahil Tongov, Vladimir Petkov</b> A THERMAL MODEL FOR WIRE ARC ADDITIVE MANUFACTURING	262
<b>Serhii Yermakov, Taras Hutsol, Igor Gerasymchuk, Pavlo Fedirko, Viktor Dubik</b> STUDY OF THE UNLOADING AND SELECTION PROCESS OF ENERGY WILLOW CUTTINGS FOR THE CREATION A PLANTING MACHINE	271
<b>Radostina Zaekova, Plamen Tashev, Yasen Hadjitodorov, Deyan Gradinarov</b> MODIFICATION OF 5083 ALUMINUM ALLOY WITH GRAPHENE VIA FRICTION STIR PROCESSING	276

### *Laser Technologies*

<b>Kevins Bulavskis, Emil Yankov, Lyubomir Lazov, Antons Pacejs</b> RESEARCHING THE PROCESS OF LASER STRUCTURING OF THE SURFACE OF ALUMINUM	282
<b>Љubova Denisova, Antons Pacejs, Emil Yankov, Lyubomir Lazov</b> ANALYSING THE INFLUENCE OF TECHNOLOGICAL PARAMETERS ON THE PROCESS OF LASER MARKING OF SURFACE OF ANODISED ALUMINIUM SAMPLES	289
<b>Nikolay Todorov Dolchinkov, Teodor Petrov, Georgi Petrov, Christian Tolev, Emanuil Dimitrov</b> FEATURES OF COLOR LASER MARKING ON METALS	297
<b>Borislav Georgiev, Tsanko Karadzhov</b> COMPARATIVE ANALYSIS OF GEOMETRIC DEVIATIONS IN CONTACT MEASURING INSTRUMENTS FOR CONTROL AND LASER CONTACTLESS SCANNING	306
<b>Veselin Hristov, Lyubomir Lazov, Nikolay Angelov, Emil Yankov</b> INFLUENCE OF BASIC PARAMETERS OF THE LASER MARKING PROCESS ON STAINLESS STEEL SAMPLES	311
<b>Tsanko Karadzhov, Lyubomir Lazov</b> COMPARATIVE ANALYSIS OF METHODS FOR MEASURING LASER POWER	316
<b>Jēkabs Lapa, Imants Adijāns, Emil Yankov, Lyubomir Lazov, Ritvars Rēvalds</b> INVESTIGATION OF LASER MARKING AND TEXTURING OF TITANIUM GR 2 WITH FIBER LASER	321
<b>Lyubomir Lazov, Ivo Draganov</b> APPLICATION OF A FINITE ELEMENT MODEL TO OBTAIN THE INFLUENCE OF THE TREATMENT'S POWER, REFLECTION AND FOCAL DIAMETER IN LASER TEXTURING OF ALUMINUM	328

<b>Lyubomir Lazov, Nikolay Padarev, Milko Yovchev, Lyubomir Linkov</b> THE CHANGE OF CONTRAST IS INVESTIGATION OF 75 STEEL SAMPLES LASER MARKED WITH DIFFERENT MODES	334
<b>Dimcho Pulov, Petar Tsvyatkov</b> OPTICAL SYSTEMS FOR REDUCING THE DIVERGENCE OF LASER BEAMS	339
<b>Daniels Raubiška, Imants Adijāns, Emil Yankov, Lyubomir Lazov</b> INVESTIGATING THE CONTRAST OF SURFACE MARKING ON DIFFERENT COLOR CONNECTORS FOR TELECOMMUNICATIONS NEEDS	344
<b>Dzintars Rāviņš, Emil Yankov, Imants Adijāns, Lyubomir Lazov, Daivis Rāviņš</b> INVESTIGATING THE IMPACT OF LASER POWER AND SCAN SPEED ON ENGRAVING ASPEN THERMOWOOD	351
<b>Petar Tsvyatkov, Emil Yankov, Lyubomir Lazov, Edmunds Teirumnieks, Karlis Pīgožnis</b> INVESTIGATION OF SURFACE ROUGHNESS OF CARBON STEEL MACHINED PARTS AFTER NANOSECOND FIBER LASER MARKING	358
<b>Petar Tsvyatkov, Emil Yankov, Lyubomir Lazov, Edmunds Teirumnieks, Erika Teirumnieka</b> COLOR MARKING OF STAINLESS STEEL AND TITANIUM WITH THE LASER OXIDATION METHOD	363
<b>Petar Tsvyatkov, Emil Yankov, Lyubomir Lazov, Edmunds Teirumnieks, Karlis Pīgožnis</b> INVESTIGATION OF THE INFLUENCE OF TECHNOLOGICAL PARAMETERS OF LASER MARKING ON THE DEGREE OF CONTRAST	370

**ENGINEERING SCIENCES  
AND PRODUCTION  
TECHNOLOGIES**

# *Study of the Influence of Road Resistance on the Fuel Consumption of a Passenger Car with an Automatic Transmission*

**Krasimir Ambarev**

Department of Transport and  
Aircraft Equipment and Technologies  
Technical University of Sofia,  
Plovdiv Branch  
Plovdiv, Bulgaria  
email kambarev@tu-plovdiv.bg

**Stiliyana Taneva**

Department of Transport and  
Aircraft Equipment and Technologies  
Technical University of Sofia,  
Plovdiv Branch  
Plovdiv, Bulgaria  
email s.taneva@tu-plovdiv.bg

**Abstract.** One of the directions in the modern automotive industry is related to optimizing processes of the working cycle of internal combustion engines, which is related on another hand to reducing fuel consumption. This article presents calculation results of fuel consumption of a passenger car Honda Accord with automatic gearbox which are based on experimentally obtained power characteristics by using a chassis dynamometer DYNO COSBER. The fuel consumption was determined at different speeds of the car on a road without a slope and with 2%, 4% and 6% slope by using the chassis dynamometer and diagnostic equipment. The results of calculations about the influence of road resistances on fuel consumption were compared and analyzed with those obtained from measurements.

**Keywords:** fuel consumption, slope, passenger car chassis dynamometer, road resistances.

## I. INTRODUCTION

Important operating properties of the car are its fuel economy characteristics. They are evaluated by the fuel consumption when the vehicle is driving in different road conditions [1]. The fuel consumption of the car depends on the fuel economy of the internal combustion engine (ICE).

Internal combustion engines are the main source of energy for vehicle for various purposes [3]. Recently, more attention is devoted to problems related to the ecology and emissions release by ICE of vehicles.

Modern cars are equipped with ICE with relatively higher power. Designers are looking for solutions to reduce weight and fuel consumption and to improve the

aerodynamic characteristics by using modern electronic systems for controlling the ICE and the vehicles as a whole. Significant portion of the currently available studies in the area of ICE and vehicle optimization are focused on the impact of the different factors on the fuel consumption. The effect of the change of the transmission efficiency of useful action on the fuel economy was determined analytically in [4], while in [5] the influence of the aerodynamic resistances on the fuel consumption was investigated.

Researches of various parameters of the car can be conducted in laboratory conditions or through road tests. In recent time, chassis dynamometers are increasingly used to conduct various tests [2, 6, 7, 8]. The chassis dynamometers are used to measure the power performances of the car and the engine, but they are also used to realize various loads and simulate road conditions [6, 7]. The researchers in [8] do investigate on the fuel consumption of a conventional car and a hybrid, with road conditions realized via chassis dynamometer.

The purpose of the study is a calculation and experimental measurement of the influence of road resistance of the fuel consumption of a passenger car with an automatic transmission. The experimental measurements were carried out on a COSBER dynamometer and with the application „Car Scanner Pro“ connected via Bluetooth LE (4.0) adapters to the electronic control unit (ECU) of ICE through which current fuel consumption data were obtained.

Print ISSN 1691-5402

Online ISSN 2256-070X

<https://doi.org/10.17770/etr2023vol3.7273>

© 2023 Krasimir Ambarev, Stiliyana Taneva. Published by Rezekne Academy of Technologies.  
This is an open access article under the [Creative Commons Attribution 4.0 International License](https://creativecommons.org/licenses/by/4.0/).

## II. METHODS OF THE DETERMINATION OF FUEL CONSUMPTION

Fuel consumption can be determined analytically and experimentally.

Resistance forces applied on a moving car are opposite to its direction of motion and they are overcome by the tractive force  $F$ . Figure 1 presents when the car with front-wheel drive without trailer steady moving on a slope. Total resistance force in steady motion can be presented by

$$F_{tot} = F_f \pm F_i + F_a \quad , \quad (1)$$

where  $F_f$  is rolling resistance force;  $F_i$  is gradient resistance force; and  $F_a$  is aerodynamic drag force.

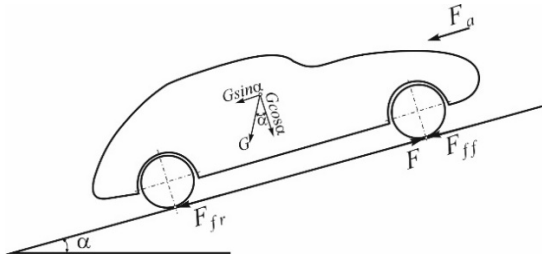


Fig. 1. Resistance forces acting on a moving car on a slope.

Rolling resistance force and gradient resistance force are represented by the sum by force  $F_\psi$ , known as road resistance and is determined by [1]

$$F_\psi = F_f \pm F_i = fG \cos \alpha \pm G \sin \alpha = \psi G \quad , \quad (2)$$

where  $f$  is rolling resistance coefficient, [-], which depends on many factors, and varies as a value, but in the study of performance properties it is usually assumed to be constant for the relevant road condition;  $G$  is the weight of the car;  $\psi$  is the road resistance coefficient and is determined by [1]

$$\psi = f + i \quad , \quad (3)$$

where  $i$  is a slope of the road, [%].

Aerodynamic drag force is distributed over the entire surface of the car, but is considered as force applied at a single point and it is determined by the formula [1]

$$F_a = \frac{1}{2} c_A \rho_A S v^2 \quad , \quad (4)$$

where  $c_A$  is the aerodynamic drag coefficient, [-];  $\rho_A$  is the mass density of air;  $S$  is the frontal area of the car, which is the projected area of the car in the driving direction, [m<sup>2</sup>];  $v$  is the car velocity, [km/h].

The fuel consumption in [l/100 km] of traveled distance with a steady speed of the car is calculated according to [1]

$$Q = \frac{g_e P_c}{10 \rho v} \quad , \quad (5)$$

where  $g_e$  is specific fuel consumption of ICE, [g/kW.h];  $v$  is the car velocity, [km/h];  $\rho$  is density of the fuel, [kg/l];  $P_c$  is the engine power, necessary for the motion of the car and can be represented by

$$P_c = \frac{F_\psi v}{3,6 \eta_t} \quad , \quad (6)$$

where  $\eta_t$  is transmission efficiency.

Taking into account the above dependencies for fuel consumption is obtained

$$Q = \frac{g_e (F_\psi + F_a)}{36 \rho v} \quad . \quad (7)$$

In the cases when the fuel economy characteristic of the engine is not available, the specific effective fuel consumption can be determined by an empirical formula [1]

$$g_e = g_p k_p k_\omega \quad , \quad (8)$$

where  $g_p$  is the specific fuel consumption at maximum engine power and it is  $g_p = (1,05 \div 1,15) g_{e_{min}}$ , [g/kW.h];  $k_p$  is the coefficient which takes into account the effect of the engine load on  $g_e$ ;  $k_\omega$  is the coefficient which takes into account the effect of the of the angular velocity of the crankshaft on  $g_e$ .

The coefficients  $k_p$  and  $k_\omega$  are determined by empirical dependences from [1].

The object of this study is a passenger car Honda Accord Executive (CL9), with petrol engine (K24A3). The electronic control unit (37820-RBB-E57) of the ICE and automatic transmission has modified Firmware. Table 1 presents parameters of the car [9] and necessary coefficients.

TABLE 1 PARAMETERS OF THE CAR AND COEFFICIENTS.

Parameters	Designation	Unit	Value
Total mass	m	[kg]	1610
Aerodynamic drag coefficient	$c_A$	[-]	0,26
Frontal area	S	[m <sup>2</sup> ]	2,11
Acceleration due to gravity	g	[m/s <sup>2</sup> ]	9,81
Rolling resistance coefficient	f	[-]	0,01
Mass density of air	$\rho_A$	[kg/m <sup>3</sup> ]	1,225
Width of the tire	$h_{tire}$	[m]	0,225
Aspect ratio of the tire	-	%	45
Rim diameter	d	[m]	0,432
Radius of the tire	$r_k$	[m]	0,310
Air pressure of tire	$p_{tire}$	[MPa]	0,23

The experimental studies were carried out by using a chassis dynamometer DYNO COSBER 4000 in a laboratory of TU-Sofia, Plovdiv branch (fig. 2). The environmental parameters in which measurements were made are presented in the table 2. The tests were performed when the hydrodynamic torque converter was operating in mode  $M_{impeller} = M_{turbine}$ , torque ratio  $k = 1$  and clutch is locked-up. In locked-up mode the impeller, turbine and stator of the torque converter rotate as one and there are no losses.

The experimental studies and calculations were made for the car steady moves on a horizontal road and at the three values of the road slope. The slopes of 2%, 4% and 6% are aligned with the regulations in [10].



Fig. 2. Experimental study of a passenger car Honda Accord 2.4.

TABLE 2 ENVIRONMENTAL PARAMETERS.

Parameters	Unit	Value
Temperature	°C	19
Pressure	kPa	101
Humidity	%	46

Figure 3 shows the input data to the chassis dynamometer software.

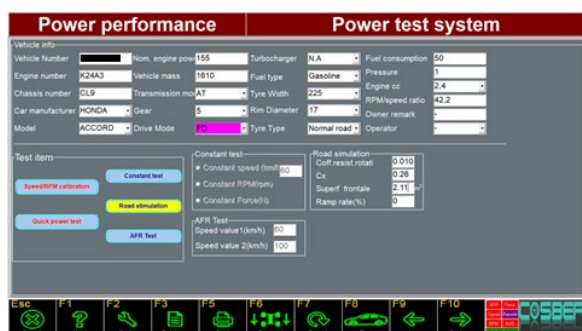


Fig. 3. Work screen with details of the passenger car and road parameters.

Figure 3 shows the „Road simulation“ mode used in the chassis dynamometer measurements. Fuel consumption measurements were made when the passenger car was in operated like a manual transmission

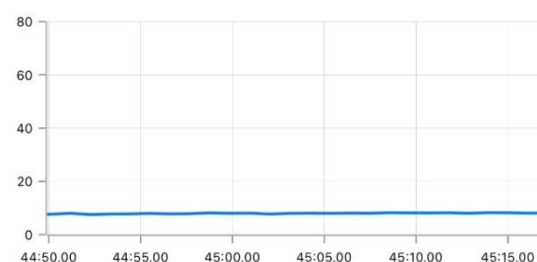
for steady speed values when driving the car in third, fourth and fifth gear respectively and at the corresponding values of road resistance without a slope, and slope 2%, 4% and 6%.



Fig. 4. „Road simulation“ mode.

The „Car Scanner Pro“ application enables real-time reading of various engine and car parameters. This data can also be saved to a log file for further processing and analysis. Figure 5 shows some of the data obtained through the experiment.

Inst. fuel cons. L/100km



Engine RPM rpm



Speed km/h

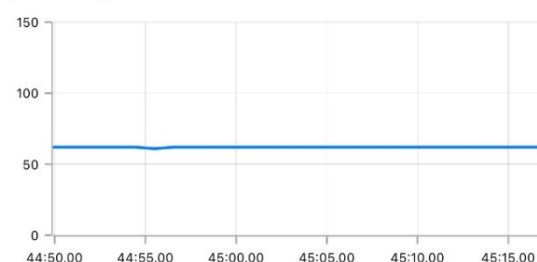


Fig. 5. Work screen of software „Car Scanner Pro“.

### III. RESULTS AND DISCUSSION

Figure 6 presents the experimentally obtained power performance of the passenger car and engine performance. The engine performance is derived from the car power performance by taking in consideration the transmission efficiency.



Fig. 6. Power performance of the passenger car and performance of the engine.

The obtained measurement result on the chassis dynamometer for maximum engine power (154 kW) with modified firmware of ECU is higher than the original one (140 kW).

The fuel consumption of the car with the third, fourth and fifth gears engaged was calculated by usage of equations (2), (3), (7) and (8) in combination with the experimentally determined power performance of the car and the engine. For the calculation of the fuel consumption for the gears, the change in the transmission efficiency was taken into account.

Figures 7, 8, 9 and 10 present the results of the fuel consumption in third, fourth and fifth gear at road resistances without a slope and slope of 2%, 4% and 6%, respectively, derived from the calculations and the experimental measurements.

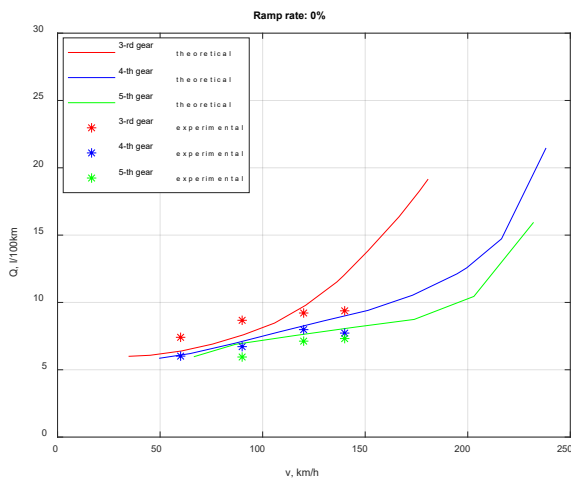


Fig. 7. Fuel consumption in third, fourth and fifth gear without a slope.

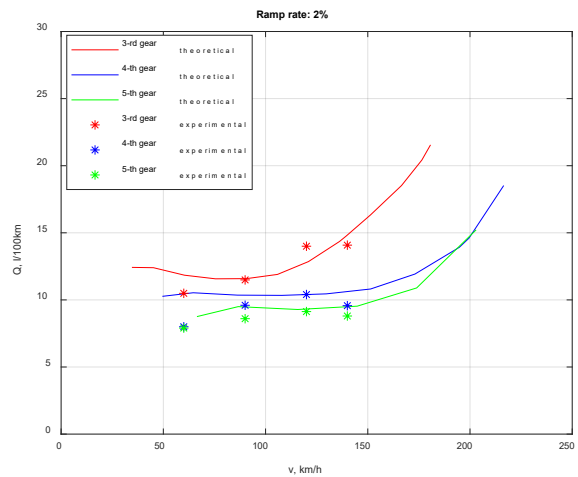


Fig. 8. Fuel consumption in third, fourth and fifth gear at 2% slope.

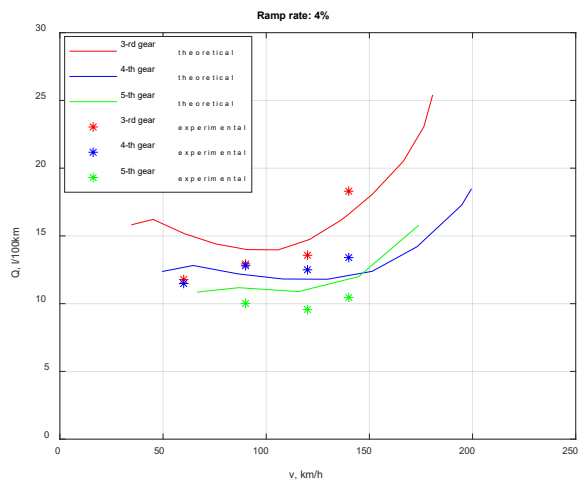


Fig. 9. Fuel consumption in third, fourth and fifth gear at 4% slope.

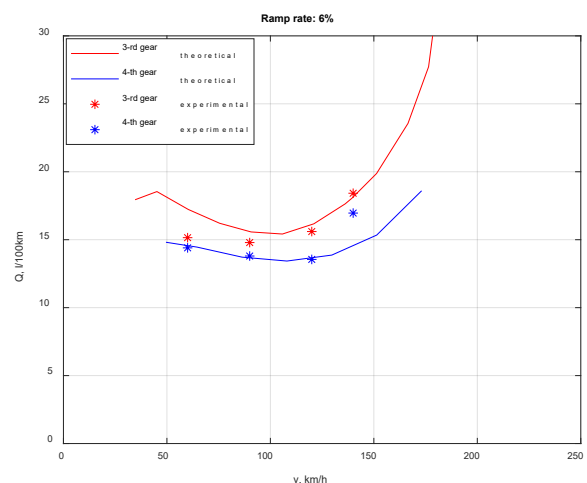


Fig. 10. Fuel consumption in third, fourth and fifth gear at 6% slope.

The fuel consumption of the car increases as the slope of the road increases. From the obtained results, it can be seen that lower fuel consumption is obtained in the fifth gear when the car is moving without a slope, and slope of

2% and 4%. At road of 6% slope the fuel consumption is lowest in fourth gear and at this road gradient the car cannot move in fifth gear.

#### IV. CONCLUSIONS

An experiment was performed to validate the results of the analytical dependences for determining the fuel consumption of a Honda Accord passenger car. The results obtained from the analytical dependences are close to the experimental results.

The small differences between the calculated and experimental fuel consumption values are due to some specifics of the system which controls the continuously variable camshaft phasing system used on the intake camshaft of DOHC engine (intelligent-VTEC) and some peculiarities in the setting of ECU's firmware of car's engine. The peculiarities of the methodology for analytical determination of fuel consumption also have an influence on this difference.

#### ACKNOWLEDGMENTS

This work was supported by the European Regional Development Fund within the OP "Science and Education for Smart Growth 2014-2020", Project Competence Centre "Smart Mechatronic, Eco-And Energy Saving Systems And Technologies", № BG05M2OP001-1.002-0023.

#### REFERENCES

- [1] S. Lyubenov, B. Angelov, I. Evtimov, „Vehicles and Tractors“- Performance properties, Ruse, 2004, ISBN: 954-712-240-1.
- [2] A. Budalā, A. Šoica, An Experimental Research on Power Losses into an Automotive Manual Transmission, International Congress of Automotive and Transport Engineering, Proceedings of the 4th International Congress of Automotive and Transport Engineering (AMMA2018), pp.527-534, DOI:10.1007/978-3-319-94409-8\_61.
- [3] E. Dimitrov, At. Tashev, CNC effect on performance parameters of diesel engine operated on duel-fuel mode, AIP Conference Proceeding, Volume 2449, Issue 1 (110.1063/5.0091441), 2022.
- [4] D. Katsov, I. Evtimov, On the influence of alteration of coefficient of efficiency on fuel consumption characteristics of automobiles, Journal of the Technical University at Plovdiv, "Fundamental Sciences and Applications", Vol. 12, pp. 21-24, 2005.
- [5] Ondrej Stopka, Branislav Sarkan, Jan Vrabel, Jacek Caban, Investigation of fuel consumption of a passenger car depending on aerodynamic resistance and related, Aspects: A case study, The Archives of Automotive Engineering - Archiwum Motoryzacji Vol. 81, No. 3, 2018, pp.111-118.
- [6] Kolator B, S. Racewics, A. Olszewski, Bench tests results of the traction parameters of the light two wheeled electric vehicle, International Automotive Conference (KONMOT2018), IOP Conference Series: Materials Science and Engineering, doi:10.1088/1757-899X/421/2/022015.
- [7] Kolator B, M. Janulin, Methodology for measuring car traction Parameters, MATEC Web of Conferences 182, 02001 (2018), 17th International Conference Diagnostics of Machines and Vehicles, <https://doi.org/10.1051/mateconf/201818202001>.
- [8] R. Šmigins, V. Pirs, D. Berjoza, Investigation in fuel consumption of a hybrid and conventional vehicle, Agronomy Research 18 (S1), Latvia, Vol. 18, Issue. 1, 2020, pp.1027-1035, <https://doi.org/10.15159/ar.20.050>.
- [9] [https://www.automobile-catalog.com/car/2008/1141430/honda\\_accord\\_2\\_4\\_i-vtec\\_executive\\_automatic.html#gsc.tab=0](https://www.automobile-catalog.com/car/2008/1141430/honda_accord_2_4_i-vtec_executive_automatic.html#gsc.tab=0).
- [10] <https://lex.bg/bg/laws/ldoc/2137187173>.

# Experimental Study of Toxic Components in the Exhaust Gases During the Operation of a Car Engine with Gasoline and LPG

**Krasimir Ambarev**

Department of Transport and Aviation  
Equipment and Technologies, Technical  
University of Sofia, Plovdiv Branch 25  
Tsanko Dyustabanov str., 4000 Plovdiv,  
Bulgaria  
E-mail: kambarev@tu-plovdiv.bg

**Valyo Nikolov**

Department of Transport and Aviation  
Equipment and Technologies, Technical  
University of Sofia, Plovdiv Branch  
25 Tsanko Dyustabanov str., 4000  
Plovdiv, Bulgaria  
E-mail: vnikolov@tu-plovdiv.bg

**Abstract.** The article presents and analyzes the results obtained from an experimental study of the content of toxic components in the exhaust gases during the operation of a car engine with gasoline and liquefied petroleum gas (LPG). The study was conducted in laboratory conditions by loading the driving wheels with a roller-type chassis dynamometer, corresponding to the established movement of the car with constant speed on a horizontal road section.

**Keywords:** Car, Engine, Exhaust Gases, Experimental Study, Gasoline, LPG and Toxic Components.

Aerodeck, with engine displacement - 1500 cm<sup>3</sup>, rated power of 84 kW/6500 min<sup>-1</sup> and meeting the environmental standard Euro 2. The car was equipped with a three-way catalytic converter with a mileage of approximately 430,000 km at the time of the experiment, and also a new catalytic converter, produced by BM Catalysts – UK. It had a car gas system (CGS) as well, installed with an LPG electronic control unit, made by the company STAG, model STAG 300 ISA2. The multiplier map for the gas ECU was done manually, not by the automatic determination algorithm.

## I. INTRODUCTION

Environmental pollution has been one of the current topics in recent decades. The road transport is one of the main polluters. The exhaust gases of internal combustion engines contain a large number of chemical compounds, the concentration of which varies depending on the type of fuel used and the nature of the combustion process [1], [2], [3], [4]. The nature of the combustion process in turn depends on the technical condition of the internal combustion engine and its mode of operation. This article aims to study the concentration of certain toxic components (CO, CO<sub>2</sub>, CH) at different car speeds and assess the pollution levels in established modes of car motion, such as constant speed driving. For this purpose, the movement of the car is simulated in laboratory conditions using a chassis dynamometer. A resistance force is created of the driving wheels, which depends on the speed of the car. A gas analyzer was used to measure the content of harmful components in the exhaust gases. The experimental study was performed on a Honda Civic

## II. MEANS FOR MEASURING AND METHODS

The roller-type chassis dynamometer used in the experiment was a the Dyno Cosber 4000. The dynamometer offers various features, including "Road simulation". Before starting the "Road simulation" mode, the car's data is entered into the system, such as vehicle's mass, rim and tire parameters, tire type, transmission type, speed/engine rpm ratio, drag coefficient, projected frontal area of the vehicle, slope angle of the road, etc., were entered into the system. The software then calculated the value of the total resistance force at the respective speed, and the chassis dynamometer loaded the driving wheels accordingly. The driving wheels of the tested car are on the front axle.

The Dyno Cosber 4000 is equipped with a digital O<sub>2</sub> sensor controller LC-2, made by Innovate Motorsports and a wideband lambda sensor Bosch LSU 4.9. This sensor is specifically designed to measure the proportion of oxygen in the exhaust gases of various types of

Print ISSN 1691-5402

Online ISSN 2256-070X

<https://doi.org/10.17770/etr2023vol3.7304>

© 2023 Krasimir Ambarev, Valyo Nikolov. Published by Rezekne Academy of Technologies.  
This is an open access article under the [Creative Commons Attribution 4.0 International License](https://creativecommons.org/licenses/by/4.0/).

automotive engines, including those, powered by gasoline, LPG, or diesel fuel. The wideband lambda sensor LSU 4.9 is a planar ZrO<sub>2</sub> dual-cell limiting current sensor with an integrated heater in it [5].



Fig. 1. Chassis dynamometer DynoCosber 4000 [6].

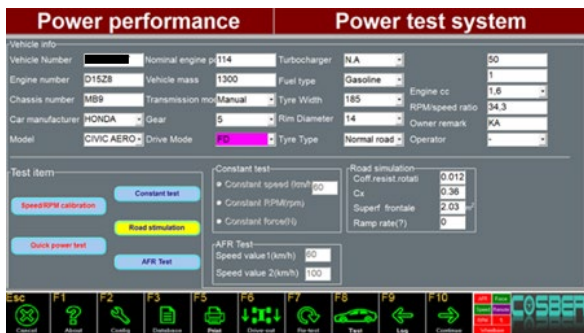


Fig. 2. Window with the technical data of the tested car [8].

TABLE 1 TECHNICAL SPECIFICATION OF A CHASSIS DYNAMOMETER

Parameter	Unit
Max. absorption power	883 kW
Max. torque	2350 Nm
Max. speed	250 km/h
Max. axle weight	2000 kg x 2
Max. continual loading time	15 min
Roller axle separation	430 mm
Roller length	860 mm
Roller diameter	216 mm
Wheel base adjustment	2180-3380 mm
Air/Fuel ratio for gasoline ( $\lambda$ )	7.35-22.39 (0.5 - 1.5)

The Dyno Cosber 4000 offers a precise simulation of defined road load conditions, enabling measurements of fuel consumption and exhaust analysis. When operating in the "Road simulation" mode with a constant speed, the PID (proportional integral derivative) controller and the power absorbing unit adjust the engine load to simulate normal road driving, accounting for a number of factors, such as slope angle, rolling resistance, and air resistance. Rolling resistance power results from the tire and road surface deformation as a function of speed, while air resistance power is proportional to the vehicle's frontal surface area and air resistance coefficient. In a "Road simulation" mode at a constant speed, the inertial drag power is zero.



Fig. 3. Gas analyzer DEK DG-04IR.

TABLE 2 TECHNICAL SPECIFICATION OF A GAS ANALYZER

Component	Measurement range	Measuring accuracy
CO	0 to 15% vol.	$\pm 0.02\%$ vol. $\pm 3\%$
CO <sub>2</sub>	or 0 to 20% vol.	$\pm 0.3\%$ vol. $\pm 3\%$
HC	0 to 15000 ppm vol. n-hexane	propane - $\pm 8$ ppm vol. $\pm 3\%$
O <sub>2</sub> (*)	0 to 25% vol.	$\pm 0.1\%$ vol. $\pm 5\%$

A DEK gas analyzer, model DEK DG-04IR [7], was used to measure the content of harmful components in the exhaust gases. The gas analyzer has a certificate for an approved type BG 04 No. 4245 of a measuring device from the State Agency for Metrological and Technical Supervision. It measures the CO, CO<sub>2</sub> and HC content of the exhaust gases. The content of CO, CO<sub>2</sub> is in %, and of HC - in ppm. The DEK gas analyzer has a clamp for measurement of the engine's rpm and a sensor for measuring the an engine's oil temperature. A screen from the gas analyzer software is shown in fig. 4. Before starting the measurement, the type of the engine's fuel must be selected - gasoline (BENZIN in gas analyzer's software) or LPG.

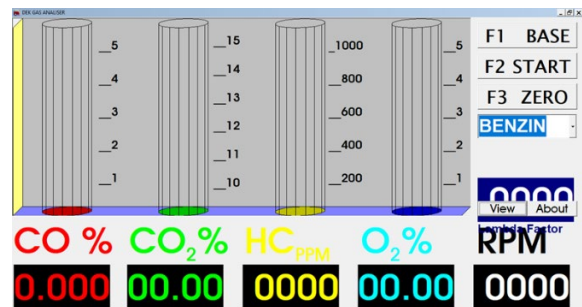


Fig. 4. Full screen mode of the DEK DG-04IR gas analyzer software.

### III. RESULTS AND DISCUSSION

The measurements were performed in laboratory conditions - fig. 5 and 6.

To ensure comparability of the results, the measurements for both fuels were performed at:

- the same adjustment of valve clearance (according to the prescriptions of the manufacturer);
- the same ignition timing setting (according to the prescriptions of the manufacturer);
- established engine temperature condition (constant coolant temperature) of the engine;
- the same atmospheric conditions (measurements conducted within a few hours).

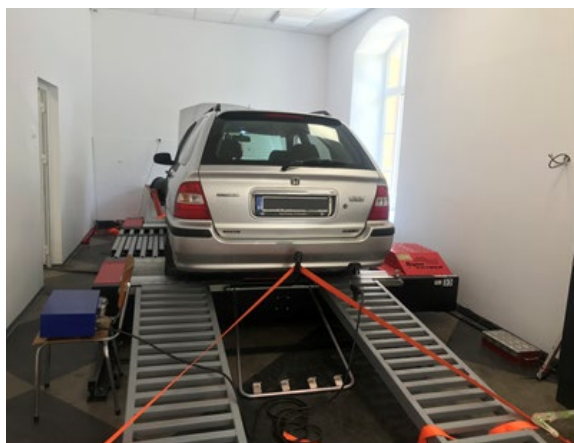


Fig. 5. Measurement of the content of toxic components in the exhaust gases.



Fig. 6. Data from the software of Dyno Cosber 4000 and the gas analyzer, used in the experimental study.

During the measurements, the car was set at its 5th gear.

The measurements were carried out at an established speed of the vehicle. The selected speed values were respectively 50, 70, 90, 110, 120, 130 and 140 km/h. The obtained results are presented graphically in Figures 7, 8 and 9.

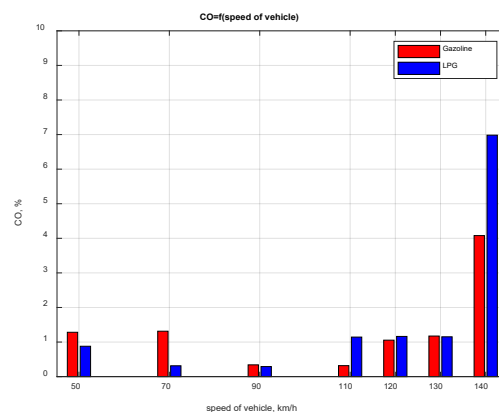


Fig. 7. Experimental study of the content of CO, [%] in the exhaust gases of a car Honda Civic Aerodeck 1.5 iLS.

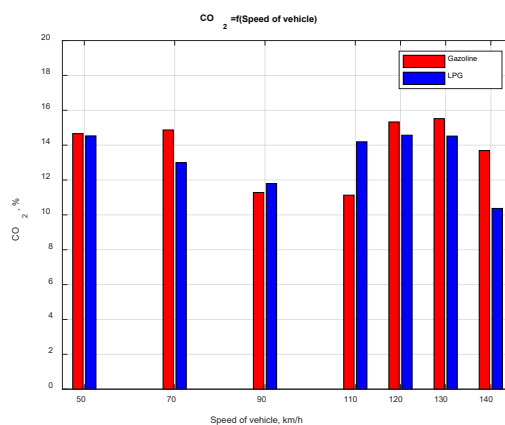


Fig. 8. Experimental study of the content of CO<sub>2</sub>, [%] in the exhaust gases of a car Honda Civic Aerodeck 1.5 iLS.

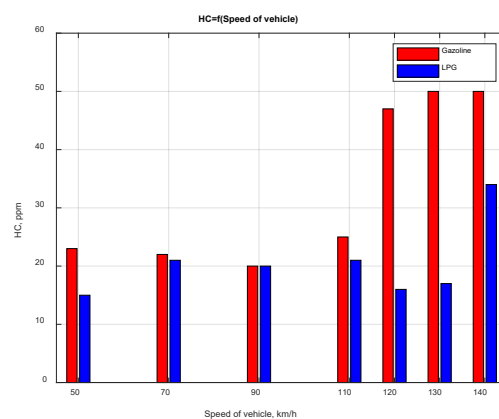


Fig. 9. Experimental study of the content of CH, [ppm] in the exhaust gases of a car Honda Civic Aerodeck 1.5 iLS.

The measurements of the air/fuel ratio (AFR) and  $\lambda$  are presented as shown by the Dyno Cosber 4000 software.

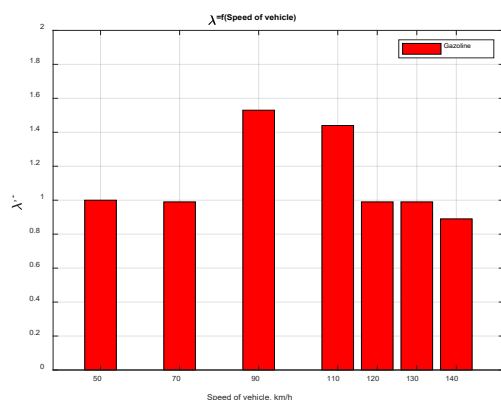


Fig. 10. Experimental study of the content of  $\lambda$  in the exhaust gases of a car Honda Civic Aerodeck 1.5 iLS.

The content of carbon monoxide depends mostly on the value of the air/fuel ratio. The content of hydrocarbons in the exhaust gases depends on both the value of the AFR and the ignition advance angle.

Figure 7 shows that the highest values of carbon monoxide in the exhaust gases are observed when the car motion speed is 140 km/h. In this case  $\lambda=0,89$  (when the engine operates on gasoline). When the engine runs on gasoline, the value of carbon oxides is 41,59% lower than when it works on LPG. The lowest values of carbon monoxide in the exhaust gases are registered at a car motion speed of 90 km/h.

Figure 8 indicates that the highest values of  $\text{CO}_2$  in the exhaust gases when the engine runs on gasoline or LPG are observed at the car motion speed of 130 km/h, and the lowest values are registered when the car motion speed is 90 km/h. There are no big differences in the measured value of carbon dioxide at different vehicle speeds.

Figure 9 illustrates that the highest values of hydrocarbons in the exhaust gases are reached when the car motion speed is 140 km/h. In this case  $\lambda=0,89$  (when the engine runs on gasoline). When the engine operates on LPG at a vehicle speed of 140 km/h, the value of hydrocarbons is 32% lower than when it runs on gasoline. The lowest values of hydrocarbons in the exhaust gases are observed at a car motion speed of 90 km/h.

In general, the nature of the change in the content of harmful components in the exhaust gases at different car speeds follows almost a similar pattern. The observed differences are due to a suboptimal multiplier map for the gas ECU.

#### IV. CONCLUSIONS

From the study of toxic components in the exhaust gases, the following conclusions and suggestions could be pointed out:

1. When driving at a constant speed and the engine is running in the mode “lean burn control“ i.e.  $\lambda>1$ , the amount of measured harmful components in the exhaust

gases is lower. The most significant difference is observed for carbon monoxide.

2. During the operation of a car engine at a constant rpm (constant car speed) with a LPG the amount of hydrocarbons in the exhaust gases is lower than it is when working with gasoline.

3. The use of an additional device to control the ignition advance angle when the engine runs on LPG will lead to lower CO values and thus improve the environmental performance of the engine.

4. For more accurate determination of fuel-air mixtures when the engine is runs on LPG, it may be recommended to use an LPG electronic control unit, which has communication on the diagnostic socket via the appropriate diagnostic communication protocol.

#### ACKNOWLEDGMENTS

This work was supported by the European Regional Development Fund within the OP “Science and Education for Smart Growth 2014 - 2020”, Project Competence Centre “Smart Mechatronic, Eco- And Energy Saving Systems and Technologies“, № BG05M2OP001-1.002-0023.

#### REFERENCES

- [1] A. Tashev and E. Dimitrov. “LPG effect on performance parameters of diesel engine operated on dual-fuel mode”. AIP Conference Proceedings, Volume 2449, Issue 1 (10.1063/5.0091488), [Online]. Available: <https://aip.scitation.org/doi/abs/10.1063/5.0091488>, 2022.
- [2] G. Palagachev. “Study of statistical characteristics of the carbon monoxide (CO) and the air ratio ( $\lambda$ ) in the exhaust gases of petrol engines”. AIP Conference Proceedings, Volume 2449, Issue 1 (10.1063/5.0103050), [Online]. Available: <https://aip.scitation.org/doi/abs/10.1063/5.0103050>, 2022.
- [3] P. Bhale, P. Ardhapurkar and N. Deshpande. Experimental Investigations to Study the Comparative Effect of LPG and Gasoline on Performance and Emissions of SI Engine, ASME 2005 Internal Combustion Engine Division Spring Technical Conference, DOI:10.1115/ICES2005-1065, January 2005.
- [4] T. Tasic, P. Pogorevc and T. Brajlilh, Gasoline and lpg exhaust emissions comparison, Advances in Production Engineering & Management 6 (2011) 2, 87-94, ISSN 1854-6250.
- [5] Bosch Motorsport, “Lambda Sensor LSU 4.9”, March 2023. [Online]. Available: <https://www.bosch-motorsport.com/content/downloads/Raceparts/en-GB/51865867208058251.html> [Accessed: March 25, 2023].
- [6] 4WD Leistungsprüfstand DynoCosber 4000, March 2023. [Online]. Available: <https://www.cosber.de/de/catalog/product/view/id/472236> [Accessed: March 25, 2023].
- [7] Gas Analyser DEK DG-04IR, March 2023. [Online]. Available: <https://www.dek.bg/main-en.php?action=diag&topic=DG04IR> [Accessed March 25, 2023].
- [8] 1998 Honda Civic Aerodeck 1.5i S (man. 5) (model since mid-year 1998 for Europe ) car specifications & performance data review. [Online]. Available: [https://www.automobile-catalog.com/car/1998/1118360/honda\\_civic\\_aerodeck\\_1\\_5i\\_s.htm#gsc.tab=0](https://www.automobile-catalog.com/car/1998/1118360/honda_civic_aerodeck_1_5i_s.htm#gsc.tab=0) [Accessed March 25, 2023].

# Thermal Characteristics of Materials in Modelling of Welding Processes

Valentin Anguelov

Center of welding (IMSETCHA) "Acad. A. Balevski"

Bulgarian Academy of Sciences

Sofia, Bulgaria

valentin.anguelov@ims.bas.bg

**Abstract.** The application of welding processes during manufacturing of metallic products result in changes of the properties of the base materials. Process simulation enables evaluation of the effect of heat application in proximity to the weld seam. The availability and use of input data, relevant for the specific material, is essential for the reliability of the results. The thermal characteristics of the materials, required for the heat modelling were identified. Their dependency on the material temperature was investigated and the formulas were presented. Particular values were found in existing data sources, for specific structural steels, stainless steels, nickel and titanium alloys. The values of the thermal characteristics were represented and in graphical and tabulated formats, facilitating direct implementation in calculations, assessment of variation trends and applicability for specific purposes.

**Keywords:** thermal characteristic, modelling, welding process.

## I. INTRODUCTION

The properties of the welded joints could not be assessed in full after the completion of the structures manufacturing. Welding is a special process [1] and control before, during and after the completion of the works is necessary, if comprehensive quality requirements are to be met [2]. In fusion welding a heat source or sources are applied to the material, melting and joining the neighbouring parts. The increase of the temperature from an initial value ( $T_0$ ) is very fast, and the decrease of the temperature is slower, depending on variable conditions, process and material characteristics. Standard recommendations regarding the process variables [3], [4] are issued for the most common materials, like ferritic steels, and information is provided by the manufacturers of advanced materials [5]. The common evaluation is based on calculation or estimation of the cooling time in the temperature range between 800 and 500 °C, the  $t_{8/5}$  time.

The calculation of the cooling time is possible according to standard formulas, valid under limited range of values of essential variables, defines by the standards [4], [6]. For example, a three-dimensional heat dissipation the equation was formulated:

$$t_{8/5} = (6700 - 5 \cdot T_0) \cdot Q \cdot \left( \frac{1}{500 - T_0} - \frac{1}{800 - T_0} \right) \cdot F3 \quad (1)$$

where:

$T_0$  – initial temperature of the material,

$Q$  – heat input,

$F3$  – seam geometrical factor.

The properties of the materials are not considered in (1), and the formula is only valid for ferritic steels.

The cooling time  $t_{8/5}$  is calculated in the immediate proximity to the weld seam, where the cooling rate is the highest. This area is considered as the most vulnerable to base material properties deterioration.

During the welding process, the  $t_{8/5}$  is regulated by controlled application of heat at specified initial temperature. At process qualification, the resulting material properties are checked by non-destructive and destructive tests on sample pieces.

This simplified approach is applicable to limited range of standard conditions. The zone of the base material, affected by the heat (HAZ) is of complicated three dimensional shapes. The properties in the volume of the HAZ vary in each direction. More detailed analysis is necessary in the cases of welding conditions outside of the limits defined by the standard [3]; for materials of chemical composition outside the defined limits; of special properties obtained by a manufacturing treatment, that could be influenced by the heat; in cases of significant importance of the structure built and in all cases when the standard approach results should be additionally verified.

Print ISSN 1691-5402

Online ISSN 2256-070X

<https://doi.org/10.17770/etr2023vol3.7202>

© 2023 Valentin Anguelov. Published by Rezekne Academy of Technologies.

This is an open access article under the [Creative Commons Attribution 4.0 International License](https://creativecommons.org/licenses/by/4.0/).

The modeling of the welding requires reliable data in order to achieve simulations in close agreement to the real process results.

## II. MATERIALS AND METHODS

### A. Overview

The simulation of the temperature profile includes building of appropriate model of the heat source (e.g. welding arc, laser beam), simulation of the heat flow within the base materials volume, as well as to and from the surrounding ambience.

The execution, validation and verification workflow of the numerical welding simulation was standardized in [7]. The application of the models and the methods used were described in a significant number of scientific papers, including [8], [9] and [10].

The simulation of the temperature profile includes building of appropriate model of the heat source (e.g. welding arc, laser beam), simulation of the heat flow within the base materials volume, as well as to and from the surrounding ambience.

The heat transfer equation,

$$\nabla^2 T = \rho \cdot \frac{c_p}{k} \cdot \frac{\delta T}{\delta t} \quad (2)$$

was initially solved for the welding processes as in [11]. It was developed in [12] as

$$c_p \cdot \rho \cdot \frac{\delta T}{\delta t} = k \cdot \left( \frac{\delta^2 T}{\delta x^2} + \frac{\delta^2 T}{\delta y^2} + \frac{\delta^2 T}{\delta z^2} \right) + q \quad (3)$$

Formulation for FEA solution was presented in [13] and depending on the welding process, developed in order to represent the specific heat source in the best way (e.g. in [14] and [15]).

### B. Modeling Input Data

In all solutions, the required input data includes:

- Process parameters, including power (i.e. welding current and voltage of arc welding), movement speed and process efficiency.

The process parameters are measured during the process or values of the parameters are decided, in order to create simulation of the changes influence. Initial values of the process efficiency could be obtained in [6]. The value of the process efficiency is used for process calibration.

- Heat source parameters, including shape and power distribution.

Multiple solutions of the heat source characteristics were developed, as described in [16]. The values of the heat source parameters are used for process calibration.

- Geometry parameters, including size of the work-piece, distance of the heat application from the edges of

the material, distance of the FEM points from the heat source.

The geometry parameters are measured or variations of the values are decided, in order to create simulation of the changes influence.

- Material characteristics, including:

$C_p$  – specific heat capacity at constant pressure,

$k$  - thermal conductivity and,

$\rho$  - material density.

### C. Material Characteristics

The specific heat capacity of a material is the amount of heat required to rise the temperature of 1 kg of mass by 1 K ( $^{\circ}\text{C}$ ) [21]:

$$Q = m \cdot C \cdot (T_2 - T_1) \quad (4)$$

where  $Q$  is the amount of heat,  $m$  is the mass,  $T_1$  and  $T_2$  are the initial and final temperatures.

$C$  is the commonly used symbol for the heat capacity, or  $C_p$  if considered at constant pressure, with unit of measurement ( $\text{J}/(\text{kg}\cdot\text{K}) \equiv \text{J}/(\text{kg}\cdot^{\circ}\text{C})$ ).

The thermal conductivity coefficient is regarded in [17]. Fourier's law defines the quantity of heat diffusing through a unit surface during a unit of time within a material subjected to a temperature gradient:

$$q = -k \cdot \nabla T \quad (5)$$

where  $k$  is the commonly used symbol for thermal conductivity, with unit of measurement  $\text{W}/(\text{m}\cdot\text{K}) \equiv \text{W}/(\text{m}\cdot^{\circ}\text{C})$ .

The density of the materials is commonly represented by the symbol  $\rho$  in units of  $\text{kg}/\text{m}^3$ .

The above characteristics are specific to each material, according to the chemical composition and internal structure and depending on the temperature value and heating rate [18].

The present investigation was targeted at the thermal characteristics of weldable metallic materials, in range representing temperatures of the base material and the heat affected zone in the period of time preceding and successive to the application of heat by a moving source. Commonly used grades of structural, low alloyed and stainless steel, nickel and titanium alloys were investigated. The range between  $-100\text{ }^{\circ}\text{C}$  to  $1400\text{ }^{\circ}\text{C}$  was considered.

### D. Data sources of thermal characteristics of the metallic materials

Limited information regarding the thermal characteristic of specific metallic material is readily available. The following types of data sources were identified:

- Regulatory specifications, including EU and USA standards and codes [19], [20]. The data includes empirical formulas of the structural carbon and stainless steel thermal characteristics at temperature ranges. The data provided in the specifications is compulsory to be considered, when calculating the properties of materials, used in construction.
- Data bases of the modelling software. The welding processes modelling software [21], [22] allows for definition of the material properties as constant, as dependent variable defined by the user, or as a data to be obtained from built-in data bases. The data in the bases built in the modelling software is limited to their material libraries.
- Data, provided by educational and research institutions [23], [24]. The data is limited to specific materials that were subject to research. In cases of different results obtained by different researchers, both results were presented in [25].
- Data provided by material manufacturers [26]. The data is limited to the materials of each steel producer.
- Other public data bases. Multiple public data bases are available online, providing information about the materials thermal characteristics. Some of the data bases provide general information, like in [27] and [28], other provide specific information, according to referenced sources [29], while some of the data was false [30].

### III. RESULTS AND DISCUSSION

#### *A. Relations of material density, specific heat capacity and thermal conductivity to temperature*

In data sources [19], [22], [27] and [29], the values of the material properties are presented as constants or by use of empirical formula calculations, depending on the temperature, as in Table 1, Table 2 and Table 3.

TABLE 1 CONSTANTS AND EMPIRICAL FORMULAS OF MATERIAL DENSITY

Material	Temperature range, °C	Density $\rho$ (T), kg/m <sup>3</sup>	Source
S 355 J2, S 690 QL	All	Constant, 7850	[19]
	All	Constant, 7800	[27]
	(-100) to 704	$7911.3 - 0.01678428 \cdot T - 8.018711 \cdot 10^{-4} \cdot T^2 + 1.172796 \cdot 10^{-6} \cdot T^3 - 1.015971 \cdot 10^{-9} \cdot T^4 + 3.677737 \cdot 10^{-13} \cdot T^5$	[22]
	704 to 788	$7116.994 + 0.5195388 \cdot T$	
	788 to 871	$8166.523 - 0.4696497 \cdot T$	
	871 to (1400)	Constant, 7630	
	All	Constant, 7850	[29]
X5CrNi18-10 (304)	All	Constant, 7850	[19]
	All	Constant, 7800	[27]
	(-100) to 1427	$7945.333 - 0.1981948 \cdot T - 3.713764 \cdot 10^{-4} \cdot T^2 + 2.213069 \cdot 10^{-7} \cdot T^3 - 5.128456 \cdot 10^{-11} \cdot T^4$	[22]
	All	Constant, 8000	[29]
X2CrNiMoN22-5-3 (2205)	All	Constant, 7850	[19]
	All	Constant, 7800	[27]
	(-100) to 20	Constant, 7790	[22]
	20 to 400	$7871.9 - 0.1918817 \cdot T - 2.088029 \cdot 10^{-4} \cdot T^2 + 8.9339 \cdot 10^{-8} \cdot T^3$	
	400 to (1400)	Constant, 7675	
	All	Constant, 7800	[29]

TABLE 1 (CONT.) CONSTANTS AND EMPIRICAL FORMULAS OF MATERIAL DENSITY

Material	Temperature range, °C	Density $\rho$ (T), kg/m <sup>3</sup>	Source
NiCr22Mo9Nb (Inconel 625)	All	Constant, 8600	[27]
	(-100) to -20	$8308.627 + 0.0376521 \cdot T - 0.001256698 \cdot T^2 + 1.529227 \cdot 10^{-6} \cdot T^3$	[22]
	-20 to 927	$8339.072 - 0.3000351 \cdot T + 2.796812 \cdot 10^{-6} \cdot T^2 - 5.001998 \cdot 10^{-8} \cdot T^3$	
	927 to (1400)	Constant, 7900	
	All	Constant, 8440	[29]
NiCu30Fe (Monel 400)	All	Constant, 8600	[27]
	(-100) to 1093	$8886.029 - 0.2533148 \cdot T - 1.860111 \cdot 10^{-4} \cdot T^2 + 4.094544 \cdot 10^{-8} \cdot T^3$	[22]
	1093 to (1400)	Constant, 8300	
	All	Constant, 8440	[29]
Titan 99.8 (Titan Grade 1)	All	Constant, 4500	[27]
	(-100) to 871	$4534.619 - 0.1176636 \cdot T + 2.570905 \cdot 10^{-6} \cdot T^2 - 1.218339 \cdot 10^{-8} \cdot T^3$	[22]
	871 to (1400)	Constant, 4385	
	All	Constant, 4500	[29]
TiAl6V4 (Titan Grade 5)	All	Constant, 4450	[27]
	(-100) to 27	$4452.817 + 0.02869485 \cdot T - 6.448869 \cdot 10^{-4} \cdot T^2 + 9.646377 \cdot 10^{-7} \cdot T^3 - 1.720215 \cdot 10^{-11} \cdot T^4$	[22]
	27 to 760	$4467.094 - 0.119171 \cdot T - 1.275079 \cdot 10^{-5} \cdot T^2$	
	760 to (1400)	Constant, 4330	
	All	Constant, 4430	[29]

TABLE 2 CONSTANTS AND EMPIRICAL FORMULAS OF SPECIFIC HEAT CAPACITY

Material	Temperature range, °C	Specific heat capacity at constant pressure $C_p$ (T), J/(kg °C)	Source
S 355 J2, S 690 QL	(-100) to 20	Constant, 443	[19]
	20 to 600	$425 + 0.773 \cdot T - 0.00169 \cdot T^2 + 2.22T \cdot 10^{-6} \cdot T^3$	
	600 to 735	$666 + \left( \frac{13002}{738 - T} \right)$	
	735 to 900	$545 + \left( \frac{17820}{T - 731} \right)$	
	900 to (1400)	Constant, 650	
	All	Constant, 470	[27]
	(-100) to 20	Constant, 500	[22]
	20 to 575	$-215.730638 + 6.0184999 \cdot T - 0.0183429321 \cdot T^2 + 2.414973 \cdot 10^{-5} \cdot T^3 - 1.07882432 \cdot 10^{-8} \cdot T^4$	
	575 to (1400)	Constant, 840	
	All	Constant, 470	[29]

TABLE 2 (CONT.) CONSTANTS AND EMPIRICAL FORMULAS OF SPECIFIC HEAT CAPACITY

Material	Temperature range, °C	Specific heat capacity at constant pressure Cp (T), J/(kg °C)	Source
X5CrNi18-10 (304)	All	$450 + 0.280 \cdot T - 2.91 \cdot 10^{-4} \cdot T^2 + 1.34 \cdot 10^{-7} \cdot T^3$	[19]
	All	Constant, 470	[27]
	(-100) to 37	$270.215 - 1.210511 \cdot T + 0.02151566 \cdot T^2 - 7.511841 \cdot 10^{-5} \cdot T^3 + 8.136796 \cdot 10^{-8} \cdot T^4$	[22]
	37 to 1038	$109.2073 + 2.571775 \cdot T - 0.006528099 \cdot T^2 + 7.787524 \cdot 10^{-6} \cdot T^3 - 4.167913 \cdot 10^{-9} \cdot T^4 + 8.090613 \cdot 10^{-13} \cdot T^5$	
	1038 to (1400)	Constant, 630	[29]
	All	Constant, 470	
X2CrNiMoN22-5-3 (2205)	All	Constant, 480	[27]
	(-100) to 20	Constant, 482	[22]
	20 to 400	$429.285931 + 0.130317584 \cdot T + 1.56721552 \cdot 10^{-4} \cdot T^2$	
	400 to (1400)	Constant, 587	[29]
	100	Constant, 530	
NiCr22Mo9Nb (Inconel 625)	All	Constant, 440	[27]
	(-100) to 20	Constant, 410	[22]
	20 to 700	$337.05099 + 0.247120722 \cdot T$	
	700 to (1400)	Constant, 580	[29]
	All	Constant, 410	
NiCu30Fe (Monel 400)	All	Constant, 439	[27]
	(-100) to 315	$-100.987409 + 4.83633162 \cdot T - 0.0170401517 \cdot T^2 + 2.74397264 \cdot 10^{-5} \cdot T^3 - 1.63381644 \cdot 10^{-8} \cdot T^4$	[22]
	315 to (1400)	Constant, 477	[29]
	All	Constant, 427	
Titan 99.8 (Titan Grade 1)	All	Constant, 540	[27]
	(-100) to 27	$-167.746811 + 7.08658306 \cdot T - 0.0297849253 \cdot T^2 + 6.04477124 \cdot 10^{-5} \cdot T^3 - 4.76258862 \cdot 10^{-8} \cdot T^4$	[22]
	27 to 627	$464.052042 + 0.152465588 \cdot T + 2.12593015 \cdot 10^{-4} \cdot T^2 - 1.72017085 \cdot 10^{-7} \cdot T^3$	
	627 to 883	$-33066.629 + 136.77383 \cdot T - 0.204810858 \cdot T^2 + 1.335041 \cdot 10^{-4} \cdot T^3 - 3.17182178 \cdot 10^{-8} \cdot T^4$	
	883 to (1400)	$352.825758 + 0.123047884 \cdot T + 6.65722934 \cdot 10^{-5} \cdot T^2$	[29]
	200	Constant, 560	
TiAl6V4 (Titan Grade 5)	All	Constant, 523	[27]
	(-100) to 30	$-167.173226 + 6.75429814 \cdot T - 0.0235237743 \cdot T^2 + 2.95625708 \cdot 10^{-5} \cdot T^3$	[22]
	30 to (1400)	$383.351385 + 0.670881806 \cdot T - 5.35234016 \cdot 10^{-4} \cdot T^2 + 1.63517247 \cdot 10^{-7} \cdot T^3$	

TABLE 3 CONSTANTS AND EMPIRICAL FORMULAS OF THERMAL CONDUCTIVITY

Material	Temperature range, °C	Thermal conductivity k (T), W/(m °C)	Source
S 355 J2, S 690 QL	(-100) to 20	Constant, 53.35	[19]
	20 to 800	$54 - 0.0333 \cdot T$	
	800 to (1400)	Constant, 27.3	
	All	Constant, 51	[27]
	(-100) to 20	Constant, 53	[22]
	20 to 800	$56.38699 - 0.00728786 \cdot T - 1.988814 \cdot 10^{-5} \cdot T^2$	
	800 to 1200	$-82.99624 + 0.1669461 \cdot T - 6.125136 \cdot 10^{-5} \cdot T^2$	
	1200 to (1400)	Constant, 30	
	All	Constant, 52	[29]
X5CrNi18-10 (304)	(-100) to 0	Constant, 14.6	[19]
	0 to 1200	$14.6 + 0.0127 \cdot T$	
	1200 to (1400)	Constant, 30	
	All	Constant, 16	[27]
	(-100) to 20	$-1.031521 + 0.1813807 \cdot T - 1.088656 \cdot 10^{-3} \cdot T^2 + 3.411681 \cdot 10^{-6} \cdot T^3 - 3.988389 \cdot 10^{-9} \cdot T^4$	[22]
	20 to (1400)	$6.742253 + 0.02864915 \cdot T$	[29]
	100	16.2	
	500	21.5	
X2CrNiMoN22-5-3 (2205)	(-100) to 0	Constant, 14.6	[19]
	0 to 1200	$14.6 + 0.0127 \cdot T$	
	1200 to (1400)	Constant, 30	
	All	Constant, 27	[27]
	(-100) to 20	Constant, 14.24	[22]
	20 to 400	$7.134798 + 0.02746063 \cdot T - 1.233173 \cdot 10^{-5} \cdot T^2$	
	400 to (1400)	Constant, 20	
	100	16	[29]
	300	18	
400	20		
NiCr22Mo9Nb (Inconel 625)	All	Constant, 10	[27]
	(-100) to 982	$5.482405 + 0.01380594 \cdot T + 1.678069 \cdot 10^{-6} \cdot T^2$	[22]
	982 to (1400)	Constant, 25.5	[29]
	All	Constant, 9.9	
NiCr22Mo9Nb (Inconel 625)	All	Constant, 23	[27]
	(-100) to 982	$14.14109 + 0.02732033 \cdot T + 2.257259 \cdot 10^{-6} \cdot T^2$	[22]
	982 to (1400)	Constant, 52	[29]
	All	Constant, 21.8	

TABLE 3 (CONT.) CONSTANTS AND EMPIRICAL FORMULAS OF THERMAL CONDUCTIVITY

Material	Temperature range, °C	Thermal conductivity k (T) , W/(m °C)	Source
Titan 99.8 (Titan Grade 1)	All	Constant, 20	[27]
	(-100) to 53	$58.17412 - 0.4851624 \cdot T + 0.00288092 \cdot T^2 - 8.255595 \cdot 10^{-6} \cdot T^3 + 8.903946 \cdot 10^{-9} \cdot T^4$	[22]
	53 to 704	$41.95804 - 0.1227486 \cdot T + 2.33331 \cdot 10^{-4} \cdot T^2 - 1.937431 \cdot 10^{-7} \cdot T^3 + 6.191111 \cdot 10^{-9} \cdot T^4$	
	704 to (1400)	$15.13513 + 0.004158454 \cdot T + 1.376649 \cdot 10^{-6} \cdot T^2$	
	All	Constant, 26	[29]
TiAl6V4 (Titan Grade 5)	All	Constant, 7.11	[27]
	(-100) to 38	$0.1560505 + 0.07648919 \cdot T - 2.883179 \cdot 10^{-4} \cdot T^2 + 3.68138 \cdot 10^{-7} \cdot T^3$	[22]
	38 to 538	$8.114005 - 0.01485211 \cdot T + 4.468662 \cdot 10^{-5} \cdot T^2 - 2.273481 \cdot 10^{-8} \cdot T^3$	
	538 to (1400)	Constant, 13.32	

*B. Graphical presentation of the physical properties of the materials*

The presentation of the physical properties values allow for the visual perception of the range of deviations in the material properties data, as well as for visualization of the values development with temperature changes, as well as transition points and extremes.

In all graphics, the data sourced were represented in the following styles:

- [22]
- - - - [19]
- · - · [27]
- - - - [29]

- S 355J2 structural steel, acc. to EN 10025-2.  
 Similar to: 1.0577, ASTM A572 gr.50, GB Q355D

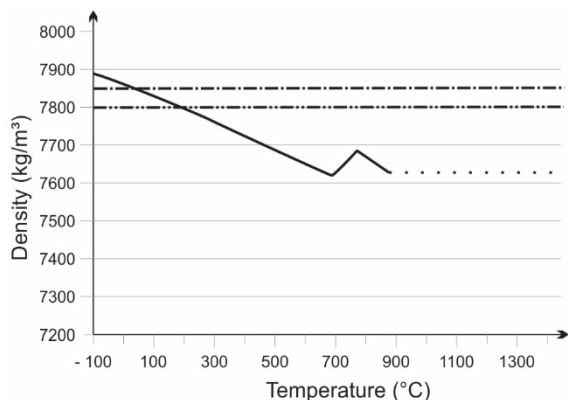


Fig. 1a Density of S 355 J2 structural steel.

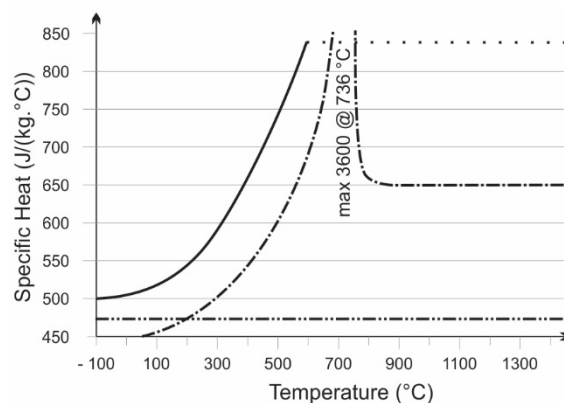


Fig. 1b Specific heat capacity of S 355 J2 steel.

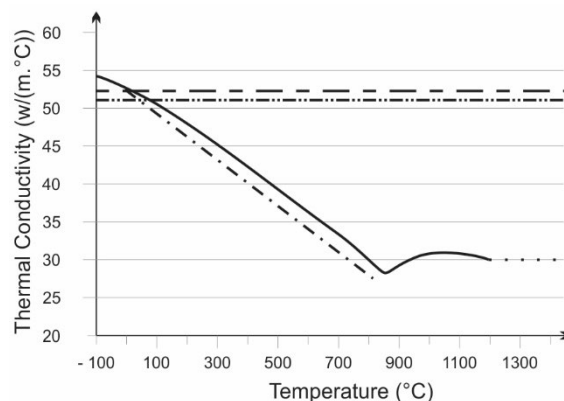


Fig. 1c Thermal conductivity of S 355 J2 steel.

- S 690 QL structural steel, acc. to EN 10025-6  
 Similar to: 1.8928, TSStE 690 V, GB Q690E

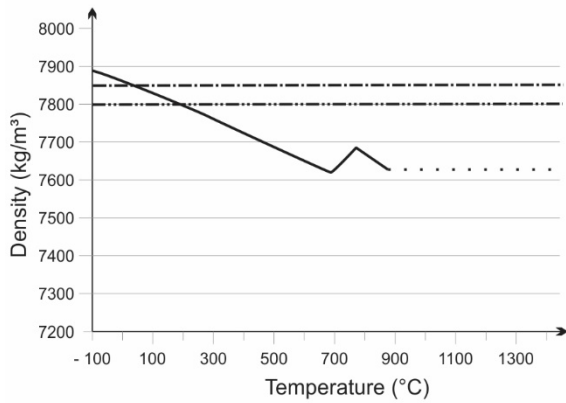


Fig. 2a Density of S 690 QL structural steel.

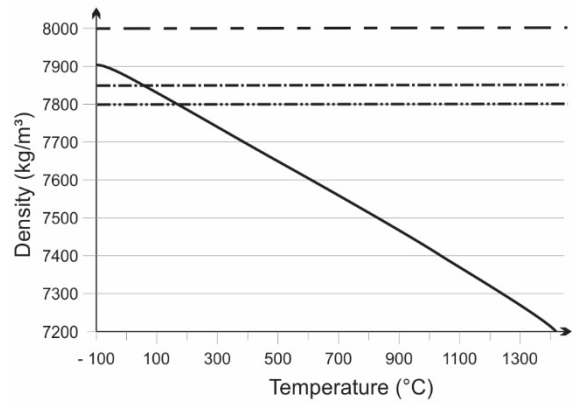


Fig. 3a Density of X5CrNi18-10 stainless steel.

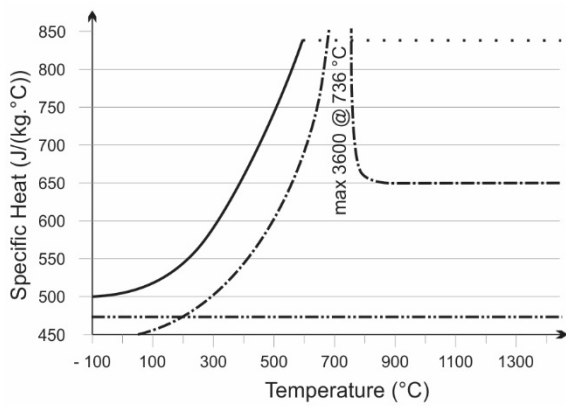


Fig. 2b Specific heat capacity of S 690 QL steel.

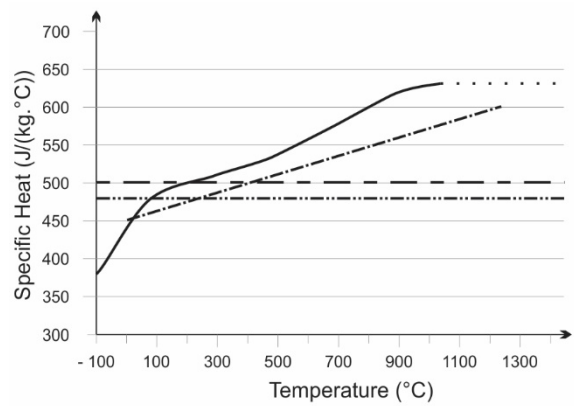


Fig. 3b Specific heat capacity of X5CrNi18-10 steel.

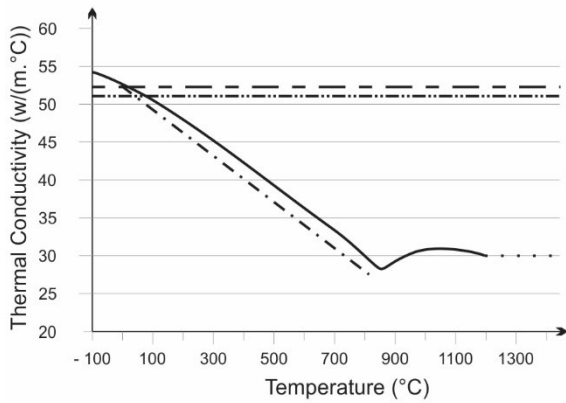


Fig. 2c Thermal conductivity of S 690 QL steel.

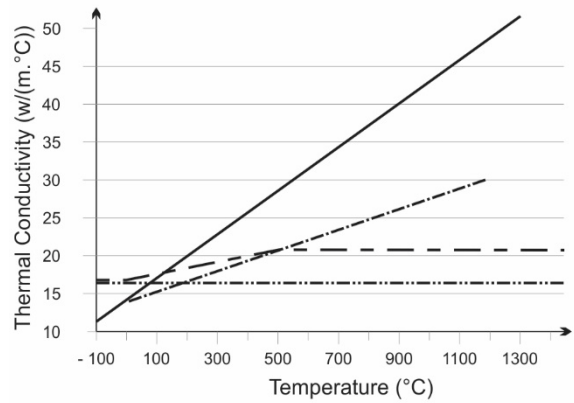


Fig. 3c Thermal conductivity of X5CrNi18-10 steel.

- X5CrNi18-10 stainless steel acc. to EN 10088-2  
Similar to: 1.4301, ASTM 304

- X2CrNiMoN22-5-3 duplex stainless steel acc. to EN 10088-2  
Similar to: 1.4462, ASTM 2205

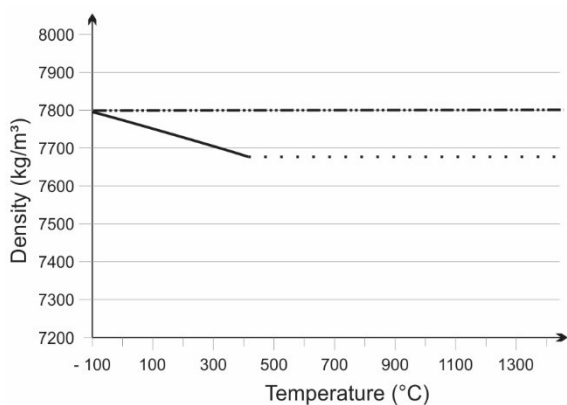


Fig. 4a Density of X2CrNiMoN22-5-3 duplex steel.

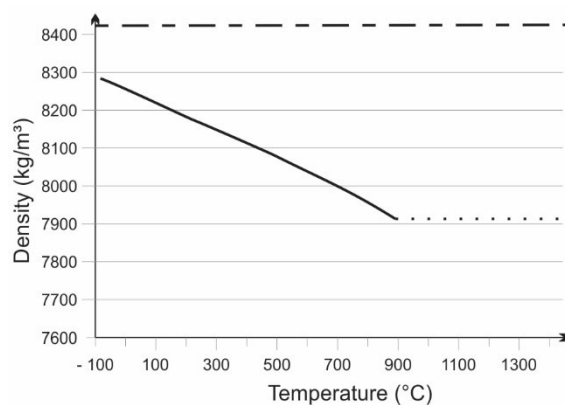


Fig. 5a Density of NiCr22Mo9Nb nickel alloy.

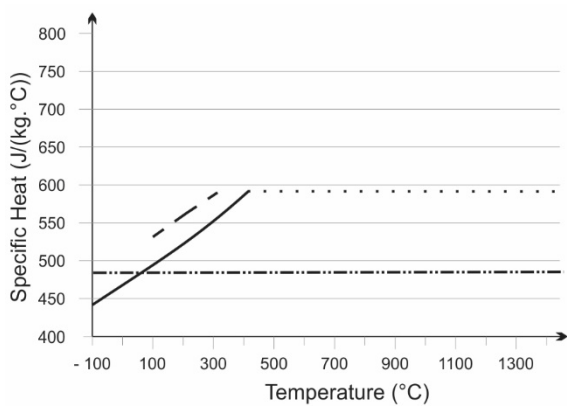


Fig. 4b Specific heat capacity of X2CrNiMoN22-5-3.

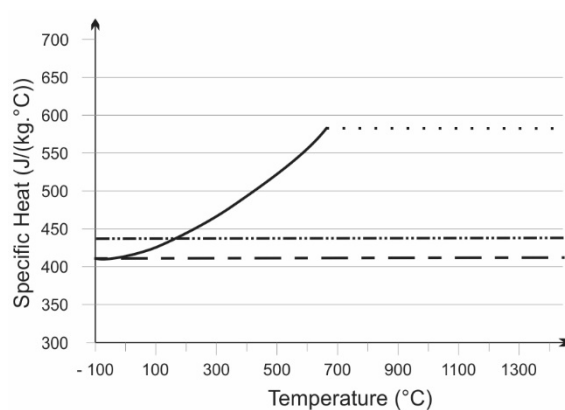


Fig. 5b Specific heat capacity of NiCr22Mo9Nb.

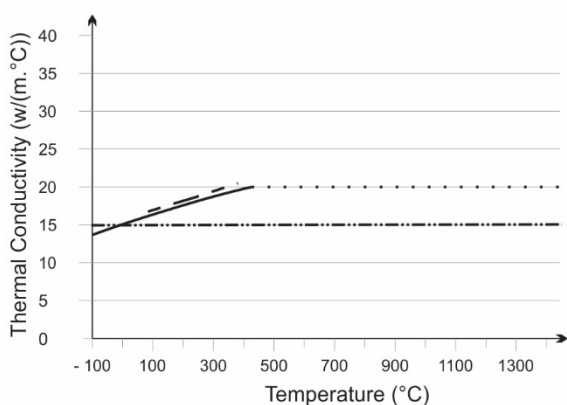


Fig. 4c Thermal conductivity of X2CrNiMoN22-5-3.

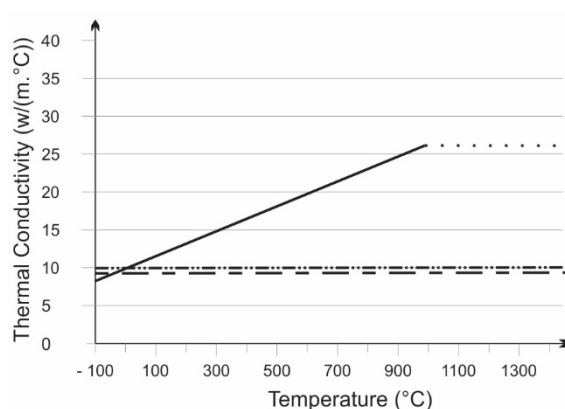


Fig. 5c Thermal conductivity of NiCr22Mo9Nb.

- NiCr22Mo9Nb nickel alloy acc. to EN 10095  
 Similar to: 2.4856, Inconel 625

- NiCu30Fe acc. to DIN 17443  
 Similar to: 2.4360, Monel 400

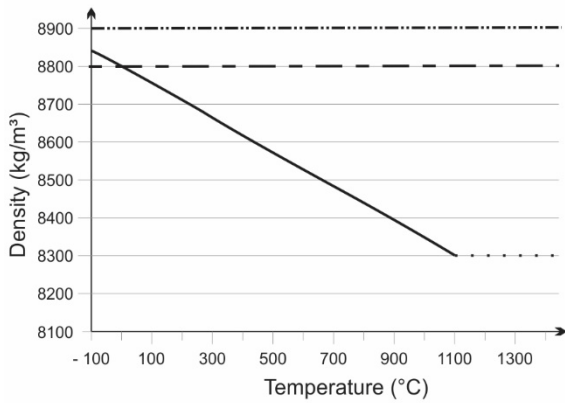


Fig. 6a Density of NiCu30Fe nickel alloy.

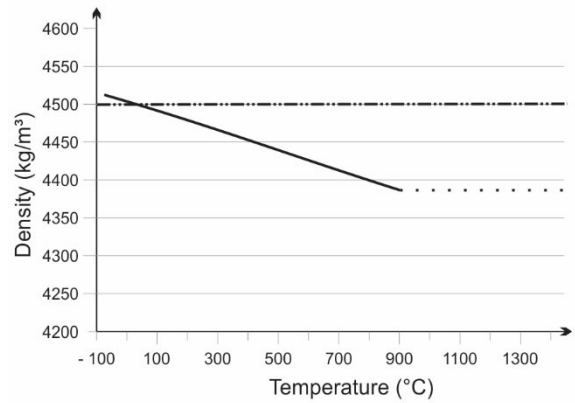


Fig. 7a Density of Ti 99.8 (Titan Grade 1).

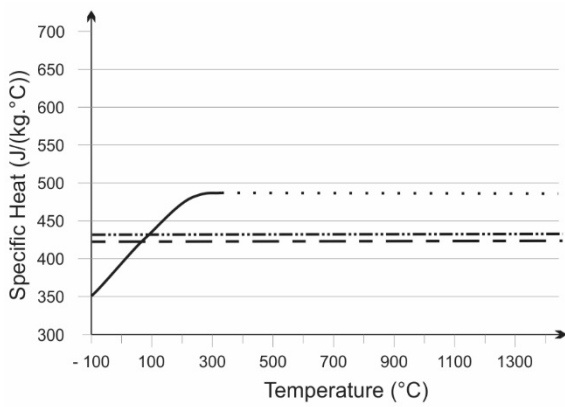


Fig. 6b Specific heat capacity of NiCu30Fe.

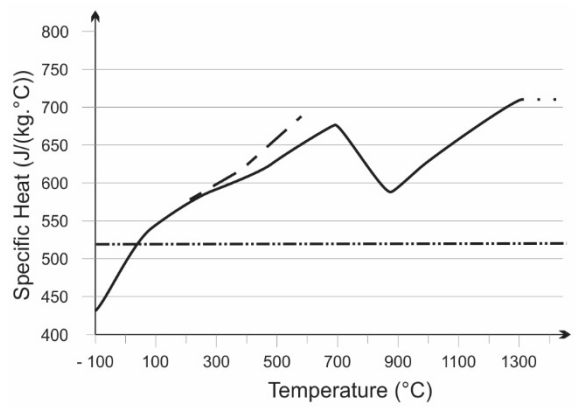


Fig. 7b Specific heat capacity of Ti 99.8.

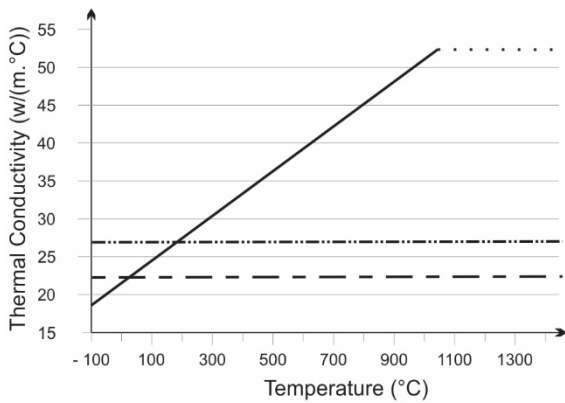


Fig. 6c Thermal conductivity of NiCu30Fe.

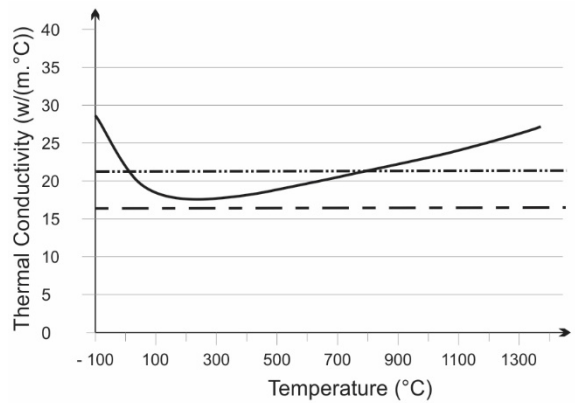


Fig. 7c Thermal conductivity of Ti 99.8.

- Titan Grade 1, Ti 99.8  
Similar to: 3.7025, ASTM B-265

- Titan Grade 5, TiAl6V4  
Similar to: 3.7165

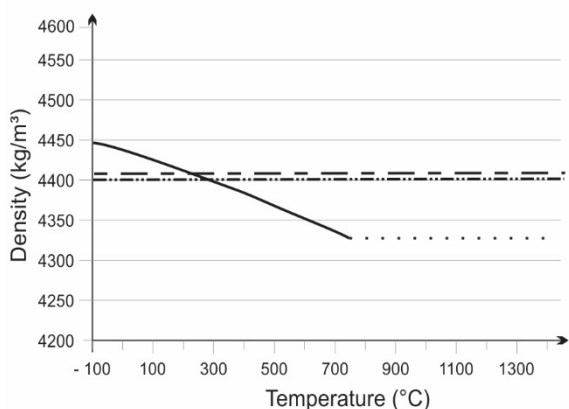


Fig. 8a Density of TiAl6V4, (Titan Grade 5).

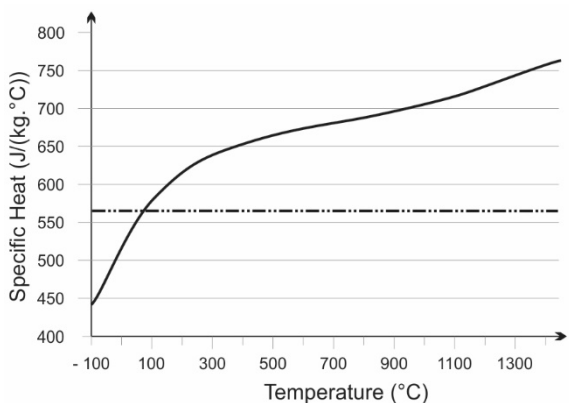


Fig. 8b Specific heat capacity of TiAl6V4.

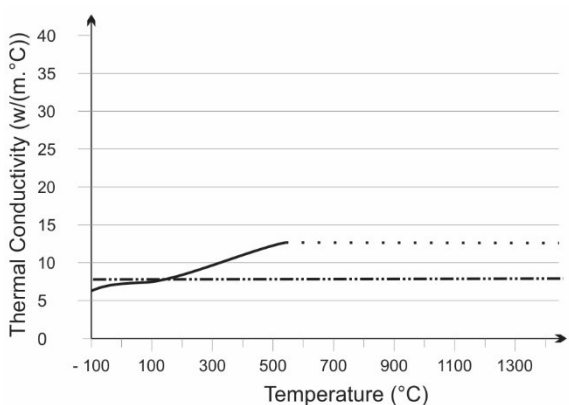


Fig. 8c Thermal conductivity of Ti 99.8.

#### IV. CONCLUSIONS

For the most common material types there are multiple sources of available data, obtained through experiments, by calculations according to empirical formulas or by estimations based on chemical and structural similarity. The application of the particular source of material properties data in model building

should consider the purpose and the application of the simulation results.

Estimation could be appropriate source of data for purpose of investigating trends and general influences.

In cases when high level of reliability or accuracy of the model results is required, input information from verified sources should be used and experimental confirmation should be considered, for the particular material type, grade, origin, manufacturing lot, and in conditions equivalent to the actual application conditions.

It should be noted, that for some types of steels there are significant differences of the material properties data, e.g. in the specific heat capacity of the structural carbon steels. The calculations according to Eurocode 3 [19] show extreme value of 3600 J/(kg °C) at 735 °C, compared to values between 400 J/(kg °C) and 800 J/(kg °C), from [22], [27] and [19]. The reason of the deviation is that in the Eurocode 3 the influence of the phase transformation energy effects were considered in a more focused way.

As visible on Fig 1 (a, b, c) and Fig 2 (a, b, c), the Eurocode do not differentiate the properties of the different grades of structural steels. The assessment of the thermal properties of structural steels described in [35] and [36] showed differences in the material properties, calculated according to Eurocode 3 [19] and the data obtained by experiments, for different grades of structural steels.

In critical applications, the use of the input data, provided by the regulations is compulsory. More than one model results, relevant to building structures, should be obtained and evaluated: according to the standard, according to data sources considered as reliable and according to test data.

#### ACKNOWLEDGMENTS

The authors are grateful to the financial support of the Bulgarian National Science Fund, Contract No KP-06-H57/10, for carrying out the necessary research.

#### REFERENCES

- [1] International Organization for Standardization Technical Committee 176, Quality management systems — Fundamentals and vocabulary, ISO 9000, 2015.
- [2] International Organization for Standardization Technical Committee 44, Quality requirements for fusion welding of metallic materials — Part 2: Comprehensive quality requirements, ISO 3834-2, 2021.
- [3] European Committee for Standardization Technical Committee 121, EN 1011-1, Welding. Recommendations for welding of metallic materials. General guidance for arc welding, 2009.
- [4] European Committee for Standardization Technical Committee 121, EN 1011-2, Welding. Recommendations for welding of metallic materials. Arc welding of ferritic steels, 2001.
- [5] Swedish Steel AB, 299 Welding of Strenx. Advanced High Strength Steels. V1, 2015, p 7.
- [6] Stahlinstitut VDEh, Stahl-Eisen-Werkstoffblatt 088 Beiblatt 2: Schweißgeeignete Feinkornbaustähle - Richtlinien für die Verarbeitung, besonders für das Schmelzschweißen; Ermittlung

- der Abkühlzeit  $t_{8/5}$  zur Kennzeichnung von Schweißtemperaturzyklen.
- [7] International Organization for Standardization Technical Committee 44, Numerical welding simulation — Execution and documentation, ISO/TS 18166, 216.
- [8] S. Afkhami, V. Javaheri, M. Amraei, T. Skriko, H. Piili, X.L. Zhao, T. Björk, Thermomechanical simulation of the heat-affected zones in welded ultra-high strength steels: Microstructure and mechanical properties, *Materials & Design* 213, 2022, <https://doi.org/10.1016/j.matdes.2021.110336>
- [9] P. H. G. Domelas, F.W.C. Farias, V.H.P.M. Oliveira, D.O. Moraes, P. Z. Júnior and J. P. Filho, FEM-thermodynamic simulation methodology to predict the influence of  $t_{8/5}$  on the coarse grain heat-affected zone of a Cr-Mo low-alloy steel pipe 60, *Journal of Manufacturing Processes*, 2020, pp 520–529, <https://doi.org/10.1016/j.jmapro.2020.10.082>
- [10] P. H. G. Domelas, J. C. P. Filho, V. H. P. M. Oliveira, D. O. Moraes and P. Z. Junior, Studying the influence of the interpass temperature on the heat-affected zone of an API 5L X65 steel welded pipe joint through computational and physical simulations, *International Journal of Pressure Vessels and Piping* 194, 2021, <https://doi.org/10.1016/j.ijpvp.2021.104548>
- [11] D. Rosenthal, Mathematical theory of heat distribution during welding and cutting, *Welding Journal* 20, 1941, pp 220–234.
- [12] D. Radaj, Heat effects of welding: temperature field, residual stress, distortion, Springer, 1992.
- [13] J. Goldak, M. Bibby, J. Moore, R. House, B. Patel, Computer modeling of heat flow in welds, *Metall Trans B* 17 (3), 1986, pp 587–600, <https://doi.org/10.1007/BF02670226>
- [14] A. Lecoanet and D. G. Ivey and H. Henein, Simulation of the Temperature Profile During Welding with COMSOL Multiphysics® Software Using Rosenthal's Approach, [Online]. Available: <https://www.comsol.com/paper/simulation-of-the-temperature-profile-during-welding-with-comsol-multiphysics-so-19689> [Accessed: Mar. 19, 2023].
- [15] E. Nart and Y. Celik, A practical approach for simulating submerged arc welding process using FE method, *Journal of Constructional Steel Research* 84, 2013.
- [16] M. Tongov, Heat Source for TIG welding modelling, Environment Technology Resources Proceedings of the International Scientific and Practical Conference 3:348-356, <https://doi.org/10.17770/etr2021vol3.6601>
- [17] Elsevier B.V., Thermal Conductivity Coefficient, [Online]. Available: <https://www.sciencedirect.com/topics/engineering/thermal-conductivity-coefficient>
- [18] Y. Xing, W. Wang and H. Al Azzani, Assessment of thermal properties of various types of high-strength steels at elevated temperatures, *Fire Safety Journal* 122, 2021, <https://doi.org/10.1016/j.firesaf.2021.103348>
- [19] European Committee for Standardization, EN 1993-1-2: Eurocode 3: Design of steel structures - Part 1-2: General rules - Structural fire design, 2005, pp 23-26.
- [20] American Society of Civil Engineers, ASCE 1992: Structural fire protection, ASCE committee on fire protection manual 78, 1992.
- [21] ESI Group, SYSWELD - User guide 2020.5, [Online]. Available: <https://myesi.esi-group.com/downloads/software-documentation/sysweld-2020.5-user-guide-visual-weld-16.0-users-guide-online>
- [22] COMSOL AB, Heat transfer module user's guide, Internal material properties library, 2018. [Online]. Available: <https://doc.comsol.com/5.4/doc/com.comsol.help.heat/HeatTransferModuleUsersGuide.pdf> [Accessed: Mar. 19, 2023].
- [23] National Institute of Advanced Industrial Science and Technology AIST Japan, Thermophysical properties database system, [Online]. Available: <https://tpds.db.aist.go.jp/tpds-web/index.aspx> [Accessed Mar. 20, 2023].
- [24] National Technical University KhPI, European steel and alloy grades, [Online]. Available: [http://www.steelnumber.com/en/steel\\_composition\\_eu.php](http://www.steelnumber.com/en/steel_composition_eu.php), [Accessed Mar. 20, 2023].
- [25] National Center for Forensic Science of University of Central Florida, Material Thermal Properties Database, [Online]. Available: [https://ncfs.ucf.edu/burn\\_db/Thermal\\_Properties/material\\_thermal.html](https://ncfs.ucf.edu/burn_db/Thermal_Properties/material_thermal.html), [Accessed Mar. 20, 2023].
- [26] Slovenian Steel Group SIJ Metal Ravne, Alphabetical Steel Index, [Online]. Available: [https://steelselector.sij.si/html/steel\\_index.html](https://steelselector.sij.si/html/steel_index.html), [Accessed Mar. 20, 2023].
- [27] Iron Boar Labs Ltd, MakeItFrom.com database, [Online]. Available: <https://www.makeitfrom.com/>, [Accessed Mar. 20, 2023].
- [28] World Material, [www.theworldmaterial.com](http://www.theworldmaterial.com/), [Online]. Available: <https://www.theworldmaterial.com/>, [Accessed Mar. 20, 2023].
- [29] MatWeb, LLC, Material Property Data, [Online]. Available: <https://www.matweb.com/search/CompositionSearch.aspx> [Accessed Mar. 20, 2023].
- [30] Steel Grades, Physical Properties of steel grade 1.4301 [Online]. Available: 1.4301 Chemical composition, 1.4301 Properties, 1.4301 Datasheet, France AFNOR 1.4301 (steel-grades.com) [Accessed Mar. 20, 2023].

# Research into the Accuracy of Holes in 3D Printing Using Taguchi Method

**Valeri Bakardzhiev**  
Technical University of Sofia,  
Branch Plovdiv  
Plovdiv, Bulgaria  
bakardzhiev@tu-plovdiv.bg

**Sabi Sabev**  
Technical University of Sofia,  
Branch Plovdiv  
Plovdiv, Bulgaria  
sabi\_sabev@tu-plovdiv.bg

**Konstantin Chukalov**  
Technical University of Sofia,  
Faculty of Industrial Technology  
Sofia, Bulgaria  
konstantin\_chukalov@abv.bg

**Plamen Kasabov**  
Technical University of Sofia,  
Branch Plovdiv  
Plovdiv, Bulgaria  
plamen.kasabov@abv.bg

**Abstract.** The article discusses the impact of two factors on the accuracy of the hole sizes - print speed and layer thickness in 3D printing. Nine samples of the ABS polymer were printed by using a 3D printer, then the impact of both of the factors on the accuracy of 3D printing of the holes was evaluated. Taguchi's method was applied with the help of DOE in Minitab to evaluate the impact of the two factors.

**Keywords:** 3D print, Taguchi's method, DOE, FDM

## I. INTRODUCTION

3D printing is used to create various models in fields such as architecture, engineering, medicine and many other areas of modern life. The main goal of 3d printing is quickly and accurately manufacturing of products that are prototypes or technologically difficult to manufacture.

We know many technologies for 3d printing, the most common types being FDM - Fused Deposition Modeling, SLA - Stereolithography and SLS - Selective Laser Sintering. Material deposition technology has gained ground with usage of polymers and creation of patterns from Acrylonitrile Butadiene Styrene (ABS), Polystyrene (HIPS) and Polylactic Acid (PLA).

ABS polymer is most often used for 3D printing, by deposition of material. Although material deposition technology was created more than 20 years ago, in the last few years it has been very actively used because it is more technological to apply. The main advantage of it is that the material, in this case the ABS polymer, is previously

created in the form of a thread, so-called filament, which is subsequently melted by an extruder with a certain polymer melting temperature of 230-250°C and an extrusion speed, thus get different layers of 3d printing.

Of scientific interest is the accuracy of 3D printed details and possibility for industrial use in various fields of technology. [1] – [9]

Parida used the experimental design proposed by Taguchi based on the L27 orthogonal array. It was found the optimal combination of different parameters in this research. [13]

Zagorski drew comparisons between the samples in terms of surface, print time, volume of material used, sample weight and the deviation from the nominal geometry. [22]

## II. METHODOLOGY

### A. Material

The object of our research is creation of a 3d model fig.1. The 3D model is octagonal prism, length of sides-80mm with a central hole diameter of which is 22 mm and 4 holes in circular pattern with diameter of 16 mm. The holes will be measured for dimensional deviations to make comparisons in different modes of operation of 3d printer using material deposition technology. ABS material has been chosen with constant extruder temperature of 235°C.

Print ISSN 1691-5402

Online ISSN 2256-070X

<https://doi.org/10.17770/etr2023vol3.7254>

© 2023 Valeri Bakardzhiev, Sabi Sabev, Konstantin Chukalov, Plamen Kasabov.

Published by Rezekne Academy of Technologies.

This is an open access article under the [Creative Commons Attribution 4.0 International License](https://creativecommons.org/licenses/by/4.0/).

**B. Equipment**

- a. 3D printer FlashForge Creator 3[10]
- b. Software FlashPrint[11]
- c. Software AutoDesk Inventor Pro 2023[12]
- d. Software Minitab 2019[13]

- Layer thickness: 0,1-0,4 [mm].
- Nozzle diameter: 0,4 [mm].

Based on the parameters in Table 1, 13 samples were printed, the printing process is shown in Fig.2. In order for more précised results, the samples were printed from same roll with ABS polymer filament.

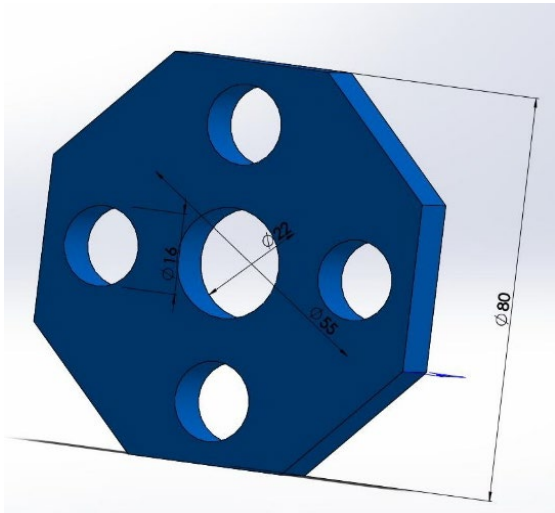


Fig.1. Model for 3D printing.



Fig.2. 3D Printing process.

**C. Parameters,**

The created 3D model was transferred to processing program slicer FlashPrint 5. For our research, we have considered optimization of printing parameters proposed by other authors[14]-[21]. We have previously created a planning of the experiment according to Taguchi's model and we have determined the values of the two parameters- printing speed and layer height shown in tab. 1.

TABLE 1 3D PRINTING PARAMETERS

Print №	Parameter 1	Parameter 2
1	0,1	10
2	0,1	45
3	0,1	80
4	0,25	10
5	0,25	45
6	0,25	80
7	0,4	10
8	0,4	45
9	0,4	80

Constant parameters as follow:

- Platform temperature: 110 °C.
- Extrusion temperature: 235 °C.
- Print speed: 10-80 [mm/s].
- Travel speed: 120 [mm/s].
- Number of shells: 3.

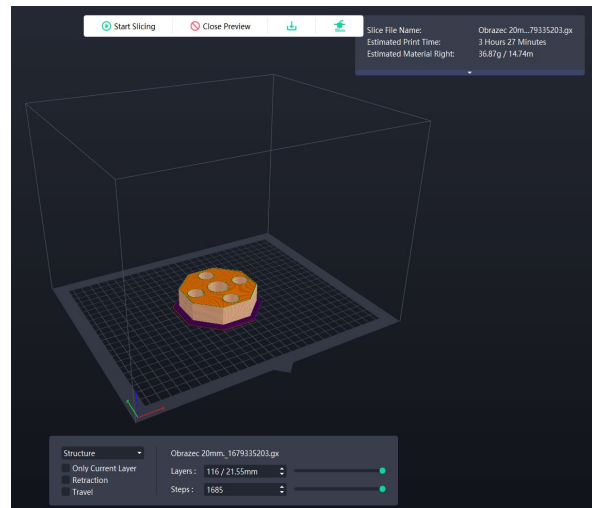


Fig.3. FlashPlot slice process.

**III. RESULTS AND DISCUSSION**

The statistical information required for the analysis is obtained by using automatic measuring system ReniShaw OMP40 mounted on the CNC Mill HAAS VS2ss. The measurement is shown in Fig.4 - 5.



Fig.4. Measurement process.

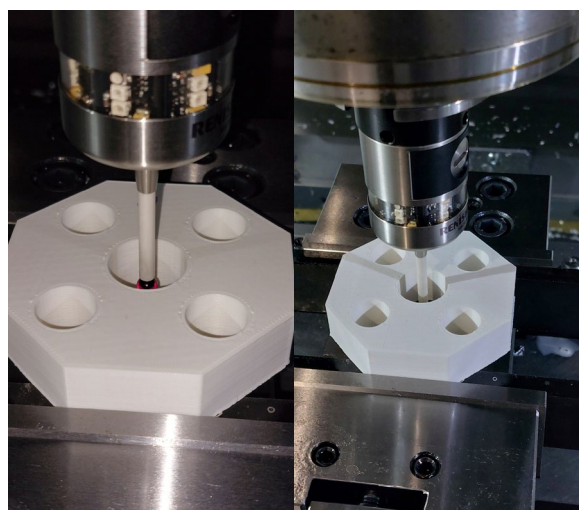


Fig.5. Measurement process.

The samples were measured in three vertical directions and in two perpendicular horizontal directions. The obtained results are averaged and shown in table 2.

TABLE 2 EXPERIMENTAL RESULTS

SAMPLE	DOWN	MIDLE	UP	S	Δ
1	21.8	21.85	21.97	21.87	0.13
2	21.71	21.85	21.95	21.84	0.16
3	21.7	21.85	21.95	21.83	0.17
4	21.7	21.72	21.84	21.75	0.25
5	21.65	21.7	21.8	21.72	0.28
6	21.62	21.62	21.65	21.63	0.37
7	21.55	21.8	21.85	21.73	0.27
8	21.56	21.81	21.89	21.75	0.25
9	21.62	21.65	21.8	21.69	0.31

Mathematical - statistical processing was performed with program product MINITAB. The data from Table 2 were processed and the following regression model was obtained:

Regression Equation

$$\ln(\delta) = -2.873 + 9.46 \text{ Layer} + 0.00294 \text{ Speed} - 13.68 \text{ Layer*Layer} - 0.0635 \text{ Layer*Layer*Speed} + 0.000268 \text{ Layer*Speed*Speed}$$

B In tables tab. 3 - 5 the results of the regression analysis are given..

TABLE 3 COEFFICIENTS FOR TRANSFORMED RESPONSE

Term	Coef	SE Coef	95% CI	T-Value	P-Value	VIF
Constant	-2.873	0.148	(-3.345; -2.401)	-19.37	0.000	
Layer	9.46	1.23	(5.54; 13.38)	7.68	0.005	38.55
Speed	0.00294	0.00187	(-0.00301; 0.00890)	1.57	0.214	4.83
Layer*Layer	-13.68	2.63	(-22.05; -5.32)	-5.21	0.014	45.13
Layer*Layer*Speed	-0.0635	0.0286	(-0.1543; 0.0274)	-2.22	0.113	21.91
Layer*Speed*Speed	0.000268	0.000143	(-0.000724; 0.000724)	1.87	0.159	22.96

TABLE 4 MODEL SUMMARY FOR TRANSFORMED RESPONSE

S	R-sq	R-sq(adj)	PRESS	R-sq(pred)	AICc	BIC
0.0729351	98.33%	95.54%	0.176326	81.53%	94.53	-16.09

TABLE 5 ANALYSIS OF VARIANCE FOR TRANSFORMED RESPONSE

Source	DF	Seq SS	Contribution	Adj SS	Seq MS	F-Value	P-Value
Regression	5	0.938602	98.33%	0.93860	0.187720	35.29	0.007
Layer	1	0.514777	53.93%	0.514346	0.514777	96.77	0.002
Speed	1	0.120495	12.62%	0.01317	0.120495	22.65	0.018
Layer*Layer	1	0.276909	29.01%	0.14421	0.276909	52.06	0.005
Layer*Layer*Speed	1	0.007888	0.83%	0.02626	0.007888	1.48	0.310
Layer*Speed*Speed	1	0.018532	1.94%	0.01853	0.018532	3.48	0.159
Error	3	0.015959	1.67%	0.01596	0.005320		
Total	8	0.954561	100.00%				

P - the coefficient of multiple correlation. The multiple correlation coefficient is insignificant if the value is less than 0.05;

The analysis of the residuals does not indicate a violation of the assumptions of the regression analysis. From fig. 6. is seen that all the standardized residuals are within the interval  $\pm 2$ . Therefore, it can be concluded that there are no gross errors. The histogram shows that the distribution of the residuals is normal.

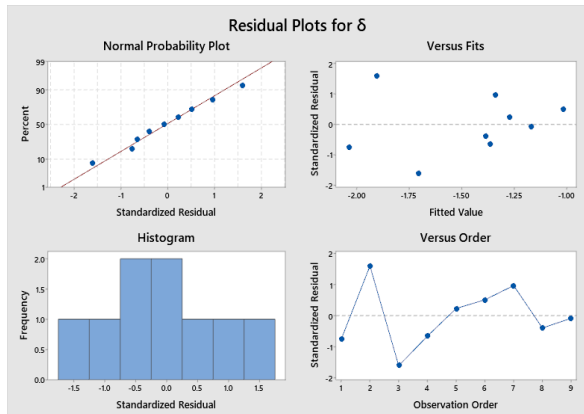


Fig.6. Standardized residual.

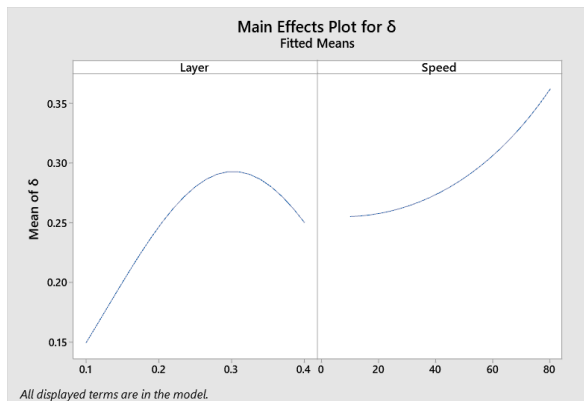


Fig 7. Main effects plot.

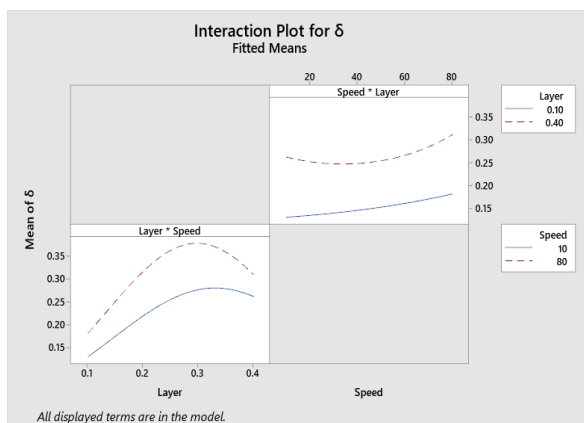


Fig 8. Interaction plot.

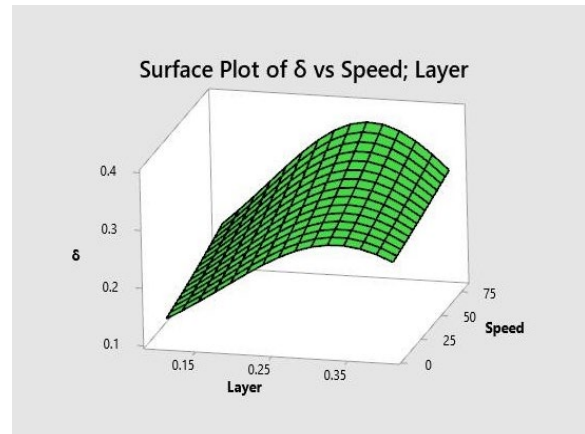


Fig 9. 3D Surface plot.

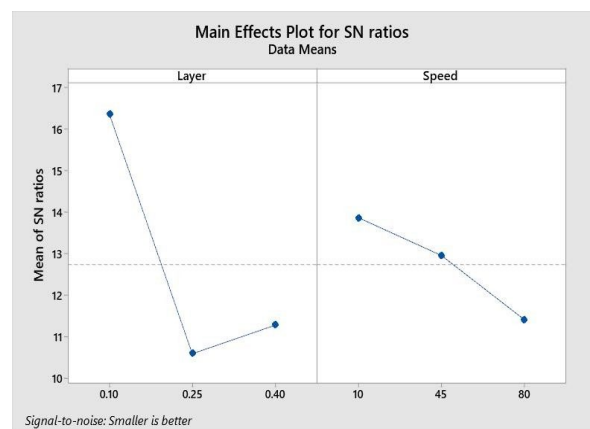


Fig. 10. S/N ratio printing parameters.

#### IV CONCLUSIONS

From the obtained results we may draw the following conclusions:

1. Regression analysis is statistically significant P-value  $< 0.05$ .
2. The coefficient of determination is over 95%, therefore the resulting analysis has a very high correlation.
3. The layer height factor has the greatest influence and mainly affects size accuracy.
4. The speed factor has a minor impact on accuracy.
5. The resulting regression model well and adequately describes the influence of speed and layer height on printing accuracy.

#### ACKNOWLEDGMENTS:

The scientific research, the results of which are presented in the paper, was financed by project BG05M2OP001-1.002-0023 - Competence Center "Intelligent Mechatronic, Eco- and Energy-Saving Systems and Technologies" of Technical University of Sofia, branch Plovdiv.

## REFERENCES

- [1] N. Cuong, N. Duy, H. Nghi, N. Tho., Application of Box-Behnken, ANN, and ANFIS Techniques for Identification of The Optimum Processing Parameters for FDM 3D Printing Parts” *Journal of Industrial Engineering and Halal Industries*. 3. p.64-86. 2022 E-ISSN 2722-8142
- [2] X. Zhao, W. Ma, W. Aiyiti, A. Kasimu, R. Jia, “Investigation of influence of printing modes on the quality of 6-PSS FDM 3D printed thin-walled parts”, *Results in Engineering*, Volume 17, 2023, ISSN 2590-1230, <https://doi.org/10.1016/j.rineng.2023.100926>.
- [3] T. Kalavathi Devi, E.B. Priyanka, P. Sakthivel, “Paper quality enhancement and model prediction using machine learning techniques”, *Results in Engineering*, Volume 17, 2023, 100950, ISSN 2590-1230, <https://doi.org/10.1016/j.rineng.2023.100950>.
- [4] S. Chowdhry, “Improving Strength of 3D Print Using RSM”, *International Journal of Engineering and Applied Sciences (IJEAS)*. 9. 6-8. 2022
- [5] S. Sunder, V. Sahithi. “Process Parameter Optimization of FDM 3D Printer Using PETG and Carbon Fiber PETG.” *Materials Science Forum*. Trans Tech Publications, Ltd., March 24, 2023. <https://doi.org/10.4028/p-y4081e>.
- [6] P. Pristiansyah, H. Hasdiansah, A. Ferdiansyah. “Pengaruh Parameter Proses Pada 3D Printing FDM Terhadap Kekuatan Tarik Filament ABS CCTREE”. *Manutech : Jurnal Teknologi Manufaktur*, vol. 14, no. 01, June 2022, pp. 15 -22, doi:10.33504/manutech.v14i01.210.
- [7] A. Bist, R. Dobriyal, M. Gwalwanshi, S. Avikal, „Influence of layer height and print speed on the mechanical properties of 3D-printed ABS“ *AIP Conference Proceedings* 8 November 2022; 2481 (1): 020012. <https://doi.org/10.1063/5.0107304>
- [8] O. Zemcik i J. Sedlak, "Application of Linear Optimization on Parameters of 3D FDM Print", *Tehnički vjesnik*, vol.26, br. 4, str. 1164-1170, 2019. [Online]. <https://doi.org/10.17559/TV-20170506140109>
- [9] V.Cabreira, R.Santana, “Effect of infill pattern in Fused Filament Fabrication (FFF) 3D Printing on materials performance”, *Matéria (Rio J.)* 25 (03) • 2020 • <https://doi.org/10.1590/S1517-707620200003.1126>
- [10] FlashFofge, *FlashForge Creator 3*, March 2023. [Online]. Available: <https://www.flashforge.com/product-detail/flashforge-creator-3-pro-3d-printer> [Accessed: March 18, 2023].  
*FlashFofge*, *FlashPrint 5*, March 2023. [Online]. Available: <https://www.flashforge.com/product-detail/FlashPrint-slicer-for-flashforge-fdm-3d-printers> [Accessed: March 18, 2023].  
*AutoDesk*, *Inventor Pro 2023*, March 2023. [Online]. Available: <https://www.autodesk.com/products/inventor/overview?term=1-YEAR&tab=subscription> [Accessed: March 18, 2023].
- [11] Minitab, March 2023. [Online]. Available: <https://www.minitab.com/en-us/solutions/analytics/statistical-analysis-predictive-analytics/> [Accessed: March 18, 2022]
- [12] A. Parida, B. Routara, R.Bhuyan, „Surface roughness model and parametric optimization in machining of GFRP composite: Taguchi and Response surface methodology approach”, *Materials Today: Proceedings*, Volume 2, Issues 4–5, 2015, Pages 3065-3074, ISSN 2214-7853, <https://doi.org/10.1016/j.matpr.2015.07.247>.
- [13] D. Shah, K. Kamdar, S.Vaity, “Optimization of EDM Process Parameters Using GRA & Taguchi Method”, *Proceedings of International Conference on Intelligent Manufacturing and Automation. Lecture Notes in Mechanical Engineering*. Springer, Singapore, 2023 [https://doi.org/10.1007/978-981-19-7971-2\\_20](https://doi.org/10.1007/978-981-19-7971-2_20)
- [14] N. Borra, V. Neigapula, "Parametric optimization for dimensional correctness of 3D printed part using masked stereolithography: Taguchi method", *Rapid Prototyping Journal*, Vol. 29 No. 1, pp. 166-184, 2023 <https://doi.org/10.1108/RPJ-03-2022-0080>
- [15] N. Lokesh, P. Pattanayak, B. Das, H.C., P. Mahanta, “Evaluation and Optimization of Process Parameter for Surface Roughness of 3D-Printed PETG Specimens Using Taguchi Method at Constant Printing Temperature”, *Recent Advances in Mechanical Engineering. Lecture Notes in Mechanical Engineering*. Springer, Singapore, 2023 [https://doi.org/10.1007/978-981-16-9057-0\\_22](https://doi.org/10.1007/978-981-16-9057-0_22)
- [16] M. Ahmad, A. Mohamad, “Analysis on Dimensional Accuracy of 3D Printed Parts by Taguchi Approach.” *Advances in Mechatronics, Manufacturing, and Mechanical Engineering. Lecture Notes in Mechanical Engineering*. Springer, Singapore, 2021 [https://doi.org/10.1007/978-981-15-7309-5\\_22](https://doi.org/10.1007/978-981-15-7309-5_22)
- [17] M.Wicaksono, F.Nugraha, “Optimization of 3D Printing Parameters Using the Taguchi Method to Improve Dimensional Precision”, *Jurnal Teknologi*, 12(2), pp. 70–75. 2022 doi: 10.35134/jitekin.v12i2.72.
- [18] I.Mitropoulou, M. Bernhard, B.Dillenburger, “Print Paths Key-framing Design for non-planar layered robotic FDM printing” *SCF '20: Proceedings of the 5th Annual ACM Symposium on Computational Fabrication* November 2020 Article No.: 6Pages 1–10 <https://doi.org/10.1145/3424630.3425408>.Galantucci, I.Bodi, J.Kacani, F. Lavecchia, Fulvio, “ Analysis of dimensional performance for a 3D open-source printer based on fused deposition modeling technique. 3rd CIRP global web conference on Production Engineering Research:Advancement beyond the state of the art.” Conference: 3rd CIRP Global Web Conference on Production Engineering Research: Advancement Beyond State of the Art, CIRPe 2014 Code 113630A: Naples; ItalyVolume: Procedia CIRP 28 (2015) 82 – 87 DOI: 10.13140/2.1.2140.1928
- [19] G.Percoco, L.Galantucci, F.Lavecchia, “Validation Study of an Analytical Model of FDM Accuracy.” In book: *DAAAM International Scientific Book 2011*Chapter: 48 Publisher: Publisher DAAAM International Vienna DOI: 10.2507/daaam.scibook.2011.48
- [20] M.Zagorski, Y.Sofronov, D.Ivanova, K.Dimova, “Investigation of different FDM/FFF 3D printing methods for improving the surface quality of 3D printed parts.” *AIP Conference Proceedings*, 2022 2449. 060001. <https://doi.org/10.1063/5.0090805>

# Research into 3D Printing Layer Adhesion in ABS Materials

**Valeri Bakardzhiev**  
Technical University of Sofia,  
Branch Plovdiv  
Plovdiv, Bulgaria  
bakardzhiev@tu-plovdiv.bg

**Sabi Sabev**  
Technical University of Sofia,  
Branch Plovdiv  
Plovdiv, Bulgaria  
sabi\_sabev@tu-plovdiv.bg

**Plamen Kasabov**  
Technical University of Sofia,  
Faculty of Industrial Technology  
Sofia, Bulgaria  
plamen.kasabov@abv.bg

**Konstantin Chukalov**  
Technical University of Sofia,  
Branch Plovdiv  
Plovdiv, Bulgaria  
konstantin\_chukalov@abv.bg

**Abstract.** The purpose of this article is to determine the impact of the two factors – layer thickness and printing speed in the adhesion of the layers in the ABS polymer. ABS control test tubes were printed and the tensile strength of each tube was measured. By means of statistical analysis, it was determined the impact of the layer thickness and the print speed on the adhesion between the layers. The research was focused on one of the most used materials in 3D printing. It can be concluded from the obtained results that the layer thickness has the greatest impact on the adhesion.

**Keywords:** Adhesion between, DOE, FDM 3D print.

## I. INTRODUCTION

3D printing is a technology that has been known for over 30 years, but its rapid use and development of the technology took place in years after 2000. New materials and new technologies were created in order to increase speed of creating 3D models and reduce printing time.

The most common technologies for 3D printing are FDM - Fused Deposition Modeling, SLA - Stereolithography and SLS - Selective Laser Sintering. Material deposition technology has gained ground with the use of polymers and the creation of patterns from Acrylonitrile Butadiene Styrene (ABS), Polystyrene (HIPS) and Polylactic Acid (PLA).

Material deposition technology is relatively easy to implement as it uses an extruder. A polymer is used in the

form of a thread that melts and builds a 3D model layer by layer. Depending on the different printing parameters, the layers have different adhesion properties and hence that increases the strength of the model being printed. In order to be able to use the printed 3D models in industry, we need to know their mechanical properties well. Achieving optimal printing parameters so adhesion between layers is maximized and results in increased strength of the 3d model. Many authors have studied the influence of temperature on the characteristics of the printed model [9]-[11].

One of the main problems of 3D printing is the adhesion between the individual layers. Better adhesion leads to better mechanical properties of the printed model and it can be used for industrial applications. In order to study the adhesion of the layers, we need to set some parameters that need to be changed. In our case, these are the main printing parameters, of which one parameter is the height of its own, and the second parameter is the printing speed.

We will work with a constant extruder temperature of 235° C to avoid some additional defects that could occur in the printing process, one of which is uneven melt flow. In addition, it is possible to clog the extruder as a result of an extremely low temperature below 220°C or an extremely high temperature above 250°C. [1] – [3].

Print ISSN 1691-5402

Online ISSN 2256-070X

<https://doi.org/10.17770/etr2023vol3.7255>

© 2023 Valeri Bakardzhiev, Sabi Sabev, Plamen Kasabov, Konstantin Chukalov.

Published by Rezekne Academy of Technologies.

This is an open access article under the [Creative Commons Attribution 4.0 International License](https://creativecommons.org/licenses/by/4.0/).

## II. METHODOLOGY

### A. Material

The object of our research is the creation of a 3d model fig.1. The three-dimensional model is a sample with a length of 100 mm and a width of 70 mm. 13 samples have been printed, which we are testing in tension. In order examination to be as accurate as possible, the samples are printed upright as shown in fig. 2. All samples are printed from one roll of ABS polymer filament. Printing takes place at a constant temperature of  $235^{\circ}\text{C} \pm 1^{\circ}\text{C}$  for each sample.

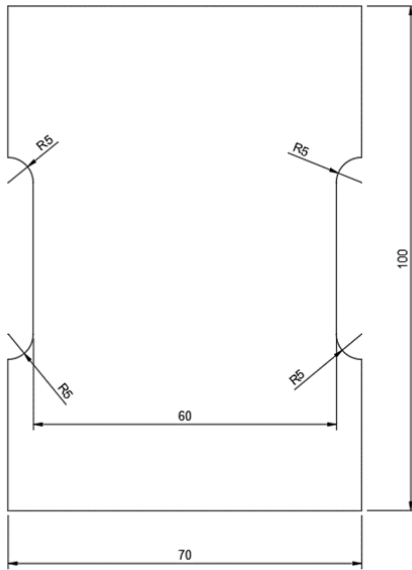


Fig. 1. Model for 3D print.

There are authors who propose different constructions of the test tube [9-10], some of which are standardized. Considering the used test equipment and the brittleness of the material, the selected model in fig. 1 is the most optimal. We will test the ultimate tensile force.

### B. Equipment

- a. 3D printer FlashForge Creator 3 [5]
- b. Software FlashPrint [6]
- c. Software AutoDesk Inventor Pro [7]
- d. Software Minitab [8]

### C. Parameters,

The created 3D model is transferred to the processing program slicer FlashPrint 5. We have set the following constant parameters:

- Platform temperature:  $110^{\circ}\text{C}$ .
- Extrusion temperature:  $235^{\circ}\text{C}$ .
- Print speed: 20-120 [mm/s].
- Travel speed: 120 [mm/s].
- Number of shells: 3.
- Layer thickness: 0,1-0,4 [mm].

- Nozzle diameter: 0,4 [mm].

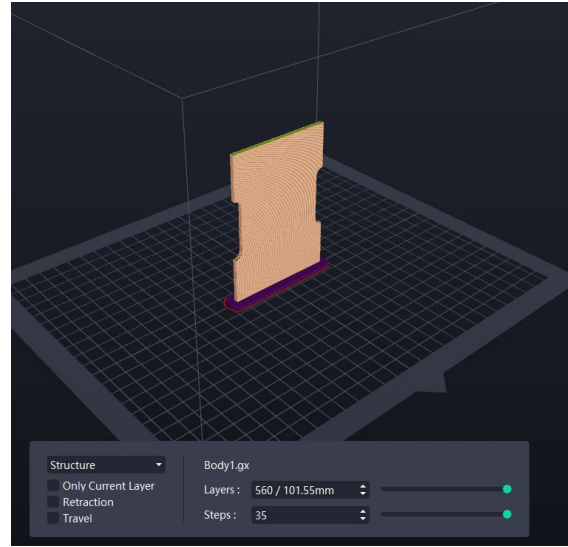


Fig. 2. Model in the FlashPrint5.

We have previously created a planning of the experiment according to Central Composite Design and have determined the values of the two parameters print speed and layer height shown in tab. 1-2.

TABLE 1 DESIGN SUMMARY

Factors:	2	Replicates:	1
Base runs:	13	Total runs:	13
Base blocks:	1	Total blocks:	1

TABLE 2 3D PRINTING PARAMETERS

Print №	Parameter 1	Parameter 2
1	0,1	80
2	0,35	52
3	0,14	52
4	0,25	80
5	0,14	108
6	0,25	80
7	0,25	80
8	0,25	80
9	0,25	40
10	0,25	80
11	0,35	108
12	0,25	120
13	0,4	80

We have used the parameters in the table. 2 and we have printed 13 samples, the printing process is shown in fig.3.



Fig. 3. 3D Printing process.

### III. RESULTS AND DISCUSSION

The specimens were tested on a calibrated electromechanical tensile machine (fig. 4)



Fig. 4. Testing machine.

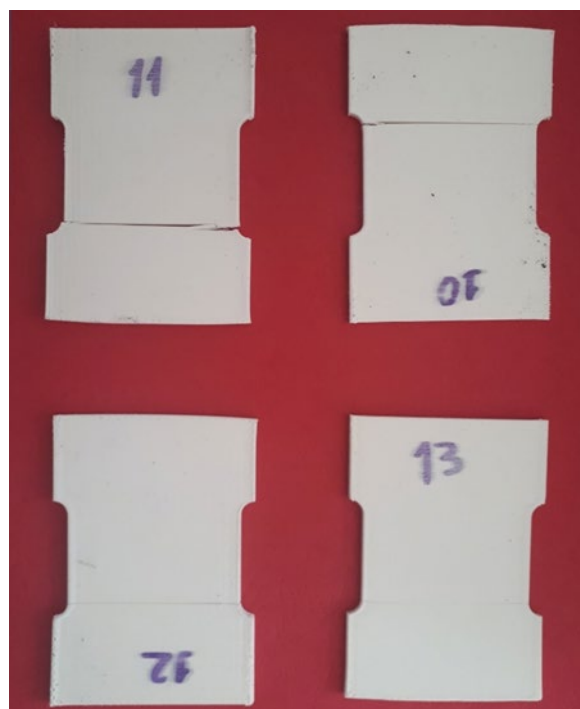


Fig. 5. Measurement process.

Thirteen specimens were tensile tested and the experimental results are presented in tabular form, Table 3.

TABLE 3 EXPERIMENTAL RESULTS

N <sup>o</sup>	Speed	Layer	kN
1	80	0.10	0.59
2	52	0.35	1.30
3	52	0.14	0.70
4	80	0.25	0.91
5	108	0.14	0.77
6	80	0.25	0.91
7	80	0.25	0.91
8	80	0.25	0.91
9	40	0.25	1.08
10	80	0.25	0.91
11	108	0.35	1.00
12	120	0.25	1.12
13	80	0.40	1.10

Statistical processing of the obtained experimental results was made in Minitab software. The obtained results of the regression analysis are shown in table 4.

#### Regression Equation

$$\begin{aligned} \text{kN} = & 0.387 + 6.063 \text{ Layer} - 0.01074 \text{ Speed} \\ & - 3.20 \text{ Layer*Layer} + 0.000115 \text{ Speed*Speed} \\ & - 0.03345 \text{ Layer*Speed} \end{aligned}$$

TABLE 4 COEFFICIENT

Term	Coef	SE Coef	95% CI	T-Value	P-Value	VIF
Constant	0,39	0,20	(-0.079; 0.853)	1,97	0,09	
Layer	6,06	0,85	(4.065; 8.062)	7,17	0,00	42,42
Speed	-0,01	0,00	(-0.01880; -0.00267)	-3,15	0,02	49,06
Layer*Layer	-3,20	1,31	(-6.30; -0.10)	-2,44	0,05	25,97
Speed*Speed	0,00	0,00	(0.000071; 0.000159)	6,22	0,00	37,87
Layer*Speed	-0,03	0,01	(-0.04903; -0.01788)	-5,08	0,00	28,7

TABLE 5 MODEL SUMMARY

S	R-sq	R-sq(adj)	PRESS
0,0387538	97,47%	95,66%	0,07
R-sq(pred)	AICc	BIC	
81,96%	-19,27	-37,71	

TABLE 6 ANALYSIS OF VARIANCE

Source	DF	Seq SS	Contribution	Adj SS	Adj MS	F-Value	P-Value
Regression	5	0,40	97,47%	0,40	0,081	53,86	0
Layer	1	0,29	69,47%	0,08	0,077	51,45	0
Speed	1	0,00	0,61%	0,01	0,015	9,91	0,016
Layer*Layer	1	0,02	4,05%	0,01	0,009	5,95	0,045
Speed*Speed	1	0,06	14,01%	0,06	0,058	38,7	0
Layer*Speed	1	0,04	9,33%	0,04	0,039	25,79	0,001
Error	7	0,01	2,53%	0,01	0,002		
Lack-of-Fit	3	0,01	2,53%	0,01	0,004	*	*
Pure Error	4	0,00	0,00%	0,00	0,000		

The regression analysis is statistically significant because the Pearson coefficient is above 95%. Figures 7-9 show the standardized residuals. Experimental results number 5 and number 12 have a deviation of more than  $\pm 2$  and appear to be inflectionally accurate to the regression equation. Figure 10 shows a normal distribution of the residuals. The factor that has the most significant influence on the ultimate tensile force of the sample is the height of the layer fig.11. The second factor indicates a negligible effect on the ultimate tensile force.

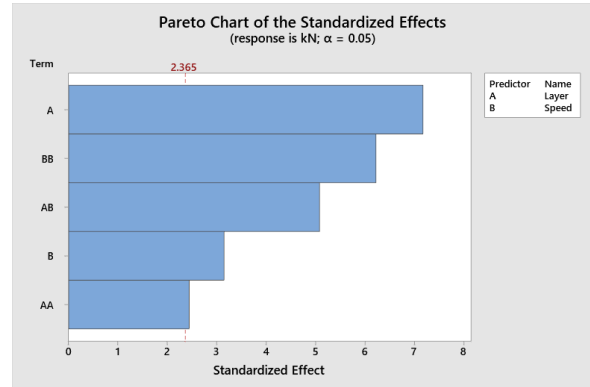


Fig. 6. Pareto chart.

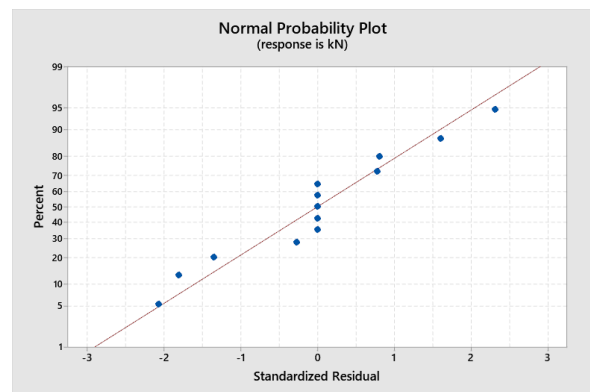


Fig. 7. Probability plot.

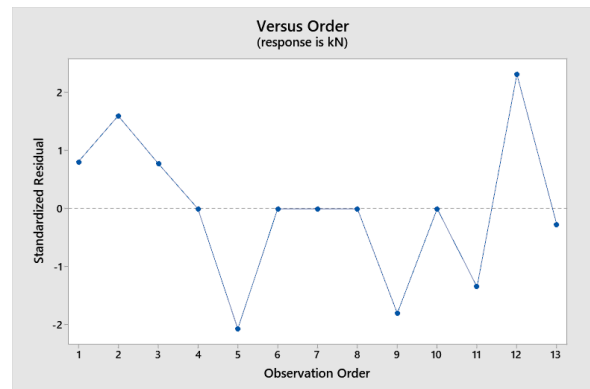


Fig. 8. Versus order.

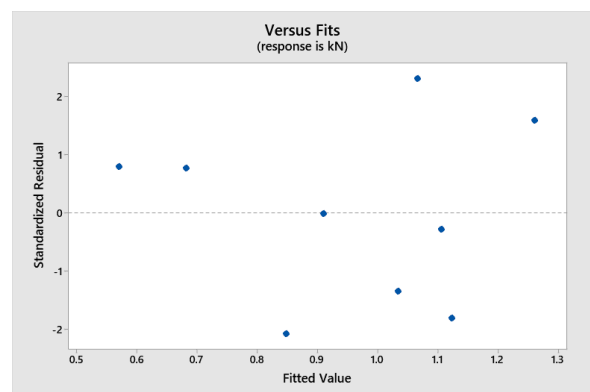


Fig. 9. Versus fits.

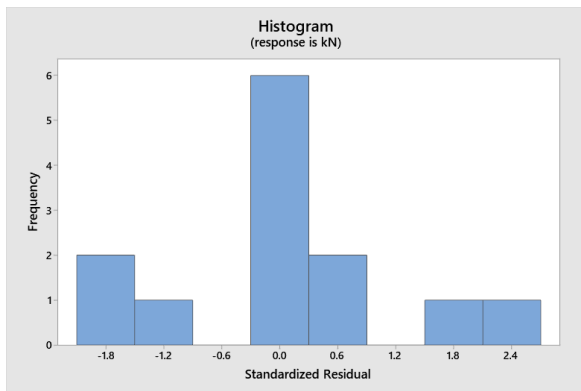


Fig. 10. Histogram.

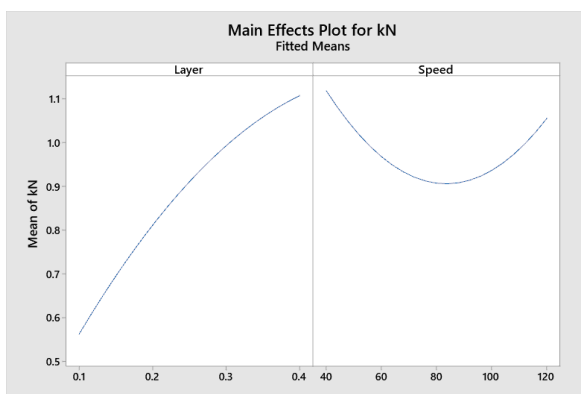


Fig. 11. Main Effects.

#### IV. CONCLUSIONS

In conclusion, we can draw the following conclusions:

- The central compositional planning made is correct.
- With the used measuring equipment we get adequate measurements.
- After the regression model analysis, the P-value values are below 0.05, therefore the factors are statistically significant. Therefore the layer thickness has the greatest importance to the tensile strength of the tested specimens. The larger the layer thickness, the larger the tensile strength of the specimen.
- The obtained results can serve in the development of 3D models requiring increased tensile strength.

**Acknowledgments:** The scientific research, the results of which are presented in the paper, was financed by project BG05M2OP001-1.002-0023 - Competence Center "Intelligent Mechatronic, Eco- and Energy-Saving Systems and Technologies" of Technical University of Sofia, branch Plovdiv

#### REFERENCES

- [1] A. Mushtaq, A. Israr, M. Fahad, J. Ahmed, "Mechanical analysis of additively manufactured polylactic acid in fused deposition modelling", Bulgarian Chemical Communications, Volume 52, Issue 1 (pp. 29-46) 2020 <https://doi.org/10.34049/bcc.52.1.4942>
- [2] M. Derise, A. Zulkharnain, "Effect of Infill Pattern and Density on Tensile Properties of 3D Printed Polylactic acid Parts via Fused Deposition Modeling (FDM)", International Journal of Mechanical & Mechatronics Engineering. 20. 54-62., 2022
- [3] A. Shafaat, H. Rezaei, "Effect of Layer Thickness and Infill Percentage on The Mechanical Characterization of Fused Deposition Modeling ABS specimens" The 5th International and 16th National Conference on Manufacturing Engineering ICME2019, 18-19 Dec 2019
- [4] S. Chowdhry, "Improving Strength of 3D Print Using RSM", International Journal of Engineering and Applied Sciences (IJEAS). 9. 6-8. 2022
- [5] FlashFofge, FlashForge Creator 3, March 2023. [Online]. Available: <https://www.flashforge.com/product-detail/flashforge-creator-3-pro-3d-printer> [Accessed: March 18, 2023].
- [6] FlashFofge, FlashPrint 5, March 2023. [Online]. Available: <https://www.flashforge.com/product-detail/FlashPrint-slicer-for-flashforge-fdm-3d-printers> [Accessed: March 18, 2023].
- [7] Autodesk, Inventor Pro 2023, March 2023. [Online]. Available: <https://www.autodesk.com/products/inventor/overview?term=1-YEAR&tab=subscription> [Accessed: March 18, 2023].
- [8] Minitab, March 2023. [Online]. Available: <https://www.minitab.com/en-us/solutions/analytics/statistical-analysis-predictive-analytics/> [Accessed: March 18, 2023].
- [9] K. Özsoy, A. Erçetin and Z. A. Çevik, "Comparison of Mechanical Properties of PLA and ABS Based Structures Produced by Fused Deposition Modelling Additive Manufacturing", Avrupa Bilim ve Teknoloji Dergisi, no. 27, pp.802-809, Nov.2021, <https://doi.org/10.31590/ejosat.983317>
- [10] C. ALVAREZ, L. Kenny; C. LAGOS, F. Rodrigo y AIZPUN, Miguel. "Investigating the influence of infill percentage on the mechanical properties of fused deposition modelled ABS parts." Ing. Investig. [online], vol.36, n.3 pp.110-116. 2016 ISSN0120-5609. <https://doi.org/10.15446/ing.investig.v36n3.56610>.  
 Zagorski, Mihail & Todorov, Georgi & Nikolov, Nikolay & Sofronov, Yavor & Kandeveva, Mara. (2022). Investigation on wear of biopolymer parts produced by 3D printing in lubricated sliding conditions. Industrial Lubrication and Tribology. ahead-of-print. <https://doi.org/10.1108/ILT-06-2021-0214>

# Conveyor-type Small Hydropower Plant for Shallow River Waters

**Vitaly Beresnevich**  
Institute of Mechanics and  
Mechanical Engineering  
Riga Technical University  
Riga, Latvia  
vitalijs.beresnevics@rtu.lv

**Marina Cerpinska**  
Institute of Mechanics and  
Mechanical Engineering  
Riga Technical University  
Riga, Latvia  
marina.cerpinska@rtu.lv

**Martins Irbe**  
Institute of Mechanics and  
Mechanical Engineering  
Riga Technical University  
Riga, Latvia  
martins.irbe@rtu.lv

**Janis Viba**  
Institute of Mechanics and  
Mechanical Engineering  
Riga Technical University  
Riga, Latvia  
janis.viba@rtu.lv

**Abstract.** This paper deals with the development of a small conveyor-type hydropower plant intended for operation in shallow river waters without construction of a dam. The proposed design offers a closed-shaped flattened conveyor equipped with flat-shaped blades. The conveyor is oriented perpendicular to the fluid flow. Several identical flat blades interacting with fluid flow are mounted on conveyor belt and move together with the belt in one straight line direction. Then after turning in the reversing mechanism, blades move in the opposite direction. The conveyor system has a built-in energy generator which drive shaft is connected with one of the reversing ends of the plant. Conveyor belt system dynamics analysis is performed on the base of equivalent model with one degree of freedom. The interaction of a moving conveyor flat blade in translation motion with fluid flow is studied by computer simulation with program Mathcad using a superposition principle. In accordance with this approach, a fast-chaotic motion of fluid particles (Brownian motion) is separated from the slow-directed flow motion, with the given average velocity. Optimization of system parameters (blade orientation angle to fluid flow, interaction constants of the braking generator) is performed, using a generated power as criterion. Simulation results confirm the serviceability and operational efficiency of the proposed hydropower plant in shallow river waters.

**Keywords:** dynamic analysis, flat blades, hydropower plant, optimization.

## I. INTRODUCTION

Hydropower generation is one of the most developed and widely applicable sources of renewable green energy. Operation efficiency of hydropower plant is primarily dependent on the hydraulic head and the rate of fluid flow in the turbine. Due to this, the problem of energetic efficiency of existing power plants is mainly solved by the construction of large dams. Worldwide there are over 58000 dams with the height up to 15 m, and number of dams continues to increase [1]. This trend has a negative environmental impact acting as a barrier to fish migration, fragmenting rivers and degrading habitats [2] – [4].

Other specific feature of existing hydropower plants lies in the practical use of turbines with rotating blades [5] – [7]. To increase generated power, such blades are often made with large radial dimensions. This gives the rise to significant vibration problems due to increased level of dynamic stresses (especially near the blades attachment to the rotor) [8]. Besides, rotating blade can damage fishes and other river species in surrounding water area.

The present paper focuses on the development of a small hydropower plant, which operates without construction of a dam and can be used in areas where water head is even lower than 1 meter. To achieve this goal, it is proposed to realize in the hydropower device a new

Print ISSN 1691-5402

Online ISSN 2256-070X

<https://doi.org/10.17770/etr2023vol3.7229>

© 2023 Vitaly Beresnevich, Marina Cerpinska, Martins Irbe, Janis Viba.

Published by Rezekne Academy of Technologies.

This is an open access article under the [Creative Commons Attribution 4.0 International License](https://creativecommons.org/licenses/by/4.0/).

operational principle based on the use of flat blades translational motion excited by fluid flow.

## II. MATERIALS, MODEL AND METHODS

Instead of conventional turbine models with rotating blades, a new design of wind power plant synthesized on the base of a closed loop conveyor equipped with flat-shaped blades is proposed (Fig. 1).

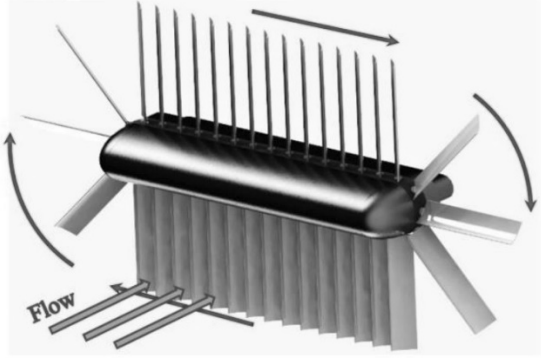


Fig. 1. Three-dimensional design of hydropower plant.

The conveyor belt is equipped with several identical flat blades, which translation motion is excited due to the action of fluid flow. Blades move together in one straight line direction, then turn in the reversing mechanism by 180 degrees and move in the opposite direction. The conveyor system has a built-in energy generator. The drive shaft of the generator can be mounted on one of the axes of the reversing ends of the conveyor belt (in Fig. 1 the drive shaft is not shown). In the proposed device, the fluid flow load is uniformly distributed over the lateral surface of the flat blades. This provides a simple way to increase the operational efficiency of the device, which can be achieved by increasing the area  $A$  of blade's lateral surface.

Principal model of the hydropower plant synthesized on the base of a closed belt conveyor is shown in Fig. 2.

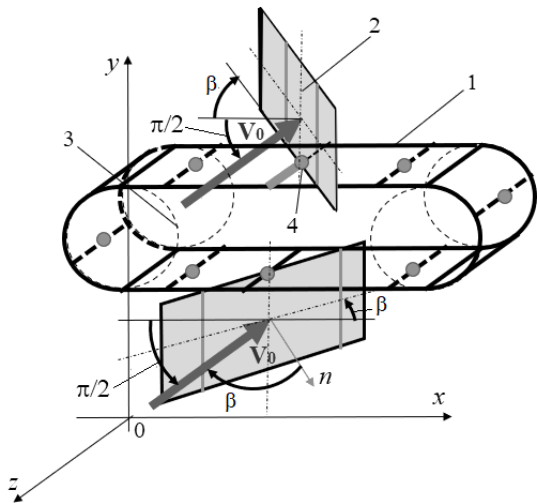


Fig. 2. Principle model of fluid flow power plant on the base of belt conveyor: 1 – closed belt conveyor; 2 – flat blade; 3 – rotor; 4 – fastening element.

Closed belt conveyor 1 forms a central part of the plant, besides the belt has an ability to move parallel to coordinate plane  $xOy$ . The conveyor is driven by a fluid flow with velocity  $V_0$ , acting on the blades 2 in parallel to the  $Oz$  axis. Power is obtained from a generator connected with rotor 3 of the conveyor 1 (Fig. 2). The flat blades 2 are attached tightly to the conveyor 1 with a fastening element 4 (welded hinge). Besides, the blades 2 are fixed at the angle  $\beta$  toward the  $x$ -axis. The model of generator has several flat blades 2. Due to the action of air flow  $V_0$ , translation motion of blades 2 along conveyor's straight and circular sections (in final turns) is excited. To obtain useful power, this translation motion of blades 2 is transformed into the rotation of generator's rotor 3.

The interaction of a moving conveyor blade in translation motion with a fluid flow is studied using superposition principle. In accordance with this approach, a fast chaotic motion of fluid particles (Brownian motion) is separated from the slow-directed flow motion, with the given average velocity. In addition, the space around the blade is divided into two zones: one zone is the interaction pressure zone on the front side of the movement, and the other zone is at the rear, or the suction zone [9], [10]. Application of the method makes it possible to study flow – blade interaction without the use of experimental lift and drag coefficients. The applicability of such approach is confirmed by experiments described in [11].

Model of fluid flow interaction with one thin flat blade is shown in Fig. 3. It is assumed that fluid flow has a constant velocity  $V_0$ , but blade is turned by angle  $\beta$  relative to flow direction. Due to the action of fluid flow and blade's translational motion along  $x$  axis, fluid interaction force  $N$  is applied to the blade.

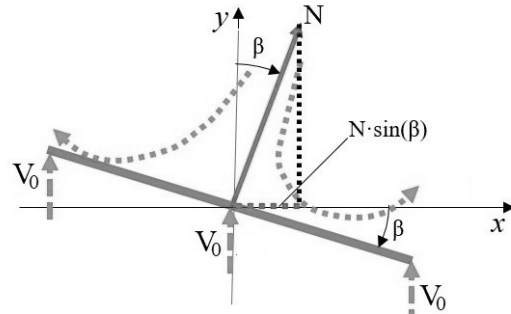


Fig. 3. Model of fluid flow interaction with one moving thin blade.

Basing on fast and slow motions separation principle, it is possible to obtain the differential relations of motion for the interaction of fluid flow with blades. For this purpose, the theorem of classical mechanics for the amount of movement changes in the differential form [12] can be used. As a result, after integration and summation over the entire system of conveyor with one degree of freedom, the following differential equation of blade translation motion is obtained [10]:

$$m\ddot{x} = (1 + C)\rho BLK \cdot (V_0 \cos \beta - \dot{x} \sin \beta)^2 \cdot \sin \beta \cdot \text{sign}(V_0 \cos \beta - \dot{x} \sin \beta) + Q, \quad (1)$$

where  $x$  is a generalized coordinate (here it is a displacement of conveyor one element);  $m$  is a mass of one blade;  $C$  is a fluid flow and blade interaction constant;  $\rho$  is a density of fluid;  $B, L$  are the width and length of one blade;  $K$  is number of blades;  $V_0$  is a fluid flow velocity in the direction perpendicular to the  $x$  axis;  $\beta$  is a blade positioning angle;  $Q$  is a remaining part of the generalized force, including resistance forces and forces of power generator.

Analysis of motion dynamics of the conveyor system is performed by the solution of differential equation (1) with program Mathcad.

### III. RESULTS AND DISCUSSION

Variants of the generator with the linear generalized resistance force  $Q$  in the equation (1) is considered:

$$Q = -b_1 \dot{x}, \quad (2)$$

where  $b_1$  is a coefficient of viscous damping in linear generator.

During simulation, power  $P$  of linear generator was calculated by formula

$$P = b_1 \dot{x}^2. \quad (3)$$

Mathematical simulation is performed assuming the following values of main system parameters:  $b_1 = 75$  kg/s;  $m = 10$  kg;  $K = 5$ ;  $\rho = 1000$  kg/m<sup>3</sup>;  $C = 0,5$ ;  $B = 1$  m;  $L = 1$  m;  $V_0 = 1$  m/s;  $\beta = 0,039$  rad;  $g = 9,81$  m/s<sup>2</sup>. Results of dynamics analysis for blade velocity  $V$  and for power  $P$  obtained in the generator are presented in Fig. 4 and Fig. 5.

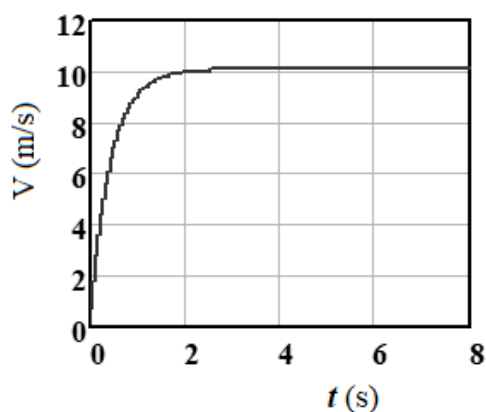


Fig. 4. Velocity  $V$  of blade translation motion along  $x$  axis versus time  $t$ .

By the analysis of diagrams presented (Fig. 4 and Fig. 5), it can be concluded that stationary motion process (when motion velocity along the  $x$  axis is almost constant) occurs very quickly (within 1,5 – 2 s), without fluctuations. The power  $P$  of the stationary process is dependent on the generator parameter  $b_1$  as well as on the flow rate  $V_0$  and blade orientation relative to fluid flow (blade position angle  $\beta$ ). For example, in the case studied here, the generated power

$P$  reaches up 7500 – 8000 W even at the relatively small fluid flow velocity of  $V_0 = 1$  m/s.

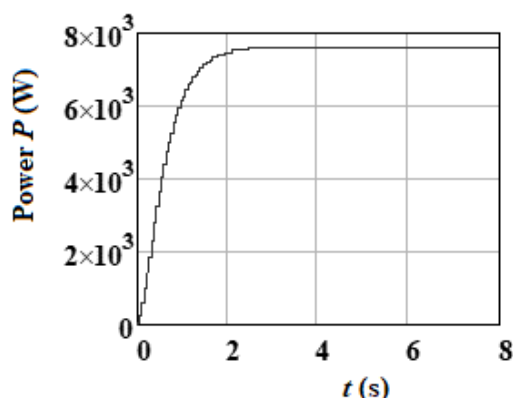


Fig. 5. Power  $P$  obtained in the generator (for the system parameters  $b_1 = 75$  kg/s,  $\beta = 0,039$  rad,  $V_0 = 1$  m/s).

As it is seen from simulation results (for example, Fig. 4), the velocity  $V$  of blade stationary motion process is almost constant, and the acceleration is close to zero. Therefore, it is possible to optimize this process.

In solution of optimization problem, the power  $P$  is considered as criterion, but the interaction constant  $b_1$  of the braking generator as well as the blade orientation (turning angle  $\beta$ ) are taken as variable parameters. Parametric optimization problem is solved with the aid of program Mathcad. The example of response curve for the criterion power  $P$  as a function of blade turning angle  $\beta$  is shown in Fig. 6.

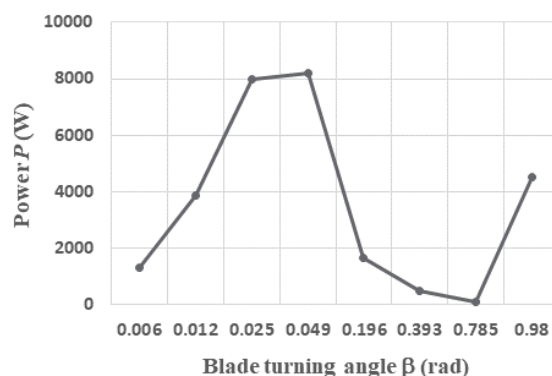


Fig. 6. Response curve for the optimization criterion  $P$  as a function of blade turning angle  $\beta$  (for the case of  $V_0 = 1$  m/s and  $b_1 = 5,5$  kg/s).

As it is seen from the diagram presented (Fig. 6), the generated power  $P$  reaches maximal values of 7-8 kW under the relatively small blade's turning angle ( $\beta = 0,025 - 0,050$  rad).

Other example of a response surface for the optimization criterion power  $P$  is shown in Fig. 7. In solution of this problem, variation of linear generator parameter  $b_1$  was held (under the constant turning angle  $\beta = 0,039$  rad).

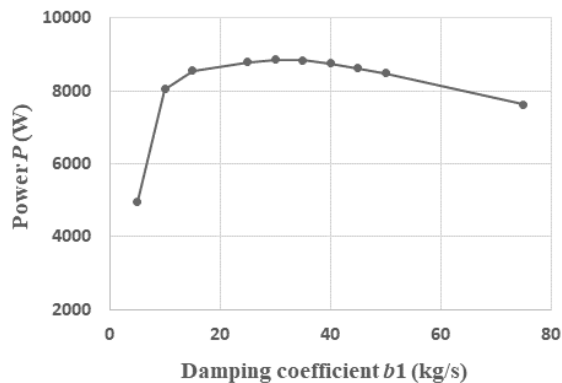


Fig. 7. Response curve for the optimization criterion  $P$  as a function of interaction constant  $b_1$  of the braking generator (for the case of  $V_0 = 1$  m/s and  $\beta = 0,039$  rad).

The renewable power  $P$  of linear generator is dependent on its viscous damping force  $-b_1\dot{x}$ , which can be varied by changing of interaction constant  $b_1$  (e.g., by changing the design of generator elements). As it is seen from the diagram presented (Fig. 7), the generated power  $P$  reaches maximal values of 8-9 kW, if damping constant  $b_1$  of braking generator lies within the range from 10 till 60 kg/s. And what is practically important, such relatively high power can be obtained under the quite a small fluid flow velocity of 1 m/s, characteristic for shallow river waters.

#### IV. CONCLUSIONS

A conveyor-type turbine for small hydropower plants (<100 kW), which can operate in shallow river waters without construction of a dam, is developed. Instead of conventional turbines with rotating blades, the proposed model generates useful power from translational motion of flat blades excited by fluid flow.

Due to excluding dams from the structure of the proposed hydropower plant, the ecological situation in surrounding aqua system will improve significantly (no barrier to fish migration, no negative influence on river fragmenting and degrading habitats, etc.). Besides, compared to turbine with rotating blades, there will be a lower risk to damage fish or other river species around the translatory moving blade in the proposed device.

The operational advantage of the conveyor-type hydropower device lies in the fact that velocities of all points of the lateral surface of the flat blade are the same (as opposed to conventional rotary-type devices, in which the speeds of the blade ends are sufficiently higher). Due to this, the side surface of the blade in the proposed device can be used more effectively than in known rotary devices [13]. By the results of computer simulation, a generated power reaches about 8-9 kW even under the quite small fluid flow velocity of 1 m/s.

Optimization of system parameters (blade orientation angle to fluid flow, interaction constant of the braking generator) is performed, using a generated power as criterion. Simulation results confirm the serviceability and operational efficiency of the proposed hydropower plant in shallow river waters.

#### REFERENCES

- [1] International Commission of Large Dams, "World Register of Dams. General Synthesis", updated April 2020. [Online]. Available: ICOLD CIGB > General Synthesis (icold-cigb.org). [Accessed: Feb. 20, 2023].
- [2] E. P. Anderson, M. C. Freeman, and C. M. Pringle, "Ecological consequences of hydropower development in Central America: Impacts of small dams and water diversion on neotropical stream fish assemblages", *River Research and Applications*, vol. 22, no. 4, pp. 397–411, May 2006, <https://doi.org/10.1002/rra.899>
- [3] J. Geist, "Editorial: Green or red: Challenges for fish and freshwater biodiversity conservation related to hydropower", *Aquatic Conservation: Marine and Freshwater Ecosystems*, vol. 31, no. 7. John Wiley and Sons Ltd, pp. 1551–1558, July 2021, <https://doi.org/10.1002/aqc.3597>
- [4] C. M. Bunt, T. Castro-Santos, and A. Haro, "Performance of fish passage structures at upstream barriers to migration", *River Research and Applications*, vol. 28, no. 4, pp. 457–478, May 2012, <https://doi.org/10.1002/rra.1565>
- [5] Ambra Giovannelli, "Development of turbomachines for renewable energy systems and energy-saving applications", *Energy Procedia*, vol. 153, pp. 10–15, October 2018, <https://doi.org/10.1016/j.egypro.2018.10.069>
- [6] J. Viba, V. Beresnevich, S. Noskovs and M. Irbe, "Investigations of rotating blade for energy extraction from fluid flow", *Vibroengineering Procedia*, vol. 8, pp. 312–315, October 2016, <https://www.extrica.com/article/17667>
- [7] J. Viba, V. Beresnevich, M. Irbe and J. Dobelis, "The control of blades orientation to air flow in wind energetic device" *Energy Procedia*, vol. 128, pp. 302-308, September 2017, <https://doi.org/10.1016/j.egypro.2017.08.317>
- [8] C. Boller, M. Buderath, "Fatigue in aerostructures – where structural health monitoring can contribute to a complex subject", *Philosophical Transactions of the Royal Society A*, vol. 365, no. 1851, pp. 561-587, February 2007, <https://doi.org/10.1098/rsta.2006.1924>
- [9] J. Viba, V. Beresnevich and M. Irbe, "Synthesis and Optimization of Wind Energy Conversion Devices", in *Design Optimization of Wind Energy Conversion Systems with Applications*, Karam Maalawi, Ed. London: IntechOpen, 2020, pp. 125-141, <http://dx.doi.org/10.5772/intechopen.90819>
- [10] I. Tipans, J. Viba, M. Irbe and S. K. Vutukuru, "Analysis of non-stationary flow interaction with simple form objects", *Agronomy Research*, vol. 17, no. 1, pp. 1227-1234, 2019, <https://doi.org/10.15159/AR.19.083>
- [11] J. Viba, V. Beresnevich and M. Irbe M. "Methods and devices for wind energy conversion", in *Wind Turbines - Advances and Challenges in Design, Manufacture and Operation*, Karam Maalawi, Ed. London: IntechOpen: 2022, pp. 247-270, <http://dx.doi.org/10.5772/intechopen.103120>
- [12] J. L. Meriam, L.G. Kraige and J.N. Bolton, *Engineering Mechanics: Dynamics*. New York: John Wiley & Sons, 2016.
- [13] G.E.M. Beshay and K.Y. Maalawi, "Structural Optimization of Wind Turbine Blades for Improved Dynamic Performance", in *Design Optimization of Wind Energy Conversion Systems with Applications*, Karam Maalawi, Ed. London: IntechOpen, pp. 69-107, 2020, <http://dx.doi.org/10.5772/intechopen.91643>

# Comparison of Potential Road Accident Detection Algorithms for Modern Machine Vision System

**Oleksandr Byzkrovnyi**

Software engineering department,  
Kharkiv National University of Radio  
Electronics,  
Kharkiv, Ukraine  
oleksandr.byzkrovnyi@nure.ua

**Kyrylo Smelyakov**

Software engineering department,  
Kharkiv National University of  
Radio Electronics,  
Kharkiv, Ukraine  
kyrylo.smelyakov@nure.ua

Vilnius, Lithuania

p.sakalys@eif.viko.lt

**Anastasiya Chupryna**

Software engineering department,  
Kharkiv National University of  
Radio Electronics,  
Kharkiv, Ukraine  
anastasiya.chupryna@nure.ua

**Loreta Savulioniene**

Faculty of electronics and informatics,  
Vilniaus Kolegija/Higher Education  
Institution  
Vilnius, Lithuania  
l.savulioniene@eif.viko.lt

**Paulius Sakalys**

Faculty of electronics and  
informatics, Vilniaus  
Kolegija/Higher Education  
Institution

**Abstract.** Nowadays the robotics is relevant development industry. Robots are becoming more sophisticated, and this requires more sophisticated technologies. One of them is robot vision. This is needed for robots which communicate with the environment using vision instead of a batch of sensors. These data are utilized to analyze the situation at hand and develop a real-time action plan for the given scenario. This article explores the most suitable algorithm for detecting potential road accidents, specifically focusing on the scenario of turning left across one or more oncoming lanes. The selection of the optimal algorithm is based on a comparative analysis of evaluation and testing results, including metrics such as maximum frames per second for video processing during detection using robot's hardware. The study categorises potential accidents into two classes: danger and not-danger. The Yolov7 and Detectron2 algorithms are compared, and the article aims to create simple models with the potential for future refinement. Also, this article provides conclusions and recommendations regarding the practical implementation of the proposed models and algorithm.

**Keywords:** Machine learning, machine vision, object detection, road accidents, CNN.

## I. INTRODUCTION

Road accidents have become a prevalent problem due to the increase in both the number of vehicles and their speed,

resulting in a higher number of victims and injuries [1-3]. Current methods of preventing dangerous situations on the roads primarily focus on the safety of individual vehicles, without considering other road users outside of their built-in safety mechanisms [4, 5].

There is a need to develop methods that can detect and notify drivers of potential dangers in areas that are currently beyond the capabilities of existing ADAS systems to scan for obstacles of varying types [6-8].

Taking in consideration the current tendencies in the tech world, the automotive safety systems should be developed using data analysis systems [9-11].

Additionally, an important factor for road safety is the driver's ability to respond appropriately to changes in traffic and information received while driving [12, 13].

The most dangerous in terms of road behavior are bicyclists and motorcyclists, which may rapidly change going trajectory [14, 15].

As a result, developing and researching new methods for monitoring driver behavior, predicting dangerous situations while driving, and notifying drivers about them is a crucial and relevant task [16-18].

Print ISSN 1691-5402

Online ISSN 2256-070X

<https://doi.org/10.17770/etr2023vol3.7299>

© 2023 Oleksandr Byzkrovnyi, Kyrylo Smelyakov, Anastasiya Chupryna, Loreta Savulioniene, Paulius Sakalys.  
Published by Rezekne Academy of Technologies.

This is an open access article under the [Creative Commons Attribution 4.0 International License](https://creativecommons.org/licenses/by/4.0/).

The key trends in terms of road safety research are:

- improvement of data mining approaches for extracting essential for road safety information from the data outdoor cameras [19, 20];
- investigation of methods for complex analysis of data mentioned before [21, 22].

Current research aims to estimate an algorithm that has the smallest prediction time, smallest size, and good accuracy for identifying and preventing road accidents based on outdoor video streams. Also, the usage of this model in robotic vision systems is one of the main points, because of surely high progress in development in this way.

The main goal of this research is defining the possibility of determining possible road accidents in a quick way, using machine learning algorithms and clarify the effectiveness and which algorithm is more applicable for explained problem for quick prediction and usage in robotic vision system.

## II. MATERIALS AND METHODS

The computer vision technologies are very rich and takes fast development. The most recent and valuable research there is Yolo [23] algorithm family which is developed to v7 and Detectron2 [24] with Faster R-CNN on backend, which has the Facebook origin. Those algorithms are very fast and efficient, so they were taken for investigation which one is more suitable for task of fast road accidents detection along with usage in robot vision system.

### A. ML MODEL METRICS

The following metrics have been used to calculate trained models' performance: Time to train, Average Precision with IoU, Model size, Loss CLS, Used GPU memory, Loss box, Inference time.

The IoU formula is the following

$$J(A, B) = \frac{|A \cap B|}{|A \cup B|}, \quad (1)$$

The Loss Box formula is the following

$$L_{box}(t^U, v) = \sum_{i \in \{x, y, w, h\}} L_1^{smooth}(t_i^u - v_i), \quad (2)$$

The Loss cls (classification) formula is the following

$$L_{cls}(p, u) = -\log \log p_u, \quad (3)$$

The Precision has the following formula

$$P = \frac{TruePositive}{(TruePositive+FalsePositive)}, \quad (4)$$

### B. DATA DESCRIPTION

Current research uses aims to determine the danger situations on the road. As far as such video data is very hard to find, the own produced video stream is used. The only one danger case explained in current article – turning left across oncoming lanes, where at least one lane is stopped for skipping the car which turn left and at least one oncoming lane without cars. The Fig. 1 display mentioned case.

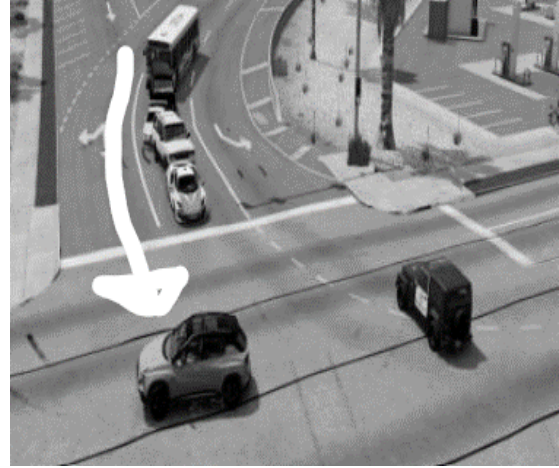


Fig. 1. Danger case explanation [25].

So, such cases can be simulated in BeamNG.drive [26] computer game and sliced in pictures. The strategy for creation of dataset for research was the following:

- Simulation of at least 5 different road crossing with different car setup, with different count of oncoming lanes.
- Do not consider night scenario, because infrared cameras are required.
- The only two classes should be explained: danger and non-danger.

The training dataset consists of 300 pictures, where 150 has danger class and 150 non-danger. The Fig.2 provides an example of dataset picture.



Fig. 2. Danger class example [25].

The resolution of pictures is 640x640.

### C. ML ALGORITHMS ARCHITECTURES

The developers of Yolov7 uses Extended ELAN architecture to control the shortest gradient path and a deeper network may learn effectively. The Detectron2 allows to use different algorithms under the hood. In current research the Faster R-CNN is used.

### III. EXPERIMENT, RESULT AND DISCUSSIONS

The experiment includes the following steps:

- Experiment planning and code preparations;
- Model training;
- Evaluation and testing;
- Results comparison.

The Google Colab was considered as a platform to train and evaluate the models. The following code is used to train models [27-28].

The following environment specs are there: Python 3 Google Compute Engine backend (GPU: Tesla T4).

The models training consists of two steps: training of Yolov7 and training of Detectron2 model.

The Detectron2 model has batch size 64, image size = 640x640 and epoch count = 1500. The Yolov7 model has batch size = 16, image size = 640x640, epoch count = 55.

The table 1 display resource consumption during training of Detectron2 model.

TABLE 1 RESOURCE USAGE DURING DETECTRON2 MODEL TRAINING

Resource Name	Time, mins
System RAM	3.7 GB / 12.7 GB
GPU RAM	8.5 GB / 15 GB
SSD	25.9 GB / 78.2 GB

The table 2 display resource usage during training of Yolov7 model.

TABLE 2 RESOURCE USAGE DURING YOLOV7 MODEL TRAINING

Resource Name	Time, mins
System RAM	5.7 GB / 12.7 GB
GPU RAM	11.4 GB / 15 GB
SSD	24.9 GB / 78.2 GB

The table 3 displays time to train each model.

TABLE 3 TRAINING TIME

Algorithm	Time, mins
Detectron2	51
Yolov7	15.9

### A. YOLOV7 RESULTS

The results of training are presented in table and chart view. The results of training and evaluation for Yolov7 model are present in Table 4.

TABLE 4 YOLOV7 RESULTS

Value	Metric
0.583	AP@.5:95
0.926	AP@.5
0.1916668 s / img per GPU	Inference time
74.8 MB	Model size

The accuracy of 58% is bad, but this was obtained on the 150 images per class. The next figures (Fig. 3, 4) represent loss metrics.

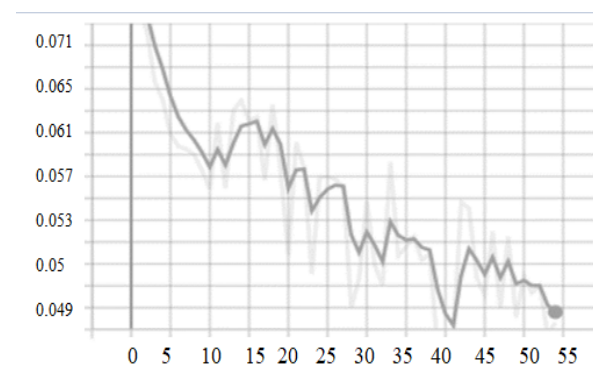


Fig. 3. The Loss box metric.

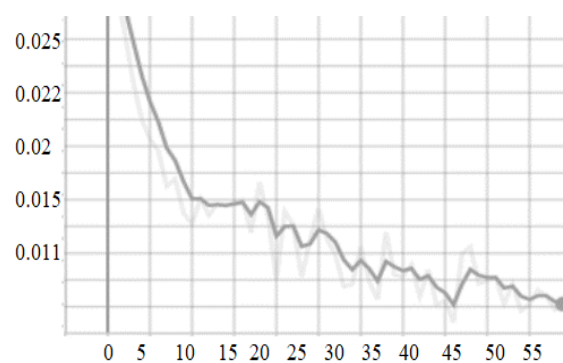


Fig. 4. The Loss classification metric.

The precision significantly decreased during ~42 epoch. The Fig. 5, 6 display that. But in case, if more pictures will be available for training, then higher precision may be for the same number of epochs.

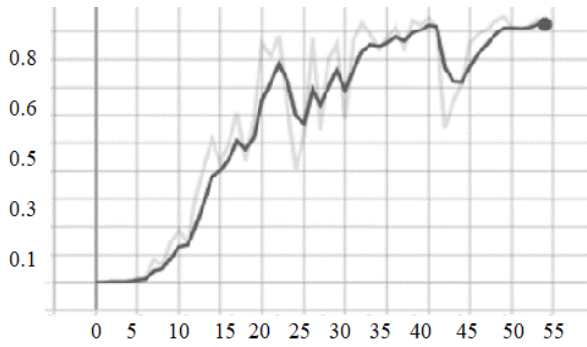


Fig. 5. AP@.5 metric of Yolov7.

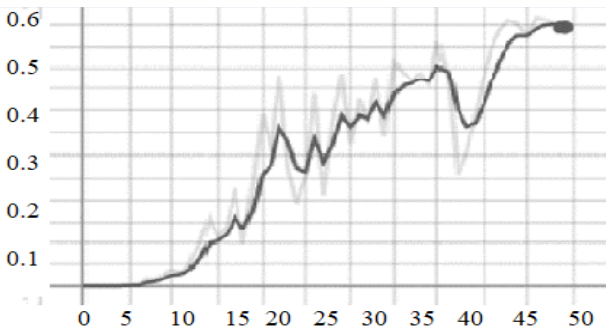


Fig. 6. Fig. 8 AP@.5:95 metric of Yolov7.

The inference results are on Fig. 7, 8. There are no mistakes or incorrect predictions was observed.



Fig. 7. Inference result of Yolov7 [25].

On the mentioned inference result the one oncoming lane presents and this is non-danger class. The model distinguish where the one oncoming lane and where two and more. This is very important in undstanding of dangerous situations. Because when the two or more lanes exist and only one lane is full and when one lane exist and it is full, these are different cases.

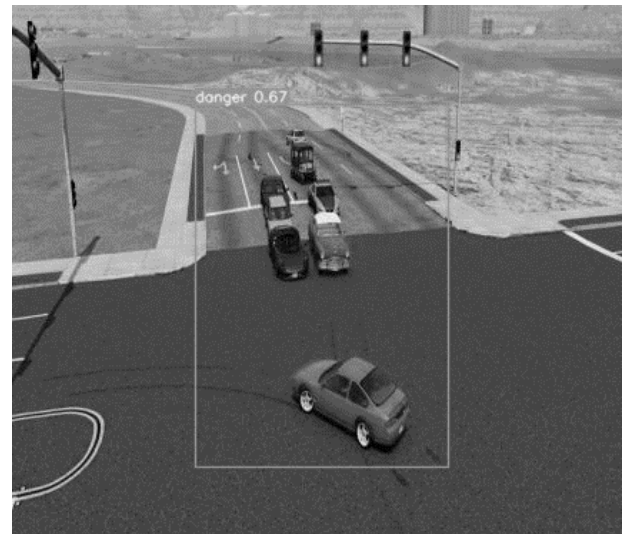


Fig. 8. Inference result of Yolov7 [25].

### B. DETECTRON2 RESULTS

The Detectron2 model has the following results values (Table 5).

TABLE 5 DETECTRON2 RESULTS

Value	Metric
0.651	AP@.5:95
0.909	AP@.5
0.198093 s / img per GPU	Inference time
815 MB	Model size

The Loss box chart is on the Fig. 9.

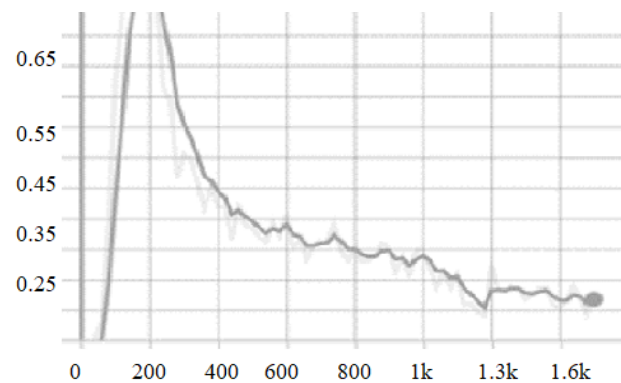


Fig. 9. Loss Box for Detectron2.

The Loss classification chart is on the Fig. 10.

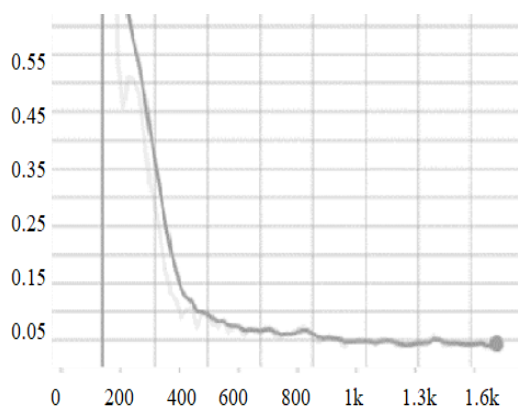


Fig. 10 Loss CLS for Detectron2.

The inference results are on the Fig. 11, 12.



Fig. 11 Inference result of Detectron2 [25].

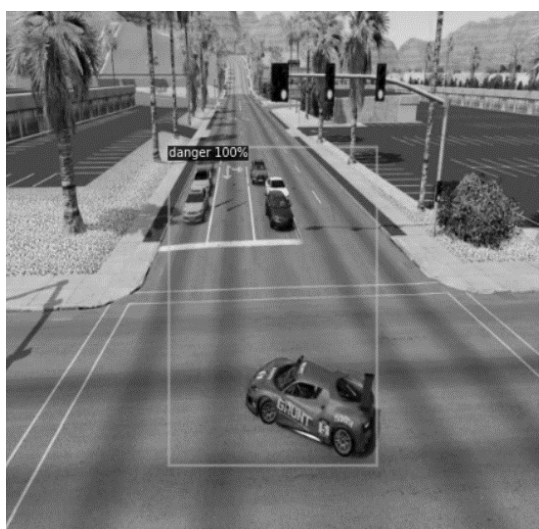


Fig. 12 Inference result of Detectron2 [25].

#### IV. DISCUSSIONS

The discussion section entails a comparison of the model's results and identification of the most appropriate algorithm for the problem of usage it in robotic vision

system. Table 6 presents the compilation results for the aforementioned algorithms.

TABLE 6 COMPILATION RESULTS

Value	Detectron2	Yolov7
AP@.5:95	0.651	0.583
AP@.5	0.909	0.926
Inference time	0.198093 s / img per GPU	0.191668 s / img per GPU
Model size	815 MB	74.8 MB
GPU RAM	8.5 Gb	11.4 GB
Time to train	51 mins	15.9 Mins
Epoch	1500	55

The results indicate that while there is only a slight improvement in accuracy, Yolov7 outperforms Detectron2 in other parameters. This is likely due to the fact that achieving similar accuracy with Detectron2 requires even greater amounts of time and resources. It is possible that a larger dataset may yield better results as using only 300 images is not sufficient for creating a high-performing model. Also, the small amount of size is better in terms of usage by autonomous system, where hardware size has big value.

#### V. CONCLUSIONS

This study presents insights into the most effective image detection and tracking algorithm for quickly identifying dangerous situations on the road. Given the alarming statistics on road accidents resulting in injuries and deaths, it is imperative to address this problem. Previous studies have focused on statistical approaches for predicting road accidents and using regression algorithms to make predictions based on various factors such as weather, road conditions, time of day, day of the week, season, speed, and car condition.

To prepare the dataset, 300 images with different road intersections, outdoor settings, and car setups were captured and labeled using the Roboflow service, which also allows for image resizing and dataset splitting. The research evaluated the performance of two algorithms, Detectron2 (with Faster R-CNN) and Yolov7, using various metrics, such as Average Precision, Inference time, Time for training, Model size, and GPU RAM usage. The research found that Yolov7 outperformed Detectron2 in terms of performance metrics.

The study also explores the potential for applying these approaches to a single-board computer or robot vision systems and provides a starting point for researchers conducting similar two-class classification

research. Overall, this study offers valuable insights into improving road safety through effective image detection and tracking algorithms.

#### REFERENCES

- [1] S. S. Thomas, S. Gupta and V. K. Subramanian, "Event Detection on Roads Using Perceptual Video Summarization," in *IEEE Transactions on Intelligent Transportation Systems*, vol. 19, no. 9, pp. 2944-2954, Sept. 2018, doi: 10.1109/TITS.2017.2769719.
- [2] W. -J. Chang, L. -B. Chen and K. -Y. Su, "DeepCrash: A Deep Learning-Based Internet of Vehicles System for Head-On and Single-Vehicle Accident Detection With Emergency Notification," in *IEEE Access*, vol. 7, pp. 148163-148175, 2019, doi: 10.1109/ACCESS.2019.2946468.
- [3] H. Hayashi, M. Kamezaki and S. Sugano, "Toward Health-Related Accident Prevention: Symptom Detection and Intervention Based on Driver Monitoring and Verbal Interaction," in *IEEE Open Journal of Intelligent Transportation Systems*, vol. 2, pp. 240-253, 2021, doi: 10.1109/OJITS.2021.3102125.
- [4] Q. Xie, X. Hu, L. Ren, L. Qi and Z. Sun, "A Binocular Vision Application in IoT: Realtime Trustworthy Road Condition Detection System in Passable Area," in *IEEE Transactions on Industrial Informatics*, vol. 19, no. 1, pp. 973-983, Jan. 2023, doi: 10.1109/TII.2022.3145858.
- [5] P. Teixeira, S. Sargento, P. Rito, M. Luís and F. Castro, "A Sensing, Communication and Computing Approach for Vulnerable Road Users Safety," in *IEEE Access*, vol. 11, pp. 4914-4930, 2023, doi: 10.1109/ACCESS.2023.3235863.
- [6] X. Mo, C. Sun, C. Zhang, J. Tian and Z. Shao, "Research on Expressway Traffic Event Detection at Night Based on Mask-SpyNet," in *IEEE Access*, vol. 10, pp. 69053-69062, 2022, doi: 10.1109/ACCESS.2022.3178714.
- [7] Q. Zhang, X. Chang and S. B. Bian, "Vehicle-Damage-Detection Segmentation Algorithm Based on Improved Mask RCNN," in *IEEE Access*, vol. 8, pp. 6997-7004, 2020, doi: 10.1109/ACCESS.2020.2964055.
- [8] A. Němcová et al., "Multimodal Features for Detection of Driver Stress and Fatigue: Review," in *IEEE Transactions on Intelligent Transportation Systems*, vol. 22, no. 6, pp. 3214-3233, June 2021, doi: 10.1109/TITS.2020.2977762.
- [9] A. Arsenov, I. Ruban, K. Smelyakov and A. Chupryna, "Evolution of convolutional neural network architectures in image classification problems", Selected Papers of the XVIII International Scientific and Practical Conference "Information Technologies and Security" (ITS 2018), Kyiv, Ukraine, November 27, 2018. In *CEUR Workshop Proceedings*, Vol-2318, 2018, pp. 35-45. <https://ceur-ws.org/Vol-2318/>
- [10] L. Hu, J. Ou, J. Huang, Y. Chen and D. Cao, "A Review of Research on Traffic Conflicts Based on Intelligent Vehicles," in *IEEE Access*, vol. 8, pp. 24471-24483, 2020, doi: 10.1109/ACCESS.2020.2970164.
- [11] K. Smelyakov, P. Dmitry, M. Vitalii and C. Anastasiya, "Investigation of network infrastructure control parameters for effective intellectual analysis," 2018 14th International Conference on Advanced Trends in Radioelectronics, Telecommunications and Computer Engineering (TCSET), Lviv-Slavske, Ukraine, 2018, pp. 983-986, doi: 10.1109/TCSET.2018.8336359.
- [12] J. Barnett et al., "Automated Vehicles Sharing the Road: Surveying Detection and Localization of Pedalcyclists," in *IEEE Transactions on Intelligent Vehicles*, vol. 6, no. 4, pp. 649-664, Dec. 2021, doi: 10.1109/TIV.2020.3046859.
- [13] H. Fan and H. Zhu, "Separation of Vehicle Detection Area Using Fourier Descriptor Under Internet of Things Monitoring," in *IEEE Access*, vol. 6, pp. 47600-47609, 2018, doi: 10.1109/ACCESS.2018.2865209.
- [14] J. E. Espinosa, S. A. Velastín and J. W. Branch, "Detection of Motorcycles in Urban Traffic Using Video Analysis: A Review," in *IEEE Transactions on Intelligent Transportation Systems*, vol. 22, no. 10, pp. 6115-6130, Oct. 2021, doi: 10.1109/TITS.2020.2997084.
- [15] J. Barnett et al., "Automated Vehicles Sharing the Road: Surveying Detection and Localization of Pedalcyclists," in *IEEE Transactions on Intelligent Vehicles*, vol. 6, no. 4, pp. 649-664, Dec. 2021, doi: 10.1109/TIV.2020.3046859.
- [16] F. Guede-Fernández, M. Fernández-Chimeno, J. Ramos-Castro and M. A. García-González, "Driver Drowsiness Detection Based on Respiratory Signal Analysis," in *IEEE Access*, vol. 7, pp. 81826-81838, 2019, doi: 10.1109/ACCESS.2019.2924481.
- [17] T. Horberry et al., "Human-Centered Design for an In-Vehicle Truck Driver Fatigue and Distraction Warning System," in *IEEE Transactions on Intelligent Transportation Systems*, vol. 23, no. 6, pp. 5350-5359, June 2022, doi: 10.1109/TITS.2021.3053096.
- [18] S. Nakashima, H. Arimura, M. Yamamoto, S. Mu and H. Lu, "Improving the Accuracy of Road Surface Distinction Based on Reflection Intensity Variations Using Ultrasonic Sensor," in *IEEE Sensors Journal*, vol. 22, no. 18, pp. 17399-17405, 15 Sept. 2022, doi: 10.1109/JSEN.2020.3033015.
- [19] X. Liu, H. Cai, R. Zhong, W. Sun and J. Chen, "Learning Traffic as Images for Incident Detection Using Convolutional Neural Networks," in *IEEE Access*, vol. 8, pp. 7916-7924, 2020, doi: 10.1109/ACCESS.2020.2964644.
- [20] C. M. Travieso-González, J. B. Alonso-Hernández, J. M. Canino-Rodríguez, S. T. Pérez-Suárez, D. D. L. C. Sánchez-Rodríguez and A. G. Ravelo-García, "Robust Detection of Fatigue Parameters Based on Infrared Information," in *IEEE Access*, vol. 9, pp. 18209-18221, 2021, doi: 10.1109/ACCESS.2021.3052770.
- [21] S. Aoki, K. Sezaki, N. J. Yuan and X. Xie, "BusBeat: Early Event Detection with Real-Time Bus GPS Trajectories," in *IEEE Transactions on Big Data*, vol. 7, no. 2, pp. 371-382, 1 June 2021, doi: 10.1109/TBDDATA.2018.2872532.
- [22] C. Yang, X. Wang and S. Mao, "Unsupervised Drowsy Driving Detection With RFID," in *IEEE Transactions on Vehicular Technology*, vol. 69, no. 8, pp. 8151-8163, Aug. 2020, doi: 10.1109/TVT.2020.2995835.
- [23] C.-Y. Wang, A. Bochkovskiy, and H.-Y. M. Liao, "Yolov7: Trainable bag-of-freebies sets new state-of-the-art for real-time object detectors," *arXiv.org*, 06-Jul-2022. [Online]. URL: <https://arxiv.org/abs/2207.02696>. [Accessed: 14-Feb-2023].
- [24] S. Ren, K. He, R. Girshick, and J. Sun, "Faster R-CNN: Towards real-time object detection with region proposal networks," *arXiv.org*, 06-Jan-2016. [Online]. URL: <https://arxiv.org/abs/1506.01497>. [Accessed: 14-Feb-2023].
- [25] O. Byzkrovnyi, "Roboflow," *Roboflow Dataset*. [Online]. URL: <https://app.roboflow.com/ds/polJ55iQ4a?key=zYXz2EmCeK>. [Accessed: 14-Feb-2023].
- [26] BeamNG.drive. [Online]. URL: <https://www.beamng.com/game/>. [Accessed: 14-Feb-2023]
- [27] "Google colab," *Google Colab. Detectron2*. [Online]. URL: [https://colab.research.google.com/drive/1vTh-bC31puePqn68K81Y41eyCAm5DrUt?usp=share\\_link](https://colab.research.google.com/drive/1vTh-bC31puePqn68K81Y41eyCAm5DrUt?usp=share_link). [Accessed: 14-Feb-2023].
- [28] "Google Colab. Yolov7," *Google Colab*. [Online]. URL: [https://colab.research.google.com/drive/1kaVsuWK6DfXykeae1PazYH0Yw-ZVzZ-I?usp=share\\_link](https://colab.research.google.com/drive/1kaVsuWK6DfXykeae1PazYH0Yw-ZVzZ-I?usp=share_link). [Accessed: 14-Feb-2023].

# Comparative Studies of the Strength Characteristics of Concrete Blocks with Titanium and Iron Rods (Bars)

**Ervins Blumbergs**

Institute of Physics, University of Latvia, 32 Miera str., Salaspils, LV-2169, Latvia

ZTF Aerkom SIA, 32 Miera str., Salaspils, LV-2169, Latvia

Faculty of Civil Engineering, Riga Technical University, 21/1 Azenes str., Riga, LV-1048, Latvia

Rīga, Latvija  
ervinblumbergs@gmail.com

**Viktors Mironovs**

Riga Technical University, Powder Materials Laboratory, Kipsalas str. 6B-319, Riga, LV-1048, Latvia

Rīga, Latvija  
viktors.mironovs@gmail.com

**Genadijs SAHMENKO**

Riga Technical University, Būvmateriālu un būvīzstrādājumu katedra, Kipsalas str. 6A, Riga, LV-1048, Latvia

Rīga, Latvija  
genadijs.sahmenko@rtu.lv

**Abstract.** The relevance of the topic of the work was shown by the accident of a multi-storey residential building in Miami, which was caused by corrosion of steel reinforcement in reinforced concrete.

There is a need to maintain the bearing capacity of structures for a long time in a humid climate, aggressive environmental influences and temperature fluctuations with a lower consumption of materials used.

The use of titanium will allow changing some parameters of titanium concrete structures in comparison with reinforced concrete structures. The protective layer of concrete, which serves to protect the reinforcement from the effects of the external environment, will be significantly reduced. This will help to reduce the mass of concrete structures while maintaining strength properties and will allow you to create lighter structures that can withstand heavy loads.

Strength tests were carried out on concrete blocks reinforced with smooth iron or titanium rods Ø10 mm, which showed the prospects of replacing steel reinforcement with titanium reinforcement in reinforced concrete.

**Keywords:** Concrete, Bending test, Concrete reinforced with titanium and iron bars, Durability.

## INTRODUCTION

Due to the high cost of titanium production, it is currently used only in those industries, where the use of such an expensive material is economically justified. When justifying the use of titanium, not only its strength and lightness are taken into account, but also corrosion

resistance which is comparable to the strength and durability of precious metals. Titanium is mainly used in the aircraft and transport industries, where the combination of strength and lightness is of particular importance [1,2,3].

In construction industry, titanium is used in the form of titanium cladding, roll roofing and facade cladding [4,5].

The utilization of titanium alloys in civil engineering is not common, but its applications are becoming more prevalent. This is due to two significant reasons: firstly, the cost of titanium has considerably decreased over time: Although, like other commodities, it is subject to price changes, when adjusted for inflation, prices generally tend to fall. As of January 2016, the price was \$3,750 per metric ton. In 2005, the price was \$21,000 a ton (Figure 1).

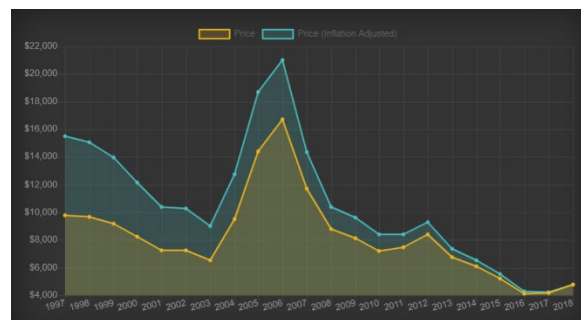


Fig. 1. Inflation adjusted cost of titanium: as of January 2016, the price was USD 3750 per ton; in 2005, the price was USD 21,000 a ton. [6].

Print ISSN 1691-5402  
Online ISSN 2256-070X

<https://doi.org/10.17770/etr2023vol3.7303>

© 2023 Ervins Blumbergs, Viktors Mironovs, Genadijs Sahmenko. Published by Rezekne Academy of Technologies.  
This is an open access article under the [Creative Commons Attribution 4.0 International License](https://creativecommons.org/licenses/by/4.0/).

Secondly, there have been occurrences of civil infrastructure collapses which have highlighted the inadequacies of using carbon steel in structures that are exposed to outdoor environments. Civil structures and infrastructures generally have a longer design life compared to aerospace or medical applications. In several developed nations, concrete bridges constructed during the economic boom of the 1950s and 1960s were often insufficiently reinforced with steel and require repair or replacement (as shown in Figure 2). These bridges are usually still functional even after 70 years, and the drawbacks of replacement are high, not only in terms of economic costs but also with regards to carbon emissions and sustainability. Recently, titanium has been utilized to renovate and prolong the life of bridges, resulting in savings in costs and time compared to replacement methods [7,8,9].

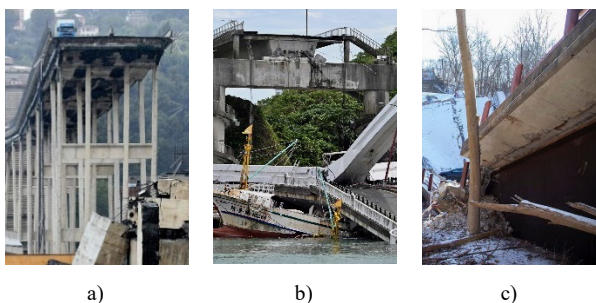


Fig. 2. Recent collapses of reinforced concrete bridges due to the corrosion of steel: a) Igaly (Genova), b) Taiwan, c) USA (Pittsburgh).

The durability of titanium is its main advantage, surpassing that of other materials such as stainless steel or composite materials. Typically, interventions on heritage masonry buildings or existing masonry structures are intended to endure for many decades, and sometimes even for centuries. These buildings are exposed to various atmospheric conditions, such as high temperatures, frost, solar radiation, humidity, and acid rain, among others, as well as the worsening impacts of climate change, resulting in new threats from natural disasters. These effects have been underestimated to some extent, not just by industry and professionals, but also by the scientific community working in conservation engineering. Numerous interventions carried out in the 1990s and 2000s using FRPs or stainless-steel exhibit signs of mechanical wear, reinforcement debonding from the masonry substrate, and corrosion. In certain instances, these impacts have caused irreparable damage to the masonry structure [10].

When investigating in the framework of ERDF No. 1.1.1.1./16/A/85 "Electroslag process for better titanium sediment morphology", the technology for the production of titanium and titanium alloys and semi-finished products from them allows the production at small and medium-sized plants similar to foundry at industrial plants. [11,12]

A large amount of accumulated titanium scrap does not find secondary use for the production of high value-added titanium products due to the large number of grades of

titanium alloys alloyed with a wide range of additives, which does not allow a correct selection of one grade of titanium alloys due to the small dimensions and weight of individual parts of titanium scrap. The main use of scrap titanium and titanium alloys is to produce ferrotitanium, which is used during steel smelting for degassing. But the entire volume of titanium scrap exceeds the needs of the steel industry. One of the possible applications of excess titanium scrap is the manufacture of rebar from titanium alloys, averaged over the chemical composition during the remelting process.

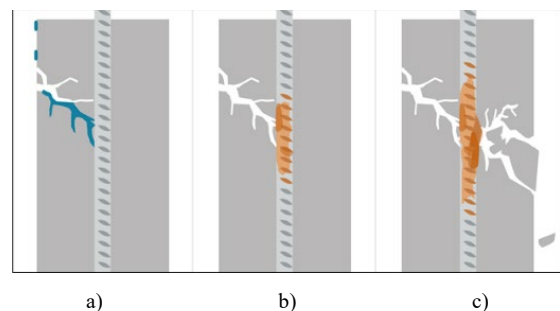


Fig. 3. Damage to reinforcement in reinforced concrete blocks in a humid environment.

- a) Water enters the concrete.
- b) Steel reinforcement starts to rust, corrosion expands.
- c) The concrete starts to crack and destroys.

The use of titanium will make it possible to change some parameters of titanium-concrete structures if compared with reinforced concrete structures. The protective layer of concrete which serves to protect the reinforcement from the external environment will be significantly reduced. This will allow to decrease the weight of concrete structures while maintaining their strength properties and to produce lighter structures that can withstand higher loads [13].

One of the directions for the effective use of titanium and titanium alloys in the construction industry is the development and implementation of methods to reduce the cost of the material. Methods for extracting cheap titanium are discussed in [14]. It has been shown that it can economically produce pure titanium metal and alloys for applications such as automobiles and electronics. Another way is to increase the strength properties of the material [15].

#### MATERIALS AND METHODS

The experimental part of the work provides for the manufacture of concrete beams 100x100x500 reinforced with steel and titanium bars. Reference mix was designed to produce concrete with strength grade C40/45 and workability class S3 (in accordance with standard LVS EN 206). The following ingredients proportions (related to 1 m<sup>3</sup> of fresh mix) were provided: Portland cement CEM I 42,5 N - 450 kg, gravel 0/8 mm - 1620 kg, water 216 kg, polycarboxilate superplasticizer 2,3 kg, water-cement ratio 0.48.

Smooth reinforcing bars with a diameter of 10 mm were used to reinforce the beams. In the frame of the experiment, the surfaces of steel and titanium bars were compared before concreting works. Optical 3D microscope Keyence 2000 equipped with VHX-20-200 lens was used for visual investigation of the surface of iron and titanium rods before concreting. Images are shown in Figure 2: On the left is steel bar surface, on the right is titanium bar surface. Comparative smoothness of iron and titanium bars showed that titanium bars are much less rough compared to iron ones.

The bars were placed in the lower part of the sample, taking into account the thickness of the protective layer of concrete 5 mm. Two samples were made with the steel reinforcement and two samples with titanium reinforcement. (Figure 4).

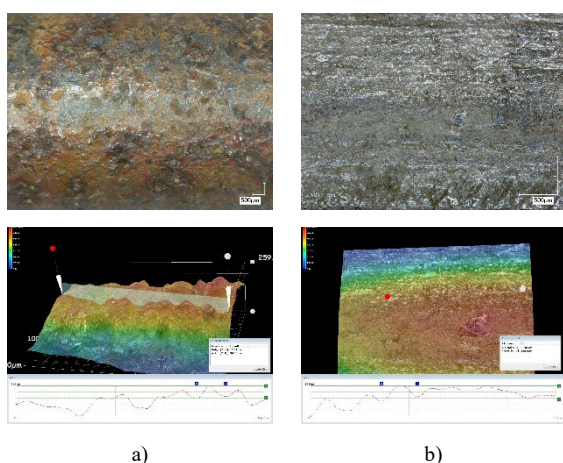


Fig. 4. Comparison of the surface of iron and titanium rods before concreting. a) iron, b) titanium.

The process of production of reinforced concrete and titanium concrete beams is shown in Figure 5. Samples were tested for three-point bending at the age of 28 days. The load was applied in the middle of the span and the distance between the supports was 420 mm (Figure 4). The load was applied in the middle of the span and during the test the numerical values of the applied force and mid-span deflection were recorded.



Fig. 5. The process of production of reinforced concrete and titanium concrete beams.



Fig. 6. Testing of concrete beams.

## RESULTS AND DISCUSSION

During the experiment, the strength characteristics of concrete samples were tested, the results of titanium and steel reinforced beams were compared. Numerical values of strength properties of concrete cubical samples and reinforced concrete beams are summarized in Table 1. Testing results of concrete samples showed average compressive strength 54.7 MPa, that confirms to designed strength class C35/45.

Bending testing curves are showed in Figure 7. The results of the bending test indicate that specimens with titanium reinforcement have average bending capacity of 15,78 kN, the specimens with steel reinforcement 25.75 kN. Thus samples with titanium reinforcement have a bearing capacity of 40% less than samples with steel reinforcement. The corresponding recalculated bending strength is 16.2 and 9.9 MPa respectively. This is not a decisive indicator, since titanium grade VT-1 was used without alloying - hardening additives.

Table 1. Strength characteristics of concrete samples and reinforced concrete beams

	Compressive strength, MPa	Maximum bending force, kN	Bending strength, MPa	Residual force at a deformation of 3.5 mm F(3.5), kN	F(3.5) / Fmax, %
Reference concrete	<b>54.7</b>				
Steel reinforced beam					
S-1		25.86	16.3	8.0	30.9
S-2		25.64	16.2	8.7	33.9
S-average		<b>25.8</b>	<b>16.2</b>	<b>8.4</b>	<b>32.4</b>
Titanium reinforced beam					
T-1		15.75	9.9	6.8	43.2
T-2		15.81	10.0	9.9	62.6
T-average		<b>15.8</b>	<b>9.9</b>	<b>8.4</b>	<b>52.9</b>

Analyzing the typical load – mid-span deflection curve (Figure 7), three characteristic areas can be distinguished. The initial linear and ascending section of the curve corresponds to the joint work of the reinforcement and the concrete matrix. The second characteristic area of the curve is the maximum value of the force at which a concrete crack is formed in the lower tensioned part of the beam and tensile load is redistributed to the reinforcing bars. The third descending section of the curve corresponds to the work of the reinforcement in tension and the concrete work on compression in the upper part of the beam section. Taking into account the above characteristic areas, the following behaviour of steel and titanium reinforced beams can be distinguished:

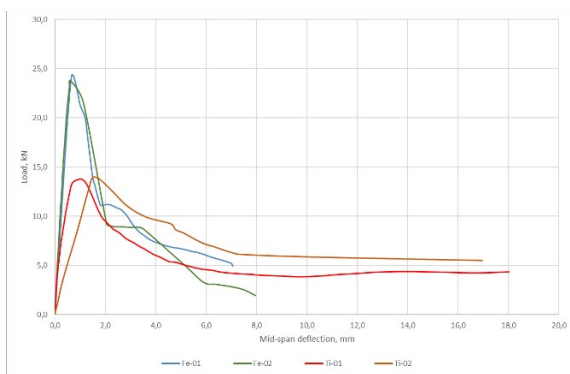


Fig. 7. Strength characteristics of concrete blocks with titanium and iron rods (rods).

In the initial linear area, the curves of specimens with titanium reinforcement have a lower angle of inclination, which can be explained by the lower modulus of elasticity of titanium (110 GPa) compared to the modulus of elasticity of steel (200 GPa).

The lower value of the bearing capacity of samples with titanium could be explained with the lower tensile strength of titanium bar compared to the strength of steel bar. Analyzing the pattern of destruction of samples with steel reinforcement (Figure 8a), it can be noted that the destruction of the beam did not occur from the rupture of steel reinforcement, but destruction occurs due to the action of transverse forces. In the case of titanium reinforcement, the beam destruction take place in the middle part of the beam (in the place with the maximum bending moment). Significant tensile deformations of titanium reinforcement cause high maximum deflection values compared to steel-reinforced beams (Figure 8b).



Fig. 8. Destruction mode of beam with steel reinforcement (a) and titanium reinforcement (b).

Evaluating the work of reinforced beams it would be advisable to analyze post-cracking areas. Specimens reinforced with titanium reinforcement, have a more pronounced area of plastic deformations. According to test results (Table 1), beams with titanium and steel carry the same residual load (8.4 kN) at the same mid-span deflection (3.5 mm). However, for beams with steel reinforcement, this load is 32% of the maximum breaking load, but for beams with titanium - 53% of the breaking load. These properties can be an additional safety factor for impact energy absorption.

Furthermore, at elevated temperatures ( $> 700^{\circ}\text{C}$ ), titanium bars are characterized by a lower decrease in strength and elastic modulus than steel. This can have a positive effect on the fire safety of structures. An additional factor of reliability is the higher chemical resistance of titanium compared to steel.

Lower strength of titanium reinforcement does not allow its use in heavily loaded reinforced concrete structures. Despite this, titanium reinforcement can find application in moderate loaded structures where high corrosion resistance, durability, impact resistance and fire resistance are required.

Reduction of concrete protective cover will help to reduce the self-weight of concrete structures while maintaining strength properties and will allow you to create lighter structures with the same bearing capacity.

## CONCLUSIONS

In this study, laboratory beams were made, using steel and titanium reinforcing bars. Comparative tests on the strength of concrete blocks reinforced with steel and titanium smooth rods showed that:

1. The bearing capacity of steel reinforced concrete beams is greater than that of titanium reinforced (25.8 and 15.8 kN correspondingly). The use of a stronger titanium alloy would have made it possible to obtain higher strength results.
2. Comparative smoothness of iron and titanium bars showed that titanium bars are much less rough compared to iron ones. When titanium bars are artificially roughened, the characteristics may be different, but this requires additional research.
3. A positive property of titanium reinforcement is a higher ductility and the ability to withstand large deformations. At the same mid-span deflection (3.5 mm) steel reinforced beams carry 32% of the maximum breaking load, but for beams with titanium - 53% of the breaking load.

Based on the obtained experimental results, a patent application and an article for publication in a high-indexed journal were prepared.

Additional reliability factors of titanium reinforcement are its significant chemical resistance and possibly higher heat resistance. These questions could be considered in the future stages of this study.

#### ACKNOWLEDGMENTS

The authors would also like to mention the support from the ERAF project No.1.1.1.1./16/A/85 “Electroslag process for better titanium sediment morphology”.

#### REFERENCES

- [1] Williams, J.C.; Boyer, R.R. Opportunities and Issues in the Application of Titanium Alloys for Aerospace Components. *Metals* **2020**, *10*, 705. <https://doi.org/10.3390/met10060705>
- [2] Boyer, R.R.; Briggs, R.D. The Use of  $\beta$  Titanium Alloys in the Aerospace Industry. *J. Mater. Eng. Perform.* **2005**, *14*, 681–685.
- [3] Cotton, J.D.; Briggs, R.D.; Boyer, R.R.; Tamirisakandal, S.; Russo, P.; Shchetinokov, N.; Fanning, J.C. State of the Art of Beta Titanium Alloys for Aerospace Applications. *JOM* **2015**, *5*, 1281–1303.
- [4] Haile, F.; Adkins, J.; Corradi, M. A Review of the Use of Titanium for Reinforcement of Masonry Structures. *Materials* **2022**, *15*, 4561. <https://doi.org/10.3390/ma15134561>
- [5] Leyens, C.; Peters, M. *Titanium and Titanium Alloys: Fundamentals and Applications*; Wiley-VCH Verlag GmbH & Co: Weinheim, Germany, 2003; ISBN 9783527305346.
- [6] PW Consulting Agency. Available online: <https://pmarketresearch.com/titanium-industry-research-report-2021/> (accessed on 17 April 2023).
- [7] Adkins, J.; George, W. Titanium finds a home in civil engineering. *Concr. Int.* **2017**, *39*, 51–55.
- [8] Higgins, C.; Knudtsen, J.; Amneus, D.; Barker, L. Shear and Flexural Strengthening of Reinforced Concrete Beams with Titanium Alloy Bar. In Proceedings of the 2nd World Congress on Civil, Structural, and Environmental Engineering (CSEE'17), Barcelona, Spain, 2–4 April 2017.
- [9] Higgins, C. Titanium Reinforcing for Strengthening RC Bridges. In Proceedings of the 32nd International Bridge Conference (IBC 2005), Pittsburgh, PA, USA, 7–11 June 2015.
- [10] Haile F, Adkins J, Corradi M. A Review of the Use of Titanium for Reinforcement of Masonry Structures. *Materials*. **2022**; *15*(13):4561
- [11] E. Platacis, I. Kaldre, E. Blumbergs, L. Goldšteins, and V. Serga, Titanium production by magnesium thermal reduction in the electroslag process. *www.nature.com/scientificreports Scientific Reports* (2019)9: 17566, November 2019, DOI: 10.1038/s41598-019-54112-2.
- [12] E. Platacis, I. Kaldre, E. Blumbergs, L. Goldšteins, and K. Gailītis, Optimization of electroslag melting towards to titanium morphology improvement in combined the Kroll process: COMPEL International Journal of Computations and Mathematics in Electrical; ahead-of-print (ahead-of-print), December 2019, DOI: 10.1108/COMPEL-05-2019-0198.
- [13] S. Platt, K.A. Harries Proposed design methodology for titanium reinforcing bars in concrete. *Eng. Struct.*, **178** (2019), pp. 543-553
- [14] Crowley, G. How to Extract Low-Cost Titanium. 2003, *Advanced Materials and Processing*, Vol. 161, pp. 25-27
- [15] Fanning, J. Near-Beta Titanium alloy for High Strength Application and Methods for Manufacturing the Same. U.S. Patent 8,454,768, 4 June 2013.

# Optical Geometric Design of Small Modular Cylindrical Gears with Asymmetric Profile

Genadi Cvetanov  
Technical University of Gabrovo  
Gabrovo, Bulgaria  
gencvet@tugab.bg

Tsanko Karadzhov  
Technical University of Gabrovo  
Gabrovo, Bulgaria  
karadjov\_st@abv.bg

**Abstract.** The article presents specific practical solutions for optimal geometric design of evolvental cylindrical gears with an asymmetric profile of cogs in the context of the basic principle of cog interlocking. In order to achieve unknown until now quality indicators, constructions with a minimum number of cogs and a maximum angle of interlocking are shown, which allow for the production of off-polar gears and significantly increase the gear ratio of the differential and planetary mechanisms. In the process of determining the geometrical parameters of the cogwheels of the gear, the “classical approach” is used by analogy with the parameters of the instrument, necessary for the production of the small-module cogwheels of the gear.

**Keywords:** *Asymmetrical profile of cogs, Geometric optimization, Border angles and number of cogs.*

## I. INTRODUCTION

In the classical theory of gear coupling, the parameters of the instrument, which is necessary for the production of the cogwheels of the gear, are accepted as the source parameters for the design. In order to perform geometric synthesis of a single evolvent cylindrical gear, four output parameters are required: Module size -  $m$ , Pressure angle -  $\alpha$ , output contour (loop) displacement factor -  $x$ , number of teeth -  $z$  [1]. The four parameters determine the axiomatic design of gear mechanisms at known instrument parameters. Through the use of asymmetrical evolvent cylindrical gears the uncertainty deriving from the choice of independent parameters has been removed and “free geometric synthesis” can be realized.

Based on the 20-years experience of the authors and over 60 publications on the problems of the asymmetrical profile, it has been found that a major problem in its use is the reversal of the direction of movement [1,2,3]. As a solution, the authors set out [4,5] a basic principle of interlocking, allowing the making of gears with an

unachievable until now quality and strength indicators [12]. On the basis of the implications of this principle, three approaches have been developed for geometric synthesis and realization of unconditional areas of existence in the field of independent variables.

## II. PRACTICAL IMPLEMENTATION AND OPTIMIZATION OF GEARS WITH ASYMMETRIC PROFILE

The free geometric synthesis of evolvent cylindrical gears [4,5] with an asymmetrical profile of the cogs, as defined by the authors, allows for various effects expressed in: increase the flow rate of hydraulic gear pumps; increasing the load capacity of ordinary and epicyclic gears; the production of self-locking gears when reversing the direction of movement.

### A. Realization in hydraulic gear pumps

In the process of manufacture, a task has been set for designing a gear with a reduced number of cogs by the method of centroid wrapping with a non-standard instrument of comb type, while maintaining the overall dimensions. When the preset requirements for the gear can not be satisfied by the symmetrical cog profile with the displacement of the output contour, then it is possible to apply asymmetry of the profile and obtain a gear with different than the previously known qualitative indicators. A gear pump is realized, using this method, that increases its actual flow rate, at the expense of increasing the effective area of the pitch surface (bottom land). The main advantage of such gear is the possibility of reversing the direction of movement while maintaining the gear ratio, but with a significant change in quality performance [6].

Print ISSN 1691-5402  
Online ISSN 2256-070X

<https://doi.org/10.17770/etr2023vol3.7279>

© 2023 Genadi Cvetanov, Tsanko Karadzhov. Published by Rezekne Academy of Technologies.  
This is an open access article under the [Creative Commons Attribution 4.0 International License](https://creativecommons.org/licenses/by/4.0/).



Fig. 1. Magnetization as a function of applied field.

A new hydraulic gear pump design was developed and experimentally tested and the following results were established by Protocol No 009/09.05.2002, on a stand of Kaproni AD — Kazanlak: The flow rate of pumps of type X3II 00C 0,5X047 — for the new design is higher by 20.2 to 23.3 %, compared to the flow rate of the existing pumps in production.

*B. Increase the load-bearing capacity of cog interception in epicyclic cog mechanisms*

In addition to the quality indicators of the interception, the asymmetrical cog profile can increase the load capacity of the gear with and without regard to reversing the direction of movement. This makes it possible to optimize gear mechanisms in terms of transmitted torque or locking stiffness, which are different when reversing the direction of movement.

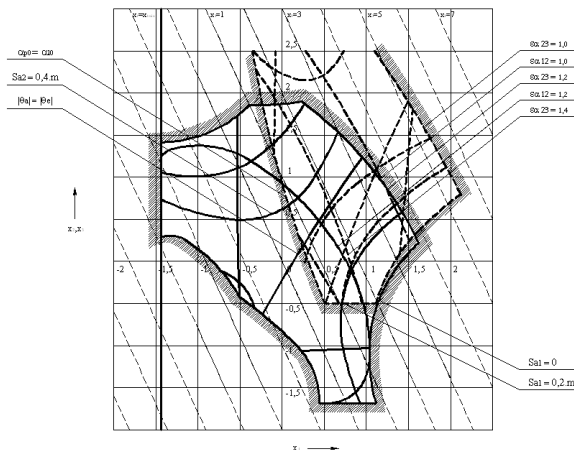


Fig. 2. Blocking contour of reverse differential 2K-H mechanism with asymmetric profile of teeth.

The use of the asymmetrical cog profile in differential and planetary mechanisms allows to increase their load capacity without changing their gear ratio [13]. In order to perform this optimization of the cog profile, blocking contours of 2K — H planetary mechanism have been developed, allowing the reconciliation of the areas of existence in the field of independent displacements of the instrument (Figure 2).

Figure 3 presents a spatial model of the differential gear, which served as the basis for the final - element analysis and a general view of the carving head “TARMATIC”, production of “Balkan” JSC — Lovech [5].



Fig. 3. Model and general view of carving head “Tarmatic”.

Similarly, a planetary 2K-H gear with an asymmetrical profile was developed in an electro-mechanical screwdriver of Gabrovo PGI (Figure 4).

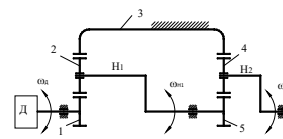


Fig. 4. Kinematic scheme and general view of electro-mechanical screwdriver of Gabrovo PGI.

In the two epicyclic mechanisms (Figure 4) with an asymmetrical profile of the cogs an effect was achieved of increasing the load capacity of the gear while preserving the number of cogs and the levels of freedom of the mechanism. Therefore, this effect should be used for mechanical devices that have a significantly higher load in one of the directions of their movement.

*C. Realization of gears with a minimum number of teeth*

Evolut cylindrical gears with a minimum number of cogs allow the creation of special gears with reduced dimensions and maximum gear ratio.

In the context of the basic principle of cog interlocking in movement, an unconditional area of existence have been developed, and a gear layout for gear ratio  $u=1$  and number of cogs  $z_1=z_2=5$  (Figure 5) .

By using an asymmetric cog profile, it is possible to reduce the minimum number of cogs by 40 % from the minimal possible for a symmetrical profile with a standard contour  $z_1=z_2=7$  to  $z_1=z_2=5$  [7].

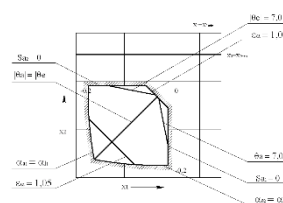


Fig. 5. Gear with asymmetric profile and minimum number of teeth.

Based on the depicted area (Figure 5), such a reverse gear with an asymmetrical profile of the cogs is realized, when the output contour is shifted  $x_1 = x_2 = -0.15$ , which has a frontal overlap coefficient of  $\varepsilon_\alpha = 1.06$  and  $\varepsilon^*_\alpha = 1.01$ .

#### D. Realization of self-locking gears

The study of the unconditional areas of existence of an asymmetrical profile and external interlocking has established the following general regularity: *as the value of one of the interlocking angles increases, the value of the other also increases, regardless of its initial value.* Therefore, the asymmetrical cog profile is characterized by: lower frontal overlap coefficients when one of the angles of intersection rises in value and higher when one of the angles of intersection is reduced (responsive to the output contour) compared to the output of symmetrical cog profile. This presupposes the existence of additional interlocking phenomena, that determines its specificity and practical limitlessness, such as the existence of a self-stop effect.

Such a gear with an asymmetrical profile was designed according to the classical approach, but due to the extreme angles of the comb-type instrument, a thread erosion method was used for the production of the wheels, with thread thickness of 0.2 mm, at Arsenal JSCo-Kazanlak [8].

In this gear with external interlock, a self-lock effect has been achieved at an angle of interlocking  $\alpha^*_w = 48,23^\circ$  (Figure 6), which cannot be achieved with a symmetrical profile. This restriction was first established by Prof. V. A. Gavrilenko, who recommended that the profile angles of the output symmetric contours to be determined by the unrestricted inequation  $\alpha \leq 35^\circ$ .

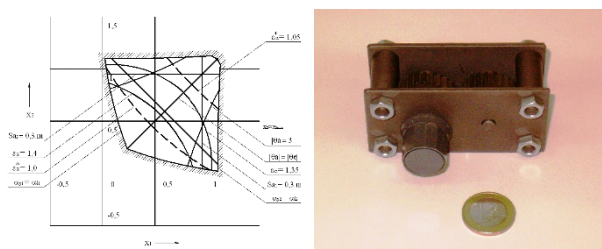


Fig. 6. Blocking contour of reverse differential 2K-H mechanism with asymmetric profile of teeth.

#### E. Realization of gears with internal interlocking and minimum number of cogs

With internal interlocking and minimal difference in the number of cogs of evolvental cylindrical gears with asymmetrical profile of the cogs, narrowing of the unconditional area of existence is observed, due to the presence of additional interference. A borderline case are the mechanisms with internal interlocking and equal number of cogs, in which there is a constant velocity of sliding at all points of the active line of interlocking for each of the profiles and different load capacity.

Figure 7 presents an evolvent cylindrical gear with asymmetrical profile, internal interlocking and equal number of cogs [9].

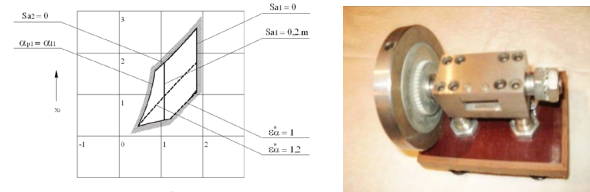


Fig. 7. Cog gear with asymmetrical profile and equal number of wheel cogs  $Z_2 = Z_1 = 44$ ; profile angles of the instrument  $\alpha = 20^\circ$  and  $\alpha^* = 30^\circ$ .

In the case of fixed gear axes, such a gear is used as a clutch, joining two parallel non-coaxial shafts. If the given gear is performed as a planetary mechanism, the satellite wheel moves translationally, the trajectory of each point being a circle with a diameter of  $2 \cdot a_w$ .

#### D. Cog gears with asymmetric profile and inclination of cogs

In order to obtain greater overlap coefficients, it is possible to realize gears with an asymmetrical profile and inclination of the cogs by using the theorem of reversing the direction of movement.

Figure 8 presents the unconditional area of existence of such gear and a layout of an evolvent cylindrical gear with an asymmetrical profile and inclination of the cogs.

Displacement factors  $x_1 = x_2 = 0.5$  were selected from it, with wheel width  $b = 5$  mm achieving overlap coefficients  $\varepsilon = 2,2$  (1.61);  $\varepsilon^* = 2,0$  (1.46).

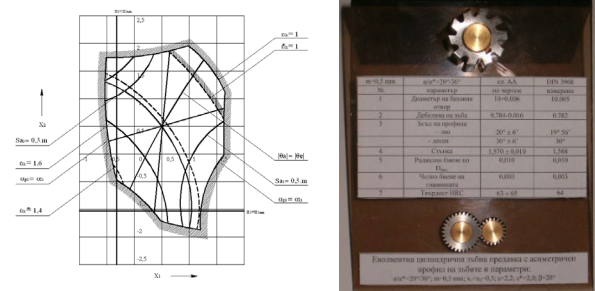


Fig. 8. Cog gear with asymmetric profile and inclination of cogs  $\beta = 20^\circ$ .

#### E. Realization of gears with variable speeds and gear ratios

The eccentric gearbox creates at its output cyclically changing speeds and gear ratios. They are modified in a similar way to gears with elliptical cog wheels (Figure 9). The distance between the geometric centers, the angle of interlocking and the overlap coefficient are variables during the movement of the gears. At a specified output angle of interlocking, the maximum variation in the distance between geometric centers is expressed by the eccentricity of the gear, which is constant [10].

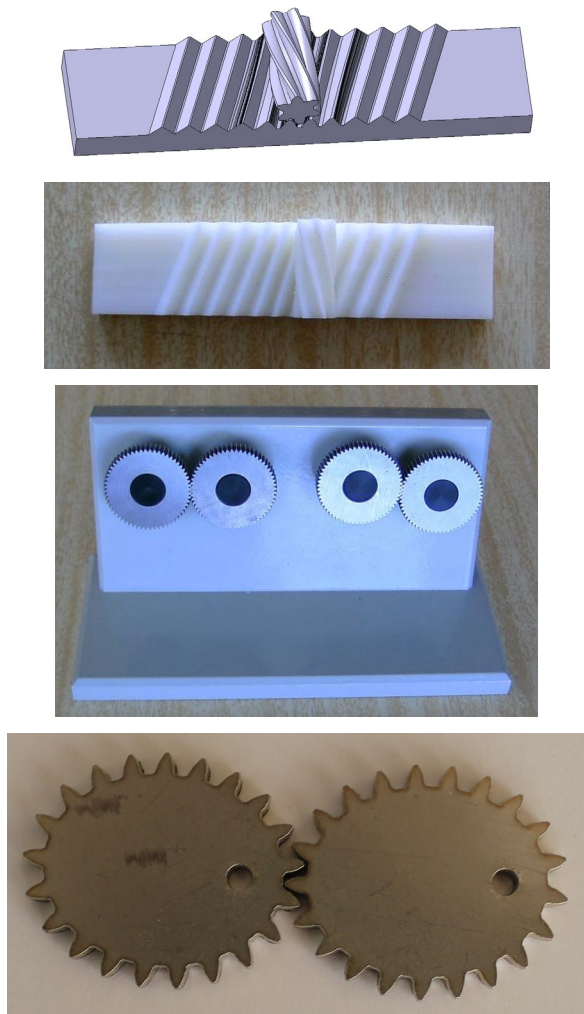


Fig. 9. Variable gears and asymmetric cog profile: model and prototype of comb gear with inclination of teeth, eccentric gear with round wheels and elliptical gears with asymmetric profile, made with laser cutting.

### III. CONCLUSION

With the help of the basic law of interlocking of evolvent cylindrical gears with asymmetric profile, free geometric synthesis and conversion of the classical theory of gear interlocking by transforming the independent variable — the non-working angle of intersection into a dependent one was carried out, which achieved optimization of quality and strength performance, excluding the geometric parameters of the instrument required for the production of the wheels of the gear.

Summarized and shown is the 20 years of experience of the authors in the optimal geometric and strength synthesis, the practical implementation of evolvent cylindrical gears with asymmetric profile of the cogs, expressed in: reduction of the number of cogs on the interlocking with preservation of the quality and strength performance, thus reduction of the overall dimensions of the gear; optimization of epicyclic cog mechanisms; realization of gears with self-locking effect; design of gear couplings with compensation of shafts with axis inconsistency and

obtaining mechanisms with variable gear ratio at a translation or rotation of the executive unit. A large part of the resulting gears with previously unknown quality and strength indicators are experimentally tested on test stands in production conditions and have been successfully implemented in practice.

### REFERENCES

- [1] Tsvetanov G. Study on small-modular cog gears with asymmetric profile, Dissertation for obtaining an educational and scientific degree: PhD, Gabrovo 2004.
- [2] Simeonov S., G. Tsvetanov, Theorem for reversing the direction of movement in evolvent cylindrical cog gears with asymmetric profile of the cogs, *Machine mechanics*, No 63, Varna, 10-12.09.2005, ISSN 0861-9727.
- [3] Cvetanov, G., Tz. Karadzhev, R. Miteva. Basic Law of the Flat Interlocking of Involute Cylindrical Gears with Asymmetric Profiles. Proceedings of the 46th international conference on application of mathematics in engineering and economics (AMEE'20), AIP Conf. PROC., 7-13 June, Sozopol, Bulgaria.
- [4] Cvetanov, G., T. Karadzhev, Consequences of the Basic Law of Flat Interlocking of Involute Cylindrical Gears. The environment. It's technology. Resources. Rezekne, Latvia, Proceedings of the 13rd International Scientific and Practical Conference. Volume 3, 54-57, 2021, Online ISSN 2256-070X, DOI: 10.17770/etr2021vol3.6576, Scopus SJR 0.11;
- [5] Cvetanov, G., T. Karadzhev, Geometric Synthesis of Involute Planetary Gears with Connected Gear Wheels of Type 2K-H. Environment. It's technology. Resources. Rezekne, Latvia, Proceedings of the 13rd International Scientific and Practical Conference. Volume 3, 49-53, 2021, Online ISSN 2256-070X, DOI: 10.17770/etr2021vol3.6643, Scopus SJR 0.11;
- [6] Simeonov S., I. Iliev, G. Tsvetanov. Möglichkeit zur erhöhung der ergebnigkeit von zahnradpumpen. IT'S 47. Internationales Wissenschaftliches Kolloquium — Technische Universität Ilmenau, 23. IT'S 26. September 2002.
- [7] Simeonov S., G. Tsvetanov. Die Konversion in den Zahnradgetriebe — ein neues Anfang. Journal of the University of Applied Sciences Mittweida, Robotic, IWKM 2006, Nr II, ISSN 1437-7624.
- [8] Simeonov S., G. Tsvetanov. St. Enchev. Self-stopping effect in evolvent cylindrical cog gears, Unitech'06 Gabrovo, comp. reports, Volume II, 24-25.11.2006, ISBN 954-683-325-8;
- [9] Simeonov S., G. Tsvetanov, M. Nencheva Possibilities for geometric synthesis in internal interlocking with asymmetric profile and minimum difference between the number of cogs, XXXIV National Seminar on the Dynamics of Mechanical Systems, Varna, 2007, ISSN 0861-9727;
- [10] Tsvetanov G., Il. Zhelezarov, An. Pumaras. Modified areas of existence in evolvent cylindrical cog gears with asymmetric profile of the cogs. *Mechanics of the machines*, Varna 2016, ISSN 0861-9727.
- [11] Dichev, D., Koev, H., Diakov, D., Panchev, N., Miteva, R., Nikolova, H. Automated System for Calibrating Instruments Measuring Parameters of Moving Objects. 59th International Symposium ELMAR, September 18-20 th, 2017, Zadar, Croatia, pp. 219-224, DOI: 10.23919/ELMAR.2017.8124472
- [12] Dichev, D., F. Kogia, H. Koev, D. Diakov. Method of Analysis and correction of the Error from Nonlinearity of the Measurement Instruments. *Journal of Engineering Science and Technology Review*. Volume 9, Issue 6, 2016, pp. 116-121, DOI: 10.25103/jestr.096.17
- [13] Pulov, D., T. Karadzhev, Optoelectronic Device for Measuring the Power of Laser Radiation. Environment. Technology. Resources. Rezekne, Latvia, Proceedings of the 13th International Scientific and Practical Conference. Volume 3, 286-290, 2021, DOI: 10.17770/etr2021vol3.6590.

# Research on Working Bodies of Hammer Crushers Employing the Finite Element Method

**Vladlen Devin**

Faculty of Engineering and  
Technology  
Higher educational institution  
«Podillia State University»,  
Kamianets-Podilskyi, Ukraine

**Serhii Yermakov**

Educational and Scientific  
Laboratory “DAK GPS”,  
Higher educational institution  
«Podillia State University»,  
Kamianets-Podilskyi, Ukraine  
dakgps@pdatu.edu.ua

**Oleg Gorbovy**

Faculty of Energy and Information  
Technologies,  
Higher educational institution  
«Podillia State University»,  
Kamianets-Podilskyi, Ukraine

**Vitaliy Pidlisnyj**

Faculty of Engineering and  
Technology  
Higher educational institution  
«Podillia State University»,  
Kamianets-Podilskyi, Ukraine

**Aleksandr Semenov**

Faculty of Engineering and  
Technology  
Higher educational institution  
«Podillia State University»,  
Kamianets-Podilskyi, Ukraine

**Abstract.** The present paper studies the issues of improving the reliability of the working bodies of hammer crushers. This machine is widely used for grinding grain material in animal husbandry and the processing industry. The main wear element of such crushers is the hammers and disks to which they are attached. To study the strength characteristics of these parts, a technique and algorithm for studying the stress-strain state of the hammer crusher disc employing the finite element method (FEM) using computer simulation software products were developed. The mathematical apparatus of finite element method simplifies the model construction where the stress-strain state must be explored. Finite element method provides solutions in the form of stress and deformation fields in almost any cross-section of structural parts. The express analysis module of the APM FEM COMPASS system was used as the software for this work. The implementation of finite element method will reduce the metal intensity of the equipment, increase the reliability of its operation and reduce the cost, improve the quality of the feed produced. The results of the study showed that the maximum stresses occur on the surface creating the internal holes in the place of attachment of the disc to the shaft, but the stresses that occur there remain within the normal range.

**Keywords:** *finite element method, hammer crusher, disc, strength characteristics.*

## I. INTRODUCTION

Hammer crushers [1-3] are widely used for feed grain grinding in livestock farms and feed mills. They are designed with maximum simplicity, flexibility, compactness, and reliability in the operation. Hammer crushers have a wide range of performances. One of the main elements of crushers is rotating discs.

The strength and durability of the discs determine the possibility of achieving high parameters of the machines and providing the necessary service life. But the fact is that traditional methods of calculating the strength and durability of rotating crusher parts can't provide further major improvements in this process [4, 5]. In this regard, the development of new methods for calculating the stress-strain state and the optimal size of working bodies for grinding grain feed machines, which have wider technological capabilities, lower energy intensity, metal intensity and provide good quality grinding, is an urgent task.

Currently, such basic machine parts as crusher shafts, shaft bearings, discs, hammers and their fastenings to the disk are calculated for strength in the process of designing structural elements of hammer crushers according to existing methods [6-11]. Strength calculations of machine parts are carried out in terms of the harshest working

Print ISSN 1691-5402

Online ISSN 2256-070X

<https://doi.org/10.17770/etr2023vol3.7197>

© 2023 Vladlen Devin, Serhii Yermakov, Oleg Gorbovy, Vitaliy Pidlisnyj, Oleksandr Semenov.

Published by Rezekne Academy of Technologies.

This is an open access article under the [Creative Commons Attribution 4.0 International License](https://creativecommons.org/licenses/by/4.0/).

conditions. Harsh working conditions suggest the highest possible speed and strict recording of the oscillatory processes in individual parts.

The shaft of the crusher is calculated for strength, rigidity, transverse and twisting oscillations. The design or preliminary calculation of the shaft for strength is carried out according to bending and torsion deformations. The section dimensions of individual shaft units are determined in this calculation. The length of the shaft units is determined for design reasons, taking into account the most compact placement of parts. After the structural design of the shaft, the machines carry out a verification calculation whereby the safety margin coefficients in the most dangerous sections are determined. The structural dimensions of the disc are selected based on the conditions of placing the hammers and ensuring the minimum required circumferential speed of the hammer [6-8]. A test calculation for determining the actual stresses and safety factors in the process of calculating the strength of the disc material is carried out. The calculation of the suspension of the hammers, the thickness of the disk, the jumpers between the holes under the axes of the suspension and the outer disk is carried out based on the deformation of the cut and crumple.

The analysis of the calculation methods for the structural elements of hammer crushers shows that these calculations, based on safety margin coefficients have limitations. They don't allow to use effectively the optimal design methods, take into account the manufacturing quality of parts and implement CAD. The classical approach in strength calculations doesn't reveal the mechanism of destruction, which can be presented in terms of fracture mechanics with sufficient accuracy.

Therefore, it is necessary to use a refined method of strength calculation (the finite element method (FEM)) in the manufacture of the main elements of hammer crushers [12-17].

The purpose of the paper is to develop a technique and algorithm for studying the stress-strain state of the hammer crusher disc using computer modeling software products.

## II. MATERIALS AND METHODS

The advantages of finite element method can be represented when calculating the disc of a hammer crusher. For this purpose, we suggest using the Ascon APM FEM COMPASS express analysis module [18-21].

According to the accepted research methodology, the main stages of solving the problem with the help of finite element method are as follows:

1. The preparation of a geometric 3D model and material selection is carried out utilizing the COMPASS-3D system. We choose the material steel 45 with an allowable voltage of 200 MPa for the disc.

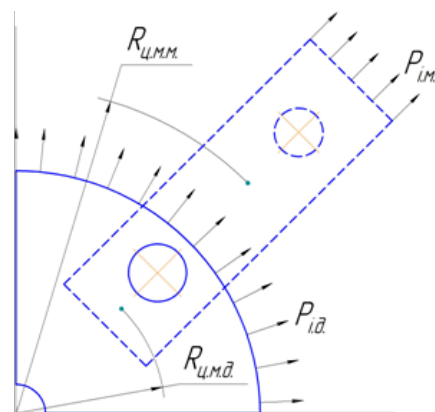


Fig. 1. Accounting scheme fourth disks of hammer crushers.

2. Analysis and determination of boundary conditions (fixation, loads). Fixing the disc sector is set by forming inner holes, in the place of its attachment to the shaft. Fixing and loads on the models are shown in Fig. 2.

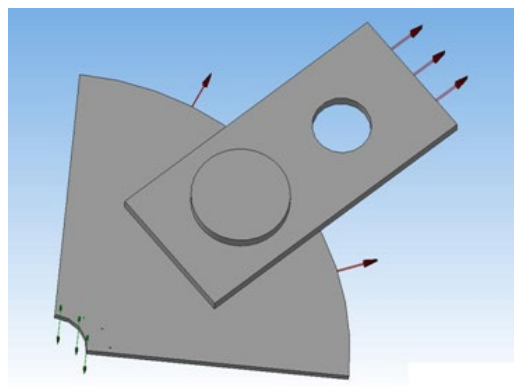


Fig. 2. Scheme of the fastening and loading models.

3. The generation of a finite element grid on a 3D model in APM FEM COMPASS is automatic, but the dimensions of the finite elements must be preset.
4. Selecting the desired type of calculation and configuring its parameters occurs in the APM FEM panel window. We select a static calculation.
5. Obtaining the results of automatic calculation in the form of a colour diagram of a deformed design model.
6. Analysis of the values of the main design characteristics (voltages, stock coefficients, displacements).

## III. RESULTS AND DISCUSSION

Centrifugal forces, the consequences of which are mechanical stresses, arise with the rotation of bodies in all elements of their volume. For each element of the volume of the body that rotates, a centrifugal force acts,  $f_{\delta} = \rho \omega^2 r$  where  $\rho$  is the specific weight of the material;  $\omega$  is angular speed,  $r$  is the rotation radius. Speed  $n$ , rpm,

is related to angular speed  $\omega$ , rad/s, by the ratio  $n = \frac{\omega}{2\pi}$ .

Since the elements of a rotating body, under the action of centrifugal forces, move in the body (within the elastic), each element is affected not only by centrifugal forces but also by the elastic forces of neighbouring elements. As a result, the distribution of mechanical stresses in a rotating body will depend on the shape of the body and elastic properties of the body  $\mu$  (the modulus of volumetric elasticity (Poisson coefficient)).

The stress distribution in a disk of constant thickness is as follows [22-24]:

radial voltages (directed parallel to the radius):

$$\sigma_R = \frac{3+\mu}{8} \rho \omega^2 \left( R^2 + R_0^2 - r^2 - \frac{R^2 R_0^2}{r^2} \right) \quad (1)$$

Tangential stresses (are directed perpendicular to radius):

$$\sigma_T = \frac{3+\mu}{8} \rho \omega^2 \left( R^2 + R_0^2 - r^2 \frac{1+3\mu}{3+\mu} - \frac{R^2 R_0^2}{r^2} \right) \quad (2)$$

where  $R$  is the external radius of the disk;  $R_0$  is the inner radius of the disk;  $r$  is the current radius (Fig. 3. (it means that the axis of rotation of the disk coincides with the axes of the radii of the disk)).

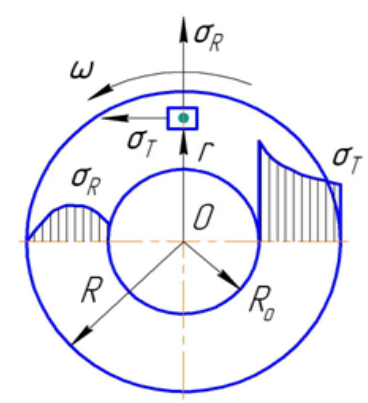


Fig. 3. Distribution radial and tangential stresses in rotating disk.

Equivalent stresses for plastic materials are determined by the fourth theory of strength, Von Mises criterion:

$$\sigma_e^{IV} = \sqrt{\sigma_1^2 + \sigma_2^2 - \sigma_1 \sigma_2} \quad (3)$$

Radial movement of the outer surface (deformation) of the disk of equal thickness from stresses is determined by the formulae:

$$\Delta R = \frac{\rho \omega^2 R^3}{4E} \left[ 1 - \mu + (3 + \mu) \left( \frac{R_0}{R} \right)^2 \right] \quad (4)$$

The disks of some machines, in addition to their inertial load, are additionally subjected to loads from the attached parts. For example, the centrifugal inertia forces of the hammers in hammer crushers are transmitted

through the suspension axes to the disks, loading them at the radius of the axe installation. Distributing these loads evenly over the circumference of the specified radius, it can be assumed that in addition to the centrifugal forces of inertia, radial forces also act on the disk, evenly distributed over concentric ring sections of the radius of the axis installation [9].

As a result, the disk can be roughly viewed as loaded around the circumference by the following force factors: radial distributed forces of inertia, which arise in the disk itself and act in its middle plane and centrifugal forces of inertia of hammers, which act on the radius of installation of the axes.

Since the disc of a crusher with four hammers is a symmetrical design in configuration and loading, it is possible to consider the equilibrium of a quarter of the disk with one hammer (Fig. 1). Using the method of kinematics, we apply the force of inertia to the rim of the disk:

$$P_d^{in} = m_d \cdot \omega^2 \cdot R_{cms}$$

where  $m_d$  is the mass of a quarter of the disk;  $\omega$  is angular speed;  $R_{cms}$  is the distance of the disk sector mass to the centre. We apply the force of inertia to the outer face of the hammer:

$$P_h^{in} = m_h \cdot \omega^2 \cdot R_{cmh}$$

where  $m_h$  is hammer mass;  $\omega$  - angular speed;  $R_{cmh}$  is the distance of mass of the hammer to the centre.

For specified values  $\omega = 314 \text{ s}^{-1}$ ,  $m_d = 0,034 \text{ kg}$ ,  $m_h = 0,02 \text{ kg}$ ,  $R_{cms} = 0,064 \text{ m}$ ,  $R_{cmh} = 0,141 \text{ m}$ , we get such values of inertial forces:  $P_d^{in} = 214 \text{ N}$ ,  $P_h^{in} = 284 \text{ N}$ .

When entering design data into the APM FEM COMPASS system, the finite element dimensions and other parameters of the geometric model (Fig.3) are set and the system automatically generates a finite element grid on the 3D model.

In a given system, the finite elements have the shape of a tetrahedron, and the number of elements in the thickness of the part should range from 4 mm to 6 mm. The thickness of the disk is 5 mm, so we take the height of the element at 1.5 mm. The finite element grid of the model is presented in Fig. 4.

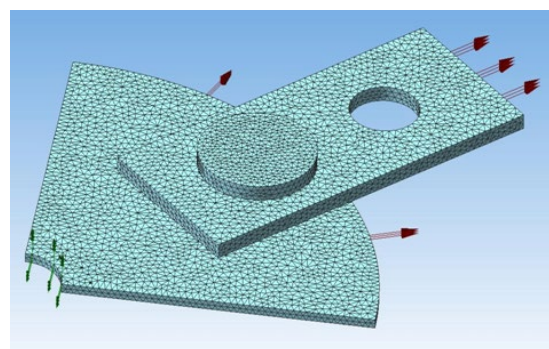


Fig. 4. Certainly element net to models.

As a result of the calculation, the diagrams of a deformed design model were obtained where the colour range depends on the level of stresses at a given place on the disk (Fig. 5). Viewing the results obtained and analyzing the values of the main design characteristics (stresses, reserve coefficients, movements) provide information for modifying the model based on the results of the calculations (you can change the geometric dimensions of the parts or material). Maximum stresses occur, as expected, on the surface creating an internal opening at the mounting point of the disc to the shaft. As the diagram (Fig. 5) shows, the voltage is normal.

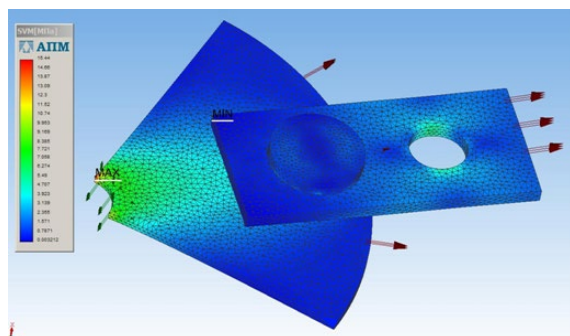


Fig. 5. Results of the calculation.

#### IV. CONCLUSIONS

The use of the mathematical apparatus of the finite element method simplifies the construction of a pattern where the stress-strain state must be explored. Finite element method provides solutions in the form of stress and deformation fields in almost any cross-section of structural parts. These advantages of the method have not been used in the design of hammer crushers up to the present time. Their implementation will reduce the metal intensity of the equipment, increase the reliability of its operation and reduce the cost, improve the quality of the feed produced.

The diagrams of the deformed design model obtained as a result of the study demonstrate the degree of stress at any point of the disk. According to the results of the study, peak stress values occur at the place of attachment of the disk to the shaft and in the places of the hammer holes. These peaks don't exceed the norm, but when changing the modes or operating conditions, as well as during grinding other material, the strengthening of the structure in these places may be needed.

#### REFERENCES

[1] S. Potapova. Klassifikatsia i otsenka izmel'chiteley zerna. MOTROL. Commission of Motorization and Energetics in Agriculture –2013. Vol. 15. No 3. 2013 pp.348-355

[2] V.V. Kirsanov, D.N. Murusydze, V.F. Nekrashev. Mechanization and animal husbandry technology. Moscow KolosS, 2007. 584 p.

[3] V.I. Trukhachev, I.V. Kapustin, O.H. Angileev, V.I. Hrebennyk. Technologies and technical means in animal husbandry. StGAU Stavropol: AGRUS, 2005. 304 p.

[4] S. Yermakov, K. Mudryk, T. Hutsol. The analysis of stochastic processes in unloading the energy willow cuttings from the hopper. Environment. Technology. Resources. Rezekne, Latvia. Vol. III. 2019, pp. 249-252, <https://doi.org/10.17770/etr2019vol3.4159>.

[5] V. Ivanyshyn, S. Yermakov, T. Ishchenko. Calculation algorithm for the dynamic coefficient of vibro-viscosity and other properties of energy willow cuttings movement in terms of their unloading from the tanker. Renewable Energy Sources, vol. 154, E3S Web of Conferences. 2020, pp. 04005, <https://doi.org/10.1051/e3sconf/202015404005>.

[6] I.V. Demyanushko, I.A. Birger. Calculation of the strength of rotating discs. Moscow: Mashinostroenie, 1978. 247p.

[7] S.V. Kharlamov. Workshop on calculation and design of food production machines and devices. Leningrad: Agropromizdat. Leningrad Department, 1991. -256 p.

[8] V.I. Sokolov. Basics of calculation and design of machines and apparatus for food production: Moscow.: Mashinostroenie, 1983. – 447 p.

[9] M.F. Mykhalev, N.P. Tretyakov, A.I. Mylchenko, V.V. Zobnyn. Calculation and construction of machines and apparatus of chemical production: examples and tasks / Ed. Mykhaleva M. F. Leningrad: Mashinostroenie, 1984.

[10] S.Yermakov, T.Hutsol, V.Devin, S.Oleksiyko, P. Potapyski. Effectiveness of cognitive digressions in classes of general technical disciplines in institutions of higher education of agro-technical direction. Engineering for rural development. 2022. pp.460-465 <https://doi.org/10.22616/ERDev.2022.21.TF154>

[11] S. Yermakov, T. Hutsol, S. Glowacki, V. Hulevskyi, V. Pylypenko. Primary Assessment of the Degree of Torrefaction of Biomass Agricultural Crops. Environment. Technologies. Resources. 2021. pp.264-267. <https://doi.org/10.17770/etr2021vol11.6597>

[12] O.V. Zhurbin, S.D. Chyzhiyomov. Analysis of engineering structures by the finite element method: Textbook. Allowance. Komsomolsk-on-Amur: GOUVPO "KnAGTU", 2004. 157p.

[13] R. Gallagher. Finite element method: fundamentals. Moscow: Mir, 1984. 428 p.

[14] O. Zenkevich. Finite element method in technology Moscow: Mir, 1975. 541 p.

[15] O. Zenkevich, K. Morgan. Finite elements and approximation. Moscow: Mir, 1986. 318 p.

[16] O. Zenkevich, I. Chang. The finite element method in the theory of constructions and mechanics of continuous media. Moscow: Nedra, 1974. 239 p.

[17] V.N. Vasilyeva. Introduction to the theory of the finite element method. Irkutsk, Irkut Publishing House. University, 1986.149p.

[18] A.N. Ivanov. Automated design and calculation of opto-electronic devices in CAD KOMPAS. Educational manual. St. Petersburg: NIU ITMO, 2012. 56 p.

[19] A. Gerasimov. Automation of work in KOMPAS-Grafik (+ CD-ROM). Moscow, BHV-Petersburg, 2010. 608 p.

[20] P. Talalai. Compass-3D V11 with examples (+ DVD-ROM). Moscow, BHV-Petersburg, 2010 616 p.

[21] N.V. Zharkov, M.A. Mineev, R.G. Why. Compass-3D V11. Full manual (+ DVD-ROM). Moscow, Science and Technology, 2010 688 p.

[22] H.S. Pisarenko. Resistance of materials. Kyiv: Higher school Main publishing house, 1979. 696 p.

[23] S.P. Fesik. Reference book on resistance of materials Kyiv: Budivelynyk, 1982. 280 p.

[24] V.I. Feodosyev. Resistance of materials. Moscow: Nauka, 1970. - 544p.

# Effect of Cu as Minority Alloying Element on Glass Forming Ability and Crystallization Behavior of Rapidly Solidified Al-Si-Ni Ribbons

Vanya Dyakova  
IMSETHAC-BAS

Materials Testing and Analyses  
Sofia, Bulgaria  
v\_diakova@ims.bas.bg

Hristina Spasova  
IMSETHAC-BAS

Materials Testing and Analyses  
Sofia, Bulgaria  
h.spasova@ims.bas.bg

Yoanna Kostova  
IMSETHAC-BAS

Materials Testing and Analyses  
Sofia, Bulgaria  
y\_kostova@ims.bas.bg

Yana Mourdjeva  
IMSETHAC-BAS

Materials Testing and Analyses  
Sofia, Bulgaria  
yana@ims.bas.bg

Georgi Stefanov  
IMSETHAC-BAS

Metal science  
Sofia, Bulgaria  
stefanov.g@gmail.com

**Abstract.** The influence of copper as a minority alloying element in the process of rapid solidification of Al-Si-Ni ribbons produced by Chill Block Melt Spinning (CBMS) was investigated. XRD and TEM analyses proved a completely amorphous structure of the alloys  $Al_{74}Ni_{16}Si_{10}$  and  $(Al_{74}Ni_{16}Si_{10})_{98}Cu_2$ . The crystallization behaviour of these alloys was studied by DSC analysis. It was found that the crystallization of the amorphous alloys  $(Al_{74}Ni_{16}Si_{10})_{100-x}Cu_x$ ,  $x=0, 2$  runs in two steps. The temperatures  $T_{x1}$  and  $T_{x2}$  of each of the crystallization steps were determined. It was proven that the addition of 2 at. % copper does not significantly change  $T_x$  temperatures. The temperature difference  $\Delta T_x$  was calculated and it showed that more thermally stable is the copper containing alloy. Crystalline analogues of the amorphous alloys were obtained by annealing of the melt-spun amorphous ribbons at a temperature which exceeded by 170°C the onset crystallization temperature. The type and size of separated crystalline phases were determined by XRD. It was found that the addition of 2 at. % Cu to  $Al_{74}Ni_{16}Si_{10}$  alloy causes a separation of new phases -  $Cu_{3.8}Ni$  and  $(Al, Cu)Ni_3$  and 54%, 24% and 7% size increase of the phases Al,  $Al_3Ni$ ,  $NiSi_2$  respectively.

**Keywords:** amorphous, nanocrystalline, aluminum, copper, silicon, nickel.

## I. INTRODUCTION

The first amorphous alloys were obtained as ribbons about sixty years ago, but the interest in them continues to be great, due to their good mechanical and physical properties and their high corrosion resistance. The most promising applications of amorphous alloys are considered to be in the field of electronics and electrical engineering. Initially, mainly iron-based amorphous alloys were studied, but in recent decades the interest in aluminum-based amorphous alloys is constantly growing [1] – [4]. Over the past decade, scientists' research has focused on studying the properties of both amorphous composites [5] and amorphous foams [6].

Amorphous aluminum alloys are generally produced from various Al-TM-RE ternary alloy compositions (TM are transition metals, RE are rare earth elements). The resulting alloys show great glass-forming ability (GFA) and high mechanical strength [7] – [11], but they contain expensive rare earth elements, which we tried to replace with cheaper ones. In our previous studies, we obtained rapidly solidified ribbons of the Al-Cu-Mg system alloyed with minority amounts of Zn, Zr and Ni and studied the influence of these elements on the GFA, crystallization and corrosion behavior on the newly produced alloys [12] – [14].

Print ISSN 1691-5402

Online ISSN 2256-070X

<https://doi.org/10.17770/etr2023vol3.7200>

© 2023 Vanya Dyakova, Hristina Spasova, Yoanna Kostova, Yana Mourdjeva, Georgi Stefanov.

Published by Rezekne Academy of Technologies.

This is an open access article under the [Creative Commons Attribution 4.0 International License](https://creativecommons.org/licenses/by/4.0/).

The aim of this research is to obtain amorphous alloys from the Al-Si-Ni system and study the influence of Cu as a minority alloying element on the GFA and crystallization behavior on the Al-Si-Ni-Cu rapidly solidified amorphous ribbons.

## II. MATERIALS AND METHODS

The base Al-Si-Ni and Al-Si-Ni-Cu alloy were synthesized from pure metals Al 99.99 %, Ni 99.99, Cu 99.99 and pure Si 99.99% in a plant comprising a resistance electric furnace installed in a water-cooled pneumo-vacuum chamber in argon atmosphere of 99.998 % purity.

The Chill Block Melt Spinning (CBMS) method was used to obtain rapidly solidified ribbons about 3 - 4 mm wide and 26 - 40  $\mu\text{m}$  thick. The production processes of the ligatures and the rapidly solidified ribbons are described in details in our previous publications [12] – [14].

Samples of the base Al-Si-Ni and of the Al-Si-Ni-Cu rapidly solidified ribbons were annealed for 2 hours at 350°C in argon atmosphere for the purposes of devitrification. The chemical composition of the produced rapidly solidified ribbons was determined by Energy Dispersive X-ray Spectroscopy (EDS) analysis using a scanning electron microscope HIROX 5500 with EDS system BRUCKER at a magnification of 100x in 10 fields with a field area of 2.5  $\text{mm}^2$ .

X-ray diffraction (XRD) analysis was performed to characterize the amount of amorphous and crystalline phases and to determine the phase composition of the crystalline part of the ribbons before and after devitrification. A Bruker D8 Advance powder X-ray diffractometer with Cu  $K\alpha$  radiation (Ni filter) and LynxEye recording in a solid-state position-sensitive detector was applied. The PDF-2 (2009) database of the International Data Diffraction Center (ICDD) and the DiffracPlusEVA software package were used to perform the qualitative phase analysis.

The microstructure of Al-Si-Ni and Al-Si-Ni-Cu rapidly solidified ribbons was studied by transmission electron microscope (TEM) JEOL 1011 at accelerating voltage of 100 kV.

Differential scanning calorimetry (DSC) analysis was performed on STA 449 F3 Jupiter calorimeter connected to a QMS 403 Aëolos Quadro mass spectrometer in Ar environment. The rate of the protective Ar flow in the apparatus during the analysis was 30  $\text{mL s}^{-1}$  and the flow rate of the purge Ar through the studied samples was 20  $\text{mL s}^{-1}$ . The heating rate was 20  $\text{K min}^{-1}$ .

## III. RESULTS AND DISCUSSIONS

The results of EDS analyses of the chemical composition of rapidly solidified ribbons Al-Si-Ni and Al-Si-Ni-Cu are presented in Table 1. Based on the obtained EDS results the Al-Ni-Si alloy will be denoted further as  $\text{Al}_{74}\text{Ni}_{16}\text{Si}_{10}$ . EDS analysis showed that the Cu content in the Al-Si-Ni-Cu rapidly solidified ribbon was close to 2 at.

% Cu, therefore, in our work, it will be denoted respectively  $(\text{Al}_{74}\text{Ni}_{16}\text{Si}_{10})_{98}\text{Cu}_2$ .

TABLE 1 CHEMICAL COMPOSITION OF THE RAPIDLY SOLIDIFIED RIBBONS AL-NI-SI AND AL-NI-SI-CU

Designation of ribbons	Al [at. %]	Ni [at. %]	Si [at. %]	Cu [at. %]
$\text{Al}_{74}\text{Ni}_{16}\text{Si}_{10}$	73.50	16.08	10.42	-
$(\text{Al}_{74}\text{Ni}_{16}\text{Si}_{10})_{98}\text{Cu}_2$	73.97	14.94	8.76	2.33

The XRD patterns of  $\text{Al}_{74}\text{Ni}_{16}\text{Si}_{10}$  and  $(\text{Al}_{74}\text{Ni}_{16}\text{Si}_{10})_{98}\text{Cu}_2$  ribbons before and after annealing and XRD-results on their structural characteristics are presented in Fig. 1 and in Table 2.

A well-defined halo is present in the XRD patterns of each of the two studied rapidly solidified ribbons (Fig. 1 (a), Fig. 1 (b)), which is an evidence of their amorphous structure. Further, in our work, these alloys will be denoted by the index "am".

The results of XRD analyzes of the amorphous structure of the rapidly solidified  $\text{Al}_{74}\text{Ni}_{16}\text{Si}_{10}$  and  $(\text{Al}_{74}\text{Ni}_{16}\text{Si}_{10})_{98}\text{Cu}_2$  ribbons were confirmed by TEM observations and electron diffraction. The diffractograms of the two alloys showed a well-defined diffraction halo and no diffraction spots, which proved that their structure was completely amorphous.

The TEM image of the microstructure of  $\text{Al}_{74}\text{Ni}_{16}\text{Si}_{10}$  alloy (Fig. 2 (a)) showed the typical for metallic glass uniform matrix. Small white spots were observed in the dark matrix of  $(\text{Al}_{74}\text{Ni}_{16}\text{Si}_{10})_{98}\text{Cu}_2$ . The absence of phase boundaries and of diffraction pixels makes us to consider they are clusters of atoms of smaller atom number (probably Al) which have formed during rapid solidification but have not succeeded to combine into a crystal lattice. The bright contrast in TEM image is due to the lower electron absorption resulting on the smaller atom number of aluminium (Fig. 2 (b))

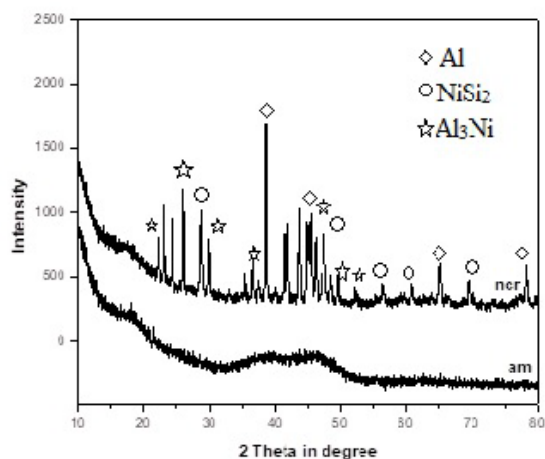
XRD analysis of the amorphous alloys subject to annealing at 350°C showed complete crystallization. Peaks of three types of crystalline phases were found in  $\text{Al}_{74}\text{Ni}_{16}\text{Si}_{10}$  alloy: Al,  $\text{Al}_3\text{Ni}$  and  $\text{NiSi}_2$  (Fig. 1 (a)) and five types of crystalline phases in  $(\text{Al}_{74}\text{Ni}_{16}\text{Si}_{10})_{98}\text{Cu}_2$

alloy: Al,  $\text{Al}_3\text{Ni}$ ,  $\text{NiSi}_2$ ,  $\text{Cu}_{3,8}\text{Ni}$  and traces of (Al, Cu) $\text{Ni}_3$  (Fig. 1 (b)).

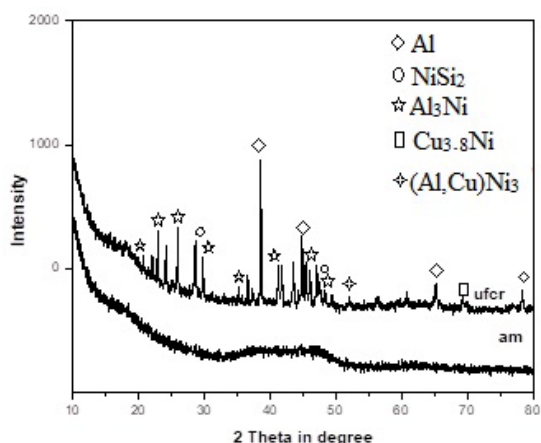
The quantity and the size of the crystalline phases were determined as nanosized in  $\text{Al}_{74}\text{Ni}_{16}\text{Si}_{10}$  and as ultrafine in  $(\text{Al}_{74}\text{Ni}_{16}\text{Si}_{10})_{98}\text{Cu}_2$  (Table 2). This gives us the reason to designate the annealed  $\text{Al}_{74}\text{Ni}_{16}\text{Si}_{10}$  alloy as nanocrystalline and the annealed  $(\text{Al}_{74}\text{Ni}_{16}\text{Si}_{10})_{98}\text{Cu}_2$  alloy as ultrafine and to use for them the indexes "ncr" and "ufcr", respectively [15].

TABLE 2 STRUCTURAL CHARACTERISTICS OF AMORPHOUS AND CRYSTALLINE  $Al_{74}Ni_{16}Si_{10}$  AND  $(Al_{74}Ni_{16}Si_{10})_{98}Cu_2$  ALLOYS

Designation of the alloy	Components of the crystal part		
	Types of phases	Quantity of the phase [mass. %]	Phase size [nm]
$Al_{74}Ni_{16}Si_{10}$ am	-	-	-
$Al_{74}Ni_{16}Si_{10}$ ncr	Al -fcc	16	88
	$Al_3Ni$ Orthorombic	72	71
	$NiSi_2$ -fcc	12	43
$(Al_{74}Ni_{16}Si_{10})_{98}Cu_2$ am	-	-	-
$(Al_{74}Ni_{16}Si_{10})_{98}Cu_2$ ufer	Al -fcc	19	136
	$Al_3Ni$ Orthorombic	64	88
	$NiSi_2$	13	45
	$Cu_{3.8}Ni$ - fcc	4	60
	$(Al,Cu)Ni_3$ -fcc	traces	



(a)  $Al_{74}Ni_{16}Si_{10}$ .



(b)  $(Al_{74}Ni_{16}Si_{10})_{98}Cu_2$

Fig. 1. XRD diagrams of  $Al_{74}Ni_{16}Si_{10}$  and  $(Al_{74}Ni_{16}Si_{10})_{98}Cu_2$  alloys.

XRD results showed that the addition of only 2 at. % Cu to  $Al_{74}Ni_{16}Si_{10}$  alloy caused a 54%, 24% and 7% size increase of the nanocrystalline phases Al,  $Al_3Ni$ ,  $NiSi_2$

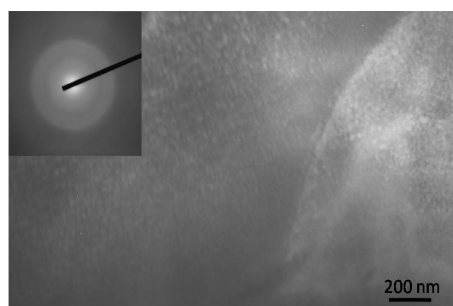
respectively, and a separation of two new phases –  $Cu_{3.8}Ni$  and  $(Al, Cu)Ni_3$ . The increased sizes, especially of the Al-containing phases can be well seen when comparing the TEM images of the two alloys (Fig. 2 (c) and 2 (d)).

Fig. 3 and Fig. 4 show DSC diagrams of  $Al_{74}Ni_{16}Si_{10}$  and  $(Al_{74}Ni_{16}Si_{10})_{98}Cu_2$  alloys in amorphous (a)-solid line and in crystalline (b) - dotted line state. The results of the DSC analyses are presented in Table 3. The DSC diagrams of each of the amorphous alloys have two exothermic peaks, indicating that crystallization takes place in two separate steps. There is no clear evidence of the glass transition effect before the temperatures of the first exothermic crystallization peak of both alloys. The absence of a glass transition (GT) feature can be explained by the formation of significant number of clusters during rapid solidification, evidence of which we observed in Fig. 2 (b). With continued heating, clusters of size above the critical nucleation size grow even at lower temperatures. Therefore, we assume that  $T_g = T_{x1}$  peak and that the GT effect is hidden below the first crystallization peak. The same vitrification effect has been observed in amorphous aluminum-based alloys by other researchers [16], [17].

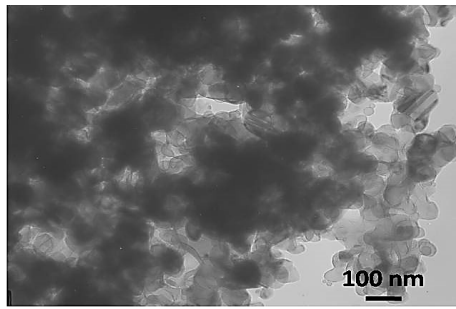
They assumed that the difference  $\Delta T_x$  between the crystallization temperature and the glass transition temperature, which mostly determines the so called supercooled liquid region of the amorphous alloy, in this case can be calculated as  $\Delta T_x = T_{x2} - T_{x1}$  [17]. The parameter  $\Delta T_x$  is directly associated with the glass stability (GS) of the alloy and it is an indication of the resistance to devitrification by the annealing above  $T_g$ . For our amorphous alloys the values of  $\Delta T_x$  are 64K and 92K for the  $Al_{74}Ni_{16}Si_{10}$  and  $(Al_{74}Ni_{16}Si_{10})_{98}Cu_2$  alloys respectively. This clearly indicates that the partial replacement of Si and Ni atoms by Cu improves the ability of the melt to form glasses [17].



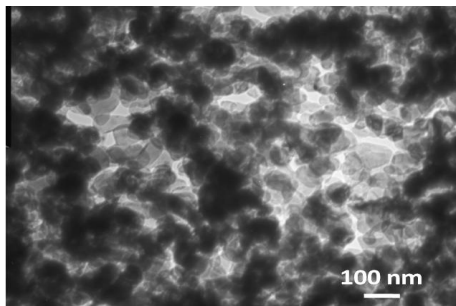
(a)  $Al_{74}Ni_{16}Si_{10}$  - am



(b)  $(Al_{74}Ni_{16}Si_{10})_{98}Cu_2$ - am



(c) Al<sub>74</sub>Ni<sub>16</sub>Si<sub>10</sub>- ncr



(d) (Al<sub>74</sub>Ni<sub>16</sub>Si<sub>10</sub>)<sub>98</sub>Cu<sub>2</sub> - ufer

Fig. 2. Microstructure of the amorphous (a), (b) and crystalline (c), (d) Al<sub>74</sub>Ni<sub>16</sub>Si<sub>10</sub> and (Al<sub>74</sub>Ni<sub>16</sub>Si<sub>10</sub>)<sub>98</sub>Cu<sub>2</sub> alloys, TEM.

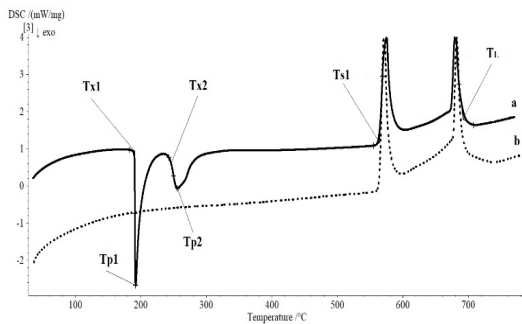


Fig. 3. DSC diagrams of Al<sub>74</sub>Ni<sub>16</sub>Si<sub>10</sub> alloy (a) amorphous; (b) nanocrystalline.

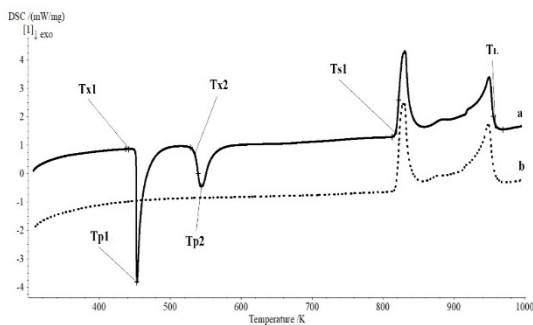


Fig. 4. DSC diagrams of (Al<sub>74</sub>Ni<sub>16</sub>Si<sub>10</sub>)<sub>98</sub>Cu<sub>2</sub> alloy (a) amorphous; (b) ultrafinecrystalline.

TABLE 3 RESULTS OF DSC ANALYSIS OF AMORPHOUS Al<sub>74</sub>Ni<sub>16</sub>Si<sub>10</sub> AND (Al<sub>74</sub>Ni<sub>16</sub>Si<sub>10</sub>)<sub>98</sub>Cu<sub>2</sub> ALLOYS

	Al <sub>74</sub> Ni <sub>16</sub> Si <sub>10</sub> - am	(Al <sub>74</sub> Ni <sub>16</sub> Si <sub>10</sub> ) <sub>98</sub> Cu <sub>2</sub> - am
Tx1, [K]	453	452
Tpeak, [K]	465	453
Tx2, [K]	529	535
Tpeak2, [K]	529	544
Ts, [K]	838	819
Tl, [K]	965	954
ΔTx, [K]	64	92

#### IV. CONCLUSIONS

Rapidly solidified amorphous ribbons Al<sub>74</sub>Ni<sub>16</sub>Si<sub>10</sub> and (Al<sub>74</sub>Ni<sub>16</sub>Si<sub>10</sub>)<sub>98</sub>Cu<sub>2</sub> and their crystalline analogues were produced by the Chill Block Melt Spinning (CBMS) method and by subsequent annealing of the amorphous alloys for 2 hours at 350°C.

It was found by DSC analyses that the crystallization of the amorphous alloys Al<sub>74</sub>Ni<sub>16</sub>Si<sub>10</sub> and (Al<sub>74</sub>Ni<sub>16</sub>Si<sub>10</sub>)<sub>98</sub>Cu<sub>2</sub> takes place in two steps. It was proven that the addition of 2 at. % copper to the Al<sub>74</sub>Ni<sub>16</sub>Si<sub>10</sub> alloy does not significantly change the T<sub>g</sub> temperature, but improve the glass forming ability of (Al<sub>74</sub>Ni<sub>16</sub>Si<sub>10</sub>)<sub>98</sub>Cu<sub>2</sub> alloy.

It was found that the addition of 2 at. % Cu to nanocrystalline Al<sub>74</sub>Ni<sub>16</sub>Si<sub>10</sub> alloy causes a 54%, 24% and 7% size increase of the separated crystalline phases Al, Al<sub>3</sub>Ni, NiSi<sub>2</sub> respectively, and a separation of new Cu<sub>3,8</sub>Ni and (Al, Cu)Ni<sub>3</sub> phases in the ultrafine crystalline (Al<sub>74</sub>Ni<sub>16</sub>Si<sub>10</sub>)<sub>98</sub>Cu<sub>2</sub> alloy.

#### V. ACKNOWLEDGEMENTS

This study is funded by the project “Study of the rheological and corrosion behavior of amorphous and nanocrystalline aluminum-based alloys”, Contract with BNSF №KP-06-H37/13 of 06 December 2019.

A part of experimental units used in this work was funded by the European Regional Development Fund within the OP “Science and Education for Smart Growth 2014 - 2020”, project CoE “National center of mechatronics and clean technologies”, No BG05M2OP001-1.001-0008-C08.

The authors are indebted to our colleagues prof. Stoyko Gyurov, PhD, Jordan Georgiev, PhD, Ivan Penkov, PhD (IMSETHAC-BAS) and prof. Daniela Kovacheva, PhD, ass. prof. Nikolay Marinkov, PhD (IIC – BAS) for their

help and support in the preparation and for the XRD and DSC analyzes of the alloys.

#### REFERENCES

- [1] Y. H. Kim., K. Hiraga, A. Inoue, T. Masumoto , H. H. Jo, “Crystallization and High Mechanical Strength of Al-Based Amorphous Alloys” *Materials Transactions, JIM*, vol. 35, pp. 293-302, 1994, <https://doi.org/10.2320/matertrans1989.35.293>
- [2] H. Kim, A. Inoue and T. Masumoto, “High Strength Bulk Amorphous Alloys with Low Critical Cooling Rates (Overview)”, *Material Transactions, JIM*, vol. 36, , no. 7, pp.866-875,1995 <https://doi.org/10.2320/matertrans1989.36.866>
- [3] I. T. H Chang, R. R. Botten, “Heat treatment of rapidly solidified Al-Ni-Mn alloys”, *Materials Science and Engineering: A*, vol. 226-228, pp.183-186, 1997 [https://doi.org/10.1016/S0921-5093\(97\)80035-4](https://doi.org/10.1016/S0921-5093(97)80035-4)
- [4] W. Kim, M. Gogebakan, B. Cantor, “Heat treatment of amorphous Al85Y5Ni10 and Al85Y10Ni5 alloys”, *Materials Science and Engineering: A*, vol. 226–228, , pp.178-182, 1997 [https://doi.org/10.1016/S0921-5093\(96\)10613-4](https://doi.org/10.1016/S0921-5093(96)10613-4)
- [5] I. Permyakova, A. Glezer, “Amorphous-Nanocrystalline Composites Prepared by High-Pressure Torsion”, *Metals*, vol.10, no. 4, p.511, 2020 <https://doi.org/10.3390/met10040511>
- [6] A. H. Brothers, D. C. Dunand, “Amorphous metal foams”, *Scripta Materialia*, vol. 54, no. 4, , pp. 513-520, 2006 <https://doi.org/10.1016/j.scriptamat.2005.10.048>
- [7] M. Gögebakan, O. Uzun, T. Karaaslan, M. Keskin, “Rapidly solidified Al–6.5 wt. % Ni alloy”, *Journal of Materials Processing Technology*, vol. 142, no.1, pp. 87-92, 2003, <https://www.sciencedirect.com/science/article/abs/pii/S0924013603004667>
- [8] M. A. Munoz-Morris, S. Surinach, M. Gich, M. D. Baro, D. G. Morris, “Crystallization of a Al–4Ni–6Ce glass and its influence on mechanical properties”, *Acta Materialia*, 51, , pp. 1067-1077, 2003 [https://doi.org/10.1016/S1359-6454\(02\)00511-6](https://doi.org/10.1016/S1359-6454(02)00511-6)
- [9] A. K. Gangopadhyay, K. F. Kelton, “Effect of rare-earth atomic radius on the devitrification of Al88RE8Ni4 amorphous alloys”, *Philosophical Magazine A*, vol. 80, , pp. 1193-1206, 2000 <https://doi.org/10.1080/01418610008212110>
- [10] N. Bassim, C.S. Kiminami, M. J. Kaufman, M. F. Oliveira, M.N.R.V.Perdigão, W.J. Botta Filho, “Crystallization behavior of amorphous Al84Y9Ni5Co2alloy”, *Materials Science and Engineering A*, 304–306, pp.332-237, 2001 [https://doi.org/10.1016/S0921-5093\(00\)01532-X](https://doi.org/10.1016/S0921-5093(00)01532-X)
- [11] T. Gloriant, D.H. Ping, K. Hono, A. L. Greer, M.D. Baro, “Segregation-controllednanocrystalization in an Al-Ni-La metallic glass”, *Applied Physics Letters*, 92, 103126, 2008, <https://doi.org/10.1063/1.2897303>
- [12] V. Dyakova, G. Stefanov, I. Penkov, D. Kovacheva, N. Marinkov, Y. Mourdjeva, S. Gyurov, “Influence of Zn on Glass Forming Ability and Crystallization Behaviour of Rapidly Solidified Al-Cu-Mg (Zn) alloys”, *Journal of Chemical Technology and Metallurgy*, 57, 6, pp. 622-630, 2020 [https://journal.uctm.edu/node/j2022-3/23\\_21-64\\_br\\_3\\_pp\\_622-630.pdf](https://journal.uctm.edu/node/j2022-3/23_21-64_br_3_pp_622-630.pdf)
- [13] V. L. Dyakova, G. N. Stefanov, D. G. Kovacheva, Y. S. Mourdjeva, N. E. Marinkov, .I. G. Penkov and J. S. Georgiev, Influence of Zr and Zn as minority alloying elements on glass forming ability and crystallization behavior of rapidly solidified AlCuMg ribbons, 2449, *AIP Conference proceedings*, 2022, <https://aip.scitation.org/doi/abs/10.1063/5.0090746>
- [14] V. L. Dyakova, B. R. Tzaneva and Y. G. Kostova, “Influence of Zn as minority alloying element on the uniform and local corrosion of amorphous rapidly solidified AlCuMg(Zn) ribbons”, 2449, *AIP Conference proceedings*, 2022, <https://doi.org/10.1063/5.0090752>
- [15] R. Birringer, H. Gleiter, P. Klein, P. Marquardt, “Nanocrystalline materials an approach to a novel solid structure with gas-like disorder?”, *Physics Letters A*, vol.102, no.8, pp. 365-369, 1984 [https://doi.org/10.1016/0375-9601\(84\)90300-1](https://doi.org/10.1016/0375-9601(84)90300-1)
- [16] M. Gögebakan, M. Okumus, Structure and crystallization kinetics of amorphous Al–Ni–Si alloy, *Materials Science-Poland*, vol. 27, no. 1, 2009, <https://materialsscience.pwr.edu.pl/>
- [17] K.L. Sahoo, R. Sahu, “Glass transition and crystallization of Al–Ni–La based metallic glasses studied by temperature modulated DSC”, *Journal of Non-Crystalline Solids*, 365, , pp. 33-36, 2013 <http://dx.doi.org/10.1016/j.jnoncrysol.2013.01.031>

# *Influence of Ni as Minority Alloying Element on the Corrosion Behavior of Amorphous Al-Cu-Mg Alloys in Chloride Solution*

**Vanya Dyakova**  
Materials Testing and Analyses  
IMSTHAC-BAS  
Sofia, Bulgaria  
v\_diakova@ims.bas.bg

**Yoanna Kostova**  
Materials Testing and Analyses  
IMSTHAC-BAS  
Sofia, Bulgaria  
y\_kostova@ims.bas.bg

**Hristina Spasova**  
Materials Testing and Analyses  
IMSTHAC-BASion  
(of Affiliation)  
Sofia, Bulgaria  
h.spasova@ims.bas.bg

**Abstract.** The influence of nickel as minority alloying element on the corrosion behavior of amorphous alloys  $(Al_{74}Cu_{16}Mg_{10})_{99}Ni_1$ ,  $(Al_{74}Cu_{16}Mg_{10})_{98}Ni_2$  and  $(Al_{74}Cu_{16}Mg_{10})_{97}Ni_3$  was investigated. The amorphous alloys were obtained as ribbons by Chill Block Melt Spinning (CBMS). The amorphous structure of the alloys was proven by X-ray diffraction (XRD) and transmission electron microscopy (TEM). The corrosion rate was calculated gravimetric using continuous immersion tests for 360 hours in 3.5% NaCl solution at a temperature of 25°C. The lowest corrosion rate was found in the alloy containing 3 at. % Ni. The chemical composition of the accumulated corrosion products was studied using XRD.

The influence of nickel on the local corrosion resistance of the amorphous ribbons of  $(Al_{74}Cu_{16}Mg_{10})_{100-x}Ni_x$   $x = 0, 1, 2, 3\%$  alloys was investigated electrochemically in a solution of 3.5% NaCl at 25°C. Pitting potential (Epitt) and repassivation potential (Erp) were determined. It was found that most resistant to pitting corrosion was the  $(Al_{74}Cu_{16}Mg_{10})_{97}Ni_3$  alloy, which showed the noblest pitting potential (Epitt -0.332 V) and repassivation potential (Erp -0.530 V).

All obtained corrosion test results of the nickel-containing amorphous alloys were compared to the base amorphous  $Al_{74}Cu_{16}Mg_{10}$  alloy.

**Keywords:** amorphous alloy, aluminum, nickel, copper, magnesium, corrosion.

## I. INTRODUCTION

The first published experimental results on the corrosion properties of amorphous alloys date back to 1974 [1]. From then until now, data have been obtained and analyzed mainly on the corrosion behavior of

amorphous iron-based alloys. The results show that amorphous alloys are more resistant to corrosion than the corresponding crystalline alloys, which can be explained by their microstructural homogeneity, the absence of defects, as well as the positive influence of some of the alloying elements [2], [3].

Aluminium-based amorphous alloys became one of the most studied metallic glasses in the last decades. The influence of various factors on their corrosion resistance continues to be the subject of many studies [4], [5].

The aim of this work is to study the influence of the Ni as a minority alloying element on the corrosion behavior of amorphous alloys  $(Al_{74}Cu_{16}Mg_{10})_{100-x}Ni_x$   $x = 1, 2, 3$  at.% in chloride-containing solution and to estimate their susceptibility to general and local corrosion.

## II. MATERIALS AND METHODS

### A. Methods of Production and Characterization of the Amorphous Ribbons

The  $Al_{74}Cu_{16}Mg_{10}$  alloy was chosen as a base alloy of the Al-Cu-Mg system, corresponding to the eutectic point E5 of the Al-Cu-Mg ternary equilibrium diagram [6]. The base  $Al_{74}Cu_{16}Mg_{10}$  alloy and 1, 2, 3 at.% Ni-containing alloys were synthesized from pure metals Al - 99.99 %, Cu - 99.99 %, Mg - 99.8 % and Ni - 99.99 %, in a plant comprising a resistance electric furnace installed in a water-cooled pneumovacuum chamber in argon atmosphere with 99.998 % purity [7]. The Chill Block

Print ISSN 1691-5402

Online ISSN 2256-070X

<https://doi.org/10.17770/etr2023vol3.7201>

© 2023 Vanya Dyakova, Yoanna Kostova, Hristina Spasova. Published by Rezekne Academy of Technologies.  
This is an open access article under the [Creative Commons Attribution 4.0 International License](https://creativecommons.org/licenses/by/4.0/).

Melt Spinning (CBMS) method was used to obtain rapidly solidified ribbons about 3 - 4 mm wide and 26 - 40  $\mu\text{m}$  thick.

The chemical composition of the produced rapidly solidified ribbons was determined by Energy Dispersive X-ray Spectroscopy (EXDS) using a scanning electron microscope HIROX 5500 with EXDS system BRUCKER. The EXDS results are presented in Table 1.

TABLE 1. CHEMICAL COMPOSITION OF THE RAPIDLY SOLIDIFIED RIBBONS AL-CU-MG-(NI)

Designation of ribbons	Al [at. %]	Cu [at. %]	Mg [at. %]	Ni [at. %]
$\text{Al}_{74}\text{Cu}_{16}\text{Mg}_{10}$	76.60	13.82	9.59	-
$(\text{Al}_{74}\text{Cu}_{16}\text{Mg}_{10})_{99}\text{Ni}_1$	74.45	15.14	9.16	1.24
$(\text{Al}_{74}\text{Cu}_{16}\text{Mg}_{10})_{98}\text{Ni}_2$	74.54	14.90	8.61	1.96
$(\text{Al}_{74}\text{Cu}_{16}\text{Mg}_{10})_{97}\text{Ni}_3$	73.23	14.84	8.72	3.21

X-ray diffraction (XRD) analysis was performed by Bruker D8 Advance powder X-ray diffractometer in order to characterize the amount of amorphous phases of the alloys. The microstructure of the rapidly solidified alloys was studied by transmission electron microscope (TEM) JEOL 1011 at accelerating voltage of 100 kV. The XRD patterns and TEM analyses of the microstructure and TEM diffraction proved that the base alloy  $\text{Al}_{74}\text{Cu}_{16}\text{Mg}_{10}$  was 98 % amorphous [8] and the three Ni – containing alloys (Fig. 1) are completely amorphous [9].

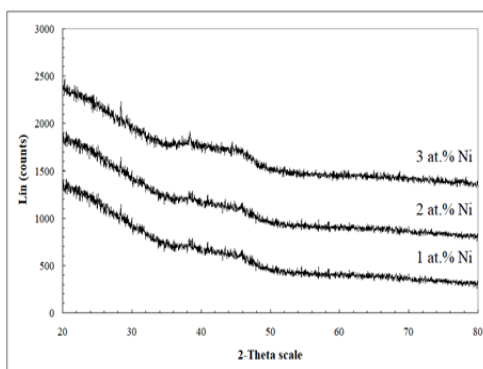


Fig. 1. XRD patterns of  $(\text{Al}_{74}\text{Cu}_{16}\text{Mg}_{10})_{100-x}\text{Ni}_x$  ribbons.

## B. Corrosion Test Methods

### 1. General Corrosion Test

General corrosion tests were performed by continuous immersion of specimens in 3.5% NaCl for 360 hours at a temperature of 25°C in a laboratory thermostat. Before

testing specimens were degreased in acetone and treated in diluted  $\text{HNO}_3$  for one minute.

The corrosion rate (CR) was calculated gravimetrically  $\text{CR} = \frac{\Delta m}{S \cdot t}$  [ $\text{g m}^{-2}\text{h}^{-1}$ ], where the mass loss index  $\Delta m = m_0 - m_1$  [g] was the difference between the weight of the test specimens before the test and after the removal of the corrosion products after the test; S is the surface area of the specimen [ $\text{m}^2$ ]; t is the test duration [h]. The weight testing was made on analytical scales. All obtained CR results are average values from three parallel tests.

After the corrosion test, the specimens were repeatedly washed with warm distilled water. The separated filtrate was dried and analyzed by XRD.

### 2. Potentiodynamic Corrosion Test

The resistance of the studied alloys  $(\text{Al}_{74}\text{Cu}_{16}\text{Mg}_{10})_{100-x}\text{Ni}_x$ ,  $x=0, 1, 2, 3$  at. % to local corrosion was determined by potentiodynamic cyclic method in a solution of 3.5% NaCl at temperature of 25°C. Test specimens of 0.8  $\text{cm}^2$  surface were degreased in alcohol, treated in diluted  $\text{HNO}_3$ . The electrochemical tests were performed in a trielectrode cell with a working electrode made from the studied amorphous alloys, a platinum counter electrode and a silver chloride reference electrode (Ag/AgCl). All potentials in this work are reported relatively to the silver chloride electrode.

The electrochemical tests were performed in a solution of 3.5% NaCl at temperature 25 °C using an Autolab galvanostat-potentiostat model PGSTAT 204 and computer software NOVA 2.1. The results of the polarization tests of studied  $(\text{Al}_{74}\text{Cu}_{16}\text{Mg}_{10})_{100-x}\text{Ni}_x$ ,  $x=1, 2, 3$  at. % alloys were compared to those obtained for the base  $\text{Al}_{74}\text{Cu}_{16}\text{Mg}_{10}$  alloy.

The specimens were kept for 60 min in 3.5% NaCl to stabilize the open circuit potential (OCP), and then were cathodically polarized for 60 s at -0.5V vs OCP to remove the natural passive layer. The cyclic potentiodynamic studies were carried out at scan rate of 1 mV/s in anodic direction from initial potential of -0.5V vs OCP until exceeding the threshold current density with more than 1  $\text{mA}/\text{cm}^2$ , after which the potential scan was reversed in cathode direction to the cross-point of the forward and the backward branches of the polarization curve.

## III. RESULTS AND DISCUSSIONS

### A. General corrosion behavior

The dependence of corrosion rate (CR) on the nickel content of the amorphous alloys  $(\text{Al}_{74}\text{Cu}_{16}\text{Mg}_{10})_{100-x}\text{Ni}_x$ ,  $x=0, 1, 2, 3$  at. % in 3.5% NaCl is shown in Fig. 2. The highest CR is measured for the alloy containing 1 at. % nickel. In the alloys with 2 or 3 at. % Ni the corrosion rate decreases to zero.

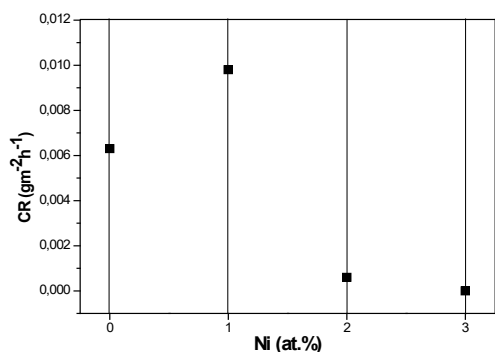
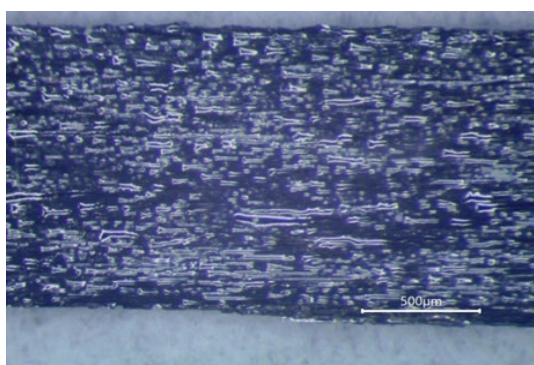
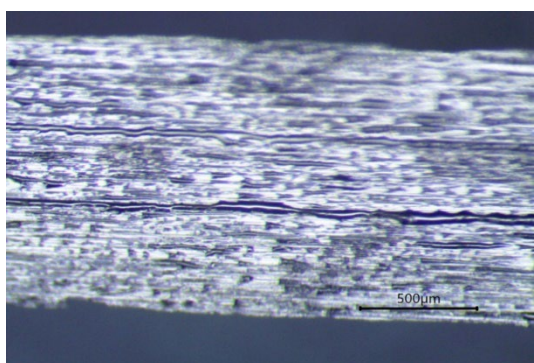


Fig. 2. Corrosion rate CR of  $(Al_{74}Cu_{16}Mg_{10})_{100-x}Ni_x$ ,  $x=0, 1, 2, 3$  at. % alloys under continuous immersion in 3.5 % NaCl for 360 hours at 25°C.

The decrease of CR of the studied alloys with increasing nickel content is explained by the fact that nickel stimulates the formation of passive film on the surface of aluminum alloys, which prevents further interaction of the alloy with the chloride containing aggressive corrosive environment [10]. This is the main reason for the reduction of corrosion losses to zero in the 2 and 3 at. % Ni alloy.



a)  $(Al_{74}Cu_{16}Mg_{10})_{99}Ni$



b).  $(Al_{74}Cu_{16}Mg_{10})_{97}Ni_3$

Fig. 3. Surface of specimens of Ni-containing amorphous alloys after 360 hours corrosion test in 3,5% NaCl at 25°C.

The pitting corrosion is the most common corrosion type of aluminum alloys in chloride solutions [11], [12] but in our case the pittings were absent in all studied Ni-containing amorphous alloys even after 360 hours corrosion test. After the test the surface of the specimens of the alloy with 1 at. % Ni was matte (Fig. 3a), while the surface of the specimens with 3 at. % Ni remained shiny, without separated corrosion products (Fig. 3b), indicating no local corrosion changes.

In order to clarify the possible mechanisms of the corrosion process of Ni-containing aluminum amorphous alloys, the phase composition of the filtrate after washing the test samples was investigated by XRD.

Although no traces of corrosion were visible on the surface of the tested specimens, XRD showed that in addition to NaCl, there were also separated oxide products in the filtrate. (Fig. 4).

An amorphous halo is visible on the onset part of the XRD patterns of the corrosion products of each of the investigated alloys in the region  $(15\div 25) 2\theta$ , followed by peaks of crystalline phases (Fig.4). This indicates that the released corrosion products are a mixture of amorphous and crystalline type. A similar structure of the layer of corrosion products was observed by other researchers also [13]. The width and the intensity of the amorphous halo at the onset of XRD patterns increases with increasing nickel content in the alloys. Based on our previous research, we can state that the film of corrosion products closest to the metal surface is amorphous mixture of aluminum oxides, oxohydroxides and chlorides [14].

It can be seen from the XRD pater that the crystal corrosion products contain copper, chlorine and oxygen phases –  $CuCl_2$ ,  $CuO$ , which, according to literature, have good protective corrosion properties [15].

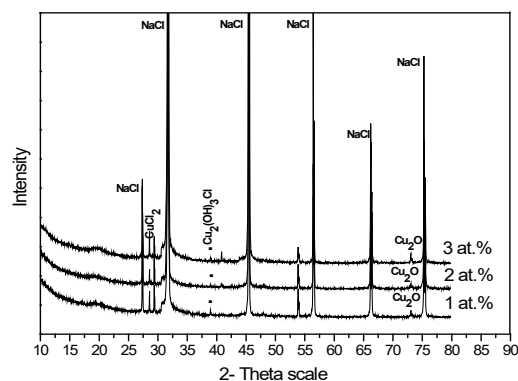


Fig. 4. XRD patterns of the corrosion products of  $(Al_{74}Cu_{16}Mg_{10})_{100-x}Ni_x$  alloys obtained after 360 hours corrosion test in 3.5 % NaCl at 25°C.

### B. Electrochemical and potentiodynamic measurements

Electrochemical corrosion test was performed in order to confirm the results of the general corrosion test and the susceptibility of aluminum amorphous alloys to pitting corrosion.

The method of open circuit potential measurements and potentiodynamic cyclic method were used for the purpose.

The open circuit potentials (OCP) of the base amorphous alloy  $\text{Al}_{74}\text{Cu}_{16}\text{Mg}_{10}$  and of the alloys with 1, 2 and 3 at. % Ni were measured in 3.5 %NaCl at 25°C for 60 min. Figure 5 displays the variations of OCP with the Ni content. Average OCP values are shown in the figure, because in all tested alloys OCP stabilization was not achieved during the 60 min test.

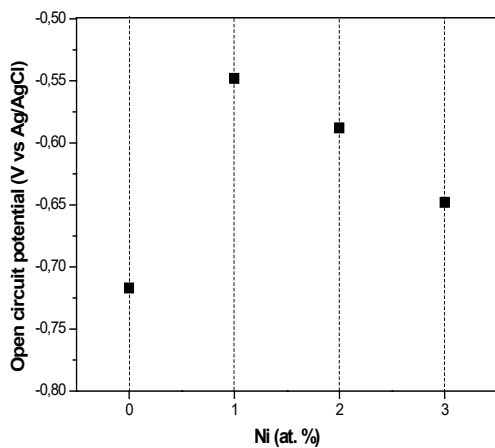


Fig. 5. Dependence of OCP on Ni content of  $(\text{Al}_{74}\text{Cu}_{16}\text{Mg}_{10})_{100-x}\text{Ni}_x$ ,  $x=0, 1, 2, 3$  alloys in 3.5% NaCl at 25°C.

It can be seen that the OCP of all three Ni containing alloys is displaced to less negative values compared to the OCP of the base alloy. The biggest displacement is observed at 1%Ni, the further increase of Ni content diminishes the displacement.

Representative potentiodynamic polarization curves of the amorphous  $(\text{Al}_{74}\text{Cu}_{16}\text{Mg}_{10})_{100-x}\text{Ni}_x$ ,  $x=0,1,2,3$  alloys in 3.5% NaCl are presented in Fig. 6. The pitting potentials  $E_{\text{pit}}$  and the repassivation potentials  $E_{\text{rp}}$  were determined and the values for Ni-containing alloys were compared with  $E_{\text{pit}}$  (solid line) and  $E_{\text{rp}}$  (dotted line) of the base alloy (Fig.7).

The OCPs of the three  $(\text{Al}_{74}\text{Cu}_{16}\text{Mg}_{10})_{100-x}\text{Ni}_x$ ,  $x=1, 2, 3$  at.% Ni alloys (Fig. 5) are more negative than their  $E_{\text{pit}}$  (Fig. 7). The biggest is the difference between OCP and  $E_{\text{pit}}$  in the alloy with 1 at. % Ni. For the base alloy  $\text{Al}_{74}\text{Cu}_{16}\text{Mg}_{10}$ , the values of OCP and  $E_{\text{pit}}$  are close.

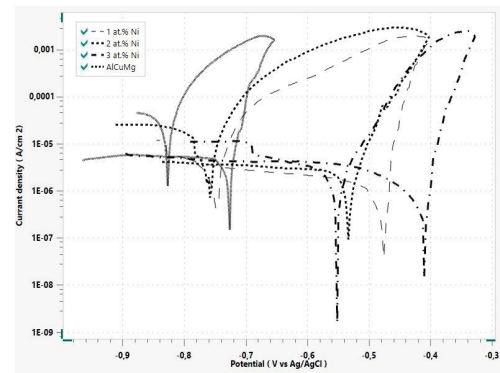


Fig. 6. Polarization potentiodynamic curves of  $(\text{Al}_{74}\text{Cu}_{16}\text{Mg}_{10})_{100-x}\text{Ni}_x$ ,  $x=0, 1, 2, 3$  alloys in 3.5% NaCl at 25°C:  $x=0$ , solid line;  $x=1$ , dash line (- -);  $x=2$ , dot line (..);  $x=3$  dash-dot line (- . - .).

No plateau was registered on the potentiodynamic polarization curves of the amorphous alloys  $(\text{Al}_{74}\text{Cu}_{16}\text{Mg}_{10})_{100-x}\text{Ni}_x$ ,  $x=1, 2, 3$  or the base amorphous alloy  $\text{Al}_{74}\text{Cu}_{16}\text{Mg}_{10}$  in 3.5% NaCl (Fig. 6). Hysteresis loops are formed on the anode part of all polarization curves. The sharp increase of current density immediately after the corrosion potentials ( $E_{\text{corr}}$ ) indicates that the alloys are in a process of active dissolution and their corrosion potentials coincide with their pitting potentials.

When increasing the nickel content in  $(\text{Al}_{74}\text{Cu}_{16}\text{Mg}_{10})_{100-x}\text{Ni}_x$ ,  $x=1, 2, 3$  alloys, the corrosion potential  $E_{\text{corr}}$  shifts in positive direction and the development of pitting corrosion begins. According to Figure 6 the most resistant to pitting corrosion is the  $(\text{Al}_{74}\text{Cu}_{16}\text{Mg}_{10})_{97}\text{Ni}_3$  alloy (dash-dot), which has the noblest pitting potential ( $E_{\text{pit}} -0.332$  V) and repassivation potential ( $E_{\text{rp}} -0.530$  V).

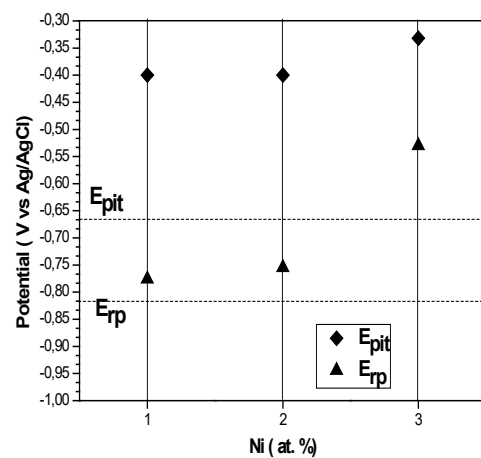


Fig. 7.  $E_{\text{pit}}$  and  $E_{\text{rp}}$  of  $(\text{Al}_{74}\text{Cu}_{16}\text{Mg}_{10})_{100-x}\text{Ni}_x$ ,  $x=1, 2, 3$  at.% and of the base  $\text{Al}_{74}\text{Cu}_{16}\text{Mg}_{10}$  alloy (dot lines).

The base Al<sub>74</sub>Cu<sub>16</sub>Mg<sub>10</sub> alloy for which the highest corrosion current was measured (Fig.2) shows the most negative pitting potential (E<sub>pitt</sub> -0.652 V) and its polarization curve (solid line) is located in the upper part of Fig. 6. The average E<sub>pitt</sub> and E<sub>pr</sub> values of the alloys with different Ni content are presented in Fig. 7. The dotted lines show the E<sub>pitt</sub> and E<sub>pr</sub> of the base alloy Al<sub>74</sub>Cu<sub>16</sub>Mg<sub>10</sub>.

The corrosion behavior of alloys is determined by the difference between the two potentials E<sub>pitt</sub> and E<sub>pr</sub> (Fig. 7). With the increase of Ni content in (Al<sub>74</sub>Cu<sub>16</sub>Mg<sub>10</sub>)<sub>100-x</sub>Ni<sub>x</sub>, x=1,2,3 amorphous alloys the zone between E<sub>pitt</sub> and E<sub>pr</sub> narrows and the zone of their cathodic potentials where they are corrosion protected expands (Fig. 6). The results indicate that most protected from pitting corrosion is the alloy (Al<sub>74</sub>Cu<sub>16</sub>Mg<sub>10</sub>)<sub>97</sub>Ni<sub>3</sub>.

#### IV. CONCLUSIONS

It was found that the addition of nickel in the range of 2-3 at % to the base amorphous alloy Al<sub>74</sub>Cu<sub>16</sub>Mg<sub>10</sub> reduces the corrosion rate of the amorphous alloys (Al<sub>74</sub>Cu<sub>16</sub>Mg<sub>10</sub>)<sub>100-x</sub>Ni<sub>x</sub>, x=2,3 from 63.10<sup>-4</sup> [g m<sup>-1</sup> h<sup>-1</sup>] to 0 [g m<sup>-1</sup> h<sup>-1</sup>]

The addition of nickel in the range of 1-3 at % to the base amorphous alloy Al<sub>74</sub>Cu<sub>16</sub>Mg<sub>10</sub> increases the resistance of the amorphous alloys (Al<sub>74</sub>Cu<sub>16</sub>Mg<sub>10</sub>)<sub>100-x</sub>Ni<sub>x</sub>, x=1, 2, 3 to pitting corrosion in a chloride-containing solution.

#### ACKNOWLEDGEMENTS

This study is funded by the project "Study of the rheological and corrosion behavior of amorphous and nanocrystalline aluminum-based alloys", Contract with BNSF №KP-06-H37/13 of 06 December 2019.

A part of experimental units used in this work was funded by the European Regional Development Fund within the OP "Science and Education for Smart Growth 2014 - 2020", project CoE "National center of mechatronics and clean technologies", No BG05M2OP001-1.001-0008-C08.

#### REFERENCE

[1] M. Naka, K. Hashimoto, T. Masumoto, J. Japan Inst. Metals, vol. 38, pp.835-841, 1974.  
[2] T. Aburada, N. Uēnlūē, J.M. Fitz-Gerald, G.J. Shiflet and J.R. Scully, "Effect of Ni as a minority alloying element on the

corrosion behavior in Al-Cu-Mg-(Ni) metallic glasses," Scripta Materialia, vol.58, pp. 623-626, 2008, <https://doi.org/10.1016/j.scriptamat.2007.11.041>  
[3] S. Dhasneem, S. S. Farhana, S. Rajendran, T. Umasankareswari, S. Shanmugapriya, D. Renita, "Corrosion resistance of metallic glasses", International journal of nano corrosion science and engineering, vol. 3, no. 1, pp. 48-59, 2016.  
[4] A. Kukuła-Kurzyniec, J. Dutkiewicz, P. Ochinn, L. Perriere, P. Dhuzewski, A. Góral, "Amorphous - nanocrystalline melt spun Al-Si-Ni based alloys modified with Cu and Zr." Archives of Metallurgy and Materials, vol. 58, no.2, pp. 419-423, 2013, DOI: 10.2478/amm-2013-0010.  
[5] Y.Q. Cheng, E. Ma, 'Atomic-level structure and structure-property relationship in metallic glasses,' Progress in Materials Science, vol. 56, pp. 379-473, doi:10.1016/j.pmatsci.2010.12.002.  
[6] Ternary Al-Cu-Mg diagram MSIT Workplace, <https://www.msiport.com/msi-research/ternary-evaluations/notes-for-authors-pdf/>, ID:10.12587(2003).  
[7] M. Gögebakan, O. Uzun, T. Karaaslan, M. Keskin, "Rapidly solidified Al-6.5 wt. % Ni alloy", Journal of Materials Processing Technology, vol. 142, no.1, pp. 87-92,2003,<https://www.sciencedirect.com/science/article/abs/pii/S0924013603004667>.  
[8] V. Dyakova, G. Stefanov, I. Penkov, D. Kovacheva, N. Marinkov, Y. Mourdjeva, S. Gyurov, "Influence of Zn on glass forming ability and crystallization behaviour of rapidly solidified Al-Cu-Mg (Zn) alloys", Journal of Chemical Technology and Metallurgy, vol. 57, no. 3, pp. 622-630, 2022, [https://dl.uctm.edu/journal/node/j2022-3/23\\_21-64\\_br\\_3\\_pp\\_622-630.pdf](https://dl.uctm.edu/journal/node/j2022-3/23_21-64_br_3_pp_622-630.pdf).  
[9] V. Dyakova, Y. Mourdjeva, N. Marinkov, G. Stefanov, Y. Kostova, S. Gyurov, "Effect of Ni as minority alloying element on glass forming ability and crystallization behavior of rapidly solidified Al-Cu-Mg-Ni ribbons", Journal of Chemical Technology and Metallurgy - in print.  
[10] G. S. Frankel, M. A. Russak, C.V. Jahnes, M. Mirzamaani, V.A. Brusic, "Pitting of Sputtered Aluminum Alloy Thin Films", J. Electrochem. Soc., vol. 136, no. 4, pp.1243-1244, 1989, DOI: <https://doi.org/10.1149/1.2096864>.  
[11] V. Harshmeet, "The corrosion behaviour of aluminium alloy b206 in seawater", M.S. thesis, University of British Columbia, Vancouver, 2016.  
[12] R. Orozco, J. Genesca, J.Juarez-Islas, "Effect of Mg Content on the Performance of Al-Zn-Mg Sacrificial Anodes", ASM Internat. JMEPEG, no. 16, p. 229-235, 2007, DOI:10.1007/s11665-007-9037-z.  
[13] V. Dyakova, Y. Kostova, S. Gyurov, D. Kichukova, H. Spasova, "The influence of Zn on the corrosion behaviour of amorphous and nanosized rapidly solidified (Al<sub>75</sub>Cu<sub>17</sub>Mg<sub>8</sub>)<sub>100-x</sub>Ni<sub>x</sub> alloys and their crystalline analogues", Mater. Sci. Non-Equilib. Phase Transform., vol. 6, no.3, pp. 73-76, 2020, <https://stumejournals.com/journals/ms/2020/3/73.full.pdf>  
[14] V. L. Dyakova, Y. G. Kostova, B. R. Tzaneva, "Effect of minority alloying elements Zn and Zr on the corrosion behavior of amorphous alloys AlCuMg(Zn) and AlCuMg(Zr) and their nanocrystalline analogues," ChemChemTech, vol. 65, no. 4, pp. 62-70, 2022, DOI: <https://doi.org/10.6060/ivkkt.20226504.6550>.  
[15] K. Dževad, K. Kozlica, J. Ekar, J. Kovač, and I. Milošev, "Roles of chloride ions in the formation of corrosion protective films on copper," Journal of The Electrochemical Society, vol.168, p. 031504, 2021, DOI:10.1149/1945-7111/ABE34A.

# Investigating the Possibility of Alloying an Alloy AlSi25Cu5Cr with Co, Cr and Mo Using Metal Powder

**Boyan Dochev**

Technical University of Sofia,  
Branch Plovdiv  
Plovdiv, Bulgaria  
boyan.dochev@gmail.com

**Desislava Dimova**

Technical University of Sofia,  
Branch Plovdiv  
Plovdiv, Bulgaria  
desislava608738@gmail.com

**Ivan Panov**

Technical University of Sofia,  
Branch Plovdiv  
Plovdiv, Bulgaria  
specialista57@abv.bg

**Abstract.** A base aluminium-silicon alloy AlSi25Cu5Cr was used to investigate the possibility of alloying aluminium alloys with hard-to-melt elements. The alloying elements Co, Cr and Mo were introduced into the melt using metal powder from a hard-melting dental cobalt-chromium-molybdenum alloy. The metal powder was packed in aluminium foil and introduced into the melt of the studied alloy at a temperature of 810° C. After alloying and mechanical stirring of the melt, it stood for 30 min. at a temperature, raised to 850° C and experimental castings were cast from it. After spectral analysis, the degree of absorption of the alloying elements by the aluminium melt was determined. The structure and mechanical properties of the thus obtained alloy were investigated.

**Keywords:** alloying, aluminium-silicon alloy, dental cobalt-chromium-molybdenum alloy, hard-melting elements.

## I. INTRODUCTION

The eutectic and hypereutectic aluminum-silicon alloys have found application in automotive industry for manufacturing pistons for internal combustion engines. The heavy loads, endured by the pistons during their operation are the reason behind the increased requirements toward the alloys, used for their production. Piston manufacturer MAHLE uses a great variety of aluminum-silicon alloys, mainly eutectic (M124, M142, M174+) and hypereutectic (M126, M138, M145, M244). The used alloying elements are copper, nickel, and magnesium in various concentrations. Copper in the alloys M124, M126, M138 and M244 is within 0,8-1,5%, while nickel and magnesium are in the range of 0,8-1,3%. The eutectic alloy M124 has won recognition as the “classic” piston alloy and it has been the basis of the vast number of pistons produced

in the recent decades. The pistons, made of hypereutectic aluminum-silicon alloys, demonstrate higher wear resistance. Of this group, alloys M138 and M244 are preferred for producing two-stroke engine pistons, while alloy M126 is used in the USA for passenger car petrol engines. Alloys M142, M145 and M174+ have been developed and used since recently. Their common feature is the increased content of the alloying elements copper (2,5-5%) and nickel (1-3%). This is the reason for their high strength at increased temperatures, which, in turn, has led to their quick launch into the market. The M142 eutectic alloy is mainly used in petrol engines, while the M174+ alloy, also of the eutectic type, is increasingly used in diesel engines. The hypereutectic aluminum-silicon alloy M145 is used in several petrol engines [1]. The development of new hypereutectic aluminum-silicon piston alloys to be competitive to those, used so far by the global piston manufacturers is the subject of many researchers [2]-[7]. The use and combination of different concentrations of alloying elements aims at increasing the strength parameters of the alloys both at normal and at high temperatures. The influence of the alloying elements on the structure and properties of the aluminum-silicon alloys is presented in [8]-[10]. In order to influence the structure and obtain aluminum-silicon alloys with high mechanical and operational properties, experiments are conducted, in which Co, Ni, Cr and Mo and combinations of them are used for alloying the alloys [11]-[15].

The aim of the present research is to establish the possibility of alloying AlSi25Cu5Cr alloy with Co, Cr and Mo by using metal powder.

Print ISSN 1691-5402

Online ISSN 2256-070X

<https://doi.org/10.17770/etr2023vol3.7180>

© 2023 Boyan Dochev, Desislava Dimova, Ivan Panov. Published by Rezekne Academy of Technologies.  
This is an open access article under the [Creative Commons Attribution 4.0 International License](https://creativecommons.org/licenses/by/4.0/).

## II. MATERIALS AND METHODS

A basic non-standardized hypereutectic aluminium-silicon alloy AlSi25Cu5Cr, whose chemical composition is shown in Table 1, was used to study the possibility of alloying aluminium alloys with hard-to-melt (churlish) elements.

TABLE 1 CHEMICAL COMPOSITION OF ALSI25CU5CR (%)

Si	Cu	Cr	Fe	Mg	Al
24,92	4,05	0,559	0,136	0,003	rest

The alloying elements cobalt, molybdenum, and part of chromium were introduced into the melt by using metal powder from the high-melting dental cobalt-chromium-molybdenum alloy WIRONIT, with a chemical composition, presented in Table 2.

TABLE 2 CHEMICAL COMPOSITION OF WIRONIT (%)

Co	Cr	Mo	Mn	Si
64	28,5	5	1	1

The metal powder was packed in aluminium foil and introduced into the melt of the studied alloy at a temperature of 810°C. After alloying and mechanical stirring, the melt stood for 30 minutes at a temperature, increased to 850°C. After metallurgical processing of the alloy, including refining, degassing and modification with phosphorus in the amount of 0.07%, experimental castings were made of it. The metallurgical processing of the melt was carried out at a temperature of 850°C, while the casting temperature was 830°C. Metal equipment, preheated to 200°C in advance, was used for casting the experimental samples.

The castings were thermally treated under the T6 mode, during which the heating for homogenizing of the structure was carried out at a temperature 510-515°C, the retention time at this temperature was 6h30min., and the used cooling medium was water with a temperature of 20°C. The artificial ageing of the samples after their hardening was carried out at a temperature of 180°C, with retention times at the chosen operational temperature 12h and 14h.

To determine the degree of absorption of the alloying elements introduced into the melt by using metal powder from the dental cobalt-chromium-molybdenum alloy WIRONIT, a spectral analysis was carried out with an ARUN Technology spectrometer. Microstructural analysis and mechanical tests of the alloy AlSi25Cu5Cr, interfused with Co, Cr and Mo, were carried out before and after its exposure to heat treatment.

## III. RESULTS AND DISCUSSION

The used amount of metal powder aimed at introducing Co-0.2%, Cr-0.09% and Mo-0.016% into the melt. The results from the performed spectral analysis show that not all amount of the metal powder was absorbed by the melt

of the studied aluminum-silicon alloy. The degree of absorption of the alloying elements Co, Cr and Mo is about 85%. Table 3 presents the chemical composition of the alloy after its modification by 0.07% P and alloying with WIRONIT.

TABLE 3 CHEMICAL COMPOSITION OF ALSI25CU5CR+ WIRONIT (%)

Si	Cu	Cr	Co	Mo	Fe	Al
24,93	4,5	0,638	0,172	0,014	0,443	rest

Increase in the amount of Cu in the composition of the alloy was also registered, which is due to the used amount of the modifier phosphorus, introduced into the melt through the ligature CuP10.

The primary Si crystals in the structure of the alloy AlSi25Cu5Cr, modified by 0.07% P and alloyed with Co, Cr and Mo before being subjected heat treatment, are 24.8 µm in size. Single crystals of Si with slightly larger sizes are observed, and their calculated arbitrary average diameter is of the order of 40-46 µm. The Si crystals in the composition of the eutectic have crystallized in the form of needles and have an average linear size of 33.4 µm (total average size). The main amount of eutectic Si crystals is up to 20 µm in size, though crystals, measuring from 30 to 80 µm are also observed (Fig.1). The mechanical properties of the alloy, infused this way, are shown in Table 4.

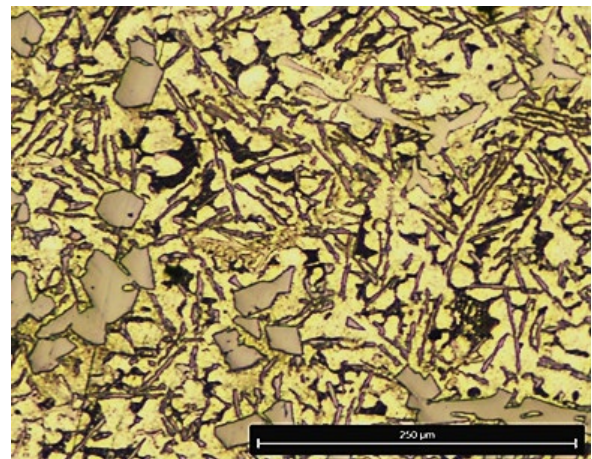


Fig. 1. Microstructure of alloy AlSi25Cu5Cr + 0.07% P + Co, Cr and Mo.

TABLE 4 MECHANICAL PROPERTIES OF ALSI25CU5CR+ WIRONIT

Alloy	Microhardness	Macrohardness	Rm [MPa]
AlSi25Cu5Cr	79.2µHV <sub>50/10</sub>	129.5HV <sub>10/10</sub>	121

After heat treatment under the T6 mode, during which the artificial ageing was carried out at a temperature of 180°C and the retention time was 12h, a change in the shape

and size of the eutectic silicon crystals was observed. From a needle-like one, their shape spheroidized, and their arbitrary average diameter, both measured and calculated, was 6.7  $\mu\text{m}$ . The main amount of primary Si crystals measured about 22  $\mu\text{m}$ . Single crystals with slightly larger dimensions of the order of 55  $\mu\text{m}$  are observed (Fig. 2). The conducted mechanical tests established an increase in the micro- and macro-hardness of the alloy, as well in its tensile strength compared to the same alloy before being subjected to heat treatment. After the heat treatment, performed in the described way, the alloy has the mechanical properties, shown in Table 5.

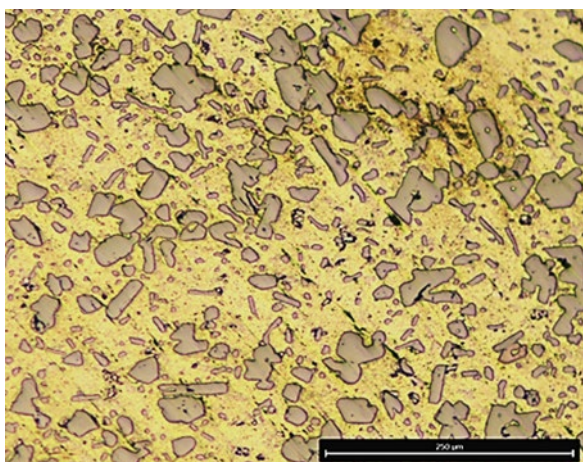


Fig. 2. Microstructure of alloy AlSi25Cu5Cr + 0.07% P + Co, Cr and Mo - T6 (artificial ageing 180°C/12h).

TABLE 5 MECHANICAL PROPERTIES OF ALSI25CU5CR+ WIRONIT+ T6 (ARTIFICIAL AGEING 180°C/12h)

Alloy	Microhardness	Macrohardness	Rm [MPa]
AlSi25Cu5Cr	86.2 $\mu\text{HV}_{50/10}$	142.1HV <sub>10/10</sub>	215

In the structure of the studied alloy after its heat treatment under the T6 mode, in which the artificial ageing was carried out at 180°C and the retention time was 14h, no significant change in the shape and sizes of the primary silicon crystals was observed. Their arbitrary average diameter was 19.7  $\mu\text{m}$ . A change in the shape and size of the silicon crystals in the composition of the eutectic was registered. Part of the crystals had a spheroidal shape and dimensions of the order of 6.2  $\mu\text{m}$ , though ones in the form of plates, about 12.5  $\mu\text{m}$  long and 2  $\mu\text{m}$  wide, were also observed (Fig. 3). With increasing the retention time (14h) during artificial ageing, an increase in the micro- and macro-hardness of the alloy is observed, but the value of the tensile strength decreases. Table 6 shows the mechanical properties of the studied alloy after heat treatment under the T6 mode, in which the artificial ageing is carried out at a temperature of 180°C, and the retention time is 14h.

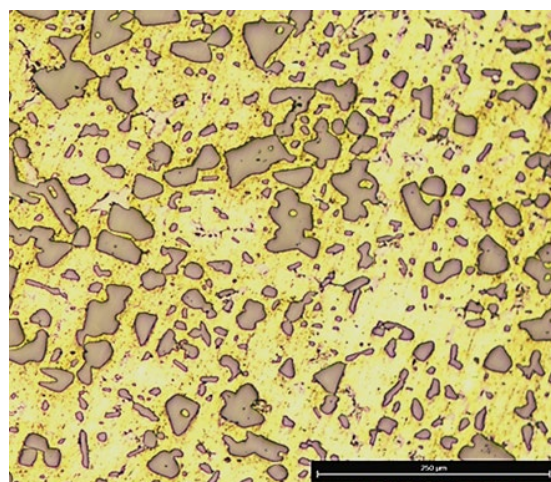


Fig. 3. Microstructure of alloy AlSi25Cu5Cr + 0.07% P + Co, Cr and Mo - T6 (artificial ageing 180°C/14h).

TABLE 6 MECHANICAL PROPERTIES OF ALSI25CU5CR+ WIRONIT+ T6 (ARTIFICIAL AGEING 180°C/14h)

Alloy	Microhardness	Macrohardness	Rm [MPa]
AlSi25Cu5Cr	89.2 $\mu\text{HV}_{50/10}$	153.2HV <sub>10/10</sub>	183

The results from the conducted studies show that the absorption of the hard-to-melt elements Co, Cr and Mo by the melt of the base aluminum-silicon alloy AlSi25Cu5Cr is not complete. One possible reason is that the metal powder of the dental cobalt-chromium-molybdenum alloy is oxidized to a certain extent, which, in turn, makes its complete absorption by the melt impossible. The other probable reason is that part of the metal powder floated on the surface of the metal melt and passed into the slag, which hindered the absorption of the hard-melting elements Co, Cr and Mo.

The T6 heat treatment leads to an increase in the mechanical properties of the studied alloy. The tensile strength and macrohardness values of the alloy are competitive with those of the standardized piston hypereutectic aluminum-silicon alloys. The selected parameters of artificial ageing after hardening lead to a change in the shape and size of the eutectic silicon crystals in the structure of the alloy. During artificial ageing at 180°C and retention time 12h the eutectic silicon crystals have a spheroidal shape and significantly small dimensions - 6.7  $\mu\text{m}$ . As the retention time during artificial ageing increases to 14h, a change in the shape of the eutectic Si is observed. Some of the crystals is in the form of plates, which, in turn, leads to a decrease in the tensile strength of the alloy.

#### IV. CONCLUSIONS

A technology for alloying hypereutectic aluminum-silicon alloys with Co, Cr and Mo by using metal powder from a dental cobalt-chromium-molybdenum alloy is proposed. With the selected parameters (temperature and

time) for the introduction of the alloying elements, their absorption by the melt of the studied alloy amounts at 85%.

After conducting T6 heat treatment, the mechanical properties of the studied alloy AlSi25Cu5Cr, interfused with Co, Cr and Mo, meet the requirements toward the standardized hypereutectic aluminum-silicon piston alloys.

The parameters (temperature and time) of artificial ageing after hardening, in which the eutectic silicon is refined and has a spheroidal shape, which, in turn, is the reason for the increased mechanical properties of the alloy, have been experimentally established. When the retention time during artificial ageing at 180°C operational temperature is increased to 14h, a change in the spheroidal shape of the eutectic silicon crystals is observed. It acquires a plate-like shape, its cutting effect on the  $\alpha$ -phase in the composition of the eutectic increases, and a decrease in the tensile strength values of the investigated alloy is observed.

**Acknowledgments:** The study was part of the „Young Researchers and Postdocs–2“ National Scientific Programme and was funded by the Technical University of Sofia, Branch Plovdiv, Faculty of Mechanical Engineering.

#### REFERENCES

- [1] Mahle GmbH „Piston materials. In: Pistons and engine testing“. ATZ/MTZ-Fachbuch. Vieweg+Teubner Verlag, Wiesbaden.2012 [https://doi.org/10.1007/978-3-8348-8662-0\\_4](https://doi.org/10.1007/978-3-8348-8662-0_4)
- [2] N. Raghukiran, R.Kumar, „Effect of scandium addition on the microstructure, mechanical and wear properties of the spray formed hypereutectic aluminum–silicon alloys“, *Materials Science and Engineering: A*, Volume 641, p. 138-147, 2015 <https://doi.org/10.1016/j.msea.2015.06.027>
- [3] P. Xing, B. Gao, Y. Zhuang, K. Liu, G. Tu, „On the modification of hypereutectic Al-Si alloys using rare earth Er“. *Acta Metallurgica Sinica (English Letters)*, Vol. 23, Issue 5, p.327-333, 2010 <https://doi.org/10.11890/1006-7191-105-327>
- [4] M. Zuo, D. Zhao, X. Teng, H. Geng, Z. Zhang, „Effect of P and Sr complex modification on Si phase in hypereutectic Al–30Si alloys“. *Materials & Design*, Volume 47, May, p. 857-864, 2013 <https://doi.org/10.1016/j.matdes.2012.12.054>
- [5] S. Miladinović, B. Stojanović, S. Gajević, A. Vencl, „Hypereutectic Aluminum Alloys and Composites: A Review“ <https://link.springer.com/article/10.1007/s12633-022-02216-2>
- [6] K. Kamarska, „ Study of the corrosion behavior of aluminum-silicon alloy AlSi18Cu3CrMn in acidic media“, *AIP Conference Proceedings* 2449, 060018, September 2022, <https://doi.org/10.1063/5.0090753>
- [7] K. Kamarska, „Corrosion of AlSi18Cu3CrMn aluminum alloy in a chloride-containing medium“, *AIP Conference Proceedings* 2449, 60019, September 2022, <https://doi.org/10.1063/5.0090754>
- [8] R. Rana, R. Purohit, S. Das, „Reviews on the Influences of Alloying elements on the Microstructure and Mechanical Properties of Aluminum Alloys and Aluminum Alloy Composites“, *International Journal of Scientific and Research Publications*, Volume 2, Issue 6, 2012, ISSN 2250-3153
- [9] O. Joseph, P. Olubambi, O. Joseph, B. Edun, J. Okeniyi, O. Abioye, „Effects of Alloying on Aluminium-Silicon Alloys – A Review“, *IOP Conference Series: Materials Science and Engineering*, Volume 1107, 2021 <https://iopscience.iop.org/article/10.1088/1757-899X/1107/1/012116/pdf>
- [10] E. Efzan, H. Kong, C. Kok, „Review: Effect of Alloying Element on Al-Si Alloys“, *Advanced Materials Research*, Volume 845, p. 355-359, 2013 <https://doi.org/10.4028/www.scientific.net/AMR.845.355>
- [11] T. Bogdanoff, A. Dahle, S. Seifeddine, „Effect of Co and Ni Addition on the Microstructure and Mechanical Properties at Room and Elevated Temperature of an Al–7%Si Alloy“, *International Journal of Metalcasting*, Volume 12, p.434-440, 2018 <https://link.springer.com/article/10.1007/s40962-017-0178-z>
- [12] J. Yeh, S. Chang, Y. Hong, S. Chen, S. Lin, „Anomalous decrease in X-ray diffraction intensities of Cu–Ni–Al–Co–Cr–Fe–Si alloy systems with multi-principal elements“, *Materials Chemistry and Physics*, Volume 103, Issue 1, 15 May, p. 41-46, 2007 <https://doi.org/10.1016/j.matchemphys.2007.01.003>
- [13] C. Nwambu, E. Nnuka, J. Odo, C. Nwoye, S.Nwakpa, „Effect of Molybdenum and Cobalt Addition on Structure and Mechanical Properties of Aluminium-12.5%Silicon Alloy“, *International Journal of Engineering Science Invention*, Volume 3 Issue 4, p.20-24, 2014 <http://www.ijesi.org/>
- [14] M. Sha, S. Wu, X. Wang, L. Wan, P. An, „Effects of cobalt content on microstructure and mechanical properties of hypereutectic Al–Si alloys“, *Materials Science and Engineering: A*, Volume 535, February, p. 258-263, 2012 <https://doi.org/10.1016/j.msea.2011.12.077>
- [15] M. Sha, S. Wu, L. Wan, „Materials Science and Engineering: A“, Volume 554, September, p. 142-148, 2012 <https://doi.org/10.1016/j.msea.2012.06.026>

# Investigation of the Structure of AlSi25Cu4Cr and AlSi25Cu5Cr Alloys

**Boyan Dochev**  
Technical University of Sofia,  
Branch Plovdiv  
Plovdiv, Bulgaria  
boyan.dochev@gmail.com

**Desislava Dimova**  
Technical University of Sofia,  
Branch Plovdiv  
Plovdiv, Bulgaria  
desislava608738@gmail.com

**Mihail Zagorski**  
Technical University of Sofia,  
Faculty of Industrial Technology  
Sofia, Bulgaria  
mihail.zagorski.tu@gmail.com

**Plamen Kasabov**  
Technical University of Sofia,  
Branch Plovdiv  
Plovdiv, Bulgaria  
plamen.kasabov@abv.bg

**Georgiya Kamburova**  
Technical University of Sofia,  
Branch Plovdiv  
Plovdiv, Bulgaria  
kgeorgiya@gmail.com

**Abstract.** The hypereutectic aluminium-silicon alloys AlSi25Cu4Cr and AlSi25Cu5Cr are heat treated T5, T6 and T7. The quenching of the alloys was carried out under the same conditions. Artificial aging at T5 was carried out at a temperature of 180° C for 2, 4 and 6h, and at T6 at 180° C for 8, 10, 12 and 14h. The artificial aging of the studied compositions at T7 was carried out at a temperature of 370° C for 20, 40 and 60 min. The influence of heat treatment on the size, shape and distribution of primary and eutectic silicon crystals in the alloy structure was investigated. It was established that the proposed heat treatment regimes do not lead to a significant change in the shape and size of the primary silicon crystals, but contribute to their uniform distribution in the structure of the studied alloys. Rounding of the silicon crystals in the composition of the eutectic of the investigated alloys was observed.

**Keywords:** heat treatment, hypereutectic aluminium-silicon alloys, structure.

## I. INTRODUCTION

The main application of alloys of the Al-Si system is for the manufacture of pistons for internal combustion engines. The hypereutectic aluminium-silicon alloys have poor casting properties, and because they crystallize over a wide temperature range, microvoid porosity is observed in the castings. To obtain solid castings, various casting methods are used - casting in stils, semi-liquid stamping, casting under gas pressure [1]-[3].

In recent years, new alloys and composites have been introduced in the automotive industry [4], [5]. In order to obtain aluminum alloys with modified structures and increased mechanical properties, new types of modifiers, rare earth elements are used, and different amounts of phosphorus are experimented with [6]-[14]. Research is being conducted on the operational properties (wear resistance and corrosion resistance) of the alloys intended for the manufacture of pistons for internal combustion engines, as well as new coatings aimed at improving their wear resistance [15]-[19].

The aim of the present work is to study the influence of different heat treatment regimes on the size, shape and distribution of primary and eutectic silicon crystals in the structure of AlSi25Cu4Cr and AlSi25Cu5Cr alloys.

## II. MATERIALS AND METHODS

The object of the present study are supereutectic aluminum-silicon alloys AlSi25Cu4Cr and AlSi25Cu5Cr. The investigated alloys were prepared by two different technologies. One technology for producing the alloys involves melting the pure metals in an electric resistance furnace and casting the resulting alloys into a block. The compositions obtained in this way are re-melted, and immediately before pouring, the metallurgical processing of the melts (refining, degassing and modification) is carried out. Phosphorus in the amount of 0.04% was used to modify the AlSi25Cu4Cr alloy, and the AlSi25Cu5Cr

Print ISSN 1691-5402

Online ISSN 2256-070X

<https://doi.org/10.17770/etr2023vol3.7181>

© 2023 Boyan Dochev, Desislava Dimova, Mihail Zagorski, Plamen Kasabov, Georgiya Kamburova.

Published by Rezekne Academy of Technologies.

This is an open access article under the [Creative Commons Attribution 4.0 International License](https://creativecommons.org/licenses/by/4.0/).

alloy was modified with 0.07% P. Experimental castings have been cast. The chemical composition of the prepared alloys is shown in Table 1 and Table 2. Castings obtained by this technology are subjected to thermal treatment T5 and T7. The heating to homogenize the structure before hardening was carried out at a temperature of 510-515°C, the holding time at the indicated temperature was 6h30min., and for hardening a cooling medium of water with a temperature of 20°C was used. Artificial aging at T5 was carried out at a temperature of 180°C and holding times were 2h, 4h and 6h. During heat treatment the T7 temperature for artificial aging is 370°C and holding times are 20min, 40min and 60min.

TABLE 1 CHEMICAL COMPOSITION OF ALSi25Cu4Cr (%) REMELTING

Si	Cu	Cr	Fe	Ni	Al
25,13	3,55	0,65	0,135	0,0051	rest

TABLE 2 CHEMICAL COMPOSITION OF ALSi25Cu5Cr (%) REMELTING

Si	Cu	Cr	Fe	Ni	Al
25,24	4,72	0,589	0,349	0,031	rest

The second technology for obtaining the studied alloys involves melting the pure metals in an electric resistance furnace, refining, degassing and modifying the melts and direct casting of experimental castings (without using remelting of previously prepared alloys). Phosphorus in the amount of 0.04% was used to modify the AlSi25Cu4Cr alloy, and the AlSi25Cu5Cr alloy was modified with 0.07% P. The chemical composition of the alloys thus prepared is shown in Table 3 and Table 4. Castings from the thus prepared compositions were subjected to T6 heat treatment, in which the hardening process was carried out as in T5 and T7. Artificial aging at T6 was carried out at a temperature of 180°C and holding times were 8h, 10h, 12h and 14h.

TABLE 3 CHEMICAL COMPOSITION OF ALSi25Cu4Cr (%) PURE METALS

Si	Cu	Cr	Fe	Ni	Al
24,98	3,69	0,538	0,16	0,005	rest

TABLE 4 CHEMICAL COMPOSITION OF ALSi25Cu5Cr (%) PURE METALS

Si	Cu	Cr	Fe	Ni	Al
25,31	4,32	0,528	0,122	0,005	rest

### III. RESULTS AND DISCUSSION

The results of the microstructural analysis show that the AlSi25Cu4Cr and AlSi25Cu5Cr alloys obtained by remelting a block and modified with 0.04% P and 0.07% P respectively at a temperature of 830°-850°C have a modified structure. The primary silicon crystals in the structure of the alloy AlSi25Cu4Cr modified with 0.04% P are finely divided and evenly distributed in its structure, with the main amount of crystals having sizes of 19-27

µm, and crystals with larger sizes are also found. The silicon crystals in the composition of the eutectic are plates, which in the observed field of the sandpaper have a needle-like shape and linear dimensions of 12-15 µm (Fig. 1).

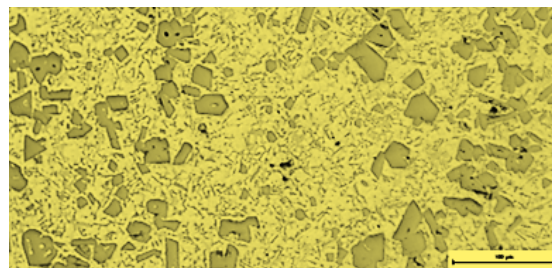


Fig. 1. Microstructure of alloy AlSi25Cu4Cr+0.04%P (remelting) x100.

In the structure of the AlSi25Cu5Cr alloy modified with 0.07% P, a large part of the silicon crystals are in the form of plates with a length not exceeding 45-50 µm and a width of 12-15 µm, single crystals with an irregular shape and a significant amount of primary silicon crystals with sizes in the range of 17 -27 µm, and eutectic silicon measures 5-7 µm (Fig. 2).

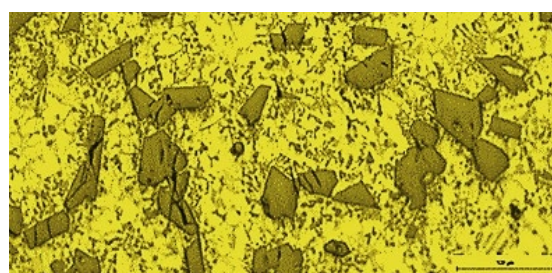


Fig. 2. Microstructure of alloy AlSi25Cu5Cr+0.07%P (remelting) x100.

In AlSi25Cu4Cr and AlSi25Cu5Cr alloys obtained from pure metals and subjected to modifying treatment with 0.04% P and 0.07% P, unmodified primary Si crystals can also be observed in their structure. The reason for this is most likely a loss of part of the used phosphorus modifier, which was introduced into the melts through CuP10 at a temperature of 900°-930°C [20], [21]. A large part of the primary Si crystals in the AlSi25Cu4C + 0.04%P alloy structure are of irregular shape and cannot be measured; those that have been measured are 35 to 50 µm in size. Eutectic Si crystals are in the form of needles with linear dimensions of 30 - 54 µm. (Fig. 3).

In the structure of the alloy obtained from pure metals AlSi25Cu5Cr and modified with 0.07%P, irregularly shaped Si crystals are observed, which are not subject to measurement. The modified crystals are polyhedral, the measured and calculated conditional average diameter is 32 µm. The silicon in the composition of the eutectic is in the form of needles with an average linear size of 25.7 µm. (Fig. 4).

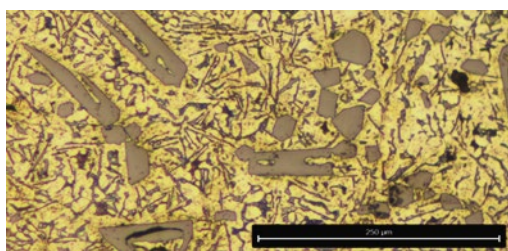


Fig. 3. Microstructure of alloy AlSi25Cu4Cr+0.04%P (pure metals) x100.

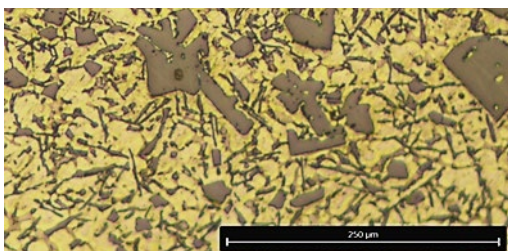


Fig. 4. Microstructure of alloy AlSi25Cu5Cr+0.07%P (pure metals) x100.

The structure of an AlSi25Cu4Cr alloy modified with phosphorus in the amount of 0.04% and subjected to T5, in which the artificial aging was carried out at a temperature of 180°C and the holding time was 2h is shown in Fig. 5. The conditional average diameter of the primary silicon crystals is in the range of 32-38μm. Crystals in the form of polygons with straight walls predominate, but primary silicon crystals in the form of plates are also observed. The silicon crystals in the composition of the eutectic are in the form of "needles" varying in size from 11 to 14 μm.

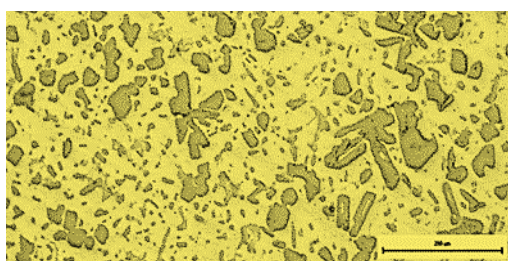


Fig. 5. Microstructure of alloy AlSi25Cu4Cr+0.04%P (remelting) T5 (180°C/2h) x100.

The microstructure of alloy AlSi25Cu4Cr + 0.04% P and subjected to T5, in which the artificial aging was carried out at a temperature of 180°C and the holding time was 4h is shown in Fig. 6. The primary Si crystals have sizes in the range of 18-29μm and are evenly distributed in the alloy structure. Some of the eutectic Si crystals have a rounded shape, there are also those in the form of plates, and their sizes are in the range from 8 to 14 μm.

After heat treatment T5, in which the artificial aging was carried out at a working temperature of 180°C and a holding time of 6h, the AlSi25Cu4Cr + 0.04% P alloy has a structure that is shown in Fig. 7. Fine and evenly distributed primary silicon crystals with sizes in the range of 21-25 μm are observed. The silicon crystals in the

composition of the eutectic are rounded in shape and 11 to 14 μm in size.

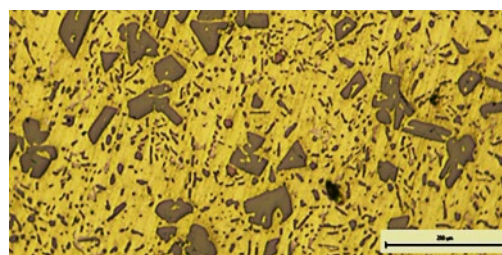


Fig. 6. Microstructure of alloy AlSi25Cu4Cr+0.04%P (remelting) T5 (180°C/4h) x100.

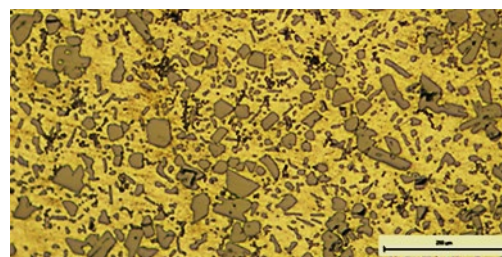


Fig. 7. Microstructure of alloy AlSi25Cu4Cr+0.04%P (remelting) T5 (180°C/6h) x100.

The AlSi25Cu4Cr alloy, which was produced from pure metals and modified with 0.04% P, was subjected to T6. The structure of the alloy, where the artificial aging was carried out at a temperature of 180°C and the holding time was 8h, is shown in Fig. 8. A large proportion of the primary Si crystals in the alloy structure are irregularly shaped and not measurable, and those measured are 43 μm in size. The eutectic Si crystals are spheroidal in shape, with one part of them having a nominal average diameter of 17 μm, and others with dimensions of 27 μm.

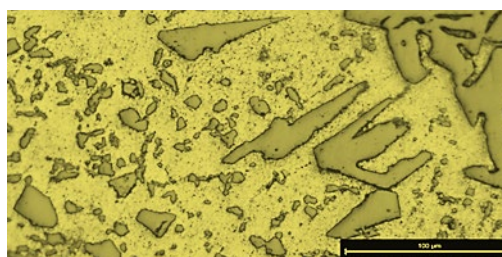


Fig. 8. Microstructure of alloy AlSi25Cu4Cr+0.04%P (pure metals) T6 (180°C/8h) x100.

After heat treatment T6 and artificial aging at a temperature of 180°C and a hold time of 10h, the modified silicon crystals in the structure of the alloy AlSi25Cu4Cr + 0.04% P were crushed. They have a conditional average diameter of 22.6 μm. A change in the shape and size of the eutectic silicon crystals is also observed, some of the crystals are spherical in shape and have a conditional average diameter of 4.5 μm, and the other part are in the form of thin plates with linear dimensions of 26.3 μm (Fig. 9).

The alloy AlSi25Cu4Cr + 0.04% P after T6 and artificial aging at 180°C and retention of 12h has a structure shown in Fig. 10. Eutectic silicon has a rounded

shape, the main amount of eutectic silicon crystals have a conditional average diameter of 5.5  $\mu\text{m}$ , a small amount with a conditional average diameter of 18  $\mu\text{m}$  is also observed. The modified Si crystals in the alloy structure are 20 to 50  $\mu\text{m}$  in size.

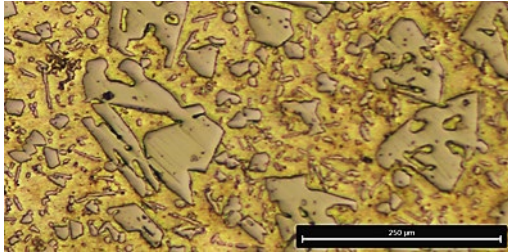


Fig. 9. Microstructure of alloy AlSi25Cu4Cr+0.04%P (pure metals) T6 (180°C/10h) x100.

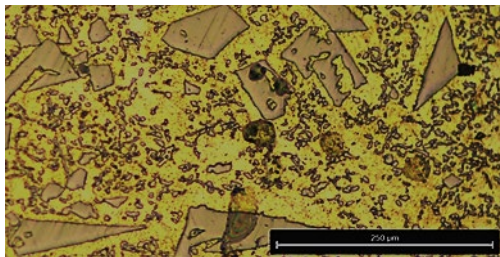


Fig. 10. Microstructure of alloy AlSi25Cu4Cr+0.04%P (pure metals) T6 (180°C/12h) x100.

Artificial aging at a temperature of 180°C and holding for 14h after quenching leads to the production of the finest crystals of eutectic silicon in the structure of the alloy AlSi25Cu4Cr + 0.04% P (Fig. 11). They are rounded in shape and have an average diameter of 7  $\mu\text{m}$ . The modified Si crystals in the alloy structure are 16 to 45  $\mu\text{m}$  in size.

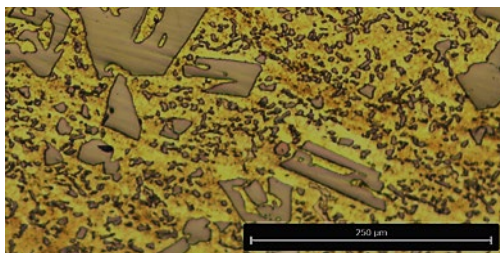


Fig. 11. Microstructure of alloy AlSi25Cu4Cr+0.04%P (pure metals) T6 (180°C/14h) x100.

With T7 heat treatment and artificial aging at 370°C and holding for 20 min. the structure of AlSi25Cu4Cr + 0.04% P alloy consists of uniformly distributed primary Si crystals with sizes of 19 to 23  $\mu\text{m}$ . Both rounded eutectic silicon crystals and in the form of plates with sizes in the range of 9-14 $\mu\text{m}$  are observed (Fig. 12).

The AlSi25Cu4Cr + 0.04% P alloy subjected to T7 and artificial aging at 370°C and holding for 40 min. has a structure shown in Fig. 13. The primary silicon crystals are finely divided and uniformly distributed with sizes ranging from 19 to 23  $\mu\text{m}$ . The silicon crystals in the composition of the eutectic have a rounded shape, there are also those

that are in the shape of plates, and their sizes are in the range of 5-8 $\mu\text{m}$ .

The microstructure of the alloy AlSi25Cu4Cr + 0.04% P subjected to T7 and artificial aging at 370°C and holding for 60 min. is composed of faceted primary silicon crystals, which have a nominal average diameter of 34-39 $\mu\text{m}$ . Individual crystals of primary silicon and of larger sizes are observed. The silicon crystals in the composition of the eutectic are in the form of plates and polygons with sizes from 3 to 7  $\mu\text{m}$  (Fig. 14).

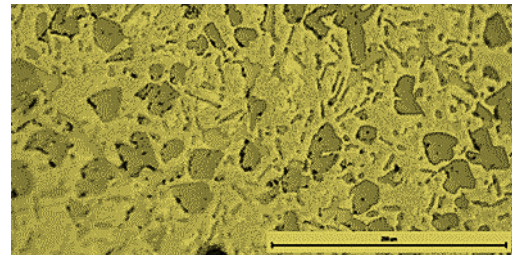


Fig. 12. Microstructure of alloy AlSi25Cu4Cr+0.04%P (remelting) T7 (370°C/20min.) x100.

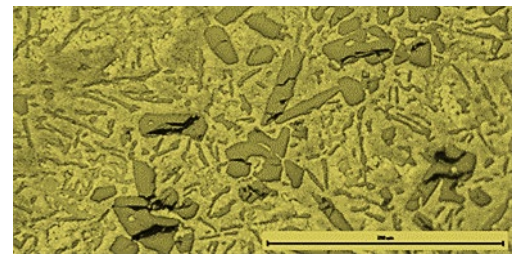


Fig. 13. Microstructure of alloy AlSi25Cu4Cr+0.04%P (remelting) T7 (370°C/40min.) x100.

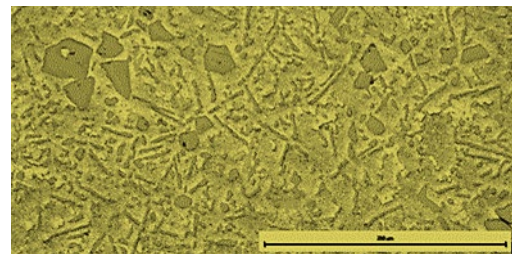


Fig. 14. Microstructure of alloy AlSi25Cu4Cr+0.04%P (remelting) T7 (370°C/60min.) x100.

The structure of AlSi25Cu5Cr alloy modified with phosphorus in the amount of 0.07% and subjected to T5, in which the artificial aging was carried out at a temperature of 180°C and the holding time was 2h is shown in Fig. 15. The primary silicon crystals are in the form of polygons with straight walls, there are also crystals with a plate shape. The conditional average diameter of the primary Si crystals is 8-13 $\mu\text{m}$ . Single plate-shaped primary silicon crystals 29-43 $\mu\text{m}$  in length are observed. The silicon in the composition of the eutectic is in the form of plates with dimensions of 4-6  $\mu\text{m}$ .

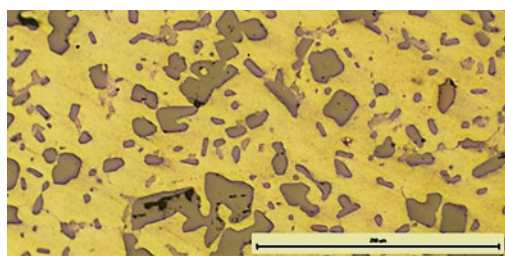


Fig. 15. Microstructure of alloy AlSi25Cu5Cr+0.07%P (remelting) T5 (180°C/2h) x100.

The microstructure of an alloy AlSi25Cu5Cr + 0.07% P subjected to T5 heat treatment, in which the artificial aging was carried out at a temperature of 180°C and the holding time was 4h is shown in Fig. 16. The primary silicon crystals are evenly spaced and have the shape of polygons and plates with an overwhelming conditional mean diameter of 19-24μm. The silicon crystals in the composition of the eutectic are in the form of needle-like platelets and rounded grains with dimensions of 9-13μm

After heat treatment T5, in which the artificial aging was carried out at a working temperature of 180°C and a holding time of 6h, the AlSi25Cu5Cr + 0.07% P, the alloy has a structure that is shown in Fig. 17. Fine primary silicon crystals are observed in the form of polygons and plates distributed uniformly in the structure. The conditional average diameter of the primary silicon grains is in the range of 11-14μm.

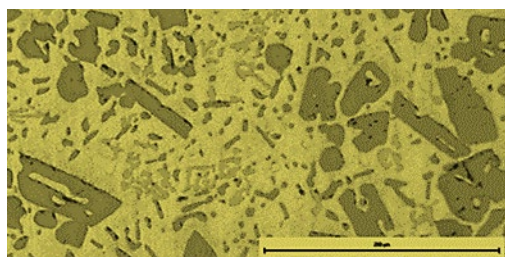


Fig. 16. Microstructure of alloy AlSi25Cu5Cr+0.07%P (remelting) T5 (180°C/4h) x100.

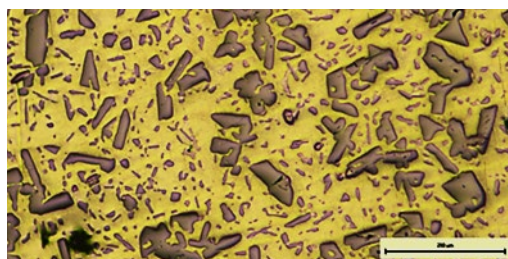


Fig. 17. Microstructure of alloy AlSi25Cu5Cr+0.07%P (remelting) T5 (180°C/6h) x100.

The alloy AlSi25Cu5Cr, which was produced from pure metals and modified with 0.07% P, was put under T6 heat treatment. The structure of the alloy, where the artificial aging was carried out at a temperature of 180°C and the holding time was 8h, is shown in Fig. 18. Most of the primary Si crystals in the alloy structure are irregularly shaped and not measurable, and those measured are 25.3 μm in size. The eutectic Si crystals are spheroidal in shape

with a conditional average diameter of 6.3 μm, and others are in the form of thin plates with linear dimensions of 22.2 μm.

After heat treatment T6 and artificial aging at a temperature of 180°C and holding time of 10h, Si crystals with a regular shape (polyhedral with straight walls) and a conditional average diameter of 20-43μm are observed in the structure of the alloy AlSi25Cu5Cr + 0.07% P. The eutectic silicon crystals have a spheroidal shape and a conditional mean diameter of 6.4 μm (Fig. 19).

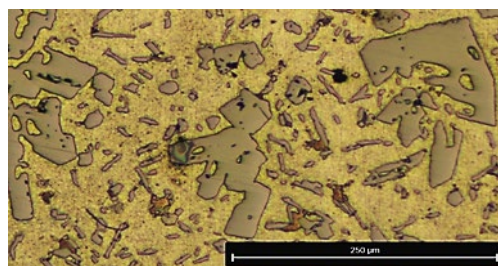


Fig. 18. Microstructure of alloy AlSi25Cu5Cr+0.07%P (pure metals) T6 (180°C/8h) x100.

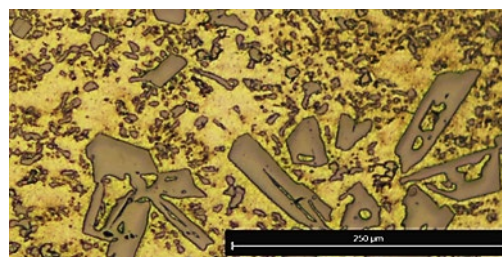


Fig. 19. Microstructure of alloy AlSi25Cu5Cr+0.07%P (pure metals) T6 (180°C/10h) x100.

The alloy AlSi25Cu5Cr + 0.07% P after T6 heat treatment and artificial aging at 180°C and retention of 12h has a structure shown in Fig. 20. The Si crystals in the composition of the eutectic are rounded in shape and up to 7 μm in size. The majority of primary Si crystals are of regular shape and reduced sizes in the range of 16 to 27 μm.

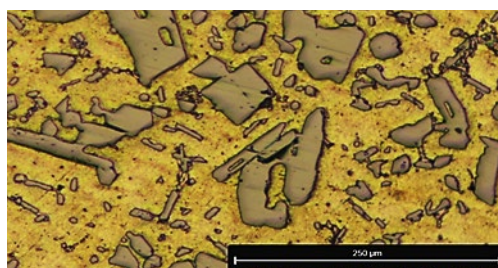


Fig. 20. Microstructure of alloy AlSi25Cu5Cr+0.07%P (pure metals) T6 (180°C/12h) x100.

Artificial aging at a temperature of 180°C and hold time of 14h after hardening leads to a change in the structure of the AlSi25Cu5Cr + 0.07% P alloy (Fig. 21). Most of the Si crystals in the composition of the eutectic are rounded in shape and up to 7 μm in size, but part of them are separated in the form of wafer with linear dimensions of 16-30 μm. The modified primary Si crystals

are in the form of polygons with straight walls and polyhedral, and the measured and calculated conditional average diameter is 25.6  $\mu\text{m}$ .

With T7 heat treatment and artificial aging at 370°C and holding for 20 min. the structure of alloy AlSi25Cu5Cr + 0.07% P consists of primary silicon crystals of regular shape - polygons with straight walls, as well as plate-shaped ones with sizes in the range of 18-27  $\mu\text{m}$ . Single crystals with an average diameter of 35-51  $\mu\text{m}$  are observed. The silicon in the composition of the eutectic is in the form of rounded crystals and plates resembling needles with dimensions of 8-10  $\mu\text{m}$ . Single plates with a length of 24-28  $\mu\text{m}$  are observed (Fig. 22).

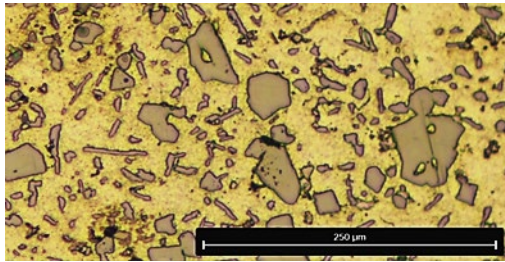


Fig. 21. Microstructure of alloy AlSi25Cu5Cr+0.07%P (pure metals) T6 (180°C/14h) x100.

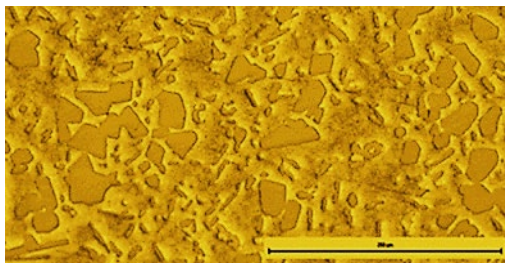


Fig. 22. Microstructure of alloy AlSi25Cu5Cr+0.07%P (remelting) T7 (370°C/20min.) x100.

The AlSi25Cu5Cr + 0.07% P alloy subjected to T7 and artificial aging at 370°C and holding for 40 min. has a structure shown in Fig. 23. Part of the silicon crystals in the composition of the eutectic are in the form of plates, but there are also those with a rounded shape and sizes from 7 to 12  $\mu\text{m}$ . The primary silicon crystals have a regular shape (polygons and plates) with dimensions of 17-22  $\mu\text{m}$ .

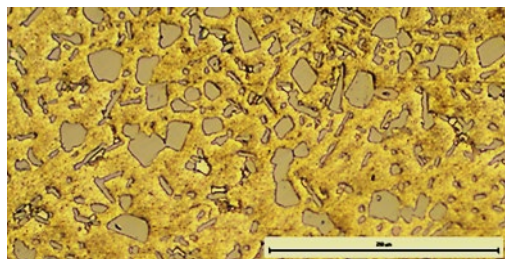


Fig. 23. Microstructure of alloy AlSi25Cu5Cr+0.07%P (remelting) T7 (370°C/40min.) x100.

The microstructure of the alloy AlSi25Cu4Cr + 0.04% P subjected to T7 and artificial aging at 370°C and holding for 60 min. consists of primary silicon crystals of regular shape and sizes in the range of 20-24  $\mu\text{m}$ . In the

composition of the eutectic, finely divided silicon crystals are observed, which are 7-10  $\mu\text{m}$  in size and have a rounded shape (Fig. 24).

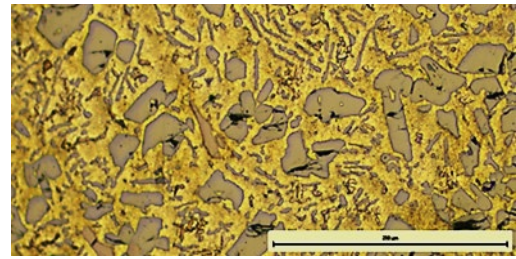


Fig. 24. Microstructure of alloy AlSi25Cu5Cr+0.07%P (remelting) T7 (370°C/60min.) x100.

In the AlSi25Cu4Cr + 0.04% P alloy subjected to T5 heat treatment, it was observed that with increasing the holding time, the shape of both primary silicon and eutectic silicon crystals was mainly affected. The primary Si crystals are uniformly distributed, of approximately the same size and regular shape. Eutectic Si crystals are rounded in shape.

The AlSi25Cu4Cr alloy, which is produced from pure metals and modified with 0.04% P, is subjected to T6 heat treatment, where the artificial aging temperature is the same as T5 (180°C). The artificial aging carried out at a temperature of 180°C and retention of 8h, 10h, 12h and 14h has the strongest effect on the eutectic silicon. It gets a rounded (spheroidal) shape. Finest eutectic silicon in the structure of the investigated alloy AlSi25Cu4Cr + 0.04% P was obtained during artificial aging at 180°C and retention of 14h.

After the heat treatment T7 in the structure of the AlSi25Cu4Cr alloy modified with 0.04% P, a tendency to increase the primary silicon crystals was observed with an increase in the holding time during the artificial aging carried out at a temperature of 370°C. With a retention time of 60 min. at 370°C the primary silicon crystals are of the largest size. No significant change in the shape and size of the eutectic silicon crystals was observed at the three retention times (20min., 40min. and 60min.) at the working temperature of artificial aging.

In the AlSi25Cu5Cr alloy modified with 0.07% P and subjected to T5, a change in the shape of the eutectic and primary silicon was observed. Silicon in the composition of the eutectic acquires a rounded shape, fine plates are also observed. Polygonization of primary Si crystals is observed, they are evenly distributed in the alloy structure.

After heat treatment T6 alloy AlSi25Cu5Cr modified with 0.07% P has in its structure eutectic silicon with a rounded shape. At artificial aging 180°C and holding for 8h, eutectic Si was observed both in spherical shape and in the form of plates. At a holding time of 10h and 12h, only rounded eutectic silicon crystals are observed in the structure of the alloy, and as the holding time increases to 14h, a tendency to change the shape of silicon in the composition of the eutectic is again observed. In addition to spherical crystals, plate-shaped crystals are also observed.

In the structure of the alloy AlSi25Cu5Cr modified with 0.07% P and subjected to thermal treatment T7, no significant changes in the shape and size of the primary silicon crystals were observed. During artificial aging at a temperature of 370°C and holding for 20 min. eutectic silicon is in the form of thin layers, rounded crystals are also found. As the retention time increases to 40 min. silicon in the composition of the eutectic is crushed and a change in the shape of the thin plates is observed as they become more massive. When held for 60 min. at the selected operating temperature of 370°C, the eutectic silicon crystals are rounded in shape.

#### IV. CONCLUSIONS

The proposed heat treatment modes do not lead to a significant change in the shape and size of the primary silicon crystals, but contribute to their uniform distribution in the structure of the studied AlSi25Cu4Cr and AlSi25Cu5Cr alloys modified with 0.04% P and 0.07% P, respectively. Rounding of the silicon crystals is observed in the composition of the eutectic of the studied alloys.

During the T7 heat treatment of AlSi25Cu4Cr alloy modified with 0.04% P, a tendency for the growth of primary silicon crystals was observed. With a retention time of 60 min. at an operating temperature of 370°C, the primary silicon crystals are of the largest size.

**Acknowledgments:** This study was supported by the Bulgarian National Science Fund № **KII-06-IIM67/12**, project title: "Investigation of the tribological properties of new nickel-free piston aluminum-silicon alloys"

#### REFERENCES

- [1] A. Velikov, S. Stanev, A. Maneva, R. Angelov, „Gas pressing" ("GP") - a method of obtaining pistons for internal combustion engines“. Proceedings of the III Scientific and Educational Conference "Mechanical Engineering-Traditions and Innovations" (MIT-2010), ISBN 978-5-94057-216, Moscow, November-December, 2010, 53-55. (In Russian)
- [2] A. Velikov, S. Bushev, „Foundry-Gas Pressing Method“. Bulgarian Society for NDT International Journal "NDT Days", Volume II, Issue 2, 2019, ISSN:ISSN: 2603-4018, eISSN: 2603-4646, 224-229.
- [3] S. Miladinović, B. Stojanović, S. Gajević, A. Vencl, „Hypereutectic Aluminum Alloys and Composites: A Review“ <https://link.springer.com/article/10.1007/s12633-022-02216-2>
- [4] S. Veličković, B. Stojanović, L. Ivanović, S. Miladinović, Milojević, „Application of nanocomposites in the automotive industry“. MVM 2019 - Volume 45 - Number 3 45(3):51–64. 2019 <https://doi.org/10.24874/mvm.2019.45.03.05>
- [5] Mahle GmbH „Piston materials. In: Pistons and engine testing“. ATZ/MTZ-Fachbuch. Vieweg+Teubner Verlag, Wiesbaden.2012 [https://doi.org/10.1007/978-3-8348-8662-0\\_4](https://doi.org/10.1007/978-3-8348-8662-0_4)
- [6] C. Gong , H. Tu, C. Wu, J. Wang, X. Su, „Study on microstructure and mechanical properties of hypereutectic Al–18Si alloy modified with Al–3B“. Journals Materials, Volume 11, Issue 3, 10.3390/ma11030456 11(3):456. 2018 <https://doi.org/10.3390/ma11030456>
- [7] K. Wang, M. Wei, L. Zhang, Y. Du, „Morphologies of primary silicon in hypereutectic Al-Si alloys: phase-field simulation supported by key experiments“. Metallurgical and Materials Transactions A volume 47, p.1510–1516, 2016 <https://doi.org/10.1007/s11661-016-3358-1>
- [8] P. Xing, B. Gao, Y. Zhuang, K. Liu, G. Tu, „On the modification of hypereutectic Al-Si alloys using rare earth Er“. Acta Metallurgica Sinica (English Letters), Vol. 23, Issue 5, p.327-333, 2010 <https://doi.org/10.11890/1006-7191-105-327>
- [9] J. Jeon, J. Shin, D. Bae, „Si phase modification on the elevated temperature mechanical properties of Al-Si hypereutectic alloys“. Materials Science and Engineering: A, Volume 748, 4 March.p.367-370,2019 <https://doi.org/10.1016/j.msea.2019.01.119>
- [10] R. Guan, D. Tie, „A review on grain refinement of aluminum alloys: Progresses, challenges and prospects“. Acta Metallurgica Sinica (English Letters) volume 30, p.409–432, 2017 <https://doi.org/10.1007/s40195-017-0565-8>
- [11] M. Zuo, D. Zhao, X. Teng, H. Geng, Z. Zhang, „Effect of P and Sr complex modification on Si phase in hypereutectic Al–30Si alloys“. Materials & Design, Volume 47, May, p. 857-864, 2013 <https://doi.org/10.1016/j.matdes.2012.12.054>
- [12] B. Njuguna, J. Li, Y. Tan, Q. Sun, P. Li, „Grain refinement of primary silicon in hypereutectic Al-Si alloys by different P-containing compounds“. China Foundry, Volume 18, p.37–44, 2021 <https://doi.org/10.1007/s41230-021-0074-2>
- [13] J. Scepanovic, V. Asanovic, S. Herenda, D. Vuksanovic, D. Radonjic, F. Korac, „Microstructure characteristics, mechanical properties, fracture analysis and corrosion behavior of hypereutectic Al–13.5Si alloy“. International Journal of Metalcasting, Volume 13, p.700–714, 2019 <https://doi.org/10.1007/s40962-019-00315-2>
- [14] W. Shi, B. Gao, G. Tu, S. Li, „Effect of Nd on microstructure and wear resistance of hypereutectic Al–20%Si alloy“. Journal of Alloys and Compounds, Volume 508, Issue 2, 22 October, p. 480-485,2010 <https://doi.org/10.1016/j.jallcom.2010.08.098>
- [15] K. Jena, J. Majhi, S. Sahoo, S. Pattnaik, „The microstructural and wear properties improvement by manganese addition in Al-14Si hypereutectic alloy“. Materials Today, Volume 62, Part10.p.5934-5941,2022 <https://doi.org/10.1016/j.matpr.2022.04.638>
- [16] K. Kamarska, „Corrosion of AlSi18Cu3CrMn aluminum alloy in a chloride-containing medium“, AIP Conference Proceedings 2449, 60019, September 2022, <https://doi.org/10.1063/5.0090754>
- [17] K. Kamarska, „ Study of the corrosion behavior of aluminum-silicon alloy AlSi18Cu3CrMn in acidic media“, AIP Conference Proceedings 2449, 060018, September 2022, <https://doi.org/10.1063/5.0090753>
- [18] M. Kandeва, Zh. Kalitchin ,Y. Stoyanova,“ Influence of Chromium Concentration on the Abrasive Wear of Ni-Cr-B-Si Coatings Applied by Supersonic Flame Jet (HVOF)“, Metals 2021, 11(6), 915, <https://doi.org/10.3390/met11060915>
- [19] M. Kandeва, T. Penyashki, G. Kostadinov, Zh. Kalitchin, J. Kaleicheva, „Wear of electroless nickel-phosphorus composite coatings with nanodiamond particles“, Journal of Environmental Protection and Ecology 19, No 3, p.1200–1214, 2018
- [20] J. Piątkowski, „Archives of foundry engineering“, Volume 9, Issue 3, p.125-128, 2009
- [21] A. Zambon, Phosphorus modification in Al-Si hypereutectic alloys: Norwegian University of Science and Technology, Department of Materials Science and Engineering, Submission date: July 2016.

# *Results and Analysis of Achieved Joint Research and Activities Between Rezekne Academy of Technology and Vasil Levski National Military University*

**Nikolay Todorov Dolchinkov**  
*Vasil Levski National Military  
University, Veliko Tarnovo, Bulgaria*  
*National Research University*  
*"Moscow Power Engineering  
Institute", Moscow, Russia*  
Veliko Tarnovo, Bulgaria  
n\_dolchinkov@abv.bg

**Abstract.** In 2018, the first group of teachers and students from Vasil Levski National University conducted experiments on laser marking in Rezekne Academy Of Technology, Latvia. Since then, joint research has been increasing every year and better results have been achieved not only in the field of laser technologies, but also in other areas of joint interest. A pilot study group is even being formed in a master's program in laser technology. As a result, the interest in laser technologies and in Latvia at Vasil Levski National University increased significantly. Research has been done on the impact of the exchange between the two institutions on the learners and their motivation to learn.

**Keywords:** *collaborative research; experiment; laser; laser marking; result; 3D printer.*

## I. INTRODUCTION

Joint research in the field of laser technologies between the Rezekne Academy of Technology, as a leading partner, and the National Military University "Vasyl Levski" has been starting since 2018. The partnership between educational institutions is even older, with the first cooperation framework agreements and Erasmus contracts being signed more than 10 years ago. Over the years, the former rector of the Rezekne Academy of Technology, Prof. Edmunds Teirumnieks, and the dean of the Faculty of Engineering, Erika Teirumnieka, have visited the military university many times, Prof. Lubomir Lazov has also visited the university and delivered public lectures to the academic staff. The National Military University was also attended by trainees from the Academy in Rezekne.

Teachers and students from the educational institution from Bulgaria have also repeatedly visited the Latvian university. During practicals, students from the National University under the guidance of Prof. Lazov carried out research and data processing from experimental and theoretical studies of various materials at the laser center in Rezekne.

Teachers and students from both universities participated in scientific conferences held in the partner country. Representatives of our educational institution from Veliko Tarnovo and Shumen are regular participants in the conference in Rezekne. Professor Lazov has delivered more than 6 plenary reports at conferences in Veliko Tarnovo and Shumen. Students from the Academy in Rezekne also regularly participate in conferences in Veliko Tarnovo. This contributes to closer ties between the two universities, exchange of information and students, and enrichment of the institutions.

## II. MATERIALS AND METHODS

In 2018, a group of 5 cadets and students and 2 teachers led by me conducted the first research at the laser center in Rezekne. The group was part of project no and a two-week mobility was carried out. During the visit to the laser center at the Academy, a rich program of research and analysis of the obtained results was carried out. During this half-month period, laser marking, laser cutting and finding the optimal values of the laser beam to perform these activities were carried out. The experiments were performed with a CO<sub>2</sub>

*Print ISSN 1691-5402  
Online ISSN 2256-070X*

<https://doi.org/10.17770/etr2023vol3.7223>

© 2023 Nikolay Todorov Dolchinkov. Published by Rezekne Academy of Technologies.  
This is an open access article under the [Creative Commons Attribution 4.0 International License](https://creativecommons.org/licenses/by/4.0/).

laser on plexiglass, textile and felt. In the study, colorless plexiglass with different sample thicknesses, 4 types of textiles and 2 types of felt were used. As a result of the conducted experiments, the optimal parameters of the laser beam for marking on the samples were found, and the minimum values of the beam power and its speed were determined for performing quality cutting on the samples. Based on the research on plexiglass, we reached the following conclusions. When the laser beam power is constant (10 W, 20 W, 30 W, 40 W or 50 W), as the beam speed increases from 5 mm/s to 30 mm/s, the measured effective perforation depth decreases. The maximum effective perforation depth is 8.324 mm for 50 W and a speed of 5 mm/s. The minimum effective perforation depth is 0.188 mm for 10 W and a speed of 30 mm/s. Furthermore, as the linear energy density decreases, the perforation depth of the efficiency also decreases [1], [2].

Laser marking and cutting can be used for artistic decoration and unique design on any surface of textile products in the fashion industry [3].

Marking, engraving and cutting can be successfully applied to all textile materials and leather materials. The choice of laser process is determined by the desired end result.

### III. RESULTS AND DISCUSSION

Marking and engraving on fabric with a composition of 65/35% CO / polyester  $\pm$  3% determined according to EN ISO 1833 quantitative chemical standard with a CO<sub>2</sub> laser was investigated and analyzed. For this purpose, an experimental methodology has been developed, which consists of the following [4]:

A matrix of 9 squares with 1x1 cm is created. The power of the laser beam is in the range of 2x26W, and its speed is in the range of 100x350 mm/s. After the experiments conducted and the analysis done, we came to the conclusion that a good cutting of the material is obtained with the following parameters: a constant power of 26 watts and a speed in the range of 100-200 mm/s, with linear energy densities of 0.26, 0.17 and 0 respectively .13 J/mm [5].

A quality mark is obtained in the range of LED values  $5 \cdot 10^{-2} \times 3.8 \cdot 10^{-2}$  J/mm for a power of 10 W, where the speed varies in the range 200-260 mm/s. The remaining highlight areas have a slight contrast that is between 5% and 10%.

The felt can be used in different directions and spheres. Most often, useful household products are made from this material, for example, for sealing in various branches of industry - mechanical engineering, paper-pulp industry, also as an insulating material, for polishing, etc. Often felt also serves as upholstery on various surfaces. After doing research, we found that a major factor in the difference in laser cutting of white and red felt is the difference in the color of the material. Another factor is its thickness – which for the white felt is 0.63mm and for the red felt is 0.67mm. Quality cutting of the material is obtained with the following parameters: for white and red felt - constant

power 26 W (9%) and speed in the range 100, 150 and 200 mm/s and LEDs are 0.26 J/mm , 0.17 J/mm 0.13 J/mm [6].

The obtained results were reported at the conference in Rezekne in 2019 and at the conference of the Scientific and Technical Unions in Borovets, Bulgaria.

In the summer of 2019, part of the group continued their research in Erasmus summer mobility at the Academy of Technology in Rezekne for 2 or 3 months. The obtained results were consolidated and the range of research was expanded. Few studies were conducted in the winter of 2020 due to the onset of the Covid epidemic. This did not allow us to conduct full-fledged research throughout 2020 [7], [8].

In 2021, the next group of trainees from Vasil Levski National University expanded the research, which was already carried out on metal plates and attention was paid to chrome-nickel alloys. For this purpose, an AISI 304 color palette consisting of fifteen colors was developed and executed. After the practical experiments, the dependence of the obtained colors on the various parameters of the laser processing was analyzed. The resulting colors were then tested using optical, scanning electron and atomic force microscopy, and the configuration of the oxide films was determined by Raman spectroscopy. The resulting colors are of appropriate uniformity, brightness and cover almost all spectral zones, and the resulting colors are of many times better quality than other metallic bases. A color standardization and palette repeatability test was also performed by evaluating the reflectance spectra of the formed colors. The color palette demonstrated high repeatability for all but one particular color. In parallel, the stability of the color markings was studied in terms of environmental, mechanical and chemical resistance. The resulting colors show high resistance to most environmental conditions; however, exposure to very high temperatures and extreme humidity (100 °C, 90%) and to low temperatures and extreme humidity (-40 °C, 90%) results in degradation of several colors. Colored brands show high hardness and excellent mechanical resistance to external influences and exceptional resistance to various chemicals, except for acid solutions and salts [9].

The result shows that with increasing power the colors do not change significantly and only the parametric window moves to higher values of the scan rate for each color. Given that greater performance can be obtained at higher intensities, the next step was to investigate the dependence of color on scan rate with a maximum continuous power of 20 W available at the same parameters of frequency, hatch spacing and duration of the impulse. Initially, the scanning speed was changed from 450 to 850 mm/s with a step of 10 mm/s, and then from 50 to 150 mm/s with the same step.

The test result revealed that specific colors such as light pink, aquamarine or bright purple can be obtained with higher frequency modes. At  $f=1000$  kHz, only silver colors are formed for the entire scan rate range; hence, the parametric color window could not be produced at the mentioned frequency, although it could be assimilated into

a final palette to produce white or silver due to its fast production speed [10].

The experiment to study the dependence of colors on the pulse duration was carried out with two different power densities  $I_0=0.8-107$  and  $I_0=1.6-107$  W/cm<sup>2</sup> and two different pulse durations  $r=4$  and  $r=8$  ns with scan speed  $V_{sc}=50-200$  mm/s with step 10 mm/s and  $H=0.01$  mm.

Product coatings and markings must withstand various environmental conditions and must not change during the period of use of the product [1], [9]. In this study, environmental testing was performed in a chamber based on four different operating conditions. Experiments are regularly conducted under temperature and humidity conditions that are not actually expected, such as a combination of extremely low or high temperatures (-40, -20, 40, 100 °C) with high humidity (70%, 90%). This ensures the stability of the samples under normal conditions and also compensates for the short duration of the test exposure (24 hours) compared to the actual operating time. The first test was conducted under ambient conditions with a temperature of -20 °C and a humidity of 70%. The result shows no change in colors or materials after 24 hours in the environmental test chamber. Optical microscope analyzes did not reveal any damage or defects in the oxide layers [11], [12], [13], [14], [15], [16], [17], [18].

The research of our cadets and students continued in 2022 under the leadership of Professor Lazov and the staff at the laser center at the Technological Academy in Rezekne.

In 2021, a pilot program for training in the master's degree in laser technologies was also launched, in which graduates and teachers from the National Military University participated. The training is within 4 semesters in a distance form of training during 2 academic years. Experiments were conducted in Rezekne, Gabrovo and Ruse again under the leadership of Prof. Lazov, and the trainees are currently working on their diploma theses. This master's program has proven to be working, and it will be thought about accrediting an already joint such program in the field of the application of laser technologies in military work. The head of the laser center in Rezekne has already been included in a master's training team at the military university [14], [19].

#### IV. CONCLUSIONS

Over the years, the two educational institutions have developed joint projects under the program "Horizon 2020", "Peter Beron" and others, and we should continue this tradition by involving more participants in joint events and research.

Over the past years, the cooperation between the Rezekne Academy of Technology and the National Military University has been constantly developing and deepening. Many mobilities took place between faculty and trainees from the two universities, research was carried out on laser marking and cutting on common and dual-purpose materials, including Plexiglas, textiles, felt, steel, chrome-

nickel, specialized metal alloys and others [2] As a result of the conducted trainings and practices, the interest of the trainees increased and as a result many of them specialize in this field and in the field of 3D printers. After the practices, 5 people bought personal 3D printers and use them rationally. With our own developments, we have participated in 3 international exhibitions with 6 exhibits, which are a consequence of the training at the Academy in Rezekne.

These studies may also be conducted with materials that may have an impact on raising the defense capabilities and combat capability of the armed forces of both countries.

In the future, we hope to increase students' interest in laser technology and 3D printers and to equip our laboratory and open a joint master's program.

#### V. ACKNOWLEDGMENTS

I express my gratitude to Professor Lyubomir Lazov for the dedicated work during these 10 years to deepen the cooperation between the two educational institutions, for the dedication in working with the trainees from the Vasil Levski National Military University and for the knowledge, experience and skills imparted.

I also thank the managements of both institutions over the years for their benevolent attitude and for the opportunity to conduct joint activities.

#### REFERENCES

- [1] Dave Ahearn, ONR Laser Power Jumps 10 Fold; Further 10-Fold Leaps Seen, Defense Today, August 4, 2004, p. 4
- [2] N. Todorov, Lyubomir L., Shterev I.J., Dimitrov N.D. and Ivanov L.L. 2019 Study of cutting and labeling of polymethylmethacrylate using a CO<sub>2</sub> laser Vide. Tehnologija. Resursi -Environment, Technology, Resources. ISBN 1691-5402, Vol 3, 20-22.06.2019 Rezekne, Latvia pp. 37-40.
- [3] S. E. Lamberson, The airborne laser, Proc. SPIE, Gas Chem. Lasers, vol. 2702, pp. 2702-1\_2 702 - 6, Mar. 1996
- [4] W. Zhang, Xiao Z. and Yan Z. 1976 Design of online laser marking system by vision guided based on template matching Journal of Physics: Conference Series 1976 012047
- [5] L. Lazov, H. Deneva, E. Teirumnieka, Influence of Defocus Position on Laser Cutting Process in Sheet Steel, Environment. Technology. Resources, Rezekne, Latvia Proceedings of the 11 th International Scientific and Practical Conference. Volume III, 163-167,
- [6] L. Lazov, Dolchinkov N., Shterev J., Peneva M. and Bozhanova D. 2019 Study of laser cutting and marking on the felt with the help of a CO<sub>2</sub>-laser Vide. Tehnologija. Resursi - Environment, Technology, Resources, ISBN 1691-5402, Vol 3 pp. 143-147.
- [7] L. Lazov, Angelov N., Teirumnieks E. and Teirumnieka E. 2019 Preliminary numerical analysis for the role of speed onto laser technological processes Vide. Tehnologija. Resursi - Environment, Technology, Resources 3 pp 137-142.
- [8] N. Petrov, Optimization of the marking process with laser radiation of samples of tool steel, dissertation, Gabrovo, 2011.
- [9] N. Dolchinkov, Lazov L., Shterev Y., Lilianova St. and Pacejs A. 2019 Use of CO<sub>2</sub> laser for marking and clearing of textile materials for manufacture of military equipment 12th International Scientific and Practical conference Environment. Technology. Resources. 3, ISBN 1691-540206.2019, Rezekne, Latvia, 32-36
- [10] N. Todorov D. 2020 Practical research of marking and cutting of textiles with increased resistance, using CO<sub>2</sub> laser Journal of Physics: Conference Series 1681 012014, doi:10.1088/1742-

- 6596/1681/1/012014, Online ISSN: 1742-6596, Print ISSN: 1742-6588
- [11] S.-T. Tse and Kan C.-W. 2020 Effect of laser treatment on pigment printing on denim fabric: low stress mechanical properties *Cellulose* 27 10385-10405
- [12] N. T. Dolchinkov 2022 Marking and Cutting of Non-metallic Products with CO<sub>2</sub> Laser, *J. Phys.: Conf. Ser.* 2224 012028 DOI 10.1088/1742-6596/2224/1/012028H, doi: 10.1109/Lighting49406.2021.9599072, Electronic ISBN:978-1-6654-3792-9, CD:978-1-6654-3791-2
- [13] L. Lazarov, Perspectives and trends for the development of electronic warfare systems, *International Conference on Creative Business for Smart and Sustainable Growth, CreBUS 2019*, 2019, 8840074
- [14] S. Stoykov, Dimitrova, S., Marinov, R., The development of educational capacity of human resources in the field of security-main priority of national security, *International Conference on Creative Business for Smart and Sustainable Growth, CreBUS 2019*, 2019, 8840062
- [15] N. Padarev, Investigation of Damage from Radiological Dispersal Device, *International Journal of Innovative Technology and Interdisciplinary Sciences*, 5(4), 2022, pp. 1052–1059. <https://doi.org/10.1515/IJITIS.2022.5.4.1052-1059>.
- [16] N. Padarev, Guidelines for improving laser targeting device in military. *Technology transfer: fundamental principles and innovative technical solutions*, 2022, 38-40. doi: <https://doi.org/10.21303/2585-6847.2022.002681>
- [17] L. Lazov, N. Padarev, Laser Safety in Army Education, *Revista, Vol. XXVIII, Nr. 1 (109)*, ED. Academiei Forțelor Terestre „Nicolae Bălcescu” Sibiu, Romania 2023, ISSN 2247-840X, ISSN-L = 1582-6384, pp. 61–68, DOI: 10.2478/raft-2023-0009
- [18] N. Padarev, Analysis of the Relation Between Climate Changes and Security Area, *International Conference Knowledge-Based Organization, Vol. XXIV. Conference proceedings 3, Applied technical Sciences and Military Technologies, Sibiu, Rom., 2018*, pp 169-173, ISSN 1843-682X, ISBN 978-973-153-329-2.
- [19] N. T. Dolchinkov 2022 Marking and Cutting of Non-metallic Products with CO<sub>2</sub> Laser, *J. Phys.: Conf. Ser.* 2224 012028 DOI 10.1088/1742-6596/2224/1/012028H, doi: 10.1109/Lighting49406.2021.9599072, Electronic ISBN:978-1-6654-3792-9, CD:978-1-6654-3791-2

# Study of Technological Chains for Rapid Prototyping of Orthodontic Dental Products

**Veselina Dukova**

Department of Materials Science and  
Technology, "Angel Kanchev"  
University of Ruse, Bulgaria  
vdukova@uni-ruse.bg

**Roussi Minev**

Department of Materials Science and  
Technology, "Angel Kanchev"  
University of Ruse, Bulgaria  
rus@uni-ruse.bg

**Emil Yankov**

Department of Materials Science and  
Technology, "Angel Kanchev"  
University of Ruse, Bulgaria  
eyankov@uni-ruse.bg

*The paper presents results from studying the possibilities of digital layering technologies (DLP SLA - Digital Light Projector Stereolithography) for construction of biomedical orthodontics devices (aligners). Experimental data on the mechanical and aesthetical properties (transparency) of the materials used has been studied in comparison with the conventional technologies for producing the aligners - Vacuum Forming (VF). The paper discuss the influence of the design of the devices (e.g. thickness) and technological parameters (e.g. stirring time) of the processes on the mechanical properties and orthodontics functionality of the materials as well as the quality and accuracy of the devices (models and functional prototypes for dental applications).*

**Keywords:** *Materials in dentistry, Orthodontics, Stereolithography.*

## I. INTRODUCTION

The treatment of orthodontic deviations aims to influence the growth of the upper and lower jaw [1]. Depending on the situation, the growth of one or both jaws can be slowed down or stimulated. The force is produced by the patient's muscles and transmitted to the teeth and jaws. Functional orthodontic appliances are used to treat deep, open and/or distal bite.

Braces, aligners and sometimes oral surgery are used for the correction of irregularly aligned teeth [2], [3]. Over the course of the patient's treatment the dentists will swap the existing aligners for new ones designed to get the teeth in place for the next phase. The dentist must have relevant information about the mechanical properties of the aligners in order to plan all phases of the treatment. Some important properties of these devices are as follow:

- (i) transparency and aesthetic appearance,
- (ii) biocompatibility,

- (iii) stability at body and food temperature,
- (iv) stiffness and rigidity.

Of the all requirements listed the mechanical properties (stiffness/rigidity) are of primary importance. Also important is the transparency of the aliners used for treting children. The rest of the properties are largely researched and predetermined by the manufacturers.

The dynamic development of digital dentistry opens wide opportunities for more and more innovative approaches in the planning and implementation of treatment by applying CAD/CAM technologies in orthodontics practice [4]. More and more often in daily practice, digital technologies such as intraoral scanners, laboratory scanners and cone beam computed tomography. 3D systems facilitate the direct fabrication of orthodontic appliances from 3D models. Known printing technologies differ in the materials and methods used to create the respective objects [5] - [8].

The first attempt to produce a retainer directly from a digital model was made in 2014 by A. Nasef et al. They report the successful fabrication of a retainer from SVST, without a physical model, using an SLS 3D-printer. Although accuracy was not evaluated, this study pioneered the use of 3D printing in orthodontics. Due to the use of an SLS printer in the study, the printed retainer is white and opaque, which is unacceptable to the most of patients [9].

Today, there are over thirty different 3D additive technologies offered by forty different companies (for example, molten material deposition, selective laser sintering, etc.) [7] - [9]. Stereolithography (SLA) is the first material-additive rapid prototyping process of this kind. Complex form models are created by sequentially

Print ISSN 1691-5402

Online ISSN 2256-070X

<https://doi.org/10.17770/etr2023vol3.7314>

© 2023 Veselina Dukova, Roussi Minev, Emil Yankov. Published by Rezekne Academy of Technologies.

This is an open access article under the [Creative Commons Attribution 4.0 International License](https://creativecommons.org/licenses/by/4.0/).

curing layers of photopolymer resin using laser beam or DLP (digital projector).

In this study we use DLP-SLA (Digital Light Projector Stereolithography technology) NextDent OrthoFlex (Vartex - Dental B.V., Soesterberg, The Netherlands) in which the model is built in a bath filled with liquid photopolymeric resin, on a vertically movable platform in a suspended position (top down approach) [10]. On the platform, supports are initially printed to ensure the stability of the physical model and especially its overhangs. DLP is controlled by the corresponding STL files performing layer by layer polymerization of the liquid material. Then the platform is immersed in the bath until the hardened layer is completely covered with liquid resin. The method finds application in dentistry in making of models, casting prototypes, surgical guides, splints, individual spoons, temporary restorations, gingival mask, prostheses, etc. It is possible to make occlusal splints and orthodontic appliances [11], [12]. The OrthoFlex is transparent class 2a biocompatible photopolymerizing material developed for the production of 3D printed occlusal splints and retainers. It has a strength of 67MPa, modulus of elasticity - 1721MPa and Charpy strength 15 kJ/mm<sup>2</sup>. This type of materials when used in less load bearing applications contain acrylate resins and photoinitiator (e.g. dimethoxy-phenolacetophenone). They are characterised by fast polymerization and relatively good geometrical accuracy and stability of the printed objects.

In this study the orthodontic devices produced with this ("digital") technology are compared with the same devices produced by "conventional" process chain covering the following stages: (i) generating a model either by scanning of the tooth profiles and production of the model by layering 3D technology or taking a replica of the patient's dental profile (in our study, the second approach was used); (ii) vacuum forming of the aligners using specialized polymer pholio made by PET-G (a copolymer that constitutes two repeating units polyethylene terephthalate and glycol which prevents the crystallization of PET upon heating and makes it clear, less brittle and more resistant to mechanical stress [13]).

## II. EXPERIMENTS

### PROCESS CHAINS

In the digital technology study, an impression was initially scanned from a patient with a Comphort+ intraoral scanner into an STL file, which was transferred to a CAD/CAM system in order to modify the resulting shell shape in thickness. The files are then fed to the control CAM program for "slicing" and determining the current sections to build. In the study, 10 aligners with different thicknesses (0.15; 0.25; 0.5; 0.75; 1.0; 1.15; 1.25; 1.5; 1.75; 2.0 mm) were made (Fig.1). The build was carried out with the following parameters optimized and recommended by the 3D printer manufacturer:

Z-axis speed 23 mm/h;  
5 min mixing before printing;

Drying 10 min;  
Post-cure 30 min;  
Printing inclination 80°-90°;  
3 mm minimum base;  
1.5 mm supports;  
Wash for 3 min. in ethanol;  
Dry for 2 min with a fan.

The "conventional" process chain includes generating a model by taking a replica of the patient's dental profile; vacuum molding of the aligners. The production of the ceramic model can be carried out in two ways: (i) scanning of the tooth profiles and production of the model by layer-by-layer 3D technology; (ii) taking a replica of the patient's dental profile. In our study, the second approach was used.

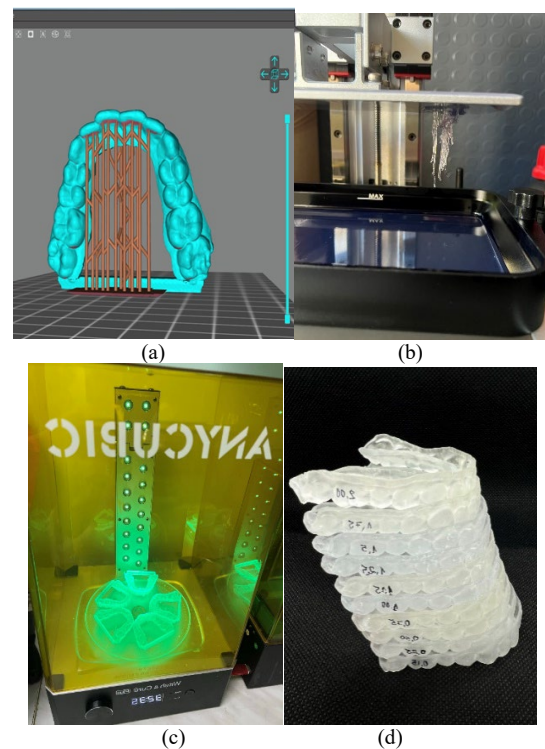


Fig.1 The CAD design of the aligners with the supporting structure (a), DLP-SLA 3D printer (b), post curing camera (c) and a set of produced aligners (d).

### STUDY OF THE TRANSPARENCY

The transparency of orthodontic aligners in different thicknesses (in the range from 0.15mm to 2.00mm) was investigated since a set of several aligners of different thickness and progressive impact on the patient's occlusal characteristics are used during the course of treatment. Other factors such as the type of technology (3D printed or moulded), the post curing time and surface texture of the printed aligners have also been investigated.

The experiments were carried out according to the scheme of Fig.2 in which light is passed through the sample and the luminous flux per unit area (Lux) is measured after passing through them.

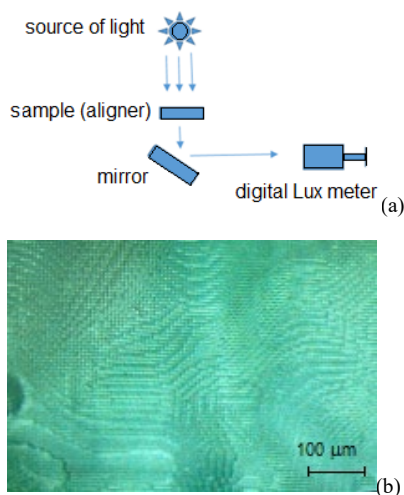


Fig. 2 Experimental set-up for transparency study (a); the texture of the printed aligner (b).

### MECHANICAL BEHAVIOUR OF THE ALIGNERS

The aligners will apply a system of forces on the teeth to shift them to desired position. Since they exert forces thanks to their particular shape they are elastically deformed in the maximum range of couple of millimetres. Therefore it is important to know their behavior under tension and compression in the elastic region of behavior (e.g. 5 mm) - Fig.2. Load-displacement curves was obtained and the stiffness  $K = \Delta F / \Delta l$  as a function of sample thickness  $d$ , mm was calculated. The deformation rate of 1 mm/min was applied and an INSTRON 3384 universal testing machine was used in the +/-0.05N force and +/-0.05mm displacement accuracy mode. The statistical error in determining the stiffness of the studied samples was within 12%.

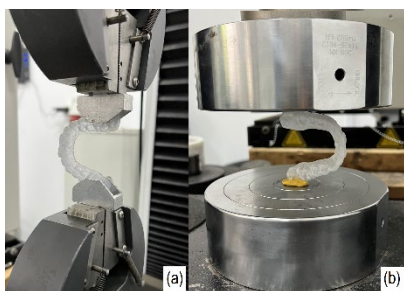


Fig. 3 Tensile (a) and compressive (b) testing of the aligners.

### III. RESULTS

#### TRANSPARENCY

In gemnaral the dependence of the sample transparency on the thickness can be assumed to be linear and its change can be calculated by the empirical formula:

$$\% \Delta I = 2.5 + 5.5 d,$$

whrere  $\Delta I$  is the change (%) in luminous flux per unit area after the light pass troug the sample with thickness  $d$ , mm.  $\Delta I$  range from 3% for small (0,15-0.5mm) ticknesses

to 12% for thicknesses of 2mm. It can be concluded that within the studied range of thicknesses, the optical qualities of the 3D printed devices with  $d < 0,5$  mm do not change significantly and for greater thicknesses (Fig.4), this change although noticeable does not unacceptably disturb the aesthetic qualities of the product.

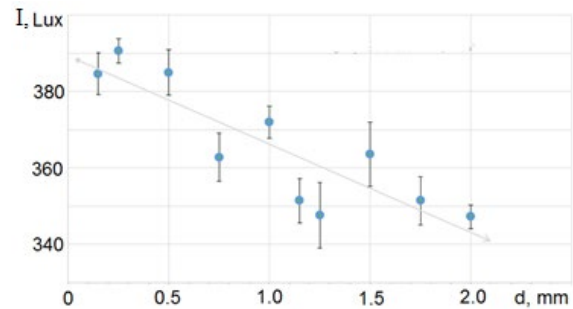


Fig.4 Transparency of aligners measured by illuminance (I, Lux) of the light passing through them as a function of their thickness (d).

The transparency of aligners made by conventional technology (Vacuum Formed) was slightly better than 3D printed (DLP SLA) - Fig.5. This difference is about 2-3% for smaller thicknesses ( $d < 1.0$  mm) and reaches 5% for thicker samples. Still the aesthetical appearance is axceptable.

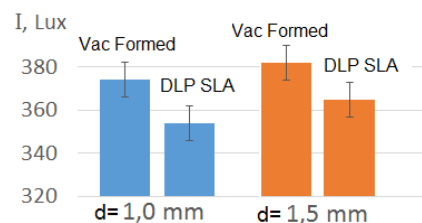


Fig.5 Comparison of the DLP SLA and Vacuum formed aligners.

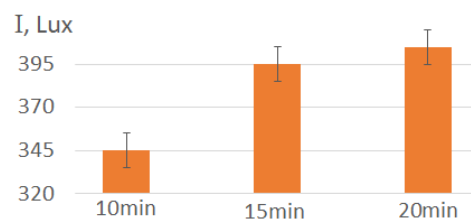


Fig.6 The influence of the resin mixing time on the transparency of the DLP SLA aligners.

Many technological factors affect the sample transparency. In the case of Vacuum formed aligners, they are well studied and come down to the influence of molding temperature and cooling rate on the degree of crystallinity of the structure. With the DLP SLA technology we have additional conditions affecting this property. For example, the roughness of the aligners resulting from the step effect during the construction of the layers leads to scattering of light and an increase in

opacity (Fig.2,b). Even more important factor is the mixing and homogenization of the resin before the photo polymerization process. Fig.6 shows the effect of stirring time on the transparency of the DLP SLA aligners. A sample with a thickness of 1.0 mm was tested. It can be seen that if insufficient mixing time is applied (less than 15 min) the transparency drops by about 20%.

**MECHANICAL PROPERTIES**

Analyses of the strain curves shown in Fig.7 reveal up to a 70% increase in the forces required to realize a 5 mm reference elastic strain of the aligner when the shell thickness is changed from 0.15 to 2.0 mm. For compressive loads the force differences are in the range of 2-7N, and for tensile loads in the range of 6-19N.

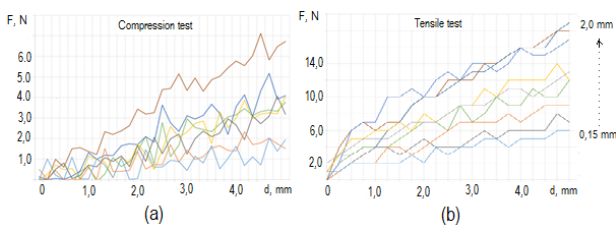


Fig.7 Compression (a) and tension (b) diagrams for aligners with thickness 0.15-2.0 mm.

The slope of the curves reveals the aligners stiffness ( $K=\Delta F/\Delta l$ ) changes within the range of 0.05-0.2 in compression and 0.3-0.8 in tension. I.e. the orthodontic structure shows about 4 times greater stiffness in tension than in compression. It should be noted that occlusal deformations (jaw closure and masticatory movements) occurring in aligners are expected to be mainly tensile making thickness variation an effective factor in determining the geometry of the orthodontic appliance set. The curves showing the  $K_{comp} = \Delta F/\Delta h$  (Fig.8,a) and  $K_{tens}=\Delta F/\Delta l$  (Fig.8,b) as a function of the aligner's thickness (d) change are not monotonous but rather show a three distinguished regions: I, II and III for "thin", "medium" and "thick" shells due to the stress state change from more pronounced plane-stressed to bulk-stressed state. Table 1 summarizes the values of the stiffness coefficient for this three regions which could be utilized for the design of the aligner's geometry.

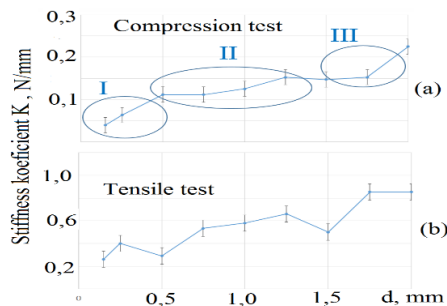


Fig.8 Stiffness in (a) - compression (b) tension as function of their thickness.

The stresses arising in the most loaded section (in the middle of the aligner, attached to the "dentes incisive") can be roughly calculated assuming the simplification of pure compression/tension load at 5 mm strain and they amount to about 0.2 MPa and 0.5 MPa respectively (for aligners with  $d = 1.0$  mm).

The comparison of the deformation diagrams of aligners manufactured by the Vacuum forming and DLP SLA technologies shows that at smaller thicknesses ( $d<1.0$ mm) the aligners manufactured by the "digital" technology have about twice the stiffness of those produced by "traditional" technology (Fig. 9,a). For thicker devices, the stiffness is practically the same (Fig.9, b).

Table 1 Stiffness coefficient (K) for aligners with different thickness (d)

d, mm	0,15-0,5	0,75-1,5	1,75-2,0
tension	0,3	0,6	0,8
compression	0,05	0,1	0,2

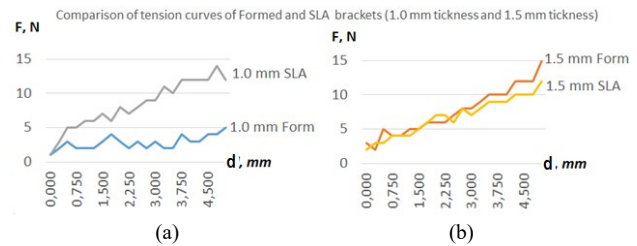


Fig.9 Deformation diagrams of aligners produced by moulding (traditional technology) and digital technology (SLA). Two thicknesses are compared: 1.0 (a) and 1.5 mm (b).

**IV. CONCLUSIONS**

1). The orthodontic devices produced by DLP SLA are not inferior to conventional ones in terms of both mechanical and optical (aesthetic) properties. This property change with the thickness of the device producing different forces on the teeth. The effectiveness of the thickness change in the "digital" devices is higher than that of the conventional onse. More particularly they show an increase of up to 70% in the forces required to deform the aligner depending on its thickness. The presented diagrams for mechanical behavior of the aligners could be used for design purposes.

2). The stiffness of the devices measured by the coefficient ( $K=\Delta F/\Delta l$ ) changes about 4 times when the thickness increases from 0.15 to 2 mm. This makes it possible to plan to use a set of aligners of different thickness to achieve progressive corrective results during the course of treatment.

3) The transparency of the aligners does not differ significantly of that of the Vacuum formed devices. Although this property of the DLP SLA devices could be improved by optimizing the technological parameters such as layer thickness and stirring time.

#### REFERENCES

- [1] T. Yordanova-Ignatova, N. Stoyanova, Y. Stoev, T. Uzunov, Retention after orthodontic treatment in the light of dental materials science: Technologies and materials for three-dimensional (3D) Printing, *Orthodontic review* 24/22, 2022, pp.18-25.
- [2] "Different Types Of Orthodontic Treatments", Baroda Dental Clinic, 7th July, 2022. [Online]. Available: <https://www.barodadental.com/types-of-orthodontic-treatment/> [Accessed: Dec. 10, 2022].
- [3] W.B. Siliguri et al.(2020). Current Trends in Orthodontics, *International Healthcare Research Journal* 4(8), pp. RV1-RV4, <https://doi.org/10.26440/IHRJ/0408.11285>
- [2] B. Ratner et al., *Biomaterials Science, An Introduction to Materials in Medicine*, 2nd Ed., Academic Press, 2004, pp.78-79.
- [4] G. Todorov, K. Kamberov, *Virtual Engineering CAD/CAM/CAE&PLM Technologies*, 2015, pp 51-78.
- [5] M. Hajeer, Assessment of dental arches in patients with class II division 1 and division 2 malocclusions using 3D digital models in a Syrian sample, *European Journal of pediatric dentistry*, vol. 15, 2014, pp. 151-157.
- [6] R. Minev, E. Minev, *Technology for Rapid Prototyping - Basic Concepts, Quality Issues and Modern Trend*, *Scripta Scientifica Medicinæ Dentalis*, vol. 2, No1, 2016, pp. 12-22.
- [7] E. Minev et al, (2015). The RepRap Printer for Metal Casting Patternmaking - Capabilities and Application, *Proceedings VIII Int. Conf. Advanced casting technologies*. MU (МИСН) Moscow, ISBN 978-5-9903239-3-3, 2015, pp. 300-303.
- [8] E. Minev, *The RepRap Printers for Metal Casting Pattern Making - Capabilities and Application*, *On Innovative Trends in Engineering and Science (SFITES) - Kavala, Greece*, Parnas Publishing House, ISBN 978-954-8483-35-6, 2015, pp. 122-127.
- [9] D. Coel, S. Bencharit, C. Carico, A. Arias, E. Tufekci, Evaluation of fit for 3D-printed retainers as compared with thermoform retainers. *American Journal of orthodontics and Dentofacial orthopedics*, 2019, pp. 592-599.
- [10]. "3D Printing Material NextDent Ortho Flex", 2023 [Online]. <https://nextdent.com/new-3d-printing-material-nextdent-ortho-flex/> [Accessed: Jan. 22, 2023]
- [11] D. Cole, Evaluation of fit for 3D printed retainers as compared to thermoform retainers - Doctoral Thesis, Department of Orthodontics, School of Dentistry, Virginia Commonwealth University, Richmond, 2018.
- [12] P. Jindal, F. Worcester, F. Siena, C. Forbes, M. Juneja, P. Breedon, Mechanical behavior of 3D printed vs thermoformed clear dental aligner materials under non-linear compressive loading using FEM, *Journal of the mechanical behavior of biomechanical materials*, vol.112, 2020, pp.24-29.
- [13] A. Masoud, E. Fayed, B. Lapatki, Clear aligners: Material structures and properties, *Pocket dentistry*, Chapter 3, 2020 [Online]. <https://www.pocketdentistry.com/clear-aligners-material-structures-and-properties/> [Accessed: Jan. 25, 2023].

# Experimental Remote Determination of the Static Characteristic of the Arc in TIG Welding

**Deyan Gradinarov**

*Institute of Metal Science, equipment,  
and technologies with Center for  
Hydro- and Aerodynamics  
"Acad. A. Balevski"  
Bulgarian Academy of Sciences  
Sofia, Bulgaria  
deyangradinarov@gmail.com*

**Marina Manilova**

*Institute of Metal Science, equipment,  
and technologies with Center for  
Hydro- and Aerodynamics  
"Acad. A. Balevski"  
Bulgarian Academy of Sciences  
Sofia, Bulgaria  
mamanil@abv.bg*

**Manahil Tongov**

*Technical University of Sofia  
Sofia, Bulgaria  
Institute of Metal Science, equipment,  
and technologies with Center for  
Hydro- and Aerodynamics  
"Acad. A. Balevski"  
Bulgarian Academy of Sciences  
Sofia, Bulgaria  
tongov@tu-sofia.bg*

**Abstract.** In the conditions of TIG welding, the magnitude of the current is set, but not the voltage of the arc. To determine the arc voltage at a set current, arc length, type of electrode, sharpening angle and others, it is necessary to know the static characteristics of the welding arc. This dependence facilitates the use of simulation modelling methods of welding processes. In the proposed study, the static characteristics of the welding arc in TIG process with 4 types of electrodes were determined experimentally. The magnitude of the current was set in the range of 20 to 200A and the arc voltage was measured. All parameters are measured remotely by a real-time welding monitoring system and transferred to a remote computer via the Internet. Graphs were built based on the recordings, and the numerical results were processed and regression relationships were obtained.

**Keywords:** TIG welding, Static characteristic of welding arc.

## I. INTRODUCTION

The welding arc is a form of gas discharge with a low degree of ionization. Arc voltage has five components – cathode spot, cathode drop zone, plasma, anode drop zone and anode spot. The static characteristic of the arc is the dependence of the arc voltage on the magnitude of the current in an established mode under unchanged conditions of existence of the arc discharge. The anodic (1÷2 [V]) and cathodic (4÷6 [V]) voltage drops are weakly dependent on the magnitude of the current and independent of the arc length. The resistance of the arc (and respectively the voltage drop) changes depending on the temperature [1÷4], the degree of ionization, the current density, etc. For this reason, it is not a constant quantity.

Thus, Ohm's law does not apply to the welding arc. Fig. 1 shows the static characteristics of the arc. At low current [2] (area 1 of the arc), as the current increases, the arc voltage decreases. This is due to the intense increase in the number of charged particles in the arc as a result of increasing the emissivity of the cathode as its temperature increases (Richardson's equation). In the second area of the arc, the characteristic is almost horizontal, which is explained on the one hand by the difficulty of the ionization processes in the arc column, and on the other by the delay in the increase of electron emission [6÷8]. In the third region of the arc, these processes are so hampered that the characteristic of the arc becomes growing - the increase in temperatures is not enough to compensate for the contraction of the arc by its own magnetic field. In this part of the arc characteristic, Ohm's law applies. As the arc length increases, the voltage required to achieve a given current increases.

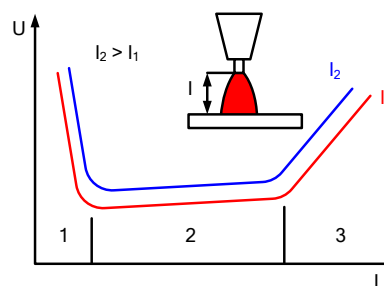


Fig. 1. Static characteristics of welding arc.

Print ISSN 1691-5402  
Online ISSN 2256-070X

<https://doi.org/10.17770/etr2023vol3.7203>

© 2023 Deyan Gradinarov, Marina Manilova, Manahil Tongov. Published by Rezekne Academy of Technologies.  
This is an open access article under the [Creative Commons Attribution 4.0 International License](https://creativecommons.org/licenses/by/4.0/).

The operation of welding current sources implementing various technological processes is mainly based on the knowledge of the static characteristics of the arc. In MMA, TIG welding, PAW and SAW with low current density, welding is done in the second area of the arc characteristic with a vertical or steeply falling static external characteristic of the current source - the magnitude of the current is stabilized. High current density MIG/MAG and SAW operate in the third region of the arc characteristic with a stiff (slightly drooping) current source characteristic and use of the arc self-regulating process.

In the present publication is reviewed the experimental construction of the static characteristic of the arc of TIG welding process.

## II. MATERIALS AND METHODS

For the purposes of this study, experiments were carried out in accordance with the scheme [9,10] shown in Fig.2 and Fig.3. The used welding current source (Cebora2030m - Fig.4) is designed for TIG welding, with the possibility of setting the current size with step 1 [A]. During the process, the magnitude of the arc current and voltage are visualized. After switching off the power source, the displayed values are saved. In addition, the current source provides a smooth increase of the current when the arc is ignited and a smooth decrease when the process is terminated. The maximum welding current of the power source is 200[A]. The welding torch was set stationary and the arc length  $l = 2.4$ [mm] was the same in all experiments performed. The arc is ignited on a plate with dimensions 6x350x120 [mm] (Fig. 5). The shielding gas (Ar) has a flow rate of 15 [l/min]. During the arc burning process, the instantaneous current and voltage values are recorded using an Arc Tracker welding process monitor (Fig.6). Data are transmitted and recorded in real time on a portable computer on which Power Wave Manager software is installed (Fig.7 and Fig.8). This software allows welding parameters to be monitored and stored in real time. The data is transmitted in real time and over the Internet using the Team Viewer software product to a remote computer where it is visualized and stored. The electrodes used are listed in table 1. The sharpening angle of the electrodes is 15°.

TABLE 1 USED ELECTRODES

№	<i>d, mm</i>	<i>Composition</i>	<i>Colour</i>
1	2.4	W+1.4÷1.6% La	Gold
2	2.4	100% W	Green
3	2.4	W+1.8÷2.2% CeO <sub>2</sub>	Grey
4	2.4	W + 1.7÷2.2% ThO <sub>2</sub>	Red

The experiments were carried out as follows. The magnitude of the current is set, and in the range from 20 to 100[A] the change is in 5[A] steps, and in the range from 100 to 200[A] – in 10[A] steps. Recording of current

values and arc voltage is started. The welding arc is ignited. After switching to the established operating mode, the values of the current source are read. The duration of arc burning for one record is 8÷20[s]. After the arc is turned off and the process is terminated, data recording is stopped (automatically). The procedure is repeated for the set currents with the four different electrodes. No other parameter is changed during the experiment (the arc voltage is varied by the current source to achieve the set current). The pause between individual experiments is such that the duration of ignited arc does not exceed 35%. A sample recording of the process parameters is shown in Fig.6. In Fig. 7 is shown screenshot of captured values with Arc Tracker welding monitoring device.

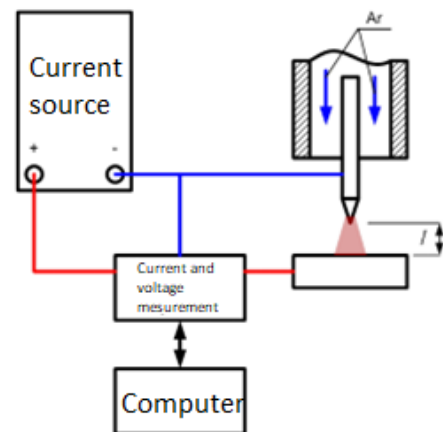


Fig. 2. Scheme of conducting the experiment.

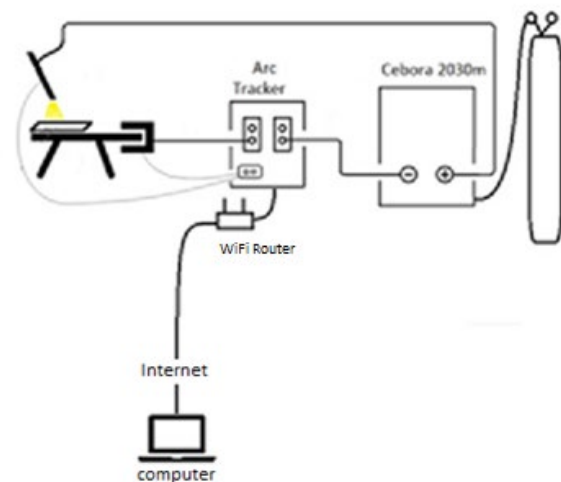


Fig. 3. Experimental set-up.



Fig. 4. Cebora2030m current source.



Fig. 6. Arc Tracker welding monitoring device.



Fig. 5. Welding arc.

grey\_25 - Notepad

File Edit Format View Help

Arc time (s)	Amperage (A)	Voltage (V)	Wire fee
0,000	9,0	10,3	0
0,250	9,8	10,3	0
0,625	11,5	10,3	0
0,828	13,1	10,3	0
1,109	14,6	10,3	0
1,375	16,1	10,3	0
1,703	17,7	10,3	0
1,969	19,2	12,4	0
2,219	20,7	13,5	0
2,484	22,2	13,3	0
2,766	22,5	12,9	0
3,047	22,4	12,9	0
3,297	22,5	12,8	0
3,609	22,6	12,9	0
3,906	22,5	12,9	0
4,172	22,5	12,9	0
4,438	22,6	12,9	0
4,688	22,7	12,9	0
4,938	22,6	12,8	0
5,203	22,7	12,7	0
5,453	22,6	12,7	0
5,719	22,5	12,5	0
5,953	22,5	12,5	0
6,234	22,5	12,5	0
6,500	22,5	12,6	0
6,781	22,5	12,6	0
7,047	22,5	12,5	0
7,328	22,4	12,3	0
7,609	22,4	12,3	0
7,969	22,3	12,3	0

Ln 106, Col 1      100%      Windows (CRLF)      UTF-8

Fig. 7. Sample recording of the process parameters – Electrode 1 at 25A.



Fig. 8. Screenshot of captures current and voltage values with Arc Tracker welding monitoring device.

### III. RESULTS AND ANALYSIS

Graphs of the dependence of the welding voltage and current on time are made from the captured parameters (in Table 2 are shown results for electrode No1 and Electrode No2). The time interval of an established process is determined from these graphs (Fig. 9). Within this time interval, the average values of the arc current and voltage are determined. The obtained results are shown in Table 3 ÷ Table 4.

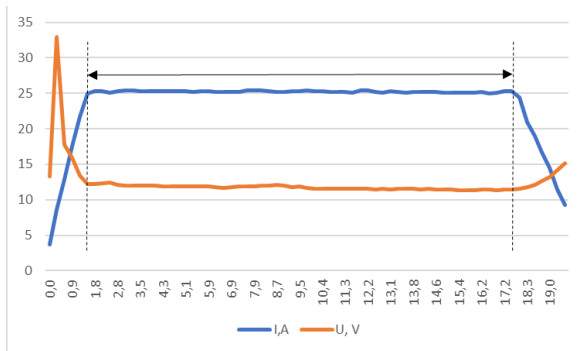


Fig. 9. Determination of time lapse of the established process for electrode No1.

TABLE 2 EXAMPLES OF RECORDED ARC CURRENT AND VOLTAGE VALUES

A	Electrode No1	Electrode N2
25		
55		
160		
200		

TABLE 3 EXPERIMENTAL RESULT FOR ELECTRODE NO1.

Set	Welding current, A		Arc voltage, V	
	Delivered	Measured	Delivered	Measured
20	21	20.1	12.5	11.8
25	25	25.2	11.45	11.7
30	30	30.3	11.25	11.6
35	35	34.9	11.45	11.6
40	39	39.4	11.2	11.3
45	44	44.0	10.5	10.6
50	49	48.5	10.4	10.5
55	54	52.9	10.6	10.4
60	58	58.1	10.5	10.2
65	62	62.3	10.5	10.2
70	68	67.7	10.5	10.1
75	72	72.7	10.45	10
80	77	76.7	10.3	9.9
85	82	80.8	10.4	9.8
90	86	86.1	10.4	9.9
95	92	90.8	10.3	9.8
100	97	96.5	10.25	9.8
110	106	104.9	9.7	9.9
120	115	115.1	10.0	10.1
130	125	124.9	10.25	10.2
140	134	133.6	10.3	10.4
150	143	143.1	10.7	10.7
160	153	152.9	11.1	11.1
170	162	161.8	11.15	11.1
180	172	171.3	11.2	11.2
190	181	181.1	11.6	11.5
200	191	190.8	11.5	11.6

TABLE 4 EXPERIMENTAL RESULT FOR ELECTRODE NO2.

Set	Welding current, A		Arc voltage, V	
	Delivered	Measured	Delivered	Measured
20	21	20.9	10.4	10.3
25	25	25.3	9.8	10
30	30	30.5	9.7	9.7
35	35	34.7	9.7	9.5
40	39	39	9.4	9.2
45	44	44.3	9.3	9.3
50	49	48.6	9.4	9.3
55	53	53	9.4	9.3
60	58	58.1	9.4	9.2
65	62	62.5	9.2	9.2
70	67	67	9.2	9.1
75	72	72.3	9.1	9.2
80	55	76.7	9.1	9.2
85	81	81.1	9.1	9.3
90	86	86.3	9.1	9.3
95	90	90.4	9.1	9.3
100	96	95.6	9.4	9.5
110	106	105.6	9.5	9.7
120	115	115.4	10.0	10.1
130	125	124.9	10.4	10.3
140	134	133.8	10.5	10.4
150	143	143.2	10.5	10.5
160	153	152.7	10.7	10.7
170	162	161.6	11.1	11.2
180	171	171.4	11.3	11.4
190	181	181.1	11.4	11.5
200	191	190.8	11.7	11.6

Static characteristics for the used electrodes were built (fig. 10 ÷ fig. 17) with based on the captured data from the experimental process. The experimental data on the static characteristics of the welding arc were processed by the method of least squares and the corresponding regression equations were obtained. Used type of equation is

$$U_w = \frac{B}{I_w} + C_0 + C_1 I_w + C_2 I_w^2 \quad (1)$$

TABLE 5 COEFFICIENTS IN EQUATION (1)

No	B	C <sub>0</sub>	C <sub>1</sub>	C <sub>2</sub>
1 - down	7.29E+01	6.78E+00	2.33E-03	1.05E-04
1 - up	1.14E+02	7.00E+00	3.14E-02	-4.25E-05
2 - down	6.53E+00	9.79E+00	-2.93E-02	2.11E-04
2 - up	1.15E+02	3.02E+00	8.81E-02	-2.60E-04
3 - down	3.17E+01	7.54E+00	1.30E-02	3.35E-05
3 - up	8.25E+01	3.52E+00	7.72E-02	-2.07E-04
4 - down	4.60E+01	5.95E+00	3.97E-02	-4.23E-05
4 - up	5.55E+01	6.36E+00	4.98E-02	-1.12E-04

The results are illustrated in Fig. 10-17. These results show that during the conducted experiments, the process parameters were such that the welding arc appeared in the first and second parts of its characteristic. Furthermore, it can be seen that the welding arc burns steadily also in the first part of its characteristic.

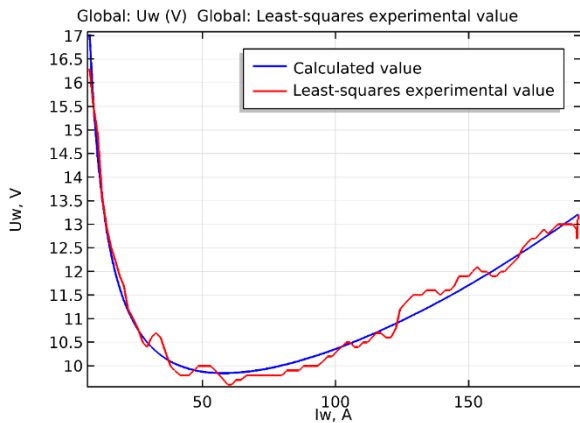


Fig. 10. Static characteristics – electrode No1 (W + 1.4÷1.6% La) decreasing welding current from 200A to 20A.

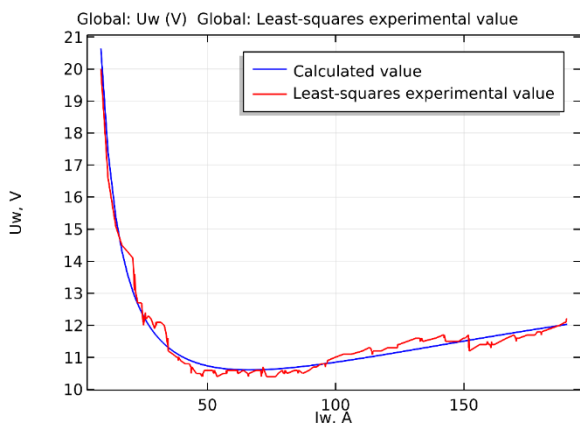


Fig. 11. Static characteristics – electrode No1 (W + 1.4÷1.6% La) increasing welding current from 20A to 200A.

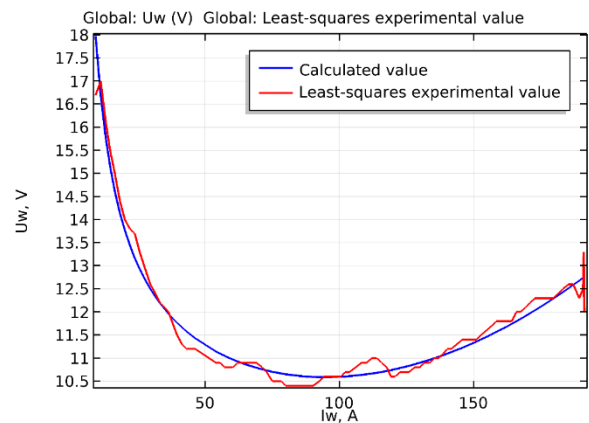


Fig. 12. Static characteristics – electrode No2 (100% W) decreasing welding current from 200A to 20A.

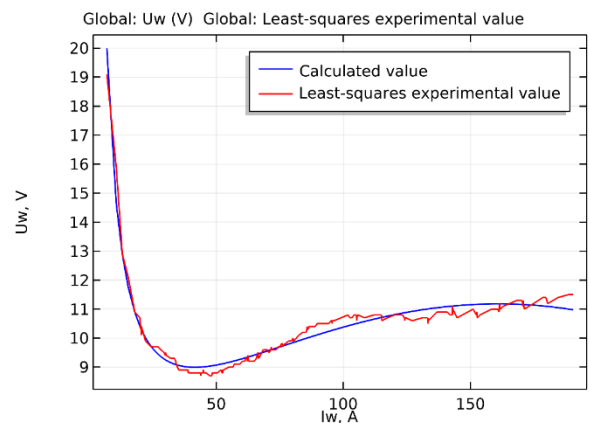


Fig. 13. Static characteristics – electrode No2 (100% W) increasing welding current from 20A to 200A.

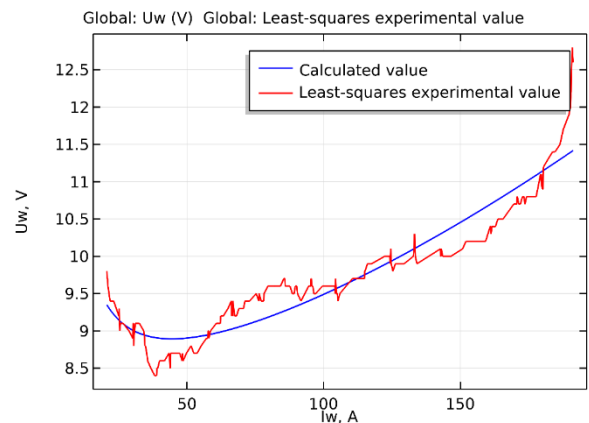


Fig. 14. Static characteristics – electrode No3 (W + 1.8÷2.2% CeO<sub>2</sub>) decreasing welding current from 200A to 20A.

The experimentally constructed static characteristics of the welding arc correspond to its qualitative representation indicated in Fig.1.

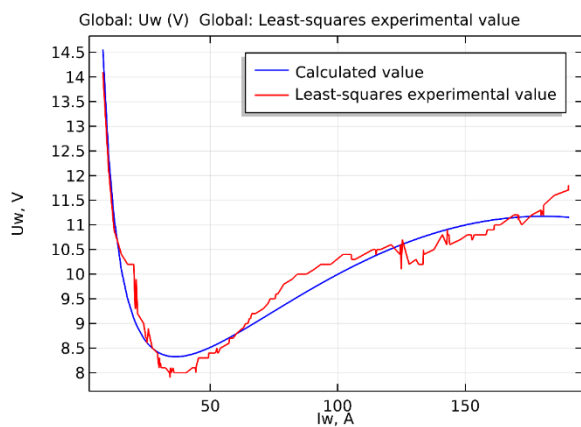


Fig. 15. Static characteristics – electrode No3 (W + 1.8÷2.2% CeO<sub>2</sub>) increasing welding current from 20A to 200A.

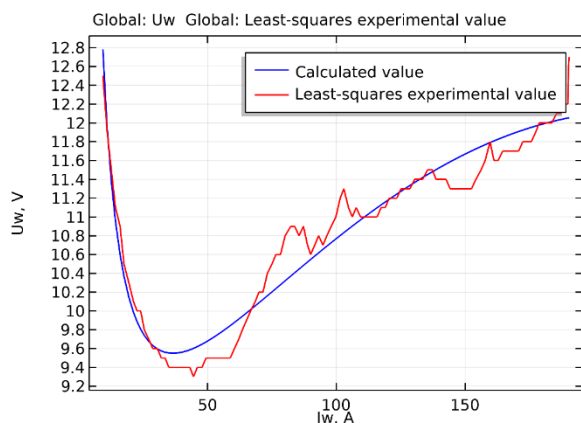


Fig. 16. Static characteristics – electrode No4 (W + 1.7÷2.2% ThO<sub>2</sub>) decreasing welding current from 200A to 20A.

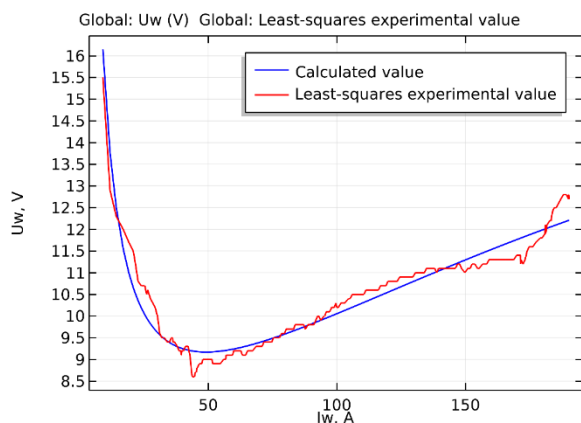


Fig. 17. Static characteristics – electrode No4 (W + 1.7÷2.2% ThO<sub>2</sub>) increasing welding current from 20A to 200A.

Several features can be observed in the presented static characteristics of the arc. First of all, there is no typical expression of the second section of the arc characteristic for electrode No 3 and electrode No 4. The increase in voltage with the increase in the magnitude of the current at electrodes No1 and No2 is observed after reaching a welding current of 90[A]. This is equivalent to a current

density of 19.9 [A/mm<sup>2</sup>]. At electrode No3 electrode No4, the rise in arc voltage begins at a current magnitude of 38.8[A]. This corresponds to a current density equal to 19.3 [A/mm<sup>2</sup>]. Comparison of these data shows that entering the third part of the arc characteristic is realized at a current density in the electrode equal to 19÷20[A/mm<sup>2</sup>].

#### IV. CONCLUSIONS

Determination of the static characteristic of the arc in TIG welding process, was successfully accomplished over the internet on remote computer by measuring welding parameters – welding current and welding voltage with real-time welding monitoring system.

It was determined that within the conducted experiments, the second part of the arc characteristic is not significantly expressed, and at a current density of 19÷20 [A/mm<sup>2</sup>], the arc voltage begins to increase with an increase in the welding current.

Further studies will determine and fill the database of the static characteristic of the arc in TIG welding process with various electrodes varying on both chemistry compound and diameter.

#### V. ACKNOWLEDGMENTS

This work was made possible by a project KP-06-N37/31, funded by the NSF.

#### REFERENCES

- [1] Álisson Fernandes da Rosa, Felipe Batista, Victor Igor Barbare Lemos, Régis Henrique Gonçalves e Silva. EXPERIMENTAL ANALYSIS ON THE PERFORMANCE OF SMA WELDING ELECTRODES. 26th ABCM International Congress of Mechanical Engineering, November 22-26, 2021. Florianópolis, SC, Brazil.
- [2] WooHo Kim, Yong-Jung Kim and Hyosung Kim. Arc Voltage and Current Characteristics in Low-Voltage Direct Current. *Energies* 2018, 11, 2511; doi:10.3390/en1102511, <https://www.mdpi.com/journal/energies>
- [3] Antoni Sawicki. Static Characteristics of Defined Ignition Voltage Used in the Modelling of Arc within a Wide Range of Current Excitation. *Bulletin of the Institute of Welding, Biuletyn Instytutu Spawalnictwa*, ISSN 2300-1674=
- [4] Li, Y., Yang, J.C., Liu, Z. Welding performance of tungsten electrodes with different contents of rare earth oxides. (2015) *Materials Science Forum*, 814, pp. 631-635. DOI: 10.4028/www.scientific.net/MSF.814.631
- [5] H. Dong ; M. Cong ; Yu. Zhang; Yu. Liu ; H. Chen, Real time welding parameter prediction for desired character performance (2017), *IEEE International Conference on Robotics and Automation (ICRA)*, 2017
- [6] Wang, R., Xue, J. Study on arc length stability of pulsed MIG welding based on average output characteristics of pulse cycle. (2012) *Jixie Gongcheng Xuebao/Journal of Mechanical Engineering*, 48 (10), pp. 50-55, DOI: 10.3901/JME.2012.10.050
- [7] Zhou, C.-F., Jiao, X.-D., Xue, L., Chen, J.-Q., Wang, Z.-H., Lu, T., Fang, X.-M. Arc static characteristics of gas tungsten arc welding under high air ambient pressure. (2008) *Shiyou Huagong Gaodeng Xuexiao Xuebao/Journal of Petrochemical Universities*, 21 (1), pp. 66-69.
- [8] Martínez, A., Blasco, N., Pérez, F.J., Vicuña, J.E., Lacámara, I., Oliva, J.A. Static output characteristic of a peak current controlled arc welding machine. (2006) *Midwest Symposium on Circuits and Systems*, 1, art. no. 4267220, pp. 636-639. DOI:

- 10.1109/MWSCAS.2006.382143W.-K. Chen, Linear Networks and Systems. Belmont, CA: Wadsworth, 1993, pp. 123-135.
- [9] Deyan Gradinarov, Set up for real time capturing of welding parameters (2021), Proceedings of the VI International Scientific Conference Winter Session. Volume 2, 259-260.
- [10] Tongov M., Gradinarov D., Tashev P., Experimental Determination of Static Characteristic of Welding Arc in TIG Welding (2022), Bulgarian Society for NDT International Journal "NDT Days", Volume V, Issue 3, Year 2022, pp.152-160.

# Modelling and Simulation of Electropneumatic Positioning System Including the Length of Pneumatic Lines

**Georgi Iliev**  
dept. Power Engineering  
Technical University of Gabrovo  
Gabrovo, Bulgaria  
spigil@abv.bg

**Hristo Hristov**  
dept. Power Engineering  
Technical University of Gabrovo  
Gabrovo, Bulgaria  
chisto@tugab.bg

**Abstract.** This paper presents a mathematical model of electropneumatic positioning system including the length of pneumatic lines for the determination of flow and pressure in unsteady operating modes. A simulation model is developed to study the dynamic processes in an electropneumatic positioning system. Simulation of the mathematical models of the screw compressor, proportional directional valve, pneumatic lines, pneumatic cylinder and PID controller were designed in “MatLab Simulink”. The simulation models of the transients in the electropneumatic positioning system at different line lengths from 1m and 10m with stepwise variation of the input setpoint are simulated developed. Graphical comparison is made of the obtained experimental results and simulation model influence of the pneumatic line length on the dynamics of the electropneumatic positioning system are made

**Keywords:** *electropneumatic positioning system; mathematical model; pneumatic lines; simulation models.*

## I. INTRODUCTION

Electropneumatic positioning system by proportional directional control valve allows adaptive positioning control to fractions of a millimeter as well as the ability to control the speed and acceleration of pneumatic actuators. Another unique characteristic of electropneumatic positioning system is smooth braking, which extends its application to metallurgy, robotics, machine tools, aerospace, food and beverage, as well as in simulators and simulators for equipment testing, etc. This calls for higher performance levels, requiring a continuous evolution of pneumatic actuators [4].

Pneumatic actuation systems as computer technology advances, control algorithms can be created and refined to make the systems better and more reliable. Through the use of advanced proportional directional control valve, various control laws can be implemented to optimize dynamic processes and improve the accuracy and quality of operation, as well as increase the system's efficiency [2], [8], [9].

Pneumatic systems are modelled in the form of a computer simulation in which a virtual system is designed. Software that uses models are primarily designed for pneumatic and hydraulic system [2], [4] or are for use in CAD environments and allow the pneumatic system to interact with external mechanical elements [5]. Most software is designed more for practicing engineers rather than for fundamental research in pneumatic systems.

Computer simulations in “MATLAB Simulink” of models for pneumatic and hydraulic systems give good results, the processes are compared with those obtained from computer modeling and simulation, and the results are used to verify the models [1], [3], [6], [8].

Despite the proven advantages of electropneumatic positioning systems, which are generally known, in the modern stage of development of science and technology there are a number of prerequisites for improving their characteristics:

- flexibility and speed compared to conventional electric and hydraulic drive systems;
- their low cost compared to other classic drive systems;

Print ISSN 1691-5402  
Online ISSN 2256-070X

<https://doi.org/10.17770/etr2023vol3.7186>

© 2023 Georgi Iliev, Hristo Hristov. Published by Rezekne Academy of Technologies.  
This is an open access article under the [Creative Commons Attribution 4.0 International License](https://creativecommons.org/licenses/by/4.0/).

– eco-friendliness and energy efficiency.

Some of the quantities under investigation, which were assumed to be negligible or were engineered guesses in the past, can now be measured, analyzed, and used to improve existing drive system models. Application of modern automated data acquisition and processing systems can substantially improve the modeling and dynamic-mode properties of electropneumatic actuator systems.

In many cases, low-order linear models are used to facilitate the studies, but a comparison with experiments reveals that the agreement in the characteristics is not very good. To improve the control process, it is necessary to use models that account for the essential nonlinearities.

The signal delay along the pneumatic lines needs further investigation. Due to the relatively few adequate models, research is needed. In practice, it is assumed that relatively short pneumatic lines have minimal impact on the system delay. However, for relatively long pneumatic lines, this delay would significantly affect the dynamics of the pneumatic system. The mathematical models presented are extremely complex and difficult to solve. Some of them use parameters that are engineering proven in practice. A more accurate and detailed mathematical model is required. It is necessary to verify the model thus created with experimental results [7-13].

## II. MATHEMATICAL MODEL

The mathematical models of the screw compressor, proportional directional control valve, pneumatic lines, pneumatic cylinder and PID controller.

For a detailed description of the complete mathematical model of the electropneumatic positioning system is in [3].

Mathematical model of the pneumatic compressed air unit:

The mass theoretical flow rate of a screw compressor is determined.

$$M_t = \left[ \rho \left( \frac{\pi}{4} (d_v^2 - d_i^2) t_v \frac{\omega}{2\pi} \right) \right] \quad (1)$$

Where:

$d_v$  - outside diameter of the screw;

$d_i$  - inside diameter of the screw;

$t_v$  - screw pitch;

$\omega$  - angular velocity;

$\rho$  - density.

The mass flow through the directional valve can be calculated by multiplying the volumetric flow rate (2) to the air density  $\rho$  in standard conditions:

$$M = \left( 8.6 \cdot 10^{-8} C_v p_{in} \left( 1 - \frac{X}{X_T} \right) \sqrt{\frac{X}{T_{air}}} \right) \rho \quad (2)$$

Where:

$C_v$  - coefficient of conductivity;

$p_{in}$  - inlet in the distributor;

$X$  - pressure relations;

$X_T$  - critical pressure drop;

$T_{air}$  - air temperature;

$\rho$  - density.

The model for the flow rate through the proportional directional control valve includes the coefficient of conductivity  $C_v$  and the critical pressure drop coefficient  $X_T$  which has to be determined experimentally [3]:

$$C_v = 0.274; X_T = 1$$

Electronic PID controller equation:

$$U = k_k \left( \Delta U + \frac{1}{T_I} \int_0^t \Delta U dt + T_D \frac{d\Delta U}{dt} \right) \quad (3)$$

Where:

$k_k$  - amplifying factor of the regulator;

$\Delta U$  - input voltage;

$T_I; T_D$  - time constants of integration and differentiation of the regulator.

### Mathematical model of pneumatic lines

We're examining a cylindrical tube (line) on fig. 1 with length  $L_t$ . The mass flow rate of the air through the line is [1], [3]:

$$M = \frac{R_r^2 L_t}{8 a_s \rho^2} e^{-\frac{R_r L_t}{2 \rho a_s}} f \left( t - \frac{L_t}{a_s} \right) \quad (4)$$

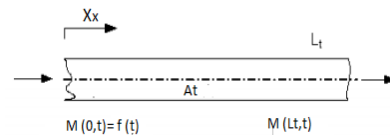


Fig. 1. Pneumatic line

Where:

$R_r$  - the tube resistance;

$L_t$  - cylindrical tube with length

$\rho$  - density;

$a_s$  - denotes the sound speed;

$t$  - time variable.

The equation for the movement of a pneumatic cylinder piston with a double sided extended rod is expressed as follows [3]:

$$m_t \frac{d^2 y}{dt^2} + \beta_c \frac{dy}{dt} + F_{mp} = (p_{c1} - p_{c2}) A_b - p_{atm} A_b \quad (5)$$

Where:

$m_t$  - mass of the load;

$y$  - cylinder rod displacement;

$A_b$  - area of the pneumatic cylinder piston;

$F_{mp}$  - static friction force;

$\beta_c$  - viscous friction coefficient;

$p_{atm}$  - atmospheric pressure;

$p_{c1}$  - pressure in the left chamber of the pneumatic cylinder;

$p_{c2}$  - pressure in the right chamber of the pneumatic cylinder;

Given that  $\frac{dm_1}{dt} = M_{b1}$ , the mass flow rate entering the pneumatic cylinder is presented in the following equation:

$$M_{b1} = \frac{1}{RT_{air}} \left[ (W_{1H} + A_b y) \frac{dp_{c1}}{dt} + p_{c1} A_b \frac{dy}{dt} \right] \quad (6)$$

Where:

$W_{1H}$  - Initial gas volume in the cylinder;

$y$  - cylinder rod displacement;

$R$  - air gas constant;

$p_{c1}$  - pressure in the left chamber of the pneumatic cylinder;

$T_{air}$  - air temperature;

$A_b$  - area of the pneumatic cylinder piston.

#### EXPERIMENTAL STUDY OF THE INFLUENCE OF THE LENGTH OF PNEUMATIC LINES ON THE ELECTROPNEUMATIC POSITIONING SYSTEM

For the study of an electropneumatic positioning system, a laboratory rig was constructed and developed as shown in fig. 2. The stand allows to experimentally investigate the dynamic processes in an electropneumatic positioning system. It is possible to model for experiments of pneumatic elements of different nature, to study the influence of the length of pneumatic lines, to determine the friction forces in pneumatic cylinders.

The process control of the experiment, data collection and processing, and data archiving is performed automatically by a personal computer and the corresponding interface board of the company "National Instruments" for the purpose of the experiment uses specialized software controlling the processes of the experiment. The "LabView" software is a state-of-the-art product capable of unlimited measurements and real-time data processing.

Two experiments were performed on the pneumatic rig under identical conditions with different length from 1m and 10 m pneumatic lines.

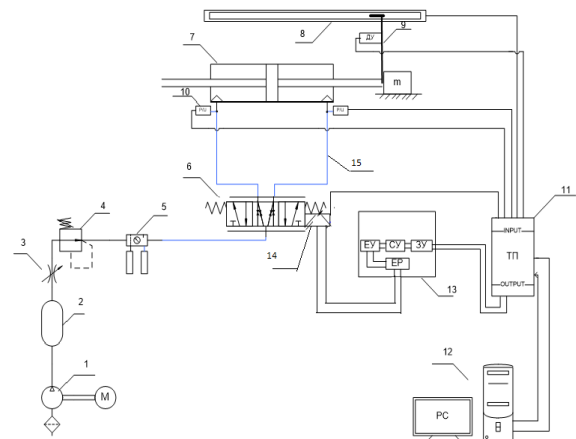


Fig. 2. Schematic representation of an electropneumatic positioning system with a measuring system.

- 1 – screw compressor; 2 - receiver; 3 - stopcock; 4 - safety valve; 5 - air preparation system preparatory; 6 – proportional directional control valve; 7 - pneumatic cylinder; 8 – position sensor; 9 - acceleration sensor; 10 – pressure/flow sensor; 11 - interface board; 12 - PC; 13 - electronic controller; 14- coil of proportional directional control valve; 15- pneumatic line.

#### VIRTUAL INSTRUMENT

For the purpose of the experiment, a virtual tool was developed to perform the following main functions Fig. 3:

Read the input channels in the following order:

Measure the input signal, measuring the pressure, flow measurement, measuring displacement of the piston pneumatic cylinder etc.

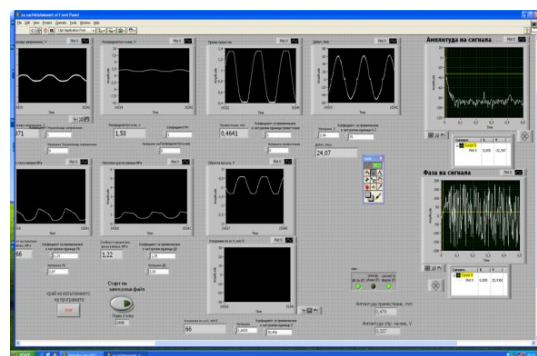


Fig.3. User interface of the virtual tool developed.

MODELLING AND SIMULATION OF THE ELECTROPNEUMATIC POSITIONING SYSTEM WITH CONSIDERATION OF THE LENGTH OF THE PNEUMATIC LINES

A mathematical model [1], [3] was simulated on the program “MatLab Simulink”, and the simulation model is shown in Fig.4.

Simulation models of the screw compressor, proportional directional control valve, pneumatic lines, pneumatic cylinder and PID controller.

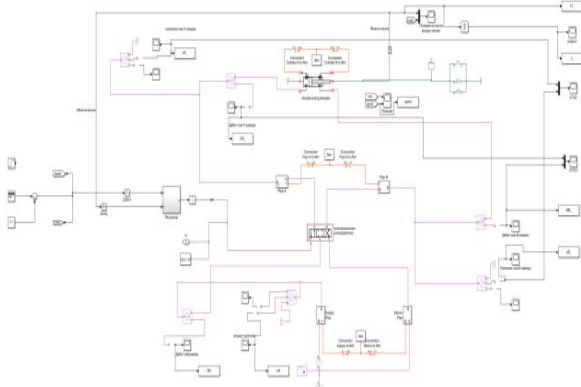


Fig. 4 Simulation model of an electropneumatic positioning system with changing length of pneumatic lines.

Results comparison of experimental and simulation transients in an electropneumatic positioning system with different length pneumatic lines fig. from 5 to 9.

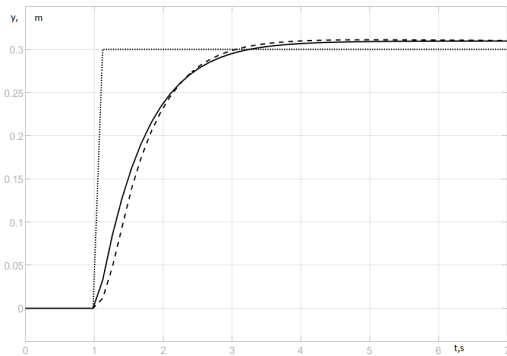


Fig. 5 Displacement of the piston rod at 1m (-) and at 10 m (- - -), input setpoint (.), computer simulation.

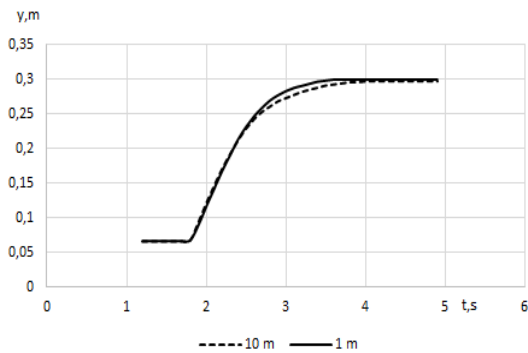


Fig. 5a Experimental data of cylinder rod displacement at 1 m (-) and at 10 m (- - -).

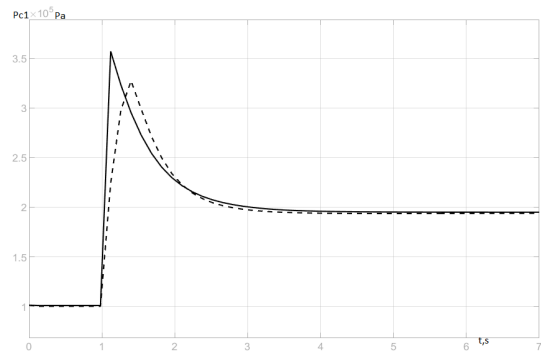


Fig. 6. Pressure in the left chamber of the pneumatic cylinder at 1 m (-) and at 10 m (- - -) computer simulation.

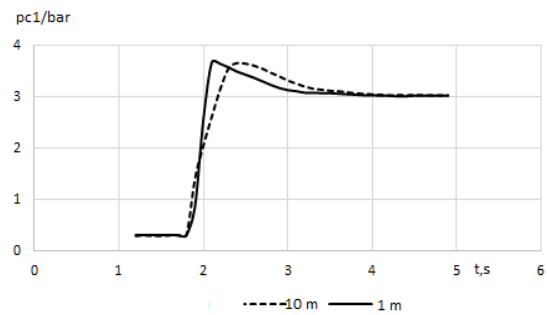


Fig. 6a. Experimental data of pressure in the left chamber of the pneumatic cylinder at 1 m (-) and at 10 m (- - -).

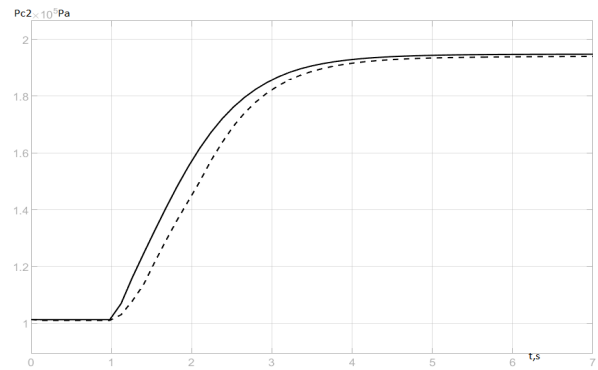


Fig. 7. Pressure in the right chamber of the pneumatic cylinder at 1 m (-) and at 10 m (- - -) computer simulation.

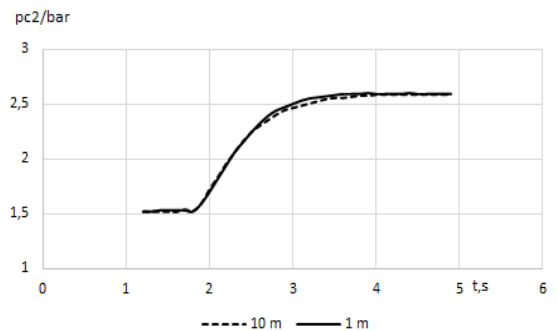


Fig. 7a. Experimental data of pressure in the right chamber of the pneumatic cylinder at 1 m (-) and at 10 m (- - -).

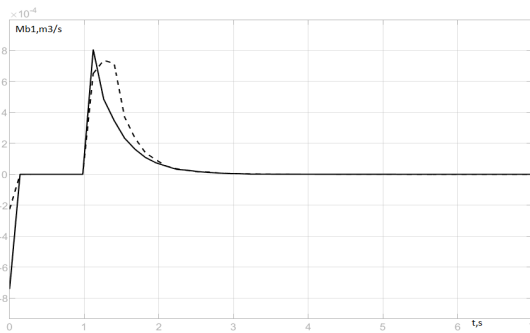


Fig.8. Mass flow rate in the pneumatic line to the cylinder left at 1m (-) length and 10 m (- -) computer simulation.

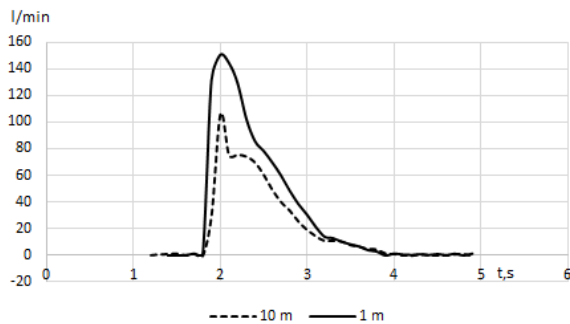


Fig. 8a. Experimental data of flow rate in the pneumatic line to the cylinder left at 1m (-) and 10 m (- -) lengths.

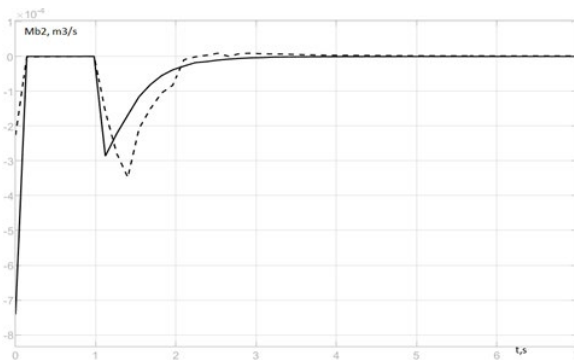


Fig. 9. Mass flow out of the right chamber of the pneumatic cylinder at 1 m (-) and at 10 m (- -) computer simulation.

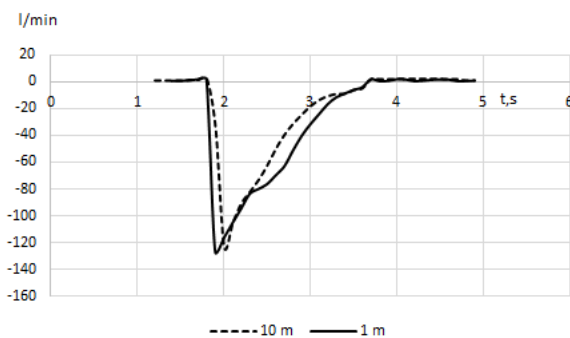


Fig. 9a. Experimental data of flow out of the right chamber of a pneumatic cylinder at 1 m (-) and at 10 m (- -) computer simulation.

The graphs show the variation of the main observed quantities - the displacement of the rod of the pneumatic cylinder, the pressure on both sides of the piston, the flow rate on both sides of the piston of the pneumatic cylinder. The input impact varies uniformly in a stepwise manner on the input setpoint, which is electrical voltage. The quantities are shown in actual values. The value of the input signal is within the working stroke of the pneumatic cylinder. Comparing the simulations, with different lengths of pneumatic lines, it is accurately seen from the differences in magnitudes that for all transients, the length of the pneumatic lines of 1 m and 10 m has a significant bias in the parameters of the electropneumatic positioning system. Longer pneumatic lines affect the system dynamics in terms of time-delay and amplitude decay.

At  $t = 1$  m and  $t = 10$  m, the time of the transition process differs by 0.4 s. It is clearly seen that the plots are almost identical to the experimentally obtained ones, from which it can be concluded that there is a signal delay at pneumatic line lengths from  $=1$  m to  $=10$  m.

### III. CONCLUSION

The proposed mathematical model of an electropneumatic positioning system with consideration of the signal delay in pneumatic lines is an adequate tool to determine the flow and pressure under unsteady operating modes of pneumatic systems. From the developed simulation model it is possible to simulate the dynamic processes in an electropneumatic positioning system. The simulation of the mathematical model in a programming environment on “MatLab Simulink”, models of the power unit, proportional distributor, pneumatic lines, pneumatic cylinder, PID controller were developed. Transients in an electropneumatic positioning system at different line lengths from 1m and 10 m with step change of input setpoint are simulated.

Graphical comparison is made of the obtained experimental results and simulation model influence of the pneumatic line length on the dynamics of the electropneumatic positioning system are made.

### REFERENCES

- [1] Andrey Andreev, Hristo Hristov, Georgi Iliev, Milena Racheva. Mathematical Model for a Pneumatic Force Actuator System. BGSIAM'15 PROCEEDINGS 10th Annual Meeting of the Bulgarian Section of SIAM. December 21-22, 2015 Sofia
- [2] Iliev, G., H. Hristov, A. Anchev. „Experimental investigation of static characteristics of pneumatic proportional directional valve. Vol. 3, pp. 318-323, UNITECH' 15, Gabrovo, 2015.
- [3] Iliev, G., Hristo N. Hristov. "Mathematical model of electropneumatic positioning system including the length of pneumatic lines" Mechanics of Machines YEAR XXXI, №3, 2023 pp(83-88); ISSN 0861-9727, Varna, Bulgaria.
- [4] Georgi Iliev. „Experimental study of dynamic processes in pneumatic lines Heat Engineering .year 8, book 1, 2017 (pp.8-12) Bulgaria
- [5] Noritsugu T. and M. Takaiwa “Robust positioning control of pneumatic servo system with pressure control loop”. IEEE International Conference on Robotics and Automation,. pp. 2613-2618. 1995.

- [6] Mihai, A., V. Constantin; "Research on the designing of pneumatic positioning units controlled with valves commanded in modulated pulses"; MATEC Web Conf. Volume 290, Number of page(s)12; [21 August 2019]  
<https://doi.org/10.1051/mateconf/201929008003>
- [7] Lucian, Bogatu, Ciprian Rizescu; "Innovative Solutions for Pneumatic Positioning Systems", Innovation, Engineering and Entrepreneurship pp 530–536 book series (LNEE, volume 505) [2018] [https://doi.org/10.1007/978-3-319-91334-6\\_72](https://doi.org/10.1007/978-3-319-91334-6_72)
- [8] Elmadbouly E. E., Abdulsadek Nour M.: Modelling, simulation and sensitivity analysis of a straight pneumatic pipeline. Energy conversion and management 35.1 [1994], 61 - 77.
- [9] Karadzhev, T., Pulov, D., Angelov, N., Contactless measuring of temperature with differential photo receiver, ENVIRONMENT. TECHNOLOGY. RESOURCES, 12th International Scientific and Practical Conference. June 20-22, 2019, Rezekne Academy of Technologies, Rezekne, Latvia, pp 101-104
- [10] Saravanakumar D., B. Mohan, T. Muthuramalingam; "A review on recent research trends in servo pneumatic positioning systems precision engineering" Journal of the International Societies for Precision Engineering and Nanotechnology volume 49, July 2017, Pages 481-492
- [11] Richer Edmond; Yildirim Hurmuzlu, "A High Performance Pneumatic Force Actuator System: Part I—Nonlinear Mathematical Mode"; J. Dyn. Sys., Meas., Control. [September 2000], 122(3)416–425. doi: <https://doi.org/10.1115/1.1286336AbstractV>
- [12] Outbib R., E. Richard, "State feedback stabilization of an electropneumatic system" j. Dyn. Sys., Meas., Control. [September 2000], 122(3): 410–415. doi: <https://doi.org/10.1115/1.1286625>
- [13] Kotkas I., N Zhurkin, A Donskoy, Zharkovskij, "Design and Mathematical Modeling of a Pneumatic Artificial Muscle-Actuated System for Industrial Manipulators" Machines [2022, 10](10), 885; <https://doi.org/10.3390/Machines10100885>

# Modelling and Simulation of Dynamic Processes of Pneumatic Lines

**Georgi Iliev**  
dept. Power Engineering  
Technical University of Gabrovo  
Gabrovo, Bulgaria  
spigil@abv.bg

**Hristo Hristov**  
dept. Power Engineering  
Technical University of Gabrovo  
Gabrovo, Bulgaria  
chisto@tugab.bg

**Abstract.** The paper presents the simulation of dynamic processes of pneumatic lines using the program "SIMULINK" from the product "MatLab". Simulation is a process of forming, preparing and entering a mathematical model in a computational environment and obtaining the results of the calculations performed in this environment. The mathematical model of the pneumatic line to be simulated is according to previously presented equations. For the simulation of the dynamic processes, various real parameters of the dimensions and lengths of the pneumatic lines with the corresponding coefficients are introduced into the model. The simulation of the transient responses was carried out with stepwise variation and sinusoidal input signal supplied by the set point device and pneumatic line lengths of 1 m, 5 m and 10 m. The simulation output data were output to the interface in the form of graphs showing the dependence of the observed quantities, the input and output pressure through the pneumatic line, and the input and output flow rates. From the mathematical model and the experiments performed, it can be concluded that the transient responses in the simulations correspond to the dynamic processes of pneumatic lines of different lengths.

**Keywords:** *pneumatic line, simulation, mathematical model, experiments.*

## I. INTRODUCTION

Electropneumatic positioning systems are widely used in modern industry. Due to the compressibility of air, the unfavourable friction characteristics in pneumatic devices and the need for different lengths of pneumatic connecting lines, complex control models are required. Electropneumatic drive systems are often applied in the drives of industrial robots, manipulators, machines and equipment, which are subject to a number of requirements related to their operation in static and dynamic modes. The experimental study of pneumatic

lines of different lengths allows to compile adequate mathematical models to be used for the study and design of pneumatic systems of high quality that meet the modern requirements of industry. Mathematical modelling plays an increasingly important and defining role in modern engineering research. This is primarily due to the fact that established and proven models are used to simulate and solve problems in actuator systems using the powerful computational complexes developed in recent times [1],[2],[4].

In this way, many more factors influencing the dynamics of the systems can be taken into account, and a comparison can be made between the different mathematical models and the experimental studies performed.

It is known that the study of dynamics for any pneumatic- or hydraulic system is directly dependent on the variation of the main parameters in the connecting lines [2],[3],[4]. In the study of dynamic processes in pneumatic actuator systems, some authors neglect the influence of pneumatic lines. This is possible in some cases, but in others it leads to inadequacy of mathematical models and real processes of the system.

In pneumatic actuation systems, one of the main problems is the consideration of the signal delay along the pneumatic line. Most studies are based on laminar flow through the pneumatic line. In order to find an adequate mathematical model for the mass flow through them, it is necessary to consider the turbulent flow regime [1-15].

Print ISSN 1691-5402

Online ISSN 2256-070X

<https://doi.org/10.17770/etr2023vol3.7190>

© 2023 Georgi Iliev, Hristo Hristov. Published by Rezekne Academy of Technologies.  
This is an open access article under the [Creative Commons Attribution 4.0 International License](https://creativecommons.org/licenses/by/4.0/).

## II. MATHEMATICAL MODEL OF PNEUMATIC LINES

We're examining a cylindrical tube (line) on Fig. 1 with length  $L_t$ . The mass flow rate of the air through the line is [1]:

$$M = \frac{R_r^2 L_t}{8 a_s \rho^2} \ell^{-\frac{R_r L_t}{2 \rho a_s}} f \left( t - \frac{L_t}{a_s} \right) \quad (1)$$

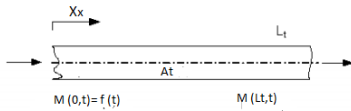


Fig. 1. Pneumatic line.

Where:

- $a_s$  denotes the sound speed;
- $\rho$  is the air density;
- $L_t$  cylindrical tube with length
- $t$  time variable
- $R_r$  the tube resistance
- $A_t$  tube cross-sectional area

## III. EXPERIMENTAL INVESTIGATION OF DYNAMIC PROCESSES IN PNEUMATIC LINES

In order to verify the obtained mathematical model for the flow through pneumatic lines, it is necessary to experimentally investigate the dynamic processes in the pneumatic lines at different input. The scheme shown in Fig. 2 is of the established experimental rig [4]. Step and sinusoidal input signal are used to obtain the experimental dynamic processes.

## IV. RESEARCH METHODOLOGY

A step input signal is applied to a discrete electro-pneumatic directional valve (6) controlled by an electrical switch (13). Pneumatic lines ( $D = 8$  mm,  $d = 6$  mm) (17) with lengths  $L_t$  (1 m, 5 m and 10 m) at an operating pressure of 5 bar are tested. Data from pressure and flow transducers at the inlet and outlet of the pneumatic line are visualized, processed and recorded by an automated real-time data acquisition and processing system.

In the process, the signals from the application and flow sensors, the input signal from the signal generator are fed to the terminal board which facilitates the user in initially switching on external signals by means of rows of terminals which are numbered and labeled.

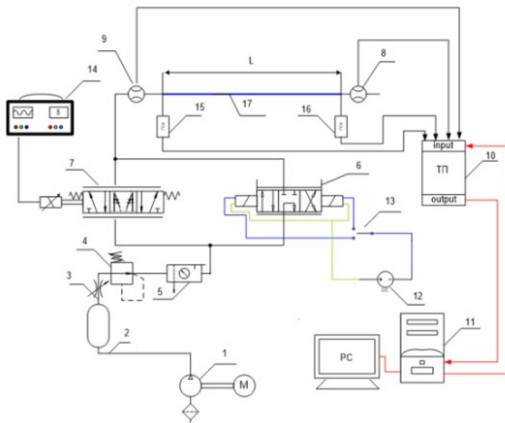


Fig. 2. Schematic of the experimental stand for the study of dynamic processes in pneumatic lines.

- 1 - screw compressor; 2 - receiver; 3 - stopcock; 4 - safety valve; 5 - air preparation system preparatory; 6 - discrete distributor; 7 - proportional directional control valve; 8, 9 - flow meters; 10 - interface board; 11 - personal computer; 12 - power supply unit; 13 - switch; 14 - signal-generator; 15, 16 - pressure sensors; 17 - pneumatic line.

Additional passive elements in the analog signal path are easily connected to the terminals. In this way, RC-filters, dividers or current signals can be implemented. The signals are processed with a virtual instrument in the LabView environment, using a DAQ board NI PSle-6351. It is an analog-to-digital 16-bit converter, using a sampling rate in the range 200...2000 samples/sec on each hardware channel. Preliminary calibration of the incoming signals from the sensors was performed in order to work in natural measurement units.

An external signal generator supplies to the terminal board a reference sinusoidal signal, serving as a time reference. Another virtual instrument, a multi-function frequency generator, was also constructed to perform the same tasks as the external signal generator. Both are used in the experiments, their choice depends on the specific needs of the experiment.

## V. VIRTUAL TOOL

For the purpose of the experiment, a virtual tool was developed to perform the following main functions Fig. 3:

Read the input channels in the following order:

- Measure the input signal;
- Measuring the pressure at the beginning of the pneumatic line;
- Measure the pressure at the end of the pneumatic line;
- Flow measurement at the beginning of the pneumatic line;
- Flow measurement at the end of the pneumatic line.



Fig. 3. User interface of the developed virtual tool.

The next function is the transition in natural units of each of the measured channels. The ability to record to a text file all input signals from a given point in time is provided. The user interface also sets the values of the recording speed, accuracy for recording to the output text file and defines the input tasks to be performed by the virtual instrument [3], [4]. In order to generate a control signal fed to the system input, a multi-function frequency generator was developed to generate an output signal with a sinusoidal shape and the ability to change frequency from 0.01 Hz to 100 kHz, amplitude from 0.01V to 10 V - Fig. 4.

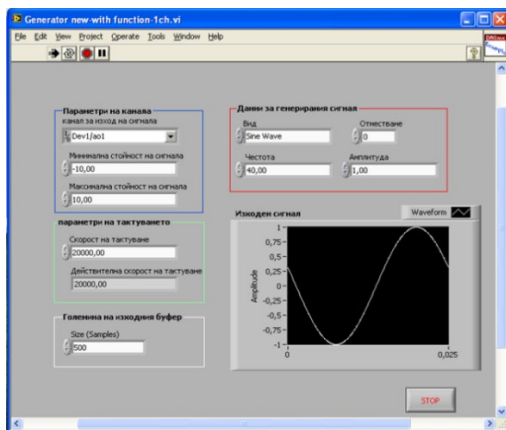


Fig. 4. Multifunction Frequency Generator User Interface.

Fig. 5 and Fig. 6 show the pressure and flow step responses at the inlet and outlet of the pneumatic line at 1 m length and 6 mm diameter. The flow and pressure values are dimensionless with respect to their maximum value.

The duration of the step responses under the flow rate variation Fig. 6. is about 0.15 s with the delay time 0.05s.

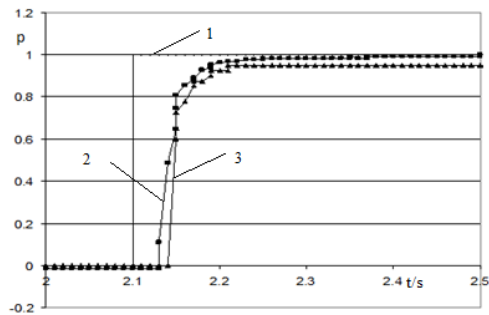


Fig. 5. Pressure at inlet (2) and outlet (3) of pneumatic line at 1 m length; (1) step input signal. (The pressure values are dimensionless with respect to their maximum value).

The transient process under the pressure variation is about 0.10s with the net delay time 0.03s. The steady-state output pressure value is less than the input pressure, Fig. 5. which is due to the hydraulic resistances in the line.

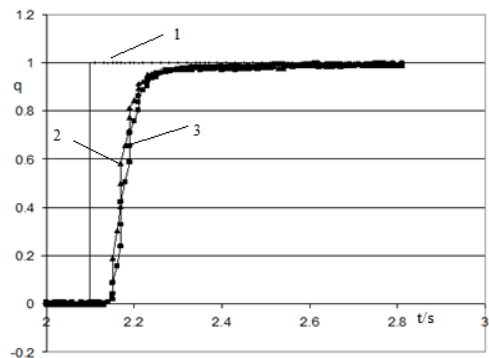


Fig. 6. Pneumatic line inlet (2) and outlet (3) flow at 1 m length; (1) step input signal (The flow values are dimensionless with respect to their maximum value.).

The Fig. 7 and Fig. 8. the pressure and flow step responses at the inlet and outlet of the pneumatic line are shown for a length of 5 m and a diameter of 6 mm.

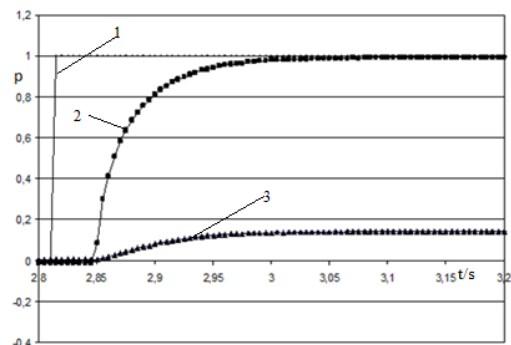


Fig. 7. Pressure at inlet (2) and outlet (3) of pneumatic line at 5 m length; (1) step input signal (The pressure values are dimensionless with respect to their maximum value).

The duration of the transition process for a pneumatic line length of 5 m is shown in Fig. 7. The flow rate variation is about 0.25 s with a delay time of 0.07 s. In Fig. 8. the transient process at pressure variation is about 0.15s with a net delay time of 0.05s

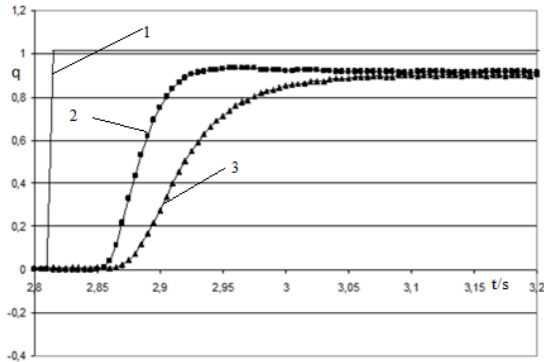


Fig. 8. Pneumatic line inlet (2) and outlet (3) flow at 5 m length; (1) step input signal (The flow values are dimensionless with respect to their maximum value).

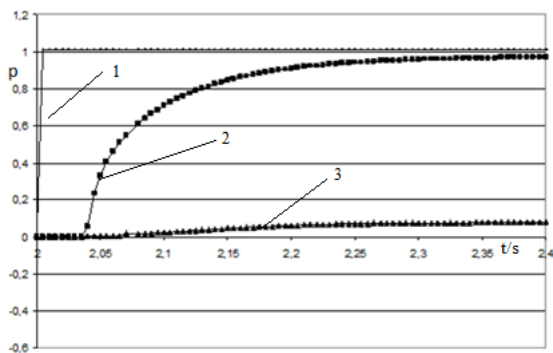


Fig. 9. Pressure at inlet (2) and outlet (3) of pneumatic line at 10 m length; (1) step input signal (The pressure values are dimensionless with respect to their maximum value).

Fig. 9 and Fig. 10 show the pressure and flow step responses at the inlet and outlet of the pneumatic line at 10m length and 6mm diameter.

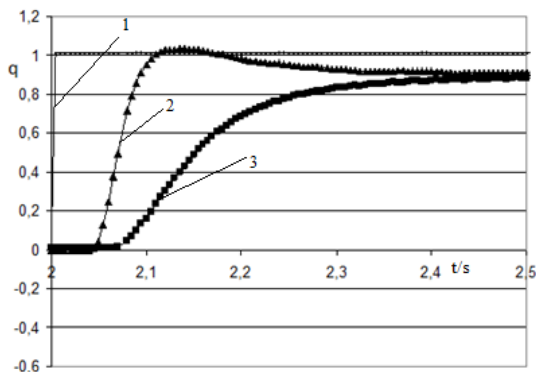


Fig. 10. Pneumatic line inlet and outlet flow at 10 m length; (1) step input signal (The flow values are dimensionless with respect to their maximum value).

The duration of the transient process for a pneumatic line length of 10 m, the flow rate variation is about 0.40 s with a delay time of 0.08 s Fig. 10. and the transient process for pressure variation is about 0.25 s with a delay time of 0.06 s Fig. 9.

When comparing the results of the study of the processes in pneumatic lines of 1m, 5 m and 10 m length, the significant influence of the larger length of the pneumatic line is observed, which affects the shape and duration of the process for flow variation changes from 0.15 to 0.40 s, and the delay time from 0.05 to 0.08 s, and the transient process at pressure variation is from 0.10 to 0.25 s, with the delay time from 0.03 to 0.06 s.

#### VI. EXPERIMENTAL STUDY OF TRANSIENTS IN A PNEUMATIC LINE OF VARYING LENGTH WITH SINUSOIDAL INPUT SIGNAL

The conduct of the experiment is analogous to the previous one, where the input signal is replaced by a sinusoidal signal set by a signal generator.

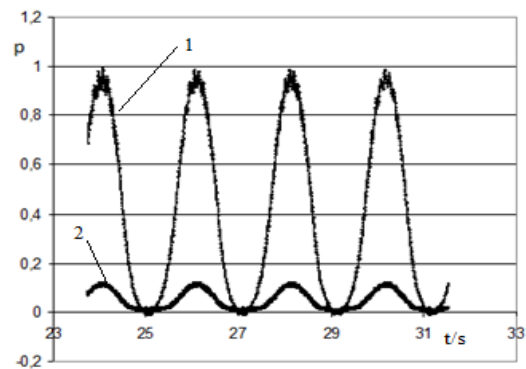


Fig. 11. Pneumatic line inlet (1) and outlet (2) pressure at 5 m length, frequency 0.5 Hz (The pressure values are dimensionless with respect to their maximum value).

A 5 m long pneumatic line was tested at different input signal frequencies of 0.3 and 0.5 Hz.

The results of the experiment-the variation of pressure and flow at the inlet and outlet-are shown in Fig. 11 to Fig.12. The corresponding flow rates and pressures are dimensionless with respect to their maximum value.

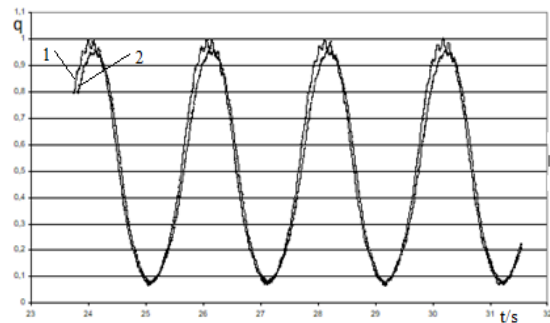


Fig. 12. Pneumatic line inlet (1) and outlet (2) flow at 5 m length, frequency 0.5 Hz (The flow values are dimensionless with respect to their maximum value).

Figure 13 and Figure 14 show the inlet and outlet flow rates and pressures for a pneumatic line length of 5 m, a frequency of 0.3 Hz and a voltage of 5 V.

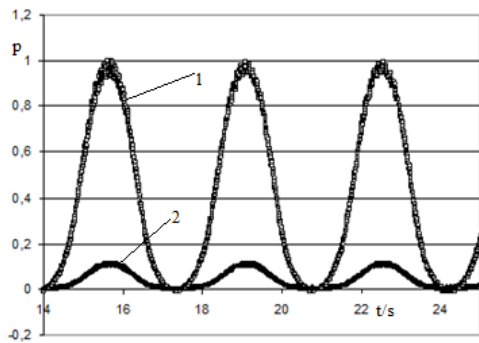


Fig.13. Pneumatic line inlet (1) and outlet (2) pressure at 5 m length, frequency 0.3 Hz (The pressure values are dimensionless with respect to their maximum value).

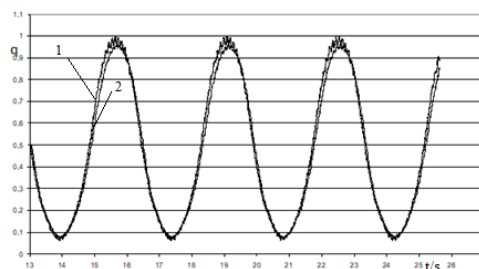


Fig. 14. Pneumatic line inlet (1) and outlet (2) flow at 5 m length, frequency 0.3 Hz (The flow values are dimensionless with respect to their maximum value).

As with step responses, transients in a sinusoidal signal show the influence of the pneumatic line length on flow and pressure variation in the dynamic regime. Phase delay and change in amplitude of the signals are observed. To study the influence of pneumatic lines in detail, it is necessary to fully investigate their frequency characteristics [1], [3],[4].

## VII. MODELLING AND SIMULATION OF DYNAMIC PROCESSES OF PNEUMATIC LINES

Simulation is the process of forming, preparing and entering a mathematical model into a computing environment and obtaining the results of the calculations performed in this environment. The mathematical model of the pneumatic line to be simulated is according to equation (1).

The simulation of dynamic processes in the pneumatic line model is carried out using MatLab SIMULINK. The block diagram of the simulation model is shown in Fig. 15.

For the simulation of the dynamic processes, various real parameters of the dimensions and lengths of the pneumatic lines with the corresponding coefficients are introduced into the model.

The model shown in Fig. 15 was created using the MatLab SIMULINK and the resulting values of the dynamic processes are presented as graphs.

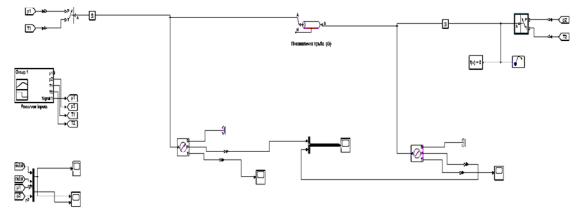


Fig. 15. Simulation model of pneumatic lines in MatLab.

The simulation of the transients has been carried out with step input supplied by the setter and with pneumatic line lengths - 1 m, 5 m and 10 m. The simulation outputs were output to the interface in the form of graphs showing the dependence of the observed quantities, the inlet and outlet pressure through the pneumatic line, and the inlet and outlet flow rates.

From the simulations performed on the mathematical model, the transients are observed at different lengths (1m, 5m and 10 m) of the pneumatic lines and when the main observed quantities (pressure and flow rate) change on both sides of the line - inlet and outlet.

The flow and pressure values in the simulation model plots are presented dimensionless with respect to their maximum value.

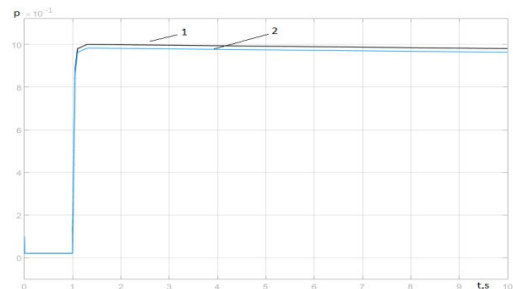


Fig. 16.a. Pressure at the inlet (1) and outlet (2) of a 1 m pneumatic.

At = 1 m the time of the transient process is between 0.1 and 0.15 s. It is clearly evident that the plots are almost identical for the inlet and outlet signals, from which it can be concluded that for a pneumatic line length of 1 m there is no large signal delay, which is analogous to the experimental results Fig.16. a. and Fig. 16.b. discussed in this chapter.



Fig. 16.b. Flow rate at the inlet (1) and outlet (2) of a 1 m pneumatic line.

At  $\tau = 5$  and  $10$  m pneumatic line length, the transition time is  $0.25$ - $0.4$  s. There is a clear signal mismatch at the inlet and outlet, from which it can be concluded that there is a signal delay at pneumatic line lengths of  $5$  m and  $10$  m, which is analogous to the experimental results Fig. 16.c. and Fig. 16.f.

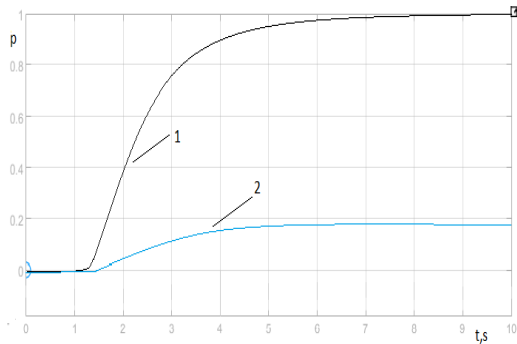


Fig. 16.c. Pressure at the inlet (1) and outlet (2) of a 5 m pneumatic line.

To better evaluate the tracking accuracy, the input and output signals are dimensionless. The analysis performed on the obtained results proves that the mathematical model is adequate and suitable for use.

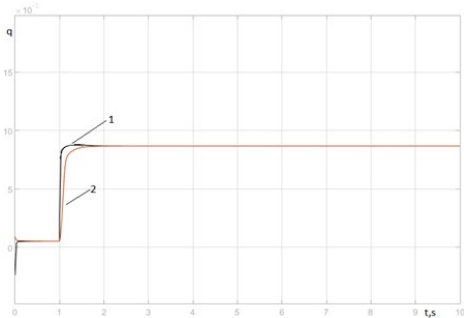


Fig. 16.d. Flow rate at the inlet (1) and outlet (2) of a 5 m pneumatic line.

Simulation of the transients is also carried out with a sinusoidal input of  $0.5$  Hz supplied by the setpoint device.

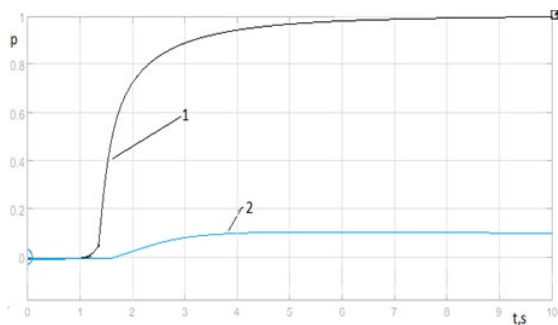


Fig. 16.e. Pressure at the inlet (1) and outlet (2) of a 10 m pneumatic line.

The simulation outputs for pneumatic line lengths of  $1$  m,  $5$  m and  $10$  m are output to the interface in the form of graphs depending on the observed quantities - inlet and outlet pressure and inlet and outlet flow through the pneumatic line. As a result of the conducted simulations the following conclusions can be drawn:

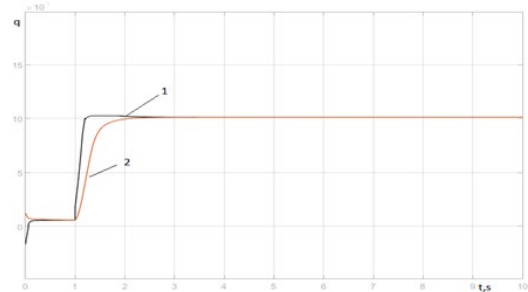


Fig. 16.f. Flow rate at the inlet (1) and outlet (2) of a 10 m pneumatic line.

Simulation of the transients is also conducted with a  $0.5$  Hz sinusoidal input signal fed through the setpoint device. The simulation outputs for  $1$  m,  $5$  m and  $10$  m pneumatic line lengths are output to the interface in the form of graphs - inlet and outlet pressure and inlet and outlet flow through the pneumatic line.

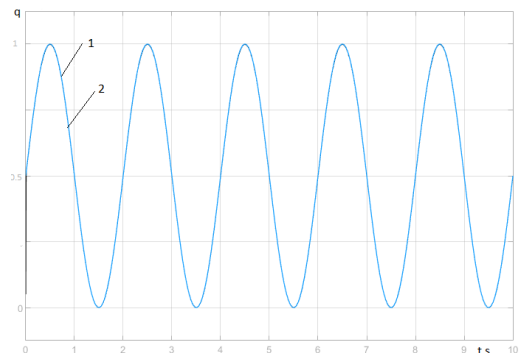


Fig. 17.a. Input (1) and output (2) pressures at 1 m pneumatic line and  $0.5$  Hz frequency.

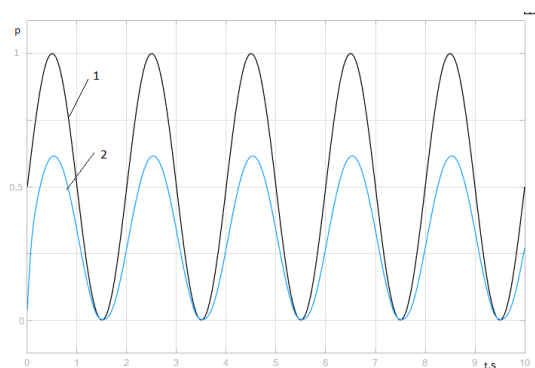


Fig. 17.b. Input (1) and output (2) pressures at 5 m pneumatic line and  $0.5$  Hz frequency.

At a frequency of the input sinusoidal signal of 0.5 Hz, a phase delay in the order of 50 – 60 Fig. 17.b and a decrease in the signal amplitude are observed, which corresponds to the experimental results Fig. 11. and Fig. 12.

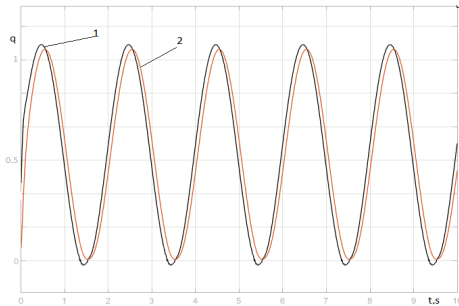


Fig. 17.c. Inlet (1) and outlet (2) flow rates at 5 m pneumatic line and 0.5 Hz frequency.

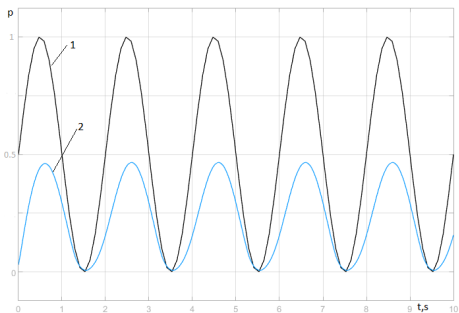


Fig. 17.d. Input (1) and output (2) pressures at 10 m pneumatic line and 0.5 Hz frequency.

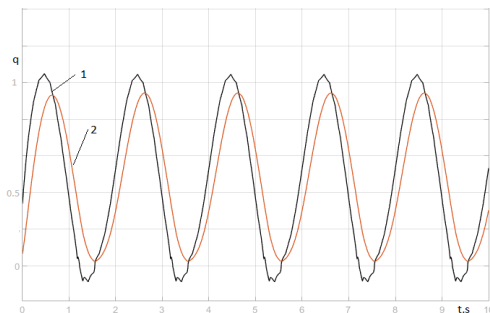


Fig. 17.e. Input (1) output (2) flow rate at pneumatic line 10 m and frequency 0.5 Hz.

For better estimation of tracking accuracy, the input and output signals are dimensionless. From the mathematical model thus presented and the experiments performed, it can be concluded that the transients in the simulations correspond to the dynamic processes of pneumatic lines of different lengths.

### VIII. CONCLUSION

The proposed mathematical model of pneumatic lines with consideration of the signal delay along their length is an adequate tool for the determination of flow and pressure in unsteady operating modes of pneumatic systems. This mathematical model is used to obtain the mass flow rate through the pneumatic lines in turbulent

flow regime. Using Fourier analysis, a new approach is applied to the study of pneumatic lines that is different from those previously described in the literature [7],[9],[10],[13]. From the study, it was found that pneumatic lines have nonlinear dynamic characteristics, delay (for flow rate 0.05 to 0.08 s, 0.03 to 0.06 s for pressure) and transient time (for flow rate 0.15 to 0.40 s, 0.10 to 0.25 s for pressure) depend on the length of the lines, the pressure and flow rate in them, and the frequency of their change. The results obtained by numerical simulation were compared with the experimental data, and excellent agreement was found.

### REFERENCES

- [1] Andreev, A., H. Hristov, G. Iliev, M. Racheva. "Mathematical model for a Pneumatic force Actuator System" Journal of the Technical University of Gabrovo, Bulgaria Vol. 53'2016
- [2] Hristov, H., K. Ormanjiev, P. Ivanov, "Investigation of the transient processes of an electro-pneumatic drive system with a hydraulic speed stabilizer" Journal of Mechanics of Machines No62, Series FH: APPLIED MECHANICS OF FLUIDS HEAT AND MASS TRANSFER, Year XIV, Book 1, Technical University of Varna Press, Bulgaria 2006
- [3] Iliev, G., A. Anchev, H. Hristov, S. Rachev. "Stand for experimental study of dynamic processes in Electro- pneumatic tracking System" XXII International Conference "Eko- Istj 2014. Bor, SERBIA (124-130)
- [4] Iliev, G., H. Hristov, A. Anchev, "Experimental study of the static characteristics of a proportional directional control valve" Volume 3, pages 318-323, UNITECH'15, Gabrovo, Bulgaria 2015.
- [5] Kreinin, G., S. Misyurin, S. Nosova. "Parametric and Structural Optimization of Pneumatic Positioning Actuator"; pp.123-129. 2020.
- [6] Mihai, A., C. Bucsan, L. Bogat; "Pneumatic Incremental Proportional Valve Part of the Lecture Notes in Networks and Systems book series" (LNNS, volume 85 20 ) July 2019
- [7] Bavaresco, D., Mathematical modeling and control of a pneumatic actuator, M.S. thesis, Mathematical Modeling Master Course, UNIJUÍ - Regional University of Northwestern Rio Grande do Sul State, Brazil, 2007
- [8] Chiara, G., D. Prattichizzo, A Mathematical Model of the Pneumatic Force Sensor for Robot-assisted Surgery IEEE World Haptics Conference (WHC) pp.121-126. 2019
- [9] Richer E., Yildirim Hurmuzlu; A high performance pneumatic force actuator system: part I—Nonlinear mathematical model: J. Dyn. Sys., Meas., Control. Sep 2000, 122(3): 416-425 (10 pages) <https://doi.org/10.1115/1.1286336>
- [10] Richer E., Yildirim Hurmuzlu; A High Performance Pneumatic Force Actuator System: Part II—Nonlinear Controller Design: J. Dyn. Sys., Meas., Control. Sep 2000, 122(3): 426-434 (9 pages) <https://doi.org/10.1115/1.1286366>
- [11] Andrzej Laski., Takosoglu Jakub Emanuel, Design of a 3-DOF tripod electro-pneumatic parallel manipulator, Robotics and Autonomous Systems Volume 72, October 2015, Pages 59-70
- [12] Jarquin Laguna A., Tsouvalas A.: Transient laminar flow in hydraulic networks based on a semi-analytical impulse response method. HERON Vol. 59 (2014) No. 1 (2014).
- [13] Dihovcni D., M Medenica, Mathematical modelling and simulation of pneumati systems, Advances in computer science and engineering 2011 pages (161-186)
- [14] Franco E.; M. Ristic Time delay controller for the position control of a MRI-compatible pneumatic actuation with long supply lines IEEE/ASME (AIM) International Conference on Advanced Intelligent Mechatronics 8-11 July 2014
- [15] Turkseven Melih, Jun Ueda, Model-Based Force Control of Pneumatic Actuators With Long Transmission Lines; IEEE/ASME Transactions on Mechatronics ( Volume: 23, Issue: 3, June 2018) Page(s): 1292 – 1302; 03 May 2018

# Effect of Boron on the Wear Behavior of High Chromium White Cast Irons

**Julieta Kaleicheva**  
Faculty of Industrial Technology  
Technical University of Sofia  
Sofia, Bulgaria  
jkaleich@tu-sofia.bg

**Krassimir Kirov**  
College Sliven  
Technical University of Sofia  
Sliven, Bulgaria  
kirov\_krassimir\_1966@abv.bg

**Valentin Mishev**  
Faculty of Industrial Technology  
Technical University of Sofia  
Sofia, Bulgaria  
v\_mishev@tu-sofia.bg

**Rumyana Lazarova**  
Institute of Metal Science,  
Equipment and Technologies with the  
Center for Hydro- and Aerodynamics  
"Acad. A. Balevski"  
Bulgarian Academy of Sciences  
Sofia, Bulgaria  
r.lazarova@ims.bas.bg

**Zdravka Karaguiozova**  
Space Research and Technology  
Institute  
Bulgarian Academy of Sciences  
Sofia, Bulgaria  
karazuzi@yahoo.com

**Abstract.** The wear behavior of high chromium white cast irons with composition: 2,6÷3,4% C; 0,9÷1,1% Si; 0,8÷1,1% Mn; 1,0÷1,3% Mo; 12,3÷13,4% Cr and 0,18 ÷ 1,25% B is investigated. The microstructure and tribological characteristics of six compositions of high chromium white cast irons (one without boron and with 0,18; 0,23; 0,59; 0,96; 1,25% boron) are studied.

After casting, heat treatment was carried out, including quenching at 950<sup>o</sup>C and tempering at 235<sup>o</sup>C for 1 h. The influence of the heating temperature in the interval 850÷1100<sup>o</sup>C, 25 min on the Rockwell hardness and the microstructure are studied.

The wear resistance during abrasive wear for samples after casting and after heat treatment is investigated as measured loss of mass in terms of dry friction under load of 1,5 kg during 10 min. The lowest mass loss during abrasive wear test in dry conditions friction is defined for cast irons alloyed with 0,18 % boron -  $\Delta m = 0,1469$  g after casting and  $\Delta m = 0,0022$  g after heat treatment. The highest mass loss is determined during abrasive testing of alloyed cast irons with 0,96 and 1,25% boron. The alloyed cast irons with 0,18 % boron show highest wear resistance.

**Keywords:** high chromium white cast iron, boron, carbides, hardness, wear resistance, microstructure.

## I. INTRODUCTION

High chromium white cast irons are an important group of materials for engineering applications of which high wear resistance and corrosion resistance are required.

Depending on the chemical composition of these materials and their chromium content, their structure may contain the following carbides:  $M_7C_3$ ,  $M_3C$  and  $M_{23}C_6$ .

These carbide phases differ in a chemical composition and morphological characteristics. The operational properties of these cast irons are determined from a predominant carbide type in their structure to a significant extent [1–3]. For this reason, the research directed towards at controlling and improving the operational properties of high-chromium white cast irons includes studying the changes in the carbide phases as a function of the alloying elements present in the structure, including the element boron [1–6].

Austempered ductile irons (ADI) with structure of lower and upper bainite, additionally alloyed with boron from 0,03 to 0,135%, become carbide austempered ductile irons (CADI). The structure of these cast irons (CADI) consists of eutectic carbides from 9 to 27% and possess up to 3 times higher wear resistance during abrasive wear compared to this one without boron (ADI) [7].

The wear resistance and strength of high chromium white cast irons depends on both the size, type and morphology of the carbide phases and on the microstructural characteristics of these alloys. The metal matrix in them can be regulate by the chemical composition and by conducting heat treatment after casting the alloy. Most of these alloys, in addition to high chromium (>10%),

Print ISSN 1691-5402

Online ISSN 2256-070X

<https://doi.org/10.17770/etr2023vol3.7294>

© 2023 Julieta Kaleicheva, Krassimir Kirov, Valentin Mishev, Rumyana Lazarova, Zdravka Karaguiozova.

Published by Rezekne Academy of Technologies.

This is an open access article under the [Creative Commons Attribution 4.0 International License](https://creativecommons.org/licenses/by/4.0/).

also contain nickel, molybdenum, copper or combinations of these alloying elements in order to prevent the formation of pearlite in the microstructure. After properly conducted heat treatment, these cast irons have a martensitic microstructure of the metal matrix for maximum abrasion resistance and toughness [8,9].

The alloying with boron and its influence on the microstructure and properties of high chromium white cast irons is poorly studied. The aim of the performed research is to determine the influence of the boron in an amount of 0,18 to 1,25% in the composition of high chromium white cast irons on their hardness and tribological characteristics.

II. MATERIALS AND METHODS

Samples of six high-chromium white cast iron melts with the following composition were examined: 2,6÷3,4% C; 0,9÷1,1% Si; 0,8÷1,1% Mn; 1,0÷1,3% Mo; 12,3÷13,4% Cr and 0,18 ÷ 1,25% B. One of the melts does not contain boron, and the other five compositions contain 0,18; 0,23; 0,59; 0,96 and 1,25% boron.

The microstructure of the samples after casting is studied by means of an optical metallographic analysis by MIT 500 microscope of the Coptic company. The test samples are processed in the reagent composition 1g KOH, 4g KMnO<sub>4</sub>, 100 ml H<sub>2</sub>O и 2g C<sub>4</sub>H<sub>6</sub>O<sub>4</sub> for 5 minutes at ambient temperature. This reagent shows carbide phases of type: M<sub>6</sub>C, M<sub>7</sub>C<sub>3</sub>, M<sub>23</sub>C<sub>6</sub> and M<sub>3</sub>C.

The samples after casting are undergone to a quenching from 950°C with air cooling and following tempering at 235°C for 1 h. The study of the influence of the heating temperature in the interval 850÷1100°C on the hardness of the cast iron is conducted (Table 1, Fig. 1) to select the proper quenching temperature. Hardness test is carried out according to Rockwell's method for the samples with different boron content after heating at 850÷1100°C at an interval of 50°C, holding at these temperatures for 25 min and subsequent air cooling to room temperature (Fig. 2).

The performance of the samples of high chromium white cast iron alloyed with boron in as-cast condition and after heat treatment with quenching on air from 950°C, 25 min. and with tempering at 235°C, 1 h is studied during abrasive wear.

TABLE 1. HRC HARDNESS OF ALLOYED WITH BORON HIGH CHROMIUM WHITE IRONS, CAST AND QUENCHED FROM DIFFERENT TEMPERATURES

№ of sample	HRC						
	cast	Quenching temperature [°C]					
		850	900	950	1000	1050	1100
2	53,5	60,33	63	65	62	59,5	55
3	53,83	61	65,5	65,83	63,3	61,5	55,5
4	56,5	61,17	62,83	65,67	64,17	62	56,67
5	57,17	62,17	64	65,67	64,33	62	57,33
6	57,5	63,33	64,33	66,33	65,17	61,67	57,83

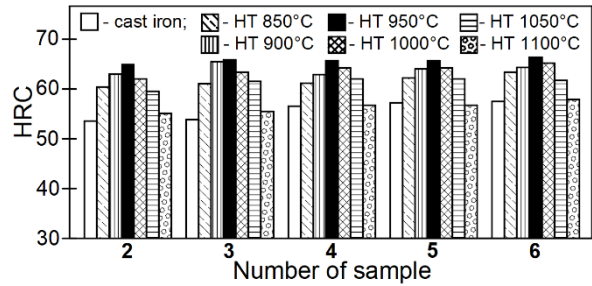


Fig. 1. Variation of HRC hardness of high chromium white cast irons depending on boron content and different heating temperatures.

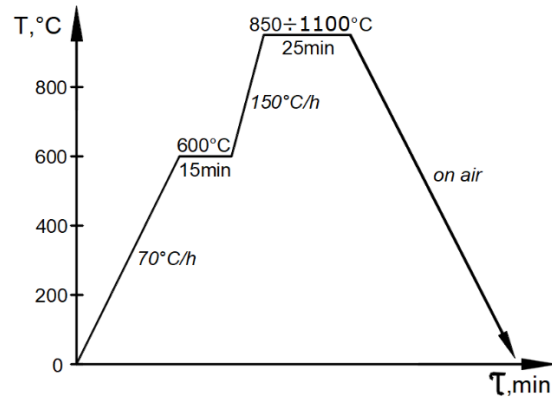


Fig. 2. Schematic diagram of the heat treatment cycle of the boron-alloyed high-chromium white cast irons.

The mass loss  $\Delta m$  is measured under the conditions of dry friction under a load of 1,5 kg for 10 min and the absolute wear resistance  $L$  was determined. A drill was used to study the wear of the different samples. The examined sample with dimensions  $\varnothing 30 \times 40 \text{ mm}$  is fixed on a rod with a socket, and the distance between the axis of the sample and the axis of the three-jaw chuck of the drill is 60 mm. A weight with a mass of 1,5 kg is attached to the vertical feed lever. The sample is rotated with  $n = 150 \text{ min}^{-1}$ , pressed on an abrasive disk with dimensions of  $250 \times 20 \times 20 \text{ mm}$ . A disk 99BA60R7V is used for the experiment. An electronic balance WPS 180/C/2 with an accuracy of 0,1 mg is used to measure the mass of the samples.

The friction road  $L$  is:

$$L = 2 \cdot \pi \cdot R \cdot n \cdot t, [m] \tag{1}$$

where:

- $R = 60 \text{ mm}$  is distance between the axis of the specimen and the axis of the chuck;
- $n = 150 \text{ min}^{-1}$  is rotation speed.

The wear layer  $h$  is:

$$h = (m_0 - m_f) / \rho \cdot A_a = \Delta m / \rho \cdot A_a, [m] \tag{2}$$

where:

- $m_0$  – sample initial mass, [kg];
- $m_f$  – final mass of the sample, [kg];
- $\rho = 7,8 \cdot 10^3 \text{ kg/m}^3$  is the density of the material;
- $A_a$  - contact area of wear, [ $\text{m}^2$ ];
- $\Delta m$  - loss of mass with wear, [kg].

Wear intensity  $i$  represents the material thickness destroyed per unit friction path:

$$i = h/L = \Delta m / (\rho \cdot A_a \cdot L) \quad (3)$$

The absolute wear resistance  $I$  is the reciprocal of the wear intensity:

$$I = 1/i = (\rho \cdot A_a \cdot L) / \Delta m \quad (4)$$

### III. RESULTS AND DISCUSSION

In the structure of high chromium white cast irons with chromium about 13% the main carbide is  $M_7C_3$  [1–3]. Carbides type  $M_3C$  и  $M_{23}C_6$  also persist in the structure of these cast irons. The cast irons studied contain about 1% molybdenum, dew to carbides type  $M_6C$  и  $M_2C$  are possible in the structure. Microstructure of the cast irons without boron and with 0,18; 0,23 and 0,59% B is subeutectic, with 0,96 % B – with 0,96% B – close to the eutectic and with 1.25% B – supraeutectic [1]. Fig. 3 shows the microstructure of high chromium white irons without boron (a) and alloyed with 0,18% (b); 0,23 % (c) and 0,59% boron. The used reagent shows the carbide phases in the microstructure in dark color. The carbide phases in different compositions of cast iron differ in shape, size and quantity (Fig. 3).

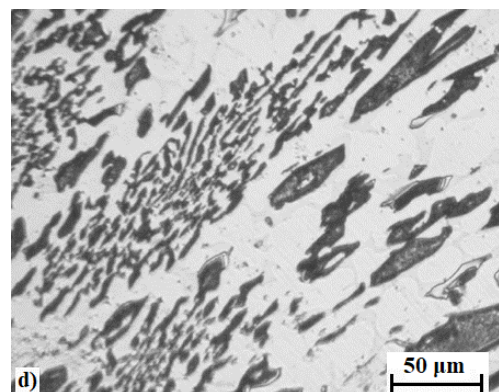
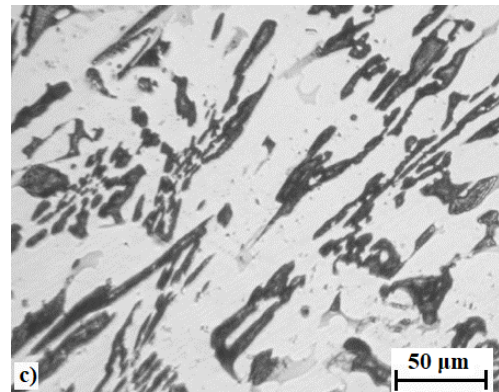
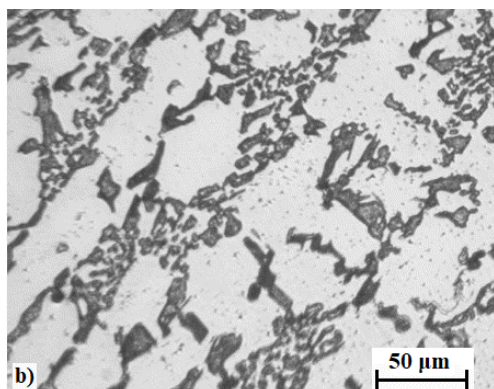
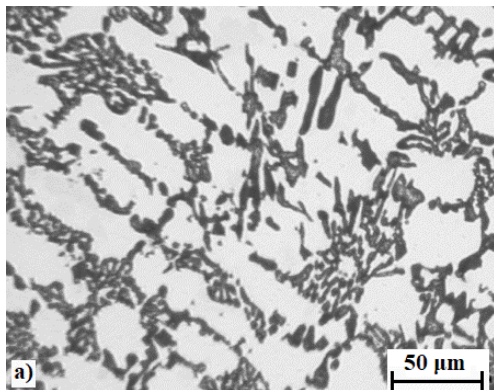


Fig. 3. Microstructure of boron-alloyed high-chromium white irons with 0% B (a); c 0,18% B (b); c 0,23% B (c) и c 0,59% B (d).

Fig. 2 shows a scheme of the tempering mode of the tested high chromium white cast irons alloyed with boron. The selected optimal mode of heat treatment of the samples for abrasive wear testing includes quenching from a temperature of 950°C with air cooling to room temperature and tempering at a temperature of 235°C, 1 hour. The heating at 950°C, 25 min and cooling in air, provides the highest hardness after quenching – 65÷67 HRC compared to the rest of the studied regimes in the temperature range 850÷1100°C. At heating temperatures of 850÷950°C for 25 min, secondary carbide phases are separated from the austenite. This leads to the impoverishment of austenite with carbon and alloying elements (the temperature  $M_s$  of the austenite-martensite transformation increases), which increases the amount of martensite in the structure of quenched cast irons and leads to an increase in hardness. At heating temperatures of 1000÷1100°C, the secondary chromium carbides dissolve in the austenite. This increases the resistance of the supercooled austenite to disintegration (the temperature of the  $M_s$  point of the austenite-martensite transformation decreases) and after quenching in the structure of the cast irons, the amount of retained austenite increases. The hardness of hardened cast iron after heating at a temperature of 1100°C decreases to 54÷58 HRC (Table 1, Fig. 1).

The data from the abrasive wear tests performed on the samples of alloyed with boron high chromium white iron in as-cast condition and after heat treatment are presented in Table 2 and 3.

TABLE 2. MASS LOSS AND WEAR RESISTANCE OF ALLOYED WITH BORON HIGH CHROMIUM WHITE IRONS IN AS-CAST CONDITION

N <sup>o</sup> of sample	B, %	m <sub>0</sub> , [g]	m <sub>f</sub> , [g]	Δ m, [g]	I.10 <sup>6</sup>
1	-	142,5032	142,2341	0,2691	1,069
2	0,18	147,4415	147,2946	0,1469	1,959
3	0,23	145,9076	145,7297	0,1779	1,617
4	0,59	143,6850	143,4546	0,2304	1,249
5	0,96	143,8705	143,5771	0,2934	0,980
6	1,25	147,6045	147,2214	0,3831	0,751

TABLE 3. MASS LOSS AND WEAR RESISTANCE OF ALLOYED WITH BORON HIGH CHROMIUM WHITE IRONS AFTER HEAT TREATMENT

N <sup>o</sup> of sample	B, %	m <sub>0</sub> , [g]	m <sub>f</sub> , [g]	Δ m, [g]	I.10 <sup>7</sup>
1	-	135,3652	135,3569	0,0083	3,467
2	0,18	142,7748	142,7726	0,0022	13,081
3	0,23	137,5008	137,4934	0,0074	3,889
4	0,59	136,4723	136,4627	0,0096	2,997
5	0,96	139,5951	139,5766	0,0185	1,555
6	1,25	140,5808	140,5520	0,0288	0,999

Fig. 4 shows the relation of the change of the mass loss Δm during wear test and the boron quantity.

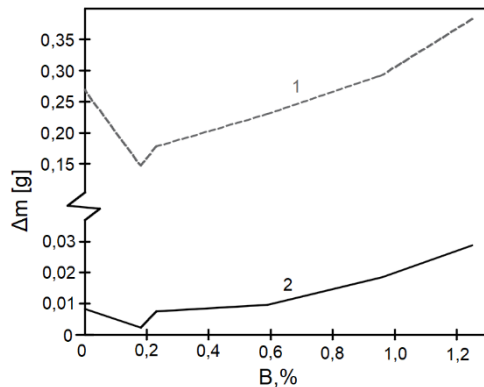


Fig. 4. Change in mass loss during wear Δm depending on the amount of boron in high chromium white cast irons: 1- in as-cast condition; 2- after heat treatment.

Fig. 5 and 6 show the absolute wear resistance I according to the boron quantity in the tested cast irons in as-cast condition and after heat treatment.

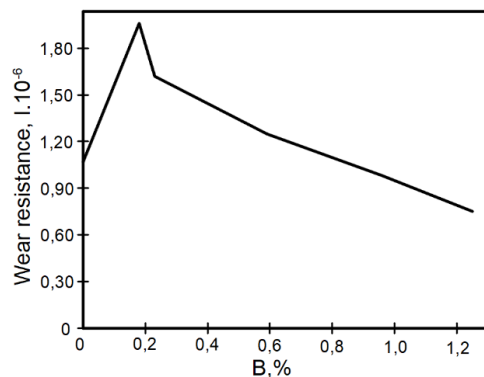


Fig. 5. Change in absolute wear resistance I depending on the boron quantity in high chromium white cast irons in as-cast condition.

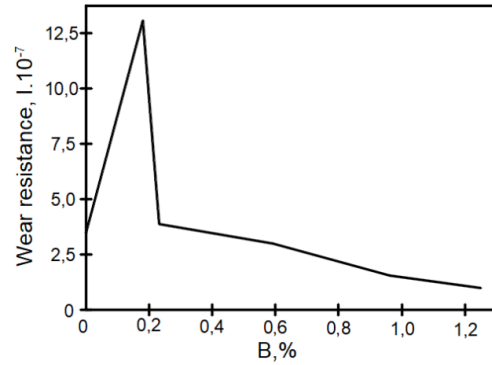


Fig. 6. Change in absolute wear resistance I depending on the boron quantity in high chromium white cast irons after heat treatment.

The lowest mass loss during wear Δm have alloyed cast irons with 0,18 % boron (Δm = 0,1469 g for cast irons in as-cast condition and Δm = 0,0022 g for cast irons after heat treatment). The cast irons in as-cast condition, alloyed with 0,18; 0,23 and 0,59% boron have smaller mass loss during wear Δm, the alloyed cast irons with 0,96 and 1,25% boron have bigger mass loss during wear Δm compared to Δm for cast iron without boron. The cast irons after heat treatment alloyed with 0,18 and 0,23 % boron have smaller mass loss during wear Δm, alloyed cast irons with 0,59; 0,96 and 1,25% boron have bigger mass loss during wear Δm, compared to Δm in the cast iron without boron. The cast irons alloyed with 0,18 % boron have highest wear resistance I (I = 1,959 .10<sup>6</sup> for irons in as-cast condition and I = 13,081 .10<sup>7</sup> for cast irons after heat treatment).

#### IV. CONCLUSIONS

The abrasion wear behaviour of high chromium white irons composition Fe-3,1C-13,1Cr-1,1Mo, additionally alloyed with 0,18; 0,23, 0,59, 0,96 and 1,25% boron is studied. It is concluded the lowest mass loss during wear Δm have cast irons alloyed with 0,18 % B – Δm = 0,1469 g for cast irons in as cast condition and Δm = 0,0022 g for cast irons after heat treatment. The same cast irons have highest wear resistance I – I=1,959.10<sup>6</sup> for cast irons in as-cast condition and I =13,081.10<sup>7</sup> for cast irons after heat treatment.

The investigation on the influence of the heat treatment in an interval 850÷1100°C for 25 min on the hardness of the quenched high chromium white irons alloyed with boron is performed. On the base of the results achieved the proper regime for the samples heat treatment is chosen for the tribological test. It includes quenching from temperature of 950°C, 25 min with air cooling to room temperature and tempering at 235°C, 1h.

#### V. ACKNOWLEDGMENTS

This work was supported by the European Regional Development Fund within the Operational Programme “Science and Education for Smart Growth 2014 - 2020” under the Project CoE “National center of mechatronics and clean technologies“-BG05M2OP001-1.001-0008.

## VI. REFERENCES

- [1] J. Kaleicheva, K. Kirov, V. Mishev and Z. Karaguiozova, "Microstructure and Properties of High Chromium White Cast Irons Alloyed with Boron", Proceedings of the 13th International Scientific and Practical Conference: Environment, Technology, Resources, Rezekne, Latvia, vol. 3, p.137-141, 2021. [Online]. Available: <http://journals.rta.lv/index.php/ETR> [Accessed March 25, 2023], <https://doi.org/10.17770/etr2021vol3.6656>
- [2] A. Nufal, "Metallurgical Aspects of High- Chromium White Irons", [Online]. Available: <https://www.foundry-planet.com/fileadmin/redakteur/pdf-dateien/13-Adel-Nofal.pdf> [Accessed: March 25, 2023].
- [3] Kh. Abdel-Aziz, M. El-Shennawy and Adel A. Omar, "Microstructural Characteristics and Mechanical Properties of Heat Treated High-Cr White Cast Iron Alloys", International Journal of Applied Engineering Research, vol. 12, Number 14, p. 4675-4686, 2017. [Online]. Available: ResearchGate, [https://www.ripublication.com/ijaer17/ijaerv12n14\\_79.pdf](https://www.ripublication.com/ijaer17/ijaerv12n14_79.pdf) [Accessed March 25, 2023].
- [4] S. Tomovic-Petrovic, S. Markovic and S. Zec, "The effect of boron on the amount and type of carbides in chromium white irons", Journal of the Serbian Chemical Society, vol. 67(10), p.697-707, 2002. [Online]. Available: ResearchGate, <https://www.doiserbia.nb.rs/img/doi/0352-5139/2002/0352-51390210697T.pdf> [Accessed March 25, 2023], <https://doi.org/10.2298/JSC0210697T>
- [5] A. Bedolla-Jacuinde, F. V. Guerra, I. Mejía, J. Zuno-Silva and C. Maldonado, "Boron Effect on the Precipitation of Secondary Carbides During Destabilization of a High-Chromium White Iron", 10th International Symposium on the Science and Processing of Cast Iron – SPCII0, 2014. [Abstract]. Available: ResearchGate, <https://www.researchgate.net/publication/271829525> [Accessed March 25, 2023], <https://doi.org/10.1080/13640461.2016.1142236>
- [6] F. Nurjaman, S. Sumardi, A. Shofi, M. Aryati, and B. Suharno, "Effect of molybdenum, vanadium, boron on mechanical properties of high chromium white cast iron in as-cast condition", AIP Conference Proceedings 1711, 020005, 2016, [Online]. Available: ResearchGate, <https://aip.scitation.org/doi/pdf/10.1063/1.4941614> [Accessed March 25, 2023], <https://doi.org/10.1063/1.4941614>
- [7] G. Rashev, V. Todorov, I. Bonev and R. Gagov, "Boron in Ductile Cast Irons". International Scientific Journal, Machines. Technologies. Materials. YEAR VI, Issue 3, pp. 8-12, 2012. (at bulgarian)
- [8] R.B. Gundlach, High alloy white irons, ASM Hand Book, Casting, 4th Edition, ASM International, 1998, pp.679-685.
- [9] J.R. Davis, Metallurgy and properties of high alloy white irons, ASM Specially Hand Book, Cast Irons, Materials Park, OH: ASM International, 1996, pp.107-30.

# *Ingredients Degradation in Steel Fiber Reinforced Concrete after Thermal Loading*

**Karunamoorthy Rengasamy Kannathasan**  
*Department of Theoretical Mechanics and Strength of Material*  
Riga Technical university  
Riga, Latvia  
Karunamoorthy.Rengasamy-Kannathasan@rtu.lv

**Andrejs Krasnikovs**  
*Department of Theoretical Mechanics and Strength of Material*  
Riga Technical University,  
Riga, Latvia  
Andrejs.Krasnikovs@rtu.lv

**Arturs Macanovskis**  
*Department of Theoretical Mechanics and Strength of Material*  
Riga Technical University,  
Riga, Latvia  
Arturs.macanovskis@rtu.lv

**Abstract.** The steel fiber reinforced concrete in structures provides good mechanical and physical characteristics and such material applications are increasing. At the same time, if structure is subjected to thermal load it is affecting both properties of reinforcement and matrix as well. The aim of the present research is to investigate the degradation of the characteristics of fibers, randomly distributed in the body of concrete block. A short steel fiber reinforced concrete slabs (400x300x18cm) [1], [2] with homogeneously distributed fibers was undergone to calefaction process from one side. dimension of 16.5x14.5x15 cm) Fiber fracture process was performed based on the single fiber pull-out test by preparing the specimens with fiber from calefacted SFRC block. Experimental curves from each layer were compared with different layer of fibers and investigation had shown that higher load-bearing capacity is there over the thermal loaded fiber. The conclusion were made with the microscopic results and the experimental data.

**Keywords:** concrete, pull out, Thermal loading, reinforced concrete, material degradation.

## I. INTRODUCTION

Concrete is a frequently utilized construction material across the world. It is brittle under tension and compression. When combined with brittleness, a high strength-to-weight ratio results leads to catastrophic tensile failure, requiring some form of tensile reinforcement. Steel rebars and cages long time have been used for that. Randomly distributed short fibers, in some situations, less efficient, in comparison to conventional rebars, at the same time, the closely spaced fibers improve

the hardness and tensile qualities of concrete and aid in fracture control. Combining fiber reinforcement with conventional steel reinforcement optimizes performance. Fiber reinforced concrete (FRC) research and development has been renewed in the last three decades because of the improved quality of fiber reinforced concrete products [3] [4] [5] [6].

Fiber reinforced concrete is made up of short, discontinuous fibers that are randomly placed throughout the concrete. Fibers made of steel, glass, polymer, or natural resources are used in cement-based composites [7] [8] [9]. Because of their close spacing, fibers can withstand breaking better than traditional reinforcing steel bars. Fiber-reinforced concrete in many situations can be replacement for standard steel bars [10]. Several applications in advanced concrete technology need the use of both fibers and continuous reinforcing steel bars. Steel fiber is the most common type of reinforcement used in FRC [11] [12] [13].

The fiber reinforced concrete is used in order to enhance the life of the concrete but that steel fiber reinforced concrete exposed to the high temperature it started to get weak, so in this research the fibers from the concrete block is treated up to the temperature of 800 degrees and are studied detailly how the mechanical properties of the steel material is changed by doing microscopic analysis. Knowledge about structure deformation and analysis of pull - out test results, performed in laboratory, will allow to know the strength factors of the fiber, studying the material under normal temperature and high temperature in situation with degrading fiber mechanical properties [14] [15].

Print ISSN 1691-5402

Online ISSN 2256-070X

<https://doi.org/10.17770/etr2023vol3.7228>

© 2023 Karunamoorthy Rengasamy Kannathasan, Andrejs Krasnikovs, Arturs Macanovskis.

Published by Rezekne Academy of Technologies.

This is an open access article under the [Creative Commons Attribution 4.0 International License](https://creativecommons.org/licenses/by/4.0/).

## II. MATERIALS AND METHODS

Steel fiber reinforced concrete (SFRC) slabs after exposure to open flame from one side [1], [2] were catted to samples with the size of 16.5×14.5×15cm. Short steel fibers were randomly distributed in the volume of each slab.

### 2.1 Properties of Steel Fibers

SFRC specimen was made up of the commercially available hooked-ended steel fibers Dramix 3D 80/60BG. Fiber properties (supplier's data) are:

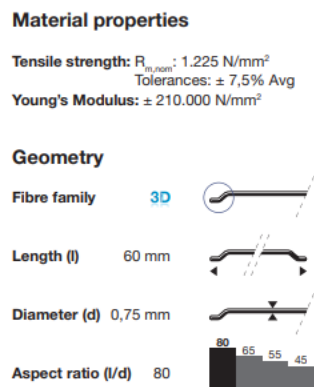


Fig.1. Fiber properties.

### 2.2 Concrete Mix Design and Materials

The concrete mix was designed using the tables and calculations provided in the standard EN-206 [1], [2]. Concrete mix design: Portland cement, sand, quartz, admixture silica fume, plasticizer, and water [16] [17] [18].

Table. 1 Mix proportion

Concrete Mixture		
S.No	Name of Ingredients	Quantity
1	Portland Cement (CEM II / 42,5 N)	2.8 kg
2	Micro silica 940-U	200 g
3	Sand (0-1 mm)	9.33 kg
4	Quartz QS 0-0.5 mm	1.67 kg
5	Plasticizer Sika D190	20 g
6	Water	2000 g

### 2.3 Collecting of fibers

In this portion of the investigation, we began by collecting every single fiber from the thermally treated concrete block (with dimensions 16.5×14.5×15cm). The block was shattered to obtain as much fiber as possible for each band width of one centimeter. To separate the fiber samples for further analysis, we shattered the block while

holding the samples, and they came out in various bits. We were especially concerned about preserving virgin fiber [19] [20] (see figure 2). For every fiber was fixed fibers central point distance from the surface subjected to open flame (heated surface).



Fig. 2. Collecting of fibers.

### 2.4 Examine of collected fiber

An Optical Microscope was used for fibers outer surface analysis. For more detail fiber surface analysis is possible to use Electron microscope facilities [21].



Fig. 3.1 Fiber from the non-heated end.



Fig. 3.2 Fiber from the heated end.

At figures 3.1 and 3.2 is possible to see two fibers. One was located in the layer with thickness 1cm from the surface subjected to the flame (figure 3.2). Second were removed from the 1 cm thick layer located at the surface of the block opposite to subjected to the flame (figure 3.1). Take a new sample of steel fiber with a cleanly cut edge and a smooth surface; the sample must be at least 6 cm in size. This sample is put under the microscope's lens, just below the view finder when viewed through the eye piece. Some analytical calculations are made to study the exact condition of fiber. After getting the clear inspection of the fiber, we can move for the next one [22].

### 2.5 Preparation of Specimens

Each block was divided into slices with thickness one and half cm. Were obtained 12 slices. 7 specimens (fibers, with central point located within the slice) for each band were obtained. Fibers removed from the concrete block were used in pull-out experiments. Were fabricated samples consisting of two concrete prisms separated by plastic film. Two prisms were connected by fiber immersed into concrete of both prisms. Initially all the concrete is mixed for the required amount no more concrete is prepared. Now the mold is ready for concreting, then concrete is poured inside the mold without steel fiber for the compression at the base for 100 mm initially, now the first frame is placed over the concrete mixture and tamped to adjust its levelling.



Fig. 4. Making of mixture.

For making the samples with fiber, fibers should be placed in the middle of the mold. So, every fiber is marked 3cm at the center and should be placed in the exact position. At first concrete is filled in each side of the specimen to check the placement fiber. Small amount of vibration is produced to remove the air molecules in the mixture. Now the opposite side of each sample is filled with the concrete and the same procedure will be followed as we did earlier. Now the cube mold is immediately covered with plastic wrapper and maintained in the laboratory where the relative humidity must be 90% but the inside temperature must be between 27, + or -2 degrees. The test samples are taken out from mold after 48 hours and are transferred to the laboratory for further curing process. The specimens must be protected from heavy temperature changes and shaking during the conveyance. Samples to be tested at one time and the average test results. The samples without fibers are considered for the compression test strength. Immerse the samples (without fiber) in the curing tank containing clean water until it is suitable for testing. The sample must be completely submerged, and more than the required water must be put down because the concrete specimen absorbs water during hydration.

### 2.6 Mechanical Testing Methods

After 28 days from the fabrication, the specimens were tested for fiber pull-out from the concrete matrix and compression test were performed. Test machine Zwick Roell Z150 was used to determine the fiber pull-out force and compression tests were done to measure the strength

of the concrete which we used to make the specimens. [23] [24]



Fig.5. Tensile strength machine setup.

## III. Experimental Results and Discussion

### 3.1 Compression Test

The cube should be positioned into the compression testing machine so that, its smooth faces land on the steel plate on the bottom side. The top surface of the finished cube must never be met with the machine's platens, as this generates unbalanced loading over the cube due to the uneven, rough surface, as opposed to the faces along the smoother side of the mold [25] [23] [26].

For cube test, standard dimensions (are commonly recommended for cube testing), 10 x 10 x 10 cm were fabricated. The loading was performed without pausing and loads was increased constantly at a rate of 150 Kg/cm<sup>2</sup>/minute, till the concrete specimen develops cracks and breaks down or it was crushed [27]. Test results are shown in the table 2.

Table 2. Compression test results

Sample	Force N	Compressive Strength MPa
1.1	341.1	34.4
1.2	317.6	31.4
2.1	239.5	24.7
2.2	244	25.5
3.1	237.7	23.9
3.2	282.3	28.1
5.1	218.8	22.8
7.1	235.7	23.7
8.1	272.3	26.7
8.2	266.1	26.5
Average		26.77

From the obtained results we can observe that the average compressive strength is 26.77 MPa, that is a good value for concrete under compression with no reinforcement and aggregates.

### 3.2 Fibers Pull-Out

Results shows the process of pulling out of seven Dramix steel fibers from the concrete matrix and indicate the average values of the peak pull-out load. Before starting the testing, all concrete samples are marked with their number and band width to identify it easily [24]. In the starting load is up to 30N fibers were in the matrix without any pull-out. Afterwards force reaches 150 N then fiber starts to slide. This reaction on the fiber is due to its shape because it is 3D 80/60BG, so it has bended ends on both sides [28] [18] [29].

Table 3. Pull out results of fiber from non-heated end

Sample	Force N	Strength MPa
1	639.34	135.67
2	607.00	128.81
3	673.89	143.00
4	682.48	144.82
5	704.41	149.48
6	595.54	126.37
7	566.08	120.12
<b>Average</b>		<b>135.47</b>

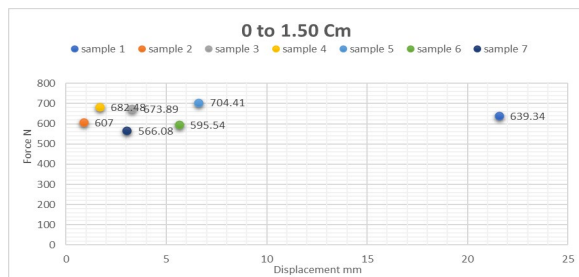


Fig.6. Force and Displacement graph for fibers obtained from first slice (0 to 1.50 cm).

Jumps in the force value may be observed during the entire pullout, this could be explained by the fact that spalling microparticles of the concrete matrix are pulled with friction-forming plugs, and that SF and concrete matrix are bonded together via a weak interface. The investigation of this interfacial behavior is critical for understanding the mechanical behavior of SFRC.

Table 3. Pull out results of fiber from heated end

Sample	Force N	Strength MPa
1	133.9	28.41
2	112.64	23.90
3	203.30	43.14
4	144.31	30.62
5	192.90	40.94
6	185.57	39.38
7	217.3	46.11
<b>Average</b>		<b>36.07</b>

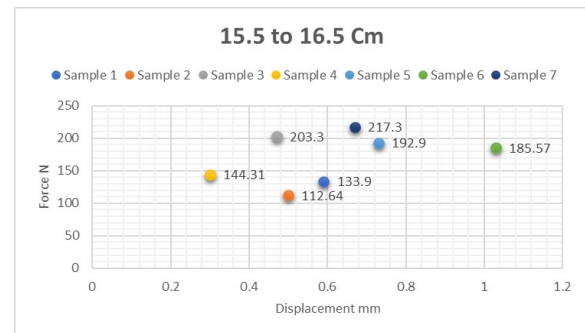


Fig.7. Force and Displacement graph for fibers obtained from last slice (15.5 to 16.5 cm).

### 3.3 Examine of tested samples

All the tested sample are collected and checked in the microscope again in order check the breakage of the fiber and to examine the surface crack of the fiber. For this process again, the same procedure is followed as was done earlier, all the fibers are viewed on the microscope and amazing images are picturized for the further analysis. Some of the images are shown below,



Fig. 8. Tested samples.



Fig. 9. Tested sample from non-heated end.



Fig.10. Tested samples from heated end.

From these pictures it is easy to notice that the oxidized layer in fiber from heated end has been destroyed during the bull-out friction applies and the core filament remains.

#### IV. CONCLUSION

1. Steel fiber degradation degree in the fiberconcrete slab depends on fiber location in the slab. Degradation was evaluated as pull-out load bearing capacity decrease.
2. Fibers located in the layer 0 to 1.5cm from the surface subjected to open flame had 3.76 times lower load bearing force comparing with fibers located in the layer 16.5 to 18cm from the surface subjected to open flame.
3. Microscopical analysis shown. Each fiber in the fiberconcrete slab, subjected to open flame is becoming "softer" yield stress is slightly decreases. Outer surface of every fiber is subjected to oxidation. Oxide has bigger volume, fiber is increasing in diameter. Oxide strength is much lower comparing with steel yield stress.

#### REFERENCES

- [1] X. K. A. W. S. Destrée, Fire Resistance of Steel Fibre Reinforced Concrete Elevated Suspended Slabs: ISO Fire Tests and Conclusions for Design, RILEM Bookseries, 2021.
- [2] X. K. A. K. J. Destree, "Fire resistance of steel fibre R. C. elevated suspended slabs: ISO fire tests and conclusions for design," in *Concrete Structures for Resilient Society*, 2020.
- [3] V. A. K. K. A. Lusic, "Concrete Reinforced by Hybrid Mix of Short Fibers under Bending," *fibers open Access*, no. MDPI, 2022.
- [4] H. P. Behbahani, "Steel Fiber Reinforced Concrete: A Review," *Published at ICSECM*, 2011.
- [5] M. P.-F. Tomasz Błaszczczyńska\*, "Steel fibre reinforced concrete as a structural material," *Operational Research in Sustainable Development and Civil Engineering - meeting of EURO*, 2015.
- [6] M. Gambhir, "Concrete Technology," *Tata McGraw-Hill*, 1995.
- [7] A. L. A. K. A. S. R. L. V. Macanovskis, "Composite fibers in concretes with various strengths," *ACI Materials Journal*, 2018 .
- [8] M. Grzybowski, "Determination of Crack Arresting Properties of Fiber Reinforced Cementitious Composites," *Royal Institute of Technology, Stockholm, Sweden*, 1989.
- [9] C. C. D. Johnston, ". "Fibre Reinforced Concrete.", " *Progress in Concrete Technology CANMET, Energy, Mines and Resources.*, 1982.
- [10] J. N. a. A. Kohoutková, "Fibre reinforced concrete exposed to elevated," *IOP Conf. Series: Materials Science and Engineering*, 2017.
- [11] G. Vitt, "Crack control with combined reinforcement," *Concrete Engineering International, issue 4,*, p. , 2005.
- [12] S. K. Sarna, "steel reinforcement bars and its important characteristics," *Ispatguru* , 2007.
- [13] C. K. Nmai, "REINFORCEMENT FOR CONCRETE-MATERIALS AND APPLICATIONS," *Materials for Concrete Construction, ACI Education Bulletin E2-00*, 2006.
- [14] I. P. Qian Chunxianga, "Properties of high-strength steel fiberreinforced concrete beams in bending," *Cement and Concrete Composites*, 1999.
- [15] D. Singh, "Thermal Properties of Concrete," *Indian Journal of Research*, 2014.
- [16] J. & B. G. Romualdi, "Mechanics of crack arrest in concrete with closely spaced reinforcement.," *Journal of the Engineering Mechanics Division., EM3. Proceedings of the American Society of Civil Engineers*, 1963.
- [17] B. V. D. K. A. Krishna Kiran Annamaneni, "Concrete, Reinforced By Carbon Fibre Composite Structure, Load Bearing Capacity During Cracking," in *Environment. Technology. Resources, Rezekne, Latvia*, 2021.
- [18] D. Y. J. Amit Rai, "Applications and Properties of Fibre Reinforced Concrete," *Amit Rai et al Int. Journal of Engineering Research and Applications*, 2014.
- [19] L. V. David Dupont, "Distribution of steel fibres in rectangular sections," *Cement & Concrete Composites*, 2005.
- [20] Z. P. B. a. M. F. Kaplan, "Concrete at High Temperatures: Material Properties and Mathematical Models," *Longman Group Limited, Essex, UK*, , 1996.
- [21] A. Haloi, " Application of Electronic Microscope Technique in Anthropological Research.," *The Anthropologist*, 21(1), 331-340., 2017.
- [22] Y. D. a. K. G. Luchun Yan, "Analysis of Environmental Factors Affecting the Atmospheric Corrosion Rate of Low-Alloy Steel Using Random Forest-Based Models," *Materials*, 2020.
- [23] A. M. Neville, " "Hardened Concrete: Physical and Mechanical Aspects", " , *ACI Monograph No. 6, ACI, Detroit.*, pp. pp 37-56, 1971.
- [24] B. Mather, " Faxed Letter to Vondran,," *U.S. Department of the Army. Vicksburg*, pp. pp 1-3, 1994.
- [25] F. F. Wafa, "Properties and Applications of Fiber Reinforced Concrete," *JKAU: Eng. Sci., Vol. 2, pp. 49-6*, 1990.
- [26] S. F. Ansel Ugural, *Advanced Mechanics of Materials and Applied Elasticity 6th edition*, International Series in the Physical and Chemical Engineering Sciences, 2019.
- [27] G. Williamson, "Response of Fibrous-Reinforced Concrete to Explosive Loading," *U.S. Army Engineer. Division* , pp. Technical Report No. 2-48, 1966.
- [28] P. P. K. a. G. L. Vondran, "DIRECT TENSILE STRENGTH TESTING AT 6 HOURS OF FIBER REINFORCED CONCRETE MORTAR FRACTIONS," in *Testing of Fiber Reinforced concrete*, American Concrete Institute, 1995, pp. 153-170.
- [29] \*. O. K. 1. A. M. 1. R. S. 3. I. L. 1. Vitalijs Lusic 1, "Experimental Investigation and Modelling of the Layered," *Fibers*, no. MDPI, 2021.

# Design and Production of a Device for Basing and Fixing Conic Details in Sine Bar Measurements

**Pavlinka Katsarova**

Mechanical and Instrument  
Engineering, Faculty of Mechanical  
Engineering  
Technical University of Sofia, branch  
Plovdiv  
Plovdiv, Bulgaria  
p\_katsarova@abv.bg

**Kliment Georgiev**

Mechanical and Instrument  
Engineering, Faculty of Mechanical  
Engineering  
Technical University of Sofia, branch  
Plovdiv  
Plovdiv, Bulgaria  
k.georgiev@tu-plovdiv.bg

**Adelina Vasileva**

Mechanical and Instrument  
Engineering, Faculty of Mechanical  
Engineering  
Technical University of Sofia, branch  
Plovdiv  
Plovdiv, Bulgaria  
adelina.bogoeva@abv.bg

**Marin Dimitrov**

odelo Bulgaria EOOD  
Kuklen, Bulgaria  
marin\_77n@abv.bg

**Abstract.** The geometric features of the conical parts measured by a sine bar requires special devices for basing and fastening. Basing and fixing conical parts on a sine bar is a problem that can lead to deviations in measurements. In the presented study, a fixture for fixing and basing conical details when measuring with a sine bar is designed and manufactured. The device is designed to facilitate the work of the operator in fixing the workpiece during the measurement, which increases the accuracy of the measurements. The developed structure is designed using SolidWorks. After the completion of the 3D model, a choice of material and technology for 3D printing is made. After that, a 3D printer is used for its production. The manufactured device is tested in laboratory studies. The designed device is installed on the sine bar without changing the measurement methodology. The conducted experiments prove its workability and applicability.

**Keywords:** design, fabrication, 3d printing, 3d modelling, device, measurement, operability.

## I. INTRODUCTION

In production practice, the control of conical details is one of the complex metrological tasks. The existing measurement and control methods are divided into three groups:

- qualitative assessment methods;
- Goniometric methods;

- Trigonometric methods;

In the present study trigonometric methods are used to control an external conical detail through the use of a sine bar.

A standard sine bar is a steel bar that is used with two properly spaced cylinders that may or may not be fastened to it. The axes of the cylinders are parallel to the adjacent sides of the sine bar and are located at a definite distance apart, usually 100, 200 and 300 mm. An angle is generated by putting different gauge blocks under the cylinders, as shown in "Fig. 1" [1].

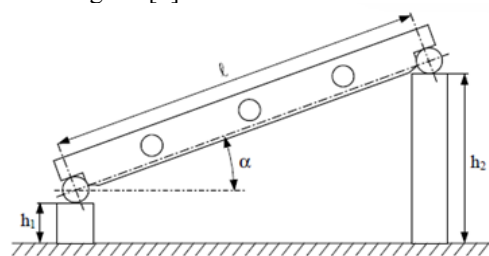


Fig 1. Standard sine bar.

$$\sin \alpha = (h_2 - h_1)/L \quad (1)$$

The most important influence on the generated angle uncertainty is parallelism deviation between the two cylinders. Too short distance between the

Print ISSN 1691-5402

Online ISSN 2256-070X

<https://doi.org/10.17770/etr2023vol3.7178>

© 2023 Pavlinka Katsarova, Kliment Georgiev, Adelina Vasileva, Marin Dimitrov.

Published by Rezekne Academy of Technologies.

This is an open access article under the [Creative Commons Attribution 4.0 International License](https://creativecommons.org/licenses/by/4.0/).

cylinders are another important influence. This fact has two consequences:

- angle changes smaller than 3.3 μm/m cannot be generated;
- the uncertainty of the gauge block calibration has a significant influence on the result;

There are several measuring methods of the taper angle of the cone, such as coloring, cylinder block, two groups of cylinders with different diameters, two spheres of different diameter measurement within the taper angle of the cone, two different diameter of the ball and the gauge block measurement taper angle, sine bar measuring taper angle. The sine bar measuring the angle of the cone is commonly [2].

The sine bar is a precision measuring tool which is used for indirect measurement or machining of precision angle by the principle of sine function. The sine bar Commonly is used to measuring the taper angle of the inner and outside cone and the head diameter of the cone, and can also measuring angle block angle, the angle between hole center line and a plane, and being a machining fixture of precision parts, especially which is the most common in the measurement of the taper angle. The sine bar can measure outside taper angle, inner taper angle, taper angle of the cylindrical cone, taper angle of the synthetic cone, taper angle of the different to cone, but the formulas of gauge which we use dimension of gauge block is different. If the dimension of gauge block size is wrong and it will directly affect the accuracy of the measurement results, so we need to clear each measurement of the dimension of gauge block size [2].

The sine bar is divided into two kinds of narrow and wide, and according to the structure of each type, they are divided into three kinds of 100mm, 200mm and 300mm. As shown in “Fig. 2”, we can see  $\alpha = \alpha_1$  by the geometrical knowledge. Based on the principle of trigonometric functions, we can see:

$$\sin \alpha = \frac{CO_1}{OO_1} = \frac{BO_1 - BC}{OO_1} = \frac{h + R - R}{L} = \frac{h}{L} \quad (2)$$

So, we know that:

$$\sin \alpha = \frac{h}{L} \quad (3)$$

In equation (3)  $\alpha$  is the nominal value of the angle of the workpiece, and  $L$  is the distance between the centers of the two cylinders of the sine bar (mm)[2].

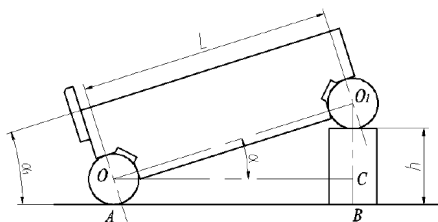


Fig. 2 Measurement principle of sine bar [2].

The methods shown in “Fig. 3” is a sine bar with a conical detail attached to it and placed on a test plate. One roller of the ruler rests on the table and the other on a block of gage blocks of the size  $h$ . The size  $h$  of the gage block is calculated in advance so that the ruler is tilted at an angle equal to the nominal value of the measured angle -  $\alpha$ . In this case, basic equipment is used to fasten the detail. The equipment for fastening the conical part is additionally made according to the views and capabilities of the operator. To achieve the required accuracy when measuring with a sine bar, it is necessary to have the measured parts fixedly attached to the sine bar[3].

Accurate and easy fixing of the controlled workpiece is one of the problems related to the operator's work when measuring with the sine bar.

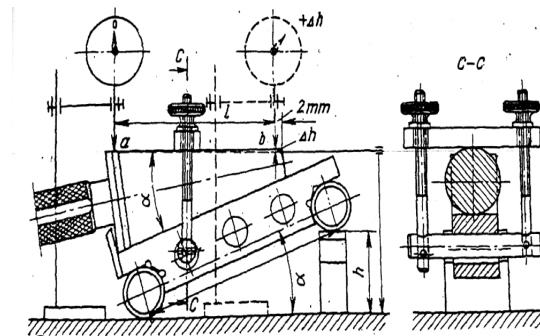


Fig. 3 principal measurement of a taper angle of outer cone with sine bar [3].

The measurement process after fixation of the workpiece follows the dependencies:

$$\sin \alpha = h/L \quad (3)$$

The size of the gage block is calculated from by the formula:

$$h = L \cdot \sin \alpha \quad (4)$$

The conicity of conical detail is determined indirectly by measuring misalignment  $\Delta h$  at a certain length  $l$ . For this purpose, a stand with a dial indicator is used, and the measurement is made at the two end points  $a$  and  $b$  at a on the surface of the detail. The deviation  $\Delta C$  from the nominal taper angle is calculated using the formula [3]:

$$\Delta C = \Delta h/l \quad (5)$$

In „Fig. 4” shows an exemplary fastening of a conical detail measured with a sine bar. This type of attachment does not provide sufficient reliability during measurement, which increases the errors and complicates the operator's work.



Fig. 4 Basing a detail on a sine bar.

The reliable fixation of the details on the sine line is of a considerable importance for the accuracy of the measurements.

In the present work, a possible solution to the problem of fixing conical details on a sine bar is presented. A special device is designed and manufactured for fastening conical details on a sine bar. The developed device is developed using SolidWorks. After the completion of the 3D model, a choice of material and technology for 3D printing is made. After that, a 3D printing technology is used for its production. The device has a simple design, easy to make and to use, also it has a low cost due to the materials and technology used.

## II. MATERIALS AND METHODS

### A. Materials

The materials used in FDM (fusion deposition modeling) technology parts are very close to conventional engineering polymers, so the suitability of the base materials is not an issue. The main difference between an FDM part and a molding is the fact that it is built in layers, which means that the inherent strength of the part will be slightly lower in the 'Z' (vertical) direction. The partial layers are relatively large - between 0.13 mm and 0.33 mm. This can lead to quite rough surfaces before surface treatment [4].

The selected material must meet the requirements for dimensional accuracy, minimum lead time and wall thickness of the structure.

Some of the most important properties when choosing materials for 3D printing are: Tensile, Bending and Tearing Strength, Modul of Elasticity and Flexibility, Elongation, Compressive Stiffness, Shrinkage, Moisture Adsorption, Heat Deformation Temperature (HDT), Point of Vicca softening and coefficient of thermal expansion [5].

When choosing a material, the requirements for dimensional accuracy, minimum execution time and wall thickness of the structure must be considered. The types of materials used in 3D printing are extremely numerous, but the chosen 3D printing technology limits us to a few materials. Since we have no special requirements for the device itself for the initial prototype, we will use PETG

(Polyethylene Terephthalate) filament with dimensions of  $1.75 \text{ mm} \pm 0.03 \text{ mm}$  as the most cost-effective material. PETG material is a thermoplastic type which has low shrinkage, strong, not brittle, and mostly layer adhesion is fantastic [6].

PETG is a polyester copolymer that has excellent technical specs like: durability, flexibility, high impact resistance, high chemical resistance, low moisture absorption and others [7]. Technical specifications of the selected material are listed in table 1 and table 2.

TABLE 1 TECHNICAL SPECIFICATION OF PETG [8]

Chemical name	Polyethylene Terephthalate Glycol Copolymer
Melting temperature	210-260 °C
Working temperature (3d printer)	250 ±10 °C
Print bed temperature	80 ±10 °C
Print speed	up to 200 mm/s
Moisture Absorption in 24 hours	0.07 %
Moisture Absorption in 7 days	0.10 %
Heat Deflection Temperature (0.45 MPa)	68 °C
Heat Deflection Temperature (1.80 MPa)	68 °C
Density	1.2 g/cm <sup>3</sup>
Tensile strength	46 ±1 MPa
Interlayer Adhesion	18 ±4 MPa
Hardness – Shore D	74

TABLE 2 MECHANICAL PROPERTIES OF 3D PRINTED SPECIMENS [8]

Property\Print Direction	Horizontal	Vertical xz	Method
Tensile Yield Strength [MPa]	47 ± 2	50 ± 1	ISO 527 - 1
Tensile Modulus [GPa]	1.5 ± 0.1	1.6 ± 0.1	ISO 527 - 1
Elongation at Yield Point [%]	5.1 ± 0.1	5.1 ± 0.1	ISO 527 - 1
Flexural Strength [MPa]	66 ± 2	70 ± 1	ISO 178
Flexural Modulus [GPa]	1.7 ± 0.1	1.6 ± 0.1	ISO 178
Deflection at Flexural Strength [mm]	9.0 ± 0.1	9.3 ± 0.2	ISO 178
Impact Strength Charpy [kJ/m2]	No break	No break	ISO 179 - 1
Impact Strength Charpy Notched [kJ/m2]	6 ± 1	3 ± 1	ISO 179 - 1

### B. Methods

The ISO / ASTM 52900 standard categorizes all the different types of 3D printing. The 3D printing technology chosen for the designed device is fused deposition modeling (FDM) "Fig 5". It is an additive manufacturing method where layers of materials are fused together in a pattern to create an object. FDM is the most cost-effective way to produce custom thermoplastic parts and prototypes.

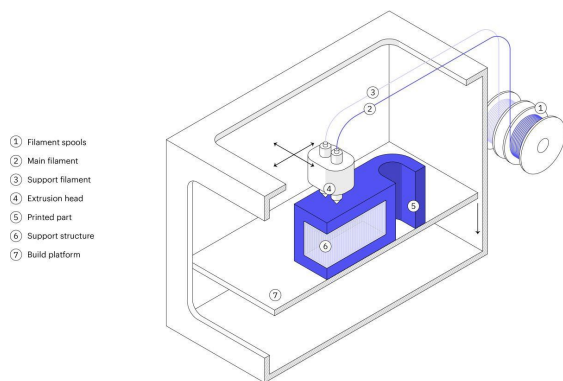


Fig 5. Schematic diagram of FDM technology.

A wide range of thermoplastic materials is available for FDM, suitable for both prototyping and some functional applications [9].

As a limitation, FDM has the lowest dimensional accuracy and resolution compared to other 3D printing technologies. FDM parts have visible lines, so for treatment on a smooth surface, subsequent mechanism is often required. In addition, the adhesion mechanism of the layer makes FDM particles inherently anisotropic. They are weaker in one direction and are unsuitable for critical applications [10].

The device used is: Prusa i3 MK3S + with additional modification for better levelling of the printer bed is shown at “Fig. 6”.



Fig. 6. Prusa i3 MK3S+.

The design of the device is done using SolidWorks. A three-dimensional model- “Fig. 7” of the Sine bar with the optimization is created - the new device /prototype/, which consists of 6 elements:

- COVER, tightly enveloping the walls of the sine bar, attached to it by PINS /1 large and 2 pcs. small pins/ snug fit in the matching process holes of the casing and the sine bar.
- STOPPER COMB, attached to the cover, in the recesses of which comb rests the so-called STOPPER.
- ARC WITH GUIDES, moving along guide channels located on both sides of the cover,

which serves to fix the measuring cone to the face of the sine bar.

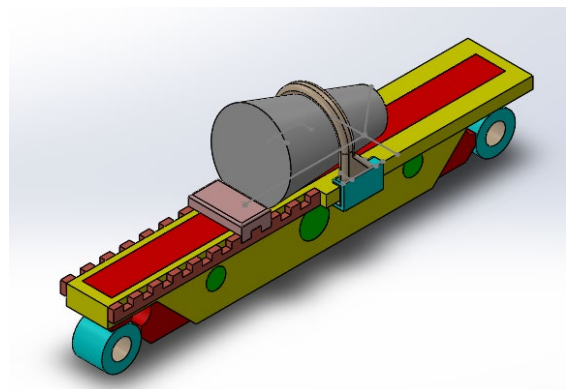


Fig. 7 3D model of the device.

“Fig.8” shows the positioning of the model on the printer table. The position of the workpiece on the printer table influences the strength of the workpiece and obtains good adhesion. Good adhesion plays an important role in the construction of the first layer. This can be improved by using a heating plate heated to 95° for PETG.

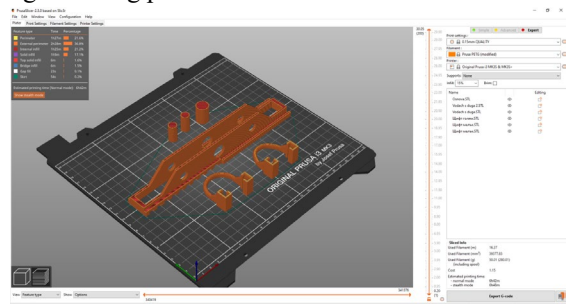


Fig .8 Details positioned on the print bed.

Setup and calibration of the printer is done immediately before starting the manufacturing process.

The purpose of the X/Y/Z calibration procedure is to measure the misalignment of the X/Y/Z axes and find the position of the 4 calibration points on the print bed for proper bed alignment. XYZ calibration can be started from the Calibration menu on the LCD panel.

The initiation of this established order performs a series of measurements in three rounds: In the first round, without the steel sheet installed, 4-sensor points on the print bed are carefully searched so as not to touch the print bed with the nozzle. In the second round, the points are improved. In the last round, with the steel sheet on, the height over 9 sensor points is measured and stored in non-volatile memory for reference. This completes the Z-axis calibration.

Mesh bed alignment can be found in LCD Menu - Calibration. This procedure is performed before each print.

During the design, all the elements of the device were made separately, but subsequently the Cover “Fig. 9” and the stopper comb as well as the Arc with the guides “Fig. 10” are assembled for easier and faster 3D printing.

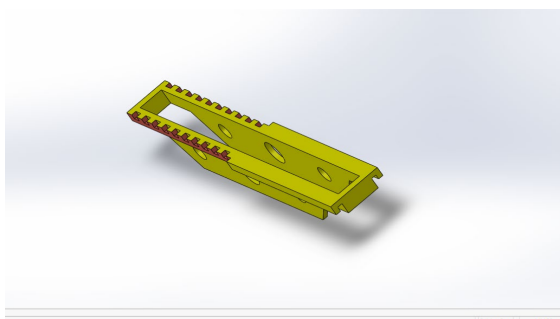


Fig.9 Cover.

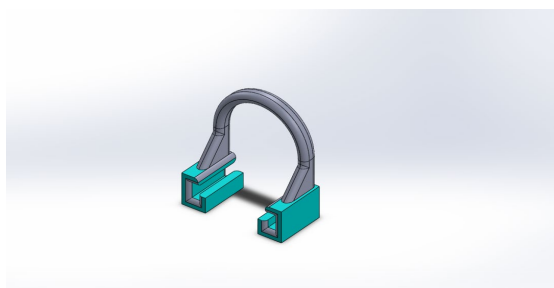


Fig. 10 Arc with guides.

In “Fig. 11” shows a manufactured device mounted on the sine bar. The fixture rests firmly on the sine bar and no clearance is observed between the sine bar and the device.



Fig.11 The device mounted on a 200mm sine bar.

### III. RESULTS AND DISCUSSION

While conducting the laboratory experiments, a sine bar with the length of 200 mm is used. Three conical details with a nominal angle  $\alpha = 5^\circ$  are measured. The data of the measured cones are listed in table 3

TABLE 3 CONE PARAMETERS

Cone №	Angle, [°]	Length, [mm]	min diameter, [mm]	max diameter, [mm]	Calculated angle, [°]
1	5°	80.00 mm	22.61 mm	29.91 mm	5° 13' 1''
2	5°	79.56 mm	22.55 mm	29.75 mm	5° 10' 48''
3	5°	79.90 mm	22.55 mm	29.82 mm	5° 12' 36''

For the laboratory experiment, a test plate with a dial indicator placed on it is used.

The sine bar with a workpiece attached to it is placed on the test plate. One roller of the ruler rests on the test plate and the other on a block of gage blocks of the size  $h$ . The size  $h$  of the gage block is calculated, so that the ruler tilts at an angle equal to the nominal value of the measured angle  $\alpha$ . If the angle being checked is equal to the nominal one, the conical part will be parallel to the test plate on which the ruler is located.

Dependency is used for this purpose:

$$\sin \alpha = h/L \quad (3)$$

Where,

$$h = L \cdot \sin \alpha \quad (4)$$

Where  $L$  is the distance between the axes of the two rollers on the sine bar,

$$h = 200 \cdot \sin 5 \quad (4)$$

$h = 17.43$  mm is the gage block size that needs to be made.

The conicity of conical parts is determined indirectly by measuring misalignment  $\Delta h$  of a certain length  $\ell$ . For this purpose, a stand with a dial indicator is used and the measurement is made at two endpoints  $a$  and  $b$ , which are 2mm apart from the workpiece faces. The distance  $\ell$  is between the two points  $a$  and  $b$  is obtained – the length of the cone minus 4 mm. The deviation from parallelism is measured with a dial indicator attached to a stand which is moved on the test table.

The measurement of the workpiece begins by placing the dial indicator in contact along the axis of the cone 2 mm from its major diameter. Then the dial indicator resets. After that, the sine bar is rotated, so dial indicator is located on the surface of the small diameter of the cone “Fig. 12”, and the value of  $\Delta h$  is measured.

The deviation  $\Delta C$  from the nominal taper angle is calculated according to the formula:

$$\Delta C = \Delta h / l \quad (5)$$

$$\Delta \alpha = \frac{\Delta h}{l} \cdot 3438 \text{ [min]} \quad (6)$$

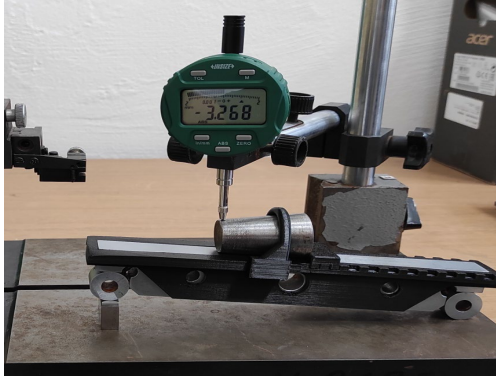


Fig.12 Measurement setup.

The results of the measurements and deviations  $\Delta C$  and  $\Delta \alpha$  are presented in table 4.

TABLE 4 RESULTS

Cone №	$\Delta h$ , [mm]	$\Delta C$ , [mm]	$\Delta \alpha$ , [°]	Calculated angle, [°]	Actual angle, [°]
1	0.146 mm	0.0019 mm	6.53 °	5° 13' 12"	5° 6' 38"
2	0.208 mm	0.0028 mm	9.63 °	5° 10' 48"	5° 9' 27"
3	0.153 mm	0.0020 mm	6.88 °	5° 12' 36"	5° 6' 55"

The conducted experiments confirm the operability of the designed device. It is easy to use and improves the accuracy of measurements.

#### IV. CONCLUSIONS

- 1) The designed fixture significantly improves the operation of the device and allows the measurement of parts of various sizes.
- 2) The technology of additive printing and materials used improves the fast and cheap production of functional prototypes and devices.

- 3) The accuracy and quality of the manufactured device increases the accuracy of the results.
- 4) The manufactured device ensures immobility when measuring the controlled cone, facilitates the operator's work and reduces measurement errors.
- 5) Experiments carried out in real laboratory conditions confirm the functionality of the device.

#### ACKNOWLEDGEMENTS

The author/s would like to thank the Research and Development Sector at the Technical University of Sofia for the financial support."

#### REFERENCES

- [1] Acko, B. (2005). Calibration of electronic levels using a special sine bar. *Precision engineering*, 29(1), 48-55.
- [2] Kan, P., & He, M. (2015, December). Analysis and calculation of dimension of gauge block in sine bar measuring taper angle. In *2015 Joint International Mechanical, Electronic and Information Technology Conference (JIMET-15)* (pp. 725-729). Atlantis Press.
- [3] Дойчо Д. Димитров. Взаимозаменяемост, стандартизация и технически измервания- Четвърто издание, Издателство „Техника“ София 1994.
- [4] Mike Ayre. 3D printing for manufacture: a basic design guide. Available on 20.06.22 at: <https://www.crucible-design.co.uk/images/uploaded/guides/3d-printing-for-manufacture-a-basic-design-guide-download-original.pdf>.
- [5] Shahrubudin, N., Lee, T. C., & Ramlan, R. J. P. M. (2019). An overview on 3D printing technology: Technological, materials, and applications. *Procedia Manufacturing*, 35, 1286-1296.
- [6] Durgashyam, K., Reddy, M. I., Balakrishna, A., & Satyanarayana, K. (2019). Experimental investigation on mechanical properties of PETG material processed by fused deposition modeling method. *Materials Today: Proceedings*, 18, 2052-2059.
- [7] Valvez, S., Silva, A. P., & Reis, P. N. (2022). Optimization of Printing Parameters to Maximize the Mechanical Properties of 3D-Printed PETG-Based Parts. *Polymers*, 14(13), 2564.
- [8] Prusament PETG Technical data sheet, available at: <https://www.prusa3d.com/product/prusament-petg-jet-black-2kg/>, 20.03.2023.
- [9] Dudek, P. F. D. M. (2013). FDM 3D printing technology in manufacturing composite elements. *Archives of metallurgy and materials*, 58(4), 1415-1418.
- [10] <https://www.3dsolid.eu/2019/09/25/procesi-v-3d-printirane/>. Available on July 2021.

# 3D Model of the Mechanical Part of a Weed Recognition System in an Agricultural Robot in 3D Experience Environment

**Kehayov Evgeni Lyubomirov**  
Agricultural Mechanization  
Agricultural University  
Plovdiv, Bulgaria

**Ivanov Georgi Borisov**  
Agricultural Mechanization  
Agricultural University  
Plovdiv, Bulgaria

**Komitov Georgi Georgiev**  
Agricultural Mechanization  
Agricultural University  
Plovdiv, Bulgaria

**Abstract.** The damage from weeds in the cultivation of agricultural crops is ubiquitous and they adversely affect the yields of agricultural production. The soil conditions of the places where the crops are grown deteriorate. Contribute to the development of diseases and the enemies on them. Apart from this, it is difficult to carry out mechanized processing and harvesting activities. Weeds also worsen the very quality of the harvested produce. That is why the availability of a recognition system to the agricultural robot is essential to reduce the adverse influence. It is part of a system of control and destruction. In this weed recognition system, an essential element is a robotic arm to enable a camera to perform video surveillance.

The aim of this paper is to modelling only the mechanical anchorage system for weed recognition elements that it does not interfere with the other elements with which it interacts. To be as effective as possible, this system must be as close as possible to the plants and at the same time close to the weed eradication system in agricultural robot.

A three-dimensional model of the weed recognition mechanical parts from system is discussed in the paper. It is designed in a 3D Experience environment, taking into account the parameters necessary for the movement of the system. Strength sizing of the structure and working simulations of the model were made.

**Keywords:** 3D model, agricultural robot for weed control, mechanical systems, strength sizing, weeds recognition.

## I. INTRODUCTION

Robots are successfully used in a variety of industries, especially those that are unattractive due to high demands on output, heavy physical labour, and low wages [1, 2]. In such conditions, agricultural robots also work – moisture, strong heat. Agricultural robots have a number of operations, such as sowing, cultivation and harvesting.

Work on these complex tasks is greatly facilitated in the use of machine vision and decision-making [3].

In the cultivation of crops, in addition to cultivated plants, weeds also grow in the soil. This creates big problems because the yields of crop plants are reduced, crops are destroyed and prerequisites for the growth of other weed species are created [4]. Weed control is a complex and costly task to begin with. Using an agricultural robot without human intervention requires serious knowledge of these weeds [5]. Weed control by robot will improve conditions in modern agriculture. The elements of the machine vision system should be placed on an equipped manipulator, as close as possible to the plant and to the work equipment [6].

The time for the creation of the weed recognition system would be shortened by using CAD modelling in the creation of the mechanical part of the system [7].

In this paper a three-dimensional model of a mechanical part of the weed recognition system is developed. It is necessary because it is part of the weed eradication system to an agricultural weed control robot. The mechanical part must be stable, carry the recognition elements themselves (the camera), and be part of the weed destruction system, while being close to the plants. It should not be influenced temperature by the heat flux in the destruction of weeds. The three-dimensional model was designed through the use of a CAD product, and some of the elements were strength sized.

## II. MATERIALS AND METHODS

The design of a mechanical part of a weed recognition and control system in this paper is reduced to the

Print ISSN 1691-5402

Online ISSN 2256-070X

<https://doi.org/10.17770/etr2023vol3.7289>

© 2023 Evgeni Lyubomirov Kehayov, Georgi Borisov Ivanov, Georgi Georgiev Komitov.

Published by Rezekne Academy of Technologies.

This is an open access article under the [Creative Commons Attribution 4.0 International License](https://creativecommons.org/licenses/by/4.0/).

development of a three-dimensional model of the system, where all the peculiarities of the process are taken into account. The recognition system consists of a camera located at a certain focal length from the plants. The camera is part of a machine vision system that directs the robot onto the weeds. The robot crosses the rows with different crops, monitoring for weed recognition. The camera data is compared with a machine-learning database and the tines perform weed removal activities.

The robot that is mounted for the weed recognition and control system is an existing self-propelled wheel with a 4x4 wheel formula. It has a variable transverse base and working height. The robot is implemented under the task of the national scientific program "Intelligent Plant Growing" in Bulgaria. The robot and the designed system are part of a patent proposal submitted to the Patent Office of Bulgaria.

In the present paper, only the mechanical weed recognition system is considered. It is part of a weed control system including an agricultural robot, a system for destroying weeds by heating, an electronic control system for weed recognition based on machine learning, a mission control system, etc.

The presented mechanical system is installed at the bottom of the robot, under its body, to be as close as possible to the plants.

The design of the mechanical part and the preparation of a 3D model is carried out on the CAD product CATIA V5, and the strength sizing was carried out through the 3D Experience development environment in the CAD laboratory of the Agricultural University – Plovdiv, Bulgaria.

### III. RESULTS AND DISCUSSION

The developed model of the mechanical part of the weed recognition and control system is shown in Fig. 1 and Fig. 2.

Fig. 1 shows the top view of the system. It consists of a 10 plate. The plate is aluminium and is fastened to the agricultural robot under its body through 14 screw M8. The plate is 4 mm thick and 500 x 500 mm in size and is consistent with the robot body gauge.

On the plate is attached the base 2, to which is connected servo motor 1. The base is made of three aluminium parts. Of these, two are vertical and one cylindrical horizontal for attachment to the plate. At one end of one vertical detail there is a separate place for fastening the servo motor. It is a product of the company "FEETECH" - FT 6560 M. The servo motor has the following parameters [8]:

Torque – 5.88 Nm; Operating voltage – 7,4 V;  
Mass – 0,2 kg; Speed – 0,15 s/60 degree.

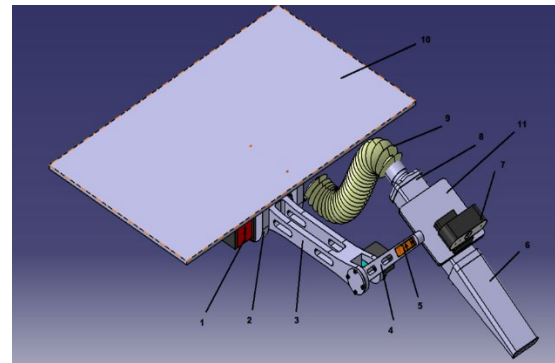


Fig. 1. Top view of the 3D model: 1, 5 – servo motors; 2 – base; 3- long shoulder; 4 – short shoulder; 6 – working tip; 7 – camera; 8 – rear tip; 9 – aluminium sleeve; 10 – plate; 11 – working plate.

The long arm 3 is attached to the servomotor by means of flanges and bearing support (in the other vertical aluminium detail). The flanges give torque to drive the arm. The bearing support is provided by the plate 1 (Fig. 2). It also serves to secure the aluminium sleeve 9. The long arm is made of PLA material by 3D printing [9,10].

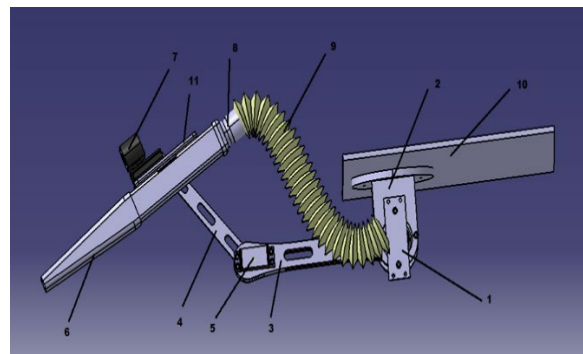


Fig. 2. Side view of the 3D model: 1 – plate; 2 – basis; 3- long shoulder; 4 – short shoulder; 6 – working tip; 7 – camera; 8 – rear tip; 9 – aluminium sleeve; 10 – plate; 11 – working plate.

It serves to position the system in a vertical position. At the other end there is a separate place for attaching servo motor 5 (Fig. 2) MG 996 R. The servo motor has the following parameters [11]:

Torque – 0,92 Nm; Operating voltage – 4,8 - 7,2 V;  
Mass – 0,055 kg; Speed – 0,17 s/60 degree.

Through flanges and bearing support, it drives the short arm 4 (Fig.1 and 2) of the system. The short arm serves for additional tilt system and more accurate positioning. It is also made by 3D printing. In the opposite of the flanges end of the arm is a separate bed for another servo motor 5 (Fig. 1). The servomotor is MG 90 S and has the following parameters [12]:

Torque – 0,18 Nm; Operating voltage – 4,8 - 6 V;  
Weight – 0.0134 kg; Speed – 0,1 s/60 degree.

The working plate 11 is attached to the servo motor (Fig. 1 and 2). It is aluminium [1] and the machine vision elements of the robot and the working bodies are fastened on it. The working plate measures 100 x 100 mm and has a thickness of 2 mm.

Machine vision is provided by camera 7 (Fig. 1 and 2). The camera is a product of HikVision DS-U02. It allows making frames with a resolution of  $1920 \times 1080 @ 30/25$  fps. This resolution allows to create frames for recognition by machine vision. It has a mass of 0.089 kg and operates in a temperature range of -10 0 -450 C at a humidity of up to 90% [13, 14].

The working parts 6 and 8 are made of stainless steel. They are used for weed control and are not relevant to this article. Fastening is by means of screws, and a thermal insulation pad is placed between them and the working plate. The aluminium sleeve 9 is attached to them.

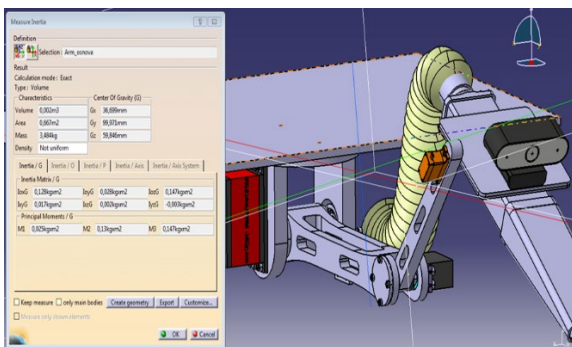


Fig. 3. Mass and moments of inertia of the 3D model.

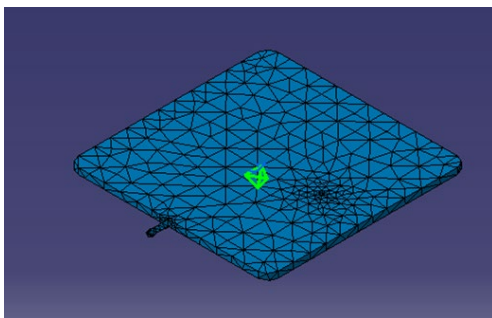


Fig. 4. Mesh for strength sizing of the working plate.

Fig. 3 shows the total mass of the system. It is 3.48 kg. The figure also shows the moments of inertia of the system along the three axes.

After 3D modelling of the system, strength sizing of the threatened parts is provided. These are the working plate, the long and short arm.

Initially, for convenience in the strength sizing of the parts, the work piece with the known parameters is based.

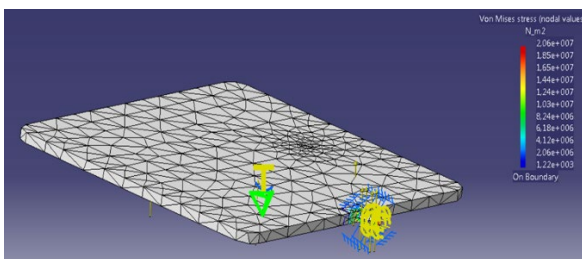


Fig. 5. Results of strength sizing of the working plate.

Fig. 4 shows the network for strength sizing of the working plate. The mesh is 8 mm in dimension, with absolute sagging set of 1,102 mm. As mentioned above, the plate is made of aluminium alloy 5052 [15].

Fig. 5 shows the results of the strength sizing of the working plate. In determining the load, the whole mass (of 0.91N) of all elements in contact with it was taken into account. The thermal load from the working members of 400 K was recorded. This temperature is without taking into account the thermal insulation coating between the plate and the working organ. The torque of 0.18 Nm generated by the servo motor was also recorded. As a result of the strength sizing, the threatened section is located in the axis for joining the servo motor and the maximum recorded load is 20.6 MPa, which is far from the limit values for aluminium alloy 5052 [15].

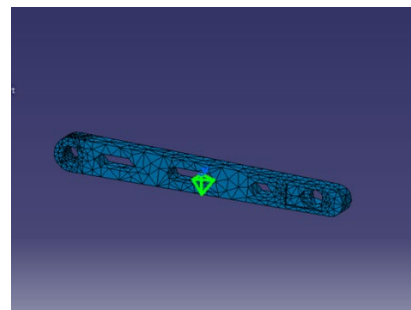


Fig. 6. Short arm strength sizing mesh.

The next detail that is subjected to strength sizing is the short arm. In Fig. 6 is given the general appearance and mesh of the work piece. The mesh used has a dimension of 12 mm, with absolute sagging set of 1,792 mm. To make the short arm was used PLA material printed at a nozzle temperature of 210°C when filling 100 % [9].

In Fig. 7 the data for the stress state analysis of the tested work piece are shown.

Here again all loads from the working plate and servo motor MG 90 S are recorded. In addition, however, the torque from the MG 996 R servo motor also enters the strength sizing. The servo motor drives the arm and the additional equipment to it. The threatened sections are located in the connection ports of the drive flanges from the servo motor. The maximum voltage that is obtained at the load thus set is 2.87 MPa, far from the limit values for the PLA material. In the figure, the software also notes the possible deformations of the material. As expected for this kind of detail this deformation is expressed in the zones of load change.

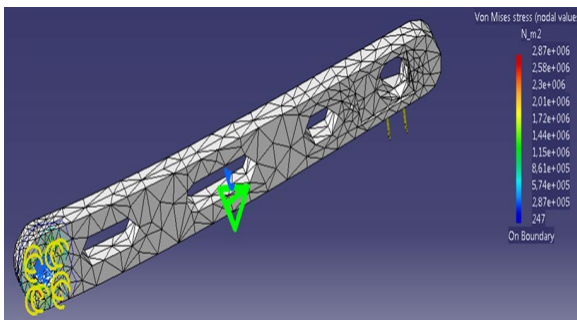


Fig. 7. Short arm strength sizing results.

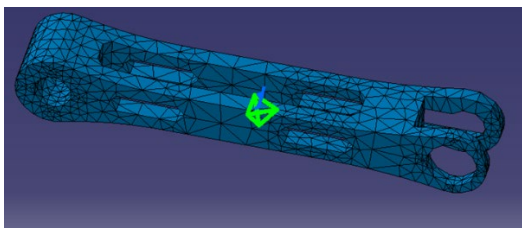


Fig. 8. Long arm strength sizing mesh.

Fig. 8 shows the mesh for the strength sizing of the long arm. The mesh used has a dimension of 16 mm, with absolute sagging set of 2,513 mm. PLA material printed at a nozzle temperature of 210 °C at 100 % filling is used to make the long arm again [9].

The analysis of the results of the strength analysis (Fig. 9) shows that the maximum load in the long arm is 0.57 MPa. This maximum stress is far from the limit for PLA materials [9]. It reappears in the zones of the connection flanges to the servo motor and support.

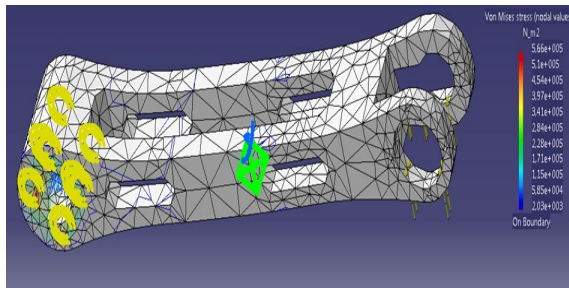


Fig. 9. Long arm strength sizing results.

#### IV. CONCLUSIONS

A 3 D model of the mechanical part of the weed recognition and control system was created. The limiting parameters in the development were an application in a self-propelled agricultural robot. The system has autonomy and can be integrated into other systems. The design of the system was carried out under CATIA V5. The mass of the designed system was reduced to 3.48 kg together with the work pieces.

To check the strength of the structure, three elements of the created 3D model of the mechanical part of the weed recognition and control system were dimensioned through the 3D Experience product.

Strength tests of the elements showed that the elements were properly sized and the structure was not loaded in strength. The maximum stresses generated in parts made of PLA materials are 2.87 MPa and 0.57 MPa, respectively, and in the aluminium work piece 20.6 MPa.

#### REFERENCES

- [1] W. Chung and K. Iagnemma, *Wheeled robots*, Springer Handbook of Robotics, pp. 575–594, 2016.
- [2] N. Reddy, A. Reddy, S. Pranavadihya and J. Kumar, A Critical review on agricultural robots. *International Journal of Mechanical Engineering and Technology (IJMET)*, 7(4), 183-188, 2016.
- [3] G. Vasconcelos, G. Costa, T. Spina and H. Pedrini, Low-Cost Robot for Agricultural Image Data Acquisition. *Agriculture*, 1-16. doi:https://doi.org/10.3390/agriculture13020413, 2023.
- [4] T. Kounalakis, G. Triantafyllidis and L. Nalpantidis, Weed Recognition Framework for Robotic Precision Farming. doi: 10.1109/IST.2016.7738271, 2016.
- [5] A. Kargar and A. Shirzadifar, Automatic weed detection system and smart herbicide sprayer robot for corn fields. *First RSI/ISM International Conference* (pp. 468-473), 2013.
- [6] A. Michaels, S. Haug and A. Albert, Vision-based high-speed manipulation for robotic ultra-precise weed control. 2015 *IEEE/RSJ International Conference* (pp. 5498–5505). *Intelligent Robots and Systems*, 2015.
- [7] B. Huang, S. Zhang, R. Huang, X. Li and Y. Zhang, An effective retrieval approach of 3D CAD models for macro process reuse. *The International Journal of Advanced Manufacturing Technology*(102), 1067–1089, 2019.
- [8] FEETECH, Model No.FT6560M. Specification of Product. China: FEETECH RC Model Co.,Ltd, 2023.
- [9] E. Yankov, MECHANICAL PROPERTIES OF PARTS OF PLA-NATURAL AS A FUNCTION OF THE TEMPERATURE OF THE 3D PRINTING BY FDM METHOD. *MACHINES. TECHNOLOGIES. MATERIALS*, 376-379, 2018.
- [10] E. Yankov and M. Nikolova, Orientation of the Digital Model for SLA 3D Printing and Its Influence on the Accuracy of the Manufactured Physical Objects for Micro- and Nano Technologies Materials Design and Applications II. *Advanced Structured Materials*(98), 283-291. doi:10.1007/978-3-030-02257-0\_21, 2018.
- [11] Datasheetspdf, MG996R Servo Datasheet PDF. High Torque Metal Gear Dual Ball Bearing Servo. Retrieved from https://datasheetspdf.com/datasheet/MG996R.html, 2014
- [12] DatasheetsPDF, MG90S Datasheet, Equivalent, Gear Servo. Metal Gear Servo. Retrieved from https://datasheetspdf.com/pdf/1106582/ETC/MG90S/1, 2014.
- [13] HIKVISION, DS-U02. 2MP Web Camera. DataSheet. Hangzhou, Binjiang, China: Hikvision Digital Technology Co., Ltd, 2020.
- [14] C. Wang, B. Liu, L. Liu, Y. Zhu, J. Hou, P. Liu and X. Li, A review of deep learning used in the hyperspectral image analysis for agriculture. *Artificial Intelligence Review*(54). doi:https://doi.org/10.1007/s10462-021-10018-y, 2021.
- [15] Atlassteels, Aluminium alloy. Data sheet 5052, 2013.

# Working Regimes for Friction Stir Processing of Aluminium Alloy A6061

**Christo Kondoff**

*Institute of Metal Science,  
Equipment, and Technologies with  
Centre for Hydro- and  
Aerodynamics,  
Bulgarian Academy of Sciences  
Sofia, Bulgaria  
hriko61@gmail.com*

**Rossen Mikhov**

*Institute of Information and  
Communication Technologies,  
Bulgarian Academy of Sciences  
Sofia, Bulgaria*

**Leoneed Kirilov**

*Institute of Information and  
Communication Technologies,  
Bulgarian Academy of Sciences  
Sofia, Bulgaria  
l\_kirilov\_8@abv.bg*

**Radostina Zaekova**

*Institute of Metal Science,  
Equipment, and Technologies with  
Centre for Hydro- and  
Aerodynamics,  
Bulgarian Academy of Sciences  
Sofia, Bulgaria*

**Plamen Tashev**

*Institute of Metal Science,  
Equipment, and Technologies with  
Centre for Hydro- and  
Aerodynamics,  
Bulgarian Academy of Sciences  
Sofia, Bulgaria*

**Abstract.** Friction Stir Processing (FSP) is a method for solid-state processing, in which a rotating tool is moved onto the material surface to modify the microstructure and thus obtain improved properties of the material surface. We study the effects of FSP on aluminium alloy A6061-T651 using a tool made at the Institute of Metal Science, Equipment, and Technologies with Centre for Hydro- and Aerodynamics (IMSETCHA) of the Bulgarian Academy of Sciences. The tool has a threaded pin with three flutes and a concave shoulder. Optimal process parameters should always be chosen for the treatment of new materials and when a new instrument is used in order to achieve target properties of processed zone. The appropriate properties, like strength, hardness, corrosion resistance, etc. require process parameters that are correctly configured. The most influential parameters on friction stir processing are direction of rotation of the tool, rotation speed, and traverse speed of the processing. In this paper, we investigate the properties of the processed zone for a total of 16 regimes: 4 rotation speeds (900, 1100, 1300, 1500 rpm) and 4 traverse speeds (15, 30, 45, 60 mm/min) using counterclockwise rotation, comparing the results with a previous study using clockwise rotation. Metallographic inquiry, hardness and tribological tests are used to estimate the stirred zone quality.

**Keywords:** aluminium alloys A6061, friction stir processing (FSP), friction stir welding (FSW), modelling.

## I. INTRODUCTION

Friction Stir Processing (FSP) is an innovative method for solid-state processing. It originates from the Friction Stir Welding (FSW) method proposed in 1991 by The Welding Institute – TWI (UK) [1]. The main principles of FSW are as follows: a rotating tool with a pin and shoulder is set between elements to be joined. The process begins with rotating of the tool and moving it into the direction of welding. The weld is a result of the mixing of the softened material as a result of the rotation and local heating. This simple and efficient way of welding is extensively studied and applied [2], [3].

Several years later, Mishra et al proposed a new method for material processing based on FSW, namely, Friction Stir Processing (FSP) [4]. The idea is by moving the rotating tool onto the material surface to modify the microstructure and thus obtain improved properties of the material surface. FSP was initially designed for superplastic materials. Throughout the years, FSP is also extensively studied [5].

Print ISSN 1691-5402

Online ISSN 2256-070X

<https://doi.org/10.17770/etr2023vol3.7235>

© 2023 Christo Kondoff, Rossen Mikhov, Leoneed Kirilov, Radostina Zaekova, Plamen Tashev.

Published by Rezekne Academy of Technologies.

This is an open access article under the [Creative Commons Attribution 4.0 International License](https://creativecommons.org/licenses/by/4.0/).

In this paper we apply a new tool for FSW and FSP made at the Institute of Metal Science, Equipment, and Technologies with Centre for Hydro- and Aerodynamics (IMSETCHA) of the Bulgarian Academy of Sciences. We study the effects of FSP with this tool on aluminium alloy 6061 because this alloy has excellent strength and corrosion characteristics. The investigated alloy has many applications, such as aerospace products, automobile applications, electrical industry, etc.

The paper is organized further as follows. In the next section we give literature overview. Next, the design of the experiments is described, followed by the results, and finally discussion and conclusions.

## II. RELATED WORK

Aluminium alloys of all series are widely involved in FSP. Hardened aluminium alloys from 6XXX series are subject to FSW and FSP through different instruments and a variety of treatment parameter values. Aluminium alloy A6061 plays a major role in the aerospace, automotive, shipping and other industries because it has good formability, weldability, machinability, corrosion resistance, and good strength compared to other aluminium alloys. It is often used in certain heavy-duty structural applications, such as truck frames, rail coaches, military and commercial bridges, ship building operations, towers and pylons, helicopter rotor skins and many others [6].

Zhang et al. present 3D modelling of material flow in FSW under different process parameters of A6061-T6 alloy, varying tool rotation speed, welding speed, and axial force [7]. A quasi-linear relation is shown between the change of the axial load on the shoulder and the variation of the equivalent plastic strain. The material flow can be accelerated with the increase of the translational velocity and the angular velocity of the pin.

Nam et al. investigate the role of traveling/transversal speed of FSW on the corrosion properties of A6061 aluminium alloy [8]. Four different traveling speeds are examined: base alloy, 40, 60 and 80 mm/min. The electrochemical tests show that increasing of the speed improves corrosion resistance. Another effect is the decreasing of the grains' size and better homogeneity of the microstructure.

Selvaraj et al. study the mechanism of weld formation during FSW of aluminium alloy [9]. The rolled 6 mm thick plate 6061 is made in the size of 150×75×6 mm. The parameters of the tool are: shoulder radius – 9 mm; pin mean radius – 3 mm; pin length – 5.5 mm; pin taper angle – 10°; normal load – 15.5 kN; rotational speeds – 300-2000 rpm; welding velocities – 300, 600, 900, 1400 and 1800 mm/min. Temperatures at different locations are measured using five K-type thermocouples embedded in the advancing side located at a distance of 4 mm, 7 mm, 10 mm, 15 mm and 25 mm from the centre line of the weld. The process parameters for quality weld are identified. The interface temperature range for defect free weld is 400-525°C.

Leon and Jayakumar investigate mechanical properties of A6061 roll plates joined with FSW [10]. The rotating tool has shoulder diameter 18 mm and pin length 5.5 mm. The probe diameter is 6 mm. Different welds are obtained by varying the rotational speed (720, 910, 1120 and 1400 rpm) and the traverse speeds (16, 20, and 31.5 mm/min). The results show that all the weldments are of high quality. When the rotation speed is more than 1200 rpm, the hardness in the weldment increases. Further, when the traverse speed increases from 16 to 31.5 mm/min, an 80-90% reduction in weldment hardness is observed in comparison to the base metal.

Emamian et al. study the influence of tool pin profile on the friction stir welding of A6061-T6 [11]. Four FSW tools with different pin profiles are made of H13 steel – threaded cylindrical, stepped cylindrical, conical, and square. The experiments are performed with three rotational speeds (800, 1200, 1600 rpm) and three traverse speeds (40, 70, 100 mm/min). The conclusion is that increasing the traverse speed influences the tensile strength. The pin profile has no significant influence on the peak temperature and the threaded shape is more efficient for mechanical properties.

Mugada and Adepu investigate the influence of different polygonal tool pin profiles combined with knurling shoulder for Al-Mg-Si alloy [12]. Several cases are considered: hexagonal, pentagonal, square, triangular and taper cylindrical pins. The square and hexagonal pins provide constant stability force in regard to the weld length/time; the square pin produces welds with better mechanical properties. Uniform mixing and distribution of plasticized material is obtained for the knurling shoulder with square tool pin.

Gadakh and Kumar determine the optimal parameter values for FSW of A6061-T6 aluminium alloy [13]. They experiment with: rotational speed, weld speed, the ratio of shoulder to pin diameter and pin geometry. It is found that the rotational speeds within [710, 1400] rpm with weld speed of 40 mm/min produce defect-free weldments; the taper cylindrical (TC) pin produces better fine-grain structure than straight cylindrical (SC) pin; the ratio  $D_{\text{shoulder}}/D_{\text{pin}} = 3$  produces better mechanical properties and fine-grain structure; and the shoulder diameter 24 mm produces better mechanical properties.

Arora et al. propose a criterion for the design of a tool shoulder diameter [14]. They use a 3D heat transfer and visco-plastic flow model developed earlier [15], [16]. The experiments are performed on A6061 with tool rotational speeds 900, 1200 and 1500 rpm; cylindrical profile with no thread and different shoulder diameters 12 to 27 mm. The formulated criterion is a function of both sticking torque and sliding torque with equal partitioning. The optimum shoulder diameter is defined depending on the maximum value of the criterion.

Takhakh and Abdulla [17] apply FSP to improve the mechanical properties of welded joint of A7075-T651 by adding SiC (silicon carbide) on the compound surface. They use a new type of tool (a hollow tool) where the SiC particles are stored, and try different values of the processing parameters.

Patil et al. [18] propose a hybrid reinforcement approach using FSP. They mix silicon carbide and fly ash particles in order to minimize wear rate and maximize microhardness.

Sharma et al. [19] optimize FSP parameters in order to have defect-free surface composites with uniform particle distribution. The experiments are done by adding silicon carbide particles into the A5083 alloy surface. The authors also experiment with dual-tool processing and tool offset overlapping.

### III. DESIGN OF THE EXPERIMENTS

In this paper, we investigate a tool, made at IMSETCHA, which has the following geometry (see Fig. 1): it has a threaded pin with three flutes and a concave shoulder. The dimensions are: tapered pin – diameter at the base 5.5 mm; pin length – 4 mm, shoulder diameter – 13 mm.

FSP was applied on a rectangular detail of A6061-T651 aluminium alloy, part of sheet metal with thickness 12 mm and dimensions 100×200 mm. The processing was performed on a machining centre HURCO VMX30 (Fig. 2). The angle between the tool and detail was a constant right angle (90°).



Fig. 1. Friction Stir Processing tool.



Fig. 2. Friction Stir Processing equipment.

For the present experiment, the direction of rotation of the tool was counterclockwise (CCW). The results are

compared against prior work of Kondoff et al. [20], where rotation direction had been clockwise (CW).

The most influential parameters on friction stir processing are rotation speed of the tool and traverse speed of the processing. We investigated the properties of the processed zone with 4 rotation speeds and 4 traverse speeds, for a total of 16 regimes:

- rotational speeds: 900, 1100, 1300, 1500 rpm;
- traverse speeds: 15, 30, 45, 60 mm/min.

### IV. RESULTS AND DISCUSSION

In all speed regimes, all of the investigated properties of the processed zone were considerably better in the experiments with counterclockwise rotation of the tool, as opposed to clockwise rotation.

This improvement is due to fact that the tool is right-hand threaded. Better compaction of the material results from the pressing action of the pin against the inner area of the mixing zone.

#### A. Metallographic Inquiry

To prepare the detail for analysing, it was cut into strips. The strips were marked, ground, polished and etched for metallographic analysis. To assess the imperfections, which in this case are metal deficiency zones (MDZ), a section was considered for each processing regime.

No MDZ imperfections could be observed with CCW rotation, which is in sharp contrast to the CW results of [20].

From the macrostructural analysis (Fig. 3), it can be seen that the size of the cross section of the stirred zone does not depend on the rotation speed and the processing speed. Regardless of the fact that the processing in the different regimes was carried out sequentially, no increase in the cross section of the stirred zone was observed at subsequently processed locations due to an increase in the temperature of the detail. This is likely due to the high thermal conductivity of the used alloy.

Fig. 4 shows the microstructure of the boundary of the processed zone. The grains of the base metal and the significantly finer grains of the stirred zone are clearly visible. The progressive and rotary movement of the tool leads to the formation of layers, known under the name of “onion rings”. They are clearly distinguishable in Fig. 5. With counterclockwise rotation of the tool, there is a tendency for the boundary between the stirred zone and the base material on the advancing side of the tool to be sharper (Fig. 6), and on the retreating side of the tool to be smoother (Fig. 7).

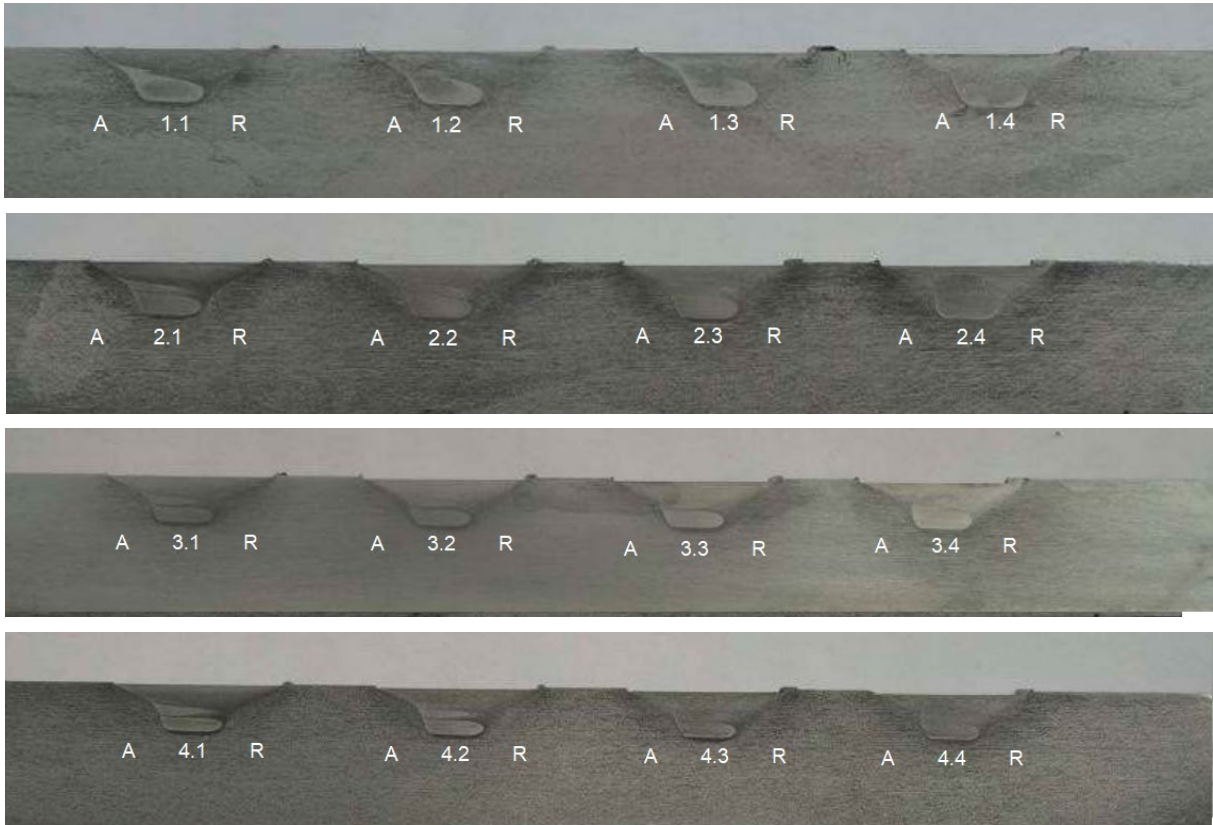


Fig. 3. Macroscopic view of cross sections of the FSP zones at different traverse speeds and rotational speeds, as follows: 1.1 – 15 mm/min, 900 rpm; 1.2 – 15 mm/min, 1100 rpm; 1.3 – 15 mm/min, 1300 rpm; 1.4 – 15 mm/min, 1500 rpm; 2.1 – 30 mm/min, 900 rpm; 2.2 – 30 mm/min, 1100 rpm; 2.3 – 30 mm/min, 1300 rpm; 2.4 – 30 mm/min, 1500 rpm; 3.1 – 45 mm/min, 900 rpm; 3.2 – 45 mm/min, 1100 rpm; 3.3 – 45 mm/min, 1300 rpm; 3.4 – 45 mm/min, 1500 rpm; 4.1 – 60 mm/min, 900 rpm; 4.2 – 60 mm/min, 1100 rpm; 4.3 – 60 mm/min, 1300 rpm; 4.4 – 60 mm/min, 1500 rpm. A – advancing side; R – retreating side.



Fig. 4. Grain size of the base and stirred metal (regime 1.1).



Fig. 6. Smooth border (regime 4.4).



Fig. 5. Onion rings (regime 1.1).

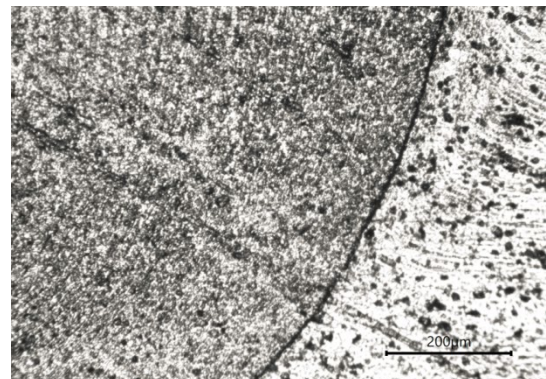


Fig. 7. Sharp border (regime 4.4).

**B. Hardness Test**

Microhardness (HV) measurements were performed with a Micro-Duromat 4000 (Reichert-Jung), with the following parameters: load – 20 gf; time for reaching the load – 10 s; hold time – 10 s; Vickers indenter. Fig. 8 is an illustration of such a measurement.

The results are listed in Table I. The measurements were performed in three different positions: under the surface, in the middle and at the base. The exact positions are illustrated on Fig. 9.

The highest average hardness is observed at regime 60/900 with a value of 75.8 kgf/mm<sup>2</sup>, which is

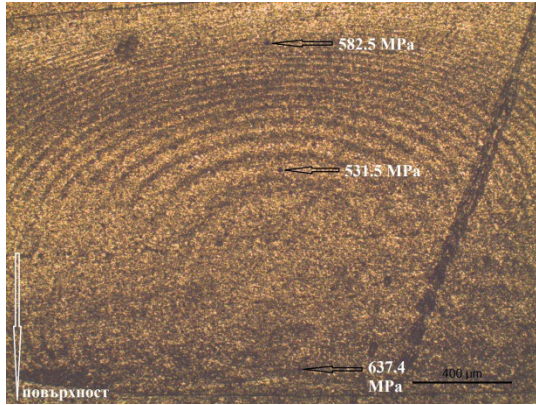


Fig. 8. Image from the microhardness measurement.

comparable to the hardness of the base material A6061-T651 with an average hardness of 73 kgf/mm<sup>2</sup>. In FSP, thermal effect occurs in the stirred zone and the thermally affected zone shows a decrease in hardness, which is due to the partial dissolution of the precipitates from the hard Mg<sub>2</sub>Si phase.

**C. Tribological Test**

Mass wear measurements were performed on a tribological installation with Ducom Pin/Ball disk tester TR-20. The counter body was a disk of special steel EN 31 with hardness 60 HRC. The other parameters were as follows: load – 20 N; speed of the counter body – 80 rpm (1 m/s); trial duration – 10 min; total distance – 600 m.

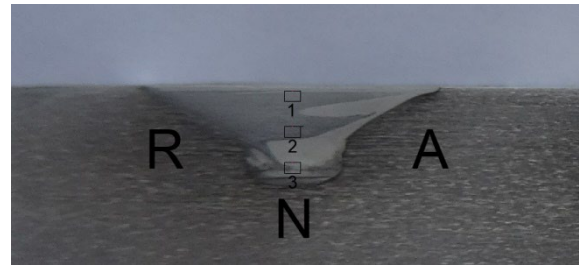


Fig. 9. Positions of the microhardness measurement. A – advancing side; R – retreating side; N – nugget; □1, □2, □3 – measurement positions “below the surface”, “in the middle” and “at the base”, respectively.

TABLE I MICROHARDNESS HV0.02/10/10

		counterclockwise (CCW) rotation				clockwise (CW) rotation			
		rotation speed, rpm				rotation speed, rpm			
		900	1100	1300	1500	900	1100	1300	1500
traverse speed, mm/min	15	HV below the surface, kgf/mm <sup>2</sup>				HV below the surface, kgf/mm <sup>2</sup>			
	30	62.1	73.6	74.0	71.5	54.6	53.1	49.3	53.8
	45	74.6	65.0	73.7	63.4	37.7	48.3	54.6	48.3
	60	67.6	59.6	63.9	63.7	33.4	48.2	41.1	62.5
traverse speed, mm/min	15	HV in the middle, kgf/mm <sup>2</sup>				HV in the middle, kgf/mm <sup>2</sup>			
	30	65.3	68.4	68.9	70.8	46.0	48.9	49.4	49.8
	45	59.6	54.2	66.8	62.8	46.2	48.9	53.1	49.8
	60	67.6	58.3	64.8	70.9	45.5	45.9	46.5	44.8
traverse speed, mm/min	15	HV at the base, kgf/mm <sup>2</sup>				HV at the base, kgf/mm <sup>2</sup>			
	30	51.4	66.7	68.9	72.4	53.4	51.8	51.4	52.8
	45	61.5	59.4	63.1	73.6	53.8	54.7	52.0	48.1
	60	67.6	59.6	59.6	72.8	53.6	56.9	54.0	55.3
traverse speed, mm/min	15	HV, average of the 3 positions, kgf/mm <sup>2</sup>				HV, average of the 3 positions, kgf/mm <sup>2</sup>			
	30	59.6	69.6	70.6	71.6	51.3	51.3	50.0	52.1
	45	65.2	59.5	67.9	66.6	45.9	50.6	53.2	48.7
	60	67.6	59.2	62.8	69.1	44.2	50.3	47.2	54.2
		unprocessed material							
		73.0 kgf/mm <sup>2</sup> (an average of 5 measurements)							

Three regimes were selected, and three samples were measured for each regime, from which a mean value was calculated (with the exception of the 15/1500 regime, for which only one sample could be measured). The results are as follows: 15/1500: 1.2 mg; 30/1100: 0.9 mg; 45/1100: 1.27 mg. For comparison, the unprocessed material had a mean mass wear of 1.13 mg (again, an average of 3 measurements).

Due to the large dispersion of the individual results, the tribological analysis establishes that there is no definite pattern regarding mass wear in the investigated regimes.

## V. CONCLUSION

The operating regimes of a tool for friction stir processing on the A6061-T651 aluminium alloy are investigated and analysed. Experiments with four levels of traverse speed and four levels of rotational speed were performed. The main results are as follows:

- The investigated tool in the aforementioned regimes with CCW rotation provides for a defect-free structure of the processed zone.
- In all speed regimes, CCW rotation of the tool is considerably superior to CW rotation, and this was observed with all of the investigated properties of the processed zone.
- The size of the cross section of the stirred zone does not depend significantly on the traverse speed and the rotation speed.
- The regime with highest average hardness of the stirred zone is 60 mm/min / 900rpm, and its hardness is comparable to that of the base material.
- No definite regularity regarding mass wear could be observed.

On the grounds of this experiment, we choose the CCW 60/900 regime as adequate for future applications. In a follow-up work, we plan to investigate the influence of adding Zn and Ti nanopowder to the FSP process under this regime.

## VI. ACKNOWLEDGEMENT

Christo Kondoff and Plamen Tashev are supported by the Bulgarian NSF under grant KP-06-India-10/02.09.2019 and by the European Regional Development Fund, Operational Programme “Science and Education for Smart Growth 2014-2020”, Project CoE “National center of mechatronics and clean technologies” BG05M2OP001-1.001-0008. Leoneed Kirilov is supported by the Bulgarian NSF under grants KP-06-N52/5 and KP-06-N52/7. Rossen Mikhov is supported by the Bulgarian NSF under grant KP-06-N52/7.

## REFERENCES

- [1] Z. Ma, “Friction Stir Processing Technology: A Review,” *Metall. Mater. Trans. A*, vol. 39, pp. 642-658, 2008.
- [2] H. Luo, T. Wu, P. Wang, F. Zhao, H. Wang, et al., “Numerical Simulation of Material Flow and Analysis of Welding Characteristics in Friction Stir Welding Process,” *Metals*, vol. 9, no. 6, p. 621, 2019.
- [3] M. S. S. El-Deeb, L. A. Khorshed, S. A. Abdallah, A. M. Gaafer, and T. S. Mahmoud, “Effect of Friction Stir Welding Process Parameters and Post-Weld Heat Treatment on the Corrosion Behaviour of AA6061-O Aluminum Alloys,” *Egypt. J. Chem.*, vol. 62, no. 8, pp. 1367-1375, 2019.
- [4] R. S. Mishra, M. W. Mahoney, S. X. McFadden, N. A. Mara, and A. K. Mukherjee, “High strain rate superplasticity in a friction stir processed 7075 Al alloy,” *Scr. Mater.*, vol. 42, no. 2, pp. 163-168, 1999.
- [5] K. Li, X. Liu, and Y. Zhao, “Research Status and Prospect of Friction Stir Processing Technology,” *Coatings*, vol. 9, no. 2, p. 129, 2019.
- [6] Howard Precision Metals Inc., “Applications of 6061 Aluminum Alloy.” [Online]. Available: <https://www.howardprecision.com/applications-of-6061-aluminum-alloy/> [Accessed: Apr. 27, 2022].
- [7] H. W. Zhang, Z. Zhang, and J. T. Chen, “3D modeling of material flow in friction stir welding under different process parameters,” *J. Mater. Process. Technol.*, vol. 183, no. 1, pp. 62-70, 2007.
- [8] N. D. Nam, L. T. Dai, M. Mathesh, M. Z. Bian, and V. T. H. Thu, “Role of friction stir welding – Traveling speed in enhancing the corrosion resistance of aluminium alloy,” *Mater. Chem. Phys.*, vol. 173, pp. 7-11, 2016.
- [9] M. Selvaraj, V. Murali, and S. R. K. Rao, “Mechanism of Weld Formation during Friction Stir Welding of Aluminium Alloy,” *Mater. Manuf. Process.*, vol. 28, no. 5, pp. 595-600, 2013.
- [10] J. S. Leon and V. Jayakumar, “Investigation of mechanical properties of aluminium 6061 alloy friction stir welding,” *Am. J. Mech. Eng. Autom.*, vol. 1, no. 1, pp. 6-9, 2014.
- [11] S. Emamian, M. Awang, P. Hussai, B. Meyghani, and A. Zafar, “Influences of tool pin profile on the friction stir welding of AA6061,” *ARPN J. Eng. Appl. Sci.*, vol. 11, no. 20, pp. 12258-12261, 2016.
- [12] K. K. Mugada and K. Adepu, “Effect of knurling shoulder design with polygonal pins on material flow and mechanical properties during friction stir welding of Al-Mg-Si alloy,” *Trans. Nonferrous Met. Soc. China*, vol. 29, no. 11, pp. 2281-2289, 2019.
- [13] V. S. Gadakh and A. Kumar, “Friction stir welding window for AA6061-T6 aluminium alloy,” *Proc. Inst. Mech. Eng. Part B*, vol. 228, no. 9, pp. 1172-1181, 2014.
- [14] A. Arora, A. De, and T. DebRoy, “Toward optimum friction stir welding tool shoulder diameter,” *Scr. Mater.*, vol. 64, no. 1, pp. 9-12, 2011.
- [15] R. Nandan, G. G. Roy, T. J. Lienert, and T. Debroy, “Three-dimensional heat and material flow during friction stir welding of mild steel,” *Acta Mater.*, vol. 55, no. 3, pp. 883-895, 2007.
- [16] R. Nandan, T. J. Lienert, and T. Debroy, “Toward reliable calculations of heat and plastic flow during friction stir welding of Ti-6Al-4V alloy,” *Int. J. Mater. Res.*, vol. 99, no. 4, pp. 434-444, 2008.
- [17] A. M. Takhakh and H. H. Abdulla, “Improving the Mechanical Properties of Al7075-T651 Welded Joint Using Direct Friction Stir Processing,” in *Proceedings of the The Second Conference of Post Graduate Researches (CPGR'2017)*, College of Engineering, Al-Nahrain Univ., Baghdad, Iraq, 2017, pp.6-10.
- [18] N. A. Patil, S. R. Pedapati, O. B. Mamat, and A. M. Hidayat Syah Lubis, “Effect of SiC/Fly Ash Reinforcement on Surface Properties of Aluminum 7075 Hybrid Composites,” *Coatings*, vol. 10, no. 6, p.541, 2020.
- [19] V. Sharma, Y. Gupta, B. V. M. Kumar, and U. Prakash, “Friction Stir Processing Strategies for Uniform Distribution of Reinforcement in a Surface Composite,” *Mater. Manuf. Process.*, vol. 31, no. 10, pp. 1384-1392, 2016.
- [20] Ch. Kondoff, V. Dykova, R. Dimitrova, Y. Hadjitodorov, and R. Zaekova, “A Layer Formation on 6061 Aluminium Alloy after FSP,” *Int. J. NDT Days*, vol. 4, pp. 2603-4018, 2021.

# Experimental Study of Surface Roughness in Vibro-impact Cutting of Optical Slugs

**Angel Lengerov**

Department of Mechanical  
Engineering and Technologies  
Technical University of Sofia,  
Plovdiv Branch  
Plovdiv, Bulgaria  
email anlen@tu-plovdiv.bg

**Sabi Sabev**

Department of Mechanical  
Engineering and Technologies  
Technical University of Sofia,  
Plovdiv Branch  
Plovdiv, Bulgaria  
email s-tu@abv.bg

**Stoyan Paliiski**

Department of Mechanical  
Engineering and Technologies  
Technical University of Sofia,  
Plovdiv Branch  
Plovdiv, Bulgaria  
email st.paliyski@abv.bg

**Abstract.** In the article, experimental studies were carried out with the aim of determining the influence of different modes of vibro-impact cutting modes of optical slugs on the roughness of obtained surfaces. From the results obtained during the measurements and their mathematical processing are evaluated the average sizes and intervals and the parameters of the roughness of treated surfaces.

**Keywords:** roughness, surface, experimental, study, optical slug.

## I. INTRODUCTION

One of the conditions for reducing the basic losses and increasing the value of the finished product is ensuring high surface quality of the optical materials, processed by cutting [1,3,10,14]. The primary task of this paper is the comparative assessment of the surface roughness, obtained both during traditional cutting and in vibro-impact cutting of optical slugs.

## II. EXPERIMENTAL DETERMINATION OF SURFACE ROUGHNESS

To determine the degree of influence of the forced vibrational oscillations on the roughness of the cut workpiece, it is necessary to study the mechanism of forming the microgeometry of the processed surfaces [2,4,5,6,7,8,9,11,12,13]. Due to the mechanical interaction of the peripheral (cutting) surface of the cutting diamond disc and the workpiece, separation of particles from the processed material begins. In result, at the starting moment, micro-irregularities appear and initial roughness of the surfaces is formed.

When the disc goes into the processed workpiece, as a result of the arising friction of the surfaces, contacting the

cutting disc, improvement in roughness is observed in the cut parts. The nature of the roughness change depends on: - the dominant type of wear in the frictional surface; - the conditions of friction and the duration of interaction of the side surfaces of the cutting disc and the machined workpiece.

The section of the cut surface of the workpiece, located at the beginning of the cutting disc, is subject to maximum wear over the duration of the friction, and the section at the exit of the cutting disc – to minimum wear.

The effect of the interaction between the cutting disc and the workpiece under the different vibro-impact modes affects the way, in which the cutting process proceeds, which influences on the conditions of forming the microrelief of the processed surfaces. The quality of the surfaces of the workpieces, subjected to vibrational cutting, is determined by the degree of influence of the amplitude-and-frequency oscillations, transmitted to the workpiece, and by the degree of manifestation of the polishing effect.

A number of experimental studies have been carried out in order to evaluate the roughness parameters ( $R_a$  and  $R_z$ ) of surfaces of optical slugs, cut by vibration. The experimental studies were carried out in three vibro-impact modes of processing (whose technological parameters are shown in Table 1), and the roughness parameters of the treated surfaces were measured.

Print ISSN 1691-5402

Online ISSN 2256-070X

<https://doi.org/10.17770/etr2023vol3.7241>

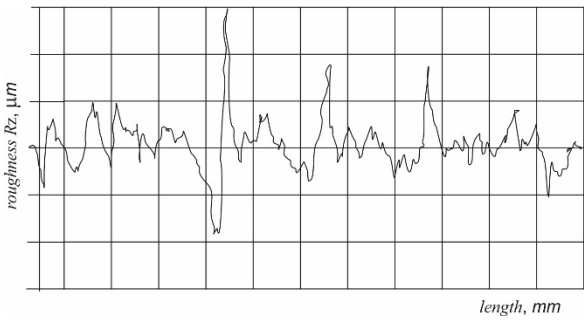
© 2023 Angel Lengerov, Sabi Sabev, Stoyan Paliiski. Published by Rezekne Academy of Technologies.  
This is an open access article under the [Creative Commons Attribution 4.0 International License](https://creativecommons.org/licenses/by/4.0/).

TABLE 1 BASIC PARAMETERS OF A CENTRIFUGAL VIBRATOR FOR THREE MODES OF CUTTING

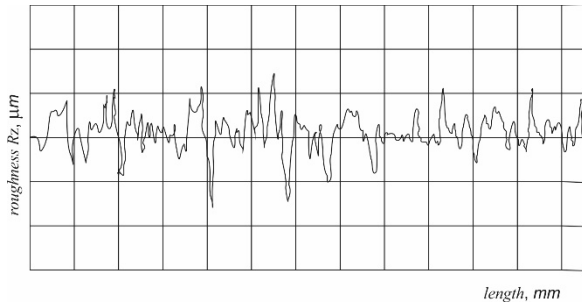
Mode of operation of the vibrator	Frequency of rotation of the electric motor shaft, min <sup>-1</sup>	Frequency of vibration of the workpiece, Hz	Amplitude of vibration of the workpiece, μm	Amplitude of the vibrational velocity, m/min	Amplitude of the vibrational acceleration, m/s <sup>2</sup>
1	2480	41,3	87,4	1,36	5,88
2	5110	85,2	32,4	1,04	9,28
3	6000	100	25,3	0,95	9,98

The measurements were made in a direction, perpendicular to the traces from the processing for all lengths from the diagonals of the sample. For all studied modes of optical slugs processing by cutting, profilograms of the sample surfaces were made, as shown in Fig. 1.

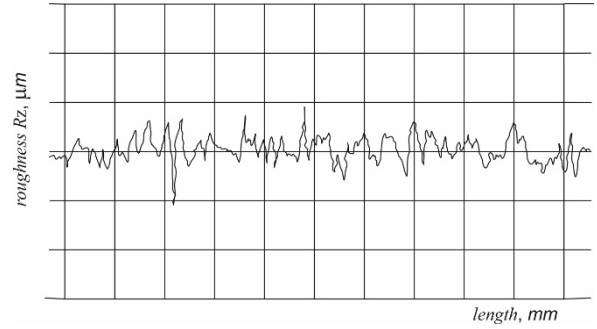
From the profilograms, taking into account the nature of the roughness height along the cut surfaces, the most expedient and optimal processing mode can be determined. Such modes (Fig. 1 c, d) prove to be the vibro-impact cutting modes 2 and 3. This is explained by the optimal combination of parameters, such as amplitude of vibrational velocity and amplitude of vibrational acceleration, primarily at a certain frequency of the forced oscillations.



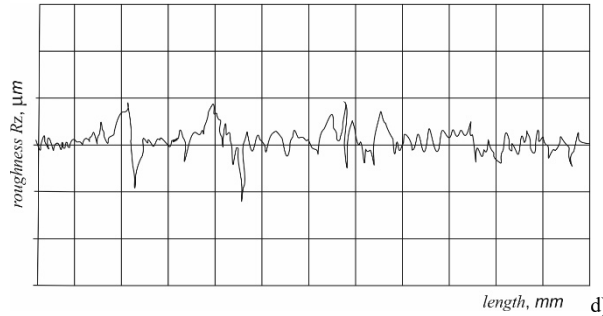
a)



b)



c)



d)

Fig. 1. Profilograms of the surfaces of the cut samples under different processing modes: a) traditional cutting; b) vibro-impact mode 1; c) vibro-impact mode 2; d) vibro-impact mode 3.

In order to clarify the degree of influence of the vibro-impact forced oscillations, implemented in the process of cutting optical slugs, the roughness parameters Ra and Rz of the machined parts of the optical samples were measured using a profilograph-profilometer. The obtained values of the Rz parameter are shown in Fig. 2.

The results of the measurements show that during vibro-impact cutting the quality parameters of the processed surfaces improve, compared to traditional cutting. The best quality was recorded for vibro-impact processing mode 2, worse for mode 3 and worst for mode 1. This is explained by the increased frequency of oscillations of the processed workpiece, which leads to a decrease in the time of dynamic impact of the single abrasive grains and the processed material of the workpiece.

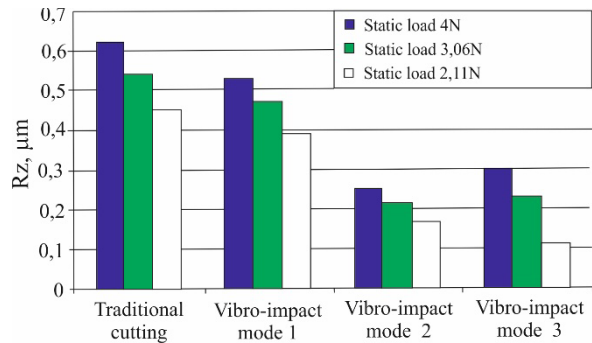


Fig. 2. Dependence of the parameter Rz of the cut surface of a brand BK7 optical workpiece on the processing mode under different static loads.

As the static load increases, the value of the Rz parameter goes up, both under normal conditions and under the

influence of forced oscillations. This is due to an increase in the pressure in the contact zone between the cutting surface of the disc and the workpiece, which leads to an increase in the separation of particles from the diamond cutting disc and the cut material. The roughness of the cut surface of the sample deteriorates. In addition to taking into account the value of the parameter  $R_z$ , measurements of the parameter  $R_a$  were also made, depending on the technological and vibrational parameters of the processing (Table 2). Vibro-impact mode 1 proved to be the most favorable. Deterioration of the roughness was observed in vibro-impact modes 2 and 3, which makes them impractical for implementation.

TABLE 2 VALUES OF THE  $R_a$  PARAMETER OF THE CUT SURFACE OF THE OPTICAL SLUG

Processing mode	Values of the parameter $R_a$ ( $\mu m$ )				
	No vibration	Vibro-impact mode1	Vibro-impact mode2	Vibro-impact mode3	
Static load, $N$	4	0,098	0,045	0,049	0,064
	3,06	0,078	0,028	0,03	0,041
	2,11	0,06	0,01	0,02	0,03

The influence of the amplitudes of the vibrational velocity and the vibrational acceleration on the value of the parameter  $R_z$  are reflected in Fig. 3., a and b.

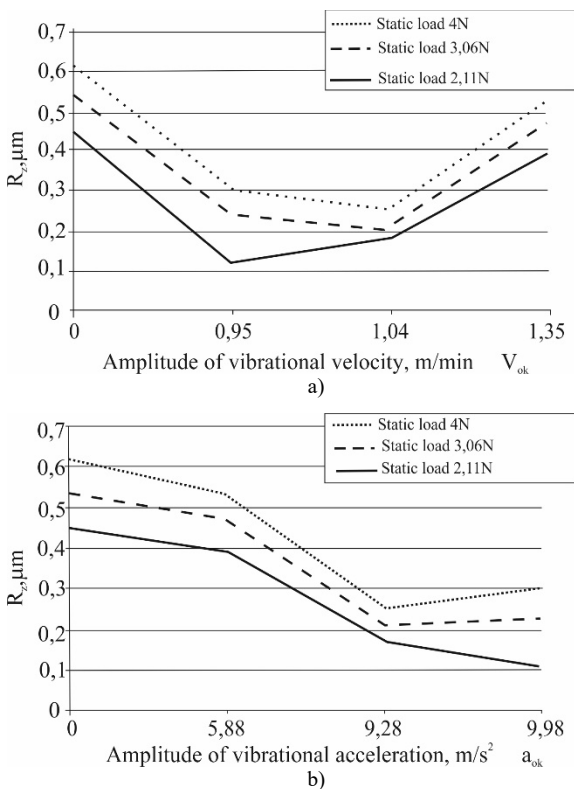


Fig. 3. Dependence of the parameter  $R_z$   $\mu m$  of the optical slugs cut surfaces at different values of the static load: a) on the amplitude of the vibrational velocity; b) on the amplitude of the vibrational acceleration.

It can be seen from the Fig.3, that with an increase in  $V_{ok}$  and  $a_{ok}$ , the value of the  $R_z$  parameter decreases and reaches a minimum value at  $V_{ok} - 0,95 - 1,0$  m / min and  $a_{ok} - 9,28 - 9,3$  m / s<sup>2</sup>, while with a further increase in  $V_{ok}$  and  $a_{ok}$  the value increases. This indicates the existence of an optimal value of and, ensuring minimum values of the parameter  $R_z$  of the cut surface. From Fig.3 it can be seen, that the reduction of the static load value from 4 N to 2,11 N leads to improvement in machining quality, which is explained by the decreased introduction of small-sized abrasive grains into the workpiece material in the cutting zone. At the same time, the sharp decrease in the roughness affects the increase in the frequency of forced oscillations in mode 3, which causes additional polishing, due to the friction of the cut surface of the workpiece with the side surfaces of the cutting disc.

### III. CONCLUSION

On the basis of the experimental studies, carried out both during vibro-impact and traditional cutting of optical slugs, it was established, that in the process of vibro-impact cutting the quality indicators of the surface roughness improve. This is explained by the additional friction between the side surfaces of the cutting diamond disc and the cut surfaces of the optical workpieces. The periodic separation of fine optical particles, caused by the oscillating vibro-impact cutting system, further contributes to improvement of the working conditions.

### IV. ACKNOWLEDGMENTS

This work was supported by the European Regional Development Fund within the OP “Science and Education for Smart Growth 2014-2020”, Project Competence Centre “Smart Mechatronic, Eco-And Energy Saving Systems And Technologies”, № BG05M2OP001-1.002-0023.

### REFERENCES

- [1] S. Hambücker, “Technologie der Politur sphärischer Optiken mit Hilfe der Synchrospeed-Kinematik,” dissertation, Berichte aus der Produktionstechnik, Shaker Verlag, Berlin, Germany, 2001.
- [2] Riemer, O.: “Trennmechanismen und Oberflächenfeingestalt bei der Mikrozerspannung kristalliner und amorpher Werkstoffe,” dissertation, University Bremen, Forschungsbericht Band 7, Shaker Verlag, Aachen, Germany, 2001.
- [3] Voss R., Fundamentals of Carbon Fibre Reinforced Polymer (CFRP) Machining. Eigenössische Technische Hochschule Zürich (ETH): Zürich, 2017.
- [4] K. Kumov, H. Metev, T. Kuzmanov. Geometric Accuracy in Machining Console Set Preparations. Mechanical Engineering and Mechanical Science, Technical University of Varna, vol. 26, pp. 127-132, ISSN 1312-8612, 2016.
- [5] T. Zhao, J.M. Zhou, V. Bushlya, J.E. Stähli, Effect of cutting edge radius on surface roughness and tool wear in hard turning of AISI 52100 steel, Int. J. Adv. Manuf. Technol. 91, pp. 3611–3618, 2017.
- [6] A.S. Vaykhinde, U.B. Bhor, V.V. Sachhe, S.P. Valte, S.B. Deokar, Review of effect of tool nose radius on cutting force and surface roughness, Int. Res. J. Eng. Technol. 4, pp. 699–703, 2017.

- [7] Agmell, M.; Ahadi, A.; Gutnichenko, O.; Ståhl, J.E. The influence of tool micro-geometry on stress distribution in turning operations of AISI 4140 by FE analysis. *Int. J. Adv. Manuf. Technol.* 89, pp. 3109–3122, 2017.
- [8] B. Denkena, A. Kroedel, T. Grove, Influence of pulsed laser ablation on the surface integrity of PCBN cutting tool materials, *Int. J. Adv. Manuf. Technol.* 10 pp. 1–12, 2018.
- [9] Filip A C, Morariu C O, Mihail L A and Oancea G, Research on the Surface Roughness of Hardox Steel Parts Machined with an Abrasive Waterjet, *STROJ VESTN-J MECH E* 65(4) pp. 230-237, 2019.
- [10] Dudutis J., Zubauskas L., Daknys E., Markauskas E., Gvozdaite R., Račiukaitis G., Gečys P. Quality and flexural strength of laser-cut glass: Classical top-down ablation versus water-assisted and bottom-up machining. *Opt. Express.* 2022;30:4564–4582. doi: 10.1364/OE.447143.
- [11] Grissa, R.; Zemzemi, F.; Fathallah, R. Three approaches for modeling residual stresses induced by orthogonal cutting of AISI 316L. *Int. J. Mech. Sci.* 135, pp. 253–260, 2018, <https://doi.org/10.1016/j.ijmecsci.2017.11.029>.
- [12] Fan, Y.H.; Wang, T.; Hao, Z.P. Surface residual stress in high speed cutting of superalloy Inconel 718 based on multiscale simulation. *J. Manuf. Process.* 2018, 31, pp. 480–493, <https://doi.org/10.1016/j.jmapro.2017.12.011>.
- [13] Wang, B.; Liu, Z.; Hou, X. Influences of Cutting Speed and Material Mechanical Properties on Chip Deformation and Fracture during High-Speed Cutting of Inconel 718. *Materials* 2018, 11, 461, DOI: 10.3390/ma11040461.
- [14] Filmetrics, User Manual: Profilm3D Optical Profiler and Analysis Software (San Diego: Filmetrics), 2018.

# Study of the Kinematic and Dynamic of Interaction of a Vibrating System for Cutting Optical Slugs

**Angel Lengerov**

Department of Mechanical  
Engineering and Technologies  
Technical University of Sofia,  
Plovdiv Branch  
Plovdiv, Bulgaria  
email anlen@tu-plovdiv.bg

**Kalin Krumov**

Department of Mechanical  
Engineering Equipment and  
Technologies  
Technical University of Gabrovo,  
Gabrovo, Bulgaria  
email  
kalin\_krasimirov\_krumov@abv.bg

**Georgi Levicharov**

Department of Mechanical  
Engineering and Technologies  
Technical University of Sofia,  
Plovdiv Branch  
Plovdiv, Bulgaria  
email glevi@tu-plovdiv.bg

**Abstract.** In the article, studies of the kinematics and dynamics of interaction of the elements of the vibration system "slug-cut disk" are made. A mathematical model describing the trajectory of a cutting arm has been created and the technological parameters of the system at which the phenomenon of resonance occurs have been determined.

**Keywords:** kinematic, dynamic, study, vibrating system, optical slug, cutting.

## I. INTRODUCTION

Mechanical systems, in which the processing is realized by introducing systematic contacts between two objects, are called vibro-impact systems [5,6].

Vibro-impact modes of processing are the basis of a different kind of actions of a wide spectrum of machines, tools and devices of different functional type [2,3,4,7,8,9]. Characteristic of these systems are the periodic modes of motion, carried out according to the scheme of forced oscillations or self-oscillations.

The theoretical evaluation of the degree of influence of the caused under conditions of vibro-impact cutting forced oscillations of optical slugs can be represented by mathematical models of the kinematics and dynamics of the interaction between a diamond cutting disk and an optical workpiece.

## II. MATHEMATICAL MODEL

The mathematical description of the trajectory and the laws of movement of the cutting arm with a centrifugal vibrator, makes it possible to analytically determine the efforts of the contact interaction between the cutting tool

and the machined workpiece at preset magnitudes of the forced oscillations.

The developed mathematical model allows for studying the kinematics and dynamics of the interaction between the elements of the vibrational system "workpiece – cutting disk" (Fig.1).

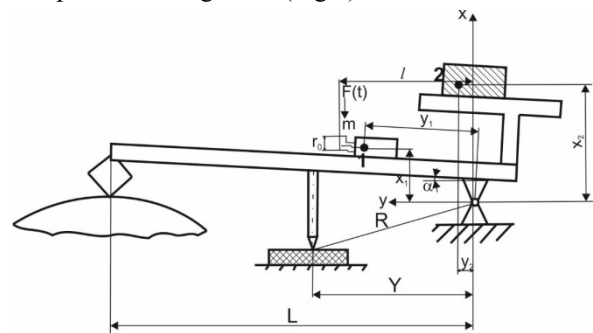


Fig. 1. Mathematical model of the cutting system.

In order to simplify the calculations, the action of the centrifugal vibrator is replaced by a driving harmonic force  $F(t)$ . According to [1] this is permissible, since the amplitude of the caused oscillations is much smaller than the radius of motion of the imbalance. The cutting arm in the hinged device is considered to be fixed so, that oscillations in the direction of the axis and perpendicular to the plane of the drawing do not exist. To simplify the calculation, the cutting arm is regarded as an absolutely rigid body, and the masses of the cutting arm, the vibrator and the devices, creating a static load on the workpiece, are replaced by two concentrated masses (points 1 and 2

Print ISSN 1691-5402

Online ISSN 2256-070X

<https://doi.org/10.17770/etr2023vol3.7242>

© 2023 Angel Lengerov, Kalin Krumov, Georgi Levicharov. Published by Rezekne Academy of Technologies.  
This is an open access article under the [Creative Commons Attribution 4.0 International License](https://creativecommons.org/licenses/by/4.0/).

in Fig.1). The axis of rotation of the cutting arm is taken as the origin of the coordinate system. The notations, used in the mathematical model, are as follows:

$\alpha$  - an angle, determining the position of the rocker, i.e., an angle between the origin and the direction of the axis of rotation - the point of contact "optical slug - cutting disk" in the counterclockwise direction;

$m$  - mass of the eccentric;

$m_1$  - mass of the system (without the counterweight);

$m_2$  - counterweight mass;

$k_1$  - damper elasticity;

$k_2$  - elastic support "detail-cutting disc";

$\xi$  - effective damping coefficient.

## 2.1. Study of the kinematics

The mass moment of inertia  $I$  of the system about the axis of rotation can be represented as

$$I = m_1(x_1^2 + y_1^2) + m_2(x_2^2 + y_2^2). \quad (1)$$

The angle  $\alpha_e$  between the contact point of the support with the damper, and the contact point of the optical slug with the cutting disk, is calculated by the dependence

$$\alpha_e = -\frac{\Delta h}{L}, \quad (2)$$

where  $\Delta h$  is the distance between the optical workpiece and the cutting disk at the moment of contact of the support with the damper.

The equilibrium equation of the system will take the form

$$(m_1 y_1 + m_2 y_2)g = \left( \alpha_0 + \frac{\Delta h}{L} \right) k_1 y^2 + \alpha_0 k_2 L^2, \quad (3)$$

where  $\alpha_0$  is the angle of the state of equilibrium.

Consequently,

$$\alpha_0 = \frac{(m_1 y_1 + m_2 y_2)g - \frac{\Delta h k_1 R y}{L}}{k_1 y^2 + k_2 L^2}. \quad (4)$$

The driving harmonic force is presented in the following form

$$F(t) = m r_0 (2\pi\nu)^2 \sin(2\pi\nu t) \quad (5)$$

Then for the driving moment we obtain

$$Me(t, \nu) = m r_0 l (2\pi\nu)^2 \sin(2\pi\nu t) \quad (6)$$

The resultant moment of the acting forces (the weight and the reactions of the supports), depending on the quantity  $\delta = \alpha - \alpha_0$ , i.e., the angular deviation of the arm position from the equilibrium state, is determined as it follows

$$\hat{M}(\delta) = \begin{cases} -\delta(k_1 y^2 + k_2 L^2) & \text{npu } \delta \geq -\alpha_0 \\ \alpha_0 k_2 L^2 - \sigma k_1 y^2 & \text{npu } \delta < -\alpha_0 \end{cases}. \quad (7)$$

The motion equation of the system can be represented as

$$I \ddot{\delta} = \hat{M}(\delta) - \xi \dot{\delta} + Me(t, \nu). \quad (8)$$

After replacing the variables

$$Y_1 = \dot{\delta} \quad Y_0 = \delta \quad \dot{Y}_0 = Y_1. \quad (9)$$

Then equation (8), taking into account (9), takes the form

$$\dot{Y}_1 = \frac{1}{I} \left[ \hat{M}(Y_0) - \xi Y_1 + Me(t, \nu) \right]. \quad (10)$$

For small disturbing forces (in case of small masses, at which the angle of deviation from the equilibrium position does not exceed  $\alpha_0$ ) there is an analytical solution.

In this case equation (8) can be written in the form

$$I \ddot{\delta} + \xi \dot{\delta} + (k_1 Y^2 + k_2 L^2) \delta = Me(t, \nu), \quad (11)$$

where it is convenient to present  $Me(t, \nu)$  as

$$Me(t, \nu) = m r_0 l (2\pi\nu)^2 \exp^{i2\pi\nu t}. \quad (12)$$

Under a steady mode of operation of the system, the solution has the form

$$\delta(t) = A \exp^{i2\pi\nu t}. \quad (13)$$

Substituting (13) into (11) with consideration of (12), we obtain

$$\begin{aligned} -A(2\pi\nu)^2 I + i2\pi\nu \xi A + (k_1 Y^2 + k_2 L^2) A &= \\ = m r_0 l (2\pi\nu)^2. \end{aligned} \quad (14)$$

Hence,

$$A = \frac{mr_0 l (2\pi\nu)^2}{(k_1 Y^2 + k_2 L^2 - (2\pi\nu)^2 I + 2\pi\nu \xi i)} \quad (15)$$

From (15) we find

$$|A| = \frac{mr_0 l (2\pi\nu)^2}{\sqrt{(k_1 Y^2 + k_2 L^2 - ((2\pi\nu)^2 I)^2 + (2\pi\nu \xi)^2)}} \quad (16)$$

The resonant frequency will be

$$\nu_0 = \frac{1}{2\pi} \sqrt{\frac{k_1 Y^2 + k_2 L^2}{I}} \quad (17)$$

In cases of large disturbing forces, when the angle of deviation of the cutting arm relative to its equilibrium position exceeds  $\alpha_0$ , i.e., when a vibro-impact mode of cutting is realized, the solution of the equation of motion of the system (8), expressed numerically, makes it possible to theoretically obtain the trajectories of motion of the cutting arm (Fig. 2).

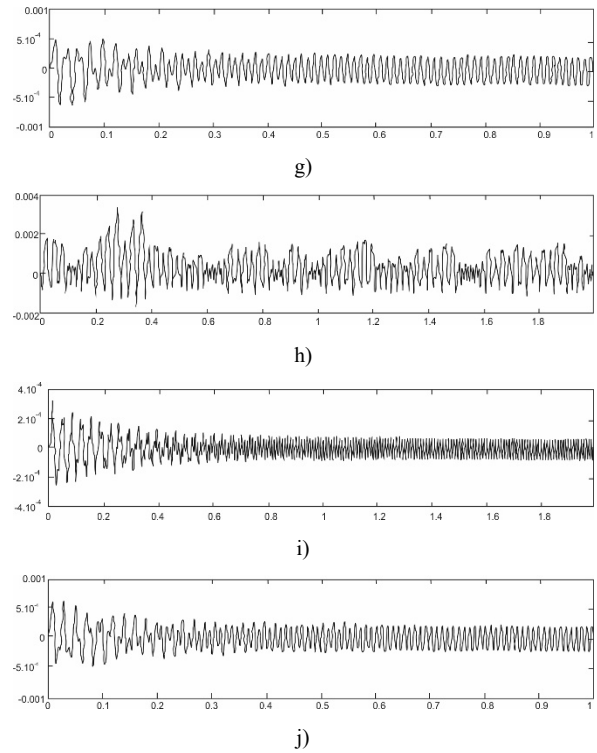
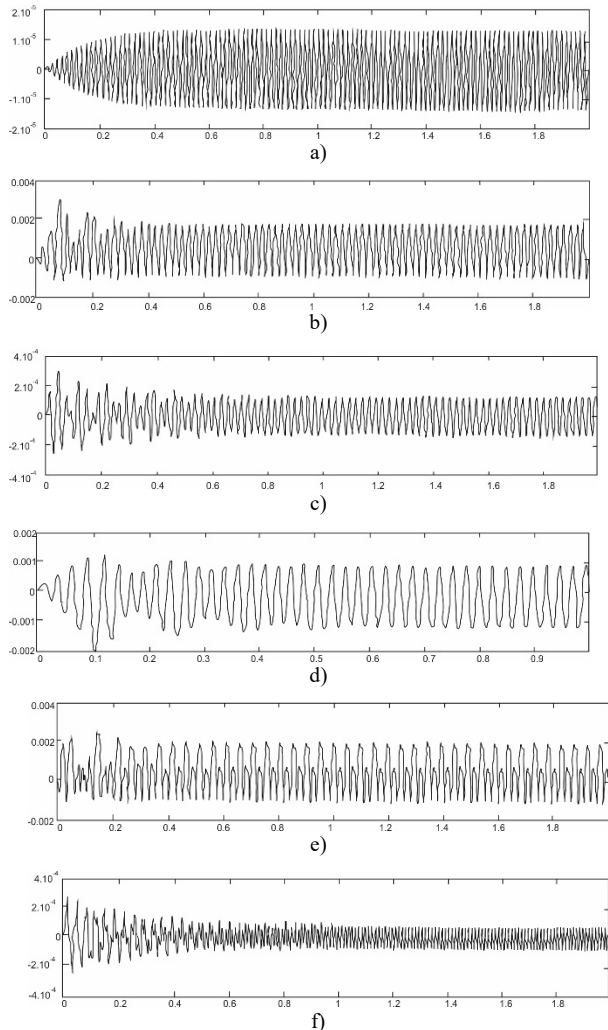


Fig. 2. Amplitude-frequency spectrum of the oscillating movements of the cutting arm: a) for a mode of processing with no impact at theoretical resonant frequency  $\nu_0 = 57 \text{ Hz}$  ; b), c), d)  $\nu_0 = 41 \text{ Hz}$  ; e), f), g)  $\nu_0 = 85 \text{ Hz}$  ; h), i), j)  $\nu_0 = 101 \text{ Hz}$  ; b), e), h) displacement  $y_1 = 0,17 \text{ m}$  ; b), c), f) i) displacement  $y_1 = 0,37 \text{ m}$  ; b), e), h) mass  $m_1 = 0,45 \text{ kg}$  ; d), g), j) mass  $m_1 = 1,45 \text{ kg}$  .

It is observed, that the frequency of the forced oscillations, for which the trajectory of movement was obtained in the cases of separation of the workpiece from the cutting disk (Fig.2 b, e, h), corresponds to the frequency of the vibro-impact modes 1-3, used in the tests for cutting optical materials.

The movement of the vibrator along the cutting arm in the direction of the machined workpiece (Fig. 2 c, f, i) leads to a significant decrease in the amplitude of oscillations (up to 10 times) which, in turn, reduces the ratio between the distances  $l/L$ , where  $l/L$  are respectively the distances from the axis of rotation of the cutting arm to the points of attachment of the vibrator and the workpiece. The reduction of the disturbing forces on the cutting arm is well presented in Fig. 2 i. When placing the vibrator close to the axis of rotation of the cutting arm and at its maximum speed of rotation (Fig.2h), stable nature of oscillations is observed, with high frequencies and an amplitude, one order of magnitude lower.

The increase in the mass of the system (e.g., when using a larger size electric motor) will increase its inertia, which leads to a decrease in the frequency of oscillation of the cutting arm and decrease in its amplitude (Fig.2 d, g, j).

## 2.2. Study of the dynamics

To evaluate the influence of the vibro-impact mode of processing when cutting optical slugs on the intensity of the process, it is necessary to study the forces, acting on the side surfaces of the cutting disk and the workpiece.

Fig. 3 illustrates part of the trajectory of movement of the cutting arm for the time of contact between the workpiece and the cutting disk. In order to perform a comparative analysis of the movements in the system, the magnitude of the angle of equilibrium  $\alpha_0$  was taken into account. This angle takes into account the deviation of the cutting arm from its initial position when the cutting tool comes into contact with the optical workpiece. The ratio between the forces, acting in a standard cutting process, and in case of forced oscillations toward the machined workpiece, will be proportional to the ratio of the perpendiculars to the straight line AE, drawn from the points B and G, respectively. It can be seen from Fig. 3 that the magnitudes of the forces of interaction between the sample and the tool in a vibro-impact mode of cutting will be significantly higher, which leads to an increase in the depth of the pre-destructive layer in the material of the workpiece, and an increase in the processing intensity.

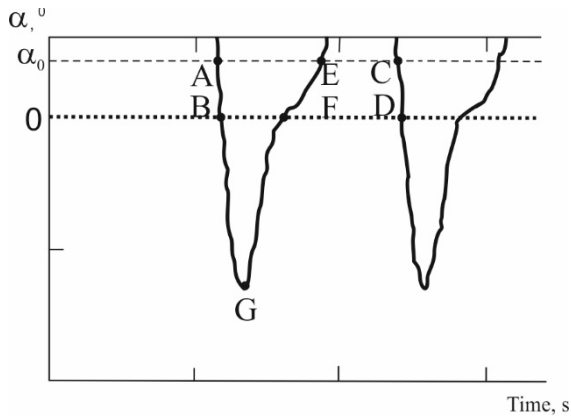


Fig. 3. Trajectory of movement of the cutting arm with the machined workpiece in the contact zone with the cutting disk.

Taking into account the fact, that the constituent forces intersect with the constituents of the free oscillations in the system, we can consider that the phenomenon of nonlinear resonance occurs.

Then the law of motion of the vibro-impact system takes the form

$$x(t) = A \cos(\omega t + \varphi) - Jx(t) \quad , \quad (18)$$

where A is the amplitude, determined when there is no impact motion;

$$J = \int_{t_a}^{t_a + \Delta} \Phi(x, \dot{x}) dt \quad - \text{impulse for the contact time } \Delta \quad (19)$$

$$\Phi(x, \dot{x}) \quad - \text{force of the impact interaction;}$$

$x(t)$  - the resulting reaction in the system of the force interaction.

To determine the unknown quantities  $J$  and  $\varphi$ , we set the conditions

$$x(0) = x_0, J(\alpha) = m(1+K)x_0. \quad (20)$$

Then  $x_0(t) = A \cos \varphi - Jx(0)$ ,

$$J = \left[ -\omega A \sin \varphi - J \dot{x}(0) \right] (1+K)m.$$

The evaluation of the stability of the oscillations, described by (18), and fulfilling the condition  $x \leq x_0, J \geq 0$ , is performed after setting the parameters of the system based on the energy function

$$E(J, \varphi) = E_1(J, \varphi) - E_2(J, \varphi),$$

where  $E_1(J, \varphi)$  is the work of the forces, created by an outer source;

$E_2(J, \varphi)$  - the work of the dissipation forces.

According to [10], the inequality

$$\left. \frac{dE}{dJ} \right|_{\substack{J=J_0 \\ \varphi=\varphi_0}} = \left( \frac{\partial E}{\partial J} + \frac{\partial E}{\partial \varphi} \frac{\partial \varphi}{\partial J} \right) \bigg|_{\substack{J=J_0 \\ \varphi=\varphi_0}} > 0, \quad (21)$$

is a sufficient condition for the instability of the considered system at  $J = J_0, \varphi = \varphi_0$ .

The most intense resonant modes and those, which are close to the free modes, significantly differ from the natural frequency of the system. This makes the first term in the right-hand side of the dependence (18) much smaller than the second.

With this in mind, we find the approximate solution for the resonant vibro-impact modes

$$x(t) = -Jx(t). \quad (22)$$

At  $x(0) = x_0$  we have  $J = -\frac{x_0}{x(0)}$  and

$$x(t) = \frac{\Delta}{x(0)} x(t).$$

At small amounts of damping due to the external influence, the expression (21) uniquely describes the resonant modes of the system.

Putting  $P(t) = P \cos(\omega t + \varphi)$  we will find the conditions for the existence of the quasi-resonant movements at any multiple of  $l$ , while balancing the work of friction forces and disturbance forces.

The period of these oscillations  $T = 2\pi l / \omega$ .

The energy balance equation describing the condition for maintaining the resonance mode takes the form

$$E_1 = E_2 + E_3, \quad (23)$$

where  $E_1 = \int_0^{\tau_1} P(t) \dot{x}(t) dt$  is the work done by external sources;

$$E_2 = \int_0^{\tau_1} G^{-1} [\varphi_\alpha x(t)] \dot{x}(t) dt \quad \text{- the loss of energy;}$$

$$E_3 = J^2 \frac{1-K}{2m(1+K)} \quad \text{- the work of the forces in case of contact friction.}$$

From the dependence of the magnitude of the impact pulses on the frequency of the external impact, the unstable modes of the system can be determined.

At higher levels of damping and excitation, the oscillations will not have a resonant character. For a system with  $x_0 > 0$ , with a gradual increase in the frequency of external impacts, the highest intensity vibro-impact modes can be realized, in which, when reaching certain characteristic magnitudes of the frequencies, determined by the conditions of the energy balance, the forces of excitation and damping decay.

For a system with  $x_0 < 0$ , the opposite situation occurs, and the oscillations in such a system arise after the transmission of additional initial impulses. When  $x_0 = 0$ , the most intense oscillations are possible to occur over the full range of used frequencies. As the natural frequencies increase, the influence of the dissipation factors also increases and the limiting magnitudes of the impact pulses decrease.

### III. CONCLUSION

On the basis of the proposed mathematical model for studying the kinematic and dynamic conditions of interaction between the machined workpiece and the cutting disk, trajectories of the oscillation displacements of the workpiece relative to the cutting tool have been obtained both for continuous (stationary) and vibro-impact modes of operation when cutting optical workpieces.

It has been established that the used modes of operation of vibrators with frequencies, equal to or multiple of the resonant frequency of the cutting arm, allow to obtain stable amplitudes of oscillations.

The change in the position of the vibrator of the cutting arm to a side of the machined workpiece, as well as the increase in its mass, lead to an increase in the static

load on the workpiece and causes a decrease in the amplitude oscillations, which, in turn, reduces the processing performance.

### IV. ACKNOWLEDGMENTS

This work was supported by the European Regional Development Fund within the OP "Science and Education for Smart Growth 2014-2020", Project Competence Centre "Smart Mechatronic, Eco-And Energy Saving Systems And Technologies", № BG05M2OP001-1.002-0023.

### REFERENCES

- [1] I.M. Bykovsky Fundamentals of the theory of vibration technology. M.: Mashinostroenie, 1998, p.362.
- [2] Sergiev A P, Vladimirov A A, Makarov A V and Shvachkin E G, The physical basis of the process of vibration cutting during turning, Scientific-theoretical journal Herald of the Belgorod State Technological University 3, pp.94 – 102, 2017.
- [3] Sergiev A P, Vladimirov A A and Shvachkin E G, Optimization of technological parameters during vibration cutting, Vestnik mashinostroeniya 3, pp. 79 – 82, 2017.
- [4] Mikheyev V V, Saveliev S V and Permyakov V B Comprehensive approach to the selection of the optimal energy-effective mode of operation of vibration rollers, Problems of mechanical engineering. Materials of the 3rd International Scientific Conference pp 158-165, 2019.
- [5] S. Sabev, P. Kasabov. The effect of feed rate and cutting speed to surface roughness during hole boring of aluminum with anti-vibration boring bar. Environment. Technologies. Resourced. Proceeding of the International Scientific and Practical Conference, 2021. 3. 314-318, doi: 10.17770/etr2021vol3.6537.
- [6] S. Sabev, P. Kasabov. The influence of feed rate and cutting speed to surface roughness during hole boring of AISI 304 with anti-vibration boring bar. AIP Conference Proceedings. 2449.060004.10.1063/5.0091006.
- [7] Śniegulska-Grądzka D, Nejman M and Jemielniak K, Cutting force coefficients determination using vibratory cutting, Ischia: 10th CIRP Conference on Intelligent Computation in Manufacturing Engineering – CIRP ICME '16. Procedia CIRP 62, pp. 205 – 208, <https://doi.org/10.1016/j.procir.2016.06.091>.
- [8] Wang G F, Hu Y B, Zhu W Q, Bao Z Y, Chen Z J, Huang Z H and Wang W, The design of a compaction parameters management system for intelligent vibratory roller, IEEE 3rd Information Technology and Mechatronics Engineering Conference (ITOEC) pp 634 – 638, 2017, DOI: 10.1109/ITOEC.2017.8122375.
- [9] Hyung Tae Kim, An Mok Jeong, Hyo Young Kim, Jong Wook An, Cheol Ho Kim, Kyung Chan Jin and Seung-Bok Choi, Lateral vibration control of a precise machine using magneto-rheological mounts featuring multiple directional damping effect, Smart Materials and Structures, Volume 27, Number 3, 2018, DOI 10.1088/1361-665X/aaad9e.
- [10] G. Scott. Experimental estimation of thermal processing possibilities of crystal glass. New works on friction and wear. M., 1989, pp. 78-84.

# *Increasing the Quality of Forming of Spinning Details of Aluminum Alloys by Controlling the Residual Stresses in Their Surface Layer*

**Dimilyan Leonov**

*Department of Mechanical  
Engineering Equipment and  
Technologies  
Technical University of Gabrovo  
Gabrovo, Bulgaria  
dimilqn@gmail.com*

**Angel Lengerov**

*Department of Mechanical  
Engineering Equipment and  
Technologies  
Technical University Sofia, Branch  
Plovdiv  
Plovdiv, Bulgaria  
anlengerov@abv.bg*

**Kalin Krumov**

*Department of Mechanical  
Engineering Equipment and  
Technologies  
Technical University of Gabrovo  
Gabrovo, Bulgaria  
kalin\_krasimirov\_krumov@abv.bg*

**Hristo Metev**

*Department of Mechanical  
Engineering Equipment and  
Technologies  
Technical University of Gabrovo  
Gabrovo, Bulgaria  
hmetev@abv.bg*

**Abstract.** In the article are analyzed the effect of technological modes and processing parameters on the stress of spinning (cold flow turning) details of aluminum alloys. As the object of the study was used a detail of aluminum alloy AMg5, obtained after 3-stage spinning with intermediate heat treatments between the stages. As a control criterion was used non-destructive resistive electro contact method, based on the correlation between the integral electric and mechanical characteristics of metals and alloys – specific conductivity or electrical resistivity within the h-layer of the metal and the amount of deformation in the crystal lattice of the material due to the residual stresses.

**Keywords:** non-destructive method, residual stresses, resistive method, spinning (cold flow turning).

## I. INTRODUCTION

When products are manufactured from metals and alloys, in many cases they are subjected to mechanical or thermal effects, which lead to plastic deformations of the crystal lattices of the materials of the products. This, in turn, results in occurrence of mechanical stresses in the deformed layer of the material, which can be the reason for destruction of the details at loads, even lower than calculated.

In a process of spinning the cause of internal stresses is the focus of the plastic deformation. The occurrence of such stresses can lead to local deformations and defects of the workpiece. An increase in the compressive stresses can cause formation of corrugations on the surface of the workpieces, while the tensile stresses can give rise to surrounding cracks. Both consequences are indicators for rejection of the products.

This determines the need for exercising reliable control of residual stresses during the technological process of producing details and during their operation [1] – [5]. Many methods are known for carrying out such a control - destructive methods (Davidenkov method, hole drilling method, the washer method, etc.) and non-destructive ones (radio-wave, ultrasonic, magnetic, X-ray diffraction method, etc.), and each of them has its own advantages and disadvantages. The research, presented here, uses a newly developed measuring complex, based on a resistive electro-contact method, which combines in one the advantages of the destructive methods (high reliability, guaranteed error for determining the residual stresses, possibility to determine the distribution of the residual stresses along the depth from the surface) and the non-destructive principle of action.

Print ISSN 1691-5402

Online ISSN 2256-070X

<https://doi.org/10.17770/etr2023vol3.7211>

© 2023 Dimilyan Leonov, Angel Lengerov, Kalin Krumov, Hristo Metev.

Published by Rezekne Academy of Technologies.

This is an open access article under the [Creative Commons Attribution 4.0 International License](https://creativecommons.org/licenses/by/4.0/).

## II. MATERIALS AND METHODS

A study of the stress states of a part, made of aluminum alloy AMg5 GOST 21631-76 by spinning, performed on a two-roll Leifeld ST-400 rotary machine, in three transitions with intermediate heat treatments between them, was conducted. The research object was a thin-walled conical body, made of aluminum alloy AMg5, whose initial wall thickness of 6 mm was reduced to 2 mm in the first spinning transition (with a cone angle of 64°), to 1, 2 mm in the second pass (with a cone angle of 43°), and up to 0.8 mm in the third one (with a cone angle of 25°) (Fig. 1).

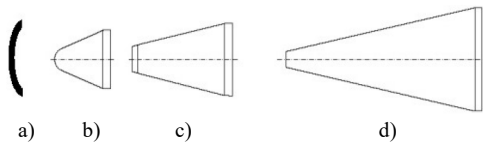


Fig. 1 Detail of AMg5, obtained after spinning in 3 transitions (the transitions are indicated by dashed lines) - a) original workpiece; b) first spinning; c) second spinning; d) third spinning.

For analysis and evaluation of the residual stresses in the process of technological processing of this part, a resistive electro-contact method for non-destructive control was applied. The method is based on the correlation between the integral electrical and mechanical characteristics of metals and alloys - specific electrical conductivity  $\gamma$  or specific electrical resistance  $\rho$  in the h-layer of the metal, and the magnitude of the deformation of its crystal lattice in result of the stresses in its surface layer q.

There is a relationship between the specific electrical conductivity  $\gamma$  (1) and the mechanical stresses [6]:

$$\gamma = \frac{e^2 E n_0}{m k T V_T N_0 \pi} \cdot d \quad (1)$$

where  $e$  is the electron charge, C;  $m$  – the rest mass of the electron, kg;  $n_0$  – the number of conductive electrons per unit volume;  $E$  – field strength, V/m;  $k$  – Boltzmann's constant, J/K;  $T$  – absolute temperature, K;  $V_T$  – speed of thermal movement of the electrons, m/s;  $N_0$  – number of atoms per unit of volume;  $d$  – period of the crystal lattice, m. The relationship between the specific electrical conductivity  $\gamma$  and the specific electrical resistance  $\rho = 1/\gamma$  is also known.

In the absence of mechanical stresses, the metal has a nominal value of the lattice period  $d_0$  and a corresponding nominal value of the specific electrical conductivity  $\gamma_0$ . Under the influence of the changes in the mechanical stresses  $\Delta\sigma$ , a change in the period of the metal lattice  $\Delta d$  is observed. In the zone of elastic deformations, this change can be assumed to be proportional to the mechanical stress. In accordance with (1), the change in the electrical conductivity  $\Delta\gamma$  is also proportional to the average mechanical stresses  $\Delta\sigma$  according to the formula (2):

$$\Delta\gamma = K_\sigma \cdot \Delta\sigma \quad (2)$$

where  $K_\sigma$  is an experimentally determined coefficient, characterizing the properties of the material.

Thus, the mechanical stresses in conductive materials can be determined by measuring their electrical properties. In doing so, it is necessary to measure the distributions of the electrical parameters and mechanical stresses along the depth of the products.

To measure the distribution of the specific resistance in depth, the skin effect phenomenon is used, in which the high-frequency currents are concentrated in that area from the surface of the conductor, which is located closest to the sources of the field, causing the currents. Based on the solution of the system of Maxwell's equations for the conductive semi-area, the penetration depth of the current  $h$  in such a conductor is determined as it follows (3):

$$h = \frac{1}{\sqrt{\pi f \mu \gamma}} \quad (3)$$

where  $f$  is the current frequency, Hz;  $\mu$  – the magnetic permeability of the material, Gn/m;  $\gamma$  – the specific electrical conductivity of the material, Ohm<sup>-1</sup>.

The magnitude of the current density decreases exponentially with increasing the depth, and  $h$  represents a value of the depth (3), at which the current density drops by "e" times compared to the initial value of the surface current. By definition  $h$  is the depth of current penetration into the conductor, i.e., the thickness of the surface layer, in which the main part of the current propagates.

The use of the skin-effect phenomenon allows to examine the surface layer of the product in depth - level by level - supplying it with currents of different frequencies and measuring the response signal, whose parameters are related to the change in the stress state of the product material. By reducing the frequency of the alternating current, applied to the product in accordance with formula (3), the depth of the investigated layer is increased. The choice of the operating frequencies ensures the required range of the measured depths of the product [7].

Based on the given method, with the aim of studying the influence of the spinning modes on the residual stresses in the surface layer of the samples, made of AMg5 material, a stress optimization process was carried out, according to the following plan:

- measurement and analysis of the stressed state of the samples by means of a resistive electro-contact method of control after each spinning transition;
- study of the influence of both the machining and heat treatment modes on the level of residual stresses in the material of the workpieces by applying the theory of experimental design;
- obtaining technological modes of processing, ensuring the lowest possible magnitude of residual stresses in the surface layer of the workpieces.

### III. RESULTS AND DISCUSSION

The SITON-TEST measuring complex (System for measuring technological residual stresses), developed by the Department of Instrumentation Technologies at the Saint Petersburg National Research University of Information Technologies, Mechanics and Optics (ITMO University), was used to determine the voltages. Based on the physical nature of the resistive electro-contact method, described above, it was implemented in this case in the following sequence:

- current with a different frequency was directed into the tested product through the supply electrodes, and measurements were performed in three points, located at an angle of 120° with respect to each other;
- the strength of the supplied current was measured for each of the set frequencies;
- the voltage of the response signal from the device was measured for each of the set frequencies;
- the distribution of the specific electrical resistance along the depth of the product material was calculated;
- a calibration dependence was derived between the specific electrical resistance and the mechanical stresses in the material of the studied product at depths, corresponding to the penetration depths of the current for the set frequencies;
- on the basis of the obtained dependence, the calculated distribution of the specific electrical resistance was converted into a distribution of the mechanical stresses along the depth of the studied product material [8].

The results of the measurements, performed according to the described algorithm, are shown in Fig. 2.

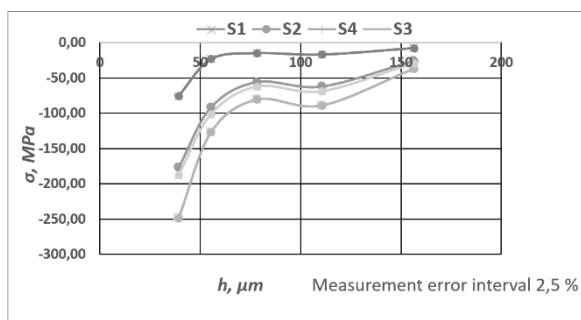


Fig. 2 Distribution diagram of the residual stresses, where S1 illustrates the stresses, measured in the original sample after heat treatment; S2 – in a heat-treated sample after the first spinning; S3 – in a heat-treated sample after the second spinning; S4 – in a heat-treated sample after the third spinning; h - depth of the studied material.

From Fig. 2 it can be seen, that after each spinning of the sample, despite the performed heat treatment, the internal stresses increase. Thus, after the last machining transition, the stresses are at the border to the yield point of the material. This justifies the need to study the influence of the technological modes of processing a

workpiece with the aim of minimizing the internal stresses in its surface layer.

The theory of experimental design was used to analyze both the obtained results and the next stage in the process of optimizing the internal stresses. The aim was to determine the lowest levels of residual stresses when varying with the factors, affecting the changes in the crystal lattice of the material in the process of its technological processing - in other words, to determine the parameter and the factors of optimization.

The magnitude of the residual stresses  $\sigma$  was determined to be the optimization parameter (the maximum values of the residual stresses measured in the surface layer of each sample were taken for the calculations).

When selecting the optimization factors, analysis of the physics of the spinning process was carried out. It is known that the successful spinning process depends on many factors [9] – [12]: degree of deformation, space between the deforming element (roller) and the mandrel, feed rate, spindle revolutions, shape and geometry of the working parts of the rolls, roll diameter, coolants, modes of intermediate heat treatment (in multi-pass spinning), etc.

The degree of deformation of the material, directly related both to its stability at a certain power of the rotary machine and to the cone angle of the workpiece, determines the necessary number of transitions for producing the finished part. To avoid making additional mandrels and fixtures for the spinning process, in this study the degree of deformation and the angle of the cone were taken with their drawing values (given above in the text, before Fig. 1).

The space between the deforming roll and the mandrel is directly dependent on the initial thickness of the original workpiece  $S_0$  and the thickness of the finished detail  $S$  and follows the well-known law of sine  $S_l = S_0 \sin \alpha$ . Any deviation from the indicated dependence leads to deterioration in stability of machining, and therefore the specified factor was not varied in the given study, while the details specified in the technological documentation were observed.

Productivity and quality of workpiece processing during spinning depend to a significant extent on the feed rate  $S$  and the radius of rounding of the working part of the roll  $\rho$ . In case of incorrect selection of these parameters, formation of cracks on the surface of the part is possible. When spinning with a feed  $f$ , greater than the allowable tool feed rate for the given material, and in case of an incorrectly selected roll shape, high tensile stresses may arise, which can lead to a complete rupture of the workpiece. Breakage may also occur in case of significant deviation of the wall thickness from the calculated value and a change in the clearance between the roller and the mandrel. Taking all this into account, the first factor of optimization was assumed to be the operational feed rate  $f$ . In the process of machining during this study, deforming

elements were used with an angle of the working part  $\varphi=20^\circ$ .

The rotational speed of the workpiece during machining should be as high as possible. The higher speed results in greater flange stability. For this reason, the level of the rotary machine spindle revolutions was determined as the second factor in the optimization process.

The modes of the performed intermediate heat treatment have the most significant influence on the relaxing properties of the material to return to its initial unstressed state after the impact of the plastic deformation. Therefore, the heat treatment temperature was chosen to be the third optimization factor in the presented study.

Thus, based on the analysis, as factors of the process of optimization were adopted the technological modes of spinning and the modes of the intermediate heat treatment performed between the spinning transitions (feed rate  $f$ , spindle revolutions  $n$ , heat treatment temperature  $T$ ).

Their basic levels are:  $f=0.41$  mm/tr,  $n=800$  min<sup>-1</sup>,  $T=350^\circ\text{C}$ . The ranges of variation of the factors were chosen based on the results of the conducted preliminary experiments (whose results are presented in Fig. 2):  $f=\pm 0.39$  mm/tr,  $n=\pm 20$  min<sup>-1</sup>,  $T=\pm 20^\circ\text{C}$ .

The conducted statistical calculation [13] allows to obtain:

- an adequate mathematical model of the process (according to Fisher's criterion), describing the relationship between the parameter and the factors of optimization (4):

$$\sigma = 207,3 + 13,7f - 3,2n - 5,8T + 2,1fn + 3,275nT + 2,75fnT \quad (4);$$

- the technological modes of processing the part (optimal for the specific production conditions), providing minimum values of residual stresses in the surface layer of the AMg5 sample in the spinning process:  $f=0.21$  mm/tr,  $n=815$  min<sup>-1</sup>,  $T=360^\circ\text{C}$ .
- the optimal distribution of the residual stresses along the depth of the surface layer of the workpieces, processed under the given modes (Fig. 3).

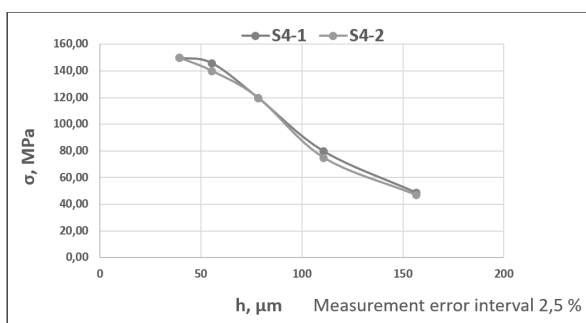


Fig. 3. Optimal distribution of the residual stresses along the depth of the surface layer of the workpieces, where S4-1 and S4-2 illustrates the optimal distribution of the residual stresses along the depth of the surface layer of two workpieces, processed under the given modes;  $h$  - depth of the studied material.

The obtained results illustrate the manageability of the residual technological stresses and prove the efficiency of using the resistive electro-contact method in search of optimization of the given parameter [14], [15]. The task, no doubt, as well as similar tasks, can be also solved by applying other methods of stress control – non-destructive (ultrasound, radio-wave, X-ray diffraction etc.) or destructive (the Davidenkov and Berger method, the method of probing holes, the ring method etc.) [16] – [23]. However, given the need for a fast, reliable, non-destructive control and a diagram of the stress distribution in the depth of the surface layer, the presented approach is accepted in this study as optimal.

To verify the mechanical properties of the material in conclusion of the study of workpieces, having a distribution of residual stresses as it is shown in Fig. 3, samples were cut in accordance with GOST 1497-84. The tests show that from the moment of yield onset of the material (at a load of 140 MPa) to the moment of rupture of the sample (at a load of 290 MPa), the relative elongation is 15%. The obtained results from the rupture test (at tension) satisfy the requirements for yield point  $\sigma_T$ , tensile strength  $\sigma_B$  and relative maximum elongation  $\delta$  of the AMg5 material.

#### IV. CONCLUSION

The proposed methodology for optimization of the residual stresses in the surface layer of details allows to study and evaluate their influence in the spinning process of thin-walled details from aluminum alloys. The means of mathematical support of the process by statistical analysis, provide possibilities to derive the optimal technological modes for quality products formation. The applied resistive electro-contact non-destructive method allows to trace the nature of the stresses in the surface layer of the details. The availability of a distribution diagram of these stresses along the depth of the surface layer illustrates their technological controllability, which can contribute to increasing the quality of the manufactured products in mechanical and instrumental engineering.

#### REFERENCES

- [1] A.Y. Ivanov, D.B. Leonov. Analysis of the methods for control and measurement of residual stress // Journal of the Technical University - Sofia, Plovdiv branch, Bulgaria «Fundamental Sciences and Applications», 2012, Volume 17. pp. 13–19.
- [2] A.Y. Ivanov, D.B. Leonov. Technological methods of providing product quality, Scientific and technical journal of SPbGU ITMO, 2011, No. 5(75), pp. 111 – 113 (in Russian).
- [3] S.P. Burkin. Residual stresses in metal products: textbook. Yekaterinburg: Publishing House of the Ural University, 2015. p. 12 (in Russian).
- [4] V.F. Bezyazychny, R.N. Fomenko. Technological support of the operational properties of gas turbine engine parts // Journal of Metalworking, Politehnika Publishing House. 2017. No. 1. pp. 16–22 (in Russian).
- [5] V.S. Mukhin. Surface. Technological aspects of the strength of GTE parts. M., 2005. p.295.
- [6] V.A. Valetov, S.D. Vasilkov, O.S. Yulmetova. Methods of researching the characteristics of the surface layer of device parts, Teaching manual, St. Petersburg, 2010 (in Russian).

- [7] A.D. Ilyina. Resistive electrocontact method for determining residual stresses in parts after machining. Young Scientists Forum.-2022, No. 5(69), 2019, pp. 145-148 (in Russian).
- [8] D.B. Leonov, A.Y. Ivanov. Control of residual stresses during spinning of aluminum alloy parts // Proceedings from the "Jubilee Scientific Conference on the occasion of 10 years since the establishment of the NVU". - Volume 7., V. Tarnovo, 2012, pp. 120–126 (in Bulgarian).
- [9] D.V. Dudka, V.I. Tregubov. Influence of technological parameters on flow formation during rotational spinning of axially symmetric parts, News of Tula State University, TulSU Publishing House, 2011, pp. 3 – 13 (in Russian).
- [10] P.M. Vinnik, T.V. Vinnik, A.I. Olehver, A.Y. Remshev. Calculation of the influence of material hardening on stresses and formed mechanical properties during successive drawings with wall thinning. Metalworking, No. 1, 2019, p. 30-34.
- [11] V.M. Kishurov, N.K. Krioni, V.V. Postnov, P.P. Chernikov, M.V. Kishurov. Processes of forming parts in mechanical engineering: textbook. M.: Journal of Mechanical Engineering, 2015. p. 496.
- [12] A. S. Chumadin1 , D.A. Baturin1. Modeling and control of the Springback Effect in the Bottom Sheet Metal Part One stage Drawing Process. Science and Education of the Bauman MSTU, 2014, no. 9, pp. 106–118.
- [13] RDMU 109-77. Method of selection and optimization of controlled parameters of technological processes. Introduction 07/01/1978. M, Standards Publishing House, 1978, p. 48 (in Russian).
- [14] D.V. Vasilkov, S.D. Vasilkov, A.V. Nikitin. Measurement of residual stresses by the resistive electrocontact method // Journal of Metalworking. 2017. No. 6. pp. 30–34.
- [15] D.V. Vasilkov, D. A. Mezentsev, A. V. Nikitin [et al.] Technological residual stresses and their deforming ability during cutting //Journal of Metalworking. 2018. No. 4. pp. 2–6.
- [16] G.V. Muratkin. Processes of formation and reduction of technological residual deformations of non-rigid parts // Journal of Metalworking. 2019. No. 6. pp. 17–26.
- [17] Saha S. Non-Destructive Evaluation of Residual Stresses in Welding. 2022. DOI: <http://dx.doi.org/10.5772/intechopen.101638>.
- [18] Suvi-Santa-aho, Laitinen A, Sorsa A, Vippola M. Barkhausen noise probes & modelling: A review. Journal of Nondestructive Evaluation. 2019;38(4): 2-4.
- [19] A.H. Mahmoudi, A. Ghasemi, G.H. Farrahi, K.A. Sherafatnia. Comprehensive experimental and numerical study on redistribution of residual stresses by shot peening // Materials & Design. 2016. N 90. P. 478–487.
- [20] N.N. Stolyarov, A.D. Sukhikh, M.V. Tabanyukhova, Residual Stresses in 3D-Printed Models. Proceedings of the Novosibirsk State University of Architecture and Civil Engineering (Sibstrin), 24-1/2(79/80) 48-54 (2021).
- [21] M. Tabanyakhova, , N. Slolyarov, A. Nagel, The issue of residual stresses in Additive Technologies. MATEC Web of conferences, Volume 376, AMEFP 2022, DOI: <https://doi.org/10.1051/mateconf/202337601008>.
- [22] G.V. Samandasyuk, I.A. Slesarev, M.S. Kozhen, Additive Technologies in Construction. Globe: Engineering Sciences 2(33) 18-1 (2020).
- [23] A.D. Sukhikh, N.N. Stolyarov, M.V. Tabanyukhova, The Issue of Residual Stresses in 3D-Printed Models. In the coll.: The Intellectual Potential of Siberia. Collection of Scientific Papers of the 29thRegional Scientific Student Conference dedicated to the Year of Science and Technology in Russia. In 5 Parts. Ed. D.O. Sokolova, Novosibirsk, 88-92 (2021).

# *Solving Functional-Technological Problems Using a Non-Parametric Approach for Control of Microgeometry of the Surfaces of Details*

**Dimilyan Leonov**

*Department of Mechanical  
Engineering Equipment and  
Technologies*

*Technical University of Gabrovo  
Gabrovo, Bulgaria  
dimilqn@gmail.com*

**Hristo Metev**

*Department of Mechanical  
Engineering Equipment and  
Technologies*

*Technical University of Gabrovo  
Gabrovo, Bulgaria  
hmetev@abv.bg*

**Kalin Krumov**

*Department of Mechanical  
Engineering Equipment and  
Technologies*

*Technical University of Gabrovo  
Gabrovo, Bulgaria  
kalin\_krasimirov\_krumov@abv.bg*

**Angel Lengerov**

*Department of Mechanical  
Engineering Equipment and  
Technologies*

*Technical University Sofia, Branch  
Plovdiv  
Plovdiv, Bulgaria  
anlengerov@abv.bg*

**Abstract.** In the article considers the effect of surface roughness on the functioning of a specific mechanism. In case of proven dependence of the studied functional property of surface microgeometry, a process of optimization of the sought parameter is carried out, in which the methods of mathematical analysis and theoretic foundations of technology of appliance and mechanical engineering are used for the basis of the theoretical studies. As control parameters of the specified optimal microgeometry, deciding the given task, the so-called non-parametric criteria are used, namely graphical of certain surface-profile functions.

**Keywords:** *surface roughness, non-parametric method, graphic images, theory of experimental planning.*

## I. INTRODUCTION

Increasing the quality of the manufacturing output is the most important task of the industry [1] – [4]. The task is especially topical for mechanical and instrumental engineering, where multiple technological problems, related to the functioning of the manufactured products need to be solved. The role of the state of the surface layer of the details in the given process is generally recognized,

though the problems, related to optimization of the surface microgeometry remain the least researched.

It has been established so far that the roughness of the surfaces affects about 20 of their functional properties (adhesion, corrosion resistance, force of friction etc.). However, the task to optimize the surface microgeometry cannot be reliably solved by using the standardized parameters (ISO 4287), since they often do not reflect the real nature of the surface relief. By setting a specific value to the roughness parameter in the technical documentation, and trying to comply with it, we can process a surface and obtain one of the numerous possible micro-reliefs, which will provide different functional properties - to give an example, two mirror-like profiles, describing totally different microreliefs, have the same parameters [5], [6].

Most surface treatment methods produce a random roughness profile. Therefore, the theory of random functions can be used to model the surface roughness, which actually means that the profile of a real surface can be regarded as a realization of a random variable.

On this basis Prof. Valetov proposed a fundamentally new approach to surface roughness evaluation and

*Print ISSN 1691-5402*

*Online ISSN 2256-070X*

<https://doi.org/10.17770/etr2023vol3.7230>

© 2023 Dimilyan Leonov, Hristo Metev, Kalin Krumov, Angel Lengerov.

*Published by Rezekne Academy of Technologies.*

*This is an open access article under the [Creative Commons Attribution 4.0 International License](https://creativecommons.org/licenses/by/4.0/).*

control – a method, using non-parametric criteria, in the role of which the graphs of various functions are taken [7] – [11]. Considering the random component in the process of forming the surface microrelief and based on the theory of random functions, it is clear that the biggest amount of information about the profile as a random variable is contained in the distribution functions and distribution density of its ordinates, as well as in the distribution functions and distribution density of the tangents of the slope angles of the profile. Thence, the conclusion about the expediency of using these functions as criteria for evaluating and controlling the roughness of the surfaces follows.

## II. MATERIALS AND METHODS

A special pneumatic mechanism, shown in Fig. 1, was used in this case as an object of study. The basis of its functioning is the outflow of air through the gap between the cylindrical surfaces (pos.  $\Delta$ ) of the sleeve (pos. 1) and the obturator (pos. 2) during the movement of the latter under the action of a spring with certain parameters (pos.3).

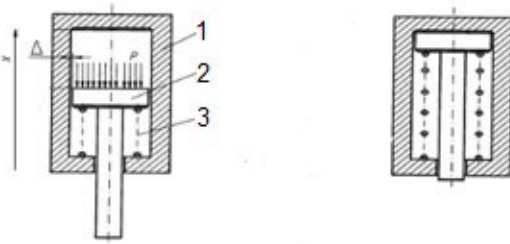


Fig. 1. Pneumatic mechanism.

The process is described by the following system of equations (1):

$$\begin{cases} m \frac{d^2x}{dt^2} = -R_{as} + cx(t) + P(t)S_n \\ \frac{dM(t)}{dt} = -Q(t) \\ M(t) = \rho(t)x(t)S \end{cases} \quad (1),$$

where  $m$  is the mass of the obturator,  $R_{as}$  – the spring tension in the composition of the assembly,  $c$  – the spring hardness,  $S$  – the area, through which the air goes out,  $Q(t)$  – amount of air per second,  $M(t)$  – air mass consumption,  $S_n$  – area of the functional surface of the obturator,  $P(t)$  и  $\rho(t)$  – air pressure and density,  $x(t)$  – movement of the obturator in the sleeve.

Modeling the process and solving the system of equations (1) in “Matlab” software environment allows for obtaining limiting values of the movement time in the range:  $104 \text{ ms} \geq t \geq 37 \text{ ms}$ . The given values match the conditions of friction between the parts (with possible intersection of the axes of the two functional details) and

the conditions of absence of friction (pure gas-dynamic process).

The results, obtained when solving the mathematical model, are difficult to reproduce experimentally, due to the impossibility to model accurately the intersection of the axes of the functional details in the mechanism. Therefore, to prove the validity of the performed calculations, a representative sample from a general set of mechanisms of the given type was considered, with fixing the time of the obturator movement in the sleeve [12]. It showed that for a batch of 12000 mechanisms a sample of 1200 pcs. is required to claim with a probability of 0,95 that the true value of the average movement time during the operation of the mechanisms will be in the range 78,86 – 81,25 ms.

In addition, the influence of the surface roughness of the nodes in the pneumatic mechanism on the movement time was also studied in the indicated range.

To construct and compare the non-parametric evaluation criteria, the Lemming software product, developed by the Department of Instrumentation Technology at the St. Petersburg National Research University for Information Technologies, Mechanics and Optics (ITMO University) was used [13] – [15].

With the help of this program, the obtained profile data were processed in the following sequence:

- Construction of the profile of the studied surface;
- Profile filtration using a straight and inverse Fourier transformation - the filtration was carried out on the basis of the given functional property of the surfaces by comparing the amplitude spectra of the profiles of the studied surfaces before and after the moment of functional impact on them.
- Calculation of the standardized roughness parameters according to ISO 4287;
- Calculation and construction of the non-parametric criteria for evaluating the profile of the surfaces.

Prior to functional property verification, roughness data were taken from the surface of each sample. After processing the obtained profile data, graphs of the non-parametric criteria for these surfaces were drawn (Fig.2).

From the graphs in Fig.2. it follows that the technologies of machining sleeves and obturators allow for providing the same standardized criteria for their surface roughness. However, the more informative non-parametric criteria indicate, that these microreliefs are different.

Another important conclusion drawn up from the conducted research is the effect of the surface roughness of the two details (sleeve and obturator) on the movement time of the obturator in the sleeve, which defines the operation of the specified mechanism. This effect justifies the necessity of carrying out a process of optimization of the respective microgeometries.

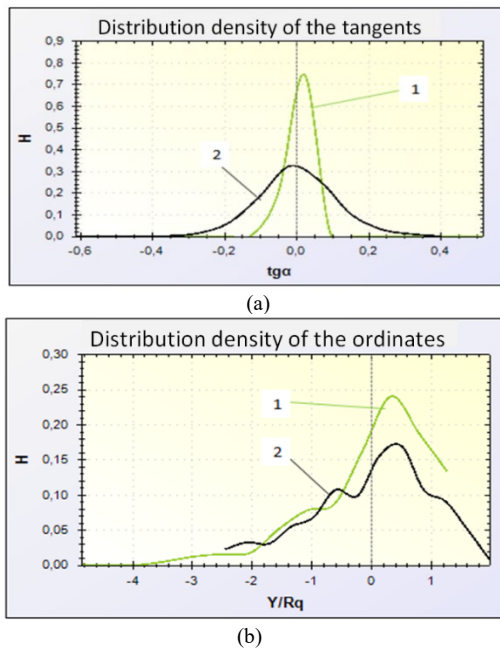


Fig. 2. Distribution densities of the tangents of the slope angles of the profiles (a) and distribution densities of the ordinates of the profiles (b) (H-frequency of repetition of the corresponding value of the tangent (a); H-frequency of repetition of the corresponding values of the dimensionless amplitude (b); 1 – sleeve surface roughness corresponding to  $R_a = 0.32 \mu\text{m}$ , 2 – obturator surface roughness corresponding to  $R_a = 0.30 \mu\text{m}$ ).

At the second stage of the research, possibly the most appropriate for specific manufacturing conditions surface roughness of sleeves and obturators, ensuring the optimal value of the functional property, were defined. With the aim of organizing the process of optimization of the microgeometry of the surfaces, the theory of experimental design was used.

The optimization, based on the theory of experimental design and the use of non-parametric criteria for evaluating the roughness of the surfaces, includes the following main stages [16], [17]:

- selecting/choosing the optimization parameter;
- determining the factors of the technological process and their changes;
- designing the experiment plan or the planning matrix;
- obtaining information about the surface roughness of each sample;
- processing of the profiles and constructing the non-parametric criteria for evaluation of the microgeometry;
- conducting the experiments according to the plan for their implementation;
- performing a statistical analysis in order to derive a regression equation, expressing the relationship between the parameter and the optimization factors;
- assessing the adequacy of the obtained mathematical model.

### III. RESULTS AND DISCUSSION

Microgeometry optimization should be understood as choosing the most suitable, possibly the best microgeometry for particular production conditions. In the given task, when justifying the parameter and the optimization factors, it is necessary to analyze the specific solutions.

The movement time ( $t$ ) of the obturator in the sleeve within the mechanism assembly was taken as an optimization parameter. The additional calculations and the experimental studies show that the optimal value of the movement time during the operation of this type of mechanisms is 80 ms with a possible tolerance of  $\pm 10$  ms.

The technological process of machining sleeves includes drilling, countersinking/chamfering, reaming, honing, zinc coating and polishing. The technological process of obturator processing includes rough turning, finish turning and grinding. The modes of finish machining of both parts were chosen as optimization factors. Based on the capabilities of the technological equipment and on the results of preliminary studies (part of their graphs are shown in Fig. 2), the ranges of their changes were selected (Table 1):

TABLE 1

Factor	Coding notation	Range of changes	Levels of factor values		
			Low (-1)	Base (0)	High (+1)
Feed rate for polishing $V_{f, pol}$	$X_1$	$\pm 0,4$ m/min	0,1	0,5	0,9
Polishing speed $V_{c, pol}$	$X_2$	$\pm 15$ m/s	20	35	50
Circular feed when grinding $V_{f, gr}$	$X_3$	$\pm 1,5$ m/min	5	6,5	8
Grinding wheel speed $V_{c, gr}$	$X_4$	$\pm 10$ m/s	20	30	40

Since the factors in the optimization process are non-uniform and have different measuring units, and the values, expressing their magnitudes are of different orders, they are reduced to a single system of calculations by a transition from the actual values of the factors to coded ones (2):

$$\tilde{X}_i = \frac{X_i - X_{ibas}}{\Delta x_i} \quad (2),$$

where  $\tilde{X}_i$  is the coded value of the factor;  $X_i$  – actual values of the factor;  $X_{ibas}$  – value of the factor at the basic level;  $\Delta X_i$  – current factor variation interval;  $i$  – number of the factor.

In result from a subsequent statistical analysis in accordance with the theory of experimental design [18], an adequate to Fisher's criterion mathematical model of the studied process was obtained in the form of a regression equation, pointing at the relationship between the

movement time of the nodes in the mechanism and the technological processes of machining the contact surfaces of the two details (sleeve and obturator) (3):

$$t = 74,25 + 17,5V_{f,pol} - 6,5V_{pol} - 5,25V_{f,gr} - 2V_{gr} - 2V_{pol}V_{f,gr} \quad (3)$$

The sign of the coefficients of the variable factors in the regression equation defines the nature of the influence of each of them on the parameter under optimization. The values of the coefficients point at the degree of influence of each of the factors on the movement time during the operation of the studied mechanism. Consequently, when controlling the process, much attention should be paid to the modes of sleeve polishing, although the obturator grinding modes, as well as the mutual interference of the polishing speed and grinding feed rate also have certain influence.

Following the described methodology in the optimization process, when controlling the roughness of the specific surfaces of the sleeves and obturators, it is proposed to use the graphs of the functions of the distribution density of the tangents of the slope angles and the dimensionless ordinates of the profiles. As an example, reference graphs are given, titled "Density of distribution of the tangents of the slope angles of the profile" and tolerances are set for possible deviations in performing control in series production of sleeves and obturators (Fig. 3). The figures present graphs, satisfying the required movement time values, which fall within the tolerance field, on the one hand, and graphs, which are outside the tolerance field because of not meeting the requirements, on the other hand.

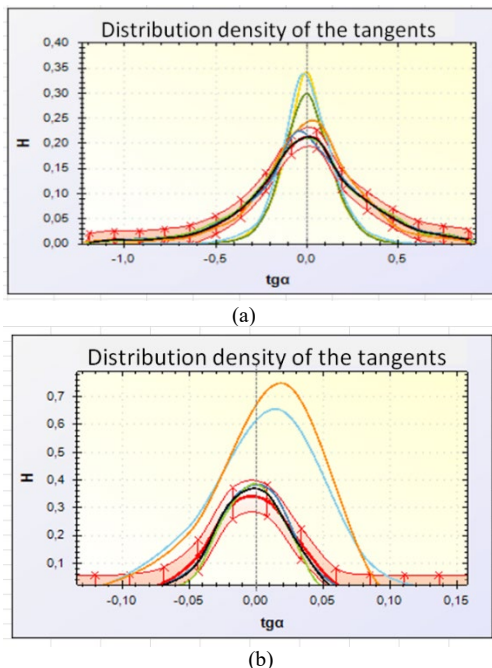


Fig. 3 - Reference graph "Density of distribution of the tangents of the slope angles of the profile" with a tolerance for possible deviations: (a) for the sleeves, (b) for the obturators.

The tolerance value in Fig.3 was chosen to be 30%, due to the scattering, resulting from superimposing of the graphs of all surfaces at an allowable value of the functional property. The given graph illustrates once again the informativeness of the non-parametric criteria for roughness control of the surfaces, while the efficiency and expedience in their use for solving tasks, related to optimization of the microgeometry, is also proved in a number of similar studies [19] – [25].

In conclusion of the study the determination of the most appropriate (reference) microrelief from the possible ones for the specific functional property of the surfaces, allows for obtaining also the technological methods of reproducing the given microrelief:  $V_{f,pol} = 0,572$  m/min;  $V_{c,pol} = 34$  m/s;  $V_{f,gr} = 49,2$  m/min;  $V_{c,gr} = 29,8$  m/s.

#### IV. CONCLUSION

The proposed methodology for optimization of the surface microgeometry can be applied in the analysis of any functional property in any type of production conditions. Moreover, the research allows for creating a database with determination of optimal technological treatment modes for specific properties of the surfaces, which can be used by other production enterprises, possessing the same type of technological equipment. The non-parametric approach, used as a basis for analysis, evaluation and control, allows to unambiguously determine the optimal microgeometry, to reproduce the technological process for achieving it, and to quickly perform quality control under the conditions of serial production by comparing with the reference. The fulfillment of these conditions allows to increase the quality of the issued production for the specific enterprise.

#### REFERENCES

- [1] V.M. Musalimov, V.A. Valetov. Dynamics of frictional interactions: Monograph: in 2 parts. - St. Petersburg: PIMash Publishing House (State St. Petersburg Institute of Mechanical Engineering LMZ-VTUZ), 2006., p. 191 (in Russian).
- [2] H. Metev, K. Krumov, A. Lengerov. Determination of inaccuracies in the reporting by turning the phenomenon of heredity technology. Journal of the Technical University - Sofia, Plovdiv branch, Bulgaria « International Scientific Conference on Engineering, Technologies and Systems TECHSYS 2018». –P. 227–232.
- [3] V.A. Valetov. Additive technologies (state and prospects). Tutorial. - St. Petersburg: ITMO University, 2015, p.63.
- [4] Chirag Patel, Mangal Bhatt. Investigation of Physical Characteristics and Machining Parameters of Improved Al-SiC MMC Using Dry EDM Process for Aerospace Industries. JoEAM. 2018. P. 15–32.
- [5] A.Y. Ivanov, D.B. Leonov. Methodology for optimization, evaluation and control of products surface roughness // Journal of the Technical University - Sofia, Plovdiv branch, Bulgaria «Fundamental Sciences and Applications». – 2012, Volume 17, pp. 19–23 (in Russian).
- [6] E. Filimonova. Automation of the control of microgeometry of machine parts and devices' surfaces using topography, IX All-Russian Mechanic University Conference of Young Scientists. 5<sup>th</sup> session of the scientific school "Problems of mechanics and accuracy in instrumentation". - St. Petersburg, 2012. - Issue. 1. - pp. 132 - 136. - 152 (in Russian).

- [7] V.A. Valetov. Feasibility of changing the standard for surface roughness of parts. Intercollegiate collection No. 6. St. Petersburg, Northwestern State Polytechnic University, 1997, pp. 118-121 (in Russian).
- [8] I.N. Gibadullin, V.A. Valetov. Image of the surface profile as a graphic criterion of its roughness. *Journal of Instrument Engineering*. 2019. Vol. 62, N 1. P. 86–92 (in Russian).
- [9] V.A. Valetov, I.N. Gibadullin. Surface roughness of parts and quality of functional properties of products // *Journal of Metalworking, Politechnika Publishing House*, 2017. V. 101, No. 5. pp. 38-43.
- [10] I.N. Gibadullin, V.A. Valetov. Automated control of the microgeometry of surfaces of parts using graphic images of profiles. *Journal of Instrument Engineering (Izvestiya vysshikh uchebnykh zavedeniy. Priborostroenie)*, 2017. V. 60, No. 3. pp. 287-289.
- [11] V.A. Valetov. Problems of optimization of workpiece surface microgeometry to ensure specific functional properties. *Journal of Instrument Engineering*, 2015, vol. 58, no. 4, pp. 250–267 (in Russian).
- [12] D.B. Leonov. Technological methods for controlling the roughness of the product surfaces // *Collection of scientific papers from the 2012 scientific session at Vasil Levski National University, Part 1., Shumen*, 2012, pp. 77–81 (in Bulgarian).
- [13] V.A. Valetov, E.A. Filimonova, Program for automated control of surface microgeometries using non-parametric criteria, *Metalworking*, No. 5, 2011, pp. 44-47 (in Russian).
- [14] V.A. Valetov, E.A. Filimonova, Automation of surface microgeometry control using non-parametric criteria, *Materials of the 14th International Scientific and Practical Conference, Saint Petersburg*, 2012 (in Russian).
- [15] E.A. Filimonova. Development of Methodology and Software for Automated Control of Instruments Surface Microgeometry using Graphical Criteria and their Application in Technological Research. *Eng. Sci. Dis. Thesis. St. Petersburg*, 2014, 24 p (in Russian).
- [16] A.Y. Ivanov, D.B. Leonov. Assessment of the influence of surface roughness on the corrosion resistance of machine-made products // *Scientific and technical journal of information technologies, mechanics and optics.* – 2013, Issue 6(88), pp. 144–147 (in Russian).
- [17] D.B. Leonov, I.L. Lilov. Methodology for optimizing the influence of surface roughness of the functional properties of details in mechanical engineering // *Machines, Technologies, Materials.* – 2015. - Issue 5. – P. 46–47.
- [18] Guidelines 109-77. Methodology of selection and optimization of controllable parameters of technological processes. *Intr.01.07.1978, M, Standards Publishing House*, 1978, 48 p (in Russian).
- [19] Yu.S. Andreev, N.A. Demkovich, R.M. Isaev, A.A. Tselishchev, S.D. Vasilkov. Determination of the microgeometry of the functional surface of a part that provides the required performance of an aviation vibration sensor // *Scientific and technical bulletin of information technologies, mechanics and optics*. 2016. V. 16. No. 6. pp. 1103–1110. D.
- [20] V.V. Maksarov, R.V. Vyushin, A.E. Efimov. Technological support of surface layer roughness based on transient modeling // *Journal of Metalworking, Politechnika Publishing House*, 2017. No. 2 (98). pp. 39–46.
- [21] S.D. Tretyakov, O.S. Yulmetova. On the problems of optimizing the microgeometry of the surface layer of instrument parts. *Journal of Instrument Engineering (Izvestiya vysshikh uchebnykh zavedeniy. Priborostroenie)*, 2010. V. 53, No. 8. pp. 12-15.
- [22] Yu.S. Andreev, V.V. Medunetsky. Research of surface microrelief changes during their sliding friction. *Journal of Instrument Engineering (Izvestiya vysshikh uchebnykh zavedeniy. Priborostroenie)*, 2012. V. 55, No. 9. pp. 30-34.
- [23] V.A. Krasny, V.V. Maksarov. Tribotechnical characteristics of mining machine parts with regular surface microgeometry, *Journal of Metalworking, Politechnika Publishing House*, 2016. No. 1 (91). pp. 29–36.
- [24] O.S. Yulmetova, M.S. Tutova, R.F. Yulmetova. Chemical analysis of thin-film's colour generation during surface laser oxidation of TiN-coating. *Journal of Physics: Conference Series*. 2018. Vol. 1124. No. 8. pp. 081010. [Тип: Статья, Год: 2018]
- [25] T.O. Tolstykh, L.A. Gamidullaeva, E.V. Shkarupeta. Key factors in the development of industrial enterprises in the conditions of industry 4.0 // *Russian journal of industrial economics*, 2018. V. 11, No. 1. pp. 11-19.

# Study about the Influence of the Process Parameters of Vibro Impact Cutting of Optical Slugs on the Productivity of the Process

**Georgi Levicharov**

Department of Mechanical  
Engineering and Technologies  
Technical University of Sofia,  
Plovdiv Branch  
Plovdiv, Bulgaria  
email glevi@tu-plovdiv.bg

**Angel Lengerov**

Department of Mechanical  
Engineering and Technologies  
Technical University of Sofia,  
Plovdiv Branch  
Plovdiv, Bulgaria  
email anlen@tu-plovdiv.bg

**Stoyan Paliiski**

Department of Mechanical  
Engineering and Technologies  
Technical University of Sofia,  
Plovdiv Branch  
Plovdiv, Bulgaria  
email st.paliyski@abv.bg

**Abstract.** In the article, experimental studies were carried out, contributing to determination of degree of influence of the parameters of the modes of vibro-impact cutting of optical slugs on the productivity of the process. The optimal frequencies of the forced oscillations of the technological system "slug-cut disc" were reported, in which the durability of the tool and the quality of the obtained surfaces are maximum.

**Keywords:** optical slug, productivity, parameter, vibro- impact, cutting.

## I. INTRODUCTION

The conducted literature review and its analysis show that after introducing ultra-sound oscillations into the zone of processing, increase in productivity of cutting optical slugs and other hard and brittle materials is observed (by 10-30%), as well as improvement in the quality of the machined surfaces – reduction of the parameter by 10-20%. The detailed clarification of all the factors, influencing on the process of cutting such materials necessitates to perform a series of experiments to confirm the results from the studies [1,2,4,5,6,7,8,9,10,11]. From the analysis of the available up to the moment research works it has been established that the oscillations depend on the type of the used vibrator and have a significant importance in the formation of the quality indicators of the surfaces, processed by cutting. The type of the vibrator should such that its installation in the cutting equipment does not require significant changes to their construction and does not hinder the course of the technological process.

The literature review shows that up to the present there is no research, showing the influence of the low-frequency

forced oscillations on the productivity and quality of the process of cutting optical materials [3].

## II. MATHEMATICAL MODEL

For a theoretical assessment of the degree of influence of the vibro-impact cutting mode on the performance of the operation of mechanical cutting of optical slugs, etc., mathematical models of the cutting process proposed in [1, 2] are used. The diagram of the process of cutting such materials is presented in Fig. 1.

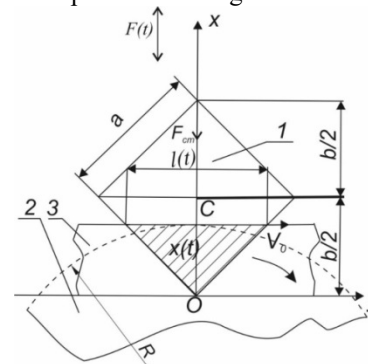


Fig. 1. Diagram of the process of cutting optical materials.

The machined optical slug 1 under the action of the applied static load  $F_{cm}$  is pressed toward the periphery of the rotating cutting disc 2, in result of which the process of cutting is accomplished conventionally, under traditional conditions. The plane of cutting the optical slug is a square with a side  $a$ . For convenience, in the further analysis the cutting disc with a radius  $R$  is presented as a rectangle 3 with a cutting edge, having the

Print ISSN 1691-5402

Online ISSN 2256-070X

<https://doi.org/10.17770/etr2023vol3.7248>

© 2023 Georgi Levicharov, Angel Lengerov, Stoyan Paliiski. Published by Rezekne Academy of Technologies.  
This is an open access article under the [Creative Commons Attribution 4.0 International License](https://creativecommons.org/licenses/by/4.0/).

same velocity as the velocity of a point from the cutting edge of the cutting disc. This is perfectly acceptable, subject to the condition that the contact size is always smaller than the radius  $R$  of the cutting disc.

We determine the time for cutting up the optical slug both under traditional conditions of machining ( $\tau_{cm}$ ) and when applying vibrational cutting ( $\tau_{ep}$ ), and quantitatively evaluate the degree of influence of the forced oscillations on the increase in cutting intensity, which we estimate according to the expression

$$\eta = \left(1 - \frac{\tau_{ep}}{\tau_{cm}}\right) 100, \quad (1)$$

assuming that  $\tau_{cm} > \tau_{ep}$ .

We connect the sample with a coordinate system  $x, y$ , as shown in Fig. 1. Based on the theory of mechanical failure of brittle materials, we express the amount of the work, expended for cutting under traditional machining conditions for time  $\Delta t$  by the expression

$$\Delta W_{up} = \alpha j_{cm} V_0 \Delta t, \quad (2)$$

where  $V_0$  is the velocity of the disc periphery (the cutting speed);  $j_{cm}$  - an impulse, transmitted to the optical sample parallel to the  $x$  axis per unit of time (the average interaction force);

$\alpha$  - a coefficient, characterizing part of the work, done by the forces during cutting, spent on destroying the optical workpiece ( $\alpha < 1$ ), (selected from a table).

The direction of the forces, performing work in traditional cutting of optical slugs should coincide with the forces, causing destruction of the workpiece surface.

The magnitude of  $\Delta W_{up}$  should match the work to destroy the sample and is equal to

$$\Delta W_{paz} = \gamma_{cm} h l(t) \dot{x}(t) \Delta t, \quad (3)$$

where  $\gamma_{cm}$  is the specific work for destruction of the material when cutting;  $h$  - width of cut;  $l(t)$  - size of the cut low along the axis, equal to  $l(t) = 2x(t)$  for the chosen shape of the slug, at  $0 < x(t) < b/2$ , where  $b$  is the depth of the cut.

For the purpose of finding the analytical solution of (2), we assume that  $j_{cm}$  is a constant, independent of the depth of the cut of the slug.

Then, from (2) and (3) the differential equation is obtained:

$$x(t) \dot{x}(t) = \frac{\alpha j_{cm} V_0}{2 \gamma_{cm} h}. \quad (4)$$

Considering the magnitude of  $\gamma_{cm}$  as constant and integrating (4) with the initial conditions  $x(0) = 0$ , we obtain the law of motion of the cutting line relative to the optical slug

$$x(t) = \beta_{cm} \sqrt{t};$$

where

$$\beta_{cm} = \sqrt{\frac{\alpha j_{cm} V_0}{\gamma_{cm} h}}. \quad (5)$$

Dependence (5) is valid for the interval  $0 \leq t \leq \tau$ , where  $\tau$  is the time to cut half of the optical slug. It is determined by the equation of the type

$$x(t) = \frac{b}{2} = \frac{a}{\sqrt{2}}; \quad \tau = \frac{a^2}{2\beta_{cm}^2} = \frac{2\pi N}{\omega}, \quad (6)$$

where  $N$  is the number of disc revolutions for the time of cutting;

$\omega$  - its angular velocity.

At  $t > \tau$  in the expression (3) it should be assumed

$$l(t) = 2[b - x(t)], \quad (7)$$

from where we obtain the differential equation

$$[b - x(t)] \dot{x}(t) = \frac{\alpha j_{cm} V_0}{2 \gamma_{cm} h}, \quad \tau < t < \tau_{cm}. \quad (8)$$

For the initial condition  $x(\tau) = b/2$  for the solution of (8) is written

$$x(t) = \frac{b}{2} \left[ 2 - \sqrt{1 - \frac{4\beta_{cm}^2}{b^2} (t - \tau)} \right], \quad \tau < t < \tau_{cm}. \quad (9)$$

The time for the complete cutting the optical slug up  $\tau_{cm}$  is determined by the condition  $x(t) = b$ , then from (6) we find

$$\tau_{cm} = \tau + \frac{b^2}{4\beta_{cm}^2} = \tau + \frac{a^2}{2\beta_{cm}^2} = \frac{a^2}{\beta_{cm}^2} = 2\tau. \quad (10)$$

According to formulas (5) and (9), the dependence  $x(t)$  is antisymmetric (odd) with respect to the points  $t = \tau, x = b/2$ .

To calculate the work, spent on cutting up half of the optical slug, the expression (3) should be summed

$$\begin{aligned} \Delta W_{\text{paz}} &= \int_0^{\tau} \gamma_{cm} h l(t) \dot{x}(t) dt = 2\gamma_{cm} h \int_0^{\tau} x(t) \dot{x}(t) dt = \\ &= \gamma_{cm} h x^2(\tau) = \frac{\gamma_{cm} h a^2}{2} \end{aligned} \quad (11)$$

When cutting under traditional conditions, when a static load  $P_{cm}$  is acting, the magnitude of the impulse per unit of time is equal to the period of the forced vibrational oscillations  $T$  and is determined

$$I_{cm} = \frac{j_{cm}}{T} = \frac{\omega_{ep}}{2\pi} \int_0^{\tau} F_{cm} dt = F_{cm}; \quad \beta_{ep} = \sqrt{\frac{\alpha F_{cm} V_0}{\gamma_{cm} h}}, \quad (12)$$

where  $\omega_{ep}$  is the circular velocity of the vibrational oscillations.

Then, the time to cut up the optical slug under traditional processing conditions according to (10) will be equal to

$$\tau_{cm} = \frac{a^2 \gamma_{cm} h}{\alpha F_{cm} V_0}. \quad (13)$$

The time to cut up optical slugs under the condition of vibro-impact cutting is determined, assuming that the vibro-impact oscillations are transmitted to the slug in its lower part below the  $x$  axis (Fig. 1). The vibro-impact mode of interaction between the periphery of the cutting part of the disc and the machined surface of the slug is realized in addition. In this case, for time  $T$ , equal to the period of the forced oscillations, the mechanical interaction between the slug and the cutting disc constitutes only the part  $t_k$  of it, and in the remaining time  $T - t_k$  we have an absence of cutting. Therefore, the chipping of diamond particles from the cylindrical surface of the disc results from the pulse impact with a frequency, equal to the frequency of rotation of the electric motor of the centrifugal vibrator, creating the forced oscillations.

Thus, in order to determine the time of cutting the optical workpiece under an introduced vibrational impact, the following correction should be made in the expressions, obtained during processing under traditional conditions: firstly, instead of  $I_{cm}$ , the magnitude of the average period of oscillation  $T$  should be taken, and the impulse of the forces of interaction between the peripheral surface of the cutting disk and the slug surface  $I_{ep}$  should be accepted; secondly, instead of the magnitude of the specific work for destruction under traditional conditions  $\gamma_{cm}$ , it should be assumed that its magnitude corresponds to the vibro-impact mode of cutting  $\gamma_{ep}$ .

Taking into account the above, expressions (12) and (13) in the conditions of a vibro-impact mode of cutting take the form

$$\Delta W_{\text{ycm.ep}} = \alpha V_0 j_{ep} \Delta t, \quad (14)$$

$$\Delta W_{\text{paz.ep}} = \gamma_{ep} h l(t) \dot{x}(t) \Delta t, \quad (15)$$

where  $\Delta W_{\text{ycm.ep}}$  and  $\Delta W_{\text{paz.ep}}$  are respectively the work, spent on cutting and the work on destructing the sample in the vibro-impact mode of processing.

Then the differential equation (14) and its solution (15) take the form:

$$x(t) \dot{x}(t) = \frac{\alpha j_{ep} V_0}{2\gamma_{ep} h} \quad (16)$$

$$x(t) = \beta_{ep} \sqrt{t}, \quad \text{където } \beta_{ep} = \sqrt{\frac{\alpha j_{ep} V_0}{\gamma_{ep} h}} \quad (17)$$

After the changes, made in expressions (8) and (9), the time for cutting the workpiece under vibro-impact action on it, will be equal to:

$$\tau_{ep} = \frac{a^2 \gamma_{ep} h}{\alpha I_{ep} V_0}. \quad (18)$$

Substituting dependencies (13) and (18) into (1), we will obtain an expression for determining the degree of increase in the intensity of cutting optical slugs

$$\eta_{\tau} = \left(1 - \frac{\tau_{ep}}{\tau_{cm}}\right) = \left(1 - \frac{F_{cm} \gamma_{ep}}{j_{ep} \gamma_{cm}}\right), \quad (19)$$

where  $j_{ep}$  is the impulse of the forces on the optical slug during the time of its contact with the cutting disc.

It follows from (19) that, other things being equal, the degree of the intensifying effect of vibration oscillations on the productivity of the process of mechanical cutting of optical materials is determined by two ratios: 1. the ratio of the specific work for destruction of the workpiece surface in the vibro-impact mode of cutting to the work, done under traditional conditions ( $\gamma_{ep} / \gamma_{cm}$ ); and 2. the ratio of the force of the impulses for the period of oscillations under traditional cutting conditions ( $F_{cm} \cdot T$ ) to the force impulse in the transmission of oscillations to the machined workpiece for the time of contact between the slug surface and the cylindrical surface of the disc  $j_{ep}$ .

If we assume that  $\gamma_{ep} = \gamma_{cm}$ , then the assessment of the degree of influence of the forced oscillations on increasing the intensity of cutting optical materials can be calculated by the expression:

$$\eta_{\tau} = \left( 1 - \frac{F_{cm} T}{j_{ep}} \right). \quad (20)$$

From analytical studies [1], using original mathematical models, the expression for determining the magnitude of  $j_{ep}$  in the case of a vibro-impact mode of cutting was obtained, which has the form

$$j_{ep} = \frac{8F_{cm}^2 \pi}{A_0 \omega_{ep} c} C.D, \quad (21)$$

where  $F_{cm}$  is the static effort;  $A_0$  - the amplitude of the vibrational oscillations;  $c$  - hardness/stiffness of the weightless vibro-element, accepted in the models;  $C$  and  $D$  – dimensionless coefficients, which can be assumed to be equal to unity, or to be more than a unity.

These coefficients will be equal to unity in continuous modes of operation of the vibrator, when  $A_0 = 2x_{cm}$ , where  $x_{cm} = F_{cm} / c$  is the value of the preliminary tightness in the system, determined by the static load.

Substituting the expression (21) into (20) and transforming, we obtain:

$$\eta_{\tau} = \left( 1 - \frac{A_0}{2x_{cm} C.D} \right). \quad (22)$$

### III. CONCLUSION

Based on the developed vibro-impact mathematical models, describing the process of cutting optical materials, a quantitative assessment of the degree of influence of the vibrational oscillations on increasing the intensity of cutting such materials can be made. With the increase in the amplitude of the vibrational oscillations, increase in the productivity of the process of cutting optical slugs is registered.

The obtained theoretical assessment of the increase in the process productivity is valid provided that the cutting resistance forces of, acting in the process of machining, are not taken into account. Taking into account the shape of the cutting disc, we can conclude that as the depth of its cut into the optical slug increases, the wedging forces, trying under the action of internal stresses to push aside the cut-off part of the workpiece, will increase. The exact evaluation of the influence of the different vibro-impact cutting modes on the productivity of machining can be performed after determining the dependencies, describing the change in the magnitude of the pulses  $j_{cm}$  and  $j_{ep}$ , transmitted to the machined samples parallel to the axis  $x$  per unit of time, while taking into account the change in the wedging forces along the depth of the cut workpiece.

### IV. ACKNOWLEDGMENTS

This work was supported by the European Regional Development Fund within the OP “Science and Education for Smart Growth 2014-2020”, Project Competence Centre “Smart Mechatronic, Eco-And Energy Saving Systems And Technologies”, № BG05M2OP001-1.002-0023.

### REFERENCES

- [1] T. Kuzmanov, H. Metev, K. Kumov. Mathematical Models of Machining Parts with Complicated Rotation Form on CNC Machines. Journal of the Technical University of Gabrovo, vol. 46, pp. 44-47. ISSN 1310-6686, 2013.
- [2] T. Kuzmanov, I. Amudzhev, K. Kumov. Influence of the Manufacturing Parameters on the Quality and the Productivity Under Treatment of Workpieces Made of Metal Ceramic Alloy by Infinite Elastic Diamond Tape. Mechanical Engineering and Mechanical Science, Technical University of Varna, vol. 11, pp. 11-14. ISSN 1312-8612, 2009.
- [3] V. S. Mironov, A. M. Bocharov, A. F. Klimovich. Increasing the productivity of the process of mechanical drilling of single crystals by using the phenomenon of electrification of the processing zone, Superhard materials, 1985, Vol. 3, pp. 1-2.
- [4] C. C. Girdu et al, Estimation of laser cutting process efficiency, IOP Conference Series: Materials Science and Engineering, 9<sup>th</sup> International Scientific Conference - Research and Development of Mechanical Elements and Systems, 5–7 September 2019, Kragujevac, Serbia, 2019, Volume 659, DOI 10.1088/1757-899X/659/1/012045.
- [5] E. Markauskas, L. Zubauskas, P. Gečys, Efficient milling and cutting of borosilicate glasses through a thin flowing water film with a picosecond laser. J. Manuf. Process. 2021;68:898–909, doi: 10.1016/j.jmapro.2021.06.013.
- [6] E. Markauskas, L. Zubauskas et al., Efficient Water-Assisted Glass Cutting with 355 nm Picosecond Laser Pulses, Micromachines 2022, 13(5), 785, https://doi.org/10.3390/mi13050785.
- [7] F. Parreño, M.T. Alonso, R. Alvarez-Valdes, Solving a large cutting problem in the glass manufacturing industry, European Journal of Operational Research, Vol. 287, Issue 1, 2020, pp. 378-388, https://doi.org/10.1016/j.ejor.2020.05.016.
- [8] Y. Huang, B. Fan, Y. Wan, S. Li, Improving the performance of single point diamond turning surface with ion beam figuring, International Journal for Light and Electron Optics-Optik, Vol. 172, 2018, pp. 540-544, https://doi.org/10.1016/j.ijleo.2018.07.039.
- [9] Y. Ito, Kizaki T, Shinomoto R et al., High efficiency and Precision Cutting of Glass by Selective Laser-assisted Milling, Journal of the International Societies for Precision Engineering and Nanotechnology Precision Engineering, Vol. 47, 2017, pp.498-507, https://doi.org/10.1016/j.precisioneng.2016.10.005.
- [10] Samuel Arba-Mosquera, Pascal Naubereit, Simas Sobutas, and Shwetabh Verma, Analytical optimization of the cutting efficiency for generic cavitation bubbles, Biomedical Optics Express, Vol. 12, Issue 7, 2021, pp. 3819-3835, https://doi.org/10.1364/BOE.425895.
- [11] X. Liu, D. Yu, D. et al., Self-tuned ultrasonic elliptical vibration cutting for high-efficient machining of micro-optics arrays on brittle materials, Journal of the International Societies for Precision Engineering and Nanotechnology Precision Engineering, Vol. 72, 2021, pp. 370-381, https://doi.org/10.1016/j.precisioneng.2021.05.007.

# A Geometrical Synthesis of Comez Textile Mechanisms of Finally Removed Possibilities

**Marin Jordanov Marinov**  
Technical University - Gabrovo  
Department of Industrial Design and  
Textile Engineering  
Gabrovo, Bulgaria  
marinov@tugab.bg

**Abstract.** A synthesis of the COMEZ spatial knitting mechanism has been developed to convert rotational motion around a moving axle in a reciprocating motion. The synthesis has been done in extremely remote positions. For practical application of the synthesis, a vector-matrix approach is proposed in Math LAB Watt programming environment. With the specific metric parameters of the head mechanism, the function definition of the position is considered and a proposed eight-pointed mechanism replacing the spatial hump of the knitting head is proposed. To establish the authenticity of synthesis is an example.

**Keywords:** Circular knitting mechanisms, metric synthesis at far-off positions, geometrical synthesis, functions of the position.

## I. INTRODUCTION

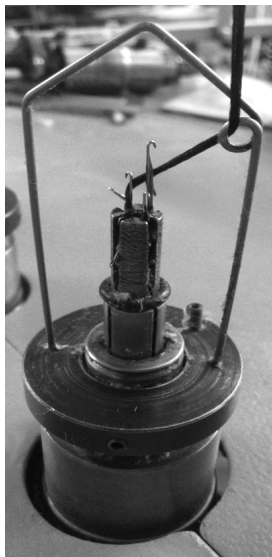


Fig.1 Real circular knitting head mechanism.

The metric synthesis of the CKM (Circular knitting mechanism) at extremely remote positions can be done by the vector-matrix method, using the generalized approach applied to planar lever mechanisms out of phase by 120° [1, 4, 5, 6, 7 and 8].

Figure 1 shows a COMEZ basic mechanism operating with three vertical needles, and Figure 2 shows the kinematic diagram of the head of the same mechanism with two symmetrical needles. This mechanism is designed to entangle a textile thread into a diameter of a line. What will be the diameter of the thread, as well as its roughness, depends on the number of entangling needles and the diameter of the hole in the middle of the head.

In order to improve the present mechanism, it is necessary to synthesize metrically and kinematically, by means of the vector-matrix method, a new structure which would create the possibility of entangling a cord from random textile threads.

The example illustrates a knitting head synthesis used in COMEZ textile machines where the main problem is the poor entanglement of thin artificial fibers caused by the high values of the accelerations at characteristic points in the movement of the knitting needle.

In order to make an optimal synthesis of the indicated mechanism with subsequent kinematic analysis and to ascertain the effect of the synthesis, the following activities were carried out:

1. Replacement of the spatial mechanism with an eight-plane flat lever mechanism was made, the function of the position of the initial and of the provided mechanisms being the same.

2. A eight-legged mechanism has been synthesized,  
Print ISSN 1691-5402  
Online ISSN 2256-070X

<https://doi.org/10.17770/etr2023vol3.7187>

© 2023 Marin Jordanov Marinov. Published by Rezekne Academy of Technologies.  
This is an open access article under the [Creative Commons Attribution 4.0 International License](https://creativecommons.org/licenses/by/4.0/).

which has been studied in detail in the characteristic points.

3. Draw kinematic schemes for the same positions.

4. The initial and conceded mechanisms are compared, each figure depicting the function of the change of the relative error of the executive unit between the initial and the resulting mechanisms.

5. The peak values of the linear accelerations of the executive unit at the characteristic points of the mechanism are minimized.

6. The author propose a unified approach to the synthesis of such mechanisms at extreme discrete positions (marginal synthesis M-synthesis) that can be applied to different types of mechanisms, both for guiding and for moving mechanisms.

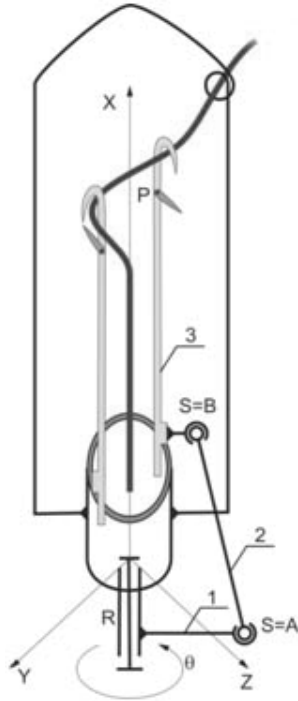


Fig.2 Kinematic diagram of a circular knitting mechanism.

## II. MATERIALS AND METHODS

II.1. Synthesis of a COMEZ mechanism intended for the Math LAB Watt programming environment.

1. Enter the relative linear displacements  $S_{li}$  of the center of the spherical pair  $B$ , the relative angular orientations  $\theta_{li}$  of link 1, the limits and steps of change of the variable parameters.

2. Enter the expressions:

$$\begin{bmatrix} X'_{Bi} \\ Y'_{Bi} \\ Z'_{Bi} \end{bmatrix} = \begin{bmatrix} 1 & 0 & 0 \\ 0 & \cos \theta_{li} & \sin \theta_{li} \\ 0 & -\sin \theta_{li} & \cos \theta_{li} \end{bmatrix} \begin{bmatrix} X_{B_i} + S_{li} \\ Y_{B_i} \\ Z_{B_i} \end{bmatrix} \quad (1)$$

to determine the coordinates  $X_{B_i}$ ,  $Y_{B_i}$  and  $Z_{B_i}$  of the center of the spherical pair  $B$ .

3. Enter the expressions:

$$\begin{aligned} a_i &= 2S_{li} \quad , \\ b_i &= -2(Y_{B_i} - Y_{B1}) \quad , \\ c_i &= -2(Z_{B_i} - Z_{B1}) \quad , \\ d_i &= Y_{B1}^2 + Z_{B1}^2 - Y_{B_i}^2 - Z_{B_i}^2 - S_{li}^2 \quad , \quad i = 2,3,\dots,n \end{aligned} \quad (2)$$

to determine the coefficients of the system of equations:

$$a_i X_{B_i} + b_i Y_{A_i} + c_i Z_{A_i} = d_i \quad .$$

4. With  $n=5$  and one variable parameter, the functions are entered

$$\begin{aligned} X_{B_1} &= X_{B_1}(Y_{B_1}) \quad , \\ Y_{A_1} &= Y_{A_1}(Y_{B_1}) \quad , \\ Z_{A_1} &= Z_{A_1}(Y_{B_1}) \quad . \end{aligned} \quad (3)$$

and

$$F(Y_{B1}) = a_5 \cdot X_{B_1} + b_5 \cdot Y_{A_1} + c_5 \cdot Z_{A_1} - d_5 \quad (4) \quad .$$

The graphs of these functions are drawn and the values of the variable and the computational parameters are determined from them.

5. With  $n=5$  end two variable parameters, the functions are introduced

$$\begin{aligned} X_{B_1} &= X_{B_1}(Y_{B_1}, Z_{B_1}) \quad , \\ Y_{A_1} &= Y_{A_1}(Y_{B_1}, Z_{B_1}) \quad , \\ Z_{A_1} &= Z_{A_1}(Y_{B_1}, Z_{B_1}) \quad . \end{aligned} \quad (5)$$

$$F(Y_{B1}, Z_{B1}) = a_5 X_{B1} + b_5 Y_{A1} + c_5 Z_{A1} - d_5 \quad (6)$$

The isoline of the surface determined by the function (6) is drawn for zero values of this function. With the coordinates of points of this isoline (which are values of the variable parameters) and the functions (5), the calculation parameters are determined.

6. With  $n=6$  and two variable parameters, the functions (5) and

$$\begin{aligned} F(Y_{B1}, Z_{B1}) &= a_5 X_{B1} + b_5 Y_{A1} + c_5 Z_{A1} - d_5 \quad , \\ Q(Y_{B1}, Z_{B1}) &= a_6 X_{B1} + b_6 Y_{A1} + c_6 Z_{A1} - d_6 \quad . \end{aligned} \quad (7)$$

The isolines of the surfaces determined by the functions (7) are drawn. The coordinates of their intersection points (which give the values of the variable parameters) are calculated from them and the calculation parameters are determined with them and the functions (5).

### III. RESULTS AND DISCUSSION

**Example:** To synthesize a **COMEZ** lever mechanism for driving the working head of the knitting machine at set:  $Z_{B1}=0,015m$ ; relative linear displacements  $S_{12}=0,1m$ ,  $S_{13}=0,023m$ ,  $S_{14}=0,020m$ ,  $S_{15}=0m$ ; relative angular orientations of the leading link  $\theta_{12}=\pi/3$ ,  $\theta_{13}=2\pi/3$ ,  $\theta_{14}=\pi$ ,  $\theta_{15}=2\pi$ .

Six discrete positions marked in Fig. 3, Fig. 4, Fig. 5, Fig. 6, Fig. 7 and Fig. 8 is fixed. To synthesize and draw the kinematic scheme of an eight-link bent mechanism for each of the six positions of the executive unit (knitting needle).

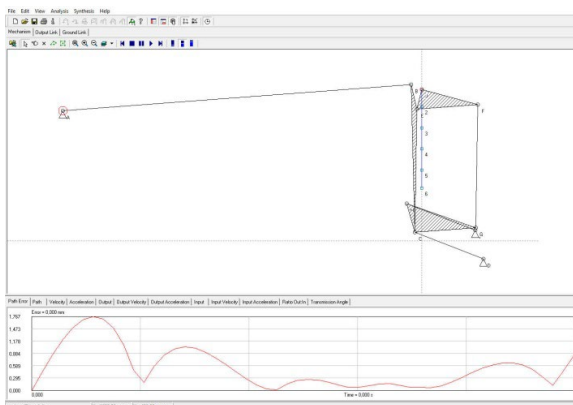


Fig.3 First extreme remote position.

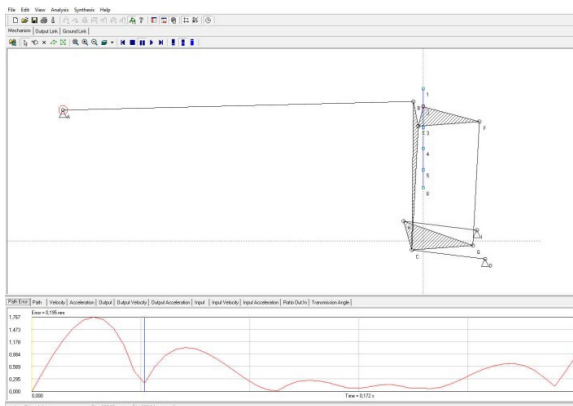


Fig.4 Second extreme remote position.

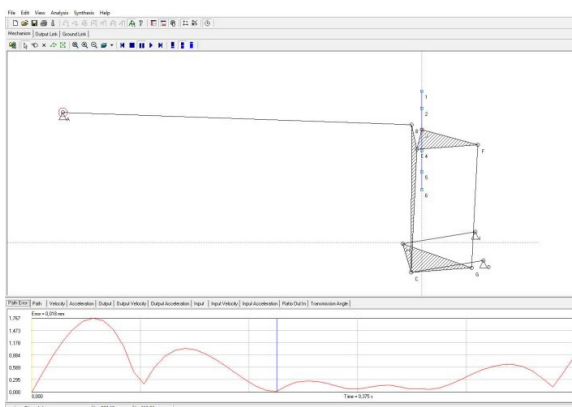


Fig.5 Third extreme remote position.

Fig. 2 shows the kinematic scheme of the knitting head, where the needles are controlled by a spatial cam, which is subsequently kinematically reduced to an eight-link lever mechanism, and the values of the variable parameter  $Y_{B1}=0,02m$  and the calculation parameters  $X_{B1}=0,02m$ ,  $Y_{A1}=-0,015m$ ,  $Z_{A1}=-0,037m$ .

In the lower part of the graphs, the relative error in the displacements of link 3 is plotted.

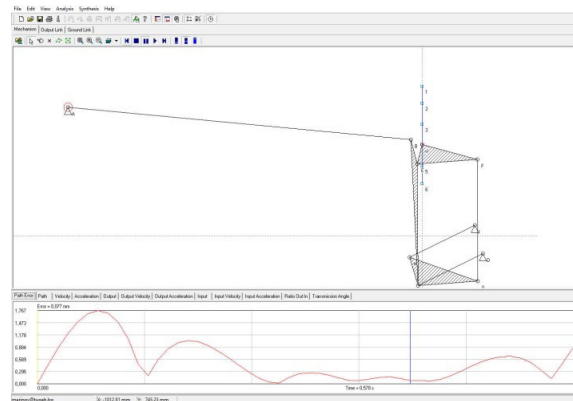


Fig.6 Fourth extreme remote position.

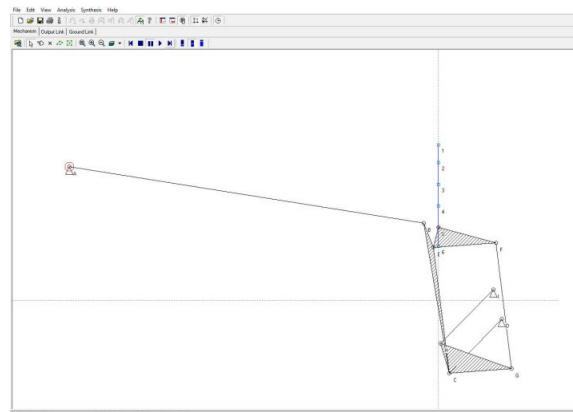


Fig.7 Fifth extreme remote position.

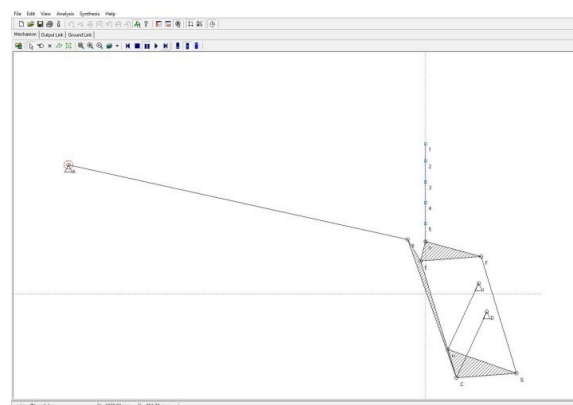


Fig.8 Sixth extreme remote position.

At the moment, a procedure for issuing a utility model (patent) has been launched at the Bulgarian Patent Office, related to increasing the capacity of the shown mechanism. This is a personal contribution of the author. It is related to studying the reliability of the displayed model. I dare to say that the synthesized mechanism is up to 15% more stable in operation than that of a company „COMEZ”.

The present problem "Geometric synthesis of COMEZ textile mechanisms at extremely remote positions" is conditionally divided into two parts. 1. Mathematical model for synthesis at extremely remote positions (six in number) and published in this article. 2. Innovative technological prototype of the circular knitting head, which is described and verified for patent purity.

More comments about the number of needles used and their gauges are the subject of the utility model I am applying for and are not subject to comment on the math model.

Moreover, in figures 3 to 8, the graphs of the kinematic parameters are drawn, which give an idea to the specialist in the field about the phase diagrams of the textile entanglement.

#### IV. CONCLUSION

The example made shows the synthesis of a knitting head used in COMEZ textile machines, where the main problem is the poor entanglement of thin artificial fibers caused by the high values of the accelerations at characteristic points during the movement of the knitting needle, namely points 1,2,3, 4,5 and 6 shown in the above figures.

In order to make an optimal synthesis of the shown mechanism with subsequent kinematic analysis and to establish the effect of the synthesis, the following activities were carried out:

1. The spatial mechanism was replaced with an eight-link planar lever mechanism, while the function of the position of the initial and reduced mechanisms is the same.

2. An eight-link mechanism was synthesized, which was studied in detail in characteristic points 1, 2, 3, 4, 5 and 6.

3. The kinematic diagrams for the same positions are drawn (fig. 3, fig. 4, fig. 5, fig. 6, fig. 7 and fig. 8).

4. The initial and reduced mechanisms are compared, and in each figure the function of the change of the relative error of the executive unit between the initial and reduced mechanisms is plotted.

5. The peak values of the linear accelerations of the executive unit at the characteristic points of the mechanism are minimized.

6. The authors propose a unified approach for the synthesis of such mechanisms at finitely distant discrete positions (marginal synthesis M-synthesis), which can be applied to different types of mechanisms, both for guiding and moving mechanisms.

7. The obtained numerical results were obtained theoretically and based on them a prototype was developed, which shows increased performance compared to that of the existing models. The prototype of the mechanism is made in a real industrial environment.

Regarding the reviewer's comment that the literature used is old, I would like to say that these are the classics in the field of the theory of mechanisms and machines. Or to put it another way, the Pythagorean Theorem and Newton's laws are old and out of date.

#### REFERENCES

- [1] Artobolevskiy I. I., Theory of Mechanisms and Machines. Science, Moscow, 1967.
- [2] Bhandari V. B., Design of Machine Elements Fifth Edition, McGraw Hill 2020.
- [3] Galabov V.B., M. J. Marinov, N.B. Nikolov, Synthesis on a guiding MF at two points, respectively phase relation and double midpoint, "Mechanics of machines" 1999, booklet 26.
- [4] Galabov V.B., M. J. Marinov, Synthesis of articulated four-link mechanism by discrete relative positions. "Mechanics of the machines", Varna, 2002.
- [5] Jhon Uicker, G. Pennok, J. Shigley, Theory of Machines and Mechanisms, Fifth Edition, Oxford University Press 2017.
- [6] Marinov M., Synthesis of planar mechanisms by extremely distant discrete positions. Dissertation abstract to get the scientific and educational degree "PhD" - TU Sofia 2002, pp.36.
- [7] Myszka David, Machines & Mechanisms: Applied Kinematic Analysis, 2011.
- [8] Marinov M.J. , B.I. Stoychev, D.M. Guteva, M.V. Georgiev, Computer modeling and geometric analysis of Click-Clack mechanisms. "Mechanics of the machines" 2016 booklet 118 pp.35-39.
- [9] Michael Stanisic, Mechanisms and machines; Kinematics, Dynamics and synthesis, Stamford 2015.
- [10] Harrisberger L.L., An overview of structural synthesis of three-dimensional mechanisms, constructing science and technology of mechanical engineering, World, Moscow, 1965.
- [11] Rusev R.A., V.B. Galabov, Structuring of rational planet-lever mechanism for passing the weft through the weaving machines. "Mechanics of machines" 2002 pp.26 booklet 33.
- [12] Sadhu Singh, Theory of Machines: Kinematics and Dynamics, Pearson Education, India 2011
- [13] Stefan Stefanov, Theoretical mechanics, statics, kinematics and dynamics, Sofia 2014.
- [14] Stoyanov P.T., Geometric precision synthesis of planar lever mechanisms. "Mechanics of the machines" 2002 p.56 vol. 33.
- [15] Timofeev G.A. Theory of Mechanisms and Machines, Moscow Urde 2010.

# Research of the Principal Model of the Electric Energy Generator of the Electric Car (Stage Combination of Mechanical and Electromechanical Parts)

**Vaidotas Matutis**

Faculty of electronics and informatics,  
Vilniaus Kolegija/Higher Education  
Institution  
Vilnius, Lithuania  
v.matutis@eif.viko.lt

**Loreta Savulioniene**

Faculty of electronics and  
informatics, Vilniaus  
Kolegija/Higher Education  
Institution  
Vilnius, Lithuania  
l.savulioniene@eif.viko.lt

**Paulius Sakalys**

Faculty of electronics and  
informatics, Vilniaus  
Kolegija/Higher Education  
Institution  
Vilnius, Lithuania  
p.sakalys@eif.viko.lt

**Laura Gzegezvske**

Faculty of electronics and informatics,  
Vilniaus Kolegija/Higher Education  
Institution  
Vilnius, Lithuania  
l.gzegezvske@eif.viko.lt

**Abstract.** The article presents the interim results of the ongoing study

(<http://journals.ru.lv/index.php/SIE/article/view/6884/5683>).

At this stage, measurements are made with a model in which we combined the mechanical part with the electromechanical part. At the presentation stage, a model demonstrating the principle operation scheme of the patented device has already been constructed as an object of research. A rotating magnet was connected to the impeller (it was rotated by the impeller). The magnet was rotating around the stationary coils and was already inducing an electric current in the coils. In this way, the generated current and generated voltage values can be used as an indicator for evaluating the efficiency of the impeller. The experiments in question are performed with three impellers of different configurations, keeping other conditions analogous. All experiments were performed using only one rotating magnetic ring and one set of stationary coils. The results of experimental measurements show a wide spectrum and possibilities of increasing efficiency and demonstrate the principle of operation of the future device. When designing an impeller with turned wings, two cavities for magnets and coils are already provided, thus preparing for the next step in improving the design of the model under study and increasing efficiency.

**Keywords:** robotic system, electricity generator, regeneration, electricity, wind.

## I. INTRODUCTION

This invention [4], on the basis of which research is organized, is primarily intended for electric cars and hybrid cars with an electric drive and a battery (for energy storage), but it can be used much more widely. At the presentation stage, a model demonstrating the operation principle of the patented device has already been constructed as an object of research. The article presents the intermediate results of the ongoing study [5]. At this stage, measurements are made with a model in which we combined the mechanical part with the electromechanical part.

The use of air flow energy is researching in studies of the practical application of wind power plants and efforts are made to maximize the use of air flow the kinetic energy. It was decided to make a practical study of this aspect in the initial stages. The essential issue of these stages was the need to determine the best number of blades for efficiency of the selected wind turbine and to improve the configuration of the blades based on the research results. The conducted studies show that it is

Print ISSN 1691-5402

Online ISSN 2256-070X

<https://doi.org/10.17770/etr2023vol3.7261>

© 2023 Vaidotas Matutis, Loreta Savulioniene, Paulius Sakalys, Laura Gzegezvske.

Published by Rezekne Academy of Technologies.

This is an open access article under the [Creative Commons Attribution 4.0 International License](https://creativecommons.org/licenses/by/4.0/).

logically to stay with six-bladed propeller and for now, continue the research the combined mechanics and electromechanics parts.

## II. THE GENERAL RESEARCH MOTIVES, SELECTED RESEARCH PHASE

Wind is moving air. As its speed increases, so does the kinetic energy associated with movement. Wind farms are designed to intercept kinetic energy, slow it down and convert it into electricity. A barrier to kinetic energy is created when the wind encounters the turbine blades, which are designed to capture the maximum amount of energy and thus create the largest possible barrier [2].

Lithuania and other European Union states are encouraged to switch to renewable energy in the Green Deal, which enshrines the aspiration to become the first climate-neutral continent. It is argued that ecology and climate issues should be the priorities of the political agenda of this period, thus harmonizing measures promoting economic recovery with the long-term vision outlined in the Green Deal - to create a cleaner Europe.

In the researches maintains a general trend to use renewable energy sources as widely as possible.

This invention relates to the transformation of wind (airflow) energy into electrical energy. It is a natural, constantly renewing source of energy for the environment around us, which is environmentally friendly and protects it. The process itself does not bring any harmful substances into the environment. However, to achieve efficiency that provides practical benefits, a complex approach is required, because mechanics, electromechanics, electronics, and several other specific areas of practical physics come together here.

In the first stages, which have already been presented, the focus was on the research of the mechanical part. Based on the research data, the impeller configuration was selected. The performance of these impellers was assessed by measurements at constant initial conditions.

At this stage, which is presented, the electromechanical part has already been connected to the mechanical part. A rotating magnet was connected to the impeller (it was rotated by the impeller). The magnet was rotating around the stationary coils and the rotating magnet was already inducing an electric current in the coils. The generated current and generated voltage values can be used as an indicator for evaluating the efficiency of the impeller.

How the generator works for electric cars (which involves the transformation of wind energy into electricity): in a wind turbine, when the air flow pressure reaches a critical value, the rotor starts rotating around the stator. Since it is a complex of several areas, a necessary condition for efficiency is the compatibility of individual parts and a positive efficiency coefficient of each step or part. The first link of this complex is mechanical - the wind turbine, so we started research from its efficiency. The accumulated measurement data of this stage already allows choosing certain impeller configurations for the next stage of research. The main criterion defining the efficiency of this

stage was the speed of rotation of the impeller measured with the help of a tachometer. The higher the rotational speed of impeller at the same airflow, the more efficient the impeller configuration.

At the current stage, after connecting the electromechanical part, the efficiency criterion is already changing. As it was already mentioned, the values of the current generated in the stationary coils and the generated voltage can be used as an indicator for evaluating the efficiency of the impeller. It opens opportunities to vary structural elements and use the same criteria for measurements. It is possible to further collect measurement data while improving the mechanical design of the vane itself (vane configuration). At the same time, it is already possible to collect measurement data of the efficiency of the electromechanical part (coil configurations). In this way, we already combine two rather important elements of the complex and two closely related areas, i.e., the impeller and the magnet rotating around the stationary coils, or the mechanical and electromechanical parts.

## III. EXPERIMENTAL PART AND DESCRIPTION OF RESEARCH

In the already presented stage, when the air flow pressure in the wind turbine reaches a critical value, the air flow pressure is concentrated on the rotor blades, thus achieving a more efficient use of energy, because according to the selected design, all pressure is concentrated at the edge of the blade. Measurements of critical points were performed with impellers of different configurations (by changing the number of blades). Measurements were also made in real conditions (mockup on the roof of the car) and for comparison in laboratory conditions. The results of these studies have been discussed in previous publications.

Based on the measurement data collected at this stage, the air flow conditions created in laboratory conditions correspond to the parameters of the passing air flow of a car traveling at a speed of 50 km/h. Under these constant conditions, further measurements and comparative analysis of various designs are carried out.

During this stage, measurements are made by changing the air flow adjustment in the incoming mock-up opening (Fig. 1).



Fig. 1. Model.

It was also possible to perform measurements by changing the air flow at the outlet (Fig. 2). This design of the model makes it possible to study the influence of

the air pocket on the work of the turbine itself, but we are not yet ready for this kind of research. So, it remains for perspective stages.

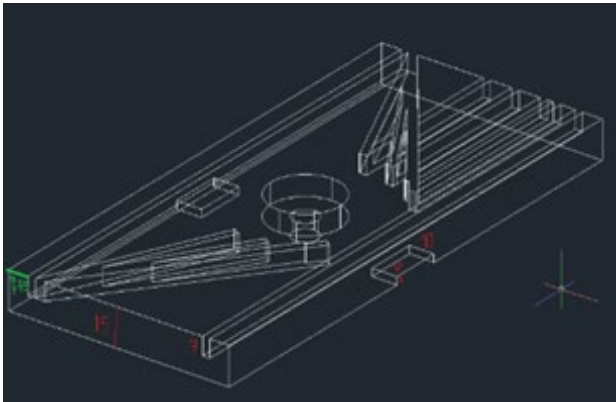


Fig. 2. Skeleton of the model.

Experiments are performed with three impellers of different configurations keeping other conditions analogous.

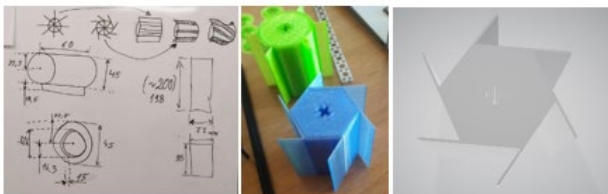


Fig. 3. Impeller (Airfoil) configurations.

As an indicator when evaluating the efficiency of impellers, we use the values of the current generated in the stationary coils and the generated voltage (tables and graphs).

All experiments were performed using only one rotating magnetic ring and one set of stationary coils. However, when designing an impeller with turned wings (Fig. 4), two cavities are already provided for magnets and coils, but this is for the next stage of experiments.



Fig. 4. Impeller with turned wings.

The most elementary active load impedance scheme was used to evaluate the efficiency of the impellers (Fig. 5).

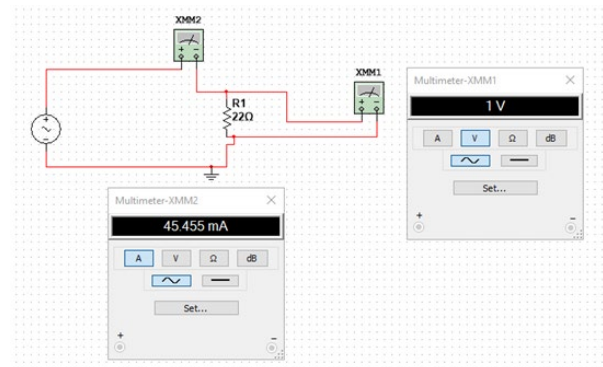


Fig. 5. Scheme of measurements.

Multimeter XMM1 (voltmeter) measured the voltage on the load resistance, and multimeter XMM2 (ammeter) measured the current flowing in the circuit.

#### IV. MEASUREMENT RESULTS AND SUMMARY

In this case, the recording and comparison of the averaged values was decided to appoint as enough. The table of characteristic data measurements looks like this (Fig. 6). One multimeter XMM1 (voltmeter) measured the averaged (in AC mode) voltage on the load resistance, while the other multimeter XMM2 (ammeter) measured the averaged current flowing in the circuit (in AC mode). When working in the environment of critical conditions, such measurement accuracy is sufficient.

sparnuotē		I, mA	V, mV	out v, km/h
	anga in1	4,8	104,2	11,7
	anga in2	3,08	68,1	11,2
	anga in3	0,4	0,1	11
	anga in1	4,5	98,3	12
	anga in2	3,93	84,3	10,5
	anga in3	0,8	13,01	10
	anga in1	1,55	35,02	11
	anga in2	0,12	2,8	11
	anga in3	0	0	12,9

Fig. 6. Table of measurement results.

The table immediately shows that in one position the impeller does not rotate at all, although the passing air flow at the outlet is even faster than in other cases. This shows that we are working in an environment of critical conditions. The line between action and non-action is very close. This provides excellent opportunities research for improving the efficiency and this is immediately noticeable in the measurement table. When the impeller is not rotating, it can be assumed that the air flow does not lose some of its kinetic energy and therefore the speed of the outgoing air flow is higher. Another rather obvious assumption based on these measurement results is that the most efficient air flow

concentration is in the gap of one wing height. When evaluating prospects, it should be taken into account that both the theory and practice of wind energy show that the energy of the air flow is proportional to the cube of its speed [1].

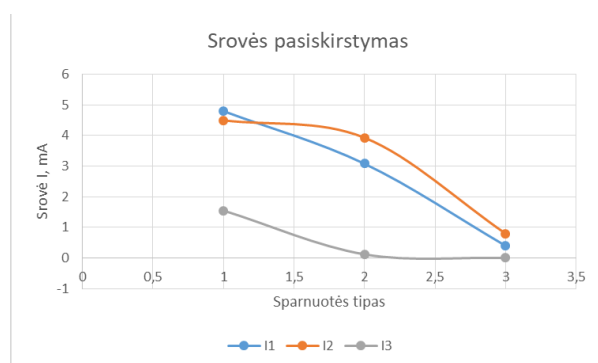


Fig. 7. Current distribution graph.

Analyzing the graphic representation of the measurement domains (Fig. 7), we drew the curves of the dependence of the current on the height of the inlet air flow for different vane configurations. Although wind energy studies emphasize that the amount of air flow energy almost directly depends on the mass of the air flow passing the vane, from the graphs we can assume a slightly different variable dependence characteristic of this design. Increasing the height of the inlet opening also increases the mass [1] of the air flow past the vane, but the energy changes slightly, and after reaching a certain value, it even starts to decrease and probably quite suddenly. This observation encourages a more careful study of structural features and the search for a combination that can ensure the highest possible efficiency. You should also pay attention to the fact that the speed of the exit air flow starts to decrease when the height of the entrance channel is increased (emphasis in the measurement table). Only in the case when the impeller is no longer rotating, the speed of the outgoing air flow has increased slightly.

The graph of current dependence was selected for analysis. The voltage and power graphs are very similar to the current dependence curves, so we will not analyze them in detail. One of these dependencies is sufficient for the examination of characteristic features at this stage.

When combining mechanical and electromechanical parts, quite a number of interesting nuances emerge, which should be studied in more detail, so the field of research can and should probably be expanded. Well, to achieve practical progress, it would be logical to choose the direction of the most promising efficiency coefficient based on the available measurement data and not to delve into possible parallel studies and solutions. This dilemma disturbs many researchers, and the decision is not easy, but necessary, as both available resources and physical capabilities must be

considered. By connecting the electrical and electronic parts to the available mechanical and electromechanical parts, the nuances that are worth investigating in more detail will probably appear even more, so the possibilities for improvement remain wide and tempting.

This research project and the scientific research areas revealed in it are relevant not only in a scientific or applied practical sense, but also their pedagogical aspect remains very important in developing the curiosity of our students and promoting cognition.

## V. CONCLUSIONS AND SUGGESTIONS

The results of experimental measurements show that the amount of electricity generated using one rotating magnet and one set of stationary coils is small for practical use, but such a mock-up already demonstrates the principle of operation of the future device. The positive efficiency factor of the mechanical part (impeller configuration) achieved at this stage already allows us to move on to the studies of the efficiency factor of the electromechanical part (coils and magnets) and the mutual coordination of these two parts. For further research, two sets of rotating magnets about stationary coils can already be used. Configuration will allow more energy to be extracted and observed, but with increased resistivity, so measures may need to be taken to maintain the boundary conditions.

## REFERENCES

- [1] R. P. Murkund, Wind and solar power systems: design, analysis, and operation. Boca Raton, 2006.
- [2] Lithuania Wind Association, "Viskas, ką reikia žinoti apie vėjo energetiką", 2020. [Online]. Available: [https://lvea.lt/wp-content/uploads/2021/01/LVEA\\_Viskas-ka-reikia-zinoti-apie-vejo-energetika.pdf](https://lvea.lt/wp-content/uploads/2021/01/LVEA_Viskas-ka-reikia-zinoti-apie-vejo-energetika.pdf) [Accessed: April 26, 2023]
- [3] L. Augulis, A. Jotautis and D. Rutkuniėnė, Fizika: mechanika, termodinamika, elektromagnetizmas: mokomoji knyga, 2012. [Online]. Available: [https://www.ebooks.ktu.lt/eb/656/fizika\\_me\\_chanika\\_termodinamika\\_elektromagnetizmas/](https://www.ebooks.ktu.lt/eb/656/fizika_me_chanika_termodinamika_elektromagnetizmas/) [Accessed: April 26, 2023]
- [4] V. Matutis and M. Matutis, "Patent description", 2019. [Online]. Available: <https://worldwide.espacenet.com/patent/search/family/068887188/publication/EP3840192A1?q=EP3840192A1> [Accessed: April 26, 2023]
- [5] G. Boyle, Renewable energy: power for a sustainable future. Oxford University Press, 2012.
- [6] V. Matutis, L. Savulioniene, P. Sakalys and T. Kasperavicius, "Energy Generator Prototypes Development and these Research Integration into the Educational Process", Society. Integration. Education. Vol 1, 2022. [Online]. Available: <http://journals.ru.lv/index.php/SIE/article/view/6884/5683> [Accessed: April 26, 2023]
- [7] A. Betz, Das Maximum der theoretisch möglichen Ausnützung des Windes durch Windmotoren. Zeitschrift für das gesamte Turbinwesen. Germany, 1920, pp. 307-309.
- [8] V. Matutis, L. Savulioniene, P. Sakalys, T. Kasperavicius, "Research of Power Generator Prototype Development and Integration into Autonomous Robotic Systems", Society. Integration. Education. Vol 5, 2021. [Online]. Available: <https://doi.org/10.17770/sie2021vol5.6453> [Accessed: April 26, 2023].

# Improvement of Operational Processes by Ensuring Work Safety in Production

**Rūta Meištė**

Faculty of Business and Technology  
Utena University of Applied Sciences  
Utena, Lithuania  
rutameiste@gmail.com

**Sandra Jakštienė**

Faculty of Business and Technology  
Utena University of Applied Sciences  
Utena, Lithuania  
sandrajakstiene7@gmail.com

**Aušra Lankauskienė**

Faculty of Business and Technology  
Utena University of Applied Sc  
Utena, Lithuania  
ausra.lankauskiene@utenos-  
kolegija.lt

*Abstract. the article analyzes the improvement of operational processes by ensuring the safety of work in production. The problem raised in the research: how to ensure work safety by improving the company's operational processes in production? The object of work is the possibilities of improving operational processes by ensuring work safety. The aim of the work is to analyze the possibilities of improving operational processes by ensuring work safety in production. Job objectives: to analyze the possibilities of improving operational processes by ensuring work safety from a theoretical aspect; to investigate the possibilities of improving operational processes by ensuring work safety in the production company; prepare a plan for the improvement of operational processes by ensuring work safety in production. Research methods: analysis of scientific literature and other informational sources; data collection and systematization method; descriptive analysis method used to report research data; the summarization method is used to evaluate the results of the analysis; the research uses data analysis and observation method.*

*After conducting the research and analyzing the measures applied in the operational processes, ensuring the safety of work in production, a plan for improving the operational processes was prepared and presented, which offers specific measures for increasing the efficiency of the processes and reducing the risk of accidents. The measures implementation plan is designed to solve existing problems in the company's operational processes, offering recommendations on how to reduce or completely eliminate accidents by ensuring work safety. The proposed plan will help minimize the risk of accidents at work by ensuring work safety in operational processes. The created plan for improving operational processes with measures by ensuring work safety and reducing the risk of accidents at work is universal and can be applied in*

*other manufacturing companies that seek to improve operational processes by ensuring work safety.*

*Keywords: operational processes, work safety, production.*

## I. INTRODUCTION

**Relevance of the topic.** Every year, accidents at work cause staggering costs in terms of loss of life, pain and suffering, lost wages for injured workers, damage to production facilities and equipment, and lost production opportunities. Accidents at work result death, injury and many lost days of work and huge costs to the company, including lost wages, medical and rehabilitation benefits, insurance administration costs, loss of property, lost production and other indirect costs. For these reasons, the safety of industrial works remains one of the most important priorities of the company's operations.

The extent of the problem can be seen in the number of accidents. More than 40 accidents<sup>1</sup> occur in Lithuania every year. The consequences of accidents at work are often complex. Since almost a third of the causes of absenteeism are factors related to the work environment, improving the work environment could reduce absenteeism.

Accidents at work are a heavy social and economic burden. Many authors [12], [7], [4] analyze the economic aspects of accidents at work, while the social aspect of accidents is highlighted by [2], [8], [3], [1], [13] and others. in their works. The consequences of an irresponsible approach to safety at work are often disastrous for both parties: employers must pay considerable compensation if an employee is injured or

<sup>1</sup> Accident statistics in Lithuania. [Looked 09-05-2022].  
<https://www.vdi.lt/PdfUploads/NAprognoseVeikla2022.pdf>

killed, and employees lose their most valuable asset - health or even life. Work safety in the company's operational processes is an important area, the purpose of which is to ensure safe and healthy working conditions. Therefore, **the scientific problem** is expressed in the question - *how to ensure work safety while improving the company's operational processes in production?*

**The object of work** is the possibilities of improving operational processes by ensuring work safety.

**The aim of the work** is to analyze the possibilities of improving operational processes by ensuring work safety in production.

**The objectives:**

1. To analyze the possibilities of improving operational processes by ensuring work safety from a theoretical perspective.

2. To investigate the possibilities of improving operational processes by ensuring work safety in a production company.

3. To prepare a plan for the improvement of operational processes by ensuring work safety in production.

**The research methods:** analysis of scientific literature and other informational sources; data collection and systematization method; descriptive analysis method used to report research data; the summarization method used to evaluate the results of the analysis; the research uses data analysis and observation method.

II. MATERIALS AND METHODS

The concept of occupational safety in the company's operational processes. Occupational safety is one of the most important conditions for work organization in the operational processes of every company. All workers have the right to work in decent and healthy conditions. Sufficient attention must be paid to the safety and health of employees, especially in high-risk production companies. The Occupational Safety and Health Act of the Republic of Lithuania requires that employers in every company, regardless of its form of ownership and lines of activity, create safe and healthy working conditions for employees.

Failure to ensure occupational safety leads to accidents at work. Accidents at work are unexpected and unplanned events, including acts of violence, arising out of or related to work, which may result in the injury, illness or death of one or more workers [6]. Since occupational accidents are considered to be travel, transport or road traffic incidents in which workers are injured and which arise out of or in the course of work, i.e. when they are engaged in economic activity, work or business activities. Accidents at work are considered to be accidents that occur not only at the workplace, but also when going to work or from work on a regular route, to places of work-related training, where they can cause death or injuries [14].

The notification of the accident and the procedure for its investigation depend on the degree of severity of the accident. According to their consequences, accidents at work are divided into:

- deadly accidents - events that cause an employee to suffer a health and life-threatening injury and die immediately or after some time as a result;
- serious accidents - events that result in an injury to the employee's health and life;
- minor accidents - events due to which the employee suffers an injury and loses his ability to work for at least one day and which is not classified as a serious accident at work;
- incidents - this is a work-related event, as a result of which the employee does not suffer health damage or does not lose working capacity due to the health damage suffered (see Table 1).

TABLE I ACCIDENT ASSESSMENT AND INVESTIGATION PROCEDURE

Grade of severity of the accident	Description of the accident	Investigation procedure
<b>Deadly accident</b>	an event that results in an injury to the worker's health and life, resulting in immediate or delayed death	The investigation is carried out by an inspector appointed by State Labour Inspection, with the participation of the employer's representative and the employee's safety and health representative.
<b>Serious accident</b>	an event that results in an injury to the employee's health and life	The investigation is carried out by an inspector appointed by State Labour Inspection, with the participation of the employer's representative and the employee's safety and health representative.
<b>Minor accident</b>	an event resulting in an injury to an employee and loss of working capacity for at least one day and which is not classified as a serious accident at work	After the investigation, a bilateral commission approved by the employer is composed of a representative of the employer, who is appointed by the company manager and a representative of the employees for safety and health.
<b>Incidents</b>	it is a work-related event that does not result in the employee suffering health damage or loss of working capacity due to the health damage suffered	After the investigation, a bilateral commission approved by the employer is composed of a representative of the employer, who is appointed by the company manager and a representative of the employees for safety and health.

An occupational injury is any bodily injury, damage to body tissue or death resulting from an accident at work. Occupational injuries result in more time lost from work, productivity and working years than any other health condition [14]. Injuries are a leading cause of worker

morbidity and mortality. Thousands of people die every year due to industrial accidents and the number of disabled people is also staggering. Many workers experience work-related injuries that result in lost work time, treatment, loss of consciousness, work or movement limitation, or transfer to another job. Injuries at work continue to take lives, harm physical and psychological well-being and drain resources of workers and their families when occupational safety is not followed. The total human, social, and financial toll of injuries at work is enormous, matching the burden of health care products such as cancer and cardiovascular disease.

It is very important to take the necessary measures to protect the safety and health of employees, including the prevention of types of occupational risk, information and professional training, as well as the necessary organizational measures to prevent accidents in the company's operational processes. Safe work is a relevant practical, theoretical and scientific problem, therefore it is necessary to analyze the existing organizational, technical and other causes of industrial injuries in the work processes that prevent the work environment from being made harmless and safe, to assess their economic damage and to provide ways to reduce them. Causes of occupational safety violations in the company's operational processes. When analyzing work safety violations in the company's operational processes, it is first necessary to clearly define the processes taking place in the company and the most common accidents in those processes.

In a production company, all processes begin with the acceptance of orders, i.e. stage of production planning according to customer demand. Service or production of goods is planned according to the number of orders. After that, the need and quantity of materials is assessed. If there is a need, materials are ordered. When the preparatory work is completed, the production phase begins, the production of the ordered quantity of goods, i.e. performing the requested service. Later, everything goes to the customer, i.e. the final process takes place - satisfaction of the customer's need.

Violations of occupational safety are observed in all processes, but in manufacturing companies they mostly occur in the stages of the production process. Therefore, it is necessary to create safe conditions and comply with work safety requirements, which could reduce the number of accidents due to work safety violations in the company's operational processes.

In both private and public companies, institutions and organizations, regardless of their type of activity, the type of employment contract concluded, the number of employees and the like, the principle of creating safe and healthy working conditions must be applied without any exceptions. Its operation and implementation is ensured by establishing the basic legal requirements for employee safety and health (i.e. work environment, workplaces, work organization), which establish the employer's duty to ensure the safety and health of employees, control over the implementation of this duty and responsibility for it [15]. Consequences of occupational safety violations in the

company's operational processes. The consequences of accidents at work are significant. At the national level, accidents at work cause negative consequences for the labor market (people's employment) and the economic development of the country, and from the company's point of view - for a decrease in operational efficiency (making a profit). In the developed countries of the world, the consequences reach 2-4 per cent of GDP [5], [10], [11], so they are often attempted to be counted, especially in those countries that pay great attention to the prevention of accidents at work [1], [9], [13], [4]. They can be broadly divided into social and economic consequences. Table 2 below shows the consequences of accidents at work.

TABLE 2 SOCIAL AND ECONOMIC CONSEQUENCES OF ACCIDENTS AT WORK

Social implications	Economic implications	
	For government	For a company
<ul style="list-style-type: none"> <li>- Early retirement due to disability;</li> <li>- Absenteeism, i.e. absence from work due to injury or occupational disease;</li> <li>- Unemployment due to reduced working capacity, when the right to pension or compensation is not granted;</li> <li>- Loss of income when family members are unable to work to care for the victim.</li> </ul>	<ul style="list-style-type: none"> <li>- Health care and rehabilitation costs;</li> <li>- Sickness benefits;</li> <li>- Incapacity compensations;</li> <li>- Death benefits;</li> <li>- Declining GDP.</li> </ul>	<ul style="list-style-type: none"> <li>- Additional costs due to replacement;</li> <li>- Additional costs for hiring and training a new employee;</li> <li>- Lost production time;</li> <li>- Damage to equipment, materials, products;</li> <li>- Increased insurance costs;</li> <li>- Managers' time dealing with accidents at work.</li> </ul>

Accidents at work, injuries at work and deaths occur for a variety of reasons. Many traditional theories about the causes of accidents at work focus on the worker. There have been many attempts to develop a predictive theory of accident causation, but none has been universally accepted to date. Researchers in various fields of science and engineering have attempted to develop a theory of accident causation to help identify, isolate, and ultimately eliminate the factors that contribute to or cause accidents.

Possibilities for improving business processes while ensuring work safety. Prevention of preventable injuries is an important task of human resource management. Intervention to reduce occupational injury should be multifaceted to be successful. In order to influence the incidence of injuries and the underlying morbidity, a combination of activities at different levels, workplace visits, risk assessment activities, development projects targeting specific risks, print and electronic media campaigns, and surveys of general public attitudes are needed. The next step in the intervention should be a thorough analysis of specific tasks and identified risks, as well as systematic collection of risk scenarios from affected workers using critical incidents and other methods. Professional and task-specific engineering, ergonomics and design solutions should be developed for

the various problems listed above. In choosing such applied developmental activities, priority should be given to reducing the severity of injuries. The significant reduction in fatal injuries may reflect changes in work organization, greater automation and better safety standards. Knowledge of predictors of work-related injuries, comprehensive training of workers can contribute to injury prevention strategies, especially among newly hired workers.

Companies with different database configurations can create a standardized occupational injury surveillance database. Personal protective equipment has dramatically reduced the incidence of injuries and days off sick leave. An effective safety program results from a multidisciplinary effort that leverages the input and interaction of many groups within an organization. Establishing a plant-level safety committee to administer the program is essential to a successful program. The selection committee should consist of top managers (plant manager or designee and production unit managers) and the plant doctor or nurse, safety manager, plant level personnel managers and labor representatives. This committee should oversee the departmental safety committees that run the day-to-day safety program and deal with plant floor issues. For a safety program to be effective, it is essential that departmental committees are formed to encourage the active participation of supervisors and hourly workers.

Senior managers must develop the security policy, build it into the program, and ensure that the program is effectively implemented.

*In summary, it can be said that the most important thing in every organization is the implemented safety policy, which includes the organization's obligations to ensure a safe environment, compliance with requirements, training of employees, planning of improvement of work safety systems, control of employees, etc.*

### III. BASIS OF EMPIRICAL RESEARCH

**The aim** of the research is to perform an analysis of accidents at work in the food production company, determining the most common causes of accidents and to prepare a plan for improving operational processes in production, ensuring work safety.

**Data used in the study.** In order to carry out an analysis of accidents at work in the food production company, company's documents are analyzed in an empirical study and observation is carried out.

**Research period.** The study was conducted in April-May, 2022. The research was conducted in accordance with the following logical structure: the research problem is formulated, then the research is designed, research methods are selected. In the next stage, an investigation is carried out, information is collected, data is analyzed, a plan for improving operational processes is prepared, and conclusions are presented.

**Research data collection method.** The following methods were used in the research: analysis of company data, observation - with the participation of the researcher

in the observation process (observation included). Monitoring was chosen because it provides a purposeful and planned opportunity to obtain data on phenomena, processes, behavior occurring in the company's environment, i.e. to see reality as it really is.

**Research ethics.** During the research, compliance with ethical principles was ensured: privacy, anonymity, confidentiality, benevolence, justice, the right to receive accurate information about the research and the results of research use, and the company's data protection was respected. Company's name is not allowed to publish.

### IV. RESULTS AND DISCUSSION

Analyzing the processes carried out in the food production company to ensure work safety, first of all it is determined how the working conditions and working tools in the company meet the requirements set out in the occupational safety and health regulatory acts, assessing the occupational risk in workplaces or other places of the company where the employee may be working on time.

There are many different processes in the company in different departments of the company, but accidents happen only in the production department during the production processes. 15 accidents occurred in the production department during the three years' period: 8 accidents in 2019, of which two were serious accidents, when the investigation was carried out by labour inspectors from the State Labor Inspectorate of the Republic of Lithuania, 4 accidents in 2020 and 3 accidents in 2021. Analyzing the data of the accidents in the company in 2019-2021, there is a trend of decreasing number of accidents.

When examining the circumstances and reasons given in the acts of accidents at work, the causes of all accidents at work are grouped into separate large groups. The analysis shows that in most cases of accidents at work there are 2 main groups of causes of accidents at work:

- 1) dangerous (extreme) situation;
- 2) inappropriate behavior that occurred in the course of production activities.

The further possible causes of the emergency situation or the sequence of events depend on the compliance of the work tool with all human safety and health requirements, on organizational and environmental factors, as well as hygienic, domestic, sanitary conditions. In the second group, risk-taking, non-observance of safe work methods and methods, violation of rules, regulations, production or behavioral errors would prevail.

Safety and health issues are an integral part of accident prevention. They are relevant all the time. In accordance with the provisions of the Occupational Safety and Health Act, the employer must plan and implement preventive measures at all stages of the company's activity, so that employees are protected from dangers and occupational risks, or it is reduced as much as possible. For that purpose, he organizes an accident risk assessment in accordance with the Occupational Risk Assessment Regulations:

- before starting or commencing operations;
- periodicity determined by normative legal acts;

- after changing the technological process or starting to use new dangerous substances;
- after the installation of collective protection measures or their modernization;
- if a serious or fatal accident at work occurs in the company and after its investigation it is established that a risk factor could have been the cause of the serious or fatal accident at work;
- upon detection of violations of Occupational Safety and Health Act normative legal acts at the request of labor inspectors, etc.

It is important for the company to be well aware of the hazards encountered in its activities, the risks posed by these hazards and the protective and preventive measures that must be applied to eliminate the hazards or reduce the risk to an acceptable level.

As the analysis of the documents shows, after taking preventive measures and installing additional devices, the number of accidents at work decreased significantly and in 2020 there were only four of them, the main reasons of which are non-compliance with safety rules, inattention, carelessness. Serious accidents at work were avoided.

Meanwhile, three accidents occurred in 2021, all of them in the production department, i.e. in production processes. The main reason is non-compliance with safety rules. Serious accidents at work were avoided. In all cases, additional training was organized to ensure that the same accidents do not recur in the future, and employees are required to be more attentive and comply with safety rules.

Since all accidents occurred due to non-observance of workers' safety rules, their incompetence, carelessness and inattention, after each accident, training is organized in which workers are familiarized with safety requirements, their powers and work tools. Courses on the implementation of occupational safety and health requirements in companies and general training on the principles of occupational safety and health assurance, which all employees must follow, are organized. An annual health check-up of employees is mandatory and the regime of work and rest time in the company is determined, in accordance with the laws and recommendations of the government.

Most accidents happen when working with devices, so potentially dangerous devices are constantly maintained and their technical condition is checked. Personal protective equipment is constantly being purchased. All premises - household, sanitary and hygienic - are equipped to ensure the safety and health of employees. Research is being conducted on the impact of physical factors (noise, vibration, heat, electromagnetic fields, lighting, microclimate) on workers' health. Constantly conducted risk assessment studies for the identification of risks of accidents in the company's operational processes. We are looking for measures that could minimize that risk. Plans are prepared and implemented, effectiveness and adequacy of measures are studied. Penalties for non-compliance with these rules have also been introduced.

After the analysis of accidents in the company's operational processes, it was found that all accidents occurred during production processes, mostly in non-compliance with safety rules.

After carrying out a study on the operational processes ensuring work safety in the production company and determining the main causes and consequences of accidents, a plan for improving the operational processes was drawn up with measures that ensure work safety and reduce the risk of accidents at work (see Figure 1).

The results of the organization's activity do not appear by themselves - they are generated in the processual interaction of activity factors. The quality of the organization's performance results directly from the quality of these interaction processes. The quality of results is influenced by various aspects of the interaction of operational factors, but one of the most important is ensuring the optimality of process management, ensuring the safety of work in the branch. The organization's activity is a complex multi-faceted activity; therefore it functions by formulating and realizing complex integrated goals, the main of which is to minimize risks and avoid accidents at work, ensuring optimal and safe working conditions for employees.

Company processes are characterized by process content, process flow and operations and process participants. The process improvement content covers three areas: accidents (dangerous situations and inappropriate behavior), periodic training and preventive measures. The course of the processes is defined by the proposed measures: introductory training, training at the workplace, general training, protective equipment, health check, collective protective equipment, occupational risk assessment, ergonomics, communication, improvement plan. These measures are divided into smaller processes that take place at all structural levels of the organization.

The created plan for improving operational processes with measures that ensure work safety and reduce the risk of accidents at work is universal and can be applied in other manufacturing companies that seek to improve operational processes, ensuring work safety.

Summarizing the results of the research, the assumption should be formulated that, by applying the created plan for improving operational processes in production, ensuring work safety, specific measures for increasing the efficiency of processes and reducing the risk of accidents are offered. The measures implementation plan is designed to solve existing problems in the company's operational processes, offering recommendations on how to reduce or completely eliminate accidents and ensure work safety. The proposed plan will help minimize the risk of accidents at work.

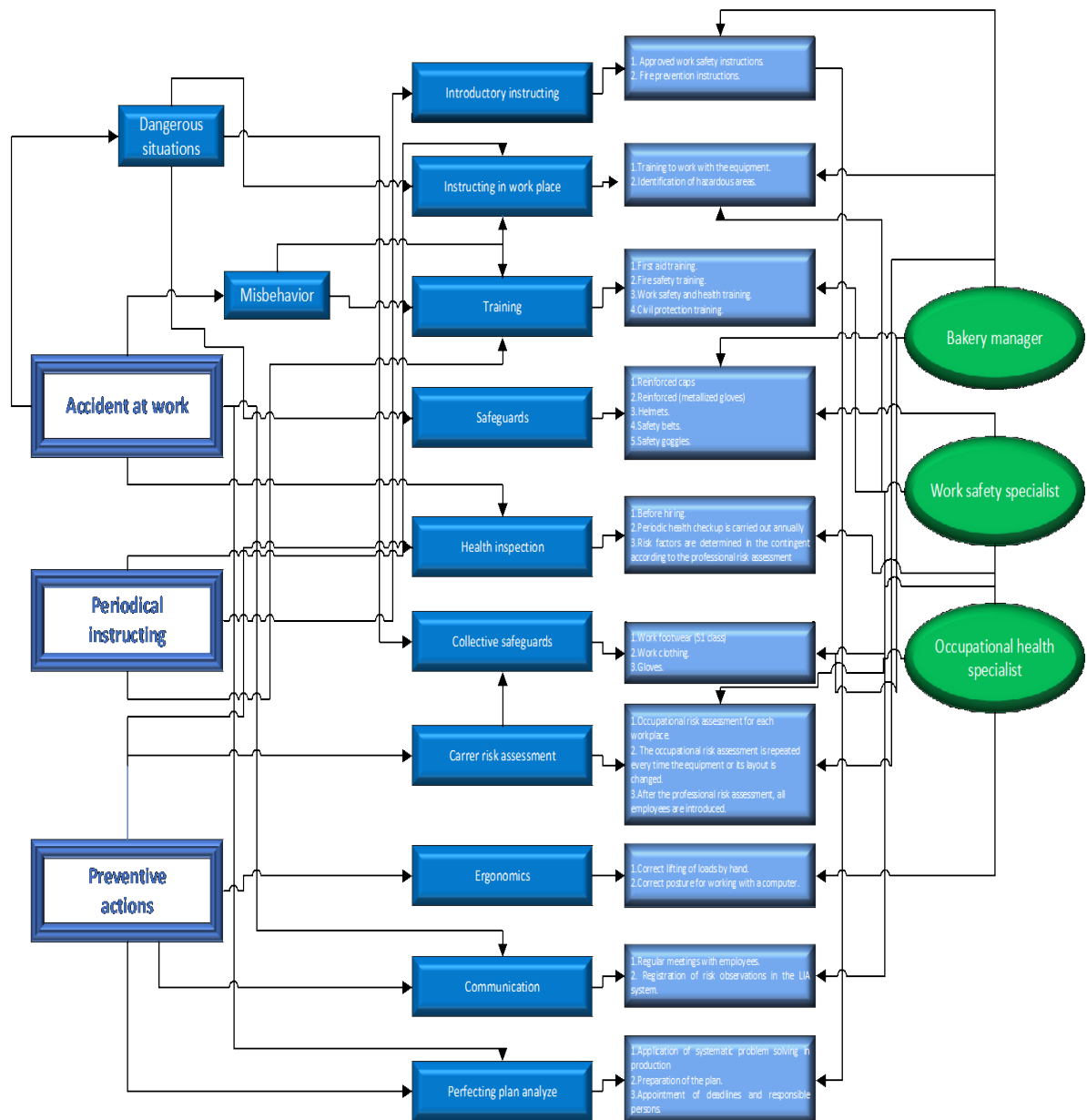


Fig.1. The measures implementation plan.

## V. CONCLUSIONS

1. After analyzing the possibilities of improving operational processes while ensuring work safety from a theoretical point of view, it can be stated that the operational processes of the organization are the practical result of the functions it performs, which are an expression of the realization of the company's goals. This shows that the goals, functions and operational processes of the organization are elastically related. And ensuring work safety and reducing the risk of accidents allows you to achieve the most efficient desired result in operational processes.

2. After carrying out a study of the possibilities of improving operational processes while ensuring work safety in the food production company, it was determined that all accidents occurred in the production process. After analyzing their causes and applied measures, it was found that the number of accidents has significantly decreased in recent years, and serious accidents have been completely avoided, which allows us to conclude that the applied measures are effective and should continue to be applied in the company's operational processes.

3. After conducting a study and analyzing the measures applied in the operational processes, ensuring the safety of work in production, a plan for improving the operational processes was prepared and

presented, which offers specific measures for increasing the efficiency of the processes and reducing the risk of accidents. The measures implementation plan is designed to solve existing problems in the company's operational processes. The proposed plan will help minimize the risk of accidents at work, ensuring work safety in operational processes.

#### VI. RECOMMENDATION

The study let form the measures implementing plan for work safety in production, ensuring the safety of work in production, improving the operational processes, which offers specific measures for increasing the efficiency of the processes and reducing the risk of accidents, is recommended to apply in any food production company. It can help to solve existing problems in the company's operational processes. The proposed plan can help minimize the risk of accidents at work, ensuring work safety in operational processes.

#### REFERENCES

- [1] V. Bell, V. and D. Wad, "Mental health of clinical staff working in high-risk epidemic and pandemic health emergencies a rapid review of the evidence and living meta-analysis," *Psychiatry Psychiatr Epidemiol*, 2021, vol. 56, p. 1–11. Available: <https://doi.org/10.1007/s00127-020-01990-x>.
- [2] T. Boeri, A. Caiumi, M. Paccagnella. "Mitigating the work-safety trade-off". *Covid Economics*, issue 2, April 2020. p. 64-70.
- [3] N. Bull, T. Riise and B. Moen, "Compensation for occupation- al injury and disease in Norway: ranking of job groups," *J Occup Environ Med*, 2000, vol. 42, no. 6, p. 621-8.
- [4] A. Dembe, J. B. Erickson and R. Delbos, "Predictors of Work Related Injuries and Illnesses: National Survey Findings," *Journal of Occupational and Environmental Hygiene*, 2004, vol. 1, p. 542-550. Available: <http://dx.doi.org/10.1080/15459620490478376>
- [5] H. J. D. Dorman and S. G. Deans, "Antimicrobial Agents from Plants: Antibacterial Activity of Plant Volatile Oils," *Journal of Applied Microbiology*, 2000, vol. 88, p. 308-316. Available: <http://dx.doi.org/10.1046/j.1365-2672.2000.00969.x>.
- [6] D. L. Gonçalves, *Coincidence Theory, Handbook of Topological Fixed Point Theory*, 2005, ISBN 978-1-4020-3221-9.
- [7] A. Hale, "Conditions of occurrence of major and minor accidents. 2-me séance du séminaire," *Le risque de défaillance et son contrôle par les individus et les organisations*, Gif sur Yvette, 2000.
- [8] J. Hovden, E. Albrechtsen and I. A. Herrera, A need for new theories and approaches to occupational accident prevention, Working on Safety Conference, September 30-October 3, 2008, Crete, Hellas.
- [9] T. W. Loushine, P. L. Hoonakker and et al, "Quality and Safety Management in Construction," *Total Quality Management and Business Excellence*, 2006, vol. 17, no. 9, p. 1171.
- [10] C. L. MacLean, I. E. Dror, "Measuring base-rate bias error in workplace safety investigators". *Journal of Safety Research* 84, 108-116.
- [11] C. Ochs, "Occupational safety and health in marine aquaculture in Atlantic Canada: What can be learned from an analysis of provincial occupational injury compensation claims data," *Aquaculture*, 2021, p. 540.
- [12] J. L. Sheu, S. L. Wu, C. Y. Lin and T. Chee, A new multi-channel MAC protocol with on-demand channel assignment for multi-hop mobile ad hoc networks, Proceedings International Symposium on Parallel Architectures, Algorithms and Networks, I-SPAN, 2000.
- [13] A. Tartilaitė, "Nelaimingas atsitikimas darbe darbuotojui esant neblaiviam: samprata, prevencija ir teisinė atsakomybė," *Socialinių mokslų studijos*, 2010, vol. 1, no. 5, p. 321–335.
- [14] E. Ūselytė, *Darbuotojų saugos ir sveikatos valdymas, kontrolė ir socialinė partnerystė*, 2017, VU, Vilnius.
- [15] X. Wu, Y. Li, Y. Yu, "CEO Inside Debt and Employee Workplace Safety". *Journal of Business Ethics*, 182, 2023. p. 159-175.

# Local Processing of Non-Metal Materials with Concentrated Energy Flow

Ivan Mitev

Faculty of Economics  
Technical University of Gabrovo  
Gabrovo, Bulgaria  
imitev@tugab.bg

Simeon Tsenkulovski

Faculty of Mechanical and Precision Engineering  
Technical University of Gabrovo  
Gabrovo, Bulgaria  
s.tsenkulovski@advanced-technology.eu

**Abstract.** In the present study, the peculiarities of local heat treatment with a concentrated light energy flow of non-metallic materials are traced. Mathematical dependences are presented for determining the surface density of the absorbed power -  $W(r)$ , the thermal power -  $P_0$ , and other characteristics in case of local thermal impact on the surface of non-metallic materials with a concentrated light energy flow.

**Keywords:** concentrated light energy flow, non-metallic materials, surface thermal effect.

## I. INTRODUCTION

Electrothermal technological processes are the basis of modern industrial development. By their nature, they are divided into two large groups [6,7,8]:

- Electrothermal physical processes;
- Electrothermal chemical processes.

Physical electrothermal processes include a large group of electroerosion, plasma, electron beam, ion and light (laser) technologies for shaping and shape change.

Electrothermal technologies, together with controlled (by composition) gas environments and vacuum, become the basis for the development of special metallurgy, the production of quartz and optical fibers, the production of metallic amorphous materials, the processing of semiconductor and dielectric materials [2,3].

The development of electrothermal technologies leads to the emergence and possibility of processing new materials (extremely necessary for the development of the electrotechnical industry, electronics, medicine and other branches of the economy) with increased operational properties, extended life and increased reliability [4]. Many of the new materials cannot be processed by existing conventional (casting, plastic deformation, etc.) technologies. In turn, the development of methods for

obtaining new materials leads to the development of new methods of processing and their modification.

The purpose of this publication is to examine the peculiarities of processing non-metallic materials by local thermal impact with a concentrated light energy flow (laser processing).

## II. RESULTS AND DISCUSSION

Under the influence of a powerful energy flow on the processed surface of the materials, the absorbed energy is converted almost instantly into heat and creates a secondary (local) source of heat on the surface or in the volume of the material. The dynamics of temperature change, the distribution of temperature fields in the material, as well as the appearance of phase transitions and opportunities for local thermal processing are mainly determined by this secondary heat source [9,10].

The thermophysical task of heating the material under the influence of the secondary heat source during laser processing has no analytical solution [1,11]. Simplifying assumptions are made about the shape of the incident energy pulse, about the thermophysical properties of the medium and their temperature variation, and about the boundary conditions, which at the present time give solutions with satisfactory accuracy.

In this regard, it is appropriate to create a method for local thermal treatment, based on simplified thermophysical considerations related to the local thermal action of pulsed heat sources in the solid body [1].

The controlled thermal (physical) state of the material in the zone of influence of the heat source, by changing the surface density of the absorbed power, by changing the focused energy spot, or by using pulses of different duration and energy is the basis of a wide class of electrophysical technologies and especially the laser ones.

Print ISSN 1691-5402

Online ISSN 2256-070X

<https://doi.org/10.17770/etr2023vol3.7275>

© 2023 Ivan Mitev, Simeon Tsenkulovski. Published by Rezekne Academy of Technologies.  
This is an open access article under the [Creative Commons Attribution 4.0 International License](https://creativecommons.org/licenses/by/4.0/).

The thermal impact on the material takes place in the area of action of the secondary source and in the area of action of the heat wave propagating as a result of thermal conduction. In this situation, an increase in the temperature of the material is accompanied by:

- change in the optical, electrical and thermal properties of the material;
- occurrence of thermomechanical stresses;
- phase transitions of the material;
- activation of diffusion processes;
- thermochemical changes in the surface layer

As a result, high heating rates are realized - up to 1010 K/s, and cooling - up to 108 K/s, which determines the large temperature gradient - 106 K/s [7].

Local laser processing of the material is the result of the appearance and use of powerful light fluxes that act on the surface of the processed product. It can be considered as localization to the maximum extent of the thermal impact along the radius -  $r$ , of the beam (most often according to the Gaussian distribution of the surface power density) and in the depth of the material - along the  $z$  axis - fig.1.

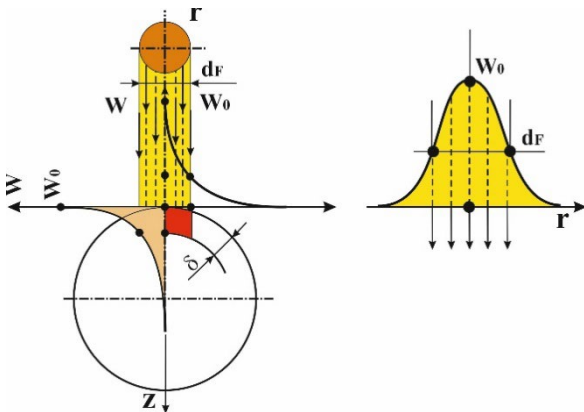


Fig.1. Schematic diagram of local surface laser thermal impact on non-metallic materials depending on the penetration depth -  $\delta$  and the size of the workpiece -  $R$ .

Depending on the transparency of the material at  $\delta \ll d_F$ , a surface heat source is formed with a different distribution of the absorbed power density  $W(r,z)$  - fig.2.

When processing non-metallic materials, the normal (Gaussian) distribution is the most common power density distribution law -  $I(r)$ , in the normal section of the energy beam (or in the contact spot). Its corresponding local heat source is also characterized by a normal distribution of the surface density of the absorbed power -  $W(r)$ , and can be calculated by formula 1:

$$W(r) = W_0 \exp(-k \cdot r^2) = A \cdot I_0 \cdot \exp(-k \cdot r^2) \quad (1)$$

where:  $k$  - flow concentration coefficient characterizing the shape of the normal distribution curve.

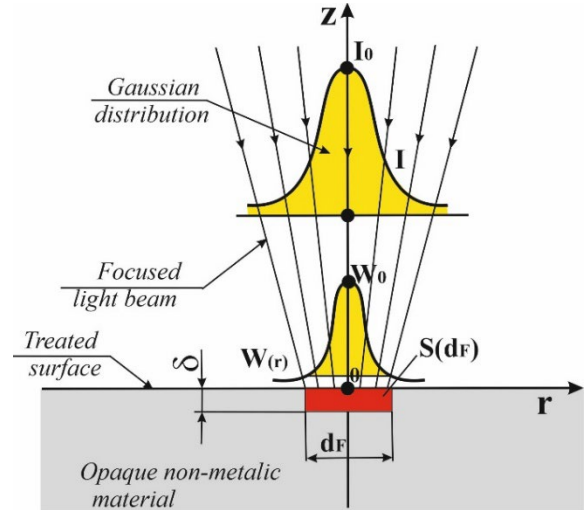


Fig.2. Formation of surface secondary heat source depending on the transparency of the material.

The thermal power of the local heat source -  $P_0$ . we can obtain by integrating the surface power density  $W(r)$  over the surface of the contact spot -  $S_F = \pi \cdot r_F^2$  (formula 2).

$$P_0 = \int_{(s)} W(r) \cdot d_F = (\pi/k) \cdot W_0 \quad (2)$$

With a uniform distribution of the surface power density -  $W(r)$  along the radius of the contact spot or with  $W = W_0 = \text{const}$  the thermal power -  $P_0$  can be determined by expression 3:

$$P_0 = S_F \cdot W_0 = \pi \cdot r_F^2 \cdot W_0 \quad (3)$$

In this situation, with the same heat power -  $P_0$ , the two distributions have the same surface power density -  $W_0$ , if the flow concentration coefficient is  $k = 1/r_F^2$  (or  $r_F^2 = 1/k$ ), we can take the radius  $r_F$  as the radius of the contact spot - fig.3

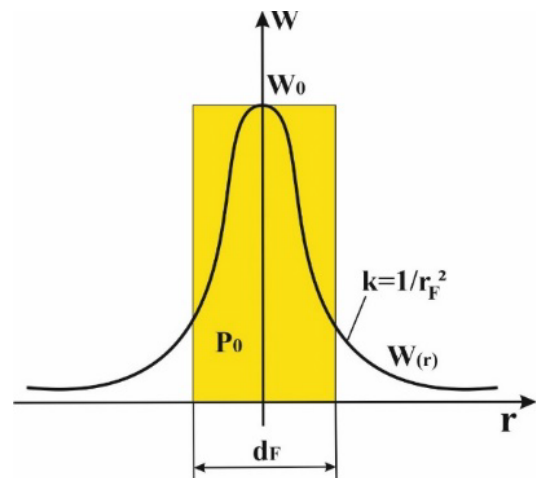


Fig.3. Power equivalence of Gaussian and uniform surface distribution of power density at  $d_F = 2r_F$ .

Therefore, we can refer to the case of a normal distribution and calculate with equation 4 all the solutions derived for a uniform distribution of the surface power density:

$$W(r) = W_0 \exp(-r/r_F)^2 \quad (4)$$

Depending on the way of absorbing the energy of the incident light beam, we can distinguish two typical cases:

- continuous absorption during the penetration of the light beam into the material;
- penetration of the light beam into the material at a certain depth -  $\delta z$ , without absorption, after which the absorption is distributed uniformly in all directions with continuous weakening with distance from the center (isotopic diffusion scattering).

When processing non-metallic materials with radiant heat transfer in laser processing, there is a continuous absorption of energy deep into the material.

Therefore, we can determine the depth of penetration with equation 5:

$$\delta = 1/\alpha \quad (5)$$

where:  $\alpha$  – attenuation coefficient of the light wave.

The dependence of absorption on the depth of penetration (Bouguer-Lambert law) is valid for a uniform distribution of the power density -  $W_0$ , in the energy spot of interaction with a diameter  $d_F$  - fig.4.

$$W/W_0 = \exp(\alpha z) \text{ или } W/W_0 = \exp(-\delta \cdot z) \quad (6)$$

where:  $\delta^2 = \rho / (\pi \cdot \mu \cdot f)$

Therefore, in the case of beam machining of non-metallic materials and a Gaussian distribution of the surface density of absorbed power in the contact spot, the depth distribution of the machined zone can be determined by the expression 7:

$$W/W_0 = \exp\{-[2r/d_F]^2 + (z/\delta)\} \quad (7)$$

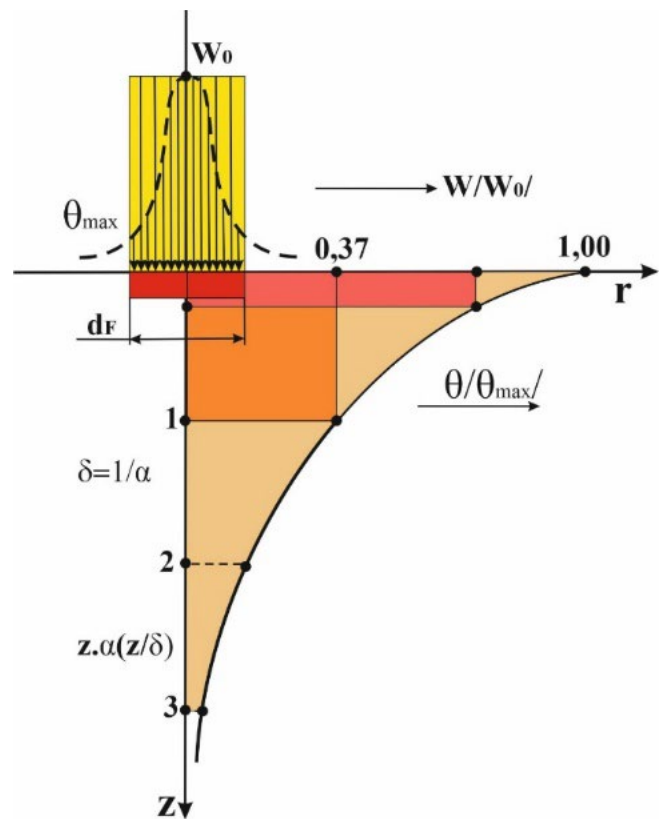


Fig. 4. Distribution of surface energy (relative power density  $W/W_0$  and relative overheating  $\theta/\theta_{max}$ ) during laser processing of non-metallic materials.

### III. CONCLUSIONS

From the conducted experiments and the results obtained, it is proved that the local heat sources during laser processing of non-metallic opaque materials are characterized by a temperature distribution field that follows the distribution of the absorbed energy density -  $W(r,z)$ .

In practice, when processing non-metallic materials with a laser-type heat source, the maximum temperature is registered on the surface of the material.

### REFERENCES

- [1] C.A. Kittel, Introduction to solid state physics, Wiley, Hoboken, 2005.
- [2] D. Petrova., Analysis of SMEs in Bulgaria – Assessment of Their Innovation Activities, Rezekne 2013, Latvia, Rezekne Higher Education Institution, Faculty of Engineering, Scientific Institute for Regional Studies, Environment. Technology. Resources, Proceedings of the 9th International Scientific and Practical Conference June 20-22, 2013, Volume 3, ISSN 1691-5402:46-49.
- [3] D.Petrova, Intelligent, Innovative and Sustainable Industry in Bulgaria – prospects and challenges, Vide I. Tehnologija. Resursi - Environment, Technology, Resources, Proceeding of the 12th International Scientific and Practical Conference „Environment. Technology. Resources“, June 20-22, 2019, Rezekne, Latvia, Volume I, pp. 210-215, ISSN 1691-5402 – print, ISSN 2256-070X – online.
- [4] I. N, Mitev, Industrial Materials, ECS-PRESS, Gabrovo, 2017, ISBN 978-954-490-556.

- [5] I. N.Mitev, Materials and blanks - part I (Materials), Credo - 3M, Gabrovo, 2021, ISBN 978-619-7100-44-0
- [6] I. N. Mitev, Materials and blanks - part I II (Unconventional electrotechnological processes for obtaining blanks), Credo - 3M, Gabrovo, 2021, ISBN 978-619-7100-46-4
- [7] I.N.Mitev, Unconventional electrotechnological processes, EX-PRESS, Gabrovo, 2020, ISBN 978-954-490-698-7
- [8] I.N.Mitev, Modern industrial technologies - part II / Electrophysical and electrochemical methods for forming /, EX-PRESS, Gabrovo, 2016, ISBN 978-954-490-413
- [9] I. N. Mitev, M.P.Georgieva, Depth of penetration during processing of powder metallurgical materials with plasma energy flow, "UNITECH, 06" Gabrovo, 2006, p. II 182 ÷ 185 ISBN 10: 954-683-352
- [10] I.N.Mitev, M.P.Georgieva, Determination of the main thermophysical properties in the treatment of powder materials with plasma energy flow, "UNITECH, 06" Gabrovo, 2006, p. II 227 ÷ 231 ISBN 10: 954-683-352
- [11] P.P.Dinev, Electrical Technology, University of Technology - Sofia, 2000, ISBN 954-438-292-5.

# Human Capital in the Changing Work Environment of Industry 4.0

Neli Nikolova  
Department Management  
Technical University of Gabrovo  
Gabrovo, Bulgaria  
e-mail: nikel@abv.bg

**Abstract.** The analysis of surveys conducted in Bulgarian companies proves that the quantity and quality of human capital to the greatest extent determine the long-term potential for sustainable organizational development. Aware of the need for investment in human capital, more and more company leaders and managers are focused on creating value for their business through training and development of their employees; building knowledge, skills, competences and motivational attitudes towards the changing working environment in Industry 4.0. The article examines flexible forms of work and creative approaches to increasing the satisfaction and engagement of employees in the implementation of strategic company goals.

**Keywords:** changing working environment, Industry 4.0, human capital, flexible forms of work.

## INTRODUCTION

Industry 4.0 completely transforms the production processes and has an impact on the world economy and politics, as well as on society and the individual - a carrier of capital and the most important resource for each company. Knowledge, intelligence and the quality of human resources have long become decisive forces for the prosperity of any nation.

In digital transformation, human capital is the core of any organization and business for the creation of value. Human capital is a system of competencies - knowledge, skills, qualities and attitudes to work (inherent in the workforce) that are driving forces for the creation of economic, social and personal well-being, through higher productivity and quality of performance and through the achievement of the strategic goals of the organization. Due to the specifics of human capital, resulting from the personal characteristics of each individual person in the organization, it is difficult to measure and therefore - the most difficult to manage. It is created and managed in a dynamic, highly competitive business environment and is

influenced by a variety of critical factors. The growing interest in human capital can be explained by the change in the understanding of economic development factors.



Fig.1. Major factors changing the work environment.

Globalization, changing economic and social conditions, the introduction of innovative digital technologies are some of the factors requiring the need for changes and restructuring of labor markets. Flexicurity is a holistic approach to labour market policy that provides workers with secure jobs the opportunity to quickly find new ones. Flexibility implies a smooth transition of workers to rapidly changing working conditions. Flexibility and security go hand in hand. They are aimed not only at employed persons, but also at the restructuring of the labor process in the organizations themselves. Flexible forms of employment enable the employer to reduce the costs associated with the cost of labor. It is also aimed at employees, who have the opportunity to improve knowledge and competences by combining their duties in other areas. The second factor is social security, guaranteeing a dignified existence, justice and solidarity for all participants in the labour markets.

Print ISSN 1691-5402

Online ISSN 2256-070X

<https://doi.org/10.17770/etr2023vol3.7177>

© 2023 Neli Nikolova. Published by Rezekne Academy of Technologies.

This is an open access article under the [Creative Commons Attribution 4.0 International License](https://creativecommons.org/licenses/by/4.0/).

## EXPOSITION

The aim of the entire European Community is to promote partnership and unity among all EU member states. Synergies, the implementation of an integrated labour policy, joint cooperation, solidarity and the development of flexible forms of employment are certainly the way to smart and sustainable growth for all European countries.

We live in a digital world where we do everything virtual, unlimited and everywhere (the new normal). Workers, firms and governments accumulate new comparative advantages in changing conditions. High-tech equipment and process robotization are changing business models and management approaches.

American futurist Alvin Toffler writes: "Today's market, technology and consumers need rapid change and in so many different ways they exert pressure on the company that the bureaucratic uniform is becoming obsolete. Since markets are constantly changing, location is less important than mobility and flexibility."

The quantity and quality of human capital determine to the greatest extent the long-term development potential of the individual, company or country. This was true as early as the 18th century, when the Scottish economist Adam Smith concluded that: "The acquisition of... Talents during... education, training or apprenticeship is a real cost that represents an invested capital in an individual. These talents are part of his well-being, and the same is true of the welfare of society." This continues to be true today.

The development of socio-behavioral, so-called. "soft" skills, such as the ability to work in a team, empathy, resolve conflicts and improve relationships, increases the human capital of the individual. Globalized and automated economies place a higher value on human capabilities that cannot be fully mimicked by machines. Abilities such as persistence in difficult situations have economic benefits that are often as great as those associated with cognitive skills.

The main objective of the article is reduced to justifying the need to invest in people, their acquisition of new knowledge and skills, lifelong learning, as factors that lead to economic and social progress. Flexible forms of work and creative approaches to increasing the satisfaction and engagement of employees in the implementation of strategic company goals are discussed.

**Methodology:** The method of content analysis of sources from the scientific field in which the study is positioned is used. A secondary analysis of the results of sociological surveys in the problem area is made. Specific case studies from social practice are analyzed. An empirical study has been conducted with the means provided by the Internet. The results of studies in Bulgarian companies prove that the quantity and quality of human capital to the greatest extent determine the long-term potential for sustainable organizational development.

Bulgarian companies and institutions are part of the global world. That is why the survey pays attention to the self-assessment of each respondent for their creative

potential and tolerance. They are convinced that organizations can achieve competitiveness in this world now, in the era of the fourth industrial revolution, provided that management teams activate their creative capital.

Particular attention is paid to the role of the environment. The summary of the examples given leads to the finding that creative places are open, tolerant of different ones and this makes them a crossroads of ideas. By breaking down barriers between different cultures, this environment becomes the epicenter of creativity and combining existing concepts into a huge number of unfamiliar ideas.

The transformation is provoked by the advent of the digital age, online platforms and fast-growing companies. The change on a global scale does not bypass the business in Bulgaria. The HR specialist is no longer just an employee of the Personnel and Labor Relations Department, but a person who helps both to achieve the company's goals and to provide a better working atmosphere for employees.

Automation through technology and robots will increase productivity and wealth and create many new opportunities for people with the right skills. People will be able instead of focusing on "tasks" identified as work, to focus on the work that makes the world a better place to live. The surveyed organizations recognize that they need to develop the digital literacy of their staff, to engage in time to respond adequately to the needs of their customers. Digital literacy enables the human resource in the organization to add value to the customer and become human capital, which is the bearer of the competitiveness of the organization in the conditions of the fourth industrial revolution. It complements material capital in the production process and makes an important contribution to technological innovation and long-term growth.

Human capital can be referred to as the value that is added to a company by an employee, which can be measured by his skills and competences. Human capital can be developed in many ways to obtain the highest economic value for the organization. The activities related to human capital formation are very diverse and include educational initiatives and self-initiatives at different levels: health, investment in geographical mobility, as well as the formation of relevant attitudes and motivation in personal and social terms.

Leaders can learn a lot about ways of communicating in business if they learn how to communicate with horses. More and more organisations in the UK are sending their managers to horse communication courses to learn to overcome business challenges, improve their performance and, of course, hone their leadership skills. The art of communicating with horses is the ability to communicate with horses in their own language, using nonverbal communication and body language. Since each horse has its own personal individuality, it is easy to make a connection between communicating with them and communicating with people, especially given the fact that the most human communication is nonverbal. According

to scientific research, only 7% of any message is conveyed through actual words, and 93% is nonverbal communication – facial expression, posture and tone. Understanding between a person and a horse is mutual respect, and achieving it can also improve the way leaders communicate with people. Working with horses can help leaders step out of their comfort zone and teach them valuable management skills in a creative and memorable way. Many managers have never approached a horse or attempted to communicate with these animals, and by learning how to do so, they also gain the ability to connect with people and have more influence as leaders.



Fig. 2. Leadership lessons with horses. [6]

The changing nature of work requires a set of skills that improve the adaptability of workers by allowing them to easily transfer from one job to another. Authors of publications in various scientific disciplines [1,2,4] as well as employers consistently indicate that they value higher-order cognitive (technical) skills and social-behavioral skills the most. In this new work environment, continuous learning is required; creativity; skills to solve unexpected problems and situations; responsibility for one's own quality and quantity of performance of work duties; changing knowledge in the field of human capital management. In a survey of industrial Bulgarian companies with business leaders and employees, the necessary skills to work in today's conditions of increasing digitalization were arranged, illustrated in Fig. 3:

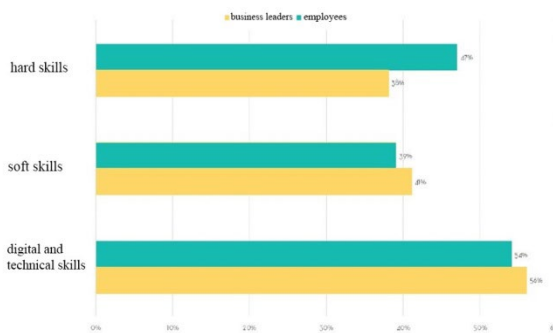


Fig. 3. The importance of skills according to employees and business leaders.

Effectively managing the collaboration between humans and artificial intelligence is a new challenge for management teams. The fourth industrial revolution, which is characterized by a fusion of technologies from the physical, digital and biological spheres, is changing the structure of the traditional labor market, increasing the demand for engineers, computer scientists and new unknown or little-known professions.

One of the main bridges between the physical and digital worlds today is the "Internet of Things" using connected technologies and different platforms. In in-depth interviews with functional and strategic managers of industrial Bulgarian companies, they find that technological platforms lower the barriers that people and companies must overcome to create material goods, changing the personal and professional work environment. Operations managers point out that digital platforms significantly reduce the cost of closing barriers. On the other hand, respondents share the concern that technology will eliminate some jobs, leading to an increase in unemployment. Examples often given as arguments are that robots are already entering the service sector, that airplanes and cars can be created by 3-D printers, and that nanotechnology and artificial intelligence are affecting more and more industries.

While it is true that technology will have a disruptive impact on the workforce as we know it today, it will not eliminate it, but rather change the spectrum of skills needed. Demand for more basic skills that can be replaced by technology is declining. At the same time, there is a growing demand for high cognitive skills, socio-behavioral skills and combinations of skills associated with greater adaptability. Rapidly developing industrial technologies and the integration of artificial intelligence require adaptability of management capacity and flexible digital literacy of personnel.

In Industry 5.0 people and machines will need to interact as harmoniously as possible to remain competitive and adapt to the new way of working. At the same time, human resources are increasingly confused and fearful about their future and often change jobs in search of security. The expression "no people" will take on a new and even more terrifying meaning in the next few years, and organizations will undergo major changes, while the question arises of what company managements can do to retain and motivate people on the team for the realization of these inevitable changes. To be designers of new processes, we must learn to see the human side of change and how to manage change as a structured process in which the human is the key factor in making effective and flexible solutions. CEOs in Bulgaria face 3 main challenges in recruiting: finding the right people for the right technology so that the business wins; to find and develop employees with the right set of skills and to respond to the differences in motivation and way of working characteristic of the representatives of the Millennials generation.

It turns out that business managers value the skills that cannot be reproduced by machines, such as problem

solving, collaboration, adaptability, emotional intelligence. The ten most necessary skills for success in the workplace in response to global change in the coming years will be [7]:

- creativity related to a new way of thinking in the changing work environment;
- emotional intelligence, distinguishing productive human relations with empathy and commitment to results and good working relations;
- analytical/critical thinking as a requirement for proactive behavior in conditions of dynamic change;
- active learning and attitude for continuous development with learning from mistakes, active experimentation for better results;
- skills for evaluating situations and more complex tasks, requiring the ability to evaluate and make independent decisions;
- effective interpersonal communication;
- leadership skills to provide opportunities, support and engage people to develop their potential for good results at work;
- understanding and skills for working in an environment of cultural and personal differences;
- technological skills;
- willingness to work and commitment in conditions of continuous change. nce, leadership, creativity and innovation.

The development of the already popular "soft skills" and leadership, including emotional intelligence, problem solving, teamwork and communication, creativity are increasingly important as a weight in the selection or promotion of an employee, as they are rarely cultivated in the family or the university, and at the same time require a long time and effort to be well developed. It is precisely these skills that technology cannot reproduce on its own, which makes them even more highly valued.

In recent years, the problem of staff recruitment and staff qualification has seriously worsened. According to employers, the majority of candidates do not have qualifications that meet the requirements of the development of the modern economy and technology. The age aspect is striking - older workers and employees are diligent and responsible, but with outdated knowledge and skills. Young people can be said to have knowledge and skills at a modern level, but they are not so motivated and demand high salaries without having the necessary experience.

Industry 4.0 gives us the opportunity to rethink the concepts of working-age population, retirement and individual life planning. New technologies are fundamentally changing the nature of work in all industries and professions [5]. The results of a survey conducted among Bulgarian companies from 10 industries show that 54% of workers performing routine and repetitive operations are exposed to risk as a result of the digital automation of production processes. The survey participants believe that in the next 3-4 years, the skills to solve complex cases and knowledge of systems will be much more in demand than physical abilities.

Only 38% of the surveyed managers indicate that the strategies they use are able to implement the upcoming changes in the organizations, ensuring their sustainable development. The majority of HR managers in the surveyed companies believe that the quality of working life and flexible working hours should be improved. More and more employers are using a "human cloud" populated by people performing specific work tasks from different locations around the world. For cloud workers, the benefits are greater job satisfaction, less stress, mobility and freedom. The challenge remains for business owners to discover new forms of social and labor contracts that respond to the changing work environment and nature of work.

Digital transformation places new demands on the quantitative and qualitative characteristics of human resources, their effective management and development. Based on the systematization of the scientific discussion on a global scale, two groups of researchers are forming, which discuss the impacts of the Fourth Industrial Revolution in the field of work. According to the first group, the consequences are reduced employment, increased inequality and economic instability. Automation, artificial intelligence, and other technological inventions are no longer only affecting uneducated, low-wage workers. Robots will be able to perform jobs that require significant qualifications and education.

Another group of authors is optimistic - the studies of the OECD, McKinsey Global Institute, Boston Consulting Group, etc., show that new digital technologies will lead to the enrichment of jobs and the creation of new ones, to a higher decentralization of decision-making and planning, transparency of business processes and improvement of social services. Digital innovations have important impacts on the way human resources participate and add value in many industrial value chains. The need for human labor is reduced, workplaces are reorganized, the dynamics of business processes and communications are changing. The accelerated pace of change requires a new management of organizations, with a reassessment of corporate culture, strategy and structure.

Many Bulgarian developments are aimed at the importance and necessity of developing non-standard forms of employment, combined with certainty for the achievement of modern, competitive labor markets, leading to economic growth and a successful market economy. According to the EC, flexicurity can be defined as an integrated strategy for simultaneously increasing flexibility and security in the labor market. Flexible employment in most European countries is mainly defined in the following categories:

- Part-time: this type of employment is when the worker is employed full-time and any reduction in his working hours is considered part-time;
- Term-time working: the employee remains at a permanent job, but can use paid/unpaid leave during the school holidays;
- Jobsharing: a type of flexible form of employment when two (or sometimes more) people share common responsibility for a given type of work;

- Floating working hours: it enables employees to choose, within limits set by the employer, how long their working day should be;
- Compressed working week (fortnights): The essence of this type of employment is the redistribution of working time into smaller but longer blocks during the week. – Working from home on a regular basis: full-time employees performing their work duties from home;
- Mobile work / remote work: In this type of employment, employees can work remotely from the organization's workplace, throughout the week or during most of it;
- Career break: this is the so-called creative leave, aimed at extended periods of leave – usually unpaid within one to five years.

A large number of processes related to HRM are being digitized. A significant part of the day-to-day administrative tasks of personnel management are supported by digital tools. This makes it possible literally in fractions of a second to perform complex operations based on the analysis of multiple factors. A variety of statements and reports are prepared; vacations are planned; salaries are managed; career development is tracked, etc. In some organizations, many training materials have been prepared in digital format - for example, for initial training when introducing a new employee into the work process. Virtual trainings help unify the information provided for every employee in the company, regardless of location. Industry 4.0 changes both the outside of companies and the way they look from the inside. Many institutions are renovating old buildings in accordance with technological and cultural changes. New ideas and alternative perspectives are accepted within the organization. The changes are not only on the surface. To rapidly innovate, companies are introducing new organizational designs based on cross-functional teams, a structure borrowed from digital companies [3].

As technology advances, the human part of the job will become increasingly important. Full-timers will gradually be replaced by temporary workers or cross-functional teams as the main source of talent. Smart offices will become their main priority. The trends are aimed at shaping open and shared workspaces, allowing free movement of people and information.

The understanding of a workplace is changing. Often teams are virtual. A new way of looking at workforce mobility. These and other changes related to globalization require a new way of thinking and new solutions from HR professionals.

Creative people have always been one of the most mobile groups in the workforce and this mobility trend is now being transferred to the business world as a whole. Regardless of the work industry, professional life is becoming more nomadic, digital and flexible in a green office, helping to organize remote work, teambuilding or outsourced work week for the whole team in nature.

Today, Coworking Bansko extends to four different locations in the city, and the number of members exceeds 100 per month. There they get everything to work well and have an even better time. The mountain town is imperceptibly turning into one of the main hubs for digital nomads.



Fig. 4. Shared workspace for digital nomads in Bansko.

The growing need for greater flexibility in the workplace is driving more and more large companies to use shared workspaces. Together with startups, they aim to keep up with new developments, to discover emerging trends and new opportunities for selling services. According to the forecasts of the World Economic Forum, by 2030 self-employed workers or so-called will make up 80% of the workforce.

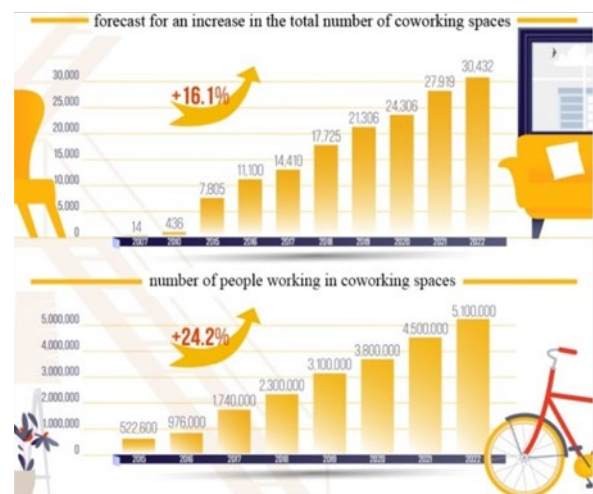


Fig. 5. Coworking spaces.

The lobby is the most suitable area in the hotel to be transformed into a shared workspace. Such an initiative could bring additional revenue to hoteliers in traditionally lean periods and attract people looking for comfortable furniture, fast free Wi-Fi, electrical outlets and ready-to-eat food and drinks. At NEST, Dubai's Tryp by Wyndham co-working space, those who pay a monthly "rent" can use the hotel's gym, swimming pool and have unlimited coffee - all while working alongside colleagues from around the world in a designer and comfortable environment.



Fig. 6. New concept for hotel lobby.

Globalization (including the diminishing importance of geographic location) is leading to the creation of multinational (and multicultural) teams and companies. For these entities to function effectively, corporate culture plays a key role. The HR specialist has a key role in building, maintaining and developing the desired corporate culture – he is its carrier, ambassador of its values and mission. What has been said can be summarized as follows:

- New software technologies (payroll, wages, vacations, career)
- AI; chat bots for recruitment, etc.; virtual trainings; digital portals – for example for introducing new employees; to introduce procedures and policies, etc.
- Tasks at a strategic level (eg strategic partner on the Board of Directors).
- Management of succession and development processes.
- Engagement – formation, maintenance, development.
- Programs for organizational well-being and satisfaction; resistance to stress.
- Managing multicultural communities.
- Balance – professional – personal life.
- Change management; agents of change.
- Perceiving the organization and managing the experience.
- Talent management.

"Factory 4.0" provides an overview of the firm as an interconnected global system at the microeconomic level. Figure 3 depicts some of the key factors: outside the factory we see "Logistics Network 4.0", the resources of the future, new customer requirements and the means to achieve them. Inside the factory, we imagine new production technologies, new materials and new ways of storing, processing and exchanging data.

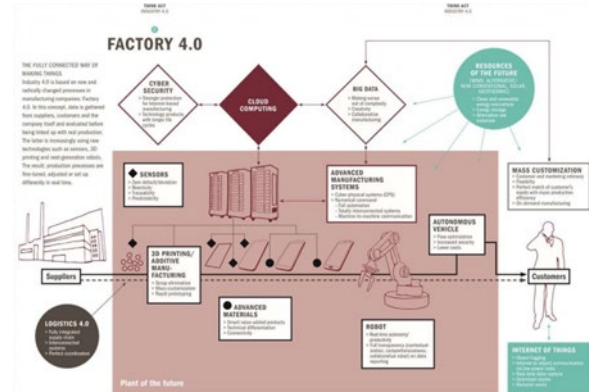


Fig. 7. General view of a smart factory.

The connected worker has a mobile hub that collects the sensor data received from the wearable devices the worker wears. These wearable sensors include various solutions, providing sensory concentration combined with pattern detection technologies in processing the data stream.



Fig. 8. Connected Worker Concept.

In many countries such as the UK, the government is pushing changes and pushing policies to encourage companies to use smart devices. In addition to smart factories, there are already cities that have taken the first steps to become "smart cities" - with smart traffic and public transport, lighting, roads and regulation, buildings and parks that are connected in a harmonious system and interact with each other, creating an environment that is both responsive to people's needs and energy efficient.



Fig. 9. Smart cities.

## RESULTS AND DISCUSSION

The analysis of the results and the implementation of the good practices in the business can lead to changes in the used business model. In this way, the value of the labor input is increased and a higher return is realized. This helps to implement optimization processes, such as the use of artificial intelligence for uniform procedures and activities.

The research carried out in the industrial sector of Bulgaria gives grounds to summarize the conditions for achieving economic and social progress in the changing working environment:

- investments in human resources;
- their acquisition of new knowledge and skills;
- lifelong learning.

The activities related to the formation of human capital are:

- educational initiatives and self-initiatives at different levels;
- investments in geographic mobility;
- formation of relevant attitudes and motivation in personal and social terms.

Developing a strategy in line with company goals and objectives is imperative. This poses the main question not only about the new role of the manager related to the management of human resources, but also about the implementation of new processes - artificial intelligence, monetary value measurement of the results of the work and its impact on the profitability of the company. All this could be achieved through the development of a single strategy meeting the company's goals.

Complex knowledge, which requires knowledge of programming in different languages, will be increasingly required. The emergence of new positions such as big database analyst and people with scientific knowledge using big databases.

## CONCLUSION

Today, with the advent of robotization and automation, taking away jobs, new digital technologies creating a virtual space, every aspect of life is changing. Variants of collaborative partner production are emerging, finding expression in significant projects without traditional hierarchical organization.

The future belongs to those organizations that realize their role in building, maintaining and developing effective interpersonal relationships in work teams. Company leaders should invest in human capital, minimize the reasons for leaving creative employees and increase the factors that increase their satisfaction and motivation to stay and develop. For successful and competitive business organizations, the use of human capital is a major factor of long-term importance, not a means of short-term exploitation and maximum profit.

More and more decisions in the changing work environment are made with the help of algorithms underlying many automated production processes and systems. They generate new forms of social and economic relationships in our increasingly digital world.

## REFERENCES

- [1] Naydenov, P., Integrated system for logistics management, Conf. Proceedings of 6th International conference "Economics and management – based on new technologies", EMoNT 2016, Vrnjacka Banja, Serbia, 16-19 June 2016, ISBN: 978-86-6075-059-6.
- [2] Petrova D., Analysis of SMEs in Bulgaria – Assessment of Their Innovation Activities, Rezekne 2013, Latvia, Rezekne Higher Education Institution, Faculty of Engineering, Scientific Institute for Regional Studies, Environment. Technology. Resources, Proceedings of the 9th International Scientific and Practical Conference June 20-22, 2013, Volume 3, ISSN 1691-5402: 46-49.
- [3] Petrova, D., Intelligent, Innovative and Sustainable Industry in Bulgaria – prospects and challenges, Vide I. Tehnologija. Resursi - Environment, Technology, Resources, Proceeding of the 12th International Scientific and Practical Conference „Environment. Technology. Resources“, June 20-22, 2019, Rezekne, Latvia, Volume I, ISSN 1691-5402 – print, ISSN 2256-070X – online.
- [4] Totev, H., The deplorable state of the Bulgarian economy requires urgent measures for its modernization, but creates enormous difficulties for the investment process, Conf. Proceedings of 4th International conference "Economics and management – based on new technologies", EMoNT 2014, Vrnjacka Banja, Serbia, 12-15 June 2014, ISBN: 978-86-6075-045-9.
- [5] Schwab, Klaus, The fourth industrial revolution, by World Economic Forum, 2016.
- [6] Leadership lessons with horses. [Online]. Available: <https://www.trainingjournal.com/> [Accessed: February 9, 2023].
- [7] The 10 Vital Skills You Will Need For The Future Of Work [Online]. Available: <https://bernardmarr.com/> [Accessed: February 17, 2023].

# *Approach to the Forming of Rational Technology for the Export Cargoes Delivery in Supply Chain on the Principles of Co-Modality*

**Oleksandra Orda**  
*Department of Transport Technologies*  
*Kharkiv National Automobile and Highway University*  
Kharkiv, Ukraine  
kost.alexandra@gmail.com

**Yevgen Nagornyy**  
*Department of Transport Technologies*  
*Kharkiv National Automobile and Highway University*  
Kharkiv, Ukraine  
nagorniyevgeniy123@gmail.com

**Natalia Potaman**  
*Department of Transport Technologies*  
*Kharkiv National Automobile and Highway University*  
Kharkiv, Ukraine  
potaman81@ukr.net

**Abstract.** In this article, we propose an approach to the forming of rational technology for the export cargoes delivery in the supply chain on the principles of co-modality in the context of effective interaction of delivery participants, which allows reducing the costs of all them through the optimal use of resources related to delivery and increasing the competitive advantages of products. Taking into account the strengthening of cooperation between road and rail transport, under modern conditions, combined transport within the international transport corridor is proposed as an alternative option to promote cargo flow in the supply chain. As a result of experimental studies carried out on the basis of the simulation model of the delivery process in the Petri Nets, the time characteristics of technological processes under alternative schemes depending on the input parameters of the model have been determined. A comparative assessment of alternative delivery schemes based on mathematical models has made it possible to establish that the rational scheme for the delivery of export cargo from Ukraine to Germany via the Pan-European Corridor III is the Rolling Highway technology, which ensures compliance with the cargo owner's requirements for delivery time and cost established by the contract. The proposed approach is recommended as a tool for making managerial decisions when planning and organising the delivery of export cargoes from Ukraine to the EU countries in order to effectively manage supply chains by minimising the cost of delivery and environmental damage.

**Keywords:** *Co-modality, export cargoes, supply chain, sustainability of transportation.*

## I. INTRODUCTION

The reorientation of the lion's share of cargo flows of export products of Ukrainian producers from sea to other

modes of transport under martial law has revealed acute problems in existing supply chains related to technological limitations, destruction of transport infrastructure and low level of development of transport and logistics technologies, intermodal and multimodal transport in Ukraine compared to global trends. All this leads to high cost of services, restructuring of logistics supply chains, and as a result, low delivery speeds within the timeframe set by customers. At the moment, the government in Ukraine is emphasising the need to create a flexible logistics system that can respond to external threats as quickly and effectively as possible. Furthermore, the ongoing process of integrating the Ukrainian transport system into the European one requires the development and implementation of advanced logistics solutions based on sustainability principles [1]. Therefore, in the current environment and with the further recovery of the transport industry, new approaches to the development of rational technology for the delivery of export goods in the supply chain are needed, which would minimise the use of resources related to the delivery, reduce the costs of all participants in their interaction, and increase the attractiveness of products for customers [2].

According to Informall BG, huge resources are currently being spent on organising complex intermodal logistics for the export of goods from Ukraine. The consequences of an increase in shipping costs by about 25-40% are the rise in global prices for Ukraine's leading export products and the increase in global prices for Ukraine's leading export products and the risks of a global food crisis [3]. The negative consequences of "Transport visa-free regime" for Ukrainian road carriers are felt both

*Print ISSN 1691-5402*

*Online ISSN 2256-070X*

<https://doi.org/10.17770/etr2023vol3.7301>

© 2023 Oleksandra Orda, Yevgen Nagornyy, Natalia Potaman. Published by Rezekne Academy of Technologies.  
This is an open access article under the [Creative Commons Attribution 4.0 International License](https://creativecommons.org/licenses/by/4.0/).

for the environment and for European carriers. And many more problems need to be resolved immediately.

Under conditions of increased risk, achieving optimal conditions in the supply chain with a certain level of efficiency is possible only with use of digital logistics technologies [4]. The development and implementation of intelligent transport systems with the introduction of integrated transport technologies based on the principles of co-modality are indicated as key areas for the transformation of the European transport system [5]. Co-modality requires increasing the efficiency, compatibility and interconnection of different modes of transport, as well as the stations and transport hubs connected between them. At the same time, all modes of transport are considered as complementary subsystems, the combination of which can provide users and society with maximum economic, environmental and social benefits [6]. The principle of co-modality is gaining relevance in the context of increased cooperation between different modes of transport, especially for Ukraine in the current environment, when the main freight flows of road and rail transport are directed to western international railway crossings to the EU. Sustainable development and optimal use of resources can only be ensured through the coordinated interaction of all modes of transport in the formation of logistics chains at the macro level [1], which can be achieved by developing delivery technologies within the framework of the ITC. Ukraine is part of several international transport corridors and Ukrainian transport networks are included in the TEN-T indicative maps. The modality of European policy is to ensure the efficiency of cargo delivery through seamless transport corridors with door-to-door service [6]. Ukrainian railways already have experience in organising container trains, the “Viking” transit train between Lithuania and Azerbaijan, and the “Yaroslav” transit train between Ukraine and Poland. Under the current conditions, it is necessary to organise new routes between Ukraine and the EU countries for running of container or contrail trains as part of combined trains. Therefore, we believe that one of the perspective areas of research is the formation of a technology for the export cargo delivery (TDC) in supply chains based on the principles of co-modality by building rational routes through International Transport Corridors (ITC).

Decision-making on the choice of delivery technology is complicated by existing problems of interaction between the players of the transport market due to constant changes in the market itself and the presence of a large number of interconnections between participants in the cargo delivery process [2]. Therefore, we are developing new approaches to the formation of TDC. Most of the approaches are based on the principles of integrated logistics [1], [2], [4], [6] – [14] and aim to solve problems of improving the efficiency of the delivery process in individual logistics chains as subsystems of the logistics system [9]. The analytical models proposed by the authors of [7], [9], [10], [15] to improve the efficiency of the delivery process by forming a rational technology and structure of the supply chain do not take into account the complex impact of random factors of the process.

The author [11] proposes a two-stage stochastic model of a sustainable multimodal system that allows taking into account the uncertainties of the delivery of the shippers and the uncertainties in the performance of the intermodal terminals, without taking into account the risks during the transportation of goods. The approach based on genetic algorithms developed in [14] to optimize a sustainable multimodal freight and logistics system in terms of time, distance, and CO<sub>2</sub> emissions allows the development of strategies to organise the transportation of containerized cargo by rail and river transport to reduce the road transport domination.

The models developed on the basis of Petri Nets in [2], [4], [13] have advantages related to ease of use and visibility compared to the approaches described above. In addition, these models allow one to take into account the probability factors, to study the behaviour of the system and its individual elements, and to obtain their characteristics. However, as a criterion for the efficiency of cargo delivery, the authors of [4], [13] propose to consider only the time parameters of the technological process without a cost estimate that affects the final consumer value of export products in the market.

The purpose of the study is to develop an approach to the forming of a rational technology for the export cargo delivery under modern conditions by choosing an effective option to move cargo flow in the supply chain in a mixed scheme within the framework of the ITC on the principles of co-modality to ensure a high level of quality of service to cargo owners by meeting the established delivery time and ensuring environmental friendliness of transportation.

## II. MATERIALS AND METHODS

We believe that the cargoes delivery within the ITC in the direction of Ukraine - EU countries can be classified as combined transport, since the transportation of cargoes along the routes can be carried out according to three alternative schemes considered in the study: by road, by rail and by contrail transit system (Rolling Highway) using road and rail.

The integrated process of combined transportation of goods from the consignor to the consignee involves the performance of certain groups of operations in each module of the system to select modes of transport, connections and transport and technological delivery schemes, prepare the cargo for transportation, load the mainline transport, load and unload and warehouse operations, transport by mainline transport, transport a consignment from the mainline transport terminal to the consignee's warehouse, unload at the warehouse [2], [15]. The set of operations in the modules of the delivery system can vary as well as the characteristics of production resources (types and number of mechanisms, number of workers), ways and methods of organising work. The determination of the rational TDC from a set of alternative ones on the basis of co-modality is determined by the technical and economic characteristics of transport modes, the availability and location of transport and logistics infrastructure of mainline carriers, as well as an indicator

that determines the level of service quality in accordance with customer requirements.

The object of research is presented in the form of a structural outline of functional links of the cargo delivery system on the route according to alternative schemes, consisting of modules and related subprocesses performed in the modules (Fig.1).

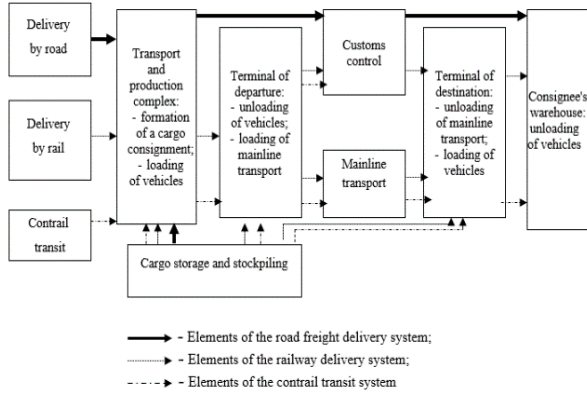


Fig. 1. Structural outline of the functional links of the export cargo delivery system through alternative schemes.

Reliability of the delivery system under certain conditions of the system's operation should be ensured by moving the cargo flow through the system modules with a minimum delay time in each module and the time of the cargo consignment in the system, in accordance with the customer's delivery time and costs.

The level of specific costs for the delivery of cargoes significantly affects the final cost of the cargo, therefore, it is proposed to consider the minimum total specific costs for the transportation of cargoes during the delivery period as an efficiency criterion, as in (1).

$$B_z(t) = f(Q, I, N_{LUI}, K_w, T_d) \rightarrow \min, \quad (1)$$

where  $B_z$  are total specific costs, [c.u./t];  $Q$  is the consignment weight, [tons];  $I$  is the time interval between the moments of current request reception and the reception of the next request in a flow, [hours];  $N_{LUI}$  is the number of mechanisms involved in servicing the material flow in the system modules, [units];  $K_w$  is the number of employees involved in the maintenance of material flow in the system modules, [people];  $T_d$  is the time of delivery of a consignment, [hours].

Delivery of cargoes is carried out on a "just-in-time" basis

$$T_d = \sum_{j=1}^n t_{ij} \leq T_{agr}, \quad (2)$$

where  $t_{ij}$  is the time for performing consecutive  $i$ -th technological operations in the  $j$ -th module of the system, [hours];  $T_{agr}$  is the delivery time according to the agreement with the cargo owner, [hours].

The chosen efficiency criterion allows for a comprehensive consideration of the interests of all

delivery participants when choosing a rational cargo delivery scheme. Of the alternative delivery schemes compared, the one with the lowest total specific costs for the delivery period under the "Just-in-time" condition is considered to be the most efficient.

We use mathematical modelling methods to establish the mathematical dependence between the parameters of the research object, to study in detail the processes of the cargo delivery system on the route, to establish accurate quantitative relationships between the input parameters of the model and the output function.

The functioning of individual elements of the cargo delivery system on the route within the ITC is considered as a set of consistently interconnected incoming flows of service requirements (vehicles, cargo delivery orders, cargo flow), service channels (checkpoints, warehouses, terminals, etc.) and outgoing flows of requirements after service. When determining the efficiency of each module and the system as a whole, it is necessary to take into account the unevenness of work that occurs at their "docking points", the occurrence of queues and delays due to downtime of rolling stock and reloading facilities.

We determine the efficiency criterion for each alternative delivery scheme.

The total specific costs of cargo delivery are determined for the delivery period [2], as in (3),

$$B_z = \frac{(B_{TPC} + \sum_1^s B_{Ts} + B_{OC} + B_{MT} + B_{Wcown})}{Q}, \quad (3)$$

where  $B_{TPC}$  is the cost of technological operations in the module TPC, [c.u.];  $B_{Ts}$  is the amount of payment for using the services of the  $s$ -th terminal, [c.u.];  $B_{OC}$  is the amount of payment to the delivery system operator determined by the cost of organising the delivery of a consignment via the ITC route, [c.u.];  $B_{MT}$  is the cost of delivery of a consignment by mainline transport, [c.u.];  $B_{Wcown}$  is the costs of performing technological operations at the warehouse of freight owners, [c.u.].

The alternative nature of the existing schemes for the delivery of export cargo within the ITC determines the search for a rational TDC of the appropriate level of service, taking into account the resource capabilities of the system elements on the principles of co-modality. The simulations based on the proposed models are carried out taking into account the average time characteristics of the cargo flow through the system, which are obtained as a result of simulation modelling. The simulation model is formalised on the basis of the developed mathematical model (3) using the mathematical apparatus of the Petri Nets (Fig.2). The properties of Petri Nets allow to study the behaviour of the system being modelled and obtain information about its most important characteristics using formal methods.

As a result of the experiment, we determine the characteristics of changes in the time parameters of the cargo delivery system depending on the input parameters. On the basis of the results obtained, we perform

mathematical modelling. To determine the dependence of the efficiency criterion on the parameters of the order flow and the numerical parameters of the production resources, we apply regression analysis methods.

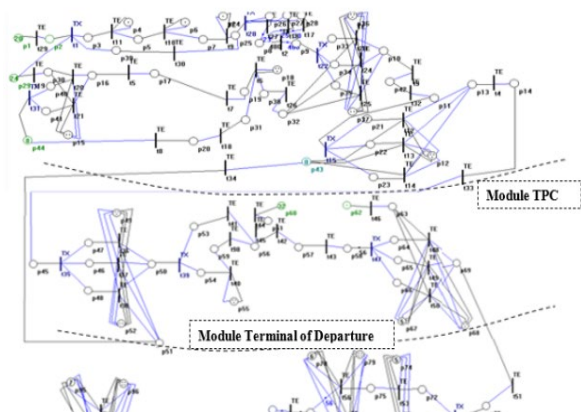


Fig. 2. Fragment of the simulation model of the cargo delivery process by routes within ITC.

To evaluate and select a rational TDC, we determine the economic efficiency of the scheme by the value of the integrated total effect ( $E_{INT}$ ): the sum of cost estimates of reducing delivery costs ( $E_1$ ), early release of money due to reduced delivery times ( $E_2$ ) and reduction of environmental damage ( $E_3$ )

$$E_{INT} = E_1 + E_2 + E_3 \rightarrow \max \quad (4)$$

The cost estimate of the reduction in delivery costs when applying the rational TDC, the early release of money due to reduced delivery times, and the reduction of environmental damage can be defined as the difference between the values of the indicators under the rational TDC and the existing option.

The value of environmental damage reduction, as a social effect, is determined by the difference in indicators that characterise changes in the environment as a result of the relevant measures. This measure is the reduction of the vehicle on the route during delivery.

The basis of calculations for determining the social effect of reducing the negative impact on the environment is the determination of fuel consumption and harmful compound emissions during delivery under the existing option (road transport) and under the rational TDC.

### III. RESULTS AND DISCUSSION

The implementation of the proposed approach is presented as an example of the case of transport processes for the Transport Company “Neolith Logistic” (Ukraine), which organises international freight transport, especially between Ukraine and the EU countries. According to the company, one of the most demanded services is cargoes delivery in the direction of Ukraine - Germany. The presented approach was used to develop the rational technology for the delivery of electrical equipment on the route “Kyiv-Berlin” by ITC № 3.

Cargoes are transported by road with a capacity of 22 tonnes using DAF FT 85.340+Schmitz SPR 24/L trucks. The company’s data report indicates that there are problems with excessive downtime while waiting for technological operations to be performed during delivery. ITC № 3 passes through the territories of Germany, Poland and Ukraine on the route Berlin (Dresden) - Wroclaw - Lviv - Kyiv. The length of public roads on the Krakowiec - Lviv - Rivne - Zhytomyr - Kyiv section is 617 km. The railway route by ITC № 3 (Mostyska - Lviv - Krasne - Ternopil - Khmelnytsky - Zhmerynka - Kozyatyn - Kyiv) is 648 km long and is fully electrified, double-tracked and equipped with auto-locking devices.

The process of cargo delivery on the Kyiv-Berlin route can be considered under three alternative schemes: TDC.1 - by road through Kyiv - Lviv – Krakow - Katowice - Wroclaw - Berlin; the total length of the route is 1640 km; TDC.2 - by rail on the Kyiv - Zhmerynka - Lviv - Mostyska - Wroclaw – Berlin route; the total length is 1046 km; TDC.3 - by contrail transit system using road and rail transport on the route Kyiv - Lviv - Mostyska - Wroclaw - Berlin as part of a combined train.

To conduct an experiment on three alternative schemes, taking into account the impact of all possible combinations of input parameters within the range of variation on the efficiency criterion, we developed a full factorial experiment plan, consisting of 64 series of experiments.

When varying the input parameters of the model, we monitor the dynamics of the system's functioning in order to solve the problem of coordinating the parameters of technological processes and obtaining optimal values of the efficiency criterion, provided that the delivery time set by the customer is met.

Based on the results of simulation modelling the dynamics of cargo flow in the system for a request with specified characteristics, we determine the time indicators that are the input data for modelling the total specific costs for each of the alternative TDCs.

These are indicators of the time a consignment is located in each module and the total time of cargo delivery, which value, according to the reporting and statistical data, differs from the result of the modelling using the Petri Nets by no more than 10%, which indicates the adequacy of the results obtained (Table 1).

TABLE I. TOTAL TIME OF CARGOES DELIVERY ON THE KYIV - BERLIN ROUTE BY ROAD

Value of incoming flow of cargoes, tonnes	Value of total cargo delivery time, hours			
	Reporting and statistical data		Modelling results	
	Minimum number of resources	Maximum number of resources	Minimum number of resources	Maximum number of resources
15	105	98	120	105
22	120	100	140	128
45	154	120	180	155

At the next stage, we perform a modelling of the total specific costs of cargo delivery based on the time characteristics of the process in the MS EXCEL

environment according to the mathematical models using alternative schemes.

The results of the regression analysis showed that among the hypotheses tested, the hypothesis of a step dependence is characterised by the smallest deviation of the variance of experimental values from the variance of the values obtained by the model. The value of the coefficient of determination, close to 1, indicates that the obtained dependence is practically functional. The obtained regression dependencies are proposed to be used to substantiate managerial decisions on the organisation of cargo delivery by routes within ITC.

On the basis of the results of the calculations, the values of the criterion for choosing the rational TDC were as follows: the rational scheme is contrail transit, which ensures compliance with the cargo owner's requirements for delivery time and delivery costs established by the agreement. Compared to the existing scheme, the reduction in specific delivery costs under the rational scheme is 9,80 c.u./t.

The determination of the rational TDC involves the optimisation of the independent variables of the model, numerical parameters of the production resources, based on the simulated time characteristics of the cargo delivery process.

The results of calculations of the components of the integrated total effect for the delivery of a cargo consignment of 22 tonnes on the Kyiv-Berlin route using the rational TDC are presented in Table 2.

TABLE II. THE VALUE OF THE CRITERION FOR THE EFFICIENCY OF CARGO DELIVERY ON THE KYIV - BERLIN ROUTE BY THE RATIONAL TDC

Cargo consignment volume, tons	Components of the total integrated effect			Value of the total integrated effect, $E_{int}$ c.u.
	Value of $E_1$ , c.u.	Value of $E_2$ , c.u.	Value of $E_3$ , c.u.	
22	90,8	15,6	22,0	128,4

When increasing the volume of a consignment or reducing the delivery time of a consignment by increasing the number of production resources at the points of "docking" of the participants' activities, it should be taken into account that delivery costs increased moderately, since the involvement of additional production resources leads to an increase in the cost of technological operations in the system module.

#### IV. CONCLUSIONS

This paper proposes an approach to the formation of the rational technology for the delivery of export cargo under modern conditions from the standpoint of sustainable logistics. The results of the analysis of the current state of export cargo delivery from Ukraine show that there are

problems, in particular, non-compliance with conditional deadlines due to exceeding the normative indicators of cargo delivery time by road. As alternative delivery schemes, the authors consider delivery by road, rail and the technology of combined transport within the framework of the ITC (Rolling Highway).

The mathematical models proposed in this paper allow us to evaluate alternative delivery schemes taking into account demand parameters resource constraints and average time characteristics of cargo flow through the system.

The developed simulation model based on the Petri Nets allows tracking the dynamics of system behaviour, modelling the time characteristics of the process for each TDC depending on the numerical parameters of demand and production resources, making timely management decisions to eliminate commercial risks associated, in particular, with failure to meet the established delivery time.

As a result of the experiment, the total unit costs of cargo delivery under alternative TDC were modelled. The regression models obtained as a result of the experiment allow us to formalise the dependence of the efficiency criterion on the numerical parameters of demand and production resources for alternative schemes. The practical significance of the obtained dependencies is to choose a rational technology under the "just-in-time" condition. It is determined that the rational technology for the TDC of export cargo on the Kyiv - Berlin route is contrail transit as part of a combined train according to the criterion of minimum specific delivery costs. Compared to the existing technology by road, the reduction in specific delivery costs is 9,80 c.u./t.

The performance indicator is integrated and takes into account the main aspects of the transport service, including economic, social and environmental components, in a comprehensive way. The use of the proposed approach ensures the selection of rational technology based on the principles of co-modality and allows taking into account the interests of all delivery participants in the conditions of uncertainty. The integral effect of the forming of a rational technology in the amount of 128.4 c.u. for the delivery of 22 tonnes of cargo is obtained.

The practical application of the proposed approach is to use it in the work of transport companies in planning and organising the delivery of export cargo within the framework of the ITC from Ukraine to the EU countries.

#### REFERENCES

- [1] V. Naumov, O. Shulika, O. Orda, H. Vasiutina, M. Bauer, and M. Olishevych, "Shaping the Optimal Technology for Servicing the Long-Distance Deliveries of Packaged Cargo by Road Transport," *Sustainability*, vol. 14, no. 12, p. 7283, Jun. 2022, <https://doi.org/10.3390/su14127283>. [Online]. Available: <https://www.mdpi.com/2071-1050/14/12/7283> [Accessed Oct. 14, 2022].
- [2] O. Orda, "Formation of strategies of the organization of intermodal container transportations in supply chains on the principles of cooperation of participants," M.S. thesis, Kharkiv National Automobile and Highway University, Kharkiv, Ukraine, 2019.

- [3] Ukrainian Shipping Magazine, "Informall BG: Resumption of direct container transportation to Ukraine is a humanitarian need," Ukrainian Shipping Magazine, 2022. [Online]. Available: <https://en.usm.media/>. [Accessed Jan. 15, 2023].
- [4] O. Pavlenko, N. Shramenko, and D. Muzylyov, "Logistics Optimization of Agricultural Products Supply to the European Union Based on Modeling by Petri Nets," In Proc. NT 2020 International Conference New Technologies, Development and Applications '128, 2020, pp. 596–604.
- [5] Publications Office of the European Union, "White paper on transport. Roadmap to a single European transport area : towards a competitive and resource efficient transport system," Publications Office of the European Union, 2011. [Online]. Available: <https://op.europa.eu/en/publication-detail/-/publication/bfaa7afd-7d56-4a8d-b44d-2d1630448855/language-en>. [Accessed: Oct. 12, 2022].
- [6] [O. Datsii, N. Levchenko, G. Shyshkanova, O. Platonov, and V. Zalizniuk, "State policy for the development of multimodal transportation by clean and energy efficient motor transport," Cuestiones Políticas, vol. 39, no. 71, pp. 884-902, 2021, <https://doi.org/10.46398/cuestpol.3971.54>. [Online]. Available: <https://produccioncientificaluz.org/index.php/cuestiones/article/download/37493/41009/> [Accessed Oct. 12, 2022].
- [7] A. Chandra, A. Pani, P.K. Sahu and S. Sushant, "Integrating Commodity-Based and Trip-Based Approaches of Freight Demand Modelling Using Trip Length Distributions," Journal of The Institution of Engineers (India): Series A, vol. 104, no. 1, March 2023. [Abstract]. Available: Springer, <https://link.springer.com/article/10.1007/s40030-023-00712-1#citeas>. [Accessed February 20, 2023].
- [8] N. Ronald, J. Yang, and R. G. Thompson, "Exploring Co-Modality Using On-Demand Transport Systems," The 9th International Conference on City Logistics, June 17-19, 2015, Tenerife, Canary Islands (Spain). Transportation Research Procedia vol. 12, 2016, pp. 203-212. [Online]. Available: <https://www.sciencedirect.com/science/article/pii/S2352146516000600> [Accessed Jan. 15, 2023].
- [9] Ye. Nagorny, V. Naumov, and A. Ivanchenko, "The model of logistics system of cargo delivery in international traffic," Automobile Transport, vol. 29, pp. 120-124, 2011.
- [10] N. Shramenko, "Rationalization of interaction between terminal complexes and cargo owners," Scientific Journal Transactions of Kremenchuk Mykhailo Ostrohradskyi National University, vol. 2 (79), pp. 109–113, 2013.
- [11] V. Badyal, W. G. Ferrell Jr, N. Huynh and B. Padmanabhan, "A two-stage stochastic model for intermodal terminal location and freight distribution under facility disruptions," International Journal of Systems Science: Operations & Logistics, vol. 10, no. 1, p. 2169055, January 2023. [Abstract]. Available: Taylor & Francis Online, <https://www.tandfonline.com/doi/full/10.1080/23302674.2023.2169055?scroll=top&needAccess=true&role=tab>. [Accessed February 26, 2023].
- [12] V. Naumov, I. Taran, Y. Litvinova, and M. Bauer, "Optimizing Resources of Multimodal Transport Terminal for Material Flow Service," Sustainability, vol. 12, no. 16, p. 6545, Aug. 2020, <https://doi.org/10.3390/su12166545>. [Online]. Available: <https://www.mdpi.com/2071-1050/12/16/6545> [Accessed Nov. 13, 2022].
- [13] O. Pavlenko, D. Velykodnyi, O. Lavrentieva, and S. Filatov, "The Procedures of Logistic Transport Systems Simulation in the Petri Nets Environment," In Proc. ICTERI 2020 16th International Conference on ICT in Education, Research and Industrial Applications. Integration, Harmonization and Knowledge Transfer. Volume II: Workshops '2732, 2020, pp. 854-868.
- [14] S. Okyere, J. Yang, and C. A. Adams, "Optimizing the Sustainable Multimodal Freight Transport and Logistics System Based on the Genetic Algorithm," Sustainability, vol. 14, no. 18, p. 11577, Sep. 2022, <https://doi.org/10.3390/su141811577>. [Online]. Available: <http://dx.doi.org/10.3390/su141811577> [Accessed Dec. 20, 2022]
- [15] Ye. Nagorny and N. Shramenko, Commercial work on road transport. Kharkiv: Kharkiv National Automobile and Highway University Press, 2010.

# Characteristics of Movements when Cylindrical Turning, Drilling, Coredrilling and Reaming

Angel Poparov

Technical University - Sofia, Branch Plovdiv  
Plovdiv, Bulgaria  
poparan@abv.bg

Agop Izmirliqn

Technical University - Sofia, Branch Plovdiv  
Plovdiv, Bulgaria  
izmirliyanx3@gmail.com

**Abstract.** In the process of work the tool angles change their value to become the working angles. This results in a variation of the work conditions of the cutting tools. The variation depends on the characteristic of the resultant cutting motion – the sum of the cutting motion and feed motion.

In this article the characteristics of motions of cylindrical turning, drilling, coredrilling and reaming are derived, which can serve as a basis for determining the relations between the tool and working angles.

These relations can be used in programming the CNC to prevent the formation of negative working clearance angle and the destruction of the tool.

**Keywords:** characteristics of movement, coordinate axes, cutting and feed motion, resultant cutting motion.

## I. INTRODUCTION

The ISO 3002-1982 standard helps to solve many engineering tasks, but it is not generally valid and computer oriented. The simultaneous existence of two standards - ASME B94.50-1975 and ISO3002-1:1984, which deal with unchangeable terminology and definitions, has a large share in the confusion and misunderstanding of the basic geometric parameters of cutting tools [1].

A critical analysis of both the advantages and disadvantages of ISO 3002-1:1984 can be found in a number of sources [1] - [6].

In the alternative methodology of [7], proposed in [2], the dependencies between tool and working angles are derived by defining in a new way the setting angles  $G$ ,  $H$  and  $L$  that give the correlation between the tool-in-hand system  $f$  and the machine system  $m$ , and the motion angles  $M$ ,  $N$  and  $T$  that connect the tool-in-use system  $f_e$  with the machine system  $m$ .

The transformations of tool angles in working ones in the process of operation is due to the feed rate  $D_f$ . The feed rate  $D_f$ , summed with the cutting motion  $D_c$ , determines the resultant cutting motion  $D_e$ . The placement of the tool in relation to the workpiece also has an impact.

For transformations of the tool angles into working ones and vice versa it is necessary that the main characteristics of the cutting motion  $D_c$ , feed rate  $D_f$  and the resultant cutting motion  $D_e$ : trajectory, path, speed, acceleration are known. The local elements of the trajectory: the tangent, the principal normal, the binormal (which form an accompanying trihedron), curvature and torsion should be known as well.

For the practical application of these dependencies the parametric equations of resultant cutting motion in cylindrical turning, drilling, coredrilling and reaming have been derived in [8] and [9]. In this article the equations of the characteristics of the cutting, feed and resultant cutting motions are derived.

## II. METHODS

*A. Equations for the resultant cutting motion and the motions of cut and feed.*

Two rectangular right oriented coordinate systems, fixed to the workpiece  $O_{1x_1y_1z_1}$  and the machine  $O_{0x_0y_0z_0}$ , respectively, were introduced. Axes  $X_0$ ,  $Y_0$  and  $Z_0$  are colinear with the axes of a standard coordinate system as in [10].

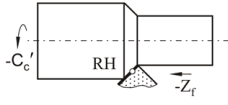
The case of cutting motion  $-C'_c$  and feed motion  $-Z_f$  is considered (Fig. 1 and Fig. 2).

Print ISSN 1691-5402

Online ISSN 2256-070X

<https://doi.org/10.17770/etr2023vol3.7259>

© 2023 Angel Poparov, Agop Izmirliqn. Published by Rezekne Academy of Technologies.  
This is an open access article under the [Creative Commons Attribution 4.0 International License](https://creativecommons.org/licenses/by/4.0/).


 Fig. 1 Cutting motion and feed motion  $-Z_f$  when cylindrical turning.

The resultant cutting motion for a point of the cutting edge of a tool with coordinates  $x = const.$ ,  $y = const.$  and  $z = -z(t)$  is defined in  $O_{0x_0y_0z_0}$  with the equation of a helix curve

$$\bar{r}_e(t) = \begin{vmatrix} x_e(t) \\ y_e(t) \\ z_e(t) \end{vmatrix} = \begin{vmatrix} r \cdot \cos[N - \varphi_{01}(t)] \\ r \cdot \sin[N - \varphi_{01}(t)] \\ Z - z(t) \end{vmatrix}, \quad (1)$$

where  $\varphi_{01}$  is the angle of rotation around  $Z_0 \equiv Z_1$  of the workpiece coordinate system  $O_{1x_1y_1z_1}$  against coordinate system of the machine  $O_{0x_0y_0z_0}$ , and

$$r = \sqrt{x^2 + y^2} = const. \quad (2)$$

The tool-in-use system  $f_e$  [8] is orientated in the machine system  $m$  (Fig.3) according to the cutting direction giving angel  $N$

$$N = \arctg\left(-\frac{y}{x}\right) = const. \quad (3)$$

The motion of cut  $-C'_c$  in  $O_{0x_0y_0z_0}$  is defined by the equation:

$$\bar{r}_c(t) = \begin{vmatrix} x_c(t) \\ y_c(t) \\ z_c \end{vmatrix} = \begin{vmatrix} r \cdot \cos[N - \varphi_{01}(t)] \\ r \cdot \sin[N - \varphi_{01}(t)] \\ z \end{vmatrix}. \quad (4)$$

The feed motion  $-Z_f$  in  $O_{0x_0y_0z_0}$  is described by:

$$\bar{r}_f(t) = \begin{vmatrix} x_f \\ y_f \\ z_f(t) \end{vmatrix} = \begin{vmatrix} r \cdot \cos N \\ r \cdot \sin N \\ Z - z(t) \end{vmatrix}. \quad (5)$$

When both the revolutions  $n$ ,  $\text{min}^{-1}$ , and the feed  $f$ ,  $\text{mm/min}$ , are constant, the values of the angular speed  $\omega$  and the feed speed  $v_f$  are

$$\omega = 2 \cdot \pi \cdot n \quad (6)$$

$$v_f = f \cdot n. \quad (7)$$

In this case the angle of rotation is

$$\varphi_{01} = \omega \cdot t = 2 \cdot \pi \cdot n \cdot t, \quad (8)$$

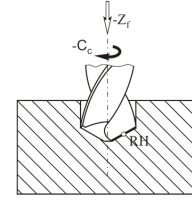
and the translation along the direction of feed is

$$z(t) = V_f \cdot t = f \cdot n \cdot t. \quad (9)$$

Then the equations (1), (4) and (5) get the form

$$\bar{r}_e(t) = \begin{vmatrix} x_e(t) \\ y_e(t) \\ z_e(t) \end{vmatrix} = \begin{vmatrix} r \cdot \cos[N - 2 \cdot \pi \cdot n \cdot t] \\ r \cdot \sin[N - 2 \cdot \pi \cdot n \cdot t] \\ Z - f \cdot n \cdot t \end{vmatrix}, \quad (10)$$

$$\bar{r}_c(t) = \begin{vmatrix} x_c(t) \\ y_c(t) \\ z_c \end{vmatrix} = \begin{vmatrix} r \cdot \cos[N - 2 \cdot \pi \cdot n \cdot t] \\ r \cdot \sin[N - 2 \cdot \pi \cdot n \cdot t] \\ z \end{vmatrix}, \quad (11)$$


 Fig. 2 Cutting motion  $-C'_c$  and feed motion  $-Z_f$  when drilling.

$$\bar{r}_f(t) = \begin{vmatrix} x_f \\ y_f \\ z_f(t) \end{vmatrix} = \begin{vmatrix} r \cdot \cos N \\ r \cdot \sin N \\ Z - f \cdot n \cdot t \end{vmatrix}. \quad (12)$$

### B. Characteristics of cut motion.

The cutting speed  $\bar{v}_c$  is:

$$\bar{v}_c(t) = \begin{vmatrix} v_{cx_1}(t) \\ v_{cy_1}(t) \\ v_{cz_1} \end{vmatrix} = \begin{vmatrix} 2 \cdot \pi \cdot n \cdot r \cdot \sin(N - 2 \cdot \pi \cdot n \cdot t) \\ -2 \cdot \pi \cdot n \cdot r \cdot \cos(N - 2 \cdot \pi \cdot n \cdot t) \\ 0 \end{vmatrix}, \quad (13)$$

and the value  $v_c$  is:

$$v_c = \sqrt{v_{cx_1}^2 + v_{cy_1}^2 + v_{cz_1}^2} = 2 \cdot \pi \cdot n \cdot r = const. \quad (14)$$

The unit vector  $\bar{e}_{v_c}$  of the cutting speed  $\bar{v}_c$  is:

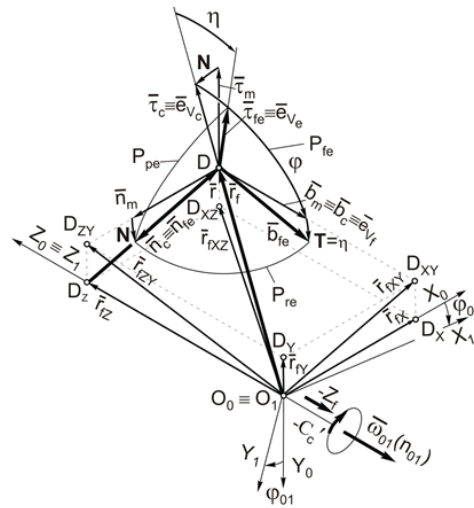
$$\bar{e}_{v_c}(t) = \frac{\bar{v}_c(t)}{v_c} = \begin{vmatrix} \sin(N - 2 \cdot \pi \cdot n \cdot t) \\ -\cos(N - 2 \cdot \pi \cdot n \cdot t) \\ 0 \end{vmatrix}. \quad (15)$$

The acceleration of cutting  $\bar{a}_c$  is:

$$\bar{a}_c(t) = \begin{vmatrix} a_{cx_1}(t) \\ a_{cy_1}(t) \\ a_{cz_1}(t) \end{vmatrix} = \begin{vmatrix} -4 \cdot \pi^2 \cdot n^2 \cdot r \cdot \cos(N - 2 \cdot \pi \cdot n \cdot t) \\ -4 \cdot \pi^2 \cdot n^2 \cdot r \cdot \sin(N - 2 \cdot \pi \cdot n \cdot t) \\ 0 \end{vmatrix}, \quad (16)$$

and the value  $a_c$  is:

$$a_c = \sqrt{a_{cx_1}^2 + a_{cy_1}^2 + a_{cz_1}^2} = 4 \cdot \pi^2 \cdot n^2 \cdot r = const. \quad (17)$$


 Fig. 3. Tool-in-use system  $f_e$  ( $\bar{r}_{f_e}$ ,  $\bar{n}_{f_e}$ ,  $\bar{b}_{f_e}$ ) and angle  $N$  when cylindrical turning with cutting motion  $-C'_c$  and feed motion  $-Z_f$ .

The unit vector  $\bar{e}_{a_c}$  of the acceleration of cut  $\bar{a}_c$  is:

$$\bar{e}_{a_c}(t) = \frac{\bar{a}_c(t)}{a_c} = \begin{pmatrix} -\cos(N-2.\pi.n.t) \\ -\sin(N-2.\pi.n.t) \\ 0 \end{pmatrix}. \quad (18)$$

The value of the tangent acceleration  $\bar{a}_{ct}$  is:

$$a_{ct} = 0, \quad (19)$$

and the value  $a_{cn}$  of the normal acceleration  $\bar{a}_{cn}$  is:

$$a_{cn} = \sqrt{a_c^2 - a_{ct}^2} = a_c = 4.\pi^2.n^2.r = const. \quad (20)$$

The radius  $R_{k_{1c}}$  of the curve  $k_{1c}$  is:

$$R_{k_{1c}} = \frac{1}{k_{1c}} = r. \quad (21)$$

The unit vectors of tangent  $\bar{t}_c$ , the principal normal  $\bar{n}_c$  and binormal  $\bar{b}_c$  of the trajectory of cutting motion are:

$$\bar{t}_c(t) = \bar{v}_{v_c}(t) = \begin{pmatrix} \sin(N-2.\pi.n.t) \\ -\cos(N-2.\pi.n.t) \\ 0 \end{pmatrix}, \quad (22)$$

$$\bar{n}_c(t) = \begin{pmatrix} a_{cx}(v_{cy}^2 + v_{cz}^2) - v_{cx}(v_{cy}.a_{cy} + v_{cz}.a_{cz}) \\ a_{cy}(v_{cx}^2 + v_{cz}^2) - v_{cy}(v_{cx}.a_{cx} + v_{cz}.a_{cz}) \\ a_{cz}(v_{cx}^2 + v_{cy}^2) - v_{cz}(v_{cx}.a_{cx} + v_{cy}.a_{cy}) \end{pmatrix} = \begin{pmatrix} -16.\pi^4.n^4.r^3.\cos(N-2.\pi.n.t) \\ -16.\pi^4.n^4.r^3.\sin(N-2.\pi.n.t) \\ 0 \end{pmatrix}, \quad (23)$$

$$\bar{b}_c = \frac{\bar{v}_c \times \bar{a}_c}{|\bar{v}_c \times \bar{a}_c|} = \begin{pmatrix} v_{cy}.a_{cz} - a_{cy}.v_{cz} \\ v_{cz}.a_{cx} - a_{cz}.v_{cx} \\ v_{cx}.a_{cy} - a_{cx}.v_{cy} \end{pmatrix} = [0, 0, -1]^T \quad (24)$$

$$\begin{aligned} & \begin{pmatrix} v_{cy}.a_{cz} - a_{cy}.v_{cz} \\ \sqrt{(v_{cx}.a_{cy} - a_{cx}.v_{cy})^2 + (v_{cy}.a_{cz} - a_{cy}.v_{cz})^2 + (v_{cz}.a_{cx} - a_{cz}.v_{cx})^2} \\ v_{cz}.a_{cx} - a_{cz}.v_{cx} \\ \sqrt{(v_{cx}.a_{cy} - a_{cx}.v_{cy})^2 + (v_{cy}.a_{cz} - a_{cy}.v_{cz})^2 + (v_{cz}.a_{cx} - a_{cz}.v_{cx})^2} \\ v_{cx}.a_{cy} - a_{cx}.v_{cy} \\ \sqrt{(v_{cx}.a_{cy} - a_{cx}.v_{cy})^2 + (v_{cy}.a_{cz} - a_{cy}.v_{cz})^2 + (v_{cz}.a_{cx} - a_{cz}.v_{cx})^2} \end{pmatrix} = \\ & = [0, 0, -1]^T \end{aligned}$$

### C. Characteristics of feed motion.

The feed speed  $\bar{v}_f$  is:

$$\bar{v}_f(t) = [0, 0, -n.f]^T, \quad (25)$$

and its value  $v_f$  is

$$v_f = f.n = const. \quad (26)$$

The unit vector  $\bar{e}_{v_f}$  of the feed speed  $\bar{v}_f$  is:

$$\bar{e}_{v_f} = [0, 0, -1]^T. \quad (27)$$

### D. Characteristics of resultant cutting motion.

The speed  $\bar{v}_e$  is:

$$\bar{v}_e(t) = \begin{pmatrix} v_{ex}(t) \\ v_{ey}(t) \\ v_{ez}(t) \end{pmatrix} = \begin{pmatrix} 2.\pi.n.r.\sin(N-2.\pi.n.t) \\ -2.\pi.n.r.\cos(N-2.\pi.n.t) \\ -n.f \end{pmatrix}, \quad (28)$$

and its value  $v_e$  is:

$$v_e = \sqrt{v_{ex}^2 + v_{ey}^2 + v_{ez}^2} = n.\sqrt{4.\pi^2.r^2 + f^2} = const. \quad (29)$$

The unit vector  $\bar{e}_{v_e}$  for the speed  $\bar{v}_e$  is:

$$\bar{e}_{v_e}(t) = \frac{\bar{v}_e(t)}{v_e} = \begin{pmatrix} \frac{2.\pi.r.\sin(N-2.\pi.n.t)}{\sqrt{4.\pi^2.r^2 + f^2}} \\ \frac{2.\pi.r.\cos(N-2.\pi.n.t)}{\sqrt{4.\pi^2.r^2 + f^2}} \\ -\frac{f}{\sqrt{4.\pi^2.r^2 + f^2}} \end{pmatrix}. \quad (30)$$

The acceleration  $\bar{a}_e$  is:

$$\bar{a}_e(t) = \begin{pmatrix} a_{ex}(t) \\ a_{ey}(t) \\ a_{ez}(t) \end{pmatrix} = \begin{pmatrix} -4.\pi^2.n^2.r.\cos(N-2.\pi.n.t) \\ -4.\pi^2.n^2.r.\sin(N-2.\pi.n.t) \\ 0 \end{pmatrix}, \quad (31)$$

and its value  $a_e$  is:

$$a_e = \sqrt{a_{ex}^2 + a_{ey}^2 + a_{ez}^2} = 4.\pi^2.n^2.r = const. \quad (32)$$

The unit vector  $\bar{e}_{a_e}$  of acceleration  $\bar{a}_e$  is:

$$\bar{e}_{a_e}(t) = \frac{\bar{a}_e(t)}{a_e} = \begin{pmatrix} -\cos(N-2.\pi.n.t) \\ -\sin(N-2.\pi.n.t) \\ 0 \end{pmatrix}. \quad (33)$$

The value  $a_{et}$  of the tangential acceleration  $\bar{a}_{et}$  is:

$$a_{et} = 0, \quad (34)$$

and the value  $a_{en}$  of the normal acceleration  $\bar{a}_{en}$  is:

$$a_{en} = \sqrt{a_e^2 - a_{et}^2} = a_e = 4.\pi^2.n^2.r = const. \quad (35)$$

Radius  $R_{k_{1e}}$  of the curve  $k_{1e}$  of the trajectory of resultant cutting motion is:

$$R_{k_{1e}} = \frac{1}{k_{1e}} = \frac{v_e^2}{a_{en}} = \frac{f^2 + 4.\pi^2.r^2}{4.\pi^2.r}. \quad (36)$$

The derivative  $\dot{\bar{a}}_e$  for acceleration is:

$$\dot{\bar{a}}_e(t) = \begin{pmatrix} -8.\pi^3.n^3.r.\sin(N-2.\pi.n.t) \\ 8.\pi^3.n^3.r.\cos(N-2.\pi.n.t) \\ 0 \end{pmatrix}. \quad (37)$$

The torsion  $k_{2e}$  of the trajectory of resultant cutting motion is

$$k_{2e} = \frac{\begin{vmatrix} v_{ex} & v_{ey} & v_{ez} \\ a_{ex} & a_{ey} & a_{ez} \\ \dot{a}_{ex} & \dot{a}_{ey} & \dot{a}_{ez} \end{vmatrix}}{v_e^4.a_{en}} = \frac{8.\pi^3.r.f}{(4.\pi^2.r^2 + f^2)^2}. \quad (38)$$

The unit vectors of tangent  $\bar{t}_{fe}$ , the principal normal  $\bar{n}_{fe}$  and binormal  $\bar{b}_{fe}$  of the trajectory of resultant cutting motion (Fig. 3) are:

$$\bar{\tau}_{fe}(t) = \bar{e}_{v_e}(t) = \left| \begin{array}{c} \frac{2\pi.r.\sin(N-2\pi.nt)}{\sqrt{4\pi^2.r^2+f^2}} \\ \frac{2\pi.r.\cos(N-2\pi.nt)}{\sqrt{4\pi^2.r^2+f^2}} \\ -\frac{f}{\sqrt{4\pi^2.r^2+f^2}} \end{array} \right|, \quad (39)$$

$$\begin{aligned} \bar{n}_{fe}(t) &= \left| \begin{array}{c} a_{ex}(v_{ey}^2+v_{ez}^2) - v_{ex}(v_{ey} \cdot a_{ey} + v_{ez} \cdot a_{ez}) \\ a_{ey}(v_{ex}^2+v_{ez}^2) - v_{ey}(v_{ex} \cdot a_{ex} + v_{ez} \cdot a_{ez}) \\ a_{ez}(v_{ex}^2+v_{ey}^2) - v_{ez}(v_{ex} \cdot a_{ex} + v_{ey} \cdot a_{ey}) \end{array} \right| = \\ &= \left| \begin{array}{c} -4\pi^2.n^4.r.(4\pi^2.r^2+f^2).\cos(N-2\pi.nt) \\ -4\pi^2.n^4.r.(4\pi^2.r^2+f^2).\sin(N-2\pi.nt) \\ 0 \end{array} \right|, \quad (40) \\ \bar{b}_{fe} &= \frac{\bar{v}_e \times \bar{a}_e}{|\bar{v}_e \times \bar{a}_e|} = \quad (41) \end{aligned}$$

$$\begin{aligned} &\left| \begin{array}{c} \frac{v_{ey} \cdot a_{ez} - a_{ey} \cdot v_{ez}}{\sqrt{(v_{ex} \cdot a_{ey} - a_{ex} \cdot v_{ey})^2 + (v_{ey} \cdot a_{ez} - a_{ey} \cdot v_{ez})^2 + (v_{ez} \cdot a_{ex} - a_{ez} \cdot v_{ex})^2}} \\ \frac{v_{ez} \cdot a_{ex} - a_{ez} \cdot v_{ex}}{\sqrt{(v_{ex} \cdot a_{ey} - a_{ex} \cdot v_{ey})^2 + (v_{ey} \cdot a_{ez} - a_{ey} \cdot v_{ez})^2 + (v_{ez} \cdot a_{ex} - a_{ez} \cdot v_{ex})^2}} \\ \frac{v_{ex} \cdot a_{ey} - a_{ex} \cdot v_{ey}}{\sqrt{(v_{ex} \cdot a_{ey} - a_{ex} \cdot v_{ey})^2 + (v_{ey} \cdot a_{ez} - a_{ey} \cdot v_{ez})^2 + (v_{ez} \cdot a_{ex} - a_{ez} \cdot v_{ex})^2}} \end{array} \right| = \\ &= \left| \begin{array}{c} \frac{f \cdot \sin(N+2\pi.nt)}{\sqrt{4\pi^2.r^2+f^2}} \\ \frac{f \cdot \cos(N+2\pi.nt)}{\sqrt{4\pi^2.r^2+f^2}} \\ \frac{2\pi.r}{\sqrt{4\pi^2.r^2+f^2}} \end{array} \right| \end{aligned}$$

### III. CONCLUSIONS

The change of tool angles in some working cases (turning acme threads, face turning, milling of complex

profile surfaces, high speed cutting) leads to significant changes in the values of clearance angles, sometimes leading to tool destruction. The coordinate systems, setting angles and motion angles, defined in ISO 3002/2-1982(E), lead to complicated, unclear and in some cases impossible transformations of tool angles to working angles.

The derived equations for the characteristics of the cutting, feed and resultant cutting motions are the basis for deriving the dependencies for straight and inverse transformation between tool and working angles in cylindrical turning, drilling, coredrilling and reaming.

**Acknowledgments:** The authors would like to thank the Research and Development Sector at the Technical University of Sofia for the financial support.

### REFERENCES

- [1] V. Astakhov, Geometry of Single-Point Turning Tools and Drills: Fundamentals and Practical Applications. Springer, 2010, pp .565
- [2] A. Vachev, Conversion Methodology to Relate Tool and Working Angles – an Alternative to ISO 3002/2, Journal of the Technical University at Plovdiv, “Fundamental Sciences and Applications”, Vol. 13 (6), 2006. Anniversary Scientific Conference’ 2006, Plovdiv, Bulgaria, (In Bulgarian), pp. 51-58.
- [3] S. Radzevich, Geometry of the Active Part of Cutting Tools (in the Tool-in-Hand System), SME Paper TPO 6PUB37:10, 2006.
- [4] S. Radzevich, Geometry of the Active Part of Cutting Tools (in the Tool-in-Use System), SME, 2006.
- [5] M. Aleksiev, Machining by rotary cutting on CNC Machine, M.S. thesis, Technical University of Sofia, Sofia, Bulgaria, 2018
- [6] M. Aleksiev, Grapho-analytical method for determining the working angles of turning tools, Journal of the Technical University at Plovdiv, Vol. `21 (2), 2015, Scientific Conference Techsys-2015, Plovdiv, Bulgaria, (In Bulgarian), pp. 61.
- [7] ISO 3002/2-1984(E), Basic quantities in cutting and grinding - Part 2: Geometry of the active part of cutting tools - General conversion formulae to relate tool and working angles.
- [8] A. Vachev and A. Poparov, Tool in use system and motion angles when turning, Journal of the Technical University at Plovdiv, “Fundamental Sciences and Applications”, Vol. 13 (6), 2006. Anniversary Scientific Conference’ 2006, Plovdiv, Bulgaria, (In Bulgarian), pp. 59-70.
- [9] A. Vachev and A. Poparov, Tool in hand and tool in use systems when boring (3D), drilling, counterboring and reaming, Journal of the Technical University at Plovdiv, “Fundamental Sciences and Applications”, Vol. 13 (6), 2006. Anniversary Scientific Conference’ 2006, Plovdiv, Bulgaria, (In Bulgarian), pp. 85-92.
- [10] ISO841-1974(E), Numerical control of machines - Axis and motion nomenclature.

# Characteristics of Motions in Facing

Angel Poparov

Technical University - Sofia, Branch Plovdiv  
Plovdiv, Bulgaria  
poparan@abv.bg

Agop Izmirliqn

Technical University - Sofia, Branch Plovdiv  
Plovdiv, Bulgaria  
izmirliyanx3@gmail.com

**Abstract.** In the process of work the tool angles change their value to become the working angles. This results in a variation of the work conditions of the cutting tools. The variation depends on the characteristic of the resultant cutting motion – the sum of the cutting motion and feed motion.

In this article the characteristics of motions of facing are derived, which can serve as a basis for determining the relations between the tool and working angles.

These relations can be used in programming the CNC to prevent the formation of negative working clearance angle and the destruction of the tool.

**Keywords:** characteristics of movement, coordinate axes, cutting and feed motion, resultant cutting motion.

## I. INTRODUCTION

The ISO 3002-1982 standard helps to solve many engineering tasks, but it is not generally valid and computer oriented. The simultaneous existence of two standards - ASME B94.50-1975 and ISO3002-1:1984, which deal with unchangeable terminology and definitions, has a large share in the confusion and misunderstanding of the basic geometric parameters of cutting tools [1].

A critical analysis of both the advantages and disadvantages of ISO 3002-1:1984 can be found in several sources [1] - [6].

In the alternative methodology of [7], proposed in [2], the dependencies between tool and working angles are derived by defining in a new way the setting angles  $G$ ,  $H$  and  $L$  that give the correlation between the tool-in-hand system  $f$  and the machine system  $m$ , and the motion angles  $M$ ,  $N$  and  $T$  that connect the tool-in-use system  $f_e$  with the machine system  $m$ .

The variation of tool angles in working ones in the process of operation is due to the feed rate  $D_f$ . The feed rate  $D_f$ , summed with the cutting motion  $D_c$ , determines the resultant cutting motion  $D_e$ . The placement of the tool in relation to the workpiece also has an impact.

For transformations of the tool angles into working ones and vice versa it is necessary that the main characteristics of the cutting motion  $D_c$ , feed rate  $D_f$  and the resultant cutting motion  $D_e$ : trajectory, path, speed, acceleration are known. The local elements of the trajectory: the tangent, the principal normal, the binormal (which form an accompanying trihedron), curvature and torsion should be known as well.

For the practical application of these dependencies the parametric equations of resultant cutting motion in facing have been derived in [8]. In this article the equations of the characteristics of the cutting, feed and resultant cutting motions are derived.

## II. METHODS

*A. Equations for the resultant cutting motion and the motions of cut and feed.*

Two rectangular right oriented coordinate systems, fixed to the workpiece  $O_{1x_1y_1z_1}$  and the machine  $O_{0x_0y_0z_0}$ , respectively, were introduced. Axes  $X_0$ ,  $Y_0$  and  $Z_0$  are colinear with the axes of a standard coordinate system as in [9].

The case of cutting motion  $-C'_c$  and feed motion  $-X_f$  is considered when facing from the center to the periphery (Fig. 1) and  $+X_f$  when facing from the periphery to the center (Fig. 2).

Depending on the placement of the tool relative to the center axis of the machine, three cases are possible [8] – position above the center axis (angle  $N>0$ ) as in Fig. 1 (a) and Fig. 2 (a); position on the axis of the centers (angle  $N=0$ ) as in Fig. 1 (b) and Fig. 2 (b); position below the axis of the centers (angle  $N<0$ ) as in Fig. 1 (c) and Fig. 2 (c).

The resultant cutting motion for a point of the cutting edge of a tool with coordinates  $x = x(t)$ ,  $y = const.$  and  $z = const.$  is defined in  $O_{0x_0y_0z_0}$  with the equation

Print ISSN 1691-5402

Online ISSN 2256-070X

<https://doi.org/10.17770/etr2023vol3.7260>

© 2023 Angel Poparov, Agop Izmirliqn. Published by Rezekne Academy of Technologies.

This is an open access article under the [Creative Commons Attribution 4.0 International License](https://creativecommons.org/licenses/by/4.0/).

$$\bar{r}_e(t) = \begin{vmatrix} x_e(t) \\ y_e(t) \\ z_e \end{vmatrix} = \begin{vmatrix} r(t) \cdot \cos[N - \varphi_{01}(t)] \\ r(t) \cdot \sin[N - \varphi_{01}(t)] \\ z \end{vmatrix}, \quad (1)$$

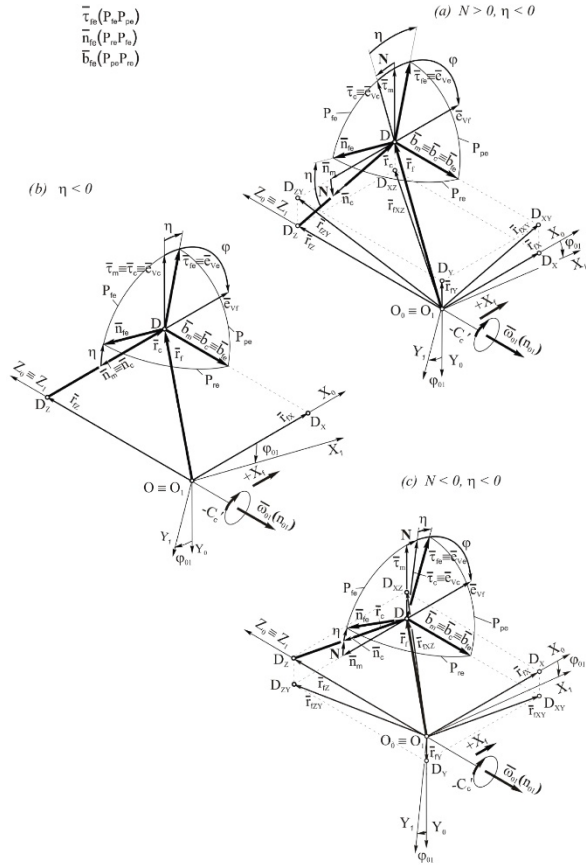


Fig. 1 Tool-in-use system  $f_e(\bar{\tau}_{fe}, \bar{n}_{fe}, \bar{b}_{fe})$  with cutting motion  $-C'_c$  and feed motion  $+X_f$ .

where  $\varphi_{01}$  is the angle of rotation around  $Z_0 \equiv Z_1$  of the workpiece coordinate system  $O_{1X_1Y_1Z_1}$  against coordinate system of the machine  $O_{0X_0Y_0Z_0}$ , and

$$r(t) = \sqrt{x(t)^2 + y^2} = \sqrt{(X + i.n.f.t)^2 + y^2} \quad (2)$$

$$x(t) = X + i.n.f.t. \quad (3)$$

The tool-in-use system  $f_e$  [8] is oriented in the machine system  $m$  (Fig.1, Fig.2) according to the cutting direction giving angle  $N$

$$N(t) = \arctg\left(-\frac{y}{x}\right) = \arctg\left(-\frac{y}{X + i.n.f.t}\right). \quad (4)$$

(1) is an equation of a flat curve, and when  $y = 0$  – archimedean spiral.

The feed motion  $-Z_f$  in  $O_{0X_0Y_0Z_0}$  is described by the equation:

$$\bar{r}_f(t) = \begin{vmatrix} x_f(t) \\ y \\ z \end{vmatrix} = \begin{vmatrix} X + i.n.f.t \\ y \\ z \end{vmatrix}. \quad (5)$$

(5) is an equation of straight line perpendicular to the axis  $Z_0 \equiv Z_1$  and lying in the plane  $Y = y$ . When the feed is  $-X_f$ ,  $i = -1$ . When the feed is  $+X_f$ ,  $i = 1$ .

The cutting motion is dependent on the feed motion and its characteristics are determined at a cutting time point  $t$ .

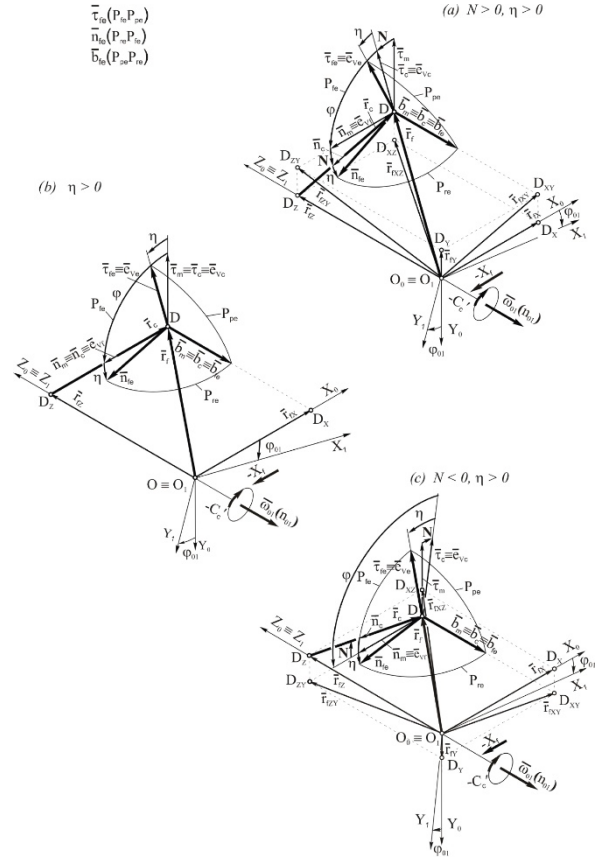


Fig. 2. Tool-in-use system  $f_e(\bar{\tau}_{fe}, \bar{n}_{fe}, \bar{b}_{fe})$  with cutting motion  $-C'_c$  and feed motion  $-X_f$ .

When both the revolutions  $n$ ,  $\text{min}^{-1}$ , and the feed  $f$ ,  $\text{mm/min}$ , are constant, the values of the angular speed  $\omega$  and the feed speed  $v_f$  are

$$\omega = 2.\pi.n \quad (6)$$

$$v_f = f.n. \quad (7)$$

In this case the angle of rotation is

$$\varphi_{01} = \omega.t = 2.\pi.n.t, \quad (8)$$

and the translation along the direction of feed is:

$$x(t) = V_f.t = f.n.t. \quad (9)$$

Then (1) gets the form

$$\bar{r}_e(t) = \begin{vmatrix} x_e(t) \\ y_e(t) \\ z_e \end{vmatrix} = \begin{vmatrix} \sqrt{(X + i.n.f.t)^2 + y^2} \cdot \cos[N - 2.\pi.n.t] \\ \sqrt{(X + i.n.f.t)^2 + y^2} \cdot \sin[N - 2.\pi.n.t] \\ z \end{vmatrix}. \quad (10)$$

B. Characteristics of cut motion.

Value  $v_c$  of cutting speed  $\bar{v}_c$  at a point in time  $t$  is:



$$= \frac{\left| \begin{array}{c} f.i.(f.i.n.t + X) \cdot \cos\left(2.n.\pi.t + \arctan\frac{y}{f.i.n.t + X}\right) - A.\sin\left(2.n.\pi.t + \arctan\frac{y}{f.i.n.t + X}\right) \\ \sqrt{(f.i.n.t + X)^2 + y^2} \cdot \sqrt{f^2.(1 + 4.n^2.\pi^2.t^2) + 4.f.i.\pi.(2.n.\pi.t.X - y) + 4.\pi^2.(X^2 + y^2)} \\ A.\cos\left(2.n.\pi.t + \arctan\frac{y}{f.i.n.t + X}\right) + f.i.(f.i.n.t + X) \cdot \sin\left(2.n.\pi.t + \arctan\frac{y}{f.i.n.t + X}\right) \\ \sqrt{(f.i.n.t + X)^2 + y^2} \cdot \sqrt{f^2.(1 + 4.n^2.\pi^2.t^2) + 4.f.i.\pi.(2.n.\pi.t.X - y) + 4.\pi^2.(X^2 + y^2)} \end{array} \right|}{0},$$

where  $A$  is defined by (16).

The unit vector  $\bar{n}_{fe}$  of the principal normal of the trajectory of resultant cutting motion is (Fig.1, Fig.2):

$$\bar{n}_{fe}(t) = \frac{\left| \begin{array}{c} a_{ex} \left( v_{ey}^2 + v_{ez}^2 \right) - v_{ex} \left( v_{ey} \cdot a_{ey} + v_{ez} \cdot a_{ez} \right) \\ a_{ey} \left( v_{ex}^2 + v_{ez}^2 \right) - v_{ey} \left( v_{ex} \cdot a_{ex} + v_{ez} \cdot a_{ez} \right) \\ a_{ez} \left( v_{ex}^2 + v_{ey}^2 \right) - v_{ez} \left( v_{ex} \cdot a_{ex} + v_{ey} \cdot a_{ey} \right) \end{array} \right|}{0} = \quad (27)$$

$$= \frac{\left| \begin{array}{c} -C \cdot \left[ D.\cos\left(2.n.\pi.t + \arctan\frac{y}{f.i.n.t + X}\right) + f.i.(f.i.n.t + X) \cdot \sin\left(2.n.\pi.t + \arctan\frac{y}{f.i.n.t + X}\right) \right] \\ E \cdot \sqrt{(f.i.n.t + X)^2 + y^2} \cdot \sqrt{f^2.(1 + n^2.\pi^2.t^2) + 2.f.i.\pi.(n.\pi.t.X - y) + \pi^2.(X^2 + y^2)} \\ C \cdot \left[ -f.i.(f.i.n.t + X) \cdot \cos\left(2.n.\pi.t + \arctan\frac{y}{f.i.n.t + X}\right) + D.\sin\left(2.n.\pi.t + \arctan\frac{y}{f.i.n.t + X}\right) \right] \\ E \cdot \sqrt{(f.i.n.t + X)^2 + y^2} \cdot \sqrt{f^2.(1 + n^2.\pi^2.t^2) + 2.f.i.\pi.(n.\pi.t.X - y) + \pi^2.(X^2 + y^2)} \end{array} \right|}{0},$$

where:

$$C = f^2.(1 + 2.n^2.\pi^2.t^2) + f.i.\pi.(4.n.\pi.t.X - 3.y) + 2.\pi^2.(X^2 + y^2), \quad (28)$$

$$D = 2.f^2.n^2.\pi.t^2 + f.i.(4.n.\pi.t.X - y) + 2.\pi.(X^2 + y^2), \quad (29)$$

$$E = f^2.(1 + 4.n^2.\pi^2.t^2) + 4.f.i.\pi.(2.n.\pi.t.X - y) + 4.\pi^2.(X^2 + y^2). \quad (30)$$

The unit vector  $\bar{b}_{fe}$  of binormal of the trajectory of resultant cutting motion (Fig.1, Fig.2) is:

$$\bar{b}_{fe}(t) = \frac{\bar{v}_e \times \bar{a}_e}{|\bar{v}_e \times \bar{a}_e|} = \frac{\left| \begin{array}{c} v_{ey} \cdot a_{ez} - a_{ey} \cdot v_{ez} \\ v_{ez} \cdot a_{ex} - a_{ez} \cdot v_{ex} \\ v_{ex} \cdot a_{ey} - a_{ex} \cdot v_{ey} \end{array} \right|}{0} = \quad (31)$$

$$= \frac{\left| \begin{array}{c} 0 \\ 0 \\ -f^2.(1 + 2.n^2.\pi^2.t^2) + f.i.\pi.(-4.n.\pi.t.X + 3.y) - 2.\pi^2.(X^2 + y^2) \\ \sqrt{f^2.(1 + n^2.\pi^2.t^2) + 2.f.i.\pi.(n.\pi.t.X - y) + \pi^2.(X^2 + y^2)} \cdot \sqrt{E} \end{array} \right|}{0},$$

where  $E$  is defined by (30).

### III. CONCLUSION

The change of tool angles in some working cases (turning acme threads, face turning, milling of complex profile surfaces, high speed cutting) leads to significant changes in the values of clearance angles, sometimes leading to tool destruction. The coordinate systems, setting angles and motion angles, defined in ISO 3002/2-1984(E), lead to complicated, unclear and in some cases impossible transformations of tool angles to working angles.

The derived equations for the characteristics of the cutting, feed and resultant cutting motions are the basis for deriving the dependencies for straight and inverse transformation between tool and working angles when facing.

**Acknowledgments:** The authors would like to thank the Research and Development Sector at the Technical University of Sofia for the financial support.

### REFERENCES

- [1] V. Astakhov, Geometry of Single-Point Turning Tools and Drills: Fundamentals and Practical Applications. Springer, 2010, pp .565
- [2] A. Vachev, Conversion Methodology to Relate Tool and Working Angles – an Alternative to ISO 3002/2, Journal of the Technical University at Plovdiv, “Fundamental Sciences and Applications”, Vol. 13 (6), 2006. Anniversary Scientific Conference’ 2006, Plovdiv, Bulgaria, (In Bulgarian), pp. 51-58.
- [3] S. Radzevich, Geometry of the Active Part of Cutting Tools (in the Tool-in-Hand System), SME Paper TPO 6PUB37:10, 2006.
- [4] S. Radzevich, Geometry of the Active Part of Cutting Tools (in the Tool-in-Use System), SME, 2006.
- [5] M. Aleksiev, Machining by rotary cutting on CNC Machine, M.S. thesis, Technical University of Sofia, Sofia, Bulgaria, 2018
- [6] M. Aleksiev, Grapho-analytical method for determining the working angles of turning tools, Journal of the Technical University at Plovdiv, Vol. '21 (2), 2015, Scientific Conference Techsys-2015, Plovdiv, Bulgaria, (In Bulgarian), pp. 61.
- [7] ISO 3002/2-1984(E), Basic quantities in cutting and grinding - Part 2: Geometry of the active part of cutting tools - General conversion formulae to relate tool and working angles.
- [8] A. Vachev and A. Poparov, Tool in use system and motion angles when turning, Journal of the Technical University at Plovdiv, “Fundamental Sciences and Applications”, Vol. 13 (6), 2006. Anniversary Scientific Conference’ 2006, Plovdiv, Bulgaria, (In Bulgarian), pp. 59-70.
- [9] ISO841-1974(E), Numerical control of machines - Axis and motion nomenclature.

# Development of a Method for Contactless Temperature Measurement in 3 Spectral Ranges

**Dimcho Pulov**

Department of Mechanical and Precision Engineering  
Technical University of Gabrovo  
Gabrovo, Bulgaria  
pulov@mail.bg

**Tsanko Karadzov**

Department of Mechanical and Precision Engineering  
Technical University of Gabrovo  
Gabrovo, Bulgaria  
karadzov\_s@abv.bg

**Abstract.** A 3-spectral method for non-contact temperature measurement has been developed. Three silicon photodiodes were used. The separation of the spectrum is done by optical bandpass filters and beamsplitters. It is possible to work in three modes: three-spectral, two-spectral (spectral ratio) and one-spectral. In the first mode, the temperature of objects with an unknown and variable emissivity can be measured. The last two modes give good results respectively for gray bodies and for objects with known emissivity.

**Keywords:** differential photo receiver, temperature, method, IR diaphragm, lens design.

## I. INTRODUCTION

Temperature is one of the main parameters that determine the state of substance. The efficient functioning of a large number of technological processes in the industry is related to maintaining the temperature within certain limits and with a specified accuracy. For this reason, accurate temperature measurement is essential to modern science and technology.

Remote methods of temperature measurement are increasingly used. These are optical methods that are based on the registration of the own thermal radiation of the investigated objects in the infrared spectrum [1]–[4]. Regardless of their advantages, optical pyrometers have one serious drawback which necessarily must be accounted for. All non-contact measurements are based on Planck's law, which relates the spectral radiant exitance of a black body  $M_{bb}(\lambda, T)$ , its temperature  $T$  and the wavelength  $\lambda$ .

$$M_{bb}(\lambda, T) = \frac{C_1}{\lambda^5 \left[ \exp\left(\frac{C_2}{\lambda T}\right) - 1 \right]} \quad (1)$$

The real objects whose temperature is measured are not black and therefore it can be recorded

$$M(\lambda, T) = M_{bb}(\lambda, T) \varepsilon(\lambda, T)$$

where  $\varepsilon(\lambda, T)$  is the emissivity.

The emissivity of real bodies varies from 0 for an ideal mirror to 1 for a black body. If  $\varepsilon(\lambda, T) = \text{const.}$ , the body is called gray.

Therefore, the pyrometer output signal depends simultaneously on two unknown quantities: the actual temperature of the object  $T_{obj}$  (which is to be measured) and its emissivity  $\varepsilon(\lambda, T)$ .

This implies an indeterminacy of the results of the measurements and the appearance of a difference  $\Delta T$  between the actual temperature of the object  $T_{obj}$  and the measured one  $T_{meas}$  ( $T_{meas} = T_{obj} - \Delta T$ ).

Several types of pyrometers are known:

- Radiation pyrometers. The measured value is equal to the temperature of a black body at which its radiance is equal to the radiance of the object under study. For them

$$T_{obj} = \frac{T_{meas}}{\sqrt[4]{\varepsilon(T)}} \quad \text{или} \quad \frac{\Delta T}{T} = 1 - \sqrt[4]{\varepsilon(T)}$$

where  $\varepsilon(T)$  is the integral emissivity in the working spectral range of the device  $\Delta\lambda$ .

Radiation pyrometers correctly measure temperatures only of black bodies or of bodies with a known emissivity  $\varepsilon(T)$ .

Print ISSN 1691-5402

Online ISSN 2256-070X

<https://doi.org/10.17770/etr2023vol3.7184>

© 2023 Dimcho Pulov, Tsanko Karadzov. Published by Rezekne Academy of Technologies.  
This is an open access article under the [Creative Commons Attribution 4.0 International License](https://creativecommons.org/licenses/by/4.0/).

- Spectral ratio pyrometers. The measured temperature  $T_{meas}$  is numerically equal to the blackbody temperature, where the ratio of the spectral radiant exitance  $M(\lambda, T)$  for two narrow spectral ranges is equal to the same ratio, but for the controlled object at its actual temperature  $T_{obj}$ . The spectral ratio pyrometers correctly measure the temperature of only gray bodies or bodies with a known  $\varepsilon_1/\varepsilon_2$  ratio [5], [6], because for them

$$\frac{1}{T_{obj}} - \frac{1}{T_{meas}} = \frac{\lambda_1 \lambda_2}{C_2(\lambda_2 - \lambda_1)} \cdot \ln\left(\frac{\varepsilon_1}{\varepsilon_2}\right) \quad (2)$$

- Spectral pyrometers. Temperature is measured by registration the radiation spectrum of the object and comparing it to the spectrum of a black body. Receiving information in many channels allows correction of the unknown emissivity [7],[8] and temperature measurement of non-gray bodies for which  $\varepsilon = f(\lambda)$ .

In this method, the separation of the spectrum is realized by using spectrometers with diffraction gratings [9], which are expensive devices. In addition, the presence of many spectral channels implies the acquisition of large data sets, as well as complex algorithms and mathematical expressions for determining the true temperature [10] – [13].

As a compromise option, an improvement of the two-wave spectral ratio pyrometer can be proposed by adding one more spectral channel. In this way, additional information about the emissivity will be obtained, which will reduce the error of measurements caused by its unknown.

The aim of the given publication is the development of a pyrometer operating in 3 narrow spectral ranges, which allows temperature measurement of non-gray bodies and the separation of the spectral channels is realized by simple beamsplitters.

## II. EXPOSITION

### A. Essence of the three-spectral method

The three-spectral method is a development and improvement of the two-spectral pyrometric method. It measures the radiant exitance in 3 narrow spectral intervals  $\Delta\lambda_i$  using 3 photodiodes. The centers of these intervals  $\lambda_i$  are respectively  $\lambda_1, \lambda_2$  и  $\lambda_3$ , for which the ratio  $\lambda_1 < \lambda_2 < \lambda_3$  applies. The approximation of the unknown emissivity with a suitable function adequately characterizing the dependence  $\varepsilon = f(\lambda, T)$  is the basis of the three-spectral method.

The signal at the output of the photo receiver in the spectral interval  $i$  is defined as

$$I_i(T) = Ad\Omega \int_{\Delta\lambda_i} M(\lambda)S(\lambda)\tau(\lambda)d\lambda \quad (3)$$

where:  $A$  – area of the entrance pupil of the optical system;  $\Omega$  – solid angle of the field of view;  $M(\lambda)$  – spectral radiant exitance of the measured body;  $S(\lambda)$  – spectral sensitivity of the photo receiver;  $\tau(\lambda)$  – transmittance of the all optical components (lens, beam splitter, filter, medium).

It can be assumed that in narrow parts of the spectrum, the spectral sensitivity of the photo receiver and the transmittance of the optical system do not change. Furthermore, when the measured body is located relatively close to the pyrometer, the transmittance of the medium can be neglected. Then expression (3) takes the form

$$I_i(T) = K_i \varepsilon_i(\lambda) M_{bbi}(\lambda) \quad (4)$$

where  $K_i$  is a constant depending on the summary characteristics of the pyrometer;  $M_{bbi}(\lambda)$  – spectral radiant exitance of a black body.

Using the Vin approximation for the short-wavelength region of the spectrum, expression (4) takes the form

$$I_i(T) = K_i \varepsilon_i(\lambda) \frac{C_1}{\lambda_i^5 \exp\left(\frac{C_2}{\lambda_i T}\right)} \quad (5)$$

It can be assumed that for narrow and closely spaced spectral sections, the pyrometer constant does not change, i.e.  $K_i = const$ . When measuring in two spectral ranges ( $i = 1, 2$ ) and from expression (5), the ratio  $I_1(T)/I_2(T)$  is expressed.

After its two-sided logarithm the temperature of the object is determined as

$$T = \frac{C_2 \left(1/\lambda_2 - 1/\lambda_1\right)}{\ln\left(\frac{I_1(T)}{I_2(T)} \cdot \frac{\lambda_1^5}{\lambda_2^5}\right)} \quad (6)$$

When measuring in 3 spectral ranges ( $i = 1, 2, 3$ ), expression (5) is converted into a system of 3 equations with 4 unknowns ( $\varepsilon_1(\lambda), \varepsilon_2(\lambda), \varepsilon_3(\lambda)$  and  $T$ ).

$$\begin{cases} I_1(T) = \varepsilon_1(\lambda) \lambda_1^{-5} \exp\left(-\frac{C_2}{\lambda_1 T}\right) \\ I_2(T) = \varepsilon_2(\lambda) \lambda_2^{-5} \exp\left(-\frac{C_2}{\lambda_2 T}\right) \\ I_3(T) = \varepsilon_3(\lambda) \lambda_3^{-5} \exp\left(-\frac{C_2}{\lambda_3 T}\right) \end{cases}$$

This system is undefined. In order for it to be solved correctly, it is necessary to introduce another equation connecting these unknown quantities. Determining the true (thermodynamic) temperature of non-gray bodies under such indeterminacy involves using a priori assumptions about the form of the function  $\varepsilon = f(\lambda, T)$ . This means modeling the behavior of the emissivity based on substantiated theoretical and experimental data. The spectral emissivities of various metals are shown in fig. 1.

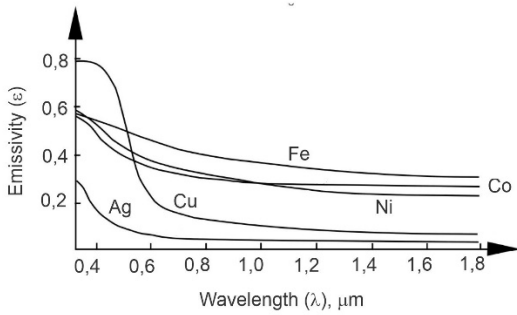


Fig. 1. Spectral emissivity of various metals.

It is shown in [14]–[17] that various approximation functions are possible, but the exponential is the most used because of the convenient mathematical operations with it. In [11],[12] various exponential functions are investigated and it is found that the emissivity of many metals is successfully approximated by an exponential function of the form

$$\varepsilon(\lambda, T) = \varepsilon_0(T) \exp(a\lambda) \quad (7)$$

where  $\varepsilon_0(T)$  is the dependence of the emissivity on temperature.

Considering expression (7) the signal at the output of the photo receiver can be written as

$$I_i(T) = \varepsilon_0(T) \exp(a\lambda) \frac{C_1}{\lambda_i^5 \exp\left(\frac{C_2}{\lambda_i T}\right)} \quad (8)$$

After logarithmizing both sides of expression (8) for the three spectral ranges ( $i = 1, 2, 3$ ), the following system of equations is obtained

$$\begin{cases} \ln(I_1) = \ln(\varepsilon_0(T)) + a\lambda_1 + \ln(C_1) - 5\ln(\lambda_1) - \frac{C_2}{\lambda_1 T} \\ \ln(I_2) = \ln(\varepsilon_0(T)) + a\lambda_2 + \ln(C_1) - 5\ln(\lambda_2) - \frac{C_2}{\lambda_2 T} \\ \ln(I_3) = \ln(\varepsilon_0(T)) + a\lambda_3 + \ln(C_1) - 5\ln(\lambda_3) - \frac{C_2}{\lambda_3 T} \end{cases}$$

This is a definite system of 3 equations with 3 unknowns ( $\varepsilon_0(T)$ ,  $a$  and  $T$ ). Its solution gives the value of the measured non-gray body temperature as a function of the measured signals at the output of the three photo receivers

$$T = \frac{C_2}{\lambda_1 \lambda_2 \lambda_3 (A + B)} \quad (9)$$

where the coefficients  $A$  and  $B$  are:

$$A = \frac{\ln\left(\frac{I_1}{I_3} \cdot \frac{\lambda_1^5}{\lambda_3^5}\right)}{(\lambda_3 - \lambda_2)(\lambda_3 - \lambda_1)} \quad B = \frac{\ln\left(\frac{I_1}{I_2} \cdot \frac{\lambda_1^5}{\lambda_2^5}\right)}{(\lambda_3 - \lambda_2)(\lambda_1 - \lambda_2)}$$

### B. Development of a block functional diagram of a three-spectral pyrometer.

In fig.2 shows the functional diagram of the developed three-spectral pyrometer. The heated object emits a flux in a hemisphere. Part of the flux falls on the objective of the pyrometer and is collected on the beamsplitter.

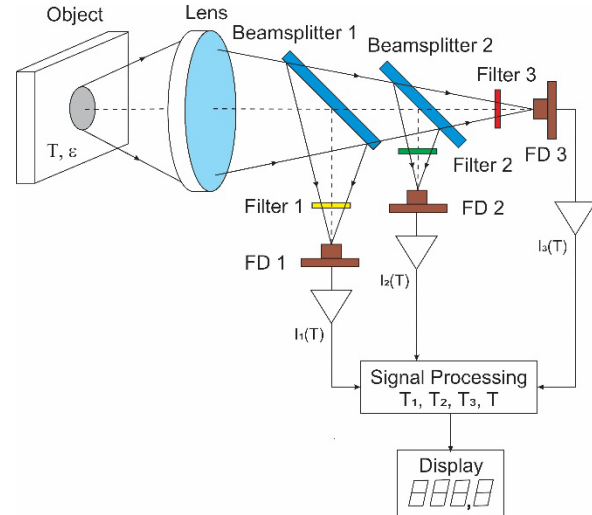


Fig. 2. Functional diagram of three-spectral pyrometer.

Three identical beamsplitters are provided in the scheme, which partially transmit and partially reflect the optical flow. The light dividers direct the radiation to three identical silicon photodiodes. Before the photo receivers, there are bandpass filters that limit the width of the spectral ranges. The parameters of the elements used in the pyrometer are shown in Table 1.

TABLE 1 THE PARAMETERS OF THE ELEMENTS USED IN THE THREE-SPECTRAL PYROMETER

	Spectral Band		
<b>Number</b>	1	2	3
<b><math>\Delta\lambda_i</math></b>	775-825nm	825-875nm	875-925nm
<b>Lens</b>	Achromatic Doublet AC254-100-B-ML - Thorlabs catalog		
<b>Beamsplitters</b>	BSW11 from Thorlabs catalog		
<b>Filters</b>	Bandpass Filters from Edmund Optics		
<b>Number</b>	# 84-789	#84-790 850	# 84-791
<b>CWL, <math>\lambda_i</math></b>	800 nm	nm	900 nm
<b>FWHM</b>	50 nm	50 nm	50 nm
<b>Photo Receivers</b>	Silicone Photodiodes Hamamatsu S2386		

### C. Schematic electrical diagram of the device

In fig.3 is shown the principle electrical circuit of device. Silicon photodiodes were used as photodetectors. Photodiodes produce electrical signals proportional to optical flow. The photocurrent  $I_{ph}$  through the photodiodes

is converted to voltage using operational amplifiers with feedback LM358.

In the block for electronic processing, these signals are amplified, their ratio is determined, which is subsequently converted into a value of the measured temperature of the controlled object.

An 8-bit microcontroller PIC18F252 is used to control the operation of the device, which has a 10-bit analog-to-digital converter. The controller has enough input-output ports and a sufficient amount of program memory in which the control program can be located.

Threshold voltages that determine the measuring range of the converter are respectively  $V_{REF-} = 0\text{ V}$  and  $V_{REF+} = 5\text{ V}$ .

The analog input signal to the ADC is represented by  $2^{10}$  or 1024 levels. The voltage increase step is determined by the formula:

$$\Delta U = \frac{V_{REF+}}{2^{10}} = \frac{5}{1024} = 4,883\text{ mV}$$

The functional scheme of the device is composed of three measuring channels. The voltage from the outputs of the current-voltage converters is fed to three analog inputs of the controller RA1/AN1, RA2/AN2 and RA3/AN3. The analog-to-digital converter is one and the inputs are switched. Only one input voltage is measured at any given time.

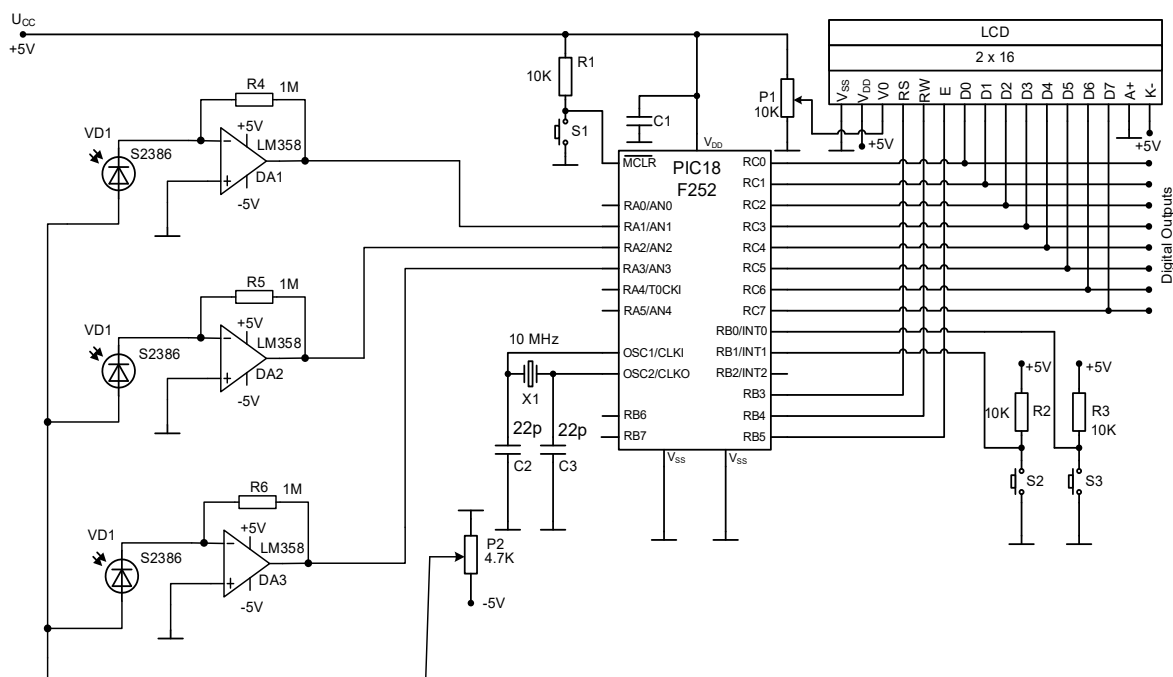


Fig. 3. Basic circuit diagram.

*D. Block chart of the algorithm of the program*

The block diagram of the control program algorithm is shown in fig. 4. At the beginning, the controller is initialized, constants and variables are defined, saving corresponding cells from the data memory for them. Next, it is determined which I/O ports will be used. Set which microcontroller pins to be digital inputs, analog inputs and digital outputs. The display is then initialized. The main program is a continuous loop that only breaks when the analog-to-digital converter has finished measuring the voltage. The processing of the result of each measurement takes place in a subroutine, which is started when an interruption occurs from the analog-to-digital converter.

*E. Connecting the LCD to the microcontroller*

At the beginning of the subroutine, the analog input for the next measurement is selected. After that, the result of the previous measurement is processed, which includes – hardware multiplication of the value of the measurement with a preset constant. The measured voltages from the three channels are compared. The result is converted from

hexadecimal to binary-decimal code. After that, the results of the measurements are displayed on the LCD display. First, the output addresses are determined, which means at which position each digit of the result should be displayed. The calculated values are then visualized. Finally, the subroutine starts the next measurement and returns to the main program.

A two-line alphanumeric LCD display is used, and 16 characters can be displayed on each line. To control the LCD module, a control bus is used, including pins RS, R/W, E, which are connected respectively to pins RB3, RB4, RB5 of the microcontroller initialized as digital outputs. The display data bus consists of 8 pins. With their help, the microcontroller communicates with the LCD module. Display pins D0, D1, D2, D3, D4, D5, D6 and D7 are initialized as inputs and are connected respectively to microcontroller pins RC0, RC1, RC2, RC3, RC4, RC5, RC6 and RC7 which are initialized as exits. At the beginning of the program, the display is also initialized.

Finally, the measured values are displayed on the display, and the user could choose different operating

modes of the device. The operation mode of the measuring system is mainly determined by the operation mode of the microcontroller, which is set by entering certain values in the registers defining the special functions. For a given measurement, the photodiodes can be used separately, and the result measured with each photodiode can be compared, or they can be used together, and a total result can be obtained.

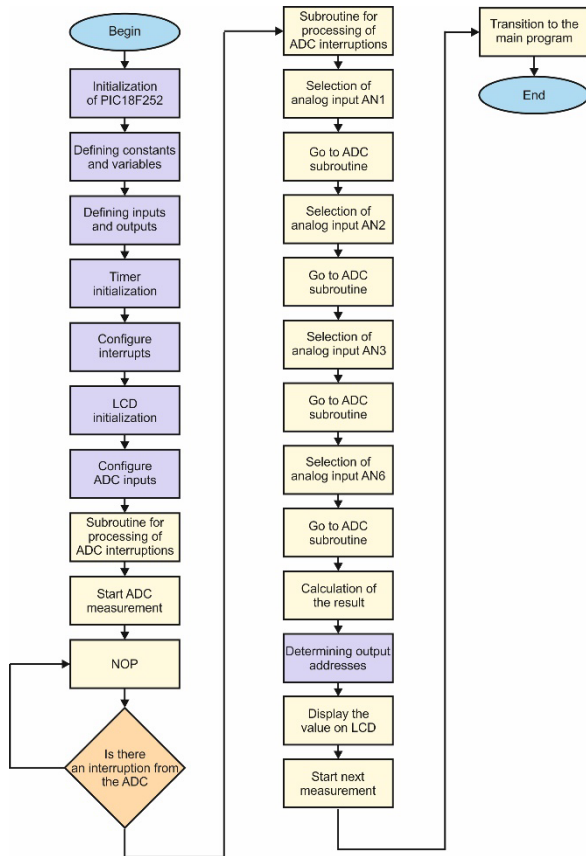


Fig. 4. Block chart of the algorithm of the program.

#### F. Algorithm for the operation of a device

The pyrometer operation algorithm can be presented with the following sequence.

1. The signals at the outputs of the three photodiodes are measured  $I_1(T)$ ,  $I_2(T)$  и  $I_3(T)$ .
2. According to expression (6), the ratio temperatures are calculated for the combinations containing two spectral ranges respectively

$$T_1 = T(\Delta\lambda_1, \Delta\lambda_2) = f\left(\frac{I_1}{I_2}\right)$$

$$T_2 = T(\Delta\lambda_2, \Delta\lambda_3) = f\left(\frac{I_2}{I_3}\right)$$

$$T_3 = T(\Delta\lambda_1, \Delta\lambda_3) = f\left(\frac{I_1}{I_3}\right)$$

3. It is checked whether the body is gray. It will be grayed out if  $T_1 = T_2$ . This equality is not strictly enforced in the general case. Nevertheless, the measured body can be assumed to be gray if the condition is met

$$T_1 = T_2 \pm \delta T \quad (10)$$

where  $\delta T$  is the permissible measurement error. If condition (10) holds, then the temperature of body is defined as

$$T = \frac{\sum_{i=1}^3 T_i}{3}$$

4. If condition (10) is not fulfilled, then the temperature of body is determined by expression (9).

The total error of the proposed three-spectral pyrometer is determined by the instrumental error, the blackbody pyrometer calibration error, the error due to the presence of parasitic reflections, the error due to the background radiation from near spaced high-temperature sources falling into the field of view of the device, and the methodological error caused by the approximation error of the emissivity [18],[19]. When measuring the temperature of highly heated metals ( $800 \div 2000$ )°C, the methodological error has the greatest influence. In the indicated temperature range, for many metals, an exponential dependence of  $\varepsilon = f(\lambda, T)$ . The use of narrow and close spectral intervals together with the exponential approximation of the emissivity leads to a small methodological error, which, depending on the temperature of the body and the width of the spectral interval, varies from 0,5% to 1%.

### III. CONCLUSION

A three-spectral pyrometer using three narrow spectral regions has been developed. Under substantiate assumptions about  $\varepsilon(\lambda, T) = const.$  temperature is determined as the average of three ratio temperatures for three wavelength pairs. In the most general case, a three-wave method is implemented by modeling the emissivity using an exponential function. The use of narrow and close spectral intervals in totality with the exponential approximation of the emissivity leads to a reduction of the uncertainty in the measurement of the temperature of non-gray bodies with an unknown dependence  $\varepsilon(\lambda, T)$ .

### REFERENCES

- [1] Z. M. Zhang, B. Tsai and G. Machin. Radiometric temperature measurements, Berlin: Elsevier, 2009.
- [2] V. Vavilov and D. Burleigh, Infrared Thermography and Thermal Nondestructive Testing, Springer International Publishing: New York, NY, USA, 2020.
- [3] K. Grujić, "A Review of Thermal Spectral Imaging Methods for Monitoring High-Temperature Molten Material Streams", Sensors, Vol. 23, Issue 3, Febr. 2023, doi: 10.3390/s23031130.
- [4] M.A. Khan, C. Allemand and T.W. Eagar, "Noncontact temperature measurement. I Interpolation based techniques", Review of Scientific Instruments, Vol. 62, Issue 2, pp. 392 – 402, 1991, doi: 10.1063/1.1142133.
- [5] T. Fu, X. Cheng and X. Yang, "Theoretical evaluation of measurement uncertainties of two-color pyrometry applied to optical diagnostics", Applied Optics, Vol. 47, Issue 32, pp. 6112 – 6123, Nov. 2008, doi: 10.1364/AO.47.006112.
- [6] B.K. Tsai, R.L. Shoemaker, D.P. DeWitt, B.A. Cowans, Z. Dardas, W.N. Delgass and G. J. Dail, "Dual-wavelength radiation thermometry: emissivity compensation algorithms", International

- Journal of Thermophysics, Vol. 11, Issue 1, pp. 269 – 281, Jan. 1990, doi: 10.1007/BF00503877.
- [7] P.B. Coates, “Multi-wavelength pyrometry”, *Metrologia*, Vol. 17, Issue 3, pp. 103 – 109, 1981, doi: 10.1088/0026-1394/17/3/006.
- [8] A. Araújo, “Analysis of multi-band pyrometry for emissivity and temperature measurements of gray surfaces at ambient temperature”, *Infrared Physics and Technology*, Vol. 76, pp. 365 – 374, May 2016, doi: 10.1016/j.infrared.2016.03.014.
- [9] W. Wójcik, V. Firago, A. Smolarz, I. Shedreyeva and B. Yeraliyeva, “Multispectral High Temperature Thermography”, *Sensors* 2022, 22, 742, doi: 10.3390/s22030742.
- [10] T. Fu, X. Cheng, X. Fan and J. Ding, “The analysis of optimization criteria for multi-band pyrometry”, *Metrologia*, Vol. 41, Issue 4, pp. 305 – 313, August 2004, doi: 10.1088/0026-1394/41/4/012.
- [11] V. Firago and W. Wojcik, “High-temperature three-colour thermal imager”, *Przeład Elektrotechniczny*, Vol. 91, Issue 2, pp. 208–214, 2015, doi: 10.15199/48.2015.02.47.
- [12] H. Madura, M. Kastek and T. Piatkowski, “Automatic compensation of emissivity in three-wavelength pyrometers”, *Infrared Physics and Technology*, Vol. 51, Issue 1, pp. 1 – 8, July 2007, doi: 10.1016/j.infrared.2006.11.001.
- [13] P. Saunders, “Reflection errors and uncertainties for dual and multiwavelength pyrometers”, *High Temperatures - High Pressures*, Vol. 32, Issue 2, pp. 239 – 249, 2000, doi: 10.1068/htrt201.
- [14] A. Sala, *Radiant Properties of Materials*, PWN & Elsevier, 1986.
- [15] D. P. DeWitt and J. C. Richmond, “Thermal radiative properties of materials,” in *Theory and practice of radiation thermometry*, 1988, pp. 171–175.
- [16] D.Y. Svet, Determination of the emissivity of a substance from the spectrum of its thermal radiation and optimal methods of optical pyrometry, *High Temp. – High Press.*, Vol. 8, Issue 5, pp. 493 – 498, 1976.
- [17] T. Hartsfield, A. Iverson and J. Baldwin, “Reflectance determination of optical spectral emissivity of metal surfaces at ambient conditions,” *Journal of Applied Physics*, Vol.124, Issue 10, Sept. 2018, doi: 10.1063/1.5042601.
- [18] M.J. Marinov, B.I. Stoychev, D.M. Guteva and M.V. Georgiev, “Computer modeling and geometric analysis of Click-Clack mechanisms”, *Journal of Mechanics of Machines*, vol. 118, pp.35-39, 2016.
- [19] Dichev, D., F. Kogia, H. Nikolova, D. Diakov. A Mathematical Model of the Error of Measuring Instruments for Investigating the Dynamic Characteristics. *Journal of Engineering Science and Technology Review*. Volume 11, Issue 6, 2018, pp. 14-19, doi: 10.25103/jestr.116.03.

# *Influence of Adding Polypropylene(PP) into Polyethylene(PE) on Mechanical Properties of Geocells*

**Sabi Sabev**  
Technical University of Sofia,  
Branch Plovdiv  
Plovdiv, Bulgaria  
sabi\_sabev@tu-plovdiv.bg

**Plamen Kasabov**  
Technical University of Sofia,  
Branch Plovdiv  
Plovdiv, Bulgaria  
plamen.kasabov@abv.bg

**Konstantin Chukalov**  
Technical University of Sofia,  
Branch Plovdiv  
Plovdiv, Bulgaria  
konstantin\_chukalov@abv.bg

**Valeri Bakardzhiev**  
Technical University of Sofia,  
Branch Plovdiv  
Plovdiv, Bulgaria  
bakardzhiev@tu-plovdiv.bg

**Abstract.** In the article, it will be considered what is the influence of the addition of 10% PP into a polyethylene mixture compared to a mixture of polyethylene on the main mechanical characteristics of geocells - hardness, maximum tensile strength, strength of the internal structural junctions (welds). It will be analyzed the interrelationships between the measured mechanical parameters

**Keywords:** geocells, PE/PP blends.

## I. INTRODUCTION

Geocells (fig.1) are a network of plastic strips that are ultrasonically welded. The most common material for geocells is PE, but due to the expanding application of these products, requirements for higher strength characteristics are also increasing especially for loading applications. One of the directions for increased strength characteristics is adding a harder material into mixture of PE such as PP. This is a rational option for increasing the strength characteristics due to the unreduced productivity during extrusion as well as easy access and cost of PP. Although the combination of PE and PP has been studied in the literature, the studies on mechanical properties of the relatively new product geocells are not many and researches about them may lead to new applications. One of the big disadvantages of geocells application is the weak strength properties.



Fig. 1. Geocells.

## II. MATERIALS AND METHODS

Strips of perforated high-density polyethylene sheets, also known as cell-walls, are welded together at locations known as junctions [1]. Geocells are used both in industrial practice mainly in construction infrastructure - highways, railways, dam walls, etc., as well as in consumer use - as a basis for various types of flooring and various garden applications [2] - [5]. Their use is increasing due to regulatory requirements for their application in first-class roads, as well as their engineering advantages - lightness, durability, possibility of occupying large roof areas, easy installation, individual sizes, etc. however, its applications

Print ISSN 1691-5402

Online ISSN 2256-070X

<https://doi.org/10.17770/etr2023vol3.7244>

© 2023 Sabi Sabev, Plamen Kasabov, Konstantin Chukalov, Valeri Bakardzhiev.

Published by Rezekne Academy of Technologies.

This is an open access article under the [Creative Commons Attribution 4.0 International License](https://creativecommons.org/licenses/by/4.0/).

are limited because of the sizeable long-term deformation under constant loading and poor tensile strength [6] - [9].

The most common used material for geocells offered by manufacturers is polyethylene with high density. This is due to the good mechanical and physical characteristics of polyethylene - hardness, elasticity, dielectric strength, moisture resistance, high chemical resistance [10].

The main disadvantages of polyethylene are the weak resistance to light and heat, but due to the specifics of its application, geocells are not exposed to direct light and high temperatures, which also predisposes to its use. From an economic point of view, there are also prerequisites for its use, because on one hand, primary polyethylene has a low cost and is widely available, and also the fact that High-density polyethylene (HDPE) is one of the most popular plastics used in industry [11], [12].

The additives that are traditionally used for geocells are different colorants, depending on the application of the product, as well as-UV stabilizer that improves the product's resistance to light [13].

Other anti-aging additives can be used to improve the technological qualities, fillers and plasticizers, etc. depending on the specific application of the product. In general, polyethylene has established itself as the main material due to the very good combination of technical and economic characteristics.

On another hand PP is a polymer with good mechanical properties-chemical resistance, weldability, stiffness, economical-easy access, low cost, ecological-recyclability. Generally polypropylene is a promising plastic by showing its great chemical, physical and mechanical properties PP applications include, but not limited to, fabrics, films, bottles, sheets and automotive products [14].

Blends of PE/PP have been largely studied because they make up 2/3 of the world's volume of plastics and are fully recyclable. For example, blow molding grade of HDPE as a bottle and injection molding grade of PP as a cap are often used to produce detergent bottles [15]. The proportions used in the article is 50/50 between virgin materials and recycled materials, because the production of geocells is associated with a large technological waste, which is reused.

The investigated properties are the major mechanical properties of geocells-hardness according to Shore D(according DIN 53505, maximum tensile strength(according ISO 10139, strength of internal structural junctions (welds) - according ISO 13426, method B. 10 samples were tested according every selected standardized method.

All tests are in accordance with the relevant test standards (fig 2), being observed the test conditions for the dimensions of the specimens, the range, the rate of deformation and the geometry of the testing machine and of the gripping jaws, as well as the surrounding environment.

The used machine equipment is calibrated according the metrology requirements. The test samples have an

average thickness of 1.4 mm (deviation of maximum 5%, width of 100 and 150 mm], the results of samples composed of 100% PE and additives for color and anti UV agent were compared, as well as samples with 90% PE and 10% PP with the same additives.

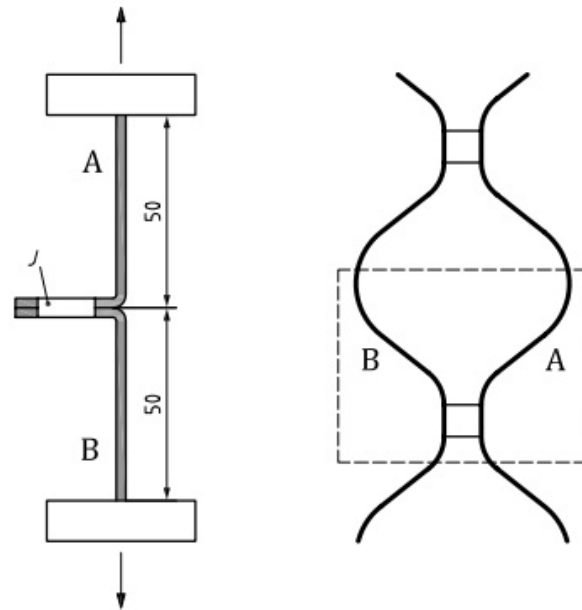


Fig. 2. Dimensions and place to take the sample (ISO 13426, method B) [16].

### III. RESULTS AND DISCUSSION

The results are statistically processed. the trends in the mechanical indicators are shown, which may be used for other ratios as well. The numbers of tested samples is sufficient for statistical sampling,

The research can be used for other products from the same materials and additives and is not limited to geocells:

- Maximum tensile strength =  $R_m$ (kN/m)  
 $R_m = F/b$   
 Where  
 F - maximum applied force (kN)  
 b - width of the sample (m)

The standardized dimension unit is kN/m.

Measured maximum tensile strength of 10 samples of both mixtures - fig 3, fig. 4. PE mixture results  $R_m$ {kN/m): 26.5, 27.7, 27.1, 27.3, 25.7, 26.9, 26.7, 27.7, 24.7, 27.3.

PE/PP mixture results  $R_m$ {kN/m): 29.6, 27.7, 26.4, 28.7, 27.8, 28.7, 26.6, 28.4, 27.2, 28.1

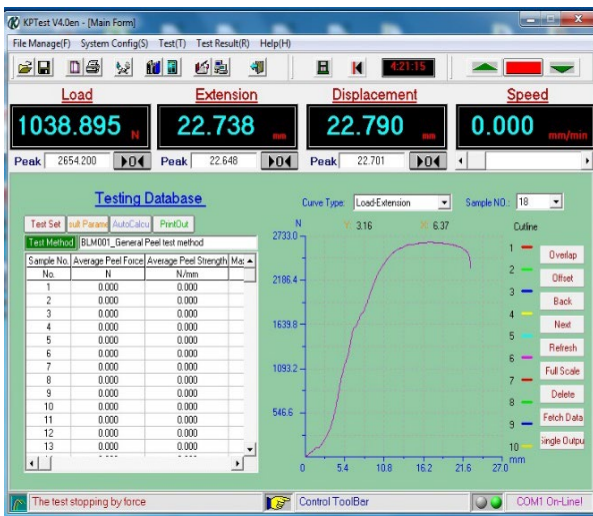


Fig. 3. Test result, sample No1, Force-1.65 kN, width of the sample-100mm, mixture PE.

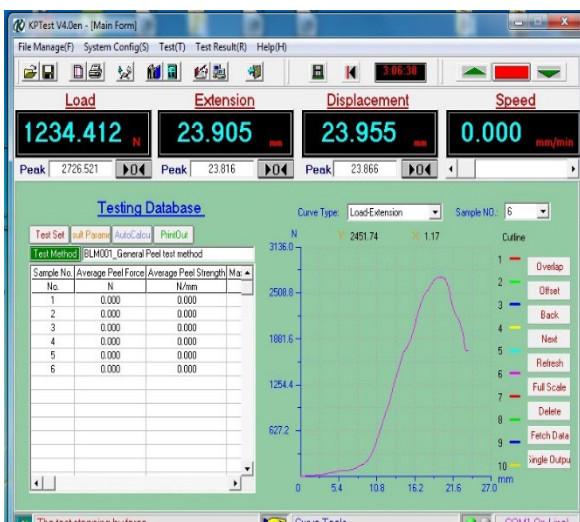


Fig. 4. Test result, sample No9, (mixture PE/PP).

The measured results show an average maximum tensile strength of a PE blend of 26.76 kN/m and an average maximum tensile strength of a blend of 90% PE and 10% PP of 27.92 kN/m or an increase in average ultimate tensile strength of 4.3% at addition of 10% PP. The results are statistically processed (fig. 5). Overall, the destruction figures are correct, no deviations are observed, testing conditions are correct, there is repeatability of the results, which is also proven by the regression analysis, although tensile strength testing of elastic materials is very sensitive.

The destruction graphs show no deviation from the test conditions. The maximum tensile strength of geocells is an essential technical characteristic in declarations of conformity and is often a leading mechanical characteristic about the standardization of geocells as a product. The increasingly wide application of geocells leads to increasingly higher required results, especially of the essential characteristics depending on their application.

The addition of PP into PE increases the average maximum tensile strength and one of the options for higher requirements of maximum tensile strength according to the specification. No differences were observed in the extrusion performance of the two blends. The current results may be used as a basis for the use of different amounts of PP in PE.

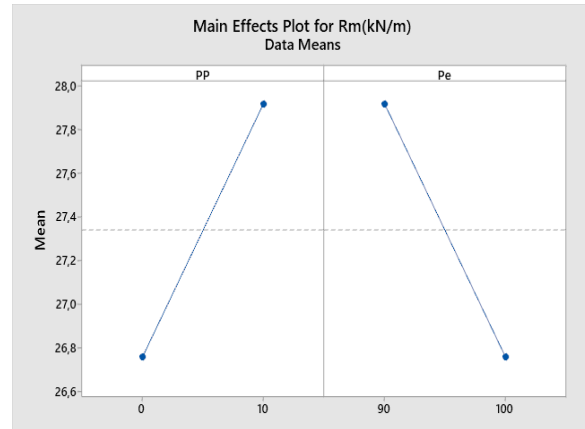


Fig. 5. Main effect plot for Rm.



Fig. 6. Test result, sample 3, mixture PE.

- Hardness

Hardness was measured according to the standardized Shore D testing method for polymers according to DIN 53505, with the range of the hardness indenter consistent with the theoretical results of the two mixtures. Hardness measures the hardness of elastomers by measuring the

penetration depth.[17] Geocell testing according Shore D is suitable because of their textured surface. Hardness is not an essential technical characteristic in the declarations of conformity, but the relationship between the results of the measured hardness and other mechanical parameters, the study is important and can be used in engineering practice, since hardness measurement is a nondestructive test. Shore-D hardness gives additional help for tribological analysis of engineering polymers and their composites[18]. Tests according Shore D are measured in dimensionless units. The results are shown in fig. 6, fig7.

Hardness results (PE mixture)-Hsh-45.8, 44.6, 48.2, 46.7, 46.5, 47.8, 44.5, 47.7, 44.5, 45.5.

Hardness results (PE/PP mixture)-Hsh-56, 56, 57.3, 59.4, 58.2, 57.7, 59.5, 57.5, 58, 58.3.

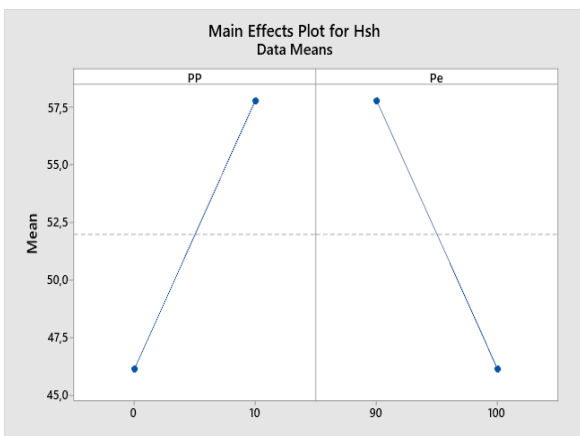


Fig. 7. Main effects plot for Hsh.

The average Shore D hardness values of both mixtures of 46.16 and 57.79 show a significant increase in hardness with the addition of 10% PP by 26.78%. It should not be overlooked that the increased hardness causes technological problems, because it slows down and makes the cutting process more difficult. Cutting is often a finishing operation during manufacturing the product. Also it is possible to get cracks as a result of the increased hardness, during cutting which affects the quality and manufacturing rate of the product. These problems may be solved by choosing technological processes for the manufacturing of the product, in which there are no cutting processes.

- Maximum tensile strength for internal structural junctions are shown in fig 8, fig 9, fig. 10.

The connection mode of junctions is crucial to the performance of geocells [19].

Maximum tensile strength for internal junctions {PE mixture}. Results {kN/m} - PE mixture: 12.2, 11.5, 11.6, 11.1, 11, 10.9, 10.6, 11.3, 10.4, 11.2.

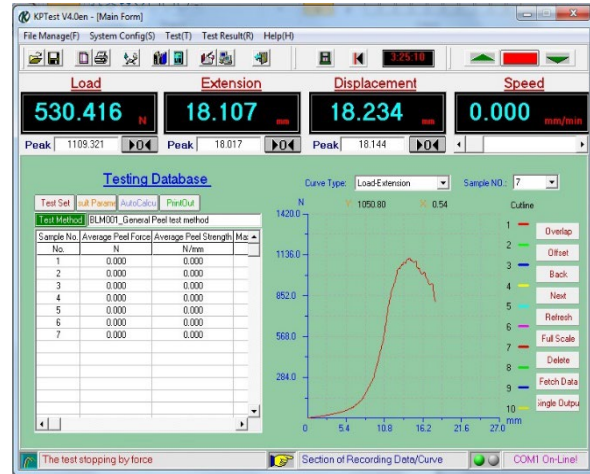


Fig. 8. Test result, sample 5, width 100 mm.

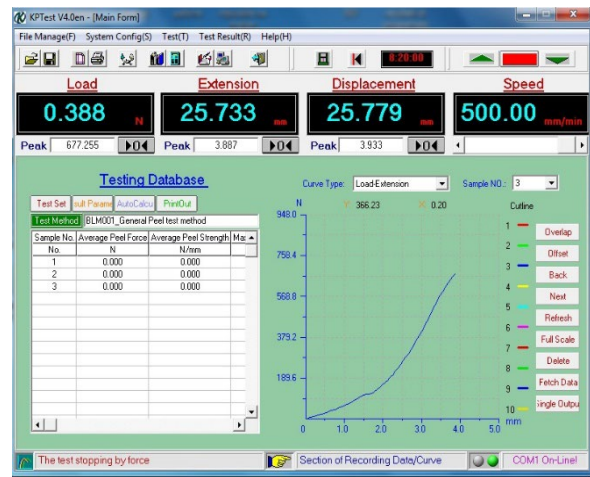


Fig. 9. Test result, sample 4, width 100 mm.

The results show a significant decrease in the strength of the internal structural junctions with the addition of 10% PE into PP. This is expected due to increased maximum tensile strength of strips and hardness with the addition of PP.

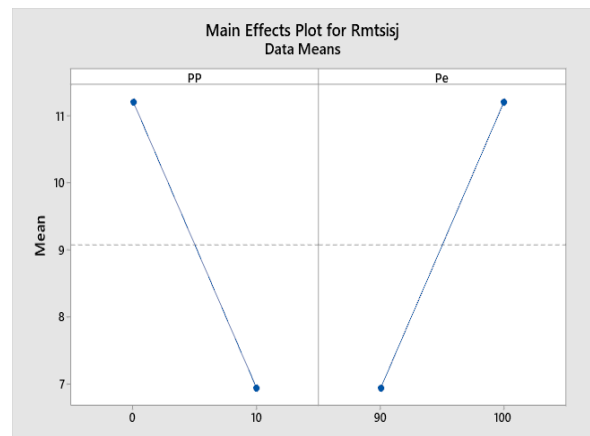


Fig. 10. Main effect plot for Rmstsj.

The results, compared with other authors [20] - [22], are reliable and no deviations were observed in the regression analyses. They may be used and applied in engineering practice. The statistical error has a negligible impact as the range of results is close.

#### IV. CONCLUSIONS

The test results showed that the addition of 10% PP in PE increased the stiffness and ultimate tensile strength, but reduced the strength of the internal connections of the structure. Given the wider application of the product and the fact that the ultimate tensile strength is part of a harmonized standard for this product, the addition of PP is justified when higher requirements are set for this property. The addition of PP does not change the productivity of the entire technological process of creating the product. However, the increase in hardness should not be ignored, which can lead to a reduced quality when cutting the product during its final processing. The results may be used as a basis and for other ratios between PP and PE. The increased strength properties may expand geocells application.

#### V. ACKNOWLEDGMENTS

The scientific research, the results of which are presented in the paper, was financed by project BG05M2OP001-1.002-0023 - Competence Center "Intelligent Mechatronic, Eco - and Energy - Saving Systems and Technologies" of Technical University of Sofia, branch Plovdiv

#### REFERENCES

- [1] Liu A., Deng A., Jaksa M., Failure mechanisms of geocell walls and junctions, *Geotextiles and Geomembranes*, 2019 - Elsevier
- [2] Chatterjee K., Singh A., Kumar A., Use of geocells is one of the most economical methods of soil improvement that is used to increase strength, Springer Singapore.2020
- [3] Song G., Song X., He S., Kong D.,Zhang S.,Soil Reinforcement with Geocells and Vegetation for Ecological Mitigation of Shallow Slope Failure.2022
- [4] Gali M., Geocells for Transportation Geotechnical Applications, *Indian Geotechnical Journal* 51(11):1-12, 2021
- [5] Arefpanan S., Sharafi A., Experimental investigation regarding the mechanical properties of poriferous Geocells produced in Iran,2022
- [6] Zhao Y.,Lu Z.,Yao H.,Nie. H.,Development and mechanical properties of HDPE/PA6 blends: Polymer-blend geocells.2021
- [7] Schary Y.,Neoloy—Developing a Novel Polymeric Alloy for Geocells, *Geotextiles and Geomembranes*, Volume 49, Issue 6, p. 1600-1612.2020
- [8] Vinayapriya M.V., Jose S., Performance of Geocell Reinforced Soil Beds. *Proceedings of the Indian Geotechnical Conference 2019, IGC-2019 Volume V*,2021
- [9] Vibhoosha M P ,Bhasi A.,Nayak S., Review on the Design, Applications and Numerical Modeling of Geocell Reinforced Soil, *Geotechnical and Geological Engineering* 39(2):1-23,2920
- [10] Zumbilev A.,*Materials science*,2006.
- [11] Bagli S.,Diverse Applications of Geocells for Highways -Two Case Studies from the North-East ,*Geotechnics for Natural and Engineered Sustainable Technologies*,2018
- [12] Chrysafi I., Asimakidou T.,Michailidou G., Xanthopoulou E., Tziamtzi T., Zamboulis A.,Bikiaris D., Characterization of the Thermal, Structural, and Mechanical Properties of Recycled HDPE,2022
- [13] Rai K.,Jaiswai D.,Pandey A.,Agrawai S.,Agrawai A.,UV-B: Boon or Curse?,2023
- [14] Hisham A. Maddah, Polypropylene as a Promising Plastic: A Review, *American Journal of Polymer Science*,2016
- [15] Karaagac E., Koc T., Archodoulaki V.,Choosing an Effective Compatibilizer for a Virgin HDPE Rich-HDPE/PP Model Blend, 2021
- [16] ISO 13426, method B, 2019
- [17] Bessling M.,Manko L.,Orlowsky L.,Quantification of the Transversal Fiber Strand Stiffness of Textiles Used in Textile-Reinforced Concrete via Shore Hardness.2022
- [18] Ando M.,Calascka G.,Czigany T.,SHORE D HARDNESS OF CAST PA6 BASED COMPOSITES,2018
- [19] Zuo Z.,Yang G.,Liu Y.,Yu F.,Experimental investigations on failure mechanism of different junction connections of geocells *Appl.Sci.* **2022**, *12*(11),5343; <https://doi.org/10.3390/app12115343>,2021
- [20] Yang G.,Su P.,Xu P.Zuo Z.,Wang.Z.,Wang H.,Experimental Investigation on Failure Mechanisms of HDPE Welded Geocell Junctions under Different Clamping Distances, *Appl. Sci.* **2022**, *12*(11),5343; <https://doi.org/10.3390/app12115343>,2022
- [21] Bhanushali S.,Srivats D.,Mishra P.,More A., Silica/coconut shell charcoal/high-density polyethylene/linear low-density polyethylene composites, DOI:10.1007/s13726-023-01146-z,2023
- [22] Gill Y.,Khurshid M.,Irfan M.,Upscale recycling of nonwoven polypropylene waste using a novel blending method, <https://doi.org/10.1002/app.52927>, 2022.

# Determination of the Dynamic Modulus of Linear Deformations of Reinforced Highly Filled Polymer Concrete Composites During Curing

**Sabi Sabev**  
Technical University of Sofia,  
Branch Plovdiv  
Plovdiv, Bulgaria  
sabi\_sabev@tu-plovdiv.bg

**Plamen Kasabov**  
Technical University of Sofia,  
Branch Plovdiv  
Plovdiv, Bulgaria  
plamen.kasabov@abv.bg

**Konstantin Chukalov**  
Technical University of Sofia,  
Branch Plovdiv  
Plovdiv, Bulgaria  
konstantin\_chukalov@abv.bg

**Valeri Bakardzhiev**  
Technical University of Sofia,  
Branch Plovdiv  
Plovdiv, Bulgaria  
bakardzhiev@tu-plovdiv.bg

**Abstract.** The objects of this study are reinforced polymer concrete composites with epoxy matrix and mineral dispersion fillers. Dynamic modulus of linear deformations has been measured according to the standardized dynamic testing method ASTM E1876 - 02. The quantitative values of the modulus are obtained by the action of longitudinal and bending. After statistical processing of the obtained results has been established the influence of fiber in the composition on the dynamic characteristic.

**Keywords:** vibrations, dynamic, epoxy based concrete, high strength polymer concrete, fillers, reinforced.

## I. INTRODUCTION

Polymer concrete (PB) composites are widely used in engineering practice, as alternative materials for bodies and housings of metal-cutting machines. The application of these composites as alternative non-metallic structural materials is an innovative activity that creates prerequisites for improving technical and operational qualities of the manufactured machines and devices such as:

- Static and dynamic stability;
- Thermal behavior;
- Corrosion resistance;

The epoxy-based PB composite used in this study has high strength and good wear resistance, sliding property, and UV stability [1]-[6]. In recent years, the use of organic and inorganic fillers, as well as waste up to 5%, has been

observed in polymer concrete to improve and modify its properties [8]-[12]. The article has an experimental focus and its main goals are:

- determining the influence of the amount of fibers on the dynamic modulus of linear deformations.
- study on change of the dynamic modulus of linear deformations during the curing of PB composites.

The composites were manufactured and tested in the laboratories of TU-Sofia, branch Plovdiv.

## II. MATERIALS AND METHODS

Determination of the dynamic modulus of linear deformations due to longitudinal and flexural fundamental freely damped oscillations.

The specimen is placed on prismatic supports clamped immovably to a base. The supports are located at a distance of 0.224l from both ends of the specimen, according to ASTM E1876-15 [7]. Impulse dynamic impact is applied to the beam with an exciter -type impact hammer, Fig.1. In this way, model of an oscillating dynamic system with distributed parameters is created.

Print ISSN 1691-5402

Online ISSN 2256-070X

<https://doi.org/10.17770/etr2023vol3.7296>

© 2023 Sabi Sabev, Plamen Kasabov, Konstantin Chukalov, Valeri Bakardzhiev.

Published by Rezekne Academy of Technologies.

This is an open access article under the [Creative Commons Attribution 4.0 International License](https://creativecommons.org/licenses/by/4.0/).

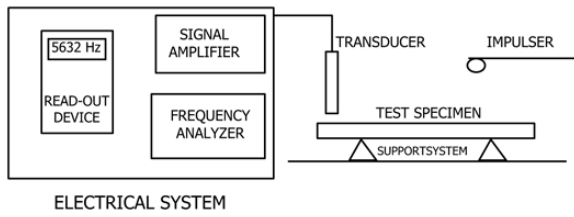


Fig. 1. Vibration test setup.

The dynamic modulus is defined as follows:

$$E_D = 0.9465(mf_f^2 / b)(l^3 / h^3)T_1 \quad (1)$$

where:

- $E_D$  - dynamic modulus of Young;
- $m$  - beam mass;
- $b$  - beam width;
- $l$  - beam length;
- $h$  - beam thickness;
- $f_f$  - Fundamental flexural resonance frequency

Fig.2 ;

$T_1$  - Correctional coefficient.

$$T_1 = \frac{1.000 + 6.585(1 + 0.0752\mu + 0.8109\mu^2)(h/l)^2 - 0.868(h/l)^4 - 8.340(1 + 0.2023\mu + 2.173\mu^2)(h/l)^4}{1.000 + 6338(1 + 0.1408\mu + 1.536\mu^2)(h/l)^2} \quad (2)$$

where:

$\mu$  - Coefficient of Planck

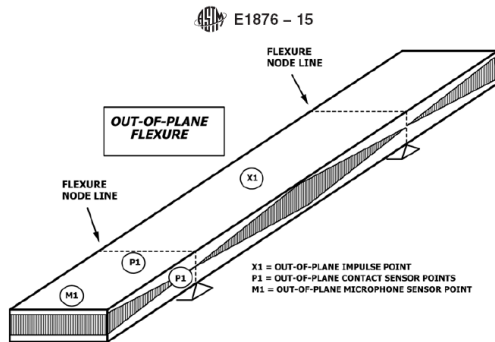


Fig. 2. Measurement of the vibrations of torque.

Determination of dynamic modulus from due to longitudinal free damped vibrations :

The specimen is placed on prismatic supports clamped immovably to a base. At one end of the beam, a frontal impulse dynamic impact is applied, and on the opposite side, the frontal response is measured using a microphone, Fig.3. In this way, longitudinal free damping oscillations are realized. The dynamic modulus of elasticity  $E_I$  will be determined according to the formula:

$$E_I = 4f_l^2 l^2 \rho_o \quad (3)$$

where:

- $f_l$  - fundamental frequency in longitudinal vibrations
- $l$  - length of a sample
- $\rho_o$  - density of a sample

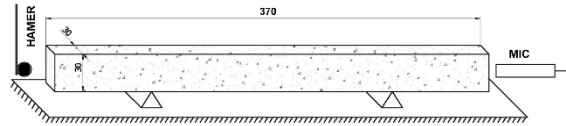


Fig. 3. Longitudinal vibration reasearch setup.

The experimental samples have a shape of a rectangular parallelepiped (beam type) with dimensions 30x30x370mm, Fig.3. They comply to the generally accepted standardization norms for polymer concrete samples. The number of PB compositions is 3, for which a total of 9 test bodies were cast (3 pieces of each composition). A vibration stand with an inverter control was used during casting, Fig.4. The samples have been vibrated for 20 min.



Fig. 4. Vibration stand.

The mold for casting the test samples is three-nested, detachable, made of wood material, Fig.5. To eliminate random errors, the equipment allows simultaneous receipt of three test samples from one PB composition.



Fig. 5. Casting shape type b.

The total amount of the mixture is taken equal to unity (or 100%), and is a part of the I component in the mixture. The components meet the following conditions:

$$X_1 + X_2 + X_3 + X_4 = 100\% \quad (4)$$

The following materials for the individual components are used:

$X_1$  - binder – epoxy resin

$X_2$  - fine filler - quartz flour;

$X_3$  -, PP Fibers M12 ;

$X_4$  - granular filler – fine and course sand.

TABLE 1 COMPONENTS

N <sub>o</sub>	X1	X2	X3	X4
4	16%	3.5%	0.3%	80.2%
5	16%	3.5%	0.0%	80.5%
6	16%	3.5%	0.7%	79.8%



Fig. 6. PB samples.

The mass of the PB samples, Fig. 6, was measured using an electronic balance, Fig. 7 with an accuracy of 1g.



Fig. 7. Electronic balance.

### III. RESULTS AND DISCUSSION

Fig. 8 shows the experimental setup for determining the two types of dynamic modules.



Fig. 8. Experimental set up.

The data about the value of the frequencies necessary for the calculation of the modules is obtained from the autospectral characteristic, Fig.9-10.

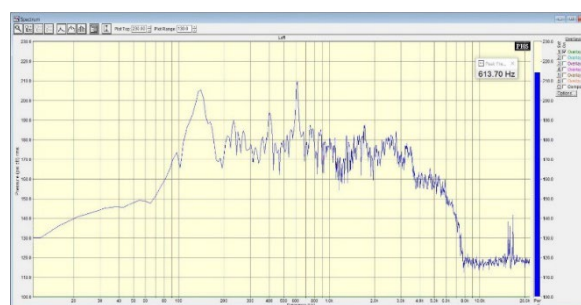


Fig. 9. Flexural spectral analysis of 5.3 day 120.



Fig. 10. Longitudinal spectral analysis of 5.3 day 120.

The obtained experimental results for the modulus of linear deformations are structured in tabular form. Table 2 presents the results of testing of sub-base 6 on longitudinal and flexural vibrations. Accordingly, Tables 3 and 4 present another results for the 5th and 6th sample.

TABLE 2 EXPERIMENTAL RESULTS

	N <sub>o</sub>	$f_l$ [Hz]	$f_f$ [Hz]	$E_l$ [Pa]	$E_f$ [Pa]
Day 2	6.1	4107	533	1.78E+10	1.18E+10
	6.2	4112	608	1.79E+10	1.55E+10
	6.3	4032	538	1.72E+10	1.20E+10
Day 8	6.1	4200	581	1.87E+10	1.40E+10
	6.2	4360	570	2.01E+10	1.37E+10
	6.3	4280	592	1.94E+10	1.46E+10
Day 13	6.1	4263	603	1.92E+10	1.51E+10
	6.2	4374	576	2.02E+10	1.39E+10
	6.3	4322	597	1.98E+10	1.48E+10
Day 21	6.1	4235	581	1.90E+10	1.40E+10
	6.2	4363	570	2.01E+10	1.37E+10
	6.3	4321	592	1.98E+10	1.46E+10
Day 120	6.1	4242	589	1.90E+10	1.44E+10
	6.2	4333	570	1.99E+10	1.37E+10
	6.3	4274	597	1.93E+10	1.48E+10

TABLE 3 EXPERIMENTAL RESULTS

	$\xi_i$	$f_l$ [Hz]	$f_f$ [Hz]	$E_l$ [Pa]	$E_f$ [Pa]
Day 2	5.1	4608	608	2.25E+10	1.54E+10
	5.2	4635	603	2.27E+10	1.53E+10
	5.3	4591	603	2.23E+10	1.51E+10
Day 8	5.1	4613	614	2.25E+10	1.57E+10
	5.2	4656	608	2.29E+10	1.56E+10
	5.3	4618	608	2.26E+10	1.54E+10
Day 13	5.1	4586	608	2.23E+10	1.54E+10
	5.2	4700	614	2.34E+10	1.58E+10
	5.3	4672	614	2.31E+10	1.57E+10
Day 21	5.1	4618	614	2.26E+10	1.57E+10
	5.2	4688	614	2.32E+10	1.58E+10
	5.3	4665	614	2.30E+10	1.57E+10
Day 120	5.1	4595	614	1.57E+10	2.23E+10
	5.2	4667	608	1.56E+10	2.30E+10
	5.3	4646	614	1.57E+10	2.28E+10

TABLE 4 EXPERIMENTAL RESULTS

	$\xi_i$	$f_l$ [Hz]	$f_f$ [Hz]	$E_l$ [Pa]	$E_f$ [Pa]
Day 2	4.1	4175	600	1.88E+10	1.50E+10
	4.2	4189	608	1.87E+10	1.56E+10
	4.3	4177	603	1.87E+10	1.51E+10
Day 8	4.1	4197	603	1.86E+10	1.51E+10
	4.2	4185	608	1.86E+10	1.56E+10
	4.3	4187	608	1.85E+10	1.54E+10
Day 13	4.1	4245	600	1.91E+10	1.50E+10
	4.2	4247	608	1.91E+10	1.56E+10
	4.3	4245	608	1.91E+10	1.54E+10
Day 21	4.1	4253	603	1.91E+10	1.51E+10
	4.2	4237	608	1.90E+10	1.56E+10
	4.3	4274	609	1.93E+10	1.54E+10
Day 120	4.1	4247	602	1.91E+10	1.51E+10
	4.2	4242	608	1.90E+10	1.55E+10
	4.3	4265	608	1.92E+10	1.54E+10

TABLE 5 CHANGA OF THE MODULUS

	Longitudinal			Flexural		
	6.1	6.2	6.3	6.1	6.2	6.3
Day 2	1.78E+10	1.79E+10	1.72E+10	1.18E+10	1.55E+10	1.20E+10
Day 8	1.87E+10	2.01E+10	1.94E+10	1.40E+10	1.37E+10	1.46E+10
Day 13	1.92E+10	2.02E+10	1.98E+10	1.51E+10	1.39E+10	1.48E+10
Day 21	1.90E+10	2.01E+10	1.98E+10	1.40E+10	1.37E+10	1.46E+10
Day 120	1.90E+10	1.99E+10	1.93E+10	1.44E+10	1.37E+10	1.48E+10
Delta	7.7%	13.1%	14.9%	28.0%	13.8%	23.1%
	11.93%			21.63%		

TABLE 6 CHANGING OF THE MODULUS

	Longitudinal			Flexural		
	4.1	4.2	4.3	4.1	4.2	4.3
Day 2	1.84E+10	1.86E+10	1.85E+10	1.50E+10	1.56E+10	1.51E+10
Day 8	1.86E+10	1.85E+10	1.85E+10	1.51E+10	1.56E+10	1.54E+10
Day 13	1.91E+10	1.91E+10	1.91E+10	1.50E+10	1.56E+10	1.54E+10
Day 21	1.91E+10	1.90E+10	1.93E+10	1.51E+10	1.56E+10	1.54E+10
Day 120	1.91E+10	1.90E+10	1.92E+10	1.51E+10	1.55E+10	1.54E+10
Delta	3.8%	3.0%	4.7%	0.9%	0.0%	1.9%
	3.8%			0.93%		

TABLE 7 CHANGING OF THE MODULUS

	Longitudinal			Flexural		
	5.1	5.2	5.3	5.1	5.2	5.3
Day 2	2.25E+10	2.27E+10	2.23E+10	1.54E+10	1.53E+10	1.51E+10
Day 8	2.25E+10	2.29E+10	2.26E+10	1.57E+10	1.56E+10	1.54E+10
Day 13	2.23E+10	2.34E+10	2.31E+10	1.54E+10	1.58E+10	1.57E+10
Day 21	2.26E+10	2.32E+10	2.30E+10	1.57E+10	1.58E+10	1.57E+10
Day 120	2.23E+10	2.30E+10	2.28E+10	1.57E+10	1.56E+10	1.57E+10
Delta	1.4%	2.8%	3.6%	1.8%	3.6%	3.6%
	2.59%			3.00%		

As can be seen from the obtained experimental results in the tables above, the modulus of PB composites was tested at 2, 8, 13, 21, 120 days.

The percentage change of the modulus of linear deformations during the curing of the samples was calculated. The results are tabulated in Tables 5-7.

For a better visualization of, the results are presented graphically, Fig.11 -16.

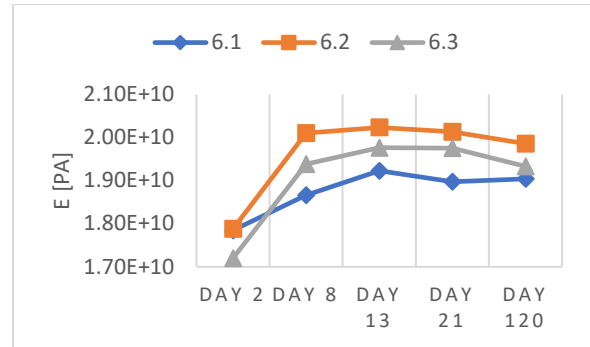


Fig. 11. Results of the modulus by longitudinal vibrations.

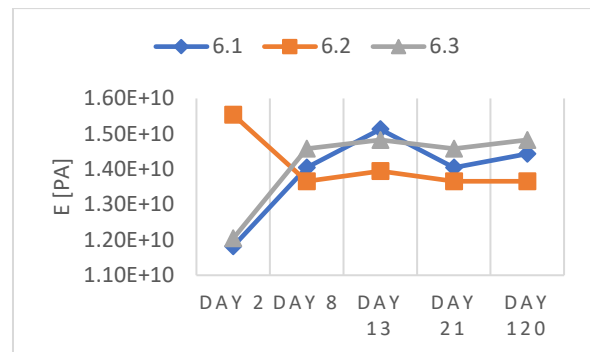


Fig. 12. The results of the modulus by flexural vibrations.

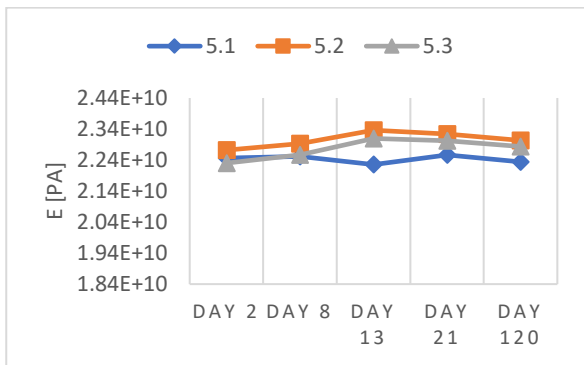


Fig. 13. The results of the modulus by longitudinal vibrations.

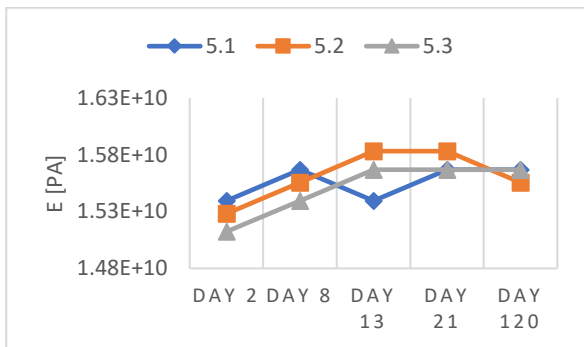


Fig. 14. The results of the modulus by flexural vibrations.

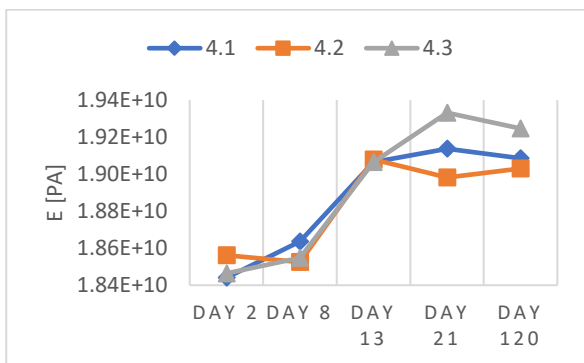


Fig. 15. The results of the modulus by longitudinal vibrations.

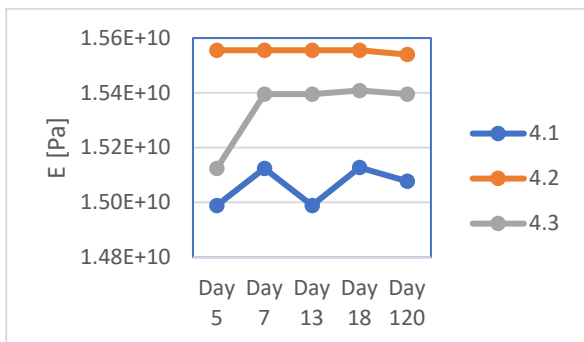


Fig. 16. The results of the modulus by flexural vibrations.

Using the Minitab software, the influence of the fibers used for reinforcement on the modulus of linear deformations was analyzed. The obtained results of the analysis are presented below.

Regression Analysis: E<sub>l</sub> versus Filler

Regression Equation

$$E_l = 2.2767 - 0.2933 \text{ Filler} + 0.05083 \text{ Filler} * \text{Filler}$$

Coefficients

Term	Coef	SE Coef	T-Value	P-Value	VIF
Constant	2.2767	0.0180	126.83	0.000	
Filler	-0.2933	0.0229	-12.82	0.000	13.00
Filler*Filler	0.05083	0.00550	9.25	0.000	13.00

Model Summary

S	R-sq	R-sq(adj)	R-sq(pred)
0.0310913	97.95%	97.27%	95.39%

Analysis of Variance

Source	DF	Seq SS	Seq MS	F-Value	P-Value
Regression	2	0.277089	0.138544	143.32	0.000
Filler	1	0.194400	0.194400	201.10	0.000
Filler*Filler	1	0.082689	0.082689	85.54	0.000
Error	6	0.005800	0.000967		
Total	8	0.282889			

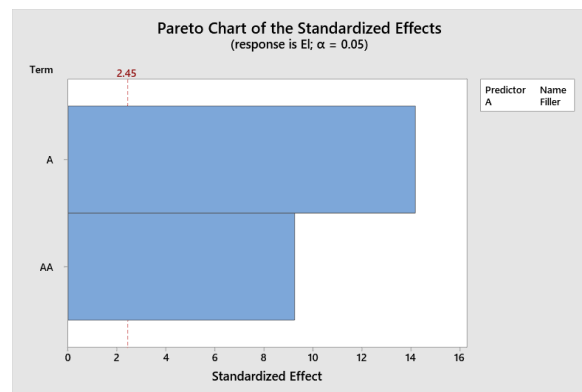


Fig. 17. Influence of fibres on a modulus during bending vibrations.

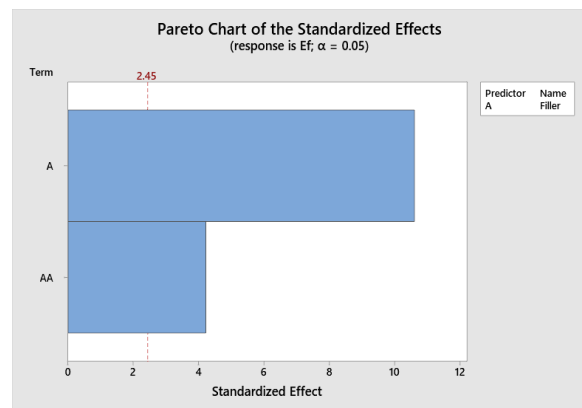


Fig. 18. Influence of fibres on the modulus by flexural vibrations.

Regression Analysis: E<sub>f</sub> versus Filler

Regression Equation

$$E_f = 1.5567 + 0.0142 \text{ Filler} - 0.01292 \text{ Filler} * \text{Filler}$$

Coefficients

Term	Coef	SE Coef	T-Value	P-Value	VIF
Constant	1.5567	0.0100	155.67	0.000	
Filler	0.0142	0.0127	1.11	0.309	13.00
Filler*Filler	-0.01292	0.00306	-4.22	0.006	13.00

**Model Summary**

S	R-sq	R-sq(adj)	R-sq(pred)
0.0173205	95.60%	94.13%	90.10%

**Analysis of Variance**

Source	DF	Seq SS	Seq MS	F-Value	P-Value
Regression	2	0.039089	0.019544	65.15	0.000
Filler	1	0.033750	0.033750	112.50	0.000
Filler*Filler	1	0.005339	0.005339	17.80	0.006
Error	6	0.001800	0.000300		
Total	8	0.040889			

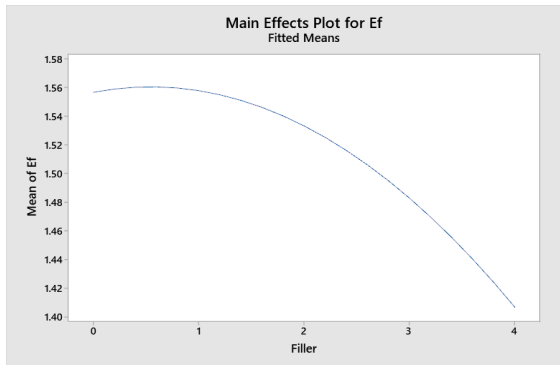


Fig. 19. Influence of fibres on the modulus by flexural vibrations.

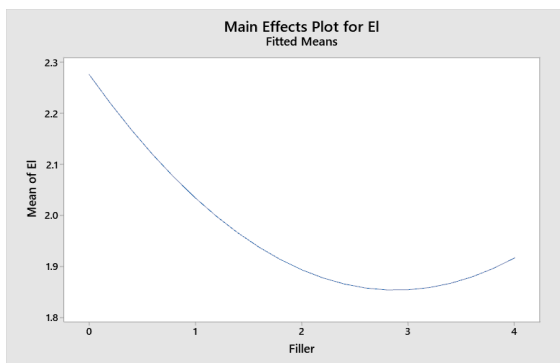


Fig. 20. Influence of fibres on the modulus by longitudinal vibrations.

**IV. CONCLUSIONS**

The results of the present work are as follow:

- A standard methodology was used for the quantitative determination of the modulus of linear deformations of PB compositions.
- A laboratory equipment that ensures the research has been designed and manufactured
- Based on the obtained experimental results from the reports and the performed analysis, it was established that as the number of fibres increases, the dynamic modulus decreases.

An analysis of the experimental results shows a change in the values of the modulus during curing change as follows:

- Composition 4 with 2g of fibers for reinforcement – 3,8 - 4,7%.
- Composition 5 with 0g fiber for reinforcement – 1-3%.

- Composition 6 with 4g fiber for reinforcement - 12-21.5%.

The dynamic modulus of elasticity during curing of polymer concrete has not been studied in the literature. Modulus of elasticity in other investigations is in the range  $10 \div 40 \text{ GPa}$ , [13]-[21].

During the curing of PB composition 4 and 5, it may be assumed that the modulus remains constant and deviation of 1 - 3% - is a measurement error.

The possibilities of obtaining reliable information about the modules for this type of composites with the proposed methodology and measuring equipment are real and adequate.

**V. ACKNOWLEDGMENTS**

The scientific research, the results of which are presented in the paper, was financed by project BG05M2OP001-1.002-0023 - Competence Center "Intelligent Mechatronic, Eco- and Energy-Saving Systems and Technologies" of Technical University of Sofia, branch Plovdiv.

**REFERENCES**

- [1] Hong S. Influence of Curing Conditions on the Strength Properties of Polysulfide Polymer Concrete. *Applied Sciences*. 2017; 7(8):833. <https://doi.org/10.3390/app7080833>
- [2] Elaloui O. Effect of Short Fibers on Fracture Properties of Epoxy-Based Polymer Concrete Exposed to High Temperatures. *Polymers*. 2023; 15(5):1078. <https://doi.org/10.3390/polym15051078>
- [3] Kumar, R. A review on epoxy and polyester based polymer concrete and exploration of polyfurfuryl alcohol as polymer concrete. *J. Polym.* 2016, 2016, 7249743. <https://doi.org/10.1155/2016/7249743>
- [4] Elaloui, O.; Ghorbel, E.; Mignot, V.; Ouedzou, M.B. Mechanical and physical properties of epoxy polymer concrete after exposure to temperatures up to 250 °C. *Constr. Build. Mater.* 2012, 27, 415–424. <https://doi.org/10.1016/j.conbuildmat.2011.07.027>
- [5] Nodehi, Mehrab. (2022). Epoxy, polyester and vinyl ester based polymer concrete: a review. *Innovative Infrastructure Solutions*. 7. <https://doi.org/10.1007/s41062-021-00661-3>
- [6] Heidari-Rarani M, Aliha MRM, Shokrieh MM, Ayatollahi MR(2014) Mechanical durability of an optimized polymer concrete under various thermal cyclic loadings—an experimental study. *Constr Build Mater* 64:308–315. <https://doi.org/10.1016/j.conbuildmat.2014.04.031>
- [7] E 1876 - 15. Standard Test Method for Dynamic Young's Modulus, Shear Modulus, and Poisson's Ratio by Impulse Excitation of Vibration.
- [8] Fauzi, & Hakim, Lukman & Simbolon, Tua. (2023). Manufacturing and Characterization of Polymer Concrete with Aggregate from Sand, Egg Shell and Sugarcane Waste with Epoxy Resin Binder as Sound Absorber. *Key Engineering Materials*. 940. 173-181. <https://doi.org/10.4028/p-2s9z9k>
- [9] Bolden,. (2013). UTILIZATION OF RECYCLED AND WASTE MATERIALS IN VARIOUS CONSTRUCTION APPLICATIONS. *American Journal of Environmental Sciences*. 9. 14-24. <https://doi.org/10.3844/ajessp.2013.14.24>
- [10] Barbuta, M & Serbanoiu, Adrian & Teodorescu, R & Rosca, Bogdan & Mitroi, Raluca & Bejan, G. (2017). Characterization of polymer concrete with natural fibers. *IOP Conference Series: Materials Science and Engineering*. 246. 012033. <https://doi.org/10.1088/1757-899X/246/1/012033>

- [11] Awwada, E.; Mabsout, M.; Hamad, B.; Farran, M. T.; Khatib, H. (2012) Studies on fiber-reinforced concrete using industrial hemp fibers. *Constr. Build. Mater.* 35 [10], 710–717. <https://doi.org/10.1016/j.conbuildmat.2012.04.119>
- [12] Jawad Ahmad, Zhiguang Zhou, Mechanical Properties of Natural as well as Synthetic Fiber Reinforced Concrete: A Review, *Construction and Building Materials*, Volume 333, 2022, 127353, ISSN 0950-0618, <https://doi.org/10.1016/j.conbuildmat.2022.127353>
- [13] Mebarkia, S., and C. Vipulanandan. "Compressive behavior of glass-fiber reinforced polymer concrete." *Journal of materials in civil engineering* 4.1 (1992): 91-105.
- [14] Martínez-Barrera, Gonzalo, et al. "Effects of  $\gamma$  radiation on fiber-reinforced polymer concrete." *Polymer Composites* 29.11 (2008): 1244-1251.
- [15] Mohamed, O.A.; Al Hawat, W.; Keshawarz, M. Durability and Mechanical Properties of Concrete Reinforced with Basalt Fiber-Reinforced Polymer (BFRP) Bars: Towards Sustainable Infrastructure. *Polymers* 2021, 13, 1402. <https://doi.org/10.3390/polym13091402>
- [16] Reis, J. M. L., and A. J. M. Ferreira. "Fracture behavior of glass fiber reinforced polymer concrete." *Polymer testing* 22.2 (2003): 149-153.
- [17] Farokhi, Ehsan & Fathi, Mojtaba & Amani, Ali. (2022). Polymer Modified Concrete containing Unsaturated Polyester by different amounts of styrene. 10.21203/rs.3.rs-2024855/v1. <https://doi.org/10.21203/rs.3.rs-2024855/v1>
- [18] Han, Tielin & Wang, Xianfeng & Li, Dawang & Li, Dong-Feng & Xing, Feng & Han, Ningxu. (2020). Influence of strain rate on mechanical characteristic and pore structure of self-healing cementitious composites with epoxy/urea-formaldehyde microcapsules. *Construction and Building Materials*. 268. 121138. <https://doi.org/10.1016/j.conbuildmat.2020.121138>
- [19] Miryala, Jayaram & Naresh, J & Thipparthi, Karhik & Kiran, Kastro. (2022). Assessment on mechanical properties of concrete with polypropylene fiber. *IOP Conference Series: Earth and Environmental Science*. 982. 012004. <https://doi.org/10.1088/1755-1315/982/1/012004>
- [20] Carrión, Francisco & Montalbán-Domingo, Laura & Real, Julia & Real, Teresa. (2014). Mechanical and Physical Properties of Polyester Polymer Concrete Using Recycled Aggregates from Concrete Sleepers. *The Scientific World Journal*. 2014. 526346. <https://doi.org/10.1155/2014/526346>.
- [21] Tian, Yaogang, et al. "Mechanical and dynamic properties of high strength concrete modified with lightweight aggregates presaturated polymer emulsion." *Construction and Building Materials* 93 (2015): 1151-1156. <https://doi.org/10.1016/j.conbuildmat.2015.05.015>

# Algorithm for Optimization of Idle Tool Moves when Milling Complex Surfaces on a Triaxial CNC Milling Machine

**Silviya Salapateva**

Faculty of Mechanical Engineering  
Technical University of Sofia,  
Plovdiv Branch  
Plovdiv, Bulgaria  
sisisal@tu-plovdiv.bg

**Iliya Chetrokov**

Faculty of Mechanical Engineering  
Technical University of Sofia,  
Plovdiv Branch  
Plovdiv, Bulgaria  
chetrov@tu-plovdiv.bg

**Bano Stefanov**

Faculty of Mechanical Engineering  
Technical University of Sofia,  
Plovdiv Branch  
Plovdiv, Bulgaria  
bano@abv.bg

**Abstract.** The idle running times of the working units of a machine tool are the sum of the idle running times for the tool change and for changing the section under treatment. The time, spent on idle running is the extra machining time. A large number of milling cutters are used for purely mechanical machining of details with complex surfaces and for a significant number of machined sections, where the complex surface is broken as a rule. This leads to an increase in the extra time for treatment. Reducing the auxiliary time in machining the parts will significantly increase the productivity of the actual milling process. When modeling the process of machining details with complex surfaces on triaxial milling machines, the optimization of the sequence of moves will allow to reduce the idle running time by up to 50% without causing deterioration in the quality of the surface layer.

**Keywords:** pure/actual/finish milling, complex surfaces, CNC machine tool, optimization.

## I. INTRODUCTION

When making parts with a complex shape on CNC milling machines the longest technological process is the finish machining. As it is known, the trajectory of movement of the tools used in this type of processing includes cutting moves and idle moves.

The idle moves of the machine working units are in fact the sum of the idle moves for changing the milling cutter and changing the section to be machined. A large number of milling cutters are used for finishing details with complex shapes and for a significant number of

machined sections, where the complex surface is broken as a rule. This leads to an increase in the extra time for treatment.

It follows from the above that the productivity of the process of finish machining on triaxial CNC milling machines can be increased, on the one hand, by reducing the cutting time, and, on the other hand, by reducing the time, spent on performing idle moves.

A number of researchers have dedicated their works [1], [2], [3], [4], [5] to defining the parameters and strategies for milling each individual section, to rational breakage of the complex surfaces into separate structural and technological sections, to selection of milling cutters of a certain size for processing each individual section, to finding and presenting methods and algorithms, allowing to optimize the process and reduce the cutting time. Positive results are thus obtained and the problem for minimizing the cutting time has been solved.

The auxiliary time optimization problem has not received much attention so far. The sequence of processing the individual sections and the sequence of tool change is determined by the technologist based on personal experience, without applying modern modeling and optimization methods. The number of options for performing the tool moves is often significant, however. Hence the choice of an optimal variant based on an exhaustive analysis of the consequences from the particular choice is impossible without the use of specific algorithms and means of programming.

Print ISSN 1691-5402

Online ISSN 2256-070X

<https://doi.org/10.17770/etr2023vol3.7193>

© 2023 Silviya Salapateva, Iliya Chetrokov, Bano Stefanov.

Published by Rezekne Academy of Technologies.

This is an open access article under the [Creative Commons Attribution 4.0 International License](https://creativecommons.org/licenses/by/4.0/).

All mentioned above determines the relevance of the present study. When modeling the process of machining details with complex surfaces on triaxial milling machines, the optimization of the sequence of moves will allow to reduce the time, spent on performing idle moves.

A number of studies of university and scientific laboratories in Austria, Great Britain, Russia, USA, Ukraine, Germany have been devoted to the choice of specific processing strategies [6], [7], [8], [9], [10], [11], [12], [13], [14], [15], [16], [17], [18]. Papers [1], [3], [4], and [16] present results from conducting a study and implementing a developed theory of optimization of the strategy for forming complex surfaces (optimal path of the milling cutter) on a triaxial CNC milling machine. The task of dividing the surfaces into sections and choosing tools for their shaping is solved in the works [1], [2], [10], [19].

As a result of the optimization of the specific processing strategies, the sections to be machined are defined, including: their boundaries, the tools and their geometry, the path of tool moves during machining, and, as a final result, the coordinates of the starting points, and the trajectory of tool incision and withdrawal.

The length of the idle-running tool moves differs significantly for the different sequences of transition from one machined section to another. Moreover, the guaranteed run time of each tool is limited by its service life, which results in additional increase in the duration of the idle running due to the need of changing the tools to guarantee the required surface quality. In this regard, to reduce the tool change time, it is necessary to minimize the number of milling cutters used to shape the sections of complex surfaces while maximizing their resource utilization.

It follows from this that the task of optimization of the general machining strategy is a search for the most profitable option, in which the idle moves during the tool passage from one section to another and during the tool change will lead to a minimum time consumption, while taking into account the minimum length of the idle tool moves from one section to another without changing the tool.

## II. MATERIALS AND METHODS

The study is aimed at the following:

- Type of equipment – a triaxial CNC milling machine, most frequently used in practice;
- Type of machining – finish milling, providing the required quality of the machined surfaces. The required quality is achieved by using low speed of idle running to reduce the influence of the dynamic error, which, in turn, results in increasing the auxiliary time. Under the high quality requirements in finish machining and limited service life of the milling cutters, regular changes of the tool typically occur. This leads to an increase in the additional time for performing idle running moves by the machine nodes;

- Tool type – tail milling cutters – flat face cylindrical, spherical face cylindrical and conical ones, all of which intended for machining complex surfaces and widely used in practice;

- Speed of idle-running moves when machining the sections by one size tool – a constant for all idle moves of the same size cutters. This assumption provides simplification in calculating the auxiliary time, and the change in the idle running tool speed by magnitude and direction has insignificant influence on the additional time;

- A guaranteed life span of the tool – in the the event of a finishing type of milling it is assumed to be the same for all cutters of one size. When processing different sections, the wear rate of the cutters of one size may be different. However, under the same cutting conditions, the tool life period of the milling cutters of one size can be assumed to be equal.

The movement of the milling cutter from one section to another and the movement for its change can be represented schematically (Fig.1).

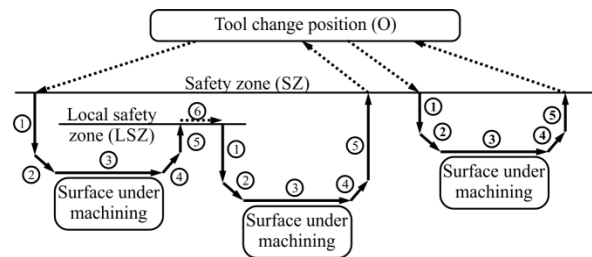


Fig. 1. Scheme of the milling cutter movement during pure machining of surfaces on a triaxial CNC machine.

The safety zone (SZ) is located at a height, greater than the highest section of the part geometry, and the local safety zone (LSP) is between two sequentially machined sections. The additional passage 1 serves to bring the cutter with an increased feed speed  $V_{f\text{ff}}$  (fast feed) from the safety zone to the point of starting the cut. The cutting movement 2 serves to move the cutter from the ending cutting point to its starting point at a speed  $V_{f\text{sp}}$ . The cutting movement 3 is carried out at the speed of the working move  $V_{f\text{wm}}$ , during which the cutter comes into contact with the surface of the workpiece. The movement for tool withdrawal 4 serves to move the milling cutter from the ending point to the starting point to bring the tool back at a speed of the working move  $V_{f\text{wm}}$ . The return movement of the tool 5 is a movement of the cutter with an increased feed speed  $V_{f\text{ff}}$  from the ending point of withdrawal 4 to the SZ or the LSZ. The transition (idle move) 6 is a rapid horizontal movement of the milling cutter at a speed of  $V_{f\text{ff}}$  from the ending point of withdrawal of the milling cutter 5 to the starting point of the next transition 1.

The idle moves with an increased feed speed take place when the tool moves from the ending point of its withdrawal to the point for its change O, and if there is a need of changing the milling cutter - during the

movement from point O to the starting point of incision and during movement from the ending point of tool withdrawal to the starting point of its incision into the workpiece to machine the next section.

Determining such a route of cutter moves, in which the length of the idle moves will have a minimum value, will allow to optimize the auxiliary time and significantly increase the productivity of the machining process and reduce the total machining time.

The operating time for machining  $T_o$  is obtained by summing the basic and the auxiliary time and can be determined by the formula:

$$T_o = \sum_{k=1}^p T_{bk} + \sum_{i=1}^q T_{ai}, \quad (2)$$

where  $T_{bk}$  is the basic time for performing the  $k^{\text{th}}$  technological transition;  $p$  – the number of technological transitions;  $T_{ai}$  – the auxiliary time for performing the  $i^{\text{th}}$  auxiliary transition;  $q$  – the number of the auxiliary transitions;

The auxiliary time  $T_{ai}$  for performing the  $i^{\text{th}}$  transition within the technological process when there is a need for changing the cutter (this includes indexing the tool magazine, transporting the tool from the magazine to the point of change, feeding it to the starting point of the section to be machined and withdrawing it from the ending point of the trajectory to the point for its change) is accepted to be calculated by the formula:

$$T_{ai} = T_{cch} + T_{imi} + \frac{l_{i0} + l_{0i}}{V_{ff}}, \quad (3)$$

where  $T_{cch}$  is the time, spent on the cutter change;  $T_{imi}$  – time for indexing the magazine, related to the sequence of arrangement of the cutters in it and the sequence of execution of the operations within the technological process;  $l_{i0}$  – length of the idle move from the ending point of the processed section to the tool change point;  $l_{0i}$  – length of the idle move from the tool change point to the starting point of the  $i^{\text{th}}$  section for machining;  $V_{ff}$  – rate at which the idle (fast) move is performed.

The length  $l_{0i}$  includes the length of the idle move from the cutter change point O to the safety zone SZ and the length of the auxiliary transition for feeding the cutter 1. The length  $l_{i0}$  includes the length of the auxiliary transition for returning the cutter from the ending point of its withdrawal to the safe zone SZ 5 and the length of the idle move from the safe zone SZ to the point for changing the milling cutter O (Fig.1).

The auxiliary time  $T_{ai}$  for performing the  $i^{\text{th}}$  transition for changing the machined sections during the technological process is determined by the expression:

$$T_{ai} = \frac{l_i}{V_{ff}}, \quad (4)$$

where  $l_i$  is the length of the idle move, which includes the tool movement from the ending point of one machined section to the starting point of the next machined section.

The length of the idle move  $l_i$  is determined by the distance traveled by the milling cutter from the ending point of its withdrawal from the machined section to the local safe zone 5, and the length of the transition 6 and the length of feeding the milling cutter for machining the next section 1.

Taking this into account, the auxiliary time  $T_a$  can be determined from the dependence:

$$T_a = \sum_{i=1}^q T_{ai} = \sum_{j=1}^n (T_{cch} + T_{imi} + \frac{l_{i0} + l_{0i}}{V}) + \sum_{i=1}^m \frac{l_i}{V_{ff}}, \quad (5)$$

where  $n + m = q$ ;  $n$  is the number of technological transitions for changing the cutter;  $m$  – the number of technological transitions for changing the machined sections.

It follows from formula (5) that the change in the sequence of machining the individual sections is accompanied by a change in the auxiliary time value.

In order to increase the productivity when machining complex workpiece surfaces by milling, the transition of the tool from one machined section to another and to the machine tool magazine for its change, should be done following the shortest route. When moving the tool along such a trajectory, the auxiliary time, spent on idle moves, should be minimum. The technological process should be realized with a minimum number of tools used and with minimum idle tool moves from one machined section to another. It should also be taken into account that when milling complex surfaces, the starting point of the cut does not coincide with the point of the tool withdrawal, and that the movement along the entire route should be carried out with a minimum number of idle moves. At the same time, the tool life period should also be taken into consideration (Fig.2).

In order to find an optimal route for all the selected tools of different sizes, it is necessary to determine the most profitable route for cutters of each size, used to machine sections, belonging to one group.

Based on the conducted research, an algorithm is proposed for determining the optimal route of milling cutters of one size when moving between a group of sections subject to machining (Fig. 3).

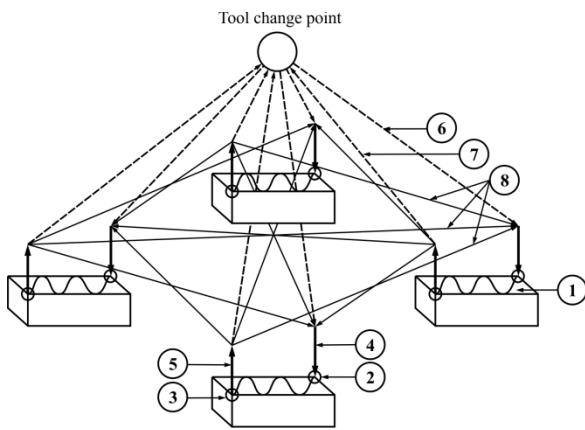


Fig. 2. Graph of the possible variants for a sequence of machining the individual sections.

1 – machined surface; 2 – point of incision of the tool; 3 – tool withdrawal point; 4 – auxiliary transition; 5 – auxiliary transition; 6 – movement of the milling cutter from the tool change point to the starting point of the machined section (fast run); 7 – movement of the milling cutter from the ending point of processing the section to the tool change point (fast run); 8 – idle tool move between two machined surfaces

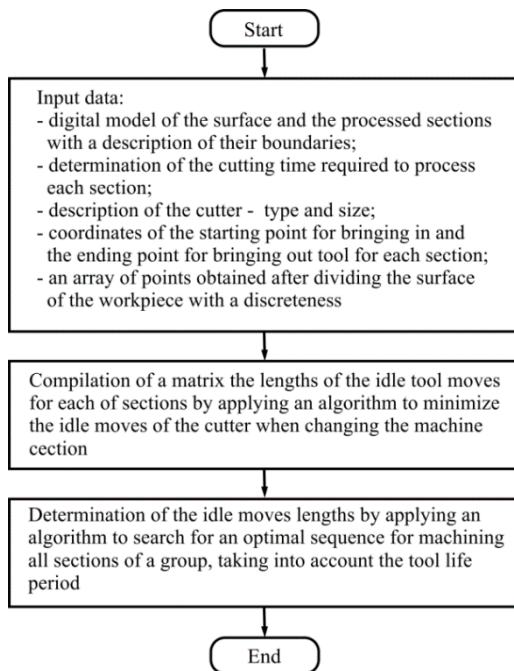


Fig. 3. Basic stages of solving the task to optimize the tool idle moves when milling complex surfaces.

The algorithm is implemented in two stages.

At the first stage, an option is sought to minimize the idle running of the tool when changing the machined section. The length of each pair of sections entering a group is checked. In doing so, it is necessary to determine the position of the local safe zone for every two consecutively machined sections.

The length  $l_i$  of the  $i^{\text{th}}$  idle tool move from the ending point  $T_1$  with coordinates  $(x_{i1}, y_{i1}, z_{i1})$  of the tool

withdrawal from the  $i^{\text{th}}$  machined section to the starting point  $T_2$  of incision into the next section with coordinates  $(x_{i2}, y_{i2}, z_{i2})$  is determined by the formula:

$$l_i = 2z_{sz} - z_{i1} - z_{i2} + \sqrt{(x_{i1} - x_{i2})^2 + (y_{i1} - y_{i2})^2}, \quad (6)$$

where  $z_{sz}$  is the height at which the local safety zone lies.

It follows from here that  $l_i$  will have a minimum value when  $z_{sz}$  is minimum, i.e.  $z_{sz} \rightarrow \min \Rightarrow l_i \rightarrow \min$ .

The minimum value of  $l_i$  can be determined from the dependence:

$$l_{i \min} = 2z_{sz \min} - z_{i1} - z_{i2} + \sqrt{(x_{i1} - x_{i2})^2 + (y_{i1} - y_{i2})^2}. \quad (7)$$

The minimum height of the local safe zone  $z_{sz}$  is equal to the sum of three parameters: the height  $z_t$ , at which the milling cutter during its movement touches the controlled geometry of the workpiece; the allowance  $a$ , and the reserve height  $h_r$ :

$$z_{sz \min} = z_t + a + h_r. \quad (8)$$

Cluster analysis of the model was used to determine  $z_t$ . A feature of this method is breaking the digital model of the detail into clusters (array of points with coordinates  $x, y, z$ ). The coordinates of these points can be obtained from the CAD system (e.g., Unigraphics).

The cluster analysis when solving the problem of determining  $z_t$  is carried out in stages:

- Determination of the points, belonging to the controlled geometry, and forming of the set  $U$ ;
- Determination of a coordinate  $z_{tj}$ , describing the local safe zone, at which the milling cutter touches points, belonging to the set  $U$ , at the  $j^{\text{th}}$  height during its movement in the direction of  $tt'$ ;
- Determination of the maximum value from the set  $\{z_{tj}\}$ , which represents the height  $z_t$ , at which the cutter touches the controlled geometry of the digital 3D model when describing the movement of the cutter along the direction  $tt'$ .

A detailed description of the developed mathematical model is presented in the work [20]. Its application results in a set of minimum values of the cutter idle run lengths when modeling all transitions from one section to another.

During the second stage, the most advantageous sequence for machining all the sections of one group is determined, taking into account the milling cutter life period and the minimum length of idle moves of the cutter determined within the first stage.

Finding a solution to the problem of searching for a minimum length of the idle moves during the tool transitions between two sections while considering the geometry of the workpiece and the task to optimize the sequence of performing the tool transitions is possible when using the well known approaches to solving vehicle routing problems for shipment.

A problem of this type can be solved in two ways: exact and approximate.

The exact method is applicable and gives an optimal solution when the machined sections are a small number.

The approximate method of finding a solution is applied in the case of a large number of machined sections. When applying it, the obtained solution approaches the optimal one.

To solve a problem, in which the number of the machined sections is less than ten, the so-called "Greedy algorithm" [21], [22], [23], [24], [25] can be applied, which belongs to the heuristic algorithms "Adaptive Large Neighborhood Search" (ALNS) [26], [27], [28], [29], [30]. The ALNS can be used to solve a problem with a number of machined sections more than ten.

### III. RESULTS AND DISCUSSION

To implement the proposed methodology for minimizing the idle moves when milling details with complex surfaces, a programming module (PM) has been developed. The PM is a synthesis of two modules. The first one, PM1, implements the method of minimizing the idle moves when the tool passes from one machined section to another, while the second one, PM2, is based both on the program module PM1 and on the method of searching for the most advantageous milling sequence for all sections, belonging to the group under processing.

The program working algorithm is shown in Fig.4.

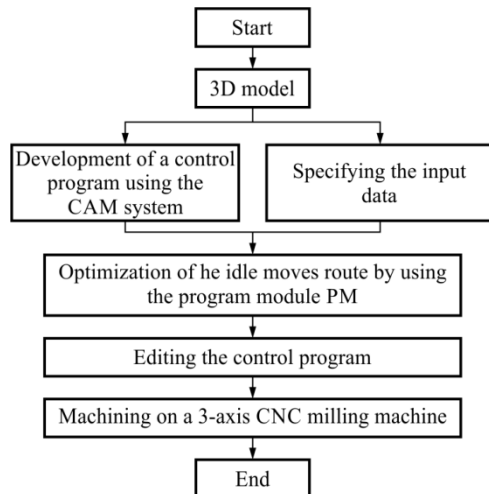


Fig. 4. Technological scheme for processing complex surfaces by milling, while using the developed PM.

The first step is related to specifying the input data: coordinates of nodal points from the surface of the workpiece, coordinates of the starting and ending points of the idle tool moves, number of machined sections, cutting time for each machined section, idle moves speed, tool life period, cutter change time.

Then, by using the PM, the sequence of processing the local sections is determined under the condition of minimizing the idle moves when passing from one machined section to another.

At the third stage of the algorithm, a process of editing the control program in accordance with the results, obtained from the previous stage, occurs.

The next stage consists in activities, related to the production of the test details. Their machining is carried out on a CNC vertical milling machine under the same modes, including cutting speed and feed rate for the same sections of the two test details with the same name, as well as the provision of tools with which the forming is carried out. The rough machining of the pair of parts is carried out by the same technology and control program, providing the same allowance for finish machining. The private cutting strategies (incision trajectory, cutting, and tool withdrawal) for the same sections of the details in purw/finish machining remain constant.

The experimental studies were carried out with a test detail, modeled by using NX 11 (Fig.5).

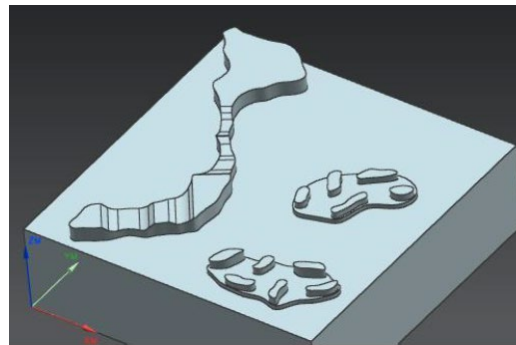


Fig. 5. 3D model of the test piece.

Details with dimensions 105 x 105 x 10 mm, made of B95 aluminum alloy, were selected for conducting the experiments.

The mechanical processing of the details was done on a vertical milling machine DMS 635 V, produce of the Deckel Maho company.

The basic rough milling was carried out initially with a 36 mm diameter flat face cylindrical cutter, then with a 10 mm diameter flat face cylindrical cutter, then with a 4 mm diameter flat face cylindrical cutter and finally with a spherical face cylindrical cutter 10 mm in diameter. The dimension tolerance after roughing was 0.1mm, the allowance for finish milling - 0.5mm.

The depth of cut and the machining allowance for rough milling for a flat face cylindrical cutter with  $D = 36$  mm was 2 mm, for the same type cutter with  $D = 10$  mm it was 1.6 mm and for the same type cutter with  $D = 4$  mm it was 1.2 mm.

The parameters of the rough milling mode are presented in Table 1.

TABLE 1  
CUTTING MODE PARAMETERS IN ROUGH MILLING

Cutter diameter D, mm	Spindle rotation frequency n, min <sup>-1</sup>	Tool feed rate V <sub>f</sub> , mm/min	Cutting feed S <sub>m</sub> , mm/min
Flat face cylindrical, D = 36 mm	<b>Rough milling</b>		
	6200	3000	1800
Flat face cylindrical, D = 10 mm	<b>Rough and finish milling</b>		
	9000	3000	2500
Flat face cylindrical, D = 4 mm	<b>Rough and finish milling</b>		
	9000	3000	800
Spherical face cylindrical, D = 10 mm	<b>Rough and finish milling</b>		
	9000	3000	1800

The finish machining of the test details, which is the purpose of the study, was carried out in two ways. In the first case, the sequence of finish milling of the sections was determined by means of the NX 11 system (variant 1). In the second one (variant 2), the sequence of finish milling of the sections was determined by using the PM optimization program module. The parameters of the finish milling mode for both variants remained constant (Table 1).

The number of individual sections machined using the different cutters is presented in Table 2.

TABLE 2  
NUMBER OF SECTIONS, MACHINED WITH CUTTERS OF ONE SIZE

Cutter	Number of sections, machined with cutters of one size
Flat face cylindrical, D = 10 mm	6
Flat face cylindrical, D = 4 mm	8
Spherical face cylindrical, D = 10 mm	18

From the table, it can be seen that the number of sections machined with Flat face cylindrical, D = 10 mm and Flat face cylindrical, D = 4 mm are less than 10. Therefore, the strategy for determining the machining sequence of these sections is by optional 1, i.e. without optimization.

As a result of the finish machining of the surfaces by means of the specified cutters, the details presented in Fig.6, were obtained.



(a) detail 1 after finish milling by the variant without optimization (b) detail 2 after finish milling by the variant with optimization

Fig. 6. Test details after finish milling.

Tables 3 present the results of the calculations obtained when preparing the control program for processing the test details based on the NX 11 system without using the optimization program module PM (variant 1), as well as the computational data, obtained by means of the algorithm, which allows to optimize the auxiliary time of idle tool moves when milling complex surfaces on triaxial CNC milling machines (variant 2).

TABLE 3  
RESULTS OF THE CALCULATIONS OBTAINED WHEN PREPARING THE CONTROL PROGRAM

Cutter	Variant of machining	
	1	2
<b>Total length of the auxiliary moves L, mm</b>		
Spherical face cylindrical, D = 10 mm	1823,27	1277,94
<b>Total time, spent on performing the auxiliary moves T<sub>a</sub>, min</b>		
Spherical face cylindrical, D = 10 mm	00.00.36	00.00.26
<b>Total time, spent on performing the working moves T<sub>o</sub>, min</b>		
Spherical face cylindrical, D = 10 mm	00.02.35	00.02.25

From the results in the table, it can be seen that even if some of the surfaces are not treated with the variant with optimization, they are reduced total length of the auxiliary moves L, total time, spent on performing the auxiliary moves T<sub>a</sub> and total time, spent on performing the working moves T<sub>o</sub>.

Based on the algorithm and the mathematical apparatus, a programming module (PM) has been developed to optimize the sequence of performing the technological transitions. The PM has been tested in practice and its performance in solving problems for minimizing the idle tool moves when machining complex surfaces by milling on CNC machines has been confirmed.

#### IV. CONCLUSIONS

The efficiency of the cutting tool route, which takes into account the mutual interests of all participants in the system, is taken as a criterion for optimizing the general strategy for mechanical processing, which means: minimum number of tools used, minimum length of idle moves during tool transitions between successively machined sections, minimum length of the idle moves when the most profitable complete tool route between all machined sections has been found.

In the calculations, the joint application of mathematical models for minimization of the idle moves in case of changing the machined sections and optimization of the sequence of machining of the individual sections, allows to obtain the most advantageous tool route when machining the individual sections with cutters of one size. The auxiliary time, spent on the idle moves when changing the milling cutter and changing the machined sections is minimized at the same time.

#### ACKNOWLEDGMENTS

The results were obtained under a project funded by the research grant at TU –Sofia -contract № 222ПД0021-24 – Optimization of the parameters of technological processes for mechanical machining on CNC machines by means of digital models.

#### REFERENCES

- [1] B. Ponomarev, Optimization of the milling strategy. Irkutsk: IRSTU, 2003.
- [2] B. Ponomarev and B. Medvedev, "Optimization of the boundaries of honeycomb milling of parts with a complex profile and artistic bas-reliefs", Scientific and Technical Conference on Improving the efficiency of technological preparation of machine-building production, November 15-18 2002, Irkutsk, 2002.
- [3] B. Ponomarev and V. Repin, A method for automatically finding the optimal parameters for strategies for fine milling of complex parts, All-Russian Scientific and Technical Conference on Computer Technologies in Science, Design and Production, January 1999, Nizhny Novgorod, Russia. State Technical University, 1999.
- [4] B. Ponomarev and V. Repin, "Improving the productivity of shaping complex parts on CNC milling machines", Journal of ISTU, vol.3, pp 50-53, 1998.
- [5] V. Danilov, Form-forming processing of complex surfaces by cutting. Minsk: Publishing House Nauka and Tekhnika, 1995.
- [6] A. Groshev. "Methods and means of improving the accuracy of processing shaped parts on CNC milling machines", M.S. thesis, Naberezhnochelni State University, Nabarezhnye Chelny, Russia, 2002.
- [7] A. Hanta, R. Grive and P. Broomhead, "Automatic CNC milling of pockets: geometric and technological issues", Journal Computer Integrated Manufacturing Systems, vol.11, pp.309-330, 1998.
- [8] A. Makarov, „Optimization of the processing of complex-shaped parts on CNC milling machines“, M.S. thesis, Lomonosov Moscow State University, Moscow, Russia, 2002.
- [9] C. Zhu, "Tool-path generation in manufacturing sculptured surfaces with a cylindrical end – milling cutter", Journal Computer in Industry, vol.7, pp.385-389, 1991.
- [10] F. Medvedev, "Creation of artistic bas-reliefs in the ArtCAM Pro software package", Scientific and Technical Conference on Modern high-performance technologies in mechanical engineering for various industries, October 6-8 2001, Irkutsk, 2001.
- [11] G. Elber and E. Cohen, "Tool path generation for freeform surface models", Journal Computer – Aided Design, vol. 26, pp. 490-496, 1994.
- [12] G. Sun, F. Wang and P. Wright, Operation Decomposition for Freeform Surface Features in Process Planning, ASME Design Engineering Technical Conference, September 12–16 1999, Las Vegas, Nevada, 1999.
- [13] H. Pottmann, J. Wallner and G. Glaeser, "Geometric criteria for gouge-free three-axis milling of sculptured surfaces", Journal ASME of Mechanical Design, June 1999, Issue 121, pp.241-248, 1999.
- [14] S. Radzevich, Shaping the surfaces of parts. Kiev: Rastan, 2001.
- [15] S. Radzevich, Formation of complex surfaces on CNC machines. Minsk: Vysha Shkola, 1991.
- [16] V. Repin, „Method for automatic selection of a strategy for finishing complex-shaped parts on a three-axis CNC milling machine“, Journal of ISTU, vol.3, pp. 54-59, 1998.
- [17] Y. Lee and T. Chang, "Application of computational geometry in optimization 2.5D and 3D NC surface machining", Journal Computers in Industry, vol.26, pp.41-59, 1995.
- [18] Y. Xiao, Z. Jiang, Q. Gu, W. Yan and R. Wang, "A novel approach to CNC machining center processing parameters optimization considering energy-saving and low-cost, Journal of Manufacturing Systems, Volume 59, Pages 535-548, April 2021.
- [19] A. Gromashev, B. B. Ponomarev and F.V. Medvedev, Vocational training of graduates of technical universities in the field of automation of design and technological work, International scientific and technical conference Mechanical engineering and the technosphere at the turn of the XXI century, June 2001, Doneck, Russia, 2001.
- [20] S. Salapatava, B. Stefanov, I. Chetrokov, "Mathematical model for minimizing a tool idle motion while milling complex surfaces on on 3-axis CNC milling machines when changing the machined area", presented at National Conference on Mechanical Engineering and Mechanical Science (It is to be published in the journal Machine Science, 2023), Varna, Bulgaria, 2022.
- [21] C. Cerrone, R. Cerulli and B. Golden, "Carousel greedy: A generalized greedy algorithm with applications in optimization", Computers & Operations Research, Volume 85, pp. 97-112, 2017,
- [22] J. Li, Y. Du, K. Gao, P. Duan, D. Gong and Q. Pan, "A Hybrid Iterated Greedy Algorithm for a Crane Transportation Flexible Job Shop Problem", IEEE Transactions on Automation Science and Engineering, Volume 19, Issue: 3, pp. 2153-2170, 2022.
- [23] J. Dubois-Lacoste, F. Pagnozzi and T. Stützle, "An iterated greedy algorithm with optimization of partial solutions for the makespan permutation flowshop problem", Computers & Operations Research, Vol.81, pp. 160-166, May 2017.
- [24] A. Brum, R. Ruiz and M. Ritt, "Automatic generation of iterated greedy algorithms for the non-permutation flow shop scheduling problem with total completion time minimization", Computers & Industrial Engineering, Volume 163, 107843, January 2022,
- [25] X. Han, Y. Han, B. Zhang, H. Qin, J. Li, Y. Liu and D. Gong, "An effective iterative greedy algorithm for distributed blocking flowshop scheduling problem with balanced energy costs criterion", Applied Soft Computing, Volume 129, 109502, November 2022.
- [26] J. Gallego, J. R. Rico-Juan and J. J. Valero-Mas, "Efficient k-nearest neighbor search based on clustering and adaptive k-values", Pattern Recognition, Volume 122, 108356, February 2022,
- [27] L. Ribeiro de Abreu, K. A. Araújo, B. de Athayde Prata, M. S. Nagano and J. V. Moccellini, "A new variable neighbourhood search with a constraint programming search strategy for the open shop scheduling problem with operation repetitions", Engineering Optimization, Volume 54, pp.1563-1582, 2022.
- [28] C. Friedrich and R. Elbert, "Adaptive large neighborhood search for vehicle routing problems with transshipment facilities arising in city logistics", Computers & Operations Research, Volume 137, 105491, January 2022.
- [29] M. Alinaghian, M. Jamshidian and E. B. Tirkolaee, "The time-dependent multi-depot fleet size and mix green vehicle routing problem: improved adaptive large neighbourhood search", A Journal of Mathematical Programming and Operations Research, Volume 71, 2022 - Issue 11: Special Issue Dedicated to the International Conference «Dynamical Control and Optimization», DCO 2021.
- [30] C. Zhang, F. Han and W. Zhang, "A cutting sequence optimization method based on tabu search algorithm for complex parts machining", Proceedings of the Institution of Mechanical Engineers, Part B: Journal of Engineering Manufacture, Volume 233, Issue, 2018.

# Mathematical Modeling of the Sequence of Machining Sections of Complex Surfaces when Milling on a Triaxial CNC Machine Tool

**Silviya Salapateva**

Faculty of Mechanical Engineering  
Technical University of Sofia, Plovdiv Branch  
Plovdiv, Bulgaria  
sisisal@tu-plovdiv.bg

**Bano Stafanov**

Faculty of Mechanical Engineering  
Technical University of Sofia, Plovdiv Branch  
Plovdiv, Bulgaria  
bano@abv.bg

**Abstract.** The idle running times of the working units of a machine tool are the sum of the idle running times for the tool change and for changing the area under treatment. The paper presents mathematical models, establishing the relationship between the additional time for performing the technological operations with the parameters of both the technological equipment and the object under treatment. The mathematical models for minimizing the idle moves when a tool passes from one machined section to another, allows to reduce the additional treatment time, which, in turn, leads to an increase in the productivity of the process of actual milling.

**Keywords:** pure/actual/finish milling, complex surfaces, CNC machine tool, optimization.

## I. INTRODUCTION

The idle moves of the working modules of a machine are the sum of the idle moves for cutter change and the idle moves for changing the machined area. The time, spent on the tool idle running is the additional part of the machine operating time. In case of finish mechanical machining of complex surfaces and of significant number of machined sections, to which, as a rule, the complex surface is broken, a great number of milling cutters is utilized. This results in increasing the additional, i.e., the auxiliary operating time. The reduction of the auxiliary time when machining details significantly increases the efficiency of the used technological equipment.

Hence, increasing the productivity of machining on triaxial CNC milling machines can be achieved, on the one hand, by reducing the cutting time, and, on the other hand, by reducing the time, spent on performing idle moves.

Reduction of the time for performing idle tool moves can be achieved by minimizing the idle moves when changing the machined sections and by optimizing the machining sequence of the individual sections.

This work studies the possibility of finding an optimal sequence of performing the transitions during all types of idle tool moves at minimum time, spent on their execution.

## II. MATERIALS AND METHODS

An algorithm for optimization of the cutting tool idle moves is presented in [1, 2, 3, 4, 5].

The mathematical model [1], developed by the authors, allows to determine the sequence of performing transitions under the conditions of: - minimizing the length of the trajectory of the tool's idle moves when passing from one given point to another; - complying with various constraints (geometry of both the machined workpiece and the fixing device, constraints, related to the dimensions of the machine working area etc.).

The authors claim that as a result of the practical implementation of the algorithm for constructing the path of the idle tool moves on multi-operational lathes when processing workpieces with a length-to-diameter ratio of less than 0.5, reduction of the auxiliary time by 20-30% is achieved, and the quality of the processed surface corresponds to the set quality.

The task of optimizing the general machining strategy is described in detail in paper [1]. The proposed algorithm provides the search for an optimal sequence of performing the transitions on multi-operational machines

Print ISSN 1691-5402

Online ISSN 2256-070X

<https://doi.org/10.17770/etr2023vol3.7194>

© 2023 Silviya Salapateva, Bano Stafanov. Published by Rezekne Academy of Technologies.  
This is an open access article under the [Creative Commons Attribution 4.0 International License](https://creativecommons.org/licenses/by/4.0/).

and their idle tool moves, at minimum expenditure of time on their execution.

When developing the algorithm, however, the authors do not take into account the tool life factor, on which the number of the cutters, used for replacement, depends, and which ultimately affects the time for performing the idle moves. The problem of minimizing the idle tool moves is solved for the case, in which the positions of the starting and the ending point of machining a section coincide. The algorithm, proposed by the authors, is intended only for a certain type of equipment, and more precisely for CNC lathes. For milling machines, in which the positions of the starting and the ending point of machining do not coincide, the application of the proposed algorithm is impossible.

In the process of mechanical machining on triaxial milling machines, the length of the idle move from one section to the next is not equal to the distance, traveled in the opposite direction, due to the mismatch of the starting and the ending point and the withdrawal of the tool, as well as due to the geometric features of the workpiece surface. Considering this, the task to determine the optimal sequence of machining individual sections can be correlated to a logistic transportation problem, namely, the Asymmetric capacitated vehicle routing problem (ACVRP). ACVRP is a combinatorial optimization and linear programming problem, in which, for vehicles of the same load capacity, located at a depot, the minimum by cost (money, time or distance) closed routes must be found, which would fully allow for servicing all customers (Fig. 1).

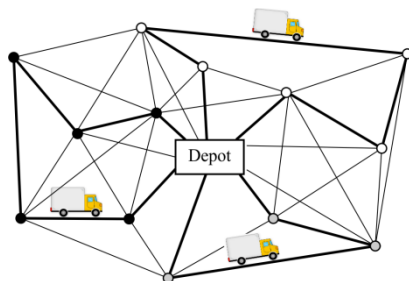


Fig. 1. Asymmetric vehicle routing problem with load capacity limitation.

At the same time, the limiting load capacity condition for the means of transport must be met for each of the routes (besides, the length of the route from A to B is not equal to the length of the route from B to A). [6].

The similarity between the problem of determining the optimal sequence of transitions from one section to another and the ACVRP is presented below as a table of analogies.

ACVRPs belong to the nondeterministic polynomial (NP) problems, whose computational complexity depends on the size of the input data. Methods for solving them are presented in the works of G. Clark, J. W. Wright [7], B. Gillet, B. Golden, T. Magnonti, H. Nguen [8], G. Laporte, F. Semet [9]., P. Toth, D. Vigo [10],

R. Baldacci, E. Hadjiconstantinou, A. Mingozzi [11], D. Pisinger, S. Ropke [12] and others.

TABLE 1  
ANALOGY BETWEEN ACVRP AND THE PROBLEM OF FINDING THE OPTIMAL SEQUENCE OF THE METAL CUTTING TOOL TRANSITIONS

Asymmetric capacitated vehicle routing problem	Problem of determining the optimal sequence of tool transitions from one section to the next
Depot;	Tool change position
A fleet of motor vehicles	Tool magazine;
Customer	Section
Automobile;	Tool
Car load capacity	Tool life period
Load requested by one customer	Needed cutting time for one section

The algorithm of Clark-Wright, consisting in merging small routes into larger ones until it becomes possible to reduce the total cost of the route, is very often used to solve the ACVRP problem (Fig. 2).

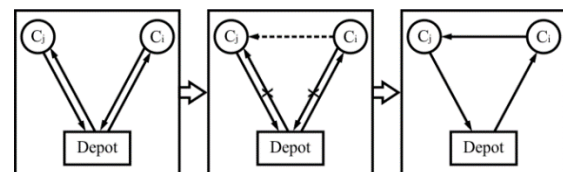


Fig. 2. Process of merging small routes into larger ones.

As a result of combining two or more routes, the total value of the solution is reduced (the authors mention the concept of "saving").

The algorithm envisages the execution of a series of steps in search for an optimal option.

The Clark-Wright algorithm belongs to the approximate iterative methods. Its advantages are its simplicity, reliability and flexibility, which allow for taking into account a number of additional factors, affecting the final solution of the problem. The solution error does not exceed 5-10%.

Disadvantages of this algorithm are: - its efficiency decreases as the end of the calculations is approached; - it takes a lot of time to find a solution, since all the options need to be calculated, stored and sorted out.

In the works of T.J. Gaskell [13], P. Yellow [14], H. Paessens [15] the Clark-Wright algorithm is modified and the above-mentioned flaws eliminated.

One of the classical heuristic transport routing problems (VPR – vehicle performance rating) is the Sweep algorithm [6], [10].

This algorithm is applied in case of polar coordinates and the depot is considered to be the origin of the coordinate system. The depot is then connected to a randomly chosen point, called the "starting point". All the other points are connected to the depot and then

represented by the angles formed by the segments, connecting them to the depot and the segment, connecting the depot to the starting point. The route begins at the starting point, and the points with increasing angles are then included, taking into consideration the given constraints. When a point cannot be included in the route as it would violate a certain constraint, that point becomes the starting point of a new route, and so on. The process is complete when all points are included in the routes (Fig.3).

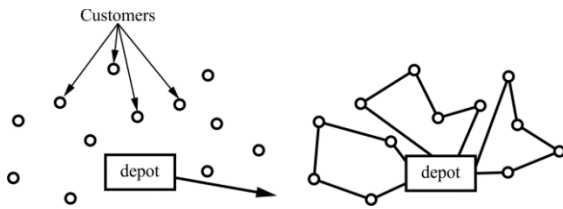


Fig. 3. Sweep algorithm.

In the event that a large number of nodes needs to be served, the Sweep algorithm is used within the “clustered routing” approach. In this case, clockwise, the ratio between the cumulative demand and the vehicle load capacity (including all other constraints) should be checked. The point, which cannot be included due to violation of the vehicle capacity or other limitations, becomes the first point in another cluster. Thus, the entire region is divided into clusters (zones). In the next step, the VRP is solved for each cluster separately. Clustering ends when all cluster points are defined (Fig.4).

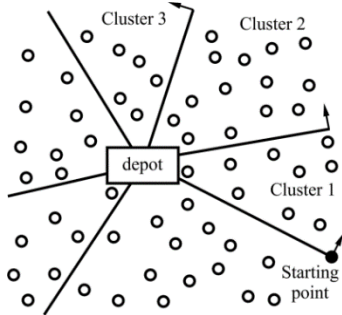


Fig. 4. Clustering by the Sweep algorithm.

It is certain that one vehicle can serve all the points within a cluster. The final solution depends on the choice of a starting point. By changing the location of the starting point, it is possible to generate different vehicle routes. The routes with the minimum total length should be chosen for the final solution

It is certain that one vehicle can serve all the points within a cluster. The final solution depends on the choice of a starting point. By changing the location of the starting point, it is possible to generate different vehicle routes. The routes with the minimum total length should be chosen for the final solution.

The merits of this algorithm are evaluated by the quality of the solution and the speed of calculation. Its

main drawback is that the first ray is turned to an arbitrary direction without imposing any conditions or principles.

Subsequently, the classical heuristics is narrowed down to metaheuristics, which allows for obtaining a qualitative solution, though with a preliminary procedure of varying the governing parameters.

In the work of D. Pisinger, S. Ropke [8], a metaheuristic method for solving the routing problem in transport is presented, which is an adapted version of the metaheuristic algorithm - Adaptive large neighborhood search (Fig. 5), which consists in generating new solutions based on the initially proposed admissible solution, while taking into account the "destroyed" and "restored" neighborhoods.

The application of this algorithm provides a sufficiently fast and accurate solution to the problem of routing the shipments with a load capacity limitation in case of high dimensionality of the problem to be solved.

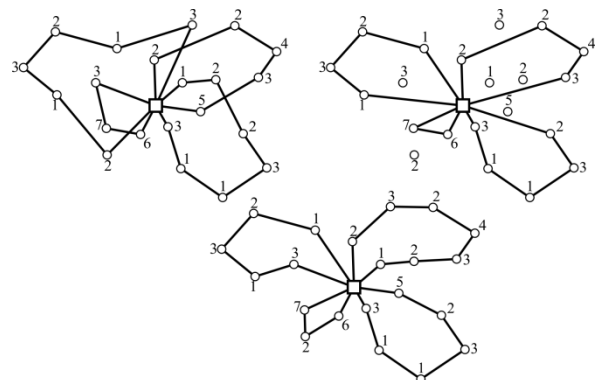


Fig. 5. An example of "destruction" and "restoration".

After analyzing the classical and modern methods for solving the ACVRP problem, an analogy was established regarding the problem of determining the sequence of changing the cutting tool and its transition from one machined section to another in a process of finishing complex surfaces on a triaxial CNC milling machine.

The efficiency of the cutting tool route, considering the mutual interests of all participants in the system, is taken as a criterion for optimization of the general strategy for mechanical processing: - minimum number of tools used; - minimum length of idle moves when passing between sequentially machined sections; - minimum length of idle moves after finding the most profitable complete tool route between all machined sections.

Finding a solution to both the problem of searching for the minimum number of idle moves during the tool transition between two sections while considering the geometry of the part, and the problem of optimizing the sequence of performing the tool transitions is possible by means of using the well known approaches for solving the vehicle routing problems.

### III. RESULT AND DISCUSSION

When searching for the most advantageous sequence of machining all sections with complex surfaces by cutters of one size, while taking into account the tool life parameters, an algorithm can be applied to minimize the idle tool moves during the transitions from one machined section to another. Such a problem can be described by a graph  $G = (V, E)$  with multiple vertices  $V = \{v_0, v_1, \dots, v_n\}$  and edges  $E \{e\}$  (Fig.6).

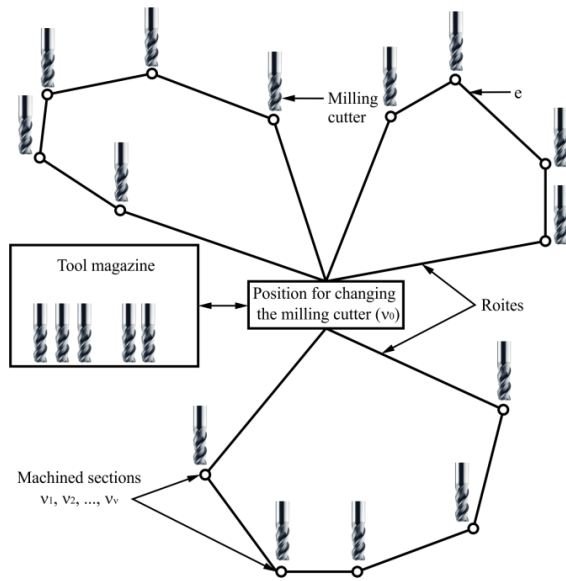


Fig. 6. Scheme for solving the tool routing problem.

The following associations can be made:  $v_0$  - position for changing the cutter;  $v_1, \dots, v_n$  - machined sections;  $e \in E$  - length of the edges connecting two of the vertices of the graph with a length, equal to the idle-running displacement  $C_e$  when changing the machined section. To build the model it is assumed that the time for the cutter to complete the machined section is  $T_i$  and the guaranteed tool life is  $Q$ .

The  $m$  routes of the milling cutter at minimum total length of the idle moves are to be found. These routes should start and end at the position of changing the milling cutter  $v_0$  and the tool should pass through each section  $v_i$  only once. Besides, each section should be completely machined by means of one milling cutter. In addition, the working time of each cutter should not exceed the set tool life period  $Q$ .

This type of a problem can be solved in two ways: exact and approximate.

The exact way of solving it is applicable and gives an optimal variant in the event that the machined sections are not a big number.

The approximate method of finding a solution is applied in the case of a large number of machined sections. When applying it, the obtained solution approaches the optimal one.

To solve a problem, in which the number of machined sections is below ten, the so-called "Greedy algorithm" can be applied, which belongs to the group of the heuristic algorithms. When the number of machined sections is bigger than ten, the "Adaptive Large Neighborhood Search" (ALNS) can be applied to find the solution to the problem.

#### A. Greedy algorithm for optimizing the sequence of machining the sections

Greedy algorithm is considered in detail by a number of authors and finds application in various areas of life [16], [17], [18], [19], [20].

This algorithm envisages the execution of the following actions:

1. Description of all possible sequence options for machining the individual sections;
2. Exclusion of the inadmissible variants;
3. Specifying multiple options for a cutter change sequence for each admissible variant;
4. Exclusion of those sequences of cutter change, in which the cutting time exceeds the tool life period;
5. Of the remaining options of cutter change sequences, choosing the ones, in which the number of cutter changes is the minimum;
6. Determining the auxiliary time, spent on idle tool moves for each variant, at a minimum number of cutter changes;
7. Choosing an optimal variant of a cutter change sequence with minimum auxiliary time, spent on idle moves of the milling cutter.

#### B. ALNS (adaptive large neighbourhood search) for searching a larger area in the process of optimizing the sequence of machining the sections

ALNS is considered in detail by a number of authors and finds application in various areas of life [21], [22], [23], [24].

ALNS represents an approach for synthesizing different methods of dismembering and joining points. The essence of the ALNS consists in "destruction" of the initially executable version of the sequence of processing individual sections and in "restoration" of the destroyed version. As a result, a new variant of the sequence for processing the sections is obtained. The advantage of the ALNS algorithm is the possibility to evaluate the degree of correspondence (relevance) of each of the methods at each stage of the problem-solving process. Each destruction/restoration method is assigned a "weight" which helps to control the frequency with which the method is used in the search process, and the "weight" of a method can be updated stage by stage [8].

To search for an optimal variant, using the ALNS algorithm, the following steps must be performed:

1. The initial variant for the sequence of machining the sections  $x$  is built;

2. Assumption is made that the constructed initial version  $x$  is the best, i.e.,  $x_b = x$ , and that the weights of the destruction/restoration methods are the same  $\rho^- = (1, \dots, 1)$ ,  $\rho^+ = (1, \dots, 1)$ ;
3. The action is repeated until the stop condition is met. For the purpose:
  - 3.1. Destruction  $d \in \Omega^-$  and restoration  $d \in \Omega^+$  methods are chosen, using their weights  $\rho^-$  and  $\rho^+$ ;
  - 3.2. A process of destruction and reconstruction takes place, resulting in a new variant  $x_t = r(d(x))$ ;
  - 3.3. Evaluation is made to decide if the variant  $x_t$  is acceptable. If this is the case, then  $x = x_t$ . The variant  $x_t$  is not accepted if this option has already been realized.
  - 3.4. The auxiliary times for each variant  $x_t$  and  $x_b$ , are compared. If the variant  $x_t$  is better than the available variant  $x_b$  ( $t_v(x_b) > t_v(x_t)$ ), then it is assumed that  $x_b = x_t$ . The weights of the destruction/restoration methods  $\rho^-$  and  $\rho^+$  are updated after that.
4. Going back to  $x_b$ .

The ALNS algorithm allows to determine the initial executable variant for a sequence of processing individual sections and makes it possible to choose an appropriate method of destruction of this initial variant. After finishing the destruction, the algorithm chooses a method to restore the destroyed version with the aim of obtaining a better one. This process is repeated until the last feasible option gets close to the optimal one (the iteration is terminated when the stop condition is met). As a result, an option for the sequence of processing individual sections is obtained, in which the additional time, spent on idle tool moves, is minimum.

This paper presents a fragment of a research, aimed at increasing the efficiency of triaxial CNC milling machines when milling parts with complex surfaces by reducing the auxiliary time for performing the individual operations, and more precisely by reducing the time for performing idle tool moves. The latter can be achieved, on the one hand, by minimizing the length of the idle tool moves when changing the machined section, and, on the other hand, by finding the most advantageous sequence for machining the sections.

Based on a conducted literature review [25], [26], [27], [28], [29], [30] a method is proposed for determining the optimal route of cutters of one size when moving among one group of sections subject to machining. The method is implemented in two stages:

- at the first stage, an option for minimizing the idle moves of the tool when changing the machined section is sought. The length of each pair of sections, included in a group, is checked. In doing so, it is necessary to determine the position of the local safety zone for every two consecutively processed sections;
- at the second stage, the most advantageous sequence for machining all the sections in a group is determined, taking into account both the tool life period

and the minimum-length idle moves of the cutter, determined during the first stage.

To implement the proposed methodology for minimizing the idle moves when milling details with complex surfaces, a programming module (PM) has been developed. The PM is a synthesis of two modules. The first one, PM1, implements the method of minimizing the idle moves when the tool passes from one machined section to another, while the second one, PM2, is based both on the program module PM1 and on the method of searching for the most advantageous milling sequence for all sections, belonging to the group under processing. PM2 implements the mathematical model considered in the present work. It is based on Microsoft Excel and the VPR Spreadsheet Solver application. The working algorithm of the PM2 module is the following:

Step 1: Entering the input data: data, obtained after the implementation of the PM1 module; cutting time when machining each of the sections; idle moves speed; tool life period; time, spent on changing the cutter.

Step 2: Based on the input data and using the means of the PM2 module, the optimal sequence of milling the sections, machined with one size milling cutters at a minimum length of the idle moves is determined.

The confirmation of the effectiveness of the proposed method for automatic determining of the sequence of execution of the technological transition during pure/finishing milling of parts with a complex shape on a triaxial CNC milling machine should be done by comparing results, obtained for the same details after applying a program module CAM of the Unigraphics system and the developed program module PM.

Test details need to be produced, following a compiled control program.

The results of both the virtual modeling and the physical realization of the machining process, which allow to determine the values of the machine time and the auxiliary time, including the time for idle moves and the time for tool change, should be presented in a tabular format. On the basis of the obtained data, an analysis should be carried out and corresponding conclusions drawn up.

The experimental studies were carried out with a test detail, modeled by using NX 11 (Fig.7).

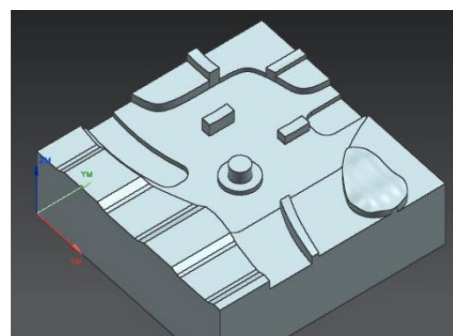


Fig.7. 3D model of the test piece.

TABLE 3

RESULTS OF THE CALCULATIONS OBTAINED WHEN PREPARING THE CONTROL PROGRAM

Cutter	Variant of machining	
	1	2
<b>Total length of the auxiliary moves <math>L</math>, mm</b>		
Flat face cylindrical, D = 10 mm	2665,8	1484,47
Spherical face cylindrical, D = 10 mm	1768,1315	1287,48
<b>Total time, spent on performing the auxiliary moves <math>T_a</math>, min</b>		
Flat face cylindrical, D = 10 mm	00.00.53	00.00.29
Spherical face cylindrical, D = 10 mm	00.00.35	00.00.25
<b>Total time, spent on performing the working moves <math>T_w</math>, min</b>		
Flat face cylindrical, D = 10 mm	00.02.14	00.01.50
Spherical face cylindrical, D = 10 mm	00.06.05	00.05.55

The finish machining of the test details, which is the purpose of the study, was carried out in two ways. In the first case, the sequence of finish milling of the sections was determined by means of the NX 11 system (option 1). In the second one (option 2), the sequence of finish milling of the sections was determined by using the PM optimization program module.

The parameters of the finish milling mode for both variants remained constant: Spindle rotation frequency  $n = 9000 \text{ min}^{-1}$ ; Tool feed rate  $V_f = 3000 \text{ mm/min}$ ; Cutting feed  $S_m = 2500, \text{ mm/min}$  – for flat face cylindrical;  $S_m = 1800, \text{ mm/min}$  – for Spherical face cylindrical. A 10 mm diameter four-tooth flat face cylindrical cutter, 10 mm in diameter, and a spherical face cylindrical cutter, 10 mm in diameter, were used for the experiments.

The number of individual sections machined by means of a flat face cylindrical cutter with 10 mm diameter and a spherical face cylindrical cutter with 10 mm diameter, is presented in Table 2.

TABLE 2  
NUMBER OF SECTIONS, MACHINED WITH CUTTERS OF ONE SIZE

Cutter	Number of sections, machined with cutters of one size
Flat face cylindrical, D = 10 mm	17
Spherical face cylindrical, D = 10 mm	11

As a result of the finish machining of the surfaces by means of the specified cutters, the details presented in Fig.8, were obtained.



(a) detail 1 after finish milling by the variant without optimization  
(b) detail 2 after finish milling by the variant with optimization

Fig.8. Test details after finish milling.

Tables 3 present the results of the calculations obtained when preparing the control program for processing the test details based on the NX 11 system without using the optimization program module PM (variant 1), as well as the computational data, obtained by means of the algorithm, which allows to optimize the auxiliary time of idle tool moves when milling complex surfaces on triaxial CNC milling machines (variant 2).

#### IV. CONCLUSIONS

The use of an adapted algorithm for solving vehicle routing problems to optimize routes by searching for the most profitable variant of a sequence of idle moves for a triaxial CNC milling machine allows to optimize the task in terms of forming a strategy for processing complex surfaces of parts by adherence to the criterion for minimizing the auxiliary time for moving the tool during milling.

The developed algorithm allows to solve the problem of optimizing the idle tool moves for the case of a complex surface, composed of up to 1000 sections. The result, obtained when applying this algorithm, is approximately accurate and with little time, spent on solving the problem.

#### ACKNOWLEDGMENTS

The results were obtained under a project funded by the research grant at TU –Sofia -contract № 222П/Д0021-24 – Optimization of the parameters of technological processes for mechanical machining on CNC machines by means of digital models.

#### REFERENCES

- [1] A. S. Azotov and V. S. Salnikov, Optimization of the tool path in multi-operation machines. Scientific and Technical Conference on Automation and informatization in mechanical engineering, 20 – 23 January 2001, Tula, 2001.
- [2] R. Faizrahmanov, R. Murzakaev and A. Poliakov, “Cutting Time Optimization Using Technology for CNC Machines”, Proceedings of International Conference on Applied Innovation in IT, Volume 6, Issue 1, pp.37-44, 2018.
- [3] J. Marcinčin and K. Albeloushy, “Optimization of cutting tool motion strategy for cnc milling technological processes”, Proceedings of the 16th International Conference on Manufacturing Systems – ICMaS ISSN 1842-3183, University POLITEHNICA of Bucharest, Machine and Manufacturing Systems Department Bucharest, Romania, 2019.
- [4] C. Feng, Y. Huang, Y. Wu and J. Zhang, “Feature-based optimization method integrating sequencing and cutting parameters for minimizing energy consumption of CNC machine tools”, The International Journal of Advanced Manufacturing Technology, volume 121, pages503–515, 2022.

- [5] Ö. Özçelik, Küçük Koç, "Evaluation of tool path strategies in cnc woodworking machines and a case study", *Wood Industry and Engineering*, Volume 2021, Issue, 2021.
- [6] N. Cristofides, A. Mingozzi and P. Toth, C. Sandi, *The vehicle routing problem: Combinatorial Optimization*, Wiley, Chichester, 1979.
- [7] G. Clarke, "Scheduling of vehicles from a central depot to a number of delivery points", *Journal Operations Research*, vol.12, pp.568-581, 1964.
- [8] B. Golden, T. Magnanti and H. Nguyen, "Implementing vehicle routing algorithms", *Networks* vol.7 (2), pp.113-148, 1977.
- [9] G. Laporte, "Classical Heuristics for the Vehicle Routing Problem", *Les Cahier du GERAD*, G98-54, Group for Research in Decision Analysis, pp.234-239, Montreal, Canada, 1998.
- [10] P. Toth and D. Vigo, *The Vehicle Routing Problem*, Society for Industrial and Applied Mathematics, 2002.
- [11] R. Baldacci, E. Hadjiconstantinou and A. Mingozzi, "An Exact Algorithm for the Capacitated Vehicle Routing Problem Based on a Two-Commodity Network Flow Formulation", *Journal Operations Research*, vol.52, pp.723-738, 2004.
- [12] D. S. Pisinger and A. Ropke, "A general heuristic for vehicle routing problems", *Journal Computers and Operations research*, vol.34 -Issue 8, pp.2403-2435, 2007.
- [13] T.J. Gaskell, "Bases for vehicle fleet scheduling", *Journal Operational research Quarterly*, vol.18, pp.281-295, 1967.
- [14] P. Yellow, "A computational modification to the savings method of vehicle scheduling", *Journal Operational research Quarterly*, vol.21, pp.281-283, 1970.
- [15] H. Paessens, "The savings algorithm for the vehicle routing problem", *European Journal of Operational research*, vol.34, pp.336-344, 1988.
- [16] C. Cerrone, R. Cerulli and B. Golden, "Carousel greedy: A generalized greedy algorithm with applications in optimization", *Computers & Operations Research*, Volume 85, pp. 97-112, 2017,
- [17] J. Li, Y. Du, K. Gao, P. Duan, D. Gong and Q. Pan, "A Hybrid Iterated Greedy Algorithm for a Crane Transportation Flexible Job Shop Problem", *IEEE Transactions on Automation Science and Engineering*, Volume 19, Issue: 3, pp. 2153-2170, 2022.
- [18] J. Dubois-Lacoste, F. Pagnozzi and T. Stützle, "An iterated greedy algorithm with optimization of partial solutions for the makespan permutation flowshop problem", *Computers & Operations Research*, Vol.81, pp. 160-166, May 2017.
- [19] A. Brum, R. Ruiz and M. Ritt, "Automatic generation of iterated greedy algorithms for the non-permutation flow shop scheduling problem with total completion time minimization", *Computers & Industrial Engineering*, Volume 163,107843, January 2022,
- [20] X. Han, Y. Han, B. Zhang, H. Qin, J. Li, Y. Liu and D. Gong, "An effective iterative greedy algorithm for distributed blocking flowshop scheduling problem with balanced energy costs criterion", *Applied Soft Computing*, Volume 129,109502, November 2022.
- [21] A. J. Gallego, J. R. Rico-Juan and J. J. Valero-Mas, "Efficient k-nearest neighbor search based on clustering and adaptive k-values", *Pattern Recognition*, Volume 122, 108356, February 2022,
- [22] L. Ribeiro de Abreu, K. A. Araújo, B. de Athayde Prata, M. S. Nagano and J. V. Moccellini, "A new variable neighbourhood search with a constraint programming search strategy for the open shop scheduling problem with operation repetitions", *Engineering Optimization*, Volume 54, pp.1563-1582, 2022.
- [23] C. Friedrich and R. Elbert, "Adaptive large neighborhood search for vehicle routing problems with transshipment facilities arising in city logistics", *Computers & Operations Research*, Volume 137, 105491, January 2022.
- [24] M. Alinaghian, M. Jamshidian and E. B. Tirkolaei, "The time-dependent multi-depot fleet size and mix green vehicle routing problem: improved adaptive large neighbourhood search", *A Journal of Mathematical Programming and Operations Research*, Volume 71, 2022 - Issue 11: Special Issue Dedicated to the International Conference «Dynamical Control and Optimization», DCO 2021.
- [25] C. Zhang, F. Han and W. Zhang, "A cutting sequence optimization method based on tabu search algorithm for complex parts machining", *Proceedings of the Institution of Mechanical Engineers, Part B: Journal of Engineering Manufacture*, Volume 233, Issue, 2018.
- [26] Y. Xin, S. Yang, G. Wang, R. Evans and F. Wu, "A tool path optimization approach based on blend feature simplification for multi-cavity machining of complex parts", *Science Progress* 2020, Vol. 103(1) 1–21, 2020.
- [27] D. Karimi and M.J. Nategh, "Contour maps for developing optimal toolpath and workpiece setup in hexapod machine tools by considering the kinematics nonlinearity", *Proc IMechE Part B: J Engineering Manufacture*, 230: pp.1572–1583, 2016.
- [28] Abu Qudeiri JE., "Production simulator system for flexible routing optimization in flexible manufacturing systems". *Proc IMechE Part B: J Engineering Manufacture*, 231: pp.1237– 1247, 2017.
- [29] Hu L, Gu Z-Q, Huang J, et al., "Research and realization of optimum route planning in vehicle navigation systems based on a hybrid genetic algorithm".*Proc IMechE Part D: J Automobile Engineering*, 222: pp. 757–763 2018, 2018.
- [30] C. Feng, H. Guo, J. Zhang, Y. Huang and S. Huang, "A systematic method of optimization of machining parameters considering energy consumption, machining time, and surface roughness with experimental analysis", *The International Journal of Advanced Manufacturing Technology*, volume 119, pages7383–7401, 2022.

# Experimental Studies of an Algorithm for Minimizing the Idle Tool Moves when Milling Complex Surfaces on Triaxial CNC Machine Tools

**Silviya Salapateva**

Faculty of Mechanical Engineering  
Technical University of Sofia, Plovdiv Branch  
Plovdiv, Bulgaria  
sisisal@tu-plovdiv.bg

**Bano Stefanov**

Faculty of Mechanical Engineering  
Technical University of Sofia, Plovdiv Branch  
Plovdiv, Bulgaria  
bano@abv.bg

**Abstract.** The idle running times of the working units of a machine tool are the sum of the idle running times for the tool change and for changing the section under treatment. The time, spent on idle running is the extra machining time. A large number of milling cutters are used for purely mechanical machining of details with complex surfaces and for a significant number of machined sections, where the complex surface is broken as a rule. This leads to an increase in the extra time for treatment. Reducing the auxiliary time in machining the parts will significantly increase the productivity of the actual milling process. When modeling the process of machining details with complex surfaces on triaxial milling machines, the optimization of the sequence of moves will allow to reduce the idle running time by up to 50% without causing deterioration in the quality of the surface layer.

In modern production a method is needed, which would allow to automatically and quickly enough make a choice of an optimal option for a sequence of performing tool moves while taking into account the durability of the metal cutting tool.

**Keywords:** pure/actual/finish milling, complex surfaces, CNC machine tool, optimization.

## I. INTRODUCTION

This paper presents a fragment of a research, aimed at increasing the efficiency of triaxial CNC milling machines when milling parts with complex surfaces by reducing the auxiliary time for performing the individual operations, and more precisely by reducing the time for performing idle tool moves. The latter can be achieved, on the one hand, by minimizing the length of the idle tool moves when changing the machined section, and, on the

other hand, by finding the most advantageous sequence for machining the sections.

In order to find an optimal route for all the selected tools of different sizes, it is necessary to determine the most profitable route for each cutter size, used to machine the sections, belonging to one group.

Based on a conducted literature review [1], [2], [3], [4], [5], [6], [7], [8], [9] a method is proposed for determining the optimal route of cutters of one size when moving among one group of sections subject to machining. The method is implemented in two stages:

- at the first stage, an option for minimizing the idle moves of the tool when changing the machined section is sought. The length of each pair of sections, included in a group, is checked. In doing so, it is necessary to determine the position of the local safety zone for every two consecutively processed sections [10];

- at the second stage, the most advantageous sequence for machining all the sections in a group is determined, taking into account both the tool life period and the minimum-length idle moves of the cutter, determined during the first stage.

To solve a problem, in which the number of machined sections is below ten, the so-called "Greedy algorithm" can be applied, which belongs to the group of the heuristic algorithms. When the number of machined sections is bigger than ten, the "Adaptive Large

Print ISSN 1691-5402

Online ISSN 2256-070X

<https://doi.org/10.17770/etr2023vol3.7195>

© 2023 Silviya Salapateva, Bano Stefanov. Published by Rezekne Academy of Technologies.  
This is an open access article under the [Creative Commons Attribution 4.0 International License](https://creativecommons.org/licenses/by/4.0/).

Neighborhood Search" (ALNS) can be applied to find the solution to the problem [11], [12], [13].

To implement the proposed methodology for minimizing the idle moves when milling details with complex surfaces, a programming module (PM) has been developed. The PM is a synthesis of two modules. The first one, PM1, implements the method of minimizing the idle moves when the tool passes from one machined section to another, while the second one, PM2, is based both on the program module PM1 and on the method of searching for the most advantageous milling sequence for all sections, belonging to the group under processing.

The working algorithm of the PM1 module is as it follows:

Step 1: Specifying the input data: coordinates of nodal points from the surface of the part; number of sections processed with cutters of one size; coordinates of the entry and exit points for each section processed with cutters of one size; shape and dimensions of the cutters; extra safety distance.

Step 2: Based on the input data, by means of programming, PM1 compiles a matrix with the minimum lengths of the idle moves during the transition of the tool from one machined section to the next, and the minimum height of tool lifting, guaranteeing the operation of the equipment without coming into contact with the workpiece.

The working algorithm of the PM2 module is the following:

Step 1: Entering the input data: data, obtained after the implementation of the PM1 module; cutting time when machining each of the sections; idle moves speed; tool life period; time, spent on changing the cutter.

Step 2: Based on the input data and using the means of the PM2 module, the optimal sequence of milling the sections, machined with one size milling cutters at a minimum length of the idle moves is determined.

## II. MATERIALS AND METHODS

### A. Methodology for conducting the experiment

The confirmation of the effectiveness of the proposed method for automatic determining of the sequence of execution of the technological transition during pure/finishing milling of parts with a complex shape on a triaxial CNC milling machine should be done by comparing results, obtained for the same details after applying a program module CAM of the Unigraphics system and the developed program module PM.

Test details need to be produced, following a compiled control program.

The results of both the virtual modeling and the physical realization of the machining process, which allow to determine the values of the machine time and the auxiliary time, including the time for idle moves and the time for tool change, should be presented in a tabular format. On the basis of the obtained data, an analysis

should be carried out and corresponding conclusions drawn up.

The test details, obtained by milling, should be evaluated for compliance with the dimensions and the shape of the digital model, as well as for the quality of the resulting surface layer.

### B. Stages of conducting the experiment

The experimental part of the study was conducted in several stages (Fig.1).

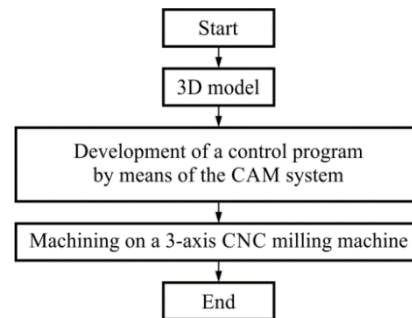


Fig. 1. Technological scheme for processing complex surfaces by milling, when using the Unigraphics system.

At the first stage, a selection of test details with surfaces of complex shape was made so that they include pieces, having biconvex and biconcave sections, as well as sections with a cylindrical, conical and spherical shape, with smooth transitions between them and with flat sections of the machined surface. When selecting the details, those were chosen, which have no less than 10 sections, and the sections can be machined by tail cylindrical cutters - flat face, spherical face and conical ones. In addition, the machining had to be carried out using a set of tools, comprising no less than three milling cutters of different sizes, made of the same material.

At the second stage, a 3D model of the test details was developed, using NX 11 Unigraphics.

The third stage consisted in developing a technology and a control program for processing the test details using the CAM module of the NX 11 Unigraphics system and the optimization options included in it.

At the fourth stage, a technology and control program for processing the test details was developed, this time using the CAM module of the NX 11 Unigraphics system, the optimization option, and the programming module (PM) for determining the sequence of machining and minimizing the idle moves when milling complex surfaces.

The program working algorithm is shown in Fig.2.

The first step is related to specifying the input data: coordinates of nodal points from the surface of the workpiece, coordinates of the starting and ending points of the idle tool moves, number of machined sections, cutting time for each machined section, idle moves speed, tool life period, cutter change time.

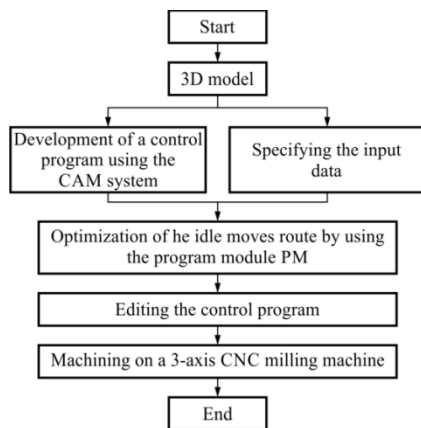


Fig. 2. Technological scheme for processing complex surfaces by milling, while using the developed PM.

Then, by using the PM, the sequence of processing the local sections is determined under the condition of minimizing the idle moves when passing from one machined section to another.

At the third stage of the algorithm, a process of editing the control program in accordance with the results, obtained from the previous stage, occurs.

The next stage consists in activities, related to the production of the test details. Their machining is carried out on a CNC vertical milling machine under the same modes, including cutting speed and feed rate for the same sections of the two test details with the same name, as well as the provision of tools with which the forming is carried out. The rough machining of the pair of parts is carried out by the same technology and control program, providing the same allowance for finish machining. The private cutting strategies (incision trajectory, cutting, and tool withdrawal) for the same sections of the details in purw/finish machining remain constant.

At the last stage of the experimental research, a check is made to assess the dimension accuracy of the pair of details and the microgeometry of the surface layer by using modern control and measuring devices.

### III. RESULTS AND DISCUSSION

The experimental studies were carried out with a test detail, modeled by using NX 11 (Fig.3).

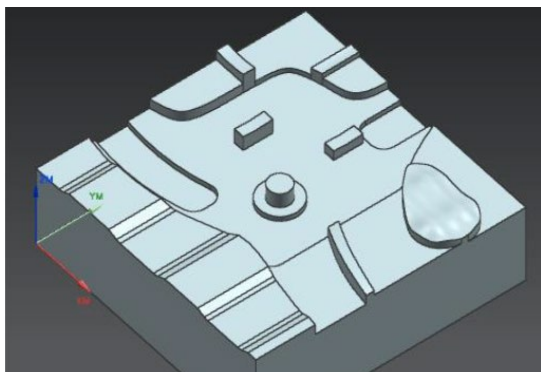


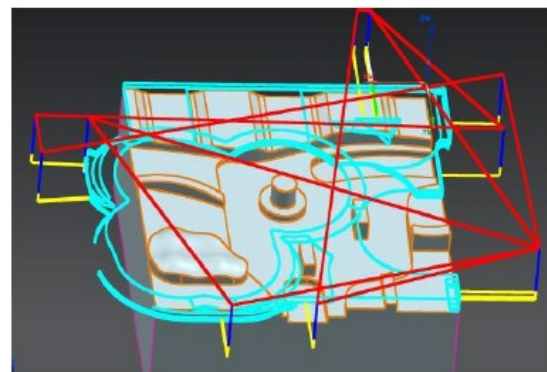
Fig. 3. 3D model of the test piece.

Details with dimensions 105 x 105 x 10 mm, made of B95 aluminum alloy, were selected for conducting the experiments.

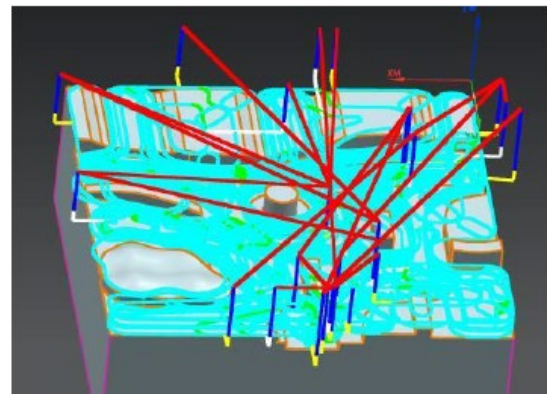
#### A. Detail processing technology

The mechanical processing of the details was done on a vertical milling machine DMS 635 V, produce of the Deckel Maho company.

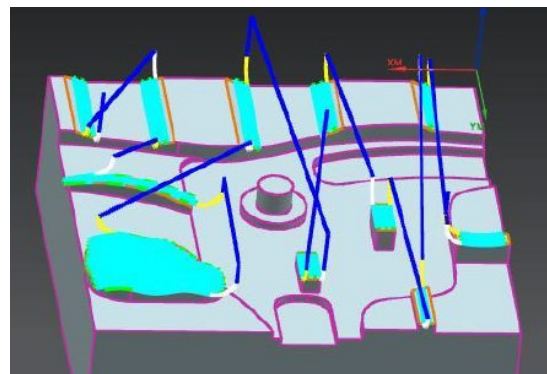
The basic rough milling was carried out initially with a 36 mm diameter flat face cylindrical cutter, then with a 10 mm diameter flat face cylindrical cutter and finally with a spherical face cylindrical cutter 10 mm in diameter (Fig.4). The dimension tolerance after roughing was 0.1mm, the allowance for finish milling - 0.5mm.



(a) flat face cylindrical cutter with D = 36 mm.



(b) flat face cylindrical cutter with D = 10 mm.



(c) spherical face cylindrical cutter with D = 10 mm.

Fig. 4. Path of tool moves during rough milling.

The depth of cut and the machining allowance for rough milling for a flat face cylindrical cutter with  $D = 36$  mm was 2 mm and for the same type cutter with  $D = 10$  mm it was 1.6 mm.

The parameters of the rough milling mode are presented in Table 1.

TABLE 1 CUTTING MODE PARAMETERS

Cutter diameter $D$ , mm	Spindle rotation frequency $n$ , $\text{min}^{-1}$	Tool feed rate $V_f$ , mm/min	Cutting feed $S_m$ , mm/min
<i>Cutting mode parameters in rough milling</i>			
Flat face cylindrical, $D = 36$ mm	6200	3000	1800
Flat face cylindrical, $D = 10$ mm	9000	3000	2500
Spherical face cylindrical, $D = 10$ mm	9000	3000	1800
<i>Cutting mode parameters in finish milling</i>			
Flat face cylindrical, $D = 10$ mm	9000	3000	2500
Spherical face cylindrical, $D = 10$ mm	9000	3000	1800

The finish machining of the test details, which is the purpose of the study, was carried out in two ways. In the first case, the sequence of finish milling of the sections was determined by means of the NX 11 system (variant 1). In the second one, the sequence of finish milling of the sections was determined by using the PM optimization program module.

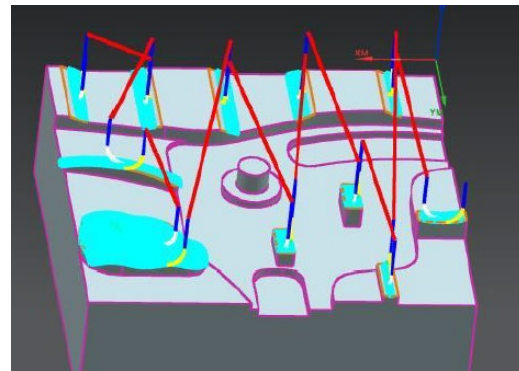
The parameters of the finish milling mode for both variants remained constant (Table 1). A 10 mm diameter four-tooth flat face cylindrical cutter, 10 mm in diameter, and a spherical face cylindrical cutter, 10 mm in diameter, were used for the experiments.

The strategy for finish machining by means of flat face cylindrical cutters with  $D = 10$  mm and spherical face cylindrical cutters with  $D = 10$  mm according to variant 1 (without optimization) is presented in Fig.5.

The number of individual sections machined by means of a flat face cylindrical cutter with 10 mm diameter and a spherical face cylindrical cutter with 10 mm diameter, is presented in Table 2.



(a) flat face cylindrical cutter with  $D = 10$  mm.



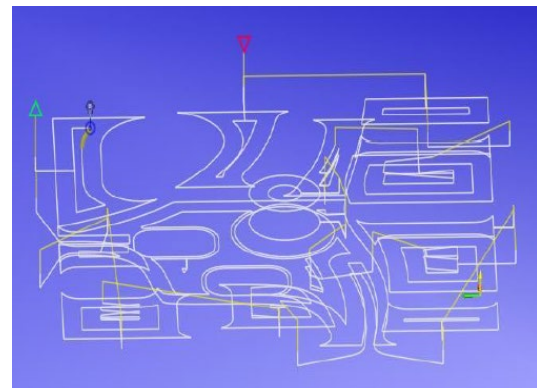
(b) spherical face cylindrical cutter with  $D = 10$  mm

Fig. 5. Path of tool moves during finish milling of a test detail according to variant 1 (without optimization).

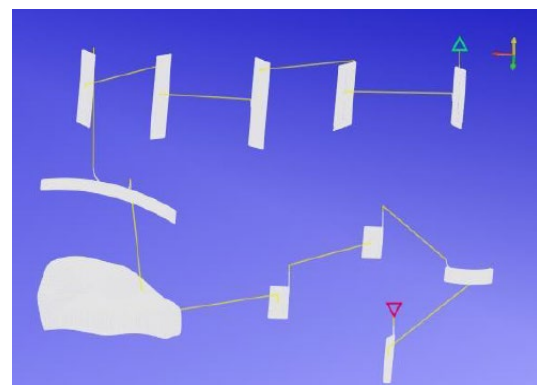
TABLE 2 NUMBER OF SECTIONS, MACHINED WITH CUTTERS OF ONE SIZE

Cutter	Number of sections, machined with cutters of one size
Flat face cylindrical, $D = 10$ mm	17
Spherical face cylindrical, $D = 10$ mm	11

The finish machining strategy, realized by means of a flat face cylindrical cutter with diameter of 10 mm, and by a spherical face cylindrical cutter 10 mm in diameter, according to variant 2 (with optimization), is presented in Fig.6.



(a) flat face cylindrical cutter with  $D = 10$  mm.



(b) spherical face cylindrical cutter with  $D = 10$  mm.

Fig. 6. Trajectory of tool movement during finish milling of a test detail according to variant 2 (with optimization).

Tables 3 present the results of the calculations obtained when preparing the control program for processing the test details based on the NX 11 system without using the optimization program module PM (variant 1), as well as the computational data, obtained by means of the algorithm, which allows to optimize the auxiliary time of idle tool moves when milling complex surfaces on triaxial CNC milling machines (variant 2).

TABLE 3 RESULTS OF THE CALCULATIONS OBTAINED WHEN PREPARING THE CONTROL PROGRAM

Cutter	Variant of machining	
	1	2
<i>Total length of the auxiliary moves L, mm</i>		
Flat face cylindrical, D = 10 mm	2665,8	1484,47
Spherical face cylindrical, D = 10 mm	1768,1315	1287,48
<i>Total time, spent on performing the auxiliary moves T<sub>a</sub>, min</i>		
Flat face cylindrical, D = 10 mm	00.00.53	00.00.29
Spherical face cylindrical, D = 10 mm	00.00.35	00.00.25
<i>Total time, spent on performing the working moves T<sub>w</sub>, min</i>		
Flat face cylindrical, D = 10 mm	00.02.14	00.01.50
Spherical face cylindrical, D = 10 mm	00.06.05	00.05.55

### B. Determination and comparison of the roughness parameters

A Form Talysurf i200 profilometer was used to determine and compare the surface roughness parameters of the test details, processed on a triaxial CNC milling machine. Measurements were carried out to determine the roughness parameters of the surfaces of each section, depending on the dimensions of the section along a certain route. The speed of the probe was 1 mm/s. As a result, average values of the roughness parameters were obtained for each measured section.

The determination of the roughness parameters was made for 28 sections (Fig.7) in accordance with the number of sections to be machined, differing in shape and size.

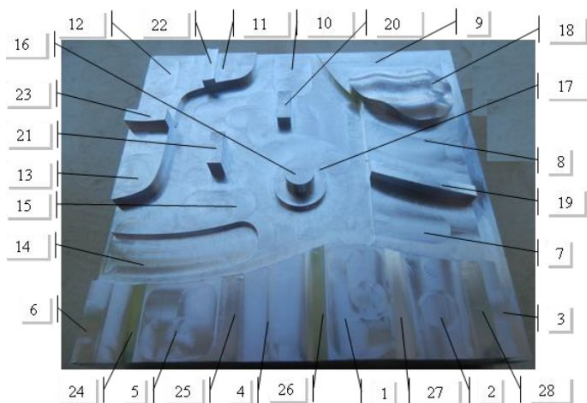


Fig. 7. The sections of the detail.

The results of the measurements are presented in Table 4.

TABLE 4 ROUGHNESS PARAMETERS RA OF THE SECTIONS OF A DETAIL

Section №	Roughness parameters Ra of the surfaces of the details (µm)	
	Variant with optimization	Variant without optimization
1	0.2570	0.2268
2	0.4257	0.4085
3	0.2975	0.3265
4	0.3054	0.3047
5	0.2697	0.2309
...	...	...
25	0.0728	0.0774
26	0.0819	0.0906
27	0.0680	0.0890
28	0.0841	0.0674

To compare the roughness parameters of the sections of the surfaces of the details, a graphical dependence was drawn, juxtaposing these parameters for the variant with and the variant without optimization (Fig. 8).

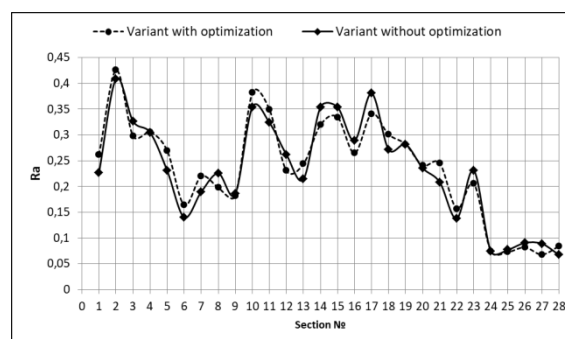


Fig. 8. Graphical dependence, presenting the deviation of the roughness parameters of the detail surfaces.

From the graphical dependence, presented in Fig.8 and the data in Table 4, it can be seen, that the deviations of the roughness parameters of the detail surfaces for the corresponding sections, machined by following the program module PM and without its use, are within the limits of the measurement error. The roughness parameter R<sub>a</sub> for the machined sections is different and varies from 0.05 to 0.4 µm, which is explained by the different cutting trajectories and the specific cutting strategies planned within the technological process for machining each section.

As a conclusion it can be said that the change in the sequence of machining the sections at an unchanged specific strategy for machining each section does not lead to deterioration in the surface quality of the machined detail.

### C. Determination and comparison of the deviation in shape and size of the test samples from the digital models

A Contura G2 Carl Zeiss coordinate measuring machine was used to determine and compare the deviations from the dimensions and the shape of the test details, machined on a triaxial CNC milling machine. In order to provide the same metrological conditions, the measurements were carried out in the same points on the surfaces of the controlled details.

The accuracy of measurement is determined by the technical capabilities of the coordinate measuring machine, i.e., is 0.001 mm. The measurement results, obtained in digital form, were imported into the automated control system for comparison with the digital reference of the test detail and determination of the deviations [15]. To compare the parameters of deviation in shape of sections of the details' surfaces, a graph was drawn, presenting the deviations of their points for the two variants of processing - with using the program module PM and without it (Fig.9).

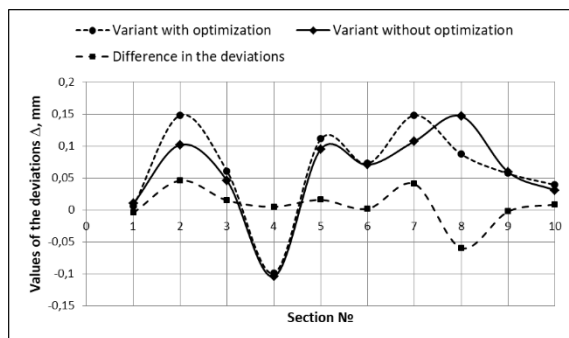


Fig. 9. Deviation in shape in points on the surface of a detail, processed both ways.

The results, obtained after comparing the deviations of the test details in shape and size from the digital model, show that the difference of the deviation parameters  $\Delta$  in the points of carrying out the measurements is within the limits of the tolerance field. This is confirmed by the fact that the change in the sequence of machining sections of complex surfaces and the application of the program module PM in order to optimize the idle tool moves preserve the accuracy of the complex surfaces of details, processed by milling.

#### IV. CONCLUSIONS

The obtained experimental data allow to conclude that the application of the program module PM to optimize the idle moves of the machine when processing complex surfaces, allows to ensure high quality of the microgeometry of the detail surface and accuracy of machining, while reducing the total machine time for processing a detail.

The greatest effect of applying the program module can be obtained for details, containing 10 or more sections to be machined.

In the calculations, the joint application of mathematical models for minimization of the idle moves in case of changing the machined sections and optimization of the sequence of machining of the individual sections, allows to obtain the most advantageous tool route when machining the individual sections with cutters of one size. The auxiliary time,

spent on the idle moves when changing the milling cutter and changing the machined sections is minimized at the same time.

#### ACKNOWLEDGMENTS

The results were obtained under a project funded by the research grant at TU –Sofia -contract № 222ΠΠ0021-24 – Optimization of the parameters of technological processes for mechanical machining on CNC machines by means of digital models.

#### REFERENCES

- [1] V. Georgiev and S. Pashov, Technology of mechanical engineering - basics of mechanical engineering technology. Plovdiv: TU-Sofia, Plovdiv branch, 2003.
- [2] V. Georgiev, R. Rachev and A. Lengerov, Technology of mechanical engineering - part two. Plovdiv: TU-Sofia, Plovdiv branch, 2005.
- [3] T. Kuzmanov and H. Metev, Fundamentals of machine-building technologies. Gabrovo: Ex-Press, 2005.
- [4] T. Kuzmanov, V. Georgiev, and H. Metev, Technological processes for CNC metal-cutting machines. Gabrovo: Ex-Press, 2007.
- [5] P. Hadjiski, Programming of CNC machines. Sofia: TU-Sofia, 2010.
- [6] "New functions of modern CNC systems in the processing of complex contours and volume-profile surfaces", pp.88+, february 2012. [Online]. Availble: Engineering Review, <http://engineering-review.bg>. [Accessed May 23, 2022].
- [7] ZZ Li, Min Zheng, Li Zheng, ZJ Wu and DC Liu, "A solid model-based milling process simulation and optimization system integrated with CAD/CAM", Review of Journal of materials processing technology, vol.138, pp.513, 2003.
- [8] GM Kim, PJ Cho, and CN Chu, "Cutting force prediction of sculptured surface ball-end milling using Z-map", Review of Journal of Machine Tools and Manufacture, vol. 40, pp.277, 2000.
- [9] M. Soori and B. Arezoo, "Virtual Machining Systems for CNC Milling and Turning machine Tools", Journal of Engineering and Future Technology, vol.18, pp.56, 2021.
- [10] S. Salapatava, B. Stefanov, I. Chetrokov, "Mathematical model for minimizing a tool idle motion while milling complex surfaces on on 3-axis CNC milling machines when changing the machined area", presented at National Conference on Mechanical Engineering and Mechanical Science (It is to be published in the journal Machine Science, 2023), Varna, Bulgaria, 2022.
- [11] . Alinaghian, M. Jamshidian and E. B. Tirkolaee, "The time-dependent multi-depot fleet size and mix green vehicle routing problem: improved adaptive large neighbourhood search", A Journal of Mathematical Programming and Operations Research, Volume 71, 2022 - Issue 11: Special Issue Dedicated to the International Conference «Dynamical Control and Optimization», DCO 2021.
- [12] C. Zhang, F. Han and W. Zhang, "A cutting sequence optimization method based on tabu search algorithm for complex parts machining", Proceedings of the Institution of Mechanical Engineers, Part B: Journal of Engineering Manufacture, Volume 233, Issue, 2018.
- [13] Y. Xin, S. Yang, G. Wang2, R. Evans and F. Wu, "A tool path optimization approach based on blend feature simplification for multi-cavity machining of complex parts", Science Progress 2020, Vol. 103(1) 1–21, 2020.
- [14] Zeiss CONTURA G2, Installation Instructions Manual, [Onlin]. Availble: <https://manualzz.com/doc/54733661/zeiss-contura-g2-installation-instructions-manual>. [Accessed: Aug. 25, 2022].

# Adaptive Image Enhancement Model for the Robot Vision System

**Kyrylo Smelyakov**

Software engineering department,  
Kharkiv National University of Radio  
Electronics,  
Kharkiv, Ukraine  
kirillsmelyakov@gmail.com

**Anastasiya Chupryna**

Software engineering department,  
Kharkiv National University of  
Radio Electronics,  
Kharkiv, Ukraine  
anastasiya.chupryna@nure.ua

**Denys Sandrkin**

Software engineering department,  
Kharkiv National University of  
Radio Electronics,  
Kharkiv, Ukraine  
denys.sandrkin@nure.ua

**Loreta Savulioniene**

Faculty of electronics and informatics,  
Vilniaus Kolegija/Higher Education  
Institution  
Vilnius, Lithuania  
l.savulioniene@eif.viko.lt

**Paulius Sakalys**

Faculty of electronics and  
informatics, Vilniaus  
Kolegija/Higher Education  
Institution  
Vilnius, Lithuania  
p.sakalys@eif.viko.lt

**Abstract.** Robotics is one of the important trends in the current development of science and technology. Most modern robots and drones have their own vision system, including a video camera, which they use to take digital photos and video streams. These data are used to analyze the situation in the robot's camera field of view, as well as to determine a real-time robot's behavior algorithm. In this regard, the novelty of the paper is special polynomial mathematical model and method for adaptive gradational correction of a digital image. The proposed model and method make it possible to independently adjust to brightness scales and image formats and optimally perform gradational image correction in various lighting conditions. Thus, ensuring the efficiency of the entire subsequent cycle of image analysis in the robot's vision system. In addition, the paper presents the results of numerous experiments of such gradational correction for images of various classes, as well as conditions of reduced and increased levels of illumination of the field of view objects. Conclusions and recommendations are given regarding the practical application of the proposed model and method.

**Keywords:** Digital Image, robotics, robot vision system, image enhancement, gradational correction.

## I. INTRODUCTION

The number of different robots and drones that we already see at the operational stage, as well as those still in development, is simply amazing [1, 2]. Most of these robots (and drones) are equipped with a video camera and their own vision system [3-5], so that the robot can independently

monitor and analyze the situation according to specified algorithms in offline mode [6].

For example, in [7] a new method for improving the input image is presented, which is based on the use of Retinex. This solution is used for robotic capture of an underwater surveillance system.

The publication [8] presents an algorithm for controlling the operation of a robot with feedback, which is based on real-time segmentation and estimation of the width of the roadway.

The paper [9] presents the results of solving the localization problem for a mobile robot. The paper proposes a new localization system that combines the use of machine vision and lidar in its work, moreover, for conditions of significant occlusion.

The publication [10] presents the results of research and proposes a new algorithm for controlling the movement of a robot based on the use of machine vision to solve the problem of self-localization. The event and deadline-based algorithm largely avoids delays in the robot control loop.

The paper [11] presents the results of a study of a complex robotic system for gesture recognition.

The work [12] presents improved algorithms for implementing the capture function by a robot, based on the use of a machine vision system, which is relevant for intelligent robots that perform complex manipulations.

Print ISSN 1691-5402

Online ISSN 2256-070X

<https://doi.org/10.17770/etr2023vol3.7300>

© 2023 Kyrylo Smelyakov, Anastasiya Chupryna, Denys Sandrkin, Loreta Savulioniene, Paulius Sakalys.

Published by Rezekne Academy of Technologies.

This is an open access article under the [Creative Commons Attribution 4.0 International License](https://creativecommons.org/licenses/by/4.0/).

A separate class of works is devoted to the development and improvement of UAV vision systems in terms of improving the efficiency of their work in offline mode [13-15].

In general, if we talk about mobile robots, the analysis of the current state of the issue shows that special attention is paid to the development and improvement of automatic image enhancement algorithms. Since the efficiency of the entire cycle of image analysis of autonomous robots depends on the efficiency of these algorithms [16-18].

In this regard, the aim of the paper is to present a mathematical model and an algorithm for adaptive gradational correction of a digital image, as well as the results of experiments for various classes of objects and conditions for obtaining images. The value of the model and the algorithm lies in the fact that they are automatically adjusted to the brightness scale and image format and carry out gradation correction of the image in automatic mode.

In addition to robotics, an effective solution to the problem of automatically improving the quality of a digital image is important for image search services that operate autonomously or as part of image storage management systems [19-21].

## II. MODELS, METHODS AND MATERIALS

The key requirement for the model and method of gradation correction of the machine vision system of an autonomous robot is that such a model (and method) should automatically adjust to the initial data. First of all, on the image brightness scale, which can vary over a wide range.

In addition, the gradation correction model should be flexible enough to provide both linear and non-linear image brightness transformation depending on the requirements of the applied task.

Currently, the main models that are used for such purposes are linear, exponential and logarithmic models. The linear model is not flexible enough, while the exponential and logarithmic models are often too harsh.

Considering these aspects, a power-law model of gradation image correction is proposed, which allows to smooth out these shortcomings.

Such a power-law model in a unified form has the form

$$h_{\gamma}(x) = \frac{d-c}{(b-a)^{\gamma}} \cdot (x-a)^{\gamma} + c. \quad (1)$$

where:

- $x$  - input brightness value.
- $\gamma$  - degree exponent.
- $h_{\gamma}$  - output brightness value.
- $[a, \dots, b]$  - the input brightness range.
- $[c, \dots, d]$  - the output brightness range.

This function was obtained in the course of transformations from the basic representation of a power function of the form

$$y(x) = k \cdot x^{\gamma}, \gamma > 0, \quad (2)$$

by substitution of coefficients  $a, b, c, d$ , where

- $[a, \dots, b]$  - the input brightness range.
- $[c, \dots, d]$  - the output brightness range.
- $k$  - normalization coefficient.
- $\gamma$  - degree exponent.

In doing so, the following conditions were met: coefficient  $k$  is determined from the condition  $y(b) = d, y(a) = c$ .

The proposed power-law model is shown in Fig. 1.

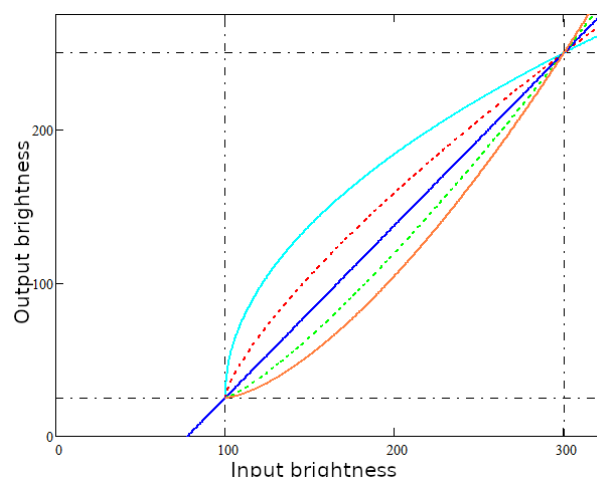


Fig. 1. A family of power-law gradation correction functions that are built with a step of 0.25 ( $\gamma = 0.5, 0.75, 1, 1.25, 1.5$ ) for brightness values:  $a = 100, b = 300, c = 25, d = 250$ ; the  $x$ -axis represents the brightness of the input image, and the  $y$ -axis represents the brightness of the output image.

With an increase in the exponent greater than one, model (1) becomes similar to an exponential. Such a model serves to significantly enhance the brighter part of the spectrum and suppress its darker part. When we decrease the exponent below one, model (1) becomes similar to a logarithm. Such a model serves to significantly enhance the darker part of the spectrum and suppress its lighter part. When the value of the  $\gamma = 1$  we get the classical linear function of the proportional change in the brightness of the image. Thus, depending on the requirements of the task, one can very flexibly tune the model (1). The model automatically adjusts to the brightness level of images when used (due to parameters  $a, b, c, d$ ).

Consider the method of applying the model (1).

At the first stage (when the model parameters are determined), for a given brightness range of the input and output images, we once, using model (1), construct a tabular function  $f(x)$  (row matrix) for converting the input brightness to the output. In order not to perform these time-consuming repetitive calculations in the gradation image correction cycle.

Then, using the  $f(x)$  table, we quickly change the brightness of the input image to the corresponding output values.

The complexity of the method is determined by the linear estimate  $O(n)$ , since in the body of the tonal correction cycle only one operation of changing the

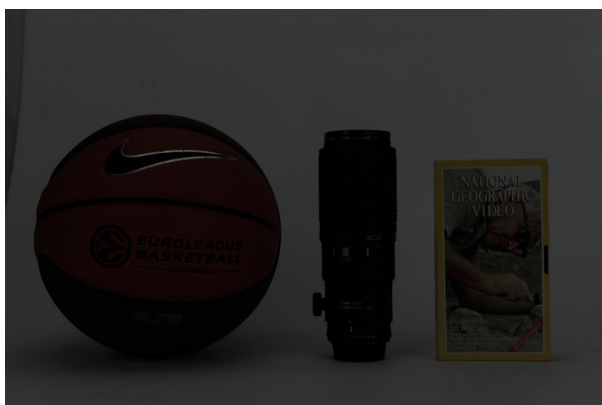
brightness of the form  $x[i, j] = f(x[i, j])$  will be performed.

The efficiency of the gradation correction method can be increased many times over by pre-trimming the tails of the brightness histogram of the original image. If you build a brightness histogram of the original image, it has tails, represented by a series of low frequency values. If they are reset to zero and new extreme values a, b are found with a non-zero frequency, when performing gradation correction, the level of image contrast will increase significantly.

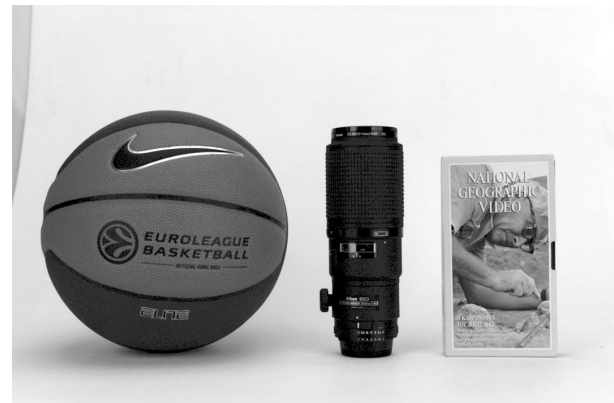
### III. EXPERIMENT

For the experiment several datasets were used. First [22] contains dark photos, taken outdoors. They vary in size, scene, and objects that are depicted on them. This dataset was chosen due to a big variety of scenes and light conditions, this helps a lot when testing of image enhancement algorithms is needed. A variety of depicted objects help for cases, when different recognition algorithms should use these images for object recognition, after enhancing by our algorithm. Also using of photos help, because these images are not perfect in terms of scene setup, so they are close to real life applications, then the laboratory images. Second dataset [23] contains indoor photos of different objects. Objects varying, as well as lighting conditions. This dataset is useful for research of how the different lighting conditions affect the perception of different objects. Also having the same objects in different lighting conditions helps to verify the work of enhancement algorithm. During the experiment we used power-law gradation correction to enhance images. The best correction was chosen by an expert.

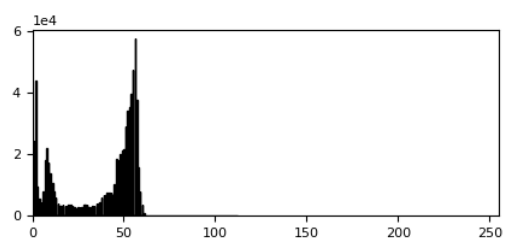
Starting with the first image of the basketball ball, camera lens and the book Fig. 2. These objects contain valuable details, like text, which is readable only after image correction.



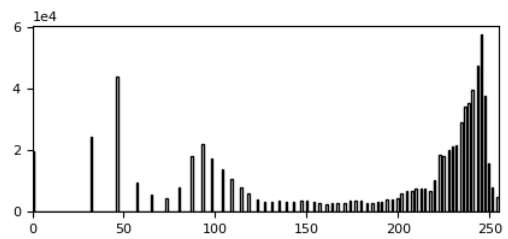
a)



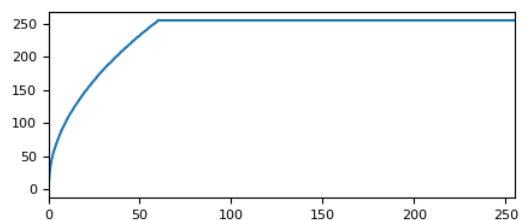
b)



c)



d)



e)

Fig. 2. Image of a basketball ball, camera lens and a book (a)[23], its brightness histogram (c). Improved image (b) and its brightness histogram (d). The scale of the change in the brightness is: 1 division corresponds to the value  $10^4$ . Image transformation function (e) x-axis represents the brightness of the input image, and the y-axis represents the brightness of the output image.

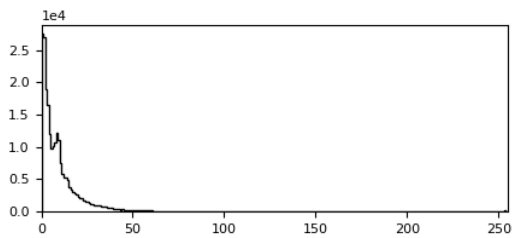
Next image on Fig. 3 is a photo of a night street, it is barely possible to see if there are any objects in this photo. After correction we can observe that there are a lot of objects on the way.



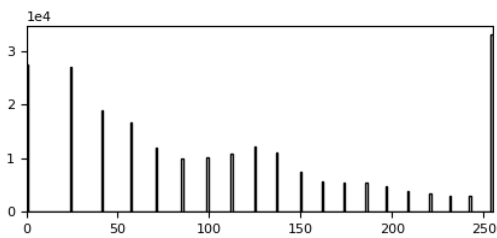
a)



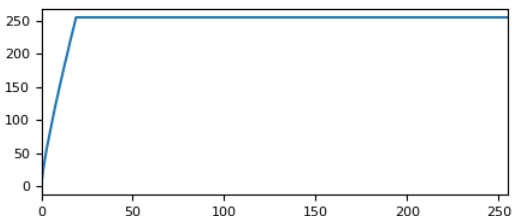
b)



c)



d)



e)

Fig. 3. Photo of a night street (a)[22], its brightness histogram (c). Improved image (b) and its brightness histogram (d). The scale of the change in the brightness is: 1 division corresponds to the value  $10^4$ . Image transformation function (e)  $x$ -axis represents the brightness of the input image, and the  $y$ -axis represents the brightness of the output image.

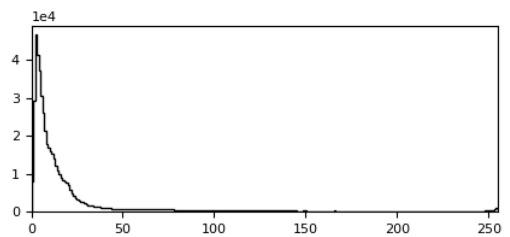
Very similar to Fig. 3 is Fig. 4. This is a photo of a house. As on previous image, in this photo it is not possible to see if there are any additional objects near the building. So, this is issue, in situation, when we need to be aware of any obstacles. Gradation correction easily fixes this issue, and it is possible to state that after correction bicycle under the window and trees are firmly visible.



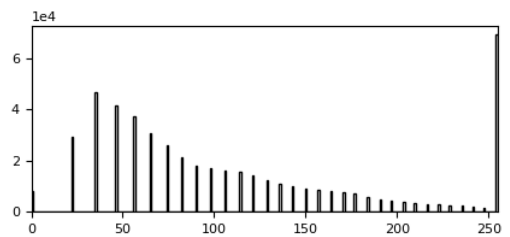
a)



b)



c)



d)

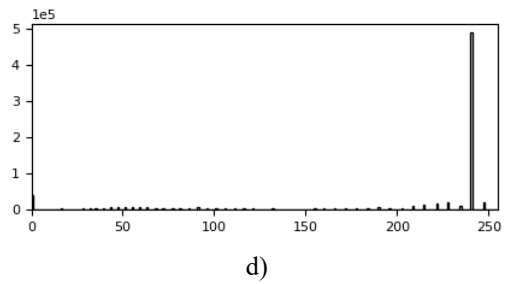
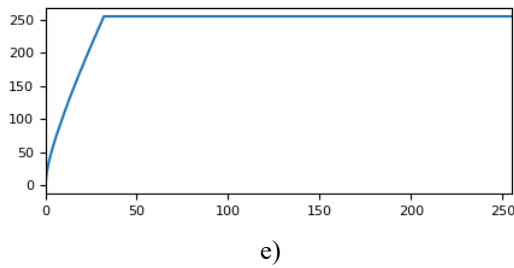


Fig. 4. Photo of night house (a)[22], its brightness histogram (c). Improved image (b) and its brightness histogram (d). The scale of the change in the brightness is: 1 division corresponds to the value  $10^4$ . Image transformation function (e)  $x$ -axis represents the brightness of the input image, and the  $y$ -axis represents the brightness of the output image.

The final example is an overexposed photo Fig. 5. Too much light is also not a good lighting condition. In this photo text is not readable, and pattern and size of the notebook is not visible. Our algorithm can handle this situation too. Please note how the transformation function for the overexposed image on Fig. 5(e) changed. Input range is shifted to the right of the  $x$ -axis.

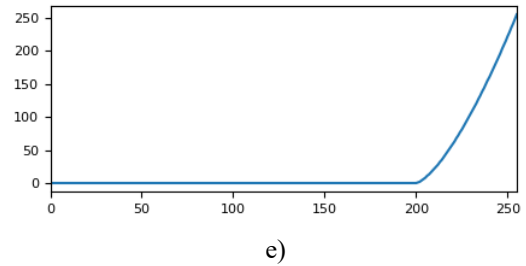


Fig. 5. Image of a book, camera lens and notebook (a)[23], its brightness histogram (c). Improved image (b) and its brightness histogram (d). The scale of the change in the brightness is: 1 division corresponds to the value  $10^4$ . Image transformation function (e)  $x$ -axis represents the brightness of the input image, and the  $y$ -axis represents the brightness of the output image.

In the course of work on the article, a large series of 200 experiments was carried out. Half of the images for the experiments were selected from the considered dataset by experts. These are the 100 most distorted images according to experts. The second half was chosen at random. This image selection refer to first dataset [22], because there are more images. And all images from the second dataset [23] where used for conducting experiments.

Test software is written using Python 3. Test hardware uses standard consumer grade PC with i5-10300H processor. Test code is not optimized for parallel execution.

To demonstrate the capabilities of the proposed model, the paper presents the results of four experiments on images chosen by experts. Analyzing the results of the experiments, the experts gave the best recommendation for the model and the method of its implementation.

Since the proposed method of gradation correction works in real time, automatically increasing the contrast of bad images up to 5-7 times, making even the worst images clearly visible (this can be seen from the above experimental results).

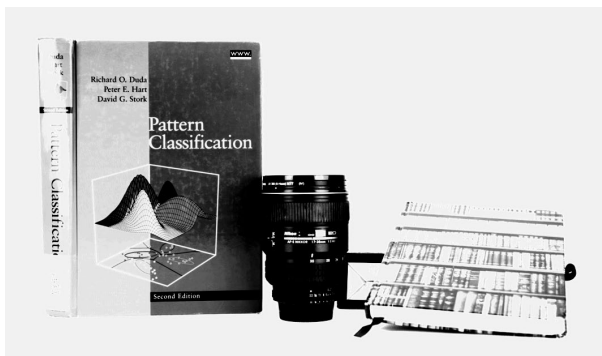
The even not optimized experimental code, used for proving of concept gives very good results is terms of performance.

#### IV. CONCLUSION

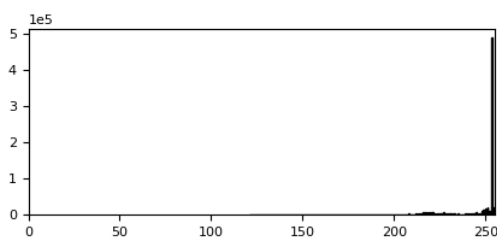
Based on publication analysis we can conclude that video input is one of the most important inputs for robot systems, as it helps to navigate, detect needed objects,



a)



b)



c)

and give much useful information. That means that the quality of the input image data is crucial for successful operation, because if input data is not good enough, even the best algorithms cannot do much. This is very well-known concept in computer science garbage in, garbage out.

The novelty of the paper is special polynomial mathematical model and method for adaptive gradational correction of a digital image. This method helps to enhance images in a very fast and efficient way. This allows using such methods even in real time applications. Which could be very handy in robot navigation applications, or video streams enhancement, even in bulk enhancement of big storages of images.

Experiment was conducted, which proved that this method works and gives good results on a wide variety of image classes which has different lighting conditions including underexposing and overexposing, different scenes, even different approaches in photograph (casual photos, and professionally made photos). But, as always, there is a space for improvement in future research, for using different functions for image processing, depending on the scene and lighting conditions.

#### REFERENCES

- [1] J. P. Queralta et al., "Collaborative Multi-Robot Search and Rescue: Planning, Coordination, Perception, and Active Vision," in *IEEE Access*, vol. 8, pp. 191617-191643, 2020, doi: 10.1109/ACCESS.2020.3030190.
- [2] I. Enebuse, M. Foo, B. S. K. K. Ibrahim, H. Ahmed, F. Supmak and O. S. Eyobu, "A Comparative Review of Hand-Eye Calibration Techniques for Vision Guided Robots," in *IEEE Access*, vol. 9, pp. 113143-113155, 2021, doi: 10.1109/ACCESS.2021.3104514.
- [3] M. Aranda, Y. Mezouar, G. López-Nicolás and C. Sagüés, "Scale-Free Vision-Based Aerial Control of a Ground Formation With Hybrid Topology," in *IEEE Transactions on Control Systems Technology*, vol. 27, no. 4, pp. 1703-1711, July 2019, doi: 10.1109/TCST.2018.2834308.
- [4] C. Zhou, Q. Sun, K. Wang, J. Li and X. Zhang, "Simultaneous Calibration of Multiple Revolute Joints for Articulated Vision Systems via SE(3) Kinematic Bundle Adjustment," in *IEEE Robotics and Automation Letters*, vol. 7, no. 4, pp. 12161-12168, Oct. 2022, doi: 10.1109/LRA.2022.3189815.
- [5] Y. Luo et al., "Calibration-Free Monocular Vision-Based Robot Manipulations With Occlusion Awareness," in *IEEE Access*, vol. 9, pp. 85265-85276, 2021, doi: 10.1109/ACCESS.2021.3082947.
- [6] R. G. Lins and S. N. Givigi, "FPGA-Based Design Optimization in Autonomous Robot Systems for Inspection of Civil Infrastructure," in *IEEE Systems Journal*, vol. 14, no. 2, pp. 2961-2964, June 2020, doi: 10.1109/JSYST.2019.2960309.
- [7] Y. Wang et al., "Real-Time Underwater Onboard Vision Sensing System for Robotic Gripping," in *IEEE Transactions on Instrumentation and Measurement*, vol. 70, pp. 1-11, 2021, Art no. 5002611, doi: 10.1109/TIM.2020.3028400.
- [8] L. Yi et al., "Reconfiguration During Locomotion by Pavement Sweeping Robot With Feedback Control From Vision System," in *IEEE Access*, vol. 8, pp. 113355-113370, 2020, doi: 10.1109/ACCESS.2020.3003376.
- [9] Y. Shi, W. Zhang, F. Li and Q. Huang, "Robust Localization System Fusing Vision and Lidar Under Severe Occlusion," in *IEEE Access*, vol. 8, pp. 62495-62504, 2020, doi: 10.1109/ACCESS.2020.2981520.
- [10] E. P. van Horsen, J. A. A. van Hooijdonk, D. Antunes and W. P. M. H. Heemels, "Event- and Deadline-Driven Control of a Self-Localizing Robot With Vision-Induced Delays," in *IEEE Transactions on Industrial Electronics*, vol. 67, no. 2, pp. 1212-1221, Feb. 2020, doi: 10.1109/TIE.2019.2899553.
- [11] L. Fiorini et al., "Daily Gesture Recognition During Human-Robot Interaction Combining Vision and Wearable Systems," in *IEEE Sensors Journal*, vol. 21, no. 20, pp. 23568-23577, 15 Oct. 2021, doi: 10.1109/JSEN.2021.3108011.
- [12] H. Cheng, Y. Wang and M. Q. . -H. Meng, "A Vision-Based Robot Grasping System," in *IEEE Sensors Journal*, vol. 22, no. 10, pp. 9610-9620, 15 May, 2022, doi: 10.1109/JSEN.2022.3163730.
- [13] G. S. Ramos, D. Barreto Haddad, A. L. Barros, L. de Melo Honorio and M. Faria Pinto, "EKF-Based Vision-Assisted Target Tracking and Approaching for Autonomous UAV in Offshore Mooring Tasks," in *IEEE Journal on Miniaturization for Air and Space Systems*, vol. 3, no. 2, pp. 53-66, June 2022, doi: 10.1109/JMASS.2022.3195660.
- [14] W. Bouachir, K. E. Ihou, H. -E. Gueziri, N. Bouguila and N. Bélanger, "Computer Vision System for Automatic Counting of Planting Microsites Using UAV Imagery," in *IEEE Access*, vol. 7, pp. 82491-82500, 2019, doi: 10.1109/ACCESS.2019.2923765.
- [15] N. H. Malle, F. F. Nyboe and E. S. M. Ebeid, "Onboard Powerline Perception System for UAVs Using mmWave Radar and FPGA-Accelerated Vision," in *IEEE Access*, vol. 10, pp. 113543-113559, 2022, doi: 10.1109/ACCESS.2022.3217537.
- [16] T. Liu, H. Liu, Y. -F. Li, Z. Chen, Z. Zhang and S. Liu, "Flexible FTIR Spectral Imaging Enhancement for Industrial Robot Infrared Vision Sensing," in *IEEE Transactions on Industrial Informatics*, vol. 16, no. 1, pp. 544-554, Jan. 2020, doi: 10.1109/TII.2019.2934728.
- [17] R. Chen, Z. Cai and W. Cao, "MFFN: An Underwater Sensing Scene Image Enhancement Method Based on Multiscale Feature Fusion Network," in *IEEE Transactions on Geoscience and Remote Sensing*, vol. 60, pp. 1-12, 2022, Art no. 4205612, doi: 10.1109/TGRS.2021.3134762.
- [18] F. Ding, K. Yu, Z. Gu, X. Li and Y. Shi, "Perceptual Enhancement for Autonomous Vehicles: Restoring Visually Degraded Images for Context Prediction via Adversarial Training," in *IEEE Transactions on Intelligent Transportation Systems*, vol. 23, no. 7, pp. 9430-9441, July 2022, doi: 10.1109/TITS.2021.3120075.
- [19] K. Smelyakov, A. Chupryna, D. Sandrkin and M. Kolisnyk, "Search by Image Engine for Big Data Warehouse," 2020 IEEE Open Conference of Electrical, Electronic and Information Sciences (eStream), Vilnius, Lithuania, 2020, pp. 1-4, doi: 10.1109/eStream50540.2020.9108782.
- [20] L. Nie, F. Jiao, W. Wang, Y. Wang and Q. Tian, "Conversational Image Search," in *IEEE Transactions on Image Processing*, vol. 30, pp. 7732-7743, 2021, doi: 10.1109/TIP.2021.3108724.
- [21] K. Smelyakov, M. Hvozdiev, A. Chupryna, D. Sandrkin and V. Martovtyskyi, "Comparative Efficiency Analysis of Gradational Correction Models of Highly Lighted Image," 2019 IEEE International Scientific-Practical Conference Problems of Infocommunications, Science and Technology (PIC S&T), 2019, pp. 703-708, doi: 10.1109/PICST47496.2019.9061356.
- [22] Loh, Yuen Peng and Chan, Chee Seng, "Getting to Know Low-light Images with The Exclusively Dark Dataset," *Computer Vision and Image Understanding*, vol. 178, pp. 30-42, 2019, doi:https://doi.org/10.1016/j.cviu.2018.10.010
- [23] V. Vonikakis, D. Chrysostomou, R. Kouskouridas and A. Gasteratos, "Improving the Robustness in Feature Detection by Local Contrast Enhancement," in *Proceedings of the IEEE International Conference on Imaging Systems and Techniques (IST '12)*, pp. 158 – 163, Manchester, United Kingdom, 16-17 July 2012.

# Frequency Analysis of an Arm of Macpherson Suspension on a Passenger Car

**Stiliyana Taneva**

Department of Transport and Aircraft  
Equipment and Technologies  
Technical University of Sofia, Plovdiv  
Branch  
Plovdiv, Bulgaria  
email s.taneva@tu-plovdiv.bg

**Krasimir Ambarev**

Department of Transport and  
Aircraft Equipment and  
Technologies  
Technical University of Sofia,  
Plovdiv Branch  
Plovdiv, Bulgaria  
email kambarev@tu-plovdiv.bg

**Stanimir Penchev**

Department of Transport and  
Aircraft Equipment and  
Technologies  
Technical University of Sofia,  
Plovdiv Branch  
Plovdiv, Bulgaria  
email spenchev@tu-plovdiv.bg

**Hristo Atanssov**

Auto center Lusi  
151 Vasil Levski Street  
Plovdiv, Bulgaria  
email h\_atan@abv.bg

**Abstract.** The smoothness, ride comfort, safety and handling of the car depends on the manner of suspension design and its corresponding details. One of main functions of the arm and the rubber bushings mounted on it is to reduce the vibrations and the noise transferred from the road to the passenger car components. This article presents the results of a frequency analysis of an arm of the MacPherson front independent suspension. For this purpose, three-dimensional geometric models of the arm and rubber bushings are created via finite element analysis (FEA) software SolidWorks, where Skoda Octavia passenger car was used as a prototype. The axial, radial and torsional stiffness of the rubber bushings were determined through analytical dependences and FEA. The obtained results had been used for calculation of the natural frequencies and mode shapes of the arm which were compared with experimentally obtained data.

**Keywords:** natural frequency, mode shape, arm, suspension, rubber bushing, FEA, experimental study.

## I. INTRODUCTION

Suspension reduces dynamic loads on the vehicle body and wheels by reducing the amount of force of shocks and vibrations. In some cases the suspension adjusts the position of the vehicle chassis.

During the suspension design the natural frequency and the vibration amplitude of the unsprung components are one of the main focus elements.

It is well known that an optimal driving comfort is achieved when the natural frequency is in the range of 1-1,5 Hz. Increase of natural frequency above 1,5 Hz, leads to decrease of the comfort. In real life vehicle applications, the natural frequency changes between 0 to 20 Hz due to road imperfections [2]. The range of the variations of the natural frequency must be taken in consideration during the design process of the suspension and its various components which are exposed to dynamic stresses. That's why the determining of natural frequencies and mode shapes is crucial.

The control arm of the suspension were investigated by various studies [2,3,5,6,7,8,9,10, 11,12,13] by means of FEA software. Study [5,7] provides results regarding the static strength and frequency analysis of lower arm of double wishbone suspension. Results regarding static strength analysis of MacPherson independent suspension obtained by FEA are presented in [6,8]. Studies [5,6,9,10,11,12] show topology optimization of an arm while in [3,7,13] dynamic analysis of lower arm via numerical and experimental study is described.

The purpose of the study is to determine the natural frequencies and mode shapes of a front arm of a MacPherson type suspension of a passenger car Skoda Octavia. To achieve the goal a FEA and up-to-date software tools Simulation module of SolidWorks were used. The simulation results of the natural frequencies

Print ISSN 1691-5402

Online ISSN 2256-070X

<https://doi.org/10.17770/etr2023vol3.7277>

© 2023 Stiliyana Taneva, Krasimir Ambarev, Stanimir Penchev, Hristo Atanssov.

Published by Rezekne Academy of Technologies.

This is an open access article under the [Creative Commons Attribution 4.0 International License](https://creativecommons.org/licenses/by/4.0/).

were confirmed by experimentally which is also part of the current study.

## II. DETERMINATION OF THE SIFFNESS OF ARM RUBBER BUSHING

The MacPherson type is mainly used for front suspension in modern passenger cars, which stands out for its compactness, small mass and significantly less ball joints. The MacPherson type suspension includes the following main elements: arm, elastic element (spring) and shock absorber. Figure 1 shows a three-dimensional geometric (3D) model of a suspension, position 1 shows the arm, position 2 shows rubber bushing 1 and position 3 shows rubber bushing 1. The the axial, radial and torsional stiffness are presented in fig.1.

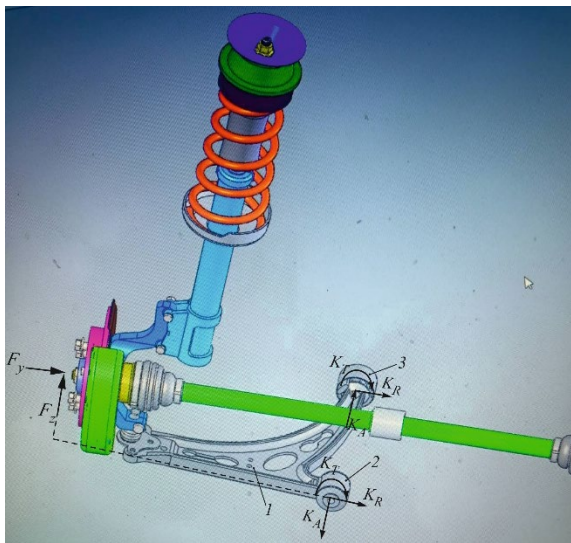


Fig. 1. Three-dimensional geometric model of a suspension and radial, axial and torsional stiffness in rubber bushing of an arm.

Natural frequencies and mode shapes of the arm are most often determined by performing a physical experiment, analytically determined or by using FEA.

The correct setting of the supports is critical in determining the natural frequencies and mode shapes of the suspension and the arm respectively.

The static stiffness of the rubber bushings can be calculated by defined mathematical equations, by FEA or experimentally.

The radial stiffness of the rubber bushing can be determined by the dependence [1, 9]

$$K_R = \frac{7,5 \cdot \pi \cdot L \cdot G}{\ln(D/d)} k_f, \quad (1)$$

where  $k_f$  is the form factor and it is defined by the graphical dependence from [9];

$G$  is the shear modulus,  $MPa$ , it is defined by Shore hardness  $H_s$ ,  $G = 0,117e^{0,034H_s}$  or through the graphical representation  $G = f(H_s)$  [4];

$D, d, L$  are the outer and inner radius respectively and the length of the rubber bushing, mm.

The dimension ratio  $\eta$  is defined as [9]

$$\eta = \frac{L}{0,5(D-d)}, \quad (2)$$

The axial stiffness and torsional stiffness of the rubber bushing can be determined by dependencies [1, 9]

$$K_A = \frac{2 \cdot \pi \cdot L \cdot G}{\ln(D/d)}, \quad (3)$$

$$K_T = \pi \cdot L \cdot G \cdot 10^{-3} \left( \frac{1}{d^2} - \frac{1}{D^2} \right)^{-1}. \quad (4)$$

## III. METHODOLOGY OF STUDY

The object of the study is an arm of the MacPherson front independent suspension on passenger car Skoda Octavia. Figure 2 shows 3D model of an arm.

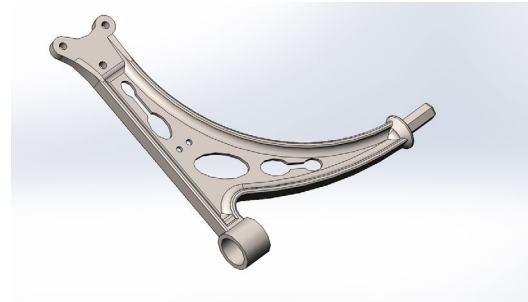
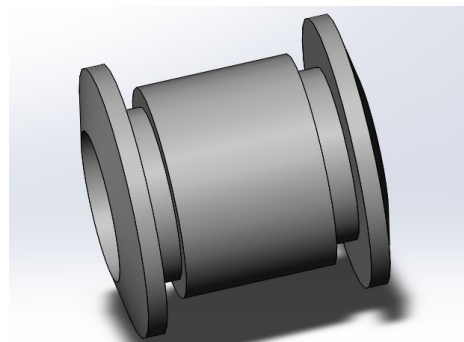


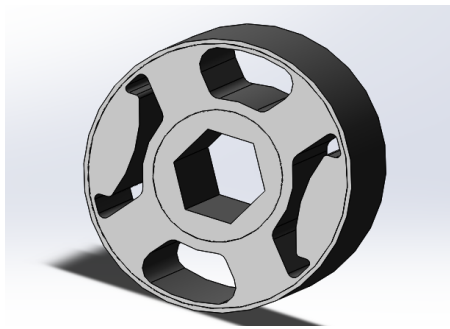
Fig. 2. Three-dimensional geometric model of an arm.

Rubber bushings were used as elastic supports of the arm therefore determining of stiffness was needed for correct definition of fixing.

Figure 3a and 3b shows 3D model of the rubber bushing 1 and 2, respectively.



a) rubber bushing 1



b) rubber bushing 2

Fig. 3. Geometric models of the rubber bushings.

The stiffness of the rubber bushings were determined via non-linear SolidWorks Simulation analysis. The elastic properties of the rubber bushings were estimated using the Mooney-Rivlin material model with five constants. The selected Shore hardness of the rubber is 70Hs. The experimental results of stress-strain relation in bi-axial tension of 70Hs from [4], had been used as an input for automatically calculation of the material constants conducted by SolidWorks. Rubber's poisson's ratio is 0,49 [1] while the density is 1130 kg/m<sup>3</sup> [1]. The metal parts of the rubber bushings are made of normalized steel 4340. A three-dimensional curvilinear finite element mesh was used for the rubber bushings.

Natural frequencies and mode shapes are determined by frequency analysis of SolidWorks Simulation. The arm is made of cast steel, according to EN10293. Its mechanical properties are shown in Table 1.

TABLE 1 MECHANICAL PROPERTIES OF THE ARM

Elastic modulus, Pa	Poisson's ratio	Mass density, kg/m <sup>3</sup>
2,1.10 <sup>11</sup>	0,28	7800

Figure 4 shows arm fixation established by elastic supports on the mounting locations of the rubber bushings surfaces.

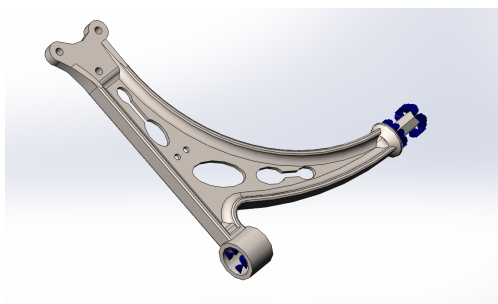


Fig. 4. Elastic supports.

A three-dimensional curvilinear mesh was generated (fig. 5). It includes 206 856 nodes and 129 636 elements.

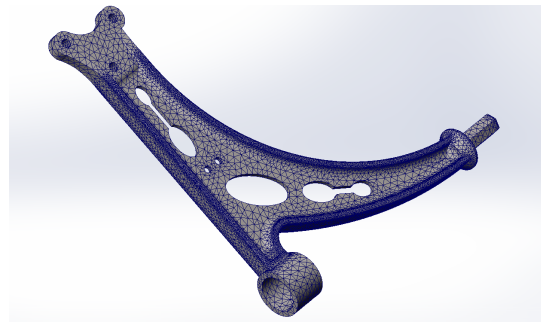


Fig. 5. FEA mesh.

The main goal of the experimental study was to determine the natural frequencies of the arm. It was carried by measuring and recording the accelerations along the three axes x, y and z at the same time. The measuring equipment includes: ADXL335 accelerometer module, power supply, multifunction I/O Device NI USB-6343, PC and a specialized software developed in LabView environment.

The accelerations on the three axes were registered by ADXL335 accelerometer. The ADXL335 is a small, thin, low power, complete 3-axis accelerometer with signal conditioned voltage outputs. The product measures acceleration with a minimum full-scale range of ±3 g. The power supply of the accelerometer is a constant stabilized voltage of 3,3 V. The information from the accelerometer is provided to the PC through the multifunction I/O Device NI USB-6343. The maximum data registration speed from the Device NI USB-6343 is 500 kSample/s, input range: ±0,2 V; ±1 V; ±5 V; ±10 V. For registration and processing of the accelerometer signals, specialized software in the environment LabView has been developed (Fig. 6).

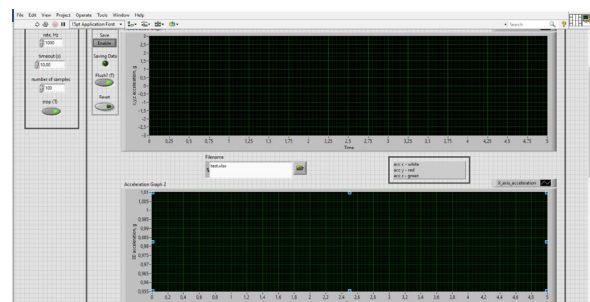


Fig. 6. Software front panel.

Figure 7 shows the object, the hammer and the measuring equipment for the experiment.



Fig. 7. Experimental determination of natural frequencies.

The accelerometer was attached to the arm. The mass of the accelerometer is 1,27 g and the mass of the arm was 3109 g. The total mass of the accelerometers of the suspension arm had negligible effects on the measurement. The FFT method in the LabView software was used, through which the data for the total acceleration in three-dimensional space were processed space. The accuracy of the method depends on the frequency resolution (1 Hz) of the measurement, since it determines the displayed peak amplitude on the PC screen that was measured.

IV. RESULTS AND DISCUSSION

Table 2 presents the results of the axial, radial and torsional stiffness of the rubber bushings obtained by FEA. For rubber bushing 1, results obtained by dependencies (1), (3) and (4) are also presented.

TABLE 2 STATIC STIFFNESS OF THE RUBBER BUSHINGS

Stiffness	Values		
	Rubber bushing 1		Rubber bushing 2
	Formula	FEA	FEA
Axial stiffness (N/mm)	526	697	144
Radial stiffness (N/mm)	4143	5806	401
Torsional stiffness (Nm/deg)	2,5	2,55	1,26

From the results presented in table 2 regarding the stiffness of the rubber bushing 1, it is observed that there is a significant difference between the results obtained by FEA and by the dependencies. This is mainly due to the simplified geometric shape of the rubber bushings in the analytically calculation. In [9], it was found that the results for the stiffness obtained by FEA are insignificant different from the experimental results, as opposed to those get from the dependencies.

Table 3 presents the obtained results of the six natural frequencies of the arm. The first, second and third mode shapes are shown on Fig. 8 a, b and c, respectively.

TABLE 3 NATURAL FREQUENCY FROM FEA

Mode number	Natural Frequency, Hz
1	10,03
2	60,52
3	112,01
4	114,13
5	188,51
6	305,7

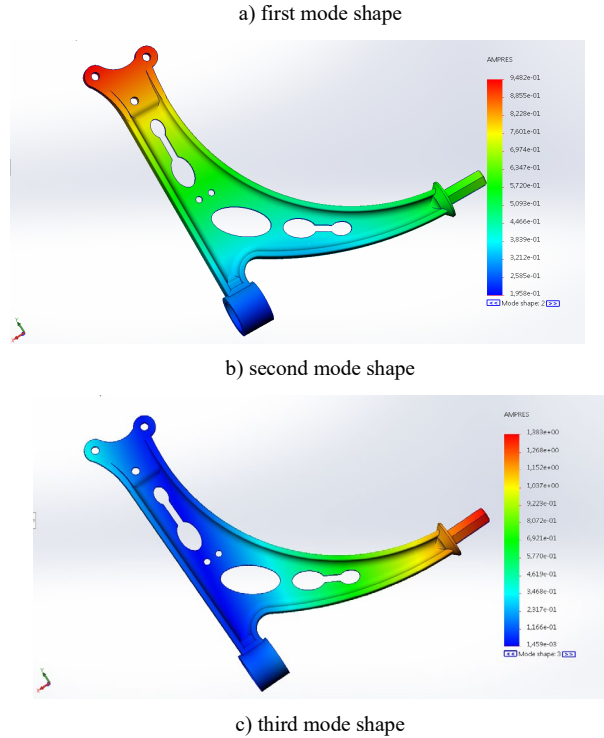
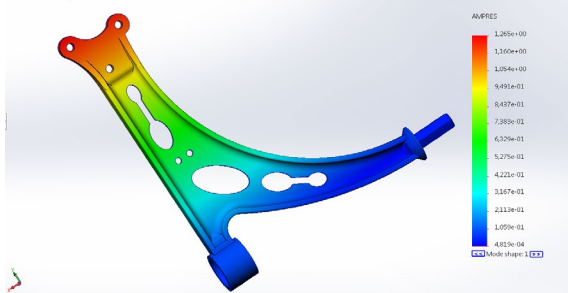


Fig. 8. Mode shapes.

Figure 9 presents the experimental results.

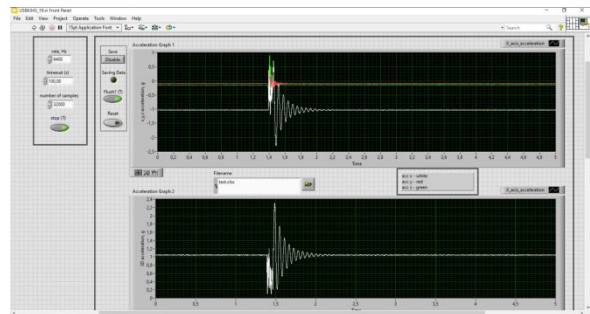


Fig. 9. Experimental acceleration results.

Table 4 presents the results regarding the natural frequencies obtained by FEA and results obtained experimentally.

TABLE 4 NATURAL FREQUENCY

Mode number	FEA Natural frequency, Hz	Experimental Natural frequency, Hz
1	10,03	16
2	60,52	75,6
3	112,01	136
4	114,13	160
5	188,51	250
6	305,7	350

The results obtained of natural frequencies by FEA are comparable to those obtained experimentally.

V. CONCLUSIONS

Based on the performed study the following conclusions are made:

It is preferable to use the FEA to determine the stiffness of rubber bushings with a complex geometry.

The results shows the lowest value of the natural frequencies of the arm is approximately 10 Hz. The next value of natural frequencies is significantly greater than the frequency of the excitation forces generated by the road surface irregularities (from 0 to 20 Hz) [2]. This means that when the car is in motion, no significant vibrations will occur in the arm, which would lead to a deterioration in the comfort of the passengers.

An experimental frequency analysis was performed to validate the FEA model developed of a front arm of a MacPherson type suspension. The results obtained by FEA are close to the results obtained experimentally.

The obtained results of the natural frequencies of the arm with fixation established by elastic supports are different from the results for the frequencies in [13], because the arm is attached with fixed supports and the geometric model is not exactly the same.

The designed suspension model, the study methodology and the obtained results can be used to topology optimization and fatigue analysis.

#### ACKNOWLEDGMENTS

This work was supported by the European Regional Development Fund within the OP “Science and Education for Smart Growth 2014-2020”, Project Competence Centre “Smart Mechatronic, Eco-And Energy Saving Systems And Technologies”, № BG05M2OP001-1.002-0023.

#### REFERENCES

- [1] A. N. Gent, *Engineering with Rubber : How to Design Rubber Components*, Hanser Publishers, Munich, 2012.
- [2] Dehkordi H., *Vibration and force analysis of lower arm of suspension system*, Masters degree, Universite du Quebec, 2014.
- [3] S. Abdullah, N.A. Kadhim, A. K. Ariffin and M. Hosseini, *Dynamic analysis of an automobile lower suspension arm using experiment and numerical technique*, *New Trends and Developments in Automotive System Engineering*, pp. 231-248, 2011.
- [4] S. Kayaci., A. K. Serbest, *Comparison of constitutive hyper-elastic material models in finite element theory*, *Otekon*, 6. Otomotiv Teknolojileri Kongresi, Bursa, pp. 121-125, 2012.
- [5] V. Kulkarni, A. Jadhav, P. Basker, *Finite element analysis and topology optimization of lower arm of double wishbone suspension using Radioss and Optistruct*, *International Journal of Science and Research*, ISSN: 2319-7064, Vol. 3, Issue 5, pp. 639-643, 2014.
- [6] A. Puranik, V. Bansode, S. Jadhav, Y. Jadhav, *Durability Analysis and optimization of an Automobile Lower Suspension Arm Using FEA and Experiment Technique*, *International Research Journal of Engineering and Technology (IRJET)*, e-ISSN: 2395-0056, p-ISSN: 2395-0072, Volume: 05 Issue: 09, pp. 1381-1389, 2018.
- [7] V. Sajjanashettar, V. Siddhartha, et al., *Numerical and experimental modal analysis of lower control arm for topography optimization*, *International Journal of Energy, Environment and Economics* 27(1), ISSN: 1054-853X, pp. 17-31, 2019.
- [8] H. Singh , G. Bhushan, *Finite Element Analysis of a Front Lower Control Arm of LCV Using Radioss Linear*, pp. 121-125, 2012, <https://www.researchgate.net/publication/305355066>.
- [9] L. Tang, J. Wu, J. Lui, C. Jiang and Shangguan, *Topology optimization and performance calculation for control arms of a suspension*, *Advances in Mechanical Engineering*, Volume 2014, Article ID 734568, 10 pages, <https://dx.doi.org/10.1155/2014/734568>.
- [10] J. Marzbanrad, A. Hoseinpour, *Structural optimization of MacPherson control arm under fatigue loading*, *Tehnički vjesnik* 21, 3 (2017), pp.917-924, doi:10.17559/TV-20150225090554.
- [11] P. Santamaria, A. Sierra and O. Estrada, *Shape optimization of a control arm produced by additive manufacturing with fiber reinforcement*, *Journal of Physics: Conference Series* 1386 012003, 2019, doi:10.1088/1742-6596/1386/1/012003.
- [12] M. Pachapuri, R. Lingannavar, N. Kelageri, K. Phadate, *Design and analysis of lower control arm of suspension system*, *The 3<sup>rd</sup> International Conference on Advances in Mechanical Engineering and Nanotechnology*, Proceedings, Elsevier Ltd., Volume 47, Part 11, 2021, pp. 2949-2956, <https://doi.org/10.1016/j.matpr.2021.05.035>.
- [13] S. Bhalshankar, *Dynamic analysis of an lower control arm using harmonic excitation for investigation dynamic behaviour*, *PradnyaSurya Engineering Works, EasyChair Preprint №5933*, 2021, <https://easychair.org/publications/preprint/8G3j>.

# Practice Oriented Heat Source Model Calibration

**Manahil Tongov**

Department of Material Science and  
Technology  
Technical University of Sofia  
Sofia, Bulgaria  
Center of welding  
(IMSETCHA) "Acad. A. Balevski" Bulgarian  
Academy of Sciences  
Sofia, Bulgaria  
tongov@tu-sofia.bg

**Valentin Anguelov**

Center of welding  
Institute of Metal Science,  
Equipment and Technologies with  
with Center for Hydro- and  
Aerodynamics (IMSETCHA) "Acad.  
A. Balevski" Bulgarian Academy of  
Sciences  
Sofia, Bulgaria  
valentin.anguelov@ims.bas.bg

**Abstract.** The modelling of the thermal process is used as a tool in determination of the properties of the materials, subject to welding. One of the most important steps in the modelling is the calibration of the heat source model. This is a necessary condition for a given model to be used to solve practical problems. The standard practice in this regard is to calibrate the model by the shape of the melted zone or by the temperature cycles at set points. In the present work, the heat source model calibration based on the maximum temperatures measured at several surface points, at different distances from the seam line, is considered. The temperature cycles in the welded joint and the penetration depth were assumed by the model, calibrated in such non-destructive way. The calculated temperature cycles were compared with records of the temperature during welding. The actual penetration depth was measured by metallographic examination of samples and compared with the assumed penetration depth. The obtained results make it possible to evaluate the suitability of the proposed methodology for determining the cooling rate in the heat affected zone.

**Keywords:** heat source calibration, thermal cycles, welding.

## I. INTRODUCTION

For the practical use of the various welding thermal processes models is necessary to calibrate, validate and verify them. The calibration of the model is realized by determination of parameters involved in the definition of the heat source, by comparing experimental and computational results. From this point of view, it is important that the process can be carried out through simple and quickly realizable experiments. In this study, it is proposed to use the maximum temperatures measured on the surface of the welded parts as such. Measuring of these

temperatures is done in proximity to the weld seam. In addition to the maximum temperatures, it is necessary to measure the distance from the seam line to the temperature measurement point. It is obvious that one of the isotherm lines, with temperature of the solidus, is located at the seam edge. The distance to the axis of the seam is equal to half of its width.

The main types of heat source models describing the interaction of the welding arc and the article are volumetric [1] ÷ [12], surface [13] ÷ [21] or a combination of both types [22] ÷ [25]. From the volumetric heat sources the Goldak's model is most often used:

$$q = \begin{cases} \frac{6\sqrt{3}\eta U I f_f}{\pi\sqrt{\pi} a_f b c} \exp\left(-3\left(\frac{x^2}{a_f^2} + \frac{y^2}{b^2} + \frac{z^2}{c^2}\right)\right) \\ \frac{6\sqrt{3}\eta U I f_r}{\pi\sqrt{\pi} a_r b c} \exp\left(-3\left(\frac{x^2}{a_r^2} + \frac{y^2}{b^2} + \frac{z^2}{c^2}\right)\right) \end{cases} \quad (1)$$

Here  $U$  is the welding voltage,  $I$  – arc current and  $\eta$  – efficiency. Since  $f_f = a_f / (a_f + a_r)$  and  $f_r = a_r / (a_f + a_r)$  it has 4 parameters that can be used for calibration –  $a_f, a_r, b$  and  $c$ .

Both volumetric and surface heat sources are defined in a movable coordinate system related to the welding arc. Surface heat sources are based on a Gaussian distribution

Print ISSN 1691-5402

Online ISSN 2256-070X

<https://doi.org/10.17770/etr2023vol3.7206>

© 2023 Manahil Tongov, Valentin Anguelov. Published by Rezekne Academy of Technologies.  
This is an open access article under the [Creative Commons Attribution 4.0 International License](https://creativecommons.org/licenses/by/4.0/).

$$q(r) = \frac{\eta UI}{2\pi R_N^2} \exp\left(-\frac{r^2}{2R_N^2}\right) \quad (2)$$

## II. MATERIALS AND METHODS

In this study, the experiments were conducted by TIG welding. The process parameters are: welding current 180 A; arc voltage – 12.6 V; welding speed – 10 cm/min. The sample for conducting the experiment is made of steel S355JR with dimensions 6x240x250 mm. During the implementation of the process, temperature cycles were recorded at two points located at different distances from the seam line (Fig.1). The distance from the first point to the seam line is 7.7mm, and from the second - 9.7 mm. From these records the maximum temperatures at these points were determined to be 1000°C and 836°C respectively. The measured width of the weld bead is 8.5mm. In this way, the distance from the seam line to the point where the temperature reaches the solidus temperature is 4.25mm.

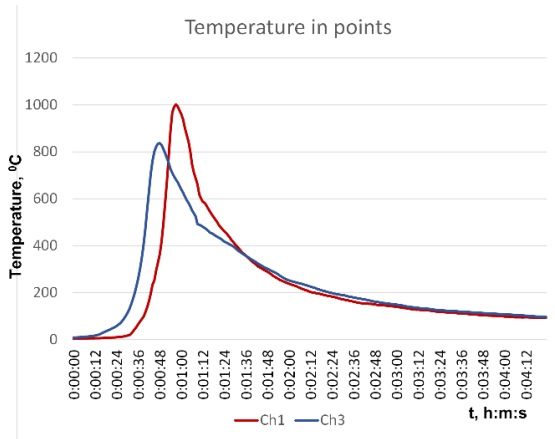


Fig. 1. Temperature records.

To solve the heat problem, the heat source described in [20] was used. The calibration was performed according to the methodology described there. The heat flux density is defined in the moving coordinate system as

$$q(r) = \eta UI A f(r) \quad (3)$$

where:

$$A = \frac{1}{\sigma\sqrt{2\pi} \exp\left(-\frac{r_0^2}{2\sigma^2}\right) + \pi r_0 \operatorname{erf}\left(\frac{r_0}{\sigma\sqrt{2}}\right)}$$

$$f(r) = \frac{1}{2\sigma\sqrt{2\pi}} \left[ \frac{\exp\left(-\frac{(r-r_0)^2}{2\sigma^2}\right)}{\exp\left(-\frac{(r-r_0)^2}{2\sigma^2}\right) + \exp\left(-\frac{(r+r_0)^2}{2\sigma^2}\right)} \right]$$

This model uses the efficiency  $\eta$ , effective heating radius  $r_{arc}$  and distribution coefficient  $\alpha_{arc} = r_0/r_{arc}$  as calibrating parameters. These parameters determine the values  $r_0 = \alpha_{arc} \cdot r_{arc}$  and  $\sigma = r_{arc} / 3$ . Minimization of the

maximum relative error was used to determine the values of the calibration parameters. In the **Table I** shows the last stage of solving the optimization problem, and Fig. 2 shows the result of the calibration process.

TABLE I. FINAL STEPS OF THE CALIBRATION PROCESS.

$\eta$	$r_{arc}, mm$	$\alpha_{arc}$	Objective
0.7000	9.540	0.3300	0.001036
0.7030	9.540	0.3300	0.001276
0.7000	9.510	0.3300	0.001167
0.7000	9.540	0.3420	7.35E-04
0.6970	9.520	0.3380	9.87E-04
0.6985	9.525	0.3360	8.92E-04
0.7000	9.540	0.3360	8.81E-04
0.7000	9.525	0.3360	8.44E-04
0.7015	9.540	0.3360	9.84E-04
0.6985	9.530	0.3400	8.36E-04
0.6993	9.533	0.3390	9.02E-04
0.7000	9.533	0.3390	7.52E-04
0.7000	9.540	0.3390	8.07E-04
0.7008	9.540	0.3390	8.55E-04
0.6993	9.535	0.3410	8.55E-04
0.6996	9.536	0.3405	7.53E-04
0.7003	9.544	0.3415	7.39E-04
0.6998	9.543	0.3422	7.16E-04
0.6995	9.544	0.3430	7.88E-04
0.7000	9.544	0.3433	7.06E-04
0.7000	9.546	0.3447	7.20E-04
0.6996	9.541	0.3435	7.25E-04
0.6998	9.542	0.3430	7.27E-04
0.6999	9.543	0.3427	7.67E-04
0.7000	9.542	0.3426	7.92E-04
0.7001	9.544	0.3424	7.36E-04
0.7000	9.546	0.3430	7.05E-04
0.7001	9.547	0.3431	7.28E-04
0.7002	9.546	0.3430	7.68E-04
0.7000	9.544	0.3428	7.56E-04
0.7002	9.545	0.3430	7.98E-04
0.7000	9.544	0.3428	7.06E-04
0.6999	9.545	0.3437	7.48E-04
0.7001	9.544	0.3427	7.46E-04
0.7000	9.545	0.3431	7.02E-04
0.7000	9.545	0.3429	7.24E-04
0.7001	9.545	0.3427	7.05E-04
0.7001	9.545	0.3429	7.37E-04
0.7000	9.545	0.3429	7.26E-04
0.7001	9.545	0.3429	7.78E-04
0.7000	9.545	0.3430	7.63E-04
0.7000	9.545	0.3430	6.99E-04

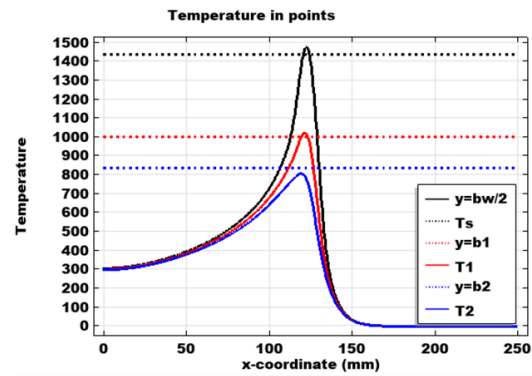


Fig. 2. Calibration result.

### III. RESULTS AND DISCUSSIONS

The general view of the temperature field is presented in Fig.3 and Fig.4. Fig. 5 shows the high temperature region with isothermal surfaces plotted for the calibration values and temperatures 800°C and 500°C. Except for the isothermal surface for the solidus temperature, the others have an almost cylindrical shape.

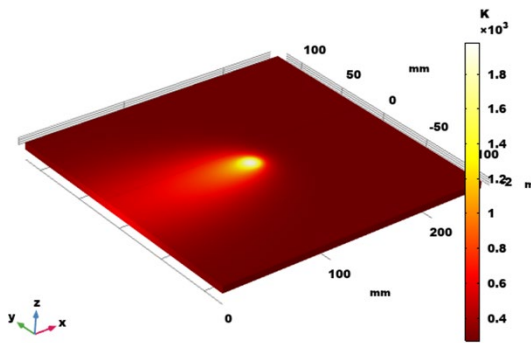


Fig. 3. Common view of temperature.

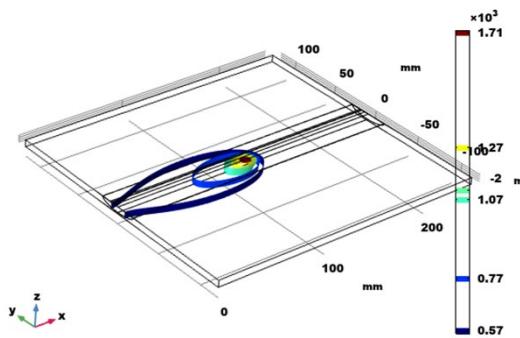


Fig. 4. Isothermal surfaces (K).

Fig. 6 shows the isothermal contours for the calibration temperatures and the liquidus temperature. It can be noted that the two-phase region is extremely small in size. Furthermore, it is also evident here that the measured temperatures have been reached at the control points. From what is shown in this figure, it follows that the deviation in the width of the 1000°C isotherm is within 0.3 mm.

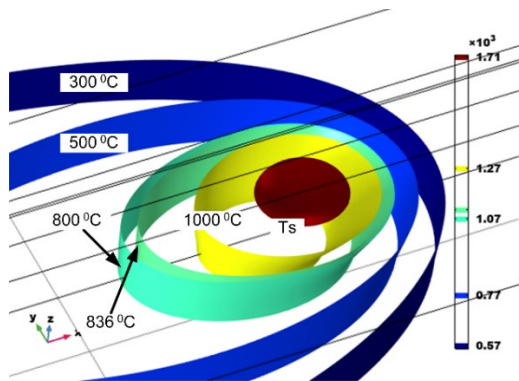


Fig. 5. Isothermal surfaces in the high temperature region.

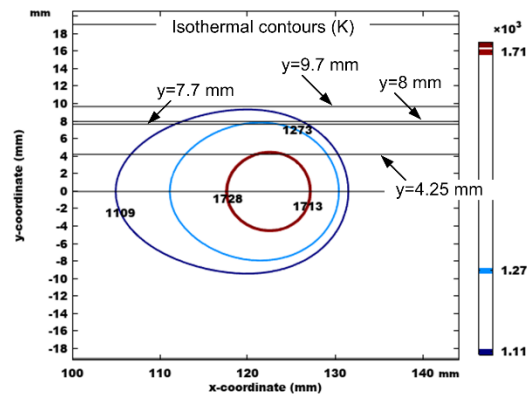


Fig. 6. Isothermal contours on top surface for calibrated distances and liquidus temperature.

One of the most important characteristics that should be determined when welding steels prone to the formation of cold cracks is the cooling time from 800°C to 500°C. Fig. 7 shows the isotherms at these temperatures. The seam line distance between these isotherms in the cooling zone is 30.5 mm. Since the welding speed is 10 cm/min, this means that the cooling time from 800°C to 500°C  $t_{8/5}$  for the points of the seam line is 18.3 s.

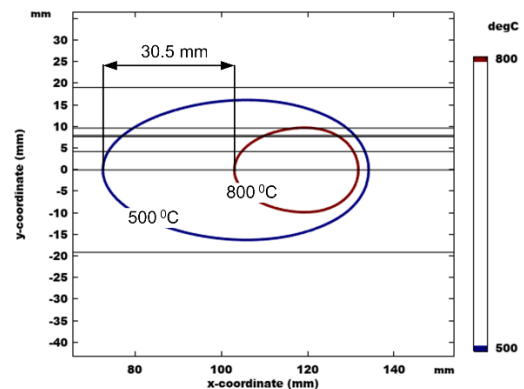


Fig. 7. Isothermal contours for  $t_{8/5}$  determining.

**Table II** shows experimental and calculated data on the cooling time at the control point reaching the maximum temperature of 1000°C. The obtained experimental data indicate that the  $t_{8/5}$  is 15 s. The result calculated by the model is 19.5 s. This shows that at the used cooling conditions (coefficient of convective heat removal  $h = 8$  W/(m<sup>2</sup>K) and emissivity  $\varepsilon = 0.4$ ) the measured values are lower than the calculated ones. Fig. 8 illustrates the influence of the distance from the axis of the seam on the duration of  $t_{8/5}$ . It can be seen that the cooling time from 800°C to 500°C is the least along the seam line.

TABLE II. EXPERIMENTAL AND CALCULATED DATA FOR COOLING RATE DETERMINING

Experimental			
$t, h:m:s$	$T, ^\circ C$	$t, h:m:s$	$T, ^\circ C$
0:01:05	800.11	0:01:13	582.84
0:01:06	746.98	0:01:14	571.02
0:01:07	712.31	0:01:15	557.55
0:01:08	687.43	0:01:16	544.28
0:01:09	662.2	0:01:17	532.52

0:01:10	619.55	0:01:18	522.28
0:01:11	600.69	0:01:19	511.00
0:01:12	586.87	0:01:20	500.32
Calculated			
$t, s$	$T, ^\circ C$	$t, s$	$T, ^\circ C$
44.25	816.37	54.75	608.18
45.00	796.65	55.50	597.67
45.75	777.59	56.25	587.56
46.50	759.67	57.00	577.84
47.25	742.57	57.75	568.50
48.00	726.22	58.50	559.48
48.75	710.66	59.25	550.80
49.50	695.75	60.00	542.41
50.25	681.56	60.75	534.30
51.00	667.95	61.50	526.47
51.75	654.94	62.25	518.87
52.50	642.50	63.00	511.52
53.25	630.56	63.75	504.39
54.00	619.16	64.50	497.47

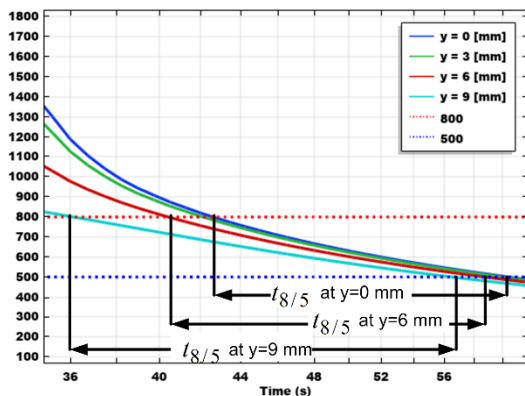


Fig. 8. Cooling time for diferend distance from seam line.

#### IV. CONCLUSIONS

Comparing experimental and simulation modelling results shows that the heat source model can be successfully calibrated to the maximum temperatures measured near the seam. When using constant values of the characteristics describing the convective and radiative heat removal, the obtained calculated values for the cooling time from 800°C to 500°C are higher than the experimentally determined ones. This means that it is important to use temperature-dependent coefficients describing the cooling process. Comparing the calculated results for points at different distances from the seam shows that, in the considered case, the lowest value of  $t_{8/5}$  was obtained along the seam line.

#### V. ACKNOWLEDGMENTS

The authors are grateful to the financial support of the Bulgarian National Science Fund, Contract No KP-06-H57/10, for carrying out the necessary research.

#### REFERENCES

[1] M. A. Malik, M. E. Qureshi and N. U. Dar, Numerical Simulation of Arc Welding Investigation of various Process and Heat Source Parameters, MED UET Taxila, 2007, pp 127÷142  
 [2] P. B. Guimarães et all, OBTAINING TEMPERATURE FIELDS AS A FUNCTION OF EFFICIENCY IN TIG WELDING BY

NUMERICAL MODELING, 21st Brazilian Congress of Mechanical Engineering October 24-28, 2011, Natal, RN, Brazil, Proceedings of COBEM, 2011, DOI: <http://dx.doi.org/10.5380/reterm.v10i1-2.61952>  
 [3] D. B. Darmadi, Validating the accuracy of heat source model via temperature histories and temperature field in bead-on-plate welding, International Journal of Engineering & Technology, October 2011, IJENS Vol: 11 No: 05  
 [4] J. Da Nobrega, D. Silva, B. Arauho, R. De Melo, T. Maciel, A. Silva and N. Dos Santos, Numerical evaluation of multipass welding temperature field in API 5L X80 steel welded joints. *International Journal of Multiphysics*, vol. 8, Issue 3, 2014, pp. 337-348.  
 [5] R. Pamnani, M. Vasudevan, T. Jayakumar, P. Vasantharaja, and K. C. Ganesh. Numerical simulation and experimental validation of arc welding of DMR-249A steel. *Defence Technology*, Vol. 12, Issue 4, August 2016, Pages 305-315, 2016, <https://doi.org/10.1016/j.dt.2016.01.012>  
 [6] W. Piekarska and K. Rek, Numerical analysis and experimental research on deformation of flat made of TIG welded 0H18N9 steel. Paper presented at the *Procedia Engineering*, vol. 177, pp. 182-187, 2017. doi:10.1016/j.proeng.2017.02.217  
 [7] Li, C. Chen, D. Zhao and C. Wu, Determination and Application of Double Ellipsoid Heat Source Model, International Conference on Material Science, Energy and Environmental Engineering (MSEEE 2017), Advances in Engineering Research, volume 125, pp. 267÷270, <https://doi.org/10.2991/msee-17.2017.49>  
 [8] C. Yan, H. Jiang, L. Wu, C. Kan and W. Yu, Numerical simulation of temperature field in multiple-wire submerged arc welding of X80 pipeline steel, *IOP Conference Series: Earth and Environmental Science* vol. 108 art. No 022048, 2018, doi:10.1088/1755-1315/108/2/022048  
 [9] P. Ferro, F. Berto, F. Bonollo and R. Montanari, Experimental and numerical analysis of TIG-dressing applied to a steel weldment, *Procedia Structural Integrity* Volume 9, pp. 64-70, 2018, <https://doi.org/10.1016/j.prostr.2018.06.012>  
 [10] H. Huang, X. Yin, Z. Feng and N. Ma, Finite element analysis and in-situ measurement of out-of-plane distortion in thin plate TIG welding. *Materials*, vol. 12, Issue 1, 2019 doi:10.3390/ma12010141  
 [11] M. Matuszewski, Modeling of 3D temperature field in butt welded joint of 6060 alloy sheets using the ANSYS program. Paper presented at the *IOP Conference Series: Materials Science and Engineering*, vol. 659 Issue 1, 2019 doi:10.1088/1757-899X/659/1/012034  
 [12] S. Zuo, Z. Wang, D. Wang, B. Du, P. Cheng, Y. Yang, P. Zhang and N. Lang, Numerical simulation and experimental research on temperature distribution of fillet welds. *Materials* 2020, vol. 13 Issue 5, art, No 1222; <https://doi.org/10.3390/ma13051222>  
 [13] H. Pengfei, L. Yan, L. Yangyang and L. Zhenyang, Numerical simulation of the temperaturbe filed in fixed-TIG welding pool, 2011 International Conference on Modeling, Simulation and Control, IPCSIT vol.10 (2011) © (2011) IACSIT Press, Singapore  
 [14] S. Yamane, T. Yamazaki, T. Kaneta, T. Nakajima and H. Yamamoto, Experiment and numerical simulation in temperature distribution and welding distortion in GMA welding. *Yosetsu Gakkai Ronbunshu/Quarterly Journal of the Japan Welding Society*, vol. 29 Issue 3, pp. 31s-34s., 2011, <https://doi.org/10.2207/qjws.29.31s>  
 [15] P. R. De Freitas Teixeira, D. B. De Araújo and L. A. B. Da Cunha, Study of the gaussian distribution heat source model applied to numerical thermal simulations of tig welding processes. *Ciencia y Engenharia/ Science and Engineering Journal*, vol. 23, Issue 1, pp. 115-122, 2014., doi:10.14393/19834071.2014.26140  
 [16] H. Liu and L. Niu, Finite element simulation research on medium plate multi-pass welding temperature field. *The Open Mechanical Engineering Journal*, Volume 9, pp.786-790, 2015  
 [17] M. B. Bjelić, K. Kovanda, L. Kolarik, M. N. Vukićević and B. S. Radićević, Numerical modeling of two-dimensional heat-transfer and temperature-based calibration using simulated annealing optimization method: Application to gas metal arc welding.

- Thermal Science*, vol. **20**, Issue 2, pp. 655-665, 2016, doi:10.2298/TSCI150415127B
- [18] M.Zhang, Y.Zhou, C. Huang, Q.Chu, W.Zhang, and J. Li Simulation of temperature distribution and microstructure evolution in the molten pool of GTAW Ti-6Al-4V alloy. *Materials* vol. 11, art. No 2288, 2018; <https://doi.org/10.3390/ma11112288>
- [19] J. Wróbel and A. Kulawik Prediction of the superficial heat source parameters for TIG heating process using FEM and ANN modeling. *Entropy*, vol. *21*, Issue 10, art. No 954, 2019, doi:10.3390/e21100954
- [20] M. Tongov Heat Source for TIG Welding Modelling, *Environment. Technology. Resources. Rezekne, Latvia, Proceedings of the 13<sup>th</sup> International Scientific and Practical Conference. Volume 3, pp. 348-356, 2021.*
- [21] M. Tongov Investigation of GMAW by Simulation Modelling, *Environment. Technology. Resources. Rezekne, Latvia, Proceedings of the 13<sup>th</sup> International Scientific and Practical Conference. Volume 3, pp. 357-362, 2021.*
- [22] A.Moarrefzadeh and M.A.Sadeghi, Numerical Simulation of Thermal Profile By Gas Tungsten Arc Welding Process in Copper, *Wseas transactions on heat and mass transfer*, Volume 5, Issue 3, July 2010, ISSN: 1790-504
- [23] Y. Saadlaoui, E. Feulvarch, A. Delache, J. Leblond and J. Bergheau, A new strategy for the numerical modeling of a weld pool. *Comptes Rendus - Mecanique*, Vol. 346, Issue 11, pages 999-1017, November 2018, <https://doi.org/10.1016/j.crme.2018.08.007>.
- [24] T.F. Flint and M.C.Smith, HEDSATS: High energy density semi-analytical thermal solutions. *SoftwareX*, Volume 10, art. No 100243, July–December 2019, <https://doi.org/10.1016/j.softx.2019.100243>
- [25] K. Agrebi, A. Belhadj and M. Bouhaf, THREE-DIMENSIONAL NUMERICAL SIMULATION OF A GAS TUNGSTEN ARC WELDING PROCESS, *IJTech International Journal of Technology*, vol. 10 Issue 4, pp. 689-699, 2019, ISSN 2086-9614, DOI: <https://dx.doi.org/10.14716/ijtech.v10i4.1849>

# A Thermal Model for Wire Arc Additive Manufacturing

**Manahil Tongov**

Department of Material Science and Technology  
 Technical University of Sofia  
 Sofia, Bulgaria  
 Center of Welding  
 IMSETCHA "Acad. A. Balevski" Bulgarian Academy of Sciences  
 Sofia, Bulgaria  
 tongov@tu-sofia.bg

**Vladimir Petkov**

Institute of Metal Science, Equipment and Technologies with  
 Center for Hydro- and Aerodynamics (IMSETCHA)  
 "Acad. A. Balevski" Bulgarian Academy of Sciences  
 Sofia, Bulgaria  
 vladimir2pe@yahoo.com

**Abstract.** Layer-by-layer detailing processes, which used wire and electric arc - wire arc additive manufacturing (WAAM), are among the most productive in 3D metal printing technologies. From this point of view, the solution of the thermal task, and subsequently of the deformation problem, are particularly relevant. It is natural that these simulation modelling processes are closely related to welding, but at the same time it is necessary to take into account particularities that are crucial for WAAM and are not always relevant in welding. In this research, one such model is proposed, which takes into account the gradual filling of the working space with the deposited metal. The specific issues related to the construction of the model, the definition of the heat source and the first layer formation in the conditions of WAAM are considered. The obtained numerical results enable the prediction of the layer dimensions.

**Keywords:** modelling; wire arc additive manufacturing.

## I. INTRODUCTION

The processes of wire and arc additive manufacturing (WAAM) are close to the corresponding welding processes. This closeness is expressed both in their realization and in their research. Simulation processes are no exception in this regard. The main directions in the study of processes and the solution of specific technological tasks through the methods of simulation modelling can be presented in several groups: solving the heat problem in the parts manufactured by WAAM [1]÷[10]; solving a heat and fluid tasks with modelling the formation of the layer [11]÷[18]; determining the geometry of the layers using the technological parameters [19]÷[25]; optimal design of the rooting [1], [9], [10], [23] and [27]. When modelling heat processes, the Goldak heat source [1÷5] is most often used. It replaces the action of the welding arc with a volumetric heat source in the metal with a density of the released

power  $q[W/m^3]$ . Equation (1) shows the definition of the base variant in a moving coordinate system related to the heat source. The effective heat output of the arc is  $q_{eff} = \eta UI$ . The density distribution function of the heat generated amount is illustrated in Fig.1. In addition to the efficiency factor  $\eta$  this heat source has 4 geometric parameters  $a_f, a_r, b$  and  $c$  (Fig.2), which can be used for its calibration.

$$q = \begin{cases} q_{eff} \frac{6\sqrt{3}f_f}{\pi\sqrt{\pi}a_fbc} \exp\left(-3\left(\frac{x^2}{a_f^2} + \frac{y^2}{b^2} + \frac{z^2}{c^2}\right)\right) & x \leq 0 \\ q_{eff} \frac{6\sqrt{3}f_r}{\pi\sqrt{\pi}a_rbc} \exp\left(-3\left(\frac{x^2}{a_r^2} + \frac{y^2}{b^2} + \frac{z^2}{c^2}\right)\right) & x \geq 0 \end{cases} \quad (1)$$

The coefficients  $f_f$  and  $f_r$  determine the energy distribution between the two ellipsoids. In order to have continuity of the function from equation (1) it is necessary to respect the ratio  $f_f/a_f = f_r/a_r$ . The sum of these two coefficients is equal to two, which is related to the normalization of the function, and they can be determined by equations (2). This heat source is convenient when there is a significant penetration and the presence of a keyhole. Varieties aimed at solving specific problems are also used - one such example is given in [2]. In the processes under consideration, the formation of a deep keyhole can be prevented, and is often undesirable.

$$f_f = \frac{2a_f}{a_f + a_r} \quad f_r = \frac{2a_r}{a_f + a_r} \quad (2)$$

Print ISSN 1691-5402

Online ISSN 2256-070X

<https://doi.org/10.17770/etr2023vol3.7212>

© 2023 Manahil Tongov, Vladimir Petkov. Published by Rezekne Academy of Technologies.  
 This is an open access article under the [Creative Commons Attribution 4.0 International License](https://creativecommons.org/licenses/by/4.0/).

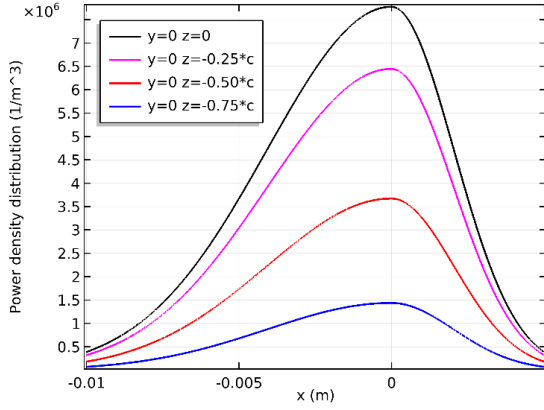


Fig. 1. Power density distribution for Goldak heat source with parameters (in mm)  $a_f = 10$ ,  $a_r = 5$ ,  $b = 8$  and  $c = 4$ .

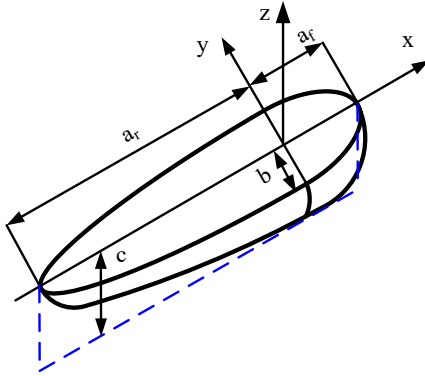


Fig. 2. Geometric interpretation of Goldak heat source.

Gaussian normally distributed heat source is also used often [6÷9, 24, 25]. It can have a different distribution along  $z$  axis (Fig. 3). The general form can be represented by equation (3). Here  $k$  is the heat source concentration coefficient ( $1/m^2$ );  $k/\pi$  is a normalizing factor for the two-dimensional normal distribution and the heat flux density along the arc axis in the plane of interaction of the welding arc with the metal is equal to  $q_{eff}k/\pi$ ;  $f(z)$  is an attenuation function of the released heat ( $1/m$ ), which is normalized according to (4) or (5) where  $h_{pr}$  is the penetration depth.

$$q = q_{eff} \frac{k}{\pi} \exp(-kr^2) f(z) \quad (3)$$

$$r^2 = x^2 + y^2$$

$$\int_{-\infty}^0 f(z) dz = 1 \quad (4)$$

$$\int_0^{h_{pr}} f(z) dz = 1 \quad (5)$$

When solving only a heat problem, the shape of the weld pool is determined by the forces acting on it. Equation (6) [2] is used to determine the weld pool free surface shape. The heat flux is transmitted through the surface of the weld pool.

$$\sigma \left[ \frac{(1 + \varphi_y^2) \rho_{xx} - 2\varphi_x \varphi_y \rho_{xy} + (1 + \varphi_x^2) \rho_{yy}}{(1 + \varphi_x^2 + \varphi_y^2)^{3/2}} \right] = \rho g \varphi + P - \lambda \quad (6)$$

where  $\sigma$  is the surface tension (N/m);  $\varphi$  – the displacement of the surface (mm);  $g$  – ground acceleration ( $m/s^2$ );  $P$  – arc pressure ( $N/mm^2$ );  $\lambda$  – Lagrange multiplier

When solving fluid and temperature problems to describe the movement of the liquid phase and the formation of the free surface of the weld pool, in addition to the heat balance equation, the fluid continuity equation and the Navier-Stokes equation, describing the movement of a viscous liquid, are solved. To describe this movement, the following factors are considered [12, 28]: the surface tensions force (equation 7); the gravitational force taking into account the change of density depending on the temperature combined with electrodynamic force (equations 8÷11); pressure of welding arc – a model (equations 12÷14) similar to the Koldak heat source model is used [12, 29]

$$P_\sigma = \sigma \kappa \quad \sigma = \sigma_L + \alpha_\sigma (T - T_L) \quad (7)$$

$$\mathbf{F}_b = (\mathbf{j} \times \mathbf{B}) - \rho g \beta \Delta T \quad (8)$$

$$P_{ex} = -\frac{\mu_m I^2}{4\pi^2 j^2 r} \exp\left(-\frac{r^2}{2j^2}\right) \times \left[ 1 + \exp\left(-\frac{r^2}{2j^2}\right) \right] \left( 1 - \frac{z}{L_0} \right)^2 \frac{x}{r} \quad (9)$$

$$P_{ey} = -\frac{\mu_m I^2}{4\pi^2 j^2 r} \exp\left(-\frac{r^2}{2j^2}\right) \times \left[ 1 + \exp\left(-\frac{r^2}{2j^2}\right) \right] \left( 1 - \frac{z}{L_0} \right)^2 \frac{y}{r} \quad (10)$$

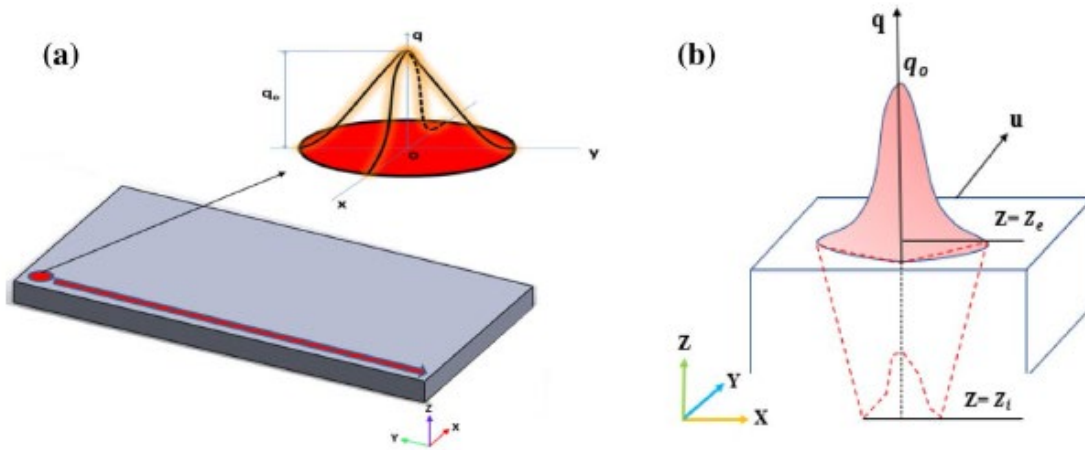


Fig. 3. Two variants of a Gaussian heat source – surface (a) and volumetric with a conical depth distribution (b) [2].

$$P_{ez} = -\frac{\mu_m I^2}{4\pi^2 j^2 r} \exp\left(-\frac{r^2}{2j^2}\right) \times \quad (11)$$

$$\times \left(1 - \frac{z}{L_0}\right) - \rho g \beta \Delta T$$

$$p_{arc}(x, y) = K_p \frac{3\mu_m I^2}{2\pi^2 (a_{pf} | a_{pr})} \times \quad (12)$$

$$\times \exp\left(-3\left(\frac{(x-vt)^2}{a^2} + \frac{y^2}{b_p^2}\right)\right)$$

$$a = \begin{cases} a_{pf} & x \geq vt \\ a_{pr} & x < vt \end{cases} \quad (13)$$

$$\iint_{\Omega} p_{arc}(x, y) dS - \frac{\mu_m I^2}{4\pi} = 0 \quad (14)$$

In [19], it was proposed that the shape of the cross section of a single welded layer (Fig. 4) be described by a second degree equation (15). After expressing the cross-sectional area of the layer by the feed rate  $v_e$ , the diameter of the electrode wire  $d_e$  and the travel speed  $v_w$ , a relationship was obtained connecting these parameters to the shape of the layer (equation 16). Experiments were then conducted with hybrid laser MIG/MAG surfacing and a regression equation was derived, enabling the height of the layer to be determined depending on the travel speed and the wire feed rate (Equation 17). The wire feed rate is changed from 4.7 to 10.4 m/min, and the travel speed is in the range of 0.6 to 1.1 m/min.

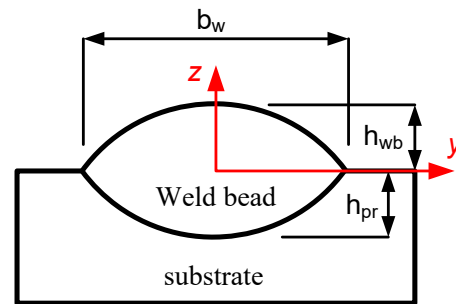


Fig. 4. Weld bead dimensions.

$$y = h_{wb} \left[1 - \left(\frac{2z}{b_w}\right)^2\right] \quad (15)$$

$$y = h_{wb} \left[1 - \left(\frac{16h_{wb}v_w}{3\pi v_f d_e^2} z\right)^2\right] \quad (16)$$

$$h_{wb} = 3.0299 - 4.9778v_w + 0.18497v_e - 0.13833v_w v_e + 2.5610v_w^2 + 0.0029945v_e^2 \quad (17)$$

The described parabolic model of the weld bead shape was used in the MIG/MAG process [20]. The profile shape of the bead can also be described using equations (18) or (19). These two models and the parabolic model are compared in [21]. The width and height of the beads were measured, as well as the cross-sectional area. The areas were calculated using the three models and it was shown that the parabolic model gives results closer to the measured ones. The parabolic model has also been used to describe the layer geometry in multipass welding [19, 22].

$$y = h_{wb} \cos\left(\frac{\pi z}{b_w}\right) \quad (18)$$

$$y = \sqrt{R^2 - z^2} + h_{wb} - R \quad (19)$$

II. MATERIALS AND METHODS

As part of this study, experiments were conducted to determine the shape of the layers. Conventional GMAW equipment was used. The filler material is SG2 with a diameter of 0.8 mm and its chemical composition according to the manufacturer's certificate is shown in Table I. WAAM starts on a 4x150x350 mm plate from S355 steel and a vertical wall is built. The parameters of the process are: welding current – 76 A; arc voltage – 17 V; feed rate – 4.6 m/min; welding speed – 12 cm/min; shielding gas Ar+18%CO<sub>2</sub>. The experimental setup used is shown in Fig. 5. To determine the shape of the applied layers, a cross-section of the layers was prepared for metallographic investigation (Fig. 6). The surface of the section was machined according to standard metallographic profile preparation procedure by grinding and polishing and was etched with 5% HNO<sub>3</sub>.

TABLE I. CHEMICAL COMPOSITION OF THE USED WELDING WIRE (BALANCED – FE), MASS. %

C	Mn	Si	P	S
0.07	1.45	0.82	0.005	0.10
Ni	Cr	V	Cu	
0.02	0.03	0.004	0.03	

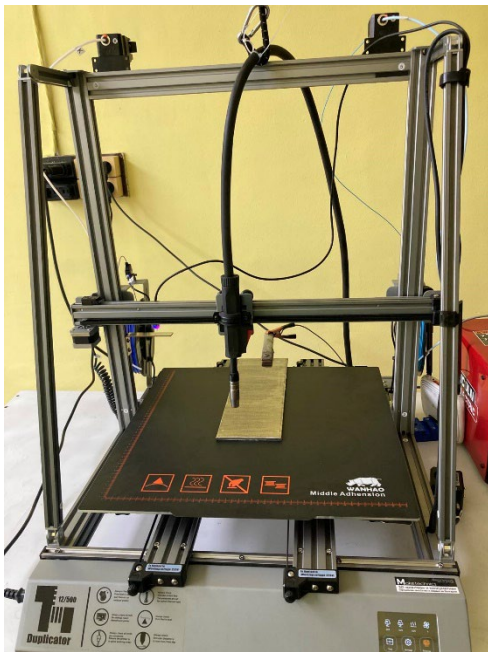


Fig. 5. Experimental set-up.

In process modelling, a heat task is solved using FEM. The used thermal properties of the metal are shown in Fig.7÷Fig.9.

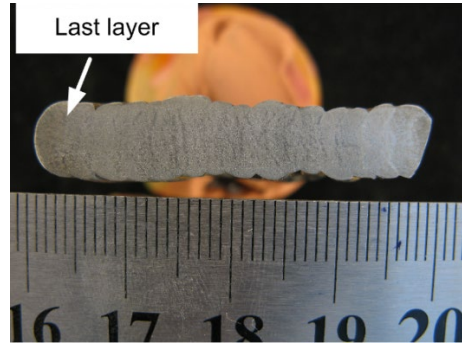


Fig. 6. Cross-section profile.

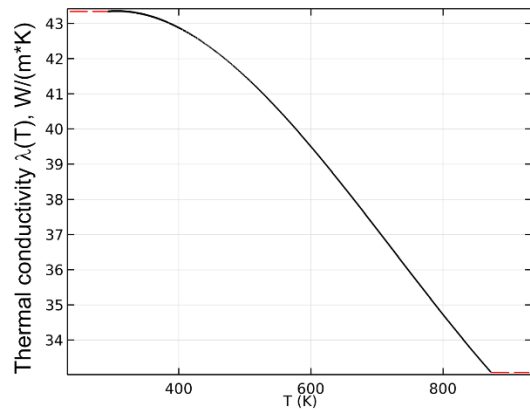


Fig. 7. Thermal conductivity of used metal.

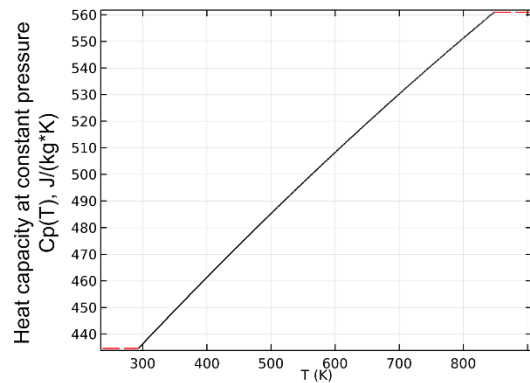


Fig. 8. Heat capacity at constant pressure for used metal.

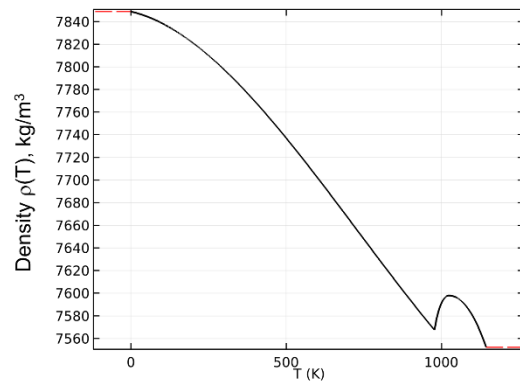


Fig. 9. Density of used metals.

### III. RESULTS AND DISCUSSIONS

The properties of the layer material are obtained by combining those of the metal and those of the air. A transition zone is defined in front of the welding arc (Fig. 10). In this transition zone, a transition function  $\varphi(x)$  is defined in the movable coordinate system associated with the welding arc (Fig. 11). The layer material properties in the moving coordinate system are defined as

$$\rho_w = \varphi(x)\rho_{air} + [1 - \varphi(x)]\rho_{steel} \quad (20)$$

$$\lambda_w = \varphi(x)\lambda_{air} + [1 - \varphi(x)]\lambda_{steel} \quad (21)$$

$$Cp_w = \varphi(x)Cp_{air} + [1 - \varphi(x)]Cp_{steel} \quad (22)$$

The change in the properties of the environment is illustrated in Fig.12 and Fig. 13.

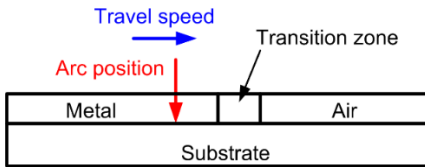


Fig. 10. Transition zone in layer material.

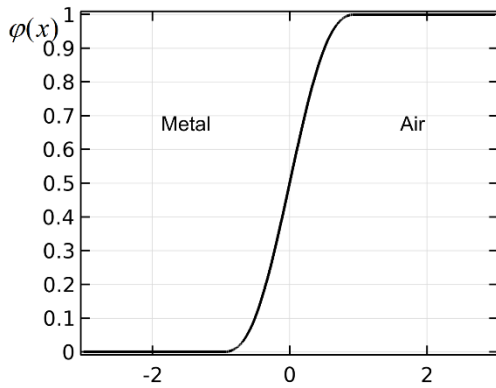


Fig. 11. Transition function.

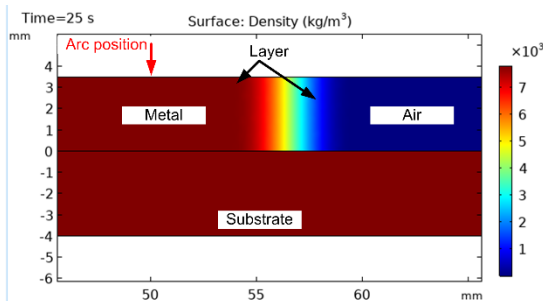


Fig. 12. Realization of transition function.

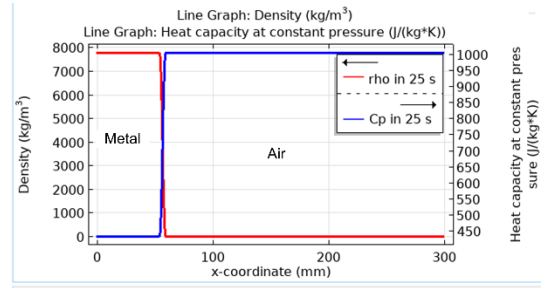


Fig. 13. Changing the properties of the medium in front of the welding arc.

The cross-sectional shape of the first layer (Fig. 14) can be represented as a segment of an ellipse with dimensions shown in Fig. 15. The area of this cross-section is defined as  $A_{wl} = ab \arccos(z_0/b) - y_0 z_0$  and is actually determined by the wire feed rate  $V_{wf}$ , the welding speed  $V_w$ , and the electrode wire diameter  $d_e$  as  $A_{wl} = 0.25 \pi d_e^2 V_{wf} / V_w$ . This area can be expressed in terms of the dimensions of the ellipse:

$$A_{wl} = \frac{b_w h_w}{2(1-\beta)} \left[ \arccos\left(\frac{\beta}{\sqrt{1-\beta^2}}\right) - \beta \right] \quad (23)$$

$$\text{where } \beta = \frac{z_0}{z_0 + h_w} \rightarrow 0 \leq \beta < 1.$$

To show that this way of representing the geometry of the first layer gives good results, we will use the experimental data from [21]. There, three different ways of representing the layer geometry are compared and it is shown that the best results are obtained when using a parabolic dependence. Using these data, the value of  $\beta$  was determined as varied in the permissible interval through 0.1, which is a rather rough determination of this quantity. Nevertheless, the accuracy with which the section of the layer is calculated is higher than that calculated by means of a parabolic section (Table 2). In this table  $A_p$  is the area of parabolic section,  $\varepsilon(A_p)$  and  $\varepsilon(A_{wl})$  are the absolute values of errors in determining  $A_p$  and  $A_{wl}$ , respectively. The mean values of these errors are  $\varepsilon_{ave}(A_p) = 5.98\%$  and  $\varepsilon_{ave}(A_{wl}) = 2.009\%$ .

To predict the dimensions of the welded bead, the heat problem is solved. When solving it, the reaching of the solidus temperature along the transition line between the substrate and the applied layer is considered as a condition (Fig. 16). At the same time, in the middle of the layer (Fig. 17), a temperature not lower than the temperature of the liquidus must be reached. The height of the layer  $h_w$  and the parameter  $\beta$ , are varied, and the width of the layer is determined by the equation

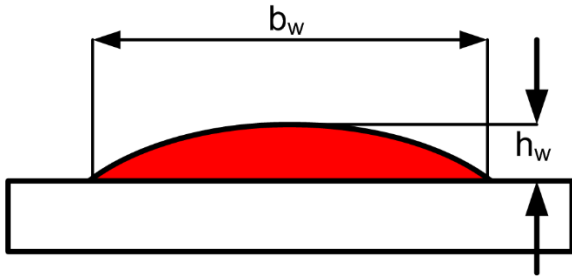


Fig. 14. Elliptical cross-sectional shape of the first layer.

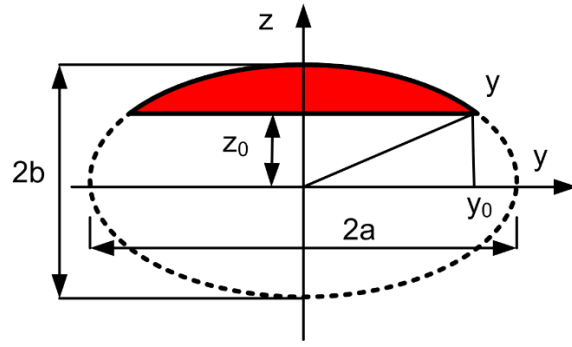


Fig. 15. Dimensions of ellipse.

TABLE II. EXPERIMENTAL DATA FOR BEAD DIMENSIONS FROM [21] AND CALCULATED PARAMETERS OF ELLIPTICAL SEGMENT

$b_w$	$h_w$	$A_{measured}$	$A_p$	$\varepsilon(A_p)$	$\beta$	$z_0$	$a$	$b$	$A_{wl}$	$\varepsilon(A_{wl})$
mm		mm <sup>2</sup>		%			mm		mm <sup>2</sup>	%
6.488	3.047	15.08	13.178	12.61	0.1	0.34	3.26	3.39	15.13	0.36
6.128	2.683	11.729	10.962	6.53	0.5	2.68	3.54	5.37	11.66	0.59
7.387	2.319	10.556	11.422	8.20	0.9999	23187	261.18	23190	11.42	8.19
4.994	2.426	8.445	8.078	4.34	0.6	3.64	3.12	6.07	8.47	0.27
8.95	2.876	18.096	17.158	5.18	0.6	4.31	5.59	7.19	17.99	0.59
7.193	2.448	10.858	11.738	8.10	0.9999	24477	254.32	24480	11.74	8.11
5.174	2.533	9.048	8.738	3.42	0.7	5.91	3.62	8.44	9.04	0.11
8.798	3.346	21.543	19.628	8.88	0.3	1.43	4.61	4.78	21.60	0.26
7.899	2.961	16.756	15.594	6.93	0.4	1.97	4.31	4.94	16.86	0.60
7.249	2.662	12.567	12.863	2.35	0.9999	26617	256.30	26620	12.86	2.37
7.193	2.533	11.6	12.149	4.73	0.9999	25327	254.32	25330	12.15	4.71
11.759	3.796	33.176	29.754	10.31	0.2	0.95	6.00	4.75	33.41	0.71
8.079	2.94	16.588	15.833	4.55	0.6	4.41	5.05	7.35	16.60	0.07
7.788	2.811	13.27	14.596	9.99	0.9999	28107	275.35	28110	14.59	9.98
7.539	2.341	11.059	11.765	6.38	0.9999	23407	266.55	23410	11.77	6.39
8.51	2.24	13.007	12.708	2.29	0.8	8.96	7.09	11.20	12.99	0.16
10.721	3.346	26.139	23.719	9.25	0.3	1.43	5.62	4.78	26.32	0.70
10.002	3.218	21.782	21.456	1.49	0.9	28.96	11.47	32.18	21.68	0.46
9.116	3.047	19.604	18.517	5.54	0.5	3.05	5.26	6.09	19.70	0.48
8.286	2.747	15.683	15.176	3.23	0.7	6.41	5.80	9.16	15.70	0.09
11.233	3.304	25.133	24.739	1.56	0.9	29.74	12.89	33.04	25.00	0.52
9.905	3.282	22.62	21.672	4.19	0.6	4.92	6.19	8.21	22.72	0.44
7.332	2.854	15.08	13.951	7.48	0.4	1.90	4.00	4.76	15.08	0.01

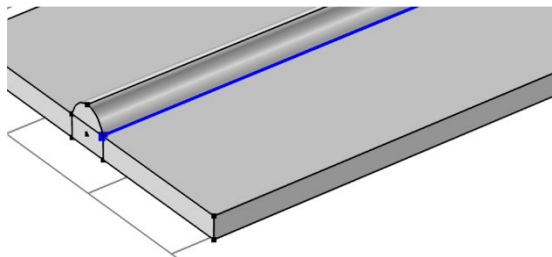


Fig. 16. On this line solidus temperature must be reached.

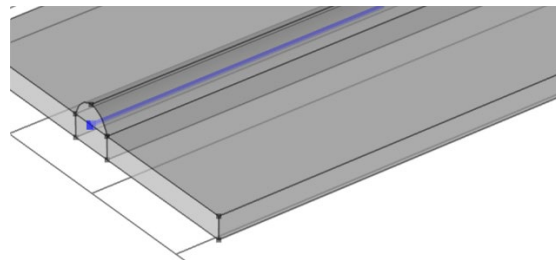


Fig. 17. The temperature reached on this line must be no lower than the liquidus temperature.

$$b_w = \frac{2(1-\beta)A_{wl}}{h_w} \left[ \frac{\arccos(\beta)}{\sqrt{1-\beta^2}} - \beta \right]^{-1} \quad (24)$$

The axisymmetric Gaussian heat source is considered as acting on the surface of the layer and substrate. It is defined in a movable coordinate system related to the

movement of the welding arc. The heat flow through the plane containing the  $y_1$  axis and perpendicular to the axis of the welding arc (Fig. 18) is described by the equation

$$f(x, y_1) = q_{eff} \frac{k}{\pi} \exp(-k(x^2 + y^2)) \quad (25)$$

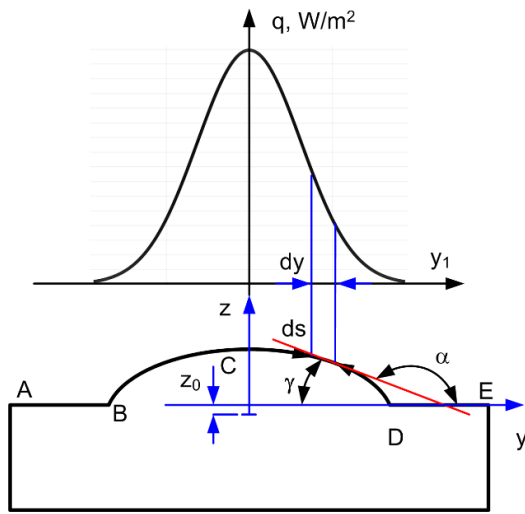


Fig. 18. Heat source.

The concentration coefficient of the heat source is related to the standard deviation and  $k = 1/(2\sigma^2)$ . The effective radius of the heating spot is  $r_{arc} = 3\sigma$  (virtually all the heat power is transmitted through the heating spot). In this way, the concentration factor of the heat source can be determined by the effective radius of the heating spot  $k = (9/2)r_{arc}^2$ . Substituting this value in (25) we get the heat flow distribution function

$$q(x, y_1) = q_{eff} \frac{9}{2\pi r_{arc}^2} \exp\left(-\frac{9}{2r_{arc}^2}(x^2 + y^2)\right) \quad (26)$$

When applying the first layer, the heat flow is transmitted to both the applied layer and the substrate. Equation (26) is used to describe the interaction of the electric arc with the substrate (sections AB and DE in Fig. 18). We determine the density of the heat flow through the surface of the applied bead as follows. In the direction of the  $x$  axis, there is no change in the way of calculation. In the direction of the  $y$  axis, we consider a section with a width of  $dy$ . The heat flow that passes through this section is distributed over a section of the surface of the applied layer with length  $ds$ . This means that in this case the dependency  $q(x, y) = q(x, y_1) \cos(\gamma)$  should be used. The curve describing the cross-section of the layer  $z(y)$  (in this case an ellipse) is defined in the  $Oyz$  coordinate system. From Fig.18 it can be seen that  $tg(\gamma) = -tg(\alpha)$  and  $\cos(\gamma) = -\cos(\alpha)$  can be determined by the derivative of the function  $z(y)$ . Equation (27) gives the final result, which is also illustrated in Fig.19

$$\cos(\gamma) = \frac{\sqrt{1 - \left(\frac{y}{a}\right)^2}}{\sqrt{1 - \left(\frac{y}{a}\right)^2 \left[1 - \left(\frac{b}{a}\right)^2\right]}} \quad (27)$$

Thus, the final model of the heat source is

$$q(x, y) = \begin{cases} q_1(x, y) & \text{for } AB | CD \\ q_1(x, y) \cos(\gamma) & \text{for } BCD \end{cases} \quad (28)$$

where

$$q_1(x, y) = q_{eff} \frac{9}{2\pi r_{arc}^2} \exp\left(-\frac{9}{2r_{arc}^2}(x^2 + y^2)\right)$$

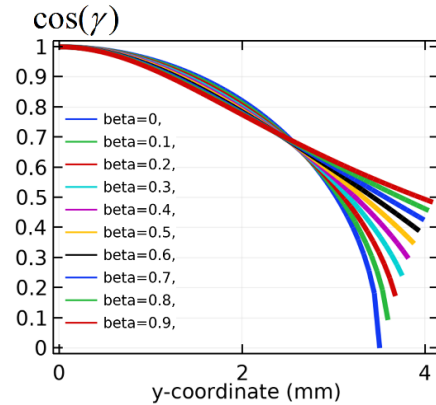


Fig. 19. Influence of the parameter  $\beta$  on  $\cos(\gamma)$ .

The results of the calculation of the temperature field are shown in Fig. 20 ÷ Fig. 25. Fig. 20 shows the temperature distribution along the upper surface of the substrate and the welded bead. It can be noted that the line delineating the width of the layer appears as a tangent to the isotherm of the solidus. This is also confirmed by Fig. 21, where the temperature distribution along the fusion line is shown. Also shown in the same figure are the temperature distributions along lines in the plane of the seam line, located at different distances from the top surface of the substrate. From these graphs, it can be concluded that the penetration depth along the seam line is slightly greater than 1 mm. Fig. 22 shows isotherms in the upper plane of the substrate. Here it can be seen that the solidus isotherm spans the entire width of the bead, i.e. there is good fusion between the substrate and the layer. In addition, here you can see the resulting width of the layer - 6 mm. The depth of the penetration along the seam line can be seen in Fig.23. This figure also shows the height of the layer. Fig. 24 and Fig. 25 show the isothermal surfaces and the general appearance of the temperature field, respectively. The resulting geometric dimensions of the layer match well with those shown in Fig. 6.

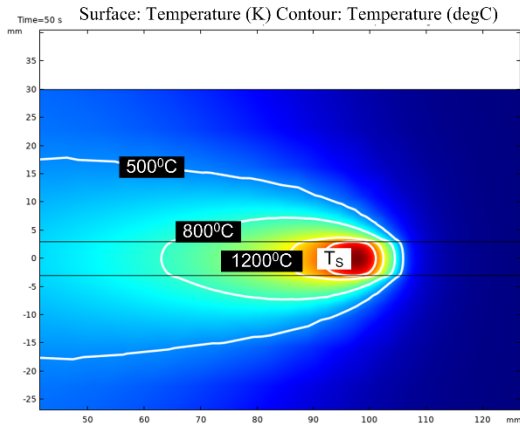


Fig. 20. Temperature distribution along the upper surface of the substrate and the welded bead.

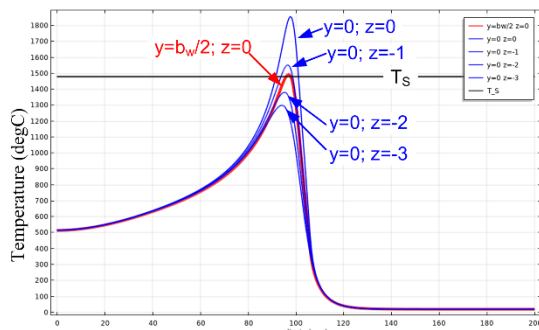


Fig. 21. Temperature distribution along the fusion line (red) and lines in the plane of the seam line at different depths in the substrate.

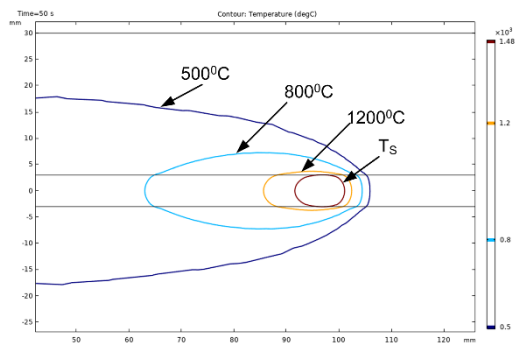


Fig. 22. Isotherms in the upper plane of the substrate.

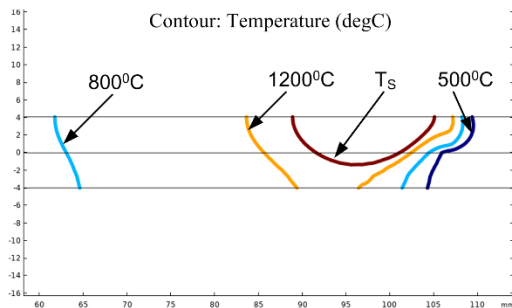


Fig. 23. The depth of the penetration along the seam line.

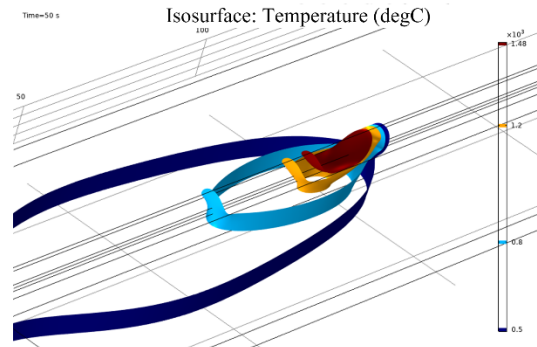


Fig. 24. Isothermal surfaces.

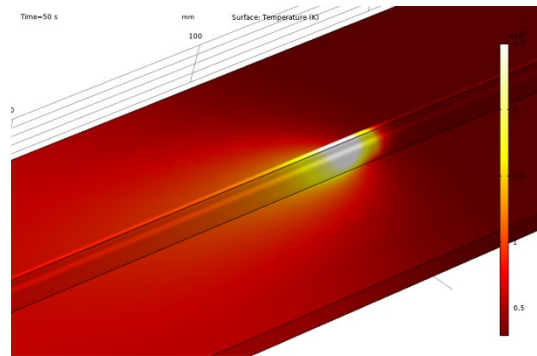


Fig. 25. General appearance of the temperature field.

#### IV. CONCLUSIONS

A methodology for simulation modeling of the thermal processes in the first layer during WAAM is proposed, which takes into account the current position of the welding torch and the completed length of the layer. It has been shown that the representation of the layer cross-section by an elliptical segment gives a more accurate calculation of the cross-sectional area of the layer compared to the parabolic form. As a result of solving the heat problem, the width and height of the obtained layer were determined at set parameters of the regime (feed rate, travel speed, welding current, arc voltage). It is shown that along the fusion line the temperature reaches that of the solidus, and that fusion between the layer and the substrate is achieved. The proposed methodology can also be used in simulation modeling of multipass welding.

#### V. ACKNOWLEDGMENTS

The authors are grateful to the financial support of the Bulgarian National Science Fund, Contract No KP-06-H57/10, for carrying out the necessary research.

#### REFERENCES

- [1] T. A. Rodrigues, V. Duarte, R.M. Miranda, T. G. Santos and J. P. Oliveira, "Current status and perspectives on wire and arc additive manufacturing (WAAM)", *Materials* vol.12, issue 7, art. ID 1121, 2019.
- [2] K. Barath and M. Manikandan, "Assessment of process, parameters, residual stress mitigation, post treatments and finite element analysis simulations of wire arc additive manufacturing technique", *Metals and Materials International*, vol. 28, pp.54-111, 2022.

- [3] V. Mishra, A. Babu, R Schreurs, U. Wu, M Hermans and C. Ayas, "Microstructure Estimation and Validation of ER110S-G steel structures produced by Wire and Arc Additive Manufacturing", *Journal of Materials Research and Technology*, vol. 23, pp. 3579-3601, 2023
- [4] T. Zhang, H. Li, H. Gong, Y. Wu, X. Chen and X. Zhang, "Study on location-related thermal cycles and microstructure variation of additively manufactured inconel 718", *Journal of Materials Research and Technology*, vol. 18, pp. 3056-3072, 2022.
- [5] J. Xiaolei, X. Jie, L. Zhaoheng, H. Shaojie, F. Yu and S. Zhi, "A new method to estimate heat source parameters in gas metal arc welding simulation process", *Fusion Engineering and Design* vol. 89, pp. 40– 48, 2014
- [6] T. Mukherjee, W. Zhang and T. DebRoy, "An improved prediction of residual stresses and distortion in additive manufacturing", *Computational Materials Science* vol. 126 pp. 360–372, 2017
- [7] H. Arora, R. Singh and G.S. Brar, "Thermal and structural modelling of arc welding processes: A literature review", *Measurement and Control*, vol 52 (7-8), pp. 955-969, 2019, SAGE Publications Sage UK: London, England
- [8] N.P. Gokhale and P. Kala "Thermal analysis of TIG-WAAM based metal deposition process using finite element method" ,*Materials Today: Proceedings*, vol. 44, pp. 453-459, 2021.
- [9] C. Xiaoxuan, S. Xin, Z. Zirong and S. Chen, "A Review of the Development Status of Wire Arc Additive Manufacturing Technology", *Advances in Materials Science and Engineering Volume 2022, Article ID 5757484, 28 pages* <https://doi.org/10.1155/2022/5757484>
- [10] S. Pattanayak and S.K. Sahoo; "Gas metal arc welding based additive manufacturing - a review", *CIRP Journal of Manufacturing Science and Technology*, vol. 33, pp. 398-442, 2021.
- [11] M. Chaturvedi, E. Scutelnicu, C.C. Rusu, L.R. Mistodie, D. Mihailescu and A.V. Subbiah; "Wire arc additive manufacturing: Review on recent findings and challenges in industrial applications and materials characterization", *Metals*, vol. 11, issue 6, art. ID 939, 2021.
- [12] W.C. Ke, J.P. Oliveira, B.Q. Cong, S.S. Ao, Z.W. Qi, B. Peng and Z. Zeng; "Multi-layer deposition mechanism in ultra high-frequency pulsed wire arc additive manufacturing (WAAM) of NiTi shape memory alloys", *Additive Manufacturing*, vol. 50, art. ID 102513, 2022
- [13] X. Chen, C. Wang, J. Ding, P. Bridgeman and S. Williams, "A three-dimensional wire-feeding model for heat and metal transfer, fluid flow, and bead shape in wire plasma arc additive manufacturing", *Journal of Manufacturing Processes*, vol. 83, pp. 300-312, 2022.
- [14] X. Zhou, H. Zhang, G. Wang and X. Bai, "Three-dimensional numerical simulation of arc and metal transport in arc welding based additive manufacturing", *International Journal of Heat and Mass Transfer* vol.103, pp. 521–537, 2016
- [15] F. Hejrípour, D. T. Valentine and D. K. Aidun, "Study of mass transport in cold wire deposition for Wire Arc Additive Manufacturing", *International Journal of Heat and Mass Transfer* vol. 125, pp. 471–484, 2018.
- [16] X. Bai, P. Colegrove, J. Ding, X. Zhou, C. Diao, P. Bridgeman, J. Hönnige, H. Zhang and S. Williams, "Numerical analysis of heat transfer and fluid flow in multilayer deposition of PAW-based wire and arc additive manufacturing", *International Journal of Heat and Mass Transfer* vol. 124 pp. 504–516, 2018
- [17] W. Ou et al. "Fusion zone geometries, cooling rates and solidification parameters during wire arc additive manufacturing", *International Journal of Heat and Mass Transfer* vol. 127, pp. 1084-1094, 2018
- [18] W. Ou et al. "Determination of the control points for circle and triangle route in wire arc additive manufacturing (WAAM)", *Journal of Manufacturing Processes* vol. 53, pp. 84-98, 2020.
- [19] S. Suryakumar, K.P. Karunakaran, Alain Bernard, U. Chandrasekhar, N. Raghavender and D. Sharma, "Weld bead modeling and process optimization in Hybrid Layered Manufacturing", *Computer-Aided Design* vol. 43, pp. 331–344, 2011
- [20] L. Nguyen, J. Buhl, and M. Bambach. "Multi-bead overlapping models for tool path generation in wire-arc additive manufacturing processes." *Procedia Manufacturing* vol. 47, pp. 1123-1128, 2020
- [21] J. Xiong, G. Zhang, H. Gao and L. Wu, "Modeling of bead section profile and overlapping beads with experimental validation for robotic GMAW-based rapid manufacturing", *Robotics and Computer-Integrated Manufacturing* vol. 29 issue 2, pp. 417-423, 2013
- [22] D. Ding, Z. Pan, D. Cuiuri and H. Li, "A multi-bead overlapping model for robotic wire and arc additive manufacturing (WAAM)", *Robotics and Computer-Integrated Manufacturing* vol. 31, pp. 101-110, 2015
- [23] B. Tomar, S. Shiva and T. Nath, "A review on wire arc additive manufacturing: Processing parameters, defects, quality improvement and recent advances", *Materials Today Communications*, vol. 31 art. ID 103739, 2022
- [24] P. Shukla, B. Dash, D.V. Kiran and S Bukkapatnam, "Arc behavior in wire arc additive manufacturing process", *Procedia Manufacturing*, vol. 48, pp. 725-729, 2020.
- [25] M. Benakis, D. Costanzo and A. Patran, "Current mode effects on weld bead geometry and heat affected zone in pulsed wire arc additive manufacturing of Ti-6-4 and Inconel 718", *Journal of Manufacturing Processes* vol. 60, pp. 61–74, 2020.
- [26] V. A Hosseini et al. "Wire-arc additive manufacturing of a duplex stainless steel: thermal cycle analysis and microstructure characterization" *Welding in the World* vol. 63 pp. 975-987, 2019.
- [27] R. Israr, J. Buhl, L. Elze and M. BamBach "Simulation of different path strategies for wire-arc additive manufacturing with Lagrangian finite element methods", *LS-DYna Forum*. 2018, Bamberg.
- [28] C.S. Wu and L. Dorn, "Computer simulation of fluid dynamics and heat transfer in full-penetrated TIG weld pools with surface depression", *Computational Materials Science* vol 2q issue 2, pp. 341-349, 1994
- [29] L. Nguyen, J. Buhl, R. Israr and M. Bambach, "Analysis and compensation of shrinkage and distortion in wire-arc additive manufacturing of thin-walled curved hollow sections", *Additive Manufacturing* vol. 47, art. ID 102365, 2021.
- [30] X. Meng, G. Qin and Z. Zou, "Sensitivity of driving forces on molten pool behavior and defect formation in high-speed gas tungsten arc welding", *International Journal of Heat and Mass Transfer* vol. 107, pp. 1119–1128, 2017.

# Study of the Unloading and Selection Process of Energy Willow Cuttings for the Creation a Planting Machine

**Serhii Yermakov**

*Educational and Scientific  
Laboratory "DAK GPS",  
Higher educational institution  
«Podillia State University»,  
Kamianets-Podilskyi, Ukraine  
dakgps@pdatu.edu.ua*

**Taras Hutsol**

*Department of Mechanics and  
Agroecosystems Engineering  
Polssia Natioinal University  
Zhytomyr, Ukraine  
wte.inter@gmail.com*

**Igor Gerasymchuk**

*Faculty of Energy and Information  
Technologies,  
Higher educational institution  
«Podillia State University»,  
Kamianets-Podilskyi, Ukraine*

**Pavlo Fedirko**

*Faculty of Engineering and  
Technology  
Higher educational institution  
«Podillia State University»,  
Kamianets-Podilskyi, Ukraine*

**Viktor Dubik**

*Faculty of Energy and Information  
Technologies,  
Higher educational institution  
«Podillia State University»,  
Kamianets-Podilskyi, Ukraine*

**Abstract.** The article highlights the problems of ensuring continuous unloading of energy willow cuttings from slotted bunkers. During the free discharge of rod-like bodies, such phenomena as crypt formations, distortions, pinching occur, which stop the discharge under the action of gravity. Finding such parameters, under which the system will work evenly and without stops, will make it possible to automate many processes related to working with such material, in particular, when developing a piecemeal selection mechanism for a planting machine. The study revealed and analyzed the possible forms of vaults that are formed during unloading from creating obstacles to movement. As a hopper model, for unloading cuttings, a slotted hopper in the form of two walls located at angles to the horizontal plane is considered. These walls form an unloading slot with adjustable width of the unloading window and an adjustable tilt angle. During the study, vaults were recorded, which are formed at different parameters of the bunker during free unloading. As research has shown, in order to ensure uninterrupted unloading of cuttings, there is such a width of the unloading window of the hopper, which will ensure uniform pouring of cuttings without crypt formations and stops associated with this process. The analysis of continuous discharge of rod-like material established that for cuttings of energy willow, the width of the window, which ensures continuous discharge, is 8-12 cm.

**Keywords:** vault formation, unloading, cuttings, energy willow, bunker, vault, automation of planting.

## INTRODUCTION

Many machines used in production technological lines use in their principle of operation such processes as loading, unloading, selection, transportation of various materials, which most often consist of the same type of particles. The high-performance and high-quality operation of such machines largely depends on the speed of unloading the product, the equipment used, and the parameters and modes of operation of the unloading devices [1-2]. The problem becomes even more complicated when it is necessary to ensure uniform and continuous discharge of material in which one size (length) significantly exceeds the other two sizes. An example of such a rod-like material is plant cuttings. The need to study this issue is dictated by the growing popularity of fuels from bioenergy crops, the volume of which requires fast and productive machines to create so-called energy plantations. One of the most common such crops is energy willow (e.g. *Salix viminalis*), which is planted vegetatively with cuttings 20-25 cm long and 8-20 mm in diameter [3-6]. Planting of energy willow plantations is carried out by machines in which the

Print ISSN 1691-5402

Online ISSN 2256-070X

<https://doi.org/10.17770/etr2023vol3.7199>

© 2023 Serhii Yermakov, Taras Hutsol, Igor Gerasymchuk, Pavlo Fedirko, Viktor Dubik.

Published by Rezekne Academy of Technologies.

This is an open access article under the [Creative Commons Attribution 4.0 International License](https://creativecommons.org/licenses/by/4.0/).

planting material is fed manually, which significantly limits the possibilities of increasing the efficiency of the units. When creating an automatic planter of such material, the task of fast and accurate feeding of cuttings arose, which led to the search for ways to justify the movement of cuttings during unloading from the storage tank [7-12]. Existing methods of automating the planting of such material are mainly reduced to the use of cassette mechanisms, however, this method requires careful preliminary preparation of the planting material and requires time spent on charging the cassettes. This study is designed to reveal the possibilities of uninterrupted gravity unloading of rod-like materials from a slotted hopper, which can be the initial stage of the development of a cassette-free planter of energy willow, which will make it possible to significantly increase the productivity of planting units, the quality of their work, as well as reduce the number of workers on the establishment of energy plantations.

It is known from the practice of functioning of bunkers that the main obstacle to the unloading of lumpy materials is the phenomenon of crypt formation, which, interrupting the natural spilling of materials, negatively affects their consumption characteristics. There is no comprehensive theoretical solution to this problem in the scientific literature. In the field of research on the dynamics of spillage of loose media from containers, fight against crypt formation, and in the field of development of crypt-destructive equipment, we note the significant contribution of the following scientists: Alfiorov K., Bilousov A., Bogomyakhi V., Goryushinskyi B., Horyushinskyi I., Gyachev L., Jenike E., Zheltkova S., Zenkov R., Kvapil R., Keglyn B., Kunakov B., Sokolovsky V., Tretyakov H., Yatsun S. and others. In their works, the main characteristics and physical and mechanical properties of bulk materials, which in one way or another affect the process of crypt formation, are considered, the general directions of research in the field of uninterrupted functioning of bunker devices and the improvement of crypt moving equipment for bulk cargoes with a wide range of physical and mechanical properties are reflected [14- 24]. Numerous studies of the process of crypt formation made it possible to establish only some dependencies that explain the essence of this process. The degree of influence of a huge number of different interdependent factors on crypt formation is difficult to assess practically and predict theoretically: it is the geometry of the hopper and outlet opening, and the physical and mechanical properties of materials, and the conditions of loading, storage and release. Precisely due to the difficulty of ensuring uniform continuous movement, which is hindered by the process of crypt formation, until now there is no universal feeding device that would work effectively with any loose material, and the variety of material that requires unloading contributes to further searches for justifications for movement one or another material.

It is also difficult to overestimate the scientific and practical importance of research into the mechanism of movement of loose materials under the influence of their

own weight, since the physical and mechanical properties of these materials and the patterns of their discharge have a decisive influence on the design of bunkers, as well as discharge devices and devices that stimulate discharge.

Scientists single out two main directions for ensuring uninterrupted discharge of bulk cargo from containers:

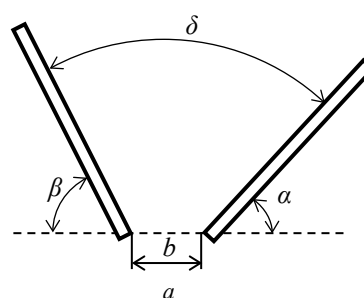
1. prevention of the occurrence of vaults, which can be achieved by the correct selection of capacity parameters;
2. destruction of the formed vaults with the use of various vaulting devices.

Both directions are relevant, but we will consider the first more progressive, since it is better to prevent crypt formation than to fight it [6]. Modeling the movement of particles of loose material during unloading, as well as the choice of means for destroying the vaults formed in the container, depends on the physical and mechanical properties of the material and the parameters of the container itself. In this work, we are interested in the behavior of rod-like heterogeneous materials (which are, in particular, cuttings of energy willow or poplar) in the process of unloading from the hopper under the action of gravitational forces, so the purpose of the article is to search and highlight the patterns of movement of rod-like bodies in the process of their discharge from the hoppers. To achieve this goal, the following tasks should be solved:

- justify the bunker model for unloading energy willow cuttings;
- to create an experimental model of the bunker that would meet the conditions for unloading rod-like materials;
- analyze the process of vault formation for rod-like materials and identify the characteristic features of vault formation for willow cuttings;
- to reveal the possibility of continuous shedding of energy willow cuttings and the nature of this process;
- create recommendations for feeder hoppers for energy willow ponds and identify directions for further study of this process.

#### MATERIALS AND METHODS

It is convenient to unload rod-like materials from bunkers with sloping walls and a slotted unloading window (Fig. 1).



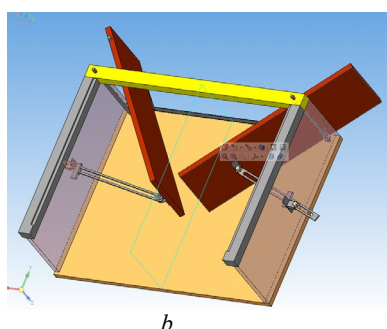


Fig. 1. Experimental installation: *a* - a model of a bunker for unloading energy willow cuttings.  $\alpha$  and  $\beta$  are the angles to the horizontal plane of the two walls,  $\delta$  is the angle of inclination of the discharge funnel formed by the two walls; *b* - the width of the unloading window; *b* - a view of the laboratory installation.

The nature of filling the bunker with such materials will be carried out in layers one above the other, therefore, in a first approximation, studying the movement in this system can be limited to the study of processes in the plane perpendicular to the bodies and walls of the bunker, neglecting the possibility of their movement in the transverse direction. Therefore, when making a working laboratory installation, let's limit the space of the bunker with two parallel walls at a distance slightly greater than the length of the material used for unloading.

The laboratory installation allows you to adjust the angles of the two walls  $\alpha$  and  $\beta$  in wide ranges, as well as to change the width of the discharge window, which is necessary for research without delay.

#### RESULTS AND DISCUSSION

In the process of conducting experiments to study the characteristics of the discharge of rod-like material through the slotted discharge window, cuttings of energy willow were loaded in a uniform layer into the bunker with the discharge window closed. When setting small window width parameters, vaults will inevitably be formed. By fixing the position of the cuttings when the movement is stopped, it is possible to identify the factors that affect the process of crypt formation of this material. And by expanding the discharge window, you can achieve conditions under which discharge will take place continuously. By using high-speed photography, it is possible to identify the regularities of such eruptions for use in the further study of this process. In the work of I.V. Horyushynskiy, I.I. Kononova, V.V. Denisov gave the following definition of the vault formation process: vault formation is the formation of vaults in containers during the release of bulk cargo [25]. Plant cuttings have a rod-like shape, therefore, excluding other factors, crypt formation here can be considered as a process in one plane, where the discharged material forms an arched structure. At the same time, the cuttings in the vault (each of them) are kept from falling by normal reactions and corresponding frictional forces of the neighboring cuttings. And the cuttings that occupy extreme positions (tangential to the walls) are held by normal reactions and frictional forces not only of the neighboring cuttings, but

also by the forces of their interaction with the material of the bunker walls (Fig. 2).

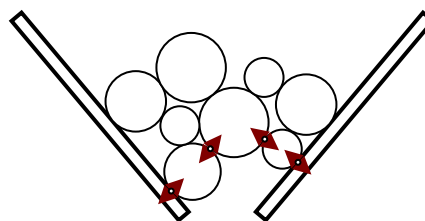


Fig. 2. Scheme of crypt formation when cuttings are shed.

In order to find possible solutions to the problem of continuous shedding of energy willow cuttings, it is important to analyze the possible forms of the formed vaults. As it was said above, when using rod-like materials in an environment limited by their length, the crypt formation can be considered only in one plane. Taking this into account, we will try to compare the formation of vaults under controlled conditions and directly for an array of cuttings.

For the first case, let's take cylindrical bodies of different diameters. In our case, coins of different denominations are quite suitable. Some variants of vaults formed during the movement of such bodies are shown in Fig. 3.

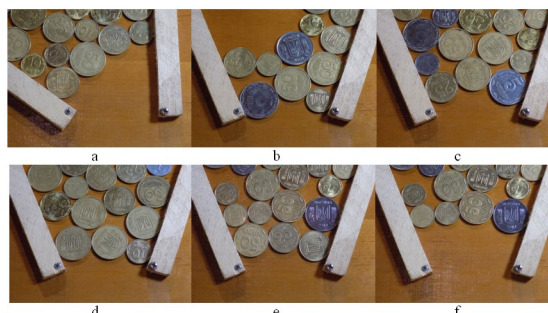


Fig. 3. Examples of vaults formed when cylindrical bodies are unloaded on a plane.

Analyzing fig. 3, it can be concluded that the formation of vaults in the system of one plane can be completely described by the laws of interaction between particles according to the positions they occupy. Moreover, the forms of the vaults themselves, although they are random, are generally formed according to one and the same laws and can be predicted in general terms. Taking into account the dimensional characteristics of plant cuttings, it is not difficult to predict that the length of the cuttings can also affect the process of crypt formation. In fig. 6 shows some variants of fixed vaults when cuttings are unloaded through the unloading hole at angles  $\alpha=90^\circ$  and  $\beta=40^\circ$ , and Fig. 7 shows the same at angles  $\alpha=60^\circ$  and  $\beta=40^\circ$ .

Thus, we can see that the shape of the vaults is significantly different from the previous vaults in one plane. The difference is at least that the extreme cuttings in the plane of the side wall do not always come into contact with the wall of the bunker, and some cuttings in this plane do not contact the neighboring cuttings at all, intertwining with them somewhere in the depth of the

layer. Often, the hanging of the cuttings provokes a non-uniform pinching of them along the length, when one of the ends is released before the other and thus trying to take a vertical position, which can be seen in fig. 4 - b, d, e.

Note that in many cases, the reason for such differences is the length of the cuttings being skewed relative to each other. Also, the reason was sometimes defects in the shape of the material - curvature, notches, taper, etc. When many of these reasons coincide in one layer, you can even observe the picture as in Fig. 5, which makes the process of uniform unloading problematic, and the controlled output of material in the desired orientation is practically impossible.

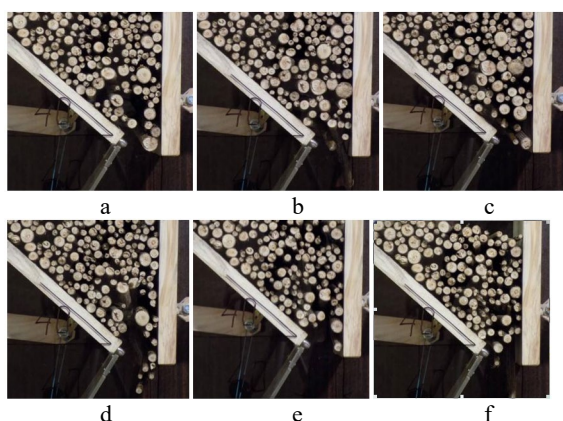


Fig. 4. Examples of vaults formed when cuttings of energy willow are unloaded.

Such problems arise with small values of the width of the unloading window, when static vaults prevail over dynamic ones. When the width of the window is increased, the unloading process is more uniform, and in this case it is possible to observe and analyze the regularities of the discharge of the material. It has been established that for energy willow cuttings, the width of the window, which ensures continuous shedding, is 8-12 cm.



Fig. 5. Problems of unloading energy willow cuttings in the area of the unloading window.

#### CONCLUSIONS

In order to solve the issues of freeing the process of planting energy willow from manual labor during the supply of planting material from storage containers to the planting site, there is a need to create an automated supply system. The selection and transportation of cuttings in

such a system can be organized using gravity unloading from the bunker. The hopper model for unloading rod-like materials consists of two walls located at an angle to the horizon, at the bottom of which an unloading window with an adjustable width is formed. The analysis of the unloading process and the shape of the vaults shows that in the case of such a rod-like material as cuttings of energy willow, in addition to the general reasons for the formation of vaults and the regularities of their shape formation, there are also other influencing factors. A feature of plant cuttings is their shape, which complicates crypt formation and causes such additional conditions and factors. such as distortions of the cuttings in the layer, irregular shape of the cuttings, unevenness of their pinching along the length, etc. When creating conditions under which there is no occurrence of static vaults, it was possible to analyze the patterns of unloading cuttings from the bunker. As a result of the study, it was established that to ensure the uninterrupted unloading of cuttings, it is possible to choose such a width of the unloading window of the bunker, which will ensure uniform pouring of cuttings without crypt formations and stops associated with this process. The use of the obtained data in further research will make it possible to more fully take into account all the factors that arise in the process of unloading and crypt formation, which is important in the study and improvement of this process.

#### REFERENCES

- [1] V.V.Adamchuk, H.L.Baranov, O.S.Baranovskiyi Suchasni tendentsii rozvytku konstrukttsii silskohospodarskoi tekhniki [Modern trends in the development of constructions of agricultural machinery]. Kyiv: Ahrama nauka, 2004 (in Ukrainian)
- [2] T. Hutsol, S. Glowacki, K. Mudryk. Agrobiomass of Ukraine – Energy Potential of Central and Eastern Europe (Engineering, Technology, Innovation, Economics). Monograph. Warsaw, 2021.
- [3] D. Baran, D. Kwaśniewski, K. Mudryk. Wybrane właściwości fizyczne trzyletniej wierzby energetycznej [Selected physical properties of a three-year-old energy willow]. Inżynieria Rolnicza. V.11., 2007. (in Polish)
- [4] J. Frączek, K. Mudryk. Jakości sadzonek wierzby energetycznej w aspekcie sadzenia mechanicznego [The quality of energy willow seedlings in terms of mechanical planting]. Inżynieria Rolnicza, 6 (66), 2005 (in Polish)
- [5] M.V. Roik, V.M. Sinchenko, Y.D. Fuchylo. Energetychna verba: tekhnologiya vy'roshhuvannya ta vy'kory'stannya [Energy willow: cultivation technology and usage]., Vinnitsa: LLC "Nilan-LTD", 2015 (in Ukrainian)
- [6] R.N. Mynko. Problema svodoobrazovanyia v emkostiakh bunkernoho tipa v uslovyiakh dlitelnoho khraneniya [The problem of arch formation in bunker-type tanks under long-term storage conditions]. Yaroslavskiyi pedahohycheskyi vestnyk, 3(1). 2017.(in Russian)
- [7] J.E. Mattsson, P.D. Kofman. Influence of particle size and moisture content on tendency to bridge in biofuels made from willow shoots, Biomass and Bioenergy, V. 24, Issue 6, 2003, P.429-435, [https://doi.org/10.1016/S0961-9534\(02\)00178-2](https://doi.org/10.1016/S0961-9534(02)00178-2).
- [8] S. Yermakov, K. Mudryk, T. Hutsol. The analysis of stochastic processes in unloadingthe energywillow cuttings from the hopper. Environment. Technology. Resources. Rezekne, Latvia. Vol. III. 2019, pp. 249-252, <https://doi:10.17770/etr2019vol3.4159>.
- [9] V. Ivanyshyn, S. Yermakov , T. Ishchenko. Calculation algorithm for the dynamic coefficient of vibro-viscosity and other properties of energy willow cuttings movement in terms of their unloading from the tanker. Renewable Energy Sources, vol. 154, E3S Web

- of Conferences. 2020, pp. 04005, <https://doi.org/10.1051/e3sconf/202015404005>.
- [10] M. Korchak, S. Yermakov, V. Maisus. Problems of field contamination when growing energy corn as monoculture. E3S Web of Conferences. Krynica, Poland. Vol.154, 2020.
- [11] M. Korchak, S. Yermakov, T. Hutsol, L. Burko, W. Tulej. Features of weediness of the field by root residues of corn. *Vide. Tehnologija. Resursi - Environment, Technology, Resources*, V. 1, 2021. pp. 122–126
- [12] A. Tryhuba, S. Komarnitskiy, I. Tryhuba. Planning and Risk Analysis in Projects of Procurement of Agricultural Raw Materials for the Production of Environmentally Friendly Fuel. *International Journal of Renewable Energy Development*, V.11(2), 2022. pp. 569–580
- [13] O. Kucher, L. Prokopchuk. Economic aspects of biomass market development in Ukraine. *Renewable Energy Sources engineering, technology, innovation*. Krynica. 2019
- [14] V.A. Bogomjagkih, A.Yu. Nesmiyanu. Funkcionirovanie bunkerov maksimalnogo rashoda v usloviyah svodoobrazuyushego istecheniya zernovyh materialov [Functioning of maximum flow bins in conditions of arch-forming outflow of grain materials]. Monograph. Zernograd. 2015. 179 p. (in Russian)
- [15] O. Kucher, L. Prokopchuk. The development of the market of the renewable energy in Ukraine. *Renewable Energy Sources: Engineering, Technology, Innovation*. Springer International Publishing AG. 2017
- [16] H. Mao, L. Han, J. Hu, F. Kumi. Development of a pincette-type pick-up device for automatic transplanting of greenhouse seedlings. *Applied engineering in agriculture*, 30(4). 2017
- [17] S.B. Savage, S.C. Cowin. *Theories for Flow Granular Materials*. American Society of Mechanical Engineers, Buffalo, N.Y. 1999.
- [18] Y. Lu, W. Jin, N. Saha, J. Lee Klinger, Y. Xia, S. Dai. Wedge-Shaped Hopper Design for Milled Woody Biomass Flow. *ACS Sustainable Chemistry & Engineering* 2022, 10 (50), 16803-16813. <https://doi.org/10.1021/acsschemeng.2c05284>
- [19] D. Barletta, R.J. Berry, S.H. Larsson, T.A. Lestander. Assessment on bulk solids best practice techniques for flow characterization and storage/handling equipment design for biomass materials of different classes. *Fuel Processing Technology*, V.138, 2015 P.540-554, <https://doi.org/10.1016/j.fuproc.2015.06.034>.
- [20] W.R. Ketterhagen, J.S. Curtis, C.R. Wassgren, B.C. Hancock. Predicting the flow mode from hoppers using the discrete element method. *Powder Technology*, V. 195. 2009. P.1-10. <https://doi.org/10.1016/j.powtec.2009.05.00>
- [21] Y.V. Horiushynskiy. Emkosty dlia sypuchikh gruzov v transportno-hruzyovkhn sistemakh [Tanks for bulk cargo in transport and cargo systems]. Samara: SamHAPS. 2003 (in Russian)
- [22] S. Yermakov, T. Hutsol, S. Glowacki, V. Hulevskiy, V. Pylypenko. Primary Assessment of the Degree of Torrefaction of Biomass Agricultural Crops. *Environment. Technologies. Resources*. 2021. pp.264-267. <https://doi.org/10.17770/etr2021vol1.6597>
- [23] S. Yermakov, T. Hutsol, V. Devin, S. Oleksiyko, P. Potapyskiy. Effectiveness of cognitive digressions in classes of general technical disciplines in institutions of higher education of agro-technical direction. *Engineering for rural development*. 2022. pp.460-465 <https://doi.org/10.22616/ERDev.2022.21.TF154>
- [24] S. Yermakov, T. Hutsol, A. Rozkosz, S. Glowacki, S. Slobodian. Evaluation of Effective Parameters Of Biomass Heat Treatment in Processing for Solid Fuel. *Engineering for Rural Development*. 2021. <https://doi.org/10.22616/ERDev.2021.20.TF241>
- [25] M. Wrobel, K. Mudryk, M. Jewiarz. Impact of raw material properties and agglomeration pressure on selected parameters of granulates obtained from willow and black locust biomass. *Engineering for Rural Development*. Jelgava. 2018

# Modification of 5083 Aluminum Alloy with Graphene Via Friction Stir Processing

**Radostina Zaekova,**

*Institute of Metal Science, Equipment and Technologies with Hydro- and Aerodynamics Center "Acad. A. Balevski" - BAS*  
Sofia, Bulgaria  
E-mail: rzaekova@ims.bas.bg

**Plamen Tashev**

*Institute of Metal Science, Equipment and Technologies with Hydro- and Aerodynamics Center "Acad. A. Balevski" - BAS*  
Sofia, Bulgaria  
E- mail: ptashev@ims.bas.bg

**Yasen Hadjitodorov,**

*Institute of Metal Science, Equipment and Technologies with Hydro- and Aerodynamics Center "Acad. A. Balevski" - BAS*  
Sofia, Bulgaria  
E- mail: jason@ims.bas.bg

**Deyan Gradinarov**

*Institute of Metal Science, Equipment and Technologies with Hydro- and Aerodynamics Center "Acad. A. Balevski" - BAS*  
Sofia, Bulgaria

**Abstract.** Graphene-modified layer is obtained on 5083 aluminum alloy sheet material via friction stir processing. A special groove is cut in the aluminum plate and filled with graphene. The processing is carried out using an innovative technology with an appropriate tool. The temperature at a chosen point in the heat affected zone is measured in real-time by a remote-control system. Test specimens were prepared from the processed plates and metallographic analysis was carried out. The microhardness of the modified layer is measured perpendicular to the direction of processing and in depth. An increase in microhardness relative to that of the base material is found.

**Keywords:** friction stir processing (FSP), friction stir welding (FSW), metallography, microhardness, parameters.

## 1. INTRODUCTION

Friction stir welding (FSW), and friction stir processing (FSP) in particular, are relatively new, successful methods for bonding or surface processing of solid-state materials. FSP has some advantages over fusion welding methods since the issues associated with cooling the liquid phase are avoided. Increasingly more studies are being conducted in order to further develop the FSP technology and to implement it faster in industrial production in order to exploit its advantages. The scientists found improved mechanical properties after FSP and FSW, such as hardness, tensile strength, bending strength, torsion strength, fatigue strength, and

ductility [1] - [3]. Grain refinement is also observed in the processed zone, which leads to a correspondingly higher strength of the weld [4] – [7]. This also applies to aluminum materials and alloys. One of the main advantages of the process FSW is conducting welding at temperatures below the melting point of the materials, thus reducing the resulting stresses and deformations [8]. Moreover, the addition of graphene in the weld improves the properties of the processed area [9] – [13]. This research examines FSP method with addition of graphene in the zone of processing. The microhardness of the modified layer transverse to the processing direction and in depth is measured and analyzed and metallographic analysis was carried out. The remote temperature measurements in the FSP area are made using the measuring system developed at IMSETCH-BAS.

## 2. 2. MATERIALS AND METHODS

### 2.1. Experimental

The experiments were conducted with addition of graphene using an innovative technology. The graphene has purity of 99.9+%, size: 5nm, S.A:170 m<sup>2</sup>/g and Dia: 30µm. The experimental blanks are made of A5083 aluminum alloy sheet material with thickness of 10mm. A groove with width of 0.5 mm and depth of 3 mm was cut at angle 45° lengthwise on the test plate of size 150x50 mm as shown in Fig. 1. The plate was

Print ISSN 1691-5402

Online ISSN 2256-070X

<https://doi.org/10.17770/etr2023vol3.7196>

© 2023 Radostina Zaekova, Plamen Tashev, Yasen Hadjitodorov, Deyan Gradinarov  
Published by Rezekne Academy of Technologies.

This is an open access article under the [Creative Commons Attribution 4.0 International License](https://creativecommons.org/licenses/by/4.0/).

mechanically cleaned and degreased with 5% acetone solution. The groove was filled with graphene and then pressed to seal it and to avoid loss of material during the subsequent processing.

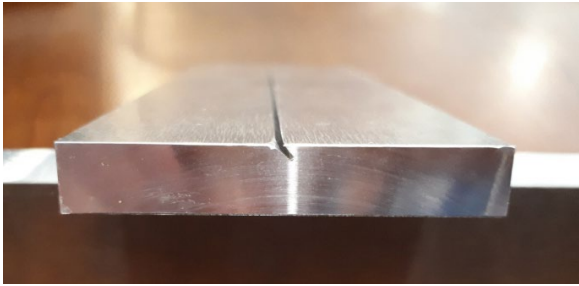


Fig. 1. Experimental plate.

The as-prepared plate was subjected to FSP of the graphene addition zone (Fig. 2). The FSP was carried out on a HURCO VMX30i vertical machining centre. A specially designed fixture was attached on the machine table for positioning and clamping the plates on a thermo-insulation pad.

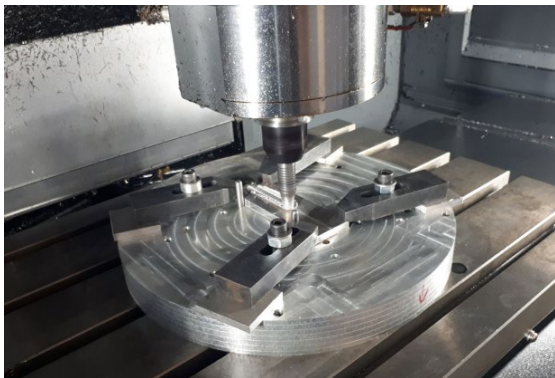


Fig. 2. FSP of the experimental plate.

The tool for FSP was designed and fabricated at IMSETCHA-BAS. It is shaped as truncated cone with length 4 mm, diameter at the base 6 mm and diameter at the tip 4 mm. A spiral groove with pitch 1 mm and three axial flutes at 120° are cut on the tapered surface. The smoothing shoulder has diameter of 13 mm. In order to better homogenize the material, the tool rotates counterclockwise.

The processing is carried out with progressive movement of the tool, first in a linear and then in a clockwise cycloid-like trajectory with offset 2 mm to the left and right from the central axis. The cycloid-like curve has radius 2 mm and pitch 2 mm.

The parameters of FSP are:

- Rotational speed 1300 rpm;
- Transverse (welding) speed 45 mm/min.

## 2.2. Remote measurement system of the temperature in the FSP-ed zone

A schematic view of the experimental setup for remote measurement of the temperature in FSP-ed zone is shown in Fig. 3. The processed sample (5) is

positioned and clamped in the fixture. The temperature is measured with eight thermocouples type B (4) connected to an eight-channel temperature recorder (1). The thermocouples (4) are spark-welded to the FSP-ed sample (5) and their ends are insulated with glass tubes. The data from the thermocouples (4) is received, visualized, analyzed and stored on a laptop (2). The recorder (1) and the laptop (2) are connected via USB cable. The data from FSP is transmitted in real time via internal wireless network created by TeamViewer between WiFi router (3) and a remote computer, where they are visualized, processed and stored.

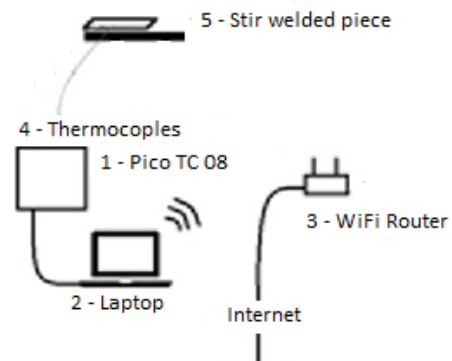


Fig. 3. Schematic view of the experimental setup.

The eight-channel temperature recorder Pico TC 08 (1) is shown in Fig. 4.



Fig. 4. Temperature recorder Pico TC 08.

The following software products are used:

- PicoLog 6 installed on laptop (2) to monitor the temperature of the thermocouples;
- TeamViewer installed on laptop (2) to establish a connection over the Internet as well as to visualize in real time the parameters and to and store them on the computer.

In Fig. 5 a macro section of the processed sample is shown, cut off in the place where the thermocouple monitoring the temperature is attached at a certain depth under the FSP-ed zone. The thermocouple is spark-welded to the bottom of a hole in the opposite side to the

side of FSP. The measurement location is shown in the photo with a yellow arrow.

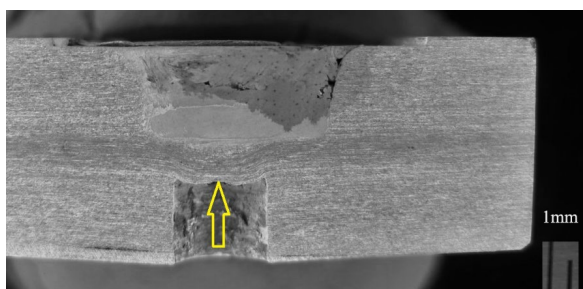


Fig. 5. Location of the thermocouple.

The temperature was measured during the processing as the tool approaches and moves away relative to the thermocouple location and the measured values were recorded (Fig. 6).

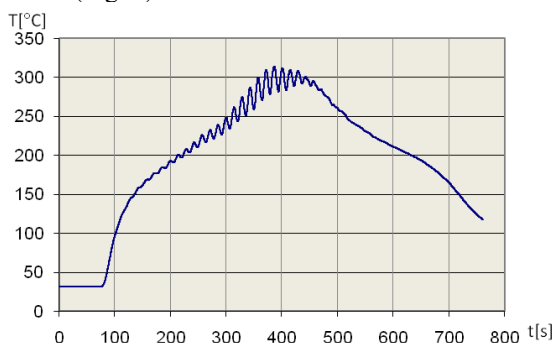


Fig. 6. Temperature curve during FSP.

The system for remote measurement of the temperature in the FSP-ed zone enables successful remote monitoring and control of this important parameter of the processing, as well as achieving predictable end results. The system also provides high degree of automation of the research work and easy and reliable archiving of the obtained data.

### 2.3. Microhardness measurements and metallography

Specimens were cut from the FSP-ed sample with added graphene and were prepared for metallographic analysis according to the standard procedure, i. e. wet grinding with sandpapers from No 400 to No 2400. The metallographic sections were developed by immersion in aqueous solution of 0.5% hydrofluoric (HF) acid. The observations were made with "PolyvarMet" metallographic microscope. The microstructure was captured using ProgRes CT3 USB digital camera with licensed software ProgResCapturePro. The analysis was conducted at temperature 24°C. The microhardness was measured with MicroDuomat 4000 microhardness tester with load 10 kg, time to reach the load 10 s and time to hold the load 10 s.

## 3. RESULTS AND DISCUSSION

The microhardness of the base material A5083 was measured. The measurement locations with the

respective values are shown on the metallographic section (Fig. 7). The measured values for Vickers microhardness (HV) of the A5083 base material are 85.2 kg/mm<sup>2</sup>, 88.5 kg/mm<sup>2</sup> and 86.0 kg/mm<sup>2</sup>. The average HV value is 86.6 kg/mm<sup>2</sup>.

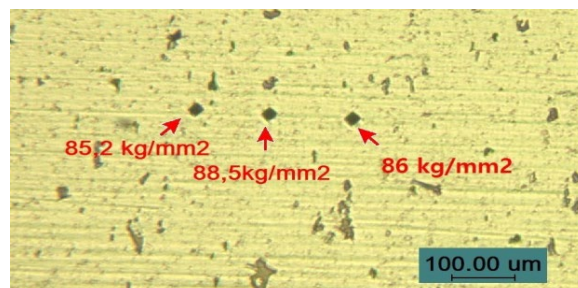
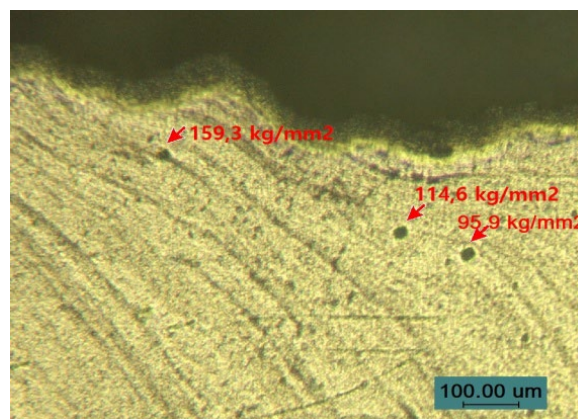


Fig. 7. Microhardness of the base metal.

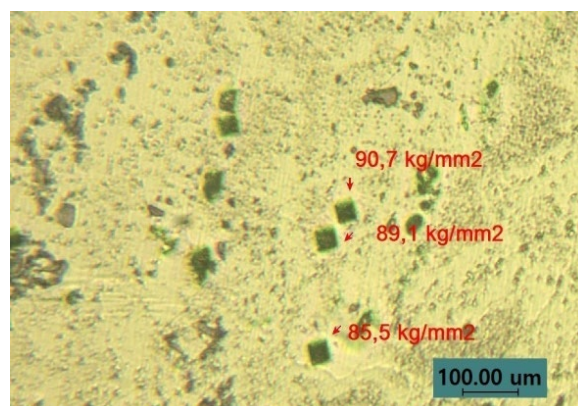
Fig. 8 (a, b) shows the measured microhardness of the FSP-ed material and the measurement locations (pointed with arrows) in two characteristic zones:

- Stir zone with visible graphene piling in wavy parallel stripes (Fig. 8a);
- Thermo-mechanically affected zone (TMAZ) (Fig. 8b).

The measurements in both zones are made in direction transverse to the direction of FSP.



a) Stir zone



b) TMAZ

Fig. 8. Microhardness of the FSP-ed material.

In the stir zone the highest microhardness value  $159.3 \text{ kg/mm}^2$  is measured in the vicinity of graphene stripes. In the TMAZ the measured microhardnesses are lower ( $85.5 \text{ kg/mm}^2$  to  $90.7 \text{ kg/mm}^2$ ).

The microhardness was also measured in depth in the same section, along a vertical line above the hole for thermocouple. Twenty-five measurements were taken at  $240 \mu\text{m}$  intervals. The curve of microhardness change in depth is shown in Fig. 9.

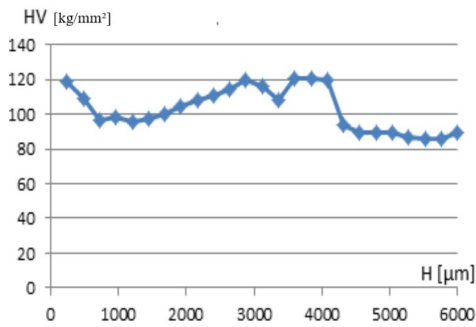


Fig.9. Curve of microhardness change in depth.

Close to the surface the measured microhardness is  $119.0 \text{ kg/mm}^2$  and the maximum measured value is  $120.7 \text{ kg/mm}^2$ . The observed decreases of the values can be explained with the uneven distribution of graphene confirmed by the metallographic analysis. After leaving the zone limited by the pin length of the tool, which defines the depth of FSP, the hardness is approximates to that of the base material.

The microhardness on the surface of the FSP-ed zone with added graphene is also measured. The measurements were made in the area of intersections of lines 1 to 7 parallel to the direction of FSP at  $2.2 \text{ mm}$  from each other, and a line transverse to the direction of FSP. The middle line 4 is located along the axis of FSP. Microhardness was measured in three points from each area.

The values of Vickers microhardness (HV,  $\text{kg/mm}^2$ ) on the surface of the FSP-ed area with added graphene are graphically visualized in Fig. 10.

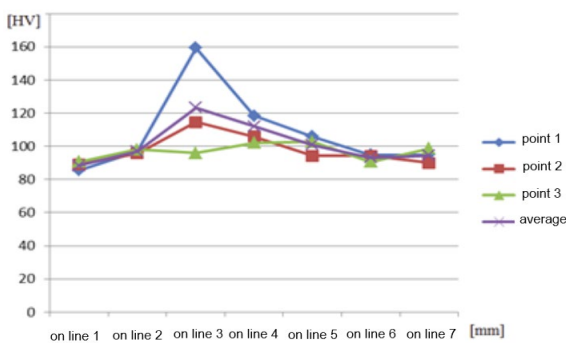


Fig. 10. Distribution of Vickers microhardness (HV,  $\text{kg/mm}^2$ ).

The analysis of the measurement results suggests that the microhardness increases when approaching the axis

of the FSP zone, i.e. the axis of the graphene groove (Fig. 10). Therein are also located the points where the highest deviations from the average microhardness value are measured, which is explained both with the higher graphene concentration and its more uneven distribution proved by the wavy parallel stripes of graphene piling observed during the metallographic analysis.

Obviously, the points of the highest measured microhardnesses are shifted from the middle line 4, i.e. from the axis of FSP zone (axis of graphene groove). We suggest that this is due to the asymmetric movement of the tool which results in uneven stirring of graphene.

#### 4. CONCLUSIONS

An innovative technology for adding graphene to aluminum alloy during FSP has been implemented. To our knowledge, there are no publications on FSP with addition of graphene using our proposed technology.

The maximum measured microhardness after FSP with added graphene is 1.8 times higher than the maximum measured microhardness of the base metal before FSP.

In the FSP areas adjacent to the graphene insertion area the reported microhardness is more than 25% higher than that of the base metal.

The largest deviations of the microhardness from the average value are observed in the areas with higher concentration of graphene and are due to the uneven distribution of graphene, confirmed by the metallographic study, which showed wavy parallel stripes of graphene.

The aims of the further research are related to both improving the technology to achieve a more homogeneous distribution of graphene and optimizing its amount.

#### 5. ACKNOWLEDGMENTS

This work was made possible by a project KP-06-N37/31, funded by the NSF.

#### REFERENCES

- [1] Omar S. Salih, Hengan Ou, W. Sun, D.G. McCartney A review of friction stir welding of aluminium matrix composites. *Materials and Design* 86 (2015), 61–71.
- [2] Johannes L, Charit I, Mishra R and Verma R 2007 Enhanced superplasticity through friction stir processing in continuous cast AA5083 aluminum *Materials Science and Engineering: A* 464 351-7.
- [3] Cui G, Ma Z and Li S 2009 The origin of non-uniform microstructure and its effects on the mechanical properties of a friction stir processed Al–Mg alloy *Acta Materialia* 57 5718-29.
- [4] Ma ZY. Friction stir processing technology: a review. *Metall Mater Trans A* 2008;39:642–58. <https://doi.org/10.1007/s11661-007-9459-0>.
- [5] Wang BB, Chen FF, Liu F, Wang WG, Xue P, Ma ZY. Enhanced mechanical properties of friction stir welded 5083Al-H19 joints with additional water cooling. *J Mater Sci Technol* 2017;33:1009–14. <https://doi.org/10.1016/j.jmst.2017.01.016>.
- [6] Zhao, Y.H.; Lin, S.B.; Qu, F.X.; Wu, L., Influence of pin geometry on material flow in friction stir welding process. *Materials Science and Technology* 2006, 22, 45–50.
- [7] Newell, J., *Essentials of Modern Materials Science and Engineering*; Wiley: Hoboken, NJ, 2009.

- [8] Ajay Kumar, Mohammad Shahal Milton, A Comparison of Welding Techniques of Aluminium Alloys, A Literature Review, USRSET2016, Volume 2, Issue 3, ISSN 2394-4099.
- [9] Abhishek Sharma, Vyas Mani Sharma, Agam Gugaliy, Pragya Rai, Surjya Kanta Pal, and Jinu Paul, Friction stir lap welding of AA6061 aluminium alloy with a graphene interlayer. *Materials and Manufacturing Processes*, 2020.
- [10] Naseer, A.; Ahmad, F.; Aslam, M.; Guan, B. H.; Harun, W. S. W.; Muhamad, N.; Raza, M. R.; German, R. M., A review of processing techniques for graphene-reinforced metal matrix composites. *Mater. Manuf. Process.* 2019, 34, 957–985.
- [11] Sahoo, B.; Girhe, S. D.; Paul, J., Influence of process parameters and temperature on the solid state fabrication of multilayered graphene-aluminium surface nanocomposites. *J. Manuf. Process.* 2018, 34, 486–494.
- [12] Jeon, C.H.H.; Jeong, Y.H.H.; Seo, J.J.J.; Tien, H.N.; Hong, S.T.T.; Yum, Y.J.J.; Hur, S.H.H.; Lee, K.J.J., Material properties of graphene/aluminum metal matrix composites fabricated by friction stir processing. *Int. J. Precis. Eng. Manuf.* 2014, 15, 1235–1239.
- [13] Khodabakhshi, F.; Nosko, M.; Gerlich, A. P. P., Effects of graphene nano-platelets (Gnps) on the microstructural characteristics and textural development of an Al-Mg alloy during friction-stir processing. *Surf. Coatings Technol.* 2018, 335, 288–305.

# **LASER TECHNOLOGIES**

# Researching the Process of Laser Structuring of the Surface of Aluminum

**Kevins Bulavskis**  
Engineering Faculty  
Rezekne Academy of Technologies  
Rezekne, Latvia  
k26bulavskis@gmail.com

**Emil Yankov**  
Engineering Faculty  
Rezekne Academy of Technologies  
Rezekne, Latvia  
emil.yankov@rta.lv

**Lyubomir Lazov**  
Engineering Faculty  
Rezekne Academy of Technologies  
Rezekne, Latvia  
Lyubomir.Lazov@rta.lv

**Antons Pacejs**  
Engineering Faculty  
Rezekne Academy of Technologies  
Rezekne, Latvia  
antons.pacejs@rta.lv

**Abstract.** In this scientific study, the ability to modify the surface using nanosecond 1064 nm fiber laser by controlling the speed and scanning line step in the marking process was demonstrated. An experimental matrix for laser marking was developed, consisting of 8 columns for marking line step and 5 rows for marking speed. The laser marked surfaces were measured using a laser scanning microscope and compared with the surface as supplied. From the obtained deviations of roughness Ra, Rz and Rq as a function of marking speed and marking line step, graphical dependencies were constructed for comparative analysis. The modified roughness is also compared with the roughness as supplied. Within this research the effect of laser treatment on the hydrophilicity/hydrophobicity of the surface was studied as well. Plots of dependences of the contact angle CA, the marking line step  $\Delta x$  and the overlap coefficient  $K_{soc}$  are plotted.

**Keywords:** laser marking, aluminum, laser texturing, laser structuring, roughness, hydrophobia.

## I INTRODUCTION

Aluminum alloys are an important engineering material in the automobile, rail, and aerospace industries as the overall performance meets the requirements of mechanical strength and low weight as well as due to their low density and high specific strength [1]. The surface quality is quite important for the efficient working of machine parts. The structure of a machined surface is one of the most important

criteria in terms of quality, and tribological properties of the machined surface. Generally, the surface quality is characterized with surface roughness. When using various kinds of solid materials, the roughness of the surface has a significant effect on their properties. Surface roughness is one of the most important characteristics of materials and affects wear resistance, contact rigidity, corrosion resistance and other functional characteristics of the surface [2]. Many approaches for increasing surface roughness have been studied over recent decades. For example, chemical etching, electrochemical etching (ECM), and laser surface texturing (LST). Among these methods, LST owns several advantages. First of all, chemical and ECM etching processes are accompanied by chemical work, which adversely affects the environment. Also, in comparison to LST, chemical etching consumes more processing time while ECM is limited to electrically conductive materials only and so LST is regarded as a more efficient, precise, and versatile approach to increase surface roughness [3]. This issue makes it necessary to study the process of laser structuring or texturing, assuming a series of experiments with varying parameters. To achieve a successful combination in the joining of dissimilar types of materials is imperative in creating a solid bond and, because the interactions take place on material surfaces, a tool or procedure for creating the bond is needed, and Laser Surface Texturing (LST) offers the perfect outcome.

Print ISSN 1691-5402

Online ISSN 2256-070X

<https://doi.org/10.17770/etr2023vol3.7271>

© 2023 Kevins Bulavskis, Emil Yankov, Lyubomir Lazov, Antons Pacejs.

Published by Rezekne Academy of Technologies.

This is an open access article under the [Creative Commons Attribution 4.0 International License](https://creativecommons.org/licenses/by/4.0/).

Enhancing fundamental characters, such as sustainability, tribological and biocompatibility, LST offers precise control regarding the main parameters of the characterization of microstructures (shape, roughness, width, depth, size, recast material, etc.) Laser surface texturing (LST) is a method to engender patterns on the surface of materials to accomplish microstructures. LST can remove the material from the surface (by dissolution, evaporation, expulsion and/or melting) to improve joining properties [4]. In addition, laser surface microstructuring has a number of advantages: high efficiency, good controllability, environmental friendly nature, and the capability of fabricating surface texture with high complexity and accuracy [5]. And also, special studies involve studying the possibility of the influence of laser structuring on hydrophilicity and hydrophobicity. In recent years, the wettability of material surface has been widely concerned, especially super-hydrophilic and super-hydrophobic [6].

Hydrophilic materials have potential for use in environmental purification, outdoor protection, medical and health, agriculture, food packaging and other fields [7].

Superhydrophobic surfaces are extremely hard to wet (low surface wettability), and such surfaces with this distinctive characteristic are found in nature. These surfaces have water contact angles greater than 150° and small roll-off angles less than 10° [12].

Wettability can be measured by water droplet contact angle (CA). CA is the angle between the surface of the liquid and the outline of the contact surface (solid surface typically). When the CA is less than 90°, the surface is hydrophilic; when the CA is greater than 90°, the surface is hydrophobic [6] [7].

There are two main factors affect the wettability of the material surface including surface roughness and surface energy, in which roughness is generally considered to be the key factor. At present, the preparation methods of super-hydrophilic and super-hydrophobic materials mainly focus on the surface roughness of the structural materials. Therefore, the micro/nanoarray structure is the key factor to make materials super hydrophilic or hydrophobic. There are several ways to fabricate the hybrid micro/nano structure on the materials, including sol-gel method, chemical vapor deposition, chemical etching, nanoimprint lithography, electrode position, self-assembly, laser fabricate, and more. Laser as an effective method could fabricate micro/nano structures directly on the material surface and to control the pattern of micro/nano structure accurately [6] [7]. Moreover, as a widely used preparation technology, laser fabricate has many advantages, including simple processing process, high preparation precision, wide processing materials, and complex structure of micro/nano preparation. The surface structure is usually stable after laser processed, which is very important to obtain the persistent micro/nano structure [6].

The purpose of this study is focused on the effect of the laser texturing process on the roughness, hydrophobicity and hydrophilicity of an aluminium surface using a fiber laser.

## II. MATERIAL AND METHODS

### 2.1. Material

Aluminum is a soft, lightweight, silvery-white metal with high thermal and electrical conductivity. Melting point 660° C. Aluminum is widely used as a structural material. The main advantages of aluminum in this aspect are lightness, pliability to stamping, corrosion resistance (in air, aluminum is instantly covered with a strong film of Al<sub>2</sub>O<sub>3</sub>, which prevents its further oxidation), high thermal conductivity, and non-toxicity of its compounds. The main disadvantage of aluminum as a structural material is its low strength, so it is usually alloyed with a small amount of copper and magnesium (the alloy is called duralumin). In Table 1 physical properties of aluminium alloy 9995 are shown.

TABLE 1 PHYSICAL PROPERTIES OF ALUMINIUM 9995

Density, (kg / m <sup>3</sup> )	2,7
Melting point T <sub>m</sub> , ° C	660
Boiling point T <sub>boil</sub> , ° C	2327
Latent heat of fusion, J/ g	393,6
Thermal conductivity l, W/ m × K (at 20 ° C)	228
Heat capacity Cp, J / (g × K) (at 0–100 ° C)	0,88
Linear expansion coefficient α × 10 <sup>-6</sup> , 1 / ° C (pr ° C)	24,3
Electrical resistance ρ × 10 <sup>-8</sup> , Ohm × m (at 20 ° C)	2,7
Ultimate strength σ in, MPa	40-60
Elongation δ, %	40-50
Brinell hardness HB	25
Normal elastic modulus E, GPa	70

### 2.2. Laser system

Within this study the nanosecond fiber laser Rofin Sinar GmbH system PowerLine f20 Varia was used to process aluminium samples within focal distance with the minimum spot size. Rofin PowerLine F20 Varia technical parameters could be observed in Table 2.

TABLE 2 ROFIN POWERLINE F20 VARIA TECHNICAL PARAMETERS

Sym-bol	Name	Value range	Step	Units
<i>kp</i>	Power regulation factor	0...1	0.001	N/A
<i>f</i>	Pulse repetition frequency	2..1000	0.001	kHz
<i>v</i>	Scan speed	1..20000	1	mm/s
$\Delta x$	Line step	0.001..120	0.001	mm
$\tau$	Pulse duration	4, 8, 14, 20, 30, 50, 100, 200	-	ns
$\Delta f$	Focus shift	-10..10	-0.5	mm

Given nanosecond laser main system parameters could be observed in Table 3.

TABLE 3 ROFIN POWERLINE F20 VARIA SYSTEM PARAMETERS

Laser type	Diode pumped Yb fiber laser
Wavelength	1065 nm ± 5 nm
Repetition rate	Programmable
Impulse energy	0.95 mJ
Beam quality, M <sup>2</sup>	<1.5
Focal spot size	40 μm

### 2.3. Microscopes

For measurements were used: 3D laser scanning microscope OLYMPUS LEXT OLS500 and a microscope Dino-Lite Premier AM7115MZT.

Roughness measurements and the resulting microstructure were examined with an Olympus model "OLS5100-EAF" laser microscope, see Fig.1. The obtained microstructural images were carried out using a 20× objective, magnification 451×, as the examined area for each measurement 1280×1280 μm with a measurement accuracy of ± 2.0 μm. From the obtained 3D images with the laser system of the microscope, the roughness Ra and Rz perpendicular to the marking lines with a length of 1280 μm, and the roughness Rq for the entire examined area 1280×1280 μm were measured. The obtained values are plotted in tables and graphical dependences of changes in roughness depending on speed and step during surface laser processing are shown. The built dependencies are presented in the results [9].



Fig.1. OLS5100-EAF" laser microscope [9].

Measurements with such laser scanning microscope gives the opportunity to observe produced structure on the surface of materials, example could be observed in Fig. 2.

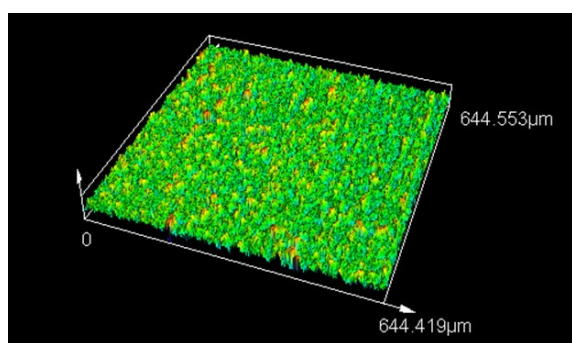


Fig. 2. The structure on the surface of material.

The Dino-Lite Premier AM7115MZT digital handheld microscope has a 5 Megapixels sensor with magnification up to 220x depending on working distance with a resolution of up to 2592x1944 [10].

Given digital handheld microscope could be observed in Fig.3.



Fig.3.The microscope Dino-Lite Premier AM7115MZT [11]

Using a Dino-Lite Premier AM7115MZT microscope and DinoCapture 2.0 software, measurements were made with the magnification 1x mode to determine the hydrophobic and hydrophilic properties of the aluminium surface ASTM D7334-08 (2022) [11]. Example of made measurements could be observed in fig. 4.



Fig.4.The measurement of the contact angle.

### 2.3. Applied laser parameters

Using the RoFin PowerLine F20 fiber laser, 2 matrixes were made on aluminium alloy. Each matrix consisted of 8 columns and 5 rows thus forming a rectangle with 40 squares inside. In the first matrix, the constant parameters were the power regulation coefficient  $P = 10\%$ ; frequency  $f = 25$  kHz; and pulse duration  $\tau = 30$  ns. In the second matrix, the constant parameters were the marking speed  $v = 50$  mm/s; pulse duration  $\tau = 30$  ns; and frequency  $f = 25$  kHz.

### 2.4. Equations

According to the formula there were made calculations to determine marking lines overlap ratio [13]:

$$Ksoc = 1 - \frac{\Delta x}{d} * 100 \% \quad (1)$$

Where:

$\Delta x$  – marking line step;  
 $d$  – laser focal spot size.

Laser surface structuring using a line-wise scanning strategy leads to a defined laser scanning line overlap ( $Ksoc$ ) which very well describe formation of periodic ripples on aluminium surfaces which lead to establish correlations of roughness and contact angle.

### III RESULTS AND DISCUSSIONS

#### 3.1. Measurement results of the Roughness on the surface.

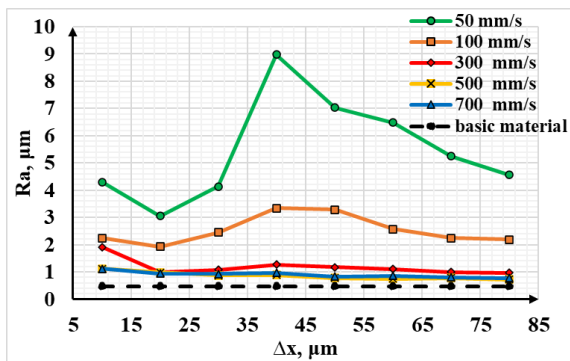


Fig.5. Dependence of the roughness  $Ra$  on the marking line step for the first matrix.

Data plotted for dependence of the roughness  $Ra$  on the marking line step could be observed in Fig.5. At a low-speed  $v = 50$  mm/s, the roughness changes with the following trend: from 10  $\mu\text{m}$  to 20  $\mu\text{m}$ , the roughness decreases. From 20 to 40  $\mu\text{m}$ , the roughness increases, and the maximum roughness value is obtained. The main reason for changes in roughness is their change in the overlap coefficient between lines. At 40  $\mu\text{m}$ , the overlap factor is 0. With an increase from 40  $\mu\text{m}$  to 80  $\mu\text{m}$ , the overlap coefficient becomes negative and the roughness decreases. This trend of roughness changes also occurs with  $v = 100$  mm/s, but with minor changes. And at a speed  $v = 300$  mm/s at the beginning with a small delta X = 10  $\mu\text{m}$  the roughness was maximum. With an increase in delta X by 20  $\mu\text{m}$ , the roughness decreases. From 20  $\mu\text{m}$  to 40  $\mu\text{m}$ , the roughness increases in the range from 40  $\mu\text{m}$  to 85  $\mu\text{m}$ , the roughness  $Ra$  decreases. At the speed  $v = 500$  mm/s from 10  $\mu\text{m}$ , the trend of  $Ra$  goes down.

And the same trend occurs at  $v = 700$  mm/s.

Data plotted for dependence of roughness on velocity  $v$  with different marking line step could be observed in Fig.6. and it shows that roughness decreases with increasing speed. At the lowest speed, roughness decreases. At the initial roughness without marking, roughness was relatively small. Roughness  $Ra$  increased in the range from 1.5 to 10.95 times, thus at  $v=50$  mm/s roughness was the highest. In the speed range from 550 mm/s to 750 mm/s, the roughness was similar.

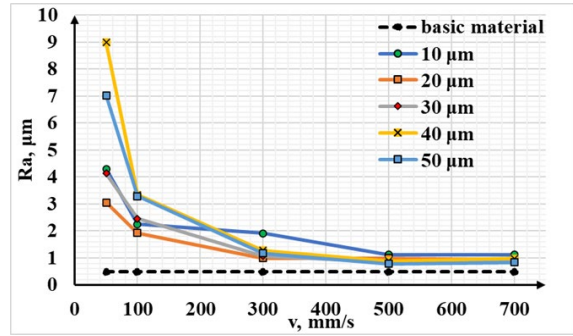


Fig.6. Dependence of roughness on velocity  $v$ , mm/s for the first matrix.

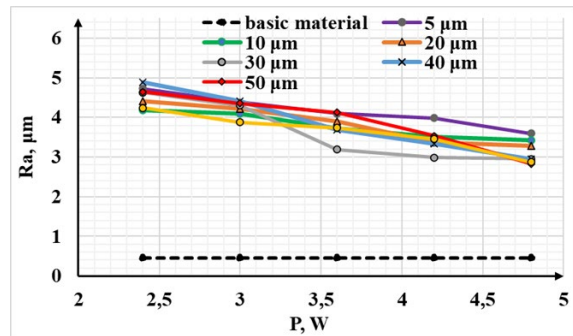


Fig.7. Dependence of roughness  $Ra$  on power  $P$ , W.

Data plotted for dependence of roughness  $Ra$  on power  $P$  with different marking line step factors could be observed in Fig.7.

With a small step of 5  $\mu\text{m}$  and a small power  $P = 2.4$  W, the surface changes and a new chaotic structure is obtained. With a step of 5  $\mu\text{m}$  and an increase in power from 3.6 W to 4.8 W, droplets are formed, which prove a decrease in roughness. In the 10  $\mu\text{m}$  range, there was a transition from evaporation to melting, in which there was a decrease in roughness. At 20  $\mu\text{m}$ , the transition zone has changed at a high power of 3.6 W and the roughness has decreased. With a step of 30-50  $\mu\text{m}$ ,  $Ra$  increases at a power of 2.4 W.

At 50  $\mu\text{m}$ , the overlap coefficient is negative between the lines and roughness  $Ra$  will be high. As the power  $P$  increases, the effects on the impact of the laser spot increase. As the power  $P$  increases, melting also occurs between the lines.

At the maximum value of 70  $\mu\text{m}$ , the line spacing is high and the power  $P$  energy at 2.4 W will result in energy reflection and little melting. As the power  $P$  increases, the roughness  $Ra$  changes with a small difference.

Data plotted for dependence of the roughness  $Ra$  on the marking line step with different power factors could be observed in Fig.8.

At a power of 2.4 W, the roughness  $Ra$  was the highest. The main reason for the high roughness  $Ra$  is the impact on the surface, which results in deep channels.

With an increase in power  $P$  by 3.0 W, the roughness  $Ra$  decreases. At power  $P = 3.6$  W, a transition zone between evaporation and melting is obtained.

At a power of  $P$  4.2-4.8, the main melting occurs on the surface and the roughness  $Ra$  decreases.

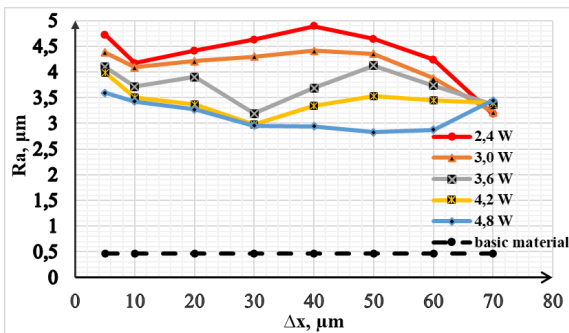


Fig.8. Dependence of the roughness  $Ra$  on the marking line step for the second matrix.

### 3.3. Measurement results of the hydrophobicity and hydrophilicity.

Data plotted for  $CA$  dependence on the line marking step with different speed factors could be observed in Fig.9.

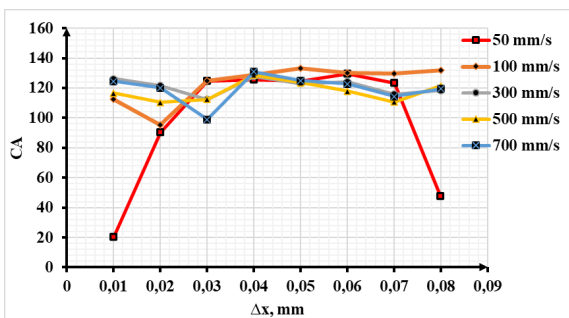


Fig.9. Dependence of the contact angle on delta x for the first matrix.

At a low speed of 50 mm/s, the droplets change depending on the pitch.

With a small step, the angle of the drop is about 20 degrees, that is, hydrophilic. The main reason is the high coefficient of spot overlap and the structure on the surface is obtained with a small roughness.

As the pitch increases to 40 μm, the roughness increases. The overlap factor between lines is reduced. And the maximum hydrophobicity is obtained at a step of 40 μm. And this structure changes from hydrophilic to hydrophobic.

With an increase in pitch from 40 μm to 80 μm the structure on the surface turns from hydrophobic to hydrophilic. At a speed of 100 mm/s and with a small step delta X, a transition zone between hydrophilic and hydrophobic is obtained on the surface structure.

An angle of about 130 degrees is achieved.

At a speed of 300-500 mm/s with a small step from 0.01 to 0.04 the surface becomes more hydrophobic. And the maximum hydrophobicity is obtained at a step of 40 μm. From 40 to 80 μm per surface structure, a decrease in hydrophobicity is obtained. At a maximum speed of 700 mm/s, the initial hydrophobicity is high. With an increase in pitch by 30 μm, which leads to a decrease in

hydrophobicity properties. At 40 on the surface is obtained.

From 40 μm to 80 μm, a change in the surface of the structure results in a smooth transient decrease in hydrophobicity. The surface structure is retained by hydrophobic compared to the speed of 50 mm/s has changed to hydrophilic.

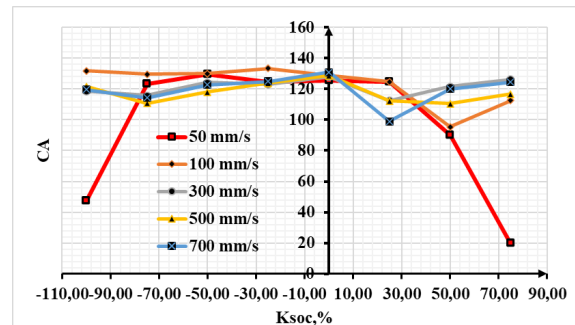


Fig.10. dependence of the contact angle on  $K_{soc}$  for the first matrix.

The graph shows changes in the angle of the drop depending on the overlap coefficient. With a small overlap ratio and a low speed of 50 mm.s, the surface changes are hydrophilic. With an increase in the overlap coefficient from -40 to 25, the surface structure becomes hydrophobic. Above 25 the overlap ratio the surface changes from hydrophobic to hydrophilic. At high speeds from 100-700 mm/s, the overlap ratio indicates little change in hydrophobicity.

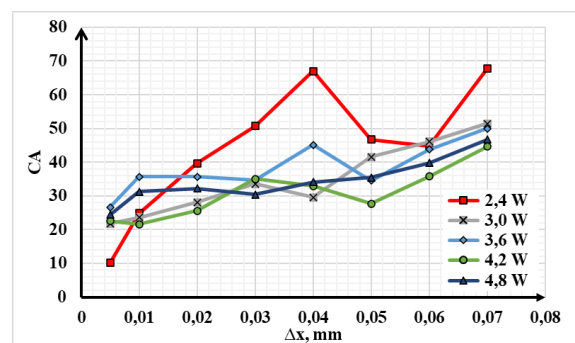


Fig.11. Dependence of the contact angle on delta x for the second matrix.

With a step of power surface treatment from 2.4 to 4.8 W, the surface structure will change from high hydrophilicity to low hydrophilicity.

At a power of 2.4 W, the changes are on the surface with the highest trend.

With a small step, the hydrophilicity is the highest. With an increase in delta X to 40 μm, the hydrophilicity decreases. With an increase in pitch from 40 μm to 60, the surface structure becomes hydrophilic. Above 60 μm a decrease in hydrophilicity is obtained.

At a power of 3.0 and 4.2 W from 10 μm to 30 μm, the hydrophilicity decreases.

The surface structure creates conditions for reducing hydrophilicity.

In a trend from 10 to 40  $\mu\text{m}$ , hydrophilicity changes poorly.

As the pitch increases from 50  $\mu\text{m}$  to 70  $\mu\text{m}$ , the hydrophilicity decreases.

At 3.6 W, the hydrophilicity decreases with a small step from 10 to 40  $\mu\text{m}$ , since the contact angle of the drop increases and the hydrophilicity decreases. In the range from 40 to 50  $\mu\text{m}$ , a transition zone is obtained - the drop angle decreases and the hydrophilicity increases. From 50 to 70  $\mu\text{m}$  the surface structure changes and the hydrophilicity decreases. With a maximum power of 4.8 W from 10  $\mu\text{m}$  to 70  $\mu\text{m}$ , the surface will gradually change to a slight hydrophilicity. This processing regime creates conditions for hydrophilicity, but not for hydrophobicity.

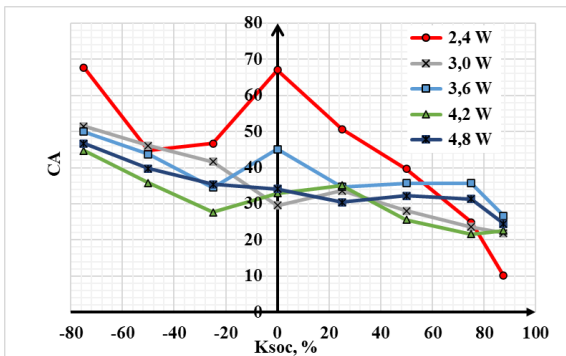


Fig.12. Dependence of the contact angle on Ksoc for the second matrix.

The overlap ratio indicates the effects of surface texture on hydrophilicity. At a low power of 2.4 W and a small Ksoc of -80 to -60, the surface texture indicates an improvement in hydrophilicity.

From -60 to 0 Ksoc the hydrophilicity decreases, the drop angle increases, and minimal hydrophilicity is obtained.

From 0 to 80 Ksoc creates conditions for improving hydrophilicity.

From 3.0 to 4.8 W, an overlap factor between lines from -80 to 90 indicates the effect of increasing hydrophilicity.

#### IV CONCLUSION

Low speed ( $v = 50 \text{ mm/s}$ ) resulted in an initial decrease in roughness (Ra) from 10 to 20  $\mu\text{m}$ , followed by an increase to a maximum at 20 to 40  $\mu\text{m}$ , attributed to the overlap coefficient between lines. Beyond 40  $\mu\text{m}$ , the overlap coefficient becomes negative, resulting in a decrease in roughness as the marking line step increases to 80  $\mu\text{m}$ . Similar trends were observed at  $v = 100 \text{ mm/s}$ . At  $v = 300 \text{ mm/s}$ , Ra reaches a maximum at 10  $\mu\text{m}$  marking line step, then decreases with an increase in delta X by 20  $\mu\text{m}$ . Roughness increases from 20 to 40  $\mu\text{m}$ , but decreases again from 40 to 85  $\mu\text{m}$ . At higher speeds ( $v = 500 \text{ mm/s}$  and  $v = 700 \text{ mm/s}$ ), the trend of decreasing roughness with increasing marking line step is also observed.

Ra increased in the range from 1.5 to 10.95 times at the lowest speed ( $v = 50 \text{ mm/s}$ ), with the highest roughness observed at this speed. In the speed range from 550 mm/s to 750 mm/s, the roughness remained similar.

Small line step of 5  $\mu\text{m}$  and low power of  $P = 2.4 \text{ W}$  resulted in changes in surface structure, with a new chaotic structure observed. With an increase in power from 3.6 W to 4.8 W, droplets are formed, indicating a decrease in roughness. A transition from evaporation to melting is observed at 10  $\mu\text{m}$ , resulting in a decrease in roughness. At 20  $\mu\text{m}$ , the transition zone changes at a high power of 3.6 W, resulting in a decrease in roughness. On the other hand, with a step of 30-50  $\mu\text{m}$ , roughness Ra increases at a power of 2.4 W. At 50  $\mu\text{m}$ , the overlap coefficient between lines becomes negative, resulting in higher roughness Ra. As the power P increases, the effects of the laser spot impact and melting between lines also increase.

At the maximum line step of 70  $\mu\text{m}$ , the energy from power P of 2.4 W is reflected with little melting, and roughness Ra changes with small differences as the power P increases.

Power factor (P) plays a significant role in the surface morphology and roughness of the marked area, with higher power levels generally resulting in lower roughness values. At a power of 2.4 W, the roughness Ra was found to be the highest, which can be attributed to the impact of the laser on the surface, resulting in deep channels and increased roughness. However, with an increase in power P to 3.0 W, the roughness Ra decreases. At a power of 3.6 W, a transition zone between evaporation and melting is observed, which affects the roughness Ra. At power levels of 4.2-4.8 W, the main melting occurs on the surface, leading to a decrease in roughness Ra.

At a low speed of 50 mm/s, the pitch between lines affects the hydrophobicity of the surface. A small pitch results in a hydrophilic surface with an angle of about 20 degrees, due to high spot overlap and small surface roughness. As the pitch increases to 40  $\mu\text{m}$ , the roughness increases, reducing the overlap factor and achieving maximum hydrophobicity. Further increase in pitch to 80  $\mu\text{m}$  changes the surface structure and increases the hydrophilicity of the surface. This is because at higher pitch values, the surface texture becomes more regular and the microstructures are spaced further apart, allowing for more water to fill in the gaps and wet the surface.

In addition to pitch, other factors such as the depth and shape of the microstructures can also affect the hydrophobicity or hydrophilicity of a surface. For example, deeper microstructures with sharp edges can create air pockets that repel water, resulting in increased hydrophobicity. On the other hand, shallower or rounded microstructures can allow for more water to penetrate and wet the surface, leading to increased hydrophilicity.

Surface roughness is another important parameter that can influence hydrophobicity or hydrophilicity. Rougher surfaces with irregular features tend to be more hydrophobic as they trap air and reduce the contact area between water and the surface. In contrast, smoother surfaces with less roughness tend to be more hydrophilic as they allow for more intimate contact between water molecules and the surface.

The hydrophobic or hydrophilic nature of a surface can have important practical applications in various fields,

including materials science, coatings, and biomedical engineering. For example, hydrophobic surfaces can be used to repel water and prevent fouling, icing, or corrosion, while hydrophilic surfaces can be used to promote wetting and adhesion, enhance heat transfer, or facilitate biological processes.

In summary, the pitch, depth, shape, and roughness of microstructures on a surface can all influence its hydrophobicity or hydrophilicity. Understanding these parameters and their effects on surface properties is crucial for designing functional surfaces with tailored wetting behaviour for specific applications.

#### ACKNOWLEDGMENT

This work was developed within the framework of Latvian Postdoctoral Research Support Program "Analysis of new industrial materials laser marking process parameters for high-tech applications" No. 1.1.1.2/VIAA/3/19/474

#### REFERENCES

- [1] Pang, Xiaobing & Dai, Jiahui & Chen, Shun & Zhang, Mingjun. (2019). Microstructure and Mechanical Properties of Fiber Laser Welding of Aluminum Alloy with Beam Oscillation. *Applied Sciences*. 9. 5096. 10.3390/app9235096.
- [2] Suker, Dhia & Alsoufi, Mohammad & Alhusaini, Majdi & Azam, Sufyan. (2016). Studying the Effect of Cutting Conditions in Turning Process on Surface Roughness for Different Materials. *World Journal of Research and Review (WJRR)*. 2. 16-21.
- [3] Zaifuddin, Amira & Aiman, M & Quazi, M & Ishak, Mahadzir & Shamini, J. (2021). Influence of Laser Surface Texturing (LST) Parameters on the Surface Characteristics of Ti6Al4V and the Effects Thereof on Laser Heating. *Lasers in Engineering*. 355-367.
- [4] Moldovan, Edit & Doria, Carlos & Ocaña, José L. & Baltes, Liana & Elena-Manuela, Stanciu & Croitoru, Catalin & Alexandru, Pascu & Roata, Ionut & Tiorean, Mircea. (2022). Wettability and Surface Roughness Analysis of Laser Surface Texturing of AISI 430 Stainless Steel. *Materials*. 15. 2955. 10.3390/ma15082955.
- [5] Przystacki, Damian & Jankowiak, M. (2014). Surface roughness analysis after laser assisted machining of hard to cut materials. *Journal of Physics: Conference Series*. 483. 012019. 10.1088/1742-6596/483/1/012019.
- [6] Zhao, Jingnan & Guo, Jian & Shrotriya, Pranav & Wang, Yan & Han, Yinfeng & Dong, Yinghui & Yang, Shuo. (2019). A rapid one-step nanosecond laser process for fabrication of super-hydrophilic aluminum surface. *Optics & Laser Technology*. 117. 134-141. 10.1016/j.optlastec.2019.04.015.
- [7] Guo, Jian & Ma, Xiaolei & Si, Xuekang & Yang, Zeng & Zhao, Jingnan. (2019). Effect of Nanosecond Laser Treatment Parameters on Surface Wettability Behaviour of Pure Aluminium. *IOP Conference Series: Materials Science and Engineering*. 538. 012021. 10.1088/1757-899X/538/1/012021.
- [8] Research Of Possibilities Of Laser Polishing Of The Surface Of Aluminum, Author: Kevins Bulavskis, Imants Adijāns, e-mail: k26bulavskis@gmail.com; Scientific supervisor: Lyubomir Lazov, Prof., Dr.sc.ing., Rezekne Academy of technologies
- [9] Olympus Global Homepage [ONLINE], 28.March 2023 AVAILABLE: <https://www.olympus-global.com/news/2017/nr00633.html>
- [10] Dino-lite microscope homepage [ONLINE], 28.March 2023 AVAILABLE: [https://www.dino-lite.com/products\\_detail.php?index\\_m1\\_id=9&index\\_m2\\_id=0&index\\_id=53](https://www.dino-lite.com/products_detail.php?index_m1_id=9&index_m2_id=0&index_id=53)
- [11] Standard Practice for Surface Wettability of Coatings, Substrates and Pigments ASTM D7334-08 (2022) standard. by Advancing Contact Angle Measurement1.
- [12] Farayibi, P. K. & Akisin, Cletus & Ijaola, Ahmed. (2020). Wettability Transition for Laser Textured Surfaces: A Comprehensive Review.
- [13] Schnell, Georg & Duenow, Ulrike & Seitz, Hermann. (2020). Effect of Laser Pulse Overlap and Scanning Line Overlap on Femtosecond Laser-Structured Ti6Al4V Surfaces. *Materials*. 13. 969. 10.3390/ma13040969.

# *Analysing the Influence of Technological Parameters on the Process of Laser Marking of Surface of Anodised Aluminium Samples*

**Ļubova Denisova**

Faculty of Engineering  
Rezekne Academy of Technologies  
Rezekne, Latvia  
ld15036@edu.rta.lv

**Antons Pacejs**

Faculty of Engineering  
Rezekne Academy of Technologies  
Rezekne, Latvia  
antons.pacejs@rta.lv

**Emil Yankov**

Faculty of Engineering  
Rezekne Academy of Technologies  
Rezekne, Latvia  
emil.yankov@rta.lv

**Lyubomir Lazov**

Faculty of Engineering  
Rezekne Academy of Technologies  
Rezekne, Latvia  
lyubomir.lazov@rta.lv

**Abstract.** The requirements for marking in terms of contrast and durability are constantly increasing. In order to meet all these challenges, it is necessary to carry out research leading to the optimisation and increase in efficiency of the technological process of laser marking. In the case of aluminium, the contrast and durability of the marking depend on the values of the laser marking parameters. In order to determine the optimal laser marking method, experimental studies have been carried out, controlling the power, speed, frequency, pulse duration and line raster step for a specific anodised aluminium. The studies carried out were analysed and subsequently optimized to obtain a contrast marking. A Rofin PowerLine F 20 Varia fiber laser system and aluminium alloy 1050 with anodised surface were used for the research. The surface changes after the laser treatment were analysed using a laser scanning microscope and contrast determination method. The dependence of contrast and roughness on speed, power, frequency and raster step was analysed. Comparative plots of contrast and roughness variations versus laser marking technological parameters were constructed.

**Keywords:** laser marking, fiber laser, laser surface texturing, aluminium, contrast, roughness.

## I. INTRODUCTION

Aluminium's distinctive chemical, electrical, thermal, and mechanical properties make it suitable for a wide range of applications. By utilizing an electrochemical process known as anodising, aluminium can produce a transparent

coating that can achieve a surface hardness like that of sapphire, depending on the thickness of the coating and the anodising procedure used. Anodising is an electrochemical technique that transforms the metal surface into a long-lasting, corrosion-resistant, decorative, anodic oxide finish that is completely fused with the aluminium base, preventing chipping or peeling. Aluminium is utilized as a raw material for a broad range of products, and these items typically require some characters or symbols to be printed directly on them. In this regard, laser marking is a widely used, dependable, and efficient process in the industry. Nonetheless, when it comes to marking aluminium, laser marking still produces unsatisfactory results since it cannot generate a dark mark, resulting in poor contrast [1] - [3].

In modern electronics and machine production, laser marking has become a crucial tool for meeting current quality control standards. Laser marking is frequently used in industrial manufacturing and trade to mark serial numbers, matrix codes, 1D and 2D barcodes, technical parameters, tables, and other operational information, as well as for monitoring production processes. This has made laser marking an integral part of the production process [4]. Laser marking is well-suited for marking intricate geometries at a rapid processing speed [5]. The three primary components of laser marking systems are the control unit, laser source, and scanner. The control

Print ISSN 1691-5402

Online ISSN 2256-070X

<https://doi.org/10.17770/etr2023vol3.7270>

© 2023 Ļubova Denisova, Antons Pacejs, Emil Yankov, Lyubomir Lazov.

Published by Rezekne Academy of Technologies.

This is an open access article under the [Creative Commons Attribution 4.0 International License](https://creativecommons.org/licenses/by/4.0/).

unit processes the commands of the laser operator and manages both the laser source and scanner. The laser source produces a beam and is regulated by input parameters such as pulse repetition frequency, pulse energy, and pulse duration. The scanner guides the laser beam and is regulated by input parameters such as scanning speed, line step, and focal length. These input parameters of both the laser source and scanner are collectively known as laser parameters [6].

The use of laser processing enables an increase in the hardness and wear resistance of aluminium surfaces [7].

Laser marking has been increasingly utilized in recent years for automated reading of alphanumeric or coded information such as bar and matrix codes on individual components or products. The laser-marked parts and details containing coded information can be automatically read, allowing for monitoring during the manufacturing process and throughout the supply chain. This is beneficial for finding service parts and repairs, filing claims, and ensuring accountability and warranty compliance [8].

In general, laser marking involves the targeted removal or melting of material from a surface using a high-powered, focused laser beam, resulting in localized heating and various modifications to the material, such as melting, vaporization, decomposition, or chemical alteration. The resulting marks or engravings are influenced by the laser and material parameters and are typically generated through material removal via ablation or the induction of a phase change [9].

In order to enhance the laser marking of aluminium products, it is crucial to determine the most appropriate marking method, as well as the optimal parameters of the laser and technological process specific to each individual case [10].

Numerous publications have investigated the influence of marking speed and raster step on the process of laser marking. Through the optimization of certain parameters, it is possible to create high-contrast markings on the surface of aluminium [11] - [13]. For marking on an anodised aluminium sample, it is recommended to use a fiber laser as it produces the darkest colour [14]. The quality of the marking is crucial when handling products in warehouses, sales outlets, and other settings [15].

The quality of laser marking is significantly influenced by the level of contrast [16]. For the laser marking process to be optimized, it is necessary to conduct experiments and optimize parameters for each new product [17].

The focus of this study is laser marking the aluminium surface of the anode, with a specific emphasis on investigating the impact of various parameters on surface roughness, including laser power, pulse frequency, scanning speed, and raster step. Furthermore, the study also examines the effect of these parameters on contrast.

## II. MATERIALS AND METHODS

### Material

For the experimental study, sulfuric acid anodised aluminium plates of 50 mm x 50 mm x 1,1 mm have been employed.

Surfaces samples were cleaned with  $C_3H_{12}O$ , to remove all dirt that would influence the results of the experiments.

### Experimental set-up

Nanosecond pulse mode was employed in the research using the Rofin Sinar Laser GmbH PowerLine F 20 Varia machine, which is a Yb-doped fibre laser, see in Fig. 1.



Fig. 1. Rofin PowerLine F 20 fiber laser.

A f-theta lens with a focal distance of 184 mm was installed on this fibre laser, resulting in a spot size of 40  $\mu\text{m}$  at the focus point. The general specifications of the employed laser system are summarized in Table 1.

TABLE 1. CHARACTERISTICS ROFIN POWERLINE F 20 FIBER LASER OF THE LASER SYSTEM

Parameter	Value
Wavelength $\lambda$ , nm	1064
Power $P$ , W	0-19.7
Pulse duration $\tau$ , ns	4-200
Frequency $f$ , kHz	2-1000
Scan speed $v$ , mm/s	1-2000

The laser processed anodised aluminium sample's structure change was examined with laser scanning microscope Lext 3D OLS5000, which is shown in Fig. 2.



Fig. 2. Lext 3D measuring G Laser microscope OLS5000.

The marked anodised aluminium samples contrast was measured with Adobe Photoshop by previously scanning samples with a HP Scanjet G3010 scanner.

### Methodology

To carry out the experiments, the Visual Laser Marker software integrated into the PowerLine F 20 Varia laser was utilized to create a matrix with 6 columns and 6 rows. A specialized matrix consisting of squares with 5 mm sides was then prepared for the study. This matrix enabled the application of different technological parameters to each square based on the selected experimental methodology. Laser marking was

conducted on two anodised aluminium samples, resulting in 2 unique and distinct laser-processed samples with varying technological parameters.

First matrix is processed with different scanning speeds ( $v$ , 25 – 150 mm/s) and raster step ( $\Delta x$ , 5  $\mu\text{m}$  -30  $\mu\text{m}$ ). General view of an exemplary experimental first matrix given in Fig. 3. The parameters that are kept constant are given in Table 2.

TABLE 2. PARAMETERS THAT DO NOT CHANGE DURING EXPERIMENTS

Parameter	Value
Power $P$ , W	3.2
Frequency $f$ , kHz	20
Pulse duration $\tau$ , ns	14

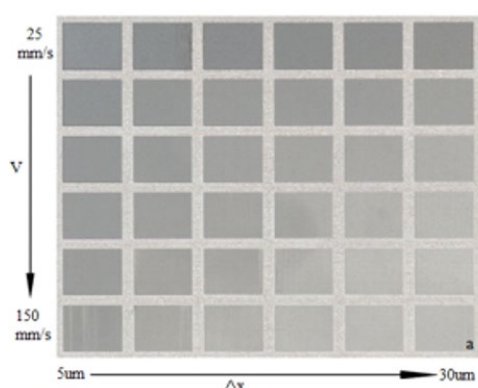


Fig. 3. General view of an exemplary experimental first matrix used in the researches.

Second matrix was marked with different average power ( $P$ , 0.1 - 2.5 W) and frequency ( $f$ , 2 – 25 kHz). General view of an exemplary experimental first matrix given in Fig. 4. The parameters that are kept constant are given in Table 3.

TABLE 3. PARAMETERS THAT DO NOT CHANGE DURING EXPERIMENTS

Parameter	Value
Raster step $\Delta x$ , $\mu\text{m}$	10
Scanning speed $v$ , mm/s	100
Pulse duration $\tau$ , ns	8

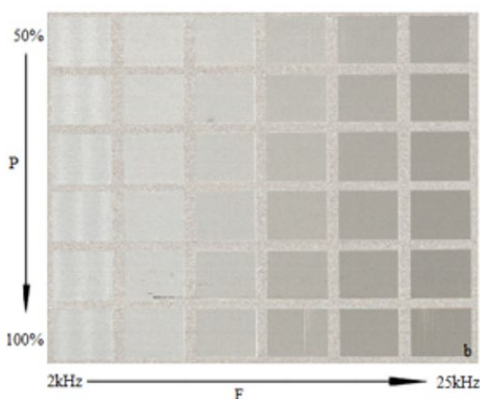


Fig. 4. General view of an exemplary experimental second matrix used in the researches.

The experiment was done in an open room. After samples were marked, they were stored in airtight bags to avoid stains.

The average power of Rofin Powerline Varia f20 laser depends on the frequency and impulse length used within the treatment process, as it is mentioned in laser system manual and confirmed using power measurement sensor OPHIR F150A-BB-26.

By observing Fig. 5 it could be seen how laser average power changes with different frequency and impulse width at different power factors (%) entered in the laser system software within 8 ns pulse duration.

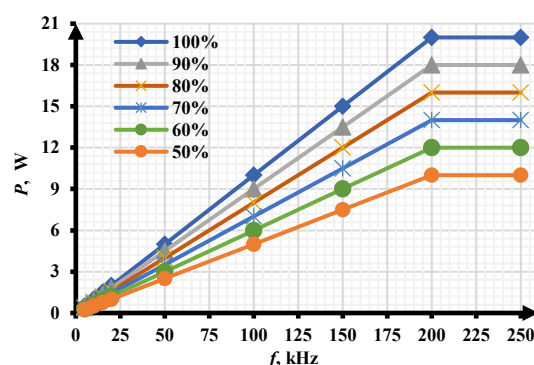


Fig. 5. Average power dependence of impulse width and frequency at different laser system software power factors.

The formula (1) was used to calculate marking contrast. The contrast is defined in percentages (%).

$$k * = \frac{N_n - N_f}{N_f} \times 100 \% \quad (1)$$

where:  $N_n$  – is the intensity of the light reflected from the affected zone on the sample;  $N_f$  - is the intensity of the light reflected from the untreated surface of the sample (from the background).

The overlap coefficient influences the roughness and contrast of the marking. There are two overlap coefficients: pulse overlap coefficient ( $K_{ov}$ ) and coefficient of overlap between lines ( $K_{soc}$ ). This coefficient determines the pulse or line overlap in percent within a single laser scanning path. They can be calculated by using formula (2) and formula (3):

$$K_{soc} = \left( 1 - \frac{\Delta x}{d} \right) \times 100 \% \quad (2)$$

$$K_{ov} = \left( 1 - \frac{v}{f \times d} \right) \times 100 \% \quad (3)$$

where:  $\Delta x$  – distance between scanning lines (mm);  $d$  – laser point diameter (mm), (for aluminium 0,04 mm);  $v$  – scanning speed (mm/s);  $f$  – laser frequency (kHz).

### III. RESULTS AND DISCUSSION

A laser-marked sample is created with a grid of 5×5 mm squares, showing how the laser-marked surface changes for each square in the matrix.

The marking contrast for each of the marked surfaces was calculated according to equation (1). A prerequisite for good readability is a permanent high contrast

between the applied marking and the surrounding material. To ensure that the Q-code is scanned accurately, the contrast between the Q-code and the surface on which it is applied should be greater than 15 %.

How different parameters affect the contrast of market anodised aluminium is shown in Fig. 6 to Fig. 9.

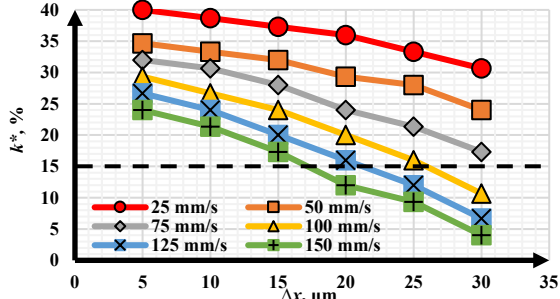


Fig. 6. Contrast dependence on the raster step and constant scanning speed.

Analysing the graph in Fig. 6, we can see that the highest contrast of 40 % is formed with a low scanning speed and raster step. Contrast marking is possible at all scanning speeds, but with a scanning speed of 100 mm/s, the contrast marking is formed with a raster step of 25 μm, with 125 mm/s up to 20 μm, and with 150 mm/s – 17 μm. The lowest contrast is formed with a large scanning speed (150 mm/s) and raster step (30 μm).

Moreover, increasing the scanning speed and the raster step decreases the colour reflection.

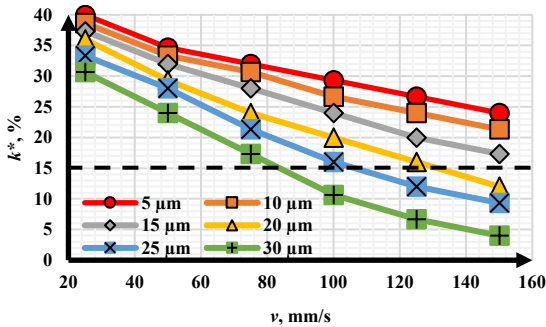


Fig. 7. Contrast dependence on the scanning speed and constant raster step.

Analysing the graph in Fig. 7, it is found that the contrast decreases with the increasing scanning speed and raster step, but the contrast is higher when the scanning speed and the raster step are the smallest.

The highest contrast is observed at a scanning speed of 25 mm/s and a raster step of 5 μm.

Changing the power and frequency of the laser, it turned out that a marking that is lighter than the material itself can be achieved.

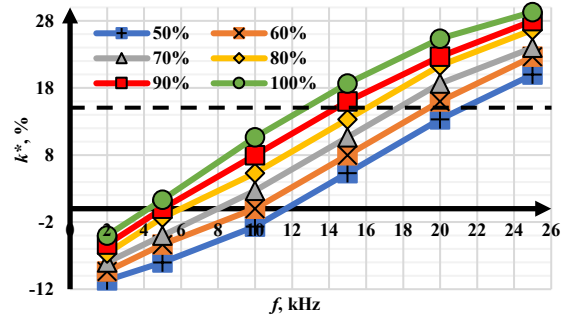


Fig. 8. Contrast dependence on the frequency and constant power.

Analysing the graph in Fig. 8, it can be observed that the contrast is higher with a high frequency and power. A contrast marking is possible if any laser power is used, but a frequency of 13 kHz and above must be used. In the graph, we can see a negative contrast because the marking appears white, which is lighter than the material itself.

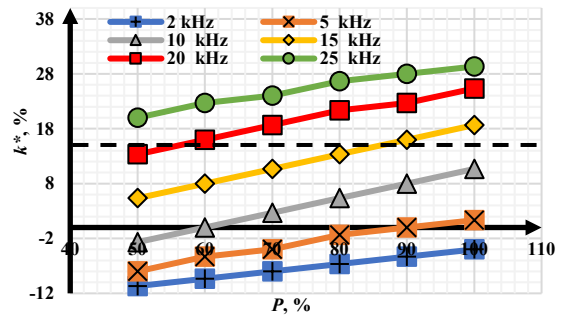


Fig. 9. Contrast dependence on the power and constant frequency.

From the analysis of the graphs in Fig. 9, increasing the laser power and frequency results in an increase in marking contrast. With a small frequency range of 2 to 10 kHz, a contrast marking is not formed. The highest contrast of 29 % is observed with a frequency of 25 kHz and power of 100%.

The effect of pulse overlap on the contrast of the marked anodised aluminium is illustrated in Fig. 10 to Fig. 13.

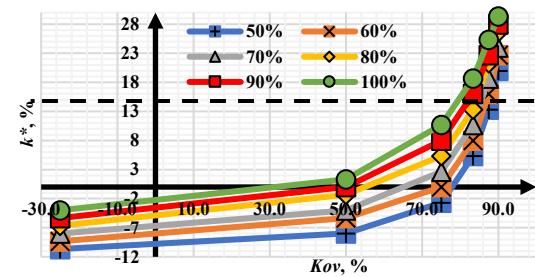


Fig. 10. Contrast dependence on the pulse overlap and constant power.

From the graph in Fig. 10, it can be observed that to achieve a contrast marking with a laser power of 10 to 100 %, a pulse overlap of 85 % of the laser pulses incident on the surface of the material is required.

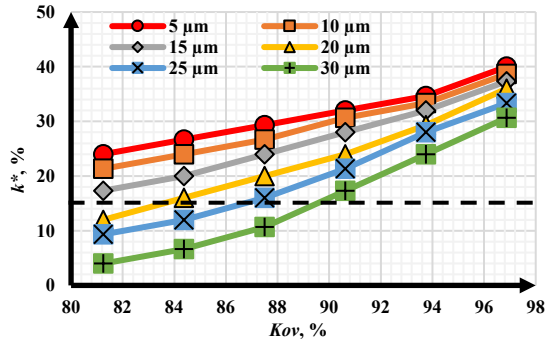


Fig. 11. Contrast dependence on the pulse overlap and constant raster step.

From the analysis of the graphs in Fig. 11, it can be concluded that contrast increases with an increase in raster step and pulse overlap. A contrast marking is possible at a raster step of 5, 10, and 15  $\mu\text{m}$ , but to obtain a contrast marking at a higher raster step, a 90 % pulse overlap of one laser scan path is required.

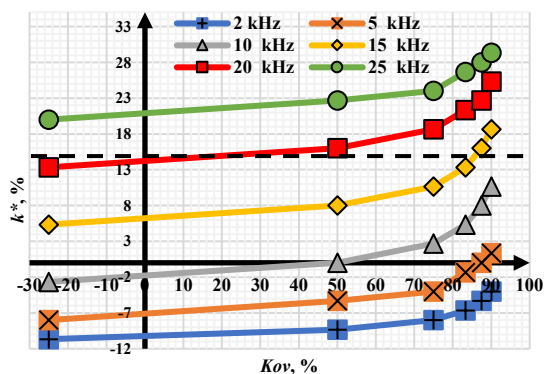


Fig. 12. Graph of the contrast of the marking from pulse overlap and frequency.

From the analysis of the graphs in Fig. 12, it can be concluded that a contrast marking is possible at a frequency of 25 kHz. With a frequency of 20 kHz, a contrast marking can be formed at a pulse overlap of 20 %.

Analysing the graph in Fig. 13, it is found that the contrast increases with an increase in pulse overlap. A contrast marking is possible with a scanning speed of 25, 50, and 75 mm/s, but a pulse overlap of 90 % is required when using a scanning speed of 100 mm/s.

The most important result of the contrast analysis after marking is that the highest contrast is formed at low scanning speed and raster step.

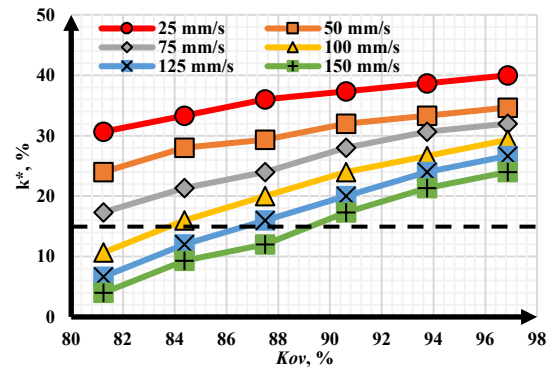


Fig. 13. Graph of the contrast of the marking from pulse overlap and scanning speed.

Analysing the roughness of a labelled sample is crucial for evaluating the durability of a part. If a part is rougher than it needs to be, there can be irregularities in the surface that will cause quicker wear and tear, breaks, and corrosion. The effect of different parameters on the roughness of the marked anodised aluminium is illustrated in Fig. 14 to Fig. 19.

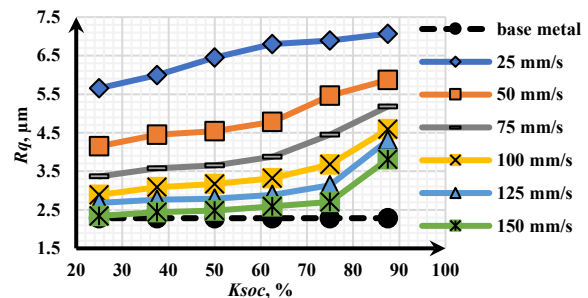


Fig. 14. Roughness dependence on the overlap between line and constant scanning speed.

From the analysis of the experimental roughness results, it can be observed that:

- The smallest roughness is formed with a scanning speed of 150 mm/s and an overlap between lines of 25 %.
- The highest roughness, on the other hand, is formed at a scanning speed of 25 mm/s.

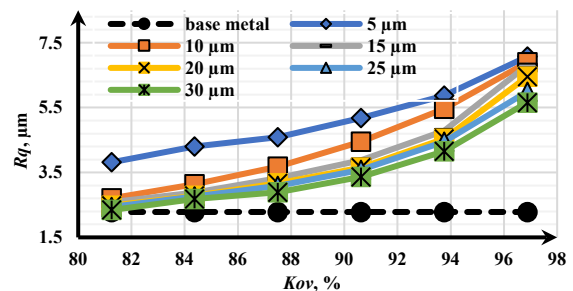


Fig. 15. Roughness dependence on the pulse overlap and constant raster step.

Analysing the structural change in anodised aluminium, a smallest roughness can be obtained with a raster step of 30  $\mu\text{m}$  and an overlap of pulses of 81%.

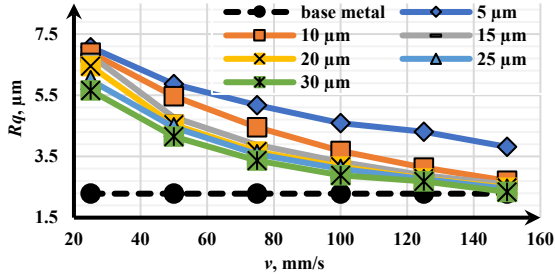


Fig. 16. Roughness dependence on the scanning speed and constant raster step.

Analysing the graph in Fig. 16, it can be observed that the roughness of the marked samples decreases as the scanning speed increases. The smallest roughness is formed at a scanning speed of 150 mm/s and a raster step of 30  $\mu\text{m}$  compared to the average unmarked sample.

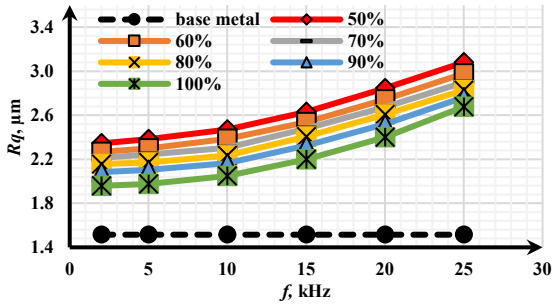


Fig. 17. Roughness dependence on the frequency and constant power.

From the analysis of the graphs in Fig. 17, it can be seen that the roughness is high with 50% power and 25 kHz frequency, while small roughness is obtained with 100% power and 2 kHz frequency.

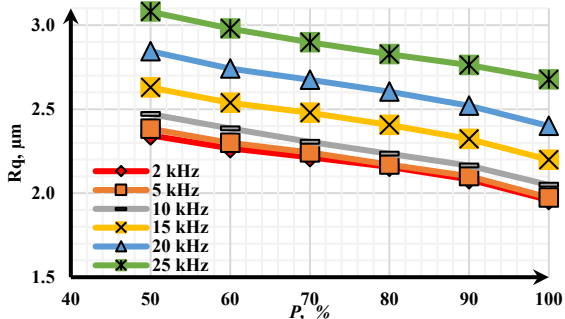


Fig. 18. Roughness dependence on the power and constant frequency.

From the analysis of the graphs in Fig. 18, it can be seen that the smallest roughness is obtained with 2kHz frequency and 100% laser power.

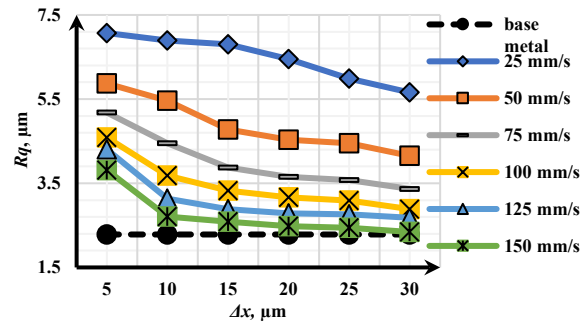
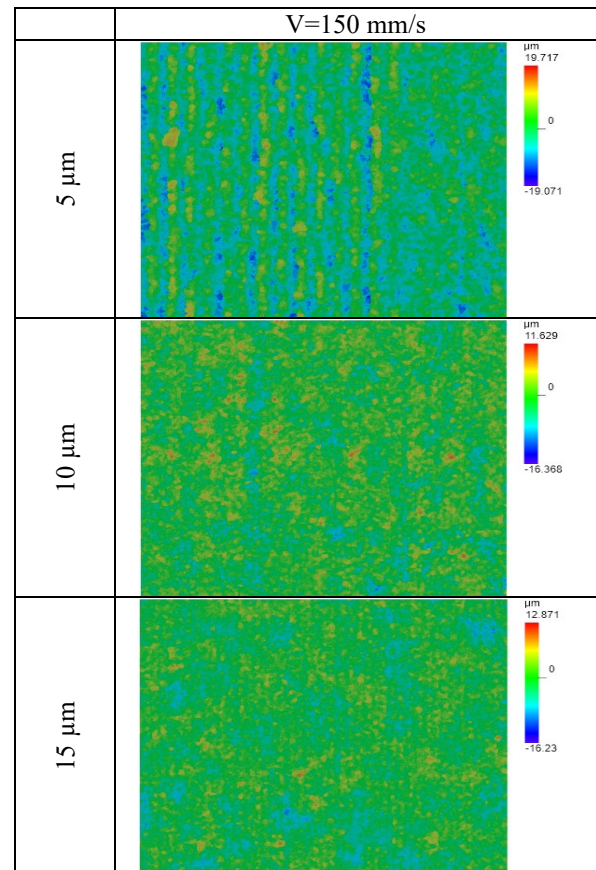


Fig. 19. Roughness dependence on the raster step and constant scanning speed.

Analysing the graph in Fig. 19, it can be observed that the highest roughness of the marked samples is 7.07  $\mu\text{m}$  and the smallest roughness is 2.34  $\mu\text{m}$ . Further analysis of the roughness data reveals the following:

- The marked samples exhibit the highest roughness at a scanning speed of 25 mm/s compared to the unmarked sample.
- The smallest roughness is obtained with a scanning speed of 150 mm/s compared to the average unmarked sample.



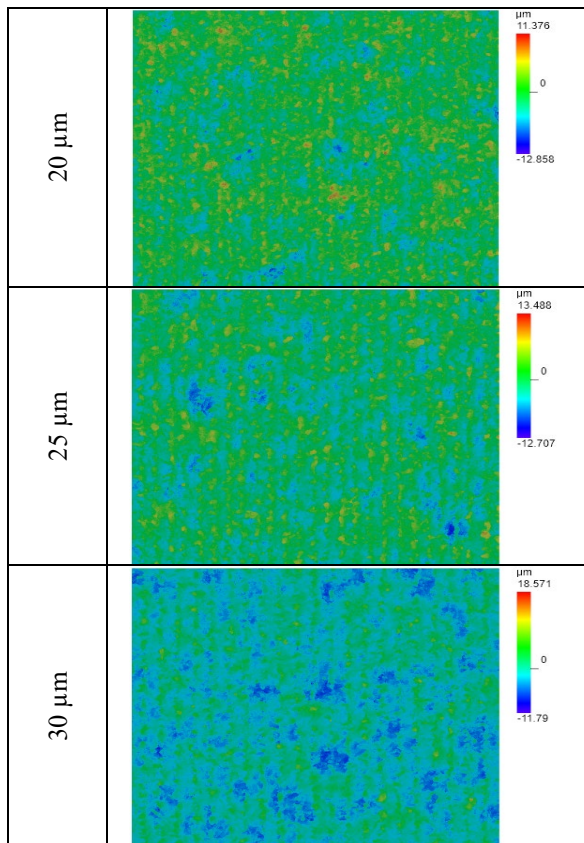


Fig. 20. Roughness changes in scanning speed 150 mm/s.

The most important result of the roughness analysis after marking is that the lowest roughness is obtained at the highest scanning speed and raster step, as shown in Fig. 20.

#### IV. CONCLUSIONS

This study used a Rofin PowerLine F 20 fiber laser to determine laser parameters impact for marking on anodised aluminium. The laser parameters were optimized to achieve high contrast marking. Based on the results of the experiment, it is possible to understand which parameters are suitable for contrast marking and which are not. From the experimental results, the main conclusions are:

- It is possible to understand which parameters are suitable for contrast marking and which are not based on the results of the experiment.
- Changing the power and frequency of the laser resulted in a lighter marking than the material itself. However, since the PowerLine F20 Varia system was used, it was impossible to make the frequency less than 2 kHz, so a contrasting white marking was not possible.
- The highest contrast was achieved at a speed of 25 mm/s and a raster step of 25 μm.
- Increasing the laser power and frequency increased the contrast of the marked surface.
- Laser marking with a frequency of 2 kHz and a laser power of 100 % produced the smallest surface roughness of anodised aluminium.
- A gradual increase in surface roughness values was observed at higher pulse and line overlap.

#### V. ACKNOWLEDGMENT

The authors gratefully acknowledge financial support by the European Regional Development Fund, Postdoctoral research aid Nr. 1.1.1.2/16/I/001 research application "Analysis of the parameters of the process of laser marking of new industrial materials for high-tech applications, Nr. 1.1.1.2/VIAA/3/19/474".

#### REFERENCES

- [1] M. Gedvilas, B. Voisiat and G. Račiukaitis, "Grayscale Marking of Anodized Aluminium Plate by Using Picosecond Laser and Galvanometer Scanner", *Journal of Laser Micro/Nanoengineering*, vol. 9, no. 3, p. 267-270, November 2014. [Abstract]. Available: ProQuest <http://www.jlps.gr.jp/jlmn/assets/8994a04d9c194b42ca9ae9d62872bfcf.pdf> [Accessed January 5, 2023], <http://dx.doi.org/10.2961/jlmn.2014.03.0017>
- [2] AAC, "What is Anodizing?". [Online]. Available: <https://www.anodizing.org/page/what-is-anodizing>. [Accessed: January 5, 2023].
- [3] J. Penide, F.Quintero, A.Riveiro, A.Fernandez, J.del Val, R.Comesana, F.Lusquinos and J.Pou, "High contrast laser marking of alumina", *Applied Surface Science*, vol. 336, p. 118-128, May 2015. [Abstract]. Available: ProQuest <https://www.sciencedirect.com/science/article/abs/pii/S0169433214022090> [Accessed January 5, 2023], <https://doi.org/10.1016/j.apsusc.2014.10.004>
- [4] L. Lazov, N. Angelov, I. Dragunov, A. Atanasov, A. Lengerov, E. Teirumnieks and I. Balchev, "Finite element modeling of laser aluminum marking", *Journal of Physics: Conference Series*, vol. 1859, September 2020. [Abstract]. Available: ProQuest <https://iopscience.iop.org/article/10.1088/1742-6596/1859/1/012017/meta> [Accessed January 5, 2023].
- [5] J. Penide, F. Quintero, F. Arias-Gonzalez, A. Fernandez, J.del Val, R. Comesana, A. Riveiro, F. Lusquinos and J. Pou, "Everlasting Dark Printing on Alumina by Laser", *Physics Procedia*, vol. 83, p. 233 - 239, September 2016. [Abstract]. Available, ProQuest <https://www.sciencedirect.com/science/article/pii/S1875389216301237> [Accessed January 5, 2023], <https://doi.org/10.1016/j.phpro.2016.08.016>
- [6] P. Narica, L. Lazov, A. Teilans, P. Grabusts, E. Teirumnieks and P. Cacivkin, "Method for color laser marking process optimization with the use of genetic algorithms", *Proceedings of the 11th International Scientific and Practical Conference*. vol. 2, p. 101 - 105, June 2017. [Abstract]. Available: ProQuest <http://journals.rta.lv/index.php/ETR/article/view/2607/2647> [Accessed January 5, 2023].
- [7] W. Pakiela, T. Tanski, Z. Brytan, G. Chladek, K. Pakiela, "The impact of laser surface treatment on the microstructure, wear resistance and hardness of the AlMg5 aluminum alloy", *Applied Physics A*, vol. 126, February 2020. [Abstract]. Available: ProQuest <https://link.springer.com/article/10.1007/s00339-020-3350-x> [Accessed March 10, 2023], <https://doi.org/10.1007/s00339-020-3350-x>
- [8] L. Lazov, H. Deneva and P. Narica, "Laser Marking Methods", *Proceedings of the 10th International Scientific and Practical Conference*. vol. 1, p. 108 - 115, 2016. [Abstract]. Available: ProQuest <http://journals.rta.lv/index.php/ETR/article/view/221/622>. [Accessed February 26, 2023], <http://dx.doi.org/10.17770/etr.2015vol1.221>
- [9] D. Austin, L. Beagle, C. Muratore and N. Glavin, "Laser processing of nanomaterials: From controlling chemistry to manipulating structure at the atomic scale", *Hybrid Atomic-Scale Interface Design for Materials Functionality*, pp. 179-208, 2021. [Abstract]. Available: ProQuest [https://www.researchgate.net/publication/350215011\\_Laser\\_processing\\_of\\_nanomaterials\\_From\\_controlling\\_chemistry\\_to\\_manipulating\\_structure\\_at\\_the\\_atomic\\_scale](https://www.researchgate.net/publication/350215011_Laser_processing_of_nanomaterials_From_controlling_chemistry_to_manipulating_structure_at_the_atomic_scale). [Accessed March 20, 2023].
- [10] A. Atanasov and A. Lengerov, "Increasing the Efficiency of Laser Marking of aluminum Alloys by Double Writing of the Symbols", *Proceedings of the 13th International Scientific and Practical Conference*, vol. 3, p. 20-24, 2021. [Abstract]. Available: ProQuest <http://journals.rta.lv/index.php/ETR/article/view/6550/5380>. [Accessed February 26, 2023].

- [11] I. Balchev, A. Atanasov, A. Lengerov and L. Lazov, "Investigation of the influence of the scanning speed and step in laser marking and engraving of aluminum", *Journal of Physics: Conference Series*, vol. 1859, 2020. [Abstract]. Available: ProQuest <https://iopscience.iop.org/article/10.1088/1742-6596/1859/1/012002> [Accessed March 10, 2023].
- [12] L. Lazov, N. Angelov, E. Teirumnieks and E. Teirumnieka, "Preliminary Numerical Analysis for the Role of Speed onto Laser Technological Processes", *Proceedings of the 12th International Scientific and Practical Conference*, vol. 3, p. 137-142, 2019. [Abstract]. Available: ProQuest <http://journals.rta.lv/index.php/ETR/article/view/4154/4167> [Accessed March 10, 2023].
- [13] J. Maltais, V. Brochu, C. Frayssinous, R. Vallee, X. Godmaire and A. Fraser, "Surface Analysis study of laser marking of aluminum", *34th International Conference and Exhibition of ICSOBA*, 2016. [Abstract]. Available: ProQuest <https://icsoba.org/assets/files/publications/2016/DS04S.pdf>. [Accessed March 10, 2023].
- [14] J. Penedi, F. Quiñtero F. Gonzalez- Arias, A. Fernandez, J. del Val, R. Comesana, A. Riveiro, F. Lusquinos and J. Pou, "Experimental study on laser marking of alumina", *Lasers in Manufacturing Conference*, 2015. [Abstract]. Available: ProQuest [https://www.wlt.de/lim/Proceedings2015/Stick/PDF/Contribution271\\_final.pdf](https://www.wlt.de/lim/Proceedings2015/Stick/PDF/Contribution271_final.pdf). [Accessed March 10, 2023].
- [15] L. Lazov, A. Atanasov and N.A. Petrov, "Investigation of the role of certain factors affecting the contrast in laser marking", *Contemporary Materials*, II-1, p. 13-17, 2011. [Abstract]. Available: ProQuest [https://www.researchgate.net/publication/268365412\\_INVESTIGATION\\_OF\\_THE\\_ROLE\\_OF\\_CERTAIN\\_FACTORS\\_AFFECTING\\_THE\\_CONTRAST\\_IN\\_LASER\\_MARKING](https://www.researchgate.net/publication/268365412_INVESTIGATION_OF_THE_ROLE_OF_CERTAIN_FACTORS_AFFECTING_THE_CONTRAST_IN_LASER_MARKING). [Accessed March 10, 2023], <http://dx.doi.org/10.5767/anurs.cmat.110201.en.013L>
- [16] L. Lazov, E. Teirumnieks, N. Angelov and E. Teirumnieka, "Methodology for automatic determination of contrast of laser marking for different materials", *Latvia Proceedings of the 12th International Scientific and Practical Conference*. vol. III, p. 134 - 136, 2019. [Abstract]. Available: ProQuest <http://journals.rta.lv/index.php/ETR/article/view/4143/4165> [Accessed March 10, 2023].
- [17] L. Lazov, E. Teirumnieks, E. Teirumnieka, P. Cacivkin, N. Angelov and T. Karadzhev, "Laboratory exercise to determine contrast in laser marking of articles", *Proceedings of the International Scientific Conference*, vol. I, p. 331-339, May 2019. [Abstract]. Available: ProQuest <http://journals.ru.lv/index.php/SIE/article/view/3906/3689> [Accessed March 10, 2023].

# Features of Color Laser Marking on Metals

**Nikolay Todorov Dolchinkov**

Vasil Levski National Military  
University, Veliko Tarnovo, Bulgaria  
National Research University  
"Moscow Power Engineering  
Institute", Moscow, Russia  
Veliko Tarnovo, Bulgaria  
n\_dolchinkov@abv.bg

**Christian Tolev**

Vasil Levski National Military  
University, Veliko Tarnovo, Bulgaria  
Veliko Tarnovo, Bulgaria  
kris997@abv.bg

**Teodor Petrov**

Vasil Levski National Military  
University, Veliko Tarnovo, Bulgaria  
Veliko Tarnovo, Bulgaria  
Tedo089@abv.bg

**Emanuil Dimitrov**

Vasil Levski National Military  
University, Veliko Tarnovo, Bulgaria  
Veliko Tarnovo, Bulgaria  
emkoto99@abv.bg

**Georgi Petrov**

Vasil Levski National Military  
University, Veliko Tarnovo, Bulgaria  
Veliko Tarnovo, Bulgaria  
gpetrov129@abv.bg

**Abstract.** In the research carried out at the Rezekne Academy of Technology, the technology for color laser marking on chromium-nickel base and other metal bases was used in industrial production from the point of view of the repeatability and stability of the produced color markings. The study and research was done during the Erasmus internship by the authors at the Academy of Technology in Rezekne, Latvia. For this purpose, an AISI 304 color palette consisting of fifteen colors was developed and implemented. After the practical experiments, the dependence of the obtained colors on the various parameters of the laser processing was analyzed. The resulting colors were then tested using optical, scanning electron and atomic force microscopy, and the configuration of the oxide films was determined by Raman spectroscopy. The resulting colors are of appropriate uniformity, brightness and cover almost all spectral zones, and the resulting colors are of many times better quality than other metallic bases. A color standardization and palette repeatability test was also performed by evaluating the reflectance spectra of the formed colors. The color palette demonstrated high repeatability for all but one particular color. In parallel, the stability of the color markings was studied in terms of environmental, mechanical and chemical resistance. The resulting colors show high resistance to most environmental conditions; however, exposure to very high temperatures and extreme humidity (100 °C, 90%) and to low temperatures and extreme humidity (-40 °C, 90%) results in degradation of several colors. Colored brands show high hardness and excellent mechanical resistance to external influences and exceptional resistance to various chemicals, except for acid solutions and salts.

**Keywords:** color marking; laser; marking; power; speed.

## I. INTRODUCTION

The marking of the various materials is an essential part of the production cycle, which provides the necessary information about the product and serves as a marketing tool to attract the attention of consumers to a particular product. Although various types of markings are applied to products, permanent markings are preferred [1], [2]. A variety of techniques can be used to create a permanent mark, including etching, electrochemical etching, engraving, dot etching, and laser marking. Nowadays, laser marking is widely used in various sections of the production line for a variety of applications to create high-quality permanent marks. The laser marking method is effective, non-contact and applies to both metallic and non-metallic surfaces. In addition, it requires no additional additives or solvents and produces no waste; thus, it is environmentally sustainable. Additionally, laser surface coloring is possible using color laser marking technology, which is the focus of this article. Color laser marking has been known for a long time, so many studies have been conducted on the use of different types of laser sources, the influence of environmental conditions on the results, and the analysis of the physical and chemical properties of surfaces before and after laser treatment. A technique for laser marking substrates such as ceramics, glass, plastic and metal was proposed by Axtell [3], [4]. In the laboratory of the Chinese scientist Li se. obtained a comprehensive view of the process of oxide formation during the interaction of an ultraviolet laser beam with stainless steel in air [5]. Modeling of coloring of stainless steel surfaces with

Print ISSN 1691-5402

Online ISSN 2256-070X

<https://doi.org/10.17770/etr2023vol3.7222>

© 2023 Nikolay Todorov Dolchinkov, Teodor Petrov, Georgi Petrov, Christian Tolev, Emanuil Dimitrov.  
Published by Rezekne Academy of Technologies.

This is an open access article under the [Creative Commons Attribution 4.0 International License](https://creativecommons.org/licenses/by/4.0/).

colored pixels by heating the surface using a laser was carried out by Lehmuchero in his laboratory. [6]. Dusser and his team demonstrated the achievement of material modifications using ultrafast laser pulses by creating polarization-dependent structures that can create specific color designs [7]. Color laser marking technology for coloring metals has also been researched at Gorny's research center. [8], [9]. The famous scientist Visco and his team researched a method for coloring metal surfaces, in which nanosecond laser pulses form small-scale periodic structures [6]. Liu and his team investigated the recent developments of laser technologies for surface coloring and three specific physical mechanisms for color generation, which are the thin-film surface oxidation effect, laser-induced periodic surface structures (LIPSSs), and laser-induced nanoparticles and nanostructures [7], [10], [11].

## II. MATERIALS AND METHODS

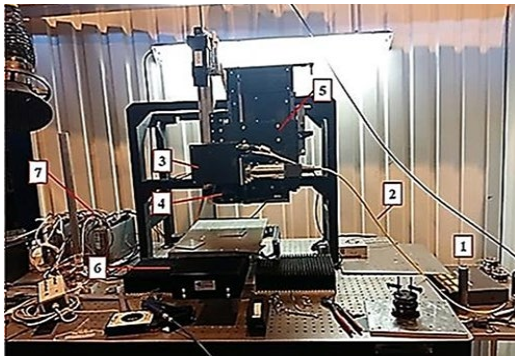


Figure 1: The configuration of the laser processing system.

Setting and parameters of the laser procedure Stainless steel contains chromium in its composition, which provides chemical stability and high heat resistance of the alloy and makes it suitable for use in the laser process. AISI 304 stainless steel plates with a thickness of 2 mm and initial roughness level  $R_z = 8.42 \mu\text{m}$ , reflectivity  $R(\lambda=1.06 \mu\text{m}) = 0.75$ , thermal diffusivity  $a = 3 \times 10^{-6} \text{ m}^2/\text{s}$ , thermal conductivity  $k = 37 \text{ W/mK}$ , melting point =  $1800 \text{ }^\circ\text{C}$  and boiling point =  $3145 \text{ }^\circ\text{C}$ . At the initial stage, the surfaces were cleaned with acetone to avoid any contamination or stains. A nanosecond pulse ytterbium fiber laser supplied by IPG Photonics Corporation  $\tau < 200 \text{ ns}$  at a repetition rate of 1.6 was selected as the source of laser radiation with a wavelength of  $1055 < \lambda < 1075 \text{ nm}$  generating pulses of 4 seconds duration  $f < 1000 \text{ kHz}$ . The configuration of the laser processing system developed for scribing and marking purposes is presented in Fig. 1 and consists of 1) IPG Photonics nanosecond fiber laser, 2) fiber optic transfer, 3) SCANLAB scanning system, 4) 100 mm objective, 5) Neff-Wiesel linear drive for vertical movement, 6) XY coordinate stage, 7) Kollmorgen ACD servo drives.

A fiber pulsed ytterbium laser was emitted and fed into a collimating system via an optical fiber to form a parallel beam output. A dual-axis galvanometer scanning system (hurrySCAN II 14 digital scanning head from SCANLAB corp. ) was installed to move along the X and Y axes. A

focusing lens with a focal distance 100 mm [11], [12]. Additional horizontal movements and vertical movements can be performed using a multi-axis linear motor coordinate stage, which allows the extension of the working space to  $250 \times 250 \text{ mm}$ . Laser radiation parameters and scan speed can be changed using the developed labVIEW code. Also, all vertical and horizontal movements can be controlled by the same code.

A focused laser beam with a diameter  $d_0$  moving at a speed  $V_{sc}$  and a pulse repetition rate  $f$  irradiates a sample surface along a line (Fig. 2). When one scan line is completed with an overlap, the laser beam continues along the Y axis along the next line with an overlap  $L_y(\%)$ , characterized by the hatch spacing  $H$ , where  $P$  is the laser power and  $d_0$  is the spot diameter. A laser beam diameter is needed to calculate the power density of the laser radiation. In this study, the diameter of the laser beam is  $40 \mu\text{m}$ .

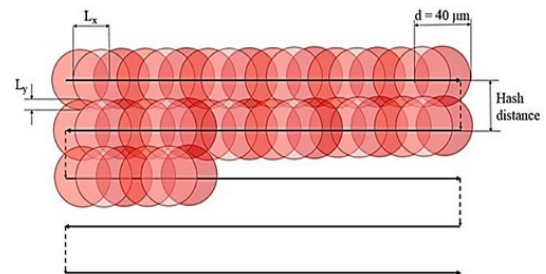


Figure 2 Focused laser beam.

### Color palette development

The color laser marking process involves sequential melting and solidification of the material, which results in oxidation and nitriding of the material surface. The final surface and oxide film formation is the result of repeated pulsed laser operation, which varies depending on the heat of the laser and the overlap value of the laser pulses [13], [14], [15]. The result of the relief and color of the surface is affected by almost all parameters of the laser source. In this study, the dependence of the obtained colors on the scanning speed, laser power, pulse duration and laser pulse frequency is investigated. The study of the dependence of the resulting color on the surface relief is not the aim of this study.

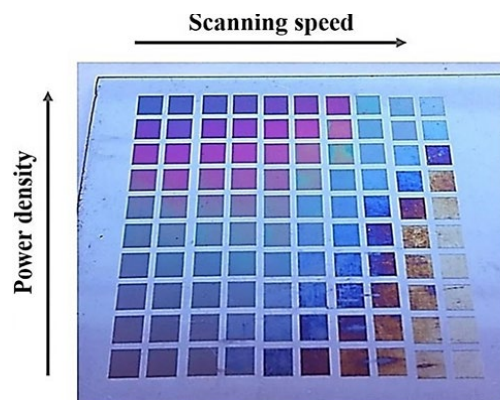


Figure 3: Dependence of obtained colors on power and speed.

The result shows that with increasing power the colors do not change significantly and only the parametric window moves to higher values of the scan rate for each color [1], [16]. Given that greater performance can be obtained at higher intensities, the next step was to investigate the dependence of color on scan rate with a maximum continuous power of 20 W available at the same parameters of frequency, hatch spacing and duration of the impulse. Initially, the scanning speed was changed from 450 to 850 mm/s with a step of 10 mm/s, and then from 50 to 150 mm/s with the same step. The results are presented in Fig. 4.



Figure 4: Obtaining a color palette at different speeds.

As shown in fig. 4, at a low scan speed, only dark gray colors appear, while as the scan speed increases, the colors vary in the following order: dark green, dark violet, wine red, orange, light green, gold, and light blue.

To investigate the dependence of colors on the frequency of laser pulses, the experiment was carried out with  $I_0=1.6-10^8$  W/cm<sup>2</sup>,  $r=100$  ns,  $H=0.01$  mm,  $V_{sc}=450-1200$  mm/s with step 50 mm/s and a changing frequency that changes from top to bottom every two lines, 100, 200, 500 and 1000 kHz respectively. Fig. 5 shows the dependence of the color on the scan rate for different frequencies.

Figure 5 shows the dependence of the produced color on the scanning speed for different frequencies ( $I_0 = 1.6 \cdot 10^8$  W/cm<sup>2</sup>,  $\tau=100$  ns,  $H=0.01$  mm,  $V_{sc}=450-1200$  mm/s,  $f=100$  kHz: lines No. 1, 2 ;  $f=200$  kHz: lines No. 3, 4 ;  $f=500$  kHz: lines No. 5, 6 ;  $f=1000$  kHz: lines No. 7, 8 .

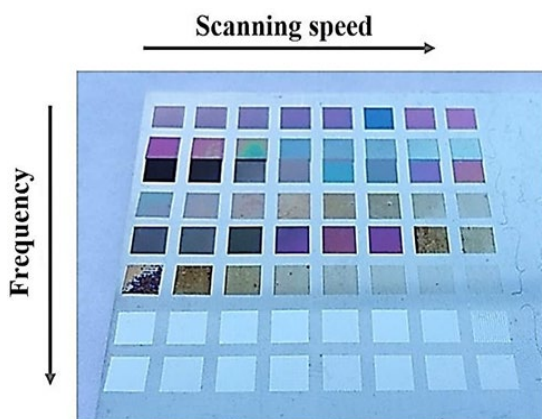


Figure 5. The dependence of the produced color on the scanning speed.

The test result revealed that specific colors such as light pink, aquamarine or bright purple can be obtained with higher frequency modes. At  $f=1000$  kHz, only silver colors

are formed for the entire scan rate range; hence, the parametric color window could not be produced at the mentioned frequency, although it could be assimilated into a final palette to produce white or silver due to its fast production speed.

The experiment to study the dependence of colors on the pulse duration was carried out with two different power densities  $I_0=0.8 \times 10^7$  and  $I_0=1.6 \times 10^7$  W/cm<sup>2</sup> and two different pulse durations  $r=4$  and  $r=8$  ns with scan speed  $V_{sc}=50-200$  mm/s with step 10 mm/s and  $H=0.01$  mm. The test result is shown in Fig. 6.

Figure 6 shows the dependence of the produced color on the scan rate for different pulse durations ( $V_{sc}=50-200$  mm/s,  $H=0.01$  mm,  $f=60$  kHz, lines № 1, 2:  $\tau=4$  ns,  $I_0=0.8 \times 10^8$  W/cm<sup>2</sup>; lines № 3, 4:  $\tau=4$  ns,  $I_0=1.6 \times 10^8$  W/cm<sup>2</sup>; lines № 5, 6:  $\tau=8$  ns,  $I_0=0.8 \times 10^7$  W/cm<sup>2</sup>; line № 7:  $\tau=8$  ns,  $I_0=1.6 \times 10^8$  W/cm<sup>2</sup>).

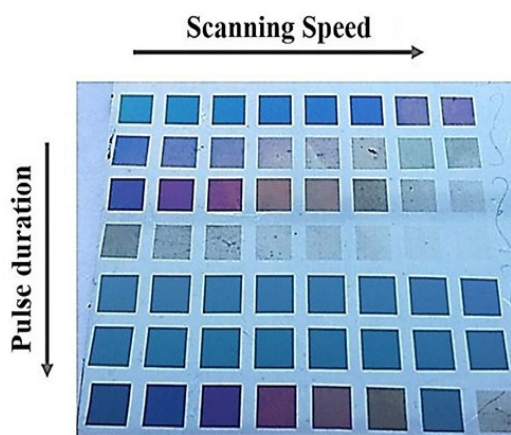


Figure 6. The dependence of the produced color on the scan rate for the different pulse durations.

As can be seen from fig. 6, the duration of the pulse has a significant effect on the color. The sequence of colors, hues and surface roughness under the color are different for shorter and longer pulse durations. For a longer duration pulse ( $r=20$  ns), visually the colors are glassy and the material underneath is smoother compared to the shorter duration pulses. In contrast, for shorter pulses, the parametric window is shifted to the scan rate with lower values, which reduces the marking efficiency.

Almost the same color dependence is observed for pulse durations of 4 ns and 8 ns; however, with a pulse duration of 8 ns, the scan rate is higher and the resulting colors are more consistent. Based on the analysis performed, the number of pulses per spot ( $N_x, N_y$ ) and the power density ( $I_0$ ) were selected to develop a color palette with fifteen different shades for AISI 304 stainless steel [3], [7], [17], [18]

Analysis of the obtained structures

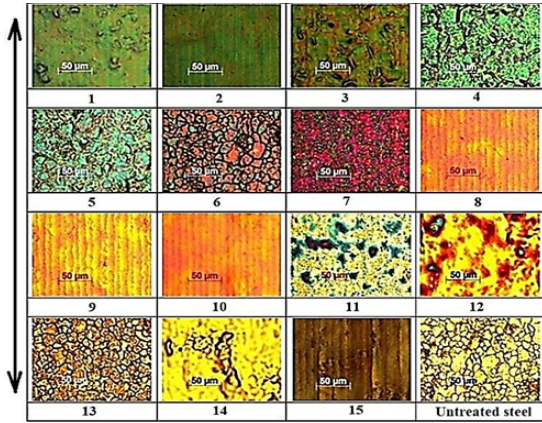


Figure 7. Micrographs of the color palette for AISI 304 stainless steel.

Optical microscopy was used to examine the microstructure of the developed colors and to analyze the oxide film structure of the color palette. The micrographs of each produced color and of the untreated surface are shown in Fig. 7.

Evaluation of the microimages shows that the created color patterns with large overlap, i.e., with large  $N_x$  and  $N_y$  values, are composed of distinct regions of different colors. In addition, the structure of the oxide film will be different depending on the overlapping and laser processing mode.

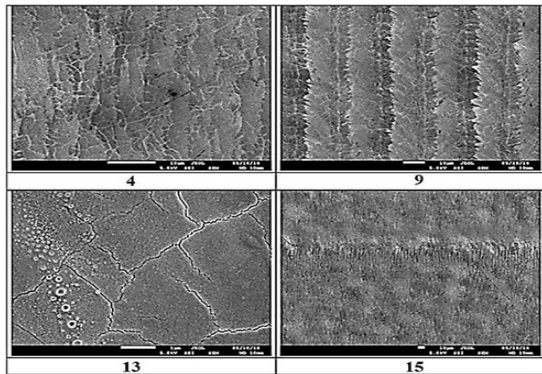


Figure 8. SEM images of the samples.

Some samples, including samples No. 8, 9, 10, 15, have a pronounced bar microstructure, while samples No. 11, 12, 14 have an irregular microstructure, and samples No. 6 and 7 have a granular structure. For a more detailed study of the structures, scanning electron microscopy (SEM) images of some samples were taken with an electron beam acceleration voltage of 5kV (Fig. 8).

The structures were also investigated by atomic force microscopy (AFM) operating in contact mode. The surface profile of specimen №9 and the 3D plane are shown in Fig. 9.

In fact, the sample has a periodically repeating relief that corresponds to the scanning geometry. The maximum and average roughness heights are nearly 2.6 and 1.5  $\mu\text{m}$ , respectively, which is quite small compared to the material surface roughness ( $R_z = 8.42 \mu\text{m}$ ).

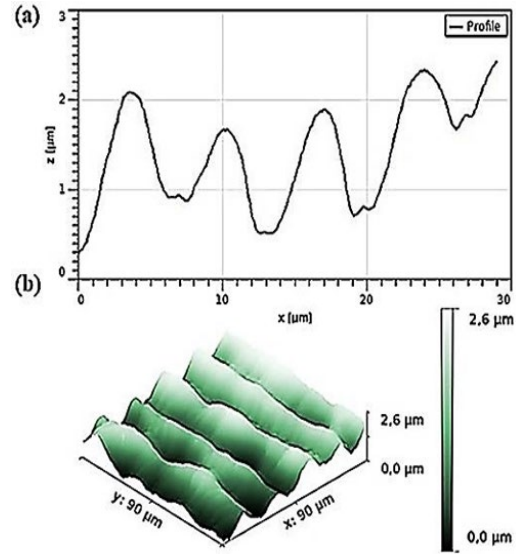


Figure 9: Profile of the studied material.

To determine the chemical composition of the obtained samples in this study, the Raman scattering method was used [5], [16], [18], [19]. A solid-state laser was used for the Raman scattering analysis. It initiates scattering on the surface of sample #9 with a wavelength of 532 nm and an output power of 1 mW (Fig. 10). A Lorentz fit function was applied to the plot to accurately characterize the position of the peaks. Seven Lorentzian peaks at 288, 332, 390, 541, 634, 674 and 715  $\text{cm}^{-1}$ .  $\text{FeCr}_2\text{O}_4$  has eigenphonon modes that coincide with 541, 634, 674  $\text{cm}^{-1}$ ; therefore, this means the presence of  $\text{FeCr}_2\text{O}_4$  in the produced films. The peaks at 288, 332, 390 and 715  $\text{cm}^{-1}$  are associated with the existence of maghemite ( $\text{Fe}_2\text{O}_3$ ) or a maghemite-rich region that may exist due to the oxide film in addition to the virgin steel.

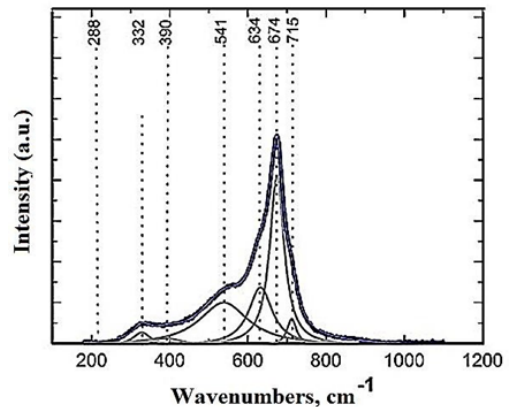


Figure 10: Dependence of intensity on distance.

### III. RESULTS AND DISCUSSION

The quality of the coating is essential for industrial production and must meet the requirements of standardization organizations, manufacturers and users [1], [5], [11]. The produced colors were tested for repeatability and stability in terms of environmental, mechanical and chemical resistance.

Repeatability is a crucial factor in color coatings in the sense that the same color can be reproduced in different production runs. Color determination is done by analyzing the reflectance and transmission spectra of the objects. In this research work, the standard CIE RGB coordinate space is used to control the colors of the samples, in which the red (R), green (G) and blue (B) components of the flux form the coordinates [8]. The additive rule in Eq. 1 is used to define colors in this system [7].

$$C = r \bar{R} + g \bar{G} + b \bar{B} \quad (1)$$

Where  $\bar{R}$ ,  $\bar{G}$ ,  $\bar{B}$  are the units of the respective primary colors, and  $r$ ,  $g$ ,  $b$  are the number of units of each primary color required to construct the particular color  $C$ . The relative color coordinates can be calculated similarly to those in the CIE XYZ system via Eq. 2-4 [4].

$$r = r / (r + g + b) \quad (2)$$

$$g = g / (r + g + b) \quad (3)$$

$$b = b / (r + g + b) \quad (4)$$

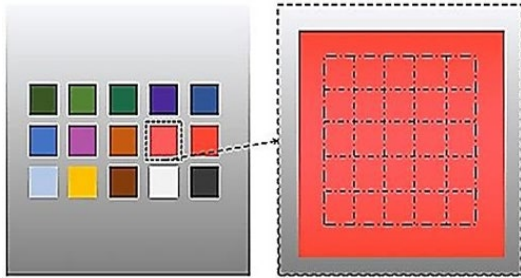


Figure 11. Matrix for conducting the tests.

The reflectance spectra of each color are needed to calculate the color coordinates. As shown in fig. 11, each color square is divided into 25 areas; therefore, the final spectrum is the average spectrum of the selected areas.

Depending on the type of peaks that appear in the wavelength, four groups of spectra can be defined. The first group (Fig. 12a) are flat spectra that do not have obvious peaks in the wavelength range and their initial appearance resembles the spectra of untreated steel. In the second group (Fig. 12b), one clear peak is observed between 500 and 700 nm. In the third group, two peaks are observed around 420 and 550 nm, respectively (Fig. 12c). In the last group (Fig. 12d), the peaks are broadened compared to the previous group. Interference effects in the denser oxide film and surface staining are suggested to be responsible for the peaks. A program was developed in LabVIEW to calculate the color coordinates in the CIE RGB space for each sample [3], [8], [20], [21].

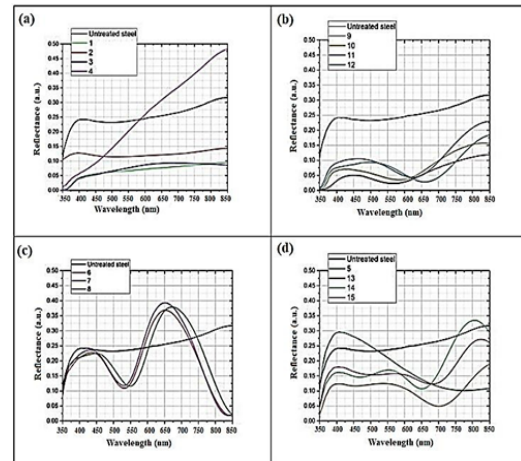


Figure 12: Spectra of the investigated material.

To investigate the repeatability, twenty color palettes were made, six of which are shown in Fig. 13.



Figure 13. Six identical color palettes produced with the same laser processing parameters.

The difference in the colors of the palettes determines the repeatability of the colors obtained by applied laser technology. The International Commission on Illumination defines the color difference standard using the definition of the Delta E concept, which represents the evaluation of the change in the visual perception of two specified colors [6], [10]. In this study, the concept of delta E was used to estimate the color difference [6], [12], [22]. For color repeatability purposes, delta E = 2 is typically used. The average value of delta E was calculated using MATLAB code for all samples of the same color, which are presented in Fig. 14.

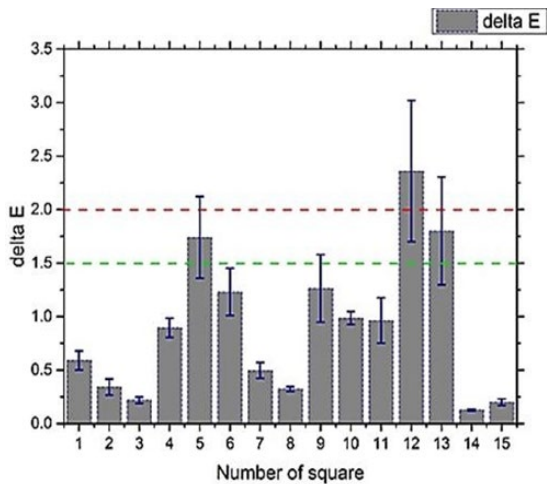


Figure 14. Delta E values of fifteen different colors averaged over ten samples.

The green line is the minimum delta E value perceived by the human eye. The red line is the maximum delta E value allowed in production.

According to fig. 14, the repeatability of all colors is satisfactory, making them suitable for use in the production line. The majority of color squares (№ 1, 2, 3, 7, 8, 14, 15) have superior delta E, so color variation is not noticeable even under close observation by an experienced observer. Samples №. 4, 6, 10 and 11 have acceptable delta E values in the sense that the color difference can only be detected by an experienced observer under suitable lighting conditions. Square #9 still has a satisfactory delta E value that is acceptable for production use. Squares №. 5 and 13 have higher average delta E values, which can be related to the corner effect [2], [12], although these colors can still be inserted into the color palette because they were not visually established differences between samples. Square №12 has the largest delta E value and correspondingly the lowest repeatability, which means that a casual observer can notice the difference. Therefore, this color cannot be recommended for further use. This problem can be solved by adjusting the laser processing parameters or by choosing different modes that can provide uniform color.

#### Environmental chamber testing

Product coatings and markings must withstand various environmental conditions and must not change during the period of use of the product [1], [14]. In this study, environmental testing was performed in a chamber based on four different operating conditions. Experiments are regularly conducted under temperature and humidity conditions that are not actually expected, such as a combination of extremely low or high temperatures (-40, -20, 40, 100 °C) with high humidity (70%, 90%). This ensures the stability of the samples under normal conditions and also compensates for the short duration of the test exposure (24 hours) compared to the actual operating time. The first test was conducted under ambient conditions with a temperature of -20 °C and a humidity of 70%. The result shows that there is no change in colors or materials after 24 hours in the environmental test chamber

as shown in Fig. 15. Optical microscope analyzes did not reveal any damage or defects in the oxide layers.



Figure 15. Color palette after 24 hours of environmental exposure in the test chamber at -20 °C and 70% humidity.

The second test was conducted under ambient conditions with a temperature of -40 °C and a humidity of 90%. The result reveals numerous minor changes to the surface after 24 hours of exposure to the environment in the chamber, as shown in Fig. 16.



Figure 16. Color palette after 24 hours of environmental exposure in the test chamber at -40 °C and 90% humidity.

Photographs of the problem areas and microimages of the defects are shown in Figs. 17a and fig. 17b. A cloudy spot with a diameter of about 400 μm appears on the surface of square No. 1 (Fig. 17a, left). Upon detailed observation under an optical microscope, it was found that the spot is a modified oxide layer with remarkable damage (Fig. 17b left). However, the rest of the square shows no changes. The presence of a stain is probably due to surface contamination or an impurity in the material. The creation of these types of defects is random in nature and occurs only once during the entire test. In square #5, the color changes slightly from blue to gray at the end of the treated area, which may be due to the partial oxidation of the sample (Fig. 17a middle). Under the microscope (Fig. 17b middle), only one damaged area with dimensions of approximately 1 × 1.5 mm is visible. Since these types of defects are characteristic of only one color, it can be concluded that they are probably related to the operating mode of the laser. In square #10, the color changed from burgundy to yellow in an area approximately 1 × 0.5 mm in size (Fig. 17a, right). Microscopic analysis presents the degraded region where the oxide film was etched while the structure was not destroyed (Fig. 17b right). This type of

defect can be caused by high humidity, which is likely to increase with increasing test exposure time. It can be concluded that, in general, laser colored stamps can withstand low temperature and high humidity environmental conditions [3], [15]. However, for these purposes, it is recommended that the color palette be slightly changed.

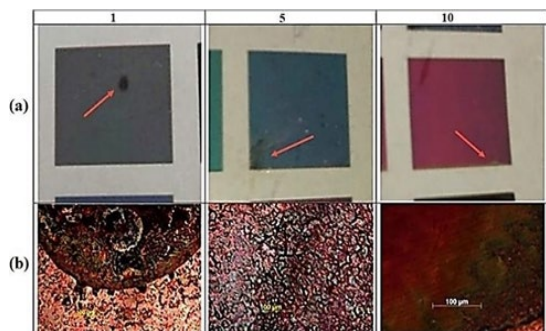


Figure 17. Color errors after 24 h exposure in an environmental test chamber at -40 °C and 90% humidity: a) photographs b) microimages.

The third test was conducted under ambient conditions: temperature 40 °C and humidity 70%. The results showed that the palette had no significant defect and no change in color or metal surface was observed after 24 hours in the environmental test chamber as shown in Fig. 18.

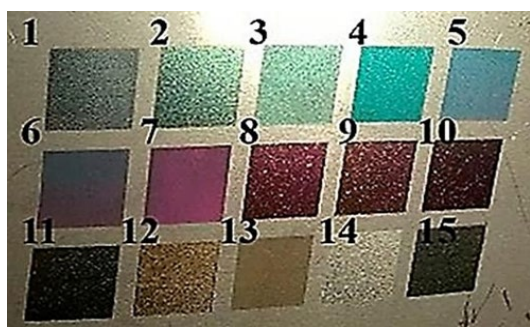


Figure 18. Color palette after 24 hours of environmental exposure in the test chamber at 40 °C and 70% humidity.

However, upon careful inspection, a spot of approximately 1 × 2 mm in size was found in one of the corners of square No. 4, visible only at a certain angle, as shown in Figure 19a. Microscopic analysis shows that the observed spot is a darkening of part of the oxide film, which may be due to the adjustments of the laser processing parameters (Fig. 19b). Overall, the color palette is relatively stable under the environmental conditions of Test 3.

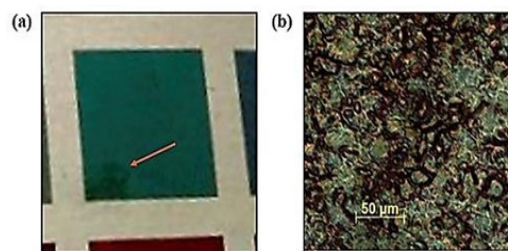


Figure 19. Color error of square No. 4 after 24 h exposure in an environmental test chamber at a temperature of 40 °C and a humidity of 70%: (a) photographs (b) microimage.

The last test was conducted under extremely harsh environmental conditions - temperature 100 °C and humidity 90%. The result showed some spots and dark spots on the metal surface itself and on the colors seen in fig. 20.

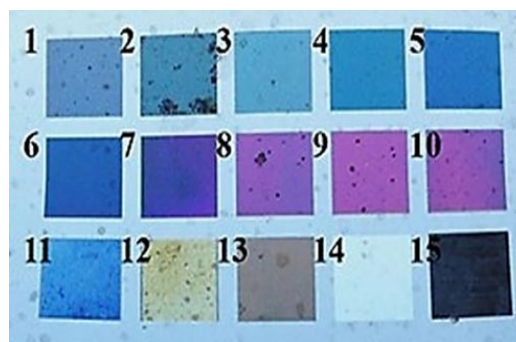


Figure 20. Color palette after 24 hours exposure in the environmental test chamber at a temperature of 100 °C and humidity of 90%.

Most of the obvious defects are presented in Fig. 21a left and center. Almost entire color squares No. 2 and No. 8 are damaged in the form of dark spots with sizes from 500 µm to 3 mm, which do not depend on the laser processing parameters. Optical microscopic analysis of Fig. 21b on the left and fig. 21b right, 21b middle means that the spots appeared are a complete breakdown of the oxide film, most likely caused by the evaporation of the condensed water on the surface due to the humidity/temperature of the test chamber. Furthermore, the untreated surface demonstrates poor resistance to such types of environmental conditions (Fig. 21a) right). When examining the surface with an optical microscope, dark spots ranging from 0.5 to 2 mm in size were found on the entire untreated steel surface (Fig. 21b, right). The darkening may be related to the rusting of certain areas of the surface caused by the condensation and subsequent evaporation of water on the metal, leading to partial oxidation.

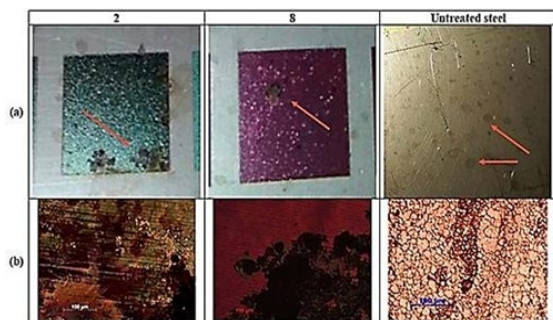


Figure 21. Color errors after 24 h exposure in an environmental test chamber at a temperature of 100 °C and a humidity of 90%:  
a) photographs b) microimages.

Therefore, the results of the test experiment show that color laser marking is not suitable for application in harsh environmental conditions with very high temperature and humidity. However, if there is adequate air circulation in the workplace, the risk of damage to the colored area can be greatly reduced.

#### IV. CONCLUSIONS

The stability of color laser marking under different environmental conditions was investigated using a climatic test chamber for four different operating conditions, including low and high temperatures and high humidity [13]. The results showed that the color palette has great persistence in most environmental conditions; however, at excessively high temperature and high humidity (100°C, 90%), limited destruction occurred in some colors and the raw metal surface was also damaged. Also, prolonged exposure to -40°C and 90% humidity results in minor discoloration of many colors that need to be replaced with more stable ones. The mechanical stability of the color palette was evaluated by determining the Vickers hardness value before and after laser treatment using a microhardness tester equipped with a diamond pyramid. After processing, the hardness of most of the samples was on average 26% less than the hardness of the base material, which still confirms the high hardness of the coatings and therefore ensures the mechanical resistance of the color markings against external influences. Moreover, given the fact that the color is not obtained by adding an additional layer of coating, but by changing the surface of the material itself, the cohesion of these labels is much higher than color markings created by conventional methods. The stability of the color palette to various chemical compounds including sulfuric acid, sodium hydroxide, ethanol, surfactant and sodium chloride was investigated. The laser color markings produced have been proven to be resistant to chemicals such as caustic soda, surfactants and alcohol. On the other hand, prolonged interaction with acid solutions and salts can damage the colored characters. Therefore, the interaction of color laser marks with environments containing acidic and salty components should be avoided.

The results of this paper make an impressive contribution to the implementation of color laser marking technology in industry. Future research directions would be to develop a color palette of AISI 304 stainless steel that

includes at least 30 different colors, and to increase the marking performance by using stronger lasers and higher frequency modes.

The laser processing system developed for the purpose of this research work is based on a nanosecond ytterbium fiber laser on a multi-axis work piece platform and the ability to move the laser scanning head vertically. In the preliminary phase, the scanning system was calibrated and the specifications of the laser beam at the focal point were determined. To find the appropriate power density value, the distribution of the laser spot on the surface is measured. The dependence of the resulting colors on laser processing parameters, including scan speed, pulse duration, emission power, and pulse repetition rate, was investigated. Based on the analysis, twenty color palettes of AISI 304 stainless steel were developed. Each sample consists of 15 squares of different colors and dimensions of 8×8 mm. The obtained oxide films were examined using optical microscopy and scanning electron microscope (SEM). The surface topology was established using atomic force microscopy (AFM). To evaluate the structure of the obtained oxide films, Raman scattering spectroscopy was performed. Peak analysis showed that four types of oxide compositions were created according to the laser processing parameters. The film consists of two main components:  $\text{Fe}_2\text{O}_3$  and  $\text{FeCr}_2\text{O}_4$ , which is consistent with data previously obtained by other researchers. Color standardization was performed based on the standard of the International Commission on Illumination. Light coordinates in the CIE RGB color space were calculated and reflectance spectra of each color were obtained using spectrophotometric measurements. The results confirm that the created colors have appropriate consistency, brightness and cover approximately all spectral regions. The repeatability of the resulting colors is proven by calculating the delta E value. Overall, the color palette confirms exceptional repeatability, although it is recommended that one particular color be replaced as it does not meet the minimum delta requirement.

#### V. ACKNOWLEDGMENTS

I express my gratitude to Professor Lyubomir Lazov for the dedicated work during these 10 years to deepen the cooperation between the two educational institutions, for the dedication in working with the trainees from the Vasil Levski National Military University and for the knowledge, experience and skills imparted.

I also thank the managements of both institutions over the years for their benevolent attitude and for the opportunity to conduct joint activities.

#### REFERENCES

- [1] Dave Ahearn, ONR Laser Power Jumps 10 Fold; Further 10-Fold Leaps Seen, *Defense Today*, August 4, 2004, p. 4
- [2] N. Todorov, Lyubomir L., Shterev I.J., Dimitrov N.D. and Ivanov L.L. 2019 Study of cutting and labeling of polymethylmethacrylate using a  $\text{CO}_2$  laser. *Vide. Tehnologija. Resursi -Environment, Technology, Resources*. ISBN 1691-5402, Vol 3, 20-22.06.2019 Rezekne, Latvia pp. 37-40.
- [3] S. E Lamberson, The airborne laser, *Proc. SPIE, Gas Chem. Lasers*, vol. 2702, pp. 2702-1\_2 702 - 6, Mar. 1996

- [4] W. Zhang, Xiao Z. and Yan Z. 1976 Design of online laser marking system by vision guided based on template matching Journal of Physics: Conference Series 1976 012047
- [5] L. Lazov, H. Deneva, E. Teirumnieka, Influence of Defocus Position on Laser Cutting Process in Sheet Steel, Environment. Technology. Resources, Rezekne, Latvia Proceedings of the 11 th International Scientific and Practical Conference. Volume III, 163-167,
- [6] L. Lazov, Dolchinkov N., Shterev J., Peneva M. and Bozhanova D. 2019 Study of laser cutting and marking on the fil with the help of a CO<sub>2</sub>-laser Vide. Tehnologija. Resursi - Environment, Technology, Resources, ISBN 1691-5402, Vol 3 pp. 143-147.
- [7] L. Lazov, Angelov N., Teirumnieks E. and Teirumnieka E. 2019 Preliminary numerical analysis for the role of speed onto laser technological processes Vide. Tehnologija. Resursi - Environment, Technology, Resources 3 pp 137-142.
- [8] N. Petrov, Optimization of the marking process with laser radiation of samples of tool steel, dissertation, Gabrovo, 2011.
- [9] N. Dolchinkov, Lazov L., Shterev Y., Lilianova St. and Pacejs A. 2019 Use of CO<sub>2</sub> laser for marking and clearing of textile materials for manufacture of military equipment 12th International Scientific and Practical conference Environment. Technology. Resources. 3, ISBN 1691-540206.2019, Rezekne, Latvia, 32-36
- [10] N. Todorov, 2020 Practical research of marking and cutting of textiles with increased resistance, using CO<sub>2</sub> laser Journal of Physics: Conference Series 1681 012014, doi:10.1088/1742-6596/1681/1/012014, Online ISSN: 1742-6596, Print ISSN: 1742-6588
- [11] S.-T. Tse and Kan C.-W. 2020 Effect of laser treatment on pigment printing on denim fabric: low stress mechanical properties Cellulose 27 10385-10405
- [12] N. T. Dolchinkov 2022 Marking and Cutting of Non-metallic Products with CO<sub>2</sub> Laser, J. Phys.: Conf. Ser. 2224 012028 DOI 10.1088/1742-6596/2224/1/012028H, doi: 10.1109/Lighting49406.2021.9599072, Electronic ISBN:978-1-6654-3792-9, CD:978-1-6654-3791-2
- [13] L. Lazov, Angelov, N., Teirumnieks, E., ...Pacejs, A., Teirumnieka, Ē., Laser ablation of paint coatings in industry, Vide. Tehnologija. Resursi - Environment, Technology, Resources, 2021, 3, pp. 187-194
- [14] E. Teirumnieka, Blumberga, D., Teirumnieks, E., Stramkale, V., Product-oriented production of industrial hemp according to climatic conditions, Agronomy Research this link is disabled, 2021, 19(4), pp. 2026-2036
- [15] L. Lazov, Teirumnieks, E., Angelov, N., Yankov, E., Modification of the roughness of 304 stainless steel by laser surface texturing (LST), Laser Physics this link is disabled, 2023, 33(4), 046001
- [16] V. Hristov, Lazov, L., Yankov, E., ...Minev, R., Angelov, N., Investigation of the laser effect of micromechanical properties of stainless steel AISI 304 during the marking process, 2021 6th Junior Conference on Lighting, Lighting 2021 - Proceedings, 2021
- [17] N. Padarev, Investigation of Damage from Radiological Dispersal Device, International Journal of Innovative Technology and Interdisciplinary Sciences, 5(4), 2022, pp. 1052-1059. <https://doi.org/10.15157/IJITIS.2022.5.4.1052-1059>.
- [18] N. Padarev, Guidelines for improving laser targeting device in military. Technology transfer: fundamental principles and innovative technical solutions, 2022, 38-40. doi: <https://doi.org/10.21303/2585-6847.2022.002681>
- [19] L. Lazov, N. Padarev, Laser Safety in Army Education, Revista, Vol. XXVIII, Nr. 1 (109), ED. Academiei Forțelor Terestre „Nicolae Bălcescu” Sibiu, Romania 2023, ISSN 2247-840X, ISSN-L = 1582-6384, pp. 61-68, DOI: 10.2478/raft-2023-0009
- [20] N. Padarev, Analysis of the Relation Between Climate Changes and Security Area, International Conference Knowledge-Based Organization, Vol. XXIV. Conference proceedings 3, Applied technical Sciences and Military Technologies, Sibiu, Rom., 2018, pp 169-173, ISSN 1843-682X, ISBN 978-973-153-329-2.
- [21] L. Lazarov, Perspectives and trends for the development of electronic warfare systems, International Conference on Creative Business for Smart and Sustainable Growth, CreBUS 2019, 2019, 8840074
- [22] S. Stoykov, Dimitrova, S., Marinov, R., The development of educational capacity of human resources in the field of security-main priority of national security, International Conference on Creative Business for Smart and Sustainable Growth, CreBUS 2019, 2019, 8840062

# Comparative Analysis of Geometric Deviations in Contact Measuring Instruments for Control and Laser Contactless Scanning

**Borislav Georgiev**

Faculty of mechanical and precision engineering  
Technical University  
Gabrovo, Bulgaria  
gborislav@gbg.bg

**Tsanko Karadzhov**

Faculty of mechanical and precision engineering  
Technical University  
Gabrovo, Bulgaria  
karadjov\_st@abv.bg

**Abstract.** The factors affecting the dimensional accuracy of 3D scanning using a measuring arm with an integrated scanner and a custom open source 3D printer using FDM technology are researched in this paper, with the purpose of isolating and reducing the sources of errors affecting the results. A consumer 3D printer is analyzed in terms of achieving accurate physical dimensions, consistent shapes, and predictable surface coverage.

**Keywords:** Geometric accuracy, laser scanning, tactile sensor, 3D printing Error.

## I. INTRODUCTION

Hardly any other technical field has developed as quickly in recent years as 3D printing. It not only finds application in the commercial, technological, industrial and scientific sectors, but also in private households. Interest in 3D printing [6][9] is growing rapidly, as is the variety of 3D printers for personal use. Factors such as easy development of customized products and reduction in production costs are driving more and more industries and companies to embrace 3D printing and incorporate it into their business. FDM (Fused Deposit Modeling) or FFF (Fused Filament Fabrication) are 3D printing processes where a filament in the form of a thermoplastic thread is heated in a print head and printed on a print platform through a nozzle. In this process, the chosen model is built up layer by layer. When talking about 3D printers, most of the time it is meant FDM printers. The so-called filament is a material that is wound on a spool and processed by the printer. There are a number of different materials (PLA, PETG, ABS, PE (nylon), etc.). They differ significantly in their properties. Filaments also available in different diameters and multiple colors.

Since layer height depends on the 3D printer used, it is one of the most important parameters of 3D printers. In general, the lower the layer height, the finer and smoother the model surface will be. On commercially available 3D printers, the average layer height is from 0.1 mm to 0.32 mm. The height of the layer depends not only on the 3D printer used, but also on the software with which a given model is cut (so-called Slicing). Today's 3D software has almost no limitations on layer height. On the other hand, however, the constantly increasing requirements for the quality of manufactured details and elements, especially in the field of mechanical engineering, lead to the need to improve both the technological equipment and the methods and means of measurement. One of the important metrological tasks in this regard is carrying out measurements with proven accuracy of the geometrical parameters of machine-building products, including both determining the deviations from the correct geometrical shape and the mutual location of the surfaces and axes, as well as all other requirements that are set in the technical drawings of engineering products. The high level of automation and intellectualization of measuring systems nowadays expands the possibilities of applying new metrological procedures based on non-contact scanning methods.

Contactless scanning systems are entering the industry more and more every day. These systems allow a significant reduction in production costs, mainly due to a significant reduction in inspection time. They allow the acquisition of a large amount of data, which provides very good levels of quality of results. Despite the well-known advantages that these systems offer, there are also some difficulties, such as the undefined and unstandardized

Print ISSN 1691-5402

Online ISSN 2256-070X

<https://doi.org/10.17770/etr2023vol3.7182>

© 2023 Borislav Georgiev, Tsanko Karadzhov. Published by Rezekne Academy of Technologies.  
This is an open access article under the [Creative Commons Attribution 4.0 International License](https://creativecommons.org/licenses/by/4.0/).

accuracy compared to traditional inspection systems based on tactile sensors with touch. This is one of the reasons for the practical absence of scanning systems in metrology applications: they have not been adequately tested for accuracy to control geometric and dimensional tolerances. In fact, these systems are mainly used as reverse engineering or multimedia applications. Two different measurement systems were analyzed: by a non-contact laser scanner and a contact tactile sensor, both mounted on a seven-degree-of-freedom Romer measuring arm. A common alignment method is defined to compare the geometry generated for the two measurement systems. Finally, an analysis was performed to compare them in terms of geometric and dimensional tolerances, being accounted for the contact measurements as a benchmark. As a result, some advice is given regarding the best scanning strategies and deviations are evaluated. Control dimensions of an aluminum part were measured by both methods (contact and non-contact). Using a 3D printer, copies of the aluminum detail were made and checked for deviations of their control dimensions and deviations from geometric accuracy (flatness and parallelism).

## II. SEQUENCE MEASUREMENT

The measurement results show that the errors of non-contact and contact measurement methods are within the tolerance of the measuring arm. The sources of most deviations are due to the printing process of the details (Table 2). The main sources of these deviations are due to: material shrinkage and deformation challenged by residual stress or rapid cooling, machine positioning errors [3], first layer adhesion problem, material extrusion problem (over or under-extrusion). Before starting any print, it is important to check the bed level. If the bed is not properly leveled, the first layer may not stick to the slab. The bed temperature is checked while printing starts. Some materials require a heated substrate to ensure that the print will stick to the substrate. The temperature of the bed can be easily controlled by the slicing software. Nozzle height can also affect layer adhesion. This is mostly a one time adjustment where the height of the nozzle from the bed is adjusted to the optimum level. If the nozzle is too high from the bed, then the deposited layer will not stick or even fall in the desired place. If the height is too low, then the nozzle itself can scrape off the build-up material. The height of the nozzle can also affect the extrusion of material, if the nozzle is too close to the build plate, then the extruder may not be able to apply the required amount of material to the bed. Therefore, it is important to set the appropriate height of the nozzle.

The HEXAGON Absolute arm 8525-7 measuring arm with 7 degrees of freedom with integrated RS5 laser scanner and OPTIV M 4.4.3 multisensor and optical coordinate measuring machines (CMM) draw on the strength of Hexagon's Enhanced Productivity Series (EPS) were used for the research.

TABLE I MEASUREMENT ACCURACY VALUES

Model	E <sub>UNI</sub> mm	P <sub>SIZE</sub> mm	L <sub>DIA</sub> mm	P <sub>FORM</sub> mm	SSA mm
8525-7	0.031	0.012	0.048	0.025	0.048

The certification specifies four accuracy values (see Table 1) known as E<sub>UNI</sub>, P<sub>SIZE</sub>, P<sub>FORM</sub> и L<sub>DIA</sub>. Each of these values represents a different aspect of the contact measurement accuracy of a portable measuring arm. The E<sub>UNI</sub> value is the maximum allowable error for unidirectional length measurements. Therefore, it most accurately reflects most measurement needs. The P<sub>SIZE</sub> value is the maximum allowable error for measuring the diameter of a sphere. Therefore, it reflects the accuracy of the feature measurements.

The value of P<sub>FORM</sub> is the maximum allowable error for the shape of a sphere. This is a value that determines the accuracy of the shoulder variance.

The L<sub>DIA</sub> value is the maximum allowable error for the articulation location. It therefore represents the repeatability of the arm. Scanning accuracy is the SSA [mm] value.

The results of determining the geometric deviations (length, thickness, flatness and parallelism) of the control aluminum detail and the printed copies using the laser scanner (laser scan copy LSC) and the tactile sensor (tactile probe copy TPC) were established using the high-precision multi-sensor measuring machine OPTIV M 443 for which a protocol has been created.

## III. ALUMINUM DETAIL RESULTS

The deviations in manufacturing of the aluminum detail are:

Length = 59,9825 mm (60mm by specification), Width = 10,5073 mm (10.5mm by specification), flatness - plane 1 = 0.009 mm and plane 2 = 0.003 mm, parallelism between plane 1 and plane 2 = 0.032mm.

All deviations are within the tolerance for the accuracy requirements of the detail.

## IV. TACTILE SENSOR RESULTS

The dimensions obtained by measuring the aluminum detail using the tactile sensors (see above) were used to print this copy. Measurement errors [5] are limited mainly by the shape deviation and roughness of the sensor sphere and the overall stability of the instrument during the measurement procedure. Deviations after printing are shown below:

Length = 59,6861 mm, Width = 10,4295 mm, flatness - plane 1 = 0.093 mm and plane 2 = 0.003 mm, parallelism between plane 1 and plane 2 = 0.484mm.

## V. LASER SCANED PART RESULTS

The dimensions (fig.1) obtained from the non-contact laser scan were used to print this copy of the detail. The laser-scanned part processing program PolyWorks allows high-end point cloud inspection to produce a CAD model in STL format. Dark, shiny and transparent surfaces cannot be scanned with this method. This is because from the experiments we have done in order to obtain a quality model of the scanned object there must be a diffuse reflection of the laser beam. During the scan operation [2], the system allows the selection of different exposure times, so that a complete image of the scanned surface can be obtained even in the conditions of the existence of areas with relatively important color differences.

Object positioning during scanning can also be a source of errors. Correct positioning must be done to avoid object surfaces being parallel to the incident beam. If this cannot be avoided, the scan will be performed in several reference positions. That is how views are obtained in which the surfaces are with sufficiently wide angles versus the incident beam to avoid gaps in the point cloud. Although non-contact scanning allows a faster point cloud, a larger number of points, and access to narrower channels or holes than contact scanning, there are situations where areas of the detail cannot be reached [12]. These surfaces are of the type of holes or narrow channels, the deep areas of which are shaded by their walls.

Sometimes it is possible to inspect them by choosing a convenient position on the detail, but there are cases when

they cannot be reached, necessitating physically cutting the piece or giving the inspection to the relevant areas.

The results after printing the model thus obtained are shown below:

Length = 59.9825 mm, Width = 10.5073 mm, flatness - plane 1 = 0.259 mm and plane 2 = 0.324 mm, parallelism between plane 1 and plane 2 = 0.267mm.

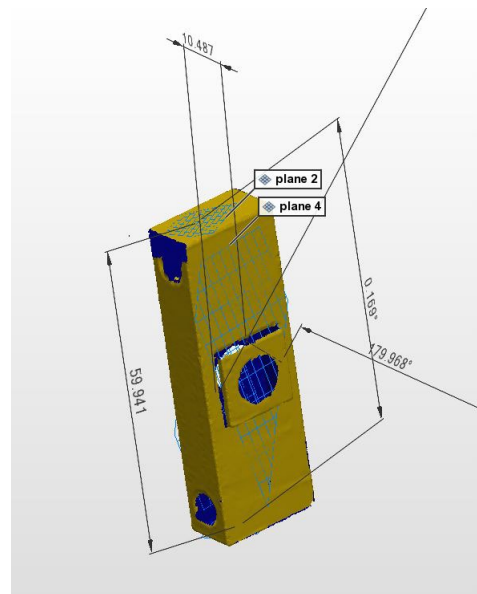


Fig.1 Laser-scanned part dimensions.

TABLE 2 MEASUREMENT PROTOCOL

Pc		PART NAME : latvia				февруари 02, 2023 11:12	
		REV NUMBER :		SER NUMBER :		STATS COUNT : 1	
	MM	FLAT1 - PLN1					
AX		NOMINAL	+TOL	-TOL	MEAS	DEV	OUTTOL
M		0.000	0.010	0.000	0.009	0.009	0.000
	MM	FLAT2 - PLN2					
AX		NOMINAL	+TOL	-TOL	MEAS	DEV	OUTTOL
M		0.000	0.010	0.000	0.003	0.003	0.000
//	MM	PARL1 - PLN1 TO PLN2					
AX		NOMINAL	+TOL	-TOL	MEAS	DEV	OUTTOL
M		0.000	0.010	0.000	0.032	0.032	0.022
	DEG	ANGL1 - PLN2 TO PLN1					
AX		NOMINAL	+TOL	-TOL	MEAS	DEV	OUTTOL
A		0.037	0.010	-0.010	0.037	0.000	0.000
	MM	FLAT3 - PLN3					
AX		NOMINAL	+TOL	-TOL	MEAS	DEV	OUTTOL
M		0.000	0.010	0.000	0.093	0.093	0.083
//	MM	PARL2 - PLN2 TO PLN3					
AX		NOMINAL	+TOL	-TOL	MEAS	DEV	OUTTOL
M		0.000	0.010	0.000	0.484	0.484	0.474
	DEG	ANGL3 - PLN2 TO PLN3					
AX		NOMINAL	+TOL	-TOL	MEAS	DEV	OUTTOL
A		0.449	0.010	-0.010	0.449	0.000	0.000
	MM	FLAT4 - PLN4					
AX		NOMINAL	+TOL	-TOL	MEAS	DEV	OUTTOL
M		0.000	0.010	0.000	0.259	0.259	0.249
	MM	FLAT5 - PLN5					
AX		NOMINAL	+TOL	-TOL	MEAS	DEV	OUTTOL
M		0.000	0.010	0.000	0.324	0.324	0.314
//	MM	PARL3 - PLN4 TO PLN5					
AX		NOMINAL	+TOL	-TOL	MEAS	DEV	OUTTOL
M		0.000	0.010	0.000	0.267	0.267	0.257
	DEG	ANGL5 - PLN4 TO PLN5					
AX		NOMINAL	+TOL	-TOL	MEAS	DEV	OUTTOL
A		180.044	0.010	-0.010	180.044	0.000	0.000

## VI. CONCLUSION

Despite the rapid growth of 3D printers in many fields of technique and household, the factors that affect the accuracy of 3D printed models have not been thoroughly studied. It is often necessary to create models by laser scanning, which are then to be printed on a 3D printer. According the results obtained in the paper, it can be concluded, that current scanning technologies allow the creation of 3D models with accuracy within tolerances, this is not always achieved when printing the model in practice. Inaccuracies are due to errors occurring during the 3D printing itself. Understanding and researching the

factors that affect the accuracy of a 3D printed model and the metrics used to measure that accuracy is key in creating methodologies leading to the reduction of these errors and the corresponding increase in the accuracy of printed models.

## REFERENCES

- [1] W.-K. Chen, Linear Networks and Systems. Belmont, CA: Wadsworth, 1993, pp. 123-135.
- [2] Z. Sheb, Tang., O. Kanaan, and Y. Cho, As-Built Error Modeling for Effective 3D Laser Scanning on Construction Sites, Proceedings of the 2013 ASCE International Workshop on

- Computing in Civil Engineering, June 23-25, Univ. of Southern California, LA, California. pp. 533-540.
- [3] D. Dichev, I. Zhelezarov, N. Madzharov. System for Measuring the Attitude of Moving Objects, using a Kalman Filter and MEMS Sensors. *Comptes rendus de l'Academie bulgare des Sciences*, Volume 72, Issue 11, pp. 1527-1536, 2019, DOI: 10.7546/CRABS.2019.11.10
- [4] D. Hernandez, Factors Affecting Dimensional Precision of Consumer 3D Printing. *International Journal of Aviation, Aeronautics, and Aerospace*, 2(4), 2015. <https://doi.org/10.15394/ijaaa.2015.1085>
- [5] D. Dichev, F. Kogia, H. Nikolova, D. Diakov. A Mathematical Model of the Error of Measuring Instruments for Investigating the Dynamic Characteristics. *Journal of Engineering Science and Technology Review*. Volume 11, Issue 6, 2018, pp. 14-19, DOI: 10.25103/jestr.116.03
- [6] M. Jadayel and F. Khameneifar, Improving Geometric Accuracy of 3D Printed Parts Using 3D Metrology Feedback and Mesh Morphing, *J. Manuf. Mater. Process.* 2020, 4, 112; doi:10.3390/jmmp4040112
- [7] E. Sachs, M. Cima, P. Williams, D. Brancazio, J. Cornie, Three Dimensional Printing: Rapid Tooling and Prototypes Directly from a CAD Model. *J. Eng. Ind.* 1992, 114, 481–488.
- [8] Ts. Zlateva-Petkova, The necessity of organizational learning and its relation to knowledge management, IV International conference “Economics and management – based on the new technologies”, EMOnt 2014, 12-15 June 2014. Vrnjachka Banja. Serbia, pp. 376-384, ISBN 978-86-6075-045-9
- [9] Z. Lianghua, Z. Xinfeng, Error Analysis and Experimental Research on 3D Printing, *IOP Conf. Series: Materials Science and Engineering* 592 012150, 2019, doi:10.1088/1757-899X/592/1/012150.
- [10] Ts. Zlateva-Petkova, Planning and forecasting future demand for employees, VI International Conference “Economics and management – based on new technologies”, EMOnt 2016, 16-19 June 2016, Vrnjacka Banja, Serbia, pp. 401-406, ISBN: 978-86-6075-059-6
- [11] H. Wang, J. Wang, Q. Zhou, Q. Xiong, Z. Wei 2017 Comprehensive Error Compensation Method of Numerical Control Machine Based on BP Neural Network. *Journal of Xi'an Jiaotong University* 6:138–145
- [12] T. Pencheva, D. Pulov, B. Gyoch, M. Nenkov Design of CCD Optical System for Thermal IR Spectral Region. In *pr. 29-th International Spring Seminar in Electronics Technology*, St. Marienthal, Germany, Verlag Dr. Markus A. Detert, 2006, pp. 413-418, ISBN 3-934142-23-0.

# *Influence of Basic Parameters of the Laser Marking Process on Stainless Steel Samples*

**Veselin Hristov**  
Department of Engineering  
University of Ruse  
Ruse, Bulgaria  
veselin-n-hristov@abv.bg

**Lyubomir Lazov**  
Department of Engineering  
RTA Larvia  
Rezekne, Latvia  
Lyubomir.Lazov@rta.lv

**Nikolay Angelov**  
Department of Economics  
Technical University of Gabrovo  
Gabrovo, Bulgaria  
angelov\_np@abv.bg

**Emil Yankov**  
Department of Engineering  
RTA Latvia  
Rezekne, Latvia  
emil.yankov@rta.lv

**Abstract.** The role of basic quantities influencing the process of laser raster marking of AISI 304 stainless steel products using a fiber laser was investigated. Some dependencies were found when changing the contrast of the marking when changing the parameters in wide intervals. As the raster step increases, a non-linear decrease in contrast occurs as the rate of contrast decrease. Regarding the influence of the speed on the contrast, it was found that as the speed increases, the contrast of the marking decreases non-linearly, and as the step increases, the speed of the contrast decrease also increases. Above 20 kHz, the frequency has relatively little influence on the contrast, as with increasing frequency the contrast slowly increases and the dependence is almost linear. The effective energy is strongly influenced by the contrast. At effective energy values below 18 kJ/cm<sup>2</sup> the contrast of the marking is insufficient for visual perception of a good quality marking, but in the interval from 6 kJ/cm<sup>2</sup> to 46 kJ/cm<sup>2</sup> the contrast increases very quickly. At values of the effective energy above 100 kJ/cm<sup>2</sup>, the contrast of the marking hardly changes.

The obtained results can be used by the operators of laser systems to evaluate the working ranges and quickly determine the boundary areas of the optimal technological parameters when obtaining a good contrast in the laser marking of stainless steels with a fiber laser.

**Keywords:** *contrast, fiber laser, frequency, laser marking, raster step, speed, stainless steel, working intervals.*

## I. INTRODUCTION

Laser marking is a technology for creating permanent alphanumeric characters, advertising logos, QR and UDI

codes directly on finished products. Laser marking provides a unique combination of speed, high positioning accuracy and flexibility [1]. Lasers can mark a wide variety of materials, they are reliable, durable and relatively economical. The technology is used in all industrial sectors and can eliminate secondary processes such as the use of consumables and secondary processing and features easy system maintenance [2]-[6]. Stainless steel materials are used in the food industry as well as in the automotive, electronics, medical and engineering industries [7]-[9]. In article [10], the influence of operating parameters on contrast, roughness and oxide layer during laser marking of AISI 304 stainless steel is investigated. In article [11], the authors use a nanosecond pulsed laser to induce surface staining of stainless steel, one of the main parameters that they change in the experiments is the focal length, the repetition rate and the scanning speed. In article [12], the authors present experiments to produce colors on stainless steel. They research how, through changes in the thickness of the resulting layers, a variety of colors can be obtained. In article [13], the authors experimented with two types of continuous mode (CW) lasers with different wavelengths 1064 nm and 532 nm to produce contrast marking on aluminum. The conclusions they draw are that the treated areas in argon and in air do not show a difference in the color of the mark, but the experiments reveal a difference in the amount of material removed, with the ablation being greater with the laser operating in the visible spectrum. In article [14], the authors modified

Print ISSN 1691-5402

Online ISSN 2256-070X

<https://doi.org/10.17770/etr2023vol3.7216>

© 2023 Veselin Hristov, Lyubomir Lazov, Nikolay Angelov, Emil Yankov.

Published by Rezekne Academy of Technologies.

This is an open access article under the [Creative Commons Attribution 4.0 International License](https://creativecommons.org/licenses/by/4.0/).

the surface of duplex stainless steel by laser processing. Experiments are done on the influence of the raster step on the roughness. In the article [15], the author gives an overview of some laser technological processes such as laser surface alloying, coating application, laser hardening.

The scientific research in this paper aim to investigate the influence of some basic parameters such as effective energy, raster step, speed, and frequency on contrast in laser marking with a nanosecond fiber laser.

## II. MATERIAL AND LASER SYSTEM

### A. Preparation of the material

AISI 304 / EN 1.4301 stainless steel with the composition shown in Table 1 was used in this study, the samples were 0.8 mm thick. The material is austenitic steel with high corrosion resistance. This grade of stainless steel has very low magnetization and is suitable for welding, forging and cold forming.

TABLE 1 CHEMICAL COMPOSITION OF THE STUDIED AISI 304 STAINLESS STEEL

Element	C	Cr	Mn	S
Content, %	≤ 0.07	17.5 ÷ 19.5	≤ 2.00	≤ 0.03
Element	Si	Ni	N	P
Content, %	≤ 1.00	8.0 ÷ 10.5	≤ 0.10	≤ 0.045

### B. Laser system



Fig. 1. Laser technological marking system.

The research was done with a laser technology system with a fiber laser. It is a pulsed laser that operates in the near infrared region ( $\lambda = 1.064 \mu\text{m}$ ). The fiber laser is characterized by high quality beam, high efficiency and low maintenance costs. The system has by high precision and good positioning accuracy. A general view of the laser technology system with which the experiments were performed is given in Fig. 1. Its main parameters are presented in Table 2.

TABLE 2 CHARACTERISTICS OF THE LASER SYSTEM

Parameters	Values
Wavelength $\lambda$ , $\mu\text{m}$	1.064
Power $P$ , W	20
Frequency $\nu$ , kHz	1 ÷ 200
Speed $v$ , mm/s	1 ÷ 2000
Focal length $f$ , mm	254
Spot diameter $d$ , $\mu\text{m}$	60
Positioning accuracy, $\mu\text{m}$	2.5
Efficiency, %	40

## III. METHODOLOGY OF EXPERIMENTS

Samples of cold-rolled steel sheet AISI 304 with a thickness of 0.8 mm were used for the experiment.

- Samples were prepared in a rectangular shape with dimensions of 100 mm × 65 mm (see Fig. 2);
- Before starting the laser marking process, the polymer film protecting the surface was removed from the samples, after which the surface was washed with isopropyl alcohol;
- The working field consists of 5 rows of 8 square modules with dimensions of 10 mm × 10 mm and a distance of 2 mm between them. An example change of the working parameters is shown in Fig. 2;
- The matrices are captured with a scanning device, the contrast  $k^*$  is determined from the grayscale images by the formula (1)

$$k_x^* = \frac{N_f - N_x}{N_f} \cdot 100\% \quad (1)$$

where  $N_f$  is the darkening value reported for the background and  $N_x$  is the darkening value reported for the particular square.

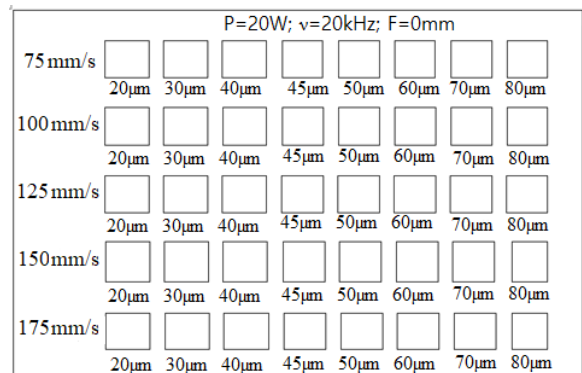


Fig. 2. Sample matrix on which the experiments are performed.

#### IV. RESULTS

The pre-prepared samples were raster marked with the fiber laser. Contrast was then determined using the gray scale for each square. The following tasks were performed:

##### A. Investigation of the influence of raster pitch on contrast

The raster step was varied in the interval  $\Delta x \in [20, 80] \mu\text{m}$ . The quantities that remained constant are given in Table 3. The resulting images for a speed of 75 mm/s are presented in Fig. 3. From the obtained data, a graphics of the dependence of the contrast  $k^*$  on the raster step  $\Delta x$  for three marking speeds 75 mm/s, 125 mm/s and 125 mm/s were drawn (see Fig. 4). The following conclusions may be made:

- As the raster step increases, contrast decreases;
- In the interval of the raster step  $\Delta x \in [20, 80] \mu\text{m}$ , the contrast changes in the interval  $k^* \in [68, 48] \%$  for a speed of 75 mm/s;
- In the interval of the raster step  $\Delta x \in [20, 80] \mu\text{m}$ , the contrast changes in the interval  $k^* \in [64, 42] \%$  for a speed of 125 mm/s;
- In the studied interval of the raster step, the contrast changes in the interval  $k^* \in [60, 36] \%$  for a speed of 175 mm/s.
- The rate of contrast change is  
 0.33 %/ $\mu\text{m}$  for speed 75 mm/s;  
 0.37 %/ $\mu\text{m}$  for speed 125 mm/s;  
 0.40 %/ $\mu\text{m}$  for speed 175 mm/s.
- The working intervals of the raster step are  
 $\Delta x \in [20, 76] \mu\text{m}$  for speed 75 mm/s;  
 $\Delta x \in [20, 63] \mu\text{m}$  for speed 125 mm/s;  
 $\Delta x \in [20, 47] \mu\text{m}$  for speed 175 mm/s.

TABLE 3 QUANTITIES THAT DO NOT CHANGE DURING THE EXPERIMENTS

Parameters	Values
Power $P$ , W	20
Frequency $\nu$ , kHz	20
Speed $v_1$ , mm/s	75
$v_2$ , mm/s	125
$v_3$ , mm/s	175
Spot diameter $d$ , $\mu\text{m}$	60
Number of repetition $N$	1
Defocus $\Delta f$ , mm	0

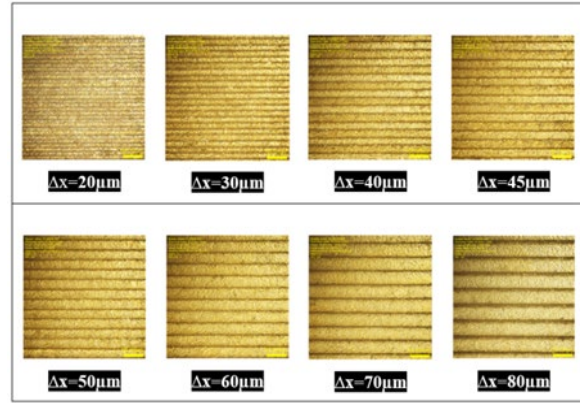


Fig. 3. Obtained images from laser raster marking for a speed of 75 mm/s and a raster step of 20  $\mu\text{m}$  to 80  $\mu\text{m}$ .

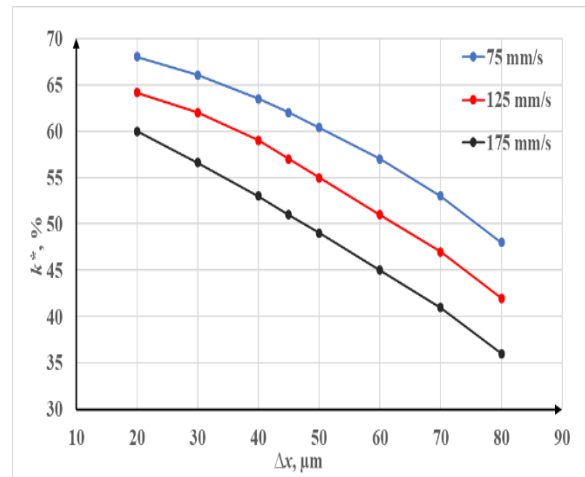


Fig. 4. Experimental graphics of the dependence of the contrast on the raster step.

##### B. Investigation of the influence of speed on contrast

The marking speed was varied in the interval  $v \in [25, 175] \text{mm/s}$ . The quantities that remained constant are given in Table 4. From the obtained data, a graphics of the dependence of the contrast  $k^*$  on the speed  $v$  for three raster steps 20  $\mu\text{m}$ , 45  $\mu\text{m}$  and 80  $\mu\text{m}$  were drawn (see Fig. 5). The following conclusions may be made:

- As the speed increases, contrast decreases;
- In the interval of the speed  $v \in [25, 175] \text{mm/s}$ , the contrast changes in the interval  $k^* \in [72, 60] \%$  for a raster step of 20  $\mu\text{m}$ ;
- In the interval of the speed  $v \in [25, 175] \text{mm/s}$ , the contrast changes in the interval  $k^* \in [66, 51] \%$  for a raster step of 45  $\mu\text{m}$ ;
- In the studied interval of the speed, the contrast changes in the interval  $k^* \in [52, 36] \%$  for a raster step of 80  $\mu\text{m}$ .
- The rate of contrast change is  
 0.08 %/(mm/s) for raster step 20  $\mu\text{m}$ ;  
 0.10 %/(mm/s) for raster step 45  $\mu\text{m}$ ;  
 0.11 %/(mm/s) for raster step 80  $\mu\text{m}$ .

- The working intervals of the speed are  $v \in [25, 175]$  mm/s for raster step  $20 \mu\text{m}$ ;  
 $v \in [25, 175]$  mm/s for raster step  $45 \mu\text{m}$ ;  
 $v \in [25, 50]$  mm/s for raster step  $80 \mu\text{m}$ .

TABLE 4 QUANTITIES THAT DO NOT CHANGE DURING THE EXPERIMENTS

Parameters	Values
Power $P$ , W	20
Frequency $\nu$ , kHz	20
Raster step $\Delta x_1$ , $\mu\text{m}$	20
$\Delta x_2$ , $\mu\text{m}$	45
$\Delta x_3$ , $\mu\text{m}$	80
Spot diameter $d$ , $\mu\text{m}$	60
Number of repetition $N$	1
Defocus $\Delta f$ , mm	0

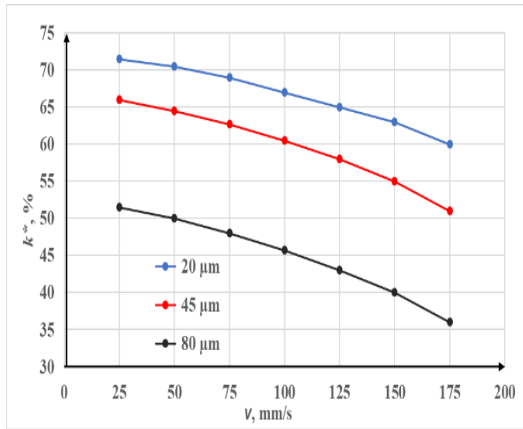


Fig. 5. Experimental graphics of the dependence of the contrast on the speed.

C. Investigation of the influence of frequency on contrast

The frequency was varied in the interval  $\nu \in [20, 200]$  kHz. The quantities that remained constant are given in Table 5. From the obtained data, a graphics of the dependence of the contrast  $k^*$  on the frequency  $\nu$  for three marking speeds 75 mm/s, 125 mm/s and 175 mm/s were drawn (see Fig. 6). The following conclusions may be made:

- As the frequency increases, contrast also decreases;
- In the interval of the frequency  $\nu \in [20, 200]$  kHz, the contrast changes in the interval  $k^* \in [68, 79]$  % for a speed of 75 mm/s;
- In the interval of the frequency  $\nu \in [20, 200]$  kHz, the contrast changes in the interval  $k^* \in [64, 72]$  % for a speed of 125 mm/s;
- In the studied interval of the speed, the contrast changes in the interval  $k^* \in [60, 65]$  % for a speed of 175 mm/s.
- The rate of contrast change is 0.061 %/(kHz) for speed 75 mm/s;  
0.044 %/(kHz) for speed of 125 mm/s;  
0.029 %/(kHz) for speed of 175 mm/s.

TABLE 5 QUANTITIES THAT DO NOT CHANGE DURING THE EXPERIMENTS

Parameters	Values
Power $P$ , W	20
Speed $v_1$ , mm/s	75
$v_2$ , mm/s	125
$v_3$ , mm/s	175
Spot diameter $d$ , $\mu\text{m}$	60
Number of repetition $N$	1
Defocus $\Delta f$ , mm	0

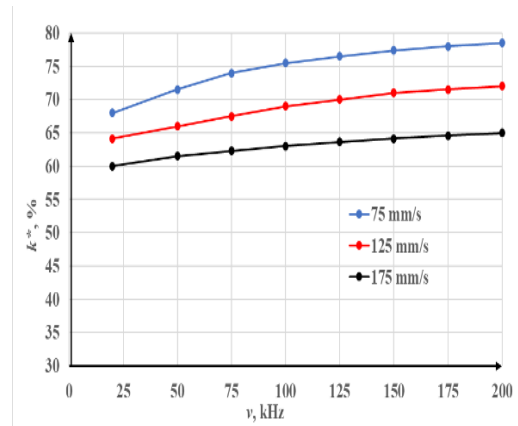


Fig. 6. Experimental graphics of the dependence of the contrast on the frequency.

D. Investigation of the influence of effective energy on contrast

The effective energy was varied in the interval  $E_{eff} \in [6, 388]$  kJ/cm<sup>2</sup>. From the obtained data, a graphic of the dependence of the contrast  $k^*$  on the effective energy  $E_{eff}$  was drawn (see Fig. 7). The following conclusions may be made:

- As the effective energy increases, contrast increases;
- In the interval of the speed  $E_{eff} \in [6, 388]$  kJ/cm<sup>2</sup>, the contrast changes in the interval  $k^* \in [6, 70]$  %;
- The rate of contrast change is 1.45 %/(kJ/cm<sup>2</sup>) for interval  $E_{eff} \in [6, 46]$  kJ/cm<sup>2</sup>;  
0.017 %/(kJ/cm<sup>2</sup>) for interval  $E_{eff} \in [46, 388]$  kJ/cm<sup>2</sup>;
- The working interval of the speed is  $E_{eff} \in [18, 388]$  kJ/cm<sup>2</sup>.

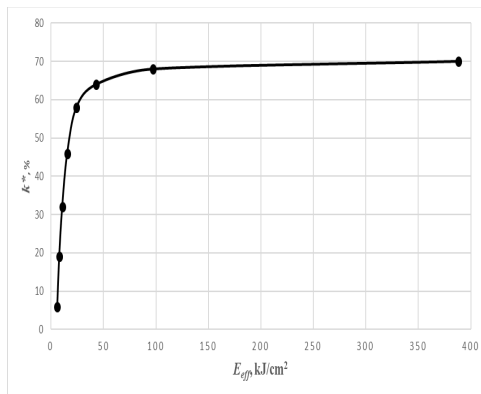


Fig. 7. Experimental graphics of the dependence of the contrast on the effective energy.

## V. CONCLUSION

Fiber laser marking experiments were performed on stainless steel samples. The influence of raster pitch, frequency, speed, and effective energy on labeling contrast was investigated. The obtained graphic dependencies of:

- the contrast  $k^*$  from the speed  $v$  of processing;
- the contrast  $k^*$  from the frequency  $\nu$  of pulses;
- the contrast  $k^*$  from the raster step  $\Delta x$ ;
- the contrast  $k^*$  from the effective energy  $E_{eff}$ ,

can be used to create technological tables defining the optimal limits of the investigated process for marking contrast satisfying the user's requirements.

The obtained results are useful for operators of laser technology systems working in production.

## VI. ACKNOWLEDGEMENT

The authors gratefully acknowledge financial support by the European Regional Development Fund, Postdoctoral research aid Nr. 1.1.1.2/16/I/001 research application "Analysis of the parameters of the process of laser marking of new industrial materials for high-tech applications, Nr. 1.1.1.2/VIAA/3/19/474".

## REFERENCES

[1] T. W. Ng, S. C., Yeo, Aesthetic laser marking assessment, *Optics & Laser Technology*, Volume 32, Issue 3, pp. 187-191, April 2000, DOI: [https://doi.org/10.1016/S0030-3992\(00\)00040-2](https://doi.org/10.1016/S0030-3992(00)00040-2)

[2] N. G. Henriksen., Z. O. Andersen, and S. M. Jellesen, Christiansen T. L., Somers A. J., Influence of Laser Marking on Microstructure and Corrosion Performance of Martensitic Stainless Steel Surfaces

for Biomedical Applications, *Journal of Heat Treatment and Materials*, June 21 2022, DOI: <https://doi.org/10.1515/htm-2022-1010>

[3] F. Bravo-Montero, D. Castells-Rufas, and J. Carrabina, High-Speed Laser Marking with Diode Arrays, *Optics and Laser Technology*, Volume 146, 107551, February 2022, DOI: <https://doi.org/10.1016/j.optlastec.2021.107551>

[4] L. Sobotova, M. Badida, Laser marking as environment technology, *Open Engineering*, 7:303-316, 2017, DOI: <https://doi.org/10.1515/eng-2017-0030>

[5] Ts. Zlateva-Petkova., Planning and forecasting future demand for employees, International Conference "Economics and management – based on new technologies", EMoNT 2016, Vrnjacka Banja, Serbia, pp. 401-406, 16-19 June 2016, ISBN: 978-86-6075-059-6

[6] D. Dichev, I. Zhelezarov, and G. Cvetanov, "Algorithm for estimation and correction of dynamic errors," 30th International Scientific Symposium Metrology and Metrology Assurance, MMA September 7 -11 2020, Sozopol, Bulgaria, 2020, DOI: 10.1109/MMA49863.2020.9254261

[7] X. Maa, X. Niea, and J. Guoa, Effect of nanosecond pulsed laser parameters on the color making of 304 stainless steel, *Optics & Laser Technology*, 106104, 2020, DOI: <https://doi.org/10.1016/j.optlastec.2020.106104>

[8] S. J. Foster, K. Carver, and S. S. Babu, Process-defect-structure-property correlations during laser powder bed fusion of alloy 718: role of in situ and ex situ characterizations, *Metallurgical and Materials Transactions*, 49:5775-98., 2018; DOI: <https://www.doi.org/10.1007/s11661-018-4870-2>

[9] A. H. Maamoun, Y. F. Xue, and S. C. Veldhuis, Effect of Selective Laser Melting Process Parameters on the Quality of Al Alloy Parts: Powder Characterization, Density, Surface Roughness, and Dimensional Accuracy, *Materials*, 11(12), 2018, DOI: 10.3390/ma11122343

[10] C. Leone, S. Genna, and I. D. Iorio, AISI 304 stainless steel marking by a Q-switched diode pumped Nd:YAG laser, *Journal of Materials Processing Technology* 210, pp. 1297-1303, 2010, DOI: <https://doi.org/10.1016/j.jmatprotec.2010.03.018>

[11] X. Maa, X. Niea, and J. Guoa, Coloring stability analysis of nanosecond pulsed laser induced surface coloring on stainless steel, *Optics and Laser Technology*, 123, 105936, 2020, DOI: <https://doi.org/10.1016/j.optlastec.2019.105936>

[12] H. Oh., J. Kim., and M. Lee, Structural coloration of stainless steel with planar thin-film surface cavity structure, *Optical Materials*, 100, 109547, 2020, DOI: <https://doi.org/10.1016/j.optmat.2019.109547>

[13] J. Penidea, F. Quinteroa, and J. Poua, High contrast laser marking of alumina *Applied Surface Science*, 336, pp. 118-128, 2015, DOI: <http://dx.doi.org/10.1016/j.apsusc.2014.10.004>

[14] Y. Arshad, R. Lingamm, and A. Qaban, Laser Surface Modification of Duplex Stainless Steel 2205 to Modify the Surface Roughness, *International Journal of Automotive and Mechanical Engineering (IJAME)*, Volume18, Issue 2, pp. 8695-8703, 2021, DOI: <https://doi.org/10.15282/ijame.18.2.2021.07.0663>

[15] R. Cottam, Laser Materials Processing for Improved Corrosion Performance, *Environmental and Industrial Corrosion - Practical and Theoretical Aspects*, pp. 3-18, 2012, DOI: <http://dx.doi.org/10.5772/52423>

# Comparative Analysis of Methods for Measuring Laser Power

**Tsanko Karadzhov**  
Technical University of Gabrovo  
Gabrovo, Bulgaria  
karadjov\_st@abv.bg

**Lyubomir Lazov**  
Rezekne Academy of Technologies  
Rezekne, Latvia  
llazov@abv.bg

**Abstract.** The application of lasers in many fields of technology and medicine is constantly increasing. This causes the development of new physical methods and principles for correct measurement of power, energy, and other parameters of laser sources. In most cases, the correct measurement of the laser power is important because the quality of the processes in which laser sources are used depends on it. In the paper, a comparative analysis of the existing methods for measuring the power and energy of laser radiation of diverse types of laser sources is made. This research aims to help users of laser equipment to choose the right measurement method depending on the laser source.

**Keywords:** laser power, measurement methods, types of measuring devices, physical principles.

## I. INTRODUCTION

The main parameter it requires control during laser processing is the power of laser radiation and its stability during the technological operation. Currently, many methods have been developed to measure the power of laser radiation because in recent years, the laser industry has developed extremely fast, with more new laser sources with new wavelengths, higher power and energy, frequencies, and modes of operation. For measurement, the power of laser radiation is necessary radiation receiver, which converts radiation into an electrical signal subject to measurements [12]. The existing radiation receivers work on various physical principles, but the most distribution received photoelectric and thermal receivers. The result and the quality for each specific laser technology such as laser welding, cutting, marking, engraving, drilling, etc. depend on many factors, including laser power therefore its measurement and control is important.

## II. CLASSIFICATION OF LASER POWER MEASUREMENT METHODS

In fig. 1 shows the classification of methods for measuring laser power. Nowadays, a wide range of high precision laser power meters are available, suitable for all professional users, some of which require high measurement accuracy. The large ranges of power and energy to be measured require a considerable number of devices because the range of any one device is relatively limited but there are already also measuring devices that are relatively insensitive to wavelength, because the greater the useful range, the less devices need to be designed, tested, calibrated, and maintained. An advantage of calorimeters, which convert radiant energy into heat and measure the amount of heat, is that they can be designed to work over a wide range of wavelengths. There are companies on the market that offer universal laser power meters capable of measuring powers from 100  $\mu$ W to 200 W over a wide wavelength range from 250 nm to 11  $\mu$ m. Such a meter is suitable for measuring the power of both CW and pulse lasers such as diode lasers, dye lasers, CO<sup>2</sup> lasers, HeCd lasers, Nd:YAG lasers and others. The operating conditions also affect the measurement. Single pulses usually require an energy measurement and CW lasers require power measurement. In some cases, it is necessary to use high-speed laser power measurement devices [6]. What has been said so far defines the wide variety of methods and principles for measuring laser power – fig. 1.

Print ISSN 1691-5402  
Online ISSN 2256-070X

<https://doi.org/10.17770/etr2023vol3.7252>

© 2023 Tsanko Karadzhov, Lyubomir Lazov. Published by Rezekne Academy of Technologies.  
This is an open access article under the [Creative Commons Attribution 4.0 International License](https://creativecommons.org/licenses/by/4.0/).

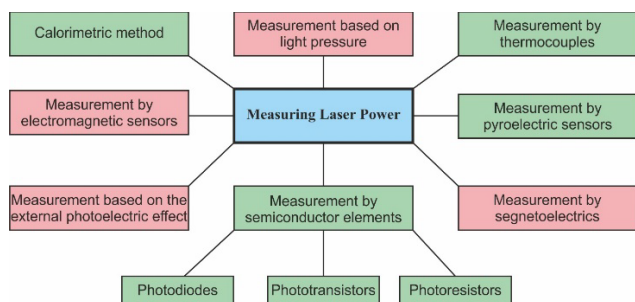


Fig. 1. Classification of methods for measuring laser power.

### III. METHODS FOR MEASURING THE POWER OF LASER RADIATION

#### A. Thermocouple laser power meter

The thermopile consists of a central, light-absorbing disk, thermocouples that surround this disk, and an annular heat sink around the ring of thermocouples – fig. 2. Laser energy falls on the absorbent disc and is converted into heat [2]. The heat then passes through the disk from the thermopile to the radiator, which is supported at a constant ambient temperature by forced cooling. The temperature difference between the absorber and heat sink is converted into an electrical signal by the thermocouples, then an electronic system converts this signal into a laser power reading.

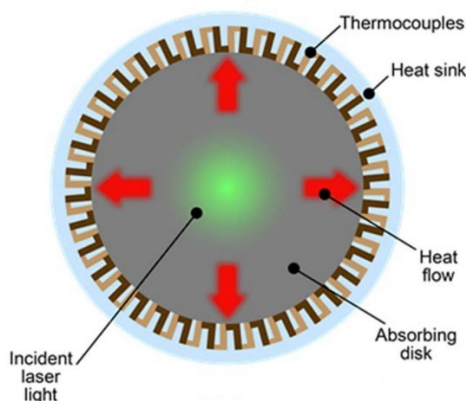


Fig. 2. Construction of thermopile.

Thermocouple sensors have the following advantages, wide spectral range, operation in a wide power range, high damage-resistance when measuring powerful laser radiations.

#### B. Measurement of laser power with pyroelectric sensors

The operation of pyroelectric receivers is fundamentally on the occurrence of charges on special faceted noncentrosymmetric crystals at temperature changes.

The output signal of pyroelectric receivers is proportional to the rate of change of the temperature of the sensitive element, which determines their high speed and rapid action – fig. 3. When a light pulse hits the absorbing surface of the detector, it heats up and polarizes the crystal, thereby creating an equal and opposite charge on both

surfaces of the detector. The surface of the detector is metallized, so the charge is collected on the parallel capacitor, regardless of where the laser beam falls on the surface [5]. Therefore, the charge on the capacitor is proportional to the pulse energy. After the pulse ends, the capacitor voltage is measured by an analog-to-digital converter and then the capacitor is discharged to measure the energy of the next pulse. The advantages of pyroelectric receivers are high speed and sensitivity. The main disadvantage is the need for modulation when measuring continuous radiation. For this reason, pyroelectric detectors are particularly suitable for measuring pulse energy in pulsed lasers. They can measure up to several thousand pulses per second and at the same time are quite sensitive. Their disadvantage is that they are not particularly durable, and for this at higher energies and powers, an optical filter is placed in front of the sensor crystal to reduce the energy on the pyroelectric crystal. Pyroelectric sensors for pulse energy measurement are now available that use an innovative technology that allows pulse measurements over a wide range, from long pulses up to 20 ms to pulses with repetition rates up to 25 kHz.

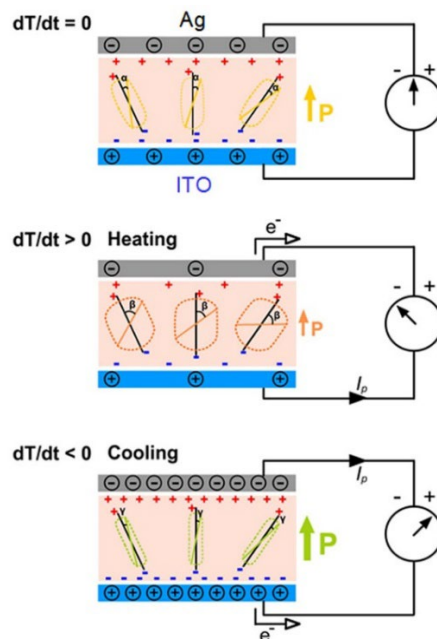


Fig. 3. Pyroelectric detectors [8].

#### C. Colorimetric sensors for laser power measuring

The calorimetric method is based on the thermal effect of optical radiation. Laser calorimetry is the measurement of laser power or energy by measuring the increase in temperature of an optical absorber irradiated by a laser beam. Radiation falls on the optical absorber, under the influence of which the temperature of the optical absorber changes [1]. By measuring the difference in the temperature of the absorber compared to the ambient temperature, one can find the energy or power of the incident radiation. Instruments that measure energy parameters of lasers in this way are called calorimeters [3]. The absorbers of the calorimeter, as a rule, are devices that are types of black bodies, for example, a cone blackened inside. At the top of the cone is a fast-acting temperature

sensor, such as a semiconductor bolometer or a thermistor, whose resistance changes with temperature. The absorber can also be made in the form of a sphere, inside which there is an insulated wire, the resistance of which changes under the influence of the thermal effect of radiation. There are calorimeters hold two absorbers, one of which is under the action of ambient temperature, and the measured radiation falls on the other. The absorbers must be identical. In this case, they are measured not the absolute values of the temperatures of the absorbers are measured, but their difference, which significantly increases the accuracy of measurements. These are the so-called differential calorimeters. The operation of the calorimeter can be described using the simplified equation for heat conduction:

$$mc \frac{dT}{dt} + \alpha S \Delta T = \Phi \quad (1)$$

where  $m$  is the mass of the absorber;  $c$  – specific heat capacity;  $\alpha$  is the coefficient of heat exchange between the absorber and the environment;  $S$  is the surface area through which heat exchange occurs;  $\Delta T$  is the temperature difference between the absorber and the environment [16].

#### D. Laser power measurement with photodiodes

The photodiode measurement principle is one of the most common methods for measuring the power of laser radiation. Photodiode sensors convert incident laser photons into charge carriers (electrons and holes), which are then measured as voltage or current. The action of the photodiode is based on increasing the reverse current of the p-n junction when it is illuminated, which is practically used to measure the intensity or power of laser radiation. Measuring the power of laser radiation with photodiodes has several advantages. They have low noise and high sensitivity, which allows them to be used in measuring of lasers with extremely low radiation power. The photodiode has the fastest response of all optoelectronic photodetectors, which is also its greatest advantage. It can be used to measure fast-changing laser radiation. The photodiode can work in two modes – photoconductive (fig. 4) and photovoltaic (fig. 5) mode, and both modes can be used to measure the intensity of laser radiation. To measure the power of pulsed lasers, so-called PIN photodiodes are used, which have a greater speed than traditional photodiodes with a PN transition [10].

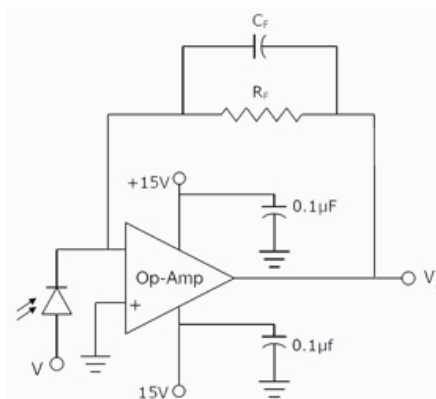


Fig. 4. Photoconductive mode [9].

Most laser power measurement circuits use light to voltage converter at which the output voltage is proportional to the luminance over the active area of the photodiode created by the laser beam fig. 4 and fig. 5. The other important advantage when measuring with photodiodes is that they have a linear light-to-current conversion characteristic, which allows more correct measurements to be made. There are also power meters that use light to frequency converter with a photodiode at the input in which the number of pulses per unit time is proportional to the power of the laser radiation.

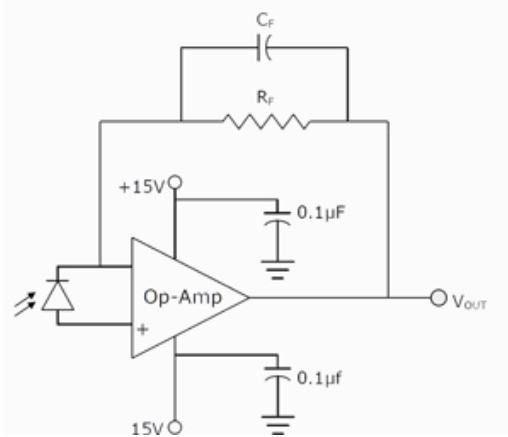


Fig. 5. Photovoltaic mode [9].

#### IV. COMPARATIVE ANALYSIS OF LASER RADIATION POWER MEASUREMENT METHODS DEPENDING ON THE TYPE AND POWER OF THE LASER

##### A. Criteria for choosing a method for measuring the power of laser radiation

Choosing a sensor and method to measure laser power or pulsed laser energy is an essential and important task. When choosing a type of device to measure, it is not always enough to know only the power range of the device and the laser, but also to consider other important characteristics of the laser that can help to choose the right method and measuring device [4]. Considering besides the power and some other important characteristics of the laser source, the choice of the most appropriate device can be optimized for accurate and correct measurements of laser power or energy without causing damage to the measuring device for a long time.

We will look at the choice of measurement method in a few steps.

1. To select the correct method for measuring laser power or energy, the operating characteristics of the laser source must be known. The wavelength of the laser must be known because there are measurement devices that can only be used to measure the power of lasers with specific wavelengths, i.e., have a narrow measurement range. Beam diameter - on which the power or energy will be measured, is the next essential element. This parameter will determine the size of the sensor's sensitive area and whether it is necessary to use optical extension lenses for the corresponding length of the laser source. One should not

choose to measure the power or energy at the focal point of the laser beam. It is recommended that the measurement sensor be positioned either before or after the laser focus point.

It is also important to know whether the laser is CW or pulsed and whether power or pulse energy will be measured.

CW Lasers – Continuous wave lasers are measured using average power from  $\mu\text{W}$  to kW. When choosing a device to measure CW laser power, one must consider what the average power will be measured. If the laser power variation range is too large, two different measurement sensors may be needed. One for low and the other for high laser power. It is important to choose a device where the power of the laser source is close to the middle of the device's measurement range, not at the lower or upper end of the range, as that is where the sensors have the highest measurement accuracy.

CW Laser – Exposure Time. Another criterion when choosing a device is to know the duration during which the laser beam will be on the sensor. Are only periodic measurements needed or will the laser beam be on the sensor the entire time the laser is running. If the laser beam hits the sensor all the time, either a larger sensor with air fins or one with a built-in fan to continuously cool the sensor will be needed.

Pulsed Lasers. With pulsed lasers, it is important to determine the energy of the pulses to be measured and from there select a measuring device with the appropriate range.

Pulse Width. The determination of the pulse width can also influence the choice of a suitable measurement device, as this parameter can reach the sensor's destruction threshold although the average laser power is less and lies within the measurement range of the device.

Pulse Rate. Another parameter to consider is the pulse repetition rate. From here it can be understood whether a device to measure the pulse energy is needed or whether a device to measure the average power of the laser source will be used. There are already pulse energy sensors on the market that can work up to 20 kHz pulse repetition rate.

2. The type of measurement to be performed must be specified.

Average Power. With most lasers, regardless of whether they are CW or pulsed, a measuring device can be used to measure the power of the laser radiation and as a result we will get a value for the average power of the laser. It is important to say that sensors that are designed to measure average power are slower. When measuring pulsed lasers with an average power sensor, there can be a discrepancy between the actual efficiency of the laser and the resulting measurement results since the energy characteristics of the pulses cannot be measured. When using a pulsed laser with a pulse repetition rate of a few kilohertz, is suitable to use a measuring device with a pyroelectric sensor that can measure the energy of each pulse is used and at even higher frequencies it is advisable to use photodiodes as measurement sensors. For powerful

lasers working in CW mode, it is best to use calorimetric measuring devices.

The main result of the comparative analysis is fixed in Table 1 which shows comparison of laser power measurements methods. This table can be useful when choosing a method and device for measuring the power of laser radiation depending on the most important parameters of laser sources.

TABLE 1 COMPARISON OF LASER POWER MEASUREMENT METHODS

Feature	<i>Thermo-pile</i>	<i>Photo-diode</i>	<i>Pyro-electric</i>	<i>Calori-meter</i>
<b>Spectral Range</b>	Broad-band	narrow band	narrow band	Broad-band
<b>Power Range</b>	Low to medium	Low	Low to medium	Very high
<b>Signal</b>	Voltage (V)	Current (A)	Voltage (V) or	Voltage (V)
<b>Response time</b>	High	Low	Low	High
<b>Wavelength dependent</b>	No	Yes	No	No
<b>Linear response</b>	Yes	Yes, up to saturation	--	--

## V. CONCLUSION

The aim of the paper is to be useful to engineers involved in laser technology in choosing a system for measuring the energy or power of laser radiation.

To achieve this aim in the paper, a comparative analysis of the most used methods for measuring the power of laser radiation is made, depending on the type and power of the laser and the accuracy of measurement. To determine the correct measurement system, it is very important to know which parameters of the laser radiation are to be measured. A methodology has been developed that covers the main criteria for choosing a method for measuring the laser power.

## REFERENCES

- [1] Y. Klimkov, M. Horoshev, Lazernaya Tehnika, Uchebnoe posobie – M.: MIIGAiK, 2014, UDK 621.375.826 (075.8).
- [2] S. Bergman, Laser power measurement: Time is money, Industrial laser solutionst for manufacturing, Santa Clara, CA.
- [3] D. A. Jennings, E. D. West, K. M. Evenson, A. L. Rasmussen, and W. R. Simmons, Laser Power and Energy Measurements, Nat. Bur. Stand. (U.S.), Tech. Note 382, 64 pages (Oct. 1969).
- [4] [Online]. Available: <https://www.ophiropt.com/laser--measurement/laser-measurement>
- [5] A. Shemyakin, M. Rachkov, M. Yakimov, Izmerenie moshtnosti lazernogo izluchenia tehnologicheskogo kompleksa s nesamostoyatelnyim tleyushtim razryadom, 2009, UDK 681.326.74.
- [6] Pulov, D., T. Karadzhov, Optoelectronic Device for Measuring the Power of Laser Radiation. Environment. Technology. Resources. Rezekne, Latvia, Proceedings of the 13th International Scientificand

- Practical Conference. Volume 3, 286-290, 2021, DOI: 10.17770/etr2021vol3.6590.
- [7] J. A. Hadler, C. L. Cromer, and J. H. Lehman, NIST Measurement Services: cw Laser Power and Energy Calibrations at NIST, NIST Special Publication (2007), Vol. 250–75.
- [8] [Online]. Available: <https://www.findlight.net/blog/laser-detectors-a-primer/>
- [9] [Online]. Available: <https://www.aptechnologies.co.uk/support/SiPDs/circuits>
- [10] Lazov, L., T. Karadzhov, Methods for Measuring Laser Power. Environment. Technology. Resources. Rezekne, Latvia, Proceedings of the 13th International Scientific and Practical Conference. Volume 3, 173-180, 2021, Online ISSN 2256-070X, DOI: 10.17770/etr2021vol3.6565.
- [11] I. Ryger and et al, “MEMS Non-Absorbing Electromagnetic Power Sensor Employing the Effect of Radiation Pressure,” in Proceeding at the Eurosensors, Graz, Austria, 2018, DOI: 10.3390/proceedings2130767.
- [12] N. Angelov, “Investigation the Influence of the Number of Repetition and Volumetric Energy Density on Laser Marking of Products,” Journal of the Academy of Sciences and arts of the Republic of Srpska „Contemporary Materials, vol. V, no. 2, pp. 250-253, 2014, DOI: 10.7251/cm.v2i5.1738.
- [13] K. Agatsuma, D. Friedrich, S. Ballmer, G. DeSalvo, S. Sakata, E. Nishida, and S. Kawamura, “Precise measurement of laser power using an optomechanical system,” Opt. Express 22(2), 2013–2030 (2014).
- [14] S. A. Kuznetsov, A. G. Paulish, M. Navarro-Cía and A. V. Arzhannikov, “Selective Pyroelectric Detection of Millimetre Waves Using Ultra-Thin Metasurface Absorbers,” Scientific Reports, vol. 6, 16 Feb 2016, DOI: 10.1038/srep21079.
- [15] P. Williams, J. A. Hadler, F. C. Maring, R. Lee, K. A. Rogers, B. J. Simonds, M. T. Spidell, A. D. Feldman and J. H. Lehman, “Portable, high-accuracy, non-absorbing laser power measurement at kilowatt levels by means,” Opt. Express , vol. 25, p. 4382–4392, 2017.
- [16] Dichev, D., I. Zhelezarov, N. Madzharov. Dynamic Error and Methods for its Elimination in Systems for Measuring Parameters of Moving Objects. Transactions of Famena, volume 45, issue 4, 2021, pp. 55-70, DOI: 10.21278/TOF.454029721.

# Investigation of Laser Marking and Texturing of Titanium Gr 2 with Fiber Laser

**Jēkabs Lapa**  
Rezekne Academy of Technologies  
Faculty of engineering  
Rēzekne, Latvia  
jekabs.lapa@gmail.com

**Imants Adijāns**  
Rezekne Academy of Technologies  
Faculty of engineering  
Rēzekne, Latvia  
imants.adijans@rta.lv

**Emil Yankov**  
Rezekne Academy of Technologies  
Faculty of engineering  
Rēzekne, Latvia  
emil.yankov@rta.lv

**Lyubomir Lazov**  
Rezekne Academy of Technologies  
Faculty of engineering  
Rēzekne, Latvia  
lyubomir.lazov@rta.lv

**Ritvars Rēvalds**  
Rezekne Academy of Technologies  
Faculty of engineering  
Rēzekne, Latvia  
ritvars.revalds@rta.lv

**Abstract.** Titanium Gr 2 is widely used in engineering and medicine due to its excellent mechanical and corrosion-resistant properties. Laser marking is a crucial process for many applications that require high-contrast, durable markings. In this study, we used a Rofin PowerLine F 20 Varia fiber laser to mark titanium Gr 2 with a 6x6 matrix of 5x5 mm squares. We varied the speed (100-1100 mm/s), power (8-18 W), and frequency (100 and 500 kHz) of the laser marking process to investigate their effects on the surface roughness and contrast of the markings. We analyzed the markings using a laser scanning microscope and Adobe Photoshop software. Our results show that the contrast and roughness of the markings were influenced by the frequency, scanning speed, and power. High marking speeds produced lighter markings, while low marking speeds produced darker markings. We also found that the surface roughness increased with higher frequency and powers. Our findings provide valuable insights into the optimal laser marking parameters for titanium Gr 2, which can enhance its performance and durability in various applications.

**Keywords:** Fiber laser, laser marking, laser texturing, laser parameter optimization, titanium.

## I. INTRODUCTION

Over the past two decades, lasers have increasingly replaced traditional processing methods in various industries due to their high quality and productivity, along with lower production costs [1].

Laser processing has become popular for marking, texturing, welding, and processing different types of materials, including metals and nonmetals [2], [3].

Comparing laser marking and texturing to other methods such as dot marking systems, CNC marking tools, sandblasting, etc., it is evident that laser marking has numerous advantages over other marking techniques, such as high marking speed, marking quality, and no need for post-processing [4].

Currently, there are many studies and scientific literature related to laser processing of various materials. For instance, researchers have studied the challenging fabrication of green color on titanium surface using laser irradiation and infrared temperature measurement [5], [6]. The method of changing the color of titanium using a laser involves the formation of oxidation layers or structures on the surface of the material so that the emitted light and the surface produce thin-layer diffraction to demonstrate the color change [7], [5].

Numerous researchers have investigated laser color marking on metals [8], [9]. To obtain the required colors, the thickness of the thin film oxide layer must meet certain parameters [10]. Relatively recently, researchers have paid attention to producing oxide layers on titanium surfaces using nanosecond fiber lasers in an atmospheric environment [11], [12].

The process of material texturing is similar to laser marking, where different material surface structure forms can be obtained by changing parameters such as scan speed, focus position, and pitch [13]. This can

Print ISSN 1691-5402

Online ISSN 2256-070X

<https://doi.org/10.17770/etr2023vol3.7251>

© 2023 Jēkabs Lapa, Imants Adijāns, Emil Yankov, Lyubomir Lazov, Ritvars Rēvalds.  
Published by Rezekne Academy of Technologies.

This is an open access article under the [Creative Commons Attribution 4.0 International License](https://creativecommons.org/licenses/by/4.0/).

induce shapes like grid, chaotic, dimpling, etc., resulting in an increase in the static adhesion resistance of the textured surface [14].

The purpose of this study is to provide insights into how the parameters of a pulsed (ns) fiber laser (wavelength 1064 nm) - power, frequency, and scanning speed - affect the results of laser marking and texturing of Gr 2 titanium.

## II. MATERIALS AND METHODS

### A. Material

The research was conducted on titanium grade 2 sheet sample with chemical element composition: Ti  $\geq$  98.9%, Fe  $\leq$  0.30%, O  $\leq$  0.25%, C  $\leq$  0.080%, N  $\leq$  0.030%, H  $\leq$  0.015%. The sample dimensions were 100x100x1 mm. The sample surfaces were cleaned with (C<sub>3</sub>H<sub>7</sub>OH) to remove all dirt and stains that could influence the results of the experiments to be performed.

### B. Laser setup

The experiments were performed using a pulsed fiber laser Rofin PowerLine F 20 Varia (Fig. 1) with a wavelength of 1064 nm, maximum power of 19 W, and variable pulse duration. The laser beam was focused using a 160 mm lens with a spot size of 40  $\mu$ m. The laser was controlled using a computer-controlled Galvano scanner with a scan field of 120x120 mm.



Fig. 1. Technological system with fiber laser Rofin PowerLine F20.

Specification of Rofin PowerLine F 20 Varia laser is shown in Table I.

TABLE I. CHARACTERISTICS OF THE LASER SYSTEM ROFIN POWERLINE F 20 VARIA

Parameter	Magnitude, Unit
Wavelength ( $\lambda$ )	1064 nm
Max. Power (P)	19 W
Max. Pulse Energy (E)	1 mJ
Scan Speed ( $v$ )	1 mm/s to 20000 mm/s
Pulse Width ( $\tau$ )	4 – 200 ns
Repetition Rate (F)	20 kHz to 1000 kHz

### C. Microscope setup

The surface roughness and structure changes of the marked titanium grade 2 (Ti Gr2) sample were examined using the Olympus LEXT OLS5000 3D Measuring Laser Microscope, as shown in Figure 2. The microscope was set to a magnification of x451, an accuracy of measurement of

0.4  $\mu$ m, a numerical aperture (N.A.) of 0.6, a working distance (W.D.) of 1 mm, a focal depth of 1.8  $\mu$ m, a focusing spot diameter of 0.82  $\mu$ m, and a measurement area of 640 X 640  $\mu$ m.



Fig. 2. Olympus LEXT OLS5000 3D Measuring Laser Microscope.

### D. Scanner

The contrast of the marked samples was scanned using an HP Scanjet G3010 scanner with a scanning area of 216 X 297 mm and a color depth of 48-bit. The scanning parameters were set to a resolution of 2400 DPI, brightness of 100, contrast of 80, and the file format used was .tif.

### E. Methodology

Laser marking was carried out using a fiber laser on Ti Gr 2 sample, size 100x100x1 mm. Before laser marking Ti Gr 2 sample was cut with a 1 kW fiber laser with a wavelength of 1064 nm. Before laser marking, the sample was thoroughly cleaned using isopropyl alcohol 99.8% (IPA) to remove any contaminants. Two matrices of 6 rows and 6 columns each were marked on the sample, which is 72 markings with different speed, power and frequency parameters and constant pulse duration of 4 ns. Experiments were conducted in ambient conditions without the use of any assist gases. The marking of Ti Gr 2 plate occurred between the three changing parameters: power  $P$  (W), scanning speed  $v$  (mm/s) and frequency  $F$  (kHz). Figure 3 shows the marking schematics of Ti Gr 2 samples.

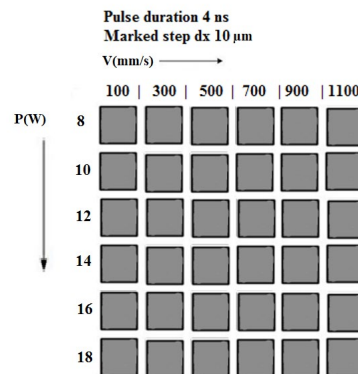


Fig. 3. Laser marking schematics of Ti Gr 2 samples.

The first matrix was marked between the values (Table II): marking speed  $v$  (mm/s), output power  $P$  (W) versus frequency at 100 kHz. For the other matrix, only the frequency has changed to 500 kHz.

TABLE II. FIBER LASER MARKING PARAMETERS FOR Ti GR 2 SHEET  
 SAMPLE AT 100 KHZ

Parameter	Magnitude, Unit
Pulse Duration ( $\tau$ )	4 ns
Output Power (P)	8/10/12/14/16/18 W
Scanning Speed (v)	100/300/500/700/900/1100 mm/s
Square Size	5×5 mm
Frequency (F)	100 kHz

The formula (1) was used to calculate the percentage, which is equal to the power, because in the used fiber laser the unit of measurement of power is entered in percentage.

$$P(\%) = \frac{100\% * P(W)}{P_{max}(W)} \quad (1)$$

Were  $P_{max}(W)$  = maximum laser power in watts and  $P(W)$  = power (in watts) used for each laser marking. The calculated power values in watts, corresponding to the power values in percent, are shown in table III.

TABLE III. POWER VALUES IN WATTS, CORRESPONDING TO THE POWER VALUES IN PERCENT

<b>P (%)</b>	41.7	52.1	62.5	72.9	83.3	93.8
<b>P (W)</b>	8	10	12	14	16	18

The contrast  $k_x$  is a percentage value [15]. To calculate  $k_x$ , we need to determine  $N_f$  volume of the unmarked area. On the other hand,  $N_x$  value of the laser marked area can be obtained directly from the marked area. The formula used to determine  $k_x$  is given by Equation (2):

$$k_x = \frac{N_f - N_x}{N_f} \times 100\% \quad (2)$$

To express the difference between two measured colors in the CIE color uniform space, we use the CIE color difference  $L^* a^* b^*$  formula [16], [17]. The total color difference  $N_x$  between two points in three-dimensional color space is expressed using Equation (3):

$$N_x = \sqrt{(\Delta L_x)^2 + (\Delta a_x)^2 + (\Delta b_x)^2} \quad (3)$$

Similarly, the total color difference  $N_f$  is expressed using Equation (4):

$$N_f = \sqrt{(\Delta L_f)^2 + (\Delta a_f)^2 + (\Delta b_f)^2} \quad (4)$$

In these equations,  $\Delta L$ ,  $\Delta a$ , and  $\Delta b$  represent the differences in lightness/darkness, red-green, and blue-yellow color channels, respectively, taken from the marked areas  $L$ ,  $a$ , and  $b$  using Adobe Photoshop color tool. The  $L$  channel refers to the lightness or darkness of the color, where  $L = 0$  represents black and  $L = 100$  represents white.

To ensure that all contrast values are positive, we take the absolute value ( $|k_x|$ ) of each calculated contrast value.

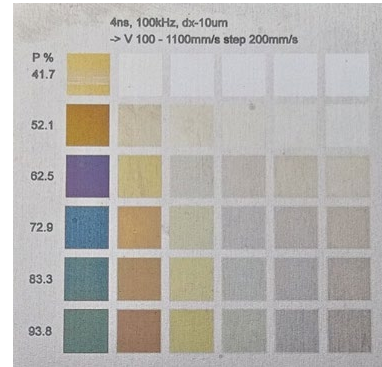
### III. RESULTS AND DISCUSSIONS

Laser treatment of Ti Gr 2 resulted in change of contrast (color marking) as well as surface roughness change, compared to untreated material. The data obtained for the marked samples of titanium Gr 2 are shown in Fig. 4. – Fig. 10.

#### A. Marking at 100 kHz

On Fig. 4 can be seen two Ti Gr 2 plates with laser markings at 100 kHz and 500 kHz frequency. Several color tones appear on both matrices. We can observe shades of gray, yellow, brown-orange, blue, purple, pink, and green. Laser color marking on Ti Gr 2 is a result of surface oxidation and chemical reaction between the titanium material and the surrounding air during laser treatment, which leads to the formation of a thin oxide layer with varying thicknesses and refractive indices, resulting in color contrast.

(a)



(b)

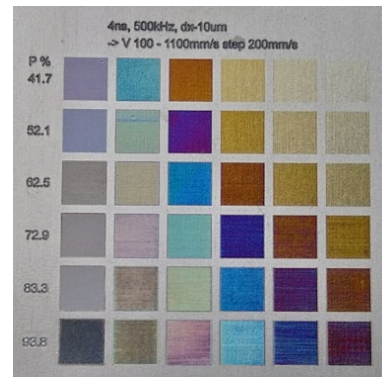


Fig. 4. Laser marked Ti Gr 2 plates with (a) 100 kHz and (b) 500 kHz frequency.

Figure 5 displays the contrast change in the laser marking at a frequency of 100 kHz. Contrast absolute value was calculated as a percentage of the difference between the marked and unmarked areas, where the unmarked area's contrast value  $N_f$  is 75.

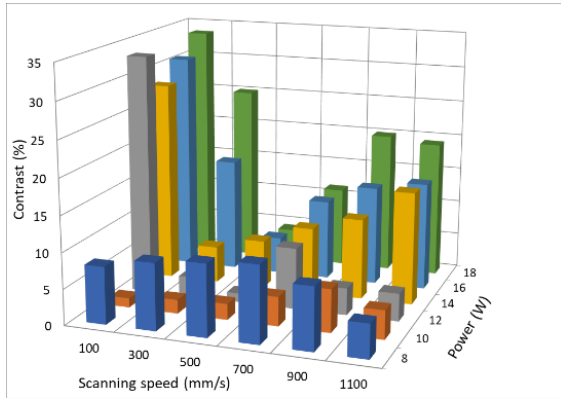


Fig. 5. Effect of power, scan speed and frequency (100kHz) on contrast absolute value change in Ti Gr 2 laser marking.

The obtained results showed that there is a clear correlation between the power and speed values and the contrast for Ti Gr 2 material. As can be seen from Fig. 5, increasing the power value from 8 W to 18 W generally led to an increase in contrast absolute values  $|k_x|$  (%). Similarly, increasing the speed value from 100 mm/s to 1100 mm/s generally resulted in a decrease in  $|k_x|$  values.

Further analysis of the obtained results reveals that the highest contrast  $|k_x|$  absolute values were achieved at the lowest speed value of 100 mm/s and the highest power value of 18 W. Specifically, a  $|k_x|$  absolute value of 33.57 % was obtained at the power of 18 W and speed of 100 mm/s. From the other hand, the lowest  $|k_x|$  absolute value of 1.24 % was observed at the scan speed of 500 mm/s and the power of 12 W. This demonstrates the importance of carefully selecting the power and speed values when aiming to achieve high contrast in laser marking of Ti Gr 2 material.

A sharp drop in contrast  $|k_x|$  was observed when scan speed was increased from 100 mm/s to 500 mm/s for power levels ranging from 12 W to 18 W. However, when the scan speed was further increased to 500-1100 mm/s, there was an increase in  $|k_x|$  values with a maximum of 19.98 % at a speed of 900 mm/s and power of 18 W.

It is worth noting that the contrast values obtained in this study were measured using Adobe Photoshop software, and thus reflect the visual contrast perceived by the human eye. Future studies could explore the correlation between the measured contrast values and other physical properties such as surface hardness.

Fig. 6 shows the effect of different scan speeds and power levels on the roughness of the marked Ti Gr 2 samples at a constant pulse duration of 4 ns and marking step of 10  $\mu\text{m}$ , with a frequency of 100 kHz.

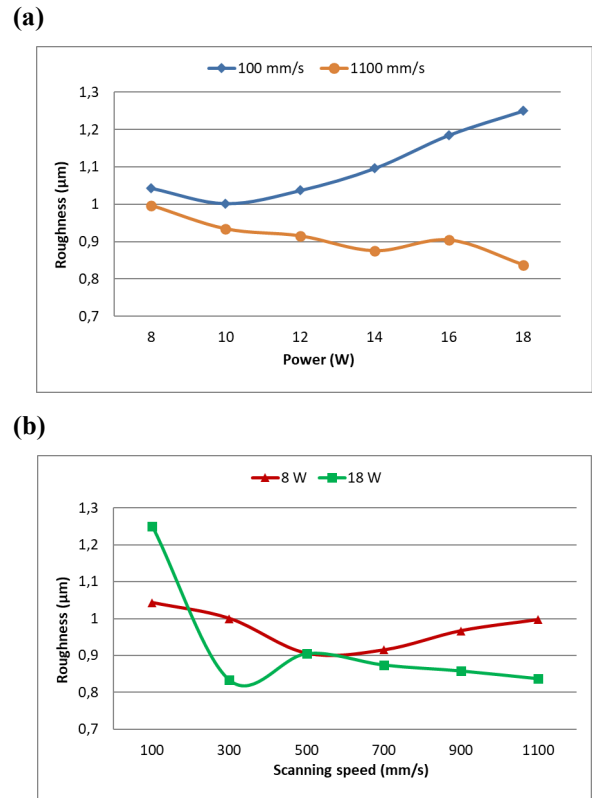


Fig. 6. Surface roughness ( $R_q$ ) of Ti Gr 2 marked samples at 100 kHz laser frequency, (a) varying power and (b) scanning speed.

The roughness of Ti Gr 2 surface after laser marking/treatment was measured using  $R_q$  parameter. The roughness values ranged from 0.8  $\mu\text{m}$  to 1.3  $\mu\text{m}$ , with an average value of 0.9  $\mu\text{m}$ . Roughness is little bit higher at power 18 W for all scan speeds, reaching its maximum value 1.3  $\mu\text{m}$  at scan speed of 100 mm/s.

It should be noted that the roughness of the non-marked Ti surface was measured to be 0.8  $\mu\text{m}$ , which is 0.1  $\mu\text{m}$  lower than the average roughness of the marked surface. It can be concluded that laser marking using these particular parameters on average slightly increases roughness of Ti Gr 2 surface.

Further studies are needed to investigate the relationship between laser marking parameters and surface roughness in more detail exploring the effects of different pulse durations or beam spot sizes on roughness. The roughness data can be used as a reference for future studies or for selecting appropriate laser marking parameters for Ti Gr 2 surfaces.

### B. Marking at 500 kHz

Fig. 7 shows the results of laser marking contrast change where are shown contrast  $|k_x|$  absolute values for different combinations of speed and power settings when marking a Ti Gr 2 plate with 500 kHz. The contrast absolute values range from 5.09 % to 59.51 %, with the highest contrast absolute value obtained at a speed of 100 mm/s and power of 18 W.

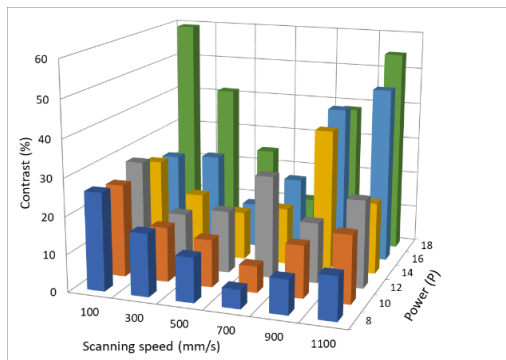


Fig. 7. Effect of power, scan speed and frequency (500 kHz) on contrast absolute value change in Ti Gr 2 laser marking.

At a fixed power setting, increasing the speed generally leads to a decrease in contrast, with the exception of the power setting of 12 W, where the contrast absolute value peaks at a speed of 700 mm/s before decreasing at higher speeds. At a fixed speed setting, increasing the power generally leads to an increase in contrast, with the exception of the speed setting of 700 mm/s, where the contrast absolute value peaks at a power of 12 W before decreasing at higher powers.

Overall, the highest contrast values are obtained at higher power settings and lower speed settings, indicating that higher energy input per unit area leads to better marking contrast on Ti Gr 2 plate at 500 kHz.

Fig. 8, 9 shows the effect of different scan speeds and power levels on the roughness of the marked Ti Gr 2 samples at a constant pulse duration of 4 ns and marking step of 10  $\mu\text{m}$ , with a frequency of 500 kHz.

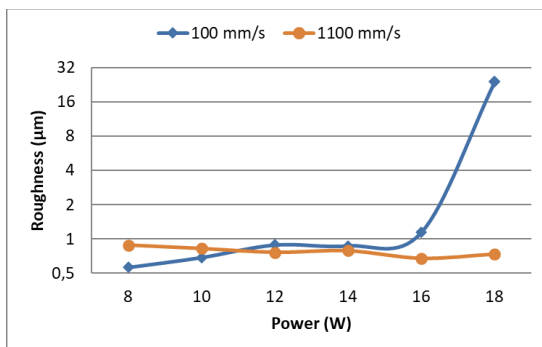


Fig. 8. Surface roughness ( $R_q$ ) of Ti Gr 2 marked samples at 500 kHz laser frequency with varying power.

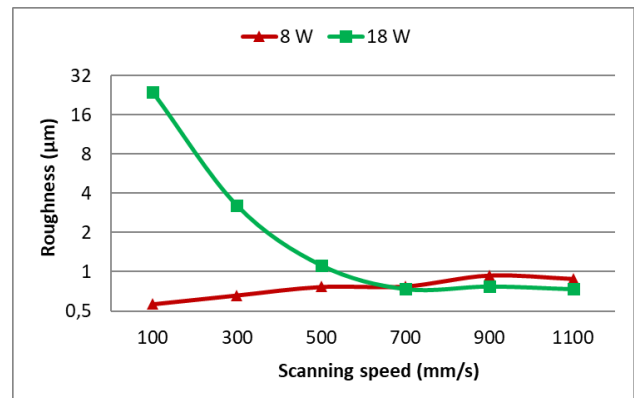


Fig. 9. Surface roughness ( $R_q$ ) of Ti Gr 2 marked samples at 500 kHz laser frequency with varying scanning speed.

From the Fig. 8, 9 we can observe that the roughness values vary significantly with changes in the marking speed and power. At lower marking speeds, the roughness values tend to be higher than at higher marking speeds, and the roughness values generally increase with increasing power. For example, at a marking speed of 100 mm/s, the roughness values range from 0.6  $\mu\text{m}$  to 23.8  $\mu\text{m}$ , while at a marking speed of 1100 mm/s, the roughness values range from 0.9  $\mu\text{m}$  to 0.7  $\mu\text{m}$ . It should be noted that the roughness of 23.8  $\mu\text{m}$  is a pronounced maximum, which is 7.4 to 39.7 times higher than the other roughness values. We can observe that the highest roughness values are obtained at the lowest marking speed and highest power levels, while the lowest roughness values are obtained at the lowest marking speed and power levels. This suggests that a trade-off needs to be made between the desired roughness level and the marking speed and power used.

Overall, the results of the roughness analysis suggest that the optimal marking conditions for achieving a desired roughness level would depend on the specific application requirements. The results can help guide the selection of marking speed and power levels for achieving the desired roughness level for a given application.

Fig 10. shows 3D and 2D laser scanning microscope images of the laser marking with the highest roughness of  $R_q = 23.8 \mu\text{m}$ . And on Fig. 11 can be seen visual color change and roughness change on Ti Gr 2 surface laser treated at specific power, scanning speed and frequency parameters, with constant step between scanning lines 10  $\mu\text{m}$  and constant pulse duration 4 ns.

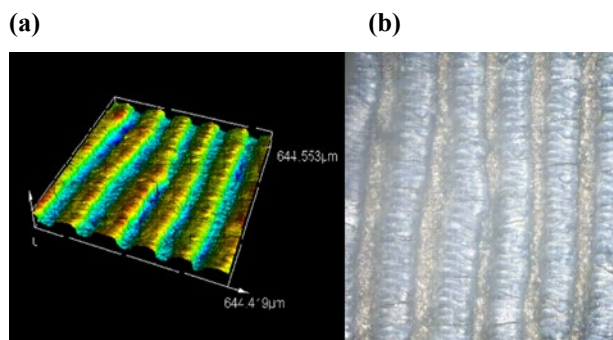


Fig. 10. Effect of laser parameter settings on surface roughness of Ti Gr 2 markings: (a) 3D laser scanning microscope image of marking with the highest roughness ( $R_q = 23.8 \mu\text{m}$ ), (b) corresponding 2D laser scanning microscope image.

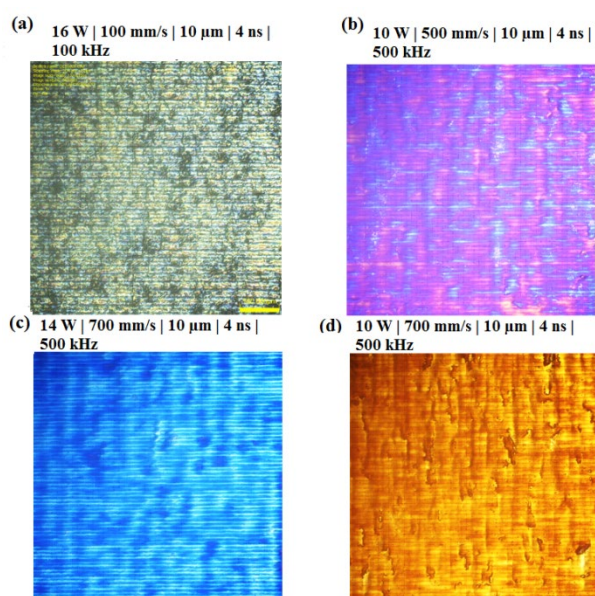


Fig. 11. Color and roughness change on Ti Gr 2 after laser treatment at specific parameters.

Our findings are consistent with the results of Johnson and Lee [18], who used a similar laser marking technique to mark titanium alloys and observed a significant influence of laser power and speed on the contrast and roughness of the markings. The results of our study are in agreement with the findings of Smith et al. [19], who also investigated the effect of laser marking parameters on titanium Gr 2 using a fiber laser.

Several studies have reported that the choice of laser parameters can have a significant impact on the surface properties of titanium and other metals (Chen et al., [20]; Wang et al., [21]). Our results support these findings, highlighting the importance of optimizing laser parameters for specific applications.

The findings presented in this study have important implications for the development of high-quality laser marking processes for Ti Gr 2, which is widely used in aerospace, medical, and automotive industries. The marking conditions identified in this study can help

improve the quality and efficiency of laser marking processes for Ti Gr 2, which can ultimately lead to more reliable and durable products in these industries.

#### IV. CONCLUSION

We investigated the effects of varying laser marking parameters on the surface roughness and contrast of titanium Gr 2 markings. Our results show that the contrast and roughness of the markings are influenced by the laser marking parameters, including frequency, scanning speed, and power. Specifically, we found that high marking speeds result in lighter markings, while low marking speeds produce darker markings.

Our findings can help to guide the development of optimal laser marking parameters for titanium Gr 2, which can lead to more effective and efficient marking for a variety of applications. The optimal laser marking parameters identified in this study can be applied in industries that require high-quality and durable markings on titanium Gr 2, such as aerospace, medical, and automotive industries. Manufacturers and engineers can use the findings of this study to develop more efficient and effective laser marking processes for titanium Gr 2, ultimately leading to cost savings and improved product quality. Additionally, the results of this study can also serve as a guide for future research on laser marking of titanium and other metals. Overall, the use of a pulsed fiber laser for marking titanium Gr 2 has shown to be a promising technique for achieving high-quality markings with desired characteristics.

#### V. ACKNOWLEDGEMENTS

The authors gratefully acknowledge financial support by the European Regional Development Fund, Postdoctoral research aid Nr. 1.1.1.2/16/I/001 research application "Analysis of the parameters of the process of laser marking of new industrial materials for high-tech applications, Nr. 1.1.1.2/VIAA/3/19/474".

#### REFERENCES

- [1] G. Annamaria un B. Massimiliano, «Laser polishing: a review of a constantly growing technology,» *The International Journal of Advanced Manufacturing Technology (2022) 120:1433–1472*, pp. 1.-7., 2022.
- [2] O. Galina, S. Nadezhda un L. Darya, «Prospects of "Colorit" Technology of Color Laser,» *ResearchGate*, pp. 2.-4., 2021.
- [3] M.-F. a. F. a. Francisca, G. Bruno, G. Michael , S. Filipe un M. Georgina, «Experimental analysis and predictive modelling of Ti6Al4V laser surface texturing for biomedical applications,» *Surfaces and Interfaces volume 35*, pp. 1.-9., December 2022.
- [4] C. W. Chung, S. P. Bhanu and T. H. Wen, "Coloring of titanium by CW fiber laser irradiation and infrared temperature measurement," *Optics Communications*, 1 february 2023.
- [5] J. Tahseen, W. Marc un D. Stefan, «Erasing and rewriting of titanium oxide colour marks using laser-induced reduction/oxidation,» *Applied Surface Science Volume 458*, pp. 849.-854., 15 November 2018.
- [6] B. Simas, J. Vytautas, K. Evaldas, S. Žilvinas, P. Domas un S. Valdas, «High-Contrast Marking of Stainless-Steel Using

- Bursts of,» *Micromachines* 14(1):194, pp. 1.-2., January 2023.
- [7] J. Tahseen, D. Sunan, B. Haider un D. S, «Laser induced single spot oxidation of titanium,» *Applied Surface Science*, pp. 617.-624., 30 November 2016.
- [8] G. Wenyang, X. Yafei, L. Guang, C. Chang, L. Benhai, H. Zhenxing, L. Kai un W. Junlong, «Investigations on the laser color marking of TC4,» *Optik*, pp. 11.-18., April 2019.
- [9] A. Yaroslava , L. Darya , M. Oleg un . L. V. C., «Laser coloration of metals in visual art and design,» *ResearchGate*, pp. 3.-6., March 2019.
- [10] A. D.P., M. R.D., S. D.J., H. D.A., R. M.A., K. P.G. un J. B.H., «Nanosecond pulsed laser irradiation of titanium: Oxide growth and effects on underlying metal,» *ScienceDirect*, pp. 38.-45., June 2014.
- [11] J. Tahseen, W. Marc un D. Stefan, «Erasing and rewriting of titanium oxide colour marks using laser-induced reduction/oxidation,» *ScienceDirect*, pp. 849.-854., 15 November 2018.
- [12] B. Matilde , L. Adrian H. A. , S. Corrado un R. Luca , «A Hybrid Approach to Surface Engineering Based on Laser,» *Journal of Manufacturing and Materials Processing* 7(2):59, pp. 3.-5., March 2023.
- [13] B. Salomé, H. Guillaume , P. H. Alina Pascale, B. Stéphane un V. Stéphane , «Effect of Texturing Environment on Wetting of Biomimetic Superhydrophobic Surfaces Designed by Femtosecond Laser Texturing,» *ResearchGate*, pp. 1.-6., 2022.
- [14] P. M. B. P. A.G. Demir, «Fibre laser texturing for surface functionalization,» *Lasers in Manufacturing Conference 2013*, pp. 763.-764., 2013.
- [15] L. Lyubomir, N. Pavels un D. Hristina, «Laser Marking Methods,» *Technology. Resources. (2015), Volume I, 108-115*, pp. 109.-112., 2015.
- [16] K. McLAREN, XIII—The Development of the CIE 1976 (L\* a\* b\*) Uniform Colour Space and Colour-difference Formula, sēj. 92, Journal of the Society of Dyers and Colourists, 1976, pp. 338-341.
- [17] A. J. Arkadiusz, S. Bogusz, K. E. Paweł un A. M. Krzysztof, «The influence of process parameters on the laser-induced coloring,» *Applied Physics A volume 115, pages1003–1013 (2014)*, March 2013.
- [18] Johnson, A. and Lee, S, « Influence of laser power and speed on the contrast and roughness of markings on titanium alloys,» *Materials Science and Engineering: A, 764: 138214. (2020)*.
- [19] Smith, J., Williams, K., and Brown, P, «. Effect of laser marking parameters on titanium Gr 2 using a fiber laser,» *Journal of Laser Applications, 27(2): 022503.*, February 2015.
- [20] Chen, C., Li, J., Wu, C., and Huang, X, « Effects of laser parameters on the microstructure and corrosion behavior of Ti6Al4V alloy laser remelted surface,» *Applied Surface Science, volume 455, pages 514-523*, July 2018.
- [21] Wang, Y., Wang, S., Dong, X., and Wu, Y, «. Effect of laser power on surface morphology and wettability of AZ31B magnesium alloy by laser surface texturing,» *Optics and Laser Technology, volume 131: 106497.*, June 2020.

# *Application of a Finite Element Model to Obtain the Influence of the Treatment's Power, Reflection and Focal Diameter in Laser Texturing of Aluminum*

**Lyubomir Lazov**

*Faculty of Engineering  
Rezekne Academy of Technologies (RTA)  
Rezekne, Latvia  
lyubomir.lazov@rta.lv*

**Ivo Draganov**

*Faculty of Mechanical and Manufacturing Engineering  
University of Ruse  
Ruse, Bulgaria  
iivanov@uni-ruse.bg*

**Abstract.** In this work, a numerical model of laser texturing is considered. A finite element model of a representative sample of pure aluminum was created. The impact of a laser pulse was simulated, assuming a Gaussian volume distribution of the heat flux. Material properties are assumed to be constant and latent heat is accounted for. Results are obtained for the thermal field and the width of the vaporized zone, assuming that the crater is characterized by its maximum width. The numerical model was used to study the influence of pulse power density, reflection, focal diameter and pulse duration. The ablation threshold at different laser pulse durations was determinate.

**Keywords:** laser texturing, pure aluminum, finite element method (FEM), vaporized zone.

## I. INTRODUCTION

Laser texturing is pulsed processing by means of a laser beam, in which ablation of the material occurs in the impact zone. By multiple repetition of this process, along a predetermined trajectory, a groove is obtained. The industrial application of laser texturing is most often done by creating a number of grooves close enough together to be perceived as a uniform area. Different modifications of the processing sequence is discussed in [1].

Laser texturing serves to improve adherence, wettability, electrical and thermal conductivity, and friction [2]. This application of laser ablation is characterized by an overlap factor less than one and a different diameter of the laser beam, and hence a different size of the resulting crater.

The obtained result depends on the characteristics of the laser machine: scanning speed, repetition rate, average

power, laser beam spot, diameter, and pulse duration. Fiber lasers [3], YAG [4] and others are suitable for laser texturing. The duration of the impact varies widely, using nanosecond [5], picosecond [6] and femtosecond lasers [7], [1].

Laser texturing is applicable to various materials, such as metals and their alloys, superalloys [8], ceramics [3], wood [9], composite materials [10] and others. Due to its wide application in industry, aluminum and its alloys are the subject of increased research, including regarding the possibilities of its laser processing [11].

The main characteristics of the laser texturing result are the width, the depth and the hatch. They can be determined directly experimentally by performing the laser texturing with the prescribed processing modes. To reduce setup time and the number of technological samples, computer models created on the basis of numerical methods, most often the finite element method (FEM), are applied. Commercial programs such as ABAQUS [9], [12], [13], COMSOL [14], [15], [16] and others are used for this purpose, as well as proprietary codes [5].

Most often, the modeling of laser texturing by the FEM to determine the resulting dimples is reduced to solving the problem of determining the temperature field by using the law of thermal conductivity. Regarding the considered area, the problem to be solved can be one-dimensional [13], two-dimensional [3], two-dimensional - axisymmetric [17] or three-dimensional [18], [9]. Depending on the number of set pulses, the models are for one pulse [9], for one transition [14] and several transitions [16]. A number of authors focus on the action of a single laser pulse [19], [5].

Print ISSN 1691-5402

Online ISSN 2256-070X

<https://doi.org/10.17770/etr2023vol3.7278>

© 2023 Lyubomir Lazov, Ivo Draganov. Published by Rezekne Academy of Technologies.  
This is an open access article under the [Creative Commons Attribution 4.0 International License](https://creativecommons.org/licenses/by/4.0/).

which allows the determination of the temperature field, and from there the resulting topography.

The modeling of the processed part as a solid body is accomplished with Fourier's law. The heat flux can be volumetric or planarly distributed Gaussian function [16], [3]. Guo et al. [9] use in the heat flow's formula a coefficient considering the plasma. Nikolidakis et al. [16] also consider the influence of the evaporated plasma layer. Some authors consider radiation and convection [19], [8], but the process is fast and the heat conduction in the solid body has a dominant effect.

Some authors model the liquid phase by solving the Navier-Stokes equations [20]. This allows obtaining results for keyholes and voids in the material and splashes. Chryssoulouris et al. [21] address the issue of plume formation. The evaporation at the melt surface is associated with the emission of neutral atoms or molecules into the gas that shields the laser-material interaction zone. Wang et al. [10] used in their work a simple finite element model to determine the plasma shielding effect in laser engraving of aluminum.

Computer determined crater dimensions can be used to validate the model. Liu et al. [22] offers a solution to the problem of measuring the diameter of such a small hole with a single laser pulse - D<sup>2</sup> method. In the modeling of laser texturing, in addition to the temperature field, some authors also determine the roughness of the obtained surfaces [15] and the stresses arising in the processing and after it [4], [3].

Numerical modeling of laser engraving can be performed by accounting for the nonlinear properties of the material [3]. A number of authors prefer the use of latent heat [20], which greatly eases the computational process.

The aim of the present research is the creation of a finite element model of laser texturing, allowing the determination of the groove width by taking into account the latent heat and the influence of the pulse power, the diameter of the laser beam, the reflection and the duration of the laser pulse.

## II. PHYSICAL LAWS DESCRIBING THE PROCESS

A complete physical description of the laser texturing process is difficult to achieve. This necessitates the use of a suitable physical-mathematical model, on the basis of which a computer model should be built, allowing the determination of the required quantities. For the needs of the presented study, it is assumed that the impact of the laser beam from the moment of its impact on the processed part, which is a solid body, will be considered.

The Fourier's law of heat conduction for solids is valid, which together with the heat balance equation has the form

$$\text{div}(\mathbf{L} \cdot \text{grad}(T)) + Q = \rho C_p \frac{\partial T}{\partial t}, \quad (1)$$

where  $\mathbf{L}$  is the tensor with the heat transfer material characteristics depending on the temperature  $T$ ,  $Q$  is the amount of heat in the considered volume,  $\rho$  is the density

of the material  $C_p$  is the material heat capacity, and  $t$  is the time.

The laser beam is a flow of electromagnetic wave in the visible spectrum, which in the process of texturing propagates in the solid body according to the Beer-Lambert law [23]:

$$I(z) = I_0 e^{-\alpha z}, \quad (2)$$

where  $I(z)$  is the intensity at depth  $z$  and  $I_0$  is the surface intensity. The equation for the absorption coefficient  $\alpha$ , is

$$\alpha = \frac{4\pi n k}{\lambda_0}, \quad (3)$$

where  $\lambda_0$  is the wave length of the laser in vacuum,  $n$  is the refraction index, and  $k$  is the extinction index. The equations for the last characteristics are [24]:

$$n = \left( \frac{\sqrt{\varepsilon_1^2 + \varepsilon_2^2} + \varepsilon_1}{2} \right)^{1/2}, \quad (4)$$

$$k = \left( \frac{\sqrt{\varepsilon_1^2 + \varepsilon_2^2} - \varepsilon_1}{2} \right)^{1/2}, \quad (5)$$

where  $\varepsilon_1$  and  $\varepsilon_2$  are the real and the imaginary part of the material's relative permittivity.

Lehmuskero et al. [25] give their own and others' results for the refractive and absorption coefficients of aluminum. For a wavelength of 578 nm,  $n = 1$  and  $k = 7$  are reported. The same values are also used in [26].

Absorption is one of the parameters of the laser impact on the processed medium, as together with the reflection,  $R$ , give the heat flow vector [27]:

$$q = I(x, y)(1 - R)e^{-\alpha z}, \quad (6)$$

The intensity of the laser beam depends on the power of the laser machine and is distributed according to a Gaussian law according to the equation

$$I(x, y) = \frac{2P_p}{\pi r^2} e^{-2 \frac{(x-x_f)^2 + (y-y_f)^2}{r^2}}, \quad (7)$$

where  $P_p$  is the pulse power of the laser,  $r$  is the radius of the laser beam, and  $x_f$  and  $y_f$  are the coordinates of the laser beam.

The phase changes from solid to liquid and from liquid to solid cause a strong nonlinearity in the specific heat capacity. In order to reduce the computational time, the latent heat is used, which is described by the equation

$$C_p = C_p^0 + L_m D_m + L_e D_e, \quad (8)$$

where  $C_p^0$  is the equivalent specific heat capacity,  $L_m$  is the latent heat of melting,  $L_e$  is the latent heat of evaporation, and

$$D_m = \frac{\exp[-(T-T_m)^2/\Delta T_m^2]}{\Delta T_m \sqrt{\pi}}, \quad (9)$$

$$D_e = \frac{\exp[-(T-T_e)^2/\Delta T_e^2]}{\Delta T_e \sqrt{\pi}}, \quad (10)$$

In the above two equations take parts, the melting temperature -  $T_m$ , the evaporation temperature -  $T_e$  and the displacements relative to them -  $\Delta T_m$  and  $\Delta T_e$ .

### III. COMPUTER MODEL

The object of research is a part of pure aluminum subjected to laser processing. The process parameters ensure that a temperature above the vaporization temperature of aluminum is reached. Due to the small size of the diameter of the laser beam and the short duration of one pulse, a representative sample (Fig. 1) of the total volume of the body is considered. This has sufficient dimensions so that the physical laws can exhibit, and in the same time the dimensions to be small enough to minimize the duration of the computational process in the computer model. The dimensions of the representative volume are  $100 \times 100 \mu\text{m}$  in the processing plane and  $70 \mu\text{m}$  in depth.

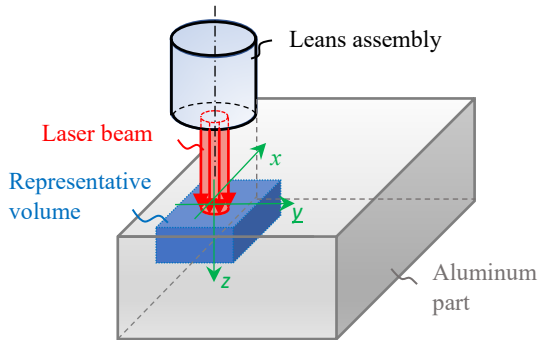


Fig. 1. General scheme of laser texturing.

The impact of a laser pulse, which creates a crater of a certain shape and size, is examined. The main properties of the crater are the width and the depth. In this work, it is accepted that the width is enough to characterize the result from the laser processing. It is based on the assumption that the formation of a groove consists of the repeated repetition of the pulse impact on the part, with the possibility of overlapping of individual craters and the presence of unprocessed areas - Fig. 2. The impact time between two pulses is long enough for the heat to spread in the considered representative volume and reach a temperature close to that of the environment at its boundaries. The

formation of a complete processed layer is done by overlapping the furrows. Various processing sequences are possible to achieve such planar overlap, but these are beyond the scope of the present study. It is expedient to introduce an overlap factor between the individual craters in the direction of the groove

$$k = \frac{vd}{l_g} = \frac{vd}{vt}, \quad (11)$$

where  $v$  is the pulse frequency and  $v$  is the speed of the laser.

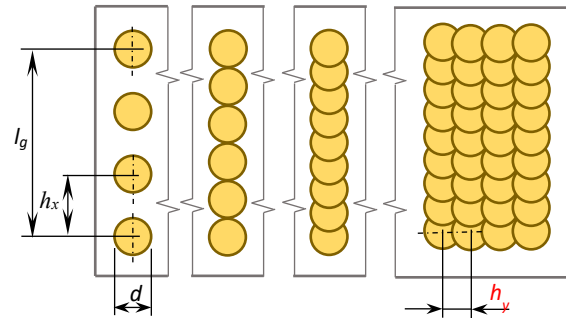


Fig. 2. Craters, grooves, layer.

A transient finite element model was created in the ABAQUS program [28]. Spatial discretization is performed using an eight-node hexahedral finite element DC3D8. The elements on the surface of laser impact are  $1 \mu\text{m}$  in size - Fig. 3. To reduce the computational work, the feature size in the thickness direction is increased, reaching a size of  $20 \mu\text{m}$  for the bottommost layer. The mesh is consist from 57222 nodes and 50500 elements.

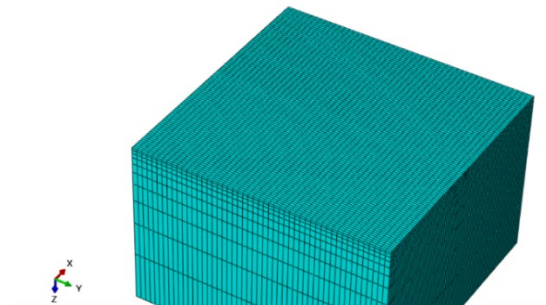


Fig. 3. Discretization of the representative volume.

The processed material is pure aluminum having the material characteristics given in Table 1. The liquid and gaseous phase changes are modeled by introducing latent heat (8), which allows the specific heat capacity to be set as constant.

TABLE 1 MATERIAL PROPERTIES

Material properties	Value
Density, $\text{kg}/\text{m}^3$	2700
Conductivity, $\text{W}/(\text{m}\cdot\text{K})$	235
Specific heat capacity, $\text{J}/(\text{kg}\cdot\text{K})$	900
Melting point, $\text{K}$	933.47

Material properties	Value
Evaporation temperature, K	2743
Latent heat of fusion, kJ/mol	10.71
Latent heat of vaporization, kJ/mol	284

It is assumed that the initial temperature of the test specimen is 20 °C. Convective and radiant heat transfer are neglected due to the short duration of the process. The time for one pulse –  $\tau$ , is 30  $\mu$ s. The pulse power is

$$P_p = P/\nu\tau, \quad (12)$$

where  $P$  is the laser average power. Engraving modes with different laser power ranging from 5.5 to 10 W were investigated.

The laser beam is modeled as a heat flux equivalent to one pulse, according to (7). A volume distribution of the heat flux by means of a Gaussian function was used. The slope coefficient of the Gaussian function is taken to be equal to 3. The heat flux is specified in the model by subroutine DFLUX [28]. It allows setting the model characteristics that are involved in the parametric analysis: laser pulse power, focal diameter and reflection. The calculations were performed by discretizing the process time in 10000 increments.

#### IV. RESULTS AND DISCUSSION

Temperature distribution results in a representative volume of a pure aluminum workpiece are obtained. In Fig. 4 shows the temperature field, at the end of the pulse, at a pulse power of 12511 W, a laser focal spot diameter of 30  $\mu$ m and a reflection coefficient of 0.3.

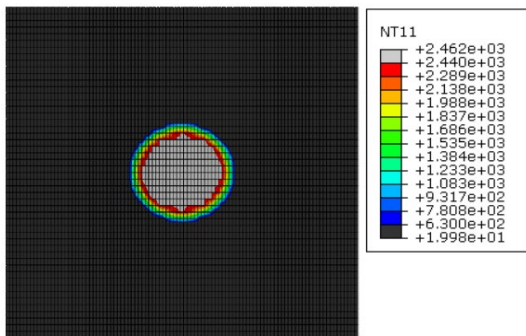


Fig. 4. Temperature distribution at  $P_p = 12511$  W,  $d = 30$   $\mu$ m,  $R = 0.3$ .

The temperatures of the evaporation point are shown with a light color, and the temperatures below the melting point with a dark color. Similar diagrams are obtained for the different laser engraving modes. By measuring the evaporation isotherm, the width of the crater in the corresponding mode was obtained.

The effect of power density on crater width at two laser beam frequencies is shown in Fig. 5.

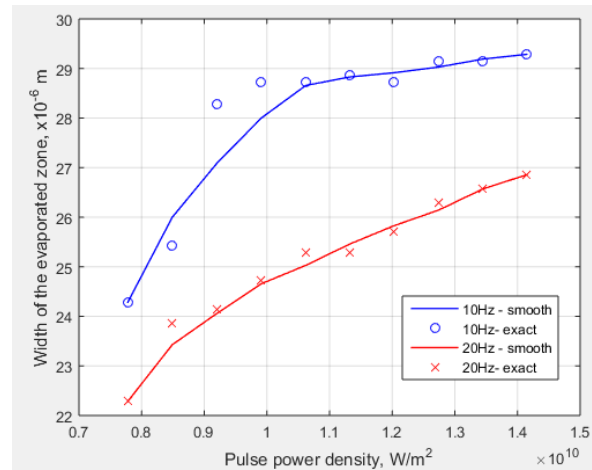


Fig. 5. Influence of pulse power density.

Figure 6 shows the dependences between the width of the vaporized zone - along the y axis and the pulse power - along the x axis. The resulting crater width results were smoothed using the smooth function in MATLAB, with the exact values given as dots. Such dependences were determined for focal spot diameters in the range from 10 to 30  $\mu$ m, with a step of 5  $\mu$ m.

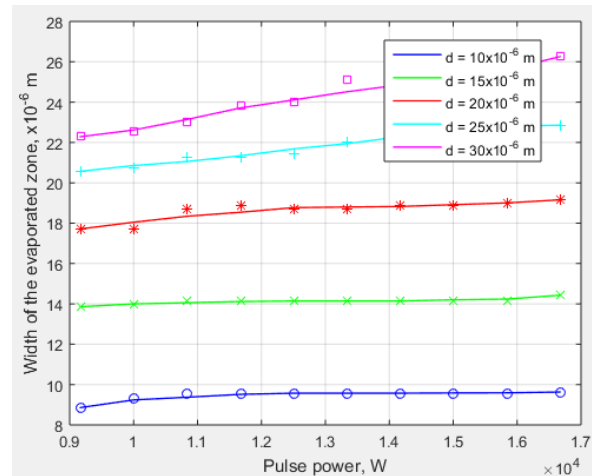


Fig. 6. Influence of pulse power on crater width at different focal spot diameters.

Increasing the pulse power leads to a smooth increase in the vaporized zone width. This trend is more distinct at larger values of the focal diameter.

The relationship between the reflection and the power at different diameters of the laser beam is shown at Fig. 7. The width of the crater decreases monotonically with increasing reflectivity. The effect of pulse power is linear.

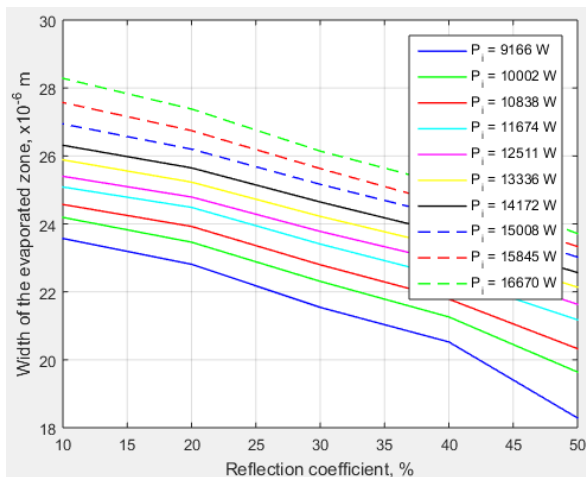


Fig. 7. Influence of the reflection.

Influence of the pulse duration on the width of the crater (Fig. 8) and the width of the molten zone – Fig 9.

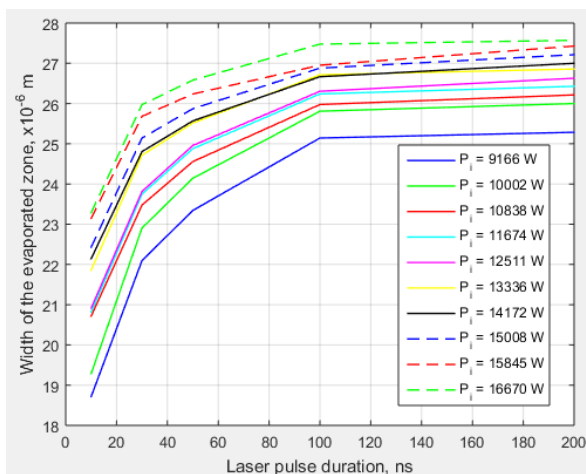


Fig. 8. Effect of pulse duration on crater width.

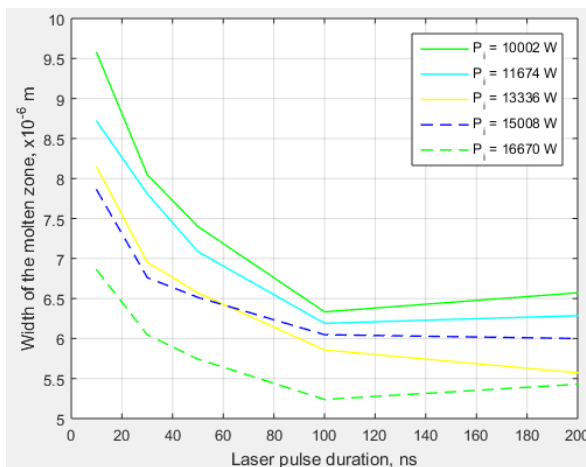


Fig. 9. Effect of pulse duration on the width of the melted zone.

It was found that as the pulse duration increased, the width of the vaporized zone increased. This tendency

decreases for larger values of time. This parameter has a greater influence than the pulse power. The width of the melted zone, which contributes to the formation of irregularities, decreases with larger values of the laser pulse duration. For pulse durations above 100 ns, a tendency to increase the width is observed, which may be due to a numerical instability of the model related to the grid density.

The ablation threshold is the power density at which the evaporation temperature is reached. Ablation threshold at different laser pulse durations is shown in Fig. 10. The slope

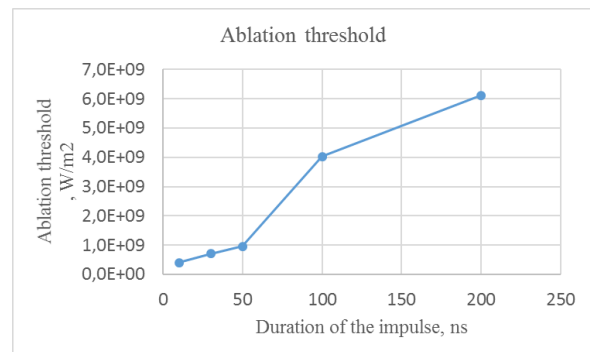


Fig. 10. Ablation threshold.

## V. CONCLUSIONS

The created finite element model allows the determination of the influence of pulse power, reflection and diameter of the laser beam on the width of the vaporized zone during laser texturing of pure aluminum.

The pulse power has a linear effect on the width of the resulting craters. The influence of this parameter is less at small values of the diameter of the laser beam.

Increasing the reflectivity of the material leads to a decrease in the width of the crater. This trend is independent of the pulse power and increases with increasing reflection.

As the pulse duration increases, the width of the crater also increases. At larger values, this trend decreases, and above 100 ns it is particularly visible. The effect of pulse duration is inverse with respect to the width of the vaporized zone. At values above 100 ns, a trend reversal is observed, which may also be due to numerical instability. This question requires further research.

## REFERENCES

- [1] D. Förster, B. Jäggi, A. Michalowski, B. Neuenschwander. Review on Experimental and Theoretical Investigations of Ultra-Short Pulsed Laser Ablation of Metals with Burst Pulses. *Materials* 14, 3331, 2021, <http://dx.doi.org/10.3390/ma14123331>.
- [2] A. Rosenkranz, P. Grützmacher, C. Gachot, H. Costa. Surface Texturing in Machine Elements – A Critical Discussion for Rolling and Sliding Contacts. *Advanced Engineering Materials*, 1900194, 2019, <http://dx.doi.org/10.1002/adem.201900194>.

- [3] S. Liu, Z. Tian, L. Shen, M. Qiu. Numerical Simulation and Experimental Investigation of Laser Ablation of Al<sub>2</sub>O<sub>3</sub> Ceramic Coating. *Materials* 13, 5502, 2020, <http://dx.doi.org/10.3390/ma13235502>.
- [4] H. D. Vora, N. Dahotre. Multiphysics Theoretical Evaluation of Thermal Stresses in Laser Machined Structural Alumina. *Laser Manuf. Mater. Process*, 2:1-23, 2015, <http://dx.doi.org/10.1007/s40516-014-0004-x>.
- [5] L. Lazov, N. Angelov. Optimization of laser marking with the help of simulation models. *Turkish Journal of Physics*, 37, pp. 145-150, 2013, <http://dx.doi.org/10.3906/fiz-1202-4>.
- [6] T. Moriya, K. Fukumitsu, T. Yamashita, M. Watanabe. Fabrication of Finely Pitched LYSO Arrays Using Subsurface Laser Engraving Technique with Picosecond and Nanosecond Pulse Lasers. *IEEE Transactions on nuclear science*, Vol. 61, No. 2, pp. 1032-1037, 2014, <http://dx.doi.org/10.1109/TNS.2014.2309347>.
- [7] J. Lopez, F. Deloison, A. Lidloff, M. Delaigue, C. Hönninger, E. Mottay. Comparison of picosecond and femtosecond laser ablation for surface engraving of metals and semiconductors. *Key Engineering Materials*, Vol. 496, pp. 61-66, 2012, <http://dx.doi.org/10.1117/12.907792>.
- [8] B. Wang, Y. Huang, J. Jiao, H. Wang, J. Wang, W. Zhang, L. Sheng. Numerical Simulation on Pulsed Laser Ablation of the Single-Crystal Superalloy Considering Material Moving Front and Effect of Comprehensive Heat Dissipation. *Micromachines*, 12, 225, 2021, <http://dx.doi.org/10.3390/mi12020225>.
- [9] Q. Guo, Y. Ma, Z. Wu, Y. Cui, C. Yang. Finite Element Analysis and Experimental Research on Micro-treatment of Coniferous Wood Surface. *Chemical Engineering Transactions*, Vol. 55, pp. 91-96, 2016, <https://doi.org/10.3303/CET1655016>.
- [10] Y. Wang, D. W. Hahn. A simple element model to study the effect of plasma plume expansion on the nanosecond pulsed laser ablation aluminum. *Applied Physics A*, 125:654, 2019, <https://doi.org/10.1007/s00339-019-2951-8>.
- [11] M. Pantawane, S. Joshi, N. Dahotre. Laser Beam Machining of Aluminum and Aluminum Alloys. *ASM Handbook*, Vol. 2A, pp. 519-541, 2018, <http://dx.doi.org/10.31399/asm.hb.v02a.9781627082075>.
- [12] Y. Wang, O. Zhupanska, C. Pasilio. Verification of a Manual Mesh Moving Finite Element Analysis Procedure for Modeling in Laminated Composite Materials. *Proceedings of the ASME IMECE2017-70623*, 2017, <http://dx.doi.org/10.1115/IMECE2017-70623>.
- [13] Y. Wang, T. Risch, C. Pasilio. Modeling of Pyrolyzing Ablation Problem with ABAQUS: A One-Dimensional Test Case. *Journal of Thermophysics and Heat Transfer*, pp. 1-4, 2018, <http://dx.doi.org/10.2514/1.T5274>.
- [14] H. Karbasi. COMSOL Assisted Simulation of Laser Engraving. *COMSOL Conference 2010 Boston*, 2010.
- [15] H. D. Vora, S. Santhanakrishnan, S. Harimkar, S. K. Boetcher, N. Dahotre. One-dimensional multipulse laser machining of structural alumina: evolution of surface topography. *Int J Adv Manuf Technol* 68, pp. 69-83, 2013, <https://doi.org/10.1007/s00170-012-4709-8>.
- [16] E. Nikolidakis, A. Antoniadis. FEM modeling simulation of laser engraving. *The International Journal of Advanced Manufacturing Technology* 105, pp. 3489-3498, 2019, <https://doi.org/10.1007/s00170-019-04603-3>.
- [17] J. Kuang, T. Hung, K. Lai, C. Hsu, A. Lin. The Surface Absorption Coefficient of S304L Stainless Steel by Nd:YAG Micro-Pulse Laser. *Advanced Material Research*, Vol. 472-475, pp. 2531-3534, 2012, <http://dx.doi.org/10.4028/www.scientific.net/AMR.472-475.2531>.
- [18] H. D. Vora, N. Dahorte. Laser Machining of Structural Alumina: Influence of Moving Laser Beam on the Evolution of Surface Topography. *Int. J. Appl. Ceram. Technol.*, pp. 1-14, 2014.
- [19] H. D. Vora, S. Santhanakrishnan, S. Harimkar, S. Boetcher, N. Dahotre. Evolution of surface topography in one-dimensional laser machining of structural alumina. *Journal of the European Ceramic Society* 32, pp. 4205-4218, 2012, <http://dx.doi.org/10.1016/j.jeurceramsoc.2012.06.015>.
- [20] A. Otto, H. Koch, K. Leitz, M. Schmidt. Numerical Simulations – A Versatile Approach for Better Understanding Dynamics in Laser Material Processing. *Physics Procedia* 12, pp. 11-20, 2011, <http://dx.doi.org/10.1016/j.phpro.2011.03.003>.
- [21] G. Chryssolouris. *Laser machining theory and practice*. New York: Springer- Verlag, 1991.
- [22] J. Liu. Simple technique for measurements of pulsed Gaussian-beam spot sizes. *Opt. Lett.* 7, pp. 196-198, 1982.
- [23] M. Pantawane, S. Joshi, N. Dahotre. Laser Beam Machining of Aluminum and Aluminum Alloys. *ASM Handbook*, Vol. 2A, Aluminum Science and Technology, pp. 519-541, 2018, <http://dx.doi.org/10.31399/asm.hb.v02a.9781627082075>.
- [24] E. Beyer. *Schweissen mit Laser*, Berlin: Springer, pp. 28-36, 1995.
- [25] A. M. Lehmuskero, M. Kuittinen, P. Vahimaa. Refractive index and extinction coefficient dependence of thin Al and Ir films on deposition technique and thickness. *OPTICS EXPRESS*, Vol. 15, No. 17, 2007, <http://dx.doi.org/10.1364/OE.15.010744>.
- [26] F. Hamadi, E. Amara, D. Bennaceur-Doumaz, R. Boutaka, H. Kellou, K. Bourai, A. Noukaz, R. Beggar. Modeling of Titanium Oxide Layer Growth Produces by Fiber Laser Beam. *Defect and Diffusion Forum* Vol. 336, pp. 11-18, 2013, <https://doi.org/10.4028/www.scientific.net/DDF.336.11>.
- [27] D. Bergström, A. Kaplan, J. Powell. *Mathematical Modelling of Laser Absorption Mechanisms in Metals: A Review*. M4PL16 - 16th Meeting on Mathematical Modelling of Materials Processing with Lasers, 2003.
- [28] ABAQUS, "Analysis User's Manual," ver. 6.14, Dassault Systemes Simulia Corp., Providence, RI, USA.

# The Change of Contrast is Investigation of 75 Steel Samples Laser Marked with Different Modes

**Lyubomir Lazov**  
Rezekne Academy of Technologies  
Faculty of Engineering  
Rezekne, Latvia  
lyubomir.lazov@rta.lv

**Nikolay Padarev**  
Rezekne Academy of Technologies  
Faculty of Engineering  
Rezekne, Latvia  
nipadarevnu@gmail.com

**Milko Yovchev**  
Technical University of Gabrovo  
Faculty of Electrical Engineering  
and Electronics  
Gabrovo, Bulgaria  
milkoYovchev1986@gmail.com

**Lyubomir Linkov**  
Rezekne Academy of Technologies  
Faculty of Engineering  
Rezekne, Latvia  
ll21172@edu.rta.lv

**Abstract.** The quality of the marked surfaces changes the optical characteristics. The aim of the study is to optimize the contrast in laser marking of Steel 75. The influence of the step in the raster marking and the influence of the repetition frequency of the pulses on the reflection coefficient were analysed. The experimental investigations of the reflectance were carried out using a spectrophotometer. For the marked samples, it was found that when directing electromagnetic radiation with a wavelength in the studied range, there are areas with absorption and reflection of light. The reflectance is plotted as a function of marking step and laser frequency for the marked Steel 75 samples.

**Keywords:** laser systems, laser safety, laser beam, optical properties.

## I. INTRODUCTION

Laser has become the most advanced and widely used tool in material processing due to its advantages such as high power, easy focus, high brightness and good directivity. The laser processing has advantages such as high precision, high speed and low cost. It can be automatically controlled by computer programming. The laser can affect materials with a complex shape. Since it is non-contact processing, it will not damage the material and is safe and dependable. Laser marking is a modern method of permanent marking. The main advantages of using a laser for marking are long life of the laser source, minimal operating costs and lack of consumables.

The laser marking is performed by interaction of laser beams with surface of material, which leads to a change in chemical composition and microstructure of materials. In fact that the surface roughness of processed material can be precisely modulated, resulting in the formation of stripes and nanostructures. The introduced micro-roughness improves diffuse effect, which is an especially important feature when considering the production of diffuse reflectors. Laser marking and laser engraving are the most sought-after identification methods and have successfully replaced inkjet markings and labels.

C75 is a standard Euronorm high carbon spring steel. It has a carbon content of 0.7-0.8% making it a multi-purpose carbon steel with good spring properties. It has numerous applications such as flat or automotive springs, machine knife blades, hand and agricultural tools, shims, doctor blades. That is why it is important to mark such details, a fast and flexible method is laser marking.

We have done several studies [1-6] in the field of changing the optical properties of marked surfaces of various materials. In research [1], a comparison of oxidant films formed on the surface of stainless-steel during laser treatment and heating in a furnace is presented. The optical properties of samples were investigated using a spectrophotometer. The reflectance spectra in the experiment were varied in the wavelength range 190–900 nm. Coloration of the treated area was seen at different

Print ISSN 1691-5402

Online ISSN 2256-070X

<https://doi.org/10.17770/etr2023vol3.7264>

© 2023 Lyubomir Lazov, Nikolay Padarev, Milko Yovchev, Lyubomir Linkov.

Published by Rezekne Academy of Technologies.

This is an open access article under the [Creative Commons Attribution 4.0 International License](https://creativecommons.org/licenses/by/4.0/).

laser parameters. The effects of laser irradiation on the surface microstructure and optical properties of ZnO films were investigated experimentally in [2]. X-ray diffraction (XRD) and atomic force microscopy (AFM) measurements have shown an improvement in crystalline quality with 514 nm Ar<sup>+</sup> laser irradiation. After laser irradiation, a significant increase in UV absorption and broadening of the optical bandgap of the films was observed. In [3] they studied the effect of laser irradiation on the optical properties of thin films of amorphous chalcogenide Ge<sub>12</sub>Sb<sub>25</sub>Se<sub>63</sub>. The structure and composition of the film were investigated by X-ray diffraction and energy-dispersive X-ray analysis, respectively. The optical properties such as refractive index and thickness of the films were found from transmission spectra based on reverse synthesis method. In article [4], the authors investigated effect of laser irradiation on the structural, electrical, and optical properties of SnO<sub>2</sub> films.

The films were treated with Nd: YAG laser pulses of different energy densities and with different pulse numbers. X-ray diffraction studies were performed to investigate the structural changes due to laser irradiation. Optical transmission studies have shown that the refractive index changes because of laser irradiation. In [5, 6, 7], CO<sub>2</sub> laser radiation on the optical properties of pure polyvinyl chloride was investigated. Optical properties (absorption, transmission, absorption coefficient, refractive index and optical conductivity) were investigated as a function of wavelength. [9, 10, 11]

One of the factors that affect the marking, along with the wear resistance, clarity and clarity of the written symbols, is the contrast. The factors that affect the contrast are related to the process of interaction of the laser radiation with the substance and the changes that occur in the treatment area (fig. 1). [12, 13]

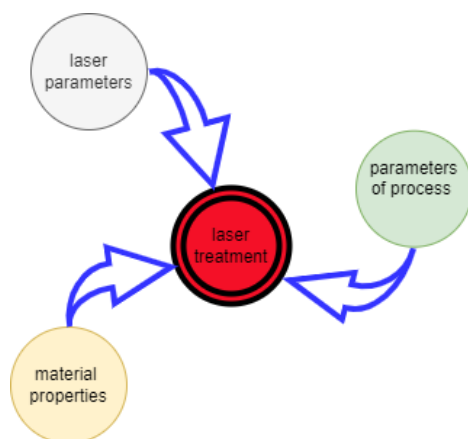


Fig. 1. Main groups of factors influencing the quality of marking.

This paper is about the study of the change of some optical characteristics of laser-treated samples of steel 75 with the aim of process optimization. That makes it relevant.

The purpose of the study:

Conducting research on the influence of changing laser parameters on optical properties of steel 75 samples. To

achieve the goal, the following scientific and research tasks are set to be solved:

- 1) To analyse the influence of the step  $\Delta x$  in raster marking on the change of reflectance and contrast
- 2) To analyse the influence of the pulse repetition rate  $\nu$  on the reflection coefficient  $\rho$  and the contrast

## II. RESEARCH MATERIALS AND METHODOLOGY

### A. Materials

The experimental work conducted was on C75 carbon steel samples. It is a carbon structural steel and belongs to the „spring-spring steel” subgroup. Its composition (shown in table 1), together with other structural steels, is shown in several literary sources - mainly reference books [7]. Steel is actively used in various industrial sectors to produce clutch discs, springs of assorted sizes, engine valves and other parts working in conditions of friction and exposed to vibration. Also, steel is used to produce cold weapons. [8]

TABLE 1 COMPOSITION OF STEEL C 75 [8]

Chemical composition	Ni	C	Si	Mn	S	Cr	P
Percentage content	≤0.25	0.70-0.80	0.17-0.37	0.40-0.70	<0.05	≤0.25	<0.04

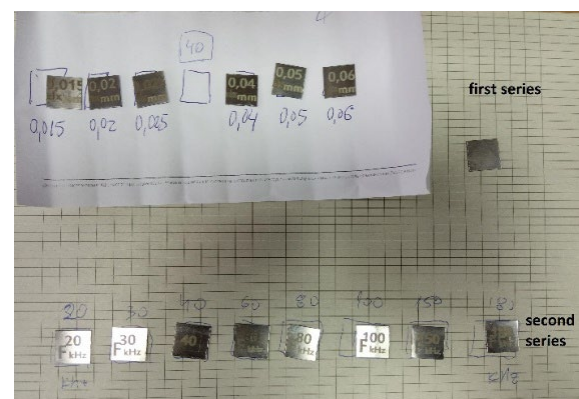


Fig. 2. Object of research.

In fig. 2 shows two series of steel 75 specimens at different marking steps  $\Delta x$  and marking frequency  $\nu$  and other process parameters held constant. The individual test samples were made with dimensions suitable for studying the optical properties in a special chamber in the SPEKOL 11 spectrometer.

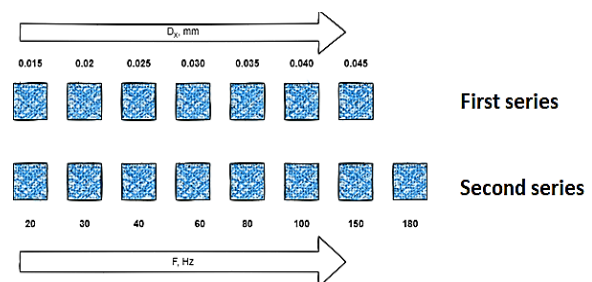


Fig. 3. Schematic of the laser treated surfaces.

Fig. 3 shows a diagram of the chosen methodology. The first series of experiments were prepared seven samples of steel 75 were laser marked with Fiber laser with the parameters showed in table 2.

TABLE 2 PARAMETERS OF LASER-MARKED WAFERS FROM THE FIRST TEST SERIES

Parameters	Sequence of the Marked Plates According to the Research Methodology						
Power P, W	15						
The pulse repetition rate $\nu$ , kHz	40						
Pulse duration $\tau$ , ns	100						
The bitmap step $\Delta x$ , mm	0.015	0.02	0.025	0.030	0.035	0.040	0.045

The second series of experiments is with eight marked plates of steel 75 with laser marking parameters showed in table. 3.

TABLE 3 PARAMETERS OF LASER-MARKED PLATES FROM THE SECOND SERIES OF RESEARCH

Parameters	Sequence of the Marked Plates According to the Research Methodology						
Power P, W	15						
Pulse duration $\tau$ , ns	100						
The bitmap step $\Delta x$ , mm	0,03						
The pulse repetition rate $\nu$ , kHz	40	30	40	60	80	100	150

### B. Apparatus used in the study

#### a. Equipment for laser marking of samples

The samples were marked with Fiber laser, the parameters of which are described in table 2 and table 3. In fig. 4 shows the laser used to mark the metal plates, and fig. 5 shows the principal diagram of creating the laser radiation with the Fiber laser.



Fig. 4. Fiber Laser from the trials.

The main parameters of the Fiber laser are:

- Wavelength  $\lambda = 1,064$  nm;
- Nominal power  $P_n = 20$  W;

- Pulse repetition frequency  $\nu = (40 \div 180)$  kHz;
- Pulse duration  $\tau = 100$  ns;
- Pulse energy  $E_p = 1$  mJ.

#### b. Apparatus for experimental studies of the reflection coefficient

The measurements were carried out with a spectrophotometer SPEKOL 11 (fig. 5 and fig. 6) of Carl Zeiss, Jena, Germany. It is a single-beam spectrophotometer with a microprocessor. In the lower part of the main body there is a diffraction monochromator, and in the upper part, executed in the form of a module, an electronic part of the device connected to the current stabilizer for the light source - a halogen lamp. Two light-sensitive vacuum photocells serve as radiation receivers: the first with spectral sensitivity in the range (340÷620) nm and the second with sensitivity in the red region of the spectrum (620÷850) nm.

To measure the spectral reflection coefficient, the Rd/0 attachment to SPEKOL 11 is used, in which the measured sample is placed - fig. 6. The Rd/0 attachment provides a comparative measurement of the reflectance with one of the CIE (International Commission on Illumination) recommended illumination geometries and measurement observation – geometry „d/0“.

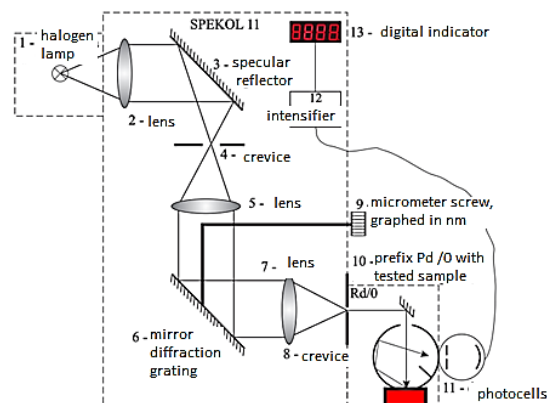


Fig. 5. Scheme of spectral reflection coefficient measurements with SPEKOL 11 spectrophotometer and attachment Rd/0.



Fig. 6. Single-beam spectrophotometer with microprocessor „SPEKOL 11“.

To reduce the influence of the specular composition of the reflected flow in case of mixed reflection of the sample, a special screen is placed in the sphere, preventing the direct impact of rays from the sample on the photocell - fig. 6.

The measurement of the reflection coefficient of the studied sample is conducted in comparison with a standard with a reflection coefficient close to 100 %. The materials recommended by the CIE are white surfaces of barium sulphate (BaSO<sub>4</sub>), magnesium oxide (MgO), etc., whose spectral reflection coefficients change slightly in the range of 0.95÷0.98 for the wavelengths of the visible spectrum of light.

The reflection coefficient is measured by irradiating the metal plates with electromagnetic radiation from a halogen lamp with a wavelength in (450÷560) nm range with a wavelength 10 nm step.

### III. RESULTS AND DISCUSSION

On fig. 7 there is a graphical dependence of the reflection coefficient  $\rho$  as a function of the wavelength  $\lambda$ .

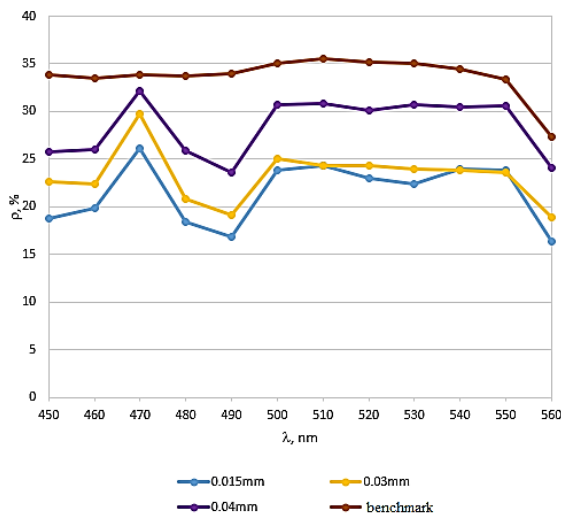


Fig. 7. Dependence of reflection coefficient as a function of wavelength for labelled samples at variable labelling step.

Measurements with a spectrophotometer revealed a different course of in separate wavelength regions. At a marking step of 0.02 mm of the laser beam, the machined surfaces have the lowest reflectivity, and at 0.04 mm the highest reflectivity. When irradiating a marked plate with a light beam with a wavelength  $\lambda$  of (500÷550) nm, a uniform contrast is observed on the surfaces.

In the second series of research, we examine the zones of laser impact when the reflection coefficient changes in the range of (470÷560) nm. In fig. 8 shows the graphical dependence of the reflection coefficient and the wavelength.

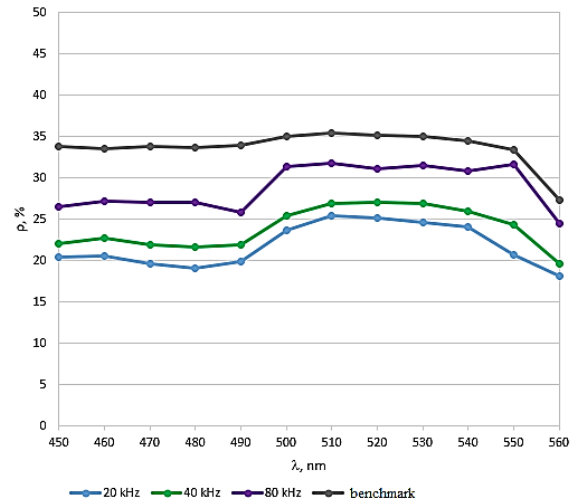


Fig. 8. Dependence of the reflection coefficient as a function of the wavelength for marked samples for the second experimental series.

For laser-marked surfaces with constant parameters and a marking frequency of 20 to 40 kHz, the same surface contrast is seen in the range of (500÷540) nm, while for surfaces marked with laser frequencies higher than 60 kHz, the range is more-wide (500÷550) nm. Marked surfaces with a frequency higher than 60 kHz in the studied range, there is no significant difference in the reflection coefficients. It was found that as the marking frequency increases, the reflection coefficient increases.

For laser-marked surfaces was determined contrast by measuring the sample with unmarked surface saturation of the resulting marking surface. The contrast of the marking was determined by the formula (1).

$$k = \frac{N_f - N_x}{N_f} * 100\% \quad (1)$$

where:

$N_f$ - background of unmarked surface

$N_x$ - the saturation of the resulting mark

On fig. 9 there is a graphically presents the dependence of the contrast  $k$  on marked samples for the first experimental series.

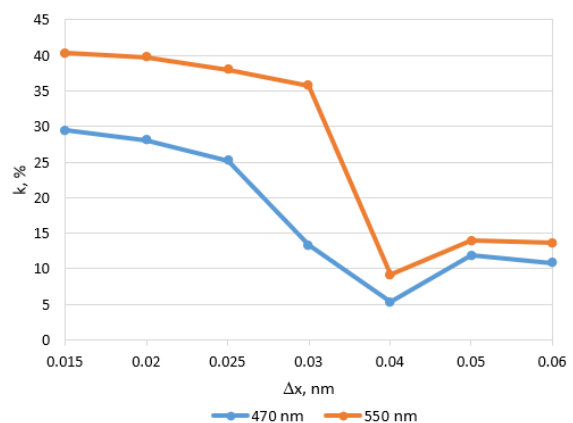


Fig. 9. Dependence of the contrast  $k$  of the mark on the step  $\Delta x$  for a sample of carbon steel C 75.

On fig. 10 as the marking step increases to 0.04 nm, the contrast decreases at both  $\lambda=470$  nm and  $\lambda=550$  nm SPEKOL irradiation.

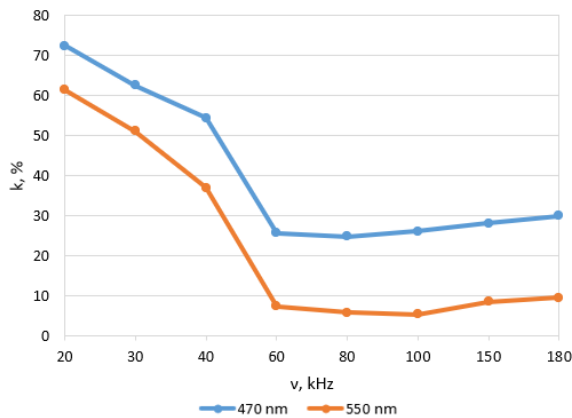


Fig. 10. Dependence of the contrast  $k$  of the mark on the frequency  $\nu$ , kHz for a sample of carbon steel C 75.

#### IV. CONCLUSION

The research we present relationship between reflectance in marking area as laser parameters change. The relationship between reflection coefficient and raster marking step  $\Delta x$  in range of 0.015 mm to 0.06 mm of laser impact area was also analysed. The influence of repetition frequency of pulses in range of 20 kHz to 180 kHz on reflection coefficient with irradiation of a light beam with a wavelength of (450÷560) nm on marked area was analysed. The variation of contrast during irradiation of marked surfaces with certain parameters was studied. A study of the influence of technological parameters on reflection coefficient, made on steel plates 75, contributes to reflectivity of marked surfaces, for example, for camouflage of various military objects. In further research, we will prepare a mathematical model on the current research as the authors in [14, 15, 16, 17, 18].

#### REFERENCES

[1] Ageev, E.I., Andreeva, Y.M., Brunkov, P.N. et al. Influence of light incident angle on reflectance spectra of metals processed by color laser marking technology. *Opt Quant Electron* 49, 50, 2017. <https://doi.org/10.1007/s11082-016-0876-4>

[2] Hui Lu, Yaoquan Tu, Xian Lin, Bin Fang, Duanbin Luo, Aatto Laaksonen, Effects of laser irradiation on the structure and optical properties of ZnO thin films, *Materials Letters*, Volume 64, Issue 19, 2010, Pages 2072-2075, ISSN 0167-577X, <https://doi.org/10.1016/j.matlet.2010.06.022>.

[3] Naik, R., Jena, S., Ganesan, R. et al. Effect of laser irradiation on optical properties of Ge12Sb25Se63 amorphous chalcogenide thin films. *Indian J Phys* 89, 1031–1040, 2015. <https://doi.org/10.1007/s12648-015-0678-8>

[4] Dawar, A. L., Kumar, A., Sharma, S. et al. Effect of laser irradiation on structural, electrical and optical properties of SnO2 films. *J Mater Sci* 28, 639–644 (1993). <https://doi.org/10.1007/BF01151238>

[5] Rafailovich, J., M. Hamad, T. K. Yusop, R. M. Al-Taa'y, Wasan A. Abdullah, Bashar Yousif, Emad. Laser Induced Modification of the Optical Properties of Nano-ZnO Doped PVC Films The effect of continuous CO<sub>2</sub> laser. pp.1687-9422. <https://doi.org/10.1155/2014/787595>, 2014, International Journal of Polymer Science, Hindawi Publishing Corporation.

[6] Лазов Л., Н. Ангелов, Изследване на контраста във функция от скоростта при лазерно маркиране на образци от стомана, International Scientific Conference, Gabrovo, 2010.

[7] Хаимович, С., Справочник по черни и цветни метали, Техника, С., 1961.

[8] <https://metinvestholding.com/bg/products/steel-grades/1075>

[9] Dolchinkov N., Practical research of marking and cutting of textiles with increased resistance, using CO<sub>2</sub> laser, *Journal of Physics: Conference Series*, Volume 1681, 2020, 1681 012014 IOP Publishing The 6th International Conference on Chemical Materials and Process 2-4 July 2020, Warsaw, Poland, doi:10.1088/1742-6596/1681/1/012014, Online ISSN: 1742-6596, Print ISSN: 1742-6588

[10] Dolchinkov N., Marking and Cutting of Non-metallic Products with CO<sub>2</sub> Laser, IOP Publishing Ltd, *Journal of Physics: Conference Series*, Vol. 2224, 2021 2nd International Symposium on Automation, Information and Computing (ISAIC 2021) Online ISSN: 1742-6596, Print ISSN: 1742-6588, pp 1-8

[11] Dolchinkov N., L. Lazov, J. Ivanov, D. Nedyalkov, L. Linkov, Study of cutting and labeling of polymethylmethacrylate using a CO<sub>2</sub> laser, 12th International Scientific and Practical conference Environment. Technology. Resources. doi.org/10.17770/etr2019, vol. 3.4203, ISBN 1691-5402, pp. 37-40

[12] Lazov, L., Petrov, N. & Teirumnieks, E.. Investigation of the influence of the number of repetitions on the process of laser marking of HS6-5-2-5 steel. *Environment. Technologies. Resources. Proceedings of the International Scientific and Practical Conference*. 3, 2021, 163-167. 10.17770/etr2021vol3.6567.

[13] Lazov L., Teirumnieks E., Angelov N.; Yankov E., Modification of the roughness of 304 stainless steel by laser surface texturing (LST), *Laser Physics, Laser Physics*, Volume 33, Number 4 , 2023, DOI 10.1088/1555-6611/acbb76.

[14] Колева, К., В. Маринова. Математическите модели в химията, Сборник научни статии „Междупредметни връзки в обучението по математика и информатика“ по проект “Междупредметни връзки в обучението по математика и информатика – дидактически модели и технологии”, Издателство „Ивис“, В. Търново, с. 28-35, 2009, ISBN 978-954-8387-49-1, COBISS.BG-ID – 1231378404,.

[15] Колева, К., Три математически модела за изравняване на химични уравнения, Сборник доклади от Годишната университетска научна конференция на НВУ “Васил Левски”, В. Търново, том 3, Научно направление „Природоматематически науки“, с. 131-144, Издателски комплекс на НВУ „В. Левски“, 2020, ISSN 1314-1937.

[16] N. Tonchev, E. Yankov, Multi-criteria support for decision-making by shifting restrictions, in Proceedings of the International Scientific Conference “Mathematical Modeling”, 12.2017, DOI: 10.13140/RG.2.2.13458.35520.

[17] Tontchev, N.; Hristov, N. Numerical Procedure to Determine the Optimal Composition of the Steel a Small Volume Database with the Same Treatment. *International virtual journal for science, technics and innovations for the industry, Machines, Technologies, Materials*, VII, 2013, 11: 54-57.

[18] Leoneed M. Kirilov, Nikolai T. Tontchev, Alexander L. Monov, Multiple Criteria Approach to Solving Problems of Metal Building-Up by Welding, IFAC Proceedings Volumes, Volume 37, Issue 19, 2004, Pages 255-260, ISSN 1474-6670, [https://doi.org/10.1016/S1474-6670\(17\)30693-6](https://doi.org/10.1016/S1474-6670(17)30693-6)

# Optical Systems for Reducing the Divergence of Laser Beams

**Dimcho Pulov**

Department of Mechanical and Precision Engineering  
Technical University of Gabrovo  
Gabrovo, Bulgaria  
pulov@mail.bg

**Petar Tsvyatkov**

Department of Mechanical and Precision Engineering  
Technical University of Gabrovo  
Gabrovo, Bulgaria  
ppeter@mail.bg

**Abstract.** The rational use of lasers as sources of radiation is also related to the development of optical systems for conversion of laser radiation. One of the ways to convert the laser radiation is related to its collimation, changing the cross-section and changing the divergence. This article presents a methodology for designing two component optical systems to reduce the divergence of laser beams. Ready-made optical elements were used, with which three different configurations were created and analyzed. The optical design was developed and subsequent optimization was performed. The resulting system has diffraction-limited quality of the outgoing laser beam and small dimensions.

**Keywords:** beam divergence, beam expander, laser, optical design.

## I. INTRODUCTION

Laser radiation has specific properties such as coherence, high monochromaticity, high focus, high spectral and surface power. These properties of lasers allow the development of highly efficient devices and machines, fundamentally different from those operating with thermal sources of radiation [1] – [6]. In recent decades, lasers have expanded their application in technological processes related to machining of metals and alloys, such as: marking, engraving, cutting, drilling, scribing, etc.

An important part of laser technological installations is the optical system which affects the capabilities and characteristics of the entire device. Therefore, in order to use lasers rationally in various technological processes, it is necessary to develop optical systems for converting laser radiation [7], [8]. The most common way to convert laser radiation is to focus it into a spot of minimal diameter [9], [10]. Such a spot may be the waist of a beam focused by a corresponding optical system. Direct use of focusing optical systems, in most cases, does not give an optimal result. In order to obtain a spot of minimum size, it is

necessary to first reduce the divergence of the laser beam and then to focus it.

## II. EXPOSITION

### A. Principles of focusing powerful laser radiation

For the efficient operation of the technological lasers, it is necessary that the required radiation power density in the material processing area is reached.

Changes in intensity are related to changes in the spatial width of the beam. They are caused by the diffraction and refraction of the beam by optical elements. To assess the effect of the laser radiation on the materials being processed, it is necessary to know the intensity of the beam at the focus and in the vicinity of the focus.

The transverse intensity distribution of a Gaussian beam operating in the fundamental mode  $TEM_{00}$  is given by the expression

$$I(r) = I(0) \cdot e^{-2\left(\frac{r}{\omega}\right)^2} \quad (1)$$

where:  $r$  is a radial distance from the axis of the beam;  $I(r)$  and  $I(0)$  are the intensity of the beam at distance  $r$  and the axis;  $\omega$  is beam radius at which the intensity decreases  $e^2$  times.

The beam waist at the output of the laser has a radius of  $\omega_0$  and is usually located inside the resonator. Outside the resonator, the width of the beam increases due to the increase in the distance and the diffraction. The Gaussian distribution of the beam is preserved, but divergence  $\theta$  appears.

$$\theta = \frac{\lambda}{\pi\omega_0} \quad (2)$$

Print ISSN 1691-5402

Online ISSN 2256-070X

<https://doi.org/10.17770/etr2023vol3.7217>

© 2023 Dimcho Pulov, Petar Tsvyatkov. Published by Rezekne Academy of Technologies.  
This is an open access article under the [Creative Commons Attribution 4.0 International License](https://creativecommons.org/licenses/by/4.0/).

Suppose this laser beam is focused by means of a single lens (Fig.1).

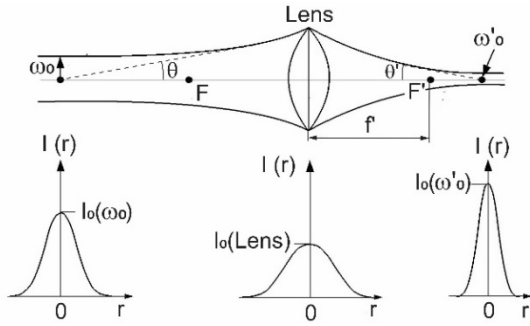


Fig. 1. The intensity distribution of a Gaussian beam before and after lens.

The diameter of the beam waist after the lens depends on the aberrations of the lens and the diffraction and is determined by the formula:

$$d_{min} = 2\omega'_0 = \underbrace{M^2 f' \frac{4\lambda}{\pi\omega_0}}_{\text{Diffraction}} + \underbrace{\frac{kD^3}{f'^2}}_{\text{Aberration}} \quad (3)$$

where:  $M^2$  – beam quality factor;  $f'$  - focal length of the focusing lens;  $D$  – diameter of the beam entering the lens;  $k$  – coefficient dependent on the lens aberrations.

For the Gaussian beam in mode  $TEM_{00}$   $M^2 = 1$ . Due to the axial propagation of laser beams, it can be assumed that off-axis aberrations are absent and only the spherical aberration is relevant. For a plano-convex lens the coefficient  $k = 0,067$ . Then from (2) and (3) it follows

$$d_{min} = 2\omega'_0 = \underbrace{\frac{2\theta f'}{f'^2}}_{\text{Diffraction}} + \underbrace{\frac{0,067D^3}{f'^2}}_{\text{Aberration}} \quad (4)$$

Expression (4) shows that there are 3 factors that affect the size of the laser spot:

- Focal length of the focusing lens  $f'$ . A decrease in  $f'$  leads to a decrease in the diffraction phenomena, and a corresponding decrease in the size of the laser spot. At the same time, as the focal length of the focusing lens decreases the spherical aberration increases. Obviously, the decrease in  $f'$  affects the spot size in various directions and at different rates. The decrease of the spot size due to the decrease of the focal length is proportional to the first power of  $f'$ . The increase of the spot due to the increase of the spherical aberration is proportional to the second power of  $f'^2$ .
- Divergence of the input laser beam  $\theta$ . A decrease in  $\theta$  leads to a decrease in the diffraction phenomena, and consequently to a decrease of the size of the laser spot.
- Diameter  $D$  of the laser beam incident on the focusing lens. The increase of  $D$  has a double effect. On the one hand, it leads to an increase in the spherical

aberration, and on the other hand to a decrease in diffraction.

Reducing  $f'$  is not a rational way to minimize the laser spot because it results in a decrease in the depth of the beam waist displacement, and accordingly limits the capabilities of the technological process. An effective way to achieve this goal is to use a focusing system composed of two groups. The first group simultaneously reduces the divergence and increases the diameter of the beam [11] – [14]. Generally, this is a collimating optical system. The second group focuses the laser beam thus formed into a spot of minimal size. A lens composed of one or more lenses can be used. The goal of this study is to develop a collimating system to reduce divergence of laser beams.

### B. Selecting the type of the collimating system

There are two types of collimating systems, designated here as Type 1 and Type 2 (Fig. 2).

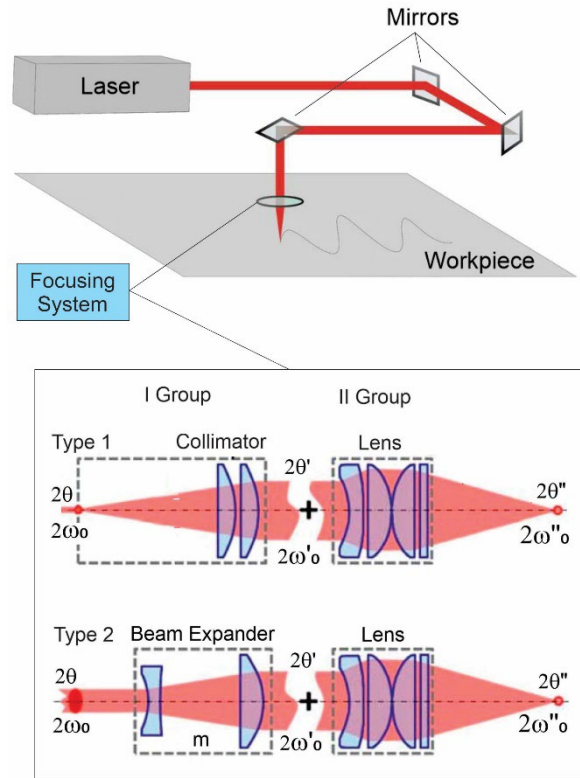


Fig. 2. Scheme of laser processing of materials.

- Type 1. A one-component collimating system, which can be composed of one or several lenses. The waist of the beam should be positioned at the front focus of the collimator. The divergence after the collimator is determined by

$$\theta' = \sqrt{\frac{2\lambda}{\pi r'_k}} = \frac{\omega_0}{f'_k} \quad (5)$$

where:  $r'_k$  - confocal parameter of the beam after the collimator;  $f'_k$  - focal length of the collimator.

It follows from expression (5) that in order to achieve low divergence, the confocal parameter must be increased, which in turn leads to an increase in the focal length of the collimator. This is an unacceptable solution because it significantly increases the overall dimensions of the system.

- Type 2. Two-component collimating system

The dimensions of the collimating system can be greatly reduced if it is made up of two components [15] – [17]. The first component focuses the beam and minimizes the size of the waist. It must therefore have a relatively short focal length  $f'_1$ . The first component can be positive or negative. The use of a negative component is preferable because it reduces the overall size of the system, the appearance of unwanted thermal phenomena is avoided due to the absence of an intermediate real image, and in such a system it is easier to correct for spherical aberration. The second component is positive. It is intended to reduce the divergence of the laser beam. For this purpose, it must first have a relatively greater focal length  $f'_2$  and secondly, be positioned so that its front focus coincides with the image of the waist from the first component.

Galileo's inverted telescopic system (beam expander) most fully meets the conditions for a two-component collimating system.

### C. Development of a two-component collimating system

The beam divergence depends on the angular magnification of the collimating system  $MP$  which is determined by the ratio between the focal lengths of the two components.

$$MP = -\frac{f'_1}{f'_2} = \sqrt{\frac{z_k}{z'_k}} = \frac{\theta'}{\theta} = \frac{\omega'_0}{\omega_0} \quad (6)$$

where:  $z_k$  and  $z'_k$  are the confocal parameters of the beam before and after the collimating system.

Expression (6) shows that in order to reduce the divergence it is necessary that  $MP < 1$ . This is achieved by proper selection of the focal lengths  $f'_1$  and  $f'_2$ , which results in the required ratio between the confocal parameters of the beam, which in turn causes a decrease in the divergence and an increase in the size of the beam waist after the collimating system.

Expression (6) is true for a precisely focussed Galilean telescopic system, i.e. for one where the back focus of the first component coincides with the front focus of the second component. Strictly speaking, after the first component of the collimating system the waist of the beam does not coincide with its back focus. Therefore, to minimize the divergence it is necessary to defocus the Galilean system and place the front focus of the second component at distance  $\Delta$  from the back focus of the first component, so that it coincides with the image of the waist from the first component:

$$\Delta = z'_1 = -\frac{z_1 f_1'^2}{z_1^2 + \frac{z_{k1}^2}{4}} \quad (7)$$

where:  $z_1$  – distance from the beam waist after the laser to the front focus of the first component of the collimating system;  $z'_1$  – distance from the beam waist after the first component to its back focus;  $z_{k1}^2$  – confocal parameter before the collimating system.

It is assumed that the type of the laser and its parameters are known:  $\lambda, \omega_0 = \omega_1, \theta = \theta_1, r_k = r_{k1}$ . The design of the two-component collimating system was developed in the following sequence:

- a) Determining the angular magnification  $MP$  by expression (6).
- b) Determining the diameter  $D_1$  of the first component.

$$D_1 \geq 2\omega_0 \sqrt{1 + \frac{2s_1}{r_k^2}} \quad (8)$$

where  $s_1$  is the distance between the laser waist and the principal planes of the first component of the collimating system.

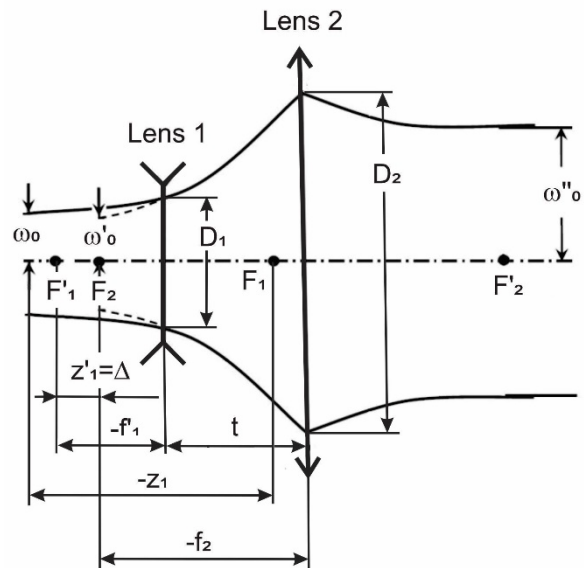


Fig. 3. Scheme of laser processing of materials.

- c) Determining the focal length of the first component  $f'_1$  so that, for aberration reasons, the focal number of the collimating system meets the condition  $F/N > 4$ .
- d) Determining the defocus of the Galilean system by expression (7).
- e) Determining the confocal parameter of the beam  $r'_{k1}$  after the first component

$$r'_{k1} = \frac{r_{k1} f_1'^2}{z_1^2 + z_{k1}^2/4} \quad (9)$$

f) Determining the beam waist  $\omega'_{01}$  after the first component

$$\omega'_{01} = \sqrt{\frac{\lambda r'_{k1}}{2\pi}} \quad (10)$$

g) Determining the focal length of the second component  $f'_2$

$$f'_2 = \frac{f_1' r_{k1}}{MP \sqrt{4z_1^2 + r_{k1}^2}} \quad (11)$$

h) Determining the diameter  $D_2$  of the second component

$$D_2 = 2\omega'_{01} \sqrt{1 - \left(\frac{2f_2'}{r_{k1}}\right)^2} \quad (12)$$

#### D. Results

A two-component collimating system was developed for a Nd-YAG laser with a wavelength  $\lambda = 1,064 \mu\text{m}$  and a beam waist diameter  $2\omega_0 = 3 \text{ mm}$ . The angular magnification of the collimating system is  $MP = 0,2^x$ , which results in a 5 times increase in beam width.

In order to simplify the design and reduce the price, ready-made optical elements [18], [19] from the Edmund Optics catalog were used. For Lens 1 and Lens 2 from Fig. 3 are chosen negative plano-concave and positive plano-convex singlet respectively. To reduce spherical aberration, rays enter the lenses through their flat surfaces. Three configurations of collimating systems have been developed that use lenses with different focal lengths. These configurations are optimized using the OSLO optical software.

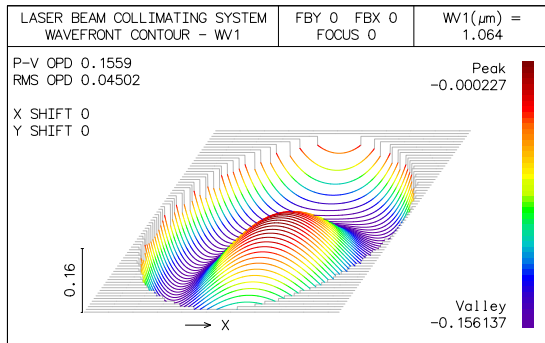


Fig. 4. Wavefront analysis of configuration 2.

The distance between Lens 1 and Lens 2 was used as a variable parameter. The distance  $t$  and the total length of the collimating system  $L$  were determined taking into

account the actual thickness of the lenses. As an optimization criterion were used the RMS wavefront error (Marechal criterion), the peak-to-valley (P-V) wavefront error (Rayleigh criterion) and RMS spot size in the image plane (Airy disc criterion).

TABLE 1 THE PARAMETERS OF THE THREE CONFIGURATIONS COLLIMATING SYSTEMS

Configuration		1	2	3
Lens 1	$f_1, \text{ mm}$	-12	-12	-24
	$D_1, \text{ mm}$	6	6	12
	Catalog №	#45-008	#45-698	#45-016
	Glass	N-BK7	Si	N-BK7
Lens 2	$f_2, \text{ mm}$	60	60	120
	$D_2, \text{ mm}$	25	25	30
	Catalog №	#45-127	#45-127	#45-243
	Glass	N-BK7	N-BK7	N-BK7
Collimating system	$t, \text{ mm}$	45,72	45,79	93.9
	$L, \text{ mm}$	51,92	52,49	103.4
	$W_{RMS}, \text{ waves}$	0,08024	0,04502	0,008107
	Marechal criterion	0,071	0,071	0,071
	$W_{P-V}, \text{ waves}$	0.2612	0,1559	0,02675
	Rayleigh criterion	0.25	0.25	0.25
	Spot radii $\beta_{RMS}, \text{ mrad}$	0,139	0,065	0,019
	Airy radii $\beta_{Airy}, \text{ mrad}$	0,084	0.083	0.086

$$\left. \begin{array}{l} \text{Rayleigh criterion} \\ \text{Marechal criterion} \\ \text{Airy disc criterion} \end{array} \right\} \begin{array}{l} W_{P-V} < \frac{\lambda}{4} \\ W_{RMS} < \frac{\lambda}{14} \\ \beta_{RMS} \ll \beta_{Airy} \end{array} \quad (13)$$

In table. 1 shows the parameters of the three configurations and the results of their evaluation according to these criteria.

- The worst quality is in the configuration 1, which is made up of lenses with small focal lengths. This configuration does not meet any of the criteria (13)
- In configuration 2, the first lens is Fused Silica. This is a compact system with the same small focal lengths.
- Configuration 3 scores many times over criteria (13), but its dimensions are the largest.

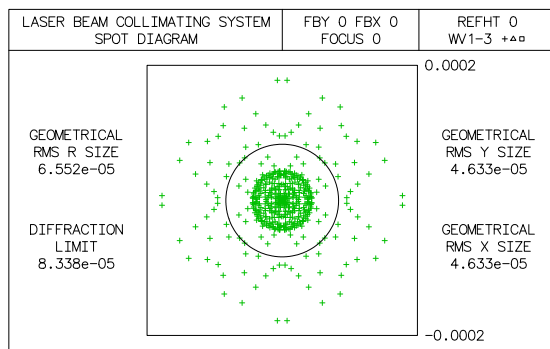


Fig. 5. Spot diagram analysis of configuration 2

Table 1 shows that configurations 2 and 3 are diffraction limited. Configuration 2 can be accepted as optimal. In Fig. 4 and Fig. 5 is shown evaluation of its wavefront and spot diagram.

### III. CONCLUSION

The principles of laser beam focusing are investigated. For increasing the intensity of the laser beam into a small spot, it is first necessary to expand it and reduce its divergence. A two-component collimating system has been developed, which is based on Galileo's inverted afocal system. Ready-made optical elements were used, with which three different configurations were created and analyzed. The resulting optical systems are optimized to minimize the peak-to-valley (P-V) wavefront error, RMS wavefront error and the RMS spot size. Configuration 2 was chosen as optimal because it fulfills these quality criteria and at the same time the focal lengths and dimensions are small.

### REFERENCES

[1] H.J. Eichler, J. Eichler and O. Lux, *Lasers: Basics, Advances and Applications*, Springer Series in Optical Sciences, Springer Nature Switzerland AG, 2018.

[2] V. Neumann, "Focusing and optical imaging in applied laser technologies", *Laser Technik Journal*, Vol.9, Issue 1, Jan.2012, pp. 41-44, doi: 10.1002/latj.201290007.

[3] I. Kolev and T. Karadzov, "Classification, parameters, characteristics and application of matrix semiconductor photoconverters", 27th International Spring Seminar on Electronics Technology, ISSE 2004, Bankya 13-16 May 2004, Vol. 3, pp. 444 - 447, doi:10.1109/ISSE.2004.1490852.

[4] L. H. J. F. Beckmann and D. Ehrlichmann, "Optical systems for high-power laser applications: principles and design aspects", *Optical and Quantum Electronics*, Vol. 27, Issue 12, pp. 1407 - 1425, Dec. 1995, doi: 10.1007/BF00326492.

[5] F. Bisti, I. Alexeev, M. Lanzetta and M. Schmidt, "A simple laser beam characterization apparatus based on imaging", *Journal of*

*Applied Research and Technology, Open Access*, Vol. 19, Issue 2, Pages 98 - 116, April 2021, doi: 10.22201/icat.24486736e.2021.19.2.157.

[6] D. Dichev, F. Kogia, H. Koev and D. Diakov, "Method of Analysis and correction of the Error from Nonlinearity of the Measurement Instruments", *Journal of Engineering Science and Technology Review*, Vol. 9, Issue 6, 2016, pp. 116-121, doi: 10.25103/jestr.096.17.

[7] P.A. Nosov, V.Yu. Pavlov, I.I. Pakhomov and A.F. Shirankov. *Aberrational synthesis of optical systems intended for the conversion of laser beams*. *J Opt Techn* 2011; 78(9): 586- 593. doi: 10.1364/JOT.78.000586

[8] B. Eppich, "Optical Design of Beam Delivery and Beam Forming Systems.", *Optik & Photonik*, Vol. 3, Issue 2, pp. 48-51, June 2008, doi: 10.1002/opph.201190193.

[9] F. Abt, A. Heß and F. Dausinger, "Focusing of high power single mode laser beams", 26th International Congress on Applications of Lasers and Electro-Optics, ICALEO 2007 - - Congress Proceedings, doi: 10.2351/1.5061053.

[10] S.A. Self, "Focusing of spherical gaussian beams", *Applied Optics*, Vol. 22, Issue 5, pp. 658 - 661, March 1983, doi: 10.1364/AO.22.000658.

[11] T. Wang, C. Cao, X. Zeng, Y. Liu and J. Ning, "Analysis of divergence angles of truncated and untruncated beams in collimation system", *Optik*, Vol. 194, Oct. 2019, doi: 10.1016/j.ijleo.2019.163130.

[12] X. Liu, J. He, X. Sun and M. Zhang, "Instrument for collimating and expanding Gaussian beams for underwater laser imaging systems", *Optical Engineering*, Vol. 37, Issue 9, pp. 2467 - 2471, Sept. 1998, doi: 10.1117/1.601770.

[13] L. Lévesque, "Divergence of far-infrared laser beam and collimation for Galilean and Keplerian system designs", *Optics and Laser Technology*, Vol. 41, Issue 5, pp. 557 - 561, July 2009, doi: 10.1016/j.optlastec.2008.10.009.

[14] R. S. Sirohi, "Optical beam collimation procedures and collimation testing: A summary", *Optical Engineering*, Vol. 59, Issue 4, April 2020, doi: 10.1117/1.OE.59.4.040801.

[15] D. Shafer, "Two-element laser beam expander", *Optics and Laser Technology*, Vol. 14, Issue 1, Pages 37-38, Febr.1982, doi: 10.1016/0030-3992(82)90066-4.

[16] A.F. Shirankov, P.A. Nosov, I.I. Pakhomov, A.G. Grigor'yants, V.P. Yakunin and R.S. Tret'yakov, *Elaboration of laser optical systems of technological installations on the base of the laser optics theory*. *Inzhenernyy zhurnal: nauka i innovatsii* [Engineering Journal: Science and Innovation], no. 9 (21), 2013, doi: 10.18698/2308-6033-2013-9-926

[17] H. Sun, "Thin Lens Equation for a Real Laser Beam with Weak Lens Aperture Truncation", *Optical Engineering*, Vol. 37, No. 11, 1998, pp. 2903-2913, doi: 10.1117/1.601877.

[18] R. G. Schuhmann, "Standardized optical components for laser applications", *Proceedings of SPIE - The International Society for Optical Engineering*, Vol. 3737, pp. 644 - 648, Design and Engineering of Optical Systems II, August 1999, doi: 10.1117/12.360063.

R. G. Schuhmann, "Quality of optical components and systems for laser applications", *Proceedings of SPIE - The International Society for Optical Engineering*, Vol. 3578, pp. 672 - 680, Laser-Induced Damage in Optical Materials, April 1999, doi: 10.1117/12.344430.

# Investigating the Contrast of Surface Marking on Different Color Connectors for Telecommunications Needs

**Daniels Raubiška**

Faculty of Engineering  
Rezekne Academy of Technologies  
Rezekne, Latvia  
e-mail: dr17057@edu.rta.lv

**Imants Adijāns**

Faculty of Engineering  
Rezekne Academy of Technologies  
Rezekne, Latvia  
imants.adijans@rta.lv

**Emil Yankov**

Faculty of Engineering  
Rezekne Academy of Technologies  
Rezekne, Latvia  
emil.yankov@rta.lv

**Lyubomir Lazov**

Faculty of Engineering  
Rezekne Academy of Technologies  
Rezekne, Latvia  
lyubomir.lazov@rta.lv

**Abstract.** The development of marking technologies for telecommunications connectors requires increasingly detailed information about their applications. One solution is to use QR codes that contain sufficient information about the connectors' applications. Accurate marking of connectors requires a precise marking system, such as a laser marking system. In this study, a Rofin PowerLine F20 Varia fiber laser was used to mark four different types of ABS plastic connectors in various colors. To achieve optimal marking for all four colors, three experiments were conducted to achieve contrasting marking and high roughness. Easy QR code reading was achieved with an average marking power of 3 W to 4.2 W, a laser marking speed of 300 mm/s to 500 mm/s, and a scanning frequency of 50 kHz to 70 kHz at a constant pulse duration of 8 ns and raster spacing of 50  $\mu$ m. The microstructural changes and change in roughness were determined using a laser scanning microscope (Olympus OLS5000), which revealed structural changes on the surface and an increase in relative roughness from 39% to 76%. This experiment shows that different parameters of the laser marking mode are required for each color.

**Keywords:** ABS plastic, Contrast, Fiber laser marking, QR code, Roughness.

## I. INTRODUCTION

Labeling is used for various goods and products today. It is necessary to identify parts and different products. Thanks to the marking, the manufacturer controls the

quality of the product and the consumer has the opportunity to obtain a quality guarantee, as well as to find out the characteristics and parameters of the purchased goods. Laser marking of materials is most often used in companies, because it is the fastest and most efficient way to mark products in large volumes [1]-[2]. Also, laser marking leaves a deep mark on the product, which is standard in many industries. Therefore, these marks cannot be removed without mechanical damage to the product. That is why the company can prevent unauthorized access to the product, mark the expiration date and improve the quality of the product. For example, a quick response (QR) code, which is a two-dimensional matrix barcode containing information about the object to which it is attached, can be used for this purpose. A QR code uses four standardized encoding modes (numeric, alphanumeric, binary, and kanji) to efficiently store data [3]. Laser marking is based on changes in the surface structure of the material being processed. Usually, this process is associated with the evaporation of material particles, as a result of which the marking appears as an indentation on the surface of the material. There is also another marking method, when the surface of the material is melted, in this way the morphological and structural changes of the surface occur, which creates a strongly pronounced marking effect [4].

Print ISSN 1691-5402

Online ISSN 2256-070X

<https://doi.org/10.17770/etr2023vol3.7263>

© 2023 Daniels Raubiška, Imants Adijāns, Emil Yankov, Lyubomir Lazov.

Published by Rezekne Academy of Technologies.

This is an open access article under the [Creative Commons Attribution 4.0 International License](https://creativecommons.org/licenses/by/4.0/).

Laser marks can be obtained using both thermal and thermal modes of beam-material interaction. Each thermal mechanism is characterized by a temperature rise that ranges from heating, melting, and vaporization [5]-[6]. The effects of material properties (such as absorptivity and melting point) and marking parameters (such as power density, focal position and marking speed) on mark readability characteristics (such as mark contrast and mark width) are reviewed [7]-[8]. Advances in direct laser marking of plastics provide unprecedented marking quality, contrast and speed. When used correctly, laser marking can provide many manufacturing benefits and improve product appearance and function [9]. To obtain high-quality images, knowledge of the interaction of the laser with plastic is necessary. [10]-[11]. A fiber laser was used for the experiments, it is a class of solid-state lasers in which the amplification medium is an optical fiber. Fiber lasers have been a key technology in the field of solid-state lasers since the first proposal to use an optical fiber as a laser mode selector. Stimulated emissions from the amplifying fiber coherently amplify the signal as the signal oscillates between two signal reflectors [12]-[13].

The purpose of the present study is to determine the influence of the color of the surface of the studied samples (telecommunications connectors), how it affects the marking process under the same conditions, technological parameters of the laser.

## II. MATERIALS AND METHODS

ABS (acrylonitrile-butadiene styrene) plastic-impact-resistant technical thermoplastic resin based on acrylonitrile copolymer with butadiene and styrene was used for the experiments. The proportions vary: 15 - 35 % acrylonitrile, 5 - 30 % butadiene and 40 - 60 % styrene. A characteristic softening temperature is 150 - 160 °C and a boiling point of 245 °C. This material is actively used in many industrial and scientific sectors.



Fig. 1. Determining the value of the contrast marking on collar connectors using Photoshop.

This material is actively used in many industrial and scientific sectors, such as chemical industry, construction industry, automobile industry, household appliances, electronic connecting connectors and other related fields [14]-[16]. Plastic connectors designed for optical fibers with four different colors - blue, cream, green and fuchsia - were used for the research (Fig.1).

The goal is to establish laser marking modes that provide contrast with an easily readable Q code. The Rofin PowerLine F20 Varia laser system (Fig.2) with a wavelength of 1064 nm was used for the experiments. The technological capabilities of the system are average power 20 W, pulse duration from 4 to 200 ns and pulse repetition frequency from 2 to 1000 kHz, line step from 1 μm to 120 mm and speed from 1 mm/s to 2000 mm/s. The maximum marking area is 120 mm × 120 mm.



Fig. 2. Fiber laser Rofin PowerLine F20 [17].

Three marking constant parameters are pulse duration 8 ns and line pitch 5 μm, diameter of working spot  $d = 40$  μm, defocusing  $\Delta f = 0$  mm and number of repetitions 1 for the fabricated matrices. In the first experiment, three marking speeds 300 mm/s, 400 mm/s, and 500 mm/s were selected, where the pulse energy ( $E_p$ ) (1) and peak power ( $P_p$ ) (2) were constant 60 μJ and 7.5 kW, respectively and line density  $N_x$  20 mm<sup>-1</sup> (3), intensity ( $I_p$ ) 11.94 W/μm<sup>2</sup> (5), energy or fluence ( $F_p$ ) 0.096 μJ/μm<sup>2</sup> (6). The pulse density ( $N_y$ ) (4) values for the three speeds are changed to 200 mm<sup>-1</sup>, 150 mm<sup>-1</sup> and 120 mm<sup>-1</sup>, respectively.

$$E_p = \frac{P}{f} [\mu\text{J}] \quad (1)$$

$$P_p = \frac{E_p}{\tau} [\text{kW}] \quad (2)$$

$$N_x = \frac{1}{\Delta x} [\text{mm}^{-1}] \quad (3)$$

$$N_y = \frac{f}{v} [\text{mm}^{-1}] \quad (4)$$

$$I_p = \frac{2 \times P_p}{\pi \times w^2} [\text{W}/\mu\text{m}^2] \quad (5)$$

$$F_p = \frac{2 \times E_p}{\pi \times w^2} [\mu\text{J}/\mu\text{m}^2] \quad (6)$$

$$E_{ef} = \frac{P \times f}{v^2} [\mu\text{J}] \quad (7)$$

Where  $E_p$  – pulse energy,  $P$  - average power,  $f$  - scanning frequency,  $P_p$  - peak power,  $\tau$  - pulse duration,  $\Delta x$  - line pitch,  $v$  - scanning in marking speeds,  $I_p$  – intensity,  $w$  - focal spot radius,  $F_p$  - density or fluence and  $E_{ef}$  - efficient energy.

In the second experiment, the changing parameter is the scanning frequency 50 kHz, 60 kHz and 70 kHz and the scanning speed is a constant 400 mm/s. In this case, the pulse energy ( $E_p$ ) 60  $\mu$ J and peak power ( $P_p$ ) change and 7.5 kW, respectively. The parameter line density ( $N_x$ ) 20  $\text{mm}^{-1}$ , intensity ( $I_p$ ) according to the scanning frequency respectively 11.94  $\text{W}/\mu\text{m}^2$ , density or fluence ( $F_p$ ) 0.096  $\mu\text{J}/\mu\text{m}^2$ . The values of pulse density ( $N_y$ ) for the three frequencies change to 125  $\text{mm}^{-1}$ , 150  $\text{mm}^{-1}$  and 175  $\text{mm}^{-1}$ , respectively.

In the third experiment, the average power ( $P$ ) is changed by 50 %, 60 % and 70 % (3.0 W, 3.6 W and 4.2 W). In an experiment, it will lead to constant values of pulse density ( $N_y$ ) 150  $\text{mm}^{-1}$  and line density ( $N_x$ ) 20  $\text{mm}^{-1}$  for the three average powers. For pulse energy ( $E_p$ ), peak power ( $P_p$ ), intensity ( $I_p$ ) and density or fluence ( $F_p$ ) change depending on the average power ( $P$ ) 3.0 W, 3.6 W and 4.2 W respectively pulse energy ( $E_p$ ) 50  $\mu$ J, 60  $\mu$ J and 70  $\mu$ J, peak power ( $P_p$ ) 6.25 kW, 7.5 kW and 8.75 kW, intensity  $I_p$  9.95  $\text{W}/\mu\text{m}^2$ , 11.94  $\text{W}/\mu\text{m}^2$  and 13.93  $\text{W}/\mu\text{m}^2$ , density or fluence  $F_p$  0.0796  $\mu\text{J}/\mu\text{m}^2$ , 0.0955  $\mu\text{J}/\mu\text{m}^2$  and 0.1115  $\mu\text{J}/\mu\text{m}^2$ .

After laser marking, the colored connectors (Fig.1) were scanned with a 2D scanner HP Scanjet G3010 to determine the contrast. To get my good image, the scan mode was at 2400 dpi, contrast 80 % and saved in \*.tiff format. The digital image is inserted into Photoshop to measure the resulting mark. Sampling of the unmarked and marked area is done at an area of 11x11 pixels in order to average the measurement. The obtained values for each measured area are recalculated according to equation (8) for contrast against the background in percentages:

$$k * = \frac{N_n - N_f}{N_f} \times 100\% \quad (8)$$

where  $N_f$  is measured background value,  $N_n$  measured value in a laser-marked area.

Roughness measurements and the resulting microstructure were examined with an Olympus model "OLS5000" laser microscope (Fig.3). The obtained microstructural images were carried out using a 10 $\times$  objective, magnification 227 $\times$ , as the examined area for each measurement 1280 $\times$ 1280  $\mu\text{m}$  with a measurement accuracy of  $\pm 2.0 \mu\text{m}$ . From the obtained 3D images with the laser system of the microscope, the roughness  $R_a$  and  $R_z$  perpendicular to the marking lines with a length of 1280  $\mu\text{m}$ , and the roughness  $R_q$  for the entire examined area 1280 $\times$ 1280  $\mu\text{m}$  were measured. The obtained values are plotted in tables and graphical dependences of changes in roughness depending on speed and step during surface laser processing are shown. The built dependencies are presented in the results.



Fig. 3. Olympus OLS5000 [18].

Determination of the percentage change in roughness after laser marking is determined by the dependence:

$$R^* = \frac{R_n - R_f}{R_f} \times 100\% \quad (9)$$

where:  $R_n$  is the roughness in the laser marked area,  $R_f$  is the roughness in the unmarked area of the sample.

### III. RESULTS AND DISCUSSION

For the contrast analysis, comparison plots were constructed for the three experiments of the four colors connectors and presented in (Fig.4) for the effect of the average power on laser marking, (Fig.5) for the effect of speed on laser marking and (Fig.6) for the effect of the frequency of laser marking.

#### A. The influence of power on contrast

With changing average power, it is found that the connector with Cream color has the highest contrast reaching from 39.58 % to 46.88 % compared to the background (Fig.4). A high contrast value is achieved at a power of 4.2 W. With the blue connector, maximum contrast (16.67 %) against the background is also achieved at the maximum experimental power (4.2 W). With the remaining two connectors Green and Fuchsia, the maximum contrast is obtained at 3.6 W, 27.94 % and 21.95 %, respectively. It should be noted that the resistor needs to be tested at higher wattages than 4.2 W for the Blue and Cream connectors.

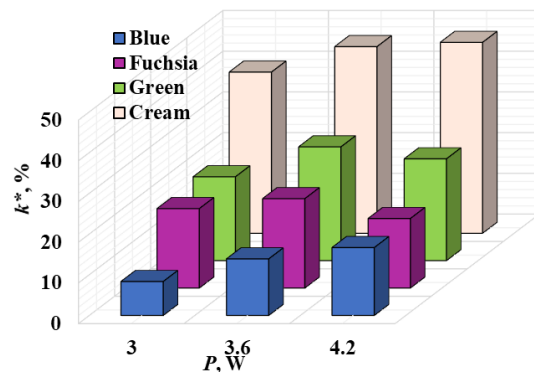


Fig.4. Comparison of power contrast.

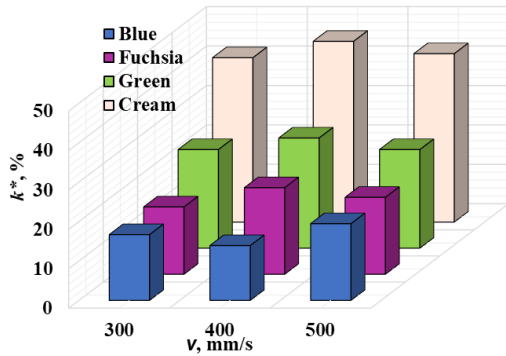


Fig.5. Comparison of speed contrast.

### B. The influence of speed on contrast

In the varying laser marking speed experiment, high contrast for the Cream, Green and Fuchsia connectors is obtained at a speed of 400 mm/s (Fig.5). While for the blue connector, maximum contrast is obtained at a speed of 500 mm/s. The highest contrast is again obtained for the connector with the color Cream 45.83 %, then for Green 27.94 % and Fuchsia 21.95 %. The pro blue connector has a contrast of 19.44%, which is the lowest value compared to the other connectors. And in this experiment, it is necessary to investigate at higher speeds to obtain a higher contrast of the blue connector.

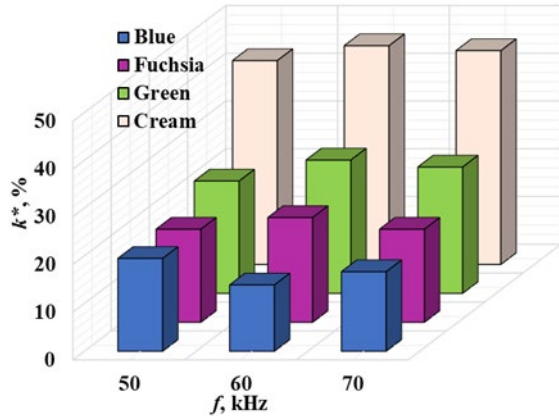


Fig.6. Comparison of frequency contrast.

### C. The influence of frequency on contrast

In the last experiment for climbing marking of colored connectors with varying scanning frequencies of 50 kHz, 60 kHz and 70 kHz, comparative contrast variation diagrams were constructed and presented in (Fig.6). At 60 kHz, the Cream, Green and Fuchsia connectors have maximum contrast, and the blue connector at 50 kHz. In the third experiment, the Cream color connector has the highest contrast 45.83 %. Next with high contrast is the connector with the color Green 27.94 %, and Fuchsia has a contrast of 21.95 %. The lowest contrast is again obtained for the blue connector 19.40 %, but this is the highest value at the three frequencies examined. In order to increase the resistance of the blue connector, it is necessary to conduct experiments at lower frequencies, which tendency is also established by the graphical dependence (Fig. 6).

The change in the roughness after laser marking compared to the roughness before marking also has an effect on the easy reading of the marking. For this purpose, comparative diagrams were built for the four colored connectors when the average power varied from 3.0 to 4.2 W (Fig.7), the speed from 400 to 600 mm/s (Fig.8) and the frequency from 50 to 70 kHz (Fig.9).

### D. The influence of power on roughness

The results of the comparison with power variation show that the power variation affects the roughness of the connectors (Fig.7). The highest percentage of change in roughness is found for the Cream connector  $R_z^* = 99.44\%$  at an average power of 4.2 W. In this case, the effective energy is the highest ( $E_{ef} = 1.58 \mu J$ ) for the conducted experiment. For the connector with blue color, the highest roughness is also achieved at 4.2 W ( $R_z^* = 55.50\%$ ), and the effective energy is the same (Tabl.1). An interesting trend for the variation of roughness is obtained for the Fuchsia color connector, with the maximum roughness being achieved at a lower average power of 3 W, where  $R_z^* = 45.12\%$ . As the power increases to 4.2 W, the roughness decreases to  $R_z^* = 8.93\%$ . The maximum effective energy for high roughness in this experiment is  $1.13 \mu J$  at a core power of 3 W.

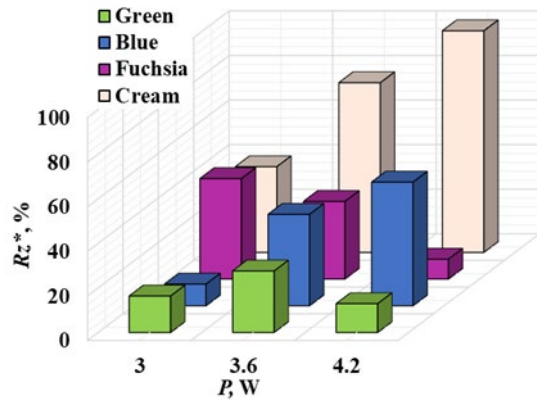


Fig.7. Surface roughness at average power changes.

With the Green connector, the maximum roughness ( $R_z^* = 27.59\%$ ) is achieved at an average power of 3.6 W, where the effective energy is  $1.35 \mu J$ . At the remaining two power values, the roughness is lower. For reading the mark in this power change experiment, one can mainly rely on the resulting contrast mark and good roughness. The main reason for the increase in roughness is the increase in pulse energy ( $E_p$ ), peak power ( $P_p$ ) and intensity ( $I_p$ ) and density or fluence ( $F_p$ ) with an increase in average power.

TABLE 1. CHANGE OF EFFECTIVE ENERGY ACCORDING TO THE AVERAGE POWER, SCAN FREQUENCY AND SPEED SCANNED

	P (W)			f (kHz)			v (mm/s)		
	3	3.6	4.2	50	60	70	300	400	500
$E_{ef}, \mu J$	1.13	1.35	1.575	0.9375	1.125	1.3125	2.4	1.35	0.864

*E. The influence of speed on roughness*

In the experiment with varying the speed of 300 mm/s, 400 mm and 500 mm/s, the roughness is varied according to the color of the connector (Fig.8). At the low scan speed of 300 mm/s, the Blue and Green connectors have the highest roughness changes,  $R_z^* = 47.75\%$  and  $R_z^* = 39.71\%$  %, respectively, where the effective energy in this experiment is 2.4  $\mu\text{J}$ . With the Cream connector, the maximum roughness ( $R_z^* = 76.16\%$  %) is obtained at a scanning speed of 400 mm/s, which is the highest for the entire experiment. The effective energy at this rate is 1.35  $\mu\text{J}$ . For the Fuchsia connector, the roughness variation has the lowest values for the experiment. A maximum value of the roughness ( $R_z^* = 35.05\%$  %) is obtained at 500 mm/s, where the effective energy is lowest for the experiment 0.864  $\mu\text{J}$ . This shows that for the Fuchsia connector, the absorbed energy at constant values of 60 kHz and average power of 3.6 W results in lower roughness changes.

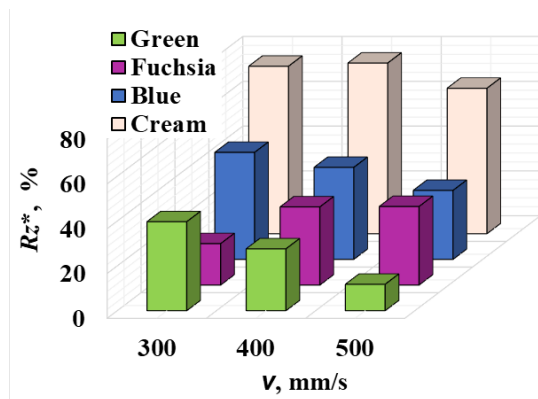


Fig.8. Surface roughness for speed change.

*F. The influence of frequency on roughness*

In a frequency change experiment, a variable parameter is the pulse density in line ( $N_y$ ), which at 50 kHz is 125  $\text{mm}^{-1}$ , 60 kHz is 150  $\text{mm}^{-1}$ , and 70 kHz is 175  $\text{mm}^{-1}$ . This change in pulse density in a line affects the change in roughness. The highest relative roughness change from baseline roughness in this experiment is achieved at the 70 kHz scan rate for the Blue, Cream, and Fuchsia connectors, where  $R_z^* = 49.48\%$  %,  $R_z^* = 76.73\%$  %, and  $R_z^* = 67.41\%$  % respectively (Fig.9). In this frequency scan, the ejective energy is the highest for the experiment 1.3125  $\mu\text{J}$ . Unlike the other connectors, the Green connector has maximum roughness at 60 kHz ( $R_z^* = 27.59\%$  %), where the effective energy is lower at 1.125  $\mu\text{J}$ . And in this experiment, the lowest values for change in roughness are found at the Green connector. All color connectors in this experiment have a result exceeding 10 % of the usable roughness. This result shows that the reading of the laser marking can be relied on the obtained contrast between the background and the marking and the resulting increased roughness.

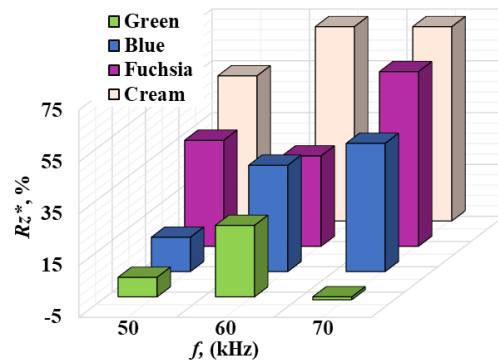


Fig. 9. Surface roughness at frequency changes.

From the laser marking experiments performed, modes were selected that gave high contrast and large roughness variation for each connector. Developed a QR code for laser marking, exploiting the established optimal modes for easy reading. In (Fig.10) the marked connectors with a developed QR code are presented.



Fig. 10. Marking the QR code.

From the marking readability check, it was found that reading the markings for the Blue, Cream and Fuchsia connectors was very easy. While the Green color connector is difficult to read. In order to determine the reason for the difficult reading, all connectors were measured for roughness changes with an Olympus OLS5000 scanning microscope, and the results are presented in (Fig.11-14). From the measurement, it is found that the roughness ( $R_z$ ) of the Blue, Cream and Fuchsia connectors are  $R_z = 2.089\ \mu\text{m}$ ,  $R_z = 8.875\ \mu\text{m}$  and  $R_z = 3.009\ \mu\text{m}$  respectively. While the Green connector has the lowest  $R_z = 1.957\ \mu\text{m}$ .

To improve readability, an experiment was conducted with two repetitions of marking, and the measured roughness increased to Green  $R_z = 12.108\ \mu\text{m}$  (Fig.15), and the contrast also improved. The (Fig.15) shows traces of melting with modification of the surface roughness. This made it possible to easily read the marking of QR code.

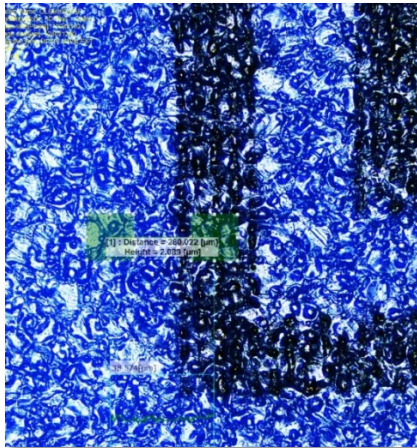


Fig. 11. Roughness connector Blue.

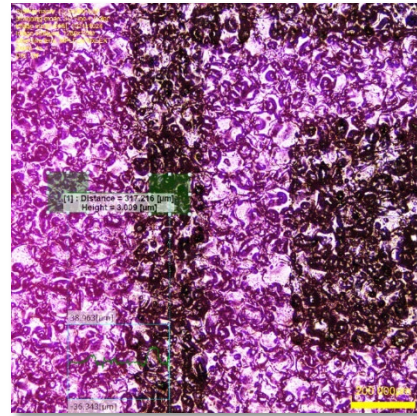


Fig. 14. Roughness connector Fuchsia.

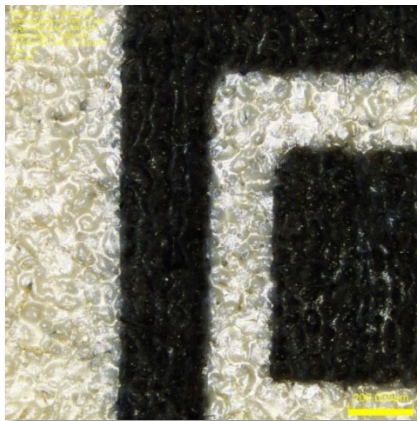


Fig. 12. Roughness connector Cream.



Fig. 15. Roughness connector Green, M-melting.

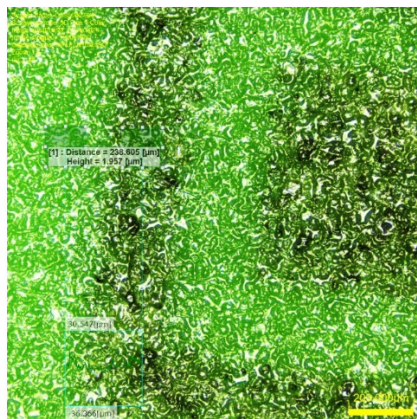


Fig. 13. Roughness connector Green.

#### IV. CONCLUSIONS

The following conclusions and findings can be made from the conducted scientific research:

- Different laser marking input parameters are required to obtain a contrast marking of QR code on a Blue, Cream, Fuchsia and Green color connector.
  - The highest contrast ( $k^* = 83.75\%$ ) is found at Cream connector at  $P = 4.2\text{ W}$ ,  $v = 400\text{ mm/s}$  and  $f = 60\text{ kHz}$ , where  $E_p = 70\text{ }\mu\text{J}$ ,  $P_p = 8.75\text{ kW}$ ,  $I_p = 0.0139\text{ W}/\mu\text{m}^2$ ,  $F_p = 0.1115\text{ }\mu\text{J}/\mu\text{m}^2$ ,  $E_{ef} = 1.575\text{ }\mu\text{J}$ ;
  - With a Green connector, the measured contrast ( $k^* = 27.94\%$ ), which is achieved at laser surface marking parameters  $P = 3.6\text{ W}$ ,  $v = 400\text{ mm/s}$  and  $f = 60\text{ kHz}$ , where  $E_p = 60\text{ }\mu\text{J}$ ,  $P_p = 7.5\text{ kW}$ ,  $I_p = 0.0119\text{ W}/\mu\text{m}^2$ ,  $F_p = 0.0955\text{ }\mu\text{J}/\mu\text{m}^2$ ,  $E_{ef} = 1.35\text{ }\mu\text{J}$ . This laser marking result was not satisfactory for the easy reading of the QR mark. During laser marking with two passes, the contrast reached values of  $k^* = 48.10\%$ , which created a prerequisite for easier reading of the QR code.
  - With connector Fuchsia contrast reaches maximum value ( $k^* = 52.70\%$ ) at laser marking parameters  $P = 3.6\text{ W}$ ,  $v = 400\text{ mm/s}$  and  $f = 60\text{ kHz}$ , where  $E_p = 60\text{ }\mu\text{J}$ ,  $P_p = 7.5\text{ kW}$ ,  $I_p = 0.0119\text{ W}/\mu\text{m}^2$ ,  $F_p = 0.0955\text{ }\mu\text{J}/\mu\text{m}^2$ ,  $E_{ef} = 1.35\text{ }\mu\text{J}$ ;

- The maximum contrast at the blue connector ( $k^* = 59.30\%$ ) is found at laser marking parameters,  $P = 3.5\text{ W}$ ,  $v = 500\text{ mm/s}$  and  $f = 50\text{ kHz}$ , where  $E_p = 70\text{ }\mu\text{J}$ ,  $P_p = 8.75\text{ kW}$ ,  $I_p = 0.0139\text{ W}/\mu\text{m}^2$ ,  $F_p = 0.1115\text{ }\mu\text{J}/\mu\text{m}^2$ ,  $E_{ef} = 0.70\text{ }\mu\text{J}$ .
- In order to improve the readability of the QR code marking, the relative roughness ( $R_z^*$ ) has also been found to have an effect. To achieve a relative roughness ( $R_z^*$ ) change of more than 10 %, different laser marking input parameters are required for the four color connectors.
  - The largest relative roughness change ( $R_z^* = 76.73\%$ ) is for the Cream connector at  $P = 4.9\text{ W}$ ,  $v = 400\text{ mm/s}$ , and  $f = 70\text{ kHz}$ , where  $E_p = 70\text{ }\mu\text{J}$ ,  $P_p = 8.75\text{ kW}$ ,  $N_y = 175.0\text{ mm}^{-1}$ ,  $I_p = 0.0139\text{ W}/\mu\text{m}^2$ ,  $F_p = 0.1115\text{ }\mu\text{J}/\mu\text{m}^2$ ,  $E_{ef} = 2.1438\text{ }\mu\text{J}$ .
  - A large relative roughness change ( $R_z^* = 49.48\%$ ) for the Blue connector is achieved in laser marking mode  $P = 4.9\text{ W}$ ,  $v = 300\text{ mm/s}$ , and  $f = 70\text{ kHz}$ , where  $E_p = 70\text{ }\mu\text{J}$ ,  $P_p = 8.75\text{ kW}$ ,  $N_y = 233.33\text{ mm}^{-1}$ ,  $I_p = 0.0139\text{ W}/\mu\text{m}^2$ ,  $F_p = 0.1115\text{ }\mu\text{J}/\mu\text{m}^2$ ,  $E_{ef} = 3.8111\text{ }\mu\text{J}$ ;
  - High relative roughness change ( $R_z^* = 67.41\%$ ) for Fuchsia connector is achieved in laser marking mode  $P = 4.2\text{ W}$ ,  $v = 500\text{ mm/s}$ , and  $f = 70\text{ kHz}$ , where  $E_p = 60\text{ }\mu\text{J}$ ,  $P_p = 7.5\text{ kW}$ ,  $N_y = 140.0\text{ mm}^{-1}$ ,  $I_p = 0.0119\text{ W}/\mu\text{m}^2$ ,  $F_p = 0.0955\text{ }\mu\text{J}/\mu\text{m}^2$ ,  $E_{ef} = 1.176\text{ }\mu\text{J}$ ;
  - Possible high relative roughness change ( $R_z^* = 39.71\%$ ) for Green connector is achieved in laser marking mode  $P = 3.6\text{ W}$ ,  $v = 300\text{ mm/s}$ , and  $f = 60\text{ kHz}$ , where  $E_p = 60\text{ }\mu\text{J}$ ,  $P_p = 7.5\text{ kW}$ ,  $N_y = 200.0\text{ mm}^{-1}$ ,  $I_p = 0.0119\text{ W}/\mu\text{m}^2$ ,  $F_p = 0.0955\text{ }\mu\text{J}/\mu\text{m}^2$ ,  $E_{ef} = 2.40\text{ }\mu\text{J}$ .

These target castings give a clear idea that the color of the connector affects the modified contrast and roughness, which is directly related to the amount of absorption (absorption) and reflection of the effective energy. Further studies are needed to determine the optimal laser marking modes for high contrast and rudeness. It is necessary to determine how the overlap parameters in pulse overlap ( $K_{ov}$ ) and coefficient of overlap between lines ( $K_{soc}$ ) affect the contrast of the marking and roughness. It is unassailable to establish the softening limits for the four connector colors when examining average powers, scan rates, and marking speeds.

#### ACKNOWLEDGMENT

The authors gratefully acknowledge financial support by the European Regional Development Fund, Postdoctoral research aid Nr. 1.1.1.2/16/I/001 research application "Analysis of the parameters of the process of laser marking of new industrial materials for high-tech applications, Nr. 1.1.1.2/VIAA/3/19/474".

#### REFERENCES

- [1] F. Bravo-Montero, D. Castells-Rufas and J. Carrabina, High-speed laser marking with diode arrays, *Optics & Laser Technology*, Volume 146, 2022, <https://doi.org/10.1016/j.optlastec.2021.107551>.
- [2] C. Lin, X. Shen, B. Hua and Z. Wang, Three-dimensional polarization marked multiple-QR code encryption by optimizing a single vectorial beam, *Optics Communications*, Volume 352, pp. 25-32, 2015, <https://doi.org/10.1016/j.optcom.2015.04.068>.
- [3] R. Kikuchi, S. Yoshikawa, P. K. Jayaraman, J. Zheng and T. Maekawa, Embedding QR codes onto B-spline surfaces for 3D printing, *Computer-Aided Design*, Volume 102, pp. 215-223, 2018, <https://doi.org/10.1016/j.cad.2018.04.025>.
- [4] В. И. Семашко, МЕТОДЫ ЛАЗЕРНОЙ МАРКИРОВКИ, Доклады - БГУИР, Минск, Беларусь 2004. [Online]. Available: <https://cyberleninka.ru/article/n/metody-lazernoy-markirovki/viewer> [Accessed May 1, 2023].
- [5] J. C. Ion, Chapter 15, *Laser Processing of Engineering Materials*, Butterworth-Heinemann, 2005, pp. 384-394.
- [6] E. Hadizadeh, S. Pazokifard, S.M. Mirabedini and H. Ashrafiyan, Optimizing practical properties of MMA-based cold plastic road marking paints using mixture experimental design, *Progress in Organic Coatings*, Volume 147, 2020, <https://doi.org/10.1016/j.porgcoat.2020.105784>.
- [7] Y. M. Noor, S. C. Tam, L. E. N. Lim and S. Jana, A review of the Nd: YAG laser marking of plastic and ceramic IC packages, *Journal of Materials Processing Technology*, Volume 42, Issue 1, Pages 95-133, 1994, [https://doi.org/10.1016/0924-0136\(94\)90078-7](https://doi.org/10.1016/0924-0136(94)90078-7).
- [8] P. Narica and J. Fedotovs, *Laser Marking of a Small Sized QR Code on a Plastic Surface, Reliability and Statistics in Transportation and Communication*, vol 117, pp 418-429, Springer, March 2020, [https://doi.org/10.1007/978-3-030-44610-9\\_41](https://doi.org/10.1007/978-3-030-44610-9_41).
- [9] M. A. Salim, Z. H. Termiti and A. Md. Saad, Mechanical Properties on ABS/PLA Materials for Geospatial Imaging Printed Product using 3D Printer Technology, Reference Module in Materials Science and Materials Engineering, Elsevier, 2019, <https://doi.org/10.1016/B978-0-12-803581-8.11357-8>.
- [10] S. R. Sabreen, "Basic Material Science for Plastics Laser Marking" The Sabreen Group, Inc. January 2009, <https://plasticsdecorating.com/articles/2009/basic-material-science-for-plastics-laser-marking/> [Accessed May 1, 2023].
- [11] R. L. Stevenson, Implementation of Beam-Steered Laser Marking of Coated and Uncoated Plastics, *Coloring Technology for Plastics*, pp. 309-315, 1999, <https://doi.org/10.1016/B978-188420778-5.50040-1>.
- [12] "Fiber laser", FiberLabs Inc., July 2021, <https://www.fiberlabs.com/glossary/fiber-laser/> [Accessed May 1, 2023].
- [13] N. Angelov, Investigation the Influence of the Number of Repetition and Volumetric Energy Density on Laser Marking of Products, *Contemporary Materials*, V-2, pp. 251-253, 2014, DOI:10.7251/COMEN1402250A
- [14] S. Olivera, H. B. Muralidhara, K.Venkatesh, et al., Plating on acrylonitrile-butadiene-styrene (ABS) plastic: a review. *J Mater*, vol 51, pp. 3657-3674, January 2016, <https://doi.org/10.1007/s10853-015-9668-7>.
- [15] C. Laveija, M. J. Clemente, L. Oriol and J. I. Peña, Influence of the Wavelength on Laser Marking on ABS Filled with Carbon Black, *Polymer-Plastics Technology and Engineering*, pp. 1599-1607, Apr 2017, <https://doi.org/10.1080/03602559.2017.1280735>.
- [16] C. Guo and S. C. Singh, *Handbook of Laser Technology and Applications: Lasers Applications: Materials Processing and Spectroscopy*, Volume 3, 2nd ed., p. 360, CRC Press, June 2021, <https://doi.org/10.1201/9781315310855>.
- [17] Engraving lasers Rofin, Home page, [Online]. Available: [https://graviranje.rs/Engraving\\_PORTAL/lasers/rofin/Rofin\\_PowerLine\\_F20.html](https://graviranje.rs/Engraving_PORTAL/lasers/rofin/Rofin_PowerLine_F20.html) [Accessed May 1, 2023].
- [18] Olympus Global Homepage, [Online]. Available: <https://www.olympus-global.com/news/2017/nr00633.html> [Accessed May 1, 2023].

# Investigating the Impact of Laser Power and Scan Speed on Engraving Aspen Thermowood

**Dzintars Rāviņš**  
Faculty of Engineering  
Rezekne Academy of Technologies  
Rezekne, Latvia  
dzintars.rav@gmail.com

**Lyubomir Lazov**  
Faculty of Engineering  
Rezekne Academy of Technologies  
Rezekne, Latvia  
lyubomir.lazov@rta.lv

**Emil Yankov**  
Faculty of Engineering  
Rezekne Academy of Technologies  
Rezekne, Latvia  
emol.yankov@rta.lv

**Daivis Rāviņš**  
Faculty of Engineering  
Rezekne Academy of Technologies  
Rezekne, Latvia  
daivis.rav@gmail.com

**Imants Adijans**  
Faculty of Engineering  
Rezekne Academy of Technologies  
Rezekne, Latvia  
imants.adijans@rta.lv

**Abstract.** This study examines the effect of pre-heat treatment on laser engraving of aspen thermowood. We used an infrared CO<sub>2</sub> laser with a wavelength of 10640 nm to engrave aspen thermowood samples with different pre-treatment temperatures, including one non-treated sample (base). The samples had a similar moisture content of about 8%, but exhibited different shades of brown depending on the pre-treatment temperature. The engraving depth and width were measured for each sample, and 8 graphs were constructed to analyze the results. Our findings show that pre-treatment temperature has a significant effect on the efficiency of laser engraving, with higher pre-treatment temperatures resulting in deeper engraving lines. The study provides valuable insights into the optimization of laser engraving parameters for aspen thermowood, and demonstrates the potential of pre-heat treatment to improve the quality of laser-engraved wooden products.

**Keywords:** Aspen thermally modified wood, CO<sub>2</sub> laser engraving, laser processing parameters.

## I. INTRODUCTION

The use of laser technology has become increasingly common in various industries since its development in the 1960s. Laser sources are utilized in different technological processes such as marking, engraving, hardening, cladding, cutting, and welding [1], [2], [3]. Lasers have been employed in the wood industry for several decades, primarily for engraving and preparing various design applications in the furniture industry. [4]

Wood is a popular decorative and construction material worldwide. Synthetic wood substitutes cannot compete with natural wood, as it saturates the air with oxygen and has a pleasant aroma. The heat treatment method, based on Finnish pioneers, provides long-lasting protection for wood against the effects of nature, which extends its service life [5].

The laser processing technology is considered one of the most promising methods for engraving. The process of laser processing is complex and depends on three groups of factors: laser source parameters, technological process parameters, and the structure and physical properties of the material being processed [6], [7], [8].

In this method, the material is ablated from the laser impact zone under the influence of the absorbed laser electromagnetic energy. The objective of this study is to investigate the laser ablation process with infrared laser radiation of 10.6 mm wavelength (CO<sub>2</sub> laser) on aspen thermowood samples.

## II. MATERIALS AND METHODS

### A. Thermally treated wood

This study uses aspen timber that has been processed by drying the wood by heating it to 180 - 230°C. In this process, a comprehensive heat exchanger performance evaluation model and average heat transfer with changes in physical properties can be observed [9], [10]. Wood is

Print ISSN 1691-5402

Online ISSN 2256-070X

<https://doi.org/10.17770/etr2023vol3.7250>

© 2023 Dzintars Rāviņš, Emil Yankov, Imants Adijāns, Lyubomir Lazov, Daivis Rāviņš.

Published by Rezekne Academy of Technologies.

This is an open access article under the [Creative Commons Attribution 4.0 International License](https://creativecommons.org/licenses/by/4.0/).

affected by changes in physical and mechanical properties with moisture content, moisture adsorption, water absorption and volume swelling ratio are reduced, while hygroscopic hysteresis is improved with increasing temperature [11], [12]. Free sugars are carbonized during heat treatment, so it is resistant to rotting, deformation and parasites [13]. Timber quality is directly related to wood moisture content, temperature, and relative humidity control during the drying process. In the process of thermal modification, exposure to high temperatures permanently changes the properties of wood, the most obvious changes and color changes. The wood chosen for processing can be freshly sawn or pre-dried. [14], [15], [16], [17].

The period of thermal treatment of aspen timber takes place with an average time cycle of 36h, as a result of which all the samples used in the experiment are treated uniformly at different temperatures.



Fig. 1. Heat-treated aspen wood samples.

As seen in Fig. 1, heat-treated aspen timber changes tone to a warm brown. The timber is known to start to change tone at roughly 180°C. In this study, six samples of aspen wood were used, including one untreated board and five boards that were heat-treated at temperatures of 180°C, 195°C, 205°C, 214°C, and 225°C, respectively. The moisture content of all samples was determined to be 8% using a digital wood moisture meter HT632. The heat-treatment process used in this study involves a rather complex process of drying the wood, which is important to consider in the analysis of the results.

### B. Equipment

For the engraving of the aspen plank samples, a CO<sub>2</sub> laser system (SUNTOP ST-CC9060) with a wavelength of 10640 nm was used (see Fig. 2).



Fig. 2. CO<sub>2</sub> laser system SUNTOP ST-CC9060.

The technical specifications of the SUNTOP ST-CC 9060 laser system are presented in Table 1.

TABLE 1. LASER SYSTEM SUNTOP ST-CC9060 TECHNICAL SPECIFICATIONS

Laser type	CO <sub>2</sub> laser
Operation mode	CW
Wavelength	10640 nm
Maximum output power	100 W
Workspace (Cutting area)	900 x 600 mm
Precision	0,02 mm
Scan speed	0 – 1000 mm/s
Laser Safety Class	4
Cooling system	Water cooling
Data formats used	dxf, plt, bmp, dst,ai
Total power	1500 W

For measuring the depth and width of the engravings, we used a Dino-Lite Edge AM7115MZT digital microscope (shown in Figure 3).



Fig. 3. Dino-Lite Edge AM7115MZT digital microscope.

The specifications of the digital microscope Dino-Lite Edge AM7115MZT are provided in Table 2.

TABLE 2. DINO-LITE EDGE AM7115MZT MICROSCOPE TECHNICAL SPECIFICATIONS

Resolution	2592 × 1944 pixels
Operating System	Windows
Magnification	20x~220x
Unit Dimension	10.5cm (H) x 3.2cm (D)
Lighting	8 white LEDs

### METHODOLOGY

In this experiment, six aspen wood samples with dimensions of 13 x 90 x 200 mm were laser engraved using different power densities  $q_s$  and scanning speeds  $v$ . The power densities used for engraving were 9.3, 2.59, 4.14, 5.39, 6.75, 7.80, and 8.45 ( $\times 10^5$ ) W/cm<sup>2</sup>, as listed in Table 4. Each set of parameters was used to engrave five lines, with a distance of 2 mm between each line and a length of 25 mm. The depth  $h$  [mm] and width  $d$  [mm] of the engraved lines were measured, and graphs were constructed as a function of the laser parameters.

The power output of the laser was measured using an OPHIR F150A-BB-26 laser power meter before starting the experiment. The recorded power values can be found in Table 3.

TABLE 3. AVERAGE POWER DEPENDENCE ON RESONATOR PUMP COEFFICIENT ( $\kappa P$ , %)

$\kappa P$ , %	10	15	20	25	30	35	40
$P$ , W	7.3	20.3	32.5	42.3	53.0	61.2	66.3

The power density  $q_s$  [W/cm<sup>2</sup>] was calculated using formula (1):

$$q = \frac{P}{S} \quad (1)$$

where  $P$  [W] is the power and  $S$  [cm<sup>2</sup>] is the cross-sectional area of the laser beam on the surface of the material to be engraved, as given in formula (2):

$$S = \pi \frac{d^2}{4} \quad (2)$$

with  $d$  [cm] being the diameter of the laser beam ( $d = 0.01$  cm). The calculated power density values in W/cm<sup>2</sup>, corresponding to the measured power values in W (shown in Table 3), are presented in Table 4.

TABLE 4. CALCULATED POWER DENSITY VALUES FOR THE CO<sub>2</sub> LASER SYSTEM

$P$ , W	7.3	20.3	32.5	42.3	53.0	61.2	66.3
$q_s \times 10^5$ , W/cm <sup>2</sup>	0.93	2.59	4.14	5.39	6.75	7.80	8.45

A matrix of laser technological parameters was generated using the computer program RDWorksV8 (shown in Fig. 4), which supports DXF, AI, and PLT formats and facilitates laser cutting and engraving operations.

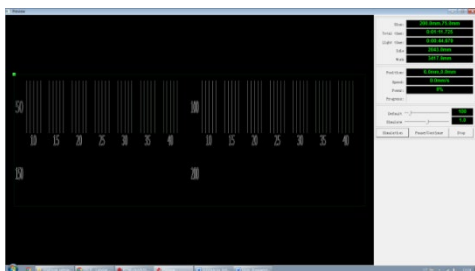


Fig. 4. Matrix of engraving lines in computer program RDWorksV8.

All six aspen wood samples, including one natural aspen wood sample and five aspen thermowood samples, were engraved according to the matrix created in RDWorksV8 (see Fig. 5).



Fig. 5. Photograph of the six aspen wood samples engraved according to the created matrix, including five aspen thermowood samples and one natural aspen wood sample on the right.

To measure the depth of engraved lines, all six aspen wood samples were cut using a circular saw in two pieces through the middle of the engraved lines.

Depth measurement on one of the samples using Dino-Lite Edge AM7115MZT digital microscope is shown in Fig. 6 and width measurement is shown in Fig. 7.

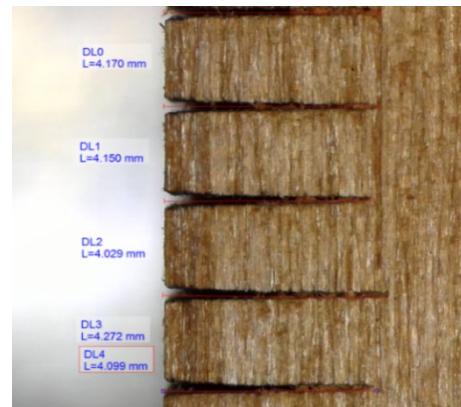


Fig. 6. Measurement of engraving depth on an aspen thermowood sample that was heat-treated at 195°C. (magnification x32).

Fig. 6 shows a heat-treated sample at 195°C with five cuts obtained using a power density  $q_s = 8.45 \times 10^5$  W/cm<sup>2</sup> and scan speed  $v = 50$  mm/s. Depth of the cuts are measured and calculated average depth  $h = 4.14$  mm.

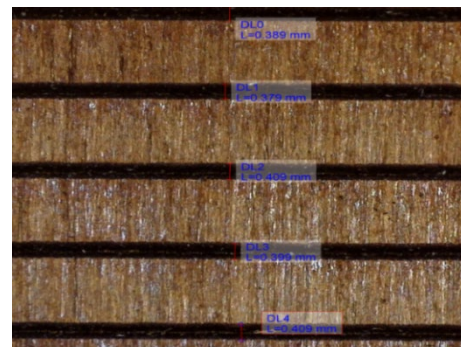


Fig. 7. Line width measurement (magnification x32) - aspen thermowood sample heat-treated at 214°C.

Fig. 7 shows a heat-treated sample at 214°C with five cuts obtained using a power density  $q_s = 4.14 \times 10^5$  W/cm<sup>2</sup>

and scan speed  $v = 100$  mm/s. The width of the cuts is measured, and the calculated average width is  $d = 0.4$  mm. The width of engraved lines is measured on the top surface of aspen wood samples, where it is maximum.

### III. RESULTS AND DISCUSSIONS

The study results are presented in graphs that depict the impact of laser power density and scan speed on the width and depth of laser engraving lines. The graphs illustrate the relationship between line width and depth as a function of energy density and scanning speed for aspen thermowood samples that have been heat-treated at different temperatures. Specifically, two graphs depict the relationship between line width ( $d$ ) and power density ( $q_s$ ) at two scan speeds (50 mm/s and 200 mm/s) for aspen thermowood samples that have been heat-treated at 180°C (Fig. 8) and 225°C (Fig. 9), respectively.

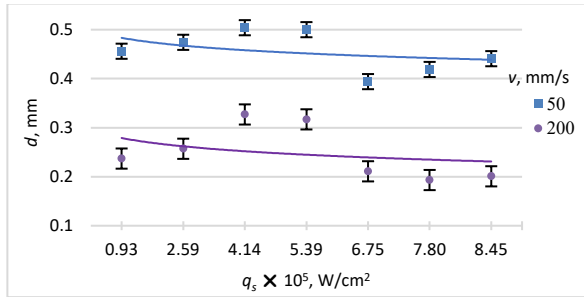


Fig. 8. Dependence of the line width  $d$  on the power density  $q_s$  at two different scan speed  $v$  for aspen thermowood sample heat-treated at 180°C.

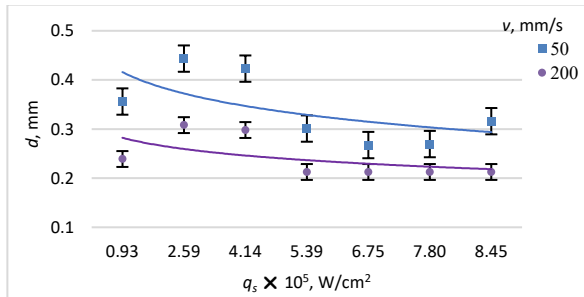


Fig. 9. Dependence of the line width  $d$  on the power density  $q_s$  at two different scan speed  $v$  for aspen thermowood sample heat-treated at 225°C.

The average line width at low scan speed 50 mm/s is 0.46 mm for aspen thermowood heat-treated at 180°C, and 0.34 mm for aspen thermowood heat-treated at 225°C. The average line width at high scan speed 200 mm/s is 0.25 mm for aspen thermowood heat-treated at 180°C, and 0.24 mm for aspen thermowood heat-treated at 225°C. The graphs for these samples are presented in Fig. 8 and Fig. 9, respectively. From these graphs, it can be seen that changes in the line width are small depending on power density, with the width of the lines slightly bigger at lower power density and smaller at higher power density.

Fig. 10 and 11 show the dependence of the line width  $d$  on scan speed  $v$  at two power density  $q_s$  2.59·10<sup>5</sup> W/cm<sup>2</sup> and 8.45·10<sup>5</sup> W/cm<sup>2</sup> for aspen thermowood sample heat-

treated at temperature 180°C (Fig. 10), and aspen thermowood sample heat-treated at temperature 225°C (Fig. 11).

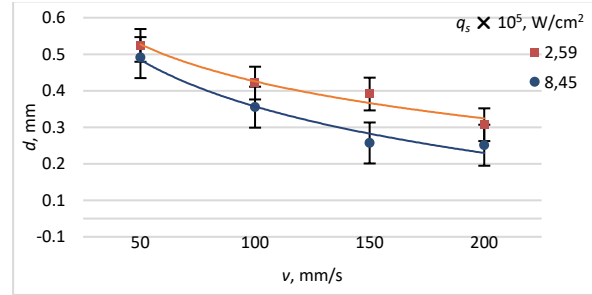


Fig. 10. Dependence of the line width  $d$  on scan speed  $v$  at two different power density  $q_s$  for aspen thermowood sample heat-treated at 180°C.

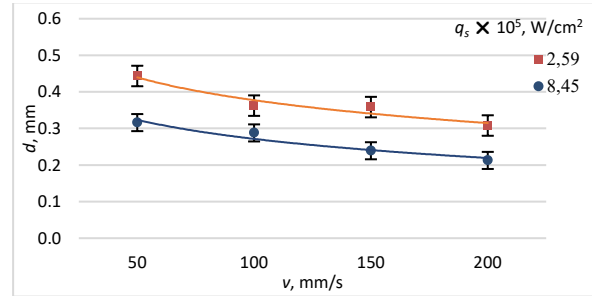


Fig. 11. Dependence of the line width  $d$  on scan speed  $v$  at two different power density  $q_s$  for aspen thermowood sample heat-treated at 225°C.

The line width decreases non-linearly with increasing scanning speed for all engraved samples. The minimum line width is observed at the highest scanning speed of 200 mm/s, reaching a value of 0.2 mm for aspen thermowood samples heat-treated at 180°C. Similarly, the maximum line width is observed at the lowest scanning speed of 50 mm/s, reaching a value of 0.47 mm for the same sample. The trends are similar for the other samples as well.

The rate of width changes  $\text{tg } d(v)$  [s<sup>-1</sup>], which depends on the scan speed, is calculated using equation (3).

$$\text{tg } d(v) = \frac{\Delta d}{\Delta v} \quad (3)$$

where  $\Delta d = d_{\text{max}} - d_{\text{min}}$  is the difference between the maximum and minimum depth, and  $\Delta v = v_{\text{max}} - v_{\text{min}}$  is the difference between the maximum and minimum scan speed. The calculated results of the rate of width changes are shown in Table 5, with units of s<sup>-1</sup>.

TABLE 5. THE RATE OF WIDTH CHANGES  $\text{tg } d(v)$  DEPENDING ON SCAN SPEED

$\text{tg } d(v), \text{ s}^{-1}$	$q_s \times 10^5, \text{ W/cm}^2$	
	2.59	8.45
180°C	0.001	0.002
225°C	0.001	0.001

Fig. 12 shows the dependence of the line depth  $h$  on power density  $q_s$  at two scan speeds  $v$  of 50 mm/s and 200 mm/s for the sample of natural aspen.

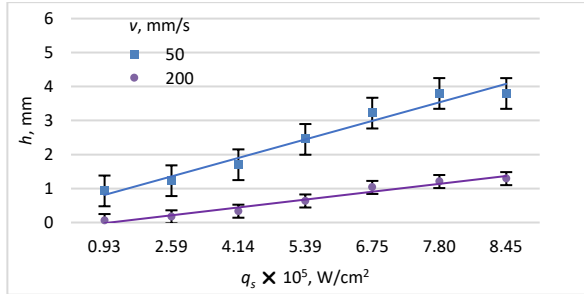


Fig. 12. Dependence of the line depth  $h$  on power density  $q_s$  at two different scan speed  $v$  for the sample of natural aspen.

Fig. 13 shows the dependence of the line depth  $h$  on power density  $q_s$  at two scan speeds  $v$  of 50 mm/s and 200 mm/s for the aspen thermowood sample heat-treated at temperature 225°C.

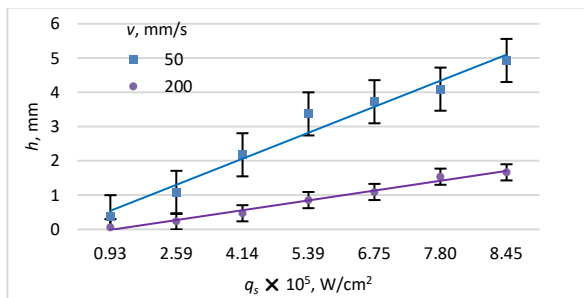


Fig. 13. Dependence of the line depth  $h$  on power density  $q_s$  at two different scan speed  $v$  for aspen thermowood sample heat-treated at 225°C.

The graphs on Fig. 12 and Fig. 13 show that line depth is smaller at low power density and bigger at high power density. The maximum depth of 4.93 mm is reached at power density of  $8.45 \cdot 10^5$  W/cm<sup>2</sup>, scan speed 50 mm/s for aspen thermowood sample heat-treated at temperature 225°C, but minimal depth of less than 0.1 mm is reached at power density of  $0.93 \cdot 10^5$  W/cm<sup>2</sup> and scan speed 200 mm/s for both samples. The graphs for the other samples are similar and are in this interval. The increase in line depth is close to linear.

The rate of depth changes  $\text{tg } h(q_s) \left[ \frac{\text{mm}}{\text{W} \times \text{cm}^2} \right]$  depending on power density is calculated using equation (4).

$$\text{tg } h(q_s) = \frac{\Delta h}{\Delta q_s} \quad (4)$$

Were  $\Delta h = h_{\max} - h_{\min}$  is difference between max depth and min depth, and  $\Delta q_s = q_{s \max} - q_{s \min}$  is difference between max power density and min power density. The calculated results of the rate of depth changes are shown in Table 6.

TABLE 6. THE RATE OF DEPTH CHANGES  $\text{tg } h(q_s)$  DEPENDING ON POWER DENSITY

$\text{tg } h(q_s), \frac{\text{mm}}{\text{W} \times \text{cm}^2}$	$v, \text{ mm/s}$	
	50	200
base	0.381	0.164
225°C	0.607	0.213

Two figures below show the dependence of the line depth  $h$  on scan speed  $v$  at low-power density  $q_s = 2.59 \cdot 10^5$  W/cm<sup>2</sup> (see Fig. 14) and high-power density  $q_s = 8.45 \cdot 10^5$  W/cm<sup>2</sup> (see Fig. 15) for the sample of natural aspen and aspen thermowood samples heat-treated at temperature 195°C and 225°C.

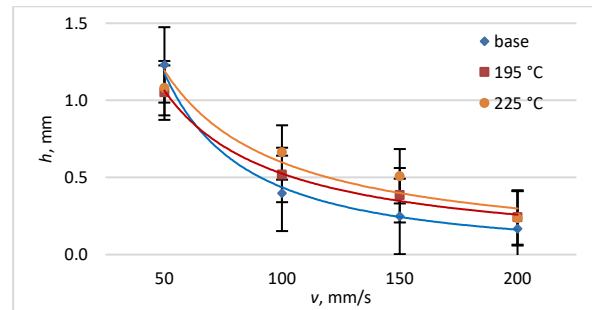


Fig. 14. Dependence of the line depth  $h$  on scan speed  $v$  at power density  $q_s = 2.59 \cdot 10^5$  W/cm<sup>2</sup>.

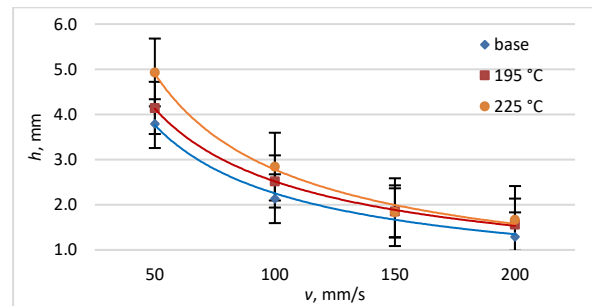


Fig. 15. Dependence of the line depth  $h$  on scan speed  $v$  at power density  $q_s = 8.45 \cdot 10^5$  W/cm<sup>2</sup>.

The depth is bigger at low scan speed 50 mm/s, and smaller at high scan speed 200 mm/s. The maximum depth of 4.93 mm is reached at power density  $8.45 \cdot 10^5$  W/cm<sup>2</sup> on aspen thermowood sample heat-treated at temperature 225°C, but minimum depth of 0.17 mm at power density  $2.59 \cdot 10^5$  W/cm<sup>2</sup> on sample of natural aspen. The decline of the lines on the graphs are non-linear.

The rate of depth changes  $\text{tg } h(v) \text{ [s}^{-1}\text{]}$  depending on scan speed is calculated using equation (5).

$$\text{tg } h(v) = \frac{\Delta h}{\Delta v} \quad (5)$$

Where  $\Delta h = h_{\max} - h_{\min}$  is the difference between the maximum depth and the minimum depth, and  $\Delta v = v_{\max} - v_{\min}$  is the difference between the maximum scan speed and

the minimum scan speed. The calculated results of the rate of depth changes are shown in Table 7.

TABLE 7. THE RATE OF DEPTH CHANGES  $tg h(v)$  DEPENDING ON SCAN SPEED

$tg h(v), s^{-1}$	$q_s \times 10^5, W/cm^2$	
	2.59	8.45
base	0.007	0.017
195°C	0.005	0.017
225°C	0.006	0.022

Calculation of depth change  $\Delta h$  in percent depending on heat-treated aspen wood obtained using equation (6).

$$\Delta h = \left( \frac{h_{max}}{h_{min}} - 1 \right) \times 100\% \quad (6)$$

Table 8 shows calculated depth change in percent for aspen thermowood samples compared to non-treated aspen wood sample. Depth measurements are taken for lines engraved at the max power density  $q_s = 8.45 \times 10^5 W/cm^2$  and min scan speed  $v = 50 mm/s$ .

TABLE 8. DEPTH CHANGE  $\Delta h$  IN PERCENT FOR ASPEN THERMOWOOD SAMPLES COMPARED TO NON-TREATED ASPEN SAMPLE AT MAX POWER DENSITY  $q_s = 8.45 \times 10^5 W/cm^2$  AND MIN SCAN SPEED  $v = 50 mm/s$

$T, ^\circ C$	$h, mm$	$\Delta h, \%$
0	3,80	0,0
180	4,02	6,0
195	4,14	9,2
205	4,20	10,7
214	4,48	18,0
225	4,93	29,8

#### IV. CONCLUSION

In this study, the laser engraving process was used to investigate the effects of power density and scan speed on the depth of engraved lines on natural aspen wood and aspen thermowood samples. The results showed that the depth of engraved lines is affected by both power density and scan speed, with higher power densities and lower scan speeds leading to deeper lines. Heat treatment of the aspen wood samples also had a significant impact on the depth of the engraved lines, with higher temperatures leading to deeper lines.

The rate of depth changes was calculated for both power density and scan speed, and the results were presented in Tables 6 and 7, respectively. Table 8 showed the depth change in percent for the aspen thermowood samples compared to non-treated samples at the maximum power density and minimum scan speed.

The findings of this study could have important implications for the use of laser engraving in the woodworking industry, particularly in the production of decorative or functional wooden objects. By

understanding the factors that affect the depth of engraved lines, manufacturers can optimize their laser engraving processes to achieve the desired results.

Further research could investigate the effects of other laser parameters, such as pulse duration and spot size, on the depth of engraved lines. Additionally, more detailed analyses could be conducted to examine the microstructural changes that occur in the wood during the laser engraving process, as well as the effects of different types of wood on the engraving results.

#### V. ACKNOWLEDGEMENTS

The authors gratefully acknowledge financial support by the European Regional Development Fund, Postdoctoral research aid Nr. 1.1.1.2/16/I/001 research application "Analysis of the parameters of the process of laser marking of new industrial materials for high-tech applications, Nr. 1.1.1.2/VIAA/3/19/474".

#### REFERENCES

- [1] Lazov L, Angelov N, Teirumnieks E, Teirumnieka E, "Preliminary Numerical Analysis for the Role of Speed onto Laser Technological Processes", 2019 Proceedings of the 12th International Scientific and Practical Conf. 3 137-142
- [2] Dolchinkov Nikolay T, Lazov L, Ivanov Jordan S, Lilyanova Stelena D, Antons P, "Use of co2 laser for marking and clearing of textile materials for manufacture of military equipment", 2019 Proceedings of the 12th International Scientific and Practical Conference. Volume III, 32-36
- [3] Artis – Stanislavs Gusts, Imants Adijāns, "Optimization of parameters for laser marking and engraving on plywood and pine wood materials" [Online]. Available: <https://doi.org/10.17770/het2021.25.6795> [Accessed February 1, 2023].
- [4] What is a laser engraving machine for wood, [Online]. Available: <https://virmer.com/what-is-a-laser-engraving-machine-for-wood/>. [Accessed February 23, 2023].
- [5] Andris M, Ilze I, Edgars B, Koksnes ķīmiskā pārstrāde un aizsardzība [Online]. Available: [https://www.mf.ltu.lv/sites/mf/files/files/lapas/koksnes\\_parstrade\\_iekasas\\_90\\_gr.pdf](https://www.mf.ltu.lv/sites/mf/files/files/lapas/koksnes_parstrade_iekasas_90_gr.pdf). [Accessed February 23, 2023].
- [6] Lazov L., N. Angelov, Basic factors determining quality of markings on metals and alloys. International Scientific Conference AMTECH - 2007, Gabrovo, Vol. I, 102-107, 2007
- [7] Lazov L., A. Atanasov, N. Angelov, Investigation of the role of certain factors affecting the contrast in laser marking, Contemporary Materials, Vol. II-1, 13-17, 2011.
- [8] Shatha M.HasanaKadhim A.HubeatirbDhuha Sh.Abdc , "Effect of CO2 laser parameters on redwood engraving process complemented by Taguchi method." [Online]. Available: <https://doi.org/10.1016/j.matpr.2020.12.580>. [Accessed February 25, 2023].
- [9] Yanchen Li, Beibei Wang, Weiye,Zhang, Junqi Zhao, Xiaoyang Fang, Jingmeng Sun, Rongqi Xia, Hongwu Guo, Yi Liu, "Processing wood into a phase change material with high solar-thermal conversion efficiency by introducing stable polyethylene glycol-based energy storage polymer." [Online]. Available: <https://doi.org/10.1016/j.energy.2022.124206>. [Accessed February 2, 2023].
- [10] Yuting He, Min Jia, Xiaogang Li, Zhaozhong Yang, Rui Song, "Performance analysis of coaxial heat exchanger and carrier fluid in medium-deep geothermal energy development" [Online]. Available: <https://doi.org/10.1016/j.renene.2020.12.109>. [Accessed February 22, 2023].
- [11] Zongying Fu, Yongdong Zhou, Xin Gao, Honghai Liu, Fan Zhou, "Changes of water related properties in radiata pine wood due to

- heat treatment” [Online]. Available: <https://doi.org/10.1016/j.conbuildmat.2019.116692> [Accessed February 22, 2023].
- [12] Cristian A.Chávez, Nelson O.Moraga, Carlos H.Salinas, Roberto C.Cabral, Rubén A.Ananías, “Modeling unsteady heat and mass transfer with prediction of mechanical stresses in wood drying”, [Online]. Available: <https://doi.org/10.1016/j.icheatmasstransfer.2021.105230>. [Accessed February 14, 2023].
- [13] Shatha M.HasanaKadhim A.HubeatirbDhuha Sh.Abdc , “Effect of CO<sub>2</sub> laser parameters on redwood engraving process complemented by Taguchi method” [Online]. Available: <https://doi.org/10.1016/j.matpr.2020.12.580>. [Accessed February 16, 2023].
- [14] Mircea Dulău, Istvan Madaras, “Development of a Monitoring and Control System for Timber’s Drying Process”, [Online]. Available: <https://doi.org/10.1016/j.promfg.2019.02.251>. [Accessed February 6, 2023].
- [15] Published press release “Thermal industry,, SIA “Ošukalns,, [Online]. Available: <https://www.osukalns.lv>. [Accessed February 16, 2023], <https://www.la.lv/zimols-owood-ar-osukalna-identitati>
- [16] SIA “Osukalns” internal safety instruction, unpublished documents: [Operating\\_instructions\\_700764\\_preliminary](#)
- [17] Mircea Dulau, Istvan Madaras, “Development of a Monitoring and Control System for Timber’s Drying Process” [Online]. Available: <https://doi.org/10.1016/j.promfg.2019.02.251>. [Accessed February 25, 2023].

# Investigation of Surface Roughness of Carbon Steel Machined Parts after Nanosecond Fiber Laser Marking

**Petar Tsvyatkov**

Faculty of Engineering  
Technical University of Gabrovo  
Gabrovo, Bulgaria  
ppeter@mail.bg

**Emil Yankov**

Faculty of Engineering  
Rezekne Academy of Technologies  
Rezekne, Latvia  
emil.yankov@rta.lv

**Lyubomir Lazov**

Faculty of Engineering  
Rezekne Academy of Technologies  
Rezekne, Latvia  
lyubomir.lazov@rta.lv

**Edmunds Teirumnieks**

Faculty of Engineering  
Rezekne Academy of Technologies  
Rezekne, Latvia  
edmunds.teirumnieks@rta.lv

**Karlis Pīgožnis**

Faculty of Engineering  
Rezekne Academy of Technologies  
Rezekne, Latvia  
karlis.pigoznis@rta.lv

**Abstract.** Laser marking with a nanosecond fiber laser is one of the most common ways to permanently mark various engineering materials. The roughness of the machined surface and its observation is essential to evaluate the impact on the contrast of the marking as well. Experimental studies of the roughness obtained as a result of the laser marking, were inspected using a 3D measuring laser microscope OLYMPUS LEXT OLS5100. Analysis of the graphical dependence of the roughness function on the four process parameters: laser power, frequency, speed of marking and step.

**Keywords:** Carbon steel, Laser marking, Roughness, fiber laser, surface texturing.

## I. INTRODUCTION

In industrial production, some of the finished components and parts are required to have a certain roughness class. The operational properties of machine parts largely depend on the quality of the surface layer of the parts. Roughness affects other surface properties such as: coefficient of friction and wear, corrosion resistance, hydrophobicity, etc.[1]. There are different techniques for superficial processing, including mechanical and chemical methods [2]. One of their biggest drawbacks is the long processing time. In the 1970s, a new reliable and relatively economical industrial technology for laser processing of materials appeared. This technology is developing

extremely fast and has been used in various industrial productions in recent years [3]. One of the directions in laser surface treatment is laser marking. In this process, a laser beam affects the surface, changing its roughness. The surface layer melts or evaporates as a result of this process, changing the roughness. When the roughness increases, we have a surface scoring effect, and when the roughness decreases as a result of laser exposure, we have a polishing effect [4]. In this effective method, through raster processing, the required grade of roughness is achieved. The advantages of the laser

method compared to the traditional ones are processing without tools, high flexibility at automation and low operational costs, high speed of processing, environmental friendliness and that it is non-contact.

The roughness of the surface during laser processing depends on several groups of factors, which are related to the parameters of the laser source, the technological process and the properties of the material [5].

Various scientific teams have investigated the changes in the roughness of products as a result of laser processing.

D Przystacki, [6] has investigated roughness in turning and laser machining. They achieved it with a laser power of 600 W roughness almost 30 % lower than that obtained by traditional turning. The Angelov, N. [7], used numerical experiments on the effect of laser wavelength

Print ISSN 1691-5402

Online ISSN 2256-070X

<https://doi.org/10.17770/etr2023vol3.7317>

© 2023 Petar Tsvyatkov, Emil Yankov, Lyubomir Lazov, Edmunds Teirumnieks, Karlis Pīgožnis.

Published by Rezekne Academy of Technologies.

This is an open access article under the [Creative Commons Attribution 4.0 International License](https://creativecommons.org/licenses/by/4.0/).

on CuBr laser ( $\lambda_1 = 511$  nm), ruby laser ( $\lambda_2 = 690$  nm), diode laser ( $\lambda_3 = 940$  nm), fiber laser ( $\lambda_4 = 1.06$   $\mu\text{m}$ ) and CO<sub>2</sub>-laser ( $\lambda_5 = 10.6$   $\mu\text{m}$ ). Numerical experiments with different types of lasers are at the same power density and lasing scan rate, and the heating temperature at the lasing wavelengths is determined. Ukar et al. [8] have achieved a change of roughness up to 80% after laser treatment on instrumental steel. Guisario et al.[9] studied the the modification on the surface, induced from high powered laser on three different surfaces. Perry et al. [10] researched the laser roughness modification process and worked on developing a model to forecast its change. Bögli et al.[11] present one of the most common tools for evaluating surface roughness.

The purpose of the present study is to evaluate the influence of the average power  $P$ , processing speed  $v$ , step  $\Delta x$  between raster lines on the roughness of a carbon steel specimen. The analysis of energy density  $E_{eff}$  shows the relationship between the increase in roughness and the energy absorbed per square centimeter on the sample.

## II. EQUIPMENT, MATERIALS AND METHODOLOGY

The experiments were carried out with a fiber laser technological system “PowerLine F-20 Varia” manufactured by GmbH ROFIN with length on the wave on the laser radiation 1.064  $\mu\text{m}$ .

The main parameters on the laser technological system are shown in Table 1.

TABLE 1 PARAMETERS ON THE LASER SYSTEM

Scanner	
Working area	120 mm x 120 mm
Scan speed	0 ÷ 20,000 mm/s
Positioning accuracy	0.5 $\mu\text{m}$
Focal length	184 mm
Laser	
Laser source	Rofin Laser
Wavelength	1064 nm
Maximum power	19.7W
Pulse energy	0.0 ÷ 1.00 m J
Operating mode	Pulsed mode
Frequency	2 ÷ 1000 kHz
Pulse duration	4,8,14,20,30,50,100,200ns

To study the roughness, samples of C75 carbon steel were marked using a raster method. The treated areas are in the shape of a square measuring 10 x 10 mm, and the distance between them is 2 mm. A series of tests were made, each line having the following parameters:

- For the speed  $v$  (mm/s)

100	200	300	400	500	600	700
-----	-----	-----	-----	-----	-----	-----

at constant power  $P = 30$  W and step  $\Delta x = 30$   $\mu\text{m}$

- For the step  $\Delta x$  ( $\mu\text{m}$ )

20	30	35	40	45	50	60
----	----	----	----	----	----	----

at constant speed  $v = 300$  mm/s and power  $P = 30$  W

- For the power  $P$  (W)

6	8	10	12.5	15	17.5	19.7
---	---	----	------	----	------	------

at constant speed  $v = 300$  mm/s and step  $\Delta x = 30$   $\mu\text{m}$

Permanent parameters for the process of laser marking for all samples are the frequency  $\nu = 40$  kHz, the duration of the impulse  $\tau = 100$  ns, the diameter of the working stain  $d = 50$   $\mu\text{m}$ , the defocus  $\Delta f = 0$  mm and the number of repetitions  $N = 1$ .

The starting material (substrate) has a hardness of from HV 442 HV to 452 HV and a roughness from  $R_a = 0.264$   $\mu\text{m}$  to  $R_a = 0.36$   $\mu\text{m}$ , from  $R_z = 13.597$   $\mu\text{m}$  to  $R_z = 21.268$   $\mu\text{m}$ , from  $R_q = 0.41$   $\mu\text{m}$  to  $R_q = 0.56$   $\mu\text{m}$ . The chemical composition of the substrate is shown in the Table 2 below.

TABLE 2 CHEMICAL COMPOSITION C75

C	Si	Mn	P	S	Cr	Ni	Al
0.70	0.225	0.662	0.009	0.001	0.214	0.071	0.01

The laser system and schematic diagram of the raster method used in processing the carbon samples are shown in Fig.1.

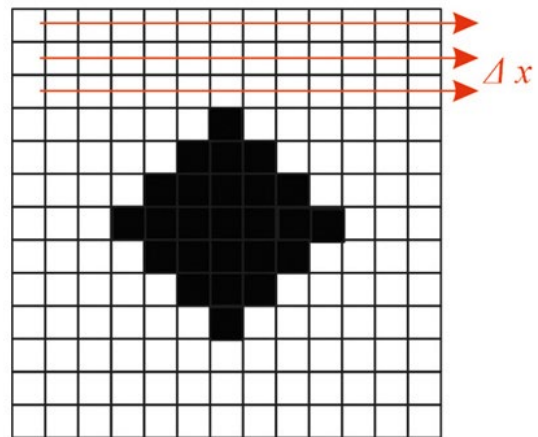


Fig.1. Fiber laser Rofin PowerLine F20 and laser marking strategy.

According to the purpose of the experiment, the present study analyzed the influence of the power  $P$ , the speed of processing  $v$  and the step  $\Delta x$  between raster lines on the surface roughness  $R_q$ . The following functional dependencies are investigated:

$$R_q = R_q(P), R_q = R_q(v), R_q = R_q(\Delta x)$$

The factors that affect the roughness of the mark are shown in Fig. 2.

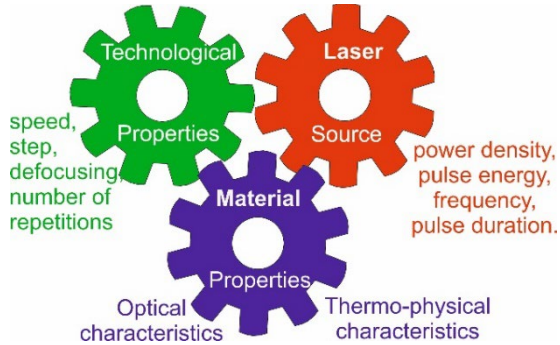


Fig. 2. Factors affecting roughness and marking.

To determine how the effective incident energy density  $E_{eff}$  affects the surface roughness, it is necessary to determine linear energy density LED (1) and linear pulse density LPD (2)

$$LED = \frac{A \cdot P}{v}, \text{ J/cm} \quad (1)$$

where  $A = 0.7$  absorption coefficient.

The LED value is numerically equal to the absorbed energy per unit length in the laser marking area.

$$LPD = \frac{v}{\Delta x}, \text{ number of pulses / cm} \quad (2)$$

The LPD value is numerically equal to the number of pulses per unit length.

The quantity  $E_{eff}$  gives the absorbed energy of the laser radiation per unit area (13) from the laser impact zone.

$$E_{eff} = LED \times LPD, \text{ J/cm}^2 \quad (3)$$

The measurements on the surface of the samples from carbon steel C75 were performed with a confocal laser scanning (CLS) microscope Olympus model "OLS5100-EAF" (Table 3). Received micro structural images were made with the help of a  $20 \times$  lens, magnification  $451 \times$ , as the examined area for each measurement  $644 \times 644 \mu\text{m}$  with a precision of measurement of  $\pm 0.03 \mu\text{m}$ . From the resulting 3D images from the laser system on the microscope are measured roughness  $R_q$  for the whole researched area  $644 \times 644 \mu\text{m}$ . For each of the treated areas ( information blocks ) five roughness measurements were made  $R_q$  with the average value of the measurement

taken as the result. From received values are built graphic dependencies on changes in roughness, depending on the power, the speed, the step and the effective incident energy density  $E_{eff}$  with laser treatment.

TABLE 3 PARAMETERS OLYMPUS OLS5000

Parameters	Value
Total magnification	$54 \times \div 17,280 \times$
Field of view	$16 \mu\text{m} \div 5.120 \mu\text{m}$
Display resolution	1 nm
Measurement accuracy	$\pm 1.5\%$
Maximum number of measuring points in a single measurement	$4096 \times 4096$ pixels
Maximum number of measuring points	36 megapixels
Wavelength of laser light source	405 nm
Power of laser light source	0.95 mW

Table 3: Basic parameters of a microscope OLS5100 – EAF

### III. RESULTS

The results from the experiment representing the graphical dependencies of the change of the roughness from the power  $R_q = R_q(P)$  are shown in Fig.3.

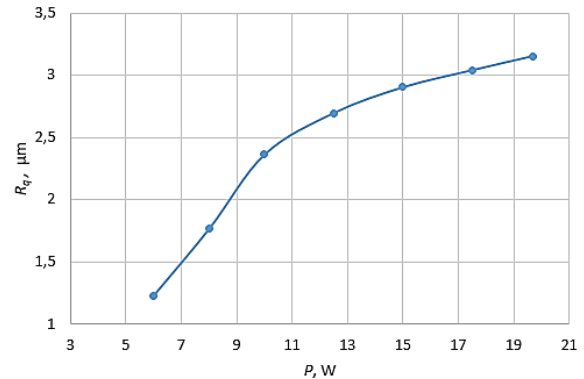


Fig.3 Experimental dependence of roughness variation on mean power.

The following conclusions can be made from the analysis of the graph:

With increasing power in the range  $P \in [6, 19.7]$  W, the processing roughness increases non-linearly;

The increase in roughness is described by the equation

$$y = 9 \times 10^5 \times x^4 - 0.004 \times x^3 + 0.0478 \times x^2 + 0.0986 \times x - 0.3393. \quad (4)$$

For powers in the range  $P \in [6, 10]$  W the rate of growth of the roughness as a function of the power  $\Delta R_q / \Delta P$  is  $0.28 \mu\text{m} / \text{W}$

For powers in the range  $P \in [10, 19.7]$  W the speed of increase of roughness as a function of power  $\Delta R_q / \Delta P$  is  $0.05 \mu\text{m} / \text{W}$ .

For powers in the range  $P \in [6, 10]$  W, the speed of change of roughness is 5 times greater than that in the range  $P \in [10, 19.7]$  W.

The results from the experiment representing the graphical dependencies of the change of the roughness from the speed  $R_q = R_q(v)$  are shown in Fig. 4.

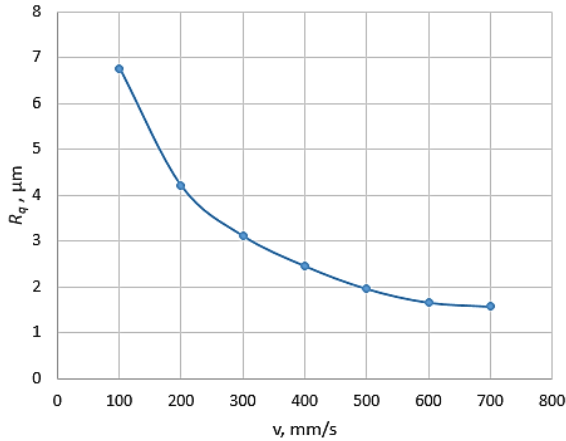


Fig. 4. Experimental dependence of roughness variation on marking rate.

The following conclusions can be made from the analysis of the graph:

When the speed increases in the range  $v \in [100, 700]$  mm/s a nonlinear decrease in roughness is observed.

For speeds in the range  $v \in [100, 400]$  mm/s the rate of roughness reduction as a function of speed  $\Delta R_q / \Delta v$  is  $0.014 \mu\text{m}/(\text{mm/s})$

For speeds in the range  $v \in [500, 700]$  mm/s the rate of roughness reduction as a function of speed  $\Delta R_q / \Delta v$  is  $0.003 \mu\text{m}/(\text{mm/s})$ , which is 4.8 times less than that in the range  $v \in [500, 700]$  mm/s

The results from the experiment representing the graphical dependencies of the roughness change from the step  $R_q = R_q(\Delta x)$  are shown in Fig. 5

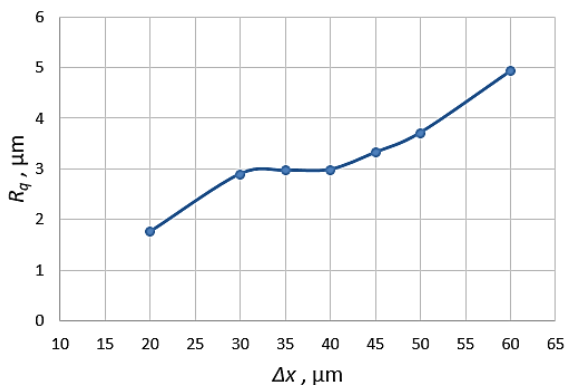


Fig. 5. Experimental dependence of roughness variation on raster marking step.

The following conclusions can be made from the analysis of the graph:

When the step increases, a logarithmic increase in roughness is observed;

For step in the range  $\Delta x \in [20, 30]$   $\mu\text{m}$  the speed of growth of the roughness as a function of the step  $\Delta R_q / \Delta x$  is 0.114.

For step in the range  $\Delta x \in [30, 40]$   $\mu\text{m}$  roughness has minimal changes

For step in the range  $\Delta x \in [40, 60]$   $\mu\text{m}$  the speed of growth of the roughness as a function of the step  $\Delta R_q / \Delta x$  is 0.001.

The results of the experiment, representing the graphical dependence of the variation of the roughness as a function of the energy density  $R_q = R_q(E_{eff})$  are shown in Fig. 6.

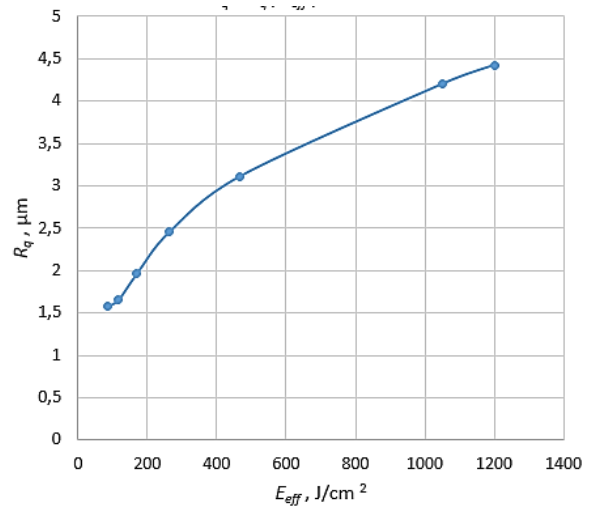


Fig. 6. Experimental dependence of roughness change on energy density.

The following conclusions can be made from the analysis of the graph:

For energy density in the range  $E_{eff} \in [116; 1200]$   $\text{J}/\text{cm}^2$  an increase in roughness is observed, the dependence being non-linear;

In the interval  $E_{eff} \in [116; 262]$   $\text{J}/\text{cm}^2$  the rate of growth of the roughness as a function of the energy  $\Delta R_q / \Delta E_{eff}$  is  $0.0054 \mu\text{m}/\text{J}/\text{cm}^2$ ;

In the interval  $E_{eff} \in [226; 1200]$   $\text{J}/\text{cm}^2$  the rate of growth of the roughness as a function of the energy  $\Delta R_q / \Delta E_{eff}$  is  $0.0021 \mu\text{m}/\text{J}/\text{cm}^2$  which is 2.5 times less than that in the range  $E_{eff} \in [116; 262]$   $\text{J}/\text{cm}^2$ ;

In the interval  $E_{eff} \in [250, 350]$   $\text{J}/\text{cm}^2$  a rapid increase in roughness is observed, which increases the efficiency in rubbing systems.

From the measurements made, the highest value of the roughness  $R_q = 6.763 \mu\text{m}$  was observed at the speed  $v = 100 \text{ mm/s}$  and  $R_q = 4.925 \mu\text{m}$  at the step  $\Delta x = 20 \mu\text{m}$

#### IV. CONCLUSION

The present study analyzes how roughness is modified by laser processing parameters: average power, speed, step and energy density. For the selected range of study, an increase in roughness is observed. The increase in roughness for some treated areas is 10 times greater than that of the substrate. The correct choice of parameters makes it possible to achieve a certain class of roughness, which is necessary in machine building.

Research is planned on the effect of the number of repetitions on the roughness of carbon steel workpieces.

#### V. ACKNOWLEDGMENT

The authors gratefully acknowledge financial support by the European Regional Development Fund, Postdoctoral research aid Nr. 1.1.1.2/16/I/001 research application "Analysis of the parameters of the process of laser marking of new industrial materials for high-tech applications, Nr. 1.1.1.2/VIAA/3/19/474".

#### REFERENCES

- [1] K. Rafiee, H. Naffakh-Moosavy and E. Tamjid, "The effect of laser frequency on roughness, microstructure, cell viability and attachment of Ti6Al4V", *Materials Science and Engineering: C*, 2020, 109, 110637. doi:10.1016/j.msec.2020.110637
- [2] S. Shaikh, S. Kedia, D. Singh, M. Subramanian and S. Sinha, "Surface texturing of Ti6Al4V alloy using femtosecond laser for superior antibacterial performance.", *Journal of Laser Applications*, 31(2), 02.2011, doi:10.2351/1.5081106
- [3] J. Walker, C. Murray, M. Nie, B. Cook, and Clare, "The effect of large-area pulsed electron beam melting on the corrosion and microstructure of a Ti6Al4V alloy", *Applied Surface Science*, A. T. 2014, 311, 534–540, doi:10.1016/j.apsusc.2014.05.105
- [4] Лазер форум, „Промышленная лазерная маркировка и гравировка металлических и неметаллических изделий“, URL: <http://laser-form.ru/technologies/tehgravirovka.html>, дата обращения: 13.02.2023
- [5] A. Lamikiz, J. Sánchez, López de Lacalle, D. del Pozo, and J. M. Etayo, "Surface Roughness Improvement Using Laser-Polishing Techniques.", *Materials Science Forum*, 2006 526, 217–222, doi:10.4028/www.scientific.net/msf.526.217
- [6] D. Przystacki, and M. Jankowiak, "Surface roughness analysis after laser assisted machining of hard to cut materials", *Journal of Physics: Conference Series*, 2014, 483, 012019, doi:10.1088/1742-6596/483/1/012019
- [7] Angelov, N., Numerical Experiments for the Study of the Influence of Wavelength in Laser Impact onto Metals and Alloys, ICEST 2013, 26-29 June 2013, Ohrid, Macedonia, pp. 603-606, 2013, [http://revt.tu-sofia.bg/ICEST2013\\_2\\_37.pdf](http://revt.tu-sofia.bg/ICEST2013_2_37.pdf)
- [8] E. Ukar, A. Lamikiz, L. López de Lacalle, D. del Pozo and J.L. Arana, "Laser polishing of DIN 1.2379 tool steel with CO2 laser and high-power diode laser", *Int. J. Machine Tools Manuf*, 2010, 50, 115–125.
- [9] A. Gisario, A. Boschetto, and F. Veniali, "Surface transformation of AISI 304 stainless steel by high power diode laser", *Optics and Lasers in Engineering*, 2011, 49(1), 41–51, doi:10.1016/j.optlaseng.2010.09.01
- [10] T. Perry, D. Werschmoeller, X. Li, F. Pfefferkorn, N. Duffie, "The effect of laser pulse duration and feed rate on pulsed laser polishing of microfabricated nickel samples", 2009, *J. Manuf. Sci. Eng.* 131, 030995–031002.
- [11] U. Bögli, A. Blatter, S. Pimenov, A. Smolin and V.I. Konov, "Smoothing of diamond films with an ArF laser", *Diamond Relat. Mater.*, 1992, 1, 782–788

# Color Marking of Stainless Steel and Titanium with the Laser Oxidation Method

**Tsvyatkov Petar**  
Faculty of Engineering  
Technical University of Gabrovo  
Gabrovo, Bulgaria  
ppeter@mail.bg

**Edmunds Teirumnieks**  
Faculty of Engineering  
Rezekne Academy of Tehnologies  
Rezekne, Latvia  
edmunds.teirumnieks@rta.lv

**Emil Yankov**  
Faculty of Engineering  
Rezekne Academy of Tehnologies  
Rezekne, Latvia  
emil.yankov@rta.lv

**Erika Teirumnieka**  
Faculty of Engineering  
Rezekne Academy of Tehnologies  
Rezekne, Latvia  
erika.teirumnieka@rta.lv

**Lyubomir Lazov**  
Faculty of Engineering  
Rezekne Academy of Tehnologies  
Rezekne, Latvia  
lyubomir.lazov@rta.lv

**Abstract.** Marking of metal products is essential in many industrial processes. It is mandatory for the finished products according to regulations of the European and world legislation. Traditional marking usually creates contrasting symbols that can easily be erased and forged.

In recent years, a new method for product identification has appeared - color marking. One of the advantages of this method is that it is difficult to counterfeit. This article aims to present the progress of color marking technology on two types of materials. Three groups of factors have been analyzed: the laser source; the technological process; material properties. Their role in obtaining a specific color marking on Ti and AISI 304 is shown. The results are presented in tables. Each color can be repeated only with strict observance of the three groups of factors.

**Keywords:** Color, Laser Oxidation method, Marking.

## 1. INTRODUCTION

Marking of machines, assemblies and parts is mandatory during the modern manufacturing process. Products on the market must be marked as required by European legislation [1].

Laser marking of parts and components is essential for the aviation, automotive, medical and other industries.

Individual marking is necessary for automatic reading of information and tracking the quality of the details during the technological process. Monochrome laser marking is widely used in production which does not

provide the necessary reliable protection against counterfeiting.

Laser color marking has many advantages: non-contact, flexibility, protection against forgery, minimal deformations after processing, good wear resistance, the possibility of color marking with high accuracy of the obtained image, environmental friendliness - a process without the use of chemicals [2]. It is necessary to improve the existing technologies, as well as to create new modern methods of laser color marking.

Color generation results from controlled surface oxidation of metal surfaces during the laser interaction[3] – [5]. This process needs further analysis and research.

This article reviews the development and methods of color marking on some metals. It is also presented how laser marking parameters affect the resulting colors on titanium and chromium nickel steel.

Print ISSN 1691-5402

Online ISSN 2256-070X

<https://doi.org/10.17770/etr2023vol3.7318>

© 2023 Petar Tsvyatkov, Emil Yankov, Lyubomir Lazov, Edmunds Teirumnieks, Erika Teirumnieka.

Published by Rezekne Academy of Technologies.

This is an open access article under the [Creative Commons Attribution 4.0 International License](https://creativecommons.org/licenses/by/4.0/).

## 2. TRADITIONAL METHODS OF COLORING AND MARKING METAL SURFACES

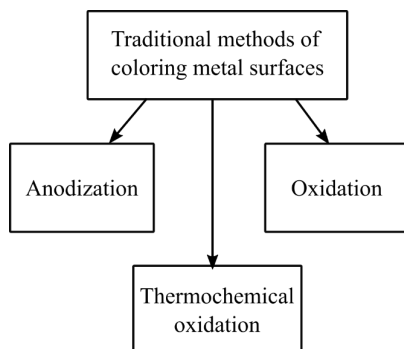


Fig. 1. Block diagram traditional methods of coloring metal.

a) Electrochemical oxidation (anodization) - obtained by electrochemical treatment in aqueous electrolytes (Fig.2). Anodizing requires high voltage and an electrolytic bath to carry out the process [6]. In these electrochemical processes, the change of metal ions in the electrolyte lead to different colors on the metal surface. The colors obtained in this technological process are limited [3], [7].



Fig. 2 Colors obtained by the anodizing method.

b) Thermal oxidation is a thermal process that takes place in thermal chambers. The essence of the method is the formation of an interference film on the surface of the metal, which has a different color[8] - [9].

c). Thermochemical oxidation occurs when the metal is heated in oxygen solutions containing, for example,  $H_2SO_4$  and  $CrO_3$  [10], [11]. The thermo- chemical method has a negative impact on the environment.

Electrochemical oxidation, thermal oxidation and thermochemical oxidation are one of the oldest industrial techniques [12]. However, the resulting films are characterized by structural weakness and the appearance of porosity, and additional processing is required to fix the colors [13].

Advantages of thermal and electrochemical technology are high performance on large areas and durability of the coating.

The disadvantages are the limited palette of colors, the inability to apply more than one color in one processing cycle. And the image has a low resolution and requires a

pre-made template . Some of the listed disadvantages find their solution in thermal printing , screen printing and ink - jet printing.

Thermal printing, colored ink -jet printing, screen printing and others are techniques for applying colored logos and markings on metal parts. Their advantage is the wide variety of colors and their accurate reproduction, as well as the high resolution of the marking compared to thermal and thermochemical processing of metal parts. A significant disadvantage is the fading of the colors and the low wear resistance of these coatings [3].

## 3. LASER COLOR MARKING OF METALS.

Laser color marking is possible via the interaction of the laser beam with the surface of the metal. This interaction can lead to obtaining different colorings, which depend on: the type of laser , the parameters of the process , the type of treated material. Marking can be applied for informative or decorative purposes in the form of colored texts, logos, barcodes or data matrix codes [14], [15].

The high resolution of the applied marking is due to the small diameter of the laser spot around 13 to 60  $\mu m$  [3], [14]. After the laser impact on the material, there is no need for additional technological treatments. Laser colored surfaces have good wear resistance and corrosion resistance, which is researched by [6], [15], [16].

The materials on which this scientific research has been carried out are chrome-nickel and titanium. They are used in the food industry and medicine.

The study of the colors obtained on chrome-nickel surface [6], [15], [17] –[19] show coloring in the pink-red, yellow-green and blue-purple color range . In the case of titanium [20] – [23], the coloring is in the blue-purple range.

## 4. LASER COLORING METHODS

a) Laser oxidation is a method of coloring metal surfaces, in which laser heating leads to the formation of a transparent or translucent oxide film [24], [25]. Light falling on the surface of the sample is reflected by the surface oxide layer, and coloration is observed in the treated areas.

b) Laser-induced periodic surface structures (LIPSS) are produced on the sample by impact using ultrashort pulses from femto or picosecond lasers [26], [27]. Typically, LIPSS have a period close to the laser wavelength and are oriented perpendicular to the polarization of the incident laser beam to metal samples. LIPSS generated colors are highly dependent on viewing angle. They were first described by Birnbaum on semiconductor materials using a ruby laser [28]. LIPSS metod coloring of Silver are shown in Fig.3.

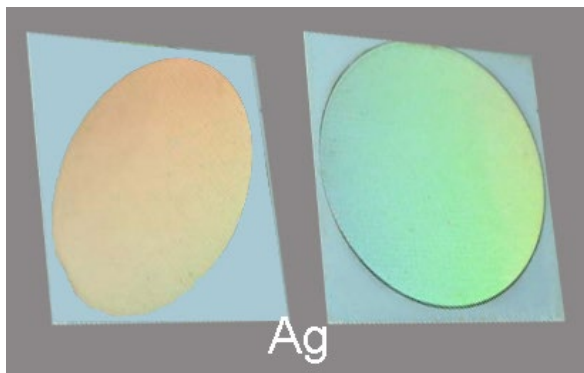


Fig. 3. LIPSS method coloring of Silver with ruby laser.

c) Surface plasmon resonance (SPR) is the third surface coloring method. The coloring is due to metal nanostructures and nanoparticles on the surface of the specimen. Unlike LIPSS, the colors observed with SPR are randomly distributed and do not change with viewing angle.

Lehmuskero [14] reported the formation of small areas of different coloration, which is due to areas of small color pixels that form as different color patches. This effect is due to different thicknesses of the oxide layer. Such coloring was achieved on chrome-nickel by heating the surface with a laser. Ackerl et.al [21] investigated laser marking and coloring of Ti-6Al-4V with ultrashort pulses. He introduces the chromaticity coefficient, which makes it possible to determine the parameters of laser processing to obtain the required color of the titanium surface. It should be noted that the same color can be achieved with different combinations of laser marking process parameters [18].

#### 5. ADVANTAGES OF LASER MARKING USING THE OXIDATION METHOD

Laser color marking using the thermal oxidation method makes it possible to obtain several colors on one part. Other important advantages of the method are non-contact, direct marking of the products, minimal heat affected area, short duration of the impact, reduced processing costs, high processing speed and environmental friendliness. Advantages of the laser method compared to the traditional one are lack of tool wear, high degree of automation, free programming with different signs and symbols [2]. Laser color marking technology provides better copy protection, wear-resistant colors that do not fade over time. The small diameter of the laser spot  $d_0 = 12 \div 65 \mu\text{m}$  makes it possible to obtain high-resolution markings and images on small areas.

#### 6. COLOR LASER MARKING REQUIRED EQUIPMENT AND PARAMETERS

The equipment used for color laser marking are pulsed UV, Nd:YAG and Fiber lasers. To ensure the necessary relative movement of the laser beam on the sample, two galvanometer-controlled scanning mirrors are used to deflect the beam. Beam focusing is performed by an F-

Theta lens with a 160 mm - 240 mm focal length. Schematic diagram of a laser system [22] is shown in Fig. 4.

There are different surface treatment strategies to obtain color markings in terms of line overlap and laser beam scanning speed. In this study, we focus on two of them. In the first strategy, the scan speed should be high  $v \in [400, 1550] \text{ mm/s}$ , in order to have a uniform distribution of heat on the surface, the distance between the lines must be small enough  $\Delta x \in [4, 6] \mu\text{m}$  to provide sufficient energy for oxide formation[23] as seen in Fig. 5a.

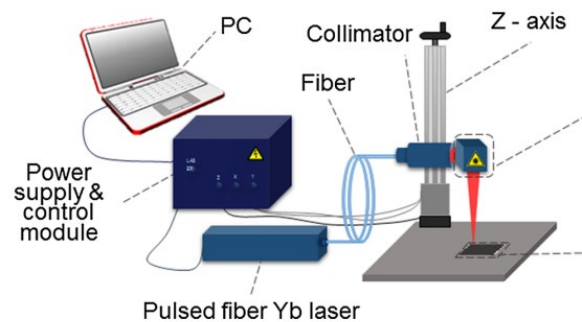


Fig. 4. Schematic diagram of a laser system.

The second strategy is achieved through relatively low speed  $v \in [66, 205] \text{ mm/s}$  per scan and large line spacing  $\Delta x \in [50, 100] \mu\text{m}$ , as seen in Fig. 5b. In this strategy, the overall appearance is a combination of two colors (photos in Fig. 5b) while one of them comes from the melting zone, the other is from the heat-affected zone, due to heat dissipation.

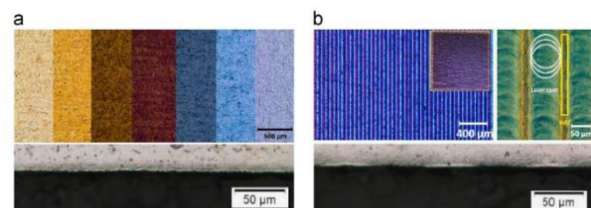


Fig. 5. Color marking according to the technological parameters of the mode.

The studied parameters for laser color marking are the average power of the laser beam in the range  $P \in [3, 30] \text{ W}$ , the scan rate in the interval  $v \in [60, 850] \text{ mm/s}$ , the scan step in the interval  $\Delta x \in [10, 50] \mu\text{m}$ , the frequency of the pulse in the interval  $\Delta \nu \in [10, 50] \text{ kHz}$ , the size of the laser spot and the pulse duration.

The change of these parameters leads to a different energy that affects the product and hence to a different coloring of the marked surface. The parameters of the laser and the technological process affect the chemical or phase composition of the marked surface and its morphology. These parameters also determine the quality of laser marking - contrast, wear resistance and corrosion resistance of the marked surface [23].

7. THE FACTORS AFFECTING COLOR MARKING

The influence of various factors on the creation of color during laser thermal oxidation is shown in Fig. 6.

They are three characteristic groups: related to the properties of the material; associated with the laser source; related to the technological process ; the properties of the material . To them must be added the factors - overlap coefficient and volumetric density of the absorbed energy.

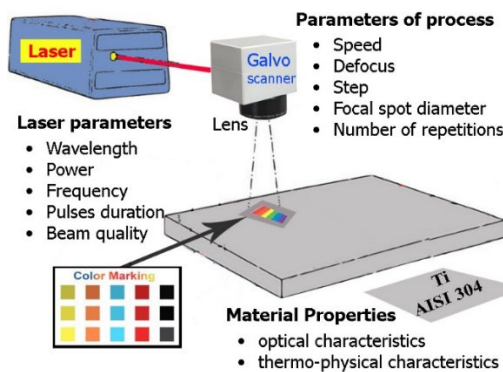


Fig. 6. Laser system during laser thermal oxidation of colors.

a) Parameters of the laser source

Laser marking of metal parts and products is mainly based on the use of solid-state ( Nd:YAG) and fiber lasers with an average power of 10 W - 30 W. These lasers work in the UV to IR range with the wavelength of 553 ns - 1064 nm with the duration of the pulses according to different authors varying from  $\tau \in [13, 200]$  ns. and frequency repetition rate interval  $\nu \in [20, 100]$  kHz. From the conducted studies, no research related to the influence can be found of the pulse duration on the resulting color. It is necessary to study this process because the duration of the pulse affects the pulse power, which is important in the formation of color on the metal surface.

The selection of the laser source is important for the implementation of the technological process of color laser marking. To achieve color reproducibility in marking, it is necessary for the laser source to have parameter stability throughout the exposure time and the ability to control the parameters [18]. In the process of color laser marking by the oxidation method, the following laser sources are used: Nd:YAG laser[20], [23], [31], [32]; Fiber laser [15], [16], [22], [30]; UV laser [3], which are reported in the papers mentioned above.

Fiber lasers are preferred for metal marking due to the low cost of laser systems, the high quality of the radiation, the low maintenance costs and their serial production.

Laser sources differ in wavelength depending on their type. Common lasers for marking are displayed in Table 1. Important for the oxidation color laser marking process is the wavelength to have good absorption by the material.

It can be seen from the table that the selected lasers mostly have a wavelength of  $\lambda = 1064$  nm.

Power is one of the important parameters to achieve color laser marking because it is related to power density.

TABLE 1 LASERS FOR MARKING

Laser type	Wavelength $\lambda$ , nm
Fiber laser	1064
Nd:YAG laser with tube pumping	1064
A diode-pumped Nd:YAG laser	1064
UV laser	450
Yb laser	1064

The authors [3], [6], [18], [19] have reported average power values around 7 W – 15 W, which is easily achievable for modern types of lasers. In Fig. 7 is shown how the color changes depending on the power [6].

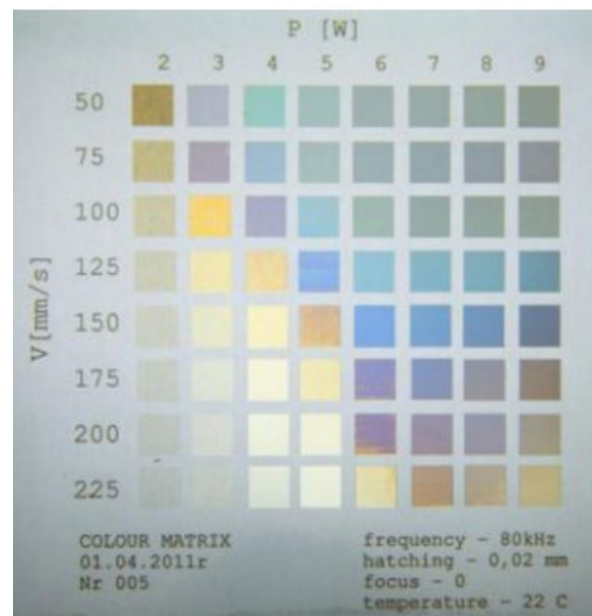


Fig. 7. Laser color marking of stainless steel.

In Fig. 7 it can be clearly seen that the color obtained on stainless steel is very sensitive to the variation of the average power, beam speed and surface temperature affecting oxidation state [3].

The power, pulse duration and pulse repetition rate are related to the energy generated by the laser. The repetition rate and overlap factor  $S$  of the pulses are interrelated. To obtain a certain color on a metal surface  $S \leq 0.1$  % is required [18].

Changes in pulse frequency and marking speed can be thought of as causing horizontal overlap of the pulses, while changes in line spacing and power result in vertical overlap.

b) Parameters of the technological process

Marking speed is a basic parameter of the technological process. The time of impact on the sample depends on it, and hence the energy absorbed in the material in the impact zone. The authors [6], [14], [15], [16], [18], [20], [23] have investigated how the speed change affects the resulting color marking. A higher scanning speed leads to a lower surface temperature, which affects the color of the oxide film obtained on the surface of the metal [3].

Focus-defocus. When the laser beam affects the material, three cases are possible: focusing on the surface of the material; defocus below the surface and defocus above the surface of the processed material. The authors [3], [14] work in focus mode. In this mode, the diameter of the focal spot is around [13] – [47]  $\mu\text{m}$ . The material in this mode absorbs a large amount of energy. In this processing, the laser spot has the smallest diameter of the three cases, and the highest temperature can be achieved at the processing site. The authors [3], [6] use defocusing under the surface of the material. As the defocus increases, the diameter  $d$  of the working spot also increases, thereby reducing the energy with which the material is processed. The dependence of the spot diameter is inversely proportional to the power density  $q_s$  of the laser radiation. It follows that the absorbed energy very rapidly decreases with increasing defocus. This dependence was investigated by the authors [6] and is shown in Fig. 8.

Coloring is obtained by using different defocus values and the same laser average power. The horizontal color bar in Fig. 8 shows how the color saturation and its gamut change at different defocus values.

The step between the laser lines in the studies of [23] show that the colors are very sensitive to the step value (hatching) and even a small change in the value of the step causes a change in the color of the titanium surfaces. A larger step between the lines results in a smaller temperature affected zone.

The number of repetitions is discussed in details by [3]. He reported that the oxide layer grew rapidly in the first and second laser passes. Growth slows down in the third and subsequent passes, which coincide with the formation of microcracks at the oxide-base metal border.

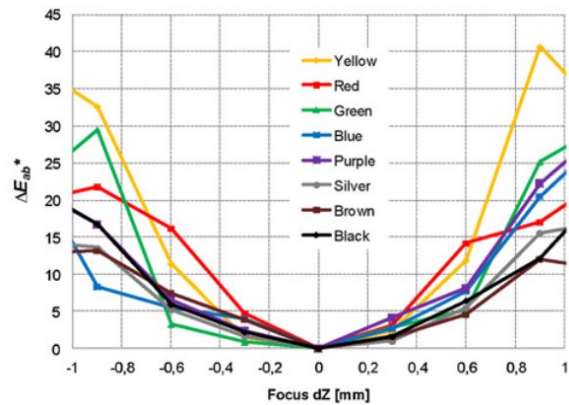
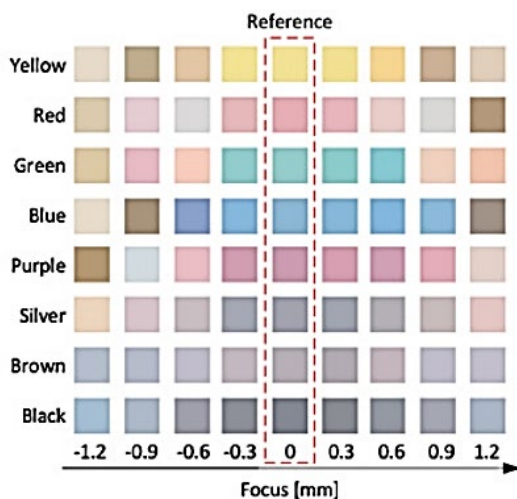


Fig. 8. Laser marking with change of focal spot.

After two laser scans at a speed of 500 mm/s, a gradual smoothing of the surface was observed with the polishing increasing as the number of passes increased. The oxide growth rate decreases with the number of laser passes and their thickness tends to stabilize, due to the diffusion of Fe into the oxide layer.

c) Complex factors affecting the process of color laser marking by the oxidation method are:

The overlap coefficient, which gives a relationship between marking speed, laser radiation power density and pulse repetition rate. Veiko et al. considered the influence of this factor [18].

The density of absorbed energy, which is related to pulse repetition frequency, laser radiation power density, marking speed, absorption capacity of the material, etc. Volumetric energy density and its characteristics have not been extensively researched for the color laser marking process.

Table 2 shows how changing the parameters of the laser source and the technological process change the color of the surface by the method of thermal oxidation.

TABLE 2 CHANGING THE PARAMETERS OF THE LASER SOURCE AND THE TECHNOLOGICAL PROCESS FOR CHANGING THE COLOR OF THE SURFACE BY THE METHOD OF THERMAL OXIDATION

RGB code	Substrates	Laser	Parameters							Autor
			$\lambda$ , nm	$v$ , mm/s	$P$ , W	$\Delta x$ , $\mu\text{m}$	$\nu$ , kHz	$\tau$ , ns	$\Delta f$ , mm	
54,30,104	Ti	Nd-YAG	1064	550	20	10	80	200	2	[23]
99,57,133	AISI 304	UV	355	400	7.1	30	40	25	-3	[3]
131,76,131	AISI 304	Fiber	1064	60	18	50	85	112	0	[14]
175,133,157	AISI 304	Fiber	1064	132	4.4	-	80	230	0	[15]
214,171,199	AISI 304	Fiber	1062	150	5	10	80	100	0	[6]
251,165,255	Ti	Nd-YAG	1064	260	53	-	-	-	0	[20]
112,89,231	Ti	Fiber	1064	60	30	-	35	200	2	[16]
124,173,250	Ti	Nd-YAG	1064	240	53	-	-	-	-	[20]
98,186,236	AISI 304	Fiber	1064	100	6	-	20	100	-	[19]
153,201,250	AISI 304	Fiber	1062	125	3.1	10	80	100	-	[6]
111,163,184	AISI 304	Fiber	1064	100	4.4	-	80	230	-	[15]
119,149,173	AISI 304	Fiber	1064	130	18	30	85	112	-	[14]
88,123,177	Ti	Nd-YAG	1064	450	20	10	80	200	2	[23]
5,121,136	AISI 304	UV	355	400	7	30	40	25	3.5	[3]
6,123,140	AISI 304	Fiber	1064	60	6	50	70	100	0	[18]
25,170,139	AISI 304	UV	355	400	7	30	40	25	3.2	[3]
98,231,236	Ti	Fiber	1064	80	30	-	35	200	2	[16]
135,227,212	AISI 304	Fiber	1062	75	3.2	10	80	100	-	[6]
146,238,201	AISI 304	Fiber	1064	500	10	-	40	100	-	[19]
193,215,114	AISI 304	Fiber	1064	80	18	50	85	112	-	[14]
252,251,142	Ti	Nd-YAG	1064	350	53	-	-	-	-	[20]
245,244,138	AISI 304	Fiber	1064	10	2	-	40	100	-	[19]
248,241,134	Ti	Fiber	1064	130	30	-	35	200	-	[16]
251,235,199	AISI 304	Fiber	1064	400	4.4	-	80	230	-	[15]
250,218,143	AISI 304	Fiber	1062	150	3	10	80	100	-	[6]
241,169,169	AISI 304	Fiber	1062	130	4	10	80	100	-	[6]
250,148,130	AISI 304	Fiber	1070	10	5	50	90	100	-	[18]
168,149,91	AISI 304	Fiber	1062	50	8	10	80	100	-	[6]
182,159,47	AISI 304	Fiber	1064	50	4.4	-	80	230	-	[15]
243,159,82	AISI 304	Fiber	1070	150	9	50	30	100	0	[18]
211,138,10	AISI 304	Fiber	1064	100	6	-	20	100	-	[19]
206,140,54	Ti	Fiber	1064	60	19.5	-	35	200	2	[16]
181,127,31	Ti	Nd-YAG	1064	100	53	-	-	-	-	[20]
183,120,7	AISI 304	Fiber	1064	80	18	50	85	112	0	[14]
169,119,60	Ti	Nd-YAG	1064	850	20	10	80	200	2	[23]
115,61,14	AISI 304	UV	355	400	8	30	40	25	3	[3]

## CONCLUSION

An increasing number of companies are interested in color laser marking and its implementation in industrial production. This technology proves its advantages and prevails over traditional laser marking. It is able to produce a palette of colors on metal surfaces. The resulting colors are sensitive to process parameters, environmental conditions and material properties. Further research is needed to improve color repeatability.

## ACKNOWLEDGMENT

The authors gratefully acknowledge financial support by the European Regional Development Fund, Postdoctoral research aid Nr. 1.1.1.2/16/I/001 research application "Analysis of the parameters of the process of laser marking of new industrial materials for high-tech applications, Nr. 1.1.1.2/VIAA/3/19/474".

## REFERENCES

- [1] L. Lazov, E. Teirumnieks, T. Karadzhev and N. Angelov, "Influence of power density and frequency of the process of laser marking of steel products", *Infrared Physics and Technology*, Volume 116, August 2021.
- [2] A. Korakana, S. Korakana, N. Ulmek, and A. Pagare, "Analyzing the effect of the parameters of laser etching process influencing the corrosion resistance and surface roughness of marine grade 316 stainless steel", *Materials Today: Proceedings*, 2020, doi:10.1016/j.matpr.2020.02.130.
- [3] Z. Li, H. Zheng, K. Teh, Y. Liu, G. Lim, H. Seng and N. Yakovlev, "Analysis of oxide formation induced by UV laser coloration of stainless steel", *Applied Surface Science* 256, 2009, pp.1582-1588.
- [4] Towards 2020, Photonics driving economic growth in Europe, Multiannual strategic roadmap 2014-2020, European Technology Platform Photonics21, 2013.
- [5] Md. Ahsan, F. Ahmed and Y. Kim, "Colorizing of the stainless steel surface by single-beam direct femtosecond laser writing", *Proc. of SPIE*, 2011, V. 7925, P.792512-1-7.
- [6] A. Antonczak, D. Kocon, M. Nowak, P. Kozioł and K. Abramski, "Laser-induced colour marking - Sensitivity scaling for a stainless steel", *Applied Surface Science* 264, 2013, pp. 229-236.
- [7] M. Wen, C. Wen, P. Hodgson and Y. Li, "Thermal oxidation behavior of bulk titanium with nanocrystalline surface layer" *Corrosion Science.*, 2012, V. 59, pp. 352-359.
- [8] B. Stellwag, "The mechanism of oxide film formation on austenitic stainless steels in high temperature water", *Corrosion Science.*, 1998, V. 40., № 2/3, pp. 337-370.
- [9] W. Sun, A. Tieu., Z. Jiang, H. Zhu and Ch. Lu, "Oxide scales growth of lowcarbon steel at high temperatures", *Journal of Materials Processing Technology*, 2004, V.156, pp.1300-1306.
- [10] S. Fujimoto, K. Tsujino and T. Shibata, "Growth and properties of Cr-rich thick and porous oxide films on Type 304 stainless steel formed by square wave potential pulse polarization", *Electrochimica Acta.*, 2001, V.47, pp. 543-551.
- [11] J. Xu, X. Bai, F. He and Y. Fan, "The growth mechanism of the colored film on the stainless steel studied by 180 tracing and nuclear reaction analysis", *Nuclear Instruments and Methods in Physics Research B.*, 1999, V.149, pp. 147-152.
- [12] R. Rusconi and J. Gold, "Color marking. Industrial Laser Solutions", pp. 16-18, 2005.
- [13] R. Crookes, "Pickling and Passivating Stainless Steel", *Material and Application Series*, Vol. 4, Euro Inox, 2007.
- [14] A. Lehmuskero, V. Kontturi, J. Hiltunen and M. Kuittinen, "Modeling of laser-colored stainless steel surfaces by color pixels", *Applied Physics B*, 2010, V.98, pp. 497-500.
- [15] K. LeRckaa and A. Antonczak, "Effects of laser-induced oxidation on the corrosion resistance of AISI 304 stainless steel", *Journal of Laser Applications*, August 2016., Vol. 28.
- [16] T. Kosec, A. Legat, J. Kovač and D. Klobčar, "Influence of Laser Colour Marking on the Corrosion Properties of Low Alloyed Ti", *Coatings* 2019, 9, 375; doi:10.3390/coatings9060375.
- [17] V. Veiko, Y. Karlagina, M. Moskvina, V. Mikhailovskii, G. Odintsova, P. Olshin, D. Pankin, V. Romanova and R. Yatsuk, "Metal surface coloration by oxide periodic structures formed with nanosecond laser pulses", *Optics and Lasers in Engineering*, Volume 96, September 2017, pp. 63-67.
- [18] В. Вейко, С. Горный, Г. Одинцова, М. Патров и К. Юдин, "Формирование многоцветного изображения на поверхности металлов при ее лазерном окислении", *Изв. Вузов. Приборостроение*. 2011. Т. 54, № 2.
- [19] E. Amara, F. Haïd and A. Noukaz, "Experimental investigations on fiber laser color marking of steels", *Applied Surface Science*, Volume 351, October 2015, pp. 1-12.
- [20] A. Pérez del Pino, J. Fernández-Pradas, P. Serra and J. Morenza, "Coloring of titanium through laser oxidation: comparative study with anodizing", *Surface & Coatings Technology* 187, 2004, pp. 106 - 112.
- [21] N. Ackerl, P. Gugger and K. Wegener, "Laser marking and coloration of Ti-6Al-4V with ultrashort pulses", *Journal of Laser Applications*, 32, pp. 032013, 2020.
- [22] E. Ageev, Y. Andreeva, P. Brunkov, Y. Karlagina, G. Odintsova, D. Pankin, S. Pavlov, V. Romanov and R. Yatsuk, "Influence of light incident angle on reflectance spectra of metals processed by color laser marking technology", *Opt Quant Electron*, 2017, 49:50.
- [23] E. Akman and E. Cerkezoglu, "Compositional and micro-scratch analyses of laser induced colored surface of titanium", *Optics and Lasers in Engineering* 84, 2016, pp. 37-43.
- [24] Z. Li, H. Zheng, K. Teh, Y. Liu, G. Lim, H. Seng and N. Yakovlev, "Analysis of oxide formation induced by UV laser coloration of stainless steel", *Appl. Surf. Sci.* 256, 2009, pp. 1582-158.
- [25] Lehmuskero, V. Kontturi, J. Hiltunen and M. Kuittinen, "Modeling of lasercolored stainless steel surfaces by color pixels", *Appl. Phys*, V. 98, 2009, pp. 497-50.
- [26] A. Vorobyev and C. Guo, "Colorizing metals with femtosecond laser pulses", *Appl. Phys. Lett.* 92, 2008, 041914.
- [27] B. Dusser, Z. Sagan, H. Soder, N. Faure, J. Colombier, M. Jourlin and E. Audouard, "Controlled nanostructures formation by ultra fast laser pulses for color marking", *Opt. Express* 18, 2010, 291.
- [28] A. Parker, "515 million years of structural colour", *J. Opt. A Pure Appl. Opt.*, Nov. 2000, V. 2., № 6., pp. 15-28.
- [29] V. Veiko, G. Odintsova, E. Ageev, Y. Karlagina, A. Loginov, A. Skuratova and E. Gorbunova, "Controlled oxide films formation by nanosecond laser pulses for color marking", *Optics express* 24343; October 2014; Vol. 22, No. 20, doi:10.1364/OE.22.024342.
- [30] L. Lavis, M. Sahour, J. Jouvard, G. Pillon, M. Marco de Lucas, S. Bourgeois and D. Grevey, "Growth of titanium oxynitride layers by short pulsed Nd:YAG laser treatment of Ti plates: Influence of the cumulated laser fluence", *Applied Surface Science* 255, 2009, pp. 5515-5518.
- [31] C. Li, J. Li, Y. Zhou, H. Xie, and Z. Zhu, "Investigation of Laser Parameters Influence of Color Marking on AISI 304 Stainless Steel", *Applied Mechanics and Materials*, 2013, 380-384, 4268- 4271, doi:10.4028/www.scientific.net/amm.380-384.4268

# Investigation of the Influence of Technological Parameters of Laser Marking on the Degree of Contrast

**Petar Tsvyatkov**  
Faculty of Engineering  
Technical University of Gabrovo  
Gabrovo, Bulgaria  
ppeter@mail.bg

**Emil Yankov**  
Faculty of Engineering  
Rezekne Academy of Technologies  
Rezekne, Latvia  
emil.yankov@rta.lv

**Lyubomir Lazov**  
Faculty of Engineering  
Rezekne Academy of Technologies  
Rezekne, Latvia  
lyubomir.lazov@rta.lvs

**Edmunds Teirumnieks**  
Faculty of Engineering  
Rezekne Academy of Technologies  
Rezekne, Latvia  
edmunds.teirumnieks@rta.lv

**Karlis Pīgožnis**  
Faculty of Engineering  
Rezekne Academy of Technologies  
Rezekne, Latvia  
karlis.pigoznis@rta.lv

**Abstract.** In modern production, each finished product entering the market is identified by a special marking. Each mark must meet requirements such as good coding, easy to see, easy to read by certain readers, stable over time, etc. In the present casting, laser marking of the C75 steel was carried out with a fiber laser with an average power of  $P = 30$  W and a wavelength of  $\lambda = 1064$  nm. For semi-contrast marking, marking speeds from 100 mm/s to 700 mm/s, average power from 10 to 30 W, raster pitch from 20  $\mu$ m to 60  $\mu$ m, scanning frequency from 20 kHz to 150 kHz were investigated as constant parameters are the pulse duration  $\tau = 100$  ns, number of repetitions  $N = 1$  and defocus  $\Delta f = 0$  mm. The influence of the changing parameters on the contrast was established, and experimental dependences were constructed. The achieved research results show that to obtain a high contrast mark, the average power should be above 20 W, the scanning speed up to 300 mm/s, the scanning frequency up to 50 kHz and the raster pitch up to 40  $\mu$ m.

**Keywords:** Laser, Marking, Contrast, Laser Power, step, Marking Speed, Frequency.

## I. INTRODUCTION

Laser technologies have developed extremely rapidly in recent years. Lasers are used in medicine, industry, electronics and other fields [1]. One of the directions in which laser technology finds mass application is surface treatment - marking. Each finished product must have a marking applied to it. It must meet the specific needs of the specific production [2]. Contrast, wear resistance and the degree of protection against forgery are part of the

mandatory requirements for the marking. Modern systems for easy reading of hatch marks and QR code require the contrast to exceed 15 % [3]-[4]. The contrast of the marking obtained on the article depends on 3 groups of factors related to: the laser source, the technological parameters and the properties of the material [5] - [6]. In the last 10 years, a lot of research has been carried out on marking metal parts using laser systems with wavelengths from 405 nm to 1064 nm. For this purpose, they change the technological parameters of the laser effect in order to obtain a contrast marking or colors marking.

The main part of the so far developed technologies is based on the use of Nd:YAG and Fiber lasers [7] – [8]. Laser sources with a wavelength of  $\lambda = 1064$  nm are most often used for laser surface treatment of metals. The low cost of Fiber laser systems, their mass production and the good absorption of this wavelength leads to their wide application in marking metal and other products [7] - [12].

In the last 4 years, the automatic scanning of QR codes has become more and more necessary, which enable more detailed information about the manufacturer of a given product and its application. Laser marking is used to apply information, due to the advantages over traditional technologies such as: non-contact, potential to mark hard-to-reach places, protection of the intellectual property of the manufacturer, etc. It is important for laser marking to meet the necessary contrast and wear-resistance requirements [9].

Print ISSN 1691-5402

Online ISSN 2256-070X

<https://doi.org/10.17770/etr2023vol3.7319>

© 2023 Petar Tsvyatkov, Emil Yankov, Lyubomir Lazov, Edmunds Teirumnieks, Karlis Pīgožnis.

Published by Rezekne Academy of Technologies.

This is an open access article under the [Creative Commons Attribution 4.0 International License](https://creativecommons.org/licenses/by/4.0/).

The widespread use of laser marking technology on many details needs study into the factors that influence the quality of the marking [10].

The aim of the present study is to determine the optimal parameters of average power ( $P$ , W), marking speed ( $v$ , mm/s), scanning frequency ( $\nu$ , kHz) and raster pitch ( $\Delta x$ ,  $\mu\text{m}$ ) in laser marking C75 steel to achieve high contrast marking.

## II. EXPERIMENTAL STAGING, MATERIAL USED AT THE RESEARCH AND METHODOLOGY

The investigations employed a fiber laser with a power of  $P = 30$  W and a wave length of  $\lambda = 1064$  nm. The movement of the laser beam along the surface was carried out using a raster method with Galvo Scanner. C75 carbon steel plates with a thickness of 1 mm are marked. Treated zones are with a form of a square with side 10 mm, and the distance between squares is 2 mm. A series of studies have been done with constant values of the pulse duration  $\tau = 100$  ns, number of repetitions  $N = 1$  and defocus  $\Delta f = 0$  mm for each examined area as follows:

**First series** with change of speed  $v$ , mm/s

100	200	300	400	500	600	700
-----	-----	-----	-----	-----	-----	-----

at constant power  $P = 30$  W, frequency  $\nu = 40$  kHz, and step  $\Delta x = 30$   $\mu\text{m}$

Dependency graph is being drawn  $k^* = k^*(v)$ .

**Second series** with a change of step  $\Delta x$ ,  $\mu\text{m}$

20	30	35	40	45	50	60
----	----	----	----	----	----	----

at constant power  $P = 30$  W, speed  $v = 300$  mm/s, and frequency  $\nu = 40$  kHz

Dependency graph is being drawn  $k^* = k^*(\Delta x)$

**Third series** with frequency change  $\nu$ , kHz

20	40	60	80	100	120	150
----	----	----	----	-----	-----	-----

at constant power  $P = 30$  W, speed  $v = 300$  mm/s and step  $\Delta x = 30$   $\mu\text{m}$

Dependency graph is being drawn  $k^* = k^*(\nu)$

**Fourth series** with change of average power  $P$ ,

10	12.5	15	17.5	20	25	30
----	------	----	------	----	----	----

at constant speed  $v = 300$  mm/s, frequency  $\nu = 40$  kHz and step  $\Delta x = 30$   $\mu\text{m}$

Dependency graph is being drawn  $k^* = k^*(P)$

The factors that affect the contrast of the marking are shown in Fig. 1.

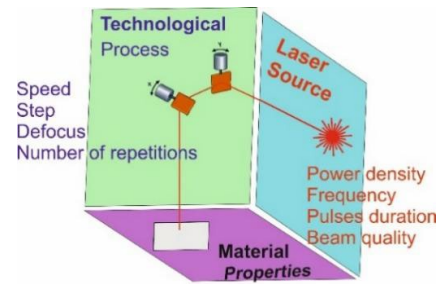


Fig. 1. Major factors affecting marking contrast.

Carbon steel C75 has the following chemical composition for Table 1.

TABLE 1. CHEMICAL COMPOSITION FOR C75

C	Si	Mn	P	S	Cr	Ni
0.70	0.225	0.662	0.009	0.001	0.214	0.071

The substrate has hardness of  $442 \div 452$  HV and roughness  $R_a$  from  $0.264 \div 0.36$   $\mu\text{m}$ ,  $R_z$  from  $13.597 \div 21.268$   $\mu\text{m}$ ,  $R_q$  from  $0.41 \div 0.56$   $\mu\text{m}$ . Investigations are made into the contrast's dependence on certain processing factors.

The influence of laser mark contrast on average power  $P$ ; speed  $v$ ; step  $\Delta x$ ; the frequency  $\nu$  is displayed graphically.

The change in the operating mode of the laser system is carried out with the help of the EZCAD software product, which changes within the set limits the studied technological parameters [11].

The parameters of the scanning system and the laser source are presented in Table 2

TABLE 2. PARAMETERS OF THE LASER SYSTEM

Scanner	
Scanning head	GalvoScan
Work area	200 mm x 200 mm
Scan speed	0 $\div$ 3000 mm/s
Positioning accuracy	0.02 mm
Focal length	290 mm
Laser	
Laser source	Raycus Fiber
Wavelength	1064 nm
Maximum power	30W
Operating mode	Pulsed mode
Frequency	20 $\div$ 200 kHz

The RFL - P 30 Q laser system used in marking the carbon steel samples is shown in Fig. 2.

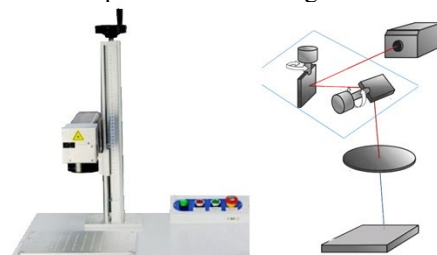


Fig. 2. The RFL - P 30 Q laser system and schematic of the experimental setup.

Analysis of the contrast  $k^*$  is performed with Adobe raster image processing software Photoshop CS 6 x64. Colorful pictures on marked samples, were loaded into the program, after which are converted to grayscale. The values of the measurements in the gray scale are taken for each of the processed areas. The range on the values varies of 0 (black) to 255 (white). Each measurement is conducted five times, and the average value is taken as the result.

Grayscale saturation values resulting with Photoshop CS6 2012 are used to determine contrast via the formula:

$$k^* = \frac{N_f - N_x}{N_f} \cdot 100, \% \quad (1)$$

The contrast  $k^*$  is determined by linear interpolation, as  $N_f$  is the value of the untreated surface, and  $N_x$ , of each treated area with different parameters.

### III. RESULTS

The results of the first experiment are given in Fig. 3, depict the graphical dependency of contrast on power  $k^* = k^*(P)$

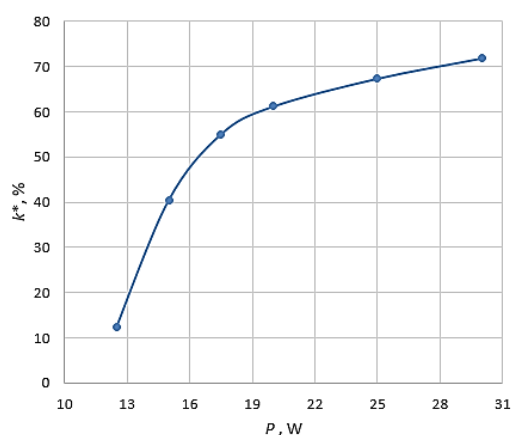


Fig. 3. Graph of the dependence of contrast on power.

The following conclusions can be made from the analysis of the graph:

With increasing power in the range  $P \in [12, 30]$  W, the contrast increases exponentially;

The increase in contrast is described by the equation  $y = -0.002x^4 + 0.1971x^3 - 7.2887x^2 + 120.53x - 691.82$ ;

For powers in the range  $P \in [12, 17]$  W the speed of contrast growth as a function of power  $\Delta k^*/\Delta P$  is 8.6 % / W

For powers in the range  $PC [17, 30]$  W the contrast growth rate in  $\Delta k^*/\Delta P$  is 1.36 % / W;

The rate of change of contrast in the interval  $PC [12,17]$  W grows 6 times faster than that in the interval  $PC [17,30]$  W

The results of the second series are summarized in Fig. 4, graphically representing the dependence

$$k^* = k^*(v)$$

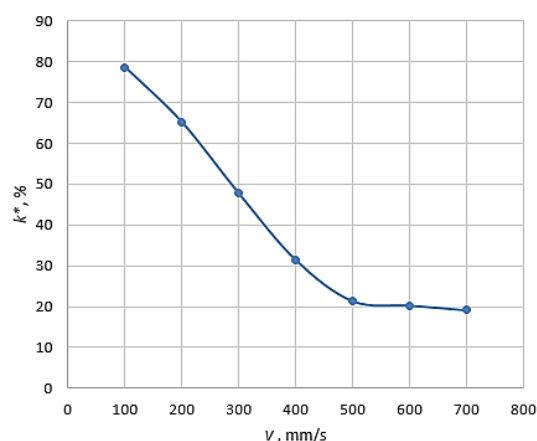


Fig. 4. Graph of the dependence of contrast on speed.

The following conclusions can be made from the analysis of the graph:

When the speed everything increases in the range  $v \in [100, 500]$  mm/s , a non-linear decrease in contrast is observed, the rate of decrease  $\Delta k^*/\Delta v$  is 0.147 % / mm/s;

For speeds in the range  $v \in [500, 700]$  mm/s no change in contrast is observed

For velocities in the interval  $v \in [400, 700]$  mm/s is not recommended to be used because the contrast of the marking is close to the minimum value of 15%, for legibility of the marking.

The results of the third series are summarized in Fig. 5, graphically representing the dependences  $k^* = k^*(v)$

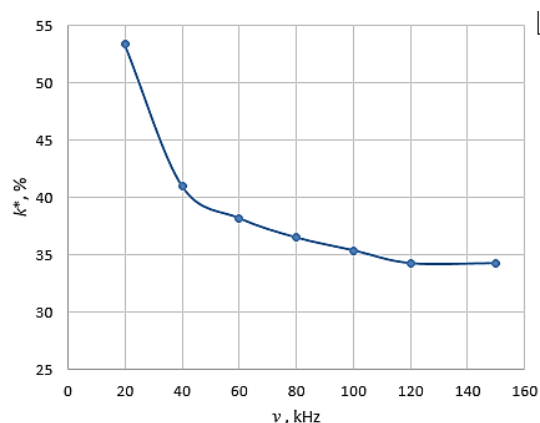


Fig. 5. Graph of the dependence of contrast on frequency.

The following conclusions can be made from the analysis of the graph:

For the investigated frequencies in the range  $v \in [40,150]$  kHz a non-linear decrease in contrast is observed, which is described by the equation  $y = -8E-09x^5 + 4E-06x^4 - 0.0007x^3 + 0.0643x^2 - 2.9088x + 90.875$

For frequencies in the range  $v \in [20, 40]$  kHz the rate of contrast decrease as a function of the rate  $\Delta k^*/\Delta v$  is 0.6 % / kHz.

For the frequency range  $\nu \in [40, 150]$  the rate of contrast reduction as a function of the rate  $\Delta k^*/\Delta \nu \in 0.087\%/\text{kHz}$ .

For frequencies in the range  $\nu \in [20, 40]$  kHz the speed of contrast reduction  $\Delta k^*/\Delta \nu$  is 7 times larger than in the range  $\nu \in [40, 150]$  kHz.

The results of the fourth series are shown in Fig. 6, graphically representing the dependence  $k^*=k^*(\Delta x)$

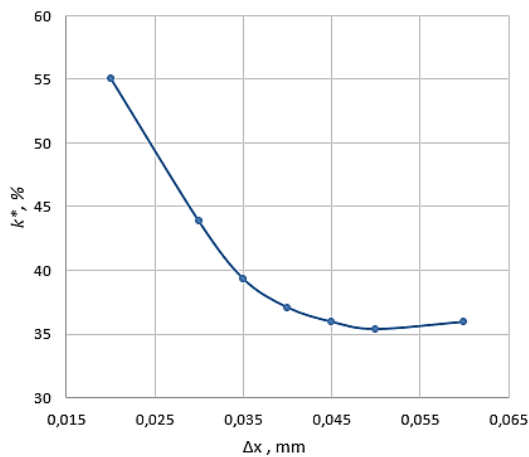


Fig. 6. Graph of the dependence of contrast on step.

The following conclusions can be made from the analysis of the graph:

As the step increases, a decrease in contrast is observed;

For a step  $\Delta x = 20 \mu\text{m}$ , the contrast  $k^*$  is 16% higher than that for a step  $\Delta x = 35 \mu\text{m}$ ;

For a step in the range  $\Delta x \in [20, 40] \mu\text{m}$  the rate of contrast decay as a function of the step  $\Delta k^*/\Delta x$  is  $0.6\%/\mu\text{m}$ ;

For the range of the step  $\Delta x \in [40, 150]$ , the speed of contrast reduction as a function of the step  $\Delta k^*/\Delta x$  is  $0.087\%/\mu\text{m}$ ;

Contrast in the range  $\Delta x \in [20, 40] \mu\text{m}$  decreased 9 times faster than that in the interval  $\Delta x \in [40, 60] \mu\text{m}$ .

From experimental studies of C75 steel to achieve the required contrast, the following optimal working intervals for marking have been determined:

- $\nu \in [200, 400] \text{ mm/s}$
- $R \in [14, 21] \text{ W}$
- $\Delta x \in [20, 35] \mu\text{m}$
- $\nu \in [20, 40] \text{ kHz}$

The largest change in contrast is observed in the speed changes in the range  $\nu \in [100, 500] \text{ mm/s}$ , with the contrast varying in the range  $k^* \in [20, 80]\%$ .

#### IV. CONCLUSION

In the present study, the following results were achieved for laser marking of C75S steel:

- The influence of the speed on the contrast of the marking was evaluated;

- The influence of the step on the contrast of the marking was evaluated;
- The influence of the power of the laser radiation on the contrast of the marking was evaluated;
- The influence of frequency on marking contrast was evaluated
- Optimization of the researched process was achieved with determination of working intervals of the technological parameters.

Future research is planned to investigate the effect of repetition number and defocus on marking contrast.

#### V. ACKNOWLEDGMENT

The authors gratefully acknowledge financial support by the European Regional Development Fund, Postdoctoral research aid Nr. 1.1.1.2/16/I/001 research application "Analysis of the parameters of the process of laser marking of new industrial materials for high-tech applications, Nr. 1.1.1.2/VIAA/3/19/474".

#### REFERENCES

- [1] L. Lazov, H.Deneva, P.Narica, "Laser Marking Methods", Environment Technology Resources Proceedings of the International Scientific and Practical Conference 1:108, June 2015.
- [2] M. Kučera, J. Martan and A. Franc, "Time-resolved temperature measurement during laser marking of stainless steel", International Journal of Heat and Mass Transfer, 125, 1061–1068, 2018, doi:10.1016/j.ijheatmasstransfer.2018.04.137.
- [3] 2D Codes Step By Step, "Connecting the dots to understand the verification report", <https://barcode-test.com/wp-content/uploads/2022/01/barcode-test-barcoding-step-by-step-guide.pdf>, last access 27/03/2022.
- [4] C. Leone, E. Bassoli, Genna, and A. Gatto, "Experimental investigation and optimisation of laser direct part marking of Inconel 718." Optics and Lasers in Engineering, 2018, 111, 154–166, doi:10.1016/j.optlaseng.2018.08.04
- [5] K. ŁeRckaa and A. Antonczak, "Effects of laser-induced oxidation on the corrosion resistance of AISI 304 stainless steel", Journal of Laser Applications · August 2016., Vol. 28, No. 3
- [6] M. Švantner, M. Kučera and Š. Houdková, "Possibilities of stainless steel laser marking", METAL 2012—21st International Conference 23. - 25.5.2012
- [7] L. Lazov and N. Angelov, "Main factors determining the quality of the marking of metals and alloys International scientific conference Amtech'07, Gabrovo, 2007, T. I, pp. 102–107.
- [8] A. Antonczak, D. Kocon, M. Nowak, P. Koziol and K. Abramski, "Laser-induced colour marking—Sensitivity scaling for a stainless steel", Applied Surface Science 264, 2013, 229–236
- [9] A. Korakana, S. Korakana, N. Ulmek, and A. Pagare, "Analyzing the effect of the parameters of laser etching process influencing the corrosion resistance and surface roughness of marine grade 316 stainless steel.", Materials Today: Proceedings. Volume 32, Part 3, 2020, Pages 452–462, doi:10.1016/j.matpr.2020.02.130
- [10] L. Lazov, E. Teirumnieks, T. Karadzov and N. Angelov, "Influence of power density and frequency of the process of laser

- marking of steel products”, *Infrared Physics and Technology* Volume 116, August 2021.
- [11] I. Shivakoti, G. Kibria, and B. Pradhan, “Predictive model and parametric analysis of laser marking process on gallium nitride material using diode pumped Nd:YAG laser”, *Optics & Laser Technology*, 2019, 115, 58–70, doi:10.1016/j.optlastec.2019.01.035
- [12] N. Angelov, Investigation the Influence of the Number of Repetition and Volumetric Energy Density on Laser Marking of Products, *Contemporary Materials*, V–2, pp. 251-253, 2014, DOI: 10.7251/COMEN1402250A